

NUWMAK - A Tokamak Reactor Design Study

B. Badger, K. Audenaerde, H. Avci, J. Beyer, D. Blackfield,
R.W. Boom, E. Cameron, E. Cheng, R.W. Conn, G.A. Emmert,
M. Gordinier, S. Hong, J. Kesner, A. Klein, G.L. Kulcinski,
L. Lao, E. Larsen, L.P. Mai, T.K. Mau, C.W. Maynard, P. Michaelson,
G. O'Donnell, M. Ortman, M. Ragheb, J. Scharer, D.C. Schluderberg,
I.N. Sviatoslavsky, D.K. Sze, T. Thornton, W.F. Vogelsang, P. Wilkes,
J. Williams, T. Wu, J. Wrazel, and W.C. Young

March 1979

UWFDM-330

FUSION TECHNOLOGY INSTITUTE

UNIVERSITY OF WISCONSIN

MADISON WISCONSIN

NUWMAK - A Tokamak Reactor Design Study

B. Badger, K. Audenaerde, H. Avci, J. Beyer, D. Blackfield, R.W. Boom, E. Cameron, E. Cheng, R.W. Conn, G.A. Emmert, M. Gordinier, S. Hong, J. Kesner, A. Klein, G.L. Kulcinski, L. Lao, E. Larsen, L.P. Mai, T.K. Mau, C.W. Maynard, P. Michaelson, G. O'Donnell, M. Ortman, M. Ragheb, J. Scharer, D.C. Schluderberg, I.N. Sviatoslavsky, D.K. Sze, T. Thornton, W.F. Vogelsang, P. Wilkes, J. Williams, T. Wu, J. Wrazel, and W.C. Young

Fusion Technology Institute
University of Wisconsin
1500 Engineering Drive
Madison, WI 53706

http://fti.neep.wisc.edu

March 1979

UWFDM-330

NUWMAK

A TOKAMAK REACTOR DESIGN STUDY

B. Badger
K. Audenaerde[1]
H.I. Avci[2]
J. Beyer
D. Blackfield
R.W. Boom
E. Cameron
E. Cheng[3]
R.W. Conn
G. Emmert
M. Gordinier
S. Hong
J. Kesner
A. Klein
G.L. Kulcinski
L. Lao
E. Larsen
L.P. Mai
T.K. Mau
C.W. Maynard
P. Michaelson[4]
C. O'Donnell
M. Ortman
M.M.H. Ragheb
J. Scharer
D.C. Schluderberg[5]
I. Sviatoslavsky
D.K. Sze
T. Thornton[5]
W.F. Vogelsang
P. Wilkes
J. Williams[6]
T. Wu
J. Wrazel
W.C. Young

Fusion Engineering Program
Nuclear Engineering Department
University of Wisconsin
Madison WI 53706 U.S.A.

March 1979

UWFDM-330

---

[1]Presently at University of Washington
[2]Presently at Battelle Columbus Laboratories
[3]Presently at General Atomic Company
[4]Presently at General Electric Corp.
[5]Babcock & Wilcox, Lynchburg VA 24505
[6]Carnegie Mellon University, Pittsburgh PA 15213

Acknowledgment

Other people in addition to the technical staff have contributed to producing the NUWMAK report. Special thanks go to Mr. Dennis Bruggink for organizing, editing, and arranging for printing and distribution and to the secretarial staff, Ms. Gail Herrington, Ms. Linda Kraft, and Ms. Connie Linehan for the typing (and retyping) that is a necessary part of any venture such as this. Financial support for this research has been provided by the U.S. Department of Energy through the Office of Fusion Energy (contract ET-78-S-02-4636) and by the Wisconsin Electric Utilities Research Foundation. We are grateful to these agencies and the people who were related to this project for their full support.

TABLE OF CONTENTS

I. Design Philosophy of NUWMAK
- I-A. Physics Design Philosophy — I-1
  - I-A-1. Power Density — I-1
  - I-A-2. Impurity Control — I-1
  - I-A-3. Duty Factor and Time Between Burns — I-2
  - I-A-4. Heating — I-2
- I-B. Magnet Design Philosophy — I-2
  - I-B-1. Toroidal Field Magnets — I-2
- I-C. Blanket Design Philosophy — I-4
- I-D. Structural Material — I-4
- I-E. Mechanical Design, Assembly, and Maintenance — I-5
- I-F. Resource Requirements and Economics — I-6

II. Overview and Summary of the NUWMAK Design Study
- II-A. Introduction — II-1
- II-B. Key Features of the NUWMAK Design — II-1
  - II-B-1. The Toroidal Field Magnet Design — II-1
  - II-B-2. Access and Maintenance — II-5
  - II-B-3. Titanium Alloy Structure — II-7
  - II-B-4. Isothermal Blanket Design with Internal Energy Storage — II-7
  - II-B-5. Plasma Heating by RF at $2\omega_{ci}$ — II-10
  - II-B-6. Plasma Operation Without a Divertor — II-11
  - II-B-7. Direct BWR Power Cycle — II-13
- II-C. Additional NUWMAK Design Characteristics — II-14
  - II-C-1. MHD Plasma Analysis and Vertical Position Control — II-14
  - II-C-2. Blanket Neutronic Analysis — II-18
  - II-C-3. Blanket Tritium Analysis — II-21
  - II-C-4. Materials Resource Implications — II-23
  - II-C-5. Economic Analysis — II-25
- II-D. Summary and Comments — II-28

References for Chapter II — II-31

III. Summary of Parameters
1. Characteristic Machine Dimensions — III-2
2. Plasma Parameters — III-2
3. Power Output — III-3
4. Reactor Coolant System — III-4
5. Intermediate Coolant System — III-4
6. Steam Generation System — III-5
7. Shield Coolant System — III-5
8. Reactor Auxiliary Systems — III-5
9. Reactor Components — III-6
10. Electrical Power Requirements — III-9
11. Buildings — III-9
12. Reactor Maintenance — III-10

IV. Plasma Analysis
IV-A. Introduction IV-1
IV-B. MHD Equilibrium and Stability of NUWMAK IV-2
IV-B-1. Introduction IV-2
IV-B-2. Equilibrium and Stability IV-2
IV-B-2-a. Equilibrium IV-2
IV-B-2-b. Stability IV-4
IV-B-2-b-i. Rigid Motions IV-5
IV-B-2-b-ii. Ideal MHD Modes IV-7
IV-B-2-b-iii. Resistive MHD Modes IV-8
IV-B-2-b-iv. β-limits and Ballooning Modes IV-10
IV-B-3. Results for NUWMAK IV-10
IV-B-4. Feedback Stabilization System IV-21
IV-B-5. Conclusion IV-29
References for Section IV-B IV-31
IV-C. Startup and Shutdown IV-32
References for Section IV-C IV-48
IV-D. Plasma Burn Analysis IV-49
IV-D-1. Why Divertorless Operation? IV-49
IV-D-2. Gas Blanket Philosophy IV-49
IV-D-2-a. Blanket Formation IV-49
IV-D-2-b. Liner/Limiter Protection IV-50
IV-D-2-c. Impurity Transport IV-52
IV-D-3. Periodic Gas Puffing Concept in NUWMAK IV-53
IV-D-4. Space-Time Transport Model IV-53
IV-D-5. Impact of Gas Puffing on Transport Model IV-55
IV-D-5-a. Neutral Atom Transport IV-55
IV-D-5-b. Dynamic Boundary Conditions at the Plasma Edge IV-56
IV-D-5-b-i. Collisionless Parallel Transport ($\lambda_{\parallel} > \pi R$) IV-57
IV-D-5-b-ii. Collisional Parallel Transport ($\lambda_{\parallel} < \pi R$) IV-62
IV-D-6. Divertorless Operation Figures of Merit IV-63
IV-D-6-a. Fractional Burnup Considerations IV-63
IV-D-6-b. Limiter Loading Considerations IV-64
IV-D-6-c. Impurity Buildup Considerations IV-64
IV-D-7. Learning Curve of Gas Puffing Simulations IV-64
IV-D-7-a. RF Startup Model IV-65
IV-D-7-b. Gas Injection Model IV-65
IV-D-7-c. Puffing Degrees of Freedom IV-67
IV-D-8. Final Results IV-69
IV-D-8-a. Pure Gas Puffing Scenario (Case A)(Not Finally Applied) IV-69
IV-D-8-b. Modified Gas Puffing Scenario (Case B)(Final Case) IV-80
IV-D-9. Analysis IV-81
IV-D-10. Conclusions IV-81
References for Section IV-D IV-101
IV-E. Vacuum System IV-103
IV-E-1. Introduction IV-103
IV-E-2. System Design IV-104
IV-E-3. Discussion and Conclusions IV-109
References for Section IV-E IV-110

V. RF Heating System
V-A. Introduction V-1
References for Section V-A V-3
V-B. Fast Magnetosonic Wave Theory V-5
V-B-1. Wave Propagation and Absorption V-5
V-B-2. The Influence of the Launching Structure and Mode Conversion on the Excited Mode Wave Spectrum V-13
References for Section V-B V-24
V-C. Reactor Startup Model V-26
References for Section V-C V-47
V-D. RF Circuit Coupling to Magnetosonic Waves in the Tokamak Reactor V-48
V-D-1. Introduction V-48
V-D-2. Cavity-Backed Aperture Antenna V-51
V-D-3. Coil Antenna V-63
References for Section V-D V-67
V-E. The Radio-Frequency Heating System for NUWMAK V-68
V-E-1. Introduction V-68
V-E-2. The Wave Generating System V-70
V-E-3. The RF Transmission System V-74
V-E-3-a. Design of the Coaxial Line V-76
V-E-3-b. Design of the Vacuum Window V-83
V-E-3-c. The Voltage Breakdown Problem V-93
V-E-3-c-i. The Pressurized Line V-94
V-E-3-c-ii. The Evacuated Line V-95
V-E-3-c-iii. The Vacuum Window V-100
V-E-4. The Coupling System V-101
V-E-4-a. The Cavity-Backed Aperture Antenna V-102
V-e-4-b. The Coil Antenna V-111
V-E-5. Prime Power Requirement for the Overall RF System V-115
References for Section V-E V-117
V-F. Summary V-118

VI. Magnet System and Energy Storage
VI-A. Introduction and Summary VI-1
VI-B. Superconducting Toroidal Field Magnets VI-4
VI-B-1. General Considerations VI-4
VI-B-2. 1.8 K Operation VI-7
VI-B-2-a. Superconductivity VI-7
VI-B-2-b. Heat Transfer in Superfluid He II VI-8
VI-B-2-c. Conductor and Magnet Assembly VI-13
VI-B-3. Optional Design VI-18
VI-C. Trimming Coil System VI-19
VI-C-1. General Considerations VI-19
VI-C-2. Description and Design Factors VI-22
VI-C-3. Mechanical Design and Construction Techniques VI-26
VI-C-3-a. General Description VI-26
VI-C-3-b. Structural Considerations VI-31
VI-D. Poloidal Field Coil System VI-37
VI-D-1. Ohmic Heating Coil System VI-37
VI-D-2. Mechanical Design of Cryogenic VF Coils VI-43
VI-D-2-a. General Description VI-43
VI-D-2-b. Structural Considerations VI-48

VI-D-2-c. Thermal Hydraulics VI-51
VI-D-2-d. Disassembly Procedure VI-53
VI-D-3. Superconducting Vertical Field Coil VI-53
VI-E. Energy Storage and Power Supplies VI-55
VI-E-1. Energy Storage Conductor VI-55
VI-E-2. Power Supplies VI-55
VI-E-2-a. Toroidal Field Magnet VI-55
VI-E-2-b. Poloidal Field Coils VI-55
References for Chapter VI VI-59

VII. Blanket Design
VII-A. Design Philosophy VII-1
VII-B. Material Selection VII-3
VII-B-1. Structural Material VII-3
VII-B-2. Breeding Material VII-5
VII-B-3. Coolant VII-7
VII-C. Blanket Design VII-9
VII-D. Heat Transfer Calculations VII-14
VII-D-1. Mathematical Formulation VII-14
VII-D-2. Results and Discussion VII-18
VII-E. Blanket Support Considerations VII-27
VII-F. Load Leveling Considerations for a Pulsed Fusion Reactor VII-30
VII-F-1. Introduction VII-30
VII-F-2. Discussion VII-30
VII-G. Conclusions VII-39
VII-H. Mechanical Design VII-40
VII-H-1. Introduction VII-40
VII-H-2. General Description VII-40
VII-H-3. Structural Considerations VII-52
VII-H-3-a. First Wall and Blanket Stresses VII-52
VII-H-3-b. Blanket and Shield Support VII-54
Appendix: Effect of Gas Puffing on the First Wall and Limiter Design VII-56
References for Chapter VII VII-67

VIII. Neutronics Analysis and Radioactivity
VIII-A. Introduction VIII-1
VIII-B. Design Goals for NUWMAK Blanket and Shield VIII-4
VIII-B-1. Tritium Breeding VIII-4
VIII-B-2. Nuclear Energy Deposition VIII-4
VIII-B-3. Magnet Shielding VIII-5
VIII-C. Methods of Calculation VIII-7
VIII-D. Survey Calculations and Discussion VIII-10
VIII-D-1. Tritium Breeding vs. Lithium Lead Composition VIII-11
VIII-D-2. Tritium Breeding vs. Percent ^{6}Li in Total Lithium VIII-14
VIII-D-3. Magnet Protection Considerations VIII-17
VIII-D-3-a. Tungsten Zone Thickness vs. Atomic Displacement Rate in Aluminum Stablilizer VIII-18
VIII-D-3-b. Lead Zone Thickness vs. Dose and Atomic Displacement Rates VIII-19
VIII-D-3-c. Tungsten Zone Height vs. Atomic Displacement, Dose Rate, and Neutron Fluence VIII-22
VIII-E. Final Results for NUWMAK Blanket and Shield Design VIII-22
VIII-E-1. Tritium Breeding, Neutron Multiplication, and Nuclear Heating VIII-27

VIII-E-2. Radiation Damage of Superconducting Magnet VIII-32
VIII-E-3. Contour Plots and Neutron Fluxes VIII-38
VIII-F. Radioactivity VIII-38
VIII-F-1. Radioactivity, Afterheat, and BHP VIII-53
VIII-F-2. ^{210}Po Production in NUWMAK VIII-65
VIII-G. Conclusions VIII-69
References for Chapter VIII VIII-71

IX. Materials Analysis
IX-A. Introduction IX-1
IX-A-1. Materials Design Philosophy for Advanced Reactors IX-1
IX-A-2. General Objectives for Materials in NUWMAK IX-3
IX-A-3. Outline of Chapter IX-4
References for Section IX-A IX-4
IX-B. General Description of Titanium Alloy Systems IX-5
IX-B-1. Introduction IX-5
IX-B-2. Microstructure Development in α+β Ti Alloys IX-5
IX-B-3. The Relationship Between Microstructure and Tensile Properties of Selected α+β Ti Alloys IX-25
IX-B-3-a. General Trends IX-25
IX-B-3-a-ii Decomposition of α' Martensite IX-29
IX-B-3-a-ii. Decomposition of Metastable β-phase IX-29
IX-B-3-a-iii.Decomposition of α" Martensite IX-30
IX-B-3-b. Property Variations IX-30
IX-B-4. The Effect of Microstructure on the Fracture Toughness of α+β Ti Alloys IX-33
IX-B-4-a. General Trends IX-35
IX-B-4-b. Toughness Variations IX-36
IX-B-5. The Effect of Microstructure on the Fatigue Behavior of α+β Ti Alloys IX-42
IX-B-5-a. Fatigue Life IX-43
IX-B-5-a-i. Smooth Bar Fatigue Life IX-43
IX-B-5-a-ii. Notched Bar Fatigue Life IX-52
IX-B-5-b. Fatigue Crack Propagation IX-52
IX-B-5-b-i. Microstructure Effects IX-53
IX-B-5-b-ii. Texture Effects IX-56
IX-B-6. The Effect of Microstructure on Creep of α+β Ti Alloys IX-58
IX-B-6-a. The Creep Behavior of α+β Ti Alloys IX-58
IX-B-6-b. The Mechanism of Creep IX-60
IX-B-7. The Physical Properties of Ti Alloys IX-62
IX-B-8. Titanium Industry and Fabrication Techniques IX-62
IX-B-8-a. The Titanium Industry IX-62
IX-B-8-b. Current Fabrication Techniques IX-64
IX-B-9. Corrosion of Ti in Liquid Metals IX-66
IX-B-9-a. Introduction IX-66
IX-B-9-b. The Solubility of Tritium and Its Alloys in Liquid Lithium and Lead IX-67
IX-B-9-c. Distribution of Oxygen, Nitrogen, and Carbon in Ti Alloys and Li-Pb Liquid IX-69
IX-B-10. Permeability and Solubility of Hydrogen Isotopes in Ti and Ti-6Al-4V IX-76
IX-B-10-a. Model for Hydrogen Permeability IX-76
IX-B-10-b. Sample Calculation for NUWMAK IX-79
IX-B-11. Previous Radiation Damage Studies of Ti and Its Alloys IX-85
IX-B-11-a. Neutron Irradiation IX-85
IX-B-11-b. Ion Irradiation Studies on Ti Alloys IX-87

IX-B-12. Displacement & Gas Production Cross Sections for Ti IX-91
References for Section IX-B IX-96
IX-C. Use of Ti Alloys in NUWMAK IX-100
IX-C-1. Operating Environment IX-100
IX-C-1-a. Neutron Environment IX-100
IX-C-1-a-i. Neutron Flux and Fluence IX-100
IX-C-1-a-ii. Neutron Energy Spectrum IX-109
IX-C-1-b. Particle Flux to the First Wall IX-109
IX-C-1-c. Displacement Rate Effects IX-109
IX-C-1-c-i. Displacement Rates IX-116
IX-C-1-d. Transmutation Rates in NUWMAK IX-123
IX-C-1-d-i. Production of Hydrogen and Helium in NUWMAK Materials IX-123
IX-C-1-d-ii. Production of Solid Transmutation Products IX-129
IX-C-1-e. Radiation Exposure to the Organic Thermal and Electrical Insulators of NUWMAK Magnets IX-129
IX-C-1-f. Temperature Levels in NUWMAK Components IX-129
IX-C-1-g. Stress Levels in NUWMAK Components IX-129
IX-C-2. Anticipated Performance for NUWMAK Structure IX-134

X. Tritium Systems
X-A. NUWMAK Fueling System X-1
X-A-1. Introduction X-1
X-A-2. Fueling Scenarios X-3
X-A-3. Deuterium and Tritium Flow Rates X-6
X-A-3-a. CaseII: A DT Gas Blanket X-6
X-A-3-b. Case II: A D_2 Gas Blanket--Tritium Pellet Fueling X-6
X-A-4. Tritium Consumption and Inventory in Storage X-7
X-A-5. The Deuterium-Tritium Separation System X-7
X-A-5-a. The Impurity Separation System X-8
X-A-5-b. The Isotope Separation System X-11
References for Section X-A X-14
X-B. Tritium Properties in and Extraction from $Li_{62}Pb_{38}$ X-16
X-B-1. The $Li_{62}Pb_{38}$ Blanket X-16
X-B-2. Thermodynamics of the Lithium-Lead-Tritium System X-16
X-B-2-a. The Liquid Lithium-Hydrogen Isotope System X-16
X-B-2-b. The Lead-Hydrogen System X-20
X-B-2-c. The Lithium-Lead System X-20
X-B-2-d. Observations on the Lithium-Lead-Hydrogen Isotope System X-20
X-B-2-e. Estimate of the Thermodynamics of the $Li_{62}Pb_{38}$-Tritium System X-24
X-B-3. Diffusivity of Tritium in $Li_{62}Pb_{38}$ X-25
X-B-3-a. Hydrogen Isotopes in Liquid Lithium X-25
X-B-3-b. Estimate of the Diffusivity of Hydrogen in Liquid Lead X-28
X-B-3-c. Estimate of the Diffusivity of Tritium in Liquid $Li_{62}Pb_{38}$ X-28
X-B-4. Tritium Extraction from $Li_{62}Pb_{38}$ X-29
X-B-4-a. Tritium Extraction With a Sweep Gas X-30
X-B-4-b. Vacuum Extraction of Tritium X-31
X-B-4-c. Tritium Extraction With a Purge Gas X-32
References for Section X-B X-38

X-C. Tritium Containment Systems X-42
X-C-1. Introduction X-42
X-C-2. Primary Containment X-42
X-C-3. Secondary Containment X-42
X-C-4. Tertiary Containment X-45
X-C-5. Tritium Removal From Cooling Water X-49
References for Section X-C X-51
X-D. Addendum X-51

XI. Assembly and Maintenance
XI-A. Introduction XI-1
XI-B. First Wall/Blanket Maintenance XI-2
XI-C. Toroidal Field Coil Maintenance XI-7
XI-D. Vertical Field Coil Maintenance XI-9
XI-E. Trimming Coil Maintenance XI-10
XI-F. Ohmic Heating Coil Maintenance XI-10
XI-F-1. General Discussion XI-10
XI-F-2. OH Coil Maintenance Procedure XI-11
References for Chapter XI XI-15

XII. Balance of Plant
XII-A. Introduction XII-1
XII-B. Description of Reference Site XII-2
XII-B-1. Topography and General Site Characteristics XII-2
XII-B-2. Site Access XII-2
XII-B-3. Population Density and Land Use XII-2
XII-B-4. Cost of Land XII-3
XII-B-5. Cooling Water and Public Utility Services XII-3
XII-B-6. Meteorology and Climatology XII-4
XII-B-6-a. Prevailing Wind XII-4
XII-B-6-b. Atomospheric Diffusion Properties XII-4
XII-B-6-c. Severe Meteorological Phenomena XII-4
XII-B-6-d. Potential Accidental Release Meteorology XII-5
XII-B-6-e. Dispersion Characteristics XII-6
XII-B-7. Geology and Seismology XII-7
XII-B-7-a. Soil Profiles and Load Bearing Characteristics XII-7
XII-B-7-b. Seismology XII-7
XII-B-8. Sewage and Radioactive Waste Disposal XII-8
XII-B-8-a. Sewage XII-8
XII-B-8-b. Gaseous and Liquid Radioactive Wastes XII-8
XII-B-8-c. Solid Radioactive Wastes XII-8
XII-C. Description of Buildings XII-8
XII-C-1. Introduction XII-8
XII-C-2. Reactor Building XII-9
XII-C-3. Auxiliary Building XII-13
XII-C-4. Hot Cell XII-14
XII-C-5. Radwaste Building XII-14
XII-C-6. Turbine Building XII-16
XII-C-7. Maintenance Building XII-17
XII-C-8. Administration and Control XII-17
XII-C-9. Other Buildings XII-19
XII-D. Plant Electric System XII-21

XIII. Materials Resource Analysis XIII-1

XIV. System Economics
XIV-A. Introduction XIV-1
XIV-B. Level of Technology XIV-1
XIV-C. Design Allowance, Contingency and Spare Parts XIV-2
XIV-D. Nuclear Island Unit Costs XIV-3
XIV-E. Supplemental Systems Unit Costs XIV-13
XIV-F. Balance of Plant Unit Costs XIV-17
XIV-G. Direct Cost Accounts XIV-19
XIV-H. Capital Costs XIV-25
XIV-H-1. Direct Costs Summary XIV-25
XIV-H-2. Indirect Costs XIV-25
XIV-H-3. Time Related Costs XIV-25
XIV-I. Operation and Maintenance XIV-27
XIV-J. Plant Availability XIV-27
XIV-K. Busbar Energy Cost XIV-28
XIV-L. Results and Conclusions XIV-29
XIV-L-1. Major Conclusions XIV-33
References for Chapter XIV XIV-34

I. DESIGN PHILOSOPHY OF NUWMAK

In many ways, the design of NUWMAK has been guided by the detailed understanding of tokamak reactor problems developed in earlier studies. The aim in NUWMAK has been to confront these key problems and to develop improvements or innovations to offset previously identified difficulties. In many (although not all) areas, such innovations or improvements have been achieved. We begin with a discussion of the key issues which confront the tokamak concept as a reactor and indicate the design approach developed in NUWMAK to deal with these issues. The design philosophy has therefore been to step back, to examine the key difficulties identified in earlier studies, and to develop solutions. The aim is to search for an end product that has the potential to be reliable, maintainable, environmentally acceptable, and reasonably economic.

I-A. PHYSICS DESIGN PHILOSOPHY

I-A-1. POWER DENSITY

The average power density in a fusion reactor is proportional to $\beta^2 B^4 S^4 f(T) g_{n,T}$ where β is the plasma beta, B is the magnetic field, S is the plasma shape factor (1 for a circle, greater than 1 for noncircles), f(T) is a function of temperature, and $g_{n,T}$ depends on the profiles of plasma density and temperature. In general, reactor costs decrease with increasing power density and in NUWMAK, we have chosen a modest total beta, ~ 7%, and a high magnetic field on axis (6T) (to provide a margin of safety against uncertainties in physics). The shape factor has been optimized using MHD calculations and a plasma height to width ratio of 1.6 has been chosen. The design philosophy has been to increase the power density by increasing the magnetic field and with this approach, the power density in the plasma in NUWMAK is ~ 10 W/cm^3. This can be compared with the power density in earlier designs which ranged from 0.5 to 2 W/cm^3.

I-A-2. IMPURITY CONTROL

The control of impurities in the plasma is key to long burn operation as well as to startup itself. A magnetic divertor is one approach to impurity control but our own and other earlier tokamak studies showed that the addition of a divertor significantly complicates reactor design, often increases the size of toroidal field magnets, and makes access and maintenance difficult.

The design philosophy in NUWMAK has been to simplify design and improve access and maintenance. We have thus developed for NUWMAK the concept of periodic gas puffing plus density-temperature profile control to simultaneously fuel the plasma, keep impurities from diffusing to the center, and maintain a sufficient impurity mantle to radiate heat that has been conducted from the plasma center. We find that such an approach has many advantages for the overall reactor design. There remain, however, key areas of uncertainty related to details of plasma transport and pumping of both recycled gas and particularly helium. This makes it difficult to conclude that the concept is feasible and further study is required.

I-A-3. DUTY FACTOR AND TIME BETWEEN BURNS

One clearly would like a steady-state burn in a fusion reactor. If this is not possible, as it may not be in a tokamak, the next feature required is a short time between burns to minimize thermal fatigue and the energy storage required to level the electrical output load. We have achieved a short time between pulses in NUWMAK (~ 15 seconds) by several techniques including a partial overlap of the current rise and RF heating phases. The duty factor is high at 0.91. In addition, a phase change blanket concept has been developed which minimizes thermal fatigue in the blanket; we will discuss this shortly.

I-A-4. HEATING

It is desirable to have an efficient plasma heating source which requires minimum access and minimum shielding. This has led in NUWMAK to the choice of RF heating at $2\omega_{CD}$ (90 MHz) using a resonant cavity located in the shadow of the limiters on the outside first wall. RF feed coaxial cables can be curved to avoid line of sight to the sources. The wave guides are constructed of V-5 Ti and are water cooled.

I-B. MAGNET DESIGN PHILOSOPHY

I-B-1. TOROIDAL FIELD MAGNETS

All earlier designs of tokamaks have a relatively large number of TF coils ($\geq$ 16) which make access difficult but which provide an acceptably small magnetic field ripple. In NUWMAK, our design philosophy is to increase access space for maintenance and other components and to accomplish this, a new approach to magnet arrangement has been developed. In essence, only

a small number of primary superconducting toroidal field magnets are used (8 in NUWMAK). Access space between coils then becomes large (greater than 5 m). The field ripple is corrected with saddle coils that do not add net toroidal field. These coils are water cooled copper magnets and are located at the back of the outer blanket. They need not encircle the vacuum vessel poloidally because the field ripple is small nearest the centerline and increases in amplitude as one moves out radially. The power consumption of these coils is modest ($\sim$ 25 MW) and the improvement in access is great.

We also required in NUWMAK some additional magnetic field strength relative to earlier designs to provide a safety factor against physics uncertainties. The field on axis is thus chosen to be 6T and the peak field at the coil is then 12T. The basic design philosophy for such large high field coils is that they be fully cryostable with a reliable solid structure to avoid magnet instability. There are two technically feasible ways to design high field (B ~ 12T) superconductive coils. One is to use NbTi superconductor at reduced temperature ($T \sim 1.8$ K) in order to have a reasonably high current density in the superconductor at the required high field. The other is to use Nb_3Sn as the superconducting material at 4.2 K. The primary design of the TF coil uses NbTi superconductor and subcooled superfluid liquid helium at 1.8 K and atmospheric pressure. The reason for these choices is that NbTi is a ductile superconductor and superfluid helium has excellent heat transfer characteristics. As an optional design, Nb_3Sn superconductor is used in pool boiling 4.2 K liquid helium. However, there is no experience in the use of either option for large magnets at the present time.

A design philosophy in NUWMAK has been to develop a highly maintainable, accessible design. The absence of a poloidal magnetic divertor allows us to minimize the number of vertical field coils inside the main TF coils. There are only four magnets inside the TF coils and these are cryogenically cooled, normal aluminum coils. They have relatively easily made joints and any slight resistive heating at the joints will not be detrimental to coil operation. The approach is consistent with the overall design philosophy that provision be made to remove and replace a TF coil in case of failure. (A TF coil need <u>not</u> be removed for blanket replacement.)

I-C. BLANKET DESIGN PHILOSOPHY

Most of the unusual problems associated with a tokamak blanket arise from the special characteristics of the tokamak D-T reactor. These special characteristics are:

a. Cyclic behavior of the plasma
b. Tritium breeding and confinement
c. Non-uniform energy distribution
d. Complicated geometry.

The blanket design developed for NUWMAK is aimed at minimizing problems associated with the above characteristics while being inexpensive, fabricable, maintainable, and providing adequate thermal efficiency. Through this new design, we have minimized thermal cycling in the bulk blanket structure, eliminated the need for both an intermediate loop and thermal energy storage in the power cycle, and developed a double-walled tube design for added reliability and minimum tritium diffusion into the coolant. Relatively low temperature operation (300-350^{o}C) has been incorporated to extend first wall lifetime. Boiling water cooling is chosen to further minimize thermal cycling and to permit the use of the well established Boiling Water Reactor (BWR) power cycle.

The blanket utilizes the Li-Pb eutectic (62% Li, 38% Pb) as the tritium breeding and thermal energy storage material. The eutectic melts at 464^{o}C and operates in two phases within the blanket. During the down part of the burn cycle, the latent heat of fusion provides the requisite energy to maintain a constant electrical output. It also means that essentially the same heat flux is incident on the cooling tubes so that there is little temperature cycling. The tritium breeding ratio is more than adequate ($\sim$ 1.5) without breeding in the inner blanket and the total energy per fusion is acceptably high at 20.6 MeV per fusion event. The Li-Pb eutectic has other important advantages related to safety such as the fact that Li-Pb is relatively inert with respect to its interaction with water and air.

I-D. STRUCTURAL MATERIAL

The materials selection in NUWMAK is influenced by the design philosophy in other areas and by the desire to develop a reactor design with a long

structural lifetime at a high neutron wall loading. The material must be compatible with various coolants and there should be a well established U.S. industrial capability.

For NUWMAK, we have selected the titanium alloy Ti-6Al-4V on the basis that it is easily fabricable and has high strength, high strength to weight ratio, excellent fatigue life and resistance to corrosion, low He production from neutron reactions and no observed void swelling as yet. The material is inherently nonmagnetic, there is a well established industry, and all the major alloying constituents are abundantly available in the United States. There are, of course, problems related to a limited operating temperature range (~ 300-450^{o}C), a very low thermal conductivity, cost, and hydriding if the temperature falls below 300^{o}C.

I-E. MECHANICAL DESIGN, ASSEMBLY, AND MAINTENANCE

The design philosophy in NUWMAK has simply been to make mechanical design and maintainability easier. The decision not to employ a poloidal divertor has led to a considerably simpler shape and mechanical design of the now compact and streamlined plasma chamber. The use of RF heating means that the launching structure becomes part of the first wall. The source and power supplies can be placed well away from the main reactor components and so are much less constrictive than are neutral beam lines and their accessories.

In the past, providing the vacuum seals between blanket modules has been one of the most difficult mechanical design problems. It is agreed that the only seal which will survive the harsh environment near the first wall is a weld. Consistent with the NUWMAK design philosophy, no seals are used between blanket modules and blanket modules are supported on rails fixed to the shield. The vacuum seals are made at the back of the shield where the seals are both accessible and maintainable. The support rails are used to guide the blanket modules during maintenance and blanket replacement.

Maintainability has been a key design philosophy behind many decisions relating to plasma chamber shape, impurity control, magnet system design, and plasma heating mechanism. Earlier studies of remote maintenance have shown that early conceptual reactors would be virtually impossible to maintain. In NUWMAK, design simplicity

has been achieved, the size and weight of blanket modules has been sharply reduced (weight per module is ~ 10 tonnes of structure and reflector), access has been sharply increased, several levels of modularity have been introduced, and a maintainable design for the ohmic heating and vertical field magnet systems has been developed.

Design simplicity has been achieved both in blanket design and in access. Provision has been made for the rapid removal of vertical field coils and those coils inside the TF magnets are normal coils with joints. Space is provided around the nuclear island to allow ready access for maintenance vehicles and the number of coolant connections has been minimized. The blanket modules can be removed individually and constitute one level of modularity. In addition, the TF coils are supported from the floor rather than from a central support column so that a reactor segment, including blanket modules, shield, and one toroidal field coil can be removed. There are eight such segments at the next level of modularity. The design philosophy is that while blanket replacement is likely, the TF coils should have a lifetime exceeding plant life. Therefore, this second level of modularity involving the removal of a TF coil is not treated as a scheduled maintenance procedure.

Finally, it is crucial to the development of a maintainable tokamak concept that a design be developed which permits access and maintenance of components in the central core of the torus. A key issue is the maintainability of the ohmic heating coil system. In NUWMAK, a design approach is developed in which the OH coils are divided into two groups, one serviced from the top, the other serviced from the bottom. The separation between the upper and lower sets can be used to join a bucking cylinder (which takes up centering forces on the TF coils) to the central column. While this approach requires further development, it shows that the central core can be maintained in a reasonable way.

I-F. RESOURCE REQUIREMENTS AND ECONOMICS

The philosophy in NUWMAK has been to develop a tokamak reactor design which minimizes the impact of fusion on mineral resource requirements and has the potential to be economically attractive. Earlier studies based on the use of stainless steel led to the conclusion that chromium

and nickel resources would be strongly impacted by fusion, particularly because U.S. resources in this area are inadequate even today. Other problem areas related to the use of Be and to the use of lithium as a coolant as well as a breeder. In this case, lithium metal fills not only the blanket but also the entire primary coolant circuit. The use of Ti-alloy reactor structure and high strength aluminum magnet structure, as well as increasing the power density of the reactor, has led us to the conclusion that the NUWMAK reactor design appears to place no significant burden on the materials used. The U.S. resource picture for all the materials employed is good except for Nb, W and Co.

As for economics, the aim has been to determine if tokamak reactor costs could potentially be competitive with other long term energy sources. The design philosophy has, therefore, been to increase the system power density, to employ moderately priced structural materials, and to develop design concepts which would allow the elimination of previously large cost items (e.g., a thermal energy storage unit in the power cycle). An economic analysis based upon a standardized format indicates a constant dollar (without inflation) electricity cost of approximately 35 mills/kWh for a NUWMAK type unit in 1978 dollars. Further, NUWMAK is designed to produce about 650 MWe. Advanced fission reactors are currently being designed and built in the 1100-1500 MWe range. For fusion reactors, there is every reason to believe unit costs will decrease with increasing plant size although this conclusion has not been established in the NUWMAK study.

II. OVERVIEW AND SUMMARY OF THE NUWMAK DESIGN STUDY

II-A. INTRODUCTION

The first generation of tokamak reactor designs[1-4] were aimed at providing a quantitative understanding of fusion reactor problems and identified those which are most important. In addition, quantitative analytic tools for different subsystem's performance were developed and these have proven to be especially useful in subsequent parametric studies.[5,6] The designs themselves provide a basis for beginning the development of more highly optimized reactor systems.

NUWMAK is part of a second generation of conceptual tokamak designs[7,8] aimed at maximizing the strengths of fusion while minimizing its weaknesses. Those strengths include an inexhaustible fuel supply, controllable levels of induced radioactivity, potentially advantageous safety and environmental features, and the fact that it is one of perhaps only three truly long term sources of electric power generation. On the other hand, the weaknesses of fusion include complex geometrical arrangements, complex access and maintenance procedures, a relatively low power density, and the apparent need or desire to combine a number of advanced technologies. These considerations were important motivating factors in developing the NUWMAK design. The key features of the design are presented in Sec. II-B, additional aspects are described in Sec. II-C, and a summary with comments is given in Sec. II-D. The relationship between NUWMAK and near term tokamaks such as TFTR (the Tokamak Fusion Test Reactor), is also discussed in the last section.

II-B. KEY FEATURES OF THE NUWMAK DESIGN

The major parameters characterizing the NUWMAK design are listed on Table II-B-1, a top view of the machine is shown in Fig. II-B-1, and a cross section view is given in Fig. II-B-2. The machine is small (major radius, 5.13 m) for the net power generated (660 MW_e) and has a high value of plasma power density (10 MW/m^3) and average neutron wall loading (4 MW/m^2).

II-B-1. THE TOROIDAL FIELD MAGNET DESIGN

The NUWMAK toroidal field system design is unique and consists of just eight superconducting coils (see Fig. II-B-1) supplemented by sixteen normal, water cooled, copper trimming coils. The trim coils do not add net field but lower the field ripple to less than 2% on the midplane at

Table II-B-1. NUWMAK Design Characteristics

Net Electric Power	660 MW_e
Gross Electrical Power	725 MW_e
Thermal Power	2097 MW_t
Net Efficiency	31.5%
Availability Factor	80%
Major Radius	5.13 m
Plasma Radius, a	1.13 m
Plasma (b/a) nominal	1.64
Plasma Current	7.2 MA
Toroidal Beta	6%
$n_e\tau_E(cm^{-3}\text{-}s)$	2×10^{14}
q(a)	2.6
Axial Toroidal Field	6.05T
Plasma Heating Method	RF
RF Frequency ($2\omega_{CD}$)	92 MHz
RF Power to Plasma	75 MW

Structural Material	Ti-6Al-4V
Coolant	Boiling Water
Coolant Temperature	300°C
Coolant Pressure	8.6 MPa (1250 psi)
Breeding Material	$Li_{62}Pb_{38}$ Eutectic
Melting Point of $Li_{62}Pb_{38}$	464°C
Max. Structure Temperature	500°C
Max. Coolant Wall Stress	103 MPa (15 ksi)
Ave. Neutron Wall Load	4 MW/m^2
Tritium Breeding Ratio	1.54
Lithium Blanket Inventory	4×10^4 g
Tritium Extraction Method	Molten Salt
Blanket Tritium Inventory	800 g
Toroidal Field at Conductor	11.94 T
Superconductor	NbTi
Stabilizer	Al
Conductor Current Density	6900 A/cm^2
S/C to Stabilizer Ratio	1:60
Energy Stored in Field	30 GJ
Number of TF Coils	8
Number of Cu Trim Coils	18

TOP VIEW OF NUWMAK

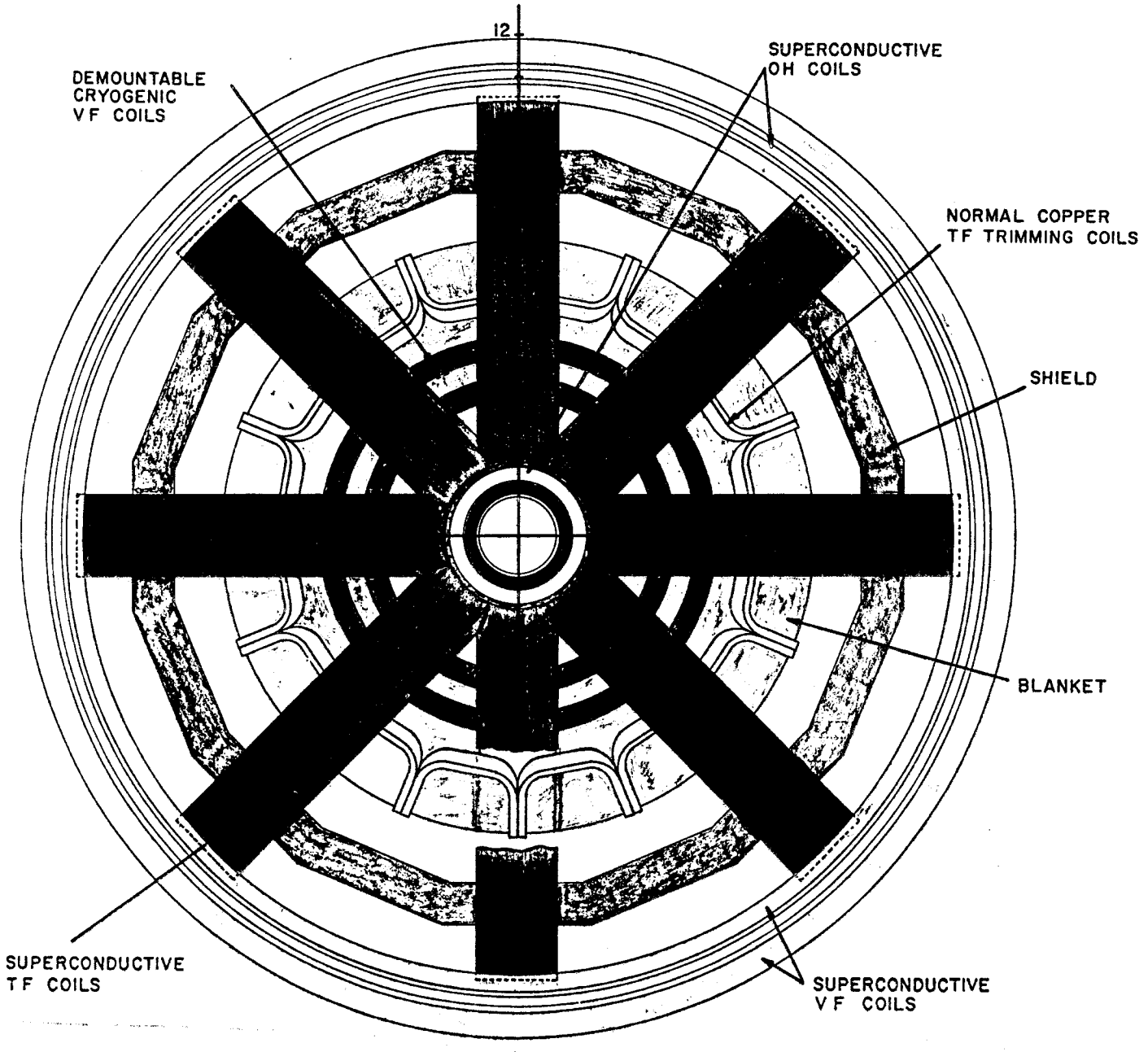


Fig. II-B-1

CROSS-SECTIONAL VIEW OF NUWMAK

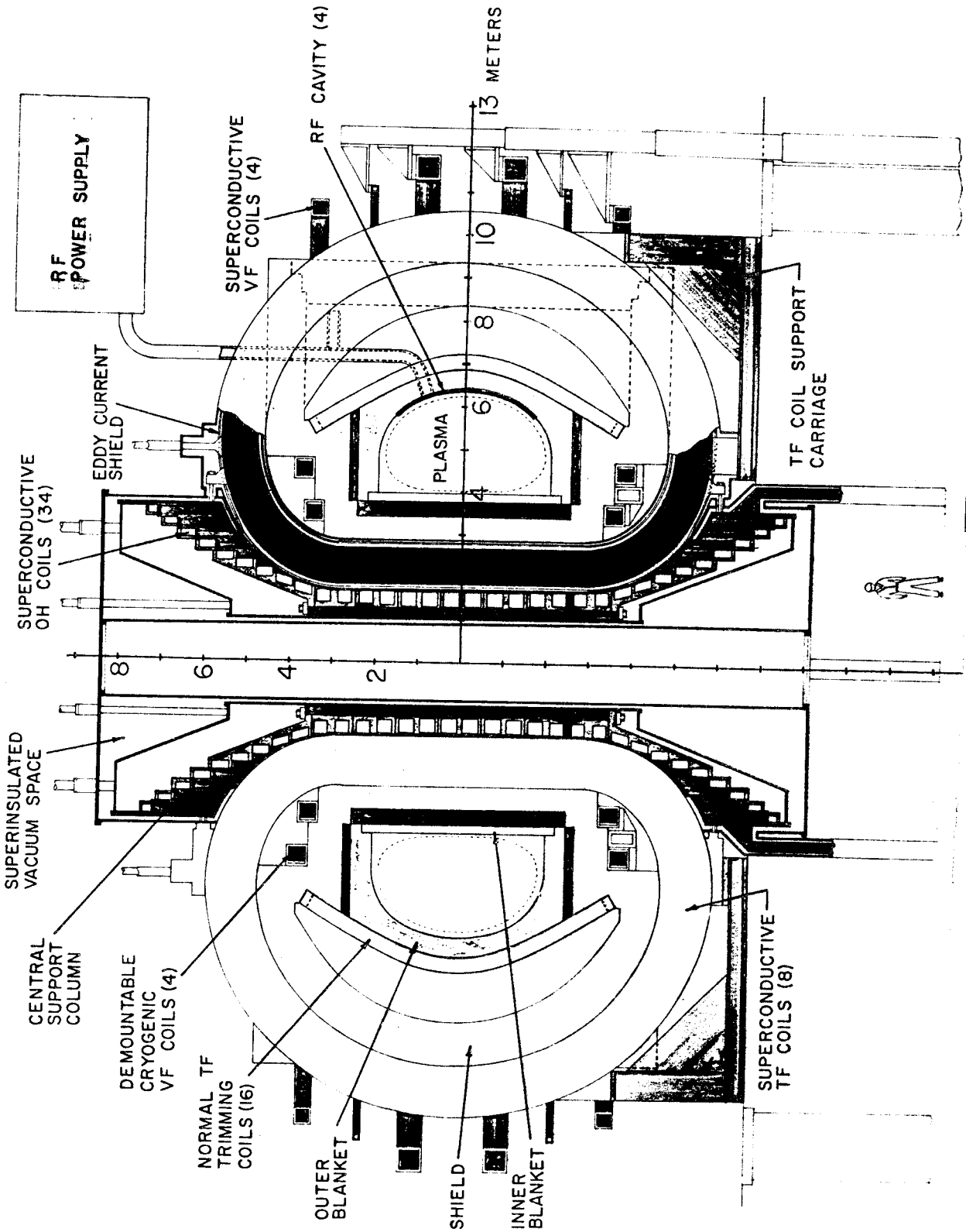


Fig. II-B-2

the plasma edge. They are located directly behind the blanket (see Fig. II-B-2). Since these trim coils do not encircle the vacuum chamber, they are readily removable.

As such, this system design represents a method to obtain the high system accessibility crucial to making maintenance feasible and practical. The distance between the outer legs of two TF coils is about 5 m.

The maximum field at the magnet is 11.9 T and the on-axis field is 6.05 T. To achieve this field, NbTi is used as the superconductor and is cooled with low pressure sub-cooled He II to 1.8 K. The advantages of this approach are that NbTi is ductile, the critical heat flux is high (0.5 W/cm^2) allowing a higher current density in the stabilizer, and the heat transfer properties of He II are excellent. The disadvantages include a high refrigeration power requirement (~60 MW), the absence of experience with this technique in large magnets, and the relatively high current density in the conductor (6900 A/cm^2)(which implies the need for fast discharging in a fault condition). High purity aluminum is used as the stabilizer and the high strength Al alloy, Al-2219, is used for the magnet structure. Other coil parameters are summarized on Table II-B-1.

II-B-2. ACCESS AND MAINTENANCE

The use of just eight superconducting TF magnets provides extensive space between each for ready accessibility. The four vertical field coils located inside the TF system (see Fig. II-B-2) are cryogenic (~18 K) aluminum (not superconducting) so that these can be disconnected and removed. A sequence illustrating the removal of a blanket segment is shown in Fig. II-B-3. The maximum weight moved per segment is just 10 tonnes.

A major advance in the NUWMAK design is the independent removability of the OH and TF coil systems. Unlike earlier studies, the TF coils are supported from the floor rather than from a central column permitting the OH system to be removed vertically without moving other elements. Likewise, an entire module consisting of one TF coil together with three blanket-shield segments can be removed independently. This design approach shows that a tokamak can have high system accessiblity and the potential for good maintainability. It need not consist of interlocking rings and an inaccessible blanket and ohmic heating coil system.

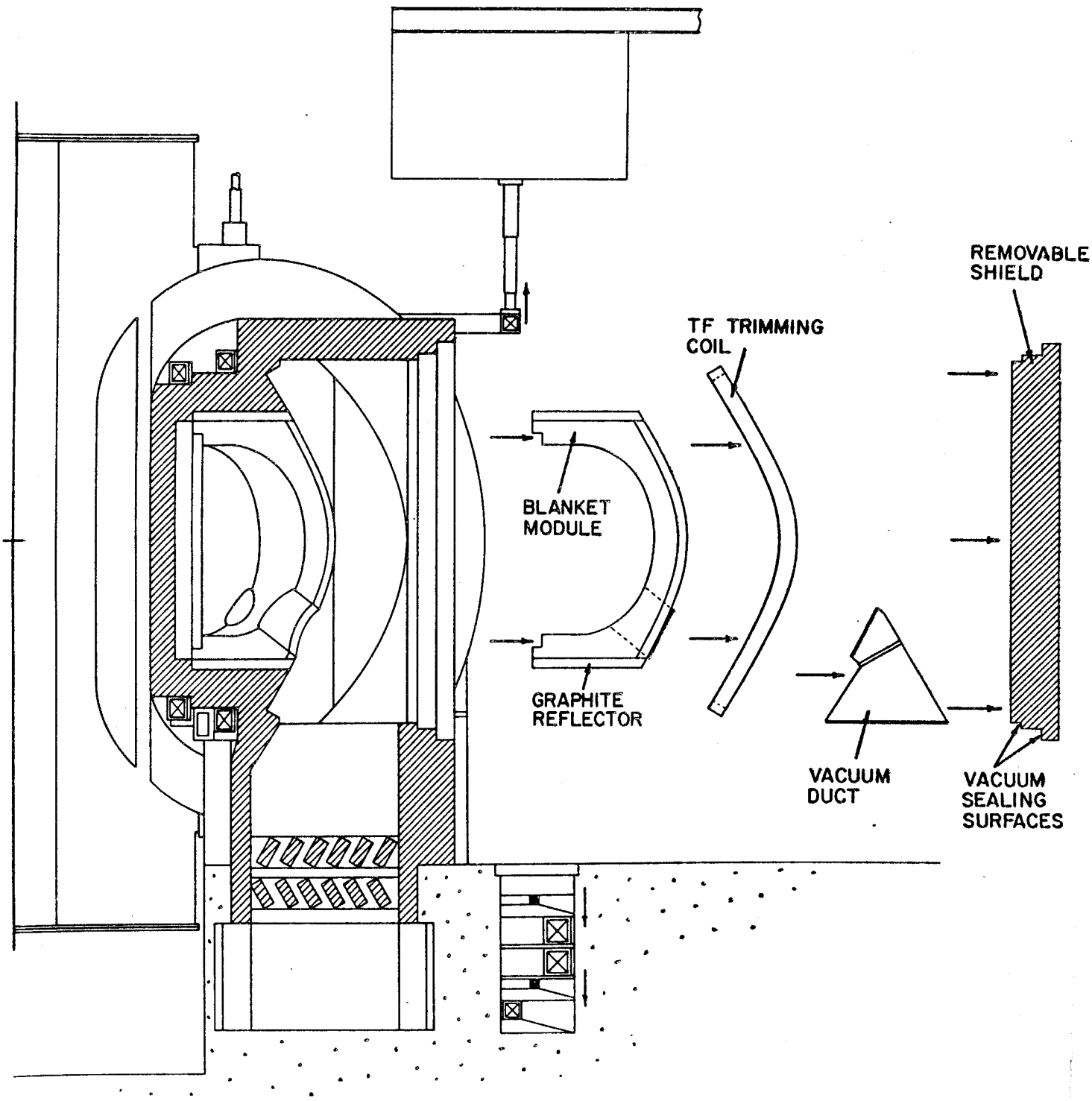


Fig. II-B-3. Sequence of steps involved in the removal of a blanket segment.

II-B-3. TITANIUM ALLOY STRUCTURE

The structural material for the reactor is the titanium alloy, Ti-6Al-4V. Titanium alloys are inherently non-magnetic and have an excellent fatigue lifetime. Also, the resistance to radiation damage appears promising and while no high neutron fluence data exist, no void swelling in either neutron irradiation or heavy ion simulations has been observed as yet. We have not determined an estimated lifetime but have used 10 MW-yr/m^2 for design purposes. Titanium does not pose any resource problems and an established industry already exists. Considerations of phase stability suggest limiting the maximum temperature to about 450°C in the high flux region while the minimum temperature is limited to 300°C to avoid hydriding. Titanium alloys have a high strength to weight ratio, good resistance to corrosion by Li or Pb, and a low neutron cross section for helium production.

Titanium alloys are also advantageous from the viewpoint of long term induced radioactivity. We find that the activity 100 years after shutdown is two orders of magnitude lower than the activity in a comparable blanket made from 316 stainless steel. The very long term activity is dominated by $^{26}Al(t_{1/2}=8\times10^5 y)$ but this should not prevent recycling or simple disposal.

II-B-4. ISOTHERMAL BLANKET DESIGN WITH INTERNAL ENERGY STORAGE

The blanket design is unique and is based upon the use of a breeding material which will operate at its melting point. The energy stored in the latent heat of fusion eliminates the need for an external energy storage system in the power cycle that would be needed otherwise to provide constant heat to the turbines. Further, the blanket is cooled with boiling water, thereby minimizing temperature cycling. The breeding material is the eutectic, $Li_{62}Pb_{38}$, which has excellent breeding and shielding properties and undergoes a solid-liquid phase change at 464°C.

The key to the isothermal operation of the cooling tubes and to the internal energy storage operation is shown in Fig. II-B-4. The temperature distribution from a coolant tube into the Li-Pb mixture is shown at different times during the plasma burn cycle. That cycle is summarized on Table II-B-2. The plasma current rises in 7 seconds to

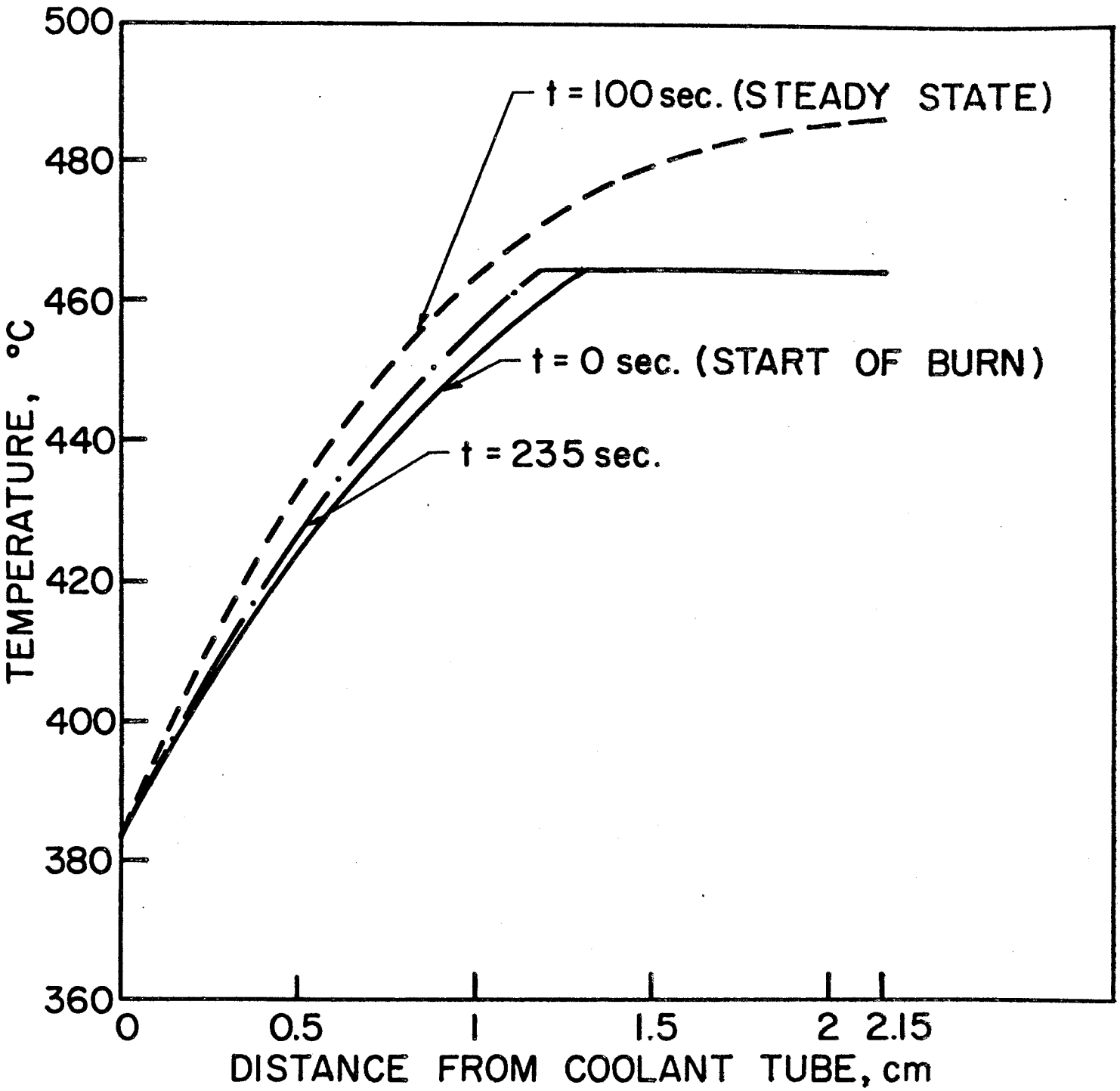


Fig. II-B-4 TEMPERATURE CHANGE OF THE BLANKET IN A BURN CYCLE (WITH PHASE CHANGE)

Table II-B-2. Burn Cycle of NUWMAK

Phase	Time (seconds)
Current Rise Time (0 to 7.2 MA)	7
RF Heating to Ignition (80 MW)	1
Plasma Burn	224
Plasma Cooling and Current Decrease	8
Additional Pumping and OH Coil Reset	5
Total Cycle Time	245
Cycle Duty Factor	0.91

7.2 MA and RF heating ignites the plasma in 2 sec. The burn time is 225 seconds. The time, t = 243 sec, on the figure is about halfway between the end of one burn and the start of another. Note that for the three quite different times during the burn, the slope of the temperature curve at the cooling tube surface changes very little. As such, both the heat flux to the coolant tube and the ΔT across the tube remain about constant during the plasma down time.

II-B-5. PLASMA HEATING BY RF AT $2\omega_{ci}$

RF plasma heating based on the fast magnetosonic mode at $2\omega_{CD}$ (92 MHz) is used in NUWMAK. This wave is approximately transverse electric (TE) with respect to the toroidal axis and is right-elliptically polarized. A cavity-backed aperture antenna is designed to couple the wave power into the plasma through the toroidal field. The wedge shaped coaxial cavity is flush mounted on the first wall as shown in Fig. II-B-2 and is fed by a coaxial line with the center conductor welded to the inner wall to form a current coupling loop.

There are four resonant cavities positioned so that they do not intersect the $\omega = 2\omega_{CD} = 3\omega_{CT}$ resonance surface over their poloidal extent. Catastrophic breakdown may occur due to anomalous acceleration of the ions if the cavity intersects such a resonant surface. The cavities have the following parameters:

Radial Width	0.1 m
Toroidal Width	1.85 m
Poloidal Width	3.5 m
Wall Thickness	0.002 m

Each cavity is water cooled and constructed of V-5Ti, chosen because of its high electrical conductivity, and each is located under a toroidal field magnet where field ripple is a minimum.

The minimum loss in a vacuum insulated coax line occurs at a characteristic resistance of 73 Ω while the maximum power handling capability occurs at about 30 Ω. Thus, a driving point resistance of about 50 Ω is highly desirable. The cavity-backed antenna designed for NUWMAK acts as an impedance transformer and, because it is resonant, nearly any driving point resistance can be found by properly locating the input coupling point to the cavity. The location of the coax feed has been determined by these considerations.

The plasma heatup phase with RF heating has been analyzed using both point and space-time plasma modeling codes. It is found from the space-time analysis that 75 to 80 MW is sufficient to ignite the plasma in about 1 second. As such, each of the four RF cavities is designed to couple in 80 MW. The overall efficiency to couple in is 80 MW. The overall efficiency of the RF driving system is estimated to be about 60% based upon an 85% efficiency for the energy store (e.g., a motor generator set), a 95% efficiency for the DC power supply, a 75% efficiency for the IPA/HPA, and a 97% efficiency for the transmission line and cavity. We thus estimate the primary power requirement during the RF pulse to be 136 MW.

II-B-6. PLASMA OPERATION WITHOUT A DIVERTOR

The operation of long pulse or steady state toroidal fusion plasmas in an appropriately clean state has been a concern from the earliest days of fusion devices. Magnetic divertors were first proposed for Stellarator reactors by Spitzer and they have been included in many recent tokamak designs,[1-4] including those of our group at Wisconsin. It has been clear that, while divertors may maintain plasma cleanliness and act as pumps, they add considerably to reactor complexity and cost. We have therefore considered an alternative for NUWMAK based on periodic gas puffing and a trapped ring of impurities which acts as a halo to radiate heat conducted from the plasma center to the chamber walls.[4]

The alpha power deposition during the NUWMAK burn is 388 MW and this must spread approximately uniformly over the first wall if it is to be a manageable heat load. The first wall area is 360 m^2 so that the average surface heating rate would be an acceptable 1.1 MW/m^2. If this heat leaves the plasma as hot ions and electrons which strike the limiter, the heat load is concentrated and would be much too high. For example, assuming escaping plasma uniformly heats two diaphragm limiters of 5 cm width, the average heat load would exceed 200 MW/m^2.

The approach in NUWMAK is based upon the assumption that impurity transport is neoclassical, as indicated by experiment. The impurities (and alpha particles) diffuse up the fuel density gradient (inward) but down the temperature gradient (outward). Periodic gas puffing maintains a

relatively flat density profile (small $\partial n/\partial r$) but the alpha heating, which varies as $n^2\langle\sigma v\rangle$ and is more sharply peaked near the plasma center, drives a very sharp temperature gradient at the plasma edge. These two effects combine to effectively keep impurities at the center to a low value.

The plasma edge behavior is intimately related to plasma wall interactions and the possible presence of a Ware pinch effect. The presence of gas at the plasma boundary implies that there is a charge-exchange neutral outflux which causes sputtering and impurities. The impurities cannot penetrate to the center and periodic gas puffing maintains a relatively flat density profile. (We find an actual density inversion near the edge which we allow to relax by stopping the gas flow.) The net effect is that a ring, or halo, of impurities is maintained in steady state and radiates the heat conducted from the center to the first wall. This loading is uniform and manageable.

Fueling and pumping are key issues for divertorless operation and are not completely resolved. If fueling is accomplished solely by puffing gaseous D-T at the plasma edge, we find fuel does diffuse to the center. However, there is a very rapid turnover of plasma near the edge because the diffusion coefficient is high and the temperature gradient is steep. Some of this fuel is simply neutralized at the limiter and recycled. However, if the edge boundary density is to decrease between puffs, gas must be pumped. This leads to very large pumping speed requirements, low tritium fractional burnup (~0.6%), and thus very high tritium inventory associated with the primary fueling system (>20 kg). This situation is unacceptable.

A workable alternative is to puff only deuterium gas and to use pellet fueling[9] to deposit fuel (mostly tritium) more deeply into the plasma where diffusion rates are lower. We find the plasma can be treated as a two region model, the core region, I, with radius r_e, and an edge region, II, of thickness δ between r_e and the plasma radius a. In region I, the diffusion rates are modest and the rate of tritium loss to region II is slow. Since most of the energy (>90%) is generated in the core, we need only fuel this zone with D and T. We now find the fractional burnup to be an acceptable 10%. Region II is dominantly deuterium in this case and is refueled solely by deuterium gas puffing. In this way, we avoid the rapid turnover of tritium due to a rapid loss of particles from the edge region alone.

A second major issue is the selective pumping of helium ash. We find that the helium can be made to diffuse into the turbulent plasma edge. The reason is the fuel density profile in the central region is flat and the only driving force for alpha inward diffusion is a fuel density gradient. Once in the edge region, however, it is necessary that the helium be pumped. The helium is a small constituent of the hydrogenic gas, is at low particle pressure, and is virtually impossible to pump. What is required is selective He pumping or trapping to prevent the ash from simply recycling and building up in the plasma. We have identified the problem in a quantitative way, namely the helium is produced at the rate of 7×10^{20} alphas per second in NUWMAK and the selective pumping speed must be about this rate to prevent alpha buildup.

At present, no established technique exists to accomplish this task. An approach which deserves further attention is to operate toroidal belt limiters at a potential of approximately 500 volts negative. Alphas will then strike the surface at normal incidence with an energy of about 1 keV. Experimental results from Sandia[10] suggest that helium can be selectively trapped in stainless steel surfaces up to a fluence of $5 \times 10^{16} - 10^{17} cm^{-2}$. This would permit only a 10-20 second burn in NUWMAK if the limiter surface is on the order of $10^5 cm^2$, a feasible figure. The limiters would have to be arranged in pairs and, as with cryopumps, the trapped gas would then have to be regenerated. This problem requires much further attention in light of its importance. At the moment, however, we must conclude the long burns without divertors are unlikely unless selective helium pumping is possible.

II-B-7. DIRECT BWR POWER CYCLE

The use of boiling water cooling and internal blanket energy storage permits the use of a simplified power cycle modelled after the direct Boiling

Water Reactor (BWR) approach. A comparison of the power cycle normally designed for tokamaks with that of NUWMAK is shown in Fig. II-B-5 and the average power flows are shown in Fig. II-B-6. The coolant temperature (300°C) and pressure (8.6 MPa or 1250 psi) are typical of a BWR cycle. The gross plant efficiency is 34.6% while the net efficiency is 31.5%. The largest recirculating power requirement is 60 MW_e for magnet refrigeration. It is expected that the absence of the equipment shown in Fig. II-B-6, particularly the intermediate heat exchanger and the hot and cold energy stores, will reflect favorably on system economics.

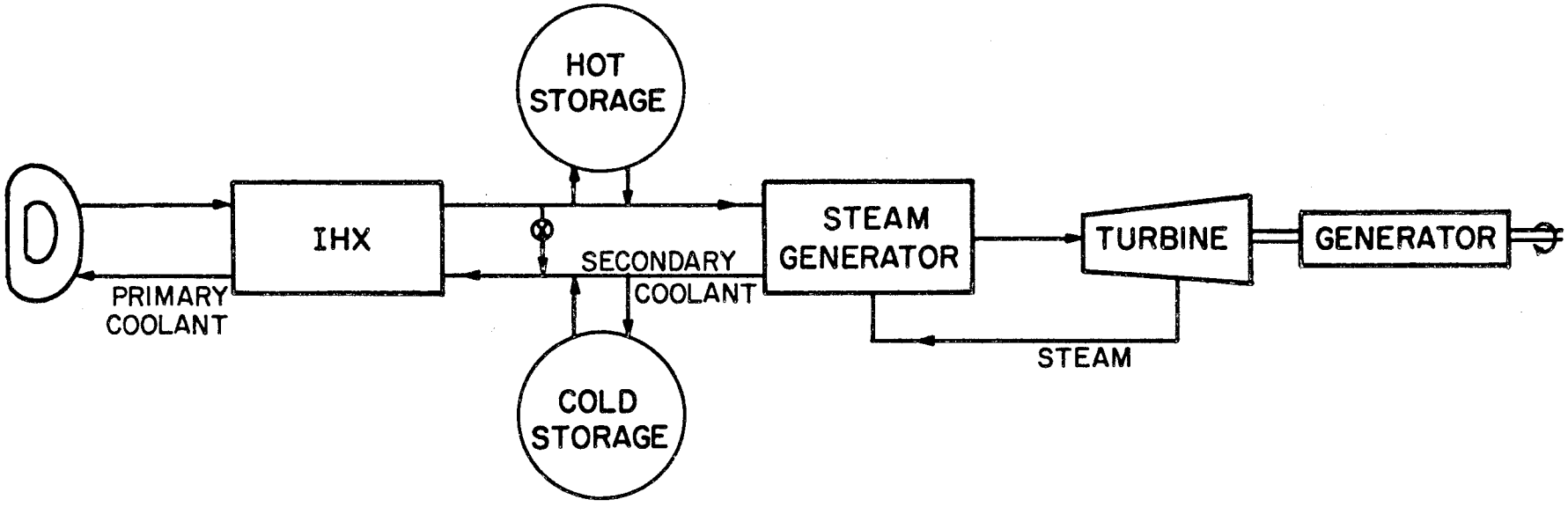
II-C. ADDITIONAL NUWMAK DESIGN CHARACTERISTICS

II-C-1. MHD PLASMA ANALYSIS AND VERTICAL POSITION CONTROL

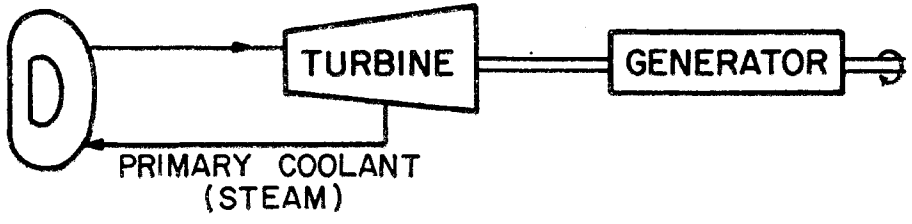
The equilibrium plasma shape for NUWMAK has been determined from MHD calculations. The final design requires just eight coils, four each above and below the plasma midplane (see Fig. II-B-2) located at the (R,Z) positions:

R(m)	Z(m)	I(MA)
3.5	±3.5	2.3
4.5	±3.75	2.0
10.5	±3.5	-2.0
11.5	±1.0	-3.5

A positive sign on the coil current signifies flow in the direction of the plasma current. The plasma shape is shown in Fig. II-C-1 and the



POWER CYCLE FOR A CONVENTIONAL TOKAMAK



POWER CYCLE FOR NUWMAK (BWR TECHNOLOGY)

Fig. II-B-5 COMPARISON OF POWER CYCLE OF NUWMAK TO A CONVENTIONAL TOKAMAK REACTOR

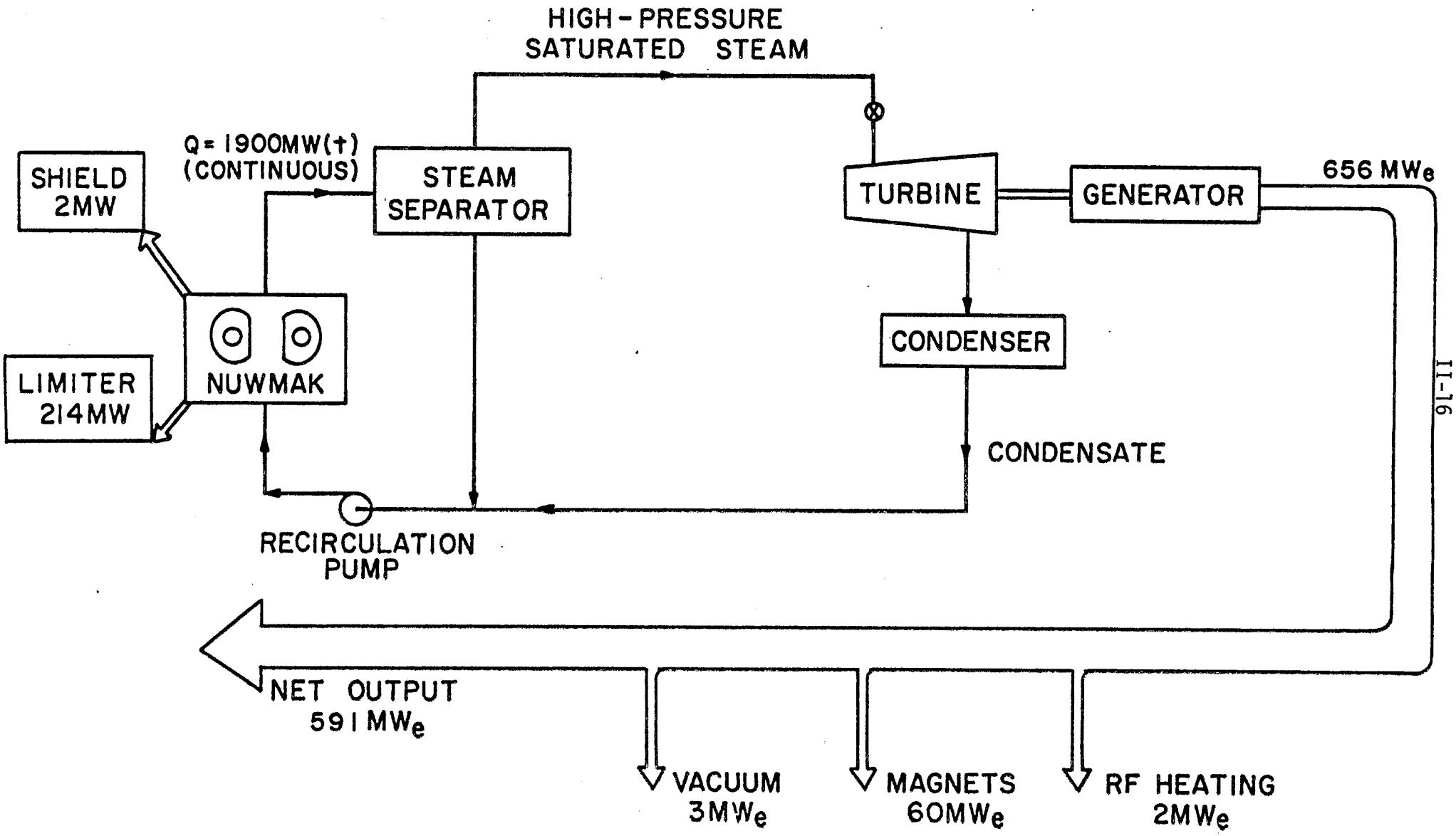


Fig. II-B-6 POWER FLOW DIAGRAM FOR NUWMAK

POLOIDAL FLUX OF NUWMAK

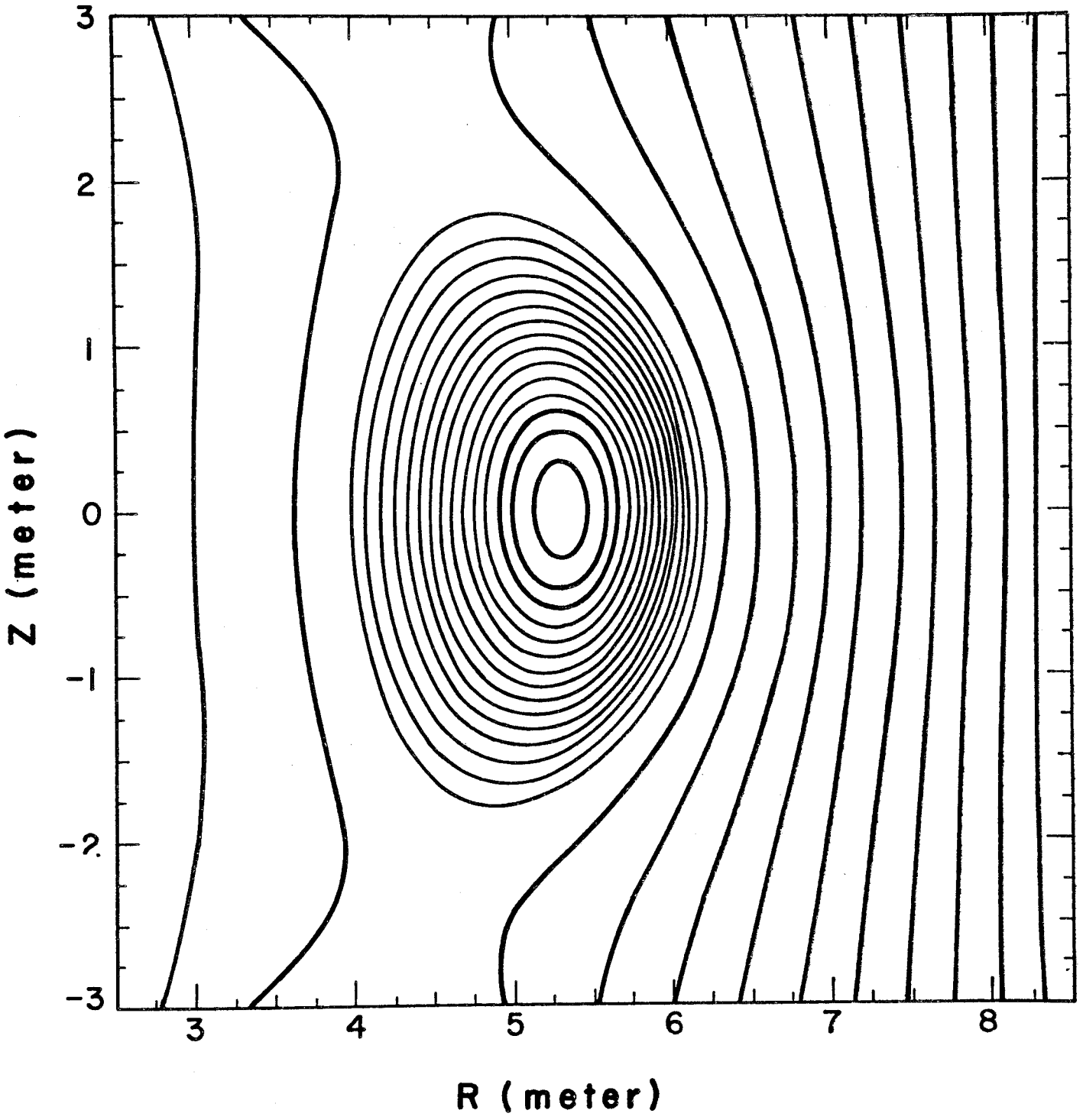


Fig. II-C-1

profile of the safety factor, q(r), as well as the stability factors, DI and DR (for ideal and resistive interchange modes), are shown in Fig. II-C-2. q(r) exceeds 1 everywhere and q(a) at the plasma edge is 2.6. The sign of DI and DR also indicates stability. The average toroidal plasma beta is 6% and the average poloidal beta ($\beta_p = \frac{2\mu_o \bar{p}}{\langle B_p^2 \rangle}$) is 3.7. We have not used the PEST code[11] to test stability against ballooning modes but 6% toroidal beta is consistent with stable β values found in other similar cases. The decay index of the vertical field, defined as $n = \frac{R}{B_\perp} \frac{dB_\perp}{dR}$, has the value of -1.13 indicating the plasma position is unstable against rigid vertical displacements. This is a familiar result found in most designs of noncircular plasmas with height to width ratios of about 1.5 or greater. In a previous study, a feedback system was designed utilizing the existing vertical field coils. The reactive power requirement was about 90 MW. The blanket in NUWMAK is more highly conducting so that the growth rate for the instability is much slower (estimated to be about 0.5 seconds). Thus, the reactive power requirement is only 1 MW.

II-C-2. BLANKET NEUTRONIC ANALYSIS

A schematic of the blanket and shield design is shown in Fig. II-C-3. The blanket has been analysed using a two-dimensional analysis to account for the poloidal variation in zone thicknesses and the different design of the inner shield. Four criteria relating to the toroidal field coils were used to design the inner shield: radiation induced changes in the critical current of the superconductor; radiation induced changes in the resistivity of the Al stabilizer; the dose limits of the super-insulation; and magnet heating. The most restrictive criterion is found to be the

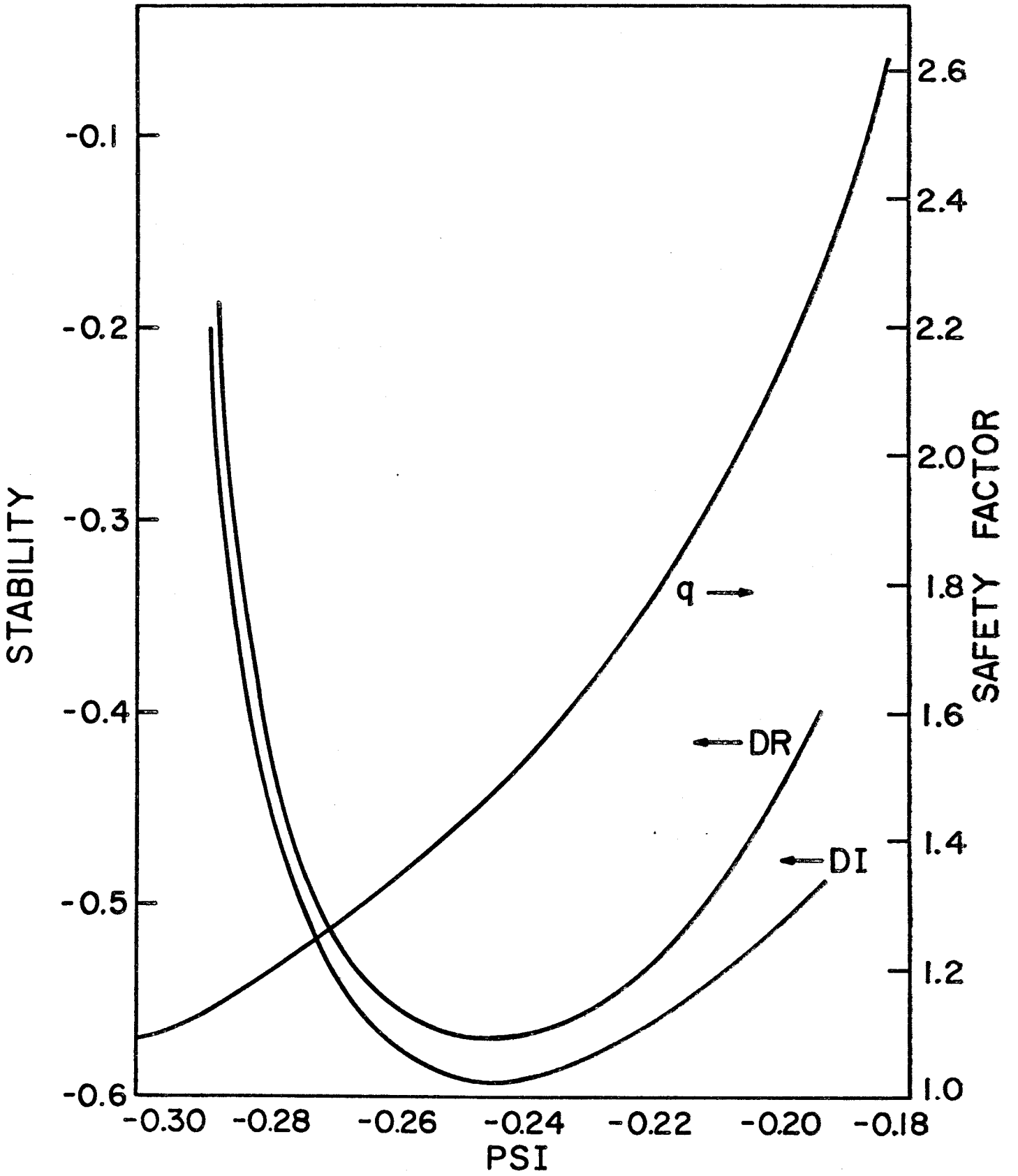


Fig. II-C-2. Plot of stability factors, DR and DI, and the safety factor, q, versus ψ surface from the plasma center to the edge.

SCHEMATIC OF THE BLANKET AND SHIELD FOR NUWMAK

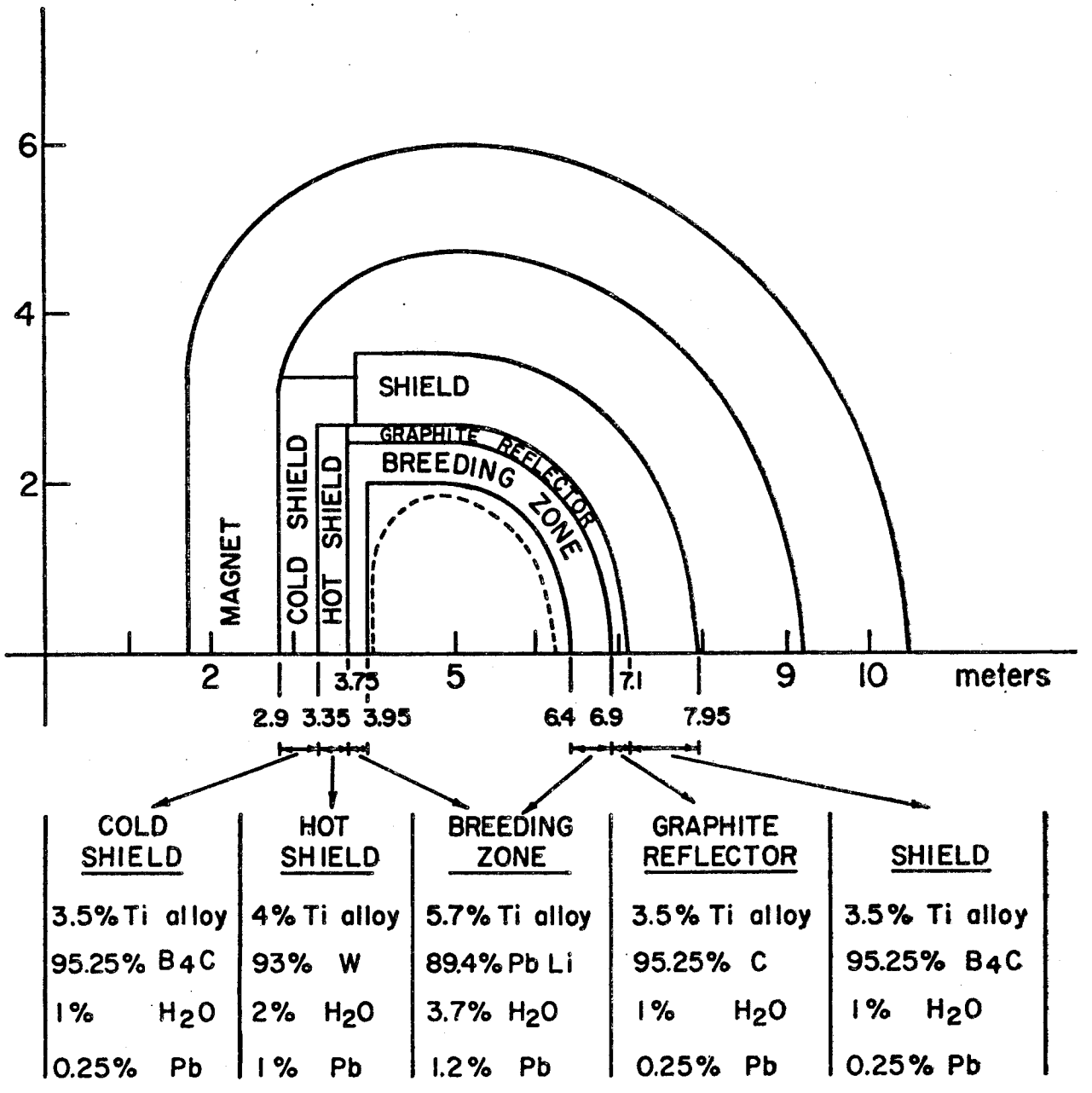


Fig. II-C-3

resistivity change of the Al stabilizer. The resistivity of the Al at 1.8 K is estimated to increase by 15%/year and although the design can operate with a 100% increase, it is proposed that this damage be annealed out by warming the coils approximately every two years. Enough margin exists so that this operation can be carried out while the reactor is shut down for other reasons. As such, it is not expected that this procedure will cause a decrease in the overall plant availability factor. The estimated change in the critical current, J_c, is just 0.5%/year. As for the superinsulation, it is found that the dose to mylar would exceed dose limits before plant life. An epoxy based superinsulator whose dose limit is 1-5 x 10^9 rads is therefore selected. At a dose rate of 1.6 x 10^7 rad/yr, the epoxy should last plant life. The remaining key neutronics parameters of NUWMAK are given in Table II-C-1. The quite high tritium breeding ratio is due to the presence of a Li-Pb zone in the inboard as well as the outboard blanket. In a previous study, UWMAK-III, the concept of breeding only in the outer blanket was developed to control the breeding ratio. The inboard shield combination was designed for maximum attenuation. In NUWMAK, the breeding ratio associated with the outer blanket alone is 1.24. However, we have retained the Li-Pb zone on the inside so as to maintain minimum thermal cycling of the structure. At this point, we have not found another compound or eutectic which can perform the same task as the Li-Pb in the same temperature range.

II-C-3. BLANKET TRITIUM ANALYSIS

The blanket in NUWMAK contains 8 x 10^5 kg of the eutectic 62 Li:38 Pb and has a very low steady state tritium inventory, only 800 g (1 wppm T). The resulting pressure of T_2 above the 62 Li:38 Pb is 5.9 x 10^{-4} torr. The tritium extraction system, which must remove the 380 g of T bred per day, is extrapolated from experimental work on the molten salt extraction of tritium from liquid Li. A stream of molten LiPb eutectic is continually removed from the blanket, heated to 500°C, and fed to a centrifugal contactor unit where the eutectic is brought into contact with an equal volume of molten salt having the composition 22 LiF:31 LiCl: 47 LiBr. The LiT is preferentially distributed in the salt phase by a

Table II-C-1. Key Neutronic Characteristics of NUWMAK

Tritium Breeding Ratio	1.54
Nuclear Heating (MeV/D-T neutron)	17.15
Total Energy Per Fusion (MeV)	20.67
Max. Displacement Rate in Al Stabilizer of TF Coil (dpa/yr)	1×10^{-6}
Dose Rate to Superinsulator (Rad/yr)	1.6×10^{-7}
Nuclear Heating in TF Coils (watts)	500
Energy Attenuation of the Blanket and Shield	1×10^{-9}

factor of approximately two, on a volumetric basis, and the salt and eutectic are then separated. The purified eutectic (0.3 wppm T) is then returned to the blanket. The salt is electrolyzed at an emf below its decomposition potential but above the decomposition potential of LiT (0.9 volts) for 30 minutes to remove the tritium. The fraction of tritium recovered from the salt in this period is approximately 90%.

The NUWMAK blanket and tritium extraction system are attractive for a number of reasons related to safety. Not only is the blanket lithium inventory low (4×10^4 kg) but the activity of Li in 62 Li:38 Pb at 464°C is only 0.6% of the activity of pure Li. Further, the eutectic mass in the contactor at any time is small (~40 kg). Since it is possible to remove tritium from pure liquid Li down to the 0.06 wppm level, the factor which ultimately limits the minimum tritium inventory is the number of times per day one can feasibly process the blanket eutectic. The relationship between the steady state blanket T inventory (I_{ss}) and the fraction of the blanket processed per day (X) is given by $X = \frac{0.59}{I_{ss}}$ where 0.59 is a factor incorporating the NUWMAK parameter for the volumetric distribution coefficient, efficiency of T recovery from the salt, and the breeding rate. To maintain the blanket tritium inventory at 800 g, it will be necessary to process 74% of the blanket eutectic per day. If the blanket could be processed more frequently, the tritium inventory could be further decreased resulting in a lower T_2 pressure.

II-C-4. MATERIALS RESOURCE IMPLICATIONS

The total materials requirements for a 300 GW_e installed capacity of NUWMAK-type reactors (~ 1500) are given in Table II-C-2. One can see that even such a large economy of reactors does not place a severe burden on materials resource requirements available at present prices from within the domestic U.S. market. Only three materials would be required from foreign sources, Nb, W, and Co. We recommend further that as fusion develops, the need for these materials be monitored. Overall, however, NUWMAK style reactors appear to place no severe burdens on resource requirements.

Table II-C-2

Group & Metal	Total Requirement for 300 GW_e (in metric tonnes x 10^3)
Group A - Materials available from domestic mines at market prices	
Boron	2,232
Carbon	1,093
Copper	1,183
Iron	56,362
Lead	2,829
Lithium	63
Magnesium	8
Zr	1.5
Mo	68
Group B - Materails available from domestic mines at 3X market prices	
Aluminum	2,240
Chromium	346
Titanium	1,286
Manganese	53
Vanadium	117
Ni	44
Group C - Materials available in adequate amounts only from foreign sources	
Niobium	75
Tungsten	1,040
Cobalt	68

II-C-5. ECONOMIC ANALYSIS

The economic analysis has been carried out in the format recently developed by the Department of Energy in the report "Fusion Reactor Design Studies - Standard Accounts for Cost Estimates", issued May 1978.

Two modes of economic analysis are used. The first is a current dollar mode (nominal dollar) which assumes that the purchasing value of the dollar changes over time. The second is a constant dollar mode which assumes the purchasing value of the dollar remains constant over time or that the inflation rates and component escalation rates are equal to zero. The cost of energy figures obtained by the constant dollar mode will be higher than the cost of energy today because the present dollar value is used without de-escalation to its value eight years ago (assuming an eight year construction period) and the interest during construction is based on the present day cost. This is an important factor to be kept in mind if one has to compare the cost of energy from NUWMAK obtained by the constant dollar mode with the cost of present day energy (fossile fuel, etc.).

In the current dollar mode the cost escalation on the estimated capital costs is assumed to exist and is accounted for in a single escalation during construction account. Further, the cost escalation on estimated operating and maintenance, scheduled component replacement and fuel costs is also assumed to exist, and is accounted for within the respective parent cost account. The current dollar analysis mode is, therefore, essentially a nominal first year facility cost and the cost of energy obtained in this way should be compared with the cost of energy from other sources eight years from now.

We have assumed an eight-year construction period for NUWMAK with a cash flow profile for interest during construction and escalation that follows the classic S-curve biased about 20% to the right. This profile appears to hold for major fossil and nuclear plant construction.

A summary of capital costs is given in Table II-C-3. While it is difficult to attach true significance to the numbers, they appear to show that fusion systems modelled after the NUWMAK design have costs that are within the range of costs projected for advanced energy systems. Busbar costs including operation and maintenance, annual fuel costs, scheduled

component replacement costs, and an estimated plant availability are also given in Table II-C-3. In the constant dollar mode, these costs are about 35 mills/kWh. In the current dollar mode, electricity cost comes to 72 mills/kWh.

A comparison of costs between two different studies we have done is given in Table II-C-4. UWMAK-III is a 2000 MW_e conceptual tokamak reactor with major radius equal to 8 m and a neutron wall loading of 2.0 MW/m^2. The design is based upon assumptions on advanced technologies and materials, such as the molybdenum alloy structure, TZM, and the advanced direct He cycle power train. The direct costs were developed by the University of Wisconsin and the Bechtel Corp. Costs have been inflated to 1978 dollars. Two costs models were used: the basis provided in the report NUS-531 on standard nuclear power plant costs; and the costing mode provided in the previously referred to 1978 DOE Guidelines. The higher power density and lower power cycle costs are primary reasons for the lower costs of NUWMAK.

Table II-C-3
Cost Summary for NUWMAK

a. Capital Costs ($\$10^6$)

	Constant Dollars	Current Dollars
Direct Costs	844	844
Indirect Costs	295	295
Time Related Costs	194	829
Total Capital Costs	1333	1968
Capital Costs	$\$2020/kW_e$	$\$2982/kW_e$
b. Busbar Costs	34.3 mills/kWh	72 mills/kWh

Table II-C-4

Cost Comparisons Between NUWMAK and UWMAK-III

	NUS-531 (1978$)	Const. Dollars (1978$)	Current Dollars (1986$)
Plant Cost			
UWMAK-III	3317 $/kW$_e$	2743 $/kW$_e$	4039 $/kW$_e$
NUWMAK	2476 $/kW$_e$	2020 $/kW$_e$	2982 $/kW$_e$
Busbar Cost			
UWMAK-III	80 mills/kWh	48 mills/kWh	100 mills/kWh
NUWMAK	58 mills/kWh	34 mills/kWh	72 mills/kWh

II-D. SUMMARY AND COMMENTS

A new conceptual design of a tokamak fusion reactor of medium toroidal field (B_T^o = 6.05 T) shows that such systems can have high power density, high neutron wall loading, modularity, and moderate size. The design is especially attractive from the viewpoints of system accessibility, first wall lifetime, low levels of long term induced radioactivity and minimum penetrations. The power density (10 MW/m^2) and electrical power output (660 MW) of this unit are chosen as typical of a full scale power reactor operating in a base-loaded mode at the turn of the centruy. Somewhat smaller tokamaks can be designed for use in a reactor development program and larger units are feasible for longer term applications when electrical grids have expanded still further.

Overall the NUWMAK design appears to be a natural and attractive extension of moderate field, moderate size tokamaks as represented by the Tokamak Fusion Test Reactor (TFTR) and the Oak Ridge-TNS design. Parameters for the three devices are given on Table II-D-1 and a pictorial size comparison is given in Fig. II-D-1. Both NUWMAK and the ORNL-TNS are about a factor of 2 larger than TFTR in linear dimension while NUWMAK extends the toroidal field and the plasma current relative to the ORNL-TNS and includes thicker blanket-shield regions which produce major differences in design. Nevertheless, the implication is that the scale-up from TFTR to the ORNL-TNS is primarily in size and to some extent in technology. Following TNS, however, a scaleup in specific technologies can then produce an interesting reactor product.

Table II-D-1 - Comparison of Key Parameters in TFTR, ORNL-TNS, and NUWMAK

	TFTR	ORNL-TNS	NUWMAK
Major Radius (m)	2.48	5.0	5.13
Plasma Radius (m)	0.85	1.25	1.13
Aspect Ratio	2.92	4.0	4.54
Plasma Current (MA)	2.5	4	7.2
Toroidal Beta	2%	3-10%	6%
Plasma Shape	Circle	"D"	"D"
Heating Method	Neutral Beams	Neutral Beams	RF
Heating Power	20MW @ 120 keV 12MW @ 60 keV	~50 MW @150 keV	75 MW @ 92 MHz ($2\omega_{cd}$)
Axial Toroidal Field (T)	5.2	4.3	6.05
TF Coil Design	Cu	Cu/NbTi/Nb_3Sn	Al/NbTi
Inner Blanket/Shield Thickness (m)	<0.5	0.54	1.10
Average Neutron Wall Loading	---	---	4.0 MW/m^2
Number of DT Pulses in Reactor Life	4×10^3	5×10^5	5×10^6
Tritium Breeding Ratio	---	---	1.54
Tritium Inventory	<1/2 g	~190 g	5-10 $\times 10^3$ g
Duty Factor	---	~50%	.91
Expected Availability	---	~20%	~ 80%

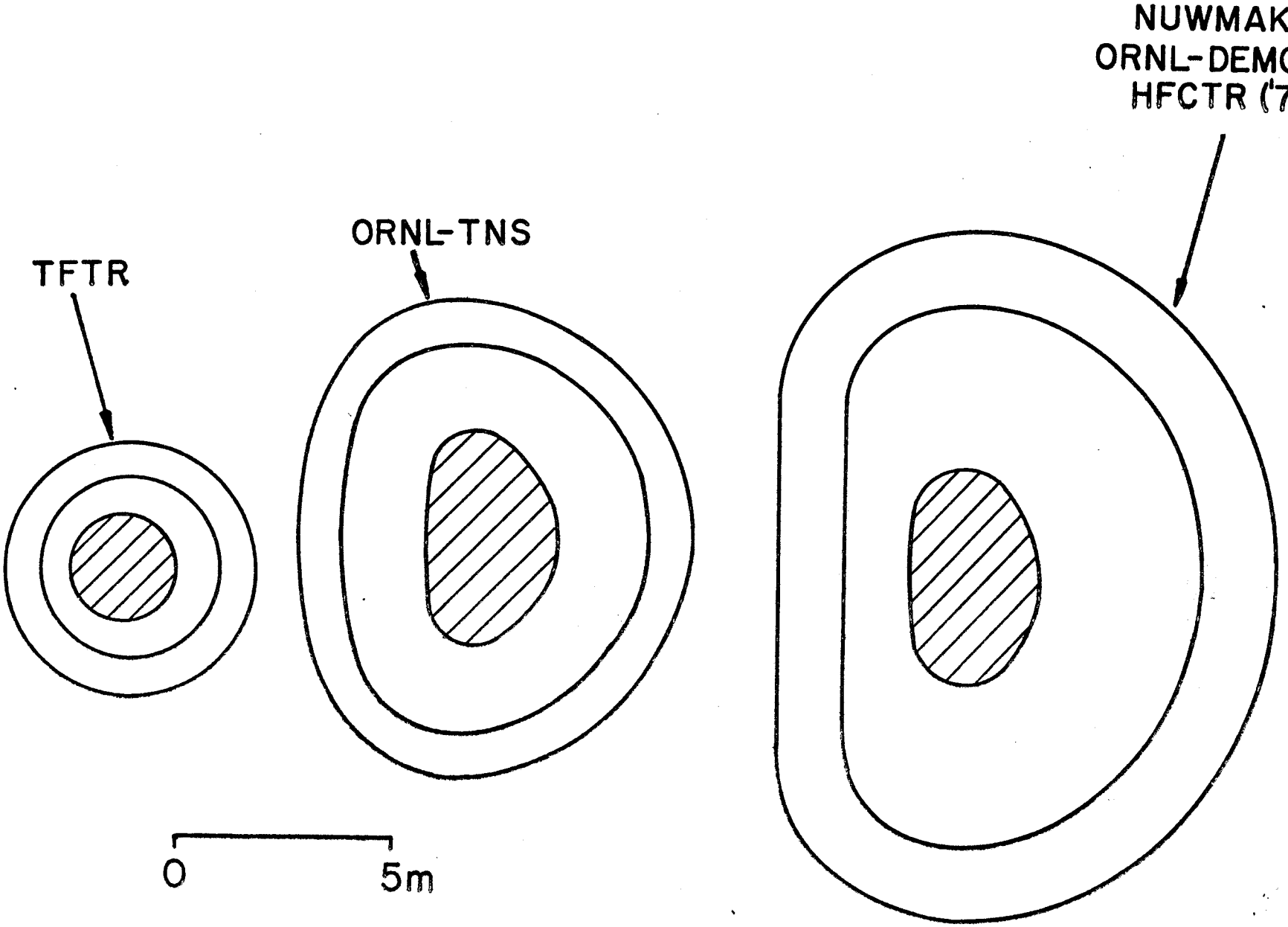


Fig. II-D-1

References for Chapter II

1. B. Badger, et al., "UWMAK-I, A Wisconsin Toroidal Fusion Reactor Design," Fusion Research Program Report UWFDM-68, Univ. of Wis., Vol. I (1973), Vol. II (1975).

2. R. G. Mills, ed., "A Fusion Power Plant," Princeton Plasma Physics Lab Report MATT-1050 (Aug. 1974).

3. B. Badger, et al., "UWMAK-II, A Conceptual Tokamak Power Reactor Design," Fusion Research Program Report UWFDM-112, Univ. of Wis., (Oct. 1975). See also Nucl. Engr. and Design 39, 5-44 (1976).

4. Fusion Reactor Design Problems, Nuclear Fusion Supplement, IAEA, Vienna (1974).

5. G. Fuller, et al., "First Wall Blanket Systems Analysis," McDonnell-Douglas Astronautics Co.-East, St. Louis (Oct. 1977).

6. M. A. Abdou, et al., "Impact of Major Design Parameters and Options on the Performance and Economics of Tokamak Power Plants," Proc. 2nd IAEA Technical Committee Meeting and Workshop on Fusion Reactor Design (to be published).

7. T. E. Shannon, Don Steiner, "The ORNL Fusion Power Demonstration Study," Proc. 2nd IAEA Technical Committee Meeting and Workshop on Fusion Reactor Design (to be published by IAEA).

8. D. R. Cohn et al., "High Field Compact Tokamak Reactor Conceptual Design," MIT Plasma Fusion Center Research Report RR-78-2 (March 1978).

9. W. A. Houlberg, et al., "Effects of Fueling Profiles on Plasma Transport," Proc. Fusion Fueling Workshop, CONF-771129, UC-20a, Dept. of Energy (March 1978).

10. W. Bauer, private communication to R. Conn.

11. Princeton Plasma Physics Laboratory, Princeton NJ.

III. SUMMARY OF PARAMETERS

Recently, the Office of Fusion Energy in the Department of Energy developed a standardized list of parameters and requested that such a list be included in all reactor design study reports. The extensive table which constitutes this chapter presents these parameters in the requisite format.

Standardized Table of Reactor Design Parameters

Reactor Concept - NUWMAK

			Unit	Value
1.	Characteristic Machine Dimensions			
	1.1	Reactor Envelope		
	1.1.1	Height	m	16
	1.1.2	Width	m	25
	1.1.3	Length ($2\pi R$)	m	32
	1.2	Vacuum Vessel		
	1.2.1	Major Radius	m	5.13
	1.2.2	Minor Radius	m	1.2-2.0
	1.2.3	Volume	m^3	190
	1.2.4	Inner Surface Area	m^2	360
2.	Plasma Parameters			
	2.1	Plasma Dimensions		
	2.1.1	Major Radius, R	m	5.13
	2.1.2	Minor Radius, a	m	1.13
	2.1.3	Plasma Elongation		1.64
	2.2	n_o, Centerline Density	m^{-3}	3.3×10^{20}
	2.3	$\bar{n}$, Average Density (ion)	m^{-3}	3.1×10^{20}
	2.4	τ_E, Energy Confinement Time	sec	1.38
	2.5	τ_e, Electron Confinement Time	sec	0.42
	2.6	τ_i, Ion Confinement Time	sec	0.38
	2.7	$n\tau_E$, (Averaged Through Plasma)	sec/m^3	4.7×10^{8}
	2.8	β_o, Centerline Toroidal Beta	%	12
	2.9	$\langle\beta\rangle$, Average Toroidal Beta	%	6.5
	2.10	β_{po}, Centerline Poloidal Beta		4.3×10^{4}
	2.11	$\langle\beta_p\rangle$, Average Poloidal Beta		5.4

		Unit	Value
2.	Plasma Parameters (continued)		
2.12	I_p, Plasma Current	MA	7.2
2.13	T_{io}, Centerline Ion Temperature	keV	15.0
2.14	$\overline{T_i}$, Average Ion Temperature	keV	9.3
2.15	T_{eo}, Centerline Electron Temperature	keV	16.8
2.16	$\overline{T_e}$, Average Electron Temperature	keV	8.6
2.17	Z_{eff}, Effective Plasma Ion Charge		2.5
2.18	q, Plasma Safety Factor		1.09-2.6
2.19	Volt-Seconds (Startup/Burn)	Volt-Sec.	67.3/16.4
2.20	Reactor Cycle	Steady State/Pulsed	Pulsed
2.20.1	Burn Pulse Length	Sec.	225
2.20.2	Total Pulse Length	Sec.	245
2.21	Fuel Cycle (i.e., D-T, D-D, etc.)		D-T
2.22	Plasma Heating Method		RF
2.23	Plasma Heating Power	MW	80
2.24	Plasma Heating Energy or Freq.	Hz	92×10^6
2.25	Plasma Energy Gain, Q_p		∞
3.	Power Output		
3.1	Plasma Power (Peak)	MW(th)	1981
3.2	Plasma Power (Total Cycle Time Average)	MW(th)	1792
3.3	Power to Blanket (Peak)	MW(th)	2283
3.4	Power to Blanket (Total Cycle Time Average)	MW(th)	2097
3.5	Blanket Power Amplification Factor		1.2
3.6	Power to Direct Convertor (Peak)	MW(th)	N/A
3.7	Power to Direct Convertor (Total Cycle Time Average)	MW(th)	N/A
3.8	Power to Divertor Peak	MW(th)	N/A
3.9	Power to Divertor (Total Cycle Time Average)	MW(th)	N/A
3.10	Plasma Chamber Power Density (Total Cycle Time Average)	MW/m^3	14.1
3.11	Nuclear Island Power Density[(a)] (Total Cycle Time Average)	MW/m^3	1.34

(a) The "Nuclear Island" is defined as everything covered by Account No. 22 in PNL-2648, "Fusion Reactor Design Studies--Standard Accounts for Cost Estimates".

			Unit	Value
3.	Power Output (continued)			
	3.12	Plant Gross Electrical Output	MW_e	725
	3.13	Plant Net Electrical Output	MW_e	660
	3.14	Thermal Cycle Efficiency	%	34.6
	3.15	Direct Convertor Efficiency	%	N/A
	3.16	Net Plant Efficiency	%	31.5
4.	Reactor Coolant System			
	4.1	Blanket Coolant Type		Boiling Water
	4.2	Blanket Outlet Temperature (Hot Leg)-Peak/Average	^oC	300
	4.3	Blanket Inlet Temperature (Cold Leg)-Peak/Average	^oC	300
	4.4	Blanket Outlet Pressure-Peak/Average	MPa	8.6
	4.5	Blanket Inlet Pressure-Peak/Average	MPa	9.0
	4.6	Blanket Coolant Flow Rate	kg/s	1500
	4.7	Blanket Coolant Pipe Material		Ti-6Al-4V
	4.8	First Wall Coolant Type		Boiling Water
	4.9	First Wall Outlet Temperature-Peak/Average	^oC	300
	4.10	First Wall Inlet Temperature-Peak/Average	^oC	300
	4.11	First Wall Outlet Pressure-Peak/Average	MPa	8.6
	4.12	First Wall Inlet Pressure-Peak/Average	MPa	9.0
	4.13	First Wall Coolant Flow Rate	kg/s	126
	4.14	Total Number of Blanket Coolant Loops		16
	4.15	Type of Blanket Coolant Circulator		Pump
	4.16	Power Input to Each Circulator	MWe	
	4.17	Peak First Wall/Blanket Temperature in Case of Loss of Coolant Flow	^oC	<500 (if plasma quenches immediately)
	4.18	Energy Storage	J	4.2×10^{10}
5.	Intermediate Coolant System			
	5.1	Coolant Type		N/A
	5.2	IHX Outlet Temperature (Hot Leg)	^oC	
	5.3	IHX Inlet Temperature (Cold Leg)	^oC	
	5.4	IHX Outlet Pressure	MPa	
	5.5	IHX Inlet Pressure	MPa	
	5.6	Coolant Flow Rate	kg/s	
	5.7	Coolant Pipe Material		
	5.8	Total Number of Coolant Loops		
	5.9	Type of Coolant Circulator		

		Unit	Value
5.	Intermediate Coolant System (continued)		
5.10	Power Input to Each Circulator	MWe	N/A
5.11	Number of IHX Per Loop		
5.12	IHX Material-Shell/Tube		
5.13	Energy Storage	J	
6.	Steam Generation System		
6.1	Steam Outlet Temperature	°C	300
6.2	Steam Outlet Pressure	MPa	8.6
6.3	Steam Flow Rate	kg/s	1500
6.4	Feedwater Temperature	°C	238
6.5	Number of Steam Generators Per Loop		N/A
6.6	Number of Modules Per SG		N/A
6.7	SG Materials, Shell/Tube		N/A
7.	Shield Coolant System		
7.1	Total Energy Deposited in the Shield	MW_t	8
7.2	Shield Coolant Type		H_2O
7.3	Shield Outlet Temperature-Peak/Average	^oC	50
7.4	Shield Inlet Temperature-Peak/Average	^oC	100
7.5	Coolant Outlet Pressure-Peak/Average	MPa	0.14
7.6	Coolant Inlet Pressure-Peak/Average	MPa	0.16
7.7	Coolant Flow Rate	kg/s	38.4
8.	Reactor Auxiliary Systems		
8.1	Vacuum Pumping System		
8.1.1	Plasma Chamber Pressure	torr	$1x10^{-5}$
8.1.2	Plasma Chamber Volume	m^3	250
8.1.3	Number of Pumps		8
8.1.4	Capacity of Each Pump	torr-litre/s	50
8.2	Magnet Cooling System	W_t	25.7×10^6
	Cooling Load		
8.3	Plasma Heating System	W_t	$7x10^5$
	Cooling Load		
8.4	Plasma Fueling System		
8.4.1	Type		Pellet plus gas injectio
8.4.2	Fuel Composition (i.e., %D, %T, etc.)		Deuterium gas--most T pellet
8.4.3	Fueling Rate (for tritium)	kg/s	$\sim 3.5x10^{-5}$
8.4.4	Pellet Size (if used)	m	Not determine

		Unit	Value
8.	Reactor Auxiliary Systems (Continued)		
8.4.5	Pellet Injection Frequency (if used)	sec^{-1}	Not Establishe
8.5	Tritium Processing and Recovery System		
8.5.1	Total Tritium Inventory	kg	22-23
8.6	Impurity Control System		
8.6.1	Type		Gas injection plus plasma profile control
9.	Reactor Components		
9.1	Blanket/First Wall		
9.1.1	Structural Material		Ti-6Al-4V
9.1.2	Breeding Material		Li_{62} Pb_{38}
9.1.3	Breeding Ratio		1.54
9.1.4	Number of Modules		16
9.1.5	Weight of Module	Tons(metric)	9.3
9.1.6	Weight of Largest Single Component	Tons(metric)	9.3
9.1.7	Dimensions of Largest Component	m x m x m	3x2.75x4
9.1.8	First Wall Loading (Peak/Average)		1.2
9.1.8.1	14.1 MeV Neutrons	MW/m^2	4.34
9.1.8.2	Alpha Particle Flux (to limiter)	MW/m^2	0.02
9.1.8.3	Electro-Magnetic Radiation[(a)]	MW/m^2	0.49
9.1.8.4	Charge exchange neutral flux	MW/m^2	0.07
9.1.8.5	Wall Life	$MW-yrs/m^2$	10
9.2	Shielding		
9.2.1	Material		Pb,B_4C,W
9.2.2	Number of Modules		16
9.2.3	Weight of Each Module	Tons(metric)	242
9.2.4	Weight of Largest Single Component	Tons(metric)	242
9.2.5	Dimensions of Largest Component	m x m x m	1x8x3.5
9.3	Magnets		
9.3.1	Toroidal Field Magnets		
9.3.1.1	Superconducting	Yes/No	Yes
9.3.1.2	Conductor Material		NbTi
9.3.1.3	Structural Material		Al
9.3.1.4	Operating Temperature	K	1.8
9.3.1.5	Coolant		He

(a) Includes electro-magnetic radiation components from synchrotron, bremsstrahlung, and impurity inputs.

		Unit	Value
9.	Reactor Components (continued)		
9.3.1.6	Maximum Stress in Coil	N/m^2	210×10^6
9.3.1.7	Maximum Force Transmitted to Building	N/m^2	-
9.3.1.8	Maximum Field	T	11.5
9.3.1.9	Field on Axis	T	6.05
9.3.1.10	Number of Magnets		8
9.3.1.11	Field Ripple-Edge/Center	%	2
9.3.1.12	Stored Energy	J	30×10^9
9.3.2	OH Magnets		
9.3.2.1	Superconducting	Yes/No	Yes
9.3.2.2	Conductor Material		NbTi
9.3.2.3	Structural Material		SS
9.3.2.4	Operating Temperature	K	4.2
9.3.2.5	Coolant		He
9.3.2.6	Maximum Stress in Coil	N/m^2	211×10^6
9.3.2.7	Maximum Force Transmitted to Building	N/m^2	
9.3.2.8	Maximum Field	T	7.3
9.3.2.9	Field on Axis	T	~6.8
9.3.2.10	Number of Magnets		34
9.3.2.11	Field Ripple-Edge/Center	%	N/A
9.3.2.12	Stored Energy	J	3.88×10^9

			Cryogenic	Superconducting
9.3.3.	VF Magnets			
9.3.3.1	Superconducting		No	Yes
9.3.3.2	Conductor Material		Al	NbTi
9.3.3.3	Structural Material		Al	SS
9.3.3.4	Operating Temperature	K	25	4.2
9.3.3.5	Coolant		He Gas	He
9.3.3.6	Maximum Stress in Coil	N/m^2	90×10^6	210×10^6
9.3.3.7	Maximum Force Transmitted to Building	N/m^2	N/A	N/A
9.3.3.8	Maximum Field	T	2.2	1.5
9.3.3.9	Field on Axis	T		
9.3.3.10	Number of Magnets		4	4
9.3.3.11	Field Ripple-Edge/Center	%	N/A	N/A
9.3.3.12	Stored Energy	J	1.42×10^8	1.84×10^9

		Unit	Value
9.	Reactor Components (continued)		
9.3.4.	Toroidal Field Ripple Correction (Trim) Magnets		
9.3.4.1	Superconducting	Yes/No	No
9.3.4.2	Conductor Material		Cu
9.3.4.3	Structural Material		None
9.3.4.4	Operating Temperature	K	335
9.3.4.5	Coolant		H_2O
9.3.4.6	Maximum Stress in Coil	N/m^2	$120x10^6$
9.3.4.7	Maximum Force Transmitted to Building	N/m^2	N/A
9.3.4.8	Maximum Field	T	6.17
9.3.4.9	Field on Axis	T	N/A
9.3.4.10	Number of Magnets		16
9.3.4.11	Field Ripple-Edge/Center	%	N/A
9.3.4.12	Stored Energy	J	
9.4	Energy Transfer and Storage		
9.4.1	Plasma Preparation		Transformer Action
9.4.1.1	Type		Superconductin
9.4.1.2	Energy Per Unit	MJ	$7.2x10^3$
9.4.1.3	Total Energy	MJ	$4x10^3$
9.4.1.4	Peak Power Transfer Rate	W	$1x10^9$
9.4.1.5	Transfer Time	Sec.	7
9.4.1.6	Depth of Discharge	%	56
9.4.1.7	Recharge Time	Sec.	5
9.4.1.8	Pulse Frequency	$Sec.^{-1}$	$4x10^{-3}$
9.4.1.9	Switching Requirements		
9.4.1.9.1	Current	A	$\pm 2.5x10^6$
9.4.1.9.2	Volts	V	
9.4.1.9.3	Number		
9.4.2	Primary Power Supply		
9.4.2.1	Type		N/A
9.4.2.2	Energy Per Unit	MJ	N/A
9.4.2.3	Total Energy	MJ	N/A
9.4.2.4	Transfer Time	Sec.	N/A
9.4.2.5	Recharge Time	Sec.	N/A
9.4.2.6	Pulse Frequency	$Sec.^{-1}$	N/A

		Unit	Value
9.	Reactor Components (continued)		
9.4.2.7	Switching Requirements		N/A
9.4.2.7.1	Current	A	N/A
9.4.2.7.2	Volts	V	N/A
9.4.2.7.3	Number		N/A
10.	Electrical Power Requirements		
10.1	Cold Start Power From Grid	MWe vs. Sec	133/7
10.2	Auxiliary Power Requirements (Normal Operation) (from grid)		0
10.2.1	Electrical Energy Storage	MWe	8
10.2.2	Magnet Power Supply (Other Than Energy Storage)	MWe	18
10.2.3	Blanket Circulators	MWe	1
10.2.4	First Wall Coolant Circulators	MWe	
10.2.5	Shield Coolant Circulators	MWe	
10.2.6	Refrigeration System	MWe	29
10.2.7	Vacuum System	MWe	4.2
10.2.8	Plasma Heating System	MWe	2.0
10.2.9	Miscellaneous Reactor Plant Auxiliaries	MWe	2.8
10.2.10	Feed Pump System	MWe	
10.2.11	Condensing System	MWe	
10.2.12	Heat Rejection System	MWe	
10.2.13	Misc. BOP Auxiliaries	MWe	
11.	Buildings		
11.1	Reactor Building		
11.1.1	Characteristic Dimensions	mxmxm	40 dia. x 35 high
11.1.2	Enclosed Volume	m^3	75,630
11.1.3	Minimum Wall Thickness for Shielding	m	3
11.1.4	Internal Pressure, Normal/Accident	MPa	0.1
11.1.5	Containment Atmosphere		
11.2	Electrical Energy Storage Building		
11.2.1	Characteristic Dimensions	mxmxm	30x40x10
11.2.2	Wall Thickness for Shielding	m	3
11.2.3	Internal Pressure, Normal/Accident	MPa	Not Calculated
11.2.4	Safety Related or Not (e.g., is it a containment building?)	Yes/No	Yes
11.3	Reactor Service Building		

11. Buildings

		Unit	Value
11.3.1	Characteristic Dimensions	mxmxm	30x40x20
11.3.2	Special Functions (i.e., hot cells, blanket processing equipment, etc.)		Special Are Provided

12. Reactor Maintenance

12.1	Blanket/First Wall Replacement	% Surface Area/Yr.	50
		Tons/Yr.	24
12.2	Radioactive Material Storage Requirement, Volume/Year	m^3/yr	8.53

IV. Plasma Analysis

IV-A. Introduction

The plasma operating mode in NUWMAK is markedly different from operating modes in our previous studies (UWMAK-I, II and III) and from other tokamak reactor designs. The major difference lies in the reliance on gas puffing in combination with partial pellet fueling to permit operation for approximately 225 seconds with adequate plasma cleanliness. During a burn, neutral deuterium gas is puffed into the plasma periodically with a time between puffs of about 0.5 seconds. We have studied puffing D-T simultaneously or injecting tritium in solid pellets which penetrate only the outer plasma mantel. The latter option is preferred to minimize the tritium inventory. The power output of the plasma varies periodically with the gas puffing and deviations from the mean are ~ 15-20%. A sharp temperature profile develops at the plasma edge which is maintained cold by both the gas puffing and by impurity introduction. However, the step temperature profile prevents impurities from diffusing towards the plasma center and we find adequate central cleanliness over the entire burn period. The intense alpha heating maintains the central plasma core in a hot burning condition. Heat conducted from the center to the edge is partially radiated (~ 50%) to the first wall where it constitutes a surface heat load. The remaining heat load is absorbed by three toroidal limiters which are actively cooled. It thus appears that both fueling and impurity control may be possible over a long burn pulse in a reactor plasma without a divertor. A key aspect of this operating mode is gas handling and ash removal and this is discussed at the end of this section.

Other features of NUWMAK plasma operation include startup of the plasma on a limiter at the outside, RF heating to ignition at 2 ω_{ci}, and feedback control of the plasma position during the plasma burn. Plasma physics is covered in this chapter (MHD, RF startup, burn dynamics, vacuum pumping) while details of RF heating and the technology of launching RF waves are covered in the next chapter.

IV-B. MHD Equilibrium and Stability of NUWMAK

IV-B-1. Introduction

One approach to the design of economic tokamak fusion reactors is to make the plasma as compact as possible with a high power density. This is most easily accomplished with a high toroidal magnetic field and noncircular plasma cross-section. The NUWMAK reactor design is based on this concept. The MHD equilibrium and stability calculations for this design have been done using the Princeton MHD Code.[1,2] An interesting feature of the design is that it utilizes only four pairs of equilibrium field coils; two pairs are normal coils inside the toroidal field magnets and the other two are superconducting coils outside the toroidal field magnets. In Sec. IV-B-2, we describe the plasma equilibrium and stability conditions; the details for the NUWMAK design are given in Sec. IV-B-3. The feedback stabilization system will be presented in Section IV-B-4.

IV-B-2. Equilibrium and Stability

IV-B-2-a. Equilibrium

In a magnetohydrodynamic (MHD) model, the equilibrium configuration is determined by the pressure balance equation

$$\nabla P = \vec{J} \times \vec{B} \ , \tag{1}$$

and by Maxwell's equations

$$\nabla \times \vec{B} = \mu_o \vec{J} \ , \tag{2}$$

$$\nabla \cdot \vec{B} = 0 \ . \tag{3}$$

From Eq. (1), $\vec{B} \cdot \nabla P = 0$, $\vec{J} \cdot \nabla P = 0$, and we see that both the magnetic field $\vec{B}$ and plasma current $\vec{J}$ lie on the surfaces of constant pressure, or magnetic surfaces.

In the axisymmetric toroidal system we choose a magnetic flux coordinate system ψ, θ, ϕ, where ϕ denotes the toroidal angle, θ is the poloidal angle and ψ is poloidal magnetic flux label,

$$\psi(\vec{x}) = \frac{1}{2\pi} \int d^3\vec{x}\, \vec{B} \cdot \nabla\theta \ , \tag{4}$$

which has the property that $\psi(\vec{x})$ = constant specifies the magnetic surfaces. In these coordinates, the magnetic field can be decomposed into poloidal and toroidal components using[3,4,5]

$$\vec{B} = \frac{1}{2\pi} \nabla\phi x \nabla\psi + R_o B_o g(\psi) \nabla\phi \ , \tag{5}$$

where R_o is the major radius and B_o is the toroidal magnetic field strength at R_o. The function g is to be defined later. Combining Eqs. (1) and (2) we obtain the Grad-Shafranov equation for the equilibrium[6]

$$x^2 \nabla \cdot \left(\frac{1}{x^2} \nabla\psi\right) = 2\pi\mu_o x J_\phi$$

$$= -4\pi^2 \left(x^2 \frac{dP}{d\psi} + R_o^2 B_o^2 \, g \frac{dg}{d\psi}\right) \ , \tag{6}$$

where x is the distance from the axis of symmetry, and J_ϕ is the toroidal current density. In cylindrical coordinates (x,z,ϕ) Eq. 1 is usually written as

$$\frac{\partial^2\psi}{\partial x^2} - \frac{1}{x}\frac{\partial\psi}{\partial x} + \frac{\partial^2\psi}{\partial z^2} = -4\pi^2 \left(x^2 \frac{dP}{d\psi} + R_o^2 B_o^2 g \frac{dg}{d\psi}\right) \ . \tag{7}$$

The code we use to solve Eq. (7) numerically was developed at Princeton Plasma Physics Laboratory. The nonlinear equation (7) is solved by prescribing the functions $P(\psi)$ and $g(\psi)$. The form employed for the functions $P(\psi)$ and $g(\psi)$ in equation (7) can have a significant effect on the equilibrium and stability of the system. $P(\psi)$ and $g(\psi)$ are chosen having the following forms[1]

$$P(\psi) = P_o \left(\frac{\psi_* - \psi}{\psi_* - \psi_o}\right)^{\alpha_1} \ , \tag{8}$$

and

$$g(\psi) = 1 - g_p \left(\frac{\psi_* - \psi}{\psi_* - \psi_o}\right)^{\alpha_2} \ , \tag{9}$$

where P_o is the given peak plasma pressure at the magnetic axis, ψ_* and ψ_o are the fluxes at the plasma boundary and magnetic axis respectively. The values of the parameters α_1 and α_2 are on the order of unity. The constant g_p is varied until ψ converges. The plasma boundary is determined consistently with the location of the external equilibrium (EF) coils. A rectangular mesh of arbitrary size is used as an outer boundary for the problem and the boundary conditions on this border are fixed by specifying the currents in the EF coils.

As such, the procedure does not require the use of a conducting external boundary. The plasma boundary can be fixed either by a limiter or by the separatrix.

IV-B-2-b. Stability

In designing a tokamak fusion reactor, not only should it reach the certain fusion power level, but it is also necessary to satisfy the equilibrium and stability criteria associated with the device.

Before we discuss the stability problem, several important parameters such as the safety factor, toroidal β and poloidal β will be defined first. The volume enclosed by a flux surface ψ is given by

$$V = \oint d^3\vec{x}; \tag{10}$$

its derivative with respect to ψ has the following form

$$V' = \frac{dV}{d\psi}$$

$$= 2\pi \oint \frac{x d\ell}{|\nabla\psi|} \quad , \tag{11}$$

where the line integral is obtained by integrating along the poloidal field line at constant ψ. Defining the toroidal flux ψ_T as

$$\psi_T \equiv \frac{1}{2\pi} \oint d^3\vec{x}\, \vec{B} \cdot \nabla\phi \quad , \tag{12}$$

then the safety factor $q(\psi)$ is given by

$$q(\psi) = \frac{d\psi_T}{d\psi}$$

$$= R_o B_o g(\psi) \oint \frac{d\ell}{x|\nabla\psi|} \quad . \tag{13}$$

The volume average plasma pressure is

$$\overline{P} = \frac{\int P \frac{dV}{d\psi} d\psi}{\int \frac{dV}{d\psi} d\psi} \, . \tag{14}$$

The toroidal-β of the system is defined as

$$\beta_T = \frac{\overline{P}}{\frac{1}{2\mu_o} \overline{B_T^2}} \quad , \tag{15}$$

where $\overline{B}_T^2 = R_o^2 B_o^2 \int g(\psi) \langle \frac{1}{x^2} \rangle \, dV$. For any quantity A, its flux surface average value is given by

$$\langle A \rangle = \frac{\oint \frac{xA(\psi) d\ell}{|\nabla\psi|}}{\oint \frac{x\, d\ell}{|\nabla\psi|}} \quad . \tag{16}$$

The poloidal β is written as

$$\beta_p = \frac{\overline{P}}{\frac{1}{2\mu_o} \overline{B}_p^2} \quad , \tag{17}$$

where $\overline{B}_p^2 = \int \langle (\frac{|\nabla\psi|}{2\pi x})^2 \rangle \, dV$. Following Zakharov and Shafranov,[7] another definition of poloidal-β (for non-circular cross section tokamaks) is

$$\overline{\beta}_p = \frac{\overline{P}}{\overline{P} - \frac{R_o^2 B_o^2}{2\mu_o} \int V(\psi) g(\psi) \frac{dg}{d\psi} \langle \frac{1}{x^2} \rangle \, d\psi} \quad . \tag{18}$$

The stability of the plasma with respect to the rigid motions of the plasma column, ideal and resistive MHD modes will be considered in the next section. The MHD stability criteria are obtained by using the energy principle with or without plasma resistivity[3,4] included.

IV-B-2-b-i. Rigid Motions

First we consider rigid displacements of the plasma. The stabilizing force tending to bring the plasma column back to its original equilibrium position requires[8]

$$\frac{\partial}{\partial R}\,(B_R R)\;R=R_o > 0$$

for stability against horizontal displacements and

$$\frac{\partial B_R}{\partial z} < 0$$

for vertical motions. Using $\nabla x\vec{B} = 0$, the stability condition is obtained and related to the sign and magnitude of

$$0 \lesssim N \lesssim 3/2\ , \tag{19}$$

where $N = -\frac{R}{B_z}\frac{dB_z}{dR}\Big|_{R=R_o}$. The positive value of the decay index assures stability against the vertical displacement. On the other hand, the decay index must not exceed 3/2 for horizontal stability. If the plasma cross section is noncircular, vertical stability is more difficult to obtain. Zakharov[9] shows that for a small elongated plasma with flat current profile the relation between decay index and elongation ratio (b/a) is

$$\frac{b}{a} = 1 + \left(\frac{a}{R_o}\right)^2 \left(\frac{3}{4}\,\ell n\left(\frac{8R_o}{a}\right) - \frac{17}{16}\right)$$

$$- N\left(\ell n\left(\frac{8R_o}{a}\right) + \beta_p - \frac{5}{4}\right)\ . \tag{20}$$

Thus, for vertical stability, the elongation must satisfy

$$\frac{b}{a} - 1 < \left(\frac{a}{R_o}\right)^2 \left(\frac{3}{4}\,\ell n\,\left(\frac{8R_o}{a}\right) - \frac{17}{16}\right)\ .$$

For moderate aspect ratio tokamaks, such as R_o = 5m and minor radius a = 1.25 m, a stable configuration can be obtained only if

$$\frac{b}{a} \lesssim 1.1\ .$$

A recent paper by Haas[10] et al. indicates that for an arbitrary cross section, aspect ratio toroidal plasma, the system will be unstable if the decay index is negative and the toroidal current decreases monotonically towards

the boundary. Therefore, additional feedback stabilization systems are required for such devices.

IV-B-2-b-ii. Ideal MHD Modes

(1) Kink Modes

The most important MHD instabilities are non-local, helical-type kink modes. They are characterized by a displacement of the form $\xi(r)\exp(i(m\theta-n\phi))$, with integral numbers for m and n (these are the poloidal and toroidal mode numbers, respectively). If a kink perturbation develops, the lines of force B_p are packed together on the concave side of a tokamak. Therefore, the magnetic pressure will increase there and further push the plasma column, causing a larger distortion on the weaker B_p sides. However, if the tension of the field lines (due to B_T) is strong enough to counter the effect of the kink distortion of the field lines (due to B_p), the kink modes can be stabilized. In circular cross section tokamaks, if the safety factor $q > 1$, all "m" modes are stabilized; this is the well-known Kruskal-Shafranov limit.[11] This places an upper limit on the plasma current. The critical q value of stability is found to be larger for noncircular cross section tokamaks.

(2) Ideal Interchange Modes

The localized internal or interchange modes are driven by plasma pressure gradients. In the singular layer near the rational surfaces ($\vec{K} \cdot \vec{B} = 0$ or $q(r_s) = m/n$), the pressure driving displacements can "interchange" with the magnetic field lines without bending them. In toroidal systems, the relevant stability condition is called the Mercier criterion[5]

$$(-\frac{dP}{dr})\ (q^2 - 1) + \frac{rB_\phi^2}{8}\ (\frac{dq/dr}{q})^2 > 0\ . \qquad (21)$$

The negative pressure gradient is destabilizing and the second term is stabilizing by the influence of magnetic shear effects. However, the stability condition has a more complicated form for general noncircular tokamaks[4]

$$DI = D + H - \frac{1}{4} < 0\ , \qquad (22)$$

where

$$D = \left\langle \frac{B^2}{|\nabla\psi|^2} \right\rangle \frac{P'V'}{(q')^2} \left(\frac{2\pi R_o g q'}{\langle B^2 \rangle} - V'' + 4\pi^2 P'V' \left\langle \frac{X^2}{|\nabla\psi|^2} \right\rangle \right)$$

$$- \left(\frac{P'V'}{q'} \right)^2 (2\pi R_o g)^2 \left\langle \frac{1}{|\nabla\psi|^2} \right\rangle , \qquad (23)$$

and

$$H = - \frac{2\pi R_o g P'V'}{q'} \left(\frac{1}{\langle B^2 \rangle} \left\langle \frac{B^2}{|\nabla\psi|^2} \right\rangle - \left\langle \frac{1}{|\nabla\psi|^2} \right\rangle \right) \qquad (24)$$

where the prime of a quantity denotes its derivative with respect to the flux function ψ. H is small for highly symmetric devices, such as circular tokamaks, and can be small for high shear systems also. The shear term $-\frac{1}{4}$ in Eq. (22) has an important contribution to the stabilization of interchange modes.

IV-B-2-b-iii. Resistive MHD Modes

(1) Resistive Interchange Modes

If the plasma has finite resistivity, the stabilizing effect of magnetic shear in ideal modes vanishes. The stability condition is modified as[4]

$$DR = D + H^2 < 0 . \qquad (25)$$

Since $DR = DI + (H - \frac{1}{2})^2$, the resistive interchange modes are more stringent than the ideal interchange modes. The effect of non-vanishing H is always destabilizing. When $DR > 0$, the growth rate scales as $\eta^{1/3}$, where η is the resistivity of the plasma; this is the gravitational mode in the study of the resistive sheet-pinch by Furth et al.[12]

(2) Tearing Modes

Unlike the ideal MHD instabilities where the field lines must remain separate during perturbations, the resistive plasma can form "magnetic islands" in a narrow region close to the rational surfaces by linking up these field lines. These resistive kink modes are called tearing modes. In the high collisional limit, $\nu > \omega$, where ν is the Coulomb collisional frequency and

ω is the mode frequency, and the modified Ohm's law is

$$\vec{E} + \frac{1}{c} \vec{v} \times \vec{B} = \eta \vec{J} \ . \tag{26}$$

Combining Eq. (26) with Maxwell's equations, we obtain the following relation

$$\frac{\partial \vec{B}}{\partial t} = \frac{c^2}{4\pi} \eta \nabla^2 \vec{B} + \nabla \times (\vec{v} \times \vec{B}) \ . \tag{27}$$

Linearization of Eq. (27) gives

$$\frac{\partial \vec{B}}{\partial t} = \frac{c^2}{4\pi} \eta \nabla^2 \vec{B} + ik_{\parallel} B_o \vec{v}_r \ , \tag{28}$$

where $\vec{v}_r$ is the perturbed radial velocity and $k_{\parallel} \cong \frac{1}{qR} (m - nq)$ in a tokamak. The resistive term ($\sim \eta \nabla^2 B$) is negligibly small compared to the second term ($\sim \vec{k} \cdot \vec{B}$) except in the narrow layer close to a rational surface where $\vec{k} \cdot \vec{B} \cong 0$. Therefore, it is appropriate to use the ideal MHD condition in the regions outside the resistive layer.

The tearing modes are unstable if DR=0 and Δ>0, where Δ is computed from matching the solutions of the MHD equation inside the resistive layer to the solutions in the ideal region on both sides of it.[12] The growth rate can be scaled as a power of the resistivity: $\eta^{(3-2H)/(5+2H)}$. If H = 1/2, the growth rate scales as $\eta^{1/3}$, which is similar to the interchange mode. When H=0, the growth rate scales as $\eta^{3/5}$; this recovers the usual tearing mode scaling.[12] Numerical calculations show that stable zones should occur if the safety factor at the plasma edge is greater than 2.5.[13]

(3) Modified Tearing Modes

When DR < 0, the unstable modified tearing modes appear with complex frequencies if

$$\Delta > \Delta_c \ , \tag{29}$$

where Δ_c is defined in Eq. (111) of Reference 4. As $H \simeq 1/2$, Δ_c approaches infinity; therefore, the mode is stable. Generally $\Delta \sim \eta^{(2H-1)/3}$; in a typical tokamak scaling, we have $1/2 \gtrsim H \gtrsim 0$. This indicates that high temperature will stabilize the modified-tearing modes.

IV-B-2-b-iv. β-Limits and Ballooning Modes

Tokamak devices always have some pressure limits either in the form of β_T or β_p. One widely used upper limit of the permissible β_p at equilibrium is that it cannot exceed the aspect ratio. At this Shafranov limit,[14] the separatrix will coincide with the plasma column boundary. If the plasma β_p is larger than the Shafranov limit, then the localized "ballooning" modes will appear. In the study of ballooning modes in the neighborhood of the magnetic axis, it is found that the stability condition for these modes is just the same as that for the localized interchange modes.[15] Consequently, there is no limit on β as long as localized modes are stable. However, using the collisionless energy principle, Rutherford et al. obtained a more general form of the β-limit to the ballooning instabilities as[16]

$$\beta < \beta_c = \frac{0.18\ a}{R_o\ q_a^{0.75}\ q_o^{1.25}} \left(1 + 0.2\ \left(\frac{a}{R_o}\right)^{3/2}\right) . \qquad (30)$$

The value of this β_c is only a few percent. Numerical studies show that the value of β_c is about 5%[17] for a D-shaped plasma, and can reach 12%[18] by proper choice of the pressure and current profiles. Generally, the critical-β value of tokamaks increases with vertical elongation but decreases with larger triangularity.[19]

IV-B-3. Results for NUWMAK

The cross-sectional view of NUWMAK is shown in Fig. IV-B-1. There are only 4 pairs of EF coils required to provide plasma equilibrium and shaping effects. The location of these coils and their currents are listed in Table IV-B-1. The 4 demountable cryogenic Al coils are located inside the toroidal field (TF) coils. The other larger 4 superconducting coils are situated outside the TF coil set; they can be moved freely when necessary. There are several advantages for some coils placed inside the TF coils. Since they are closer to the plasma column, the required currents are found to be much smaller than that of outside coils and they still can provide

CROSS SECTION OF NUWMAK THROUGH A TF COIL (with outer RF cavity)

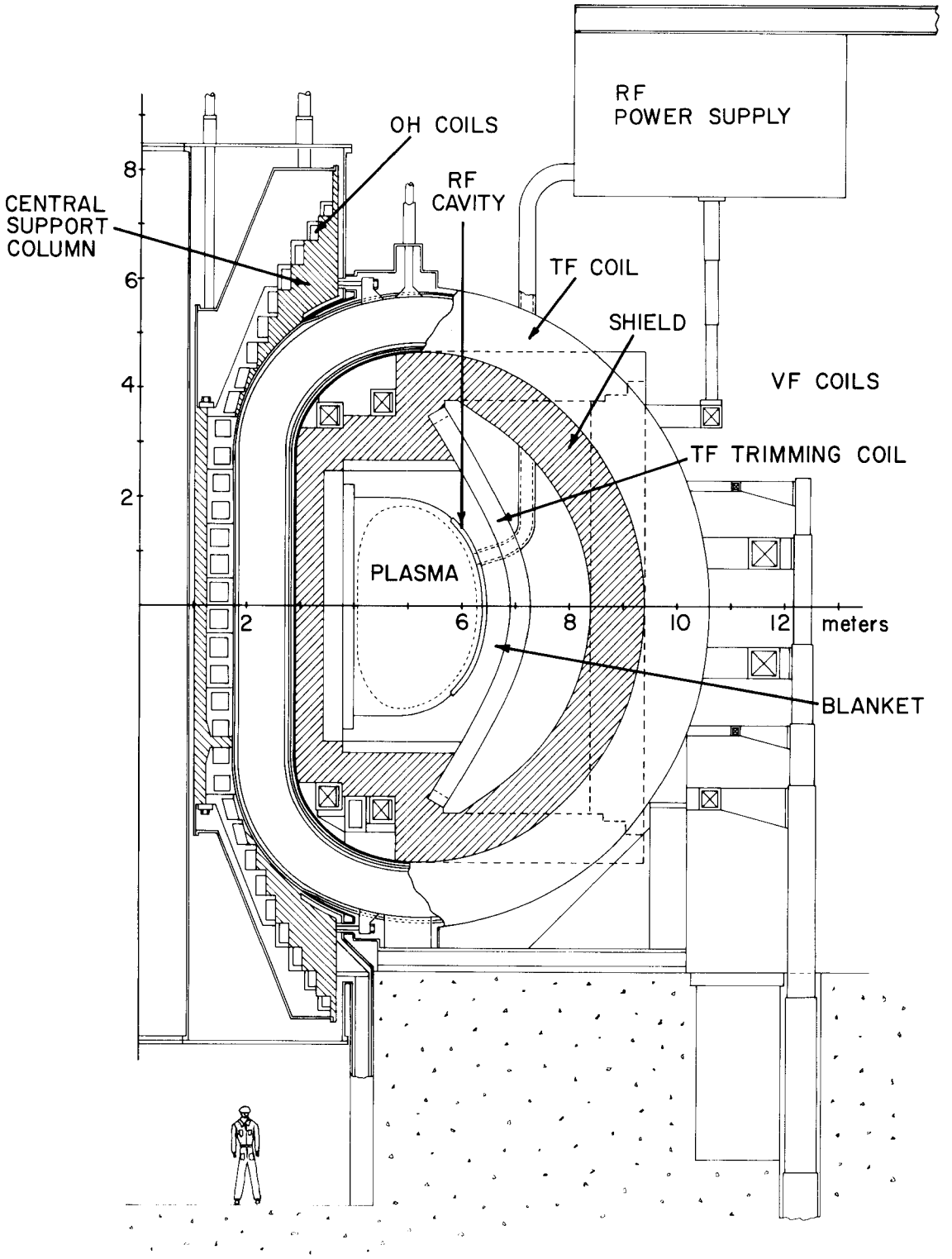


Fig. IV-B-1

TABLE IV-B-1. Equilibrium Field Coils of NUWMAK

	Z(m)	R(m)	I(MA)
1.	± 3.50	3.50	2.30
2.	± 3.75	4.50	2.00
3.	± 3.50	10.50	-2.00
4.	± 1.00	11.50	-3.50

the same effect on equilibrium and shaping. These cryogenic coils are demountable; consequently, they will not interlock with the TF coil set. Furthermore, they can save space for the Ohmic Heating (OH) coils and support structure. The available space problem can be an important issue, especially when the aspect ratio is small and when the device is compact.

Table IV-B-2 lists the plasma parameters and power density of NUWMAK. The plasma current is 7.2 MA, the major radius is about 5.13 m with minor radius a = 1.13 m and elongation ratio about 1.64. The on-axis toroidal magnetic field is 6.05 Tesla, the toroidal β about 6%, the poloidal β is 3.67 and the safety factor at the magnetic axis and plasma edge is 1.09 and 2.63, respectively. The neutron wall loading in this system is about 4.3 MW/m^2 while the plasma power density is 10.1 MW/m^3. It should also be noted that the decay index is -1.13; therefore, a feedback stabilization system is required for vertical stability. Figure IV-B-2 shows the flux surface plot. As can be seen, the plasma has a vertically elongated cross section and there are two stagnation points located outside the plasma boundary. The pressure and current profiles as a function of radius on the midplane are shown in Fig. IV-B-3. It is interesting to note that the magnetic axis is shifted about 0.18 m from the plasma geometric center, while the position of peaked current is shifted about 0.47 m further away from the magnetic axis.

The contour plot of toroidal current density is shown in Fig. IV-B-4 while the perspective views of the toroidal current density and pressure profiles are presented in Fig. IV-B-5 and IV-B-6, respectively. The toroidal magnetic field as a function of radial position with and without plasma is shown by Fig. IV-B-7. The presence of plasma reduces the strength of the toroidal magnetic field within the plasma column. The maximum diamagnetic effect is about 5% for NUWMAK. Figure IV-B-8 indicates the $|B|$ surfaces in NUWMAK. The heavy closed line shows the plasma boundary. The diamagnetic effects dominate inside the plasma while the poloidal effect due to plasma current is important at the outside edge as seen from the direction of curvature of the $|B|$ contours. Fig. IV-B-8 also provides useful information for the RF antenna design. This figure indicates that the second harmonic ion cyclotron resonance surface corresponding to a magnetic field of 6 Tesla does not intersect the RF launching cavity (Ch. V) so that breakdown due to anomalous acceleration of ions can be avoided.

TABLE IV-B-2. Plasma Parameters of NUWMAK

Plasma current	I_p = 7.2 MA
Toroidal field	B_o = 6.05 T
Major radius	R_o = 5.125 m
Minor radius	a = 1.125 m
Elongation	b/a = 1.64
Aspect ratio	R_o/a = 4.55
Toroidal β	β_T = 6%
Poloidal β	β_p = 3.67
Average poloidal β	$\bar{\beta}$ = 2.56
Safety factor (center)	q(o) = 1.09
Safety factor (edge)	q(a) = 2.63
Decay index	N = -1.13
Average power density	$\bar{P}$ = 10.1 MW/m^3
Neutron wall loading	W_d = 4.34 MW/m^2

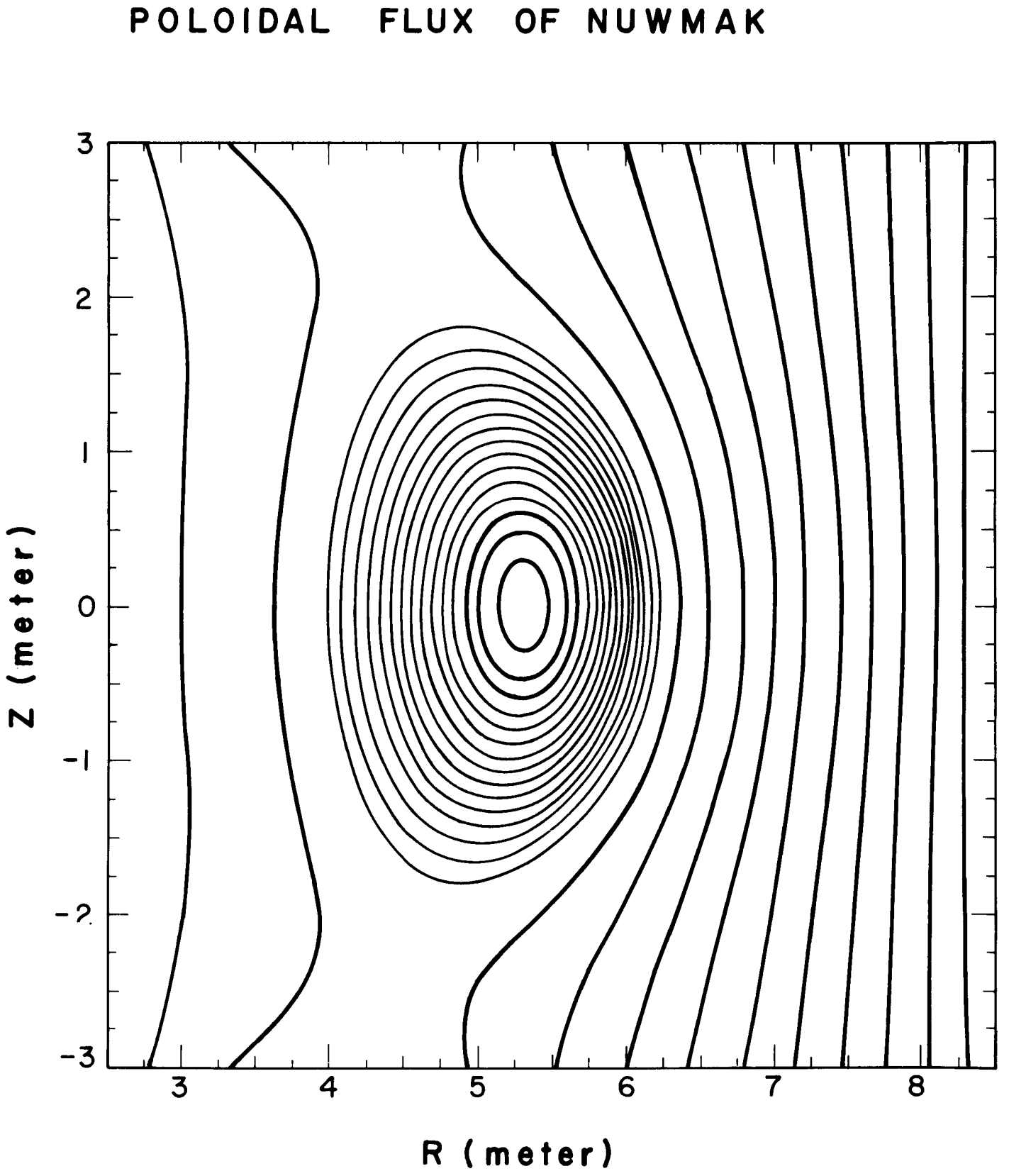


Figure IV-B-2 Flux Surfaces ψ in NUWMAK

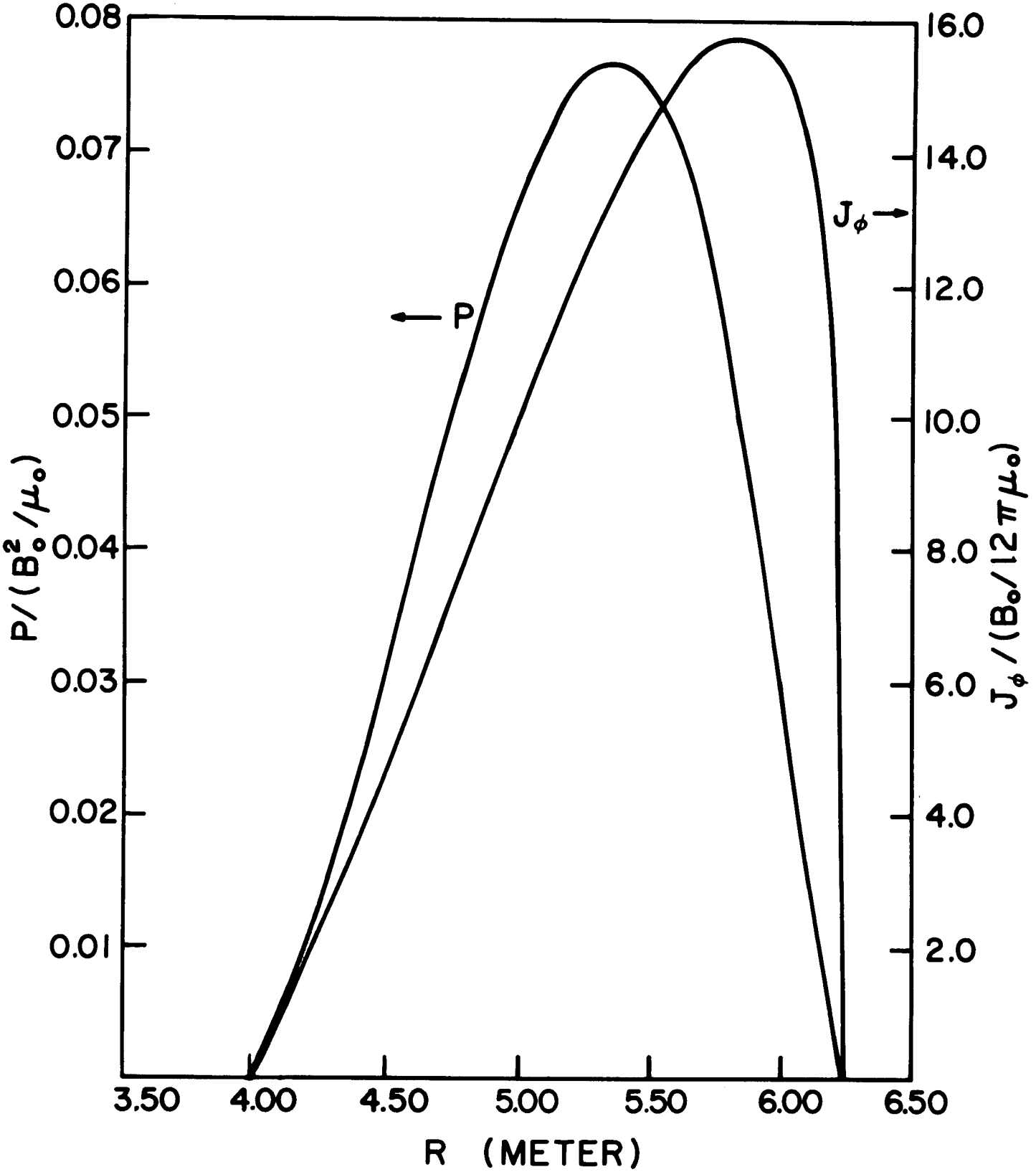


Figure IV-B-3 Pressure and Toroidal Current Profiles in the Mid-Plane

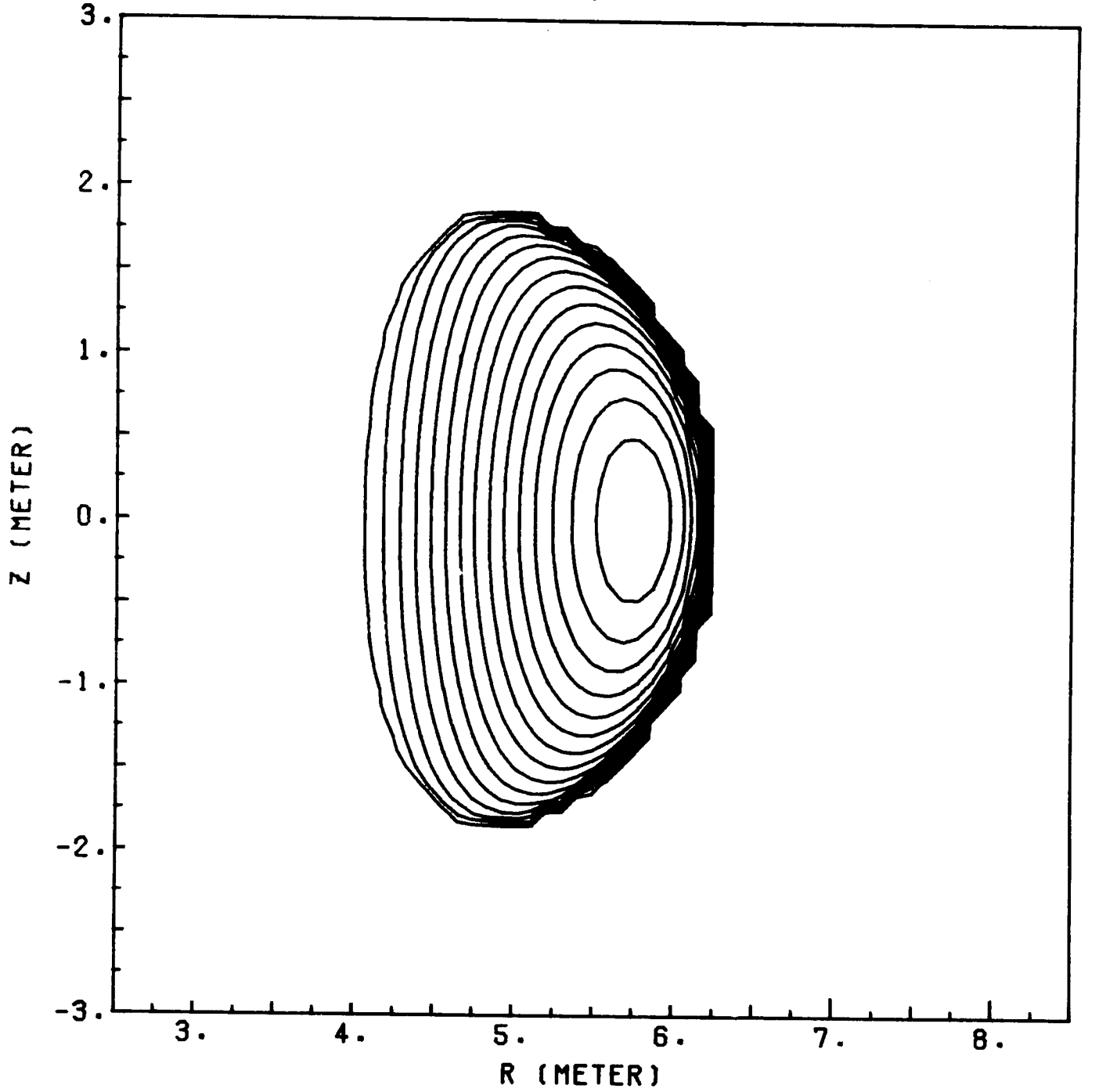


Fig. IV-B-4. Toroidal Current

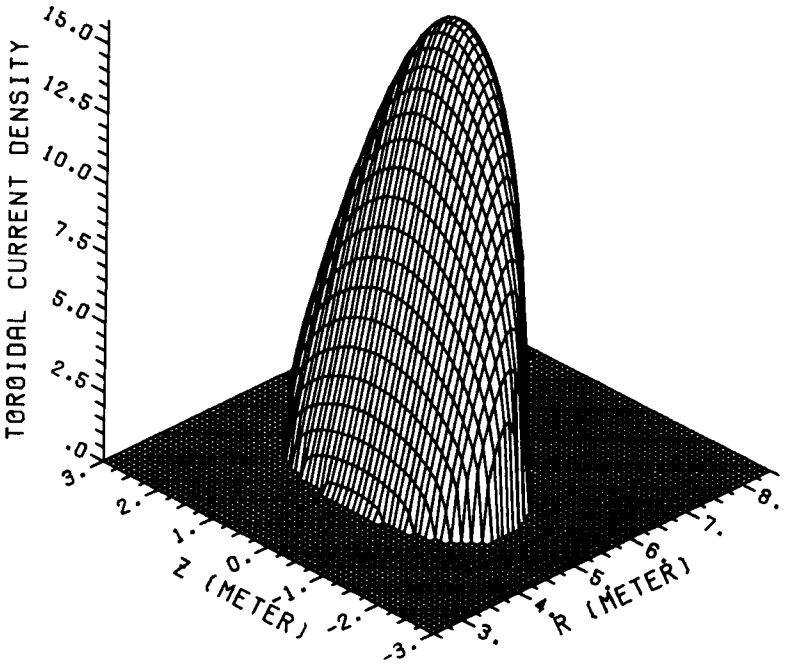


Fig. IV-B-5. Perspective View of Toroidal Current Density

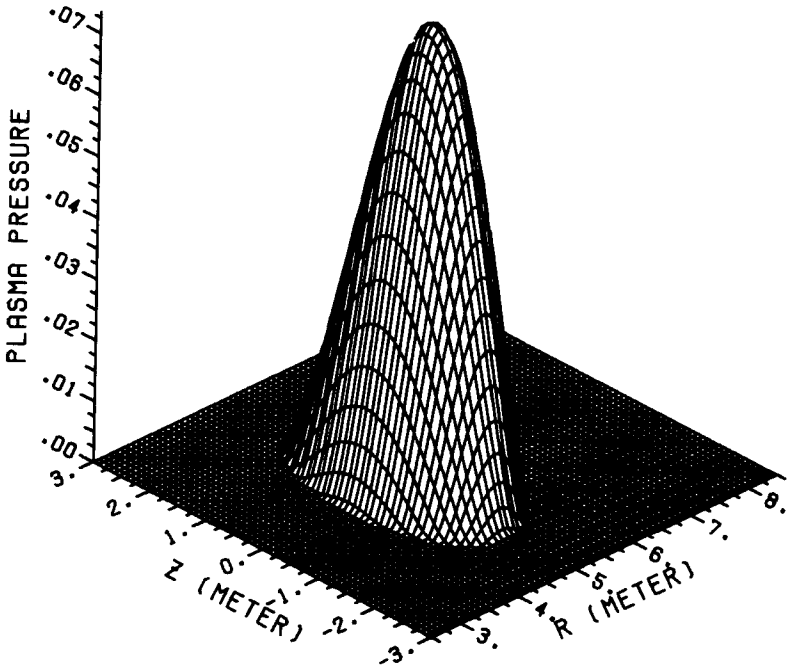


Fig. IV-B-6. Perspective View of Pressure Profile

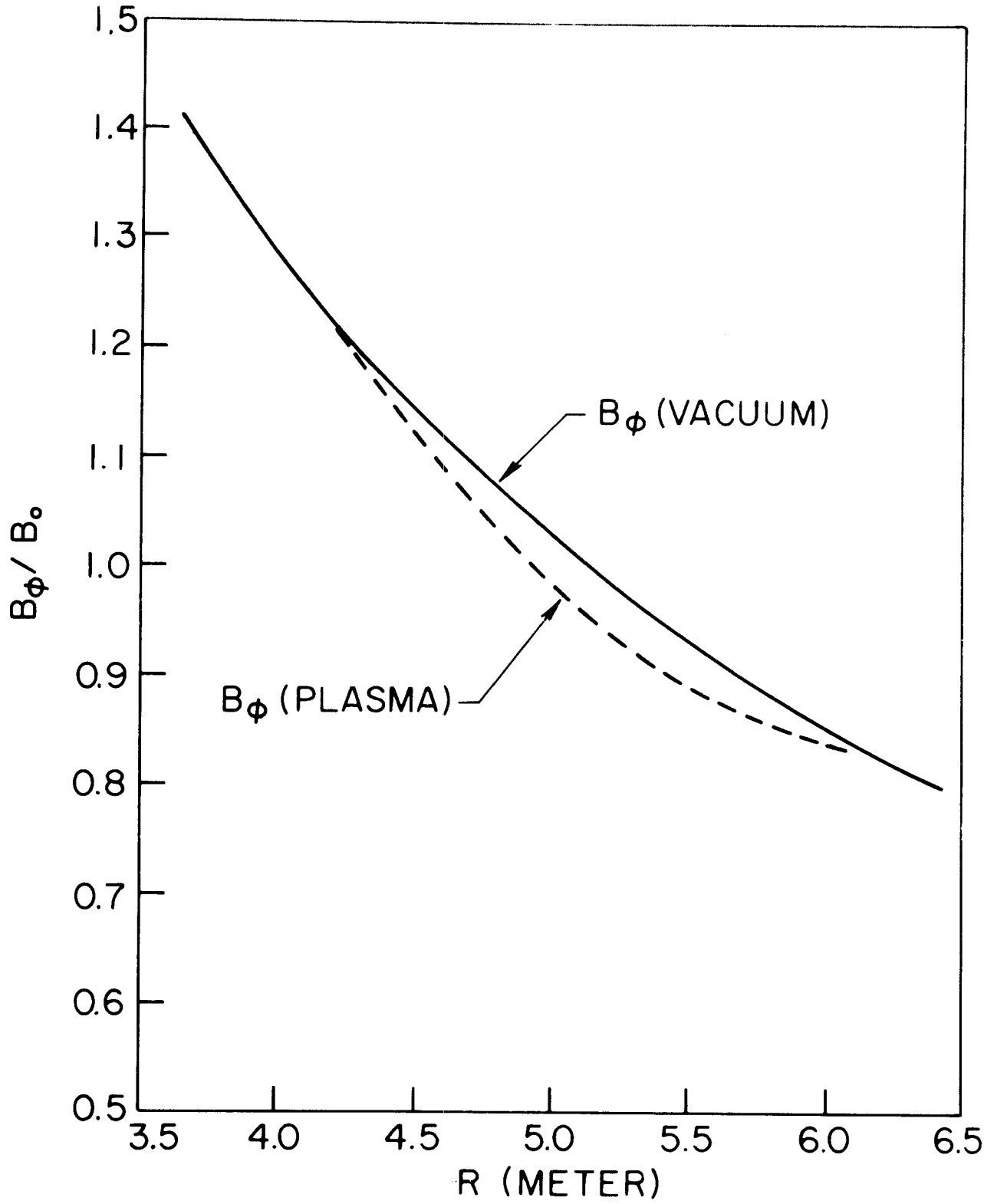


Fig. IV-B-7. Toroidal Magnetic Field

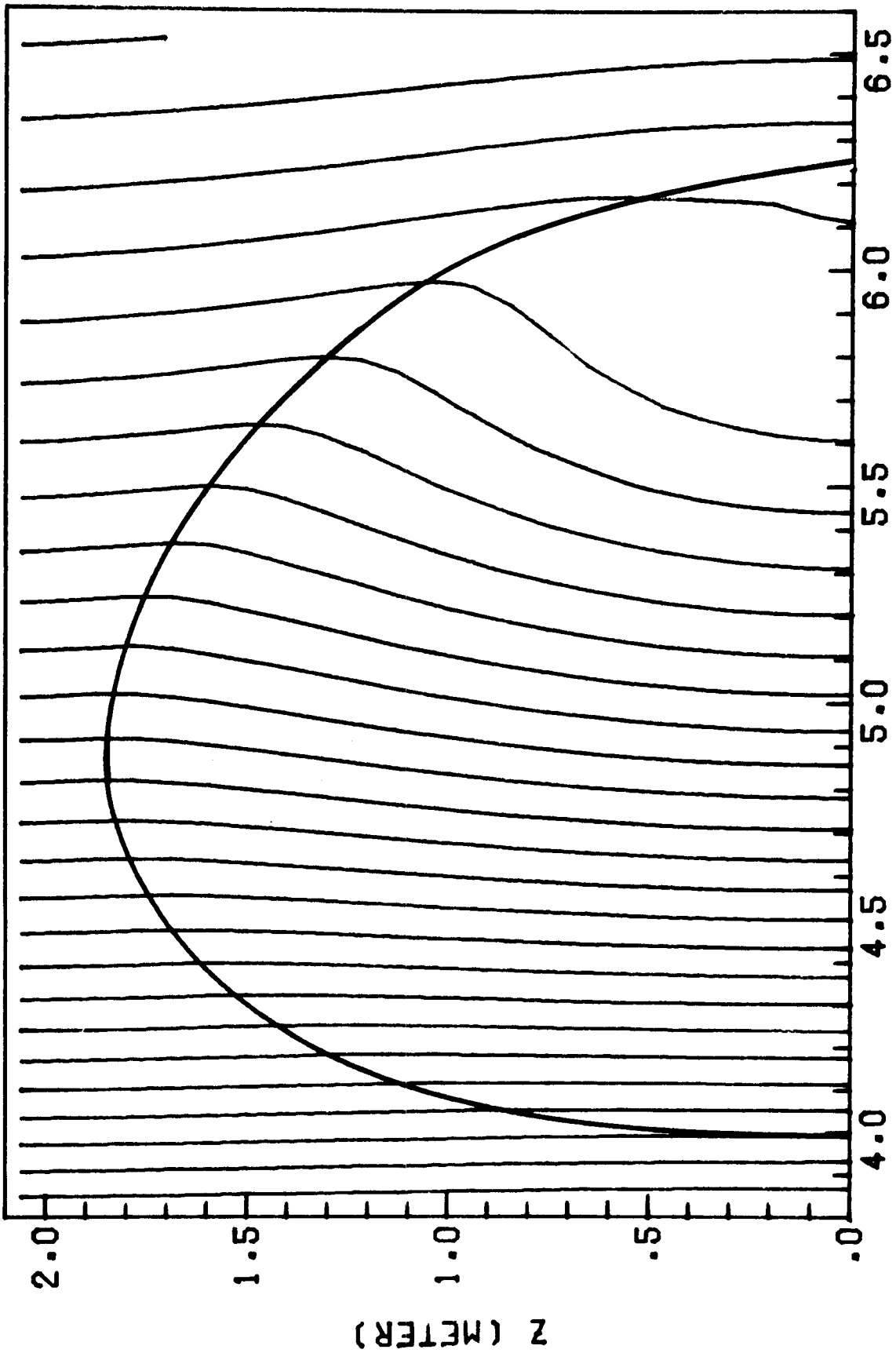


Fig. IV-B-8. Plot of Constant |B| Surfaces. The Heavy Closed Line Indicates the Plasma Boundary

Two important parameters H and D for the MHD stability analysis are shown in Fig. IV-B-9 as a function of ψ. The minimum ψ is about -0.30; this corresponds to the location of the magnetic axis. The ψ value at the plasma edge is -0.18. The profiles of DI (ideal interchange), DR (resistive interchange) and q are shown in Fig. IV-B-10. We see that both ideal and resistive interchanges are stable in NUWMAK. Since DR < 0 and H > 0 everywhere, the tearing mode is stabilized. On the other hand, the modified tearing modes are stabilized due to small positive values of H ($0.2 \lesssim H \lesssim 0.4$), and the high temperature of the plasma. The safety factor at plasma edge is about 2.63; this can ensure the stability of general kink modes in this system.

Although Eq. (27) gives a value for β_c of about 2% for NUWMAK parameters, this analytical criterion is good for circular tokamaks only. As indicated earlier, D-shaped plasmas can have a higher β-limit; for the moderate value of β_T($\sim$ 6%), and since β_p($\sim$ 3.67) is still below the Shafranov limit ($\sim$ 4.54), it appears that ballooning modes are stable in NUWMAK.

IV-B-4. Feedback Stabilization System

As discussed in the previous section, the plasma is unstable with respect to a displacement in the vertical direction. Consequently, a feedback stabilization system is required to keep the plasma at its proper position. The feedback system detects a displacement of the plasma and applies a restoring force to cause the plasma to return to its equilibrium position. The restoring force is generated by a radial magnetic field; this produces a Lorentz force, $\vec{J} \times \vec{B}$, in the vertical direction.

An analysis of linear feedback stabilization of the vertical position was presented in the TETR report.[20] This analysis included the effect of eddy currents in a "thin" shell surrounding the plasma. These eddy currents have two effects. First, they reduce the growth rate of the instability by adding "viscous damping" to the system. This is because the eddy currents, which also cause a restoring force, are proportional to the rate of change of the plasma position. Second, they also reduce the radial magnetic field generated by the feedback system. This is also a velocity effect. This analysis can be applied directly to NUWMAK, where the shell is the lithium-lead blanket

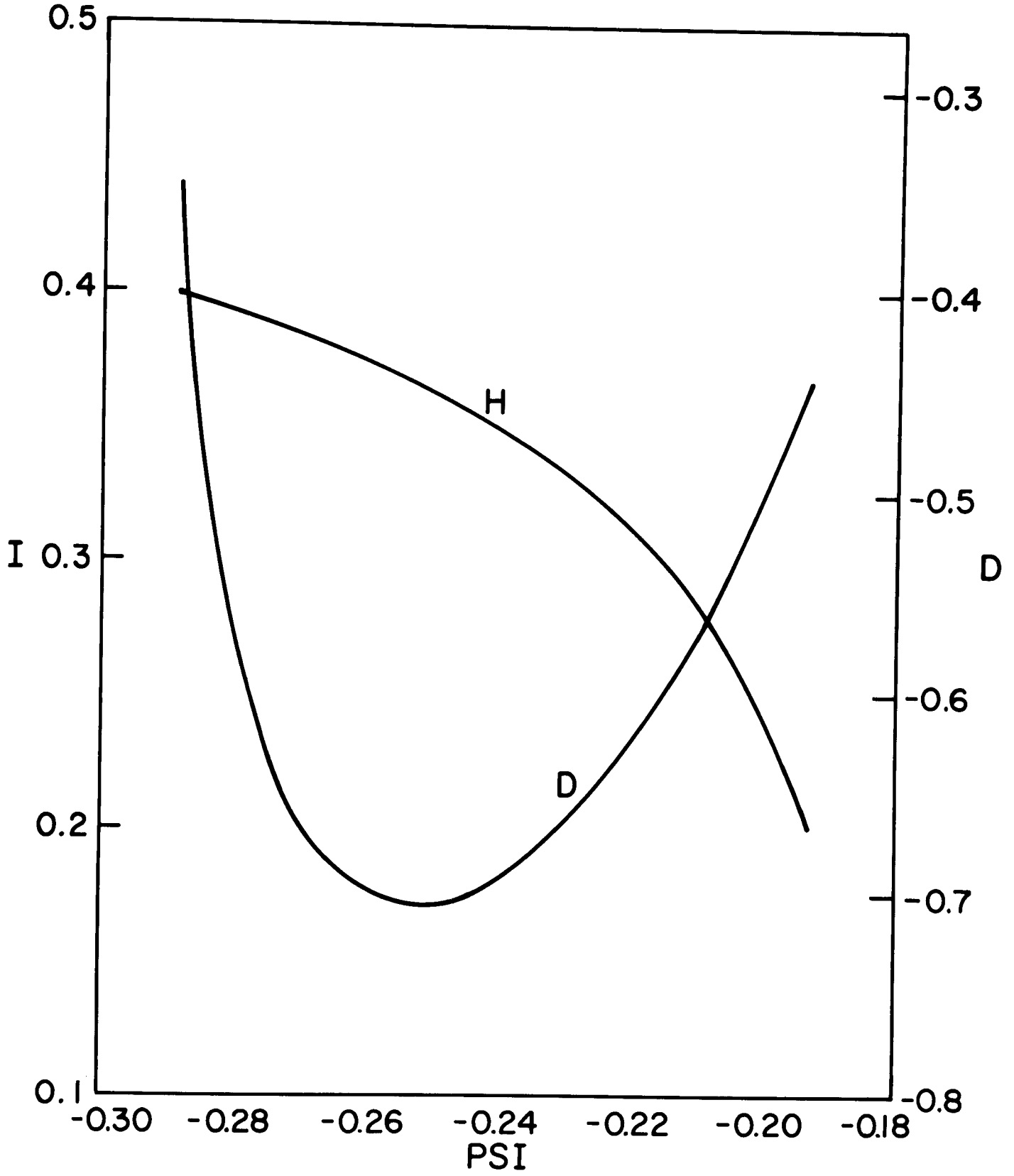


Figure IV-B-9 Parameters H and D as Functions of ψ

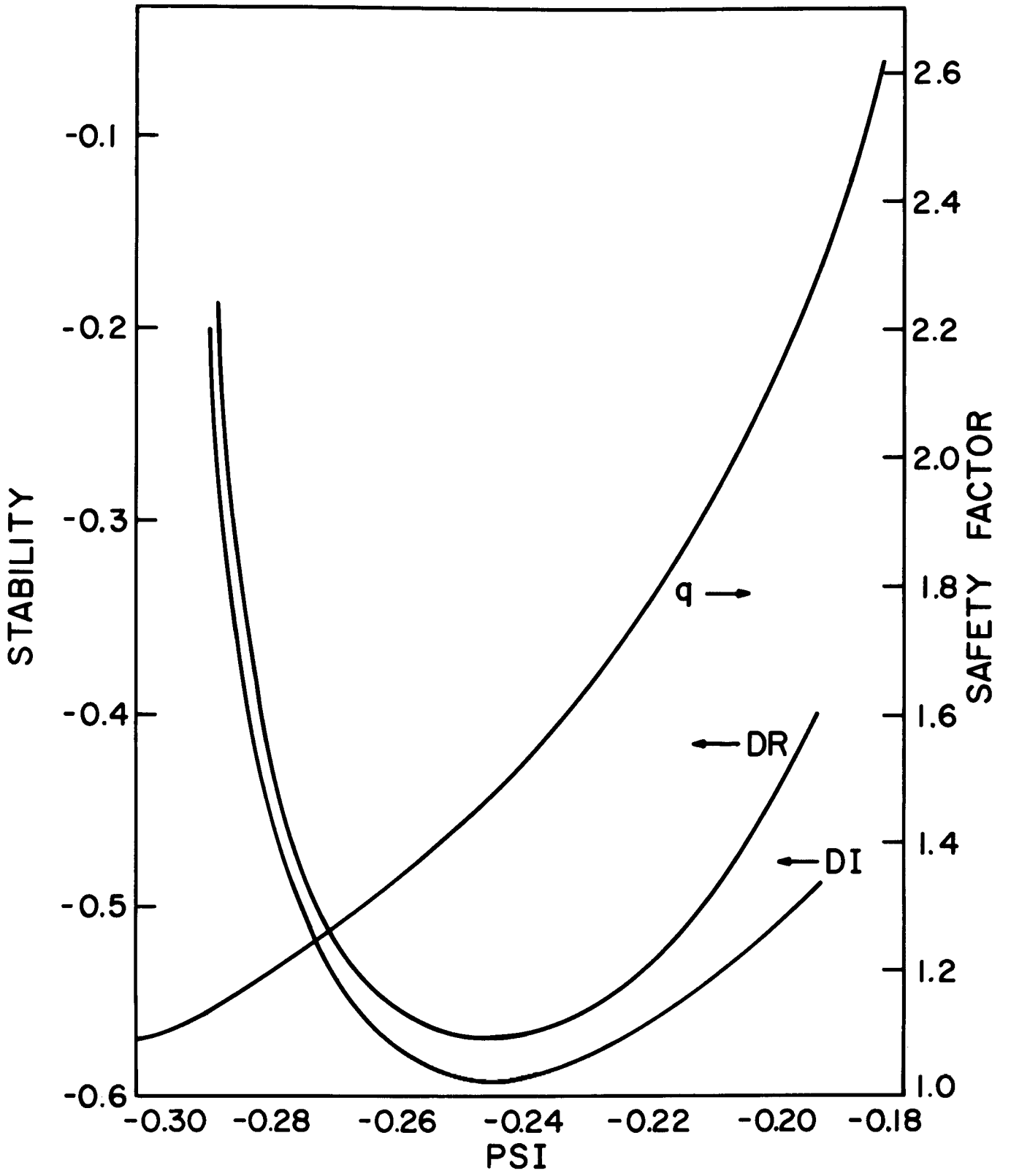


Figure IV-B-10 Stability Criteria DI, DR and Safety Factor q as Functions of ψ

surrounding the plasma. This blanket is 40 cm thick and only marginally satisfies the thin shell approximation (shell thickness less than the skin depth). Nevertheless, the estimates for the time constants and feedback system requirements ought not be seriously in error.

Frantz, Chao, and Yang[21] have given an analysis of the degree of passive stabilization caused by changes in the poloidal field coil currents as the plasma moves. For the ORNL-TNS this effect was substantial.[21] A similar analysis has been done for NUWMAK; in our case, however, the effect is small since there are considerably fewer coils and they are farther from the plasma.

The physical parameters used in the feedback calculations are listed in Table IV-B-3 and the results of the feedback system analysis are listed in Table IV-B-4. We see that the growth time is quite long, much slower than in TETR. This is because of the large amount of conducting material surrounding the plasma. Because of the reduced growth rate, the required power for the feedback amplifiers is correspondingly reduced. The power shown is based on an initial displacement of 3 cm before the feedback system begins to respond. The relevant initial displacement is based on the resolution of the sensor system; one will need to do better than this since there is only 10 cm between the plasma and the wall at the top and bottom of the plasma. During this design transient, the plasma will move 4.2 cm from its equilibrium position.

The radial magnetic field of the feedback system can be obtained by a small change in the currents in the EF coils inside the toroidal field magnets and in the trim coils. For example, the ΔI values shown in Table IV-B-5 produce a radial magnetic field of 80 Gauss. Alternate trim coils have $\pm \Delta I$ current change, as shown schematically in Fig. IV-B-11. This is equivalent to continuous poloidal field coil carrying current ΔI at the position of the top leg of the trim coil and another continuous poloidal field coil carrying current $-\Delta I$ at the position of the bottom leg. This system simplifies the structural design since it does not introduce physically different coils. The current change in the coils ($\sim$ 50 kA during an extreme

TABLE IV-B-3 NUWMAK - Physical Parameters

Plasma Current, I	7.2×10^6 A
Major Radius, R	5.13 m
Cross-Sectional Area, a	5.82 m^2
Vertical Field, B_z	5.6 kG
Decay Index, n_r	-1.13
Average Density, $\bar{n}$	2×10^{14} cm^{-3}
Ion Mass	4.2×10^{-27} kg
Wall Radius, ρ_w	2 m
Wall Thickness, δ	40 cm
Wall Conductivity, σ	1.6×10^6 mho/m

TABLE IV-B-4. Feedback Parameters - NUWMAK

Growth Rate - No shell, γ_o	4.3×10^5 sec^{-1}
Growth Rate With Shell	.65 sec^{-1}
β (L/R Time Constant of Shell)	.80 sec
Skin Time ($1/2\ \mu_o \sigma\ \delta^2$)	.16 sec
Minimum Gain for Stabilization	12.5 Gauss/cm
Design Gain	19.2 Gauss/cm
Maximum Allowable Delay Time	.74 sec
Design Delay Time	.50 sec
Required Power @ $\varepsilon(0)$ = 3 cm	250 kW
Maximum Excursion for $\varepsilon(0)$ = 3 cm	4.2 cm

TABLE IV-B-5 Feedback Currents

Coil	I (nominal), MA	ΔI^*, amps
EF	2.30	41×10^3
EF	2.30	-41×10^3
EF	2.00	49×10^3
EF	2.00	-49×10^3
Trim	.40	$\pm 33 \times 10^3$

*These correspond to the maximum ΔI during a transient starting from a 3 cm initial displacement.

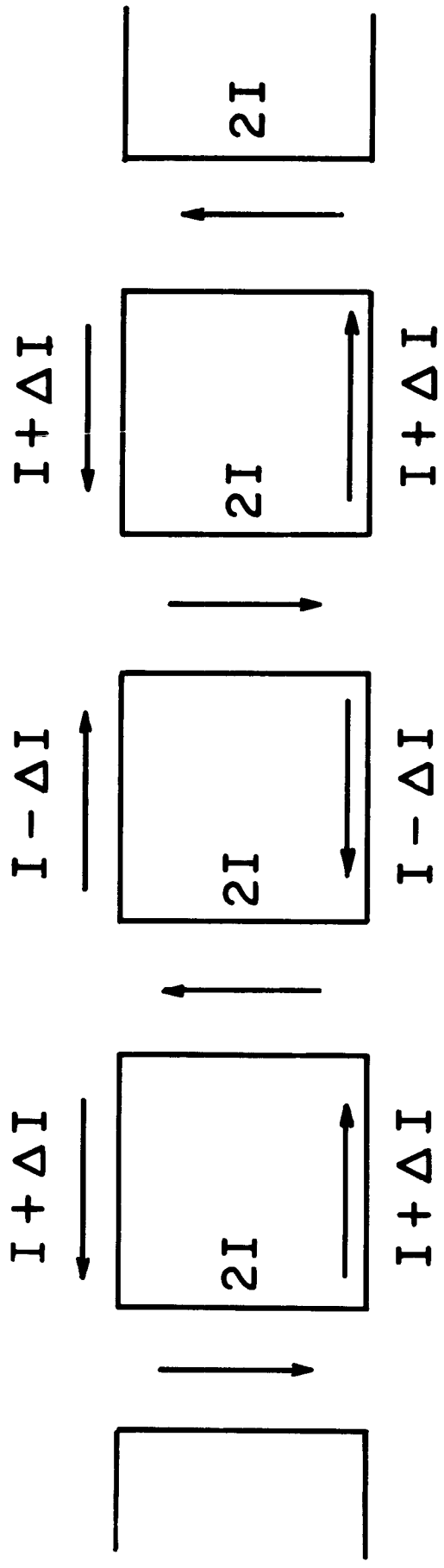


Fig. IV-B-11
Current Flow in Trim Coils

transient) is a small percentage of the steady-state current carried by these coils.

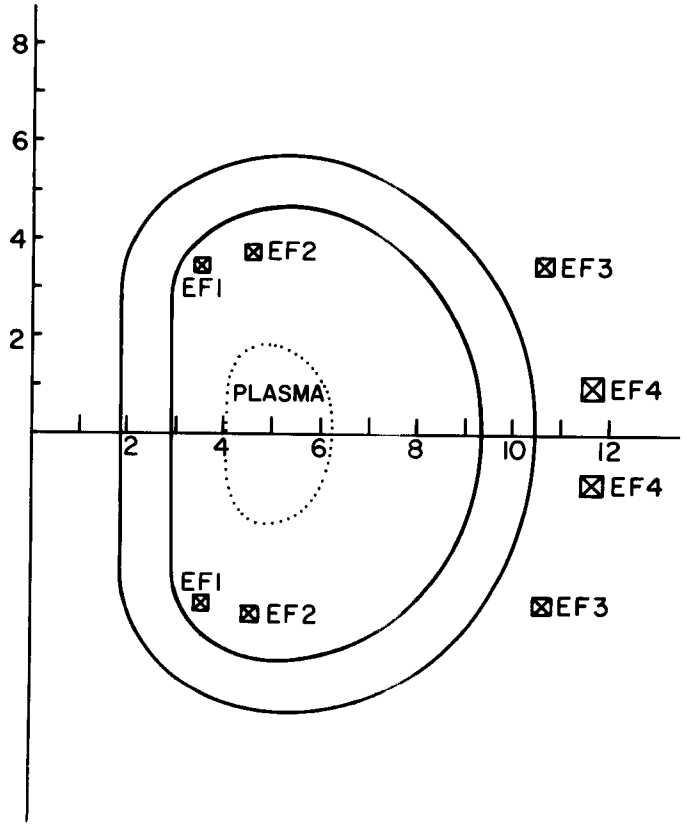
The role of the feedback amplifiers can be fulfilled by the Gratz bridges used to power the coils during startup and burn. The dI/dt due to the feedback circuit responding to a displacement of the plasma is less than the nominal dI/dt during startup. This requires that the coils be divided into 6 independent circuits, each with its own bridge. By controlling the commutation angle of these bridges separately, one has a separate control on the vertical and radial fields at the plasma and on the plasma current through the OH system. The division of the coils into these circuits is shown in Table IV-B-6. This feedback system has the advantage that it does not require additional hardware, other than the relatively minor, but very important, position sensors and electronics for controlling the bridges.

IV-B-5. Conclusion

For a reactor design without a divertor such as the NUWMAK system the overall design tends to be simple and serviceable. There are only four pairs of EF coils required for plasma equilibrium and shaping. The MHD modes are found to be stable but a feedback stabilization system is required for vertical stability. This feedback stabilization can be accomplished with only a modest investment in amplifiers and circuitry. The feedback system uses only the coils required for the equilibrium field and the trim coils; additional coils are not required.

TABLE IV-B-6. Poloidal Field Coil Circuits

Circuit	Coils
1	OH coils
2	EF1, EF2 (top)
3	EF1, EF2 (bottom)
4	Trim Coils (1/2)
5	Trim Coils (1/2)
6	EF3, EF4 (top and bottom)



References for Section IV-B

1. M.S. Chance, R.L. Dewar, A.H. Glasser, J.M. Greene, R.C. Grimm, S.C. Jardin, J.L. Johnson, B. Rosen, G.V. Sheffield, K.E. Weimer, Proc. 5th IAEA Conf. on Plasma Phys. and Cont. Nucl. Fus. Research, 1974 (IAEA, Vienna, 1975), Vol. I, p. 463.

2. T.F. Yang and R.W. Conn, UWFDM-152, Nuclear Engineering Department, Univ. of Wisconsin (Nov. 1975).

3. J.M. Greene and J.L. Johnson, Plasma Phys. 10, 729 (1968).

4. A.H. Glasser, J.M. Greene, and J.L. Johnson, Phys. Fluids 18, 875 (1975).

5. A.H. Glasser, J.M. Greene, and J.L. Johnson, Phys. Fluids 19, 567 (1976).

6. J.D. Callen and R.A. Dory, Phys. Fluids 15, 1523 (1972).

7. L.E. Zakharov and V.D. Shafranov, Soviet Physics - Technical Physics 18, 151 (1973).

8. S. Yoshikawa, Phys. Fluids 7, 278 (1964).

9. L.E. Zakharov, Soviet Physics - Technical Physics, 16, 645 (1971).

10. F.A. Haas and J.C.B. Papaloizou, Nucl. Fusion 17, 721 (1977).

11. V.D. Shafranov, Plasma Physics and the Problem of Controlled Thermonuclear Reactions (Pergamon, Oxford, 1969), Vol. 2, p. 197.

12. H.P. Furth, J. Killeen, and M.N. Rosenbluth, Phys. Fluids 6, 459 (1963).

13. H.P. Furth, P.H. Rutherford, and H. Selberg, Phys. Fluids 16, 1054 (1973).

14. L.A. Artsimovich, Nucl. Fusion 12, 215 (1972).

15. G. Laval, E.K. Maschke, and R. Pellat, Phys. Rev. Letters 24, 1229 (1970).

16. P.H. Rutherford, et al., PPPL-1418, Feb. 1978.

17. G. Bateman and Y.-K.M. Peng, Phys. Rev. Letters, 38, 829 (1977).

18. A. Sykes, J.A. Wesson, and S.J. Cox, Phys. Rev. Letters 39, 757 (1977).

19. J.P. Freidberg and W. Grossmann, Phys. Fluids 18, 1494 (1975).

20. B. Badger, et al., "A Near Term Tokamak Engineering and Materials Test Reactor - TETR", Nuclear Engineering Dept. UWFDM-191, University of Wisconsin-Madison, February 1977.

21. E.R. Frantz, Y.A. Chao, T.F. Yang, "Vertical Instability in TNS", ANS Topical Meeting on the Technology of Controlled Nuclear Fusion (May 9-11, 1978, Santa Fe, New Mexico).

IV-C. Startup and Shutdown

The design philosophy of the transformer coils to drive the plasma current during startup, burn and shutdown is similar to previous reports.[1,2] The plasma of the tokamak fusion reactor serves as a single turn secondary of the air core transformer. The startup flux necessary to bring the plasma to full operation current is provided by the transformer (OH) coils and assisted by the vertical field (VF) coils. Once the plasma reaches its full plasma current the currents in the vertical field coils remain constant while those in the transformer coils keep changing to provide the driving force for the constant induced plasma current. Because the plasma impurities, maximum allowable magnetic field and its time rate of change on the superconducting coil can all limit the startup and down time, the reactor is usually operated in a pulsed phase. The startup and burn study for the transformer design has been done using the code supplied by Dalhed.[3] The detailed result of the full reactor cycle is outlined in Table IV-C-1. Some characteristics of the burn cycle are shown in Table IV-C-2. The total flux required for a seven-second startup and 225-second burn is about 84 volt-seconds. The time for reactor shutdown is chosen to be eight seconds while the transformer system requires an additional five seconds for recocking. The overall duty factor of NUWMAK is about 92%.

The locations and currents carried in the transformer coils at different phases are listed in Table IV-C-3. All the transformer currents are proportional to the value of the T1 coil. Fig. IV-C-1 shows the positions of the transformer and vertical field coils in the reactor. The location and size of the vertical field coils can have an important effect on the design of the transformer system. In the case of NUWMAK, there are four VF coils located inside the toroidal field coils rather than outside. For the same effect on the plasma equilibrium inside coils require smaller currents. These VF coils can save important space for the arrangement of the OH coils and support structure, especially when the

Table IV-C-1 Reactor Cycle of NUWMAK

Time (sec)	Phase
0-7	Startup: Plasma and vertical field coil currents rise to full value; transformer currents begin to drop; ohmic heating to raise the plasma temperature to 750 eV, then use RF heating for 2 seconds to bring the plasma to burn conditions.
7-232	Burn: Vertical field currents are kept constant; transformer currents drop to maximum negative value.
232-240	Shutdown: Plasma and vertical field currents drop to zero; transformer currents rise to a certain positive value.
240-245	Recocking: The transformer currents reset to initial values. Pump out the toroidal chamber and then refill with fresh fuel.

Table IV-C-2 Characteristics of Burn Cycle

Time (sec)	I_1 (MA)	B_{max} (1) (T)	$\dot{B}_{max}$ (2) (T/sec)	Power (MW)	Stored Energy (MWHR)
0	2.40	6.92		-595	0.403
7	-1.97	5.68	1.80	1010	0.769
232	-2.87	7.32		-1030	1.044
240	1.50	4.32	1.46	390	0.158
245	2.40	6.92	0.52	217	0.403

(1) B_{max} is the maximum magnetic field measured at the surface of the superconducting transformer coil.

(2) $\dot{B}_{max}$ is the peak time rate of change of the magnetic field measured at the superconducting transformer coil.

Table IV-C-3 Transformer Programming

Coil Number	R (m)	Z* (m)	Initial Current (MA)	Current at End of Start-up (MA)	Current at End of Plasma Burn (MA)
T1	1.46	0.25	2.4000	-1.9700	-2.8700
T2	1.46	0.75	2.3976	-1.9680	-2.8671
T3	1.47	1.25	2.3928	-1.9641	-2.8614
T4	1.48	1.74	2.3808	-1.9542	-2.8470
T5	1.49	2.25	2.3544	-1.9326	-2.8155
T6	1.52	2.75	2.3112	-1.8971	-2.7638
T7	1.56	3.25	2.2416	-1.8400	-2.6806
T8	1.71	3.72	2.1624	-1.7750	-2.5859
T9	1.89	4.19	2.0640	-1.6942	-2.4682
T10	2.07	4.65	1.9248	-1.5800	-2.3017
T11	2.25	5.12	1.8072	-1.4834	-2.1611
T12	2.43	5.59	1.7088	-1.4026	-2.0434
T13	2.68	6.01	1.5024	-1.2333	-1.7966
T14	2.95	6.44	1.2432	-1.0205	-1.4867
T15	3.21	6.86	1.0224	-0.8392	-1.2226
T16	3.48	7.28	0.8400	-0.6895	-1.0045
T17	11.00	2.25	0.1800	-0.1478	-0.2153

*For each coil at location (R,Z), there is a similar coil at (R,-Z).

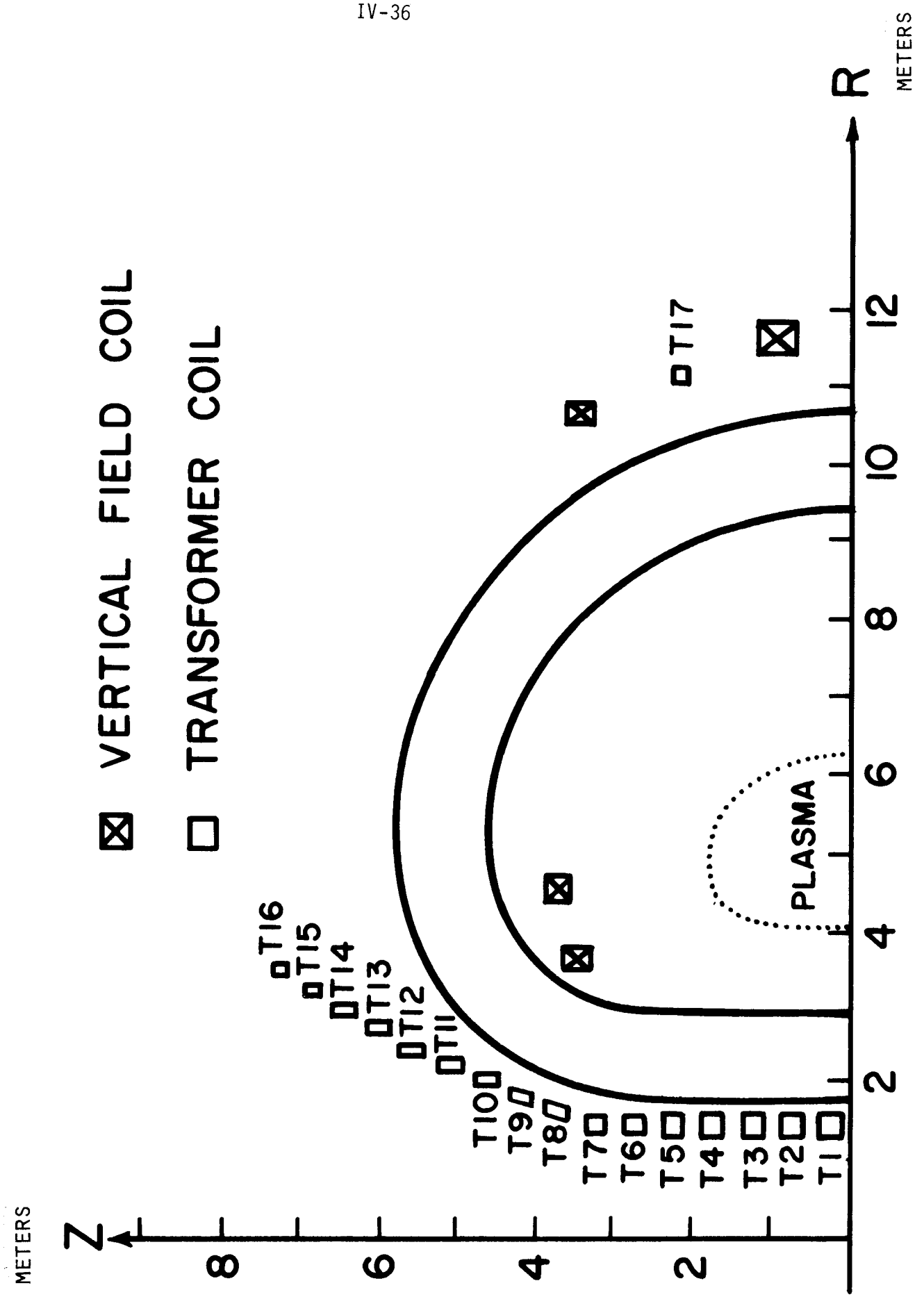

VERTICAL FIELD COIL
TRANSFORMER COIL
PLASMA
Z
R
METERS
METERS
T1
T2
T3
T4
T5
T6
T7
T8
T9
T10
T11
T12
T13
T14
T15
T16
T17
2
4
6
8
10
12

Fig. IV-C-1

reactor size is compact and the aspect ratio is small as in NUWMAK.

During the seven-second startup time, the required flux to raise the plasma current linearly from zero to 7.2 MA is 67.3 volt-seconds. This amount of flux is supplied by the linear change of currents in the VF and OH coils. The largest rate of change of the magnetic field in the reactor cycle occurs during the startup phase with a magnitude of 1.8 tesla/sec, which is far below the maximum permissible value of 6 tesla/sec. The peak power supplied to the transformer system is 1000 MW which occurs at the end of startup. The current changes of the plasma and Tl coil in the reactor cycle are shown in Fig. IV-C-2. The power supply and total poloidal energy storage of the system for different operating phases are shown in Fig. IV-C-3 and Fig. IV-C-4, respectively.

The ohmic heating and radio frequency (RF) heating of the plasma for the reactor startup are simulated by a 0-D point code.[2] Fig. IV-C-5 shows the plasma current and plasma radius change during the startup phase. The plasma current is assumed to rise linearly from 0.6 MA to 5.2 MA in 5.5 seconds, while the radius increases from 38 cm to 112.5 cm at the same time, where a constant current density is assumed, or, consequently, the q-value (safety factor) at the plasma surface is kept at 2.6. Due to the non-circularity of the plasma cross-section, the resultant current rise as calculated in the 0-D code does not closely agree with the MHD results. Fig. IV-C-6 shows the plasma temperature change as a function of time for the startup phase. The electron and ion temperatures are roughly the same for the first 4.5 seconds. At the time t = 4 seconds, when the plasma temperature is about 750 eV, 75 MW of RF power is applied to the plasma for two seconds to heat the plasma to ignition conditions. Since most of the RF power is absorbed by the ions between time t = 4.5 seconds and t = 5.7 seconds, the ion temperature is higher than that of the electrons. However, after t = 5.75 seconds, the production of fusion alpha particles increases rapidly; therefore, the electrons have higher temperatures after this stage. After the shut-off of RF power it is estimated that the plasma temperature requires one more second to reach an equilibrium. The equilibrium

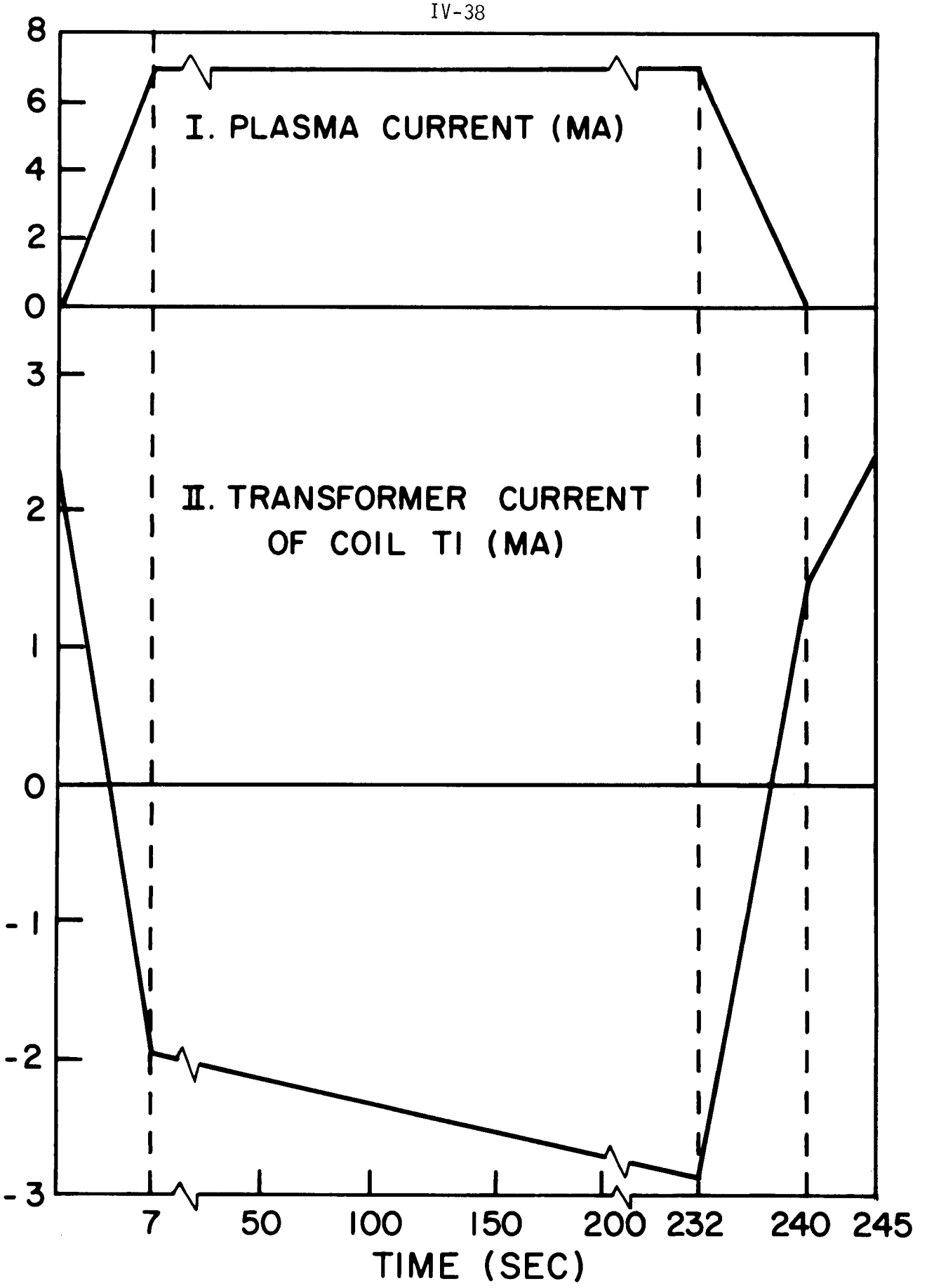

8
6
4
2
0
I. PLASMA CURRENT (MA)
3
2
1
0
-1
-2
-3
II. TRANSFORMER CURRENT
OF COIL TI (MA)
7
50
100
150
200
232
240
245
TIME (SEC)

Fig. IV-C-2

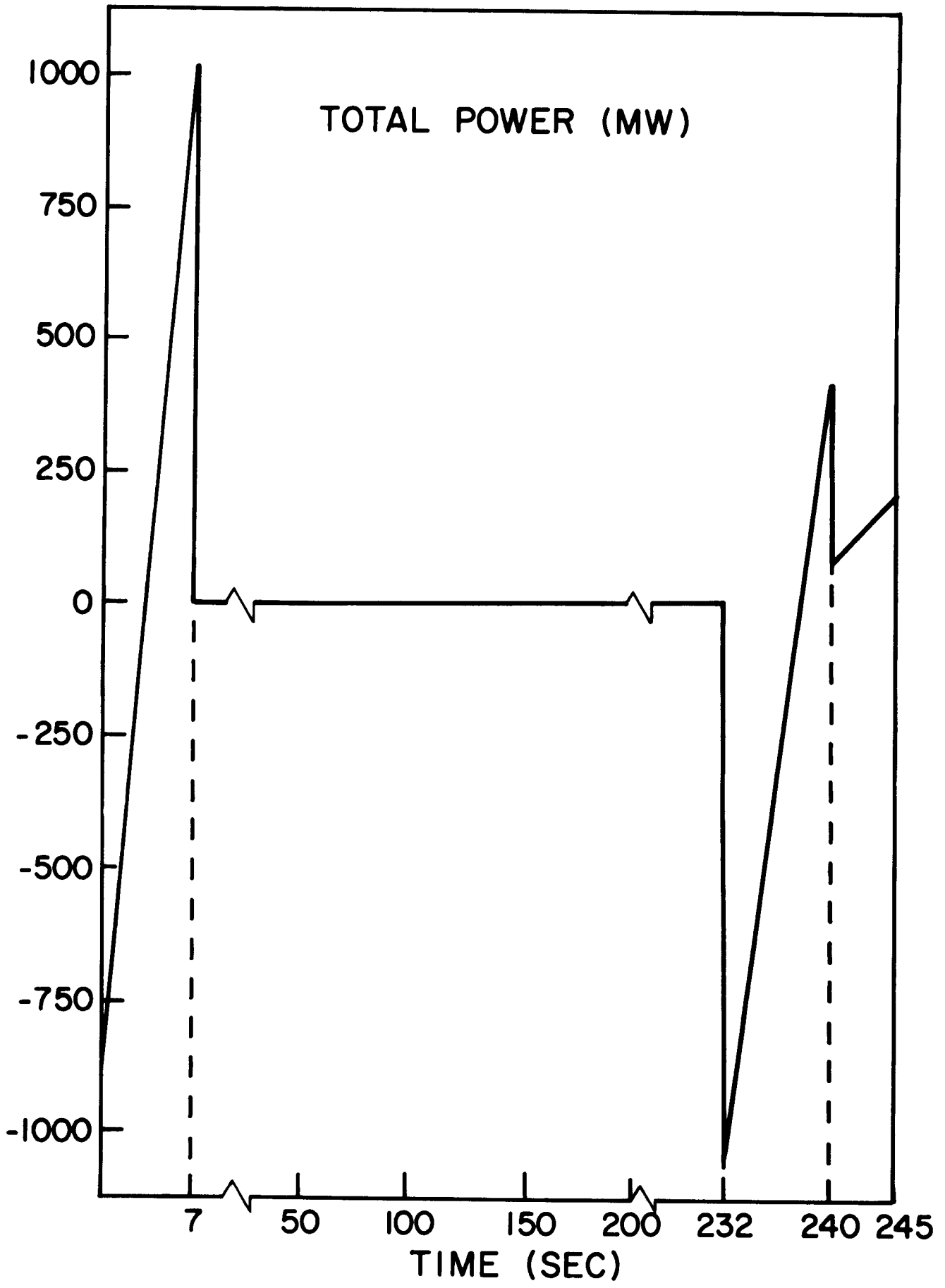

TOTAL POWER (MW)
1000
750
500
250
0
-250
-500
-750
-1000
7
50
100
150
200
232
240
245
TIME (SEC)

Fig. IV-C-3

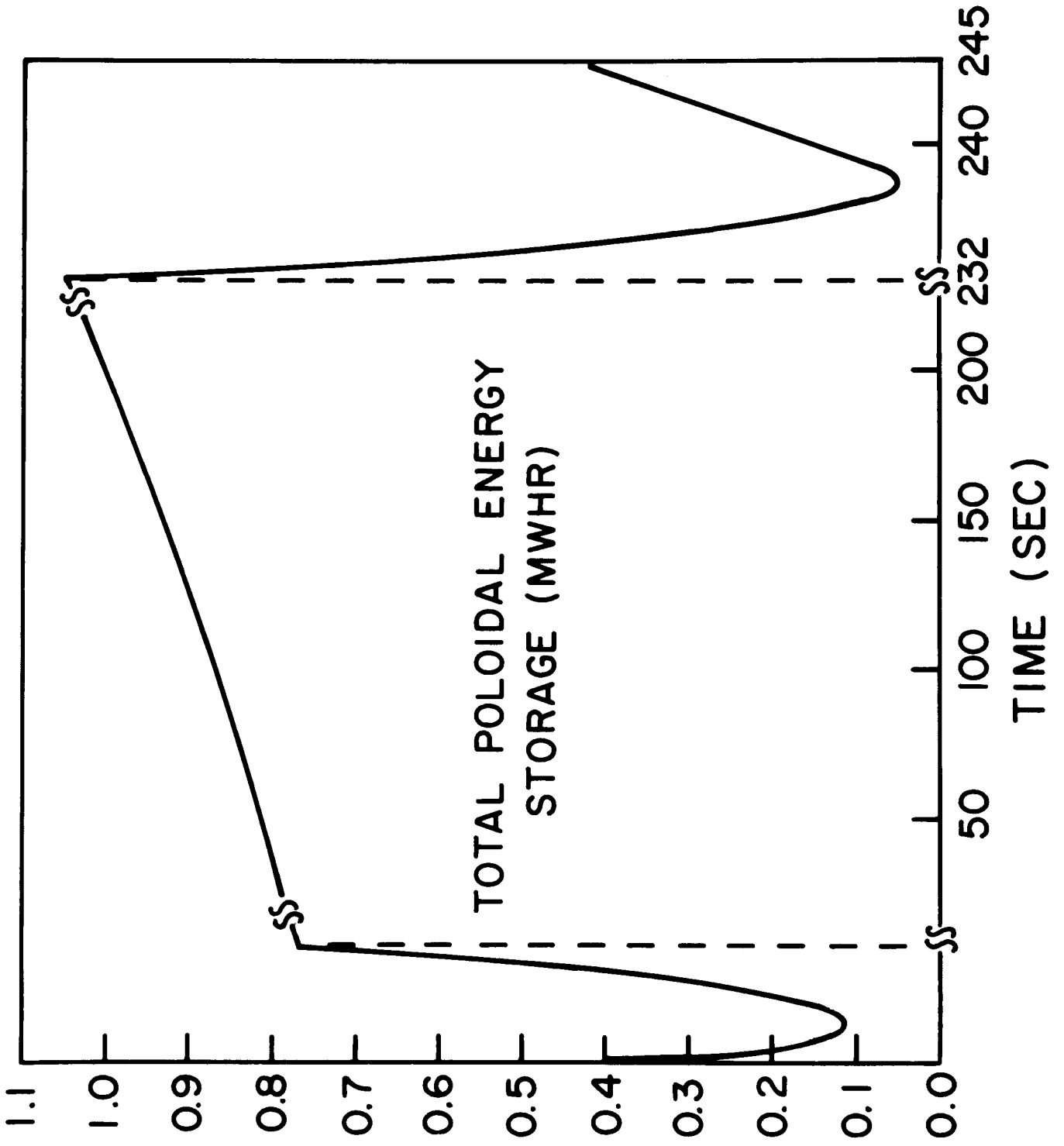

TOTAL POLOIDAL ENERGY
STORAGE (MWHR)
TIME (SEC)
0.0
0.1
0.2
0.3
0.4
0.5
0.6
0.7
0.8
0.9
1.0
1.1
50
100
150
200
232
240
245

Fig. IV-C-4

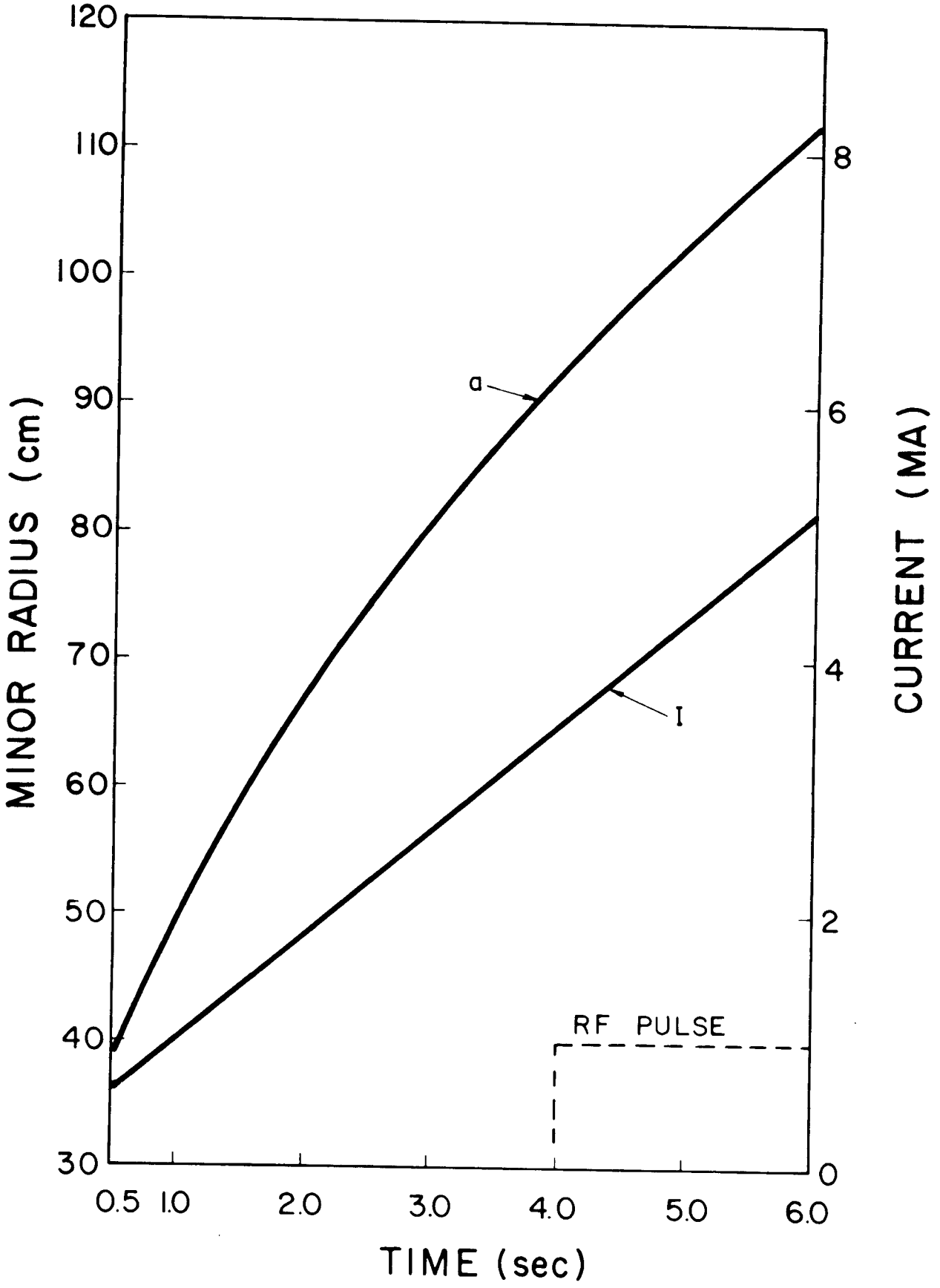

120
110
100
90
80
70
60
50
40
30
MINOR RADIUS (cm)
8
6
4
2
0
CURRENT (MA)
a
I
RF PULSE
0.5
1.0
2.0
3.0
4.0
5.0
6.0
TIME (sec)

Fig. IV-C-5

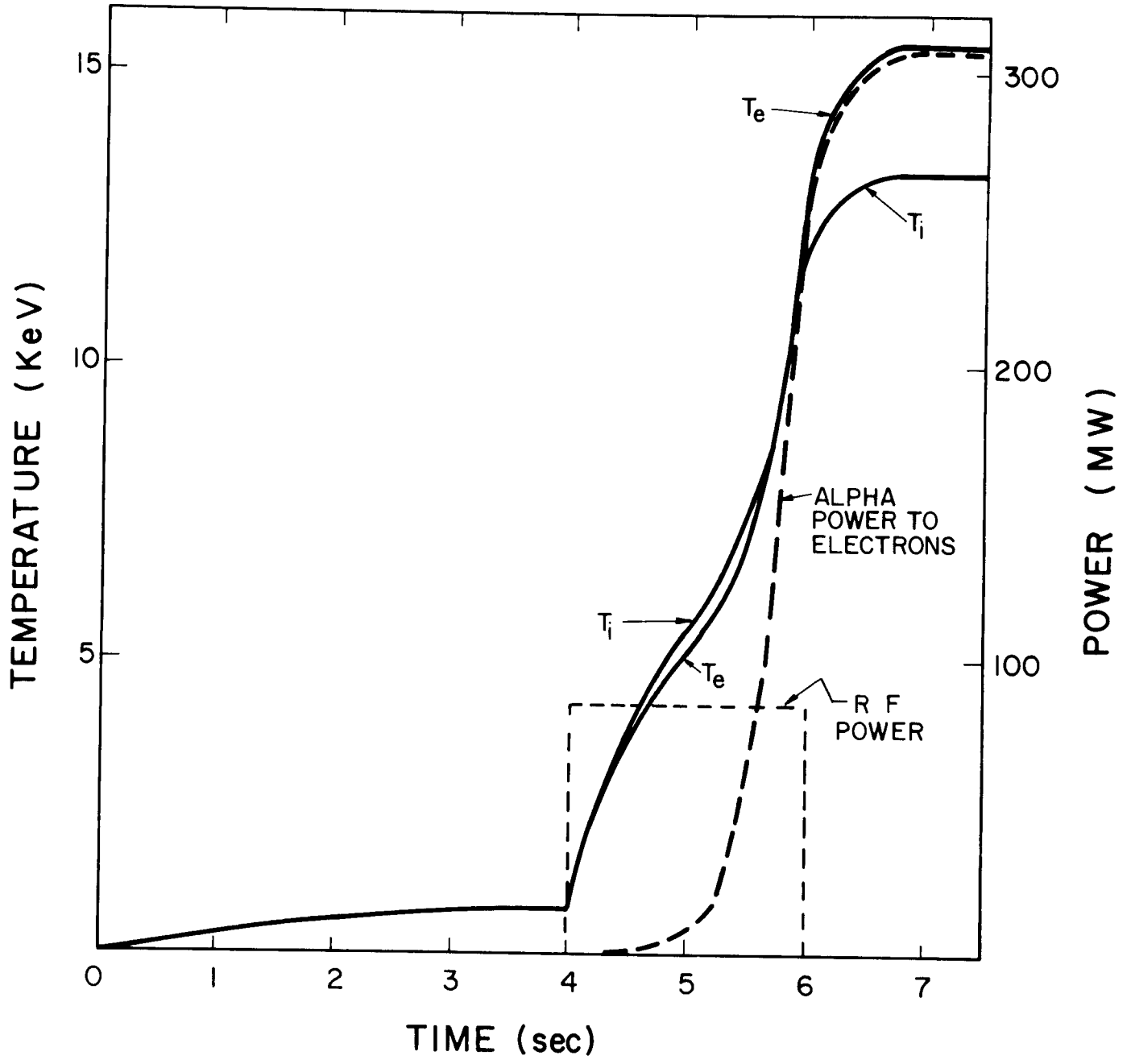

15
10
5
0
1
2
3
4
5
6
7
300
200
100
TEMPERATURE (KeV)
POWER (MW)
TIME (sec)
T_e
T_i
ALPHA POWER TO ELECTRONS
T_i
T_e
R F POWER

Fig. IV-C-6

ion temperature is 13.3 keV while the electron temperature is 15.5 keV and is kept constant during the entire burn phase.

The volt-second requirement for the plasma burn is determined using the space-time code described in section IV-D. This flux is calculated by the multiplication of the plasma loop voltage and burn time. The conductivity of plasma with neoclassical correction[4] is

$$\sigma = \sigma^{*}_{s\rho} \left(1 - 1.95 \left(\frac{r}{R_o}\right)^{1/2} + 0.95 \left(\frac{r}{R_o}\right)\right)$$

where $\sigma^{*}_{s\rho}$ is the Spitzer conductivity corrected to Z_{eff}, R_o is the major radius and r is the radius of the plasma. Using this equation and the plasma current profile, the plasma loop voltage, averaged over the plasma cross section was determined to be about 0.06 volts. This gives 16.4 volt-seconds as the flux to be provided by the transformer during the burn. A plasma Z_{eff} of 1.2, as calculated by the 1-D space time code, has been used for the estimation of the burn flux. During the burn the power required in this period is a few MW only, while the stored energy increases to a peak value of 1.04 MWHR as indicated by Fig. IV-C-4. The maximum transformer coil current is -2.87 MA corresponding to the peak magnetic field at the superconducting coil T1 surface of 7.32 tesla, which occurs at the end of the burn.

After the burn the plasma current decreases linearly from 7.2 MA to zero in eight seconds. At the same time, the currents in the VF coils reduce from their full values to zero, while the transformer currents increase linearly from a peak negative value of -2.9 MA to a positive value of 1.5 MA for the preparation of the next cycle of reactor operation.

The 0-D point code is used to examine the plasma behavior in the shutdown phase. In this code, to simulate a reactor shutdown, it is assumed that deuterium ions replace tritium ions in time, thereby reducing the rate of fusions with a corresponding decrease in plasma temperature. Though the 0-D code assumes a constant overall ion plasma density in time, the fraction of tritium in the plasma (f_{TP}) can be varied.

In Figure IV-C-7, we see that the plasma current decreases linearly while the plasma minor radius drops to 16.2 cm in eight seconds with the plasma q at the edge remaining at a constant value of 2.6. During this shutdown phase, the plasma ion temperature decreases from 13.3 keV to 50 eV as shown in Fig. IV-C-8.

We assume that deuterium replaces tritium with the typical particle scale period of the reactor so that f_{TP}, the fraction of tritium in the plasma, varies as

$$f_{TP} = f_{TP_o} e^{-t/\tau_p} \quad , \tag{31}$$

where τ_p is the particle confinement time

$$\tau_p \sim \frac{a^2}{D} \quad , \qquad \text{(see Sec. V-C)}$$

and f_{TP_o} is the equilibrium value of f_{TP}, in our case $f_{TP_o} = 0.5$.

Using Eq. (31) we find that f_{TP} decreases to 0 within 6.5 sec. The decreasing values of f_{TP} and T_i during this phase of operation cause the alpha power production to decrease from 1.98 W/cm^2 to less than .015 W/cm^2, as shown in Fig. IV-C-9.

From Figs. IV-C-8 and IV-C-9 it is concluded that within 8.0 secs of the initial in-flux of deuterium into the plasma, shutdown occurs. Though the in-flux of deuterium may not be as fast as Eq. (31) indicates, there are two factors which would tend to counteract this effect. First,

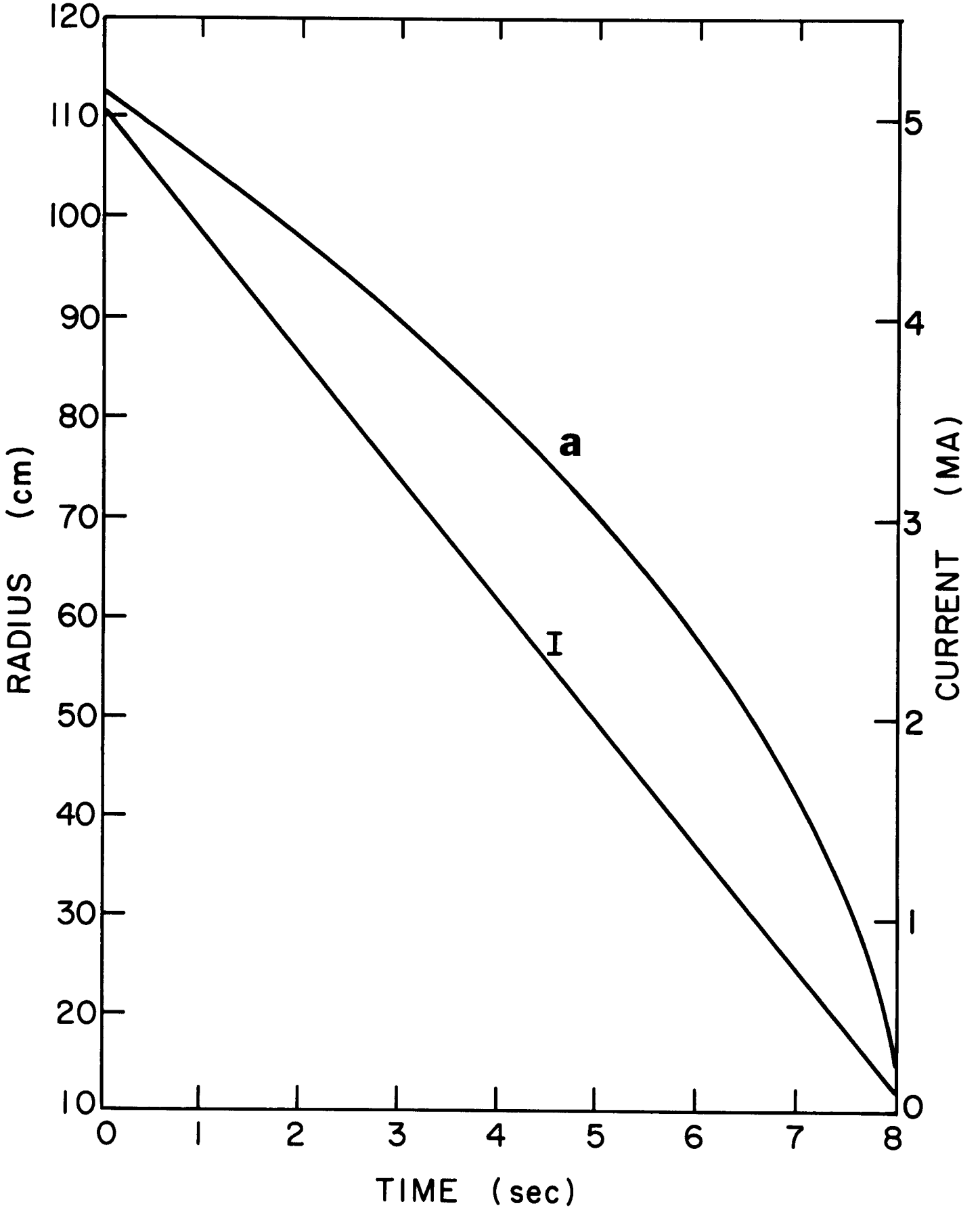

120
110
100
90
80
70
60
50
40
30
20
10
RADIUS (cm)
0
1
2
3
4
5
6
7
8
TIME (sec)
5
4
3
2
1
0
CURRENT (MA)
a
I

Fig. IV-C-7

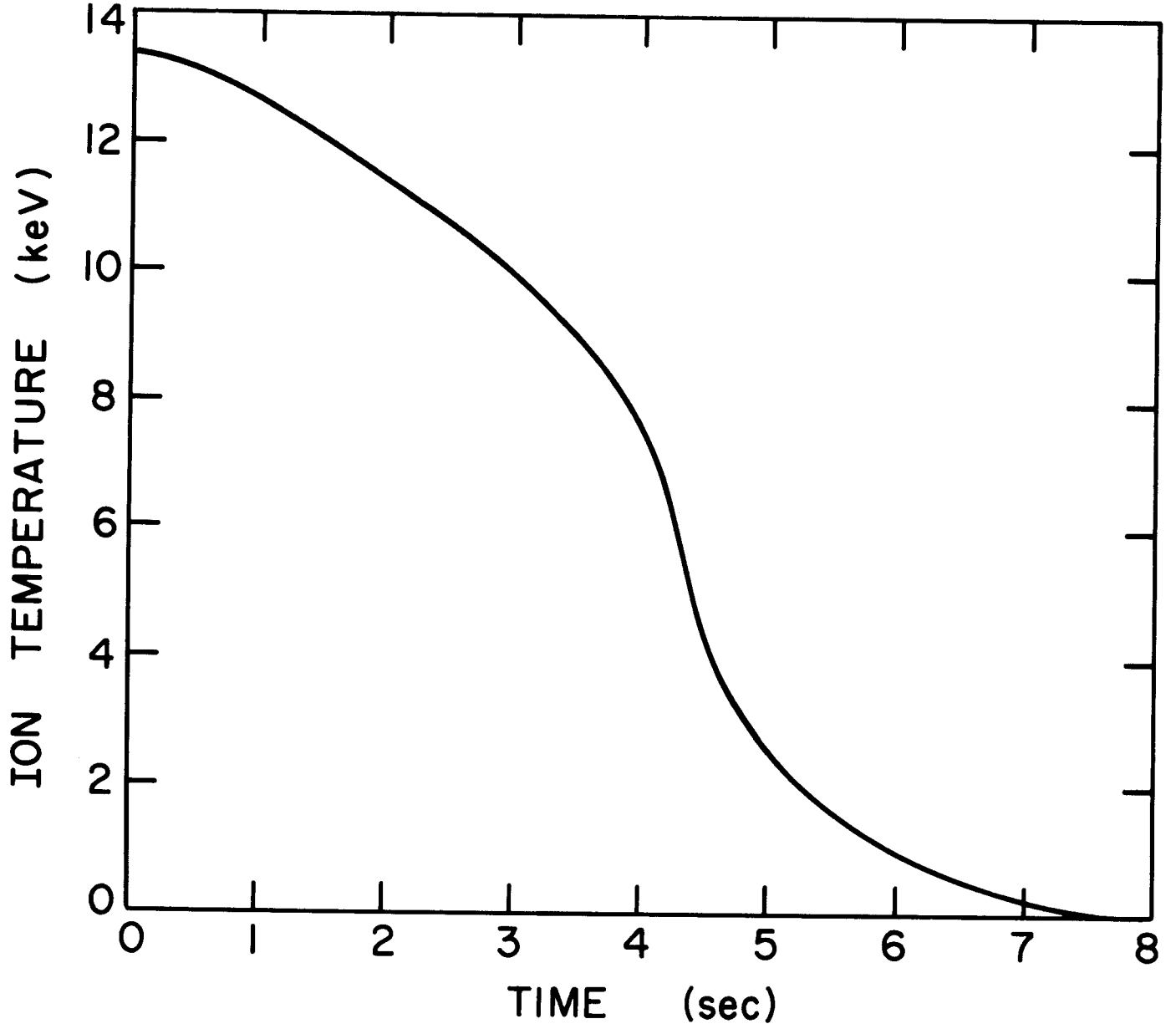


Fig. IV-C-8

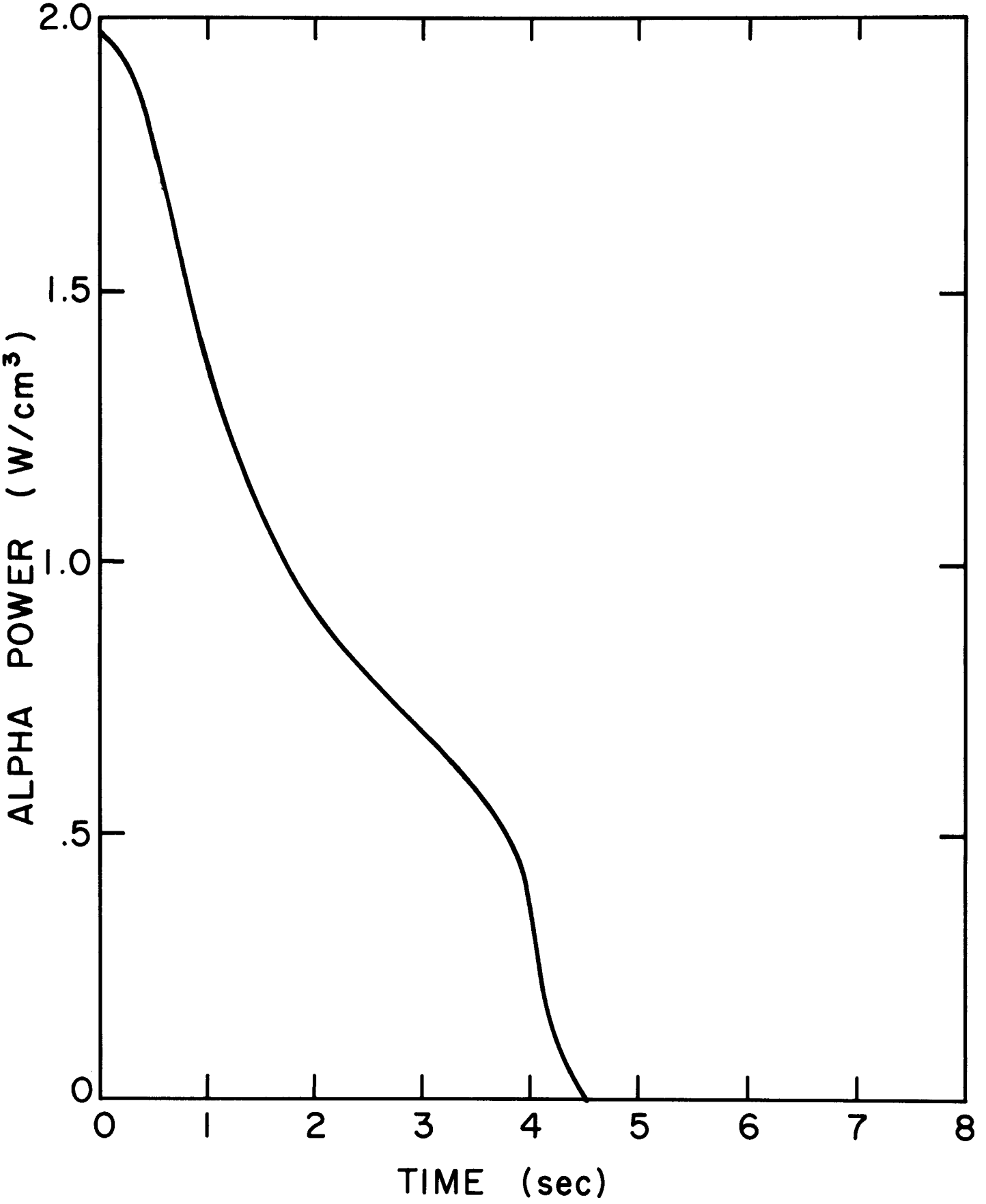


Fig. IV-C-9

a cold deuterium gas would probably be injected into the plasma which is not assumed to be the case since the 0-D code cannot deal with different ion temperatures. It is assumed that all ions have the same temperature. Secondly, the 0-D code contains no impurities; hence, $Z_{eff} = 1$. Since radiation losses increase with increasing Z_{eff}, impurities would tend to make the plasma cool faster. Hence, a reactor shutdown at 8.0 seconds appears to be feasible.

The last phase of the reactor cycle is recocking. During this five minute interval, the transformer currents are reset to the initial values, while the gas in the toroidal chamber will be pumped out and then refilled with fresh fill for the preparation of the next operation cycle.

References for Section IV-C

1. B. Badger et al., "UWMAK-I, A Wisconsin Toroidal Fusion Reactor Design", UWFDM-68, Dept. of Nuclear Engineering, University of Wisconsin (1974).

2. B. Badger, et al., "UWMAK-III, A Noncircular Tokamak Power Reactor Design", UWFDM-150, Dept. of Nuclear Engineering, University of Wisconsin (1976).

3. Sam Dahled, private communication.

4. M.N. Rosenbluth, et al., Physics Fluids 15 116 (1972).

IV-D. Plasma Burn Analysis

IV-D-1. Why Divertorless Operation?

Impurity control, fueling and alpha ash removal are key elements required for the long burn operation of tokamaks. Previous Wisconsin reactor designs have attempted to meet these challenges by incorporating magnetic divertors and pellet fueling schemes. While such devices may ultimately prove to be a necessary part of any viable reactor, they represent complicating factors in both the design and economic efficiency of the system.

In light of these drawbacks, the desirability of a divertorless tokamak becomes obvious. The key issue is whether some simplified process might be employed which would perform divertor functions. The design goal sought by the NUWMAK plasma group was two-fold: 1) to perform divertor functions with the process of Periodic Gas Puffing (PGP) and 2) to discover a gas puffing and/or pellet fueling scheme which would be compatible with the constraints placed upon the system by all other engineering groups. Before the PGP process is described in detail, we give a short review of the properties of gas blankets.

IV-D-2. Gas Blanket Philosophy

The formation of a high density, low temperature plasma surrounding a hot central core has long been recognized as a means of first wall and limiter protection.[1-8] To understand the utility of gas blankets, the following sections sketch the process of blanket formation, the shielding effects of a blanket and finally the influence of a gas blanket on impurity transport.

IV-D-2-a. Blanket Formation

Employing the expressions for the plasma flux in each neoclassical regime and requiring that a steady-state solution exist, relationships between plasma density and temperature are found which allow for the creation of a cool, dense plasma blanket at the plasma edge.[9]

The expressions for particle flux in each neoclassical regime are given by:

$$\text{Banana:}^{(10)} \quad -D_{\perp} q^2 n \left[.62 \frac{\partial}{\partial r}(\ell nT) - 2.24 \frac{\partial}{\partial r}(\ell nn)\right] \left(\frac{r}{R}\right)^{-3/2} \tag{1}$$

$$\text{Plateau:}^{(11)} \quad -D_{\perp} qn \left[\frac{\partial}{\partial r}(\ell nn) + 3/2 \frac{\partial}{\partial r}(\ell nT)\right] * \left(\frac{V_e}{R\nu_e}\right) \tag{2}$$

Pfirsch-Schlüter:[12] $$- 2D_{\perp}\, q \left[\frac{.66}{T}\frac{\partial}{\partial r}(nT) - .27\left(\frac{n}{T}\right)\frac{\partial T}{\partial r}\right] . \qquad (3)$$

Assuming relations between density and temperature of the form:

$$nT^{\alpha} \equiv \text{constant}$$

and solving for the value of α which makes each flux vanish leads to the results:

Banana: $$nT^{-.28} = \text{constant} \qquad (4)$$

Plateau: $$nT^{1.5} = \text{constant} \qquad (5)$$

Pfirsch-Schlüter: $$nT^{.59} = \text{constant} \qquad (6)$$

Highly-Collisional: $$nT = \text{constant} . \qquad (7)$$

If the temperature profile is assumed Gaussian-like, then the above relations yield a density profile as seen in Fig. IV-D-1. Thus, the neoclassical expressions for plasma transport yield a "blanket solution" (cool temperature, high density plasma) in steady-state.

IV-D-2-b. Liner/Limiter Protection

Obviously a low blanket temperature decreases ion-induced sputtering of the first wall and limiters. In addition, if the blanket thickness is sufficient to attenuate energetic neutrals born at the plasma center, then the liner can be protected from high energy neutral sputtering. The criteria for an effective blanket thickness is easily derived.

For the attenuation process to be effective, the blanket thickness must exceed several mean free paths of a fast neutral produced upon charge exchange with a cool blanket ion. Let Δ be the blanket thickness. If we demand that the blanket be at least 3 mean free paths thick, then

$$\Delta \gtrsim 3\lambda = \frac{3V_o}{n_i \langle\sigma v\rangle_{cx}}$$

$$n_i \Delta \gtrsim \frac{3V_o}{\langle\sigma v\rangle_{cx}} \qquad (8)$$

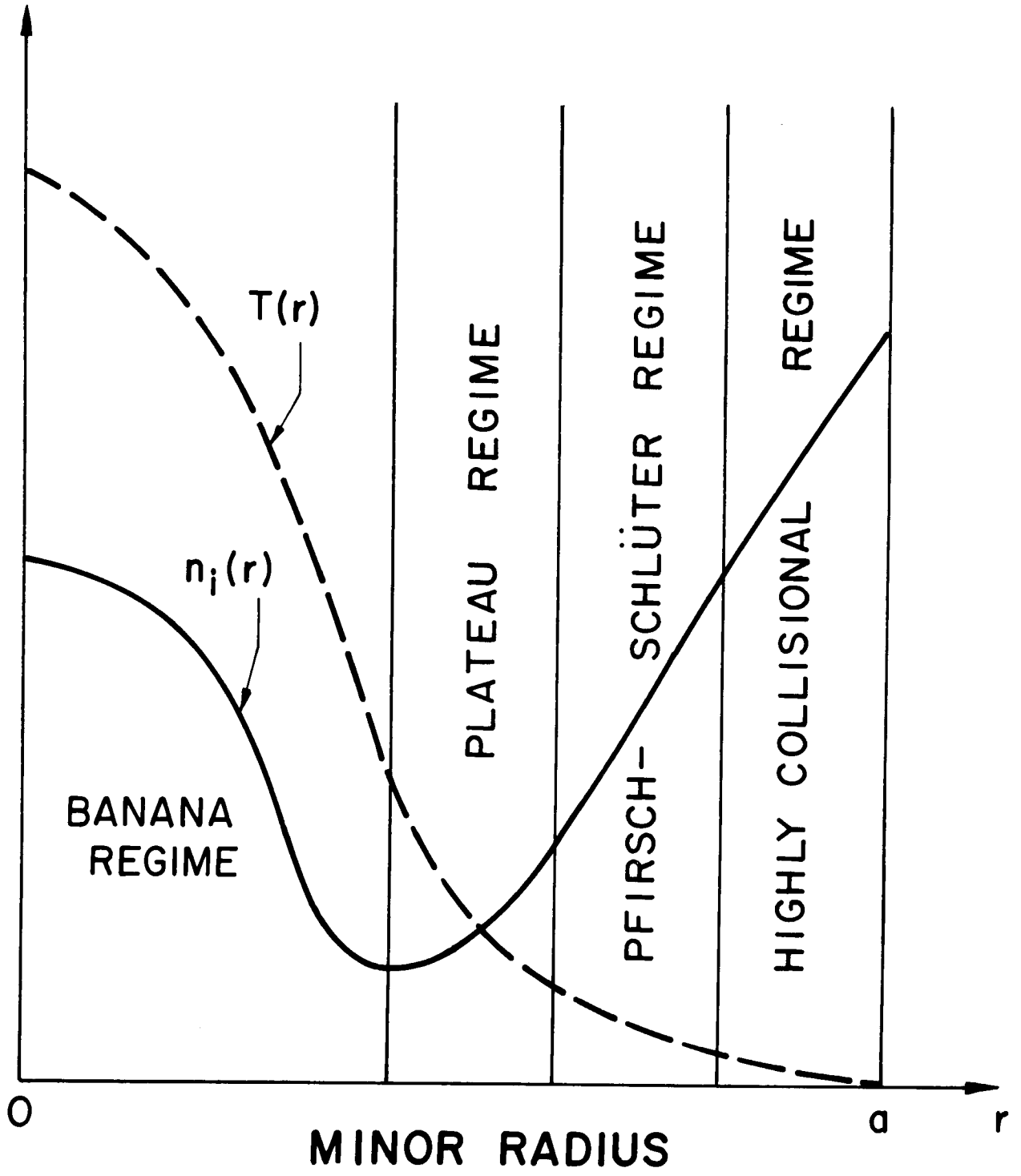


Fig. IV-D-1 Steady-state gas blanket formation

where V_o is the velocity of the hot neutral atom and $\langle\sigma v\rangle_{cx}$ is the rate coefficient for charge-exchange. Since protection from multi-kilovolt neutrals will be necessary, the criteria for liner protection can be expressed approximately as:[13]

$$n_i \Delta \gtrsim 3 \times 10^{15} \text{ cm}^{-2} . \tag{9}$$

It has been assumed that $\langle\sigma v\rangle_{cx} \simeq 7 \times 10^{-8}$ cm^3/sec.[14] The condition (9) signifies that for a blanket density of 3×10^{14} cm^{-3}, a thickness of 10 cm is required for protection.

IV-D-2-c. Impurity Transport

In addition to providing protection to the first wall and limiters, the presence of a cool gas blanket at the plasma edge may prevent the inward radial transport of externally generated impurities. This is illustrated by the following example. Consider a plasma composed of singly charged ions and an arbitrary impurity species. In steady-state the fluid equations yield the following force balances:[15]

$$\begin{aligned} \bar{\nabla} P_i &= n_i e \, (\bar{E} + \bar{V}_i \times \bar{B}) + \bar{R} \\ \bar{\nabla} P_z &= n_z \, Ze \, (\bar{E} + \bar{V}_z \times \bar{B}) - \bar{R} \end{aligned} \tag{10}$$

where $\bar{R}$ denotes the frictional force between the ions and impurities due to collisions. Taking the toroidal component of these equations (in the limit of large aspect ratio) yields:

$$n_i \, V_{ir} = - \, n_z \, Z \, V_{zr} . \tag{11}$$

Using Fick's law, we can write:

$$V_{ir} = \frac{-D_\perp}{n_i} \left(\frac{\partial n_i}{\partial r}\right) \tag{12}$$

so that Eqn. (11) becomes:

$$D_\perp \left(\frac{\partial n_i}{\partial r}\right) = + \, n_z \, Z \, V_{zr} . \tag{13}$$

Thus, employing only simple momentum conservation, the following observation can be made: if the plasma density gradient can be made either relatively flat or inverted near the edge so as to make $(\partial n_i/\partial r) \gtrsim 0$, then $V_{zr} \gtrsim 0$, i.e. the flux of impurities will be radially outward. This leads to plasma cleaning and applies to the pumpout of both alpha particle ash and impurities.

Since the gradient flattening or inversion process occurs automatically in the creation of a gas blanket, a blanket not only represents a possible wall protection mechanism (via cool ion temperatures and hot neutral attenuation) but also may supply the necessary divertor action required for ash removal, impurity control and thus long plasma burn.

IV-D-3. Periodic Gas Puffing Concept in NUWMAK

As demonstrated in the previous section, a gas blanket may be able to provide the divertor action necessary for the maintenance of a clean plasma as well as offer protection to the liner and limiters. By periodically puffing cold fuel (50-50 DT mixture) at the plasma edge, a gas blanket can be created. If the magnitude and duration of these puffs could be made large and long enough, the plasma density could be inverted at the edge. In addition to possible divertor action, this gradient would also cause D-T to flow inward, thereby providing a fueling mechanism for the core. Finally, the impurities trapped in the blanket would form a so-called mantel or "radiating halo", dissipating via radiation a large fraction of the plasma alpha power. In this scenario the limiters will not then be subjected to a large heat flux.

Periodic gas puffing and its impact on the burn dynamics of a reactor plasma forms the basis for the NUWMAK plasma simulation study. The fluid transport model used in the simulations and those aspects of gas puffing which required alterations in this model will now be described.

IV-D-4. Space-Time Transport Model

The one-dimensional space-time model used in the NUWMAK simulations solves the following coupled particle and energy balance equations in cylindrical geometry:

$$\frac{\partial}{\partial t}\left(\frac{3}{2} n_e KT_e\right) = \frac{n_i^2 \langle\sigma v\rangle}{4} E_\alpha U_{\alpha e} - \frac{1}{r}\frac{\partial}{\partial r}\left[r\left(Q_e + \frac{3}{2} KT_e \Gamma_e\right)\right] - Q_{ei} - P_{Rad} + P_\Omega \quad (14)$$

$$\frac{\partial}{\partial t}\left(\frac{3}{2} n_i KT_i\right) = \frac{n_i^2 \langle\sigma v\rangle}{4} E_\alpha (1-U_{\alpha e}) - \frac{1}{r}\frac{\partial}{\partial r}\left[r\left(Q_i + \frac{3}{2} KT_i \Gamma_i\right)\right] + Q_{ei} - P_{cx} \quad (15)$$

$$\frac{\partial n_i}{\partial t} = -\frac{1}{r}\frac{\partial}{\partial r}(r\Gamma_i) - \frac{n_i^2 \langle\sigma v\rangle}{2} + S_i \quad (16)$$

$$\frac{\partial n_\alpha}{\partial t} = \frac{-1}{r}\frac{\partial}{\partial r}(r\Gamma_\alpha) + \frac{n_i^2 \langle\sigma v\rangle}{4} \quad (17)$$

$$\frac{\partial n_z}{\partial t} = \frac{-1}{r}\frac{\partial}{\partial r}(r\Gamma_z) + S_z \quad (18)$$

where all terms have their usual meanings:

n_e:	Electron density $\equiv n_i + 2n_\alpha + Zn_z$
Q_{ei}:	Electron-ion rethermalization term.
P_{rad}:	Bremsstrahlung, line, recombination, ionization and synchrotron losses
P_Ω:	Ohmic heating term
Γ_j, Q_j:	Species j particle, energy flux
P_{cx}:	Charge exchange loss term
S_i:	Source of ions due to gas puffing, pellets and recycle
S_z:	Source of impurities.

The solution to this set of coupled partial differential equations is obtained via the Cranck-Nicholson method in which the balance equations are transformed into an implicit set of difference equations.[16]

In general, the transport coefficients (D, χ_e, χ_i) are treated explicitly and are assumed to vary in functional form as the plasma changes collisionality. The impurity transport coefficients are those of Rutherford, et al.[17] The high collisionality regime reflects pseudoclassical scaling[18] and, as the plasma heats, the transport is assumed to be caused by turbulence, passing successively into regimes dominated by the presence of the trapped electron mode,[19] the trapped ion mode[20] and the collisionless trapped particle interchange mode.[21] Transport coefficients based on estimates of the linear growth rates for these modes has been summarized by Dean et al.[22] In the trapped electron regime, the relationship between

χ_e and χ_i is not known. Rather than optimistically assuming χ_i remains neoclassical in this regime, it is assumed that $\chi_i = \varepsilon\chi_e$, where ε is the local inverse aspect ratio.

To allow for a general variation of the transport coefficients, the general form:

$$D,\ \chi_e,\ \chi_i = C\ T_e^{S1}\ T_i^{S2}\ n_i^{S3}\ B^{S4}\ (\nabla n)^{S5}\ (\nabla T)^{S6}\ (\nabla q)^{S7}\ (1-T_e/T_i)^{S8} \qquad (19)$$

is used in which the coefficients C and S1, S2, ... are determined by the dominant mode present.

The fast and accurate simulation of gas puffing requires that two areas of the model be revised: (1) the transport of neutral atoms and (2) the evaluation of boundary conditions at the plasma edge.

IV-D-5. Impact of Gas Puffing on Transport Model

IV-D-5-a. Neutral Atom Transport

Neutral atom transport is clearly an integral part of the gas puffing concept. Unfortunately, most neutral transport codes are computationally far too slow and bulky to allow for their repeated use in a space-time transport code. In order to economically model repeated gas puffs in detail, an exceptionally fast and accurate neutral transport model, SPUDNUT,[23] has been developed.

Since the mean free path of a cold edge neutral entering the plasma is much less than the plasma minor radius, the model assumes a slab geometry. This assumption has been justified in comparison studies between the Oak Ridge slab model,[24] FASLAB, and the cylindrical Princeton Monte Carlo code.[25]

Given a density of cold fuel molecules at the plasma edge, it is assumed they undergo Franck-Condon dissociation:

$$H_2^o + e^- \rightarrow H_1^o + H_1^+ + 2e^-$$

in which the resulting neutral atom is characterized by an energy of 5 eV. This isotropic source of atoms gives rise to a flux of neutral atoms into the plasma. As the atoms traverse the plasma they can become ionized or charge-exchange on the background plasma. These energetic charge exchange atoms then can either escape directly from the plasma to the liner or again become ionized as they transport within the plasma.

The entire neutral transport problem is formulated in terms of an integral equation for the charge-exchange collision density. The equation is solved via a matrix technique which in effect follows an infinite number of charge exchange "generations". Once the charge-exchange collision density is known, the model yields the ionization source rate profile, the loss of plasma energy due to ionization and charge exchange events and finally the magnitude and energy spectrum of those charge-exchange neutrals which escape directly from the plasma and impinge upon the liner. This latter information is required to evaluate the erosion rate of the liner and also the source of high-Z impurities which enter the plasma.

IV-D-5-b. Dynamic Boundary Conditions at the Plasma Edge

In most plasma simulations, the boundary conditions on density and temperature at the plasma edge are static. That is, either a value is assigned to the parameter of interest at the edge, or a characteristic length, $\ell_\perp$, is defined via the logarithmic derivative formalism:

$$\frac{1}{x_i}\left(\frac{\partial x_i}{\partial r}\right)\Big|_{r=a} \equiv \frac{-1}{\ell_\perp} \quad . \tag{20}$$

In either case, the boundary conditions are fixed in time as initial conditions. Since gas puffing will significantly alter the plasma density and temperature near the edge as a function of time, this static approach is unacceptable. A more dynamic approach to this problem would be to calculate the characteristic lengths in a manner consistent with the time dependent edge parameters. In the following section, one such method is outlined.

In a divertorless tokamak the slope of the density and temperature profiles at the plasma edge are determined by the particle and energy transport processes in the interface or blanket zone defined by the (toroidal or poloidal) limiter. A very simple two-dimensional model has been developed which describes this transport and yields values for the profile slopes which can be used as boundary conditions in a one-dimensional transport model. It is obvious that a different transport model will have

to be used depending on how the mean free path for ions in the toroidal direction compares to half the toroidal circumference.

The dominant collision mechanism contributing to an appreciable change in ion momentum is charge exchange with neutrals. This occurs with the frequency $n_o \langle\sigma v\rangle_{cx}$ where n_o is the neutral density, and $\langle\sigma v\rangle_{cx}$ is the charge exchange rate coefficient. Hence, the mean free path in the z-direction, $\lambda_{\parallel}$, is:

$$\lambda_{\parallel} = \frac{v_{th}^{i}}{n_o \langle\sigma v\rangle_{cx}} \quad , \tag{21}$$

v_{th}^{i} being the thermal velocity of the ions defined as $(2\ kT/m)^{1/2}$. The quantity $\langle\sigma v\rangle_{cx}$ is known as a polynomial.[26]

The average distance to the limiter is πR (half the toroidal circumference). For NUWMAK this is 1.6×10^3 cm, and thus the longitudinal ion transport will be collisionless except for extremely high neutral densities (e.g. during gas puffing).

IV-D-5-b-i. Collisionless Parallel Transport ($\lambda_{\parallel} > \pi R$)

In this case the ions can be assumed to stream freely towards the limiter and their parallel flux is independent of z: $\partial\Gamma_{\parallel}/\partial z = 0$. In the blanket we have

$$\nabla\cdot\Gamma = \frac{1}{r}\frac{\partial}{\partial r}(r\Gamma_{\perp}) = \text{sources - sinks} \ .$$

There are no ion sources in the blanket, but per cm^3 $\Gamma_{\parallel}/2\pi R$ particles are lost. Hence, the continuity equation in the blanket becomes

$$\frac{1}{r}\frac{\partial}{\partial r}(r\Gamma_{\perp}) = -\frac{\Gamma_{\parallel}}{2\pi R} \tag{22}$$

where $\Gamma_{\parallel}$ is given by

$$\Gamma_{\parallel} = n_o \int_{-\infty}^{+\infty} dv_x \int_{-\infty}^{+\infty} dv_y \int_{0}^{\infty} dv_z \ v_z \ f(v) = \langle n_o v\rangle = n_o \ v_{th} \ .$$

But also $\Gamma_{\parallel} = n_i \frac{\pi R}{\tau_{\parallel}}$,

where $\tau_{\parallel}$ is the time needed to cover the distance πR. Hence,

$$\tau_{\parallel} = \pi R / v_{th} \ .$$

The continuity equation now becomes

$$\frac{1}{r} \frac{\partial}{\partial r} (r \Gamma_{\perp}) = - \frac{n_i}{2\tau_{\parallel}} \ . \tag{23}$$

Bohm diffusion is assumed in the blanket. If the plasma edge can be kept at a sufficiently low temperature (e.g. by maintaining a halo of radiating impurity ions around the plasma), T_e, and hence D_B, depends only weakly on the radial position in the blanket compared to $n_i(r)$, and, using Fick's law, the continuity equation reduces further to

$$\frac{\partial}{\partial r} \left(r \frac{\partial n_i}{\partial r} \right) = \frac{n_i}{2\tau_{\parallel}} \frac{r}{D_B} \ .$$

This expression can be written out as

$$r \frac{\partial^2 n_i}{\partial r^2} + \frac{\partial n_i}{\partial r} - \frac{n_i r}{2\tau_{\parallel} D_B} = 0 \ . \tag{24}$$

The solution of this ordinary differential equation is a zeroth order modified Bessel function. The requirement $\lim_{r \to \infty} n_i(r) = 0$ leaves only

$$n_i(r) \sim K_0 \left(\frac{r}{\sqrt{2\tau_{\parallel} D_B}} \right) \quad \text{for } r \geq a \ .$$

Matching $n_i(r)$ at the interface $r = a$, i.e. requiring $n_i(a)$ to have a prescribed value yields

$$n_i(r) = \frac{n_i(a)}{K_o\left(\frac{a}{\sqrt{2\tau_{\parallel} D_B}}\right)} K_o\left(\frac{r}{\sqrt{2\tau_{\parallel} D_B}}\right) .$$

Using $K_o'(z) = - K_1(z)$ we find

$$\frac{dn_i}{dr} = - \frac{n_i(a)}{K_o\left(\frac{a}{\sqrt{2\tau_{\parallel} D_B}}\right)} K_1\left(\frac{r}{\sqrt{2\tau_{\parallel} D_B}}\right) \frac{1}{\sqrt{2\tau_{\parallel} D_B}} .$$

Evaluating this for $r = a$:

$$\frac{1}{n_i} \frac{dn_i}{dr} \Big|_{r=a} = \frac{-1}{\sqrt{2\tau_{\parallel} D_B}} \frac{K_1\left(\frac{a}{\sqrt{2\tau_{\parallel} D_B}}\right)}{K_o\left(\frac{a}{\sqrt{2\tau_{\parallel} D_B}}\right)} . \qquad (25)$$

For large arguments, $K_1(z) \simeq K_o(z)$ and

$$\frac{1}{n_i} \frac{\partial n_i}{\partial r} \Big|_{r=a} = \frac{-1}{\sqrt{2\tau_{\parallel} D_B}} .$$

If the characteristic length for the ion density is defined by:

Then:
$$\lambda_{n_i} = \left(- \frac{1}{n_i} \frac{d_{ni}}{dr} \Big|_{r=a}\right)^{-1}$$

$$\lambda_{n_i} = \sqrt{2\tau_{\parallel} D_B} . \qquad (26)$$

A similar reasoning can be set up for the parallel energy transport: $\partial Q_{\parallel}/\partial z = 0$. If the energy transport in the parallel direction is assumed to be entirely convective, then:

$$\langle Q_{\parallel} \rangle = \int_{-\infty}^{+\infty} dv_x \int_{-\infty}^{+\infty} dv_y \int_{0}^{\infty} dv_z \frac{mv^2}{2} v_z f(v) = \sqrt{\frac{2}{\pi}} m_i n_i \left(\frac{kT_i}{m_i}\right)^{3/2} \tag{27}$$

i.e.

$$Q_{\parallel} = 2kT_i \Gamma_{\parallel} .$$

Hence,

$$Q_{\parallel} = 2kT_i n_i \frac{\pi R}{\tau_{\parallel}}$$

and

$$\frac{1}{r}\frac{\partial}{\partial r}(rQ_{\perp}) = -\frac{n_i kT_i}{\tau_{\parallel}} . \tag{28}$$

We proceed by matching the energy flux at the interface (as opposed to matching the temperatures). If no particles or energy reach the wall, then eqs. (23) and (28) can readily be integrated to yield

$$Q_{\perp}(a) = \frac{1}{a}\int_{a}^{a+d} \frac{n_i kT_i}{\tau_{\parallel}} r dr \tag{29}$$

and

$$\Gamma_{\perp}(a) = \frac{1}{a} \int_{a}^{a+d} \frac{n_i}{2\tau_{\shortparallel}} \, rdr \, . \tag{30}$$

If $T_i(r)$ can be regarded as constant for $a < r < a + d$, then

$$Q_{\perp}(a) = 2 \, kT_i \, \Gamma_{\perp}(a)$$

and, from

$$\Gamma_{\perp}(a) = - D \frac{\partial n_i}{\partial r} \Big|_{r=a} ,$$

$$Q_{\perp}(a) = - 2 \, kT_i \, D \frac{\partial n_i}{\partial r} \Big|_{r=a} .$$

Continuity of the energy flux requires to lowest order

$$Q_{\perp}(a) = - n\chi \frac{\partial kT_i}{\partial r} - \frac{3}{2} kT_i \, D \frac{\partial n_i}{\partial r} \, . \tag{31}$$

Hence,

$$n_i \, \chi \frac{\partial kT_i}{\partial r} + \frac{3}{2} kT_i \, D \frac{\partial n_i}{\partial r} = 2 \, kT_i \, D \frac{\partial n_i}{\partial r}$$

or

$$\frac{1}{T_i} \frac{\partial T_i}{\partial r} = \frac{1}{2} \frac{D}{\chi} \frac{1}{n_i} \frac{\partial n_i}{\partial r}$$

i.e.

$$\frac{1}{T_i} \frac{\partial T_i}{\partial r} = - \frac{D}{2\chi} \frac{1}{\sqrt{2\tau_{\shortparallel} D_B}} \, .$$

Thus, the characteristic length for the ion temperature is given by

$$\lambda_{T_i} = \frac{2\chi}{D} \sqrt{2\tau_{\shortparallel} D_B} \, . \tag{32}$$

IV-D-5-b-ii. Collisional Parallel Transport ($\lambda_{\parallel} < \pi R$)

In this case the parallel particle transport depends on the density gradient in the z-direction:

$$\Gamma_{\parallel} = - D_{\parallel} \frac{\partial n_i}{\partial z} . \tag{33}$$

Bohm diffusion is still assumed in the radial direction:

$$\Gamma_{\perp} = - D_B \frac{\partial n_i}{\partial r} . \tag{34}$$

The continuity equation now is $\nabla \cdot \vec{\Gamma} = 0$ because there are neither sinks nor sources. Written out this becomes

$$\frac{1}{r} \frac{\partial}{\partial r} (r \, \Gamma_{\perp}) = - \frac{\partial \Gamma_{\parallel}}{\partial z} \tag{35}$$

or

$$\frac{1}{r} \frac{\partial}{\partial r} (r \, \Gamma_{\perp}) = \frac{\partial}{\partial z} (D_{\parallel} \frac{\partial n_i}{\partial z}) \simeq D_{\parallel} \frac{\partial^2 n_i}{\partial z^2} \simeq - D_{\parallel} \frac{n}{\lambda_{\parallel}^2}$$

where $D_{\parallel} = \frac{1}{3} \frac{\lambda_{\parallel}^2}{\tau_{\parallel}}$ and hence $\frac{D_{\parallel}}{\lambda_{\parallel}^2} = \frac{1}{3\tau_{\parallel}}$. Writing the continuity equation out yields

$$\frac{\partial n_i}{\partial r} + r \frac{\partial^2 n_i}{\partial r^2} - \frac{n_i r}{3\tau_{\parallel} D_B} = 0 . \tag{36}$$

The solution of this ordinary differential equation again is a zeroth order modified Bessel function $K_o \left(\frac{r}{\sqrt{3\tau_{\parallel} D_B}}\right)$. In a similar way as described in the previous section we find:

$$\frac{1}{n_i} \frac{\partial n_i(r)}{\partial r} = \frac{-1}{\sqrt{3\tau_{\parallel} D_B}} \frac{K_o(\ldots)}{K_o(\ldots)} = \frac{-1}{\sqrt{3\tau_{\parallel} D_B}}$$

and

$$\lambda_{n_i} = \sqrt{3\tau_{\parallel} D_B} \tag{37}$$

i.e. only a factor $\sqrt{3}/2$ larger than in the collisionless case. Similarly, we find

$$\lambda_{T_i} = \frac{2\chi}{D_\perp}\sqrt{2\tau_{\parallel}D_B} \quad . \tag{38}$$

It should be noted that in practice the temperature boundary conditions were taken to be fixed values of T_e and T_i for numerical stability. However, the characteristic lengths for density decay in the limiter shadow were calculated using the model just described.

IV-D-6. Divertorless Operation Figures of Merit

In order to evaluate the attractiveness of one puffing scheme against another, the following figures of merit have been chosen: (1) the fractional burnup, (2) the limiter heat loading and (3) the buildup of plasma impurities as a function of time. These three have been adopted as useful evaluation criteria since each value will have a significant impact on the feasibility of a particular reactor burn scenario.

IV-D-6-a. Fractional Burnup Considerations

The fractional burnup, f_B, is defined in such a way as to be a useful parameter in calculating the cryopumping and tritium handling requirements of the reactor:

$f_B \equiv$ (# ions burned per second)/(# of ions introduced into plasma (gas puff + pellets) per second).

If f_B is very low, the pumping and tritium handling requirements will be prohibitively large. In addition to pure gas load considerations, divertorless operation will tax the pumping capacity of the system due to the low flow conductance between chamber and pumps. This conductance is now a factor since the recycling gas is not dumped directly into the pumping ports, as in the divertor case, but rather must be drawn through a more resistive piping network.

IV-D-6-b. Limiter Loading Considerations

In divertorless operation, the limiters will be subjected to a heat load associated with those electrons and ions which are diffusing from the system. To calculate this heat load, a simple power balance can be made between the alpha power and all non-diffusive energy losses, i.e. radiation and charge-exchange. The steady-state power to the limiters, P_{LIM}, is then

given by:

$$P_{LIM} = P_{\alpha} - (P_{rad} + P_{cx}) \ .$$

Ideally, from a heat transfer point of view, the alpha power should be very close to the radiated plus charge-exchanged power. The power to the limiters will then be minimized. However, the constraints placed upon the system by the average thermal power and tolerable impurity density may make this optimum condition only partially realizable. An attractive design would incorporate a puffing scheme in which P_{LIM} is as small as possible.

IV-D-6-c. Impurity Buildup Considerations

Long burntimes are essential if fusion power is to be an economically viable source of energy. Of all the processes under consideration which can limit the burntime none is more critical than the question of plasma ash and impurity buildup. In divertor designs, the divertor shields the plasma from externally generated impurities as well as provides a sink for internally generated helium ash. In a divertorless device, these functions are assigned to the gas blanket.

Two measures of the success with which gas puffing prevents burntime degradation is the time history of the alpha and high Z population densities. If $\dot{n}_{\alpha}$ or $\dot{n}_{Z} >> 0$ (in a global sense or at the plasma center), the burntime will be shortened due to enhanced radiative losses and possible beta limitations.

Therefore, even if all the other benefits of gas puffing can be realized, if impurity buildup in the plasma is so severe that the plasma burntime is significantly reduced, then the puffing scheme in question is of marginal utility. A good design will thus yield $n_i/\dot{n}_{\alpha}$ and $n_i/\dot{n}_{Z} >> \tau_{burn}$.

IV-D-7. Learning Curve of Gas Puffing Simulations

Initially it was hoped that only pure gas puffing would be necessary in order to achieve the design goals of NUWMAK. Unfortunately, we find that such gas puffing simulations result in a high limiter heat loading and low fractional burnup. These less than optimum trends constituted severe problems for the cryopumping and heat transfer groups.

In an effort to improve the concept, a modified gas puffing scheme has been created which incorporates shallow pellet fueling and deliberate impurity contamination. The pure to modified modes of operation represent the learning curve followed by the plasma group over a period of time. Before getting into the specifics of each scenario, the plasma startup, gas injection model, and periodic puffing constraints, all common elements of each scheme, will be described.

IV-D-7-a. RF Startup Model

After heating the plasma ohmically, 100 MW of RF power is introduced into the plasma for 0.5 seconds. Lacking a detailed model of RF heating, the absorbed power is assumed to be spatially represented by a peaked Gaussian. The ions receive 70% of the injected power while the electrons receive 30%. Employing this model, the core of the plasma can achieve ignition.

At the moment of RF termination, a single 60 msec gas puff is made in order to raise the plasma density and power. As the plasma power approaches the design value of 2300 MW, periodic gas puffing is initiated, where the puff duration is now 10 msec and the time between puffs is 400 msec.

Approximately one second after PGP starts, plasma density, temperature and power begin to vary in a sinusoidal fashion with a period corresponding to the time between puffs.

IV-D-7-b. Gas Injection Model

The following model has been adopted to simulate the periodic injection of cold neutral gas into the plasma. During a gas puff of duration Δt, the cold neutral edge density is assumed constant at a value n_1 (Fig. IV-D-2). This density gives rise to a neutral flux into the plasma, the magnitude of this flux being an input to the neutral code. The edge density is then assumed to fall exponentially in time to a value n_2. This reduction of edge neutral density is in response to active cryopumping. The e-folding period of the pumps has been set at 100 msec. The gas puffing cycle then repeats itself.

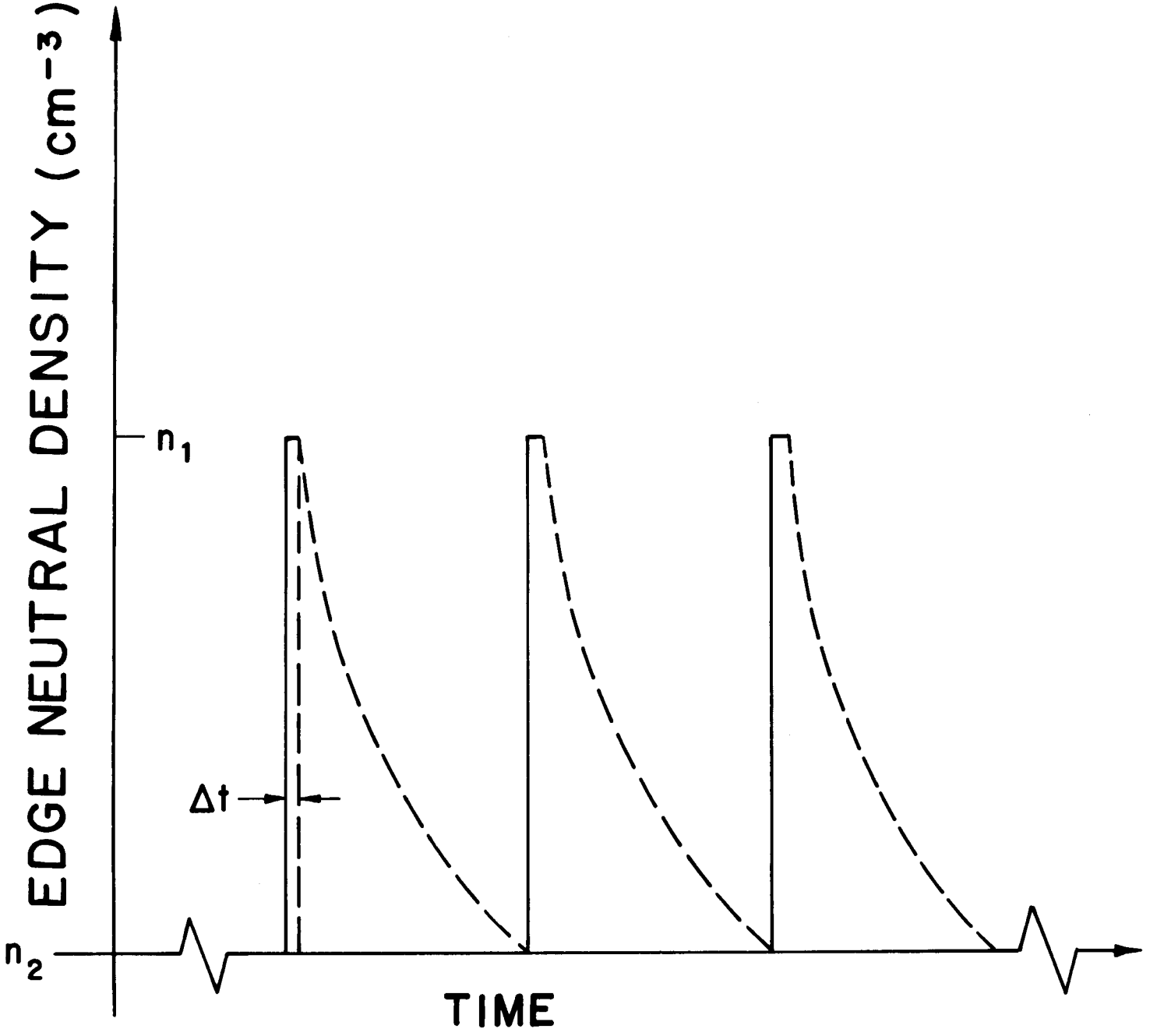


Fig. IV-D-2 Franck-Condon edge density as a function of time.

IV-D-7-c. Puffing Degrees of Freedom

There are three "degrees of freedom" involved in the search for an acceptable periodic gas puffing scenario: (1) the magnitude of the puff, (2) the duration of the puff, and (3) the time between puffs. Some combination of these three parameters must be determined which will induce a periodic, stable plasma burn while simultaneously satisfying the many engineering design constraints placed upon the system.

The magnitude and duration of a gas puff determines the fueling rate and ultimately the plasma power. Since the fueling is periodic, the power produced by the plasma now becomes a function of time. This dynamic behavior represents a new and important facet in reactor modelling. The magnitude of these power oscillations will have an impact upon the design of the limiter and blanket. The period of these oscillations is also a concern if they are close to the thermal time constant of the wall or limiters. Since these are only a few of the many engineering constraints placed upon the puffing scenario, it is clear that the puffing scheme cannot be chosen arbitrarily.

In order to achieve periodic plasma behavior, the plasma must be driven as if it were a harmonic oscillator. If periodic gas puffs are simply initiated at some arbitrary point in the plasma power cycle, it has been observed that large amplitude, non-periodic power excursions are produced. An early simulation in which such excursions were produced is shown in Fig. IV-D-3. Two concepts which were instrumental in determining the correct puffing sequence are: (1) puff/power lag time, and (2) thermal inertia.

"Puff/power lag time" refers to the observation that a characteristic amount of time, τ, elapses before the plasma power increases in response to a gas puff. For NUWMAK, this time is approximately 100 msec. "Thermal inertia" refers to the observation that once the plasma power has peaked and begins to drop, it is difficult to slow its rate of decline.

As an illustration of these two concepts, define the average power output required as $\bar{P}$. If at some point in time the power is greater than $\bar{P}$, and if no fueling takes place, the power will begin to fall towards $\bar{P}$. If a gas puff is applied when the power equals $\bar{P}$, then by definition, τ seconds will elapse before the power starts to increase. During this time, however, thermal inertia has driven the power well below $\bar{P}$. The power thus starts its climb towards $\bar{P}$ from a point well below

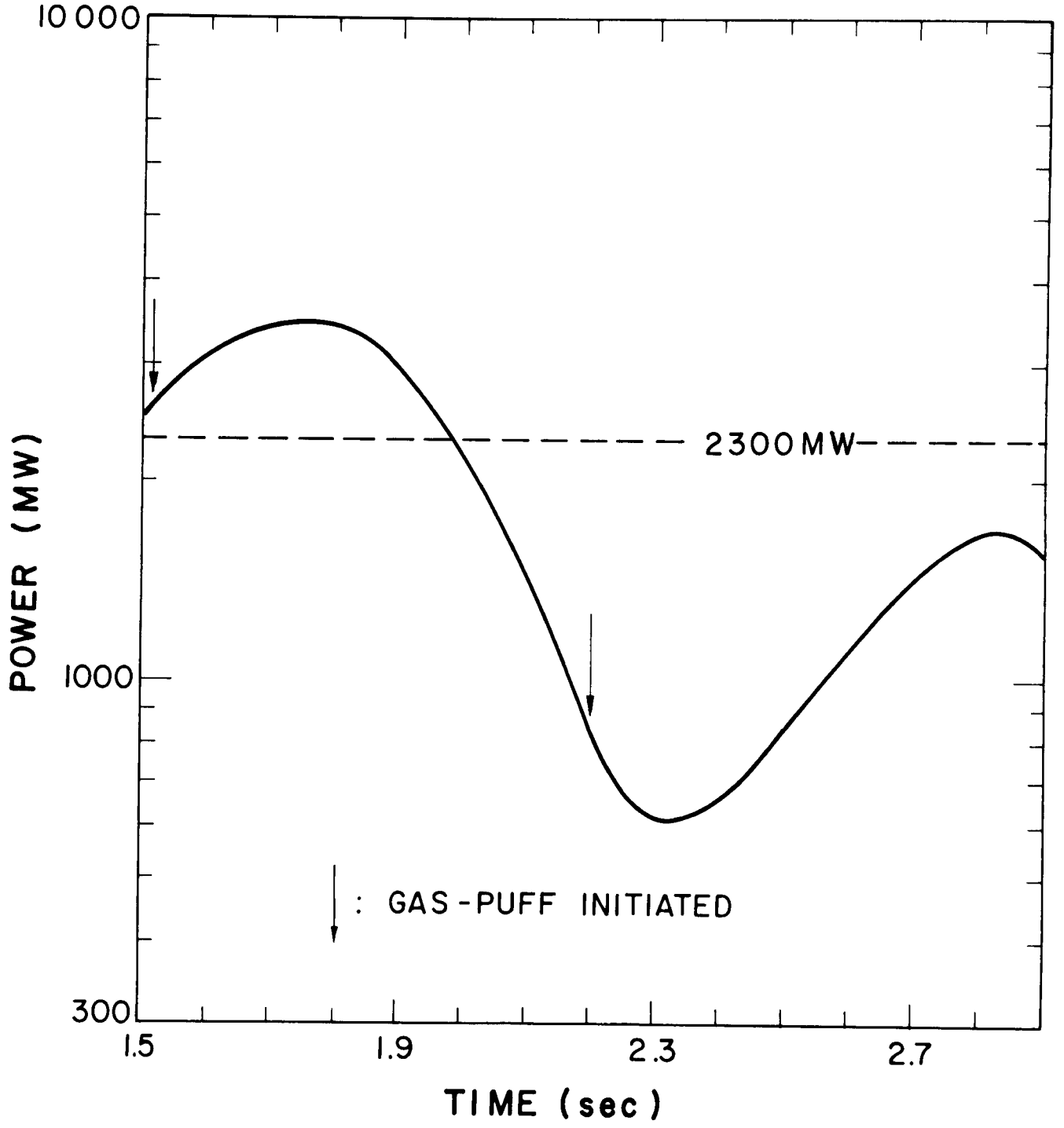


Fig. IV-D-3 Plasma power excursion due to arbitrary puffing scheme

$\bar{P}$, giving rise to large, unacceptable power excursions.

The correct puffing sequence must obviously be to initiate the puff a short time before the power falls to $\bar{P}$ so that after τ seconds, the plasma power will begin to increase from a level not too far from $\bar{P}$. This is in analogy to the well known phase relationship between a harmonic oscillator and an outside driving agency.

Having examined some of the commom elements and strategies of each gas puffing scheme, the results of an unacceptable pure gas puffing simulation will be reported. By analyzing the resulting figures of merit, the modifications necessary to formulate a better (modified) gas puffing scenario will be determined. This improved case has been chosen as the final NUWMAK plasma scenario.

IV-D-8. Final Results

IV-D-8-a. Pure Gas Puffing Scenario (Case A) (Not Finally Applied)

In this scheme: (1) all fueling is via gas puffing and (2) all impurities which contaminate the plasma arise from liner sputtering. We tabulate in Tables IV-D-1 to IV-D-5 the results of this simulation. Three-dimensional plots of the plasma density and temperature as a function of time are shown in Figs. IV-D-4 to IV-D-8. We find the following difficulties with this scenario:

(1) The fractional burnup is low, 0.37%, creating pumping and tritium handling problems; (2) a low fraction (16%) of the alpha power is radiated to the first wall, placing a large heat load on the limiters; and (3) impurity buildups on the order of $3 \times 10^{11}/cm^3$-sec for both the alpha and high-z densities, values which may be incompatible with the assumed burn time of 225 seconds.

On the positive side, it is found that: (1) any power level could be achieved by modestly modifying the puff duration, and (2) plasma parameters such as density, temperature and power were highly periodic and reproducible in time. These two features of gas puffing, while not representing a definitive proof of principle, are highly suggestive and encouraging. Low fractional burnup appears to be an unavoidable feature of pure gas puffing since not all fuel admitted into the scrape-off region enters the plasma and becomes ionized.

Table IV-D-1
NUWMAK Physical Parameters

Major Radius (cm)	512.5
Equiv. Circular Plasma Radius (cm)	144.
Plasma Radius at Midplane (cm)	112.5
Toroidal Magnetic Field on Axis (T)	6.05
Plasma Current (MA)	5
Plasma Volume (cm^3)	2.1×10^8
Wall Surface Area (cm^2)	3.6×10^6

Table IV-D-2

Plasma Parameters: Case A

Mean Ion Temperature (keV)	10.1
Mean Electron Temperature (keV)	9.4
Mean Ion Density (cm^{-3})	2.8×10^{14}
Mean Electron Density (cm^{-3})	2.9×10^{14}
Mean Alpha Density (cm^{-3})	1.9×10^{12}
Mean Impurity Density (cm^{-3})	3.0×10^{11}
Total Toroidal Beta, β_ϕ(%)	6.2
Total Poloidal Beta, β_θ	5.2
Energy Content of Plasma (GJ)	.29
Particle Confinement Time (sec)	.3
Energy Confinement Time (sec)	1.1
$\overline{n_e}\ \tau_E$ (sec/cm^3)	3.19×10^{14}

Table IV-D-3
Power Parameters: Case A

Energy Per Fusion Event (MeV)	20.67
Thermal Power During Burn (MW)	2160±300
Peak to Average Power Fluctuation (%)	14
Period of Power Fluctuation (msec)	400
Average Plasma Power Density (W/cm^3)	8.8
14 MeV Neutron Production Rate (sec^{-1})	6.52×10^{20}
Total Power to Wall (MW)	1585
Radiation (MW)	60
Neutrals (MW)	54
Neutrons (MW)	1471
Neutron Wall Loading (MW/m^2)	4.1
Total Power to Limiters (MW)	254±48
Peak to Average Limiter Loading (%)	18
Average Charge-Exchange Flux to Wall (cm^{-2} sec^{-1})	2.38×10^{17}
Effective Temperature of Maxwellian Neutral Spectrum (eV)	324

Table IV-D-4

Fueling Parameters: Case A

Max. Neutral Edge Density (cm^{-3})	1×10^{12}
Min. Neutral Edge Density (cm^{-3})	1×10^{10}
Time Gas Puff On (msec)	10
Time Gas Puff Off (msec)	390
Time Between Gas Puffs (msec)	400
e-folding Pump Time (msec)	100
Average Tritium (D) Consumption Rate (sec^{-1})	6.52×10^{20}
Average Tritium Burnup Rate (kg/day)	.21
Average Deuterium Burnup Rate (kg/day)	.14
Average (T) Fueling Rate (kg/day)	56.8
Average (D) Fueling Rate (kg/day)	37.8
Fractional Burnup, f_B (%)	.37
Total Particle Leakage (D+T+α)	2.0×10^{23}/sec

Table IV-D-5

Figures of Merit: Case A

Fractional Burnup (%)	.37
Limiter Heat Loading (MW)	254
Radiated Power/Alpha Power (%)	16
$\dot{\bar{n}}_{\alpha}$ (cm^{-3}-sec)	2.9×10^{11}
$\dot{\bar{n}}_{Z}$ (cm^{-3}-sec)	2.7×10^{11}
Erosion Rate of Wall (mm/yr)	.22
Average Energy of Diffusing Particles (eV)	4200

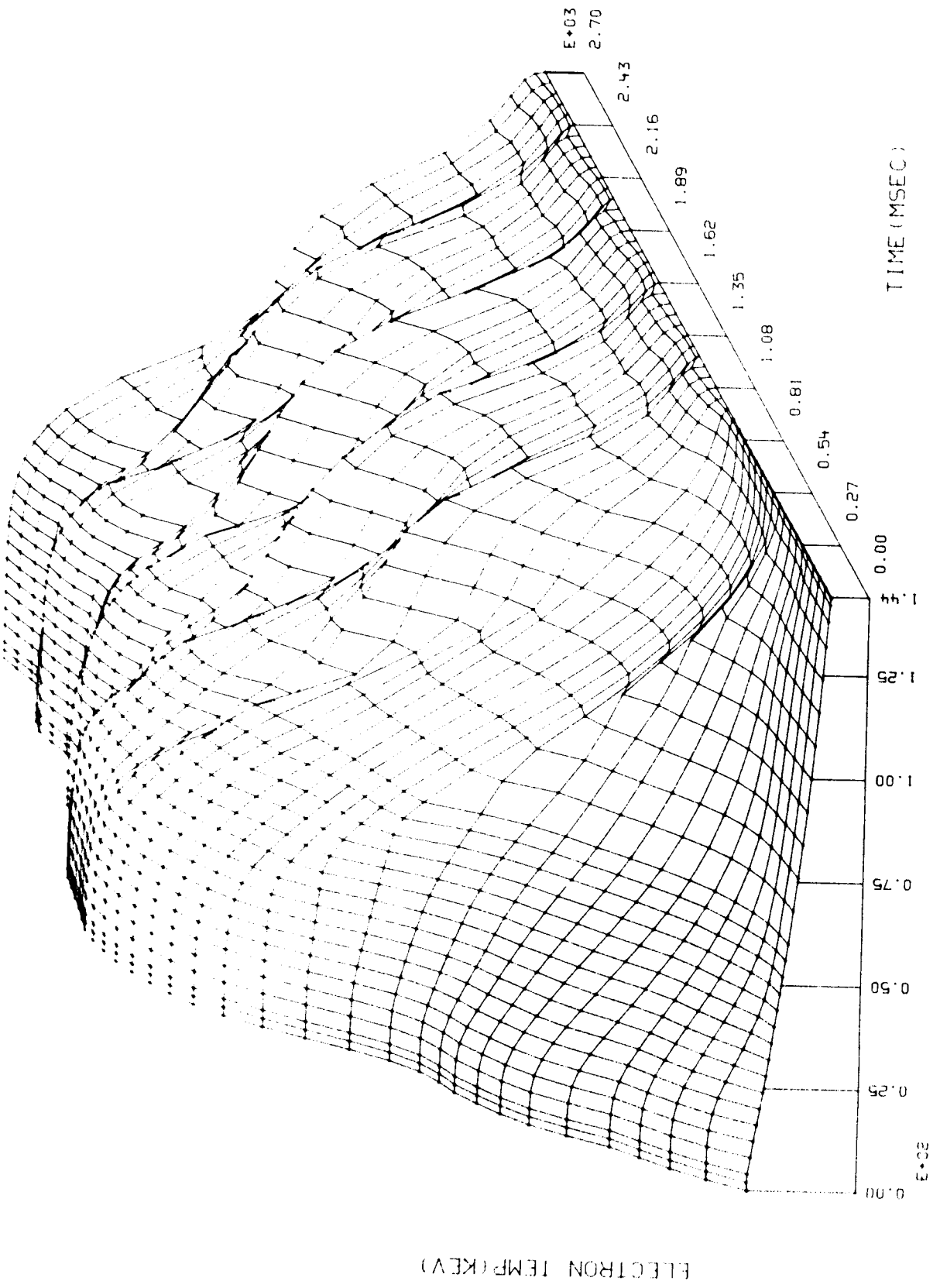


Fig. IV-D-4 Three dimensional time history of electron temperature: Case A

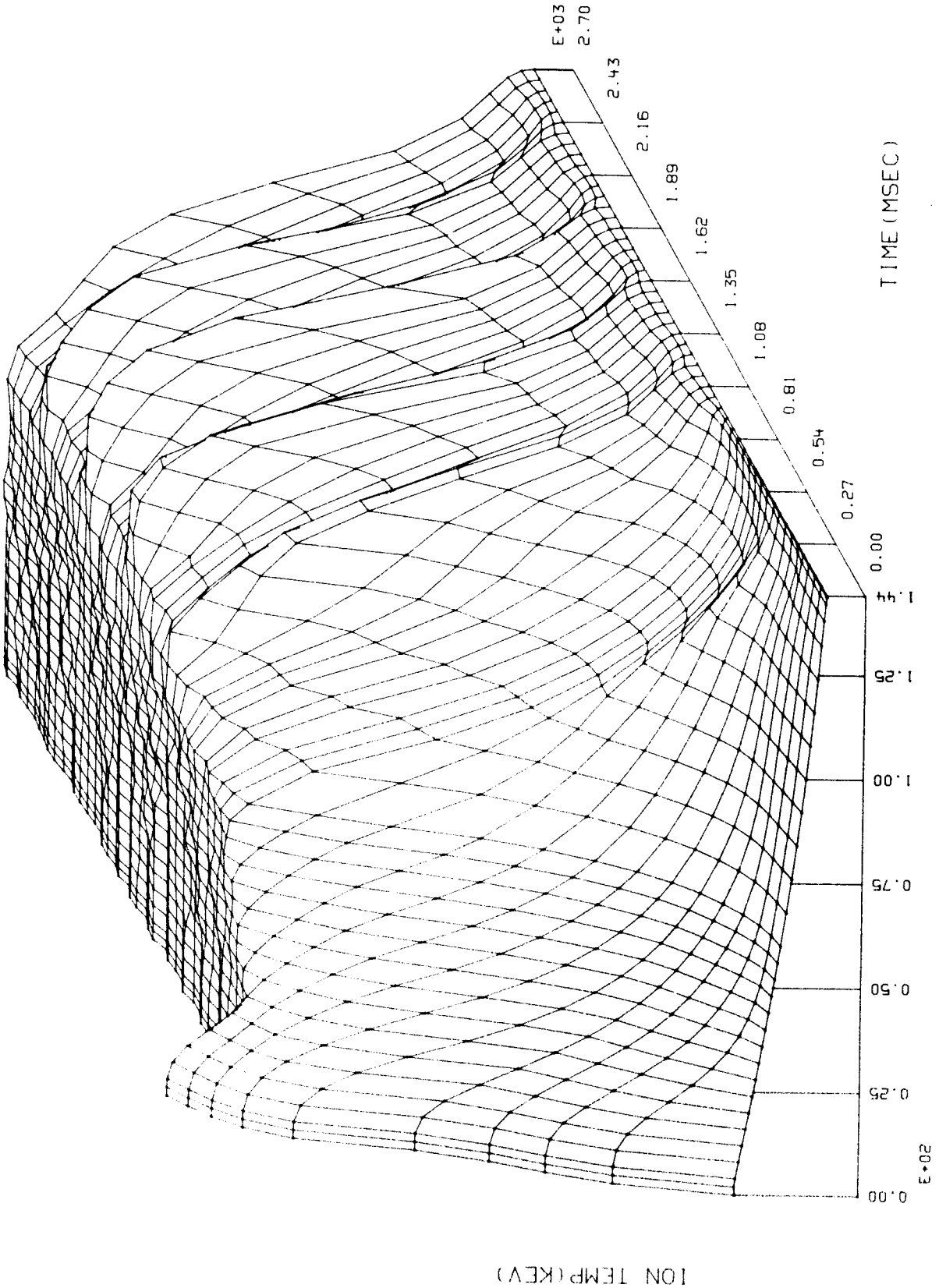


Fig. IV-D-5 Three dimensional time history of ion temperature: Case A

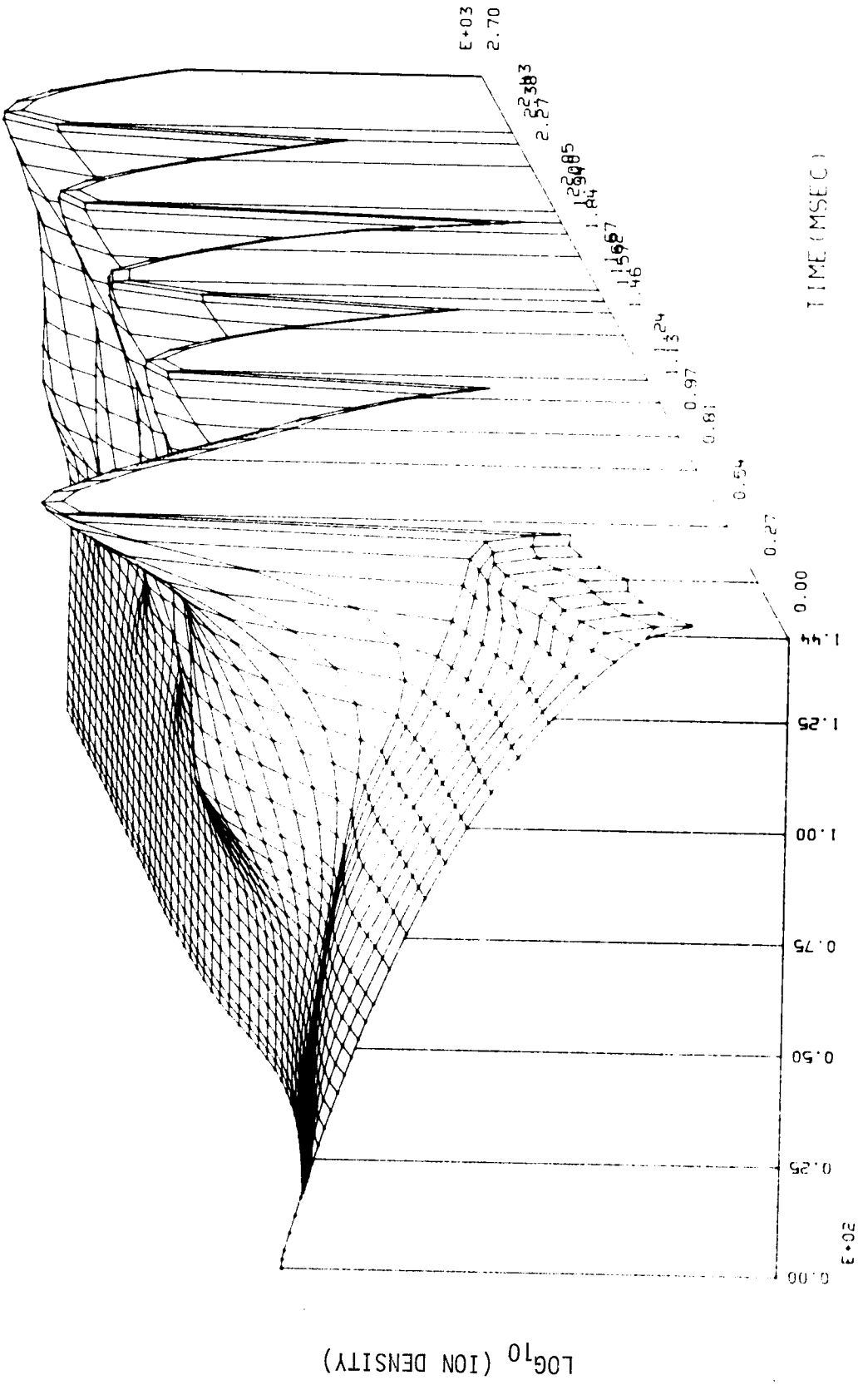


Fig. IV-D-6 Three dimensional time history of ion density: Case A

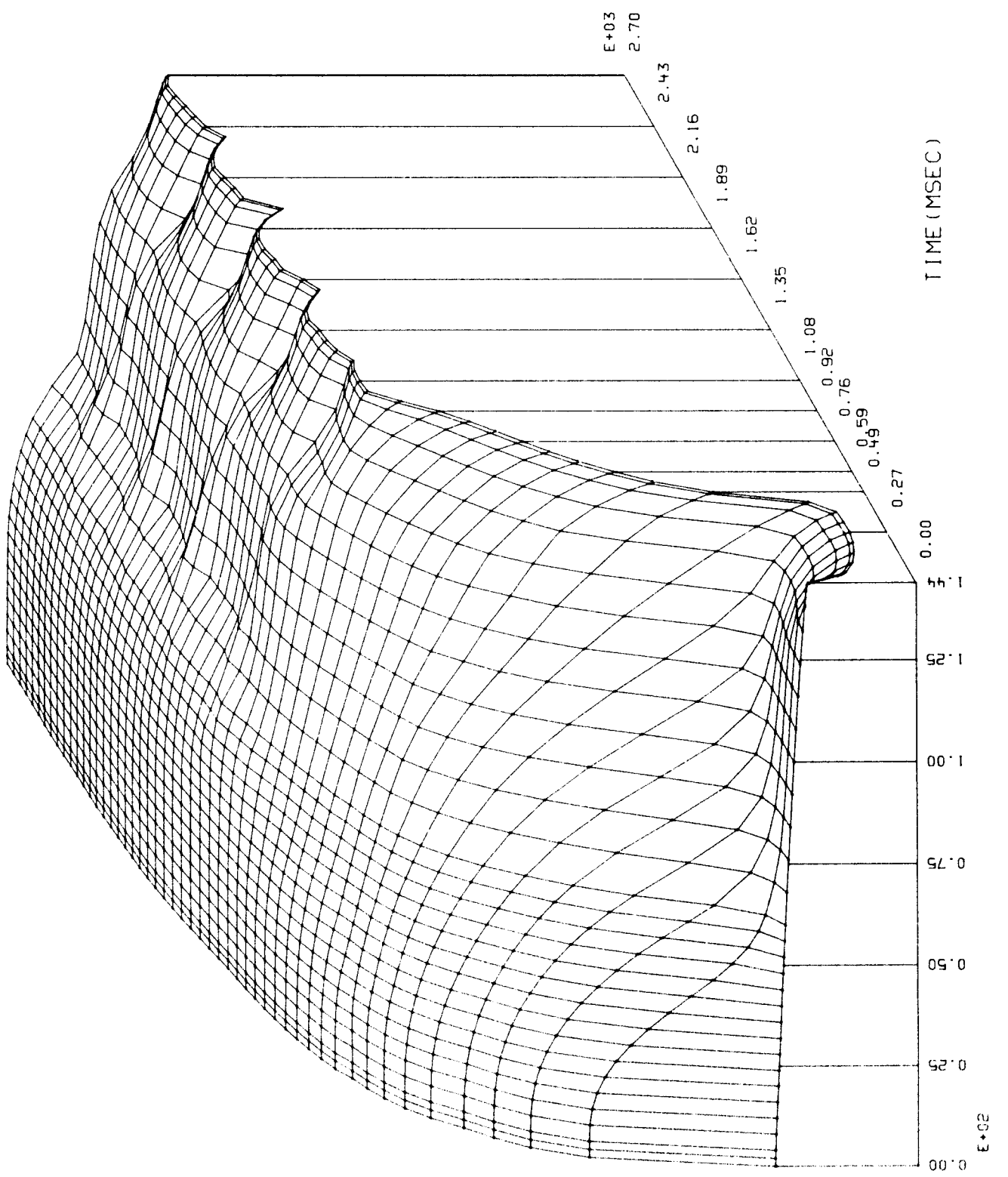


Fig. IV-D-7 Three dimensional time history of alpha density: Case A

Fig. IV-D-8 Three dimensional time history of high-Z impurity: Case A

To understand the alpha buildup, note that the ion temperature profile and alpha density profile are extremely flat over much of the plasma. Since $\nabla n_\alpha \simeq \nabla T_i \simeq 0$ in these regions, the alphas born here feel no driving force. Hence, their transport is reduced and the alpha density tends to increase as a function of time.

In addition to the alpha buildup problem, note that the average energy per diffusing particle is approximate 4200 eV. As these particles will impact upon the limiter, the limiter will sputter. However, in this early simulation, this source of impurities is not accounted for. In the modified puffing scheme to follow, an additional impurity source is provided to model this effect.

The treatment of the helium ash which does diffuse from the plasma deserves some comment. Those alphas which diffuse from the system will travel along field lines which ultimately intersect the limiters. At this point, they neutralize and are lost from the calculation, i.e. they are assumed to be pumped away with perfect efficiency. This is not consistent with the treatment of the ions since a large fraction of these ions are assumed to recycle as neutrals off the limiters and back into the plasma. Clearly, a more sophisticated recycling model is needed to self-consistently analyze this critical aspect of divertorless operation. In the summary we discuss one possibility for selective He gas pumping as required for divertorless operation.

In light of these difficulties, a modified gas puffing scenario was implemented which attempted to improve the figures of merit obtained in the pure gas puffing simulations.

IV-D-8-b. Modified Gas Puffing Scenario (Case B) (Final Case)

This scheme attempts to improve upon the pure gas puffing scenario by: (1) reducing the magnitude of the gas puffs; (2) performing some fueling via shallow "pellet" injection, and (3) increasing the radiative losses of the plasma halo by creating an impurity source localized at the plasma edge in addition to liner sputtering, thereby controlling the edge temperature.

By replacing one large gas puff with a smaller puff plus a constant step source of fuel at the plasma edge, the large temperature gradient at the edge would be reduced. This would increase the magnitude of ∇n_α and ∇T_i over much of the plasma, providing a driving force for alpha ash removal from the plasma core.

Deliberate edge contamination by a constant step source of high Z

impurities would increase the radiation from the plasma, reducing the heat loading to the limiters. The divertor action of the blanket would hopefully keep these impurities out of the plasma core, thus improving the likelihood of a long plasma burn.

In Tables IV-D-6 to IV-D-9, we tabulate the parameters of this simulation while three-dimensional plots of the plasma density and temperature are given in Figs. IV-D-9 to IV-D-13. Radial plots of density, temperature and power are given in Figs. IV-D-14 to IV-D-20.

IV-D-9. Analysis

In the scenario, the temperature gradients are reduced in response to the decreased magnitude of the gas puffs. This has a very beneficial effect upon $\dot{\bar{n}}_\alpha$ and $\dot{\bar{n}}_Z$. By comparison with the pure gas puffing case, the modified scenario reduces $\dot{\bar{n}}_\alpha$ and $\dot{\bar{n}}_Z$ by factors of 2 and 6, respectively. Thus, the chances for long burn operation are improved.

The injection of extra impurities has increased the radiation from the halo, reducing the heat load to the limiters. This procedure more than doubles the previous P_{rad}/P_α ratio. As a result, the average energy of particles which diffuse from the plasma is decreased although we find the value is still too large.

Finally, the fractional burnup has been increased by nearly a factor of 2. This reduces the problems associated with the handling of tritium although the pumping requirements are still excessive.

IV-D-10. Conclusions

The results here suggest the possibility of using periodic gas puffing and pellet fueling to maintain a clean plasma which can be fueled for an extended burn period. We have found, however, a number of fundamental issues which will likely only be clarified by experiment.

First, the pumping of helium ash without a divertor is unresolved. While our model a priori assumes that all helium incident upon the limiters is perfectly absorbed, there are indications that helium ash may be selectively trapped in the limiters, and thus pumped, this process being a consequence of the potential sheath surrounding the limiters.

Table IV-D-6

Plasma Parameters: Case B

Mean Ion Temperature (keV)	9.3
Mean Electron Temperature (keV)	8.6
Mean Ion Density (cm^{-3})	3.1×10^{14}
Mean Electron Density (cm^{-3})	3.4×10^{14}
Mean Alpha Density (cm^{-3})	2.0×10^{12}
Mean Impurity Density (cm^{-3})	1.0×10^{12}
Total Toroidal Beta, β_ϕ (%)	6.5
Total Poloidal Beta, β_θ	5.4
Energy Content of Plasma (GJ)	.29
Particle Confinement Time (sec)	.38
Energy Confinement Time (sec)	1.38
$\overline{n_e}\ \tau_E$ (sec/cm^3)	4.7×10^{14}
$\overline{Z}_{eff}$	2.5

Table IV-D-7

Power Parameters: Case B

Energy Per Fusion Event (MeV)	20.67
Thermal Power During Burn (MW)	2283
Peak to Average Power Fluctuation (%)	8
Period of Power Fluctuation (msec)	400
Average Plasma Power Density (W/cm^3)	9.3
14 MeV Neutron Production Rate (sec^{-1})	6.89×10^{20}
Total Power to Wall (MW)	1731
Radiation (MW)	151 ± 15
Neutrals (MW)	25
Neutrons (MW)	1555
Neutron Wall Loading (MW/m^2)	4.3
Total Power to Limiters (MW)	214 ± 20
Peak to Average Limiter Loading (%)	9
Average Charge-Exchange Flux to Wall (cm^{-2} sec^{-1})	1.7×10^{17}
Effective Temperature of Maxwellian Neutral Spectrum (eV)	214

Table IV-D-8

Fueling Parameters: Case B

Max. Neutral Edge Density (cm^{-3})	2×10^{11}
Min. Neutral Edge Density (cm^{-3})	1×10^{10}
Time Gas Puff On (msec)	10
Time Gas Puff Off (msec)	390
Time Between Gas Puffs (msec)	400
e-Folding Pump Time (msec)	100
Average Tritium (D) Consumption Rate (sec^{-1})	6.89×10^{20}
Average Tritium Burnup Rate (kg/day)	.22
Average Deuterium Burnup Rate (kg/day)	.15
Average (D) Fueling Rate (kg/day)	24.2
Pellets: 19.8	
Gas Puff: 6.8	
Average (T) Fueling Rate (kg/day)	37.1
Pellets: 30.3	
Gas Puff: 6.8	
Fractional Burnup, f_B (%)	.62
Total Particle Leakage (D+T+α)	1.8×10^{23}/sec
Constant Step Pellet Source on Outer 4% of Plasma	$1.1 \times 10^{16}/cm^3$-sec
Constant Step Impurity Source on Outer 4% of Plasma	$3 \times 10^{14}/cm^3$-sec

Table IV-D-9
Figures of Merit: Case B

Fractional Burnup (%)	.62
Limiter Heat Loading (MW)	214 ± 20
Radiated Power/Alpha Power (%)	39
$\dot{\bar{n}}_\alpha$ (cm^{-3}-sec)	1.7×10^{11}
$\dot{\bar{n}}_z$ (cm^{-3}-sec)	4.6×10^{10}
Erosion Rate of Wall (mm/yr)	.10
Average Energy of Diffusing Particles (eV)	3723
Erosion Rate of Limiters (mm/yr)	17
Atoms Pumped Per Second	3.1×10^{22}

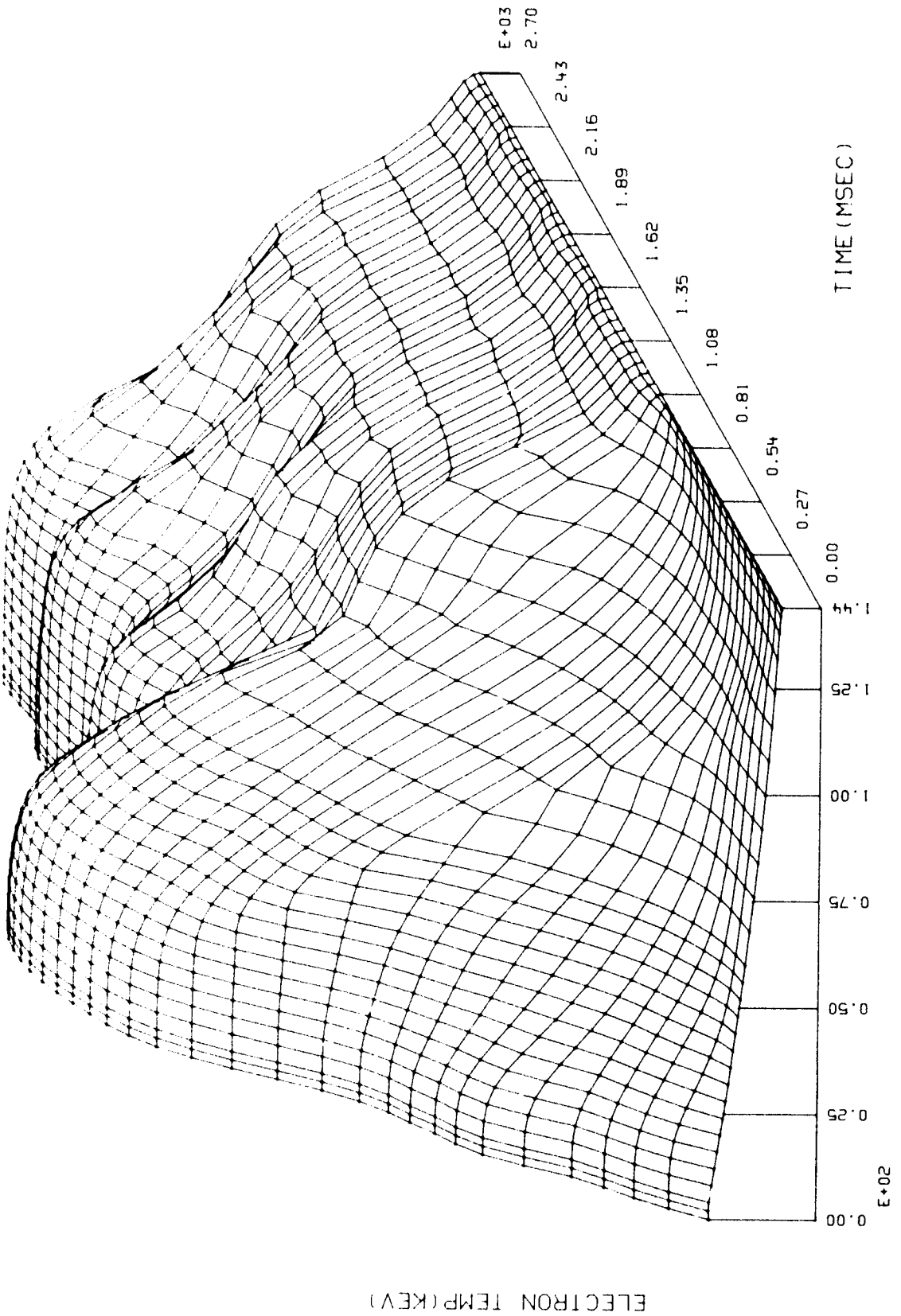


Fig. IV-D-9 Three dimensional time history of electron temperature: Case B

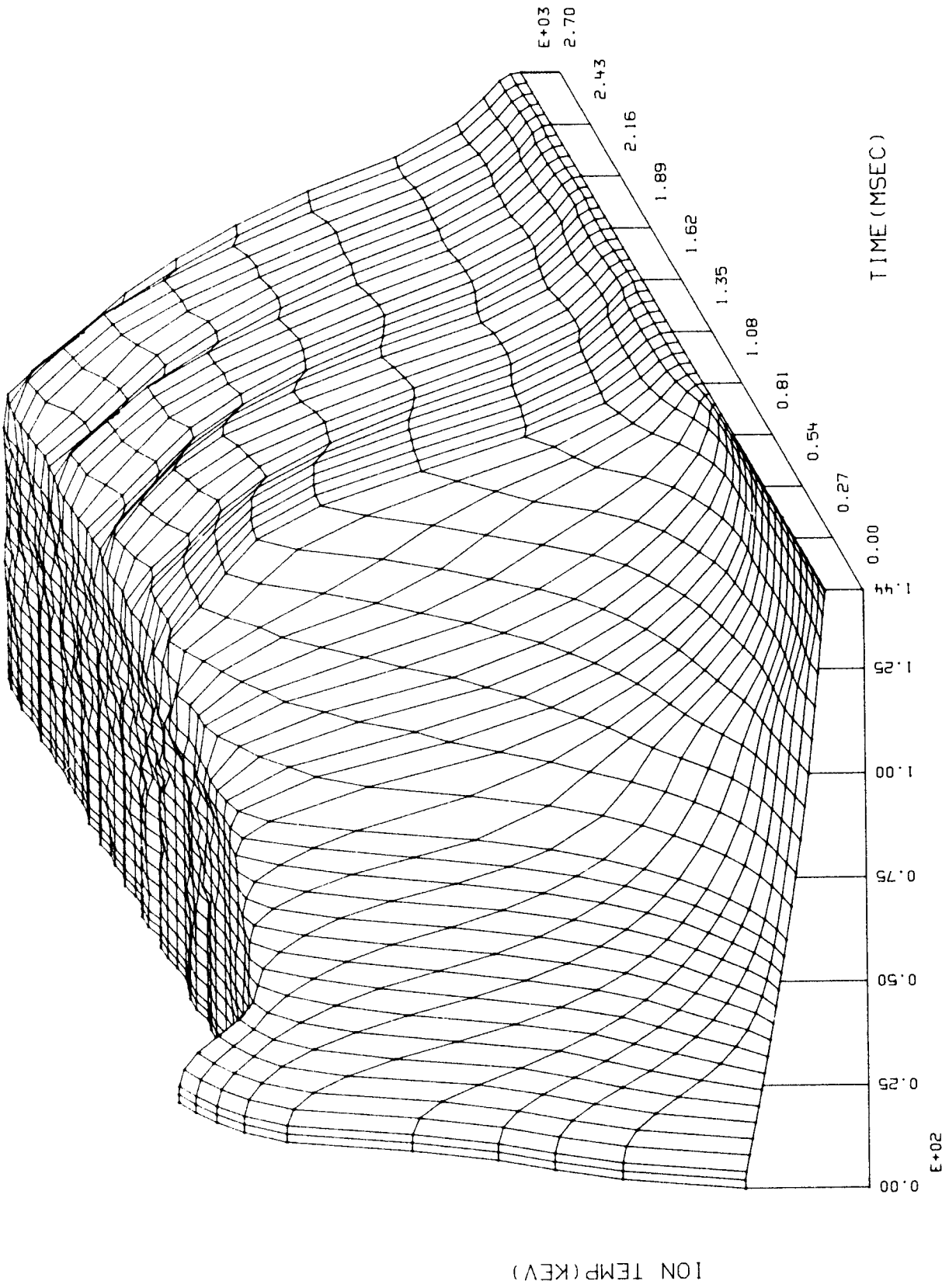


Fig. IV-D-10 Three dimensional time history of ion temperature: Case B

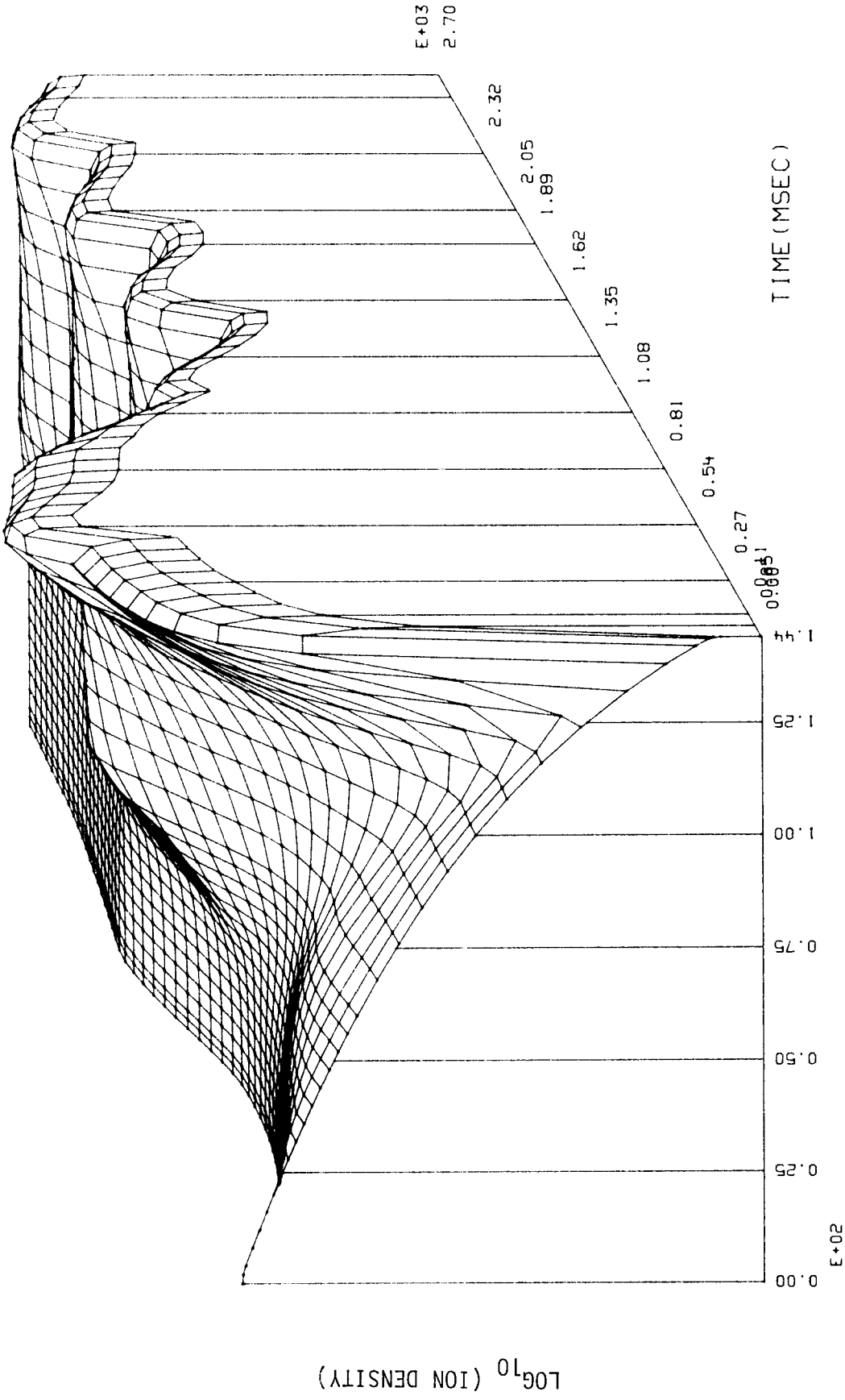


Fig. IV-D-11 Three dimensional time history of ion density: Case B

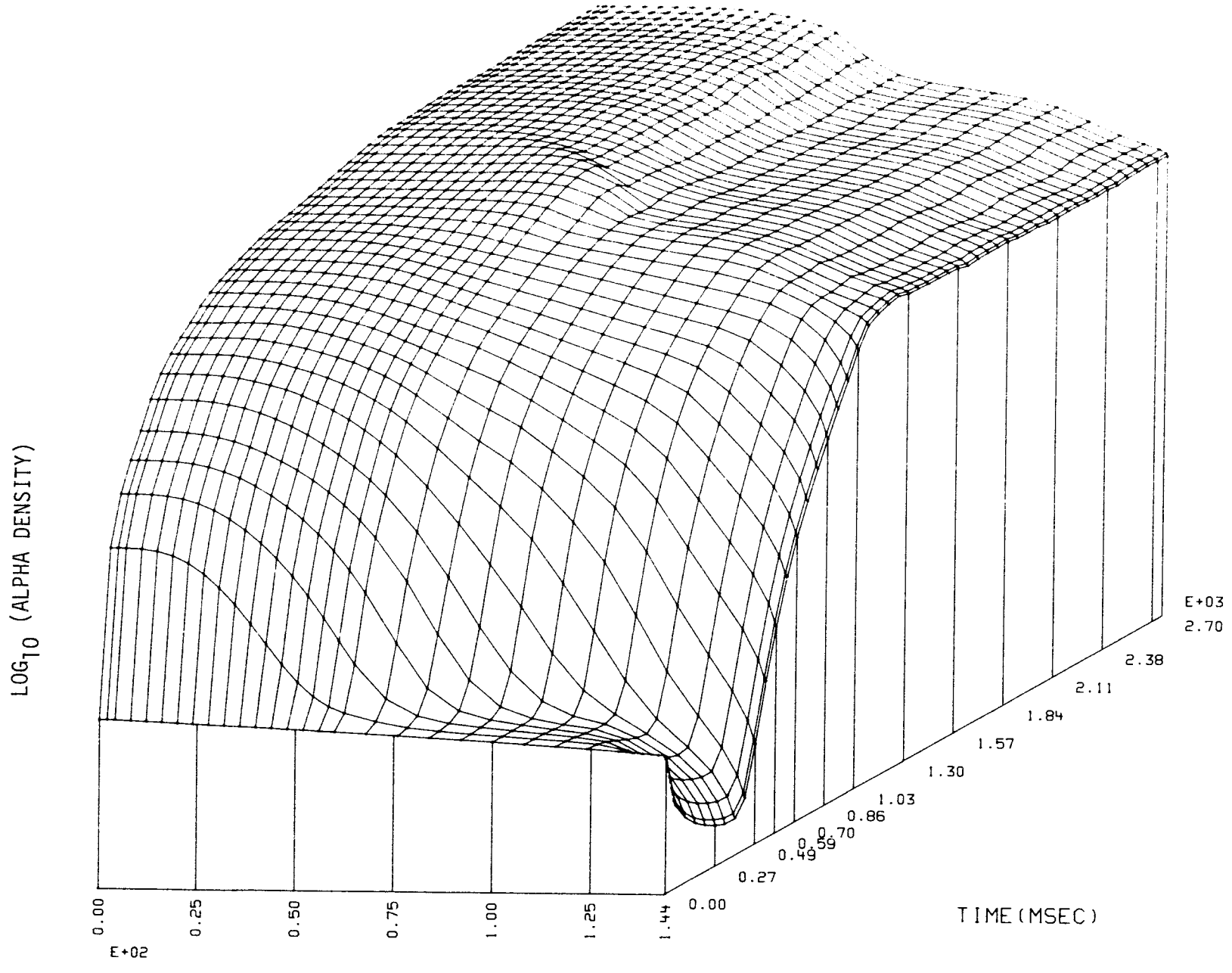


Fig. IV-D-12 Three dimensional time history of alpha density: Case B

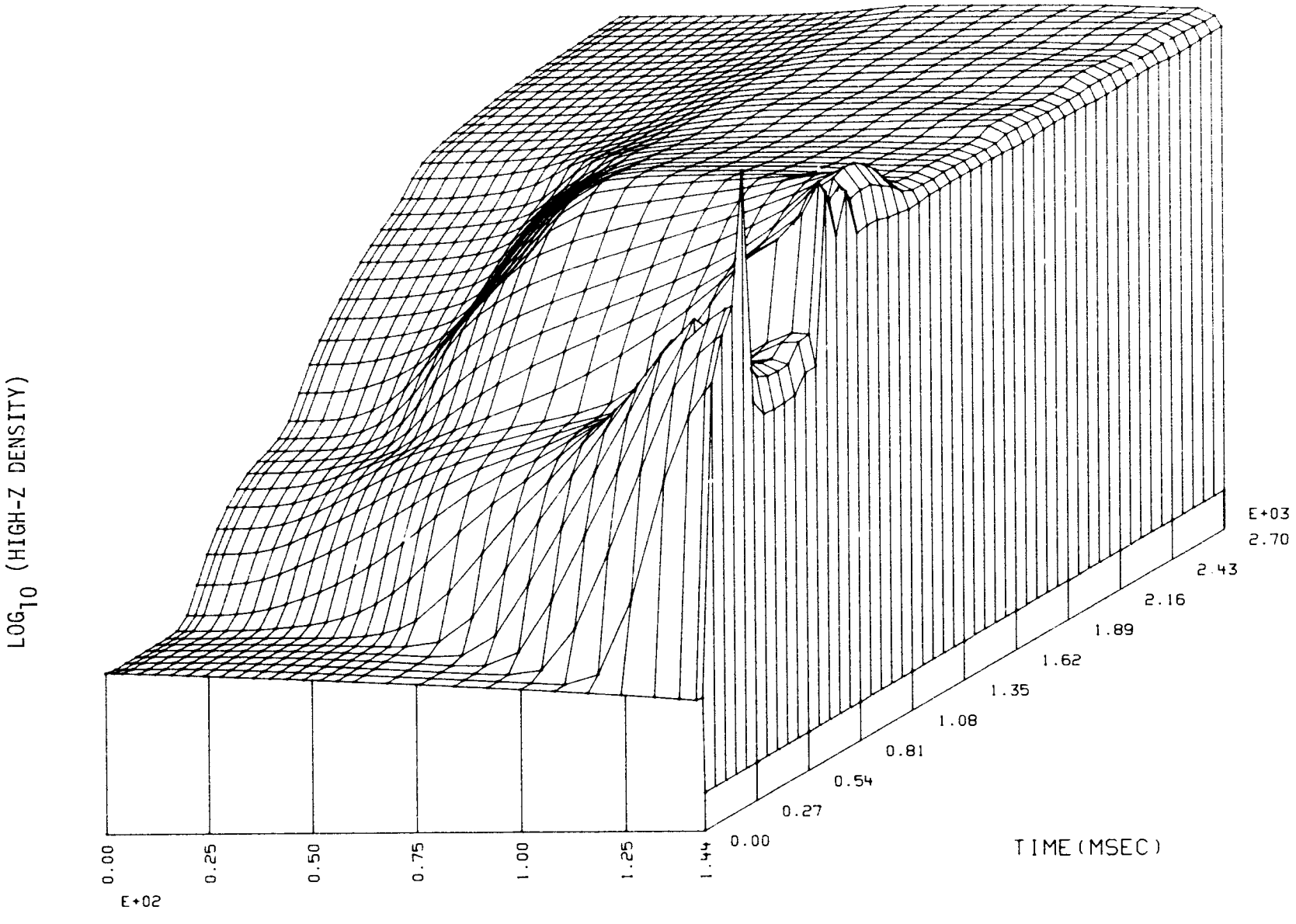


Fig. IV-D-13 Three dimensional time history of impurity density: Case B

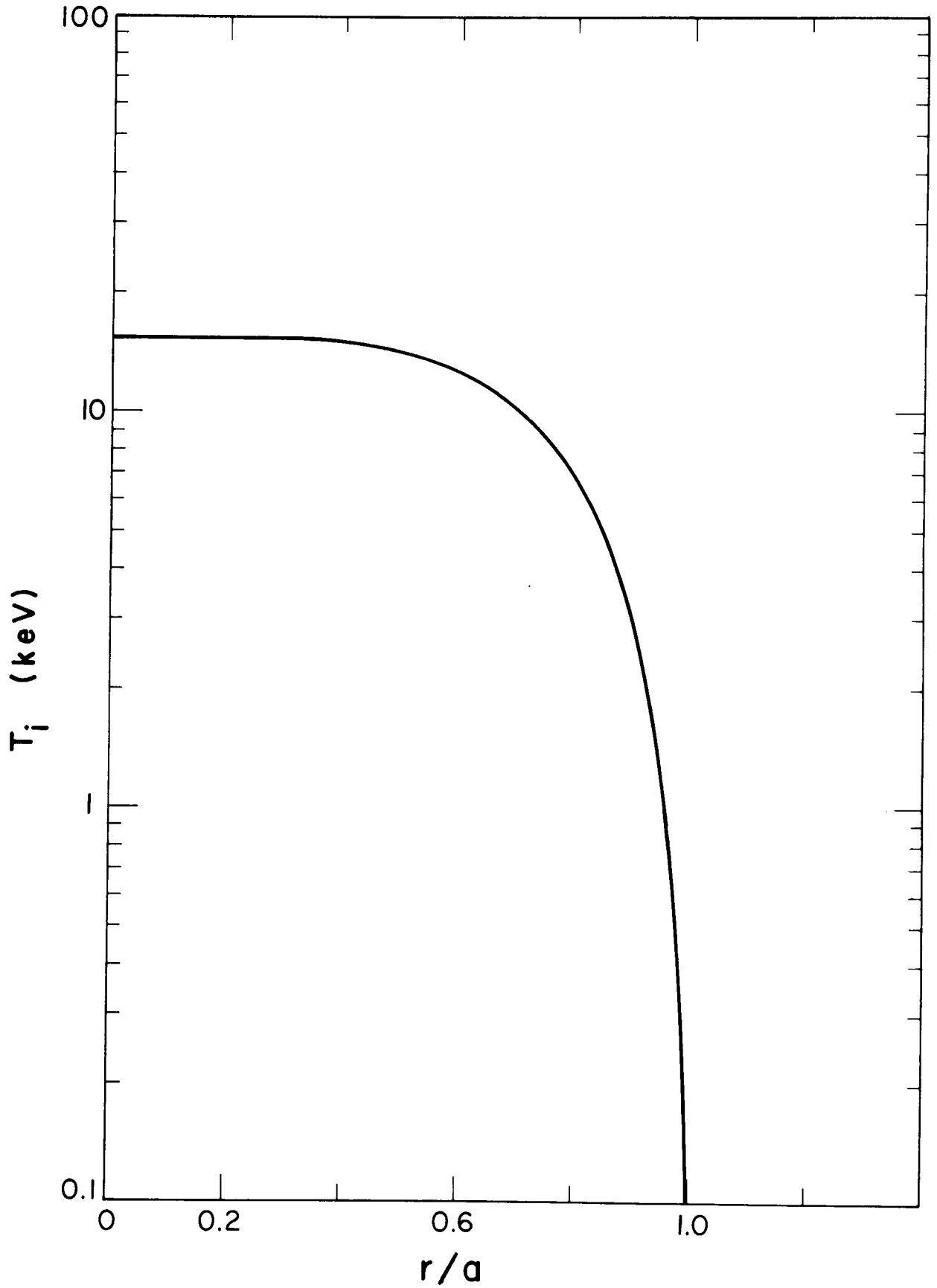


Fig. IV-D-14 Ion temperature vs. (r/a): Case B

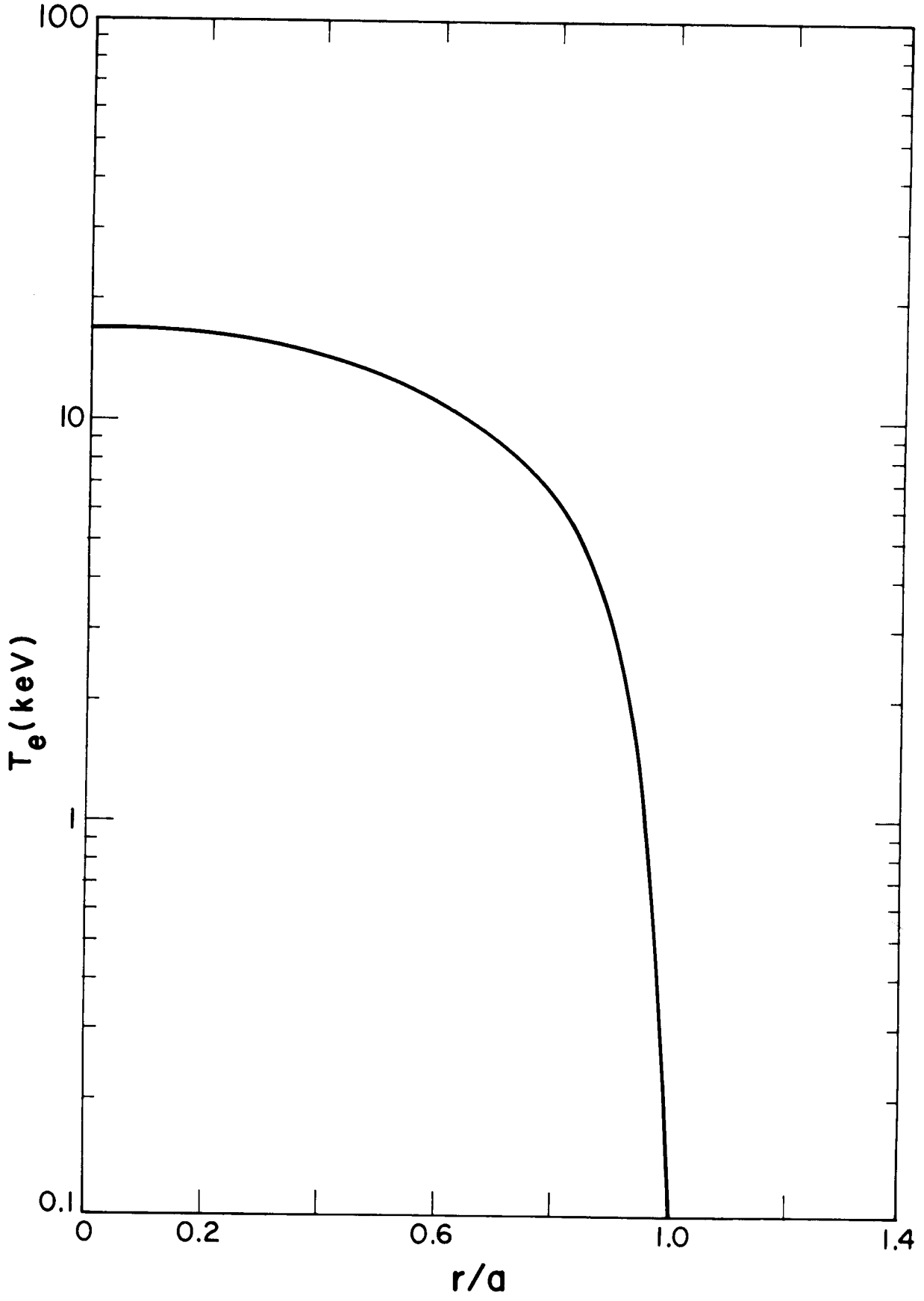


Fig. IV-D-15 Electron temperature vs. (r/a): Case B

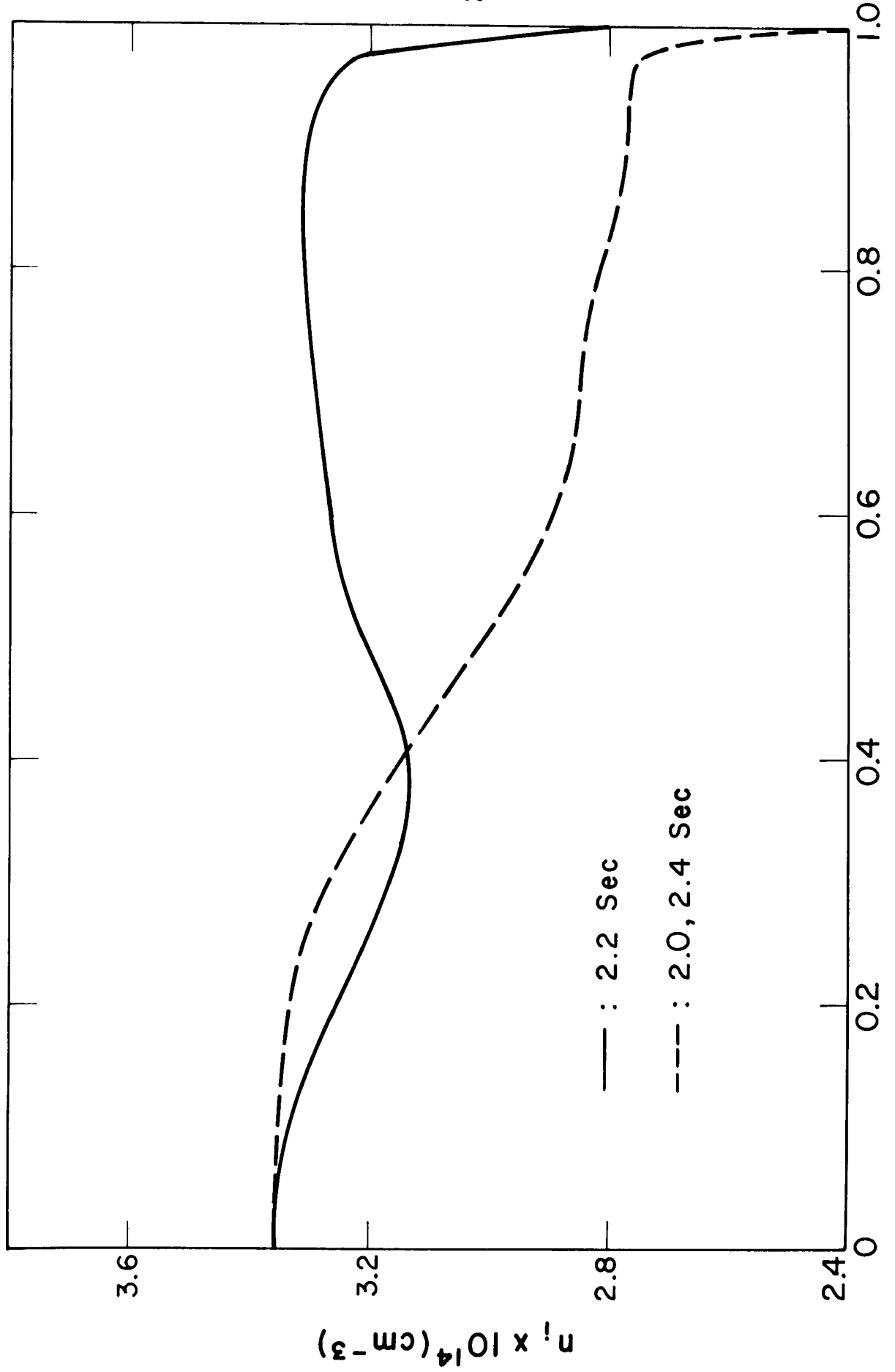


Fig. IV-D-16 Ion density vs. (r/a): Case B

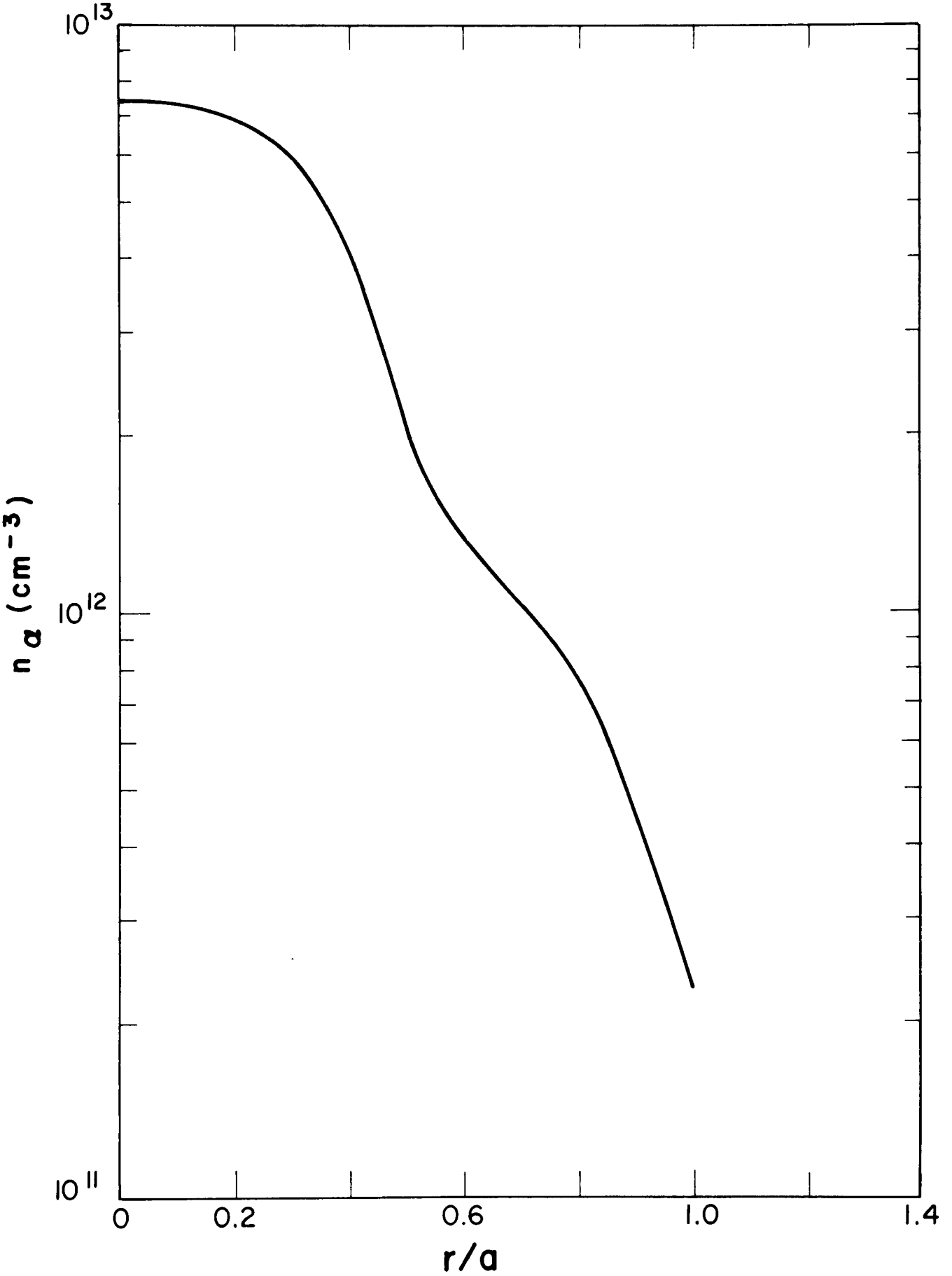


Fig. IV-D-17 Alpha density vs. (r/a): Case B

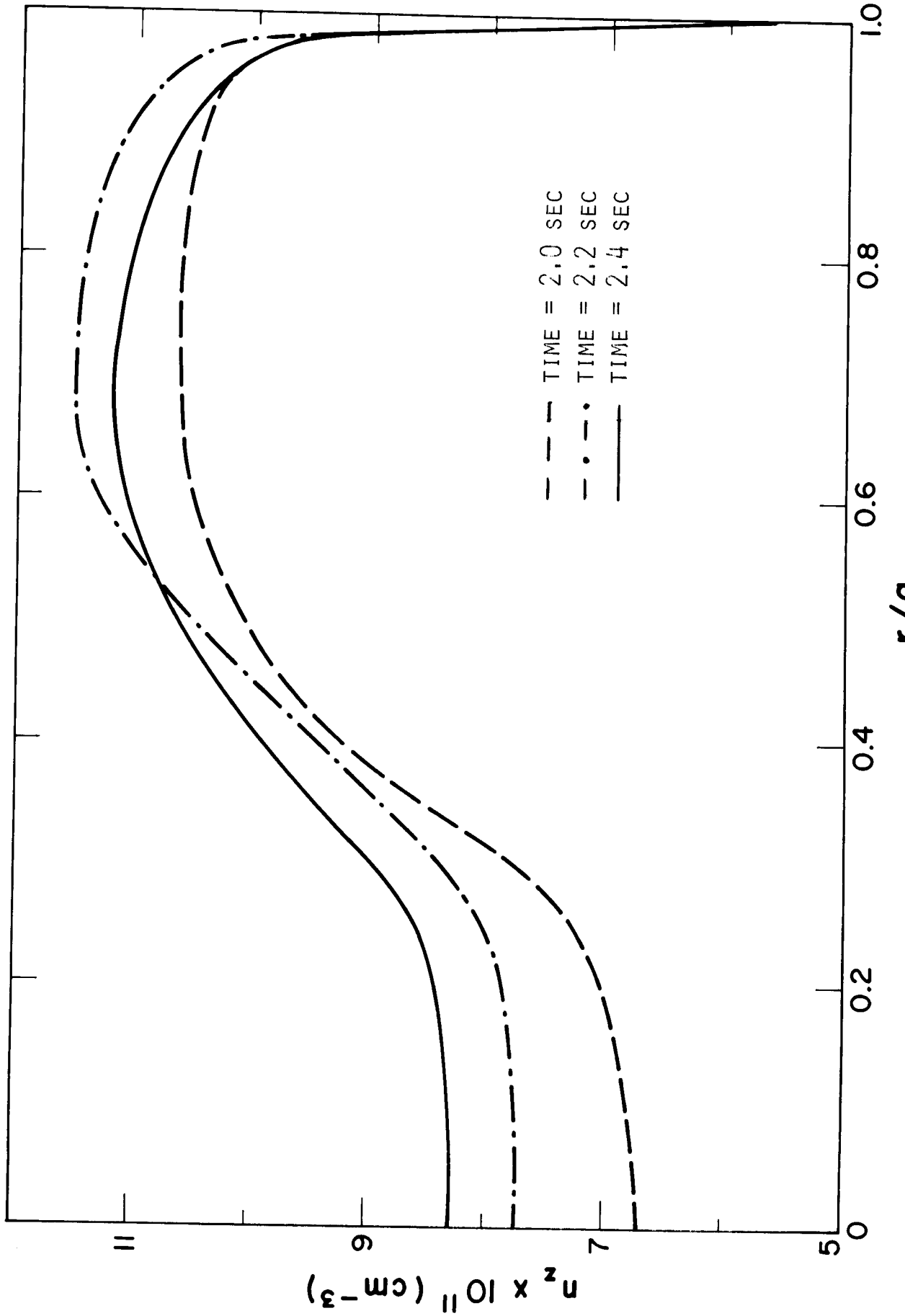


Fig. IV-D-18 Impurity density vs. (r/a): Case B

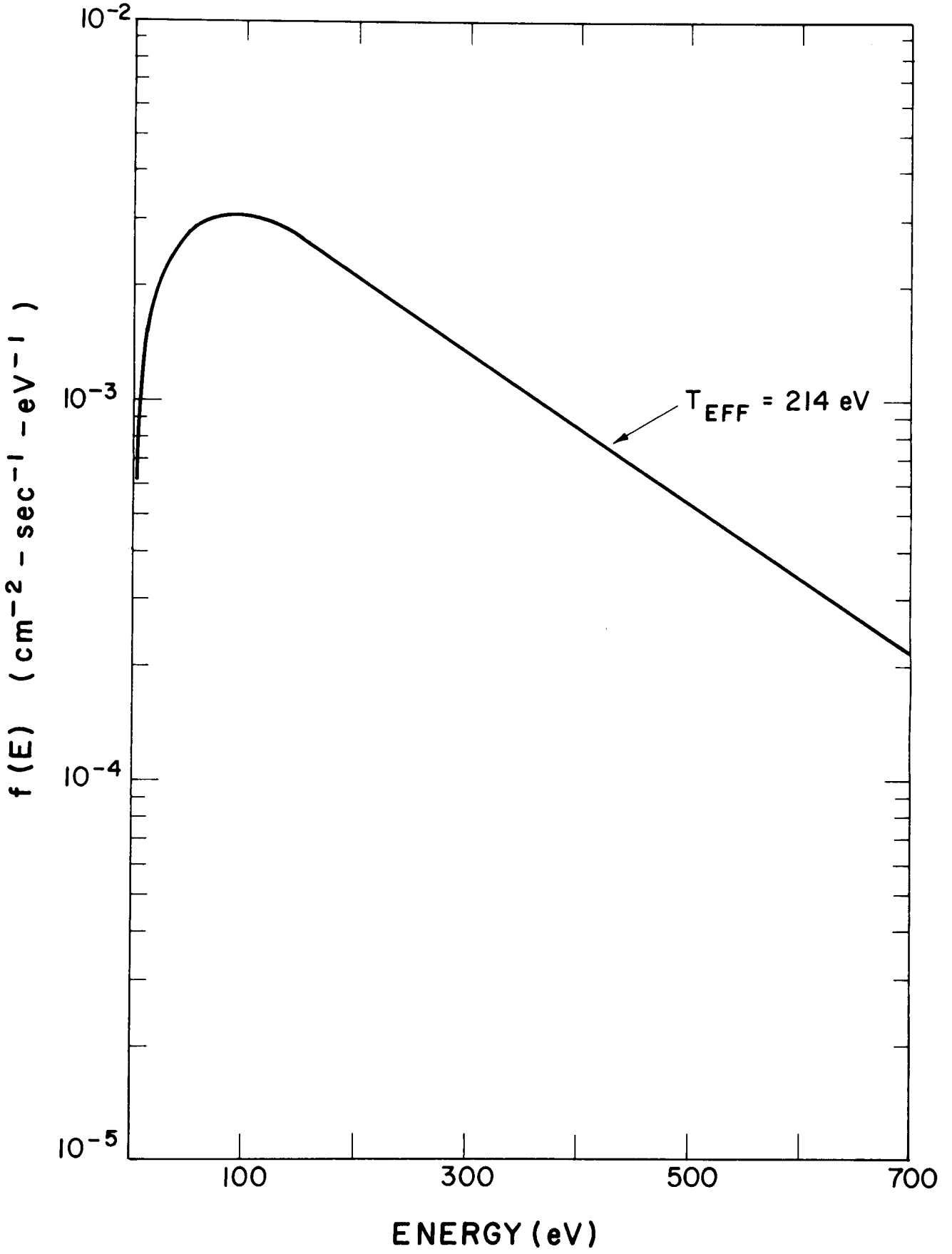


Fig. IV-D-19 Charge exchange flux energy spectrum: Case B

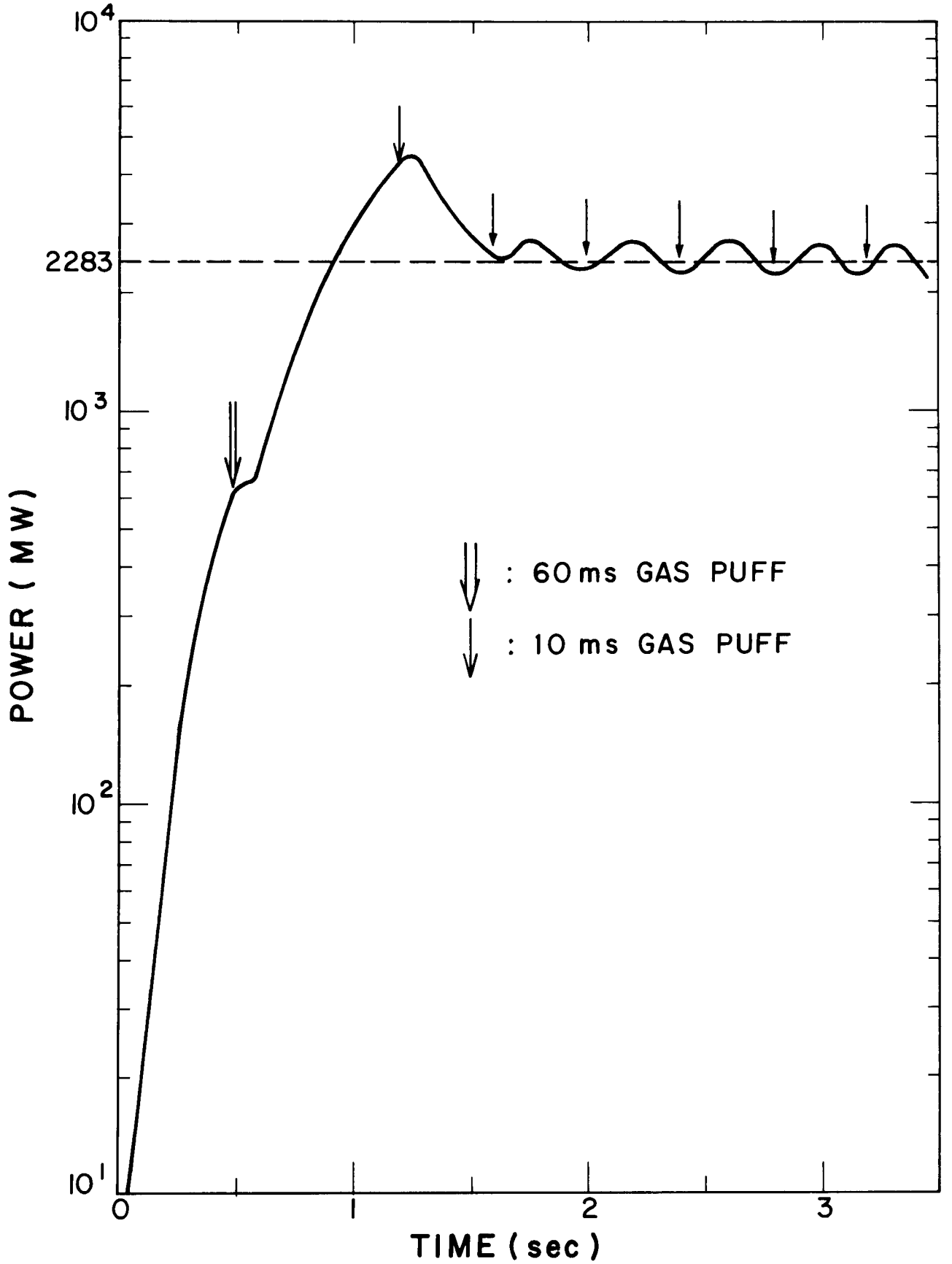


Fig. IV-D-20 Time history of NUWMAK plasma power

The sheath potential will be ~ 4 times the edge electron temperature. Alpha particles which are doubly ionized will be accelerated normal to the limiter surface and attain a directed energy of ~ 8 times the edge electron temperature. These alphas may then have sufficient energy to trap in the limiters. If these energies are insufficient, then the limiter might be placed at an artificially large negative potential. For example, if 1 keV He^{++} ions are required for trapping, a potential of 500 volts would be applied.

The question of saturation must also be addressed if this pumping mechanism is to be credible. For NUWMAK, 3×10^{20} alphas are produced per GW of fusion power. If toroidal belt limiters can supply 10^5 cm^2 of area, then the alpha flux to the limiters will be approximately 3×10^{15} α/cm^2-sec. For one 200 second plasma burn, the limiter fluence will be 6×10^{17} α/cm^2, a value close to saturation. Note that the limiter voltage and area could be tailored to obtain a burn time consistent with the maximum allowable fluence. In addition, moving limiters or limiters which are coated with an unsaturated material between plasma burns might also be employed.

In any event, the viability of adequate helium pumping via this or any other scheme is likely only to be established by experiment.

Second, we find that puffing DT fuel at the plasma edge results in unacceptable tritium handling requirements. This follows as a direct consequence of the low value of τ_p near the plasma edge (Fig. IV-D-21). If, however, only deuterium gas were puffed and tritium fueling accomplished by pellets to an ablation point where $\tau_p >> \tau_p^{EDGE}$, then the tritium diffusing from the plasma would be substantially reduced, thus improving the handling requirements.

Simple estimates show that by pellet fueling to $(r/a) \sim .6$, the burn fraction can be increased by a factor of 10, i.e., .6% → 6%. Thus, pellet fueling of tritium into regions of larger τ_p and deuterium gas puffing at the edge should substantially improve the attractiveness of the periodic gas puffing concept.

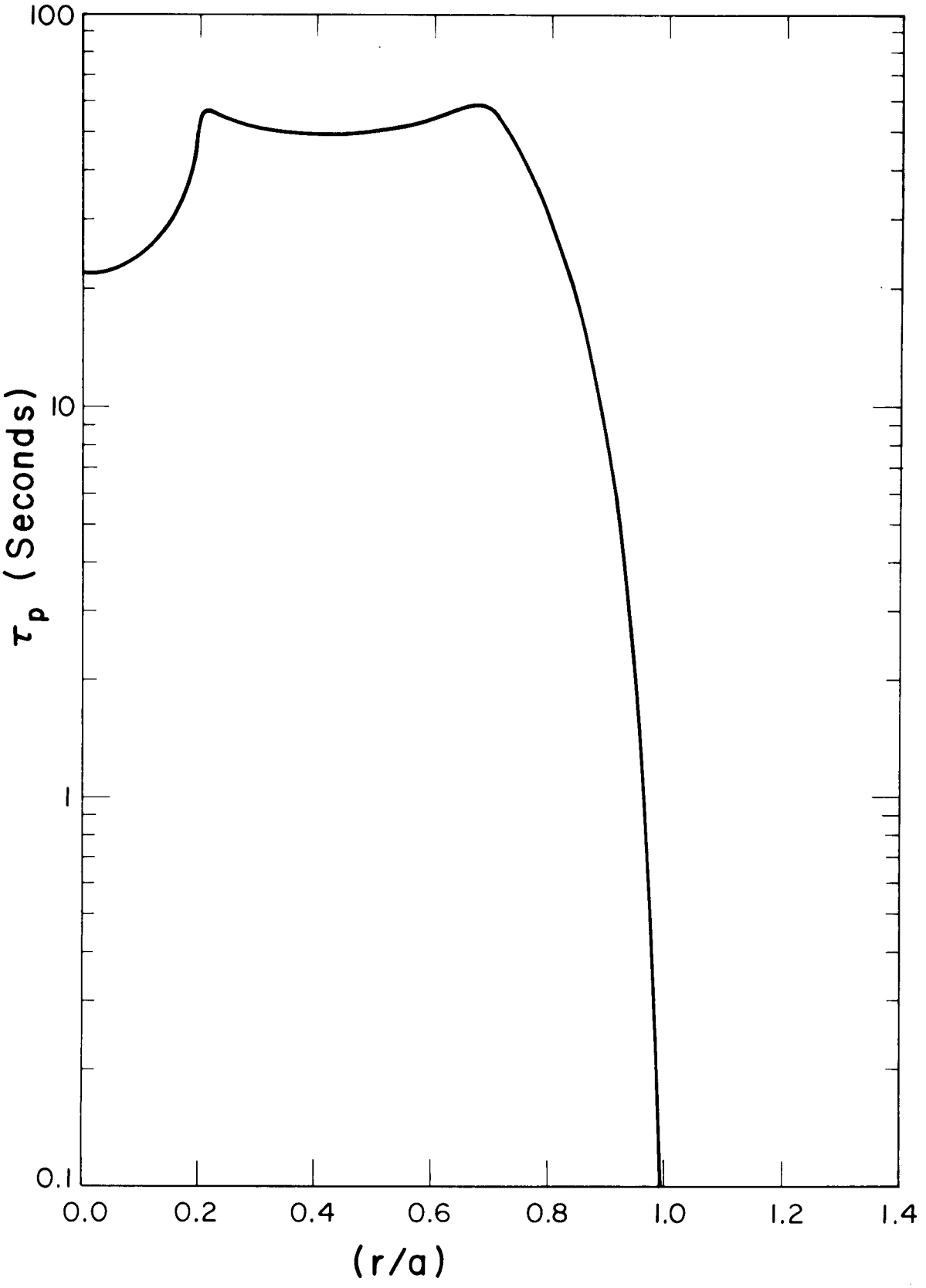


Fig. IV - D - 21 Particle confinement time vs. (r/a)

Third, our plasma/wall interaction model, while more sophisticated than in earlier work, still requires great improvements. Specifically, transport of plasma at the edge in the presence of an intense neutral source needs further study.

While in present experiments the inversion of the density profile is not observed during gas puffing, the density inversion of a reactor-sized plasma is unresolved. Examine the ratio of the density gradient scale length to the plasma radius. In present experiments this ratio is large, while for reactor plasmas, the ratio will be small. Since this ratio has an important effect on stability and performance, any extrapolations based upon present devices to future reactor plasmas are questionable. Again, we are faced with an issue which can only be clarified by future experiments, since the behavior of plasmas under full thermonuclear conditions ($T_i \sim T_e \sim 15$ keV, $n_i \sim 10^{14}$ cm^{-3}, $\beta \sim 5$-10%) must still be verified.

Fourth, the particle heat flux to the limiters is high. This characteristic of divertorless systems is analogous to the problem of handling the intense heat load to the divertor collector plates in a reactor with a divertor, a problem which remains without accepted solution even though it was identified many years ago.

Overall, we would conclude that operation with a divertor is more likely to resolve the problem of impurity control for long burn tokamak operation, but such a solution would add significant technical complexity to an already complex system. While operation without a divertor is clearly the more risky approach, the concept has great appeal and can be tested in detail in the next set of large, long pulse tokamak experiments.

References for Section IV-D

1. Verboom, G.K., Rem, J., Nuclear Fusion 13 (1973), 69.

2. Volkov, T.F., Igitkhanov, Yu. L., Tokar, M.Z., "Stationary Temperature Profile in a Tokamak Reactor Operated in the Neoclassical Regime", IAEA-CN-35/I9-3.

3. Igitkhanov, Yu. L., et al., Nuclear Fusion 18 (1978), 415.

4. Gross, R.A., Nuclear Fusion 15 (1975), 729.

5. Lehnert, B., Nuclear Fusion 13 (1973), 958.

6. Göedheer, W.J., Proceedings of the International Symposium on Plasma-Wall Interaction, Jülich, 1976.

7. Verboom, G.K., Plasma Physics 11 (1969), 903.

8. Gibson, A., Journal of Nuclear Materials (76 & 77) (1978), 92.

9. Engelmann, F., Nocentini, A., Schrijver, H., "Application of the Collisional Transport Model to the Cold-Plasma Blanket Problem", IAEA-CN-35/B7.

10. Hazeltine, R.D., Hinton, F.L., Physics of Fluids 16 (1973), 1883.

11. Hinton, F.L., Rosenbluth, M.N., Physics of Fluids 16 (1973), 836.

12. Hinton, F.L., Hazeltine, R.D., Rev. Mod. Phys. 48 (1976), 239.

13. Lehnert, B., Nuclear Fusion 13 (1971), 69.

14. Freeman, R.L. and Jones, E.M., "Atomic Collision Processes in Plasma Physics Experiments", Report CLM-R137, Culham (1974).

15. Burrell, K.H., Phys. Fluids 19 (1976), 401.

16. M.M. Widner, R.A. Dory, Bull. Am. Phys. Soc. 11 (1970), 1418. See also Oak Ridge National Lab. Report ORNL-TM-3498 (1971).

17. Rutherford, et al., Phys. Fluids 17 (1974), 1782.

18. L. Artsimovich, J.E.T.P. Letts. 13 (1971), 70.

19. B.B. Kadomtsev, O.P. Pogutse, Nuclear Fusion 11 (1971), 67.

20. B.B. Kadomtsev, O.P. Pogutse, Sov. Phys. Dokl. 14 (1969), 470.

21. J.D. Callen, B. Coppi, R. Dagazlan, R. Gajewski, D.J. Sigmar, in Plasma Physics and Controlled Nuclear Physics Research (Proc. Madison Conf., June 1971) (IAEA, Vienna 1972), Vol. II, pg. 51.

22. S.O. Dean, et al., "Status and Objectives of Tokamak Systems for Fusion Research", U.S. Atomic Energy Commission, WASH-1295 (1974).

23. Audenaerde, K., Emmert, G.A., Gordinier, M., "SPUDNUT: A Transport Code for Neutral Atoms", Univ. of Wisconsin Nuclear Engineering Department Report UWFDM-259 (1978) (to be published in the Journal of Computational Physics).

24. Howe, H. (personal communication).

25. Gilligan, et al., "Multi-Group Calculations of Low Energy Neutral Transport in Tokamak Plasmas", Princeton Plasma Physics Report PPPL-1384 (1977).

26. Freeman, R.L. and Jones, E.M., "Atomic Collision Processes in Plasma Physics Experiments", Report CLM-R137, Culham (1974).

IV-E. Vacuum System

IV-E-1. Introduction

Long burn operation in tokamaks depends in part on impurity control, fueling and ash removal. In earlier designs[1,2,3,4] these needs were accommodated with the use of a divertor for impurity and ash removal and with solid pellet injection for fueling. It may prove to be that these components are indispensable to the viable operation of long burn tokamaks, however, they do represent complicating factors in the design and subsequent maintenance of the reactors.

A divertorless tokamak is extremely attractive from several standpoints, in particular from the standpoint of assembly and maintenance. These advantages are also reflected in smaller TF coils and fewer VF coils within the toroidal bore, which can be translated into substantial economic benefits. However, such a reactor is faced with the problem of handling an enormous quantity of gas without the benefit of a divertor. This appears to be a problem that will be difficult to overcome for long burn tokamak reactors with a duty cycle high enough to make them economically attractive.

In tokamaks with poloidal divertors[1,2,3,4], charged species leaving the plasma confinement are guided out of the plasma chamber along magnetic field lines. Once outside the plasma torus, the charged particles are neutralized on collecter plates and subsequently pumped out. The poloidal divertor slots usually account for a very small percentage of the first wall area. Since the charged particles follow the field lines through the slots they are not in any way impeded by the narrow apertures provided for that purpose. On the other hand, in a divertorless tokamak, the charged particles are neutralized within the chamber and are pumped out as neutrals. In the molecular flow regime, conductance through the vacuum ports is determined by the collision of the molecules with the walls of the ducts. Obviously, the conductance of the vacuum ports can be increased if a larger fraction of the first wall is devoted to them. But there is a practical limit which is somewhere between 5 - 10% of the first wall area and is usually determined by such considerations as neutron streaming, space limitation, and interference with other reactor components.

A divertorless tokamak is faced with another equally challenging problem, namely that of neutralizing the ions at a point where they can be easily pumped out. It is difficult to distribute pump ports uniformly over the whole first wall surface. In most designs, the pump ports are located at one or two azimuthal levels, and are uniformly distributed circumferentially. The location of the limiters must be such that the neutrals scattering from them can be pumped out before they diffuse back into the plasma. It has been proposed[5] that the limiters can be designed with a steep obtuse angle such that the neutrals can be scattered directly into a pump port. This may be difficult to implement. The whole problem of pump port/limiter design, sizing and location in divertorless tokamaks is very complex and will require a great deal of investigation and experimentation.

IV-E-2. System Design

The periodic gas puffing scheme has been discussed in great detail earlier in this chapter. The scheme requires that the scrapeoff zone surrounding the plasma be periodically cycled between two neutral atom densities:

$$(n_0)^{max.} \sim 3.5 \times 10^{11} \text{ cm}^{-3}$$

$$(n_0)^{min.} \sim 1.3 \times 10^{11} \text{ cm}^{-3} \quad .$$

The higher density is maintained for about 10 msec and then pumped down to the lower density value in about 400 msec. It was decided that the only credible way of maintaining such a pressure profile is by means of a system of venetian blinds located slightly downstream from the pump ports. The idea is to have the venetian blinds undergo a 180^{o} rotation in about 20 msec every 400 msec, thus effectively placing a very high impedence in the pumping system which coincides with the gas puff in the plasma chamber. Because the whole sequence will remain in the molecular flow regime, the plasma chamber will be effectively isolated from the pumps for the duration of the pulse. The mechanical drive and the venetian blind system was designed in detail by a mechanical engineering student for his senior year project, although it is not included in this report.

The vacuum system in NUWMAK is characterized by the following:

1. There are no seals between the blanket modules, but the region between the blanket and the shield is maintained at a pressure of 1×10^{-4} torr.
2. Eight large cryosorption pump stations are located below grade between the TF coils as shown in Fig. IV-E-1. Each pump station has $20m^2$ of compound condensation and cryosorption surface.
3. The pumps are designed with front and back pumping surfaces, such that while the front side is in operation, the back side is being regenerated. Such a pump is shown in Fig. IV-E-2.
4. There are sixteen 1.2m x 1.5m rectangular pump ports in the plasma chamber amounting to ~ 10% of the first wall area. Each two ports are ducted to one of the eight pump stations by means of removable ducts. The ducts are water cooled and are surrounded with a shield.
5. A massive chevron shield which is water cooled attenuates the neutron streaming to the pumps. The pump surfaces are parallel to the ducts further alleviating the problem of neutron streaming.

Table IV-E-1 gives the major specifications of the vacuum system for NUWMAK.

CROSS SECTION OF NUWMAK BETWEEN TF COILS (with inner RF cavity)

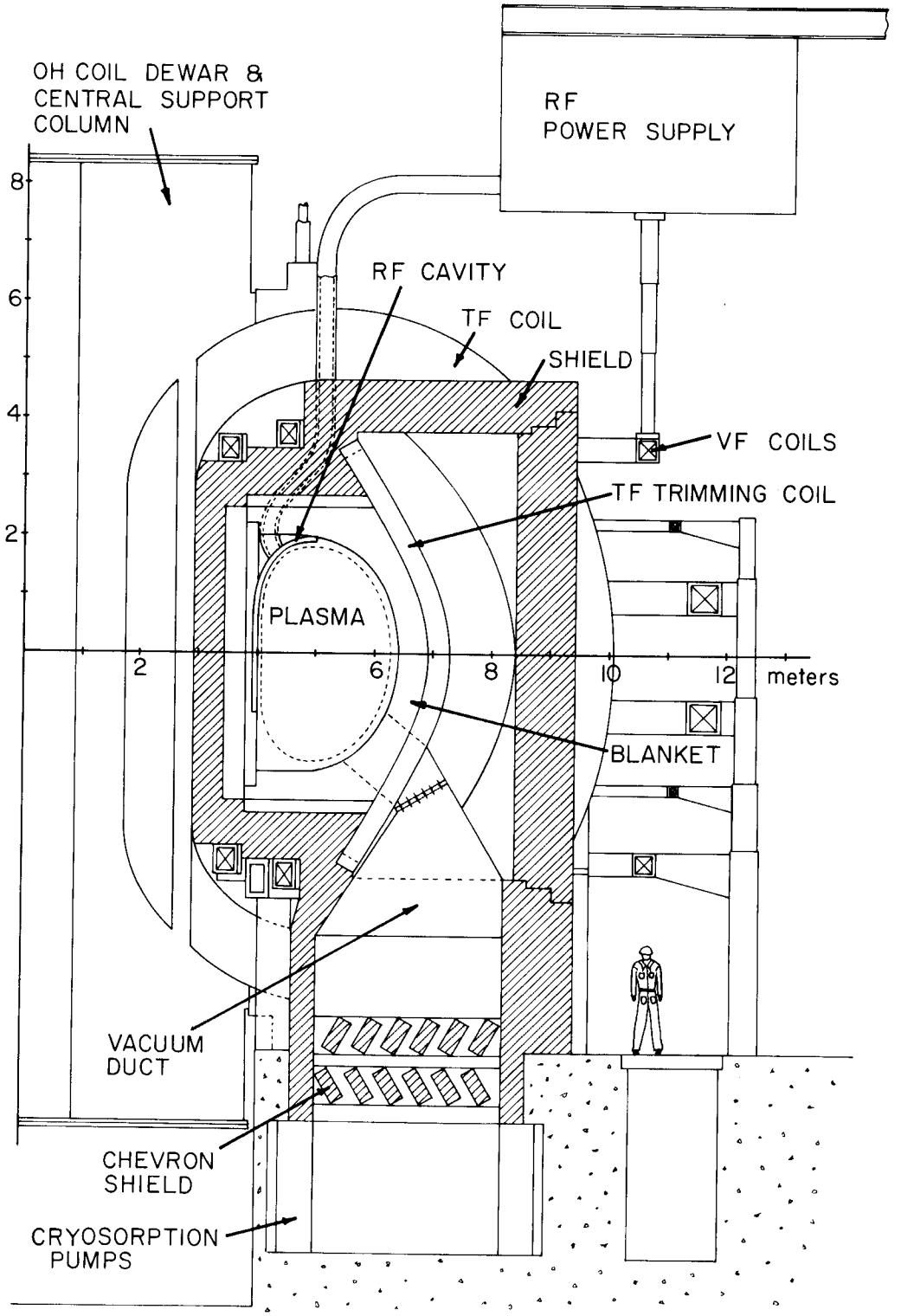
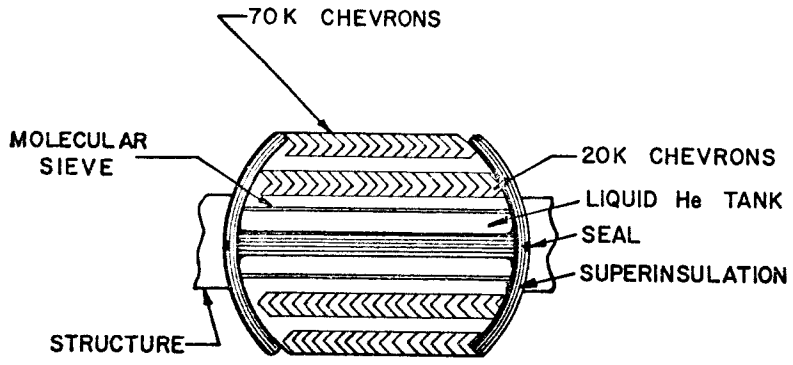
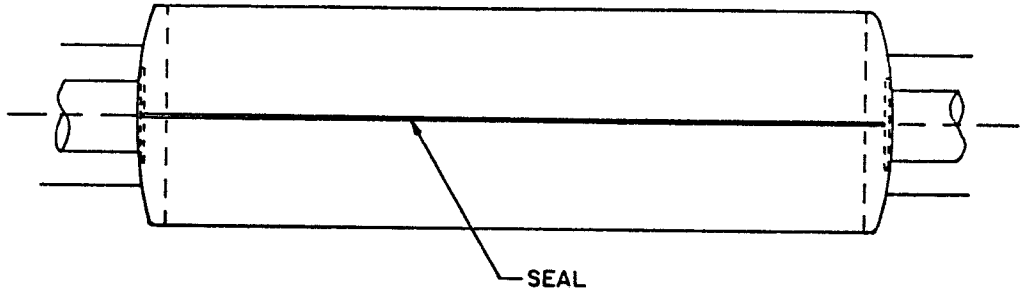


Fig. IV-E-1





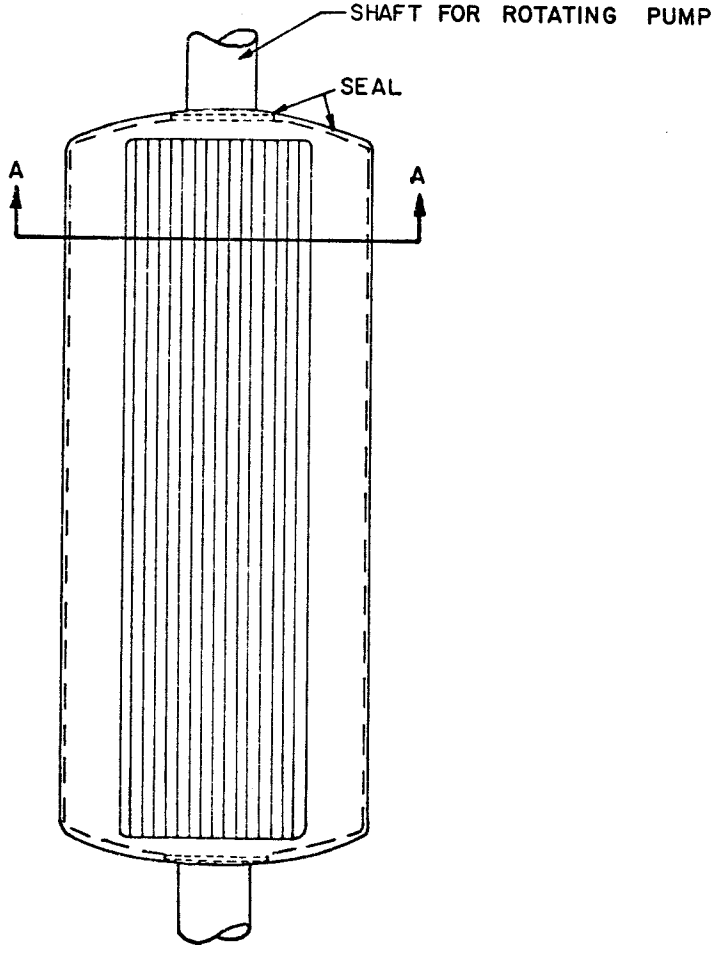


FIGURE IV-E-2

Sketch of Proposed Rotatable Cryosorption Pump

Table IV-E-1 NUWMAK VACUUM SYSTEM SPECIFICATIONS

NUMBER OF PUMP STATIONS	8
ACTIVE PUMPING AREA PER STATION (m^2)	20
NUMBER OF PUMP PORTS IN PLASMA CHAMBER	16
SIZE OF EACH PUMP PORT (m)	1.2 x 1.5
CONDUCTANCE OF EACH PUMP PORT (ℓ/s)	9×10^5
CONDUCTANCE OF EACH SET OF VENETIAN BLINDS (ℓ/s)	7.3×10^5
CONDUCTANCE OF EACH SET OF CHEVRON SHIELDS (ℓ/s)	5×10^8
EFFECTIVE PUMPING SPEED FOR D_2 & T_2 (ℓ/s)	4×10^6
EFFECTIVE PUMPING SPEED FOR HELIUM (ℓ/s)	2.3×10^6
D & T ATOM LEAKAGE /sec	2.95×10^{22}
α PARTICLE LEAKAGE /sec	6.8×10^{20}
D_2, T_2 & DT GAS THROUGHPUT (torr - liters/sec)	1000
He GAS THROUGHPUT (torr - liters/sec)	49
REQUIRED D & T BASE PRESSURE (torr)	1×10^{-5}
ATTAINABLE D & T BASE PRESSURE (torr)	2.5×10^{-4}
REQUIRED He BASE PRESSURE (torr)	2×10^{-6}
ATTAINABLE He BASE PRESSURE	2.1×10^{-5}
LIQUID He CONSUMPTION (liters/day)	42×10^3
LIQUID N_2 CONSUMPTION (liters/day	300×10^3
TOTAL POWER CONSUMPTION (MW)	3.8

IV-E-3. Discussion and Conclusions

It is clear from Table IV-E-1 that the major difficulty in the vacuum system is pumping the helium. Obviously, the ideal fusion pumping system is one which can selectively pump the helium while allowing the hydrogen to recycle back into the plasma. Although mention has been made of possible helium gettering, no credible system which can do that has yet been proposed thus far.

In NUWMAK the lowest attainable He partial pressure is 2×10^{-5} torr. This value is based on a pumping speed for helium of $2\ell/sec - cm^2$. Such pumping speeds are achievable today at low mass loading rates. However, the molecular sieve tends to load up rapidly at high mass loading rates such as will be encountered in a tokamak. Compound pumps, in which the hydrogen is cryosorbed or cryocondensed on 15K chevrons before it reaches the helium cryosorption panel are presently being tested. Initial results are very encouraging.[6] There is clear evidence, however, that hydrogen cannot be pumped on the same panel with helium under fusion reactor conditions.[6]

The lowest attainable D_2 & T_2 pressure in NUWMAK is 2.5×10^{-4} torr, a factor of four higher than the required minimum of 1×10^{-5} torr. The pumping speed for D_2 & T_2 was taken as $6\ell/sec - cm^2$. Although hydrogen pumping speeds of 8-15 $\ell/sec - cm^2$ have been reported,[7] experiments at ORNL have shown speeds on the order of 3-6$\ell/sec - cm^2$ [8,9]. It is readily conceded that improvements in design and control can increase the pumping speed somewhat. This clearly indicates that the problem of cryopumping both with respect to hydrogen and helium requires extensive investigation and development.

Only small increases in the overall pumping capacity can be expected with improvements in pump design. For example, a factor of two increase in the pumping speed at the cryopanel will only contribute 50% to the overall capacity due to the limitations in the conductance of the ports and ducts. One can conclude, therefore, that improvements in pump design alone will not be sufficient to bridge the gap between what is needed and what is attainable in the way of helium and hydrogen pumping in a divertorless tokamak such as NUWMAK.

To summarize the vacuum system problems we can say the following:

1. Limiter design and placement is very critical from the standpoint of neutralizing the charged particles at a location where the neutrals can be pumped out by the vacuum system.
2. Even with 10% of the first wall devoted to pump ports, it is difficult to provide adequate pumping speed to maintain a low enough He and hydrogen partial pressure suitable for proper plasma conditions in a divertorless tokamak.
3. Unless the requirements on the helium partial pressure are relaxed in a divertorless tokamak, the power output may be dictated to a large extent by the practical amount of pumping capacity that can be provided by the vacuum system.

References for Section IV-E

1. B. Badger et al., "UWMAK-I-A Wisconsin Toroidal Fusion Reactor Design," UWFDM-68 (1973).

2. B. Badger et al., "A Conceptual Tokamak Reactor Design, UWMAK-II," University of Wisconsin, UWFDM-112 (1975).

3. R.W. Conn et al., "UWMAK-III, A Noncircular Tokamak Power Reactor Design," University of Wisconsin, UWFDM-150 (1976).

4. B. Badger, et al., "TETR-A Tokamak Engineering Test Reactor to Qualify Materials and Blanket Components for Early DT Fusion Power Reactors," University of Wisconsin, UWFDM-191 (1977).

5. D.R. Cohn et al., "High Field Compact Tokamak Reactor (HFCTR) Conceptual Design," M.I.T. Plasma Fusion Center Research Report RR-79-2 (1979).

6. J.S. Watson and P.W. Fisher, "Cryosorption Vacuum Pumping Under Fusion Reactor Conditions," Seventh International Vacuum Congress and Third Intern. Conf. on Solid Surfaces, Vienna, Austria (Sept. 1977).

7. V.B. Yuferov et al., "Cryogenic Pumping of Fusion Reactors," Physical Technical Institute of the Ukrainian Academy of Sciences, Kharkov, USSR (1975).

8. P.W. Fisher, J.S. Watson, "Cryosorption Vacuum Pumping of D_2, He and H_2 at 4.2 K for Controlled Thermonuclear Reactor Application" , ANS Transactions, 1976 Winter Meeting, Vol. 24, p. 501.

9. J.S. Watson et al., "Current CTR Related T_2 Handling Studies at ORNL," Proc. of the 2nd Topical Meeting on the Technology of Controlled Nuclear Fusion, Sept. 1976, Richland WA.

V-A. Introduction

It is clear that a supplementary heating system will be required to heat a tokamak plasma from the efficient Ohmic heating limit of a few keV to the 7-10 keV required for reactor ignition conditions. In this paper we consider the scaling of fast magnetosonic wave heating at the second ion cyclotron harmonic for the NUWMAK tokamak reactor. While a considerable amount of theoretical[1-10] and experimental[11-15] work has been done on recent and current tokamaks including PLT, ATC, TFR, T-4, and ST, relatively little work has been done on the scaling to reactor size machines[16-20]. This work is directed toward clarifying the reactor heating problem and discussing the hardware associated with coupling to a tokamak.

The work starts with a review of fast magnetosonic wave theory including hot plasma dispersion, absorption, eigenmode density and mode conversion processes. In a reactor the competition between the dense spectrum of eigenmodes and the mode conversion from fast magnetosonic waves to electrostatic ion Bernstein modes near the first harmonic resonance surface with the consequent decrease in "Q" is a most important consideration. At the two extremes one has either a dense spectrum of modes which can be excited with some selectivity provided by the launching structure or a plane wave picture where all the power launched by the antenna is essentially absorbed in a single pass via mode conversion. A brief discussion of this aspect is made and its implication in terms of the coupling structure is presented.

Next, the problem of reactor startup utilizing fast magnetosonic wave heating is addressed. A spatially-averaged, time-dependent

transport code which simultaneously solves the ion and electron energy balance equations is presented. A local weak damping approximation is used to derive the RF heating term in the equations. The code includes alpha-particle and RF heating terms, species equilibration, and conduction, convection, bremsstrahlung, and synchrotron losses. It is found that 80 MW of power absorbed by the plasma for a period of three seconds is sufficient to increase the alpha particle heating rate so that the plasma ignites and reaches its equilibrium operating conditions in a sufficiently short time.

In order to provide the power assumed to be propagating in the machine in the startup model, the problem of efficient coupling from external RF generators to desired fast magnetosonic wave modes in the plasma is addressed. The coupling structure must match impedance levels between the generator and plasma waves so that a maximum power transfer with low external losses is achieved. This must be done without exceeding RF breakdown conditions. The launching structure must be compatible with the high neutron flux emanating from the plasma and the access constraints imposed by a high field, high density, minimum size tokamak reactor. Finally, a summary is presented.

References for Section V-A

1. J. Adam and A. Samain, Association Euratom - C.E.A. Report EUR-CEA-FC-579 (Fontenay-aux-Roses, 1971); J. Adam, Report EUR-CEA-FC-711 (Fontenay-aux-Roses, 1973).

2. F. W. Perkins, Symposium on Plasma Heating and Injection, Varenna, Italy (1972).

3. R. R. Weynants, Phys. Rev. Letters 33, 78 (1974).

4. D. G. Swanson and Y. C. Ngan, Phys, Rev. Letters 35, 517 (1975).

5. D. G. Swanson, Phys. Rev. Letters 36, 316 (1976).

6. T. H. Stix, Nuclear Fusion 15, 737 (1975).

7. R. Klima, A. V. Longinov, and K. N. Stepanov, Sov. Phys. Tech. Phys. 21, 409 (1976).

8. J. E. Scharer, B. D. McVey, and T. K. Mau, Nuclear Fusion 17, 297 (1977); J. E. Scharer, B. D. McVey, and T. K. Mau, Proceedings 3rd International Meeting on Theoretical and Experimental Aspects of Heating of Toroidal Plasmas (C.E.A., Grenoble, 1976) Vol. 1, p. 79; J. E. Scharer, T. K. Mau, D. T. Blackfield and B. D. McVey, Proc. Seventh European Conference on Controlled Fusion and Plasma Physics, p. 145, Lausanne, September, 1975.

9. J. Jacquinot, B. D. McVey, and J. E. Scharer, Phys. Rev. Lett. 39, 88 (1977).

10. F. W. Perkins, Nuclear Fusion 17, 1197 (1977).

11. J. Adam, M. Chance, H. Eubank, W. Getty, E. Hinnov, W. Hooke, J. Hosea, F. Jobes, F. Perkins, R. Sinclair, J. Sperling, and H. Takahashi, Proceedings 5th International Conference on Plasma Physics and Controlled Nuclear Fusion Research (IAEA, Vienna, 1975) p. 65.

12. V. L. Vdovin, N. V. Shapotkovskii, and V. D. Rusanov, Proceedings 3rd International Meeting on Theoretical and Experimental Aspects of Toroidal Plasmas (C.E.A. Grenoble, 1976) Vol. 2, p. 349.

13. H. Takahashi, C. C. Daughney, R. A. Ellis, R. J. Goldston, H. Hsuan, T. Nagashima, F. J. Paoloni, A. J. Sivo, and S. Suckewer, Phys. Rev. Letters 39, 31 (1977).

14. V. V. Buzankin, V. A. Vershkov, N. V. Ivanov, I. A. Kovan, V. A. Krupin, I. A. Popov, I. B. Semenov, and Yu. A. Sokolov, Proceedings of the 6th International Conference on Plasma Physics and Controlled Nuclear Fusion Research, (IAEA, Vienna, 1977) p. 61.

15. Equipe TFR, Proceedings 6th International Conference on Plasma Physics and Controlled Nuclear Fusion (IAEA, Vienna, 1977) 39; Proceedings 3rd International Meeting on Theoretical and Experimental Aspects of Heating of Toroidal Plasmas (C.E.A., Grenoble, 1976) Vol. I, p. 87; Proceedings 3rd Symposium and Workshop on Plasma Heating in Toroidal Devices (Varenna, 1976).

16. J. E. Scharer, R. W. Conn, and D. T. Blackfield, EPRI Report ER-268, (1976).

17. J. Adam and J. Jacquinot, Report EUR-CEA-FC-886, Fontenay-aux-Roses (1977).

18. T. H. Stix, Third Symposium of Plasma Heating in Toroidal Devices, Varenna (1976). PPPL Report-1298.

19. J. C. Hosea, Third Symposium of Plasma Heating in Toroidal Devices, Varenna (1976). PPPL Report-1309.

20. B. W. Reed, O. N. Bowen, H. M. Hill, J. Q. Lawson, W. G. Newman, and A. J. Sivo, PPPL Report-1410 (1977).

V-B. Fast Magnetosonic Wave Theory

V-B-1. Wave Propagation and Absorption

In this section we present the wave propagation, absorption, eigenmode, and mode conversion properties for the fast magnetosonic wave. Early theoretical works by Adam and Samain[1], Perkins[2], and Weynants[3] have presented the basic wave propagation and absorption mechanisms for the mode in the ion cyclotron frequency range (ICRF). The operative absorption mechanisms are cyclotron harmonic damping of the wave by the ions and Landau and transit-time damping of the wave by the electrons. Stix[6] has shown that when cross terms in the dielectric tensor are included in the electron damping calculation that for TFTR parameters the net electron damping is Landau damping and has a value which is half that for the transit time considered separately. We have found from computational studies that this is generally the case for reactor oriented machines.

We now present a brief derivation of the fast magnetosonic wave hot plasma dispersion relation. Assuming an $e^{-i\omega t + i\bar{k}\cdot\bar{r}}$ Fourier component of wave quantities, the wave equation is obtained as $\bar{k} \times (\bar{k} \times \bar{E}) + (\omega/c)^2 \overline{\overline{K}} \cdot E = 0$ where $\overline{\overline{K}}$ is the dielectric tensor as defined in Stix[21]. By noting that in the magnetosonic regime that the Bessel function argument $\lambda_j = k_\perp^2 \rho_j^2/2$ is small for both ion and electron terms, one can obtain a tractable dispersion relation in which first-order finite gyroradius effects are included by expanding to first order in λ_j. Further, the K_{zz} component of the dielectric tensor is so large compared to other elements involving the z component that the dispersion relation can be obtained to a very good approximation by expanding the 2 x 2 minor of the K_{zz} component. The dispersion

relation then becomes ($k_\perp = k_x$, $k_\parallel = k_z$) to the fourth order in $k_\perp$

$$\begin{vmatrix} (\omega/c)^2 K_{xx} - k_\parallel^2 & (\omega/c)^2 K_{xy} \\ (\omega/c)^2 K_{yz} & (\omega/c)^2 K_{yy} - k_\parallel^2 - k_\perp^2 \end{vmatrix} = 0 \qquad (1)$$

where

$$K_{xx} = 1 + \sum_{\alpha=i,e} (\omega_{p\alpha}^2/2\omega k_\parallel v_\alpha)(Z_1^\alpha + Z_{-1}^\alpha) - k_\perp^2 \sum_{\alpha=i,e} (\omega_{p\alpha}^2 v_\alpha/4\omega k_\parallel \omega_{c\alpha}^2)(Z_1^\alpha + Z_{-1}^\alpha - Z_2^\alpha - Z_{-2}^\alpha),$$

$$K_{yy} = K_{xx} + k_\perp^2 \sum_{\alpha=i,e} (\omega_{p\alpha}^2 v_\alpha/\omega k_\parallel \omega_{c\alpha}^2)\,[Z_0^\alpha - 1/2(Z_1^\alpha + Z_{-1}^\alpha)],$$

$$K_{xy} = -K_{yz} = -i \sum_{\alpha=i,e} (\omega_{p\alpha}^2/2\omega k_\parallel v_\alpha)(Z_1^\alpha - Z_{-1}^\alpha) + ik_\perp^2 \sum_{\alpha=i,e} (\omega_{p\alpha}^2 v_\alpha/4\omega k_\parallel \omega_{c\alpha}^2)(2Z_1^\alpha - 2Z_{-1}^\alpha - Z_2^\alpha + Z_{-2}^\alpha)$$

and Z_ℓ^α denotes the Fried and Conte plasma dispersion function $Z((\omega + \ell\omega_{c\alpha})/k_\parallel v_\alpha)$. The dispersion relation then includes wave absorption due to finite ion gyroradius effects, cyclotron damping, and electron transit-time damping (a factor of 2 greater than the resulting Landau damping obtained from the 3 x 3 dispersion relation).

The power absorbed by the ions and electrons per unit volume can be obtained in the weak damping limit in a manner following Stix[6] as $p = \xi\omega\bar{E}^* \cdot (\bar{\bar{K}}^a \cdot \bar{E})/2(\text{watt/cm}^3)$ where $\bar{\bar{K}}^a$ is the anti-Hermitian part of the dielectric tensor. The finite ion gyroradius damping term becomes

$$p_i = \pi^{1/2} \varepsilon_o \omega_{pi}^2 \mathrm{Re}(\lambda_i)^{\ell-1} |E_+|^2 e^{-((\omega - \ell\omega_{ci})/k_\parallel v_i)^2/4k_\parallel v_i} \qquad (2)$$

In a similar way the electron Landau damping term can be obtained from the anti-Hermitian part of the K_{yy}, K_{yz}, K_{zy}, and K_{zz} elements and written as

$$P_e = \pi^{1/2}\varepsilon_o(\omega_{pe}/\omega_{ce})^2 k_\perp^2 |E_y|^2 v_e e^{-(\omega/k_\parallel v_e)^2}/4k_\parallel \quad . \tag{3}$$

In the above equations, ℓ is the harmonic number $\omega = \ell\omega_{ci}$, E_+ is the left-hand circularly polarized electric field component rotating in the sense of the ions, and E_y is the rectangular component of the electric field. $|E_+|^2 = |1-\chi|^2|E_y|^2 = |1+x^2|^{-1}|E_y|^2$ where

$\chi = iE_x/E_y \simeq \dfrac{-i\ K_{xy}}{K_{xx} - n_\parallel^2}$ is the polarization factor for the second harmonic and

$$x^2 = 3\pi^{1/2}\ k_\perp^2 v_\perp^2/(8\ k_\parallel v_i \omega_{ci}) \quad .$$

The ion cyclotron harmonic absorption term occurs in a region of finite width in the tokamak minor cross section due to the thermal effects and the 1/R variation of the toroidal magnetic field. For the second harmonic, this width is $\Delta R = k_\parallel\ v_i R/\omega_{ci}$. It is further assumed that the energy deposited in the slab is uniformly distributed over the circular flux surface intersecting the radial element on the slab due to the rotational transform.

To take rotational transform effects into account in the ion heating expressions we write

$$B_T = \frac{B_o}{1 + \frac{r}{R}\sin\theta} \tag{4}$$

where B_o is the B-field on axis.

For a large aspect ratio device, we may approximately write

$$B_T \approx B_o \left(1 - \frac{r}{R} \sin\theta\right) . \qquad (5)$$

By averaging over a flux surface, we can define

$$\langle p_i(r)\rangle_\theta = \frac{1}{2\pi} \int_0^{2\pi} p_i(r,\theta)\, d\theta \qquad (6)$$

where

$$\langle p_i(r)\rangle_\theta = \frac{\pi^{1/2} \varepsilon_o\, \omega_{pi}{}^2\, \lambda_i{}^{\ell-1}}{4\, k_\parallel v_i} |E_+|^2\, e^{-\gamma^2 \sin^2\theta} \qquad (7)$$

and

$$\gamma^2 = \frac{\ell^2 \omega_{cio}{}^2\, r^2}{R^2\, k_\parallel{}^2\, v_i{}^2} \text{ , and } \omega_{cio} = \frac{q\, B_o}{m_i} .$$

Then equation (6) yields

$$\langle p_i(r)\rangle_\theta = \frac{\pi^{1/2} \varepsilon_o\, \omega_{pi}{}^2}{4\, k_\parallel\, v_i}\, \lambda_i{}^{\ell-1}\, I_o\left(\frac{\gamma^2}{2}\right)\, |E_+|^2 \qquad (8)$$

where we have assumed that $|E_+|^2$ is not an explicit function of θ. For $\gamma^2/2 \gg 1$ we find that

$$\langle p_i(r)\rangle_\theta = \varepsilon_o(\omega_{pi}{}^2/\omega_{cio})\, (R/r)\, \mathrm{Re}(\lambda_i)^{\ell-1}\, |E_+|^2/4\ell . \qquad (9)$$

Note that this provides a strong peaking of the energy deposition to the ions at the plasma core. By integration over the tokamak cross section these equations are adapted to a time-dependent model for the startup calculation in NUWMAK.

Fig. V-B-1 shows the dispersion relation for the magnetosonic wave for NUWMAK parameters. The parameter $\lambda_D = k_\perp^2 \rho_D^2/2$ (D = deuterium) is plotted as a function of the minor radius on the horizontal plane of the machine with parabolic density and temperature profiles assumed over the cross section. The parallel wavelength ($k_\parallel = 10\ m^{-1}$) is assumed constant over the cross-section and a peak temperature of $T_i = T_e = 5$ keV and peak density $n = 4 \times 10^{14}/cm^3$ is assumed on the axis with values at the plasma edge ($r = 1.25$ m) dropping to one percent of those on axis. The wave frequency is 92 MHz which corresponds to second or third cyclotron harmonic resonance for deuterium or tritium at 60 kG on axis, respectively.

From the dispersion curve in Fig. V-B-1, one notes that the imaginary part of the roots for λ_D corresponds to absorption, mode conversion, and evanescent regions. The roots labelled F correspond to the fast magnetosonic mode and those labeled B correspond to an electrostatic ion Bernstein branch. In the region where the two roots coalesce, some of the wave power propagating in the fast wave branch can be coupled into the backward wave mode ion Bernstein branch and some can be transmitted through. Works by Swanson, Ngan, Scharer, McVey, Mau, Jacquinot and Perkins[4,5,8,9,10,22] have treated this problem. No exact model has been put forth that will describe the amount of wave energy which tunnels through and is absorbed by cyclotron harmonic absorption and the amount of incident fast wave energy that is mode converted for

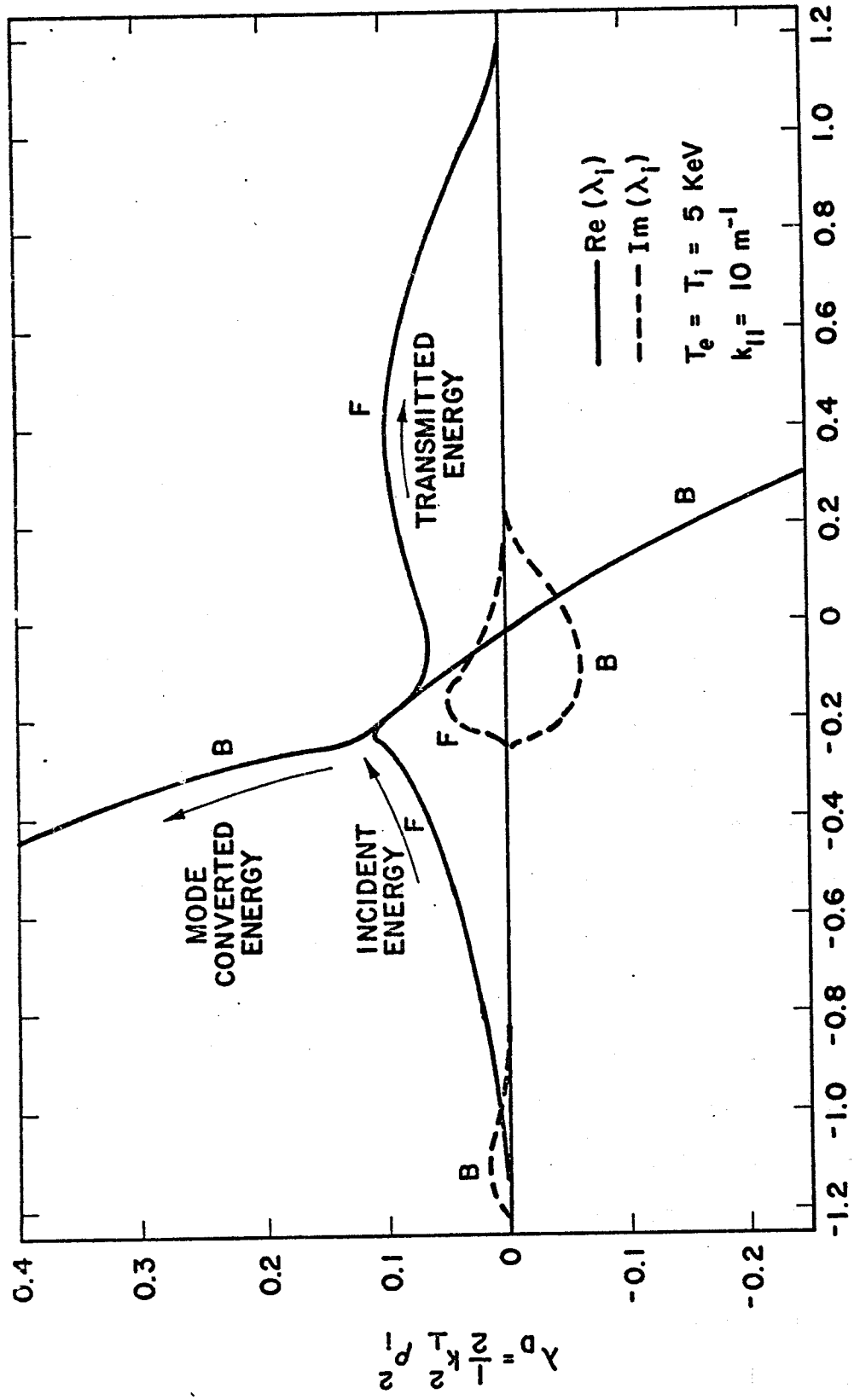


Fig. V-B-1 Local fast magnetosonic dispersion relation for a plasma profile given by $n_e = 2n_D = 2n_T = 4 \times 10^{14}$ $(1-(r/a)^2)cm^{-3}$, $T_e = T_i = 5\ (1 - 0.9(r/a)^2)^2$ keV, $k_{||} = 10\ m^{-1}$, f = 92 MHz and B_o = 60 kG on axis.

all values of $k_{\parallel}$ and plasma parameters. However, in the limit where $k_{\perp}^2\rho_i/k_{\parallel} >> 1$, computational results predict that fast wave energy incident from the high magnetic field side of the cyclotron harmonic resonance is essentially all converted to the backward wave ion Bernstein mode and wave energy incident from the low magnetic field side is completely reflected from the cyclotron harmonic resonance zone. In this limit the eigenmode description of fast magnetosonic waves is not appropriate and wave energy propagating along the fast wave branch from the high field side of resonance can be visualized as being completely absorbed in a single pass via mode coupling to the more strongly damped ion Bernstein mode.

Perkins[10] has shown that once the wave energy flows along the ion Bernstein branch, the effect of the poloidal component of the magnetic field provided by the rotational transform from the Ohmic heating current greatly modifies the local $k_{\parallel}$ and strong absorption can result. McVey and Scharer[22] have done ray tracing studies incorporating this effect and obtained a dispersion relation for the ion cyclotron range of frequencies (ICRF) which accurately describes the dispersion of the ion Bernstein branch for all ranges of the parameter $\lambda_i \lesssim 10$. The results show that strong ion or electron absorption of waves launched from the high field region can occur in the low $k_{\parallel}$ regime, dependent on the orientation of the initial ray direction at the plasma edge and its location in the vertical profile.

For sufficiently large $k_{\parallel}$ (20 m^{-1} for NUWMAK parameters), the mode conversion process can be neglected and fast wave tunneling

through the second ion cyclotron harmonic absorption region is possible. However, even though the weak absorption limit $|k_i|/|k_r| \ll 1$ is locally valid in this regime, the harmonic absorption width in a reactor, ΔR, is sufficiently large so that the wave is substantially damped in a single pass through the resonance zone. This lowers the wave Q in the machine and makes an eigenmode description of the fields inadequate.

Nevertheless, we adopt the eigenmode description of wave fields in our reactor study due to the relative ease of formulating the coupling problem. The final verdict on the role of mode conversion in absorption in the ICRF range awaits more detailed experimental measurement on scaling as the size of tokamaks is increased.

A further condition that must be met in order to have high Q eigenmodes is that the impurity proton concentration which is at the fundamental ion cyclotron resonance must not exceed $n_H/n_D = \beta_i$ [10] so that fundamental proton absorption or mode conversion near the two-ion hybrid resonance does not dominate the deuterium cyclotron harmonic absorption and strongly reduce the mode Q. As a practical matter for a reactor such as NUWMAK the proton concentration should not exceed fractions of a percent ($n_H/n_D = 0.003$).

Finally, if mode conversion processes are ultimately shown to dominate the absorption in a reactor, the resultant spatial and plasma species absorption rates can be incorporated in the time dependent transport code for startup calculations in a similar manner as we have done for the case of fast wave eigenmode absorption. However, the formulation of the coupling problem and calculation and antenna radiation impedance for the wave absorption via mode conversion will be much more formidable.

V-B-2. The Influence of the Launching Structure and Mode Conversion on the Excited Mode Wave Spectrum.

Fast magnetosonic wave experiments on the ST, ATC, TFR, T-4, TM-1-VCh, PLT, MACROTOR, CALTECH, ERASMUS, and TEXAS TECH tokamaks have observed high Q eigenmodes under appropriate conditions at the second harmonic of the ion cyclotron frequency. When this occurs an enhanced radiation resistance of the antenna is present and the coupling from the RF generator to plasma waves is very efficient. In this section we determine the possible dense spectrum of eigenmodes in the plasma and consider the influence of wave processes such as mode conversion and the spectrum of the launching structure in determining the composite heating picture and loading of the antenna.

Stix[18] and Hosea[19] have considered the density of eigenmodes in a cold homogeneous cylindrical plasma such that the axial RF magnetic field varies as $B_z \sim J_m(k_r r) \exp(im\theta + in\phi - i\omega t)$ where m is the poloidal mode number, $n = k_{\parallel} R$ is the toroidal mode number, and k_r is the radial wave number. Stix calculates the density of eigenmodes when the radial (μ), azimuthal (m), and toroidal (n) indices are varied assuming a perfectly conducting wall at radius r=a. The boundary conditions determine that eigenmodes appear whenever $k_r a \approx \pi(\mu + |m/2|)$ where μ and m are the radial and poloidal mode numbers. If one lets $\nu = \pi(\mu + |m/2|) > 1$, then eigenmodes appear at half-integral values of ν with a $(2\nu-1)$ multiplicity due to the various combinations of μ and m yielding the same ν. By integrating over the values of ν and n, subject to the approximate cold plasma dispersion relation,

$$k_{\perp}^2 + \left(\frac{\omega + \omega_{ci}}{\omega_{ci}}\right) k_{\parallel}^2 = (\omega/v_A)^2 \ , \qquad (10)$$

Stix obtains the total number of propagating modes as

$$N = \frac{2}{3\pi^2} \left(\frac{\omega + \omega_{ci}}{\omega_{ci}}\right)^{-1/2} a^2 R \left(\frac{\omega}{v_A}\right)^3 \tag{11a}$$

where R is the major radius and v_A is the Alfvén speed. The mode separation $d\omega$ necessary to increase N by 1 is

$$d\omega/\omega = dN/3N = 1/3N \tag{11b}$$

For reactors the size of NUWMAK with a = 1.25 m, R = 5.0 m, $\bar{n}_e$ = $2 \times 10^{14}/cm^3$, B_0 = 60 kG, and $\omega = 2\omega_{ci}$ the separation in eigenmode frequencies is about one part in 6×10^5 when compared to the first ion cyclotron harmonic for deuterium. The argument then follows that the antenna can provide a poloidal and toroidal resolution of 100 with individual Q's of order 100 so that about 60 modes are simultaneously excited. If too many modes are simultaneously excited, the cumulative field intensity is in phase near the antenna, but due to radial phase shifts can be out of phase and destructively interfere at regions in the plasma core. This can lead to undesirable surface heating of the plasma.

The above analysis assumed that all mode indices were equally excited and that the excitation spectrum of the antenna provided a combined poloidal and toroidal resolution of about 100. A more complete picture of an ideal launching structure would include the following considerations. First, the launching structure would have a Fourier spectrum which peaks at fairly low values of m and becomes negligible for $|m| > 3$. This greatly reduces the number of modes over which substantial RF power is distributed and thus the effective

density of modes. Secondly, the low $k_{\parallel} = n/R$ modes as we have seen are those which are most readily mode converted and have an equivalent low Q. If competition for power density among the mode spectrum takes place, the strongly mode converted "modes" might receive the least amount of wave power and the higher Q eigenmodes corresponding to the higher $k_{\parallel}$ part of the spectrum would receive most of the wave power due to their enhanced radiation resistance.

Hosea[19] has looked at the mode density question for larger machines and noted that the spectrum is quite dense for higher $k_{\parallel}$ modes but that it is relatively sparse for lower $k_{\parallel} \approx 0$ modes. He suggests an antenna structure which preferentially excites low $k_{\parallel}$ modes and uses frequency tracking and gas puffing for density control to excite the desired modes. It would appear that due to the preferential mode conversion process for low $k_{\parallel}$ modes and the higher density of modes for larger $k_{\parallel}$, the presence of low $k_{\parallel}$ eigenmodes and selective tracking of higher $k_{\parallel}$ eigenmodes in a reactor is very difficult technologically and somewhat academic. The resolution of this question awaits further detailed experimental evidence on the mode conversion process and eigenmode scaling in larger tokamaks such as PLT and TFTR.

Hosea further points out that density fluctuations in the plasma can effectively scan over modes so that tracking a single mode becomes very difficult. It should also be kept in mind that plasma heating via mode conversion processes can offer the advantage of a well defined process dominating cyclotron harmonic absorption. One possible disadvantage is the reduced radiation resistance for absorption via mode conversion processes when compared with that where the dominant absorption is via cyclotron harmonic damping for high Q eigenmodes.

For reactor size machines longer resonant half-wavelength antennas can be considered rather than the electrically short coils used in present day machines. This will act to enhance the radiation resistance and counter the expected decrease due to mode conversion processes providing efficient coupling of the RF power to the fast magnetosonic wave for plasma heating.

We now calculate the mode spectrum and spacing for fast magnetosonic waves in a tokamak. Due to the weak rotational transform effects in a tokamak compared to the circumference, we adopt the cold, uniform plasma-filled guide problem discussed by Bernstein and Trehan[23]. For waves in the ion cyclotron frequency range the TE mode solution ($E_z = 0$) is derivable from the axial magnetic field component given by

$$H_z = H_1 J_m(k_r r) e^{im\theta+in\phi-i\omega t} \tag{12}$$

where H_1 is an amplitude coefficient, k_r is the radial wavenumber, m is the poloidal mode number and $n = k_{\parallel} R$ is the toroidal mode number corresponding to an eigenmode. The dispersion relation is given by

$$k_r = [k_{\parallel}^4/S - 2k_0^2 k_{\parallel}^2 + k_0^4 RL/S]^{1/2} [k_0^2 - k_{\parallel}^2/S]^{-1/2} \tag{13}$$

where S, R, L, and D are defined in the Stix[21] notation and $k_0 = \omega/c$. For our case $S = \omega_{pi}^2/(\omega_{ci}^2 - \omega^2)$, $RL/S = \omega_{pi}^2/\omega_{ci}^2$, and $D/S = -\omega/\omega_{ci}$.

The θ component of the electric field which is the tangential electric field at the edge of the cylindrical column can be calculated via Maxwell's equations and is

$$E_\theta = i\omega \mu_0 H_1 [a_2(m/r) J_m(k_r r) + a_1 k_r J_m'(k_r r)] \tag{14}$$

where $a_1 = -k_r^{-2} = (k_\parallel^2/S - k_0^2)/\Lambda$ and $a_2 = (D/S)k_0^2/\Lambda = (-\omega/\omega_{ci})k_0^2/\Lambda$ are polarization factors and $\Lambda = k_\parallel^4/S - 2k_0^2k_\parallel^2 + k_0^4RL/S$. Applying the boundary condition for a plasma filled guide with a conducting boundary $E_\theta\ (r=a) = 0$ yields

$$a_2(m/a)\, J_m(k_r a) + a_1\, k_r\, J_m'(k_r a) = 0$$

or

$$k_r a\, J_m'(k_r a)/J_m(k_r a) = m(\omega/\omega_{ci})k_A^2/(k_\parallel^2 - k_A^2 - k_\parallel^2(\omega/\omega_{ci})^2) \qquad (15)$$

where $k_A = \omega/v_A$ and v_A is the Alfvén velocity.

We now investigate the eigenfrequencies and frequency spacing as the radial (μ), azimuthal (m), and toroidal (n) indices are varied. We assume that the wave launching structure and large reactor size satisfy the following conditions: 1) $k_r a \gg m$, 2) $k_r \simeq k_A \gg k_\parallel$, and 3) $\omega \simeq 2\omega_{ci}$. By using the asymptotic form of the Bessel functions

$$\lim_{k_r a \gg m} J_m'(k_r a)/J_m(k_r a) \to -\tan\left(k_r a - \frac{m\pi}{2} - \frac{\pi}{4}\right) ,$$

Eq. (15) can be written in the form

$$k_r a - m\pi/2 - \pi/4 = \mu\pi + m(\omega/\omega_{ci})/(k_r a) \qquad (16)$$

where $\mu > 0$ is the radial eigenvalue related to the number of radial half-wavelengths that fit in the machine.

Since $\tan(\phi) = \tan(\phi - \mu\pi)$ we can write

$$\tan(k_r a - \nu\pi - \pi/4) = m(\omega/\omega_{ci})/k_r a \qquad (17)$$

where $\nu = \mu + m/2$.

We now consider the shift in eigenmode frequencies due to various changes in the mode indices. The smallest shift will be due to a

shift in m and μ while maintaining constant ν and n indices. We note that $|k_r a - \nu\pi - \pi/4| \ll 1$ and let $\Delta k_r = k_{r1} - k_{r2}$. Thus,

$$\Delta k_r a = \Delta m(\omega/\omega_{ci})/(k_r a)$$

and since $$\Delta k_r = \Delta\omega/v_A \simeq \Delta\omega\ k_r/\omega$$

we have

$$\Delta\omega(\mu,m)/\omega|_{\nu,n} = \Delta m(\omega/\omega_{ci})/(k_r a)^2 \ . \tag{18}$$

In a similar fashion we obtain

$$\Delta\omega(\mu)/\omega\Big|_{n,m} = \Delta\mu\pi/(k_r a) \tag{19}$$

and

$$\Delta\omega(m)/\omega\Big|_{n,\mu} = \Delta m\pi/(2\ k_r a) \ . \tag{20}$$

For $\Delta\omega(n)/\omega\Big|_{\mu,m}$ we must use a more accurate dispersion relation for finite $k_{\parallel} = n/R$. The cold plasma dispersion relation can be written

$$(\pi\nu/a)^2 + ((\omega^2 + \omega_{ci}^2)/\omega_{ci}^2)(n/R)^2 = (\omega/v_A)^2 \tag{21}$$

where the second term is small for our regime of interest. Thus

$$2\ \omega\ \Delta\ \omega \simeq v_A^2\ ((\omega^2 + \omega_{ci}^2)/\omega_{ci}^2)\ 2n\Delta n/R^2$$

and utilizing $v_A \simeq \omega/k_r$, we obtain

$$\Delta\ \omega(n)/\omega\Big|_{\mu,m} = \Delta n((\omega^2 + \omega_{ci}^2)/\omega_{ci}^2)\ n/(k_r R)^2 \ . \tag{22}$$

For the NUWMAK tokamak with $\bar{n} = 2 \times 10^{14}/cm^3$, $B_0 = 60$ kG, $R = 5$ m, $a = 1.25$ m, $n = 100$ and a 50/50 DT plasma treated as a single ion species with AMU = 2.5, the previous results yield

$$\Delta\omega(\mu,m)/\omega \Big|_{\nu,n} = 1.7 \times 10^{-4} \Delta m \ , \tag{23}$$

$$\Delta\omega(\mu)/\omega \Big|_{n,m,} = 2.6 \times 10^{-2} \Delta\mu \ , \tag{24}$$

$$\Delta\omega(m)/\omega \Big|_{\mu,n} = 1.3 \times 10^{-2} \Delta m \ , \tag{25}$$

and

$$\Delta\omega(n)/\omega \Big|_{\mu,m} = 3.0 \times 10^{-3} \Delta n \ . \tag{26}$$

The above results show the spacing between adjacent eigenmodes for the variation of a single mode index. Note that since the dispersion relation for Alfvén waves varies as $\omega^2 = k_r^2 v_A^2 \sim n_e^{-1}$ that $\Delta\omega/\omega = -\Delta n_e/2n_e$ and that the above expressions can be interpreted as the shift in density required to shift to an adjacent mode. It is noted that the density fluctuations in a tokamak discharge should ultimately be taken into account in obtaining the time-average heating and absorption rates for ion cyclotron harmonic waves. We now look at ways in which the launching structure and mode conversion processes tend to limit the spectrum of excited modes.

There are currently two main processes being considered in the propagation and absorption of wave energy in a tokamak. The first involves ion cyclotron harmonic absorption near the second harmonic resonance. In today's machines this can lead to high Q eigenmodes with weak absorption processes. As larger, more dense, and hotter plasmas are created suitable for a reactor device the second process of mode conversion from fast magnetosonic wave modes to ion Bernstein modes is expected to become more substantial. An adjustment of the $k_{\parallel}$ spectrum is then required if one wishes to insure that the wave is absorbed by ion cyclotron harmonic processes. Computations by McVey[22] show that $k_{\parallel}$ must be increased to 20 m^{-1} in a reactor device in order that mode conversion processes can be neglected and that the local weak damping description is valid. By increasing $k_{\parallel}$, the width $\Delta R = k_{\parallel} v_i R/\omega_{ci}$ of the cyclotron harmonic absorption zone is substantially increased so that even though the weak damping limit ($k_i/k_r \ll 1$) is satisfied locally, the cumulative effect over the whole absorption zone is such as to strongly damp the wave and yield a low Q situation. As mentioned earlier, this means that efficient coupling to the cavity requires a transformation of impedance levels such as that found in the aperture coupled cavity or the use of resonant half-wavelength coil antennas.

We now consider the desirable properties of a launching structure so that efficient wave coupling and heating in a tokamak can be achieved.

With regard to the poloidal spectrum, we note that the spatial heating profiles for an eigenmode vary as $J^2_{m-1}(k_r r)$ so that an antenna which excites a low m spectrum is desirable to provide core heating and avoid edge heating of less well confined plasma particles. As an example, the expression for the current in a coil which covers half the poloidal angle and is of uniform amplitude and phase is $I(\theta) = I_0(H(\theta + \pi/2) - H(\theta - \pi/2))$ where the H stands for the Heaviside function. The current can be represented as

$$I(\theta) = \sum_{m=0}^{\infty} I_m e^{im\theta}$$

where the Fourier coefficient can be calculated as $I_m = \frac{1}{2\pi} \int_0^{2\pi} I(\theta) e^{-im\theta} d\theta$.

Thus

$$I_m = \begin{cases} 1/2 \ (m=0) \\ \frac{1}{\pi |m|} \ m \text{ odd; } m = \pm 1, \pm 3, \pm 5, \ldots \\ 0 \quad m \text{ even; } m = \pm 2, \pm 4, \pm 6, \ldots \end{cases}$$

Since the excited power is proportional to I_m^2 for slowly varying radiation resistance, we can assume that most of the power launched will be in the $|m| \leq 3$ part of the spectrum. It should be noted that the above current excitation could only be excited with a poloidal array of properly phased, electrically short ($\ell << 0.1\lambda$) current elements. If a resonant half-wavelength antenna were used, the cosine-shaped exciting current amplitude about the feed point would produce substantially more power in the higher m part of the spectrum.

For the toroidal spectrum, we assume that a peak at $k_{\parallel} = 20\ m^{-1}$ is excited to insure heating via finite ion gyroradius effects at the

second harmonic resonant zone. A plasma density profile which is sufficiently sharp at the edges is assumed so that the wave evanescent zone is not appreciable and the wave propagates over most of the plasma cross section. We assume a toroidal array of an even number of elements (N_A) with a 180° time-phase shift between successive elements spaced $2\pi R/N_A$ apart. The toroidal current distribution is given by

$$I(\phi) = \sum_{n=0}^{\infty} I_n e^{in\phi} \qquad \phi = z/R$$

where $$I_n = (2\pi)^{-1} \int_0^{2\pi} I(\phi) e^{-in\phi} d\phi$$

The toroidal Fourier spectrum is given by the well-known form

$$I_n = \sin((2n - N_A)\pi/2)/(2\pi\sin((2n - N_A)\pi/2N_A)). \tag{27}$$

The spectrum peaks at $n = k_{\parallel}R = (2p+1)N_A/2$ where p is an integer and has a width $\Delta k_{\parallel}/k_{\parallel 0} = 2/N_A$ corresponding to $\Delta n = 2$ for large N_A.

We now calculate the number of modes for which an appreciable Fourier spectrum excitation coefficient exists.

$$N_E = \int_{\nu_{min}}^{\nu_{max}} D(\nu) d\nu \int_{n_{min}}^{n_{max}} dn \tag{28}$$

where $D(\nu)$ is a degeneracy factor taking into account different combinations of m and μ for the same ν.

If only $|m| = 3$, 1, and 0 modes are appreciably excited we have $D(\nu) = 5$. The width of the n spectrum is $\Delta n = 2$ about the peak and we have two regions of $k_{\parallel}$ below the $k_{\parallel\ max}$ fast wave cutoff for $k_{\parallel 0} = 20\ m^{-1}$. Thus we have

$$N_E = 5 \cdot \Delta\nu \cdot 2 \cdot \Delta n(=2) \ . \tag{29}$$

Now the fast wave dispersion relation can be written

$$(\pi\nu/a)^2 + ((\omega + \omega_{ci})/\omega_{ci})(n/R)^2 = (\omega/V_A)^2 \ .$$

For fixed frequency the above dispersion relation yields

$$d\nu = -3(a/\pi)^2(n/\nu)\ dn/R^2. \qquad (30)$$

For $\Delta n = 2$, $n = 100$, $\nu = 110$, $a = 1.25$ m, and $R = 5$ m we have $\Delta\nu = 0.10$. Thus $N_E = 5 \cdot (0.1) \cdot 2 \cdot 2 = 2$ modes. To complete the problem one has to consider the Q of generator and fast wave modes.

The previous calculation shows that the array can substantially reduce the mode spectrum to provide heating. The practical implementation of a large array in the NUWMAK reactor environment is much more difficult. The excited spectrum is likely to be larger than the ideal case previously calculated due to access constraints and a limit on the number of elements in the array.

References for Section V-B

1. J. Adam and A. Samain, Association Euratom - C.E.A. Report EUR-CEA-FC-579 (Fontenay-aux-Roses, 1971); J. Adam, Report EUR-CEA-FC-711 (Fontenay-aux-Roses, 1973).

2. F.W. Perkins, Symposium on Plasma Heating and Injection, Varenna, Italy (1972).

3. R.R. Weynants, Phys. Rev. Letters 33, 78 (1974).

4. D.G. Swanson and Y.C. Ngan, Phys. Rev. Letters 35, 517 (1975).

5. D.G. Swanson, Phys. Rev. Letters 36, 316 (1976).

6. T.H. Stix, Nuclear Fusion 15, 737 (1975).

7. R. Klima, A.V. Longinov, and K.N. Stepanov, Sov. Phys. Tech. Phys. 21, 409 (1976).

8. J.E. Scharer, B.D. McVey, and T.K. Mau, Nuclear Fusion 17, 297 (1977); J.E. Scharer, B.D. McVey, and T.K. Mau, Proceedings 3rd International Meeting on Theoretical and Experimental Aspects of Heating of Toroidal Plasmas (C.E.A., Grenoble, 1976), Vol. 1, pp. 62 and 79.

9. J. Jacquinot, B. D. McVey, and J. E. Scharer, Phys. Rev. Lett. 39, 88 (1977).

10. F. W. Perkins, Nuclear Fusion 17, 1197 (1977).

11. J. Adams, M. Chance, H. Eubank, W. Getty, E. Hinnov, W. Hooke, J. Hosea, F. Jobes, F. Perkins, R. Sinclair, J. Sperling, and H. Takahashi, Proceedings 5th International Conference on Plasma Physics and Controlled Nuclear Fusion Research (IAEA, Vienna, 1975), p. 65.

12. V. L. Vdovin, N. V. Shapotkovskii, and V. D. Rusanov, Proceedings 3rd International Meeting on Theoretical and Experimental Aspects of Toroidal Plasmas (C.E.A., Grenoble, 1976) Vol. 2, p. 349.

13. H. Takahashi, C. C. Daughney, R. A. Ellis, R. J. Goldston, H. Hsuan, T. Nagashima, F. J. Paoloni, A. J. Sivo, and S. Suckewer, Phys. Rev. Letters 39, 31 (1977).

14. V. V. Buzankin, V. A. Vershkov, N. V. Ivanov, I. A. Kovan, V. A. Krupin, I. A. Popov, I. B. Semenov, and Yu. A. Sokolov, Proceedings of the 6th International Conference on Plasma Physics and Controlled Nuclear Fusion Research, (IAEA, Vienna, 1977), p. 61.

15. Equipe TFR, Proceedings 6th International Conference on Plasma Physics and Controlled Nuclear Fusion (IAEA, Vienna, 1977) 39; Proceedings 3rd International Meeting on Theoretical and Experimental Aspects of Heating of Toroidal Plasmas (C.E.A., Grenoble, 1976) Vol. I, p. 87; Proceedings 3rd Symposium and Workshop on Plasma Heating in Toroidal Devices (Varenna, 1976).

16. J. E. Scharer, R. W. Conn, and D. T. Blackfield, EPRI Report ER-268, (1976).

17. J. Adam and J. Jacquinot, Report EUR-CEA-FC-886, Fontenay-aux-Roses (1977).

18. T. H. Stix, Third Symposium of Plasma Heating in Toroidal Devices, Varenna (1976). PPPL Report-1298.

19. J. C. Hosea, Third Symposium of Plasma Heating in Toroidal Devices, Varenna (1976). PPPL Report-1309.

20. B. W. Reed, O. N. Bowen, H. M. Hill, J. Q. Lawson, W. G. Newman, and A. J. Sivo, PPPL Report-1410 (1977).

21. T. H. Stix, The Theory of Plasma Waves (McGraw Hill, New York, 1962).

22. B. D. McVey and J. E. Scharer, Proceedings of the Third Topical Conference on Radiofrequency Plasma Heating, paper D6-1, Pasadena (1978). B. D. McVey, Ph.D. Thesis, University of Wisconsin, 1978. Accepted for publication in Nuclear Fusion.

23. I. B. Bernstein and S. K. Trehan, Nuclear Fusion 1, 3 (1960).

V-C. Reactor Startup Model

In this section, we examine various ways in which a reactor may be heated to ignition using RF auxiliary heating. Time varying temperature as well as various heating and loss mechanism curves are obtained by solving the time dependent ion and electron energy balance equations. The RF heating terms are calculated assuming a linear, weak damping, finite Larmor radius theory. A computer point code, based on a spatially independent, "0-D" model is used to solve the energy balance equations. The energy balance equations can be obtained from the Boltzman equation,[1,2,3]

$$\frac{df_j}{dt} + \vec{v} \cdot \vec{\nabla} f_j + \frac{e_j}{m_j} (\vec{E} + \vec{v} \times \vec{B}) \cdot \vec{\nabla}_v f_j = C_j \qquad (1)$$

where C_j is the Fokker-Planck collision operator.[4]
By taking the second velocity or energy moment of Eq. 1 we obtain

$$\frac{\partial}{\partial t} (\frac{3}{2} n_j kT_j) = - \vec{\nabla} \cdot (\frac{3}{2} kT_j \vec{\Gamma}_j + \vec{Q}_j) - n_j kT_j \vec{\nabla} \cdot \vec{V}_j + n_j e_j \vec{E} \cdot \vec{V}_j + m_j \int v^2 C_j d^3v \qquad (2)$$

$$\vec{Q}_j \equiv \int \vec{v} (\vec{v} - \vec{V}_j)^2 f_j d^3v \qquad (3)$$

where use has been made of both the particle and momentum conservation equations.[1]

Averaging over a magnetic flux surface yields the spatially dependent fluid energy equations for both electrons and ions. For electrons we have

$$\frac{\partial}{\partial t}\left(\frac{3}{2} n_e k T_e\right) = \frac{n_i^2 \langle \sigma v \rangle_{DT}}{4} E_\alpha U_{\alpha e} + \frac{1}{r}\frac{\partial}{\partial r}\left[r\left(Q_e + \frac{3}{2} k T_e \Gamma_e\right)\right]$$

$$- Q_{ei} - P_{rad} + P_{Ohm} + P^e_{INJ} + P^e_{RF} \qquad (4)$$

where a source term for an external injection of power either from RF or beams as well as loss terms from bremsstrahlung and synchrotron radiation have been added. The radiation loss terms are calculated assuming that a local Maxwellian temperature occurs for the electrons over time scales much longer than the relaxation scale in Eq. 1.

The ion equation is

$$\frac{\partial}{\partial t}\left(\frac{3}{2} n_i k T_i\right) = \frac{n_i^2 \langle \sigma v \rangle_{DT}}{4} E_\alpha U_{\alpha i} + \frac{1}{r}\frac{\partial}{\partial r}\left[r\left(Q_i + \frac{3}{2} k T_i \Gamma_i\right)\right]$$

$$+ Q_{ei} + P^i_{INJ} - P_{cx} + P^i_{RF} \qquad (5)$$

where

n_e, n_i = electron and ion densities, with $n_i = n_D + n_T$

T_e, T_i = electron and ion temperatures, with $T_D = T_T$ due to the short ion-ion equilibration time

$U_{\alpha e}$, $U_{\alpha i}$ = fraction of alpha energy to electrons and ions

Q_{ei} = electron-ion rethermalization term

P_{rad} = bremsstrahlung, line, recombination and synchrotron radiation losses

P_{Ohm} = Ohmic heating

P^e_{INJ}, P^i_{INJ} = electron and ion heating sources from beams

P_{cx} = charge exchange energy loss

Γ_e, Γ_i = electron and ion particle fluxes

Q_e, Q_i = electron and ion energy conduction terms

P^e_{RF}, P^i_{RF} = electron and ion RF power absorption terms

To obtain the particle flux terms in Eqns. 4 and 5 we examine the particle conservation equation of the zeroth moment of Eq. 1

$$\frac{\partial n_i}{\partial t} = \frac{1}{r}\frac{\partial}{\partial r}(r\Gamma_i) - \frac{n_i^2 \langle\sigma v\rangle_{DT}}{2} + S_p(r,t) \tag{6}$$

where $S_p(r,t)$ is the particle source due to neutral beams, pellet injection, or gas puffing and we may write[1]

$$\Gamma_i = D_i \frac{\partial n_i}{\partial r} \tag{7}$$

$$Q_{e,i} = \chi_{e,i} \frac{\partial (kT_{e,i})}{\partial r} \tag{8}$$

To obtain the ion-electron equilibration term in Eqns. 4 and 5 we use the classical expression which is in agreement with experimental results,

$$Q_{ei} = \frac{3n_e}{\tau_{ei}} \frac{m_e}{m_i} k(T_e - T_i) , \tag{9}$$

where τ_{ei} is the electron-ion equilibration time which for the neoclassical banana regime is given by[5]

$$\tau_{ei} = \frac{3\, m_e^{1/2}\, T_e^{3/2}}{4(2\pi)^{1/2} e^4 n_i \ell n\Lambda} . \tag{10}$$

The Ohmic heating term is evaluated from the neoclassical model

$$P_{Ohm} = E_\phi J_\phi \tag{11}$$

$$E_\phi = \eta_{nc} J_\phi \tag{12}$$

where η_{nc} is the neoclassical resistivity obtained from the Spitzer resistivity by[1,6]

$$\eta_{nc} = \eta_{sp} [1 - 1.95(r/R)^{1/2} + .95(r/R)]^{-1} \quad (13)$$

The energy loss from bremsstrahlung may be written as[2,5]

$$P_B = 4.8 \times 10^{-31} Z_{eff} n_e^2 T_e^{1/2} \text{ watts/cm}^3 \quad (14)$$

with T_e in keV.

The synchrotron loss term is[8]

$$P_{syn} = 1.55 \times 10^{-14}(1 - r_w)^{1/2}[5. + .17(5-A)]^3 \frac{n_e^{1/2} B_T^{5/2}}{a^{1/2}} T_e^{2.1} \text{ W/cm}^3 \quad (15)$$

where

A = aspect ratio

r_w = wall reflectivity

T_e in keV

B_T = toroidal field in Tesla

a = minor radius

Finally Eqns. 4 and 5 become[9]

$$\frac{\partial n_e T_e}{\partial t} = 4.28 \times 10^{-11} n_e n_i \frac{(T_i - T_e)}{T_e^{3/2}} + \frac{1}{1.5r}\frac{\partial}{\partial r}(r n_e \chi_e \frac{\partial T_e}{\partial r}) - \frac{1}{r}\frac{\partial}{\partial r}(r n_e V_e T_e)$$

$$+ 4.17 \times 10^{15} \{n_D n_T \langle\sigma v\rangle U_{\alpha e} + \bar{E} \cdot \bar{J} + P_{inj}(U_{be} + f(\frac{E_\alpha}{E_b}) U_{\alpha e})$$

$$- P_B - P_S\} + P_{RF}^e \quad (16)$$

and

$$\frac{\partial n_i T_i}{\partial t} = -4.28 \times 10^{-11} n_i n_e \frac{(T_i - T_e)}{T_e^{3/2}} + \frac{1}{1.5r}\frac{\partial}{\partial r}\left(r n_i \chi_i \frac{\partial T_i}{\partial r}\right) - \frac{1}{r}\frac{\partial}{\partial r}\left(r n_i V_i T_i\right)$$

$$+ 4.17 \times 10^{15} \{n_D n_T \langle\sigma v\rangle_{DT} U_{\alpha i} + P_{inj}\left(U_{bi} + f\left(\frac{E_\alpha}{E_B}\right) U_{\alpha i}\right)\} + P_{RF}^i \qquad (17)$$

$T_{e,(i)}$ is the electron (ion) temperature (eV), B_p is the poloidal magnetic field (Gauss), $n_{e,(i)}$ is the electron (ion) density (cm^{-3}), V_i is the ion velocity (cm/ms), J is the toroidal current density (amp/cm^2), E is the toroidal electric field (volt/cm), r is the radius (cm), t is time (ms), $\chi_{e,(i)}$ is the electron (ion) thermal diffusivity (cm^2/ms), η_{NC} is the neoclassical resistivity (ohm-cm), D is the diffusion coefficient (cm^2/ms), $U_{bi,(e)}$ is the fraction of beam energy going to ions (electrons), and f is the fraction of deuterons in the neutral beam which undergo fusion as they slow down in a tritium target plasma. P_B, P_S represent bremsstrahlung, synchrotron, radiation, respectively (watts), and E_B is the beam energy, and $P_{RF}^{i,e}$ is the ion (electron) power absorption (watts).

Since the point code is spatially independent, we need to eliminate the gradients in both the conduction and convection terms. Therefore, we may replace the conduction term by[10]

$$\frac{2}{3}\frac{\partial}{\partial r}\left[r n \chi \frac{\partial T}{\partial r}\right] \rightarrow \frac{nT}{\tau_c} \qquad (18)$$

where τ_c is a characteristic thermal conduction time. For the convection term we have[10]

$$\frac{1}{r}\frac{\partial}{\partial r}\left(r\, nVT\right) \rightarrow \frac{nT}{\tau_D} \qquad (19)$$

where τ_D is a characteristic thermal diffusion time.

Qualitatively, we can replace τ_c and τ_D by

$$\tau_c^{i,e} \rightarrow \frac{a^2}{\chi_{i,e}} \tag{20}$$

$$\tau_D \rightarrow \frac{a^2}{D} \tag{21}$$

where a is the plasma minor radius and D is the diffusion coefficient, and χ is the thermal conduction coefficient.

To calculate D and $\chi_{i,e}$[11] we first must examine single particle orbits. Particles may travel along magnetic field lines which, if closed and in the absence of drifts, result in no particle losses. However, due to the 1/R variation in the magnetic field, as a particle travels along a given field line it passes through regions of varying field strengths. For a maximum magnetic field strength on that line of B_{max} particles with energy $E < \mu B_{max}$ will be reflected from the high magnetic field regions and become trapped in weak magnetic wells, undergoing periodic motion between reflection points. The bounce frequency for this periodic motion is approximately

$$\omega_b \simeq \frac{v_T}{Rq} \sqrt{2\varepsilon} \tag{22}$$

where $\varepsilon = r/R$ and q is the safety factor

$$q = \frac{rB_T}{RB_p} \quad . \tag{23}$$

Besides this bounce motion, particles also experience an effective gravitational force again caused by the inhomogeneity in the magnetic

field. The resultant drift of particles may be characterized by the velocity

$$V_D \simeq (mv_{\parallel}^2 + \mu B) \frac{B \times \nabla B}{eB^3} \sim \frac{m}{eB} \frac{v_T^2}{R} \tag{24}$$

The combination of bounce motion with drift produces a banana-shaped orbit whose width is given by

$$\Delta r_T \simeq \frac{2V_D}{\omega_b} \simeq 2\rho_\theta \sqrt{\varepsilon} = 2q\ \rho/\sqrt{\varepsilon} \tag{25}$$

where $\rho_\theta = \frac{V_T m}{eB_p}$.

A general particle diffusion coefficient may be defined by $D \sim (\Delta x)^2/\Delta t$ where Δx is the mean spatial step size caused by the scattering process during the time Δt. In the absence of bounce motion and drifts, simple Coulomb collisions produce particle transport. For low β machines, the classical diffusion coefficient is written[11] as

$$D \sim \nu_{ei}\rho^2 \tag{26}$$

where ρ, the gyroradius, is the step size and

$$\nu_{ei} = \frac{4\sqrt{2\pi}\ n_i Z^2\ e^4 \ell n\Lambda}{3\sqrt{m_e}\ T_e^{3/2}} = \text{electron-ion collision frequency.} \tag{27}$$

However, when banana orbits are present in tokamaks, this simple diffusion picture becomes more complicated.

For low ν, the trapped particles have a step size on the order of the banana width rather than their gyroradius. This step size is valid when the collision frequency for the scattering of trapped particles

out of the region of trapped particle velocity space is small compared to the bounce frequency. Since Coulomb collisions are small angle processes we define

$$\nu_{eff} \sim \frac{\nu_{90°}}{(\Delta\theta)^2} \sim \frac{\nu_{ei}}{\varepsilon} \tag{28}$$

The condition for trapped particles to be considered "collisionless" is that

$$\nu_{eff} < \omega_b \text{ or } \nu < \varepsilon^{3/2} V_T/Rq \tag{29}$$

In this "neoclassical" regime, the diffusion coefficient due to trapped particles is

$$D \sim \nu_{eff} (\Delta r_T)^2 f_T \sim \nu \rho^2 q^2 \varepsilon^{-3/2} \tag{30}$$

where f_T is the fraction of trapped particles

$$f_T \equiv \frac{B_{max}}{B_{min}} - 1 \equiv \sqrt{2\varepsilon} \tag{31}$$

For ions in this neoclassical regime $\chi_i \sim D$.

Since plasmas in tokamaks are neither spatially uniform nor Maxwellian, they are subject to both macroinstabilities and microinstabilities. Microinstabilities may be driven by velocity space anisotropy or temperature, density and pressure gradients. Microinstabilities lead to enhanced or "anomalous" transport of which, for tokamaks, the most important kind are those driven by the various gradients present in all tokamaks.

In an inhompgeneous plasma, there is an apparent drift of particles in the $\bar{B}X\nabla n$ direction given by

$$V_d = \frac{T}{eB}\frac{1}{n}\frac{dn}{dr} = \frac{\rho}{r_n} v_T \tag{32}$$

where r_n = effective plasma radius = $(\frac{1}{n}\frac{dn}{dr})^{-1}$.

When there exists an E_θ in the $\bar{B}X\nabla n(\theta)$ direction, with wave number k_θ, this field produces a drift wave with frequency

$$\omega_* = k_\theta V_D \ . \tag{33}$$

Since $\frac{1}{r} < k_\theta < \rho_i^{-1}$ we may have a range of drift frequencies with

$$\omega_{*min} \simeq \frac{V_d}{r} \sim \frac{v_{thi}}{r}\frac{\rho_i}{r_n} \tag{34}$$

$$\omega_{*max} \simeq \frac{V_d}{\rho_i} \sim \frac{v_{thi}}{r_n} \ . \tag{35}$$

There is no energy or momentum exchange between species since E_θ causes both ions and electrons to drift in the $\bar{E}_\theta X\bar{B}$ direction, hence no instability develops. However, various mechanisms exist which may retard one of the drifting species, resulting in a net exchange of either momentum or energy with the drift wave causing an instability to grow. These mechanisms which result in enhanced transport may be classified between various natural frequencies in the plasma ω_{*min}, ω_{*max}, ω_b and the curvature drift frequency $\omega_D \equiv k_\theta v_D$. In tokamaks, we usually have

$$\omega_{Dmin} < \omega_{*min} << \omega_{bi} << \omega_{*max} < \omega_{be} \ .$$

Therefore, we may order the various types of instabilities due to drift waves in order of decreasing collision frequency.

For $\nu_{eff} > \omega_{be}$ but $\nu < \omega_{*max}$, i.e., trapped particles collide before a full bounce period is completed, drift dissipative modes develop and we have the following "pseudoclassical" transport coefficients

$$\chi_e \sim C_o \nu_{ei} \rho_{\theta e}^2 \qquad \text{and} \qquad D \sim C_1 \nu_{ei} \rho_{\theta e}^2 \tag{36}$$

with $C_o = 10$ and $C_1 = 10/3$ for NUWMAK.

For $\nu_{eff_e} < \omega_{be}$, $\nu_{eff_e} > \omega_{*min}$ trapped particles bounce before undergoing Coulomb collisions, hence are "collisionless". When a temperature gradient exists, these collisions do not retard the $\bar{E}\bar{X}\bar{B}$ drift of the trapped electrons and the dissipative trapped electron mode develops with transport coefficients

$$\chi_e \sim \frac{3\,\varepsilon^{3/2}\, r^2\, \omega_{*min}\, \omega_{*min}^T}{\nu_{ei}} \qquad \text{with } \omega_{*min}^T = \frac{1}{e\,Br}\frac{\partial T}{\partial r} \tag{37}$$

$D \sim \varepsilon\chi_e \sim \chi_i$.

For $\nu_{eff_e} < \omega_{be}$, $\nu_{eff_e} < \omega_o \sim 0.1\,(r/\rho_{\theta e})\,\omega_{*min}$ again we have a dissipative trapped electron mode instability developing. However, in this lower collision frequency regime the effective wave number k of this mode is determined by the magnetic shear and we obtain

$$\chi_e \sim C_2 \nu_{ei} \rho_{\theta e}^2 \qquad \text{where } C_2 = 0.06\,\varepsilon^{1/2}\,\frac{d\ell nT}{d\ell nn}\,\frac{m_i}{m_e}\,\frac{B_p}{\theta B} \tag{38}$$

$D \simeq \varepsilon\chi_e \sim \chi_i$. = constant of order 10^2 depending upon the magnetic shear

$$\theta \equiv r_n/L \rightarrow \theta = r_n/L_S$$

Finally for $\nu_{eff_i} \ll \omega_{bi}$ the frequency of this mode is below the ion bounce frequency. The drift wave in this case is supported by only trapped particles and we have

$$D \sim \chi_e \sim \chi_i \sim \frac{\varepsilon^{5/2} r^2 \omega_{*min}^2}{\nu_{ei} (1 + T_e/T_i)^2} \tag{39}$$

In the point code, all of the above transport coefficients are first calculated and the largest values for D and $\chi_{i,e}$ are used in the energy balance equations.

To eliminate the spatial dependency in density and temperature, we use the following expressions for the average density and temperature[9,10]

$$\bar{n} = 2 \int_0^a \frac{n(r) r dr}{a^2} \tag{40}$$

$$\bar{T} = \frac{\int_0^a n(r)\ T(r)\ r dr}{\int_0^a n(r)\ r dr} \tag{41}$$

where both T(r) and n(r) are assumed of parabolic form

$$n(r) = 2\ n_o\ (1 - \frac{r^2}{a^2})^{\alpha} \tag{42}$$

$$T(r) = 2\ T_o\ (1 - \frac{r^2}{a^2})^{\beta} \tag{43}$$

where α and β are set equal to 1 for the cases we analyze.

Since NUWMAK is noncircular, a shape factor S is defined[10] by

$$S = \frac{\text{circumference of plasma}}{\text{circumference of prescribed circular plasma}} \tag{44}$$

so that the stability factor q is given by

$$q = \frac{S}{A} \frac{B_T}{B_p} \tag{45}$$

where A is the aspect ratio of the smaller inscribed circular plasma and B_p is the poloidal field at the plasma edge.

In the point code, we assume that through some fueling mechanism, such as low energy neutral beams or pellets, the density of deuterium and tritium remains constant, although the ratio of the two species may vary if neutral deuterium beams are used. The resultant alphas from both main body and TCT fusions are calculated and we may find the resultant electron density by the charge neutrality condition

$$n_e = n_D + n_T + 2n_\alpha \tag{46}$$

We now spatially average the RF heating expressions (Eqns. (9) & (3) in Section V-B) assuming the parabolic expressions 42, 43 and define

$$PRFI = \sum_{\ell=2}^{3} \int_0^a \frac{\varepsilon_o \omega_{pi}^2(r)}{4\ell\, \omega_{cio}} \frac{R}{r} \left[\frac{\langle k_\perp^2\rangle v_{thi}^2(r)}{2\,\omega_{ci}^2(r)}\right]^{\ell-1} |E_+|^2 \, rdr \Big/ \int_0^a rdr \tag{47}$$

where $\ell = \frac{\omega}{\omega_{ci}} = 2$ for deuterium and 3 for tritium

$$PRFE = \frac{\displaystyle\int_0^a \frac{\pi^{1/2}\varepsilon_o}{4\,k_\parallel} \frac{\omega_{pe}^2(r)}{\omega_{ce}^2(r)} \langle k_\perp^2\rangle v_{the}(r)\,(1 + x^2(r))\,|E_+|^2\, e^{-\left(\frac{\ell^2\omega_{cio}^2}{k_\parallel^2 v_{the}^2(r)}\right)} rdr}{\displaystyle\int_0^a rdr} \tag{48}$$

In the expressions for PRFI and PRFE we have previously averaged $k_\perp^2$ over the resonant heating zone whose width is given for both ion species by

$$\Delta R = \frac{2\, k_{\parallel}\, v_{thi}\, R}{\ell\, \omega_{cio}} \tag{49}$$

while for the electrons, ΔR is taken to be the entire plasma cross section since electron Landau heating as well as transit time magnetic pumping occur over the entire plasma radius. With this model we have neglected possible effects due to coupling problems as well as multiple modes. With this we find that

$$PRFI = \frac{|E_+|^2}{2\ell\omega_{cio}a^2}\, \varepsilon_o R \int_0^a \omega_{pi}^2(r) \left[\frac{\langle k_\perp^2\rangle\, v_{thi}^2\,(r)}{2\,\omega_{ci}^2\,(r)}\right]^{\ell-1} dr \tag{50}$$

$$= PRFI'\ |E_+|^2$$

$$PRFE = \langle k_\perp^2\rangle \frac{|E_+|^2}{2k_{\parallel}a^2}\ \pi^{1/2} \int_0^a \frac{\omega_{pe}^2(r)}{\omega_{ce}^2(r)}\, v_{the}(r)\,(1 + x^2(r))e^{-\ell^2\omega^2_{cio}/k_{\parallel}^2 v^2_{the}} dr \tag{51}$$

$$= PRFE'\ |E_+|^2 \tag{52}$$

$$\text{TOTAL RF INJECTED POWER} = |E_+|^2 \times (PRFI' + PRFE') \times \text{VOLUME}\ . \tag{53}$$

In the point code, we input the total power deposited in the plasma; therefore, we normalize $|E_+|^2$ such that

$$|E_+|^2 = \frac{\text{TOTAL RF INJECTED POWER}}{(PRFI' + PRFE') \times \text{VOLUME}}\ . \tag{54}$$

First of all, Figure V-C-1 shows how the ion and electron temperatures as well as the amount of alpha power deposited in the electrons varies with time. From 0.0 to 4.0 seconds the plasma is ohmically heated while from 4.0 to 6.0 seconds 75 MW of RF power is assumed to be deposited in the plasma. As seen in Fig. V-C-1, the plasma reaches the equilibrium ion temperature of 13.2 keV and 15.4 keV for the electrons 500 to 1000 ms after the RF is shut off. Once the RF is turned on, T_i is greater than T_e because most of the RF power goes to the ions (see Fig. V-C-3). However, 1800 ms after the RF is turned on the plasma reaches a high enough temperature so that a significant number of fusions occur. Since most of the fusion alpha energy is deposited in the electrons as they thermalize, T_e becomes greater than T_i. As seen in Figs. V-C-1 and V-C-4, the alpha power to the electrons rises sharply 1500 ms after the RF is turned on reaching an equilibrium value of 310 MW.

Figure V-C-2 shows how the plasma minor radius and current changes during the current rise-RF heating phase of operation. The plasma current rises linearly from 1.0 MA to 5.2 MA in 5.5 sec while the plasma minor radius increases from 38 cm to 112 cm in such a way as to keep the safety factor q at a value of 2.6 at the edge. It should be noted that in order to have agreement with the space-time and MHD codes, q was kept constant for all three codes but since the codes determine q in slightly different ways, the plasma current varies between these codes. When the RF is supplied the plasma radius is initially at a value of 92 cm which is 82% of its final value.

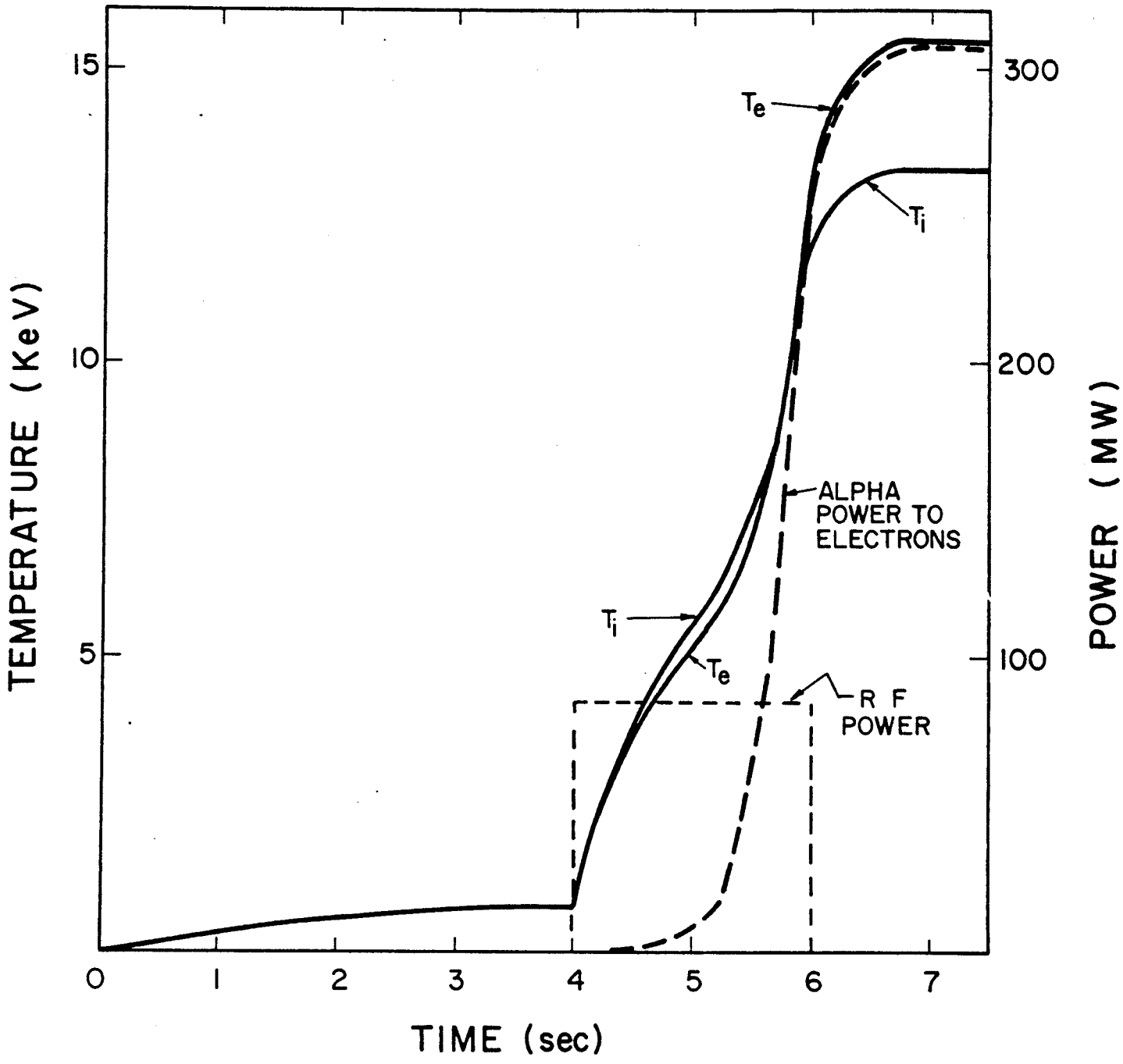

TEMPERATURE (KeV)
POWER (MW)
TIME (sec)
15
10
5
0
1
2
3
4
5
6
7
300
200
100
T_e
T_i
ALPHA POWER TO ELECTRONS
T_i
T_e
R F POWER

Fig. V-C-1

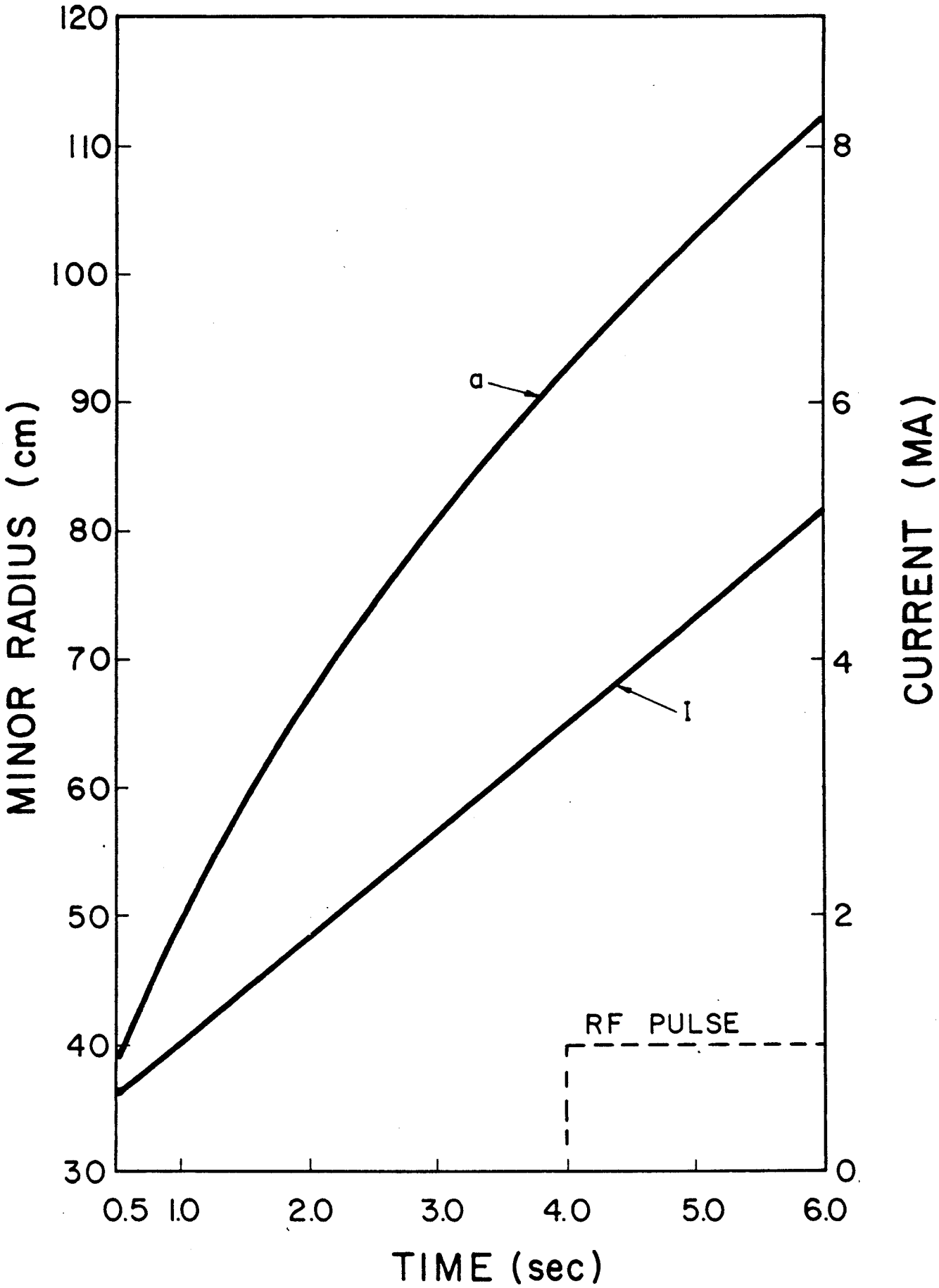

120
110
100
90
80
70
60
50
40
30
MINOR RADIUS (cm)
8
6
4
2
0
CURRENT (MA)
a
I
RF PULSE
0.5
1.0
2.0
3.0
4.0
5.0
6.0
TIME (sec)

Fig. V-C-2

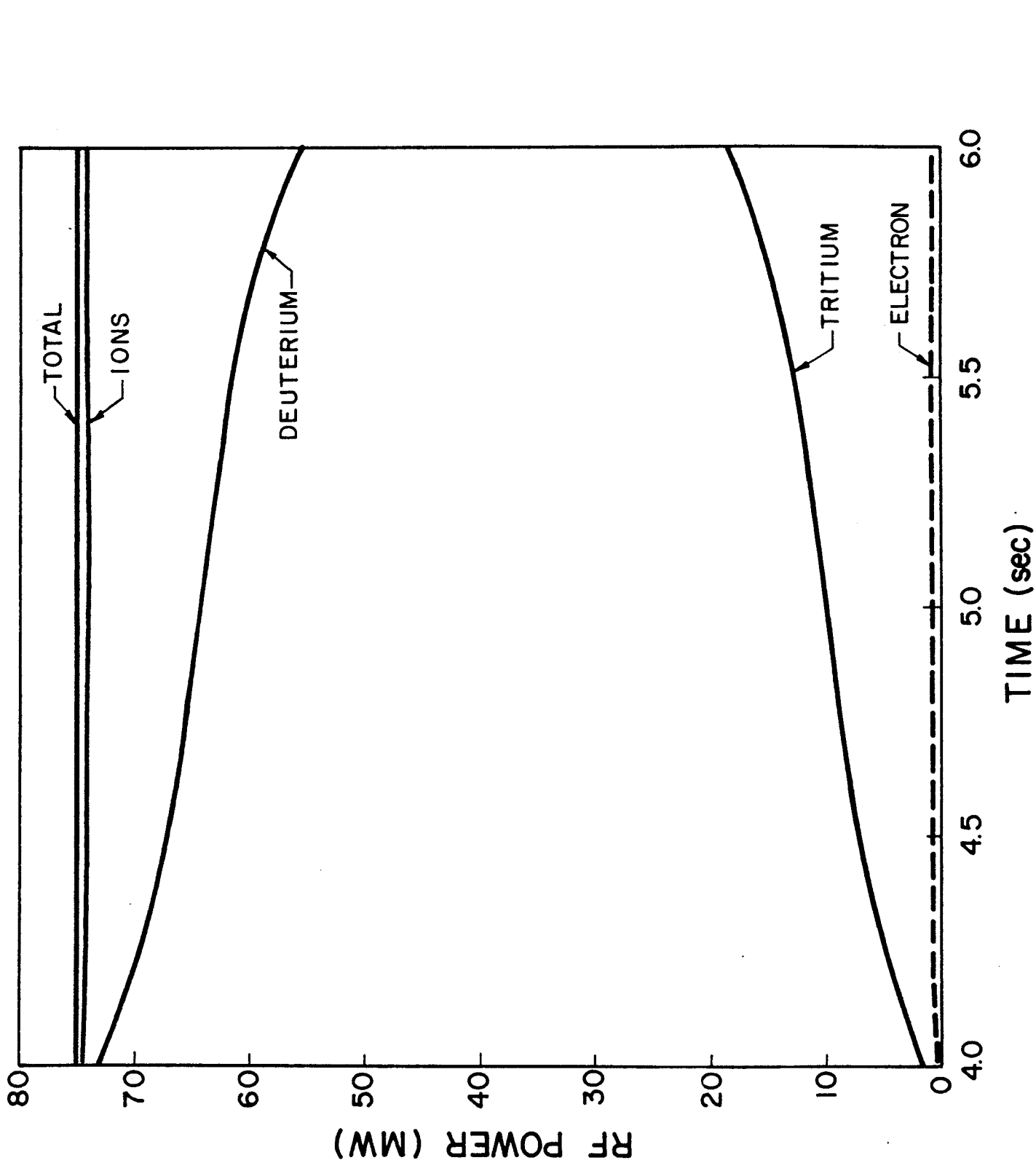

TOTAL
IONS
DEUTERIUM
TRITIUM
ELECTRON
RF POWER (MW)
80
70
60
50
40
30
20
10
0
4.0
4.5
5.0
5.5
6.0
TIME (sec)

Fig. V-C-3

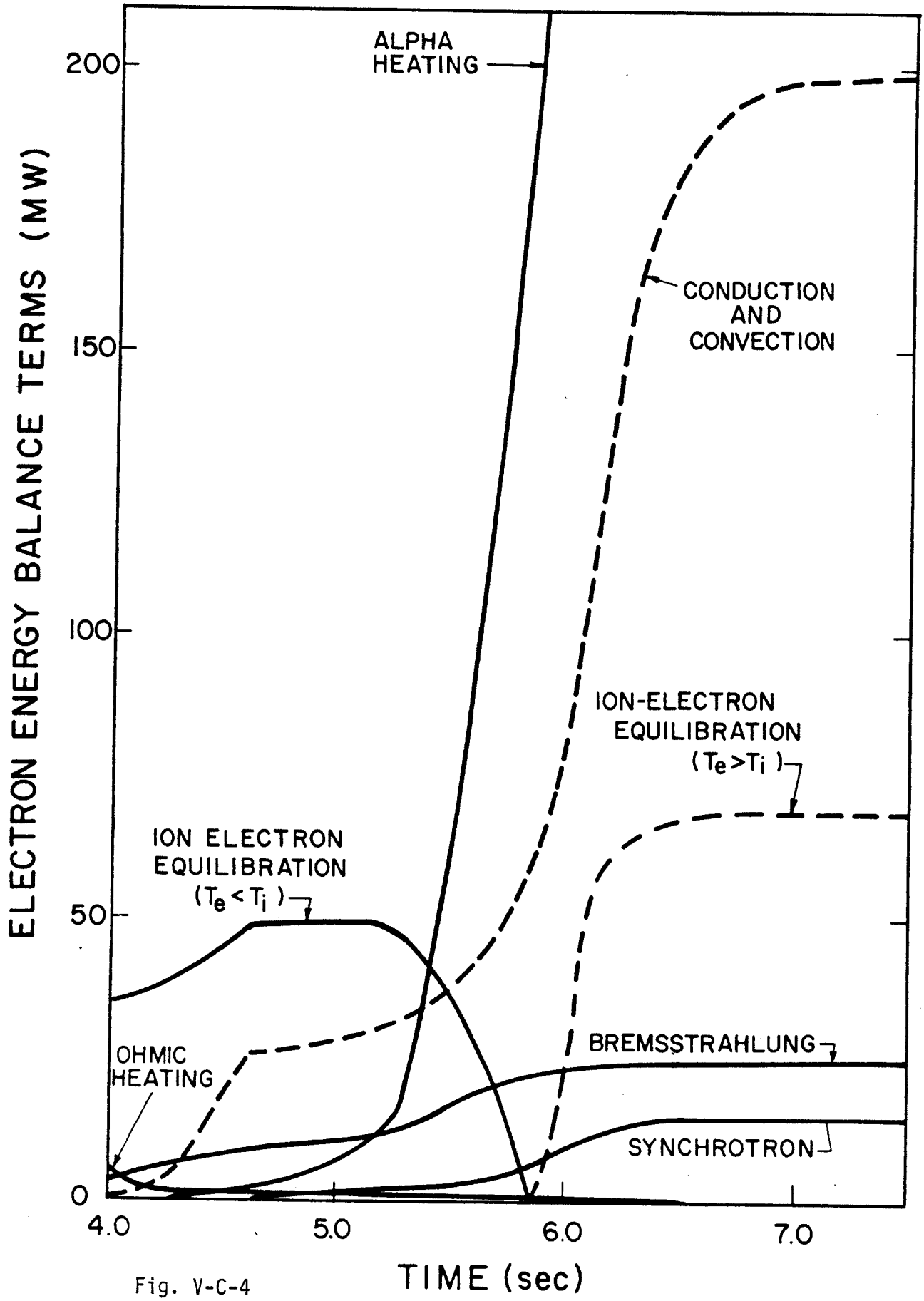

ALPHA HEATING
CONDUCTION AND CONVECTION
ION-ELECTRON EQUILIBRATION ($T_e > T_i$)
ION ELECTRON EQUILIBRATION ($T_e < T_i$)
BREMSSTRAHLUNG
OHMIC HEATING
SYNCHROTRON
ELECTRON ENERGY BALANCE TERMS (MW)
TIME (sec)
200
150
100
50
0
4.0
5.0
6.0
7.0

Fig. V-C-4

In Figure V-C-3, we see the amount of RF power deposited in each species. Most of the power supplied goes to the ions, decreasing slightly from 75 MW to 74 MW. As the plasma temperature increases the power flow to deuterium decreases from 73 MW to 56 MW while that to tritium increases from 1.6 MW to 18 MW. This change in power ratio is due to the fact that $\frac{P_T(3\omega_{CT})}{P_D(2\omega_{CD})} \propto T_i$. The power supplied to the electrons remains at the relatively low level of 500-600 kW. In order to explain this low level we first notice that in Figs. V-C-1 through V-C-5 an averaged value of $k_\perp^2$ was used. For the ions $\langle k_\perp^2 \rangle = 2.45\ cm^{-2}$ where $k_\perp^2$ is averaged over the resonant ion width ΔR where

$$\Delta R = \frac{2k_\parallel v_{TH_i} R}{n w_{cio}}$$

while for the electrons $\langle k_\perp^2 \rangle = 1.5\ cm^{-2}$ and $k_\perp^2$ is averaged over the entire plasma cross section since electron heating occurs throughout the plasma. The electron heating term is small because the exponential factor in Eq. 51 is larger, thus making PRFE small. The magnitude of the spatially averaged electric field $|E_+|$ drops steadily from a peak value of 980 V/m to 212 V/m. As time increases, the plasma conductivity increases, hence the magnitude of E_+ must decrease if we wish the supply of RF power to the plasma to remain constant.

Figures V-C-4 and V-C-5 show the terms in the electron and ion energy balance equations. Dashed lines indicate energy loss mechanisms while solid lines indicate heating terms. In Fig. V-C-4, we see that at these high plasma

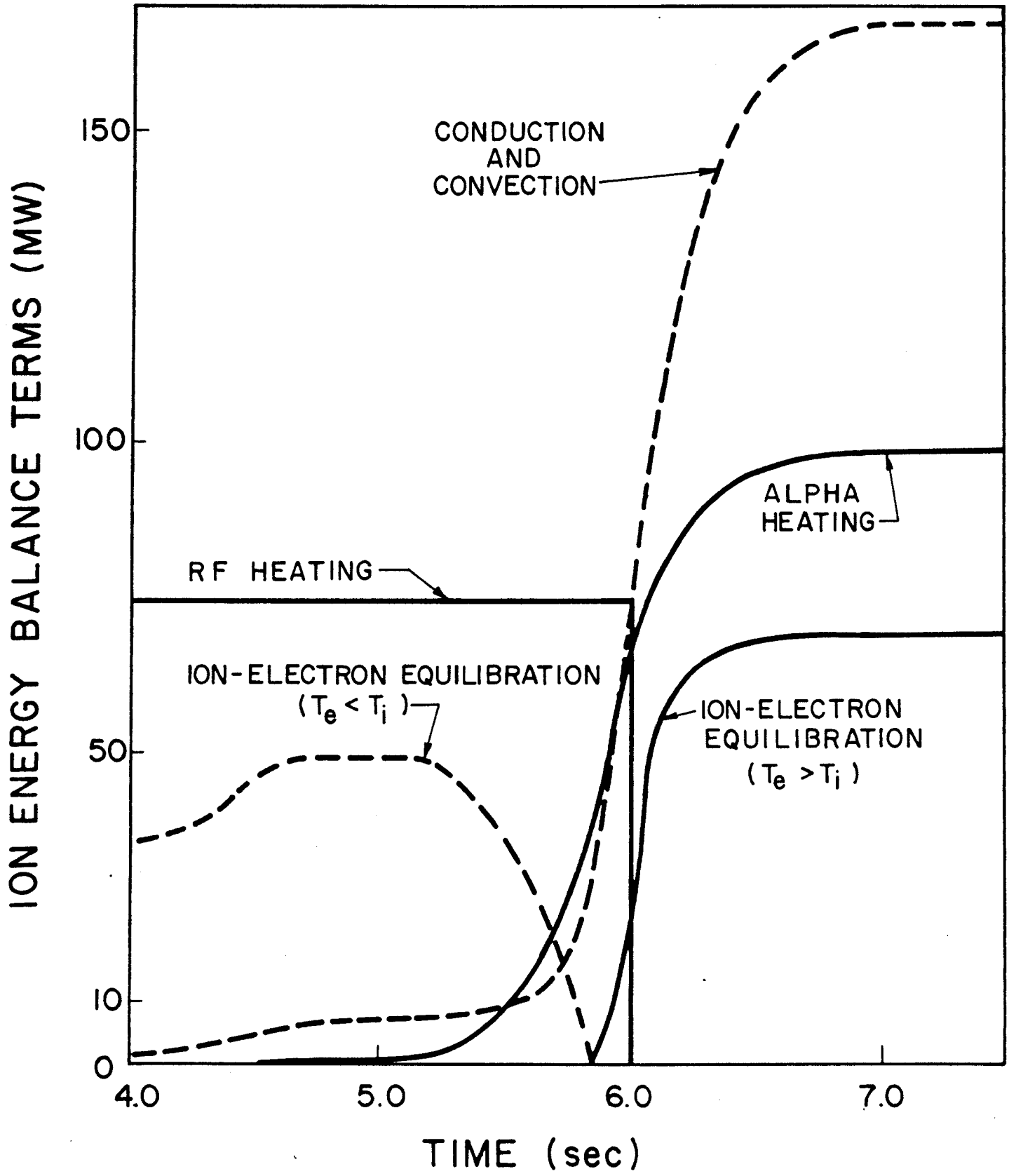

ION ENERGY BALANCE TERMS (MW)
150
100
50
10
0
4.0
5.0
6.0
7.0
TIME (sec)
CONDUCTION AND CONVECTION
ALPHA HEATING
RF HEATING
ION-ELECTRON EQUILIBRATION
($T_e < T_i$)
ION-ELECTRON EQUILIBRATION
($T_e > T_i$)

Fig. V-C-5

temperatures the Ohmic heating term is quite small, decreasing as the plasma temperature increases from 5 MW to 100 kW. After 1700 ms, the alpha heating term becomes so large that even if mode conversion processes were present causing most of the power to be deposited in the electrons, our results would still be the same. As Fig. V-C-1 shows, $T_i \simeq T_e$, the electron-ion equilibration time is quite short, indicating that heating of the electrons would drag the ion temperature along with it, thus not changing our results. Equilibrium is reached when the loss terms equal the heating terms. In the case of the electrons, at equilibrium as shown in Fig. V-C-4, the electrons lose 15 MW from synchrotron radiation, 25 MW from Bremsstrahlung, 200 MW through conduction and convection, and since $T_e > T_i$ at equilibrium, the electrons lose 70 MW to the ions from the equilibrium term. However, as shown in Fig. V-C-1, the electrons receive 310 MW from the thermalization of the alphas. As for the ions at equilibrium, Fig. V-C-5 shows that the ions lose 168 MW through conduction and convection, but receive 70 MW from the electrons due to the equilibration term and also receive 98 MW from the thermalization of the alphas.

Earlier NUWMAK studies showed that a 3 second, 75 MW RF pulse was needed to heat the plasma to ignition when the RF was supplied after the ohmic heating-current rise phase. By overlapping the RF heating phase with the current rise phase, we need only provide 75 MW for 2 seconds. Thus less energy is needed to heat the plasma to ignition and the plasma reaches equilibrium 3 seconds sooner, thereby increasing the duty cycle.

References for Section V-C

1. W. Houlberg, Ph.D. Thesis, (1977) University of Wisconsin-Madison, Madison, Wisconsin.

2. S. I. Braginskii, Review of Plasma Physics, M. A. Leontovich, Ed., Plenum Publishing Co., New York, Vol. I, p. 205, (1965).

3. N. A. Krall and A. W. Trivelpiece, Principles of Plasma Physics McGraw-Hill Book Co., New York (1973).

4. F. L. Hinton and R. D. Hazeltine, "Theory of Plasma Transport in Toroidal Confinement Systems", Reviews of Modern Physics 48, 239 (1976).

5. R. W. Conn, "Plasma Equations and Energy Equilibria and Stability", Nuclear Engineering Department Report UWFDM-16, p. 4, (University of Wisconsin-Madison, July 1972).

6. Lyman Spitzer, Jr., Physics of Fully Ionized Gases, Interscience Publishers, New York (1962).

7. D. J. Rose and M. Clark, Jr., Plasmas and Controlled Fusion, MIT Press, p. 233, Cambridge (1961).

8. T. F. Yang, H. K. Forsen and G. A. Emmert, "The Calculation and Parametric Study of the Synchrotron Radiation Loss for Tokamak Reactors", Nuclear Engineering Department Report UWFDM-49 (University of Wisconsin-Madison, 1973).

9. J. E. Scharer, R. W. Conn and D. T. Blackfield, "Study of Fast Magnetosonic and Neutral Beam Heating of Large Tokamaks", EPRI Report ER-268 Project 237-3 Topical Report, Sept. 1976.

10. B. Badger, et al. "UWMAK-III, A Noncircular Tokamak Power Reactor Design", Nuclear Engineering Department Report UWFDM-150 (Univ. of Wisconsin-Madison, July 1976).

11. "Status and Objectives of Tokamak Systems for Fusion Research" U.S. Atomic Energy Commission Report WASH-1239 UC-20.

V-D. RF Circuit Coupling to Magnetosonic Waves in the Tokamak Reactor

V-D-1. Introduction

Coupling structures in present tokamaks are often small with respect to a wavelength. Loop coupling at a point of high RF magnetic field intensity using external lumped capacitance to resonate with the loop inductance has been commonly employed. In reactors where the larger size allows self-resonant coupling structures a different approach may be used to advantage. If, on such large structures, a high voltage point can be used as the driving point then such a point will exhibit a high radiation resistance and will have considerable advantage from the standpoint of the driving system. Considering that air insulated coax line will be used, minimum loss occurs at a characteristic resistance, Z_0, of 73Ω and maximum power handling capacity occurs at a Z_0 of 30Ω, hence, driving point resistances of the order of 50Ω have considerable practical advantage.

One might expect that a $\lambda/2$ dipole would be a structure exhibiting these qualities. However, due to the physical constraints imposed by the reactor the dipole must be located near a conducting wall. Hence, the dipole's image is located near the dipole and as a result the driving point impedance is lowered. For example, to estimate the effect consider self and mutual impedance data for free space dipoles spaced $\lambda/10$ apart.

$$z_{11} = 73\Omega$$

$$z_{12} = 70 + j\ 10\Omega$$

Then considering antenna 2 in Fig. V-D-1 to be the short circuited image antenna, one finds for the driving point impedance

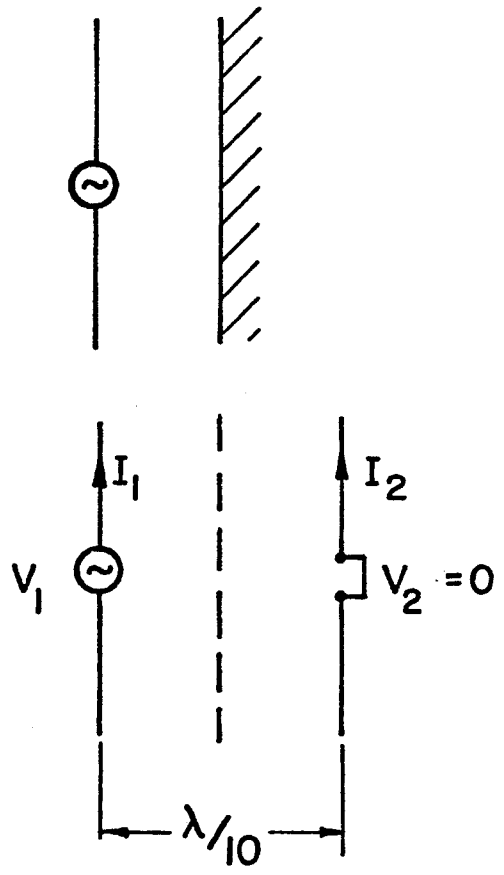


Fig. V-D-1 Illustration of the effect of a conducting wall on a half-wavelength dipole antenna.

$$V_1 = I_1 Z_{11} + I_2 Z_{12}$$

$$V_2 = I_1 Z_{21} + I_2 Z_{22} \qquad (1)$$

$$\frac{V_1}{I_1} = Z_{11} - \frac{Z_{21}}{Z_{22}} Z_{12}$$

$$\tilde{=} 5\Omega$$

This is rather low for efficient coupling. However, a higher impedance drive point may be selected away from the center of the antenna which will improve this value.

V-D-2. Cavity-Backed Aperture Antenna

Let us consider now another method of obtaining a high driving point impedance, that of aperture coupling by using a cavity backed antenna. Such a concept has advantages from the reactor point of view since the coupling apertures are located flush with the first wall. In addition, from the RF driving system viewpoint the cavity acts as an impedance transformer and since it is in resonance, nearly any desired driving point resistance can be found by properly choosing the input coupling point to the cavity. Also the cavity can be conveniently tuned to accommodate changing reactor conditions. Figure V-D-2 shows a proposed TE_{101} mode cavity antenna system. The cavity is a TE_{10} waveguide C meters wide and B meters high that is one half guide wavelength long in the A dimension. Figure V-D-3 shows the resonance curve for the C and A dimensions at 92 MHz. (Note: In this mode B does not affect the resonant frequency). Because of the given reactor dimensions we have chosen A = 3.5 m, B = 10 cm and C = 1.85 m. The height B = 10 cm was chosen to accommodate the input coupling structure in the outer blanket.

In order to further understand the choice of mode and cavity orientation one must consider the wave mode in the reactor. This mode is approximated by a TE_z cylindrical waveguide field description and since the H_z field at the outer wall is large, coupling via this field is used. Furthermore, since efficient core plasma heating is accomplished with low poloidal mode numbers, ($m=0, \pm 1$) apertures over only half of the A dimension are used so that the reactor fields are not affected by the reversed H field over the other half of the antenna cavity. Figure V-D-4 then shows the antenna cavity fields and their relationship to the reactor fields.

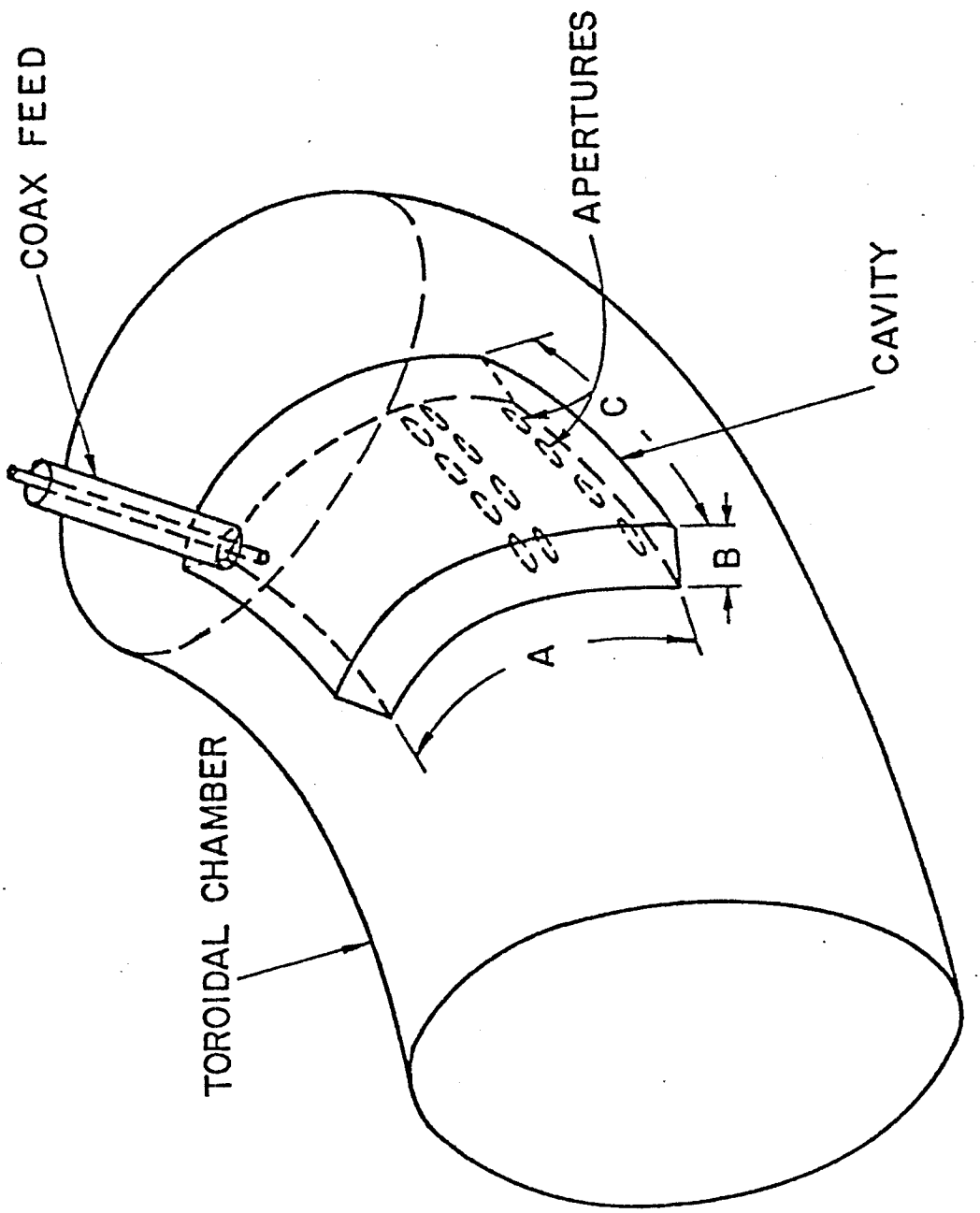


Fig. V-D-2 Schematic of proposed TE_{101} mode cavity antenna system mounted on a torus.

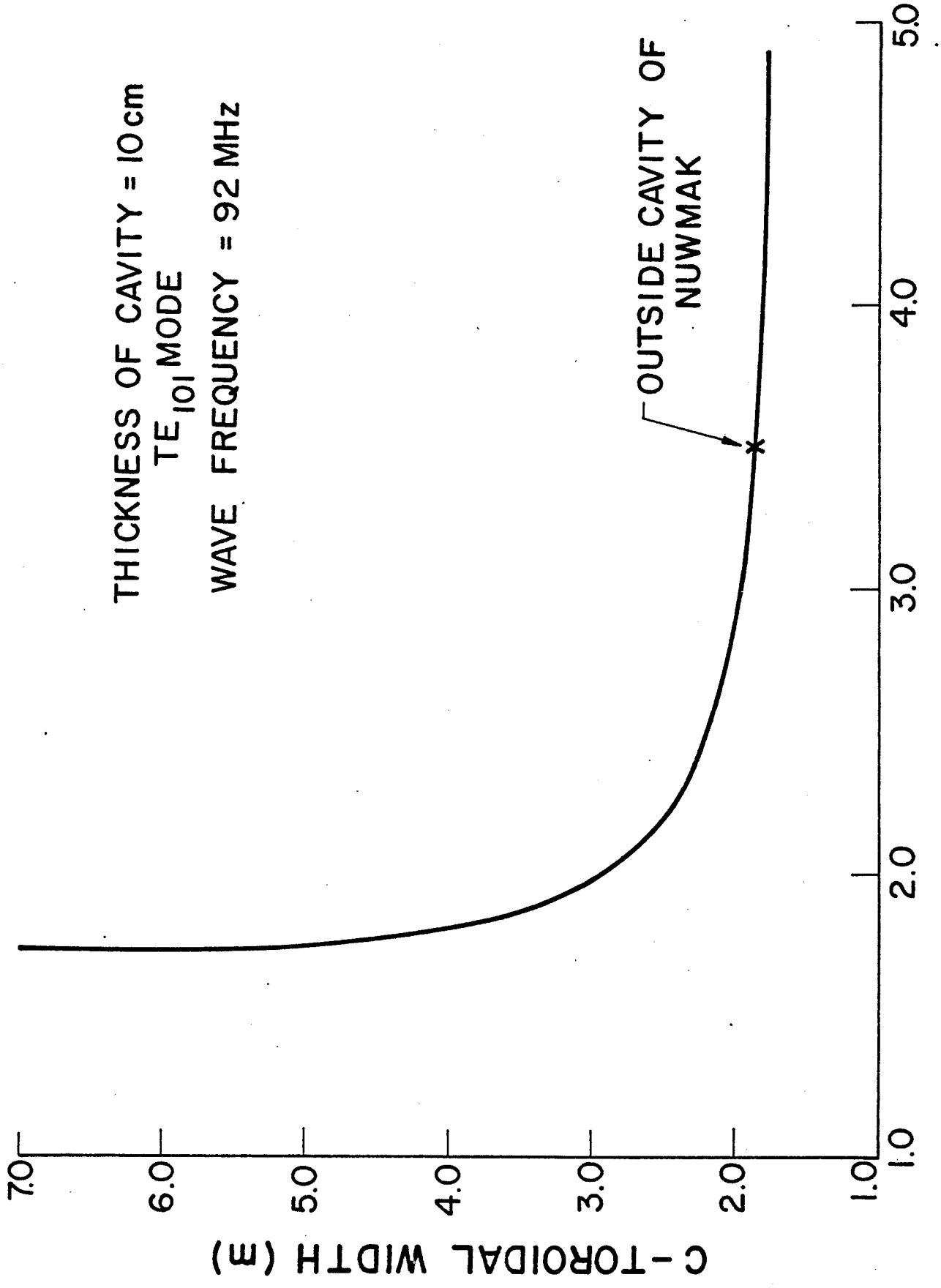


Fig. V-D-3 Resonance curve of the C and A dimensions of the cavity antenna at 92 MHz.

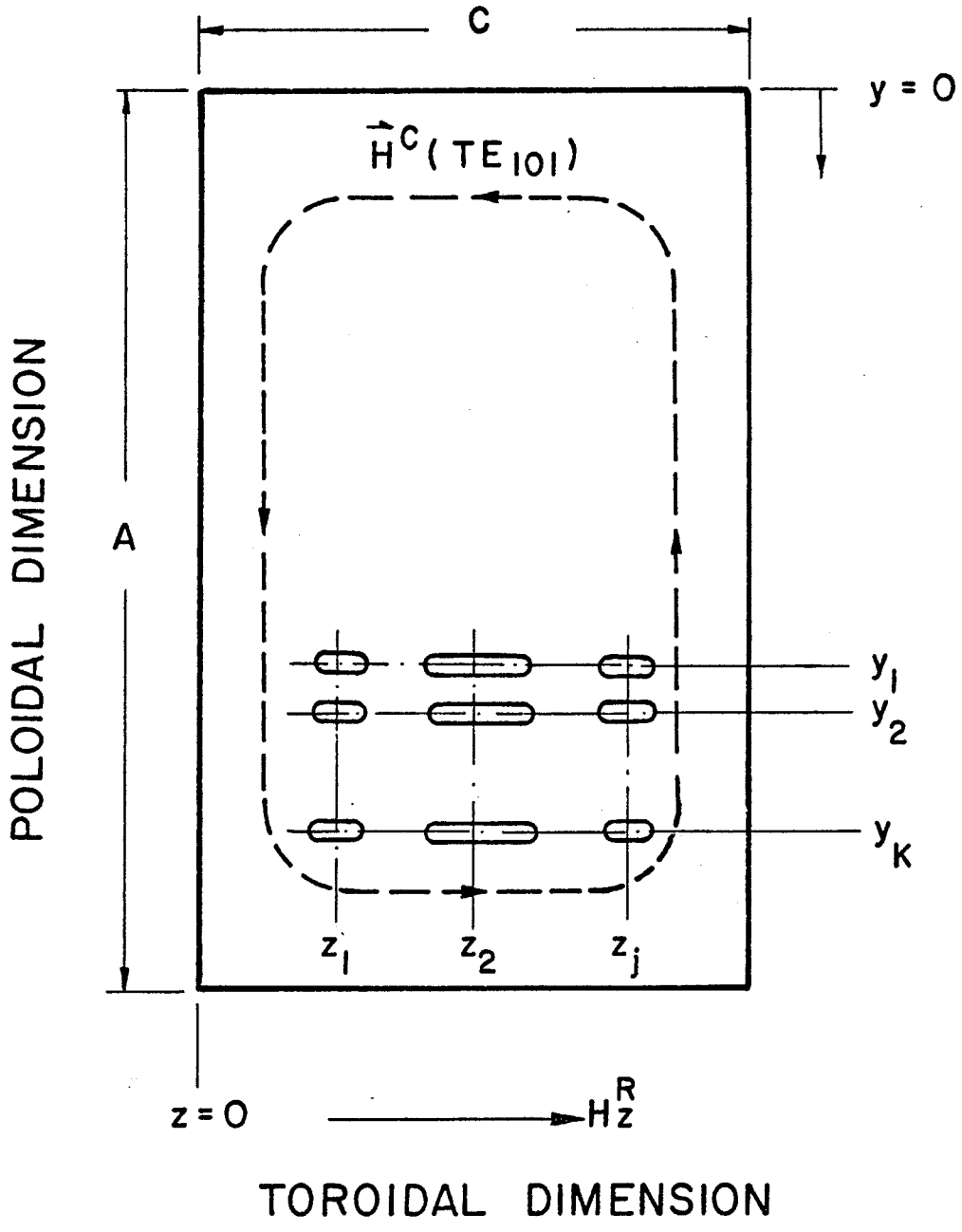


Fig. V-D-4 Schematic of antenna cavity and reactor fields.

In the following equations the superscript R will designate reactor fields while the superscript C will be used for antenna cavity fields. Furthermore, the subscript m will indicate normal mode fields normalized according to

$$\iiint \mu_0 \bar{H}_m \cdot \bar{H}_m^* \, dV = 1 \tag{2}$$

For a description of the fields and normalization coefficient consider the following fields in a plasma-filled cylindrical waveguide which is an approximation to a toroidal cavity of minor radius a and major radius R. For the fast magnetosonic mode in a cold plasma, we can assume $E_z = 0$ (TE-mode).

Assume a single eigenmode of the form

$$H_z^R = h_{m0} J_m(k_r r)\, e^{i(k_\parallel z + m\theta - \omega t)} \tag{3}$$

where $k_\parallel = n/R = 20\ m^{-1}$ where n is the toroidal mode number.

m = poloidal mode number

$$k_r^2 = \Lambda/(k_0^2 - k_\parallel^2/S)$$

with $\Lambda = k_\parallel^4/S - 2k_0^2 k_\parallel^2 + k_0^4 \frac{RL}{S}$

$$S = 1 + \sum_\alpha \omega_{p\alpha}^2/(\omega_{c\alpha}^2 - \omega^2)\ ,\quad R = 1 - \sum_\alpha \frac{\omega_{p\alpha}^2}{\omega^2}\left(\frac{\omega}{\omega+\omega_{c\alpha}}\right)\ ,\quad L = 1 - \sum_\alpha \frac{\omega_{p\alpha}^2}{\omega^2}\left(\frac{\omega}{\omega-\omega_{c\alpha}}\right)$$

$k_0 = \omega/c$, $\omega_{c\alpha} = \frac{\varepsilon_\alpha e B_0}{m_\alpha}$ and $\varepsilon_\alpha = +1$ for ions and -1 for electrons.

The other field components are then given by

$$H_r^R = -ik_\parallel h_{m0}\left[a_2 \frac{m}{r} J_m(k_r r) + a_1 k_r J_m^r(k_r r)\right] \tag{4a}$$

$$H_\theta^R = k_\parallel h_{m0}[a_1 \frac{m}{r} J_m(k_r r) + a_2 k_r J_m'(k_r r)] \qquad (4b)$$

where $a_1 = -k_r^{-2}$, $a_2 = (D/S)\, k_0^2/\Lambda$, and $D = \frac{1}{2}(R-L)$.

For an eigenmode, the boundary condition $E_\theta^R = -\frac{\omega}{k_\parallel} \mu_0 H_r^R = 0$ at $r = a$ is given by

$$a_2 \frac{m}{a} J_m(k_r a) + a_1 k_r J_m'(k_r a) = 0 \qquad (5)$$

Together with Eqs. (4), (5), and the normalization integral in Eq. (2), we obtain

$$h_{m0} = [2\pi^2 a^2 R_0 \mu_0 F_m(k_r a)]^{-1/2} \qquad (2a)$$

where h_{m0} is the normalized H-field amplitude as in Eq. (3), and

$$F_m(x) = 2 G_m(x) + k_\parallel^2 k_r^2 [(a_1 + a_2)^2 G_{m-1}(x) + (a_1 - a_2)^2 G_{m+1}(x)]$$

$$\text{with } G_m(x) = \frac{1}{2} J_m^2(x) \left(1 - \frac{m^2}{x^2}\right) + \frac{1}{2} J_m'^2(x) .$$

Let us first consider an overview of the coupling calculation. To find the cavity driving point impedance we work back from the reactor fields. From the computer simulation of the plasma heating equations the magnetic field in the reactor, H^R, is known everywhere for a given power delivered to the plasma, P_{diss}. We now assume that the reactor H^R field is excited by magnetic dipole equivalent sources at the coupling apertures. The required dipole moment is thus determined for a given P_{diss}. It is then a simple matter to relate the dipole moment to the magnetic field in the cavity, H^C. Knowledge of this field in turn will then give its source current on the input coupling structure. The terminal current on this

structure can then be calculated and since the input power is known (P_{diss}), and $P_{diss} = I^2_{drive} R_{drive}$, the driving point resistance is determined.

We begin by determining the source currents necessary to produce the required reactor fields. We assume that

$$\bar{H}^R = \sum_m B_m \bar{H}^R_m \tag{6}$$

where B_m is the amplitude coefficient of the mth normal mode field $\bar{H}^R_m$ normalized according to Eq. (2). For a surface distribution of magnetic current, $\bar{m}_s$, on the reactor wall, one finds for a particular mode m,[1]

$$(\omega_m^2 - \omega^2) B_m = - i\omega \iint \bar{m}_s \cdot \bar{H}^{R*}_m \, ds \tag{7}$$

where ω_m is the resonant mode frequency. In order to simplify the analysis for our case, we will assume a single mode exists in the reactor, hence m = 1. Since the coupling apertures are small with respect to a wavelength, each aperture can be accurately represented by a single magnetic dipole of moment $\bar{M}$ rather than a surface distribution of magnetic current. The integral on the right hand side of Eq. (7) can then be written as $\sum_{j,k} i\omega\mu_o \bar{H}^{R*}_m(r=a)\cdot\bar{M}_{jk}$ where $\bar{M}_{jk}$ is the magnetic moment of an aperture of the jth column and kth row of the array. With the further assumption that the reactor Q > 10,

ω_m in Eq. (7) may be approximated as

$$\omega_m^2 \simeq \omega^2 (1 + i1/Q) \ . \tag{8}$$

Noting that both $\bar{H}_m^R$ and $\bar{M}_{jk}$ are z-directed and using Eq. (8) in Eq. (7), we obtain

$$B_m = -iQ \sum_{j,k} \mu_o H_m^{R*}(a) M_{jk} \ . \tag{9}$$

Furthermore, the magnetic moment of an elliptical aperture, small with respect to a wavelength, may be written as[3]

$$M_{jk} = \frac{4\pi \ell_1^3 e_a^2 H_{jk}^c}{3[K(e_a)-E(e_a)]} \tag{10}$$

where $e_a = (1 - (\ell_2/\ell_1)^2)^{1/2}$ is the eccentricity of the ellipse and $2\ell_1$ and $2\ell_2$ are its major and minor axes, respectively. In Eq. (10) $K(e_a)$ and $E(e_a)$ are elliptic integrals given by

$$\left.\begin{aligned} K(e_a) &\simeq \ell n(4\ell_1/\ell_2) \\ E(e_a) &\simeq 1 \end{aligned}\right\} \text{ for } e_a \text{ near unity} \ . \tag{11}$$

To describe the field at the coupling apertures we refer to Fig. V-D-4 with the fields for the TE_{101} mode given by

$$H_z^c = h_o^c \cos \frac{\pi y}{A} \sin \frac{\pi z}{C} \tag{12a}$$

$$E_x^c = i\, h_o^c\, \eta \left(1 + \frac{A^2}{C^2}\right)^{1/2} \sin \frac{\pi y}{A} \sin \frac{\pi z}{C} \tag{12b}$$

where $\eta(= 377\Omega)$ is the intrinsic impedance. Hence,

$$H^c_{jk} \cong h^c_o \cos \frac{\pi y_k}{A} \sin \frac{\pi z_j}{C} \quad . \tag{13}$$

For elliptic apertures with $e_a \sim 1$, we substitute Eqs. (10), (11) and (13) into Eq. (9) to obtain

$$B_m = -iQ \sum_{j,k} \frac{4\pi \ell_1^3 \mu_o H^{R*}_m(a)}{(\ell n\, 4\frac{\ell_1}{\ell_2} - 1)} \; h^c_o \cos \frac{\pi y_k}{A} \sin \frac{\pi z_j}{C} \quad . \tag{14}$$

We now express B_m in terms of an assumed power dissipated within the plasma. Let P_{in} be the power input per RF module and N be the number of modules. For the fast magnetosonic mode we can approximate the time-averaged wave energy density $\langle W \rangle$ by $\frac{1}{2}\mu_o \langle \overline{H}^R \cdot \overline{H}^{R*} \rangle$, and from the definition of Q, we have

$$\langle W \rangle = \frac{QNP_{in}}{\omega V} \cong \frac{1}{2}\mu_o |B_m|^2 h^2_{mo} F_m (k_r a) \tag{15}$$

where V is the plasma volume. Using Eq. (12a) in Eq. (15) results in

$$|B_m| = \left(\frac{2QNP_{in}}{\omega}\right)^{1/2} \quad . \tag{16}$$

We now calculate the driving point resistance at the cavity feed point (y_o, z_o). We assume the coax line center conductor is connected to the wall of the cavity opposite the feed point. Hence, a cosinusoidal surface current is assumed on the coupling structure with a maximum at the wall, given by $\bar{J}_s = \frac{I_o}{4\ell} \cos(kx)\, \hat{u}_x$ where $k = 2\pi/\lambda_o$, and ℓ is the circumferential length of the structure. We now determine I_o from the known power input, namely

$$P_{in} = \frac{1}{2} \text{Re} \iint \bar{E}^{c*} \cdot \bar{J}_s \, ds \tag{17}$$

where the surface integral is evaluated over the coupling structure. For $B << \lambda_o$, we obtain for a structure uniform in x,

$$P_{in} = \text{Re}\,(ik_o^c)\, I_o \eta \left(1 + \frac{A^2}{C^2}\right)^{1/2} B \frac{1}{4\ell} \oint_c \sin \frac{\pi y}{A} \sin \frac{\pi z}{C} \, d\ell \tag{18}$$

where the contour integral is over the structure circumference centered at (y_o, z_o). Furthermore, since $I_{drive} \simeq I_o$, we have

$$R_{in} = 2P_{in}/I_o^2 \tag{19}$$

where R_{in} is the driving point resistance at the coax to cavity junction. Noting that $H_m^{R*}(a) \simeq (\mu_o V F_m(k_r a))^{-1/2} J_m(k_r a)$ and combining Eqs. (14), (16), (18) and (19) to eliminate B_m, h_o^c and I_o, we arrive at the following matching equation

$$R_{in}^{1/2} = \left(\frac{NVF_m(k_r a)}{Q\omega\mu_o}\right)^{1/2} \left(\ell n \frac{4\ell_1}{\ell_2} - 1\right) \eta \left(1 + A^2/C^2\right)^{1/2} B \left| \frac{1}{4\ell} \oint_c \sin \frac{\pi y}{A} \sin \frac{\pi z}{C} \, d\ell \right|$$

$$/2\pi \left| J_m(k_r a) \right| \ell_1^3 \sum_{j,k} \cos \frac{\pi y_k}{A} \sin \frac{\pi z_j}{C} \, . \tag{20}$$

Following a similar procedure, we obtain the cavity electric field distribution as

$$|E_x^c| = \left(\frac{NP_{in}VF_m(k_r a)}{2\mu_o\omega Q}\right)^{1/2} \left(\ell n \frac{4\ell_1}{\ell_2} - 1\right) \eta \left(1 + A^2/C^2\right)^{1/2} \left|\sin \frac{\pi y}{A} \sin \frac{\pi z}{C}\right|$$

$$/2\pi \left| J_m(k_r a) \right| \ell_1^3 \sum_{j,k} \cos \frac{\pi y_k}{A} \sin \frac{\pi z_j}{C} \, . \tag{21}$$

Equation (20) describes the possible locations of the coax feed point (y_o, z_o) coupling to a single fast wave eigenmode in the reactor through an array of elliptical apertures and matched to a coax of characteristic impedance R_{in}. From Eq. (21) a design constraint on high voltage breakdown may be imposed.

Let us now consider Eqs. (20) and (21) for NUWMAK parameters: $R = 5$ m, $a = 1.25$ m and $\omega = 2\pi \times 9.2 \times 10^7$ rad/sec, with the toroidal resonance conditions given by $k_{\parallel} = 20\ m^{-1}$, $m = 1$, $k_r a = 106$, $a_1 = -1.39 \times 10^{-4}\ m^2$ and $a_2 = -2.75 \times 10^{-4}\ m^2$. For a total input power of 80 MW through 4 RF modules, Eqs. (20) and (21) become

$$\left|\frac{1}{4\ell} \oint_c \sin \frac{\pi y}{A} \sin \frac{\pi z}{C}\, d\ell\right| = 6.96 \times 10^{-4} (R_{in}\, Q)^{1/2} \qquad (22)$$

and

$$|E_x^c|_{peak} = 456\, Q^{-1/2}\ \text{kV/cm} \qquad (23)$$

where a 12 x 4 array of elliptical apertures with $2\ell_1 = 6\ell_2 = 15$ cm as shown in Fig. V-E-12 is assumed.

Both the position of the feed and shape of the coupling structure are design parameters that can be used to advantage to match the coax drive line properly to the cavity. For a 30Ω coax drive line of 30 cm outer diameter the left hand side of Eq. (22) is bounded by

$$10^{-2} \lesssim \left|\frac{1}{4\ell} \oint_c \sin \frac{\pi y}{A} \sin \frac{\pi z}{C}\, d\ell\right| < 1\ . \qquad (24)$$

From Eqs. (24) and (22), only certain combinations of the coax impedance R_{in} and the wave Q can be matched properly to a single toroidal eigenmode, namely, those with $R_{in}\, Q \gtrsim 206\Omega$. Shifting the poloidal mode number m

changes $F_m(k_r a)$ only slightly and the matching condition remains relatively stable. For the case of NUWMAK, a feed point of $y_o = z_o = 15.25$ cm at the upper left corner as shown in Fig. V-E-12 has been chosen. For the above 30Ω coax located at the upper corner of the cavity, Q factors of the order of 10 can be accommodated. It should be noted that the collective summation over several modes in a reactor will tend to lower the axial wave magnetic field at the edge, raise the wave impedance there, and allow a match for the coax further from the corner of the external cavity. In addition, the peak electric field strength in the matching cavity will be reduced.

We note that Eq. (23) determines the scaling with Q of the peak electric field inside the cavity antenna as found in NUWMAK. The detailed implication of this equation on RF high voltage breakdown in the cavity is beyond the scope of the present work. However, with the limited supply of information[4] in this area, we have attempted a plausible assessment on this problem. For edge neutral pressures ($\lesssim 10^{-4}$ torr) and temperatures ($\lesssim$ 30 eV) commonly used in reactor studies,[5] particle collisions are scarace so that the inside of the cavity can be treated as a virtual vacuum. It follows that breakdown may only occur through processes on the surface of the electrodes. For an interelectrode spacing of 10 cm, the field emission current is probably too low to initiate any breakdown current. On the other hand, the typical time scale for the formation and vaporization of microparticles between electrodes which eventually lead to breakdown is long compared to the time (~ 5 ns) between field reversals. In addition, the presence of a strong transverse magnetic field tends to set all electrons and ions in oscillatory drift motion, the amplitude of which is small compared to the cavity dimensions for 100 kV/cm < E^c_{peak} < 200 kV/cm. This oscillatory motion

acts to inhibit a direct flow of current between the electrodes and further reduces the possibility of breakdown. At any rate a comprehensive theory of RF breakdown in the presence of a transverse magnetic field, coupled with a series of simulation experiments, appear necessary for verifying the above assessment.

Besides the volume breakdown problem, substantial electric fields may also build up at the apertures. Using the averaged Poynting flux approach, with 20 MW transmitted per port, the aperture field is found to be of the order of 6 kV/cm. Thus, a.c. multipactor breakdown[6] may be possible in the apertures but proper treatment of the conductor surface can presumably suppress it.

V-D-3. Coil Antenna

We have also considered an alternative method of coupling using a nearly self-resonant coil antenna type of structure. In general, there are two types of resonant coil antennas which can be used. The first kind is a center-fed half-wavelength dipole, open at its ends, which can be expected to have a relatively low driving point resistance. The second kind is the same as the first except that the structure is shorted at the ends, as shown in Fig. V-D-5. Since this antenna is driven at a high voltage point, the driving point resistance can presumably be raised to match the 30 ohm coaxial line feeding the antenna.

We have calculated, in a rudimentary fashion, the loading resistance for the two kinds of antennas, each coupling to a single fast wave eigenmode in NUWMAK, to assess the possibility of matching. To obtain a realistic picture for the plasma, we have adopted a two-step density profile model over the minor cross-section. The coil antenna is assumed to be located in the low density region at the wall. Preliminary analyses, assuming

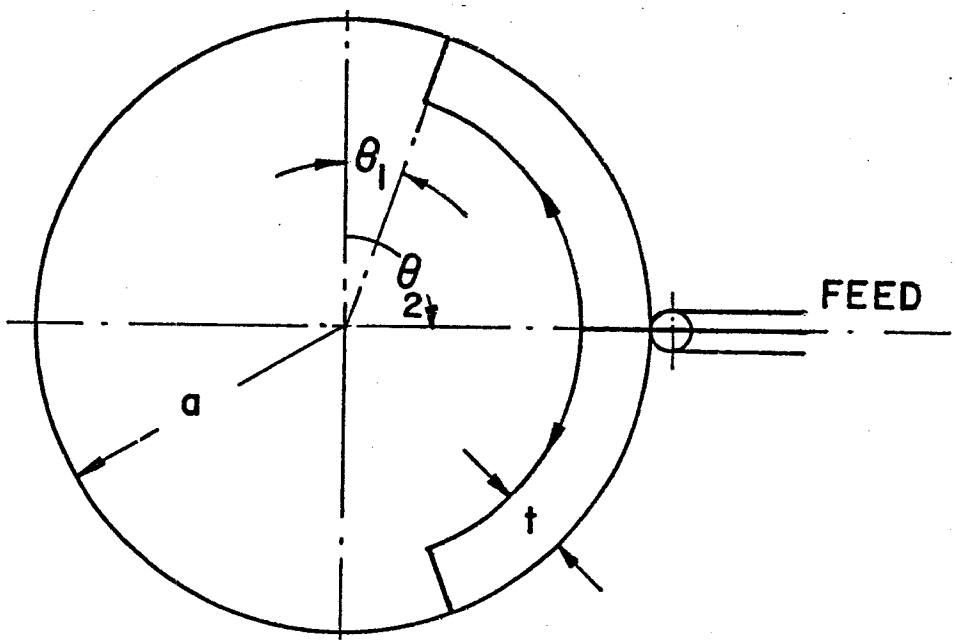


Fig. V-D-5 Schematic of a center-fed half-wavelength dipole antenna.

that the low density region approaches a vacuum, show that for open-ended antennas,

$$R_L \propto Q \left| J_m^2(k_\perp a) \right| F_+^2(m,\Delta\theta) \tag{25a}$$

while for short-ended antennas,

$$R_L \propto \{Q \left| J_m^2(k_\perp a) \right| F_-^2(m,\Delta\theta)\}^{-1} \tag{25b}$$

where R_L is the loading resistance at the feed point, Q is the wave quality factor of an eigenmode of poloidal number m, a is the plasma radius and

$$F_{\pm}(m,\Delta\theta) = \frac{\sin(m\Delta\theta - \frac{\pi}{2})}{m - \frac{\pi}{2\Delta\theta}} \pm \frac{\sin(m\Delta\theta + \frac{\pi}{2})}{m + \frac{\pi}{2\Delta\theta}}$$

is the mode excitation coefficient with $\Delta\theta = \theta_2 - \theta_1$ being the poloidal angle the antenna subtends. In the context of the plasma model we adopted, it appears that matching at 30-50 ohms to low m single modes in NUWMAK is rather difficult to achieve unless the wave Q exceeds 1000. However, it is well-known that in a reactor-sized plasma the damping length of a fast wave mode due to cyclotron absorption is comparable to a toroidal circumference. If mode conversion to ion Bernstein modes is significant, a further drop in Q is expected. Thus, we assume that the Q for a fast wave mode in a reactor is between 10 and 50.

To get optimum coupling to a poloidal mode m via a self-resonant antenna requires the length of each coil to be $\frac{1}{2|m|}$ of the minor circumference, which means the frequency and hence the magnetic field have to be properly adjusted. These conditions cannot always be met in real situations.

By examining Eqs. (25a,b) and noting that $H_z \propto J_m(k_\perp r)$, we observe that the wave toroidal field H_z at the edge is extremely low compared to its peak value towards the core, resulting in a mismatch with the coax feed. If the plasma density is decreased, $k_\perp$ will drop resulting in a more gradual fall of the field amplitude in the radial direction. With

a decrease in plasma radius, $J_m(k_\perp a)$ will approach unity, making matching a much easier task, as found in small tokamaks. Thus, we believe that if a radial density profile is assumed and the wave equation properly solved by numerical methods, the matching problem should be greatly improved.

There are also engineering methods by which we can externally match to a low Q mode, such as

(i) Increasing the number of modules and the number of antennas in each module.

(ii) Connecting antennas in each module in parallel and matching each antenna to a coax feed of $R_L = N_m Z_o$, where N_m is the number of coils in each module and Z_o is the impedance of the main transmission line.

(iii) Feeding the antenna asymmetrically.

Although the problem of matching of a self-resonant coil antenna has not yet been solved completely, a preliminary engineering design of the coil antenna system is proposed and detailed in the next section, as an alternative to the cavity antenna.

References for Section V-D

1. R. F. Harrington, Time Harmonic Electromagnetic Fields, McGraw-Hill (1961), pp. 432-434.

2. R. E. Collin, Field Theory of Guided Waves, McGraw-Hill (1960), p. 291, Eq. 59.

3. Ibid, p. 298, Eq. 68b.

4. J.M. Meek and J.D. Graggs (Editors), Electrical Breakdown of Gases (John Wiley & Sons, 1978).

5. A. Gibson, J. Nuclear Materials 76 & 77, 92 (1978).

6. A.J. Hatch and H.B. Williams, J. Appl. Phys. 25, 417 (1954).

V-E. The Radio-Frequency Heating System for NUWMAK

V-E-1. Introduction

In the conceptual design of the NUWMAK tokamak fusion reactor, the radio-frequency (RF) supplementary heating method in the ion cyclotron range of frequencies (ICRF) is employed. It is proposed to launch the fast magnetosonic wave into a 50-50 DT plasma and heat the ions at the second harmonic cyclotron frequency of deuterium.

Most of the present-day magnetic fusion reactor designs advocate the use of neutral beams for heating and fueling purposes. However, as a supplementary heating scheme, RF has its potential advantages over beams which should not be overlooked. For instance, the technological demands for a successful RF heating system appear less severe than for the injection system in terms of high-power source development. With a properly designed RF system, the problem of material and equipment damage caused by prolonged radiation and neutron bombardment can be minimized. On the other hand, in the beam injection scheme the line-of-sight requirement places the beam accelerator directly in the path of neutron and radiation outflux from the plasma and results in a very stringent design criterion.

The RF supplementary heating system consists of the wave generator, the transmission line and the coupling structure. The wave generating system is responsible for producing an RF pulse of the required power level, frequency and duration during the start-up phase of the reactor duty cycle. The transmission system delivers the RF energy to the wave launching structure inside the reactor chamber, where the wave energy is coupled into and absorbed by the plasma.

In the design considerations outlined in the following sections, emphasis will be placed on the engineering problems associated with high power transmission and coupling to the plasma in a reactor environment. In particular, the problem of high voltage breakdown and the choice of structural materials to withstand radiation damage will receive special attention. For simplicity, only the fast magnetosonic wave heating scheme in the ion cyclotron range of frequencies will be presented. For lower hybrid wave heating, for example, the transmission and antenna design criteria are quite different, being in a higher frequency range, and have been dealt with in other works[1],[2].

Because of the preliminary nature of this work, alternative design schemes have been presented. As much theoretical calculation as possible will be incorporated into the design consideration to support the feasibility of the resulting system. Due to the limited scope of this work, no detailed cost analysis of the RF engineering system has been undertaken. But it is believed that the RF system cost will comprise only a small portion of the total estimated cost for building the reactor. Finally, it should be pointed out that much theoretical and experimental work has yet to be performed to provide a concrete understanding of the high power behavior of RF systems under the reactor environment. It is hoped that future experiments on large tokamaks such as PLT, TFTR and JET may just serve this purpose.

V-E-2. The Wave Generating System

The design of an efficient wave generating system is closely related to the amount of energy needed to heat a plasma the size of NUWMAK to ignition. Once ignition is reached, the sharply increased production of alpha-particles provides further heating of the plasma. A point is finally reached when the RF can be turned off while the plasma approaches a sustained burn condition, relying completely on alpha-particle heating.

Assuming that before the RF is on, the plasma has reached a temperature of 1 keV by Ohmic heating and that the RF pulse is turned off at about 8 keV after ignition, the required net input of energy to the plasma is about 100 MJ for NUWMAK. Taking into account the losses through radiation, energy transport, and impurity heating, a conservative estimate of 240 MJ of RF energy will be needed. To optimize the duty factor of the burn cycle, an RF pulse of 1 to 3 seconds duration is desirable in the start-up phase of the Ohmic heating current. This implies a minimum power requirement of 80 MW for 2-3 seconds which translates to 20 MW per module for a system of four RF transmission ports. The wave generating system design specifications can be summarized as follows:

Total power transmitted at first wall	20 MW/port for each of 4 ports
Pulse duration	2-3 sec.
Pulse repetition period (burn cycle)	245 sec.
Nominal center frequency	92 MHz

The frequency of 92 MHz in the table corresponds to the second harmonic ion cyclotron frequency of deuterium on the toroidal axis of the minor cross-section. For this reason, the idea of driving the RF system with super-power oscillators with drifting frequencies tuned to the loading circuits is not very practical. By far, the most efficient RF generator uses the driver, exciter and high-power amplifier (HPA) combination[1], which delivers full power into a matched load at a fixed frequency.

For reasonable operating conditions and design simplicity, power tubes capable of delivering at least several megawatts CW for 2-3 seconds at 92 MHz have to be used. At this frequency and power range, the RCA "coaxitron" is recommended as the HPA unit. A "coaxitron" is a super-power triode upgraded to the 100 MHz range by including the tuned cavities as part of the vacuum envelope. However, "coaxitrons" of MW-level power output are not presently available although their development is not believed to be a major technological problem and should pose no serious obstacle in the overall development of the RF system. Assuming that 5 MW "coaxitrons" are available in the future, four such units will be needed for each module, making it a total of sixteen units for the entire system.

Presumably, conventional power tubes, such as tetrodes, can be modified to meet the frequency and power demands for the NUWMAK RF system. In this respect, RCA[3] recently came up with the A3012, a liquid cooled super-power beam power tetrode, which has capabilities with some modifications of generating large amounts of

power within one vacuum enclosure. At present, they have a tube and circuit capable of over 50 kW of C.W. power at 100 MHz which can serve as a drive source for the larger tube. However, modification of the A3012 will not be undertaken until a sufficient market is assured to justify the expenditure.

The schematic of a module of the proposed RF generating system[2] is outlined in Fig. V-E-1. Power is drawn independently from the utility line, passed through a series of high-voltage step-up transformers and subsequently converted to DC by means of an SCR bridge converter. It is then fed in parallel to four ignition turn-on switches, each of which produces a DC pulse of 3 sec duration for every 245 sec. Any remaining ripples in the pulse can be filtered out by a low-pass capacitive network and the pulsed energy is then used to drive four HPA-IPA (intermediate power amplifier) units in parallel. Each HPA is composed of either a super-power tetrode or coaxitron with an output capability of 5 MW while the IPA consists of a high power (50kW) tube driven by a 92 MHz signal generator.

To ensure continuous and safe operation, a fault detecting circuit is included in the system. Connected in series with the transmitter is the fault detector consisting of a saturated time delay transformer (STDT) which acts as a current limiter when an arc is drawn in either the transmission or coupling system. The STDT also initiates a switch-regulator tube to remove the high voltage from the amplifier circuit in case of an arc fault. If the arc persists for more than a cycle, the crowbar will be energized through a crowbar time delay (CTD) circuit and the main power line will be disconnected by mechanical vacuum circuit breakers.

For this design, all switching and crowbarring will be performed at 40 kV levels and 125 A, which may necessitate a moderate improvement in tube technology. In the absence of an energy storage unit, the pulsed nature of the load will create disturbances on the main line and increase operation costs through "peak demand charges" by the utility company.

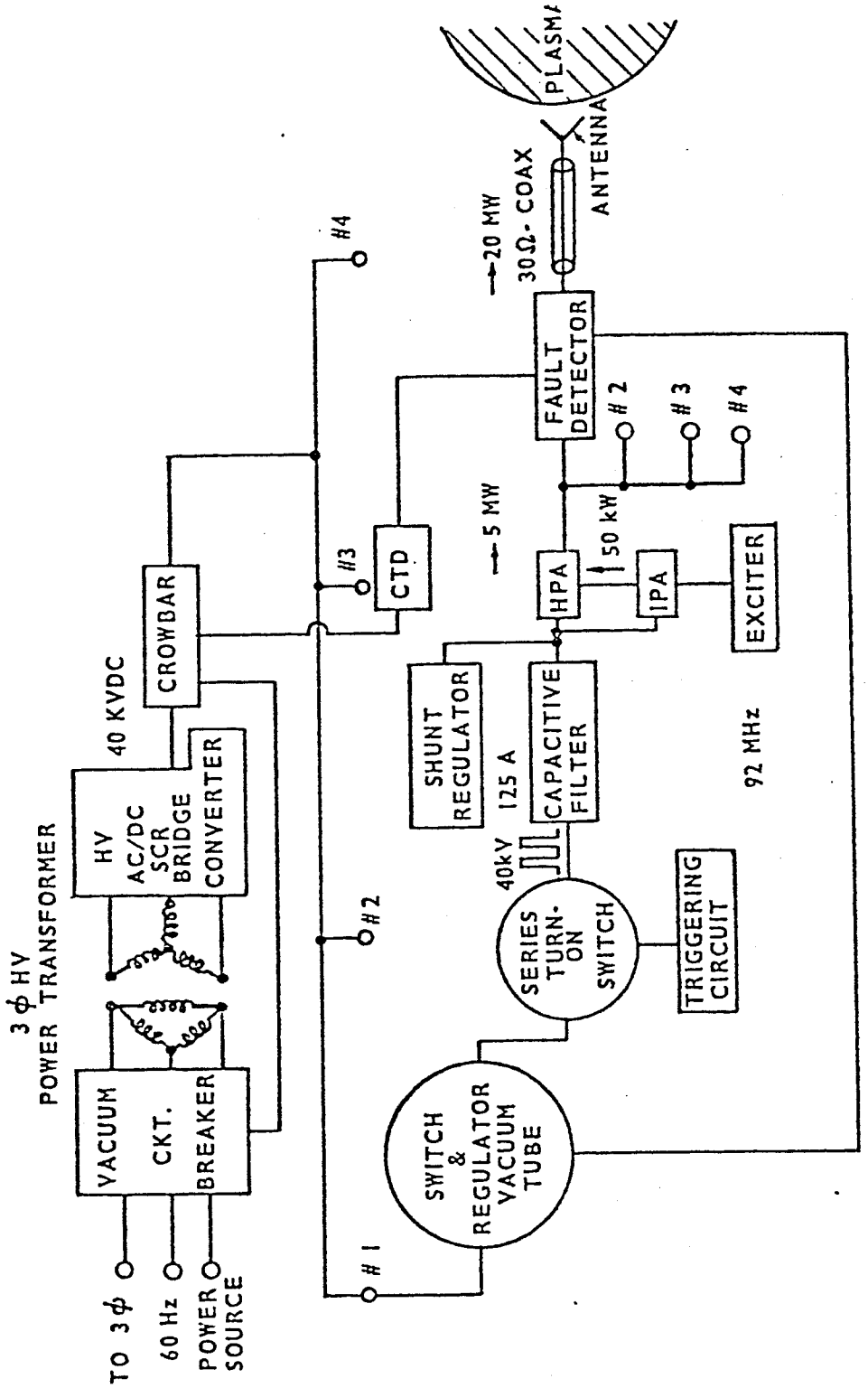


Figure V-E-1 Schematic of HV Power Supply and Transmitter for One RF Module in NUWMAK

V-E-3. The RF Transmission System

The overall objective of the transmission system design is to choose or construct a transmission line capable of handling 20 megawatts of RF power at 92 MHz over a distance of 10 meters from the generator to the coupler. The requirement of handling megawatt levels of power precludes the use of open transmission lines, such as the slab line and the strip line. The enclosed transmission lines which can be considered are the coaxial line, waveguides (rectangular, circular or ridged) and balanced TEM lines.

Because the balanced TEM transmission lines are three-conductor systems, they are very difficult to construct and design as far as support, matching, and cooling are concerned. Therefore they will be ruled out of consideration in spite of their many advantageous features.

Waveguides are the most ideal transmission lines to work with basically because of their simple one-conductor geometry. However, in the ion cyclotron range of frequencies (ICRF), they are usually intolerably bulky and take up valuable space in the reactor walls. For instance, to propagate a TE_{10} mode in a vacuum-filled rectangular waveguide at 92 MHz will require a cross-section of a 1.63 m minimum width. Ridged waveguides filled with a ceramic material having a dielectric constant much greater than unity can considerably reduce the size of the system[4]. However, the dielectric medium will be directly exposed to neutrons and radiation from the plasma, and the choice of material which can withstand a continuous radiation loading of several MW/m^2 still awaits years of experimental testing.

In addition, there is a lower cutoff frequency for the dominant mode which, for a fixed-size waveguide, tends to limit the range of operating frequencies. The waveguide mode is inherently narrow band, imposing a restriction on the bandwidth of the generator.

By far, the coaxial line represents the most practical choice for high power transmission in the 100 MHz frequency range and is adopted by the NUWMAK group as the basic unit in the RF transmission system. There are many advantages of the coax over the other candidates and they are listed as follows.

Advantages of the Coaxial Line

(1) There has been ample experience in the industrial use of high-power coaxial lines, such as in radio stations, and in experimental design, with proven reliability.

(2) There is no low frequency cutoff.

(3) Because the TEM mode is the dominant propagating mode, the coax is inherently broad band. Thus a coax can easily be designed for a certain operating frequency without exciting the TE and TM modes.

(4) Although the coax is a two-conductor system which complicates the design of electrical components, its generally hollow center conductor can serve as a cooling pipe through which a coolant is circulated.

It is felt that enough industrial experience has been gained that the design of vacuum seals, tuning elements and dc breaks with coaxial lines can be achieved without a major technological advancement. Finally, through the use of rigid vacuum windows and quarter-wavelength stubs, insulating spacers may not even be needed to provide support for the center conductor.

V-E-3-a. Design of the Coaxial Line

There are many types of high-power coaxial lines which are commercially available. As an example, the Prodelin Rigid "800" series[5] offers the following types:

Line Diameter (in.)	Characteristic Impedance (Ω)	Peak Power Rating (MW)
1-5/8	50	0.509
3-1/8	50	1.998
4-1/8	50	3.479
6-1/8	50	7.809
6-1/8	75	5.077
9.166	75	11.535

The peak power ratings given above are nearly constant with frequency and are based on a VSWR of unity and one atmosphere of dry air pressure at sea level and 50°C ambient temperature. Higher peak power ratings can be achieved by simply pressurizing with air or other gases having a dielectric strength greater than air. Sulphur hexafluoride, SF_6, with a dielectric strength twice that of air, is a commonly accepted choice. As an illustration, the curves[5] in Fig. V-E-2 show an increase in peak power ratings as a function of absolute pressure both in air and in SF_6. Usually if the cooling of both the inner and outer conductors is efficient, the coax can operate close to the peak rated power, especially when the RF pulse is short.

In coax design, there are a few basic equations which need to be considered. A simple cross-sectional view of a typical coaxial line is shown in Fig. V-E-3, together with the important design parameters. For a TEM mode, the field components are given by[6]:

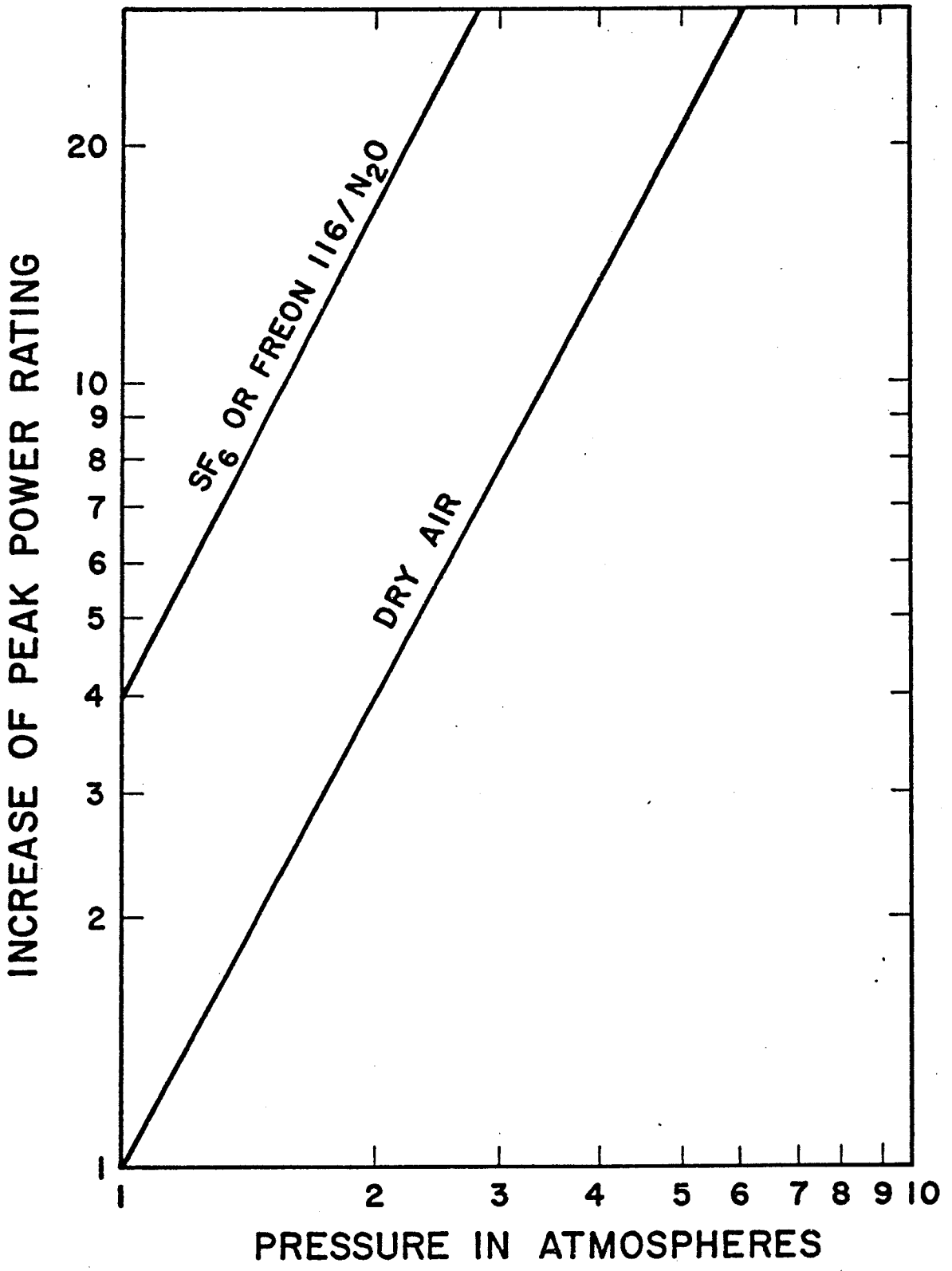
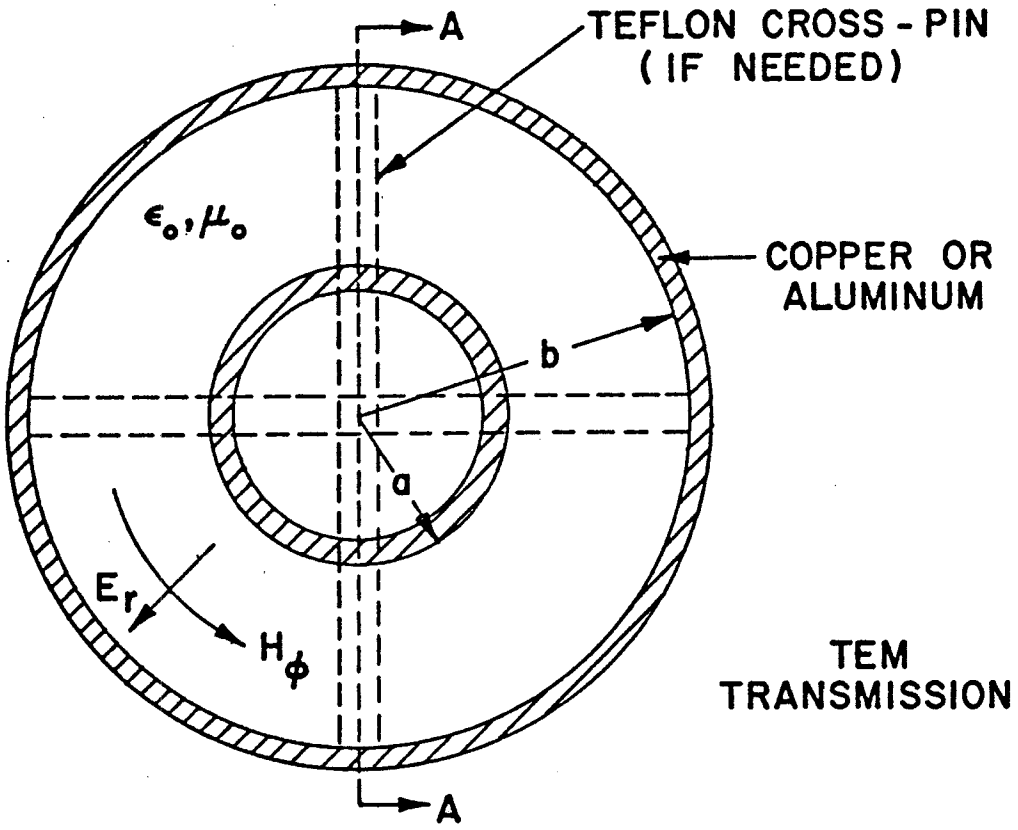
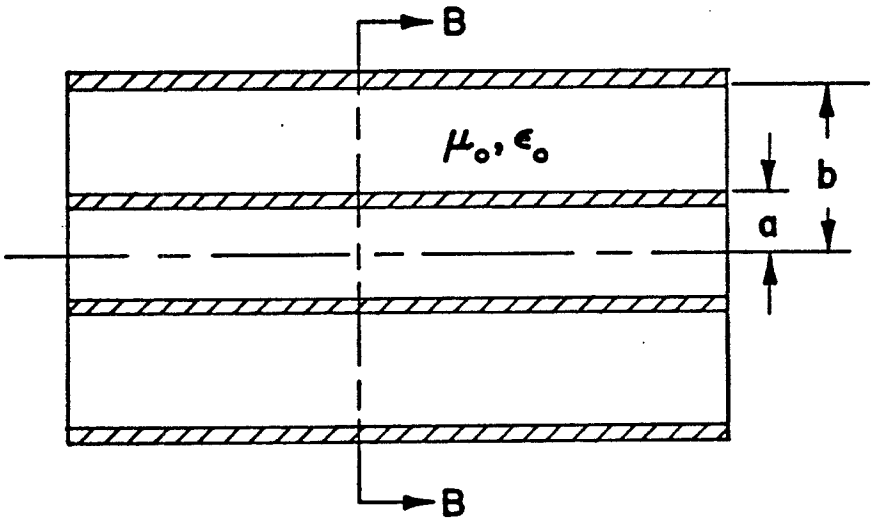


Fig. V-E-2 Coax peak power ratings as a function of pressure and gas type. (Reproduced from Ref. 5).

a = OUTER RADIUS OF INNER CONDUCTOR
b = INNER RADIUS OF OUTER CONDUCTOR



CROSS-SECTIONAL VIEW B-B



CUTOUT SIDE-VIEW A-A

Fig. V-E-3 A typical coaxial line.

$$\vec{E} = \hat{r}\, E_o \left(\frac{a}{r}\right) e^{ik_o z} \qquad (1a)$$

$$\vec{H} = -\hat{\phi}\, \frac{E_o}{Z_o} \left(\frac{a}{r}\right) e^{ik_o z} \qquad (1b)$$

with the characteristic impedance

$$Z_o = \frac{1}{2\pi} \left(\frac{\mu_o}{\varepsilon}\right)^{1/2} \ln\left(\frac{b}{a}\right) \quad \text{(ohms)} \qquad (1c)$$

$$\text{and wave number } k_o = \omega\sqrt{\mu_o \varepsilon} \qquad (1d)$$

The total transmitted power is given by

$$P = \frac{E_o^{\,2}}{2Z_o} \left[a \ln\left(\frac{b}{a}\right)\right]^2 \quad \text{(watts)} \qquad (2)$$

and the attenuation constant α_w due to dissipation on the conductor surfaces is

$$\alpha_w = R_s \left(\frac{\varepsilon}{\mu_o}\right)^{1/2} \frac{(1 + a/b)}{a \ln (b/a)} \quad \text{(nepers/m)} \qquad (3)$$

with the surface resistance $R_s = (\omega\mu_o\rho/2)^{1/2}$ (Ω-m.), where ρ (Ω-m) is the resistivity of the conductor material. Copper and aluminum are the most commonly used conductor materials in commercially available coax lines. If one substitutes the dielectric strength of air divided by a safety factor (usually 2-3) for E_o in Eq. (2), one obtains the peak power rating of the coax at one atmosphere of dry air and 50°C ambient temperature. The dielectric strength of air is listed at 30 kV/cm.

It should also be noted that ρ, the metal resistivity, and hence α_w, are very sensitive to the temperature changes of the conductor.

In Fig. V-E-4, correction curves showing an increase in attenuation due to a rise in the inner conductor temperature are depicted[5].

Should support for the center conductor be needed, teflon or other ceramic cross-pins at intervals in the axial distance can be used. These pins can be designed and spaced appropriately along the axis to provide minimum wave reflection.

There are some design constraints on the efficiency of RF transmission in coax lines which need to be taken into account. For an air-insulated coax with a fixed size, minimum loss occurs at Z_0 = 73 Ω (b/a = 3.6) while maximum power handling capacity can be achieved at Z_0 = 30 Ω (b/a = 1.65). The commonly found line impedance of 50 Ω represents a compromise between the maximum power and minimum loss conditions.

One of the major concerns in designing a coax in a reactor environment is the heavy dose of radiation and neutron outflux it encounters for the portion in direct line of sight of the plasma. To date, there is little available experimental data on the effect of intense radiation on the performance of a coaxial line. The general consensus is that it enhances the possibility of breakdown in the coax. Therefore a safe margin will have to be established between the operating parameters and the maximum power rating in design considerations. The coax will be pressurized with static SF_6 to a pressure of one atmosphere, which will increase the maximum rated power by four fold (see Fig. V-E-2). However, to avoid chemical breakdown of the gas by neutron bombardment, the vacuum seal is located outside the reactor shield while coax bends near the first wall are desirable for reducing the number of energetic neutrons hitting the window.

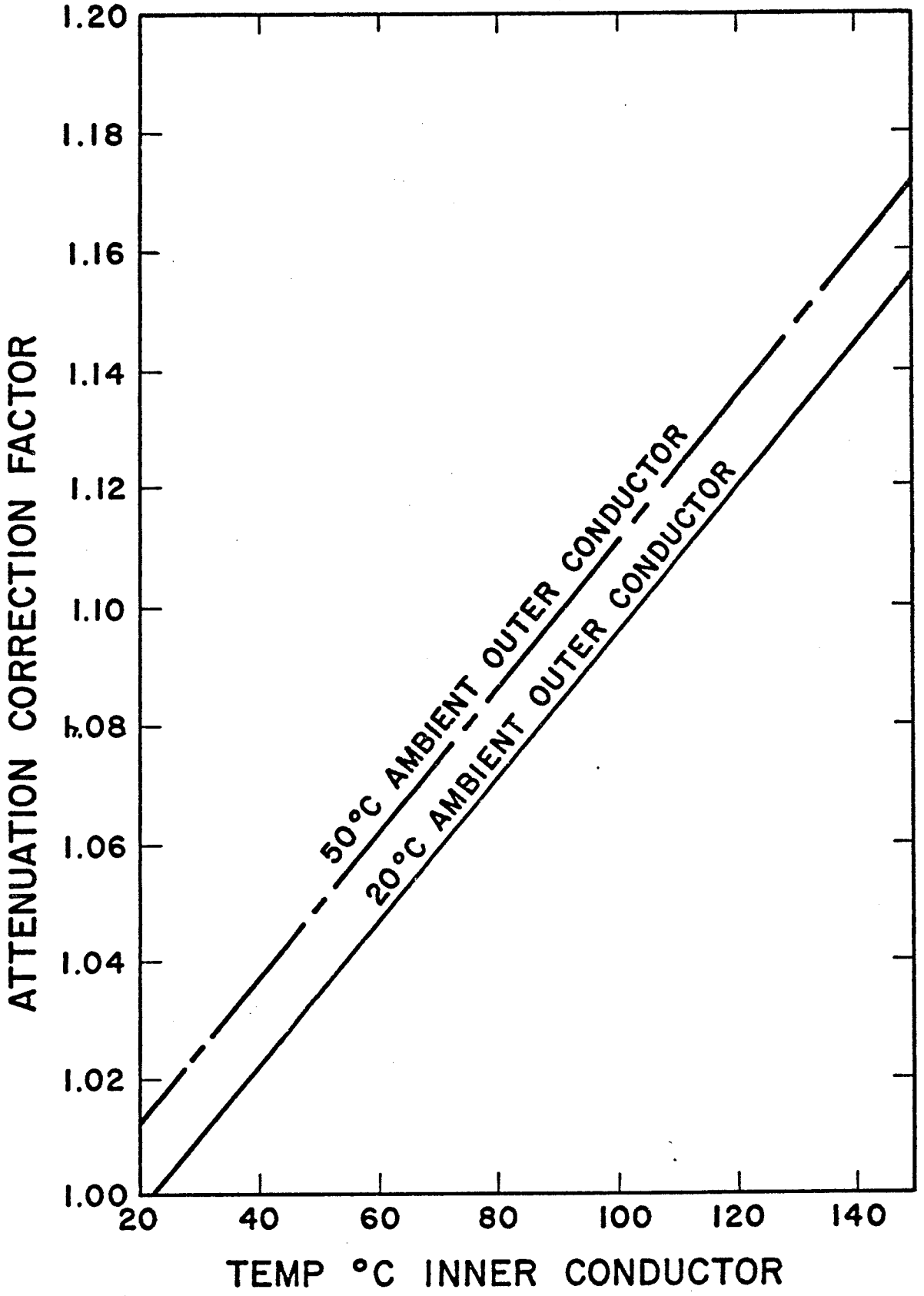


Fig. V-E-4 Attenuation correction factor vs. temperature for coax. (Reproduced from Ref. 5).

Such a configuration will leave half of the entire coaxial line evacuated and reduce considerably the burden of the cryopumps if a gas-puffing scheme is used to refuel the plasma.

Since none of the commercially available coaxial lines have a power rating as high as 20 MW, a super-power coaxial transmission line needs to be deployed. Preliminary calculations indicate that in the ICRF the resistive losses will only be 1-2% of the total power over a length of 10 meters and sufficient cooling of the conductors will be achieved to permit operation close to the peak rated power. In this respect, a 30 Ω line looks particularly attractive. To maintain a safe operating condition, a conservative value of 12 in. is chosen as the outer diameter of the outer conductor. Assuming air insulation, the following parameters are obtained:

12" - 30 ohm Coaxial Transmission Line Characteristics

Material	Copper (vanadium + 5% Ti)
Insulator	Air
Outer conductor	12.000" O.D. x 11.800" I.D.
Inner conductor	7.152" O.D. x 6.952" I.D.
Characteristic Impedance	30 ohms
Peak power rating (safety factor = 3)	35.5 MW
E_0 (r=a) at 20 MW	7.6 kV/cm
Attenuation constant α_w (50°C Ambient temp., 150°C inner cond.)	6.16×10^{-4} np./m.
Percentage power loss/10 m.	1.23%
Insulator supports (if needed)	Teflon cross-pins, spacing approx. $\lambda_0/2$, $\lambda_0 = c/f$ (At f=92 MHz., $\lambda_0/2 \cong 1.5$ m.)

In a reactor environment, lower energy ions and neutrals tend to deteriorate the copper surface over a long period of time, resulting in

higher resistivity and power loss. Therefore, the part of the coax which is exposed directly to radiation near the coupler feed point should be made of a vanadium + 5% titanium alloy, which can withstand high radiation and neutron wall loadings in a reactor environment[7].

V-E-3-b. Design of the Vacuum Window

As mentioned earlier, a pressurized coaxial line is used to alleviate the possibility of arcing over part of the transmission system. For this reason, a coaxial vacuum window is needed to seal off the pressurized portion of the line from the evacuated part.

First, the theoretical aspect of vacuum window design[6] is briefly reviewed. The cut-out side view of a typical coaxial window is shown in Fig. V-E-5. This window is assumed to be made of a ceramic material of dielectric constant $\varepsilon_r > 1$. Let P_i, P_r and P_t be the incident, reflected and transmitted power respectively in the axial direction. Assuming a lossless dielectric, the following power ratios are obtained:

$$|R|^2 = \frac{P_r}{P_i} = \frac{(\varepsilon_r - 1)^2}{(1+\varepsilon_r)^2 + 4\,\varepsilon_r \cot\beta'\ell} \tag{4a}$$

$$|T|^2 = \frac{P_t}{P_i} = \frac{4\,\varepsilon_r \csc^2 \beta'\ell}{(1+\varepsilon_r)^2 + 4\,\varepsilon_r \cot\beta'\ell} \tag{4b}$$

where $\beta' = \omega\sqrt{\varepsilon_r\varepsilon_o\mu_o}$ is the wave number in the dielectric medium and ℓ the axial length of the window. Note that in accordance with the lossless assumption, $|R|^2 + |T|^2 = 1$. It is immediately clear from Eqs. (4) that for minimum reflection, the condition

$$\ell = n\,\frac{\lambda'}{2}\,, \quad n = 0, 1, 2, 3, \ldots \tag{5}$$

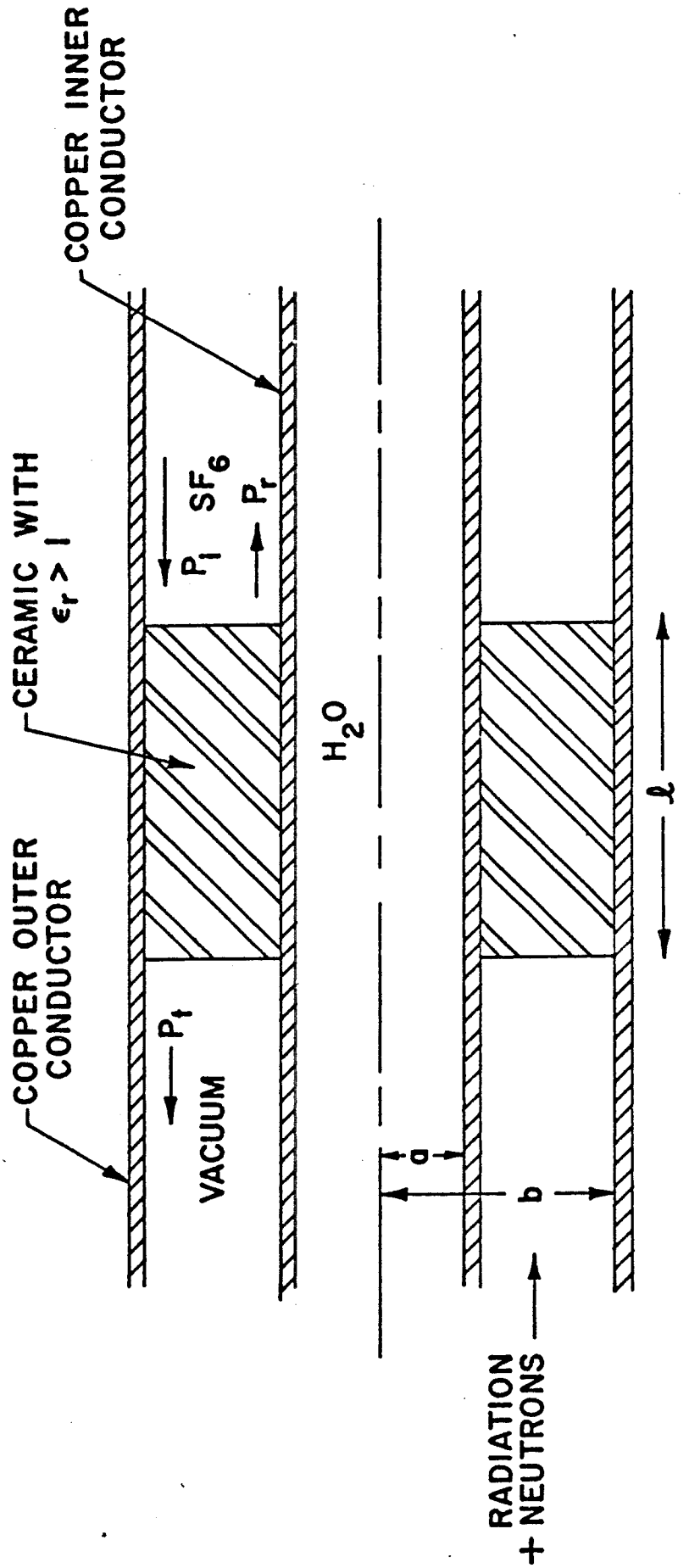


Fig. V-E-5 Coaxial vacuum window configuration (side-view).

has to be met, where $\lambda' = 2\pi/\beta'$. As an illustration, the power reflection coefficient $|R|^2$ is plotted as a function of $\beta'\ell$ for $0 < \beta'\ell < \pi$ in Fig. 6, for $\varepsilon_r = 6.5$. It is clear from this curve that there are two practical configurations for the vacuum window, namely, (i) the thin window ($\ell << \lambda'$) and (ii) the half-wave window ($\ell = \lambda'/2$). A third useful configuration consists of two thin windows spaced $\lambda_o/2$ apart, where $\lambda_o = c/f$ with f being the wave frequency and c the speed of light in vacuum.

For the thin window structure, it can be seen from Fig. V-E-6 that the window must be sufficiently short or wave reflection may become excessive. As an example, for a ceramic with $\varepsilon_r = 6.5$, a 5 cm. long window gives rise to a reflection coefficient of 0.065, which represents a 1.3 MW reflected power in a system carrying 20 MW of power. In addition, such a thin window may be insufficient for rigid support of the center conductor or may become brittle and crack after long periods of exposure to heavy doses of radiation.

The double-window configuration possesses some merits from an engineering point of view. The space between the windows can be used for cooling purposes but this is not essential if a ceramic with a high thermal conductivity is used. The windows tend to compensate for changes in their dielectric properties due to radiation damage so that the transmission coefficient remains stable. However, a standing wave is set up between the windows with a VSWR equal to

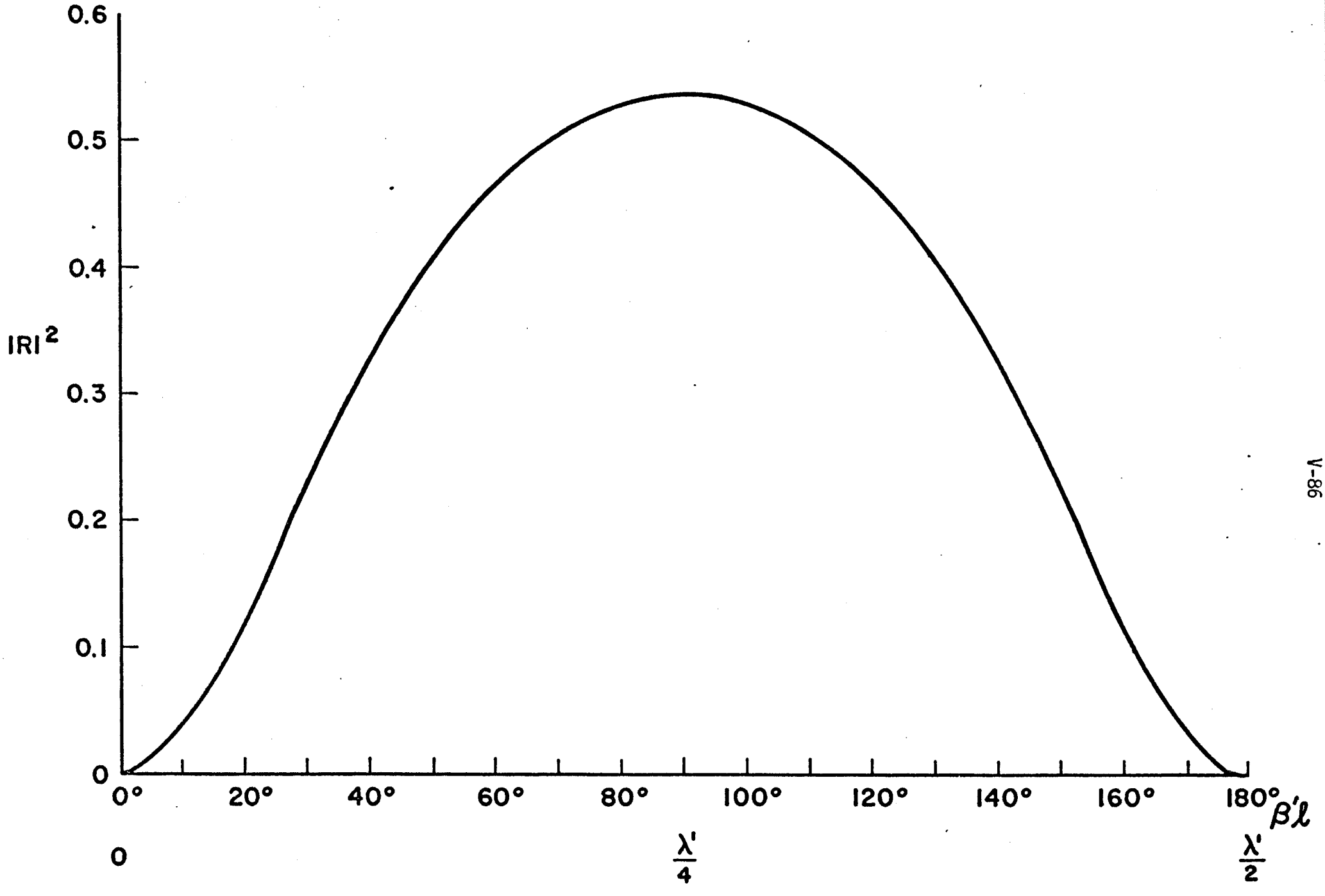


Fig. V-E-6 Power reflection coefficient as a function of window length. ε_r = 6.5 for BeO.

$$\text{VSWR} = \frac{1 + |\rho|}{1 - |\rho|} \quad \text{where } \rho = \frac{\sqrt{\varepsilon_r} - 1}{\sqrt{\varepsilon_r} + 1}$$

For $\varepsilon_r = 6.5$, $\rho = 0.44$, VSWR = 2.57 and the peak electric field inside the window is increased by a factor of $1 + |\rho|$. Thus the peak power rating of the coaxial line has to be reduced by a factor of $(1 + |\rho|)^{-2}$, which is equal to 0.48 for $\varepsilon_r = 6.5$.

Based on the above arguments, the half-wave window configuration appears to be the best choice to fulfill its intended function. Because of the bulk size of this window, a ceramic with an exceptionally high thermal conductivity has to be used, as cooling is only provided by running water along the conductors of the coax. From the RF point of view, the ideal location of the vacuum seal in a pressurized line is at the first wall of the reactor where the antenna is generally positioned. However, the window will be exposed directly to a tremendous thermal energy throughput in the form of neutron and radiation flux. To date, tests[8] are still being carried out to find a window material which can absorb the kind of loading typical in reactor first walls without long-term deleterious effects. The most practical solution is to place the window outside the reactor shield and have bends in the coax near the first wall to reduce the number of energetic neutrons which may reach the window. In this configuration, the radiation loading at the windows is drastically reduced so that commonly used ceramics such as beryllium oxide (BeO) and aluminum oxide (Al_2O_3) can be considered.

A ceramic suitable for window construction in a reactor RF heating system should possess the following basic features:

(i) Highly resistant to radiation and neutron bombardment

(ii) High thermal conductivity

(iii) High specific heat

(iv) Low coefficient of thermal expansion

(v) Stable electrical properties under long periods of exposure to radiation and thermal stresses

(vi) Low loss tangent

(vii) High surface dielectric strength

Under a mild radiation environment, beryllium oxide is the most ideal ceramic to use, primarily because of its very high thermal conductivity and specific heat. However, more extensive tests should be performed to insure the stability of this material subject to repetitive pulses of 20 MW RF power over a long period of time. The extent of swelling under tremendous thermal stresses and interface effects in bonded ceramic-copper coax windows should also be investigated. For comparison, the properties of a few commonly used ceramics are listed in the following table:[9]

	Sintered Beryllia	Sintered Alumina	Sintered Yttria
Composition	99.8% BeO	99.8% Al_2O_3	99.8% Y_2O_3
Porosity (vol. %)	3-7	3-7	2-5
Fusion Temperature (°C)	2570	2030	2410
Max. Normal Use Temperature (°C)	1900	1900	2000
Density (gm./c.c.)	3.03	3.97	4.50
Specific Heat (cal./gm./°C)	0.50	0.26	0.13

	Sintered Beryllia	Sintered Alumina	Sintered Yttria
Linear Expansion (10^{-6} in./in./°C.) (20-1000°C.)	8.9	8.6	9.3
Thermal Conductivity (cal./sec./c°/cm)	0.500(100°C) 0.046(1000°C)	0.069(100°C.) 0.014(1000°C)	0.02(100°C) --------
Modulus of Rupture (psi)	20,000(100°C) 10,000(1000°C)	30,000(100°C) 22,000(1000°C)	-------- --------
Modulus of Elasticity (10^6 psi)	45	53	--------
Thermal Stress Resistance	Excellent	Good	Fair-Poor
Electrical Resistivity (1 MHz) (ohm-cm.)	10^{16}(23°C.) 10^9(500°C.)	$5x10^{13}$(23°C) 10^{13}(500°C.)	-------- --------
Dielectric (1 MHz.) Constant (100 MHz.)	6.7 6.5	9.6 8.0	-------- --------
Loss tangent (100 MHz.)	$7x10^{-4}$	10^{-4}	--------

From the table, $\varepsilon_r = 6.5$ for beryllium oxide at 100 MHz and the required length ℓ of the coax window is 64 cm at 92 MHz. The loss tangent of a dielectric is defined as

$$\tan\delta = \frac{\sigma}{\omega\varepsilon}$$

where σ is the conductivity under the operating conditions. For a loss tangent of 0.0007, $\sigma \simeq \varepsilon_r\varepsilon_o\ \omega \tan\delta = 2.91 \times 10^{-6}$ mhos/m. Then, with Eq. (1a), the radial profile of power dissipation in the window is found to be

$$P_{diss} = \sigma E^2 = 1.64(\frac{a}{r})^2 \text{ watts /cm}^3 \qquad (7)$$

which is shown in Fig. V-E-7, so that a substantial portion of the heat

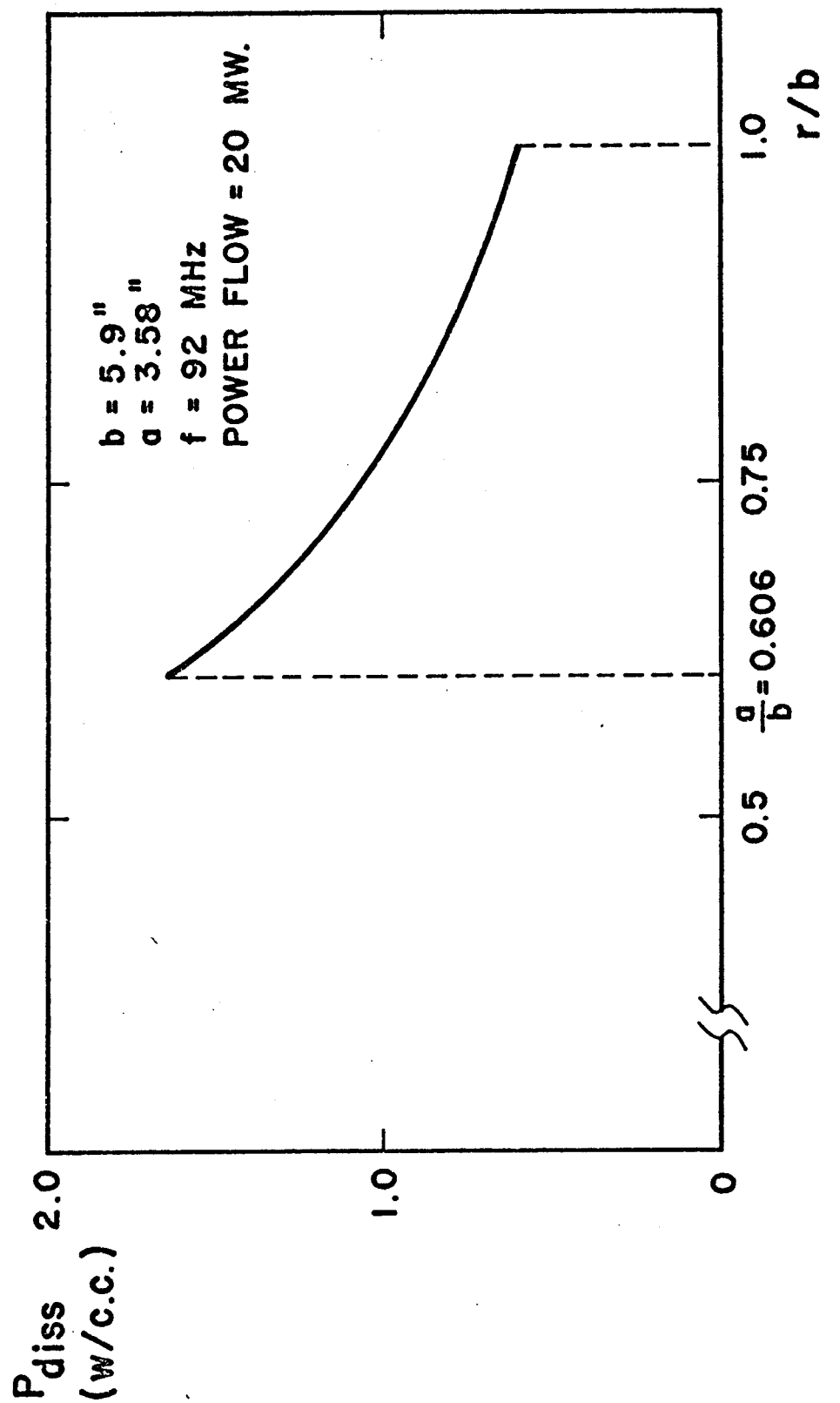


Fig. V-E-7 Radial profile of RF dissipation in coaxial BeO windows.

is generated near the inner conductor surface. The total power dissipated over the entire volume of the BeO window is then

$$P_{total} = 2\pi\ell\ \sigma E_o^2\ a^2 \ell n(\frac{b}{a}) = 28.15\ kW \qquad (8)$$

This corresponds to 84.5 kJ of heat deposition over a period of 3 seconds for each burn cycle. For a specific heat of 1255J/kg °K at 100°C, a conservative estimate of a one degree centigrade temperature rise is predicted, if heat conduction is neglected.

In Fig. V-E-8 is shown the minor cross-sectional view of the basic orientation of the coax and the wave coupler with respect to the reactor blanket and the shield. This particular configuration indicates that the coax window is located between the blanket and the shield on the outside of the toroidal chamber. At the coax feed point to the coupler, the wall loading is at a maximum of 5 MW/m^2, which corresponds to a 16.2 $watts/cm^3$ absorption at the first wall. At the location of the window, the volume dissipation is reduced by several orders of magnitude to about 1.5×10^{-3} $watts/cm^3$ which corresponds to a total of 9.8 kJ over a burn time of 225 seconds. Compared to the number for RF power, an approximate 0.1 degree centigrade rise in window temperature is predicted for each cycle without cooling.

Combining the dissipative effects of RF and radiation, a temperature rise of 1°C is predicted over one duty cycle in the vacuum window made of BeO. However, this number is generally conservative and should drop significantly when thermal conduction is taken into account. Nevertheless, it is important that an efficient cooling system be devised to stabilize the temperature, and hence the electrical and mechanical properties, of the vacuum window.

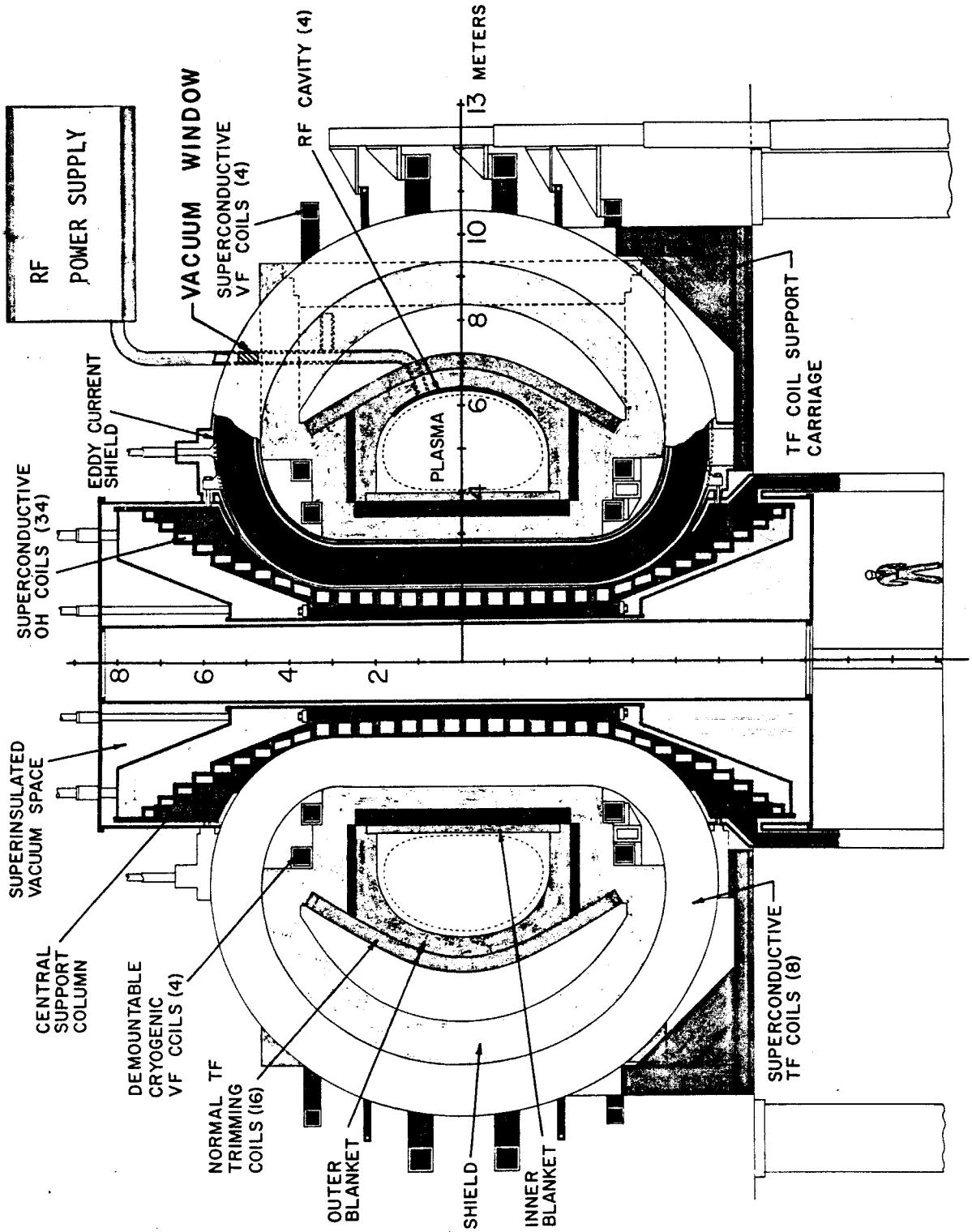


Fig. V-E-8 Cross-sectional view of NUWMAK.

Preliminary calculations[10] also show that the RF power imposes a radial temperature gradient of less than 1°C across the window, while the corresponding value for radiation dissipation is much less than 1/3°C. Thus the stresses exerted by these thermal gradients are expected to be negligible over a reasonable period of time.

From Eqs. (4), it is evident that once ℓ is fixed, the performance of the window is very sensitive to changes in ε_r due to radiation damage. At the window position in NUWMAK, a neutron flux of 4.2×10^9 n/cm^2/sec is anticipated, which corresponds to a dosage (n.v.t.) of 1.3×10^{17} cm^{-2} over a period of one year[11]. Therefore an experiment to test the stability of the electrical parameters of beryllia under such a dosage should be undertaken to consolidate the above window design. If the change in ε_r is tolerable, the window may still have to be replaced once every year together with the first wall blanket. In the case of a highly unstable dielectric constant, additional shielding should be used or the double-window configuration may have to be considered.

V-E-3-c. The Voltage Breakdown Problem

In designing a high-power RF system, it is essential to provide sufficient insulation to the system to prevent breakdown which may disrupt operation and inflict severe damage to equipment. Design problems related to high-voltage breakdown in the transmission system are considered for three separate regions, namely, the pressurized line, the evacuated line, and the vacuum seal.

V-E-3-c-i. The Pressurized Line

For the most part, the coaxial transmission line is insulated with SF_6 at a pressure of one atmosphere. Within this pressure range, the motion of an electron is primarily dominated by collisions with the gas molecules. In the presence of a continuous electric field, the electrons maintain a constant drift velocity given by[12]

$$\vec{v} = \mu \vec{E} \tag{9}$$

where μ is the electron mobility given by $\mu \simeq \frac{e}{m_e \nu}$, with ν being the collision frequency. Since the velocity is in phase with the force, the electron absorbs a mean power[12]

$$\overline{P}_e = \overline{\nu \mu E} = \frac{e^2 E_o^2}{2 m_e \nu} \tag{10}$$

From this equation, one observes that the electron gas behaves essentially as a resistive medium. An electron-molecule collision may result in ionization of the molecule, producing more charged particles. If the process is allowed to continue, eventually a large number of charged particles will be accumulated. In the presence of a large electric field, an avalanche electron current is triggered, resulting in breakdown.

Free electrons which trigger the avalanche current can be produced by any one of the following processes:[13]

(i) Photoelectric emission in the gas or from the metallic conductors, caused by impinging gamma rays from a radioactive source or bremsstrahlung radiation.

(ii) Thermionic emission from the conductor surface.

(iii) Secondary emission from the walls by electron or heavy ion impact.

(iv) Field emission from the wall due to an electric field normal to the surface, resulting in lowering of the work function.

(v) Emission by neutral atom or alpha-particle impact.

To prevent breakdown in a pressurized line, the most effective method is to use a gas with a high ionization energy or dielectric strength, since ionization is the main cause for such a process. Sulfur hexafluoride (SF_6), which fulfills the above requirements and is commonly used in industry, is apparently the ideal choice under the present conditions.

V-E-3-c-ii. The Evacuated Line

The prevention of breakdown in the evacuated portion of the coax presents a completely different problem from the one in the previous section. Two aspects of this problem need to be clarified. The first one is whether or not this region can be treated as a virtual vacuum as far as breakdown is concerned. The second one concerns the validity of dc breakdown theory under the prescribed conditions.

The NUWMAK reactor employs a gas puffing scheme to re-fuel the plasma from the low-field side of the chamber. Therefore, the scrape-off region and the vicinity of the coax feed to the coupler contains a weakly ionized plasma. It is reasonable to assume a 10% ionized gas, with $T_{neut.} \simeq 5$ eV and $T_i = T_e = 30$ eV, with a density of 10^{10} cm^{-3}. The kinetic pressure of the gas is 1.26×10^{-4} Torr. Apparently, this number is a little high since the presence of pumping ports in each blanket segment has been neglected.

The electron mean free path is calculated by

$$\ell_{mfp} = \frac{\langle v_e \rangle}{\nu} \qquad (11)$$

where $\langle v_e \rangle$ is the mean thermal speed and ν is the collision frequency. By including ν_{ei}, ν_{ee} and ν_{en} in ν, ℓ_{mfp} is found to be of the order of 10^5 m , while the interelectrode distance d is 6 cm. Thus

$$\ell_{mfp} >> d \tag{12}$$

which implies that practically no collision occurs during an electron transit between the electrodes. Thus one can treat the coax as a "vacuum"-insulated line and conclude that only emissions from the electrodes play a part in causing a breakdown.

When the RF frequency is sufficiently high such that the wave period 1/f is short compared to the transit time τ of an electron between electrodes, i.e., $f\tau \geq 1$ the dc breakdown theory is inadequate. For the coax system, $\tau = d/\langle v_e \rangle$, f = 92 MHz so that $f\tau \gtrsim 1$ implies $T_e \leq 142$ eV, while the estimated T_e is only 30 eV. Thus ac breakdown theory must be used for the evacuated coax.

For simplicity, consider two parallel electrode plates separated by a distance d and an electric field normal to the plates given by $E = E_a \sin(\omega t + \theta_o)$. Then the collisionless equation of motion for a free electron is[12]

$$\ddot{x} = -\frac{e}{m_e} E_a \sin(\omega t + \theta_o) \tag{14}$$

with $\dot{x} = v_o$ and $x = x_o$ at $t = 0$. The solution to Eq. (14) is

$$\dot{x} = v_o - \frac{eE_a}{m_e \omega} [\cos\theta_o - \cos(\omega t + \theta_o)] \tag{15a}$$

$$x = x_o + (v_o - \frac{eE_a}{m_e \omega} \cos\theta_o)t - \frac{eE_a}{m_e \omega^2} [\sin\theta_o - \sin(\omega t + \theta_o)] \tag{15b}$$

Note that unlike the collisional case considered in the pressurized line, the electron velocity and the force acting on it are in quadrature, resulting in no energy absorption from the wave.

In the absence of collisions with gas molecules, multiplication of electrons is dominated by secondary-electron emission from the walls. Breakdown is then possible through a secondary-electron resonance or "multipactor" effect[14]. For a certain range of E_a and θ_o, the secondary-emission time phase angle, it is possible for electrons to travel from one electrode to the other in approximately one-half period (1/2f) of the wave field. When these "primary" electrons strike an electrode, they produce secondary electrons which are emitted in a reversed field and accelerated to the opposite electrode in half a cycle of the field. If the secondary-emission coefficient is greater than unity, repetition of this process will accumulate a large number of these oscillating electrons, eventually triggering an avalanche breakdown current.

Now, by setting $t = \pi/\omega$ in Eqns. (15) and letting $v_a = \dot{x}(t=\pi/\omega)$ and $d = x(t=\pi/\omega)$, where v_a is the arrival velocity of the electron, one obtains the following criterion for multipactor breakdown[14],

$$E_a = \frac{\omega^2 d}{(e/m_e)\,\Phi} \tag{16a}$$

where $\Phi = \frac{k+1}{k-1}\,\pi\cos\theta_o + 2\sin\theta_o, \qquad -60° < \theta_o < 18°$ (16b)

with $k = v_a/v_o$. The limits of θ_o are determined experimentally[14]. From Eqns. (16), it is evident that for fixed ω and d, there is a range of E_a values within which multipactor breakdown may take place.

Minimum E_a is reached when Φ is a maximum, with

$$(\theta_o)_{min} = \tan^{-1} \left(\frac{k - 1}{k + 1} \cdot \frac{2}{\pi}\right) \tag{17}$$

which gives k=3 for $(\theta_o)_{min} = 18°$. There is also a low end cutoff frequency f_{co}, below which it is impossible to trigger a multipactor breakdown. This cutoff frequency f_{co} can be roughly determined by the empirical relation

$$f_{co} = C_b/d \tag{18}$$

where $C_b \approx 79$ MHz-cm is found from experiments[14].

The multipactor breakdown analysis for a coaxial transmission line is relatively complicated due to the radially varying electric field. However, a good qualitative picture can be deduced if one assumes E_a to be the averaged electric field across the two conductors. This gives the relation

$$E_a = \frac{E_o a}{b - a} \ln \left(\frac{b}{a}\right) \tag{19}$$

which results in $E_a = 0.77\ E_o$ for the designed coax. The multipactor breakdown regime for the evacuated coax is plotted in Fig. V-E-9. At f = 92 MHz, breakdown occurs for 0.175 kV/cm $< E_a <$ 0.8 kV/cm which translates to the range of power 0.019 MW < P < 0.385 MW. It is found[14] that if the rise time of the RF pulse is sufficiently short that $\Delta t < \frac{1}{2f}$, where Δt is the time interval for the line power to pass through the breakdown region and $\frac{1}{2f}$ corresponds to the electron transit time, multipactor breakdown may not be initiated. For f = 92 MHz, Δt must be less than 5.4 nsec., which is very unlikely to be achieved

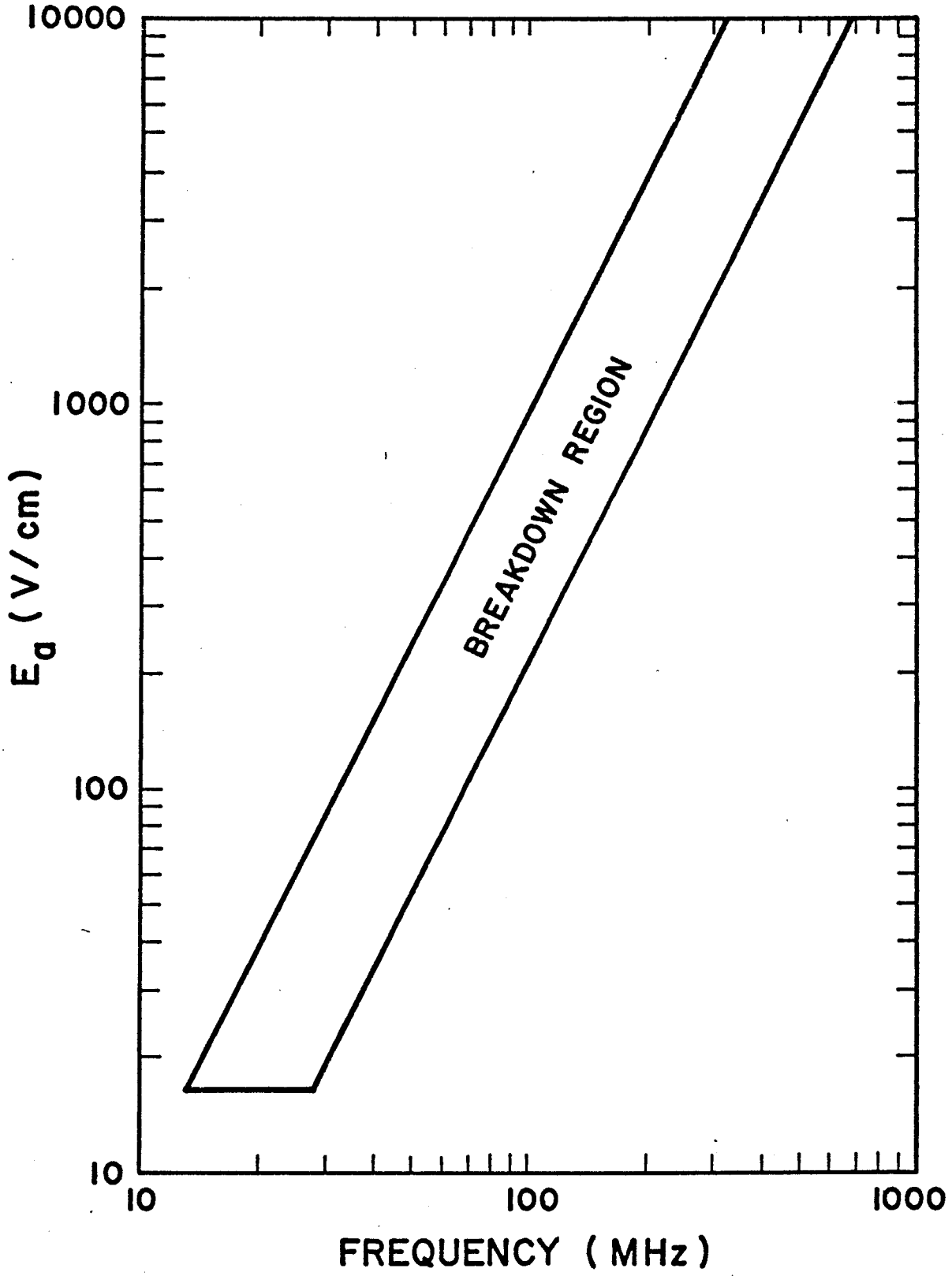


Fig. V-E-9 Fundamental multipactor breakdown region; plate separation = 6 cm and $-60° < \theta_o < 18°$, k = 3.

due to the presence of shunt regulators in the generator. Thus some method to suppress this breakdown mechanism must be used. There are two commonly suggested techniques[1]:

(i) A thin coating (thickness < skin depth) of metal with a low secondary emission coefficient such as titanium on the conductor surfaces.

(ii) Surface grooving to introduce electric field inhomogeneities near the conductor surface.

It should be noted that the above multipactor analysis for the coax is only approximate. Clearly a theory involving the electric field variation in a cylindrical geometry should be developed to correctly determine the breakdown region. The effect of the presence of a magnetostatic field inside the coax should also be considered. Tests on the quenching mechanisms should also be conducted to determine their effectiveness.

V-E-3-c-iii. The Vacuum Window

Because of the difference in the dielectric constants of vacuum and BeO a standing wave is established inside the window. For ε_r = 6.5, the reflection coefficient is ρ = 0.44 and the VSWR = 2.57. Thus the field at the inner conductor surface (r=a) varies between 2.9 kV/cm and 7.5 kV/cm inside the window. The dielectric strength of BeO is listed as 94 kV/cm so that breakdown within the window is very unlikely. Surface breakdowns, especially those caused by surface multipactor effect, may cause trouble, but they can generally be suppressed by the methods mentioned in the previous section.

V-E-4. The Coupling System

The main goal of the RF coupling system design is to construct a launching antenna which couples wave energy efficiently to the plasma and is structurally sound to survive in a radiation environment found in NUWMAK. Several aspects of antenna design need to be considered.

(1) The antenna must be well matched to a vacuum-bounded toroidal plasma so that undesirable wave reflection at the first wall is minimized. This can generally be achieved by carefully choosing a wave mode at an appropriate frequency and wave number, or by the use of an impedance matching network. However, the matching circuit tends to create a large amount of reactive power between the tuner and the antenna. Thus the impedance matching concept is not highly recommended in this system.

(2) Due to the high power requirement, special emphasis should be addressed to the high-voltage arcing problem in the antenna structure.

(3) The coupler should be compact in size and positioned close to the first wall to avoid obstruction of the flow of plasma in the torus.

(4) The structure should be constructed of a radiation resistant material with a stable electrical conductivity so that losses can be kept low.

(5) An efficient cooling system should be developed to stabilize the temperature of the launcher during the burn cycle.

(6) The wave absorption mechanism should be properly identified to determine the wave mode to be launched. The spectral requirement for the wave should also be considered from the point of view of launching and absorption efficiencies.

In the NUWMAK reactor, the fast magnetosonic mode at the second harmonic deuterium cyclotron frequency (~ 92 MHz) is to be launched. This wave is approximately transverse electric (TE) with respect to the toroidal axis and is right-hand elliptically polarized. It can be coupled to the plasma through the poloidal electric field (E_ϕ) or the toroidal wave magnetic field (B_z). Waveguide[4] and balanced TEM line[1] coupling to the plasma in the ICRF have been previously investigated. In these configurations, the wide side of the line is aligned parallel to the toroidal axis so that the electric field points in the poloidal direction at the aperture. Up to this date, poloidal current loops, which couple through the B_z-field, have been employed successfully in RF experiments in present day tokamaks, such as ST, ATC and TFR.

Two coupler designs have been proposed for NUWMAK, one using a cavity-backed aperture antenna and the other a current loop. The latter scheme has been proven successful in smaller machines but may be susceptible to radiation damage in reactors, while the former has advantages mentioned in Sec. V-D. The cavity-backed aperture coupler needs extensive testing to evaluate its performance. It is felt that both plans should be developed in parallel until experimental results in the next generation of tokamaks are available to determine the final choice.

V-E-4-a. The Cavity-Backed Aperture Antenna

The conceptual design of this antenna consists of a wedge coaxial cavity flush-mounted on the first wall of the torus as shown in Fig. V-E-10. The cavity is fed by a coaxial line on its outer wall, with the center conductor welded to the inner wall, forming

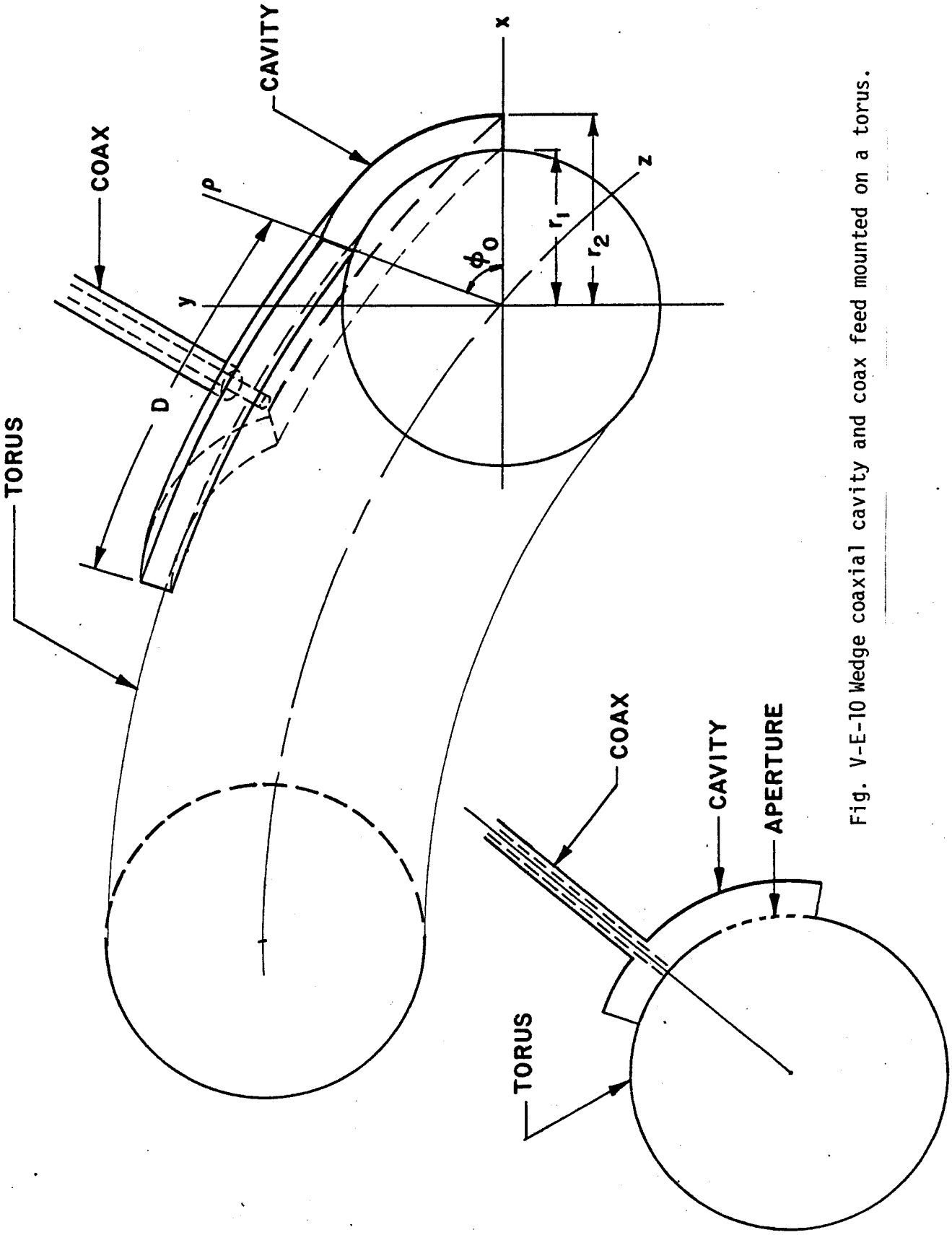


Fig. V-E-10 Wedge coaxial cavity and coax feed mounted on a torus.

a current coupling loop. On the lower side of the cavity, an array of apertures is cut out which serves as an antenna radiating wave energy into the plasma.

To determine the condition for eigenmode excitation, one has to look at the field structure inside the cavity. With reference to Fig. V-E-10, the poloidal component of the electric field E_ϕ for the $TE_{mn\ell}$ mode in the cavity is[15]

$$E_\phi^{mn\ell} = k_\rho^{n\ell} B_{mn\ell} \sin(\frac{m\pi}{D} z) \cos(n\phi) \{J_n'(k_\rho^{n\ell}\rho) + A N_n'(k_\rho^{n\ell}\rho)\} \qquad (20)$$

where m, n, ℓ are the toroidal, poloidal and radial mode numbers respectively, with $n = p\pi/\phi_o$, (p = 0, 1, 2, 3, ...) and ϕ_o the poloidal angle subtended by the cavity. In Eq. (20), $k_\rho^{n\ell}$ is the ℓ th resonant radial wave number for poloidal n, J_n' and N_n' are derivatives of Bessel functions of the first and second kind with respect to the argument and $B_{mn\ell}$ is the amplitude factor for the mode. The boundary conditions of $E_\phi^{mn\ell} = 0$ at $\rho = r_1$ and $\rho = r_2$ yield the resonant condition

$$J_n'(k_\rho^{n\ell} r_1) N_n'(k_\rho^{n\ell} r_2) - N_n'(k_\rho^{n\ell} r_1) J_n'(k_\rho^{n\ell} r_2) = 0 \qquad (21)$$

for which the dispersion equation is given by

$$(k_\rho^{n\ell})^2 = \omega^2 \mu_o \varepsilon_o - (\frac{m\pi}{D})^2 \quad . \quad m = 1, 2, 3, \ldots \qquad (22)$$

Given p, ϕ_o (and thus n), m and ℓ, and the dimensions r_1, r_2 and D, one can determine the resonant frequency for the $TE_{mn\ell}$ eigenmode by using Eqs. (21) and (22). In particular, from Eq. (22), one notes that for given ω and m, the toroidal length D has to exceed a minimum value for a propagating mode, i.e., $(k_\rho^{n\ell})^2 > 0$.

The fundamental mode of oscillation in this cavity is given by the mode numbers: m=1, p=1 ($n = \pi/\phi_o$) and ℓ=1, which is equivalent to the TE_{101} mode in a rectangular cavity. Clearly it is desirable to excite only the fundamental cavity mode in the NUWMAK RF coupling system. The primary design calls for the cavity to be mounted on the outside wall of the torus, as shown in Fig. V-E-8. In spite of the D-shaped minor cross-section, the profile of the outer first wall is well approximated by a circular arc of radius r_1 = 2.4 m. For a 10 cm radial thickness ($r_2 - r_1$ = 10 cm), Eqs. (21) and (22) are solved numerically for the fundamental mode at an operating frequency of 92 MHz. The possible toroidal and poloidal widths of the cavity are plotted in Fig. V-E-11. As a comparison, the corresponding dimensions of a rectangular cavity for the TE_{101} mode are plotted in the same figure. Note that, except for operation near cutoff which occurs at ϕ_o = 39°, the simpler rectangular cavity analysis is evidently a very good approximation to that for the wedge coaxial cavity.

For the NUWMAK RF system, the following cavity parameters are chosen:

Resonant Cavity Parameters

Radial Width	10 cm
Toroidal Width	1.85 m
Poloidal Width	3.5 m
Wall Thickness	0.2 cm
Material of construction	vanadium + 5% titanium alloy

The vanadium + 5% titanium alloy is chosen as the material of construction because vanadium maintains a high conductivity under

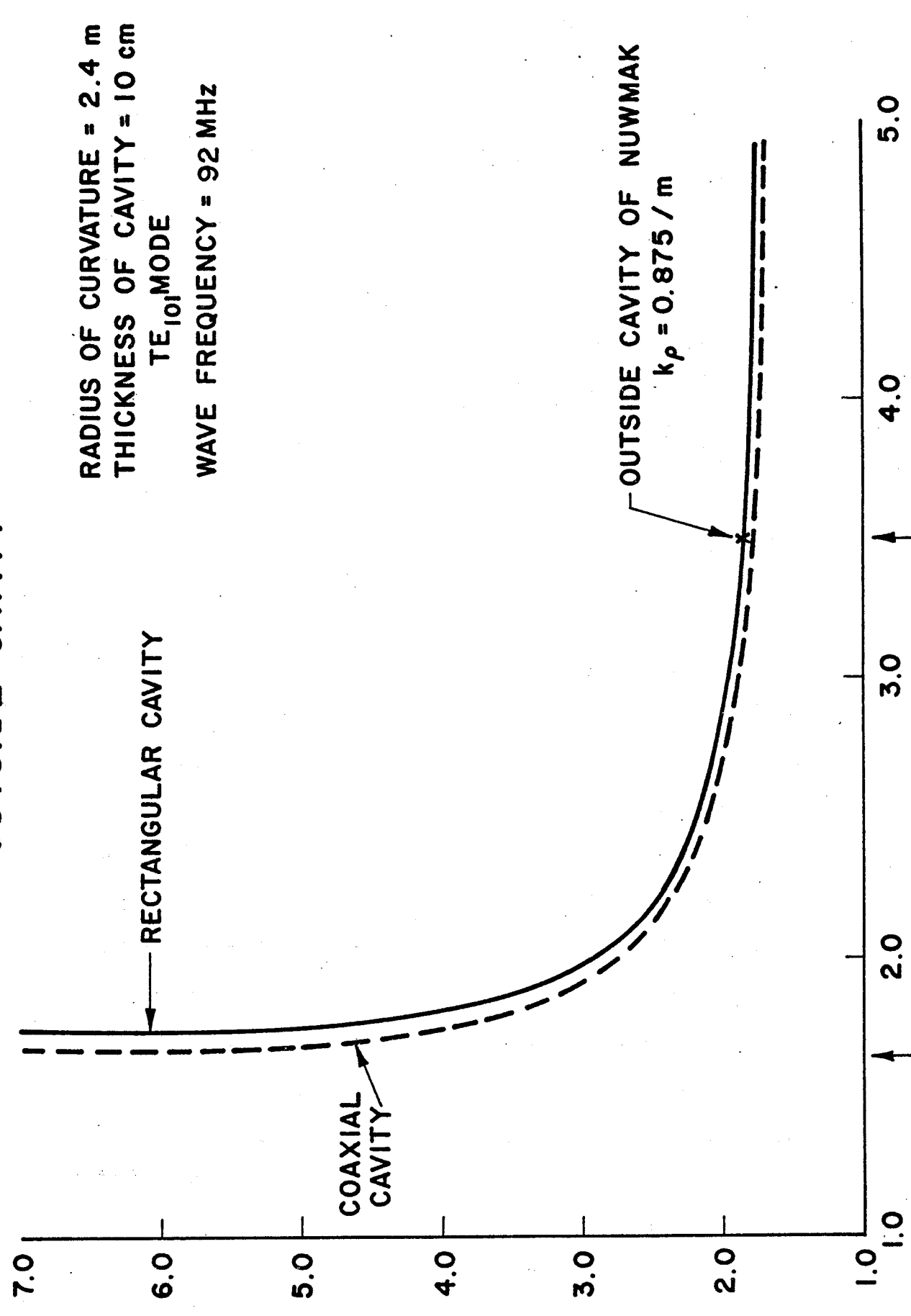


Fig. V-E-11 Exact and approximate TE_{101} resonance curves for the poloidal and toroidal dimensions of the outer cavity at 92 MHz.

severe radiation environment and titanium is present to protect the surface from excessive damage by neutrals, neutrons and radiation. Cooling pipes containing running water are installed on the inside of the inner wall to maintain the first wall temperature at 300°C. These pipes also form grooves on the surface to prevent multipactor breakdown. The toroidal and poloidal dimensions of the cavity are chosen so that each unit can be mounted on a movable blanket segment and does not interfere with the pumping port located on the lower side of the outer first wall. The cavity is also positioned so that it does not intersect with the $\omega = 2\omega_{CD} = 3\omega_{CT}$ resonance surface (Fig. V-E-8) over its poloidal extent. Catastrophic breakdown may occur due to anomalous acceleration of the ions if the cavity intersects such a resonance surface.

Preliminary design of a launching array of apertures on the cavity has been considered. Coupling of the fast wave is achieved via the toroidal wave magnetic field, which is B_z in the cavity (Fig. V-E-10). For the TE_{101} mode, B_z reverses its direction from the upper to the lower poloidal half. In order that the fields radiated from the apertures do not cancel one another far away from the wall, the array is located entirely on the lower poloidal half while the coax is fed into the upper half on the opposite wall, shown in Fig. V-E-12.

As discussed in an earlier section, a wave spectrum centered at $k_{\parallel} = k_z = 20\ m^{-1}$ is desirable if one wishes to minimize the effect of mode conversion[16] which complicates the picture of cyclotron absorption. For any array of apertures on the cavity, it seems inevitable that

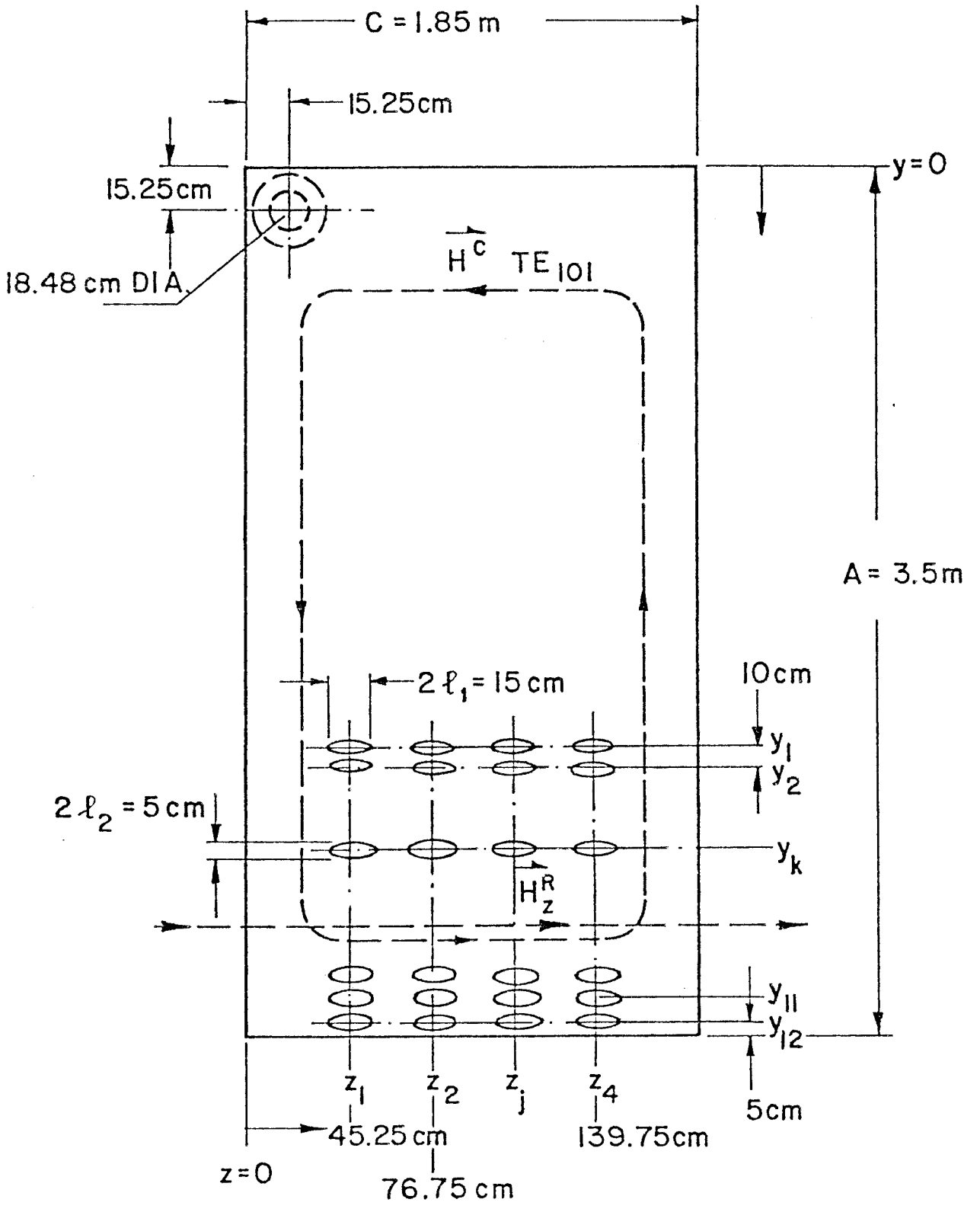


Fig. V-E-12 Aperture array on outer cavity as viewed from the major axis

some $k_{\parallel} = 0$ component is always present in the radiated field. However, a sideband centered at $k_{\parallel} = 20\ m^{-1}$ can be achieved if the apertures are spaced 31.5 cm apart toroidally, which corresponds to one toroidal wave length. In Fig. V-E-12, an array of 12 x 4 apertures is drawn as a preliminary design. The holes are elliptical in shape to achieve optimal coupling efficiency[17] and to prevent breakdown at sharp corners.

A detailed theoretical analysis should be carried out to determine the wave number $k_{\parallel}$-spectrum of the radiated field from the array of apertures shown in Fig. V-E-12.

An auxilliary coupling system using the cavity-backed aperture antenna is shown in Fig. V-E-13. In this scheme, the cavity is mounted on the inner first wall where space is extremely limited. Thus the cavity thickness is reduced to 5 cm while the other dimensions remain the same as the outer cavity. A relatively sharp bend in the cavity is needed to accommodate the structure, but the rectangular cavity approximation is still valid above cutoff. The merit of this system is that the wave is now launched from the high field side and the mode conversion heating mechanism can be utilized and is particularly efficient for the $k_{\parallel} = 0$ wave component. Thus the aperture array design is much simpler than the previous one. However, the incorporation of this inner cavity into the reactor is considerably more complicated than for the outer cavity.

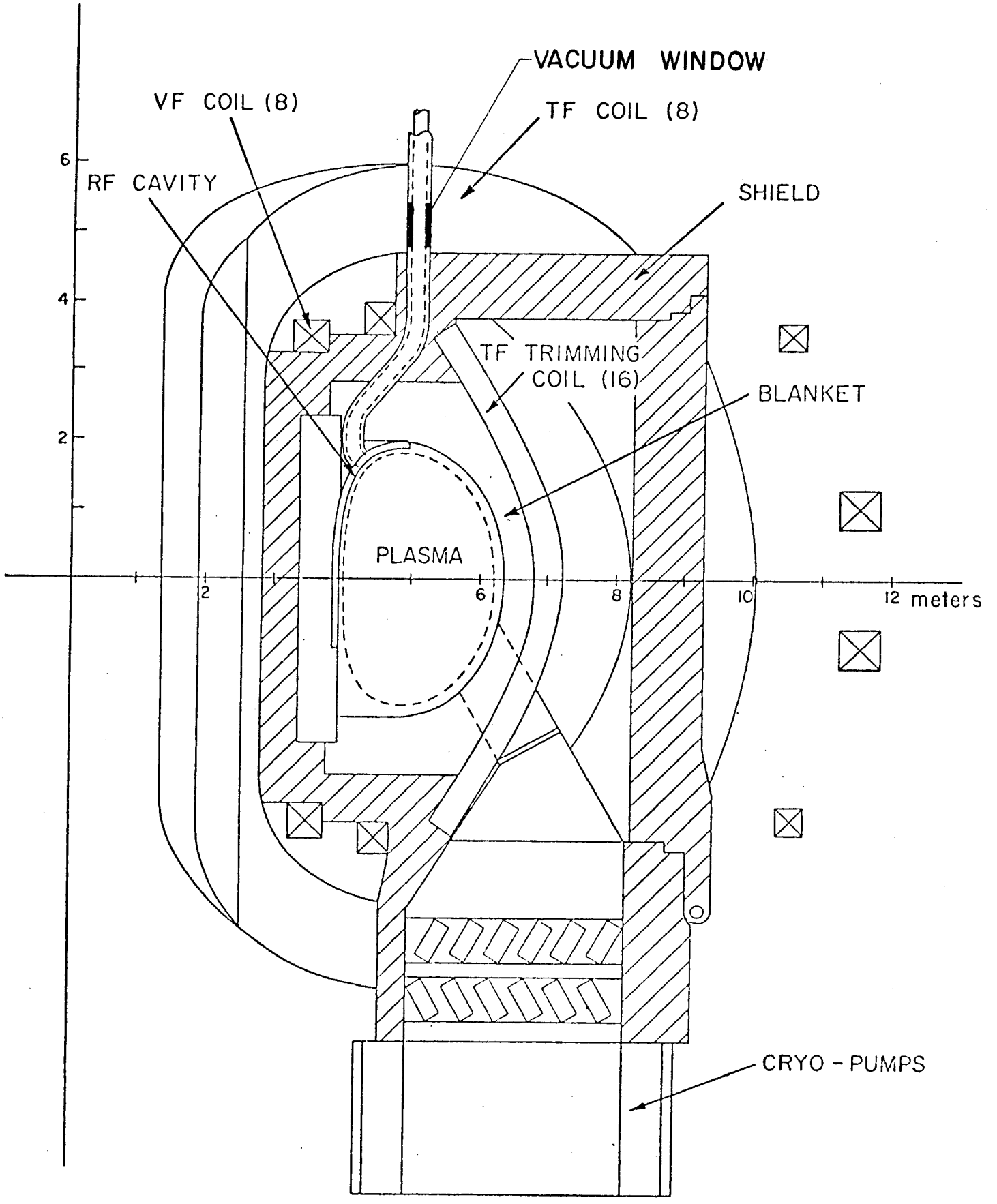


Fig. V-E-13 Cross-section of NUWMAK between TF coils (with inner RF cavity).

As mentioned earlier, four RF modules are needed to deliver 80 MW of power over a period of 3 seconds. In Fig. V-E-14 is shown the top view of the NUWMAK reactor together with the location of the four resonant outer cavities and their coax leads. Each cavity is placed directly under a toroidal field (TF) coil, where field ripples are at a minimum, so that the plasma column remains stable during the RF pulse.

V-E-4-b. The Coil Antenna

A parallel design of coil launching structures has been made because of their proven success in present-day machines. If properly designed and matched, very high coupling efficiencies (90%) can be achieved. In Fig. V-E-15, the basic scheme of such a system for NUWMAK is shown. The top view shows a total of four RF modules located on the outer wall of the toroidal chamber. Each module consists of a pair of coil antennas, driven in phase separately by coaxial transmission lines. For each antenna, a coax is fed through the first wall with the center conductor split poloidally to form two quarter-wavelength current loops connected in parallel along the minor cross-section circumference, as illustrated in Fig. V-E-15(b). For $f = 92$ MHz, $\lambda_o = 3$ m so that each current loop is 75 cm long poloidally.

Because of the size of the coils and their coaxial feed lines, there is a restriction as to how close together they could be placed without affecting their coupling efficiency. For this reason, coil coupling to a wave field with a high toroidal wave number presents a formidable problem. To excite a wave with $k_{\parallel} = 20\ m^{-1}$, the two coax feeds in each RF module have to be 31.5 cm

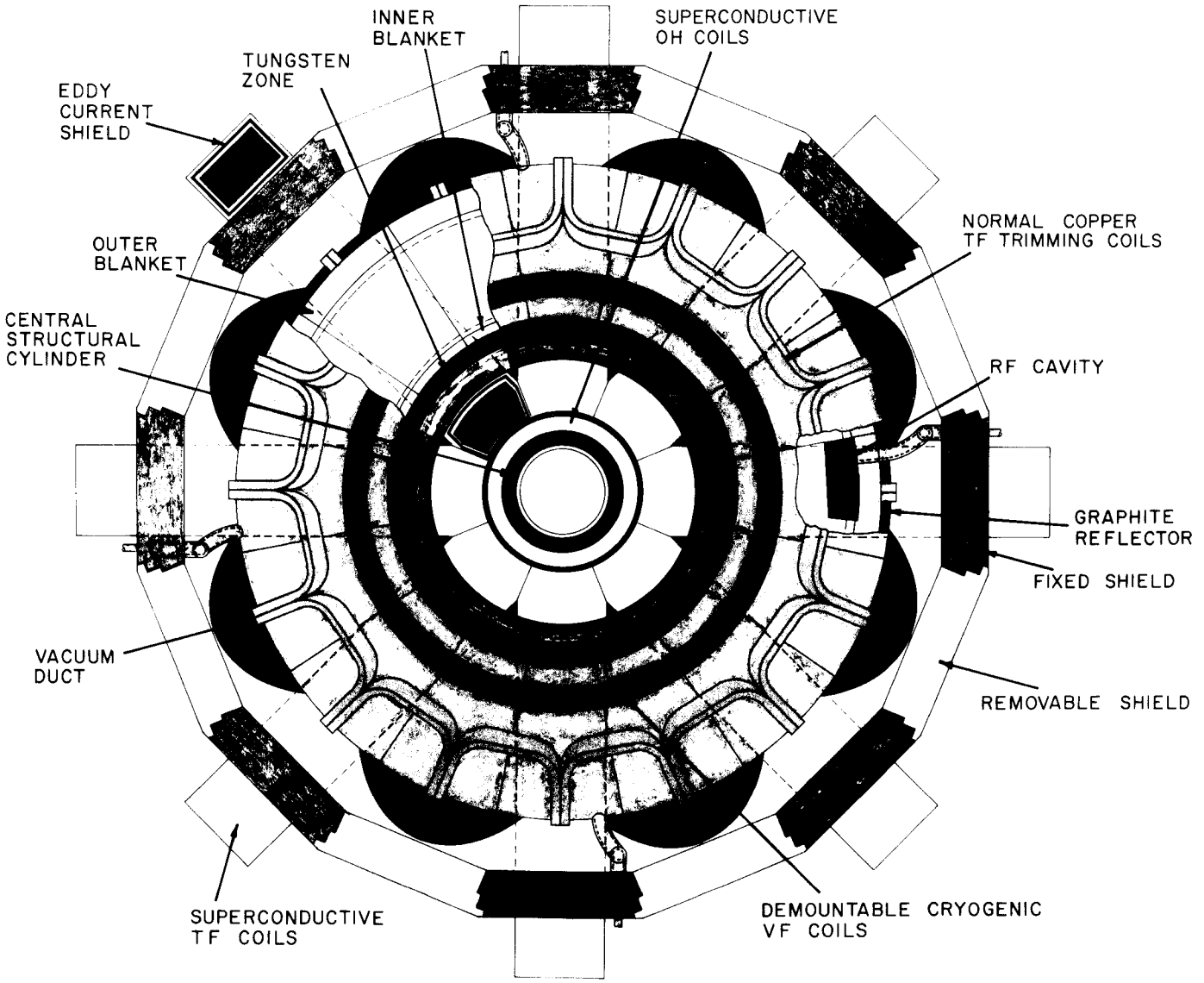


Fig. V-E-14
Top view of NUWMAK.

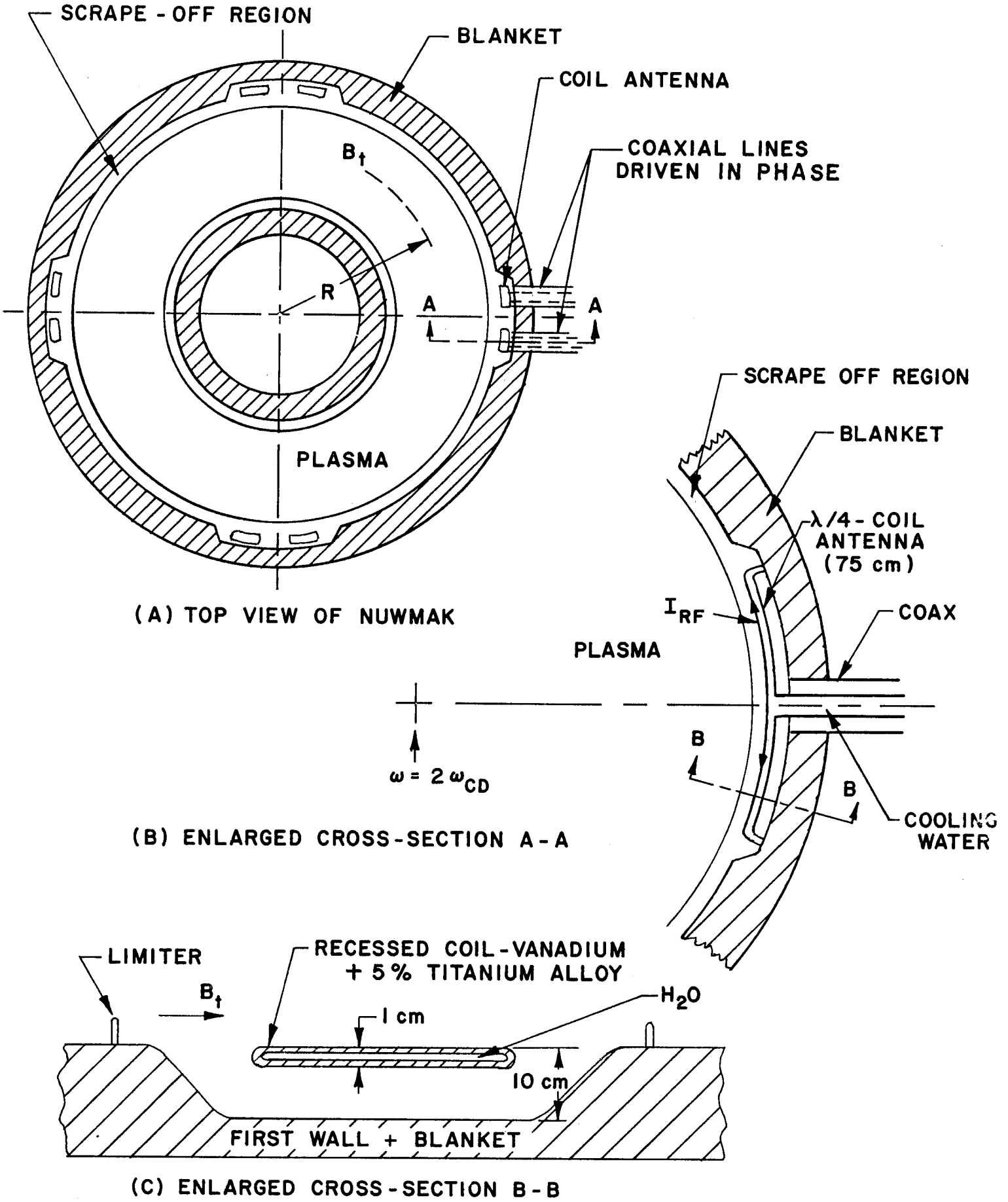


Fig. V-E-15 Base design of RF coils coupling array for NUWMAK.

($\lambda_n/2$) apart. The original 12"-coax has to be tapered gently to a 9.166"-coax towards the first wall. Keeping the characteristic impedance at 30 Ω, the inner conductor diameter becomes 14 cm. The short section of 9.166"-coax is required to carry 10 MW of power with a 3 sec pulse, and its peak power rating is 21 MW.

As shown in Fig. V-E-15(c), the coil antenna is recessed into a 10 cm deep groove in the first wall so that its profile remains essentially undisturbed. The edges of the coil and the groove are rounded, to prevent field disruption in their vicinity. The current coil and its 9.166"-coax feed are constructed of a vanadium alloy with 5% Ti so that they can withstand a constant wall loading of 4 MW/m^2 during the reactor burn cycle. Each coil is 14 cm wide toroidally and 1 cm thick, with a hollow inside through which pressurized water from the coax center conductor is run to keep the surface temperature at 350°C. The coil is placed 9 cm away from the surface of the groove to insure a matched 30 ohm driving impedance.

V-E-5. Prime Power Requirement for the Overall RF System

Numerical calculations using a global energy balance model indicate that a 2-3 sec RF pulse of 80 MW power is required at the first wall to ignite the plasma. However, considerably more power is needed from the utility lines to compensate for losses due to dissipation along the intermediate stages. A total prime power requirement will be assessed according to the efficiency of each subsystem.

Power is assumed to be supplied primarily by a utility source. A series of three-phase high voltage step-up transformers, which has a nominal efficiency of 85%, delivers power to the entire high voltage end of the RF system at the required level. Each RF module consists of a high-voltage (~ 40 kV, 125 A) pulse generator which serves as a DC power supply for the tubes in the IPA/HPA stage. The efficiency of a SCR bridge power supply is about 95%. For each IPA/HPA stage, the efficiency is essentially determined by the HPA as long as its power gain is sufficiently high (~ 20 dB). For a class C coaxitron at 92 MHz CW with a 1 MHz bandwidth and 2.5-5 MW output, the projected efficiency is 75-80%. A corresponding super-power triode operating class C narrowband will have a higher efficiency (~ 90%) but has yet to be developed with the 2-3 sec pulse widths required. Dissipation losses along the 10 meter long coax, the BeO window, and the resonant cavity walls amount to about 3% of the power flow. These results are summarized as follows:

Subsystem	Efficiency
HV Transformers	85%
DC Power Supply	95%
IPA/HPA	75%
Transmission Line + Cavity	97%
Cascaded Total	59%

For a power absorption of 80 MW by the plasma, a prime power of 136 MW is required from the line. This number may be somewhat optimistic because of the uncertainty of the HPA efficiency, but it, nevertheless, provides some ideas about the overall efficiency of the RF heating system.

References for Section V-E

1. B. W. Reed, O. N. Bowen, H. M. Hill, J. Q. Lawson, W. G. Newman and A. J. Sivo, PPPL Report - 1410 (1977).

2. W. M. Stacey, Jr., et al., Argonne National Laboratory Report ANL/CTR-76-3, Vol. 1 (1976).

3. Private communication with J. D. Stabley, RCA, Lancaster, Pennsylvania.

4. J. E. Scharer, R. W. Conn and D. T. Blackfield, EPRI Report ER-268 (1976).

5. Prodelin, Inc., General Catalog (1976).

6. W. M. Stacey, Jr., et al., Argonne National Laboratory Report ANL/CTR-76-3, Vol. 2 (1976).

7. S. Ramo, J. R. Whinnery and T. Van Duzer, Fields and Waves in Communication Electronics, John Wiley & Sons, New York (1965).

8. The Task Group on Special Purpose Materials, U.S. Department of Energy Report DOE/ET-0015 (1978).

9. Walter H. Kohl, Handbook of Materials and Techniques for Vacuum Devices, Reinhold Publishing Corporation, New York (1967).

10. Private communication with D. K. Sze, Nuclear Engineering Department, University of Wisconsin, Madison (1978).

11. Private communication with E. Cheng, Nuclear Engineering Department, University of Wisconsin, Madison (1978).

12. R. Papoular, Electrical Phenomena in Gases, American Elsevier Publishing Company, Incorporated, New York (1965).

13. A. M. Howatson, An Introduction to Gas Discharges, Pergamon Press, Oxford (1965).

14. A. J. Hatch and H. B. Williams, J. Appl. Phys. 25, 417 (1954).

15. R. F. Harrington, Time-Harmonic Electromagnetic Fields, McGraw-Hill Book Company, New York (1961).

16. D. G. Swanson and Y. C. Ngan, Phys. Rev. Lett. 35, 517 (1975); J. E. Scharer, B. D. McVey and T. K. Mau, Nuclear Fusion 17, 297 (1977); J. Jacquinot, B. D. McVey and J. E. Scharer, Phys. Rev. Lett. 39, 88 (1977).

17. R. E. Collin, Field Theory of Guided Waves, McGraw-Hill Book Company, New York (1960).

V-F. Summary

We have examined the use of fast magnetosonic wave heating in the ion cyclotron frequency range for heating a conceptual tokamak reactor to ignition. The current status of theoretical work on the subject was first reviewed. The linear local dispersion and absorption properties for the fast magnetosonic branch and coalescence in spatial regions near the second ion cyclotron harmonic with the ion Bernstein branch are well understood. The competing processes of ion cyclotron harmonic absorption and mode conversion to the ion Bernstein branch in spatial regions near the second ion cyclotron harmonic was discussed.

Researchers have found that for low values of $k_{\parallel}$, mode conversion processes can dominate the absorption process. Further, as reactor parameters of higher density and temperature are reached, the mode conversion process is expected to become more pronounced and contribute to a reduction in the fast magnetosonic wave Q for lower values of $k_{\parallel}$. This, together with a stronger finite ion gyroradius absorption of the fast wave branch for higher $k_{\parallel}$ in the reactor regime are expected to contribute to a lower wave Q situation than was previously anticipated. Finally, the importance of rotational transform in tokamaks in determining the local $k_{\parallel}$ in the absorption zone and its relation to electron Landau damping via the ion Bernstein mode or ion cyclotron harmonic absorption is noted. According to ray tracing studies, this, together with the poloidal location and $k_{\parallel}$ spectrum excited by the launching structure essentially determine the species, spatial deposition profile, and efficiency of heating in the ion cyclotron frequency range. The formulation and solution of a tokamak heating, startup, and coupling

problem taking mode conversion processes into account is quite formidable and will have to await further detailed work on the subject.

This work uses the weak damping approximation to calculate local ion and electron power absorption density. The resulting ion absorption, when averaged over a flux surface in a tokamak, yields a spatial deposition profile which is highly peaked on the axis, in agreement with previous work by Stix.

The problem of eigenmode density in a reactor as the radial, poloidal, and toroidal indices are varied is then addressed. It is shown that for the compact size of the NUWMAK reactor, the mode density is considerably lower than that for previous reactor designs. Ideally, a wave launching structure with low azimuthal mode number, $|m| < 3$, and a narrow but moderate $k_{\parallel}$ spectrum, $k_{\parallel} \simeq 20\ m^{-1}$, can be used to minimize mode conversion processes and ensure substantial ion cyclotron harmonic absorption near the plasma core. The launching structure spectrum can, ideally, provide selectivity so that several modes are excited at any one time and complex mode tracking is not required. However, the selectivity is such that several modes are simultaneously excited but that large numbers are avoided so that destructive interference of total wave fields far from the launching structure is not substantial.

Next, the ion and electron absorption expressions are averaged over the tokamak cross-section and incorporated in a spatially independent, time dependent model which solves the ion and electron energy balance equations. The results show that for an absorbed power level of 75 MW for 2 seconds, an equilibrium ion temperature of 13.5 keV can be reached within 1 second after the Ohmic heating phase. If the RF is used when the plasma is at full current, earlier studies have shown that 75 MW for 3 seconds of RF power was needed to reach the same equilibrium conditions within 4 seconds after the end of the current rise phase. Heating during the current rise phase, asuming that the coupling efficiency from the launching structure to the plasma is not degraded, results in a reduced net energy input requirement and more time for the thermonuclear burn phase of the reactor power cycle. However, the practicality of its implementation and possible benefits for the reactor cycle must await more detailed work.

For the reactor startup calculations, the power levels quoted are those absorbed by the plasma. The problem of efficient coupling from an external generator through a launching structure to the plasma was investigated. It was immediately recognized that, due to the moderate wave Q and low wave impedance in a reactor, a coupler which performs an impedance transformation between the plasma and a higher impedance transmission line is desired. Cavity-backed aperture and coil antennas located near the torus wall were proposed.

A coupling calculation was made for the driving point impedance at the coaxial feed point to the TE_{101} mode aperture cavity. By assuming a single eigenmode within the reactor, the field at the apertures is calculated for a given power absorbed in the plasma. It is found that by making a twelve by four array of 15 cm major axis elliptical apertures in the lower part of the external cavity, the desired impedance transformation is achieved by locating the coaxial feed near a corner in the upper part of the cavity. The cavity-backed aperture coupler is particularly attractive since it is flush mounted with the torus wall, achieves the impedance transformation through the location of the coaxial feed point and apertures, and reduces the RF field intensity at the torus wall by distributing the power flow over the large surface area of the aperture. This preliminary calculation indicates the potential of such a technique and suggests that implementation of aperture coupling on current ICRF experiments should be encouraged.

For coil antenna coupling, resonant $\lambda/2$ antennas may be used to enhance the radiation resistance in reactors. We considered an antenna about $\lambda/2$ long fed from a higher voltage point near the ends of the antenna. This design allows a solution for a vacuum zone between the antenna and wall of about 10 cm.

In the last section the technological and hardware design for the radiofrequency heating system was presented. The RF generators provide 20 MW/port for each of four ports at the first wall of the reactor. The frequency is 92 MHz and coaxitrons or tetrodes having 5 MW output/tube are used in units of four to provide the required power.

A 30 Ohm coaxial line of one foot (= 30.5 cm) outer diameter is used to transport the RF energy over 10 meters from the generators to the antenna systems mounted on the torus. A half-wavelength beryllium oxide window is placed just outside the shield so that radiation damage is not a problem. By bending the coaxial line and filling the center conductor with borated water for cooling, the neutron flux down the annulus of the coax can be essentially eliminated at the position of the RF window.

The problem of RF breakdown in the coupling system is solved by proper design of the coaxial system to accommodate 20 MW power levels. A safety factor for multipactor and ionization breakdown is provided by either vacuum pumping or pressurized operation of the coaxial line.

The cavity-backed aperture antenna has a radial width of 10 cm, a toroidal length of 1.85 m, and a poloidal heigth of 3.5 m corresponding to a TE_{101} mode resonance at 92 MHz. The cavity is constructed of 95% vanadium and 5% titanium alloy yielding a high conductivity, low induced radioactivity level with good strength and thermal conductivity properties for cooling. The wall thickness is 2 mm allowing the neutrons to pass through the cavity region and be collected in the reactor blanket. Cooling pipes of 0.5 cm diameter are located on the inside of the cavity. Pressurized water is used to cool the cavity to 300°C during the burn cycle so that the electrical and mechanical properties of the cavity are maintained. An alternative coil coupling system is also considered which is close to $\lambda/2$ long and fed from the end in order to improve the radiation resistance to match a 30 Ohm line. The coil is made from the same materials as the cavity

design and is flush mounted with the torus wall with a 10 cm groove cut behind the antenna in order to reduce image currents. The coils are 14 cm in toroidal width by 1 cm thick with a hollow center to provide water cooling to keep the surface temperature at 300°C.

Finally, the overall electrical efficiency of such a high power heating system including the HV transformers (85%), D.C. power supply (95%), RF amplifiers (75%) and transmission line and cavity (97%) is 59%. For an 80 MW power absorption by the plasma, 136 MW are required from the line for a three second startup period.

It is recognized that considerable experimental investigation of high power ICRF heating is required to validate it as a means for igniting a tokamak reactor. However, this preliminary investigation of scaling to reactor size should provide some degree of optimism, as well as identifying problems which require more work before the ignition of a tokamak reactor by ion cyclotron harmonic heating can be realistically achieved.

VI. Magnet System and Energy Storage

VI-A. Introduction and Summary

The designs for the toroidal field, ohmic heating, and vertical field magnet systems are described in this chapter, along with magnetic field mapping results, heat loads and cryogenic refrigerators, d.c. and pulsed power supplies, and the superconducting energy storage magnet system for pulsed power.

NUWMAK, an optimized reactor based on the knowledge obtained from the previous design studies[1,2,3,4], is a compact reactor of high plasma power density (10 MW/m^3), high average neutron wall loading (4 MW/m^2) and high β_T (6%). The plasma requires a magnetic field B_0 of 6.05 tesla at a major radius R_0 of 5.13 m, which means a maximum field of 12 tesla at the magnet. Because of the compactness of the reactor, an innovative approach was needed in the magnet design to allow access for maintenance and repair of the system. One of the unique features of NUWMAK is that it has no divertor. Instead, periodic gas puffing is used for impurity control, fueling and ash removal. Therefore, the number of vertical field coils inside the toroidal field (TF) coils can be minimized and the TF coils can be located close to the plasma. Although this reduces the magnet costs, it increases the toroidal field ripple at the plasma edge and hampers accessibility to the system through the spaces between the TF coils. To provide the needed access for maintenance and repair, NUWMAK is designed with only eight large superconducting coils and the increased ripple is corrected with 16 saddle shaped trimming coils located inside the shield. All the ampere turns needed to supply the required flux ($2\pi R_0 B_0 / \mu_0$ = 155 MA turns) are provided by the superconducting coils. The normal copper trimming coils, which are located close to the plasma, smooth out the field by adding ampere turns between TF coils and subtracting them in line with the TF coils. The cross section of NUWMAK is shown in Figure VI-A-1.

CROSS SECTION OF NUWMAK THROUGH A TF COIL (with outer RF cavity)

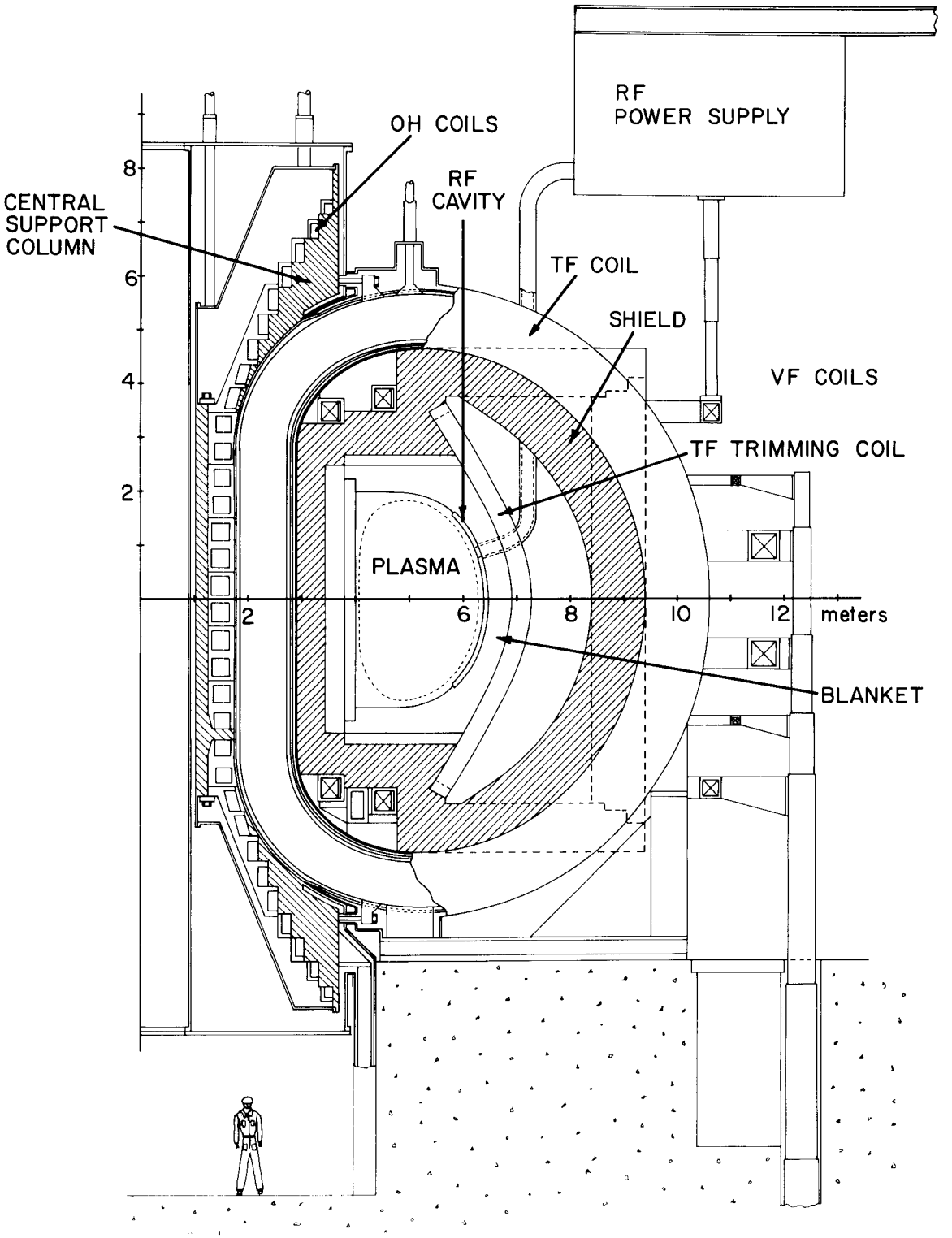


Fig. VI-A-1

The eight superconducting coils are cryostable and of a constant tension "D" shape. The embedded conductor in a solid "D" shaped structural form is used as in the earlier designs[1,2,3,4] to minimize the material requirements while providing maximum strength and stiffness. It appears that there are two technically feasible ways for designing high field (B ~ 12 T) superconductive coils. One is to use NbTi superconductor at reduced temperatures (T < 4.2 K) in order to have a reasonably high current density in the superconductor at the required high field. The other is to use Nb_3Sn as the superconducting material at 4.2 K. The primary design of the TF coil uses subcooled superfluid liquid helium at 1.8 K and atmospheric pressure, in order to use ductile NbTi superconductor and the excellent heat transfer characteristics of the superfluid[5]. As an optional design the Nb_3Sn superconductor is used in pool boiling 4.2 K liquid helium. However, there is no experience in the use of either option for large magnets at the present time.

The TF coils are supported on the reactor floor permitting the ohmic heating coil system to be removed vertically for servicing without disturbing other elements. An entire module consisting of one TF coil together with a blanket and shield segment can be removed independently. Details on the maintenance are described in Chapter XI.

There are four cryogenic vertical field coils inside of the TF coils and four superconducting coils at the outside of the TF coils to maintain the elongated plasma. As usual, the ohmic heating coils are located inside the central core of the reactor system. Due to this poloidal field coil system, the pulsed field component along the TF coil is relatively large (ΔB ~ 1 tesla) and the component is screened out by the high purity aluminum shield (field) surrounding the TF coil.

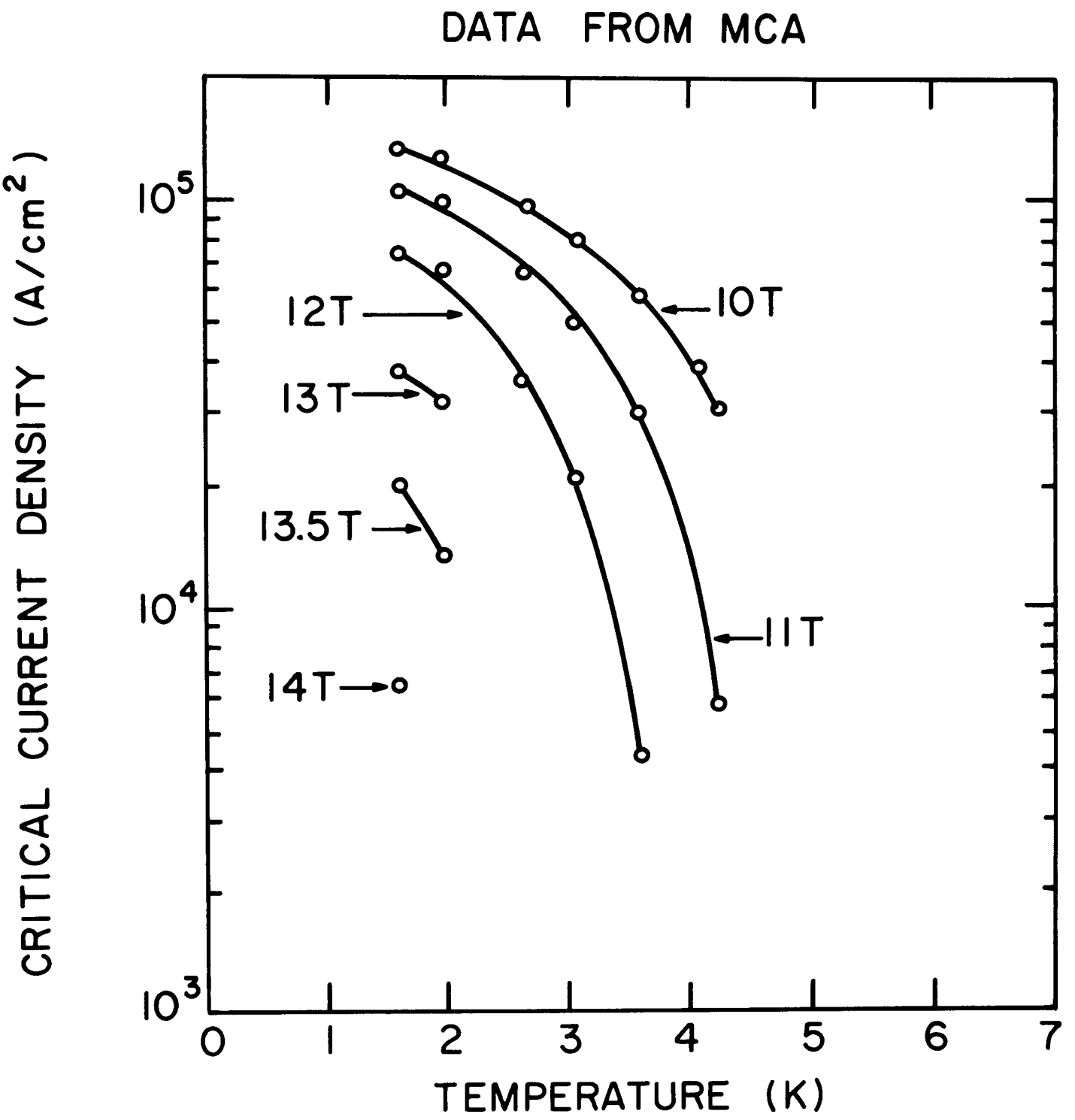
VI-B. Superconducting Toroidal Field Magnets

VI-B-1. General Considerations

The basic design philosophy of the superconducting toroidal field magnets is unchanged from that of earlier designs.[1,2,3,4] Because of the large size and high field, full cryostability and a reliable, solid structure are essential to avoid magnet instability.

The critical current density of NbTi at B = 11.48 tesla and 4.2 K is too low for practical use in magnets and multifilamentary Nb_3Sn superconductor has only been used in small magnets. However, Nb_3Sn is quite brittle and there are concerns about the use of this material in large magnets, although some reactor design studies have been performed in which this material has been proposed for TF magnets.[6] The use of NbTi at B = 10 tesla and a reduced temperature (T ~ 3 K) has been proposed in order to avoid the use of the brittle Nb_3Sn material.[7] The critical current of NbTi at B = 12 tesla and T ~ 2 K is comparable to the critical current of multifilamentary Nb_3Sn at T = 4.2 K and the same field strength (see Figs. VI-B-1 and 2).[8,9] An extensive study has been performed on the use of 1.8 K superfluid He for large superconductive energy storage magnets[10] and its application to TF magnets has been proposed.[5] The advantages of the 1.8 K subcooled superfluid helium operation are: 1) high critical current density in the ductile NbTi superconductor, 2) large critical heat flux, and 3) excellent heat transfer in He II.

In the UWMAK-III[3] and TETR[4] design studies high purity aluminum was chosen for the stabilizer and high strength aluminum alloy for the structure. The main reasons for the choices are 1) the induced radioactivity in aluminum is less compared to copper or steel, 2) the aluminum design allows a savings in weight and cost, compared to copper and steel, and 3) it appears that aluminum supply is better than that of copper and stainless steel. However, no large superconducting magnets exist with aluminum stabilizer at present, and a considerable amount of research and development work is needed.



TEMPERATURE DEPENDENCE OF CRITICAL CURRENT IN Nb-46.5% Ti WIRE

Fig. VI-B-1

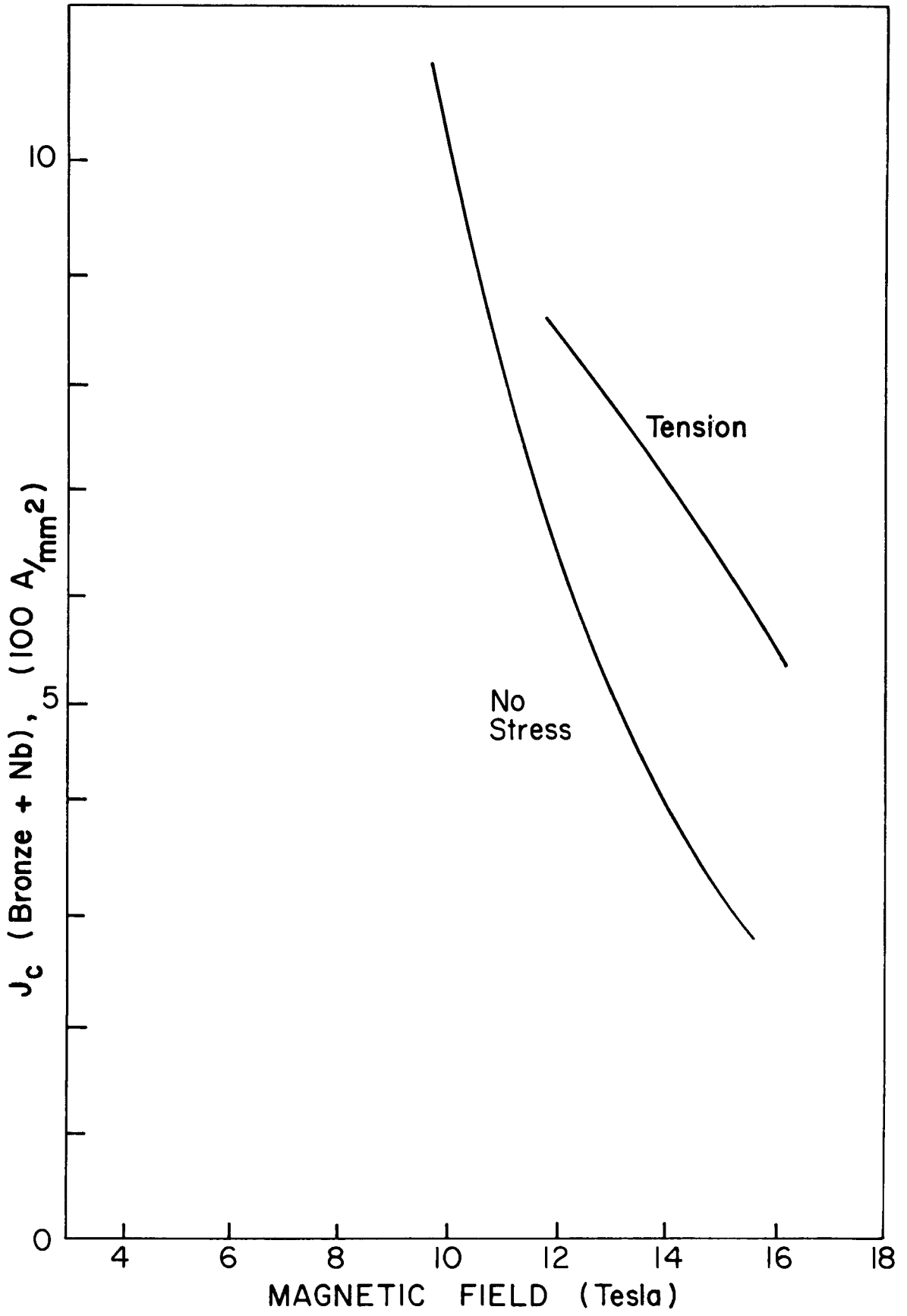


Fig. VI-B-2 Critical Current Density of Nb_3Sn

Considering the background of the present technology of superconducting magnets and the timing of the first generation reactor, NUWMAK, we choose the use of NbTi in a subcooled superfluid helium (He-II) bath at 1.8 K as a primary design, and Nb_3Sn in 4.2 K pool boiling liquid helium as an optional one.

VI-B-2. 1.8 K Operation

VI-B-2-a. Superconductivity

The upper critical field (H_{c_2}) of the superconductor NbTi is about 11 tesla at 4.2 K. In practice, the magnet may be operated at a field of at least 2 or 3 tesla below H_{c_2} because of the available critical current density and thermal margin of stability. The critical current of commercial NbTi at reduced temperature as shown in Figure VI-B-1 indicates that the current density at B ~ 12 T and T ~ 2 K is high enough to be used in the magnet. Furthermore, an experimental effort is underway at the University of Wisconsin[10] to increase the H_{c_2} of NbTi based on the ternary alloy system. In the Ginzburg-Landau-Abrikosov-Gorkov theory (generally known as GLAG) of type II superconductors, the upper critical field H_{c_2} is given by the relationship

$$H_{c_2}(0\ K) = 3.1\ \rho_n\ \gamma T_c\ (\text{tesla})$$

where ρ_n is the normal state resistivity, γ the electronic specific heat coefficient (which is proportional to the electron density of states) and T_c the superconducting critical temperature. This theory works well for a wide range of superconductors but it is found that for very high field superconductors with $H_{c_2} > 10$ tesla (e.g. Nb-Ti, Nb_3Sn, V_3Ga) the observed H_{c_2} values are reduced below those given by the equation. The origin of this discrepancy lies in the neglect in GLAG theory of the spin paramagnetism of the normal state. Although the normal state susceptibility is small, the paramagnetic energy $1/2\chi_n H^2$ can approach the superconducting condensation energy $H_c^2/8\pi$ at fields of 10 tesla and above, provoking a transition to the normal state at fields considerably less than that expected by GLAG. The GLAG

theory has been extended for this case by Maki and by Werthamer, et al., and good agreement between theory and experiment has been obtained for the behavior of some practical alloys. An interesting conclusion of the theory is that it is possible to lower the energy of the superconducting state (and hence increase H_{c_2}) by partially disordering the spins of the superconducting state. In the ground state at 0 K the electrons at the Fermi surface are aligned antiparallel to the field in Cooper pairs. However, at finite temperatures and in appreciable magnetic fields, and particularly when the mean free path is short (i.e., ρ_n high), and elements of high atomic number are present, there can be substantial short term electron spin disordering due to spin orbit scattering. The difference between the spin susceptibilities of the normal and superconducting states is thus reduced, leading to an increase in H_{c_2}. Based on the above theoretical background the experimental effort is pursuing the higher electrical resistivity and larger spin orbit scattering alloy system. The preliminary indication is that H_{c_2} at 1.8 K increases by $\sim$ 1 tesla.

VI-B-2-b. Heat Transfer in Superfluid He-II

Another advantage of operating superconducting magnets at low temperatures besides the significant gains in the critical current density and upper critical field is the use of the excellent heat transfer characteristics of superfluid helium (He-II). One of the unique properties of liquid helium is that a second order phase transition occurs as the temperature becomes lower from the normal fluid (He-I) to the superfluid (He-II) state as shown in Figure VI-B-3. At this phase transition there is no latent heat; however, there is a large discontinuity in specific heat as shown in the upper corner of Figure VI-B-3 and the viscosity of the superfluid becomes zero. Heat is carried by a conduction mechanism in He-II rather than by a convection mechanism as in He-I, which may lead to problems like vapor locking. A few proposals have been made to use He-II in large superconducting magnets by taking advantage of the excellent heat transfer characteristics. The characteristics found in the experimental study[5] will be reviewed here in some detail.

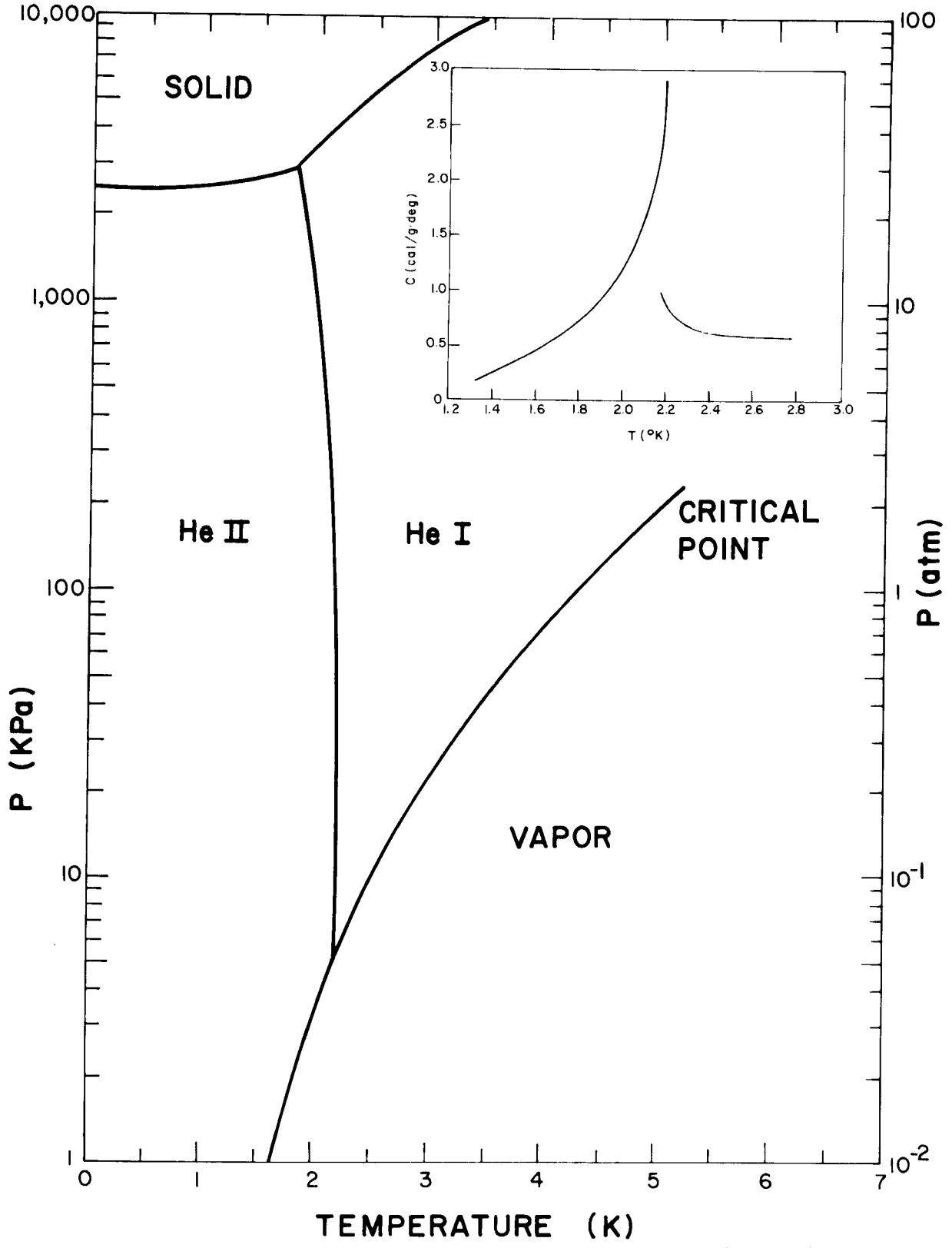


Fig. VI-B-3 Phase diagram and specific heat of He

At temperature 1.8 K,where the magnet is going to be operated because of a reason which will become clear later, the saturated vapor pressure is 12 Torr (0.016 atm) and the breakdown voltage of helium vapor is low[11] because the voltage is proportional to the vapor density and gap distance between two electrodes. Based on this reason, it is suggested that the magnet be operated in subcooled He II using the heat exchanger.

Figure VI-B-4 shows the critical heat flux from aluminum to He-II. The peak heat flux into the subcooled He II at 1.9 K and 1.3 atm is $q^* = 2.3$ W/cm^2 and its recovery heat flux is $q^R = 1.8$ W/cm^2. These values are significant improvements over those for normal liquid helium at 4.2 K and 1 atm which are also shown in the figure. The critical heat flux of 1.9 K superfluid at the saturated vapor pressure is inferior to the subcooled He II at 1 atm pressure. This fact is another reason for operating the magnet in subcooled He II. Due to the large value of q in the subcooled He II, the amount of stabilizing material may be minimized.

He II is a unique fluid in that it transports heat by a mechanism which is quite similar to conduction in a solid. Resistance to heat flow is due to what is called mutual friction, which results from the interaction between the superfluid and normal components of the fluid. For the moderate system, heat flow is governed by an equation

$$\nabla T = f(T,p)\ q^m$$

where f(T,p) is a function of the thermodynamic state of the liquid helium and m is a constant which is approximately 3, and the effective thermal conductivity is defined as

$$K_e = \frac{1}{f(T,p)\ q^2}$$

and plotted as a function of temperature in Figure VI-B-5 (q is the critical heat flux). Now the reason for operating the magnet at 1.8 K is clear since the conductivity is maximum at a temperature around 1.8 K with values about 1000 times larger than in copper. The magnet helium channel should be short enough so that a heat flux q applied at one end can be carried without thermal breakdown.

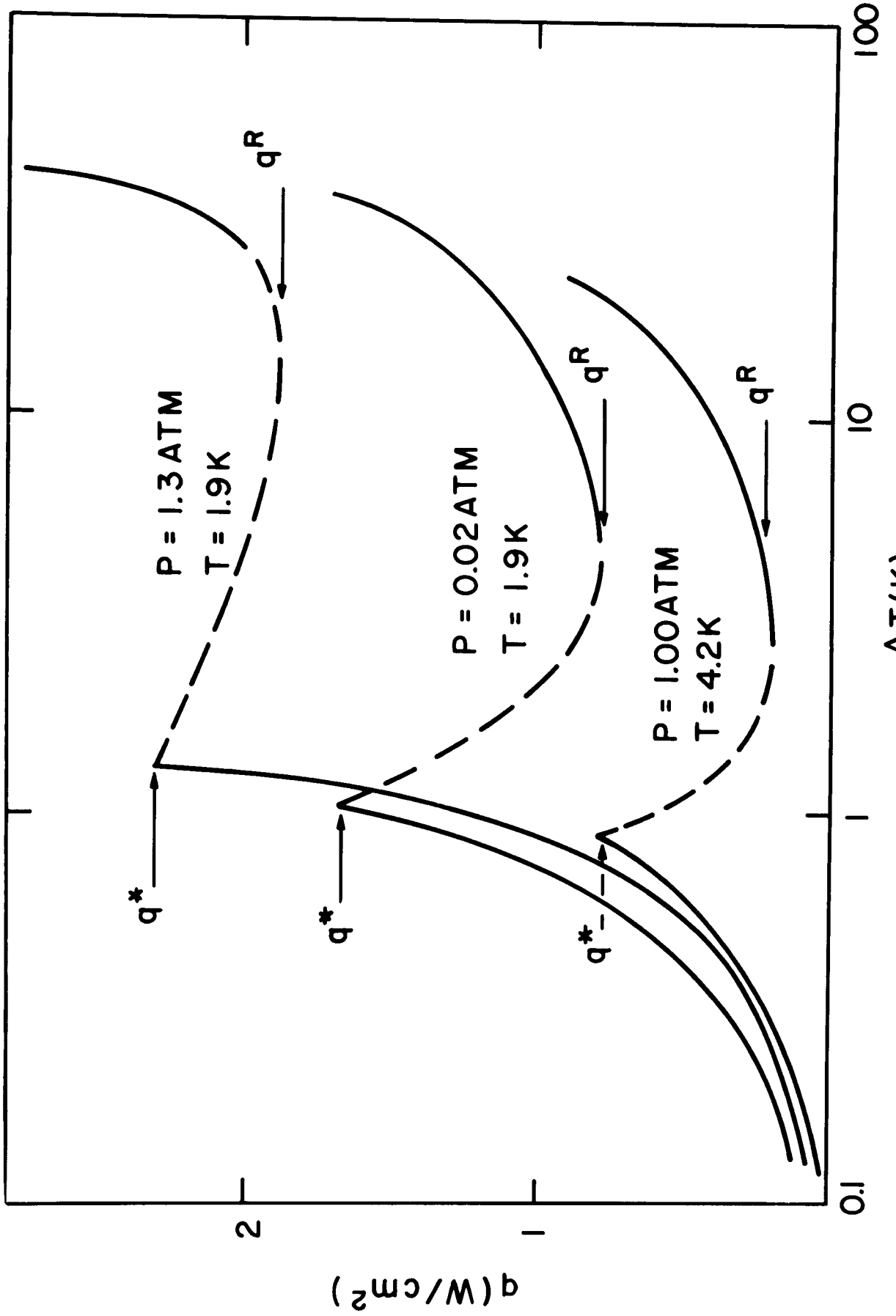


Fig. VI-B-4 CRITICAL HEAT FLUX

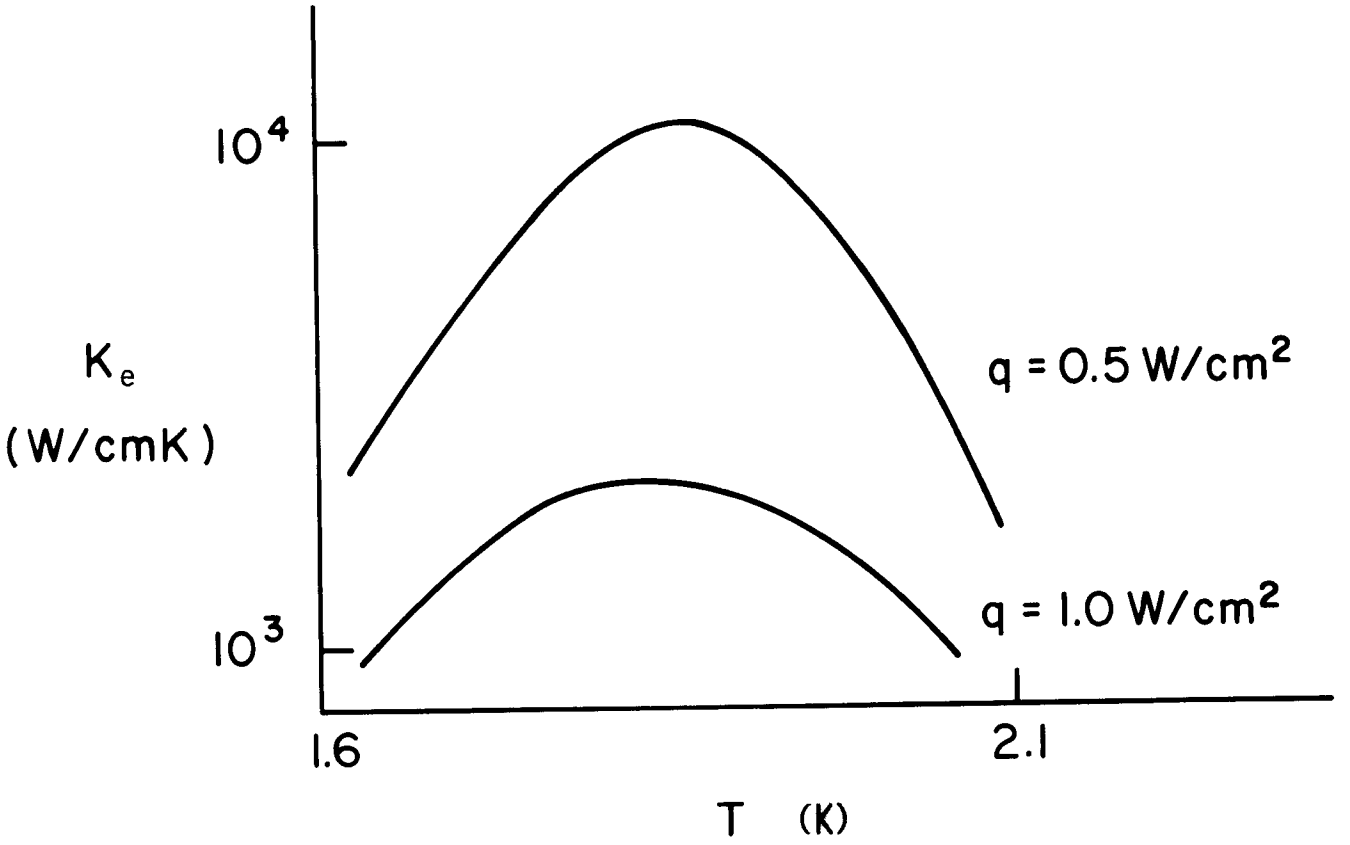


FIG. VI-B-5 EFFECTIVE THERMAL CONDUCTIVITY OF HE II

The magnet designer should design the channel length smaller than a critical length in which the hot end temperature is the λ point 2.17 K, the phase boundary of He I and He II.

In spite of these advantages of the magnet operation in He II, a major objection to He II cooling has been due to the increased refrigeration at low temperatures. The cost of refrigeration increases rapidly with decreasing temperature. Energy use for refrigeration is approximately proportional to the Carnot factor (T_w-T_c/T_c), where T_w is room temperature and T_c is the cryogenic environmental temperature. Reasonable estimates of real optimized refrigeration place power requirements at 1.8 K at about three times that at 4.2 K. However, with effective shielding, refrigeration at 1.8 K can be minimized with the result that the total power due to room temperature conduction and radiation is only increased by approximately 30%.[12] Thermal loading such as nuclear heating and induced currents in the stabilizer contribute a substantial loss mechanism. Taking these heat loads at 1.8 K, with an associated increase in refrigeration power, may prove to be economically unacceptable, and the system may require an intermediate temperature thermal interception.

VI-B-2-c. Conductor and Magnet Assembly

Designs of conductor and structure are very much like those in earlier designs.[1,2,3,4] The critical heat flux q = 0.5 W/cm^2 is used for the proposed 1.8 K subcooled superfluid helium operation of the NUWMAK TF coil compared to 0.3 W/cm^2 for the earlier design. The stabilizer in the conductor is chosen to be high purity aluminum. The resistivity of the aluminum is taken as 1×10^{-8} ohm cm throughout the entire field range. The strain in the conductor is held below 0.3% because of the indication that the resistance of high purity aluminum increases beyond this strain limit.[13] The 15,000 A conductor, 2.18 cm wide and 1.38 cm thick assembly is embedded with fiberglass epoxy into the spiral grooves in the 2219 aluminum alloy structural disk as in Figure VI-B-6. The epoxy insulation facing the liquid helium is 2 mm thick to prevent dielectric breakdown in the liquid helium at the interface between the structure and conductor. The breakdown voltage in the liquid helium across clean interfaces was reported to be about 20 kV/mm[11] and during the fast discharge period

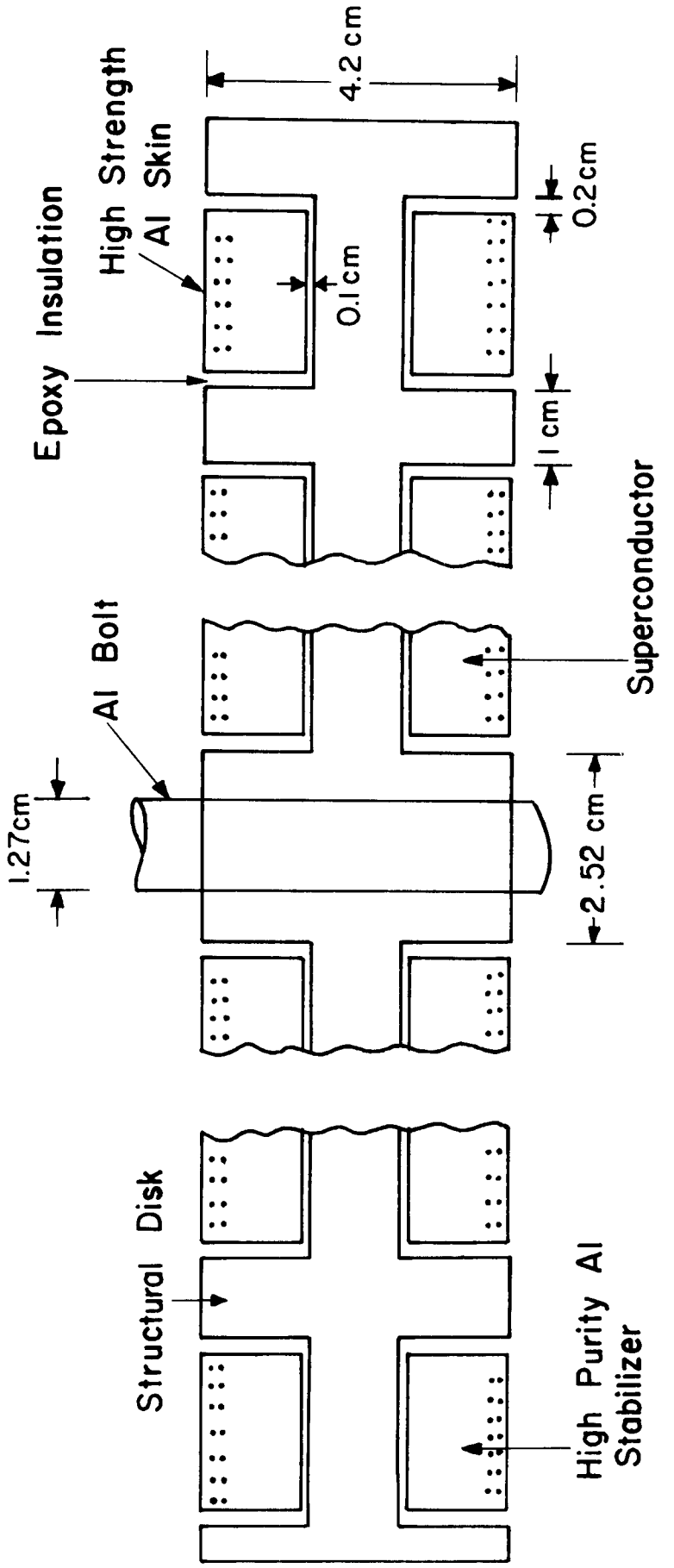


Fig. VI-B-6 Cross section of magnet disk

resulting from a fault condition, a considerable voltage can be withstood by the 2 mm gap. The conductor is encapsulated in 1/2 mm of high strength aluminum alloy to prevent plastic flow of the high purity aluminum due to the high magnetic force. It is similar to the conductor designed for the energy storage magnet.[14] Twenty-nine disk pancakes with 23 conductor turns on each side with micarta spacers covering half of the surface are bolted together to form a coil. The coil is a constant tension D shape obtained with the aid of the analytic expression derived by Moses.[15] The TF coil specifications are given in Table VI-B-1 and compared to UWMAK-III.

The lateral loads on the magnets due to the pulsed poloidal field coil system as well as the forces occurring because of the failure of one or more TF coils are transmitted to the dewar walls by means of reinforced epoxy struts. Between magnets these forces are reacted with the neutron shield designed to withstand the large lateral loads without excessive deflection as in the earlier UWMAK studies.[2,3] In order to minimize the conduction heat load to the 1.8 K helium both the struts are thermally anchored to the high purity aluminum shield. The shield surrounding the magnet is used to screen the ac component of the pulsed poloidal field in order to stabilize the magnet mechanically and electrically. This scheme has been suggested earlier.[7] The 6 cm thick shield is operated at 4.2 K at the straight leg portion of the TF magnet, since the OH coils and the central support system are operated at 4.2 K, and space is limited in the area. However, enough space is allowed between the inner dewar (1.8 K) and the outer dewar (4.2 K) walls to prevent excessive heat leak into the 1.8 K bath.

Assuming all the ac field components are screened out from the TF coil, then heat loss in the 1.8 K coil is 1300 W, of which conduction loss is 500 W, nuclear heating 500 W and joint loss 300 W. The refrigeration power required to remove this heat is 1.3 MW, which is quite small. One TF magnet contains about 5000 ℓ of liquid helium and 1.8×10^6 joules are required to raise the helium temperature from 1.8 K to 2.1 K (the difference in enthalpy from 1.8 K to 2.1 K is $\Delta H = 0.36$ joule/cm^3). It is interesting to point out that the I^2R losses will be about 2.9×10^6 watts in a magnet if the whole conductor goes normal, although there may not be any way to stabilize the magnet against this condition. Assuming that a 4000

Table VI-B-1

Specifications of Toroidal Field Magnets

	NUWMAK	UWMAK-III
Number of Superconducting TF Magnets	8	18
Operating Temperature	1.8 K	4.2 K
Superconductor	NbTi	NbTi
Stabilizer	High Purity Al	High Purity Al
Number of Trimming Coils	16	-
Maximum Field at Winding	11.48 T	8.75 T
Inductance of Coil (Total)	290 H	2370 H
Stored Energy	30 GJ (8.3 MWh)	108 GJ (30 MWh)
Total Amp. Turns	155 M Amp. Turns	164 M Amp. Turns
Current/Turn	15 kA	10 kA
Number of Disks/Magnet	29	16
Number of Turns/Disk	23 (each side)	32
Conductor Cross Section	2.18 x 1.38 cm	1.5x1.5 cm
Current Density in Conductor	5000 A/cm^2	4400 A/cm^2
Disk Cross Section	4.2 x 87.4 cm	5 x 116 cm
Average Stabilizer to Superconductor Ratio	10:1	19:1
Design Stress in Structure (2219 Al)	210 MPa (30,000 psi)	3.11 MPa (45,000 psi)
Design Strain	0.3%	0.38%
Weight of Each Magnet	100 t	174 t

watt at 1.8 K refrigerator is provided (which is three times larger than needed in normal operation) the capital equipment cost is c_p = \$6,000 x $(4,000)^{0.8}$ = \$4.6 x 10^6, which is not excessive.

The construction technique is similar to that of UWMAK-III.[3] The straight leg of the TF coil is located between R = 182.6 cm and 270 cm and the center of the OH coil T_1 is at R = 146 cm. Its maximum current is 2.87 MA, and the coil size is 40 x 40 cm, which leaves the gap of 16.60 m between half of the TF and OH coil. This space is enough for the Al shield and vacuum space to prevent the excessive heat leak into the 1.8 K bath. The inward pressure of the TF coil is transmitted into the support cylinder inside the OH coil through the fiberglass epoxy struts and the steel structure between the OH coil (see Figure VI-A-1).

The lateral support structure should be designed for the case of one magnet failure. The design requirements for the torsional loading produced by the poloidal fields is minimal compared to the catastrophic failure mode. Since there are only eight superconducting coils, their mutual inductive coupling is relatively small compared to the case of a large number of coils and in case one of the coils fails the induced current increases. The adjacent coil current is about 15% of the normal operation current. There is enough superconductor to carry this current and the critical heat flux is q = 0.66 W/cm^2, which still is a fairly conservative value considering the peak critical heat flux q = 2.3 W/cm^2. Here it is worthwhile to mention that the coupling between the saddle trimming coil and the superconducting TF coil is minimal because they are coupled to each other with nearly a 90^o angle.

The force developed in the coil next to a failed coil is 5.5 x 10^7 N/m at the inner leg portion and 1.1 x 10^7 N/m at the outer leg. This force is transmitted into the dewar wall by epoxy struts and consequently to the shell structure between dewars. By assuming about 400 MPa compression design stress of an epoxy fiber strut, the total cross sectional area of an epoxy strut at the high-force portion covers about 15% of the magnet side cross section and 3% at the outer leg portion. Ten percent of the epoxy struts are actually in contact with the magnet and dewar wall through the conical spring cap as in earlier designs[2,3] to minimize the thermal load during normal operation since the torsional force due to the pulsed

field is small. The rest of the struts are actually in contact with the dewar wall only in the case of failure.

VI-B-3. Optional Design

As discussed in earlier sections, there may be significant advantages to using subcooled He II as the coolant of a large superconducting magnet. However, there is almost no experience in this area, and the system will be generally more complicated than in using pool boiling 4.2 K helium because of the subcooling system, the thermal loss interception scheme at intermediate temperatures, and the heat exchanger pump. The major objection to this scheme is due to the large refrigeration requirement, which is about 3 times larger than that of 4.2 K refrigeration.

From results of the extensive development effort of the inherently brittle superconductor Nb_3Sn, fine multifilamentary composite conductors can be produced by growing diffusion layers of the compound at a Cu-Sn bronze - Nb interface. In this composite the superconductivity of Nb_3Sn is depressed because the material is exercising compression due to the differential thermal contraction between bronze and Nb. The typical reaction temperature of the composite is about 1000 K. The thermal contraction from 1000 K to 4.2 K is about 0.77% for Nb_3Sn, 0.71% for Nb and 1.82% for bronze. The greater change in length of the bronze leads to additional shrinking of the Nb_3Sn and Nb, which puts the Nb_3Sn under compression. The magnitude of the compression of Nb_3Sn is dependent on the relative cross-sectional area of the Nb_3Sn. As a consequence the critical current of the composite increases as the strain increases and the current reaches its peak at strain (ε_m) where the pre-compression of Nb_3Sn is presumably relieved completely.

Beyond the strain the critical current tends to decrease. The fact that the critical current rises as the strain ($\varepsilon < \varepsilon_m$) is a fortunate fact for the practical usage of Nb_3Sn. The current rise has an even larger effect in high field regions as shown in Figure VI-B-2, where the J_c is increased by 100% at the magnetic field of about 15 tesla.[9]

However, even with this favorable development of multifilamentary bronze based Nb_3Sn, handling of Nb_3Sn requires a great deal of caution in constructing magnets and consequently its cost will be high and its technology needs much development.

With the expectation of successful development of Nb_3Sn conductors, we have carried out an optional design of the TF coil system with the conductor. The magnet will be operated at 4.2 K in a bath of liquid helium. Considering the brittleness of the superconductor, strain is limited at 0.1%. Because of the low design stress, the structural material is chosen as 316 stainless steel and the stabilizer is OFHC copper. The critical heat flux $q = 0.32\ W/cm^2$ is used and the conductor size is 5.11 cm x 1.75 cm in the inner high field region and is linearly tapered to 2.67 cm x 1.75 cm in the outer low field regions. The disk is 4.4 cm thick and 98.8 cm wide. The maximum stress in the conductor is $8000\ N/cm^2$, which is below the yield point of copper. In the inner turns where the field is higher than 8 tesla Nb_3Sn is used and the remaining outer turns are of NbTi since they are in the low field region. Some specifications of the magnet in this optional design are in Table VI-B-2.

Because of the relatively large pulsed field components along the TF coil ($\Delta B \sim 1$ tesla), the high purity aluminum shield surrounding the TF coil will also be used in 4.2 K operation to provide stability for the magnet. The shield in the inner vertical leg portion will be cooled with the liquid helium in the same bath which is cooling the magnet because of the lack of space. If the VF coil system is designed in such a way that the pulsed field component is minimal along the TF coil as in one design study,[6] then the 4.2 K operation may be quite a bit more advantageous than the 1.8 K option because one may then afford to let the ac losses be dissipated in the conductor without the shield.

VI-C. Trimming Coil System

VI-C-1. General Considerations

Trimming magnets are used in this design to reduce field ripple (variation in the strength of the magnetic field) throughout the plasma

Table VI-B-2 Specifications of Optional TF Magnet

Superconductor	Nb_3Sn
Stabilizer	OFHC Copper
Structure	316 SS
Operating Temperature	4.2 K
Design Strain	0.1%
Design Stress in Structure	210 MPa
Current Density:	
High Field Region	1700 A/cm^2
Low Field Region	3400 A/cm^2
Number of Turns/Disk	21
Number of Disks/Magnet	32

region. The trimming magnets are normal metal copper magnets located close to the plasma. By including the trimming magnets, the number and size of superconducting TF magnets may be reduced from conventional designs to provide access for maintenance, and room for penetrations for blanket cooling, vacuum pumping, and plasma heating schemes.

In tokamak fusion power reactors the strength of the toroidal magnetic field in the plasma region varies along the toroidal direction, the field being higher beneath a TF magnet and lower between TF magnets. If this field ripple is too large, larger than perhaps 2% at the outer plasma edge, then the plasma will leak out due to instabilities and the confinement time will be degraded.

Also, in Ion Cyclotron Range of Frequencies (ICRF) heating and transport studies for the T-10 tokamak reactor, the effect of toroidal field ripple has been shown to have an important effect on the maximum ion temperature reached. In computer studies by Vdovin, et al.,[16] 2 MW of ion cyclotron wave heating for a 182 millisecond period resulted in a central hydrogen ion temperature increase from T_{io} = 800 eV to T_i = 3.1 keV when a toroidal field ripple effect is included (that is, enhanced diffusion due to trapped particles in the toroidal field ripples). When the heating program is run without toroidal field ripple included, the central ion temperature reaches almost 4 keV.

The field ripple has been maintained at low enough values in past conceptual designs by using large TF magnets with outer legs far removed from the plasma region and/or a large number of TF magnets. However, TF magnets are expensive, representing a signficant fraction of the direct costs of fusion power reactors, and consequently it is worthwhile to try to reduce their size and/or number. Reducing their size will also reduce the overall size and cost of the necessary containment building. In addition, access to the interior regions of the reactor during normal operation and for routine and emergency maintenance is enhanced by using fewer TF magnets with larger spaces between the magnets.

In order to maintain a low field ripple, reduce the size and number of TF magnets, and increase access to the interior regions of the reactor we

have designed a TF magnet system that includes eight superconducting magnets and sixteen normal metal trimming coils, as shown in Fig. VI-C-1.

VI-C-2. Description and Design Factors

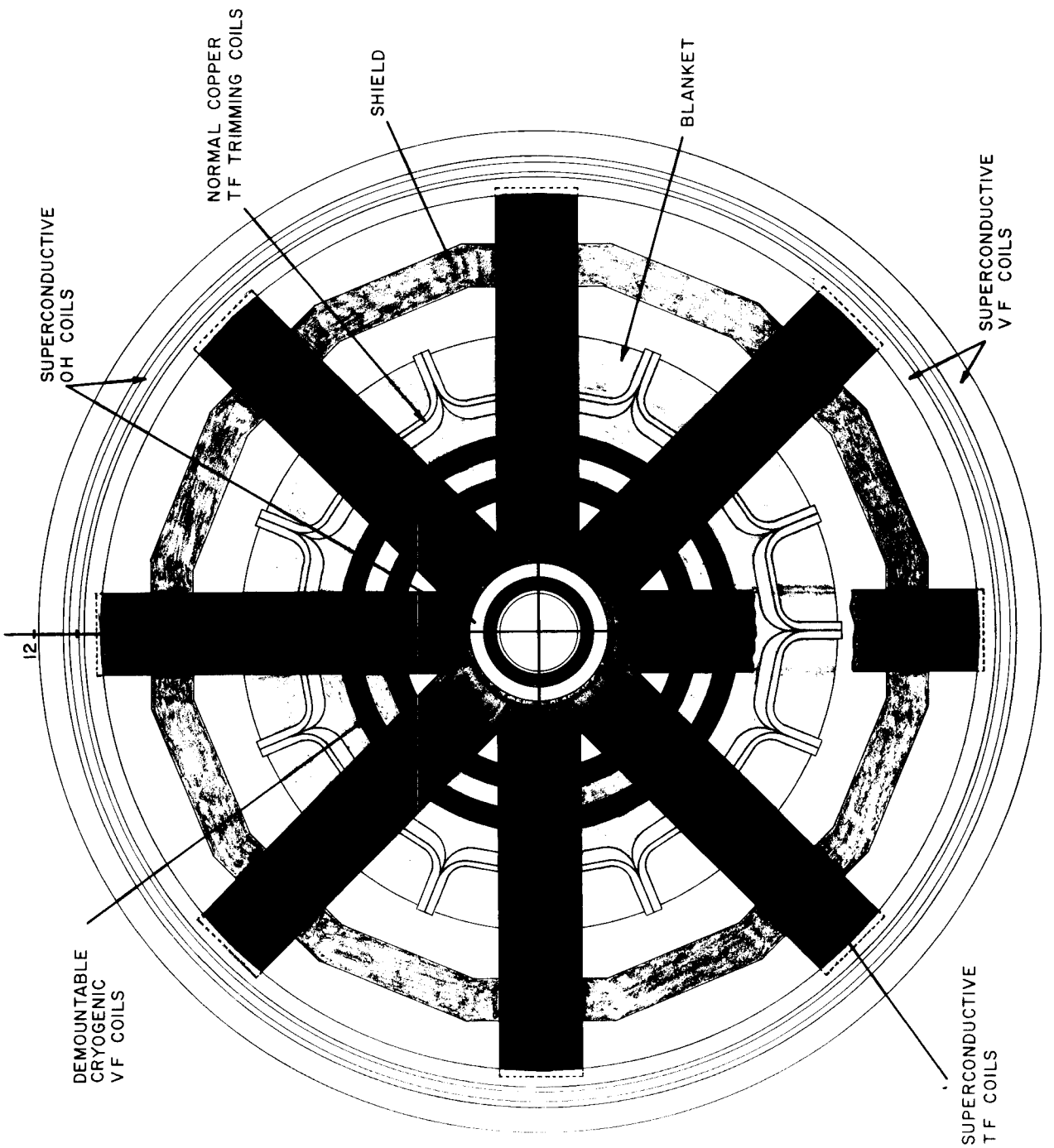
The normal metal field trimming coils chosen for use in NUWMAK are "saddle" shaped. The current runs vertically up one coil leg (shaped to fit along the outside of the blanket) to a cross member at the top of the plasma region, through the cross member in the toroidal direction to the next coil leg, down the leg to a cross member at the bottom of the plasma region, and through this bottom cross member to the starting coil leg. The current paths in the 16 trimming coils are independent of each other.

The coil shape when viewed from the top is shown in Figure VI-C-1, and when viewed from the side is shown in Figure VI-A-1, and was chosen to conform to the plasma shape for minium coil size at a given ripple reduction. The saddle coils can be replaced without cutting any components, such as the blanket or plasma chamber.

The normal coils are not located close to and just inside of the superconducting coils, as is the case in a usual hybrid magnet system. In the usual hybrid system the normal coils are present to augment the field from the superconducting coils and thereby go to higher fields than would be attainable with superconducting coils alone. Such systems have operating costs that are lower than those with normal coils alone. In our proposed design for NUWMAK, the functions of the normal and superconducting coils are quite separate and distinct. The superconducting coils supply the full toroidal field. The normal coils reduce the field in some regions and add to it in others in a symmetrical way that smooths out the field, thus reducing the ripple.

Originally the coil position was intended to be right behind the first wall, but radiation damage and neutron heating in the coils and the reduction in the tritium breeding ratio in the blanket behind the coils were too big and for these reasons the coils were moved back to a position just behind the blanket. We chose not to move the coils back any further than this because access would have been reduced and the current needed for ripple control, the I^2R

Fig. VI-C-1 TOP VIEW OF NUWMAK



losses and the coil mass would all have increased. Even when located behind the blanket the trimming coils still must be normal rather than superconducting because the nuclear heat load precludes cooling either cryogenic or superconducting coils economically. Only coils located behind the shield have a low enough nuclear heat load to be economically cooled to cryogenic temperatures.

Material choices other than copper may be considered for the conductor such as aluminum, vanadium, or liquid sodium, which would produce low residual activity in the coils. However, copper is still the material of choice at this point because of its relatively attractive combination of high conductivity, relatively low cost, good structural strength and reasonable availability. A titanium alloy ring supporting the top legs of the Cu coils and another ring supporting the bottom legs is used to resist the alternating inward and outward forces from the vertical coil legs.

The choice of eight TF coils for NUWMAK is an optimized number based mainly on the competing demands of ripple correction required and access space, both as functions of coil number. As shown in Figure VI-C-2 (using for example a machine with a 4.5 m radius and with 6T toroidal field on the plasma axis), tokamaks with fewer than 8 TF coils would have significantly more ripple, or field variation at the outer plasma edge, requiring much larger and more power consuming trimming coils. Increasing the number of TF coils above 8 does not decrease the ripple enough to be seriously considered when the loss in access is taken into account. Another machine, of different size and purpose, may have a different optimum number of TF coils.

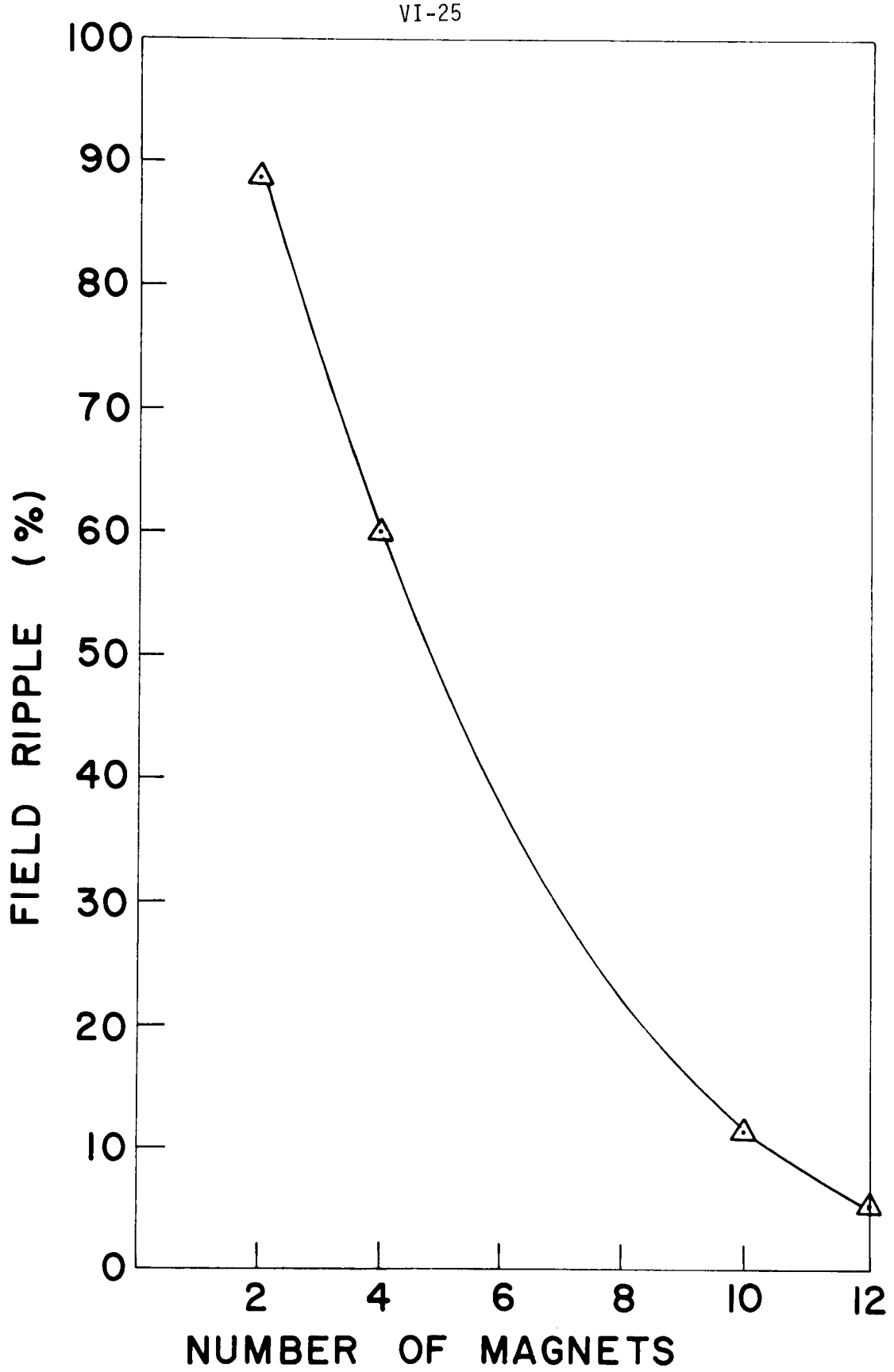


Fig. VI-C-2 Field Ripple vs. Number of Magnets

VI-C-3. Mechanical Design and Construction Techniques

VI-C-3-a. General Description

The proximity of the toroidal field (TF) trimming coils to the plasma preclude the possibility of using superconductors, both from radiation damage and heat load considerations. The same applies to the use of cryogenic coils. It was, therefore, decided to make the trimming coils from normal copper water cooled conductors operating at relatively low temperature and not make any attempts to recover the energy in the power cycle. With the exception of finding a suitable insulator to use in this environment, the technology for making such coils is very straightforward.

The conductor selected is made of quarter hard OFHC copper, has a rectangular cross section 17.6 cm long and 2.3 cm thick. It has 8 1.14 cm diameter holes for cooling, equally distributed through it. Each coil has 16 turns in it, consisting of two layers of 8 turns, as shown in a cross-sectional view in Fig. VI-C-3. Since the major constituent of the field at the coil is toroidal, producing a radial force on the coil, the conductors are oriented with the major dimension perpendicular to the plasma chamber to better resist the radial forces and the attendant bending moments. In Fig. VI-C-4, therefore, the shorter of the two dimensions of the coil cross section would face the plasma chamber. This also means that the sharp 90^{o} bend needed to wind the coil will be made across the narrow dimension and only the gradual curvature needed to make the coil fit the outside of the blanket will be made across the wide dimension. The chosen geometry makes winding of the coil relatively easy.

Because of the closeness of the coils to the plasma chamber (the coils are immediately behind the blanket), conventional insulators of the fiberglass epoxy type cannot be used. After considering several options, including ceramic insulators, we have decided to use graphite tape as the insulator. Although one does not normally think of graphite as an insulator, it would be possible to use a tightly woven tape of graphite

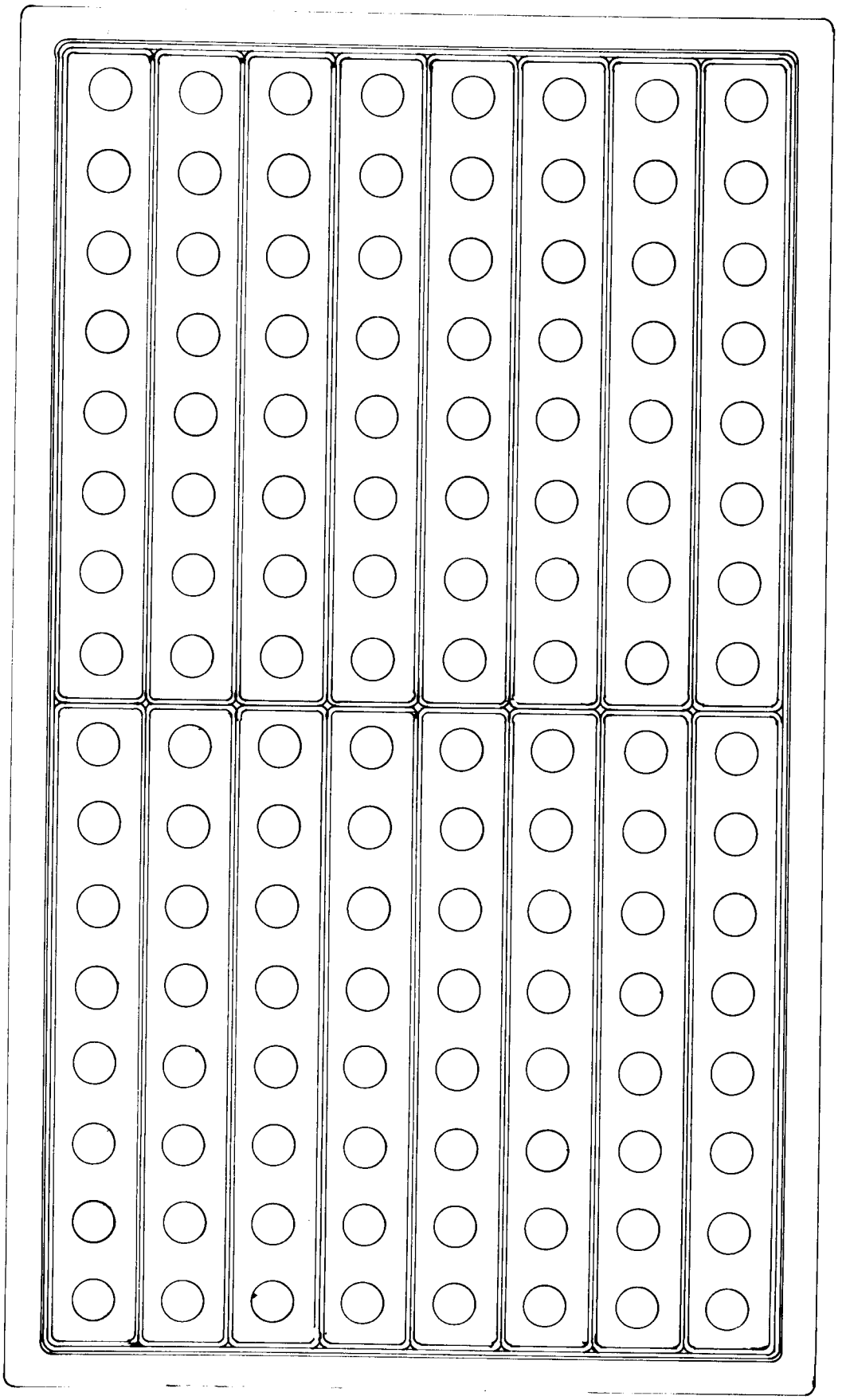


Fig. VI-C-3 Cross section of trimming coil.

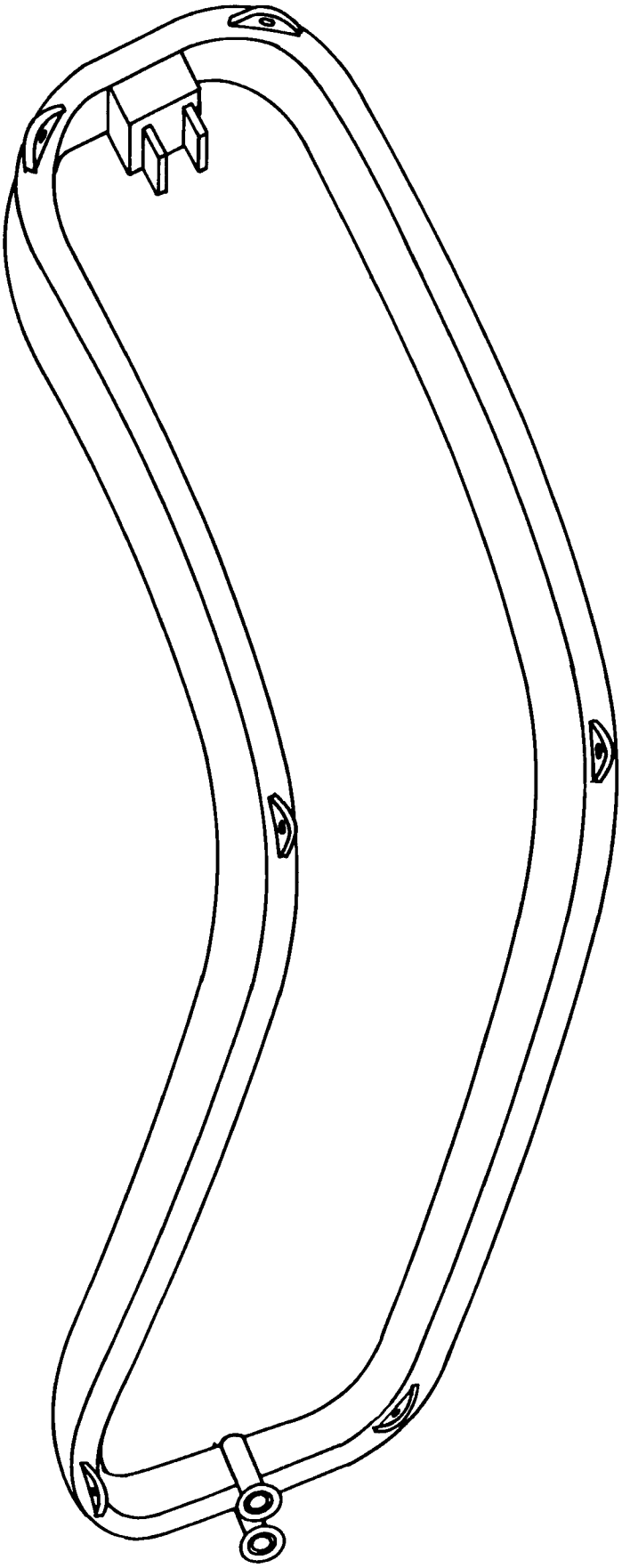


Fig. VI-C-4 Trimming coil.

fibers in place of the more conventional glass tape. Turn to turn voltage will be on the order of 3 volts and the maximum potential to ground, less than 60 volts.

It is envisaged that the conductor is wrapped with the graphite tape prior to winding and then the whole coil is wrapped with several thicknesses of the tape. The coil is then welded shut into a 1 cm thick titanium casing after which it is vacuum impregnated with a suitable epoxy and sealed. The epoxy will deteriorate very rapidly from the neutron and gamma fluxes but will remain in the voids, providing body for the graphite tape and allowing it to stay in place within the casing. At the low operating temperature of the coils (avg. temp. $\sim 60^{o}C$) the runaway swelling regime for graphite will be reached in a relatively short time. However, it is difficult to decide on a criterion upon which to base the ultimate uselessness of the irradiated graphite as an insulator. A great deal of swelling of the graphite fibers can be accommodated with no adverse effects. Moreover, swelling perpendicular to the fiber direction would be easier to accommodate than swelling parallel to it. Present graphite manufacturing techniques can insure that the graphite fibers will have the desired swelling characteristics. It should be emphasized that even if the coils cannot be designed to survive the full lifetime of the reactor, replacing them with new coils would in no way decrease plant availability. The trimming coils have to be removed for blanket replacement and then a scheduled coil renewal operation can be performed simultaneously with blanket renewal. The frequency at which coil replacement has to be made depends on the criterion adopted for the usefulness of graphite as an insulator as a function of the neutron and gamma ray dose.

Except for the method of insulating, the same coil manufacturing technique was proposed in TETR[4] for the vertical field coils. Joints will be made by induction brazing with low frequency RF using BAg filler. With proper preparation, the heat affected zone can be minimized. Copper inserts are used in the channels to provide alignment, strengthen the joint and improve sealing. Fig. VI-C-5 shows a typical brazed joint in the conductor.

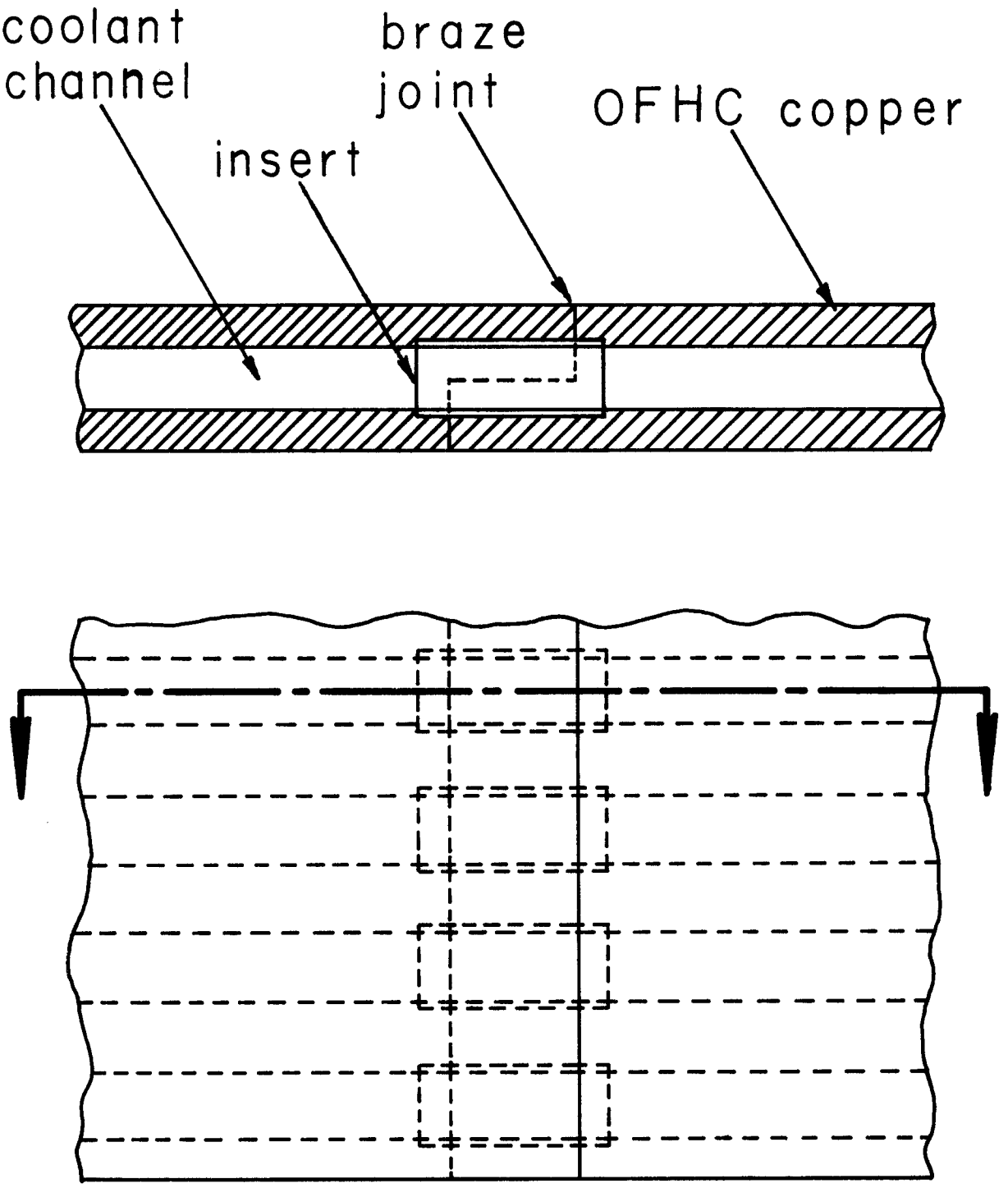


Fig. VI-C-5 Brazed joint in trimming coil.

The trimming coils are cooled with water entering at ~ 45 C and exiting at ~ 65 C. The maximum temperature of the conductor is 75 C and it occurs on the edge of the conductor facing the plasma in the first hole cooling area. Nuclear heating in the first hole area constitutes ~ 40% of the total heat removed by the coolant in the hole producing a temperature rise of 30 C in the water. In the last hole (16th) the nuclear heating is only 1% of the total in that zone. The total nuclear heating in each coil is 0.17 MW and the ohmic heating 1.10 MW, for a total of 1.27 MW.

Figure VI-C-6 shows the water routing through the pancakes of each trimming coil. There are three inlet connections and two return connections per pancake. The two end inlet connections each supply 1.98 ℓ/s of water, while the center inlet connection, which provides water flow in both directions, supplies a total of 3.96 ℓ/s. The two return connections each handle 3.96 ℓ/s. Temperature gradients are minimized by providing counter current heat exchange between the turns in all except the outermost and innermost turns. Table VI-C-1 gives a listing of the trimming coil specifications.

VI-C-3-b. Structural Considerations

There are two major forces acting on the trimming coils:

1 - an attractive force between adjacent vertical legs of two coils with the current going in the same direction in each.

2 - a force on the combined vertical leg due to the interaction of the current with the local magnetic field.

To calculate the second force, the net radial load on the combined vertical leg of two adjacent trimming coils, we need the magnitude of the field in that vicinity. Table VI-C-2 gives the various components and the total field as a function of radius and vertical distance. The total field $|B|$ is primarily toroidal since the major contribution comes from the toroidal field B_θ.

The force resulting from the interaction of the current with the local field $|B|$ (which is primarily toroidal) is radial and will alternate in direction, being inward for vertical legs located in line with a TF coil

1- INLET (1.98) l/sec.
2- INLET (3.96) l/sec.
3- INLET (1.98) l/sec.
4- OUTLET (3.96) l/sec.
5- OUTLET (3.96) l/sec.

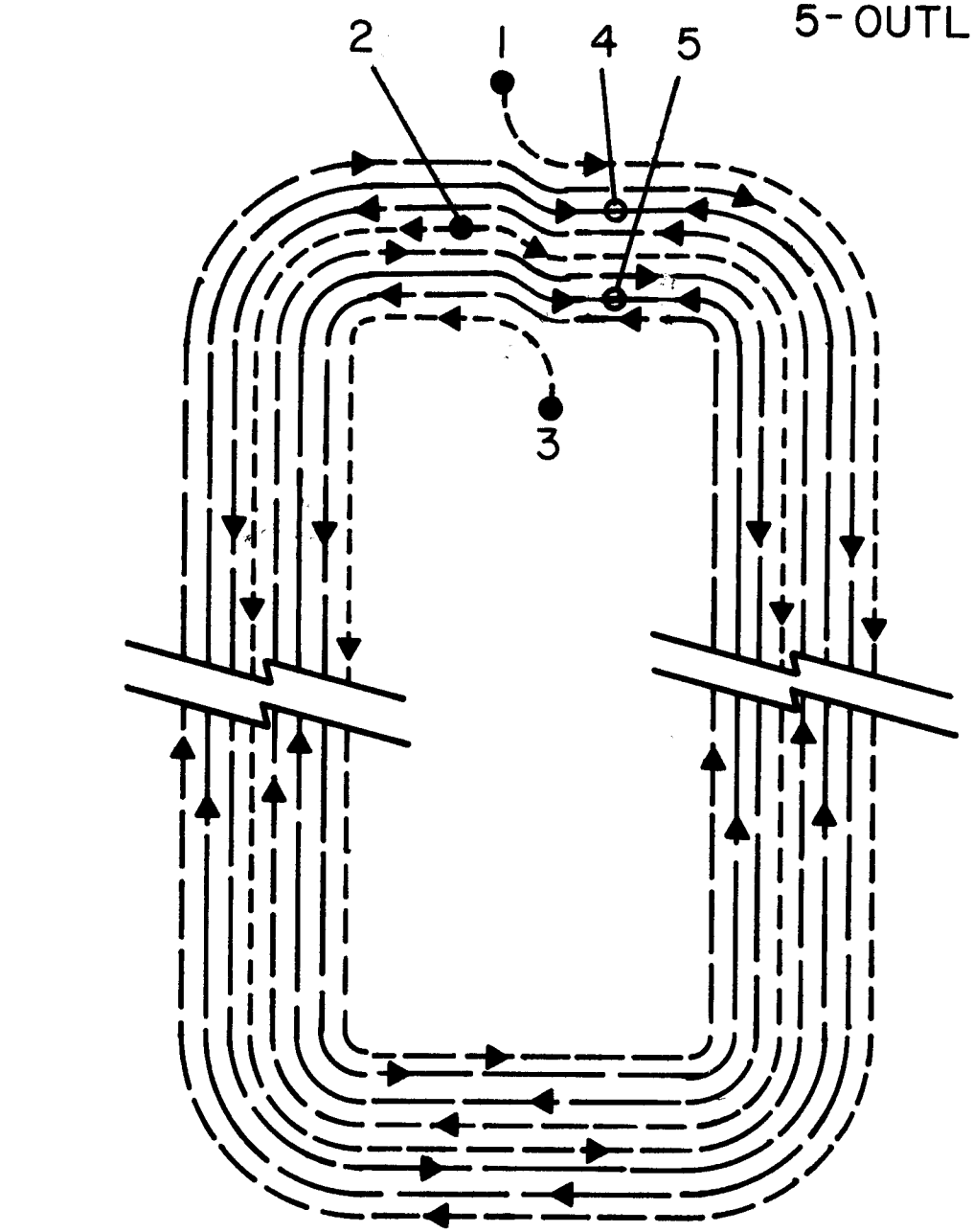


Fig. VI-C-6 Cooling water routing

Table VI-C-1
Trimming Coil Specifications

No. of Coils	16
No. of Turns/Coil	16
Ampere Turn/Coil (MA turn)	0.4
Current in Conductor (kA)	25
Conductor Dimension (cm)	2.3 x 17.6
Conductor Effective Copper Area (cm^2)	32.2
Resistivity at 60 C (μ ohm cm)	1.9
Current Density (A/cm^2)	815
Resistance of Coil (m Ω)	1.764
No. of Cooling Holes in Cond.	8
Diameter of Cooling Holes (cm)	1.14
Ohmic Heating in Each Coil (MW)	1.103
Nuclear Heating in Each Coil (MW)	0.17
Water Inlet Temp. C	45
Avg. Water Outlet Temp. C	65
Maximum Coil Temp. C	75
Water Flow/Coil (ℓ/s)	16
Total Water Flow (ℓ/s)	256
Maximum Water Pressure Drop (N/m^2) (psi)	3.4×10^5 (50)
Mass of Copper/Coil (tonnes)	9.0
Mass of Ti Alloy/Coil (tonnes)	1
Total Weight of Trimming Coils (tonnes)	160
Total Power Needed (time average) (MW) (over duty cycle of .918)	16.2

Table VI-C-2
Fields Along the Trimming Coils

R(cm)	Z(cm)	B_Z(Tesla)	B_R(Tesla)	B_θ(Tesla)	|B|(Tesla)
700	0				4.300
690	0	-1.43	.000146	4.312	4.543
670	130	-0.951	0.4568	4.695	4.8132
650	180	-0.7451	0.4071	4.8483	4.9221
630	220	-0.634	0.3339	4.8718	4.9242
610	250	-0.5733	0.27704	5.0329	5.0731
590	290	-0.55087	0.20349	5.3217	5.3541
570	320	-0.5629	0.16462	5.5447	5.5757
550	340	-0.60114	0.15154	6.1427	6.1739

and outward for those between TF coils. The magnitude of the force varies, depending on the local field. At the top and bottom extremities of the trimming coils the force is:

$$F_2 = (0.8 \times 10^6)\ A\ (6.174)\ \text{Tesla} = 4.939 \times 10^6\ \text{N/m}$$

and at midplane, it is

$$F_2 = (0.8 \times 10^6)\ A\ (\ 4.30)\ \text{Tesla} = 3.44 \times 10^6\ \text{N/m}\ .$$

Although these are substantial forces, they appear manageable if one approaches the problem with the thought of making the coils constant tension (or compression, depending on the direction of the force). If a constant tension (compression) curve is plotted and superimposed on the coil axis at midplane, it will be discovered that the coil shape deviates from it only slightly in several locations. This opens up two possible solutions to managing the radial force:

1. Make the shape of the coils conform to the constant tension curve and provide enough structure to reduce the tensile (compressive) stress in the copper to acceptable values.
2. Provide additional external structure to resist the bending moments at the points where the coil deviates from the constant tension curve.

In order for either of these solutions to be valid, mechanical restraint must be provided at the top and bottom of the vertical legs of the coils to transfer the tensile (compressive) forces to structure running circumferentially around the reactor. It should be pointed out that the net force on this structure will be zero, although there will be substantial bending moments in it from the alternately applied tensile and compressive force transmitted by the vertical legs.

It will be assumed that the trimming coils will be shaped to conform perfectly to the constant tension (compression) curve over most of the span from a meter at the top to within a meter of the bottom. A simple calculation yields the order of magnitude of the stress.

Taking the radial force at midplane and converting it into a tensile or compressive force in the coil for a radius of curvature of 4 meters, we get:

$$F_{coil} = 1.376 \times 10^7 \text{ N} .$$

The area of the copper and Ti alloy casing in the composite vertical leg is $\sim$ 1150 cm^2 and, therefore, the stress is:

$$\sigma_{con.} = 1.197 \times 10^8 \text{ N/m}^2 \text{ (17,370 psi)} .$$

This stress is below the creep limit for 1/4 hard OFHC at 75°C which seems to be a reasonable criterion to use in this case.[4] Also the fatigue limit at this stress is $\sim$ 10 x 10^6 cycles,[4] which in NUWMAK would be almost 100 years.

Bolted clamps will have to be provided for the mechanical restraint at the top and bottom. To facilitate removal of the clamps the bolts can be made captive and pneumatic tools used to disconnect them. Although this complicates the superconducting TF coil removal process, the advantage gained by providing the trimming coils is well worth the trouble.

Finally, a word should be said about the buckling of a vertical leg composite under compressive loading. This is not a simple problem in this case and no attempt will be made to solve it. It will be assumed that adequate lateral restraint can be provided by the blanket module to prevent the initiation of instability which would lead to buckling of the coil under compression.

VI-D. Poloidal Field Coil System

Because the poloidal field coils are entangled with the TF coil system, the positioning of the coils is one of the key issues for the maintenance of the tokamak reactor. By using the feature of gas puffing instead of a divertor for impurity control, the number of vertical field coils was minimized to only four pairs of coils, two of them located inside the "D" of the TF coil and the other two at the outside of the "D". This represents a trade-off between the power requirement to shape the plasma effectively and maintenance. The coils located inside of the TF coil are designed as cryogenic coils of high purity aluminum. Since the magnetic field in the region is rather high ($\sim$ 10 T), the coil should be dismountable for the maintenance of the system. The vertical field coils located outside of the TF coil as well as the ohmic heating coils are of superconductor.

The pulsed nature of these coils poses problems associated with ac losses in the conductor and a special design is required to minimize the losses and to obtain mechanical stability. Although the plasma rise time in NUWMAK (7 sec.) is relatively larger than in near term machines, we adopted a conductor developed and successfully tested with a prototype solenoid by Argonne National Laboratory for a pulse rate dB/dt $\simeq$ 8 T/sec.[17]

Generally OH coils are embedded in the central support structure of the TF coil system and it has been very difficult to allow for maintenance of the coils. However, the OH coils are designed to be serviceable in NUWMAK and the details of this feature are discussed in Chapter XI.

VI-D-1. Ohmic Heating Coil System

The ohmic heating coil system is designed to supply the flux swing needed to raise the plasma current and compensate for the voltage drop due to plasma resistance during the burn period, but it should produce no magnetic field at the plasma. To meet this requirement the OH coils are distributed as shown in Figure VI-D-1 and their specifications are given in Table VI-D-1. The plasma current reaches its maximum in seven seconds and the maximum rate of change in the magnetic field is dB/dt $\simeq$ 1.8 T/s. The plasma burns for 225 seconds.

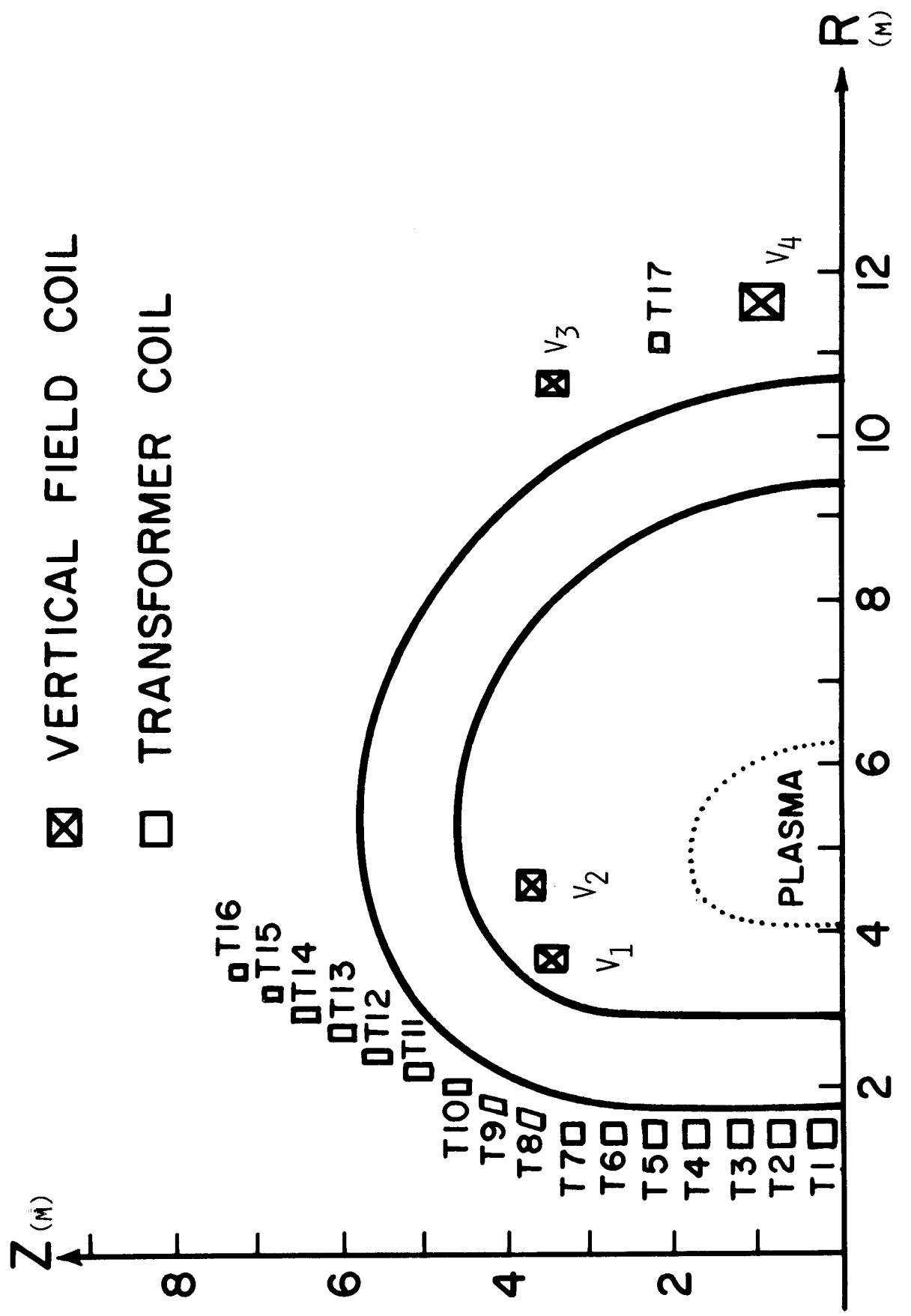

VERTICAL FIELD COIL
TRANSFORMER COIL
Z (M)
R (M)
8
6
4
2
2
4
6
8
10
12
T1
T2
T3
T4
T5
T6
T7
T8
T9
T10
T11
T12
T13
T14
T15
T16
T17
V1
V2
V3
V4
PLASMA

Fig. VI-D-1

Table VI-D-1

Ohmic Heating Coil Characteristics

Coil No.	R(m)	Z(m)	I(MA)	B_{max}(T)	$\dot{B}$(T/s)
T-1	1.46	0.25	2.87	6.8	1.67
T-2	1.46	0.75	2.87	6.85	1.68
T-3	1.47	1.25	2.86	6.9	1.7
T-4	1.48	1.78	2.85	7.1	1.75
T-5	1.49	2.25	2.82	7.1	1.75
T-6	1.52	2.75	2.76	7.2	1.77
T-7	1.56	3.25	2.68	7.3	1.80
T-8	1.71	3.72	2.59	6.1	1.50
T-9	1.89	4.19	2.47	5.4	1.33
T-10	2.07	4.65	2.30	5.2	1.28
T-11	2.25	5.12	2.16	5.1	1.25
T-12	2.43	5.59	2.04	4.5	1.11
T-13	2.68	6.01	1.80	3.8	0.93
T-14	2.95	6.44	1.49	3.3	0.81
T-15	3.21	6.86	1.22	2.6	0.64
T-16	3.48	7.28	1.00	2.4	0.54
T-17	11.00	7.25	0.22	1.2	

Argonne National Laboratory has designed a cable conductor[17] for the OH coil system of TNS and performed tests on a solenoid coil built with the cable conductor to demonstrate magnet stability with respect to dB/dt. It was demonstrated that the coil can be charged with pulse rate dB/dt ≃ 11 T/sec. The proposed conductor is shown in Figure VI-D-2. The basic strand consists of a superconducting composite and six pure copper wires. The pure copper wires are stranded around and soft-soldered to the superconducting composite with high resistivity solder in order to minimize the induced current path. Full stabilization is realized within the basic strand. The basic strand is coated with thin organic insulation to reduce the eddy current losses. The coating is thin enough so as not to hinder heat transfer characteristics.

Three basic strands, each of 1.56 mm diameter are transposed to form a basic cable. The final cable consists of 56 basic cables fully transposed around a stainless steel strip as shown in Figure VI-D-2 and carries 30,000 A at peak field B = 7.3 tesla. The stainless steel strip is about 3 mm thick. Turn to turn insulation is provided by G-10 strips 3 mm thick. The overall current density within the coil structure is about 2500 A/cm^2. Although the structure inside the winding is minimal, most of the stress is taken through the coil form to the central support structure of the TF coil where most of the OH coils are embedded. The support structure is under compression due to the centering force of the TF coil system.

The ac loss scaled for the OH coil system from ANL measurements is about 1000 W over a cycle. This value is relatively low because of the small dB/dt compared to the value of dB/dt ~ 8 T/s for which the conductor is designed. Somewhat larger values of loss may be affordable and the size of each strand can be larger to obtain better mechanical reliability in larger magnet systems.

Coil T-17, which is located near the outside vertical leg of the TF coil, is designed to carry its stress by the coil itself. This coil does not have other structures to carry the force as in the other OH coils which are buried in the central support structure. The conductor is similar to the one proposed in UWMAK-III[3] and is shown in Figure VI-D-3. This conductor was proposed and developed by D. Cornish for MFTF.[18] Three segments of cold reduced copper and a stainless steel segment are soldered together on

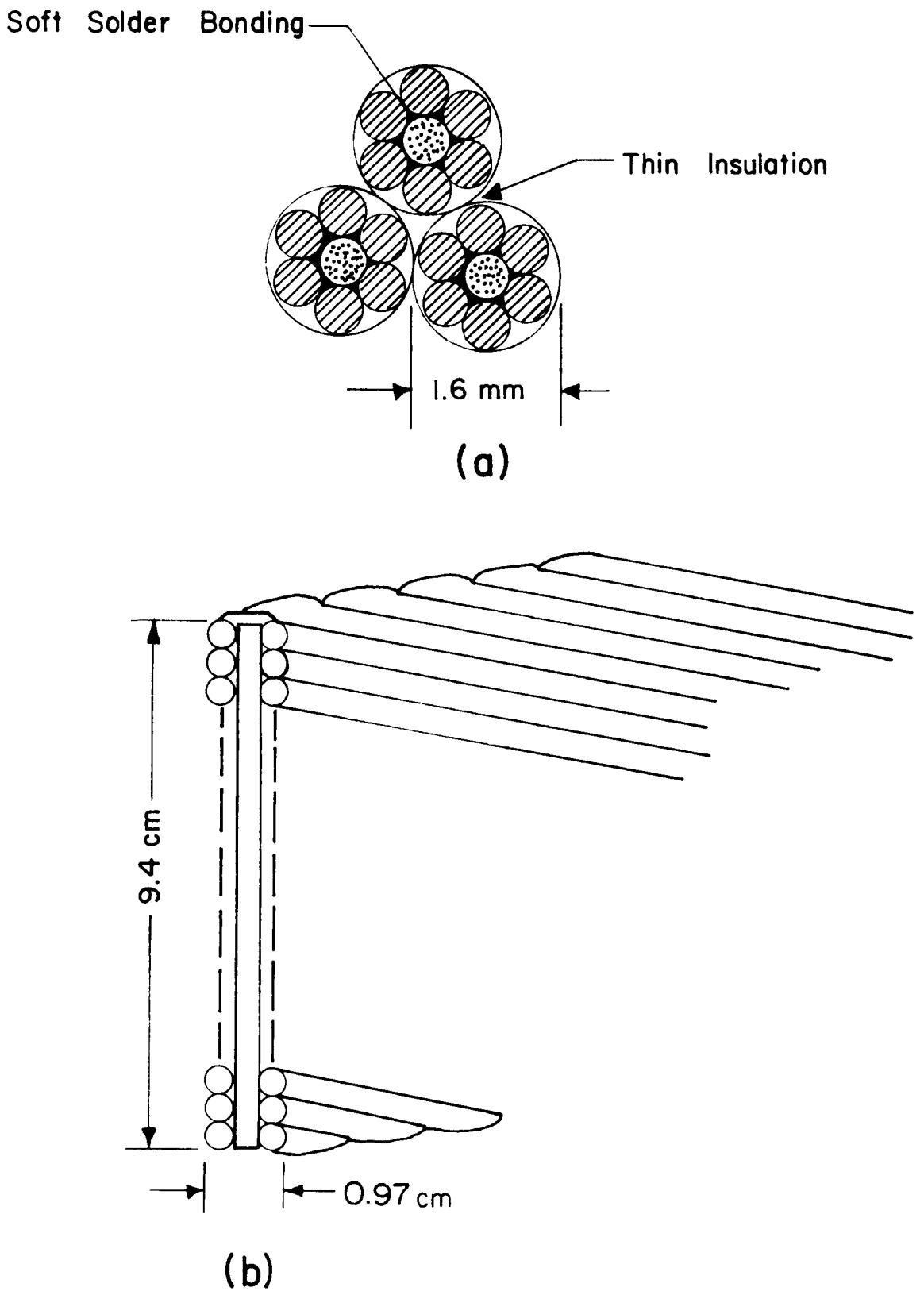


Fig. VI-D-2

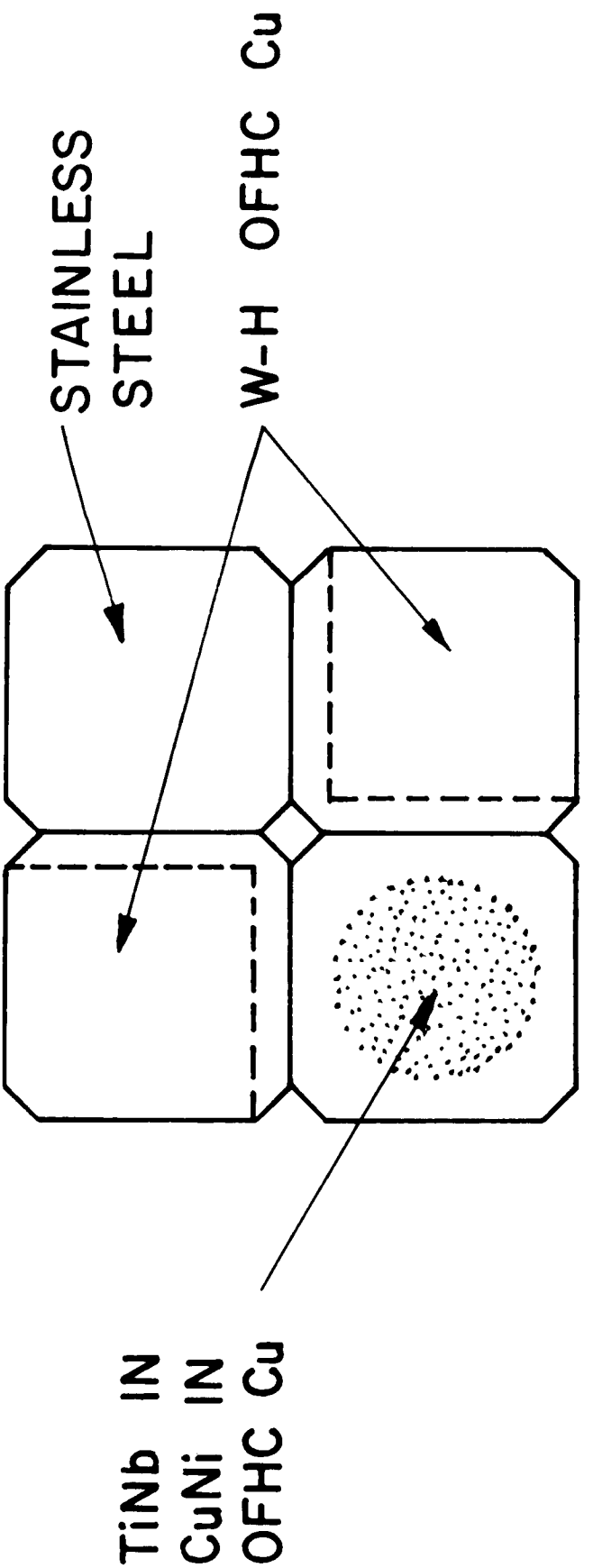


Fig. VI-D-3 Conductor cross section of ohmic heating coil T17

50 percent of their adjoining surface. The remaining 50% of the adjoining surface is devoted to the internal cooling passages. The combined lateral channels provided by these grooves and the longitudinal channels provided by the corners give excellent cooling characteristics and permit higher current density. The turn to turn insulation is provided by a spiral warp of B cured fiberglass reinforced epoxy tape covering 50% of every other conductor. The stainless steel carries the electromagnetic force and diagonally opposes the segment containing the superconductor. The design stress in the OFHC copper of the conductor is 1.2×10^8 N/m^2 (10% cold reduced OFHC copper) and 2.11×10^8 N/m^2 in 316 stainless steel. The conductor carries 11,000 A and the coil consists of 20 turns of the conductor.

VI-D-2. Mechanical Design of Cryogenic VF Coils

VI-D-2-a. General Description

The vertical field coil system in NUWMAK is divided into two groups; coils that are external to the toroidal field (TF) magnets and those that are within the TF bore. Because of the adopted philosophy in NUWMAK, namely that provision be made for removing and replacing TF coils in case of failure, it was necessary to make the latter group of VF coils (those within the TF bore) of a design that would make it possible for them to be taken apart. Although some groups[19] have proposed superconductive coils that can be taken apart and reassembled, we have decided not to follow that idea. Instead, we propose to use cryogenic high purity aluminum coils which are cooled with helium gas at ~ 30 K. The following considerations were used in making the selection:

1. Joints in cryogenic coils can be made relatively easily and have proved to be reliable. Moreover, any slight resistive heating at such a joint will not be detrimental to the operation of the coil.
2. As a measure of efficiency, a plot of the product of the resistivity for high purity aluminum (RRR 450) and the refrigeration factor as a function of temperature is given in Fig. VI-D-4. It yields a minimum between 25 K and 35 K.
3. In this temperature range there are only three logical cooling mechanisms:
   a. Liquid neon has a boiling point of 27.2 K at atmospheric pressure and is an excellent heat transfer medium. It was

PRODUCT OF THE RESISTIVITY OF 430 RRR HIGH PURITY ALUMINUM AND THE REFRIGERATION FACTOR AS A FUNCTION OF TEMPERATURE.

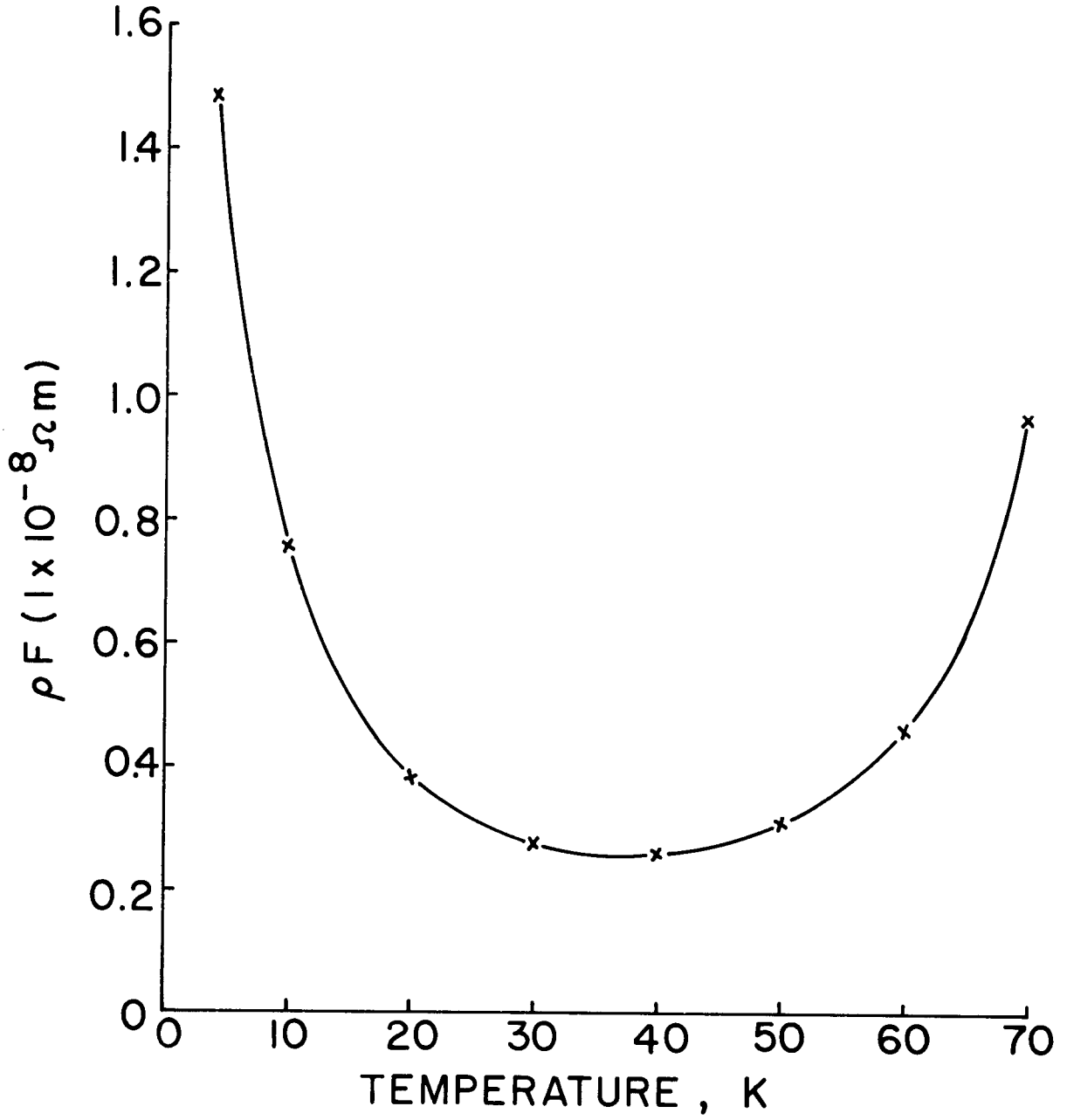


Fig. VI-D-4

rejected on the grounds of cost and availability of neon.

b. Liquid hydrogen - boiling point 20.4 K and also a good heat transfer medium. Hydrogen was rejected because of safety considerations.

c. Gaseous helium - this appears to be the logical choice. It is available in large quantities in fusion reactors, has good heat transfer properties in this temperature range and can be used in a low pressure system.

Designing a cryogenic coil is not that difficult but giving it the capability of disassembly is much more challenging. After considering several options we finally settled on a Bitter type coil design. In such a design the conductors carry large currents and are made in the form of thin discs stacked on top of each other and separated with insulators. Helium gas for cooling flows between the turns in the radial direction.

Since high purity aluminum has a very low yield strength, the conductor will be completely encapsulated within a casing of high strength aluminum. The high strength casing prevents the high purity aluminum from creeping under stress. The conductor sized for a current of 50 kA is 1.1 cm thick and 60 cm wide, of which the casing constitutes 2 mm all around. Coil V-1,which carries a current of 2.3 MA will have 46 turns and coil V-2, which carries 2.0 MA will have 40 turns.

The coils are designed with a single removable section $\sim$ 220 cm wide. Since the primary purpose for making the coil with a removable section is to make it possible to extract a TF magnet from the reactor, it will be assumed that the cryogenic VF coils can be rotated 360^{o} to allow the removable section to be aligned with the TF magnet being extracted. Providing the capability for rotation is much simpler than making the coil with eight removable sections (or more in the case of reactors with a large number of TF coils). Figure VI-D-5 is a side view and Fig. VI-D-6 a top view of a removable coil section. In the side view the removable section (bounded by the heavy line) is shown smaller in scale than is needed. Four turns are shown grouped together and then a micarta dummy turn is provided to reduce the extent of the joint at each end of the removable section. In the actual design 10 turns will be grouped together. Although this adds 5 cm to the overall height of the coil, it reduces the extent of each joint from 80 cm to 20 cm. The overlap between individual conductor turns at the splice is 2 cm and over this area, the casing is removed to

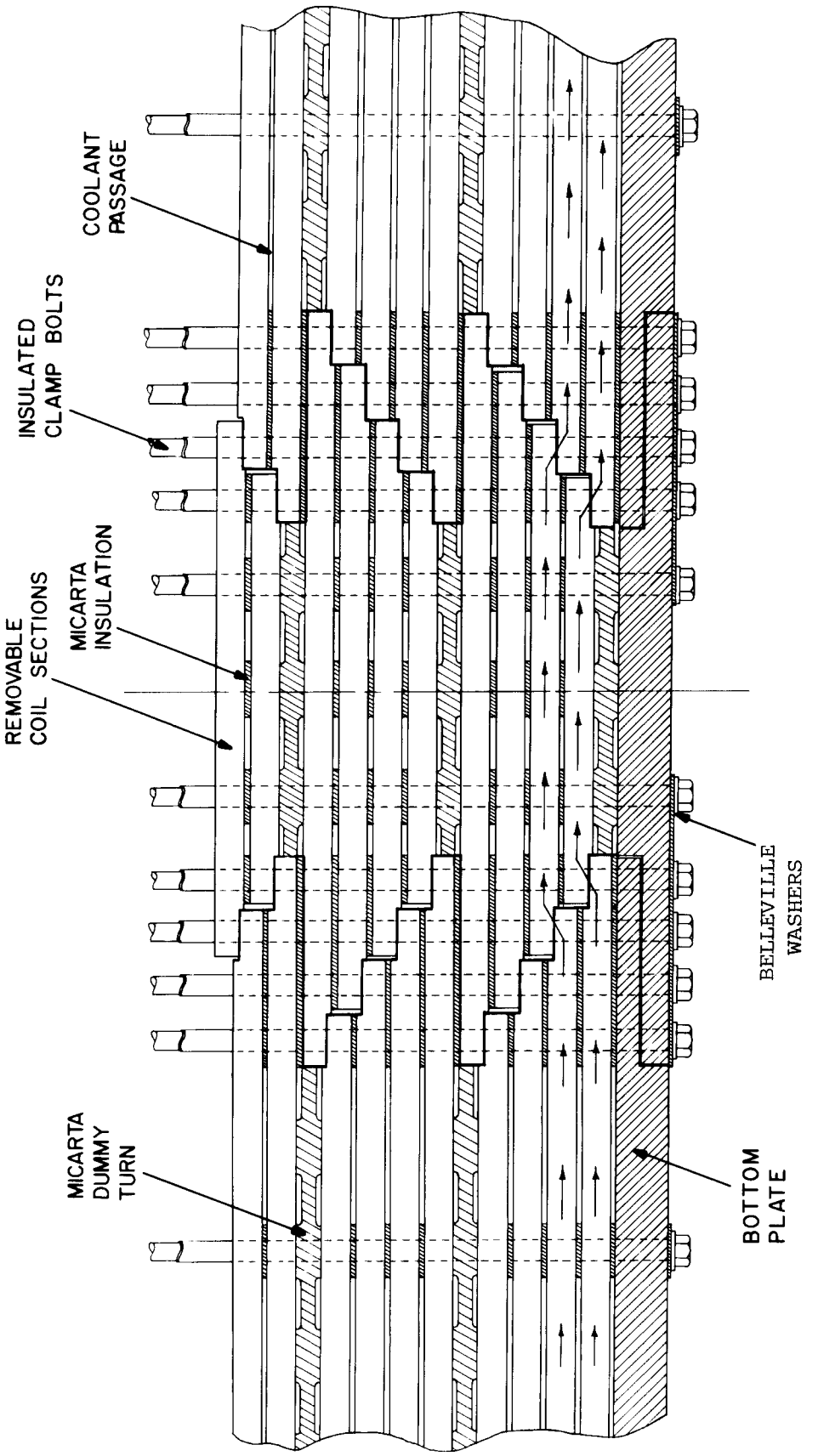

COOLANT PASSAGE
INSULATED CLAMP BOLTS
MICARTA INSULATION
REMOVABLE COIL SECTIONS
BELLEVILLE WASHERS
MICARTA DUMMY TURN
BOTTOM PLATE

Fig. VI-D-5

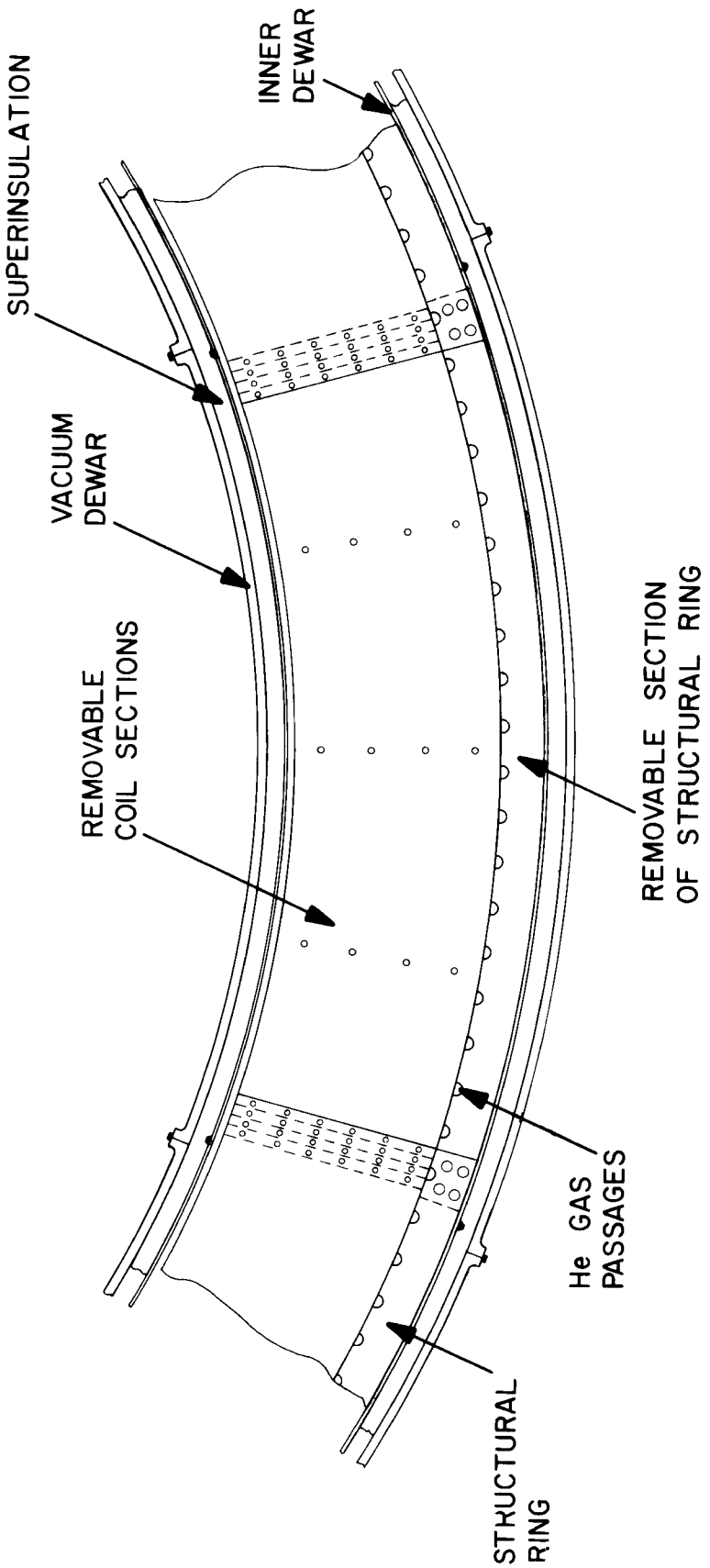

SUPERINSULATION
INNER DEWAR
VACUUM DEWAR
REMOVABLE COIL SECTIONS
REMOVABLE SECTION OF STRUCTURAL RING
He GAS PASSAGES
STRUCTURAL RING

Fig. VI-D-6

allow high purity aluminum contact between conductors. The path of the current is indicated by the arrows in Fig. VI-D-5. Some experimental work is needed to establish the best surface preparation which will provide a low electrical resistance at the splice without bonding the conductors to each other. High strength aluminum bolts, appropriately insulated, provide the clamping force between conductors. These bolts are not intended to restrain the conductors against the magnetc hoop forces. Rather, the conductors will be allowed to slide relative to each other at the joint and transfer the hoop load to a structural ring located on the outer radius of each coil. These bolts are also interspersed throughout the rest of the coil to tie the conductors together for handling.

The helium gas pressure boundary is called the inner dewar and will be made of 0.5 cm thick aluminum plate appropriately ribbed to contain the 2 atm of helium gas pressure. This will be followed by 5 cm of superinsulation in an evacuated space. The vacuum dewar is also made of aluminum plate 1 cm thick. Micarta spacers will be used to transmit the vertical forces across the vacuum superinsulated space. Table VI-D-2 gives the material specifications for coils V-1 and V-2.

VI-D-2-b. Structural Considerations

Table VI-D-3 gives the magnetic field values and the resultant forces on the cryogenic VF coils V-1 and V-2. The radial force on the coils is proportional to B(z)I, where B(z) is the total vertical field and I the current in the coil. The total vertical field in turn is composed of the local vertical field and the coil self field. The fields add up such that V-1 is in tension and V-2 in compression.

The joints in the coils are designed to slip under load, thus transferring the radial force to a structural ring located at the outer or inner radius of the coil depending on the direction of the forces (see Fig. VI-D-6). Obviously, the structural ring will also need a removable section. It is envisaged that interleaving joints with tapered pins can be provided for this purpose. The stresses at the joints will determine the size of the ring.

Table VI-D-2

Material and Power Specifications for the Cryogenic VF Coils V-1 and V-2

	V-1	V-2
Major radius (m)	3.5	4.5
Total current (MA)	2.3	2.0
Conductor current (kA)	50	50
Number of turns	46	40
Cross section of current carrying conductor (cm^2)	0.7x59.6	0.7x59.6
Overall cross section of conductor (cm^2)	1.1x60	1.1x60
Mass of HPA in cond./coil (tonnes)	11.5	12.7
Mass of HSA in cond./coil (tonnes)	6.8	7.5
Mass of HSA in structural ring/coil (tonnes)	4.2	4.1
Mass of HSA in dewars/coil (tonnes)	2.82	3.47
Mass of micarta spacers/coil (tonnes)	3.82	4.41
Total mass of each coil (tonnes)	29.14	32.18
Time average ohmic heating/coil (kW)	60	68
Room temp. power requirement/coil (MW)	1.56	1.77

HPA - high purity aluminum
HSA - high strength aluminum

Table VI-D-3

Magnetic Fields and Forces for the Cryogenic VF Coils V-1 and V-2

	V-1	V-2
Major radius (m)	3.5	4.5
Vertical location (m)	$\pm$ 3.5	$\pm$ 3.75
Current (MA)	2.3	2.0
Local vertical field (tesla)	0.446	-0.504
Self field at inner radius (tesla)	1.78	1.51
Self field at outer radius (tesla)	1.28	1.15
Total vertical field B(z) at inner radius (tesla)	2.23	1.00
Total vertical field B(z) at outer radius (tesla)	0.834	1.65
Radial field B(r) (tesla)	0.122	0.3
Radial force (N/m)	3.21×10^6	$-1.3 \times 10^{6*}$
Vertical Force (N/m)	2.8×10^5	6×10^5

*Negative value indicates a compressive force

The stresses at the joints in the structural ring will be maintained at 3.4×10^8 N/m^2 (50,000 psi). Since only one-half of the material will carry the load at the joint, the stresses in the structural ring itself will be 1.7×10^8 N/m^2 (25,000 psi). Coil V-1 which is in tension will require a structural ring 10 cm thick and 65 cm high (the same height as the coil). Coil V-2 is in compression and will also require a 10 cm thick structural ring 58 cm high. Precautions against buckling of the ring will have to be provided in this case.

The vertical loads on the coils are proportional to B(r)I. No net force will result from them because they will be balanced by the top and bottom coil sets. However, the load between the sets will be reacted by the shield structure.

VI-D-2-c. Thermal Hydraulics

The conductor turns are separated by a 0.2 cm gap for the helium gas to flow through. The cooling helium is introduced at the inner radius, flows radially outward between the turns and exits through manifolds on the outer radius. One-half of the surface area between turns will be covered with micarta spacers. This means only one-half of the conductor surface area will be actively cooled. If the spacers are 10 cm long then the gap between them will be 10 cm long.

In this design the high purity aluminum will be operated at 35 K, where its average resistivity is $\sim 1 \times 10^{-8}$ ohm cm.[20] The steady state ohmic heating in coil V-1 is 60 kW and the surface heat flux is 0.01 W/cm^2.

The incoming helium gas is assumed to be at 25 K and 2 atmospheres. If we assume a temperature rise of 0.1 K in the gas, then the mass flow would have to be 114 kg/sec and the velocity in the coil $\sim$ 30 m/sec. The thermal hydraulic parameters for the cryogenic coils are given in Table VI-D-4.

The total power needed to drive the four cryogenic coils is 256 kW. This energy has to be extracted at 25 K. In addition, conduction and radiation losses are estimated at 80 kW for a total of 336 kW. The refrigeration power needed (using a refrigeration factor of 34) is 11.4 MW.

Table VI-D-4

Thermal Hydraulics Parameters for the Cryogenic Coils V-1 & V-2

Cooling medium	Helium gas
Inlet temperature	25 K
Inlet pressure	2 atm.
Density, ρ	3.9×10^{-3} g/cm^3
Thermal conductivity, k	0.308×10^{-3} W/cm K
Viscosity, μ	41.6×10^{-6} g/cm-s
Prandtl number, N_{pr}	0.711
Specific heat, c_p	5.264 J/g K
Sonic velocity, c	296 m/s

	V-1	V-2
Ohmic heating, kW	60	68
Mass flow, kg/s	114	129
Gas temp. rise, K	0.1	0.1
Velocity in the coil, m/s	29.6	30.3
Pressure drop, N/m^2 (psi)	2.4×10^4 (3.4)	2.5×10^4 (3.5)
Reynolds number, N_{re}	1.1×10^5	1.1×10^5
Heat transfer coefficient, W/cm^2 K	1×10^{-3}	1×10^{-3}
Surface heat flux, W/cm^2	1×10^{-2}	1×10^{-2}
Average conductor temperature, K	35	35

VI-D-2-d. Disassembly Procedure

In order to disassemble one of the cryogenic coils, the following steps have to be taken:

1. The coolant is pumped out.
2. The coolant lines and electrical connections are disconnected.
3. The coil is rotated to align the removable section with the disassembly location.
4. Some shield segments are removed to provide access to the coil.
5. A segment of the vacuum dewar is removed by machining off the welds on the upper lid and outer side of the dewar.
6. Superinsulation is removed.
7. The helium dewar segment is removed in the same manner as in (5).
8. Clamp bolts in the removable section region are removed and the top plate taken off.
9. Tapered pins are pulled out of the structural ring removable section and the section removed.
10. The upper group of conductor sections can now be lifted up and out. Subsequent sections are slid radially out after the joints are loosened.
11. The bottom plate is removed.
12. Remaining bottom and inner sides of the dewars are machined off and removed.

The coil is now completely disassembled, making it possible to remove a TF coil through the resulting gap. The reverse procedure is followed in replacing the removable section.

VI-D-3. Superconducting Vertical Field Coil

Two pairs of vertical field coils, V-3 and V-4 in Fig. VI-D-1, located outside of the "D" of the TF coils are of superconducting material. Unlike V-1 and V-2 they do not have to be dismounted in the process of removing TF coils. The conductor for these coils is similar to T-7 and is illustrated in Figure VI-D-3. Each turn carries 10,000 A. The specifications of these coils are listed in Table VI-D-5.

Table VI-D-5
Specification of Superconducting Vertical Field Coils

	V-3	V-4
Radius (m)	10.50	11.50
Vertical location (m)	±3.5	±1.0
Current (MA)	-2.00	-3.50
Maximum field	-1.2 T	-1.5T
Average B(R)	-0.6 T	-0.26 T
Maximum B(z)	-1.0 T	-1.2 T
Current/turn (A)	10,000	10,000
No. of turns	225 (15x15)	361(19x19)
Stress in conductor	$1.56 \times 10^8 N/m^2$	$1.71 \times 10^8 N/m^2$
Stress in structure	$2.66 \times 10^8 N/m^2$	$2.91 \times 10^8 N/m^2$
Strain	0.13%	0.14%

VI-E. Energy Storage and Power Supplies

VI-E-1. Energy Storage Conductor

The superconductive energy storage unit for NUWMAK stores 2 MWh (7.2×10^9 J) of which 56% is cycled in and out of storage. Two MWh storage units proposed and designed for UWMAK-III and the NAL accelerator ring by the University of Wisconsin are used.

VI-E-2. Power Supplies

VI-E-2-a. Toroidal Field Magnet

The estimated inductance of the "D" magnet L is about 290 H is 30 GJ (8.3 MWh). Assuming 12 hrs. charging time, the voltage rating of the power supply will be about 100 volts and an ac/dc bridge rated at 1,500 kW is required for the power supply of the "D" magnets.

VI-E-2-b. Poloidal Field Coils

Figure VI-E-1 shows the plasma current and the current in coil T_1 of the transformer. The form of the time variation in current in the remaining coils of the transformer is the same as that in coil T_1 and the current in the vertical field coils varies as in the plasma. Figure VI-E-2 shows the power requirement of the poloidal field coil system as a function of time for a reactor cycle and the stored energy in the system is shown in Figure VI-E-3. The peak power required for the system is 1010 MW at 7 sec position. This power will be delivered from the 2 MWh energy storage units through a dc/ac/dc bridge. The circuit arrangement for the storage inductor and dc/ac/dc convertor unit can be found in the UWMAK-III report.[3]

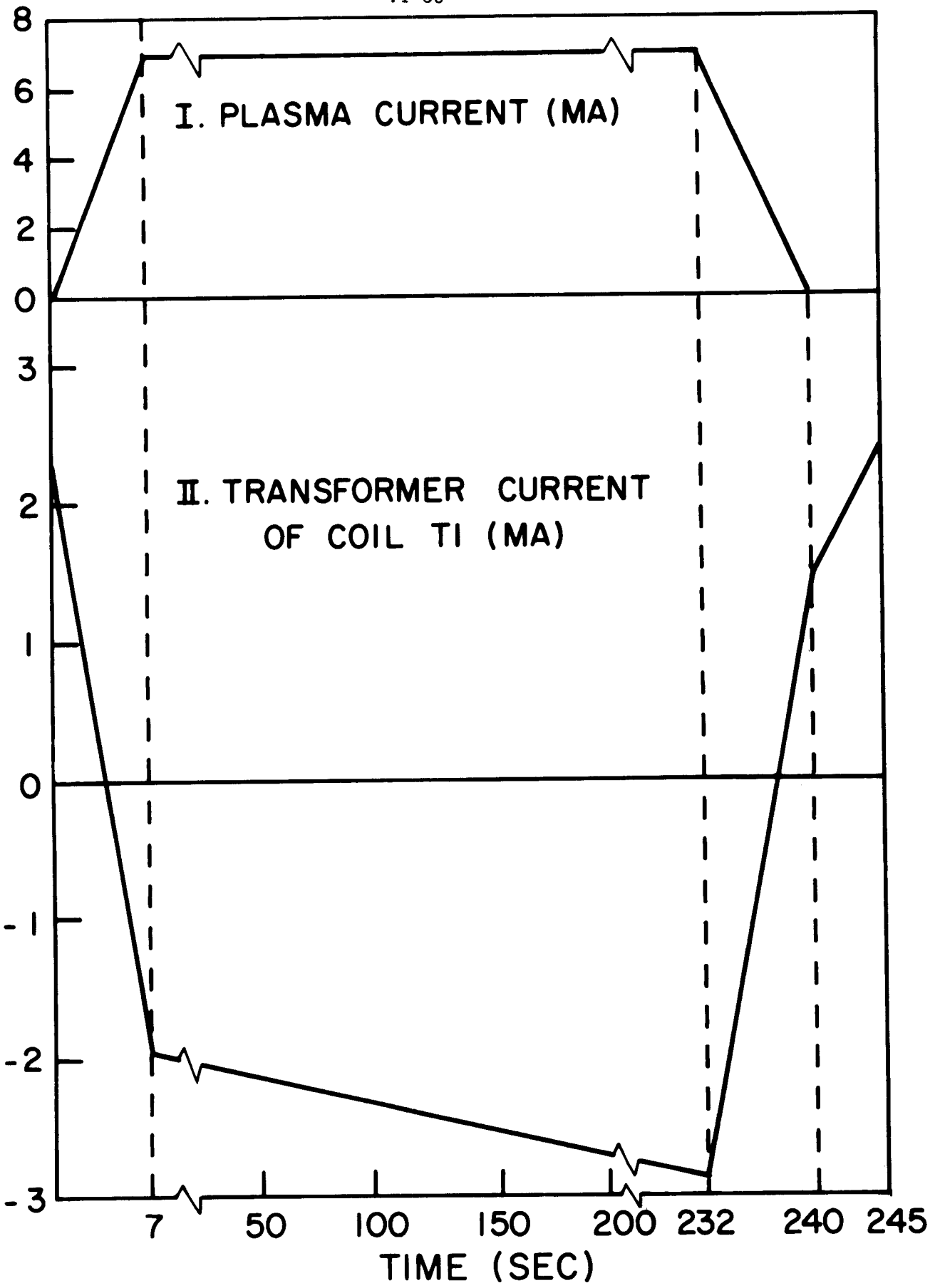

I. PLASMA CURRENT (MA)
II. TRANSFORMER CURRENT OF COIL TI (MA)
8
6
4
2
0
3
2
1
0
-1
-2
-3
7
50
100
150
200
232
240
245
TIME (SEC)

Fig. VI-E-1

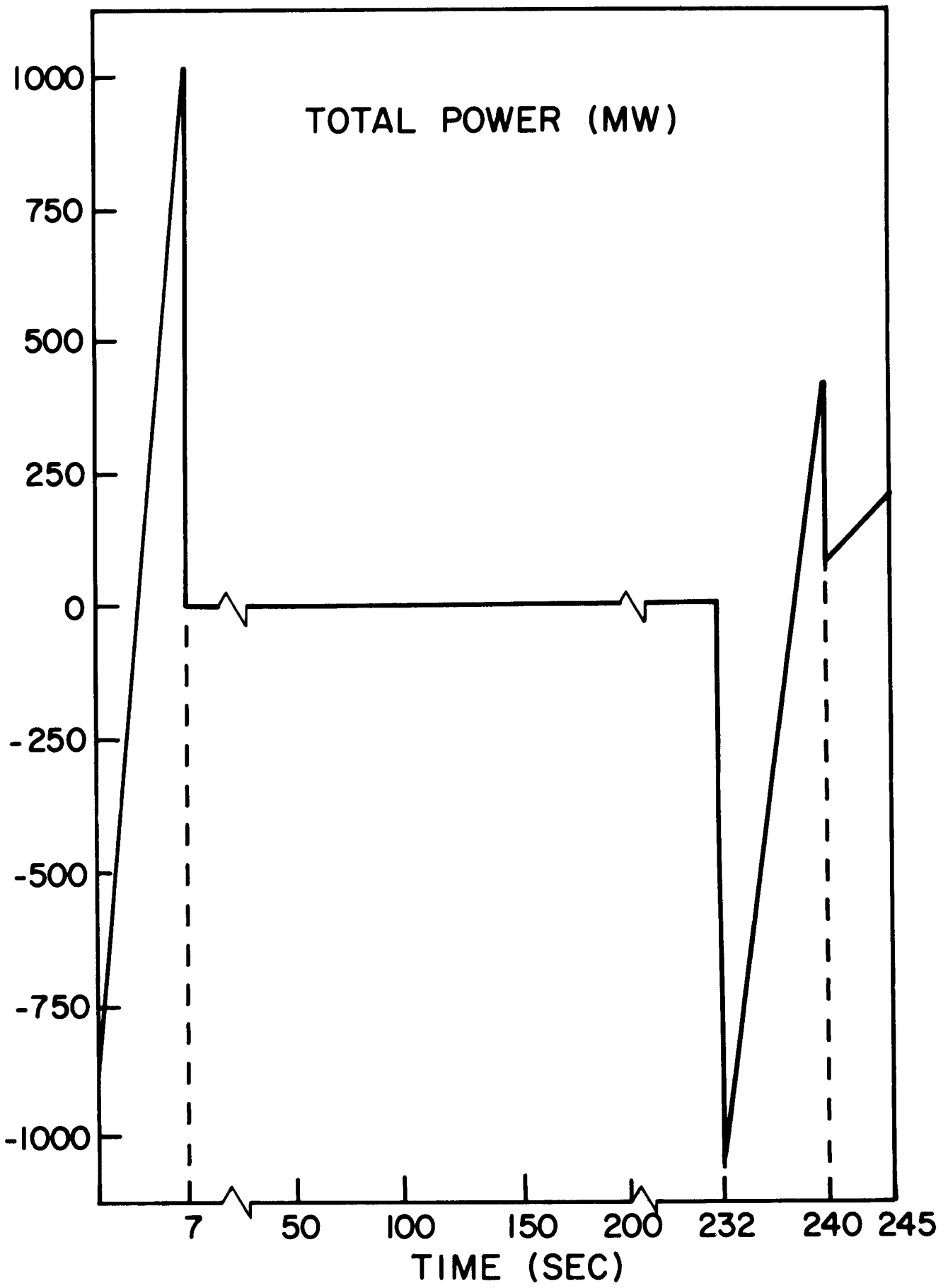

TOTAL POWER (MW)
1000
750
500
250
0
-250
-500
-750
-1000
7
50
100
150
200
232
240
245
TIME (SEC)

Fig. VI-E-2

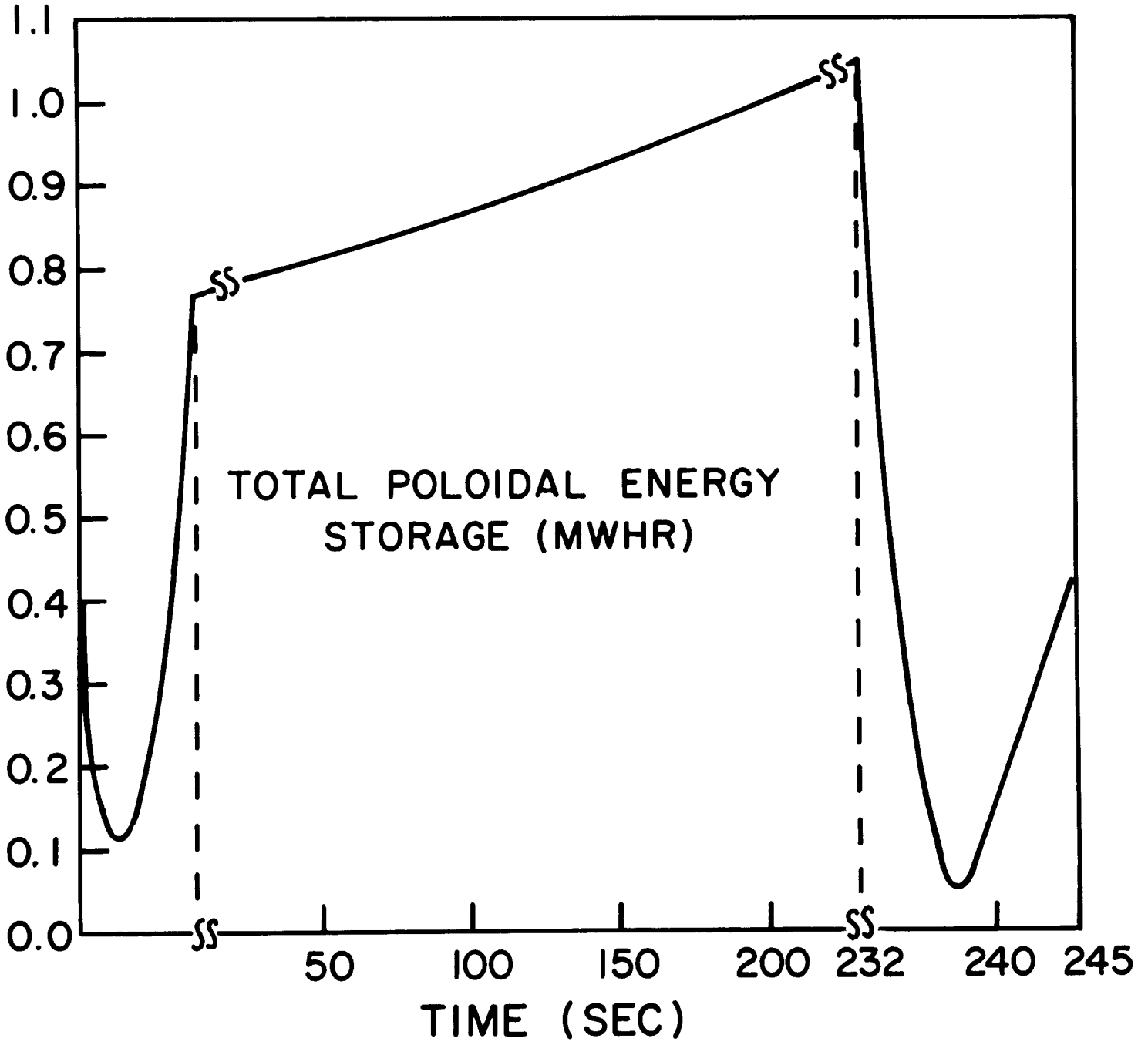

1.1
1.0
0.9
0.8
0.7
0.6
0.5
0.4
0.3
0.2
0.1
0.0
TOTAL POLOIDAL ENERGY
STORAGE (MWHR)
50
100
150
200
232
240
245
TIME (SEC)

Fig. VI-E-3

References for Chapter VI

1. B. Badger, et al., UWMAK-I, UWFDM-68, Dept. of Nuclear Eng., University of Wisconsin (Nov. 1973).

2. B. Badger, et al., UWMAK-II, UWFDM-112, Dept. of Nuclear Eng., University of Wisconsin (May 1975).

3. B. Badger, et al., UWMAK-III, UWFDM-150, Dept. of Nuclear Eng., Univ. of Wisconsin (July 1976).

4. B. Badger, et al., "TETR - A Tokamak Engineering Test Reactor", UWFDM-191, Dept. of Nucl. Engr., University of Wisconsin (December 1977).

5. S.W. Van Sciver, proceedings of the 7th Symposium on Eng. Prob. of Fusion Research, p. 690 (1977).

6. J.W. Lue and J.N. Laton, IEEE Trans. on Mag., Vol. MAG-13, No. 1, p. 601 (1979).

7. S.T. Wang, et al., IEEE Trans. on Mag., Vol. MAG-13, No. 1, p. 605 (1977).

8. H.R. Segal, et al., IEEE Trans. on Mag., Vol. MAG-13, No. 1, p. 807 (1979).

9. S.O. Hong and D.C. Larbalestier, IEEE Trans. on Mag., Vol. MAG-13, No. 1, p. 784 (1979).

10. D.C. Larbalestier - private communication.

11. K.F. Hwang and S.O. Hong, Proc. of the 7th Symposium on Eng Prob. of Fusion Research, p. 1531 (1977).

12. Hilal and McIntosch, Advances in Cryogenic Engineering 21 p. 69 (1975).

13. H.R. Segal, IEEE Trans. on Mag., Vol. MAG-13, No. 1, p. 109 (1977).

14. R.W. Boom, et al., Energy Storage Project Report, Vol. II, University of Wisconsin (1978).

15. R.W. Moses, Jr. and W.C. Young, Proc. of the 6th Symposium on Eng. Prob. of Fusion Research, p. 917 (1975).

16. V.L. Vdovin, et al., "Ion Cyclotron Heating in the T-10 Tokamak", presented at the USA-USSR Meeting on High Frequency Heating of Toroidal Devices, June 1978, Sukhumi, USSR.

17. S.H. Kim, et al., IEEE Trans. on Mag., Vol. MAG-15, No. 1, p. 840 (1979).

18. D. Cornish, et al., IEEE Trans. on Mag., Vol. MAG-15, No. 1, p. 530 (1979).

19. J. Powell, D. Hsieh, J. Lehner, "Deals: A Demountable Externally Anchored Low Stress Superconducting Magnet System for Fusion Reactors", BNL-50616.

20. "Handbook of Materials for Superconducting Machinery", Metals and Ceramic Information Center, Battelle Columbus Lab., Nov. 1975.

21. "Cryogenic Energy Storage System Design Report", Fermi National Laboratory Report FN-264 (1974).

VII. Blanket Design

VII-A. Design Philosophy

The NUWMAK design philosophy is to incorporate our experience from the UWMAK series, combine it with the recent developments in plasma physics, to design a more optimized tokamak reactor. It is aimed at maximizing the strengths of fusion, while minimizing its weaknesses. Its end product is a reliable, maintainable and reasonably economical power reactor. It should be environmentally acceptable and economically competitive. It should alleviate or avoid as many problems as possible which were uncovered in the first generation of fusion reactor design studies, i.e., the UWMAK series. The blanket design is consistent with this philosophy.

Most of the unusual problems associated with a tokamak blanket arise from the special characteristics of the tokamak D-T reactor. These special characteristics are:

a. Cyclic behavior of the plasma
b. Tritium breeding and confinement
c. Non-uniform energy distribution
d. Complicated geometry.

In the early designs, many problems were found in the course of the design process, and the remedies for those problems usually came as an afterthought. For instance, to provide a constant energy input to the power cycle, two large thermal energy storage units were provided. However, such a remedy increases the complexity and cost to the reactor system. For the second generation system studies, many of the problem areas have been discovered. To provide a sound system design, those problem areas should be kept in mind so that the system design can be aimed at solving as many problems as possible.

In order to avoid or alleviate as many problems as possible, it is essential to list those problems before the design starts. The causes of these problems should be located and a solution or solutions for each of these problems should be planned. The difficult part is that the solution of each problem was not only to be consistent with solutions for other blanket problems, but also consistent with other requirements of a tokamak fusion reactor. Table VII-A-1 tabulates the problems associated with the blanket, their causes, and the solutions provided in the NUWMAK design. The solutions provided here are consistent with each other, and also satisfy the requirements

Table VII-A-1 Problems, Causes and Possible Solutions for a Tokamak Blanket

Problems	Caused By	NUWMAK Solution
Thermal Fatigue	Cyclic Plasma	Ti Structure, Boiling Water Cooling
Thermal Storage	Cyclic Plasma	Phase Change (of Breeding Material) Thermal Storage
Intermediate Loop	H_2O-Li Compound Reaction Possibility	Li_{62} Pb_{38} Breeding, Redundant Structure
T-Diffusion	Toward Cooling Water	Multiple Layer Coolant Tube Design
High 1st Wall Thermal Load	High Wall Loading, No Divertor	Ti Structure, Boiling Water Cooling
Coolant Tube Maintenance	Tube Leak	Double Wall Tubes (Redundancy)
Waste Disposal, Reprocessing	Radioactivity	Ti Structure
Blanket Life	Radiation Damage	Low Operating Temperature

of materials, radiation damage, and neutronics analyses.

VII-B. Material Selection

VII-B-1. Structural Material

The structural material for the NUWMAK blanket is Ti-alloy. Ti-alloy is used for its high strength-to-weight-ratio, good fatigue resistance, high resistance to crack growth, fabricability, low long term residual activity, and well established industry. A detailed discussion of the applicability of Ti-alloys for use in a fusion reactor environment appears in Chapter IX. Ti-6Al-4V was chosen for the first wall and coolant tube material because of its weldability, while Ti-6Al-2V-4Sn-2Mo was chosen for the internal blanket structure and tube support because of its relatively high temperature stability. Some of the physical and mechanical properties of Ti-6-4 are summarized in Table VII-B-1. Chapter IX provides more detailed information.

The advantages and problem areas of using Ti-alloys as structural material are summarized in Table VII-B-2. From a thermal hydraulic point of view, there are two unique properties of Ti-alloys, especially for Ti-6-4, which have to be further discussed. The first is the very low thermal conductivity, which is about half that of 316 SS. This low thermal conductivity produces a large temperature difference across the coolant tube wall. This large temperature difference results in a fairly high thermal stress, though not as high as 316 SS at similar conditions. The second problem, which further compounds the problem caused by low conductivity, is that titanium alloys have a very narrow range of operating temperature. The minimum operating temperature, which is determined by solubility of hydrogen isotopes in titanium, is 300^{o}C with the presence of tritium. The maximum operating temperature is determined by phase stability and, for Ti-6-4, is probably limited to 430^{o}C. In order to include a safety factor and to account for the uncertainties encountered, a maximum design temperature of 400^{o}C is used. The maximum design temperature for Ti-6242

Table VII-B-1 Physical Properties of Ti-6-4 (at $400^{o}C$)

Atomic Weight	45.9
Melting Point	$1668^{o}C$
Mass Density	$4.4\ g/cm^{3}$
Yield Strength	530 MPa
Modulus of Elasticity	85 GPa
Yield-to-Weight Ratio	120 N•m/g
Thermal Conductivity	.12 W/cm•K
Coefficient of Thermal Expansion	$10 \times 10^{-6}/^{o}C$
Heat Capacity	668.8 J/kg•K

Table VII-B-2 Advantages and Problems Associated With Ti Structure

Advantages (Relative to Stainless Steel)

1. Higher Strength
2. High Strength to Weight Ratio
3. Better Fatigue Life
4. Better Corrosion Resistance - Li
5. Lower He Production
6. No Void Swelling (Yet)
7. *Inherently Non-Magnetic
8. *Fairly Well Established Industry
9. *Abundant Resources

*Not Relative to Stainless Steel

Problems

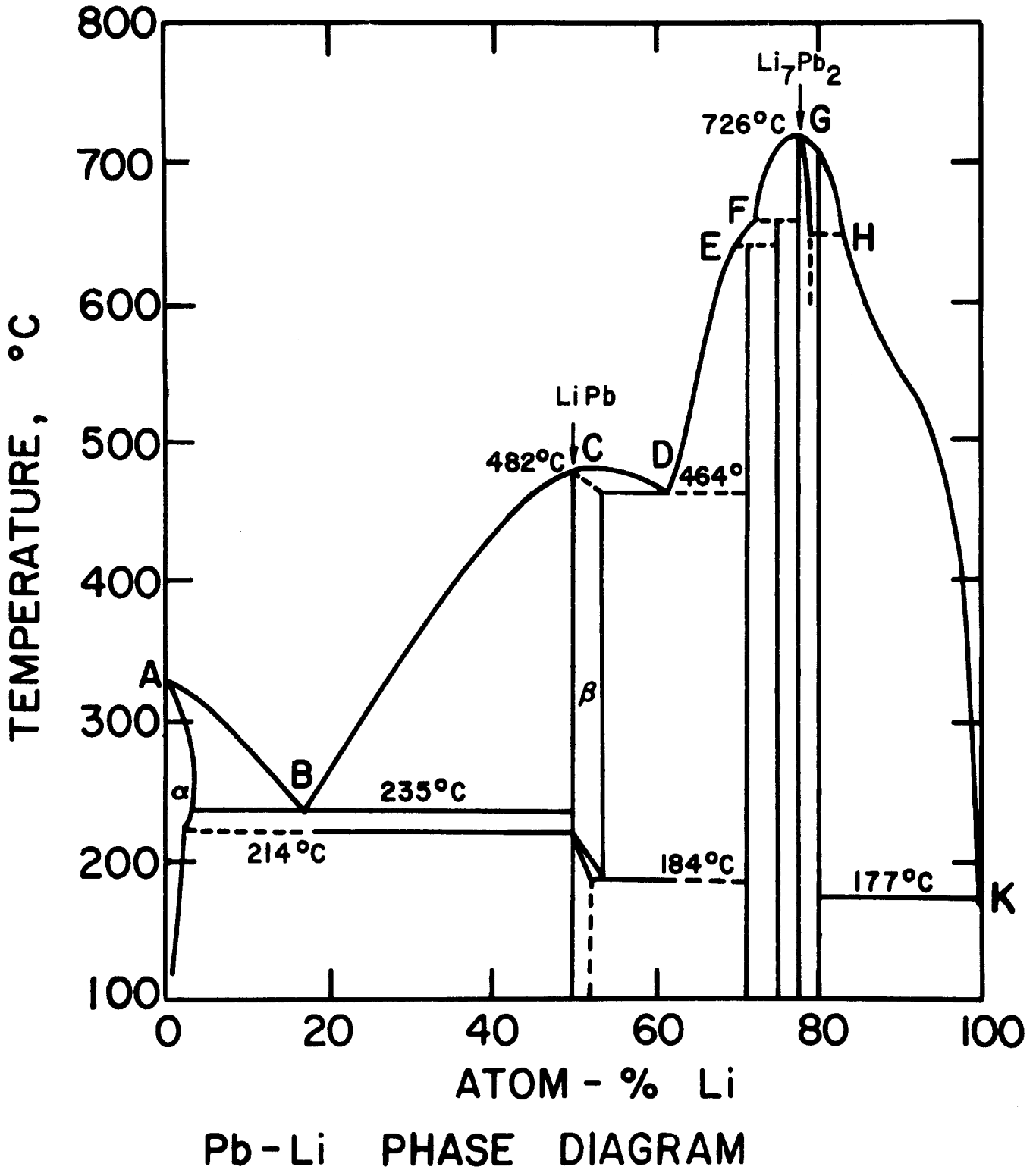
1. Very Limited Operating Temperature Range
2. Very Low Thermal Conductivity
3. More Costly
4. Lack of High Flux n Data
5. Hydriding < $300^{o}C$

is picked at 500°C. This poor thermal conductivity and the narrow operating temperature range causes severe restrictions to the thermal hydraulic design of the blanket. A coolant with a relatively larger coolant temperature rise, $(T_{in} - T_{out})$, and a small heat transfer coefficient, h, will cause a large first wall temperature fluctuation during a plasma cycle. This temperature fluctuation can easily exceed the temperature limits. Thus, for example, helium cooling can be essentially ruled out for a fusion power reactor first wall with titanium structure.

VII-B-2. Breeding Material

Natural lithium is usually considered the primary candidate for the breeding material.[1] However, corrosion, tritium recovery and magneto-hydrodynamic problems cause concern of using lithium to breed. More recent efforts have studied the possibilities of using Li_2O[2,3] and Li_7Pb_2[4] as the breeding materials. A diffusion study[5] shows that the tritium diffusivities through both Li_2O and Li_7Pb_2 are relatively high so that tritium can be recovered by the diffusion process. Li_7Pb_2 is the lithium-lead compound with the highest melting point of 726°C. This melting temperature is still relatively low so that careful design must be provided to keep the breeding material below its melting temperature. However, sintering may still be a problem because Li_7Pb_2 becomes a big chunk at a high temperature. If this happens, the diffusion path of tritium increases and tritium recovery becomes difficult.

Lithium-lead compounds are interesting materials. The activity of lithium is very low due to the presence of lead, so that the solubility of tritium in Li-Pb is much lower than that in pure lithium. Therefore, the tritium inventory can be much smaller and/or tritium recovery can be much easier. This compound is also relatively inert in water. It was reported that[6] "LiPb (50-50 mixture) resembles Pb in every respect except density. LiPb would not ignite even when exposed to the flame of a gas-air torch." Fig. VII-B-1 shows the phase diagram of a Li-Pb two component mixture.



Pb-Li PHASE DIAGRAM

Fig. VII-B-1

Of all the different compounds and mixtures, Li_{62} Pb_{38} is of most interest due to its proper melting temperature of 464°C. Therefore, we can take advantage of using the latent heat of phase change to provide energy storage. For this reason, Li_{62} Pb_{38} is picked as the breeding material, and serious effort is made to design the blanket to resemble a phase change energy storage unit.

One of the uncertainties of using Li_{62} Pb_{38} eutectic as the breeding and energy storage material at this time lies in the unavailability of physical properties data. Table VII-B-3 lists some of the properties used in this design study. They are mostly educated guesses at best and should not be taken as correct data.

VII-B-3. Coolant

The cyclic behavior of the plasma introduces a new problem which did not face the fossil or fission power plants, i.e., thermal fatigue. This fatigue problem is particularly severe for the first wall since the thermal flux is large, while there is very little thermal inertia. The temperature change of the structure is the combination of three effects as listed below:

1. $T_{coolant,out} - T_{coolant,in}$ or coolant temperature rise
2. $T_w - T_{coolant}$ (= Q/h), or film temperature drop
3. $\Delta T = Q\chi/k$, or temperature difference across the first wall.

Since Q, the heat deposited on the first wall, disappears during the plasma down time, the temperature of the first wall facing the plasma decreases by the summation of those three ΔT's combined. While the third ΔT is structurally dependent, the first two ΔT's are coolant dependent. Therefore, to minimize the thermal fatigue, a coolant must be picked with small coolant temperature rise which simultaneously provides a large heat transfer coefficient, h. A boiling heat transfer coolant is, therefore, a perfect choice. Since steam will be required for the steam cycle, boiling water becomes the logical choice.

Table VII-B-3 Physical Properties (Used)* of $Li_{62}Pb_{38}$

Solid Density	6.5 g/cm^3
Liquid Density	5.0 g/cm^3
Thermal Conductivity	.35 $W/cm-^oC$
Latent Heat of Fusion	140 kJ/kg
Heat Capacity	174 J/kg-K
Melting Temperature	464^oC

*The numbers listed on this table, with the exception of melting temperature, are educated guesses at best and should not be referred to as exact figures. The melting temperature is experimentally verified.

Water has been shown to be an economical and safe coolant in current fission reactors. However, there are serious safety questions associated with keeping water in close proximity with lithium or lithium compounds in the blanket. Another problem, perhaps equally serious, has to do with the difficulty of separating tritium from water. If large amounts of tritium diffuse into the coolant from the breeding material, tritium recovery from hydrogeneous coolants may be impractical. In a conventional fusion reactor design, an intermediate loop is usually recommended to keep water and tritium bearing lithium compounds separate. This is expensive, complex, and at the same time significantly increases the difference between the blanket operating temperature and steam temperature.

In the NUWMAK blanket, Li_{62} Pb_{38} is used as the breeding material. The activity of lithium is reduced significantly by the presence of lead. Therefore, the safety problem caused by the water-lithium reaction is much less severe. To minimize tritium diffusion into the cooling water, we propose to use a multi-layer coolant tube design, which will be discussed further later in this chapter. The use of a low chemical activity breeding material combined with a multi-layer coolant tube design gives us the confidence that boiling water cooling can be both safe and environmentally acceptable.

VII-C. Blanket Design

The blanket of NUWMAK is shown in Fig. VII-C-1. The blanket structure is Ti-6Al-4V, and is designed with a maximum temperature of 400°C at the coolant tube wall for phase stability. The maximum design temperature in the blanket is 500°C. The coolant is boiling water at 300°C. The coolant pressure is 8.6 MPa (1250 psi). The design life for the blanket module is two years.

The reactor has 8 independent modules, one for each superconducting TF coil as shown on Fig. VII-C-2. Each module has two blanket units; the inner blanket near the machine axis and the outer blanket far away from the machine axis, as shown on Figure VII-C-1. The coolant is fed and discharged

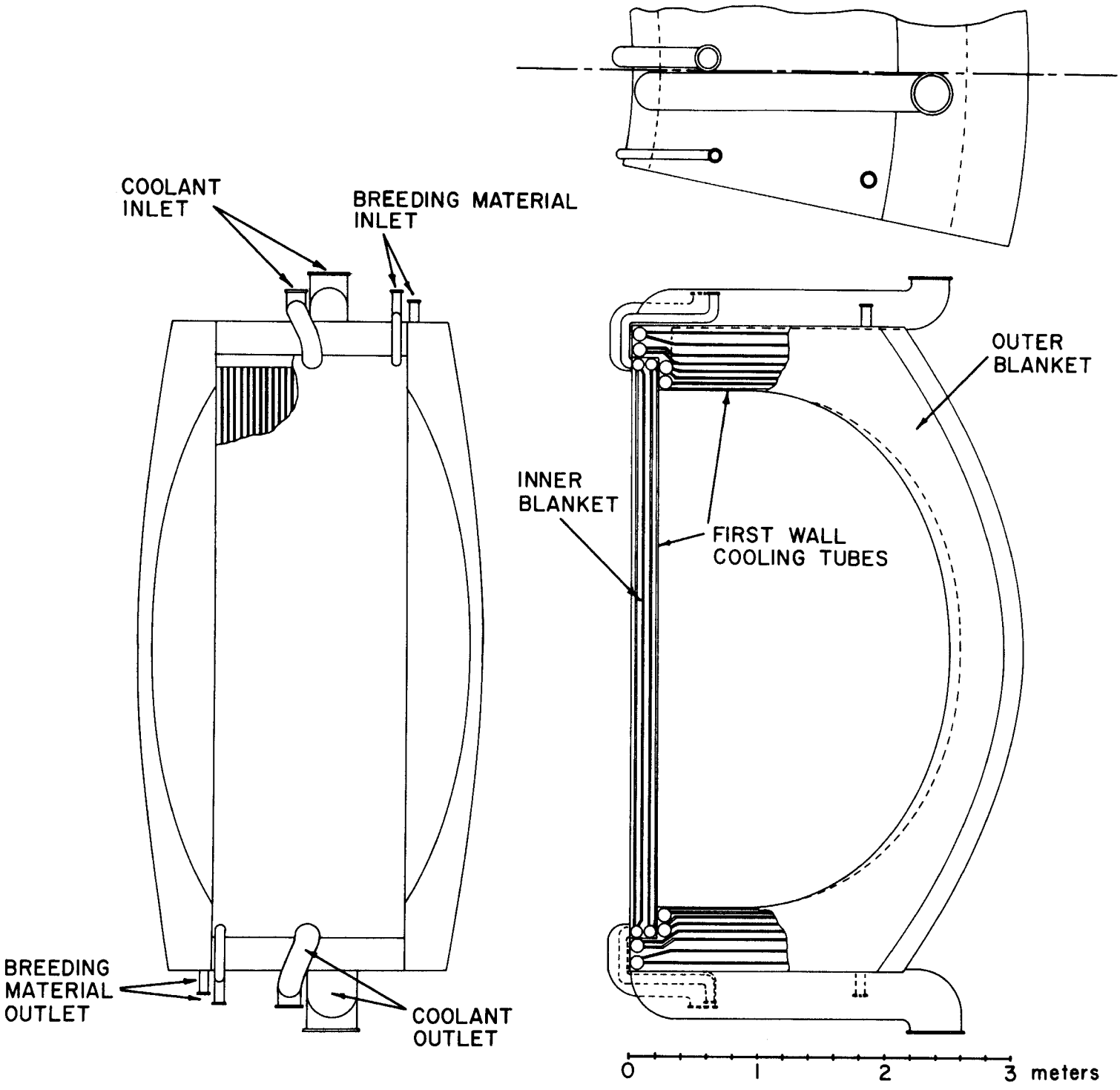
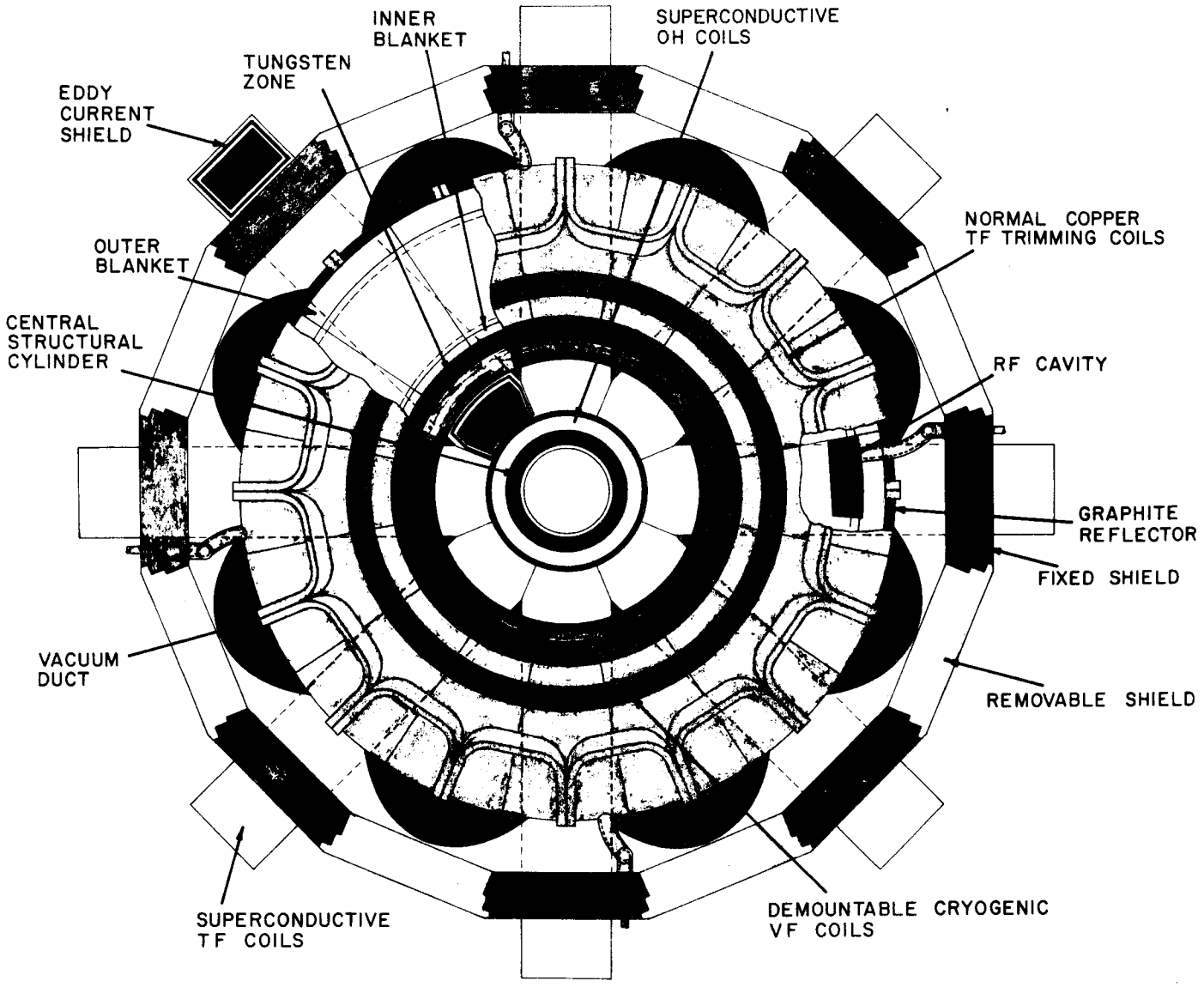


Fig. VII-C-1. Cross-Sectional View of Blanket

Fig. VII-C-2 TOP VIEW OF NUWMAK



from each module separately. Breeding material inlets and outlets are also provided for each blanket unit, both for tritium recovery and for dumping procedures. Therefore, the inner blanket and outer blanket are completely separated and will be removed independently when maintenance is required.

The coolant is supplied to and removed from the blanket through feed and discharge pipes, respectively. Each pipe is inserted between the TF magnets, and connected to a toroidal header. The toroidal headers distribute coolant in the toroidal direction and supply coolant to the coolant tubes. The coolant is fed in the form of saturated water and is removed as a two-phase mixture. A very high moisture content is always kept to insure stable boiling in the coolant tubes. The two-phase mixture is fed to a steam drum where water and steam can be separated.

The blanket resembles a large phase change energy storage tank. The first wall is formed by a continuous bank of tubes. The coolant tubes within the blanket are on a triangular pitch, with the distance between two tubes inversely proportional to the nuclear heating rate. The space in between the tubes is filled with Li_{62} Pb_{38}, the breeding and energy storage material. The breeding material temperature is between 400 and 500^{o}C, while its melting temperature is 464^{o}C. Therefore, the breeding material is always in solid form around the coolant tube, always in liquid form in between coolant tubes. The movement of the solid-liquid interface provides energy storage.

A cross-sectional view of a coolant tube is shown on Fig. VII-C-3. The coolant tube is designed to maximize blanket reliability. Double walled tubes are used throughout the blanket for redundancy. A layer of lead fills the gap between the two concentric tubes to increase the thermal conductance across the composite tube wall. Outside surfaces of both tubes are coated with a nitride coating to reduce the tritium diffusion into the coolant. The inner surface of the outer tube is coated with Zr which acts as a getter to absorb the tritium diffusing through the outer wall. Such a

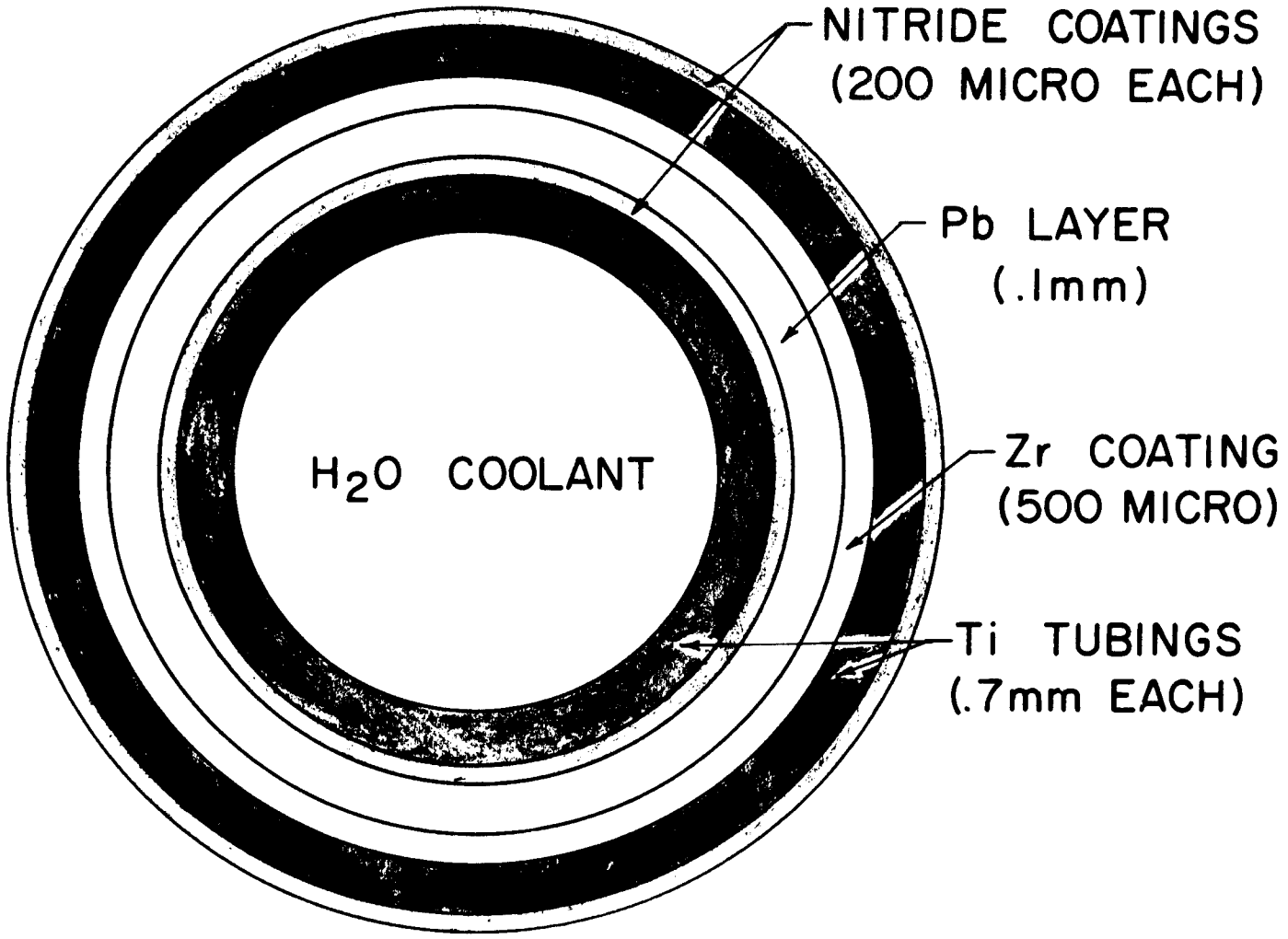


FIGURE VII-C-3 CROSS-SECTIONAL VIEW OF A COOLANT TUBE

double walled tube will minimize tritium loss to the water while providing a reliable blanket. The cost of fabricating such tubes is undoubtedly high, but can be justified in view of the advantages gained.

The blanket design described above has a major impact on the power cycle. A conventional power cycle and the one proposed for NUWMAK are shown in Fig. VII-C-4 for comparison. The conventional power cycle is not only much more complicated and, therefore, much more expensive, it also reduces the steam temperature from the primary coolant temperature by $\sim 100^{o}C$. Use of a multi-layered coolant tube, a breeding material with a low lithium chemical activity and latent heat energy storage in the blanket makes a BWR type power cycle possible. The cost saving should be significant.

VII-D. Heat Transfer Calculations

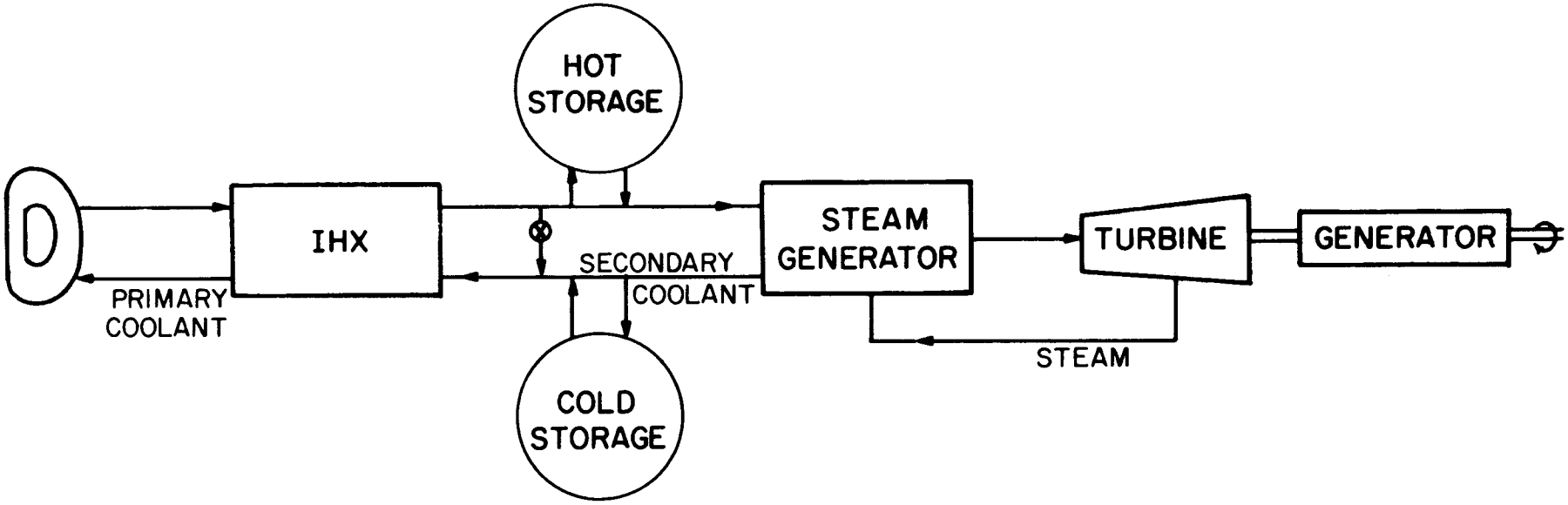
VII-D-1. Mathematical Formulation

The heat transfer problem associated with NUWMAK is a complicated one. There are phase changes in both the coolant and breeding material. A recent plasma calculation shows that the plasma output is not a constant during the burn. Due to the periodic gas puffing, the energy output varies with the same period. This variation can be as high as $\pm$ 50% from the steady state and adds severe problems to heat transfer, thermal fatigue, and radiation damage. However, by combining gas puffing and pellet injection as the fueling mechanism, this variation is significantly reduced. Chapter IV discusses in detail the effect of gas puffing on the plasma power output.

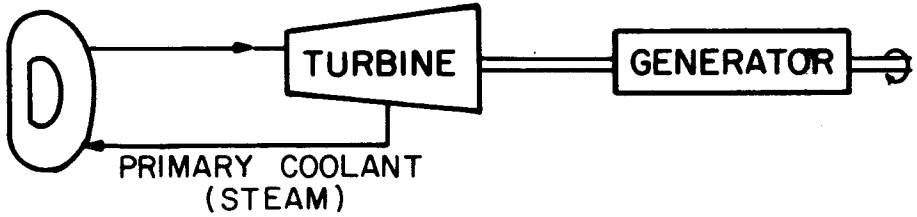
When the major portion of the heat transfer work calculations were made, the effect of gas puffing was not understood and the plasma cycling within a gas puffing period was not taken into consideration. In this calculation, we assumed:

1. A steady state burn of 245 seconds with a 20 second down time
2. The boiling water coolant is at a constant temperature of $300^{o}C$
3. The heat transfer coefficient of boiling water = $(20{,}000\ BTU/hr\text{-}ft^{2}\text{-}^{o}F)$
4. A cylindrical heat transfer model, as shown in Figure VII-D-1.

The cyclic plasma behavior due to the gas puffing has no significant impact on the heat transfer problems in the interior of the blanket due to the large thermal inertia. The temperature response of the first wall due to this cycling will be discussed in the appendix to this chapter.



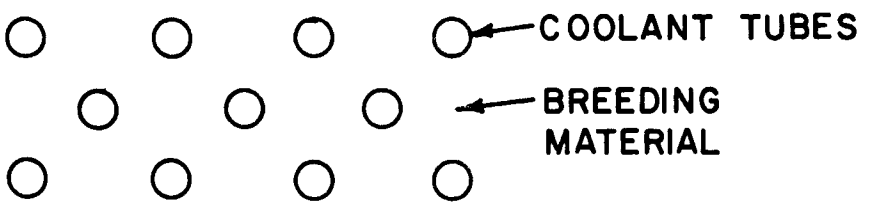
POWER CYCLE FOR A CONVENTIONAL TOKAMAK



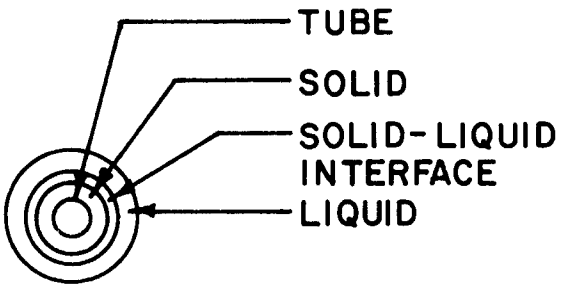
POWER CYCLE FOR NUWMAK (BWR TECHNOLOGY)

FIGURE VII-C-4 COMPARISON OF POWER CYCLE OF NUWMAK TO A CONVENTIONAL TOKAMAK REACTOR

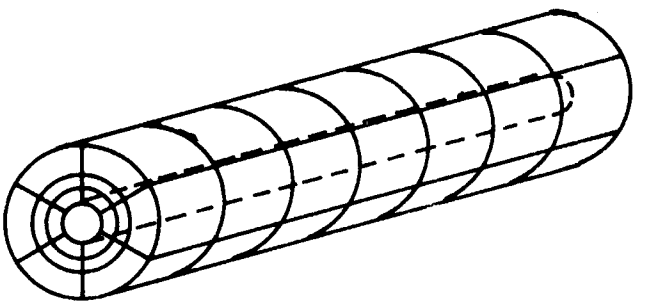
NUWMAK BLANKET



ACTUAL GEOMETRY



PHYSICAL MODEL



MATHEMATICAL MODEL

Fig. VII-D-1

A two-dimensional, finite difference heat transfer code was developed for calculating the temperature distribution in the blanket as a function of time in a burn cycle. The coolant can be either with boiling heat transfer, or with convective heat transfer. Four types of different zones exist in the blanket. They are:

1. Blanket zone without phase change
2. Blanket zone with phase change
3. Coolant zone without phase change
4. Coolant zone with phase change.

The governing equation in the finite difference form can be written for each zone:

$$V_i \rho c_p (T_i' - T_i) = [\sum_j COND_{ji} (T_j - T_i) + V_i Q_i'''] \Delta\theta \quad (1)$$

$$V_i \rho \Delta H (\chi_i' - \chi_i) = [\sum_j COND_{ji} (T_j - T_i) + V_i Q_i'''] \Delta\theta \quad (2)$$

$$V_i \rho c_p (T_i' - T_i) = [\sum_j COND_{ji} (T_j - T_i) + V_i Q_i''' + vA\rho c_p (T_{i-1} - T_i)] \Delta\theta \quad (3)$$

$$V_i \rho \Delta H' (y_i' - y_i) = [\sum_j COND_{ji} (T_j - T_i) + V_i Q_i''' + vA\rho c_p (T_{i-1} - T_i)] \Delta\theta \quad (4)$$

with the time step $\Delta\theta$ defined as

$$\Delta\theta \leq [V_i \rho c_p / \sum_j COND_{ji}]_{min} \quad (5)$$

in which

V_i	is the volume for zone i
ρ	is the density of the material
c_p	is the specific heat
T_i	is the temperature of zone i before the iteration
T_i'	is the new temperature of zone i
$COND_{ij}$	is the conductance between zone i and j

Q''' is the heat generation rate

ΔH is the latent heat for the breeding material

χ_i is the fraction of liquid in zone i

v is coolant velocity

A is coolant channel cross-sectional area

$\Delta H'$ is the latent heat of coolant

y_i is the fraction of vapor in zone i.

Assuming an initial temperature distribution, all the temperatures after a time step of $\Delta\theta$ can be calculated by Eqs. 1 through 4. The cyclic behavior of the plasma can be simulated by defining the heat generation rate Q''' as a function of time. The maximum time step is defined by Eq. 5 to insure convergence of the iteration. The iteration process should be carried over a number of plasma cycles until the temperature profile is established. By using this program, the temperature profile for the entire blanket can be calculated.

VII-D-2. Results and Discussion

The heat transfer calculations are based on the input from the neutronics calculation results. The spatial nuclear heating rate, for both inner and outer blanket, is shown on Fig. VII-D-2. The maximum nuclear heating rate in the blanket is 40 watts/cm^3. The first wall thermal loading is 108 W/cm^2. This high heat flux is due to the high neutron wall loading and the elimination of the divertor. The summary of the heat transfer calculations is listed on Table VII-D-1.

Figure VII-D-3 shows the temperature change of the first wall during a burn cycle, and compares it with a helium cooled first wall. Boiling water is a very good coolant and the first wall is kept within the design temperature limit. The poor thermal conductivity of titanium, combined with a high surface wall loading, results in a very large temperature difference across the first wall. Therefore, the surface temperature of the first wall on the plasma side reaches 400°C, which is acceptable. The other important point is the temperature response of the first wall when the plasma

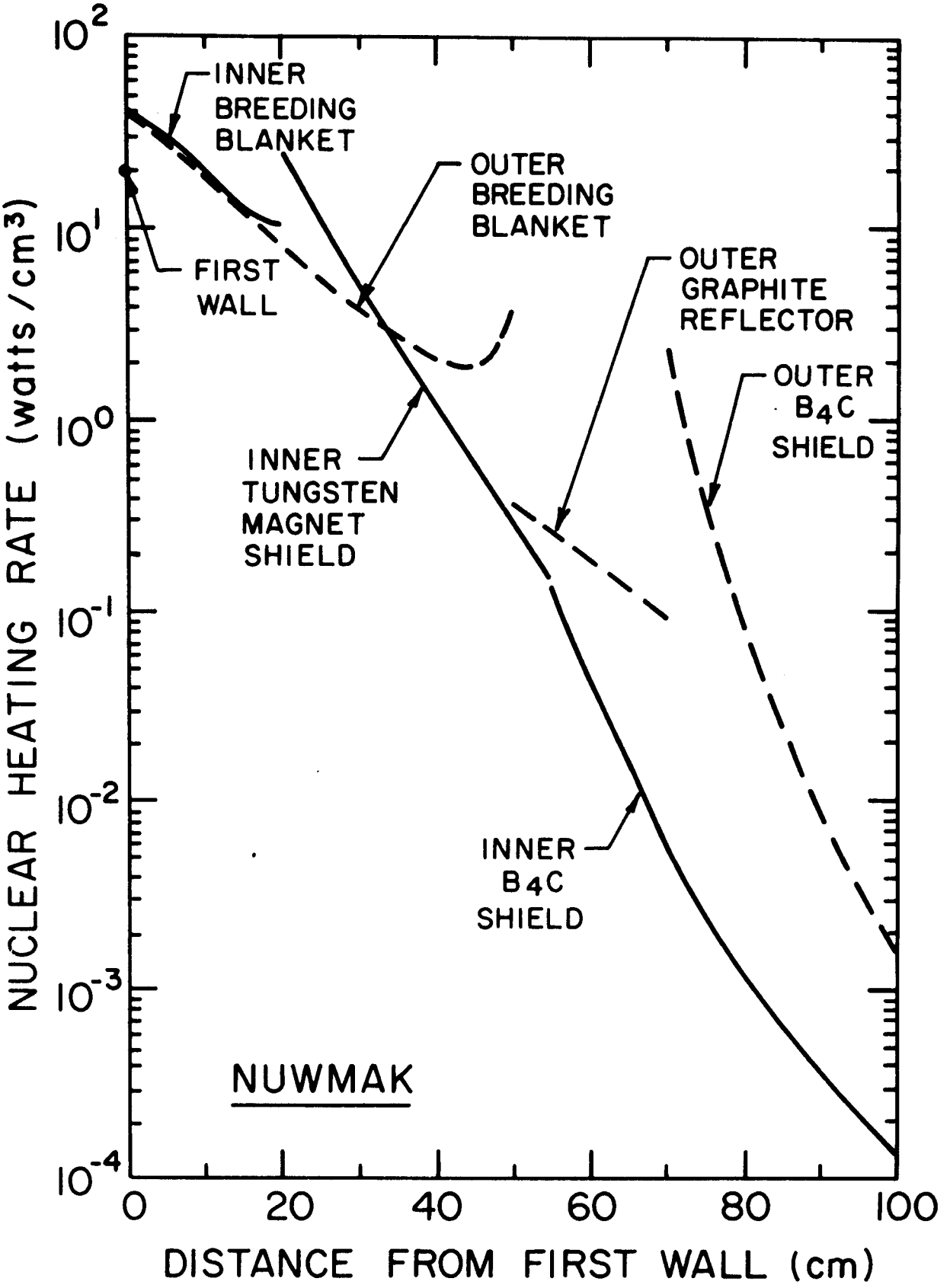


Fig. VII-D-2 SPATIAL NUCLEAR HEATING RATE

Table VII-D-1 Summary of Heat Transfer Calculations

Power Output (During Burn)	2283 MW
Blanket Energy (Continuous)	1900 MW
Neutron Wall Loading	4.34 MW/m^2
First Wall Area	360 m^2
Total Thermal Wall Loading	6.34 MW/m^2
First Wall Thermal Loading	1.08 MW/m^2
Plasma Burn Time	225 Second
Plasma Down Time	20 Second
Structure	Ti Alloy
Breeding Material	Li_{62} Pb_{38} Eutectic
Energy Storage Material	Li_{62} Pb_{38} Eutectic
Coolant	Boiling H_2O
Coolant Temperature	300°C
Coolant Pressure	8.6 MPa
Maximum Coolant Wall Temperature	400°C
Maximum Coolant Wall Stress	100 MPa
Maximum Blanket Temperature	500°C
Average Coolant Tube Thermal Load	44 W/cm^2
Total Coolant Tube Surface Area	4350 m^2
Net Power Output (Continuous)	660 MW(e)
Net Thermal Efficiency	31.5%

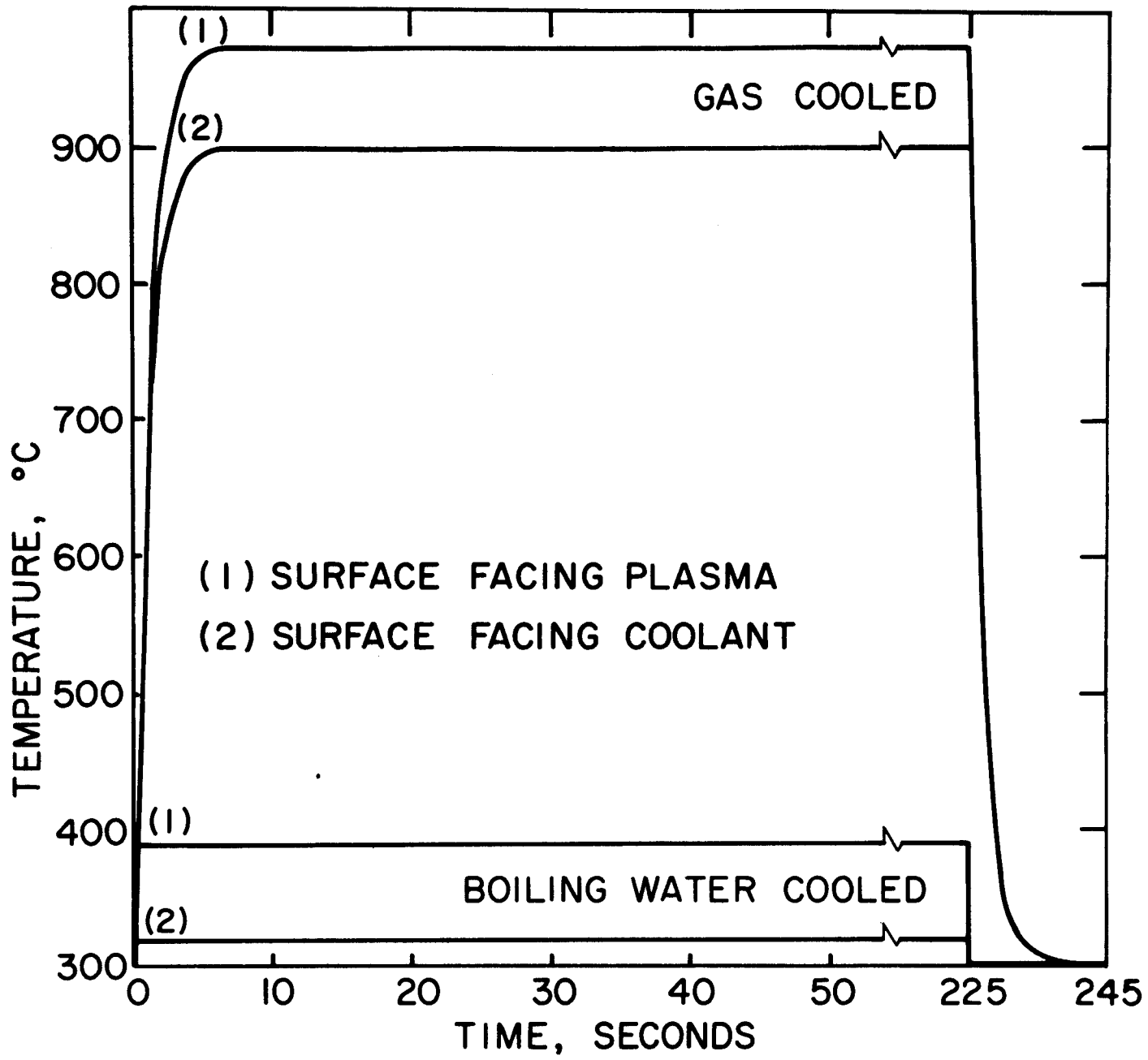


Fig. VII-D-3 TEMPERATURE RESPONSE OF THE FIRST WALL DURING A BURN CYCLE, He VERSUS BOILING WATER COOLING

is shut off. It reaches the coolant temperature within ~ 0.1 second of plasma shutdown. The stress associated with such a thermal shock is yet to be calculated, but a first order estimate indicates it is acceptable. The total stress in the first wall is 110 MPa and is reasonable. It is worth noting that if the first wall is helium cooled, both the high first wall temperature during the burn, and the large structure temperature drop at the end of a burn, result in an unacceptable design.

Figure VII-D-4 shows the temperature of the Li_{62} Pb_{38} between a coolant tube wall and midway between two coolant tubes at three different times during a burn cycle. One can clearly see the effect of the latent heat of the blanket material on the temperature changes in the blanket. After the burn is terminated, the liquid temperature drops to the melting temperature of Li_{62} Pb_{38} in a short time. After this the latent heat of fusion supplies energy to the coolant tubes. The maximum temperature change in the blanket during a complete burn cycle is only $\leq 30^{o}C$. The temperature of the coolant tubes remains almost constant. The slope of the temperature curve at the coolant tube wall and, consequently, the energy supply to the power cycle also remains almost constant during a burn cycle. For comparison, Fig. VII-D-5 shows the result for an identical system but without phase change. The maximum temperature change in the blanket is $150^{o}C$ and the slope change of the temperature curve becomes significant. The effect of phase change on the magnitude of the temperature cycling and the energy storage capacity in the blanket is clearly demonstrated in those two figures.

Figure VII-D-6 shows the variation of the energy input to a coolant tube at three different locations in the blanket. For an ideal case, the curves should be constant. For the NUWMAK blanket, the maximum variation is about 30% from steady state. Figure VII-D-7 shows the benefit obtained from using latent heat energy storage. Without phase change in the blanket, the fluctuation in the blanket energy during a burn cycle is significantly larger. Such a system would definitely need auxiliary thermal storage.

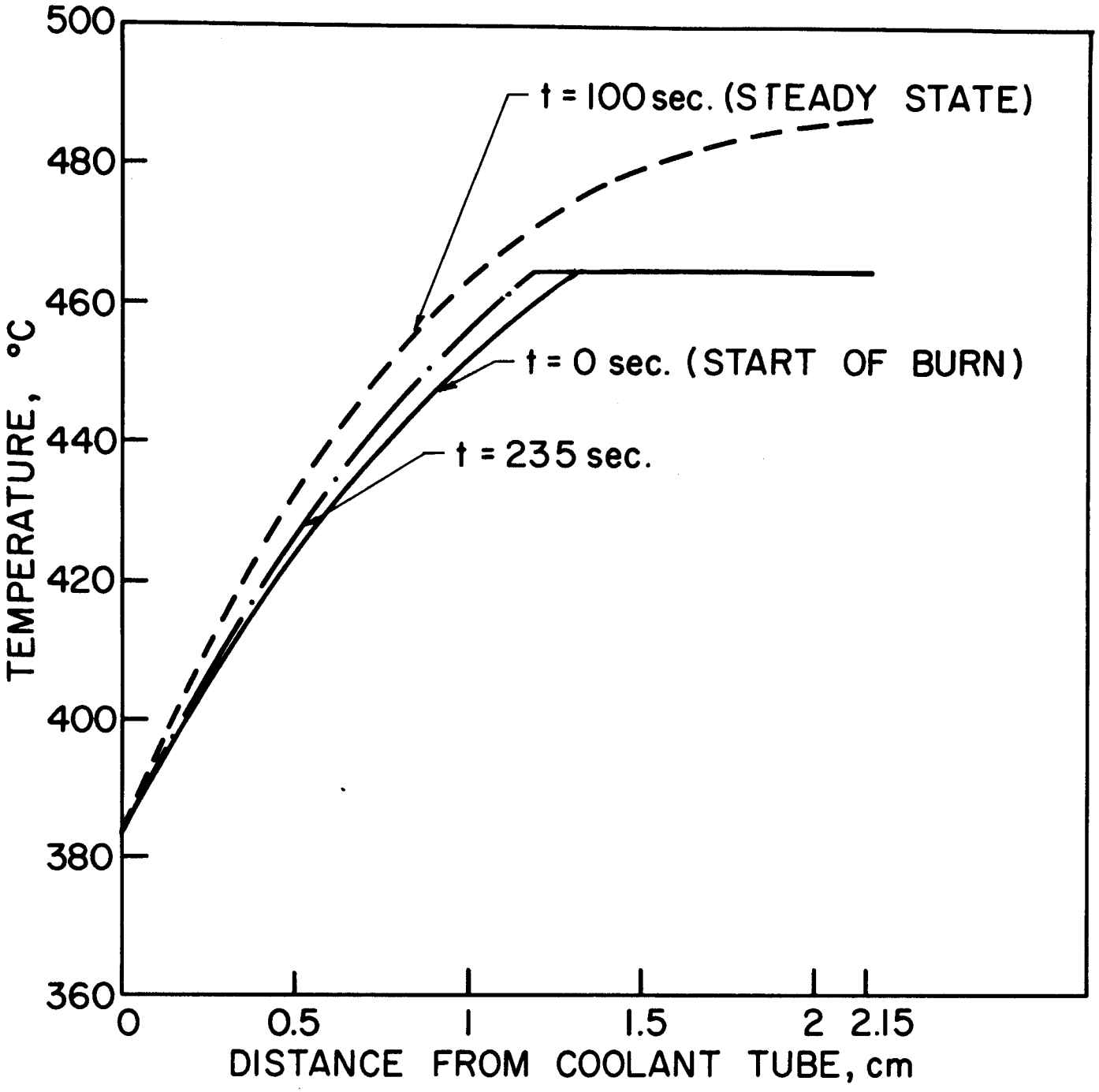


FIGURE VII-D-4

TEMPERATURE CHANGE OF THE BLANKET IN A BURN CYCLE (WITH PHASE CHANGE)

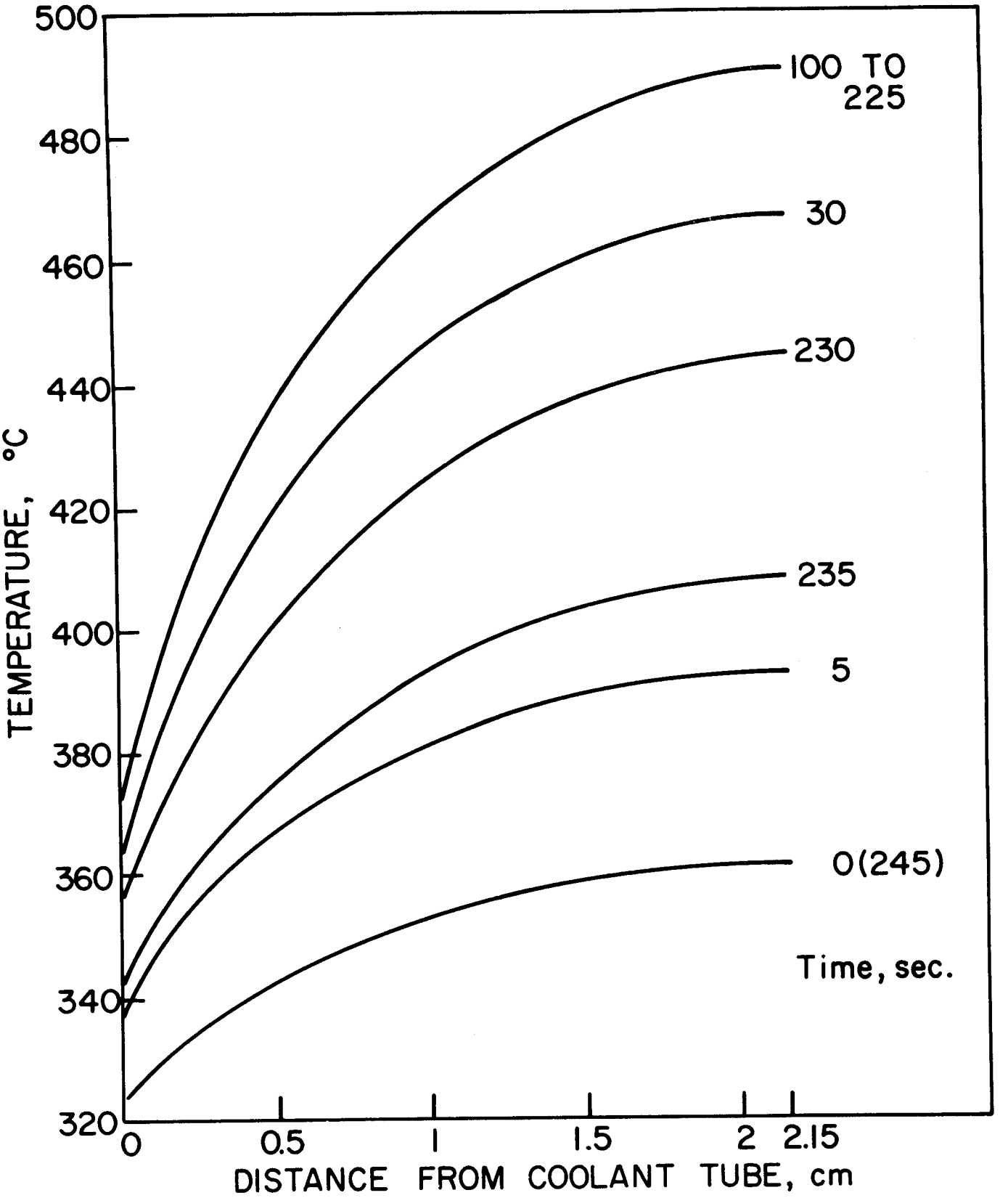


FIGURE VII-D-5

TEMPERATURE CHANGE OF THE BLANKET IN A BURN CYCLE (WITHOUT PHASE CHANGE)

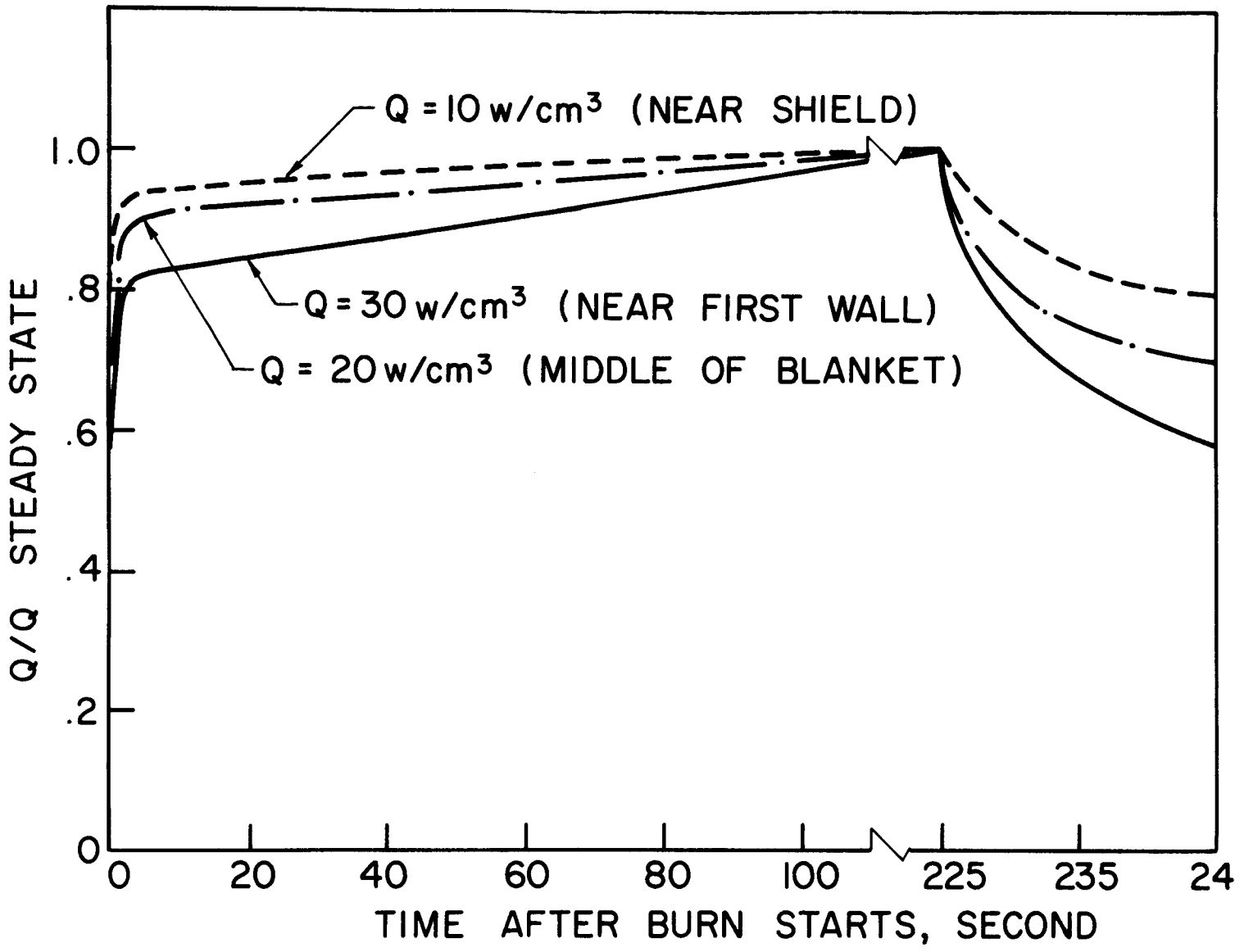


FIGURE VII-D-6 BLANKET ENERGY OUTPUT DURING A BURN CYCLE, FOR THREE DIFFERENT LOCATIONS IN BLANKET

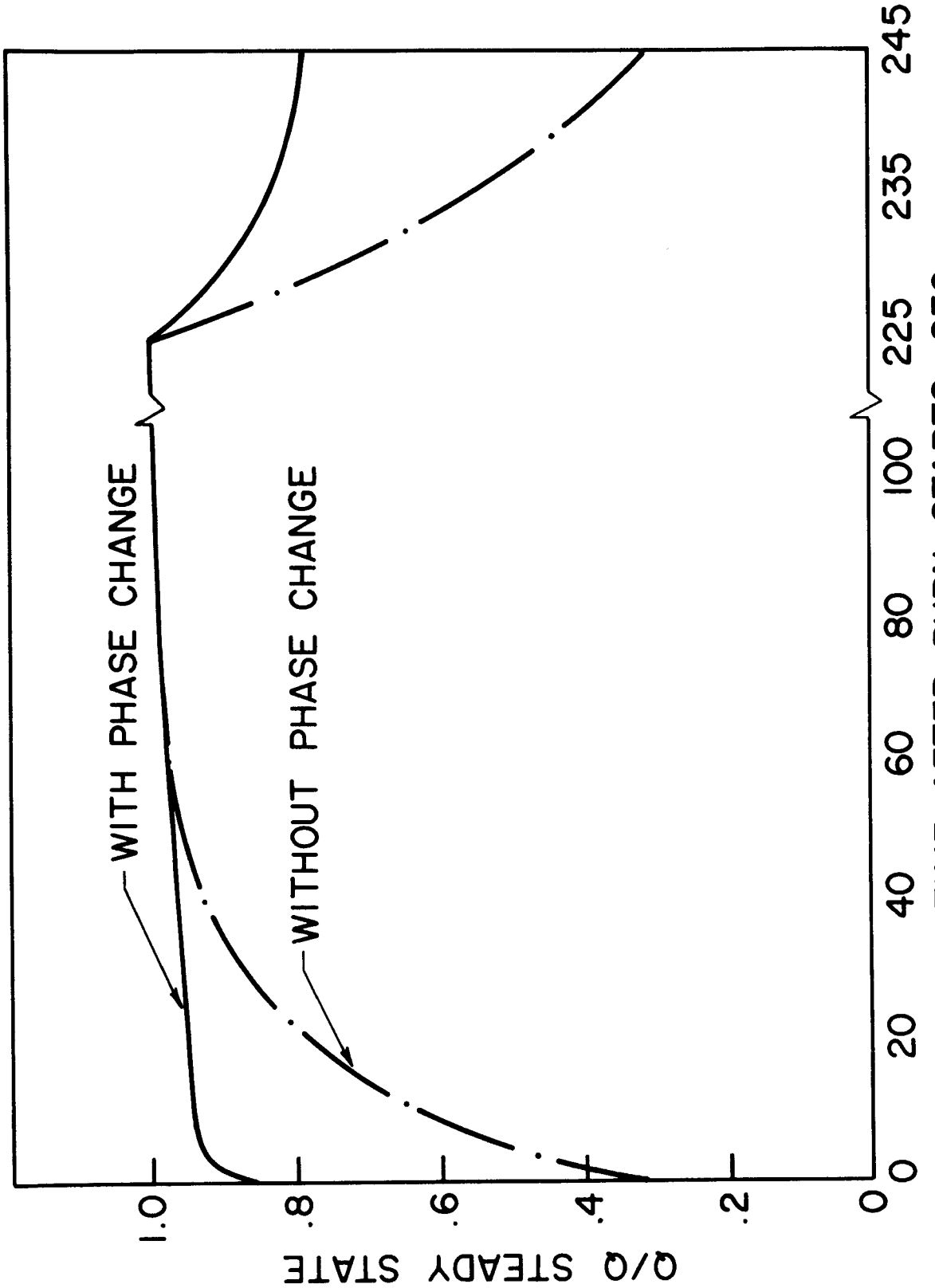


FIGURE VII-D-7 EFFECT OF PHASE CHANGE ON BLANKET ENERGY OUTPUT

A 30% energy output variation is still unacceptable to the turbine. This variation can be further reduced by using the steam drum and adjusting the feed water temperature, as will be discussed later in this chapter.

Figure VII-D-8 shows the change of the solid-liquid interface during a burn cycle, at the same three locations as in the previous calculations. These three lines are the constant temperature lines in the blanket. Since

$$Q = kA \frac{\Delta T}{\Delta \chi} \quad , \tag{6}$$

the change of the location of the interfaces, consequently the change of $\Delta\chi$, results in a non-uniform heat flux to the coolant tube.

The power flow diagram for NUWMAK is shown in Fig. VII-D-9. The gross thermal efficiency is 34.5%. The total auxiliary power requirement is 65 MW; the cooling of the magnets consumes 60 MW. The net power output is 660 MWe. The net thermal efficiency is 31.5%.

VII-E. Blanket Support Considerations

The blanket in NUWMAK is divided into 16 equal modules each consisting of an inner and an outer blanket segment. Fig. VII-C-1 shows a cross-section of a blanket module. It is 5 m high, 3.2 m deep and is 1.5 m and 2.7 m wide at midplane at the inner and outer radii, respectively. The first wall in both inner and outer blanket segments consists of a continuous bank of tubes joined together which are connected to a toroidal header at the top and bottom. In order for the constant diameter tubes to fit the toroidal geometry in the outer blanket, they will have to be gradually flattened as they approach midplane.

Each blanket module will have radial plates 0.2 cm thick spaced every 20 cm, joining the first wall to the back plate. The side plates in each module are 0.3 cm thick. In addition, struts will be used to keep the cooling tubes within the body of the blanket evenly spaced and supported. The side and intermediate plates combine to form a very strong structure.

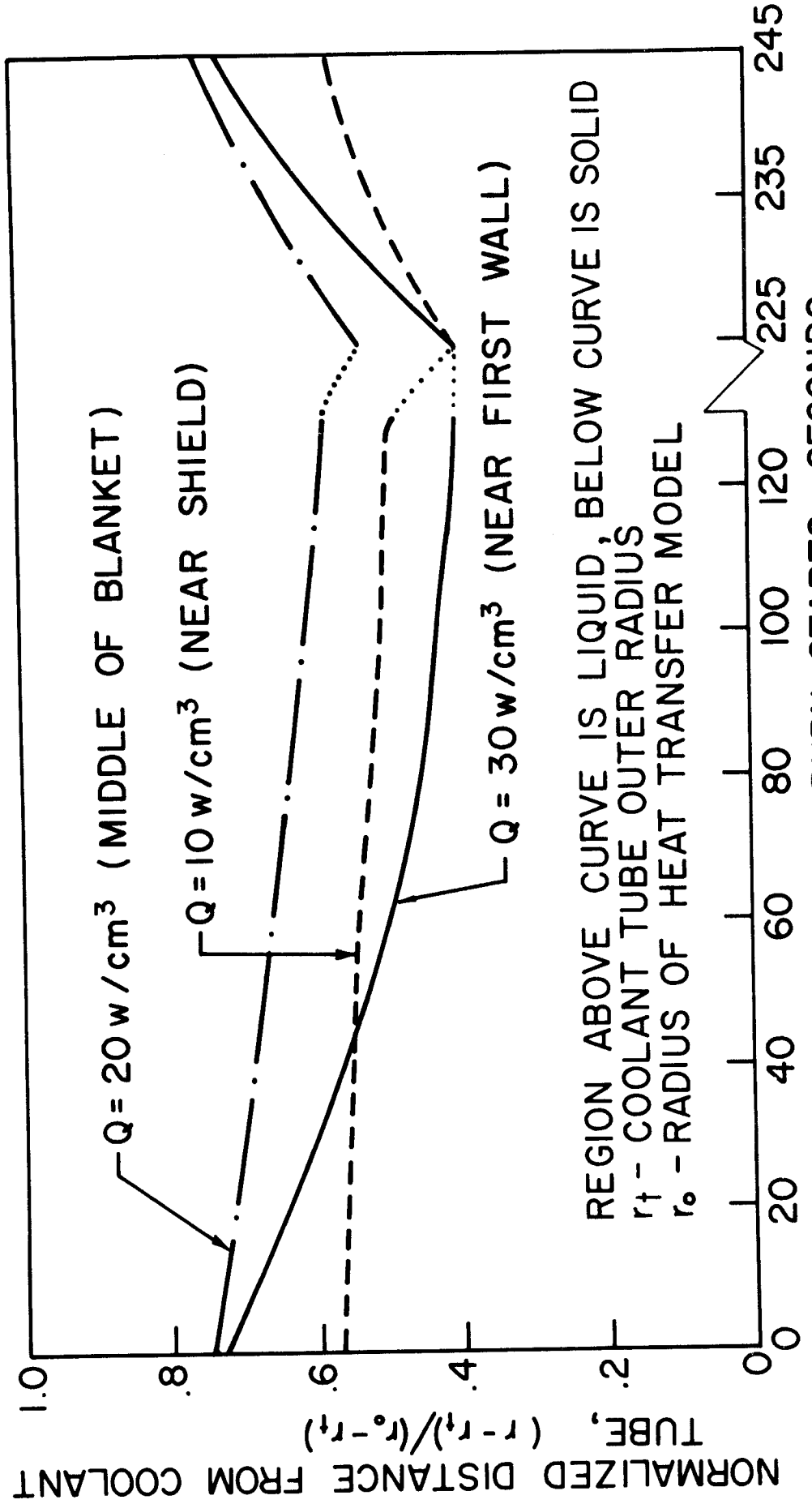


FIGURE VII-D-8

CHANGE OF SOLID-LIQUID INTERFACE IN A BURN CYCLE, FOR THREE DIFFERENT LOCATIONS IN BLANKET

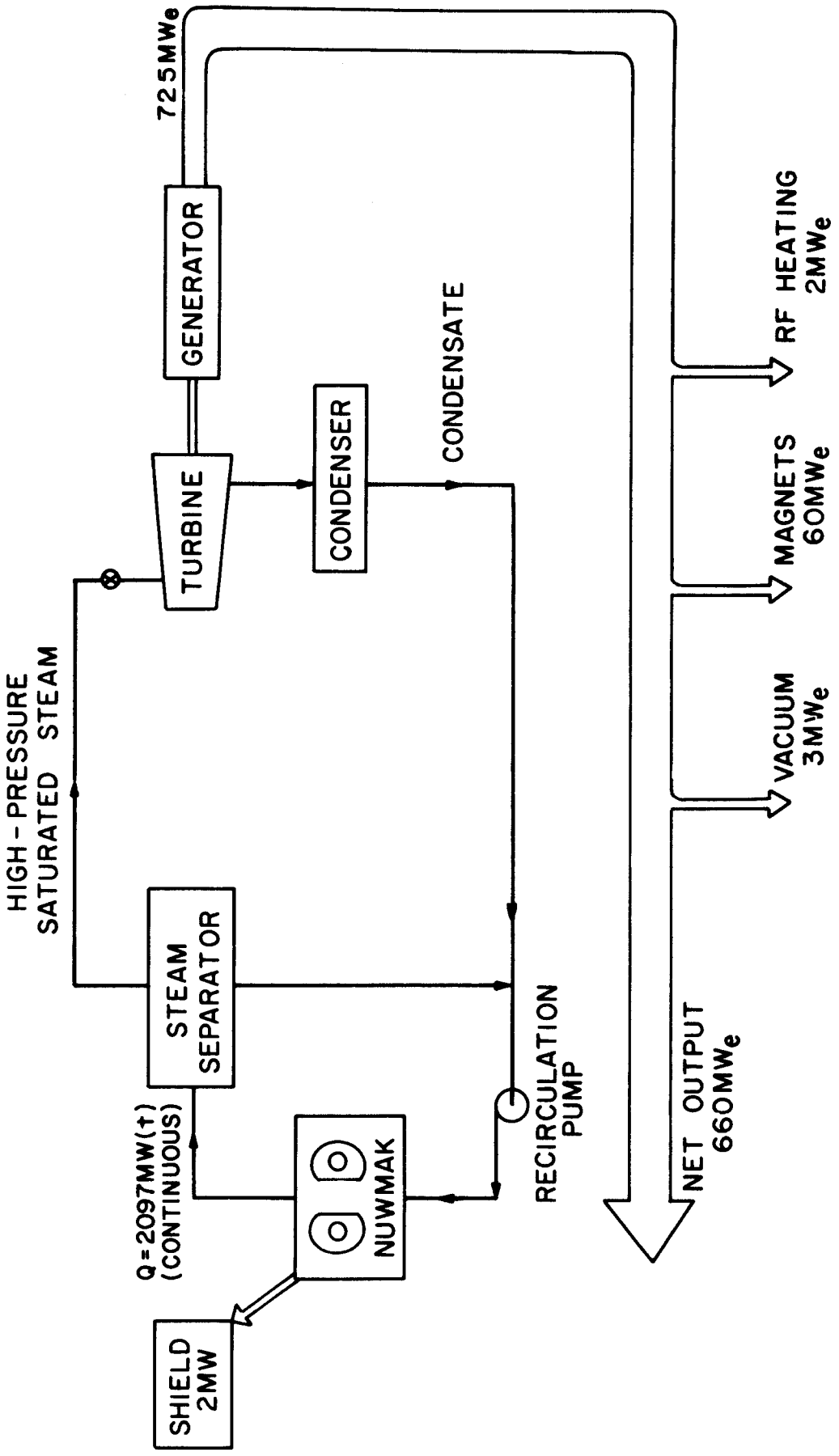


FIG. VII-D-9 POWER FLOW DIAGRAM FOR NUWMAK

The outer blanket segment is designed to be free standing and capable of supporting the full load of the breeding material. In actual practice, however, the inner blanket segment will support the overhanging portion of the outer segment. In this way the bending moment and the resulting stress at midplane are minimized. The weight of the blanket is transferred to the shield by direct bearing and is ultimately transferred to the reactor floor through columns between the TF coils.

VII-F. Load Leveling Considerations for a Pulsed Fusion Reactor *

VII-F-1. Introduction

This section is intended to briefly describe load leveling features of the NUWMAK reactor blanket and steam cycle which combine to provide constant plant electrical output in a direct cycle with a minimum amount of extra equipment cost.

VII-F-2. Discussion

Steam is generated directly in the blanket by a heating surface immersed in a fusible Li-Pb eutectic alloy. This breeding alloy exists during operation as a two phase solid-liquid mixture. Each blanket steam generator tube is surrounded by a solid phase layer of this alloy which becomes thinner during a burn period and thicker during the off-power period to provide a phase change type of thermal energy storage. Results produced are shown in Figure VII-F-1.

This energy storage feature provides a considerably smoothed blanket power output when compared to the pulsed power output of the plasma. An 11.65 MWh_t blip is reduced to a smoothed out characteristic having 3.20 MWh_t above and below the average.

The advantage of the eutectic alloy phase change was clearly discussed. Without it, minimum power falls to about 30 percent of steady state power whereas in NUWMAK, the power level falls only to 70 percent.

A momentary drop in blanket power to 30 percent tends to call for elaborate thermal storage capabilities in the nuclear steam supply system. This would characteristically involve an intermediate loop having large hot and cold storage vessels for sodium, hot oil or pressurized water.

*This section was written by D.C. Schluderberg at Babcock and Wilcox and was finished before the final plasma calculation, accounting for inconsistency with the rest of the chapter.

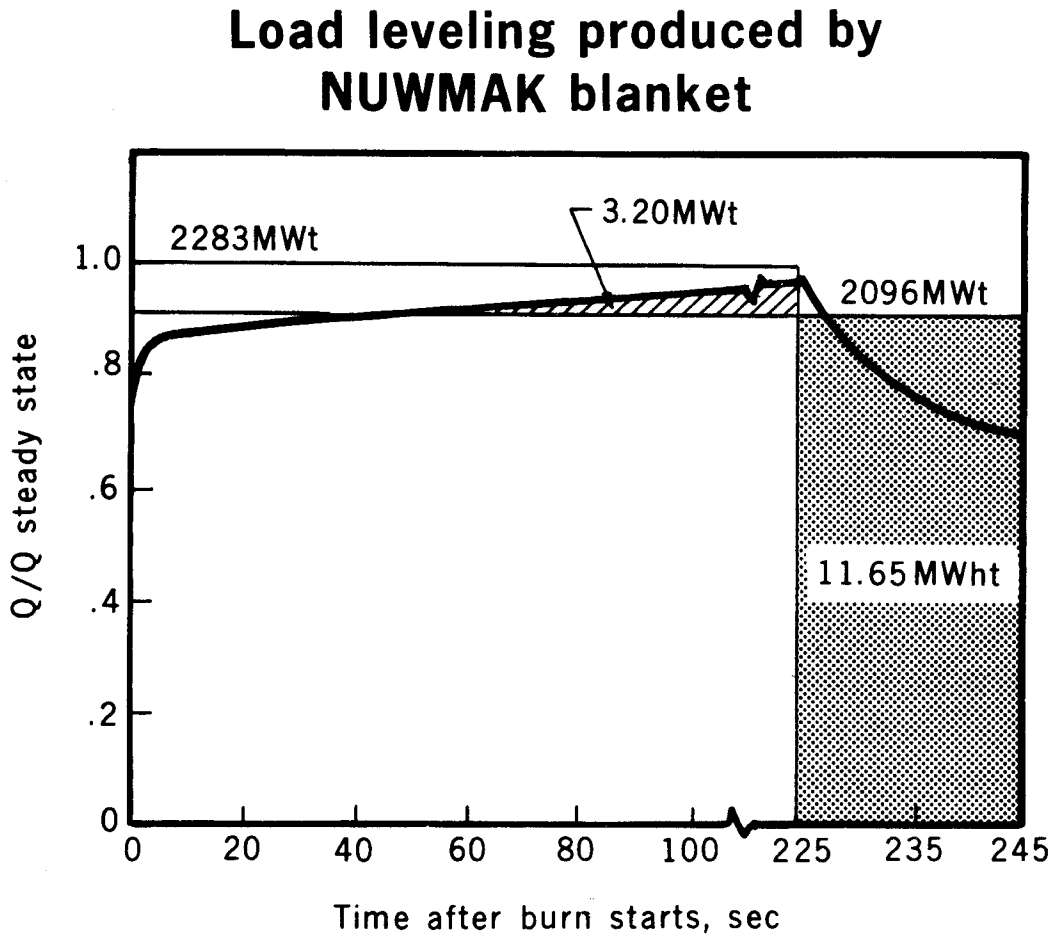

Load leveling produced by
NUWMAK blanket
2283MWt
3.20MWt
2096MWt
11.65MWht
Q/Q steady state
1.0
.8
.6
.4
.2
0
0
20
40
60
80
100
225
235
245
Time after burn starts, sec

Fig. VII-F-1

In contrast, the improved NUWMAK blanket and first wall power output characteristic hold out hope that a relatively inexpensive direct cycle system could be used to complete the load leveling task and provide constant electrical power output.

The remainder of this section describes a proposed approach to achieve this goal.

The first measure was to add a relatively small amount of pressurized water thermal storage to smooth out the power output from the first wall. This structure is not immersed in the lead-lithium alloy and thus does not benefit from the phase change of this material. Without equivalent thermal storage, first wall heat input to the power cycle varies much more rapidly as shown in Figure VII-F-2.

Figure VII-F-3 attempts to show the effect of first wall power output on the total reactor output vs. time. By adding thermal storage to maintain a more uniform first wall power output to the power cycle during the 20 second blip in reactor power, it becomes possible to materially improve the combined power output characteristic as shown.

This is done by incorporating the features listed below:

(1) Use first wall as steam generator economizer.

(2) Set feedwater temperature to provide saturated water leaving economizer.

(3) Discharge into four 35 m^3 storage drums.

(4) Discharge from drums to water space in boiler drums.

A schematic representation of this system is shown in Figure VII-F-4. An interesting aspect of this approach is that it allows use of sensible heat storage in system water inventory without an appreciable effect on steam pressure and steam flow at the turbine throttle. Fig. VII-F-4 also indicates the expected rise and fall of boiler drum water level due to modulation of feedwater flow as will be described below.

The final load leveling is now accomplished by the following steps which modulate steam cycle power input required to maintain a constant electrical output.

1. Modulate feedwater flow.
2. Let this also modulate ext. steam flow.
3. Add extra feed flow direct to steam space in drums.

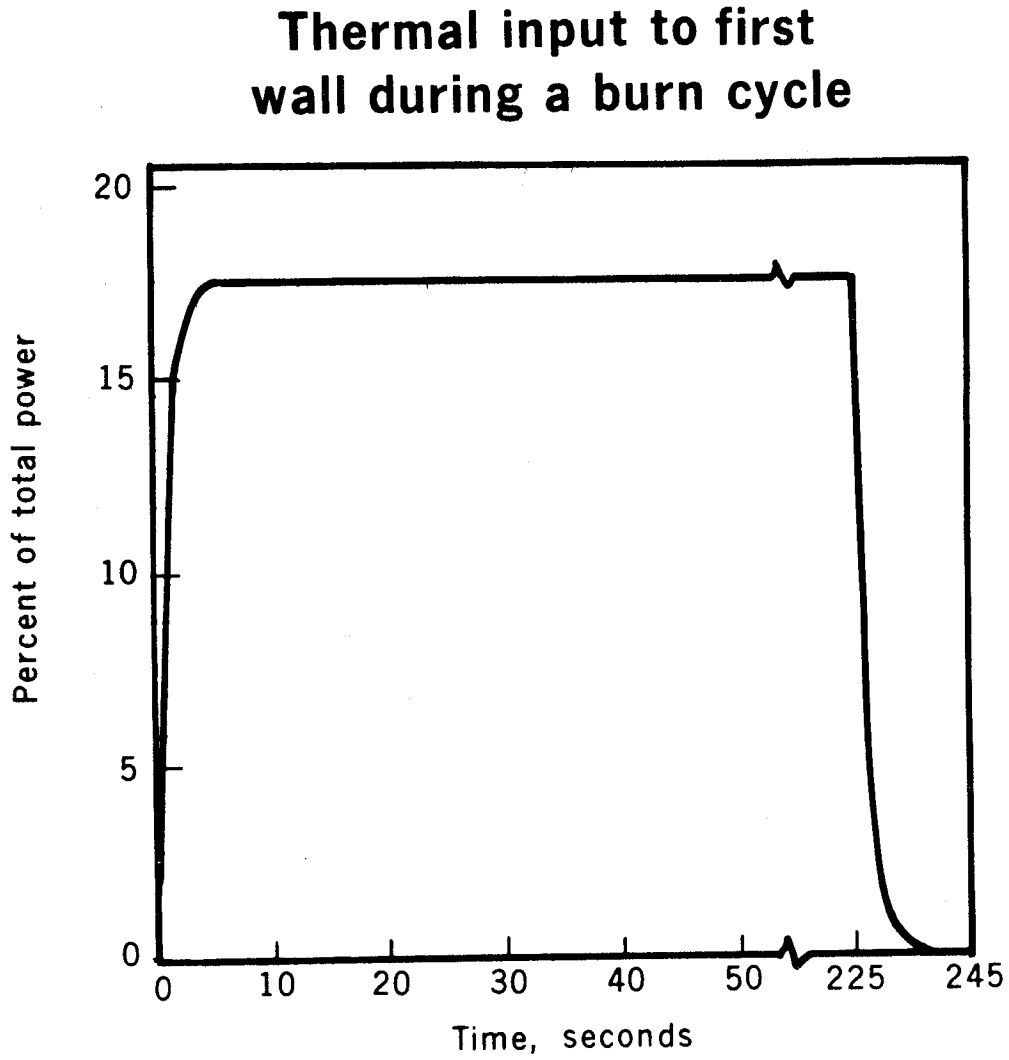

Thermal input to first wall during a burn cycle
Percent of total power
20
15
10
5
0
0
10
20
30
40
50
225
245
Time, seconds

Fig. VII-F-2

Application of thermal storage to first wall energy absorption

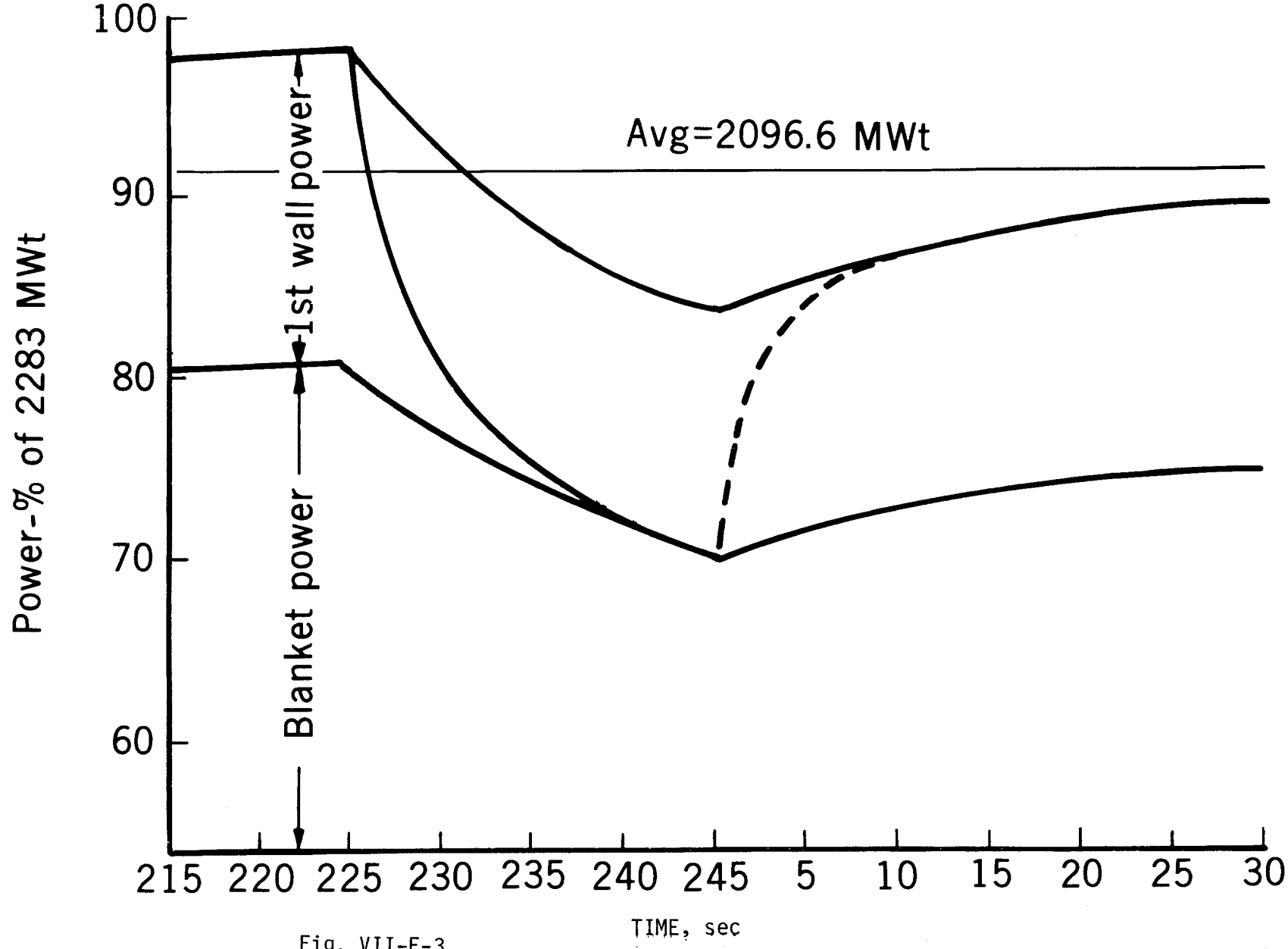


Fig. VII-F-3

Schematic showing components in NUWMAK-NSSS

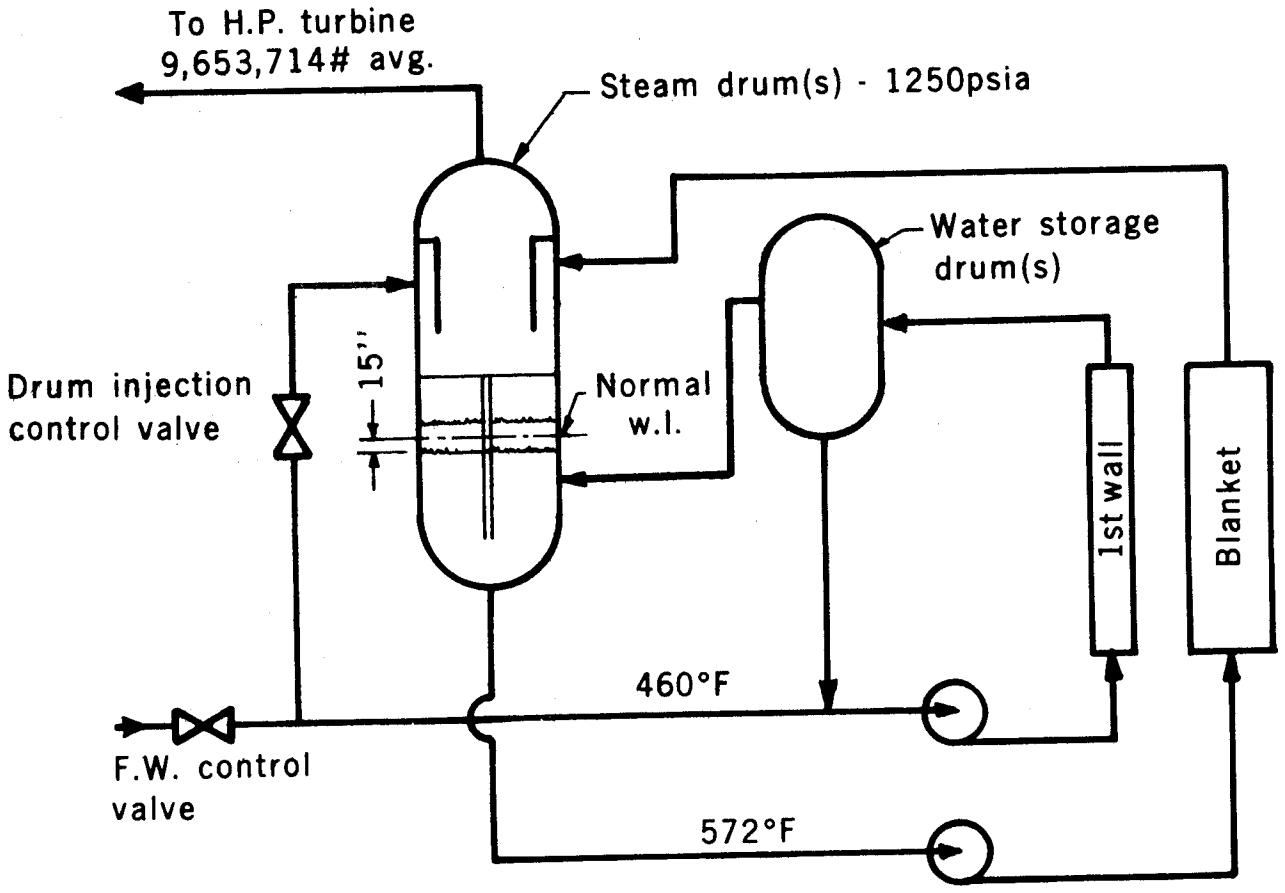


Fig. VII-F-4

The result is shown in Figure VII-F-5. Small variations between normal steam generator output and the combined effects of the above features will result in small variations of steam pressure. The largest variation corresponds to a mismatch of .04 MWh_t. Water stored in the steam generator drums, headers and tubes (170 m^3) will experience an enthalpy increase of .52 BTU/lb. This will produce a 3.8 psi pressure rise causing a rise in electrical output of only .44 percent.

Minor modification to the feedwater strings to produce the feed and extraction steam flow modulation is shown in Figure VII-F-6. The surge tanks and flow resistors are used to reduce wear and tear on the flow modulation valves. Heater size should not increase to maintain the desired average terminal temperature difference.

Factors contributing to reduced costs for load leveling are as follows:

1) Turbine modifications are minimal and an intermediate coolant loop is avoided.
2) Blanket material provides 83% of required thermal storage at no extra cost.
3) Cycle efficiency is not compromised by load leveling.

In terms of extra equipment one would need the following:

1) Four 35 m^3 cylindrical pressure vessels (1500 psi design pressure).
2) Low pressure gas loaded accumulator(s) (125 psia) capable of handling total surge volume of 12 m^3.
3) High pressure gas loaded accumulator(s) (1500 psia) capable of handling total surge volume of 12 m^3.
4) Feed modulating control valves, bypass lines and flow resistors.
5) Control valve and piping to permit direct injection of feed to each boiler drum (4).
6) Instrumentation and controls.

An appropriate conservative estimate of capital expenditure for the above equipment was calculated as follows:

(1) Most expensive component, the 35 m^3 high pressure tanks were estimated to sell for $192,000 fob based upon actual cost of similar components.
(2) The 12 m^3 accumulator capacity was assumed to be handled by the use of single high and low pressure vessels each having 35 m^3 capacity. The H.P. (1500 psi design pressure) vessel fob cost was also assumed

Feedwater and ext stm modulation to match modulation of thermal input to steam cycle

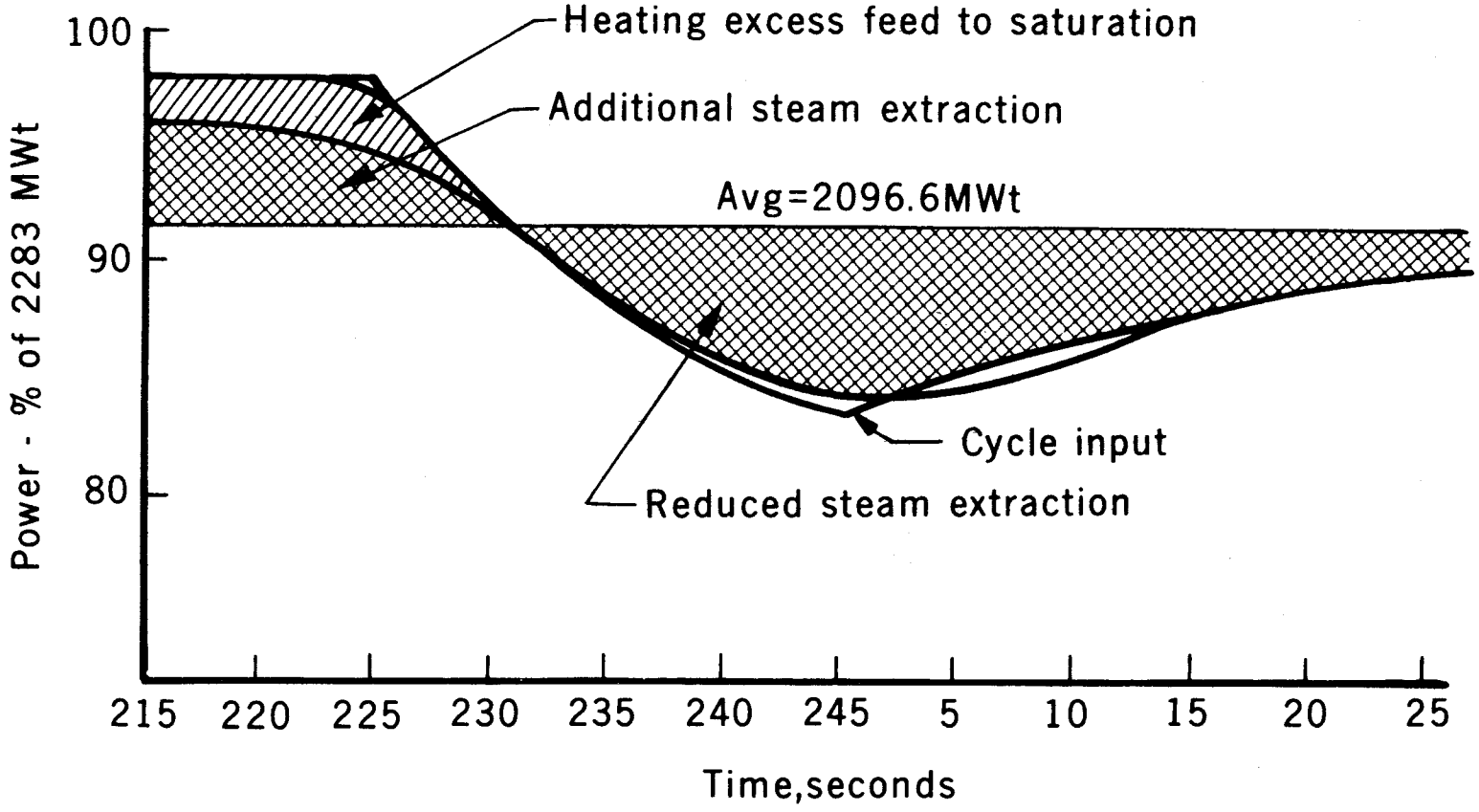
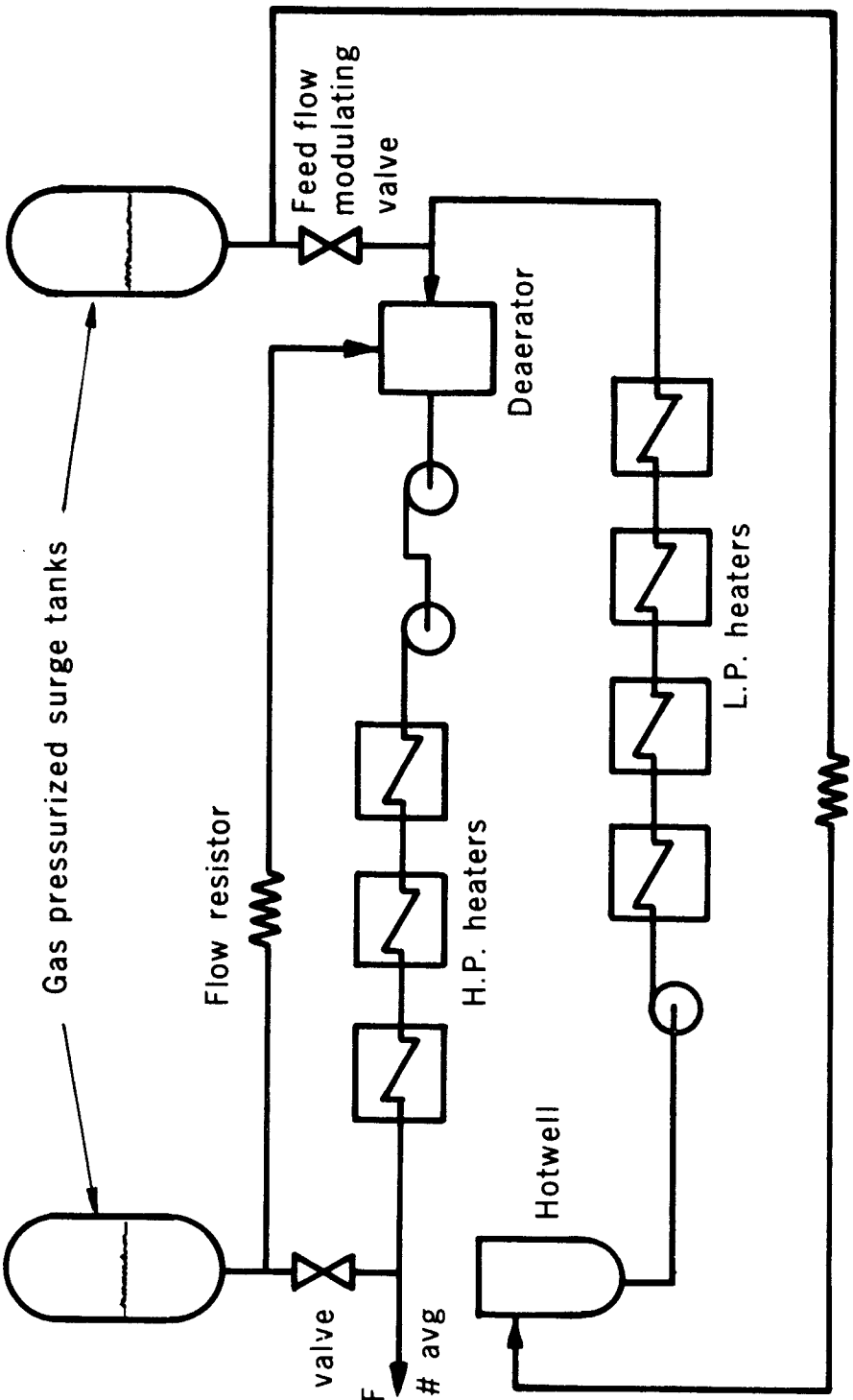


Fig. VII-F-5



Pumps designed for 12% extra flow above avg feed flow rate

Valves allow max bypass flow (each line) = 24% avg feed flow

Fig. VII-F-6

to be \$192,000. The low pressure (125 psi design pressure) vessel was assumed to cost $(125/1500)^{.25}$ x 192,000 = \$103,000.

(3) Cost of the above vessels totals \$1,063,400 (fob).

(4) With respect to this figure, the multipliers to obtain total direct cost (including the above valves and piping) are as follows (in percent).

Installation	40
Inst. and Controls	20
Piping (installed)	50
Electrical (installed)	10
	120

Thus, total direct costs are $\frac{(100 + 120)}{100}$ x 1,003,400 = \$2,339,480.

Using a characteristic ratio of 1.7 between total capital investment and total direct cost yields a total capital investment of \$3,977,000. On the basis of 660 MW_e net output, this expenditure amounts to only \$6.03/kW_e. Since the total capital expenditure will probably exceed \$2,000/kW_e in 1978 dollars, the above equipment should amount to no more than about three percent of the total plant investment.

VII-G. Conclusions

The design of a blanket for NUWMAK, a compact medium power tokamak reactor, has been carried out with the aim of alleviating the effects of several generic problems of tokamak blankets; in particular, the cyclic plasma and the need for tritium breeding. By using boiling water as the coolant and the latent heat of the breeding material for energy storage, the energy output of the reactor has been smoothed out considerably, in spite of the cyclic nature of the plasma. The use of multi-layer coolant tubes throughout the blanket has minimized tritium diffusion into the coolant to a level where an intermediate loop is no longer needed. Elimination of the intermediate loop and steam generator should result in a significant cost saving to the reactor system.

VII-H. Mechanical Design

VII-H-1. Introduction

The three factors which have provided the major impact on the mechanical design of the NUWMAK blanket are:

1 - The decision not to use a divertor

2 - RF heating instead of neutral beams

3 - No vacuum seals between blanket modules.

The decision to forego a poloidal divertor and opt for a different scheme of impurity control has considerably simplified the shape and consequently the mechanical design of the plasma chamber. In the UWMAK series of reactors[8,9,10] the poloidal divertor and the slots provided for it made it impossible to design a compact streamlined plasma chamber. Moreover, the chamber was surrounded with field shaping coils making access and servicing extremely difficult. These studies have shown that although a divertor may be a necessary part (indeed, an indispensable part) of the reactor, its inclusion immensely complicates the mechanical design. Investigation of alternate schemes of impurity control and ash removal should be pursued.

From a designer's perspective RF heating is preferable to neutral beams. In NUWMAK the frequency used is 92 MHz ($2\omega_{ci}$) which means that the launching mechanism can be made a part of the first wall. Although the power supply packages needed to drive the RF are sizeable, they can be placed out of the way and are not as constrictive as are neutral beam lines and their associated accessories.

Providing vacuum seals between blanket modules has been one of the most difficult problems from a mechanical standpoint. Most people agree that the only seal that can survive the harsh environment of the first wall is a welded seal. However, these would be difficult to make and break, especially since this operation has to be made by remote control. The obvious solution is not to have any seals between the blanket modules and instead make the seals back at the shield where they are accessible and maintainable from the outside. This concept will be discussed in more detail in the following section.

VII-H-2. General Description

The plasma chamber in NUWMAK is D shaped in cross section, being flat on the inner radius and curved on the outer as shown in Figs. VII-H-1 and VII-H-3. It is constructed entirely of Ti-6-4, a weldable and relatively

CROSS-SECTIONAL VIEW OF NUWMAK

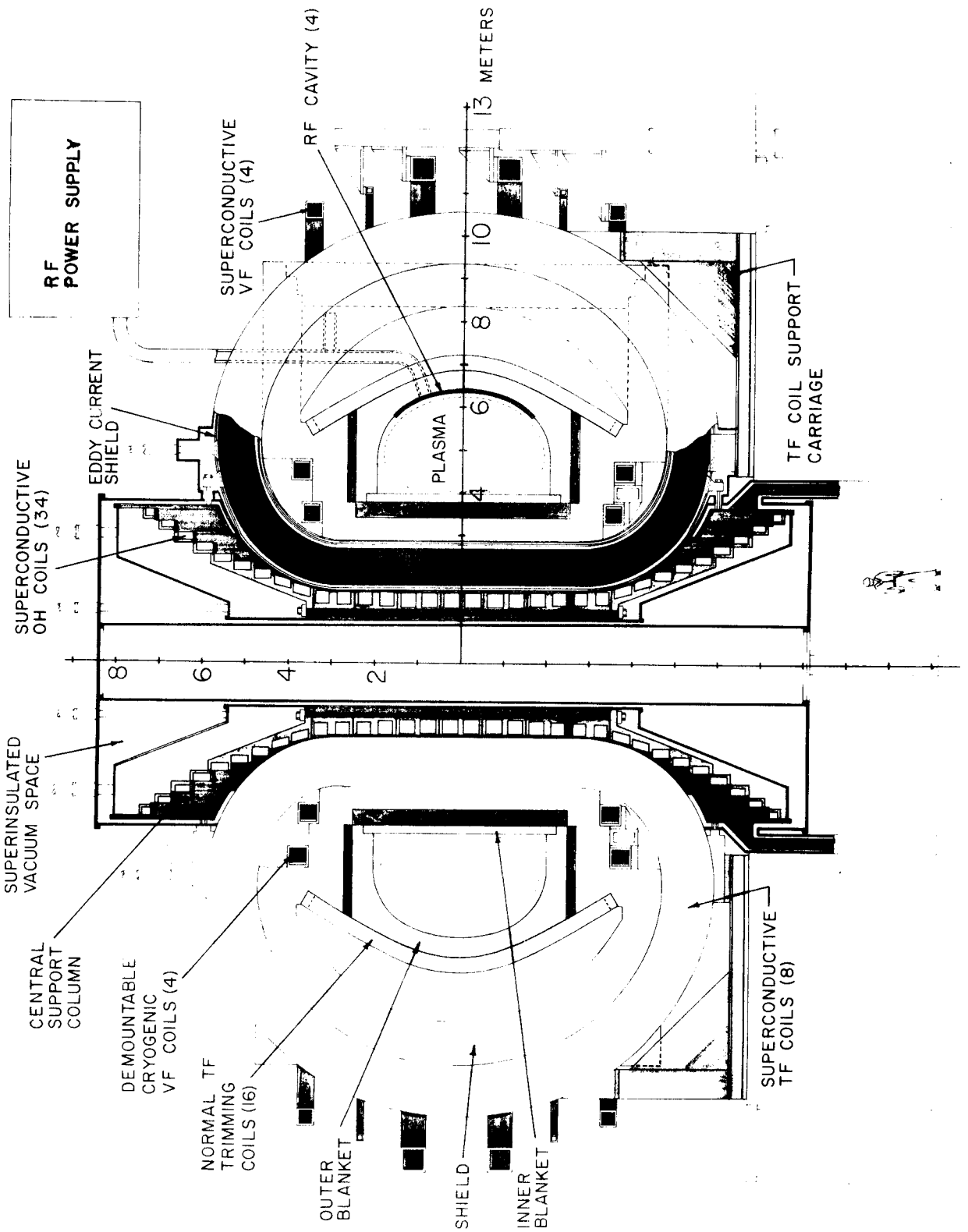


Fig. VII-H-1

TOP VIEW OF NUWMAK

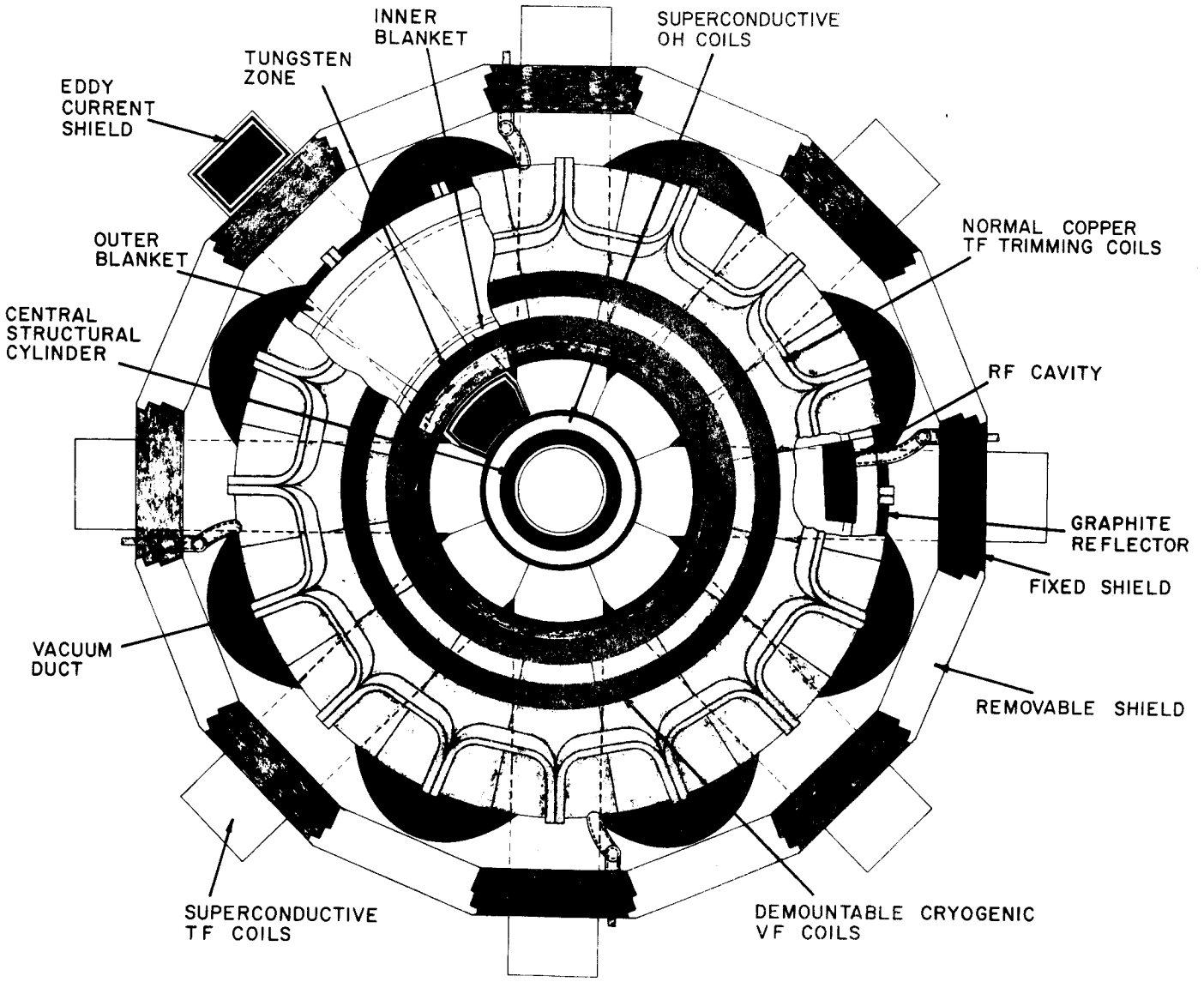


Fig. VII-H-2

CROSS SECTION OF NUWMAK THROUGH A TF COIL (with outer RF cavity)

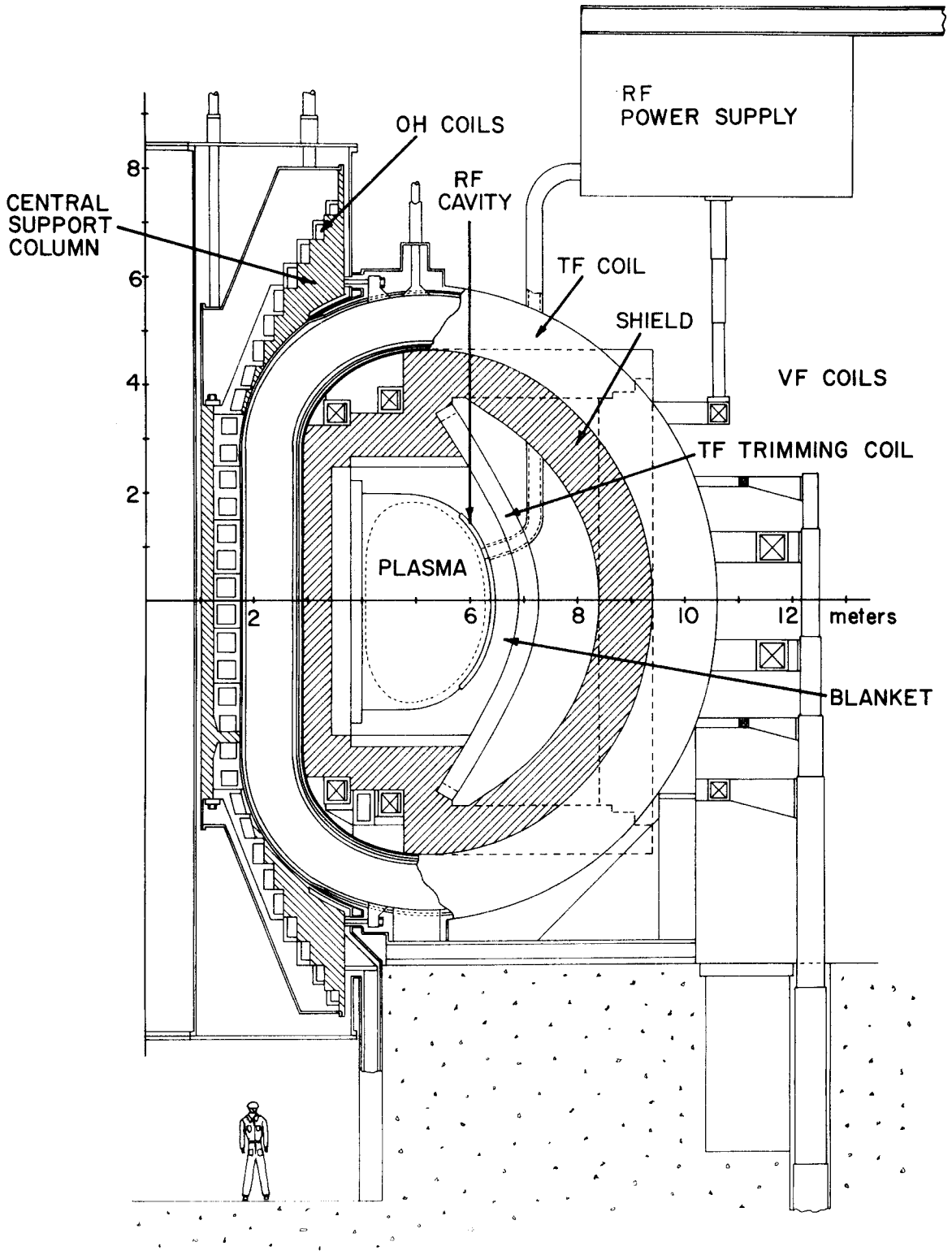


Fig. VII-H-3

easily fabricable titanium alloy very commonly used in the aircraft industry. Physically the chamber is 4 m high, the inner radius is 4 m and the outer 6.4 m, giving an aspect ratio of 1.7. In the radial direction the blanket is divided into two distinct parts, hereon referred to as the inner and outer blankets. The inner blanket is comprised of the straight section covering the inner radius and the outer blanket, the entire curved section lying between the junctions with the straight section at the top and bottom. Circumferentially the blanket is divided into 16 equal modules of $22\text{-}1/2^{o}$ each. Eight of the modules lie in line with the eight toroidal field (TF) coils and the remaining eight, between the TF coils. Four of the modules which are in line with TF coils have cavity backed aperture antennae for RF power built into the first wall of the outer blankets. The coaxial transmission line connections are made at the back of the outer blanket as shown in Figs. VII-H-2 and VII-H-3.

There are only eight TF coils in NUWMAK and thus the spaces between them at the back leg are quite large producing an unacceptable field ripple at the outer edge of the plasma. In order to mitigate this condition, normal copper saddle shaped trimming coils discussed in detail in Chapter VI are provided immediately behind the outer blanket. The parting line between two adjacent trimming coil vertical legs falls in the center of a blanket module (see Fig. VII-H-2) and the parting line between adjacent blanket modules falls in the center of a trimming coil. The junctions between adjacent blanket modules are unobstructed by the trimming coils, thus providing an ideal place for locating vacuum ports. Each two vacuum ports are ducted to a single pump station, of which there are eight located between TF coils. The pump stations are placed below grade and have a chevron shield in the duct to alleviate the problem of neutron streaming as shown in Fig. VII-H-4 which is a cross section of NUWMAK taken between TF coils.

The blanket in NUWMAK is cooled with boiling water at $300^{o}C$. The breeding and moderating material in the blanket is $Li_{62}\ Pb_{38}$ eutectic mixture which is essentially static. The coolant tubes are immersed in the breeding material absorbing the thermal energy produced by nuclear heating. During reactor down time, the latent heat of fusion of the $Li_{62}\ Pb_{38}$ is

CROSS SECTION OF NUWMAK BETWEEN TF COILS (with inner RF cavity)

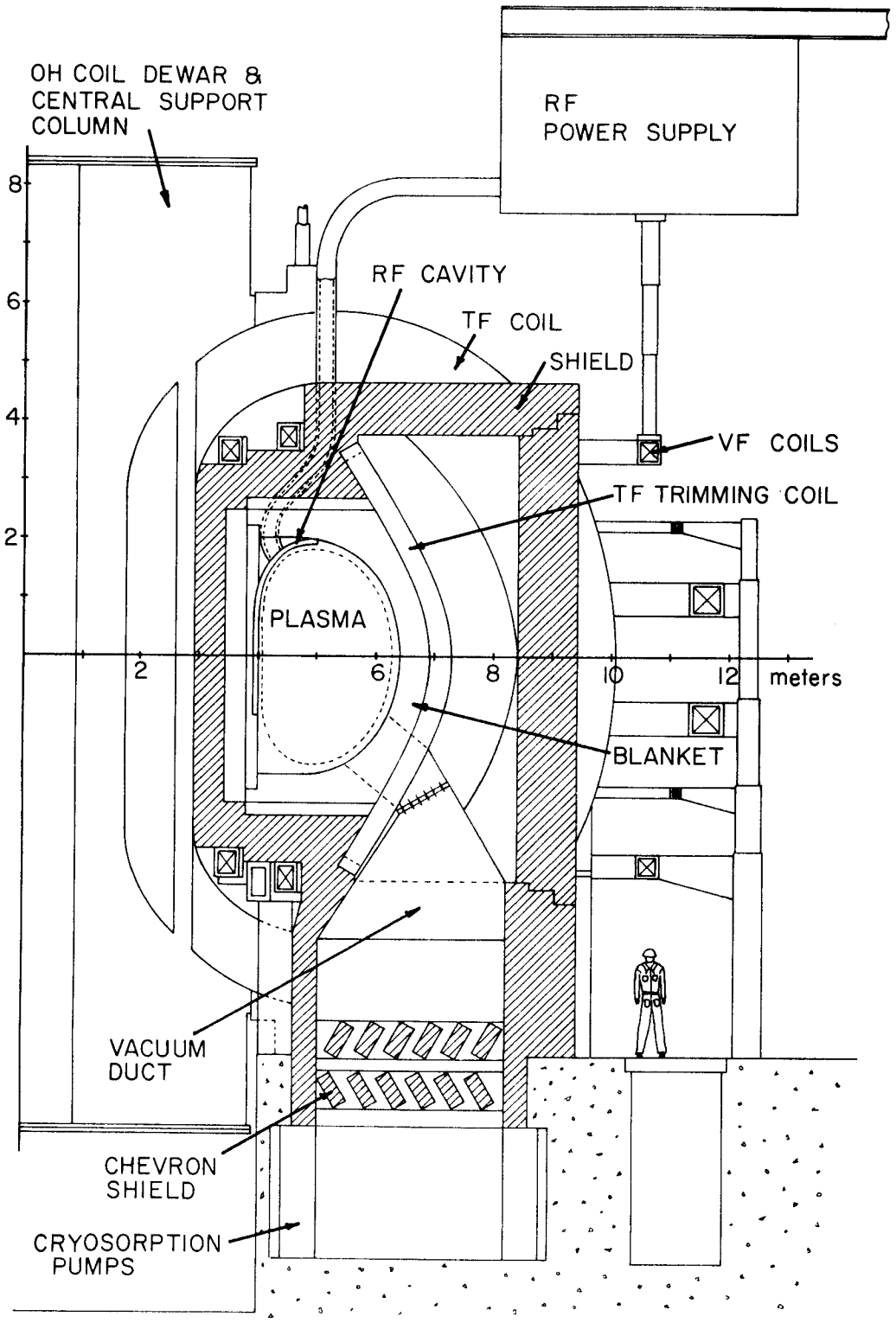


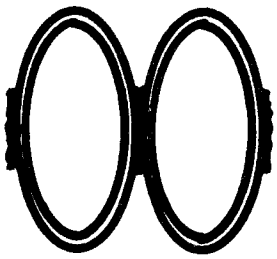
Fig. VII-H-4

used to maintain an almost constant thermal load on the turbine generators. This feature of the NUWMAK blanket considerably mitigates the problem of fatigue due to thermal cycling.

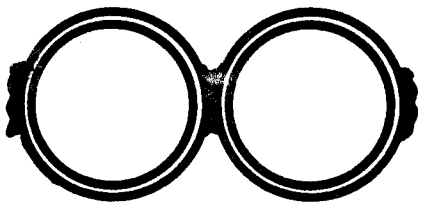
The first wall consists of a continuous bank of tubes running in the vertical direction. In the outer blanket, the circumference at midplane is 63% larger than that at the junction between it and the inner blanket. The only way to accommodate this change in geometry with a constant number of tubes running vertically is to vary the shape of the tubes. We have assumed that first wall panels can be fabricated from constant diameter tubes joined together. The dimension of the panel can be decreased by upsetting the tubes perpendicular to the panel and increased by squashing them parallel to the panel. Figure VII-H-5 shows the resultant tube shapes and Table VII-H-1 gives the dimensions of the tubes. Since the first wall consists of a composite of two tubes within each other, we take the liberty of assuming that the coated inner tubes are inserted into the panel before the tubes are upset. Obviously a lot of development has to take place before such techniques can be used for fabricating first walls of fusion reactors.

Beyond the first wall, the blanket is cooled with rows of tubes running in the vertical direction. The spacing between the rows, and the spacing between the tubes in each row is progressively increased toward the back of the blanket to account for the radially decreasing nuclear heating. An attempt is made to maintain a uniform temperature throughout the blanket. Figure VII-H-6 is a cross section of an outer blanket module at midplane, showing the continuous first wall and the cooling tubes beyond. The size and number of the tubes is out of proportion in the drawing for clarity. Radial struts, 0.2 cm thick are spaced at 20 cm intervals throughout the blanket connecting the first wall tubes to the back plate. They are needed to reinforce the first wall against the hydrostatic pressure of the breeding material. The side plates of the blanket modules are 0.3 cm thick and the back plate is 0.5 cm thick.

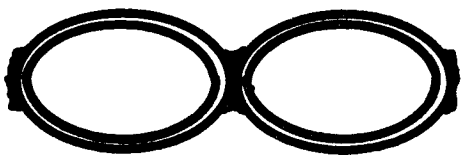
The first wall and blanket tubes are connected to circumferential headers at the top and bottom as shown in Fig. VII-H-7. A single supply line



a. Tube cross section at extremity of blanket module



b. Tube cross section at point intermediate between extremity and midplane



c. Tube cross section at midplane

Fig. VII-H-5 First wall tube shapes for NUWMAK

Table VII-H-1

First Wall and Blanket Tube Specifications

	First Wall (original dimensions)	Inside Blanket
OD of outer tube (cm)	1.3	1.3
ID of outer tube (cm)	1.16	1.16
Material of outer tube	Ti-6-4	Ti-6-4
OD of inner tube (cm)	1.14	1.14
ID of inner tube (cm)	1.06	1.00
Material of inner tube	Ti	Ti-6-4
	(squashed dim.)	
Outer tube width at midplane (cm)	1.4	
Outer tube depth at midplane (cm)	0.92	
Outer tube width at junction between inner and outer blanket modules (cm)	0.85	
Outer tube depth at junction between inner and outer blanket modules (cm)	1.50	

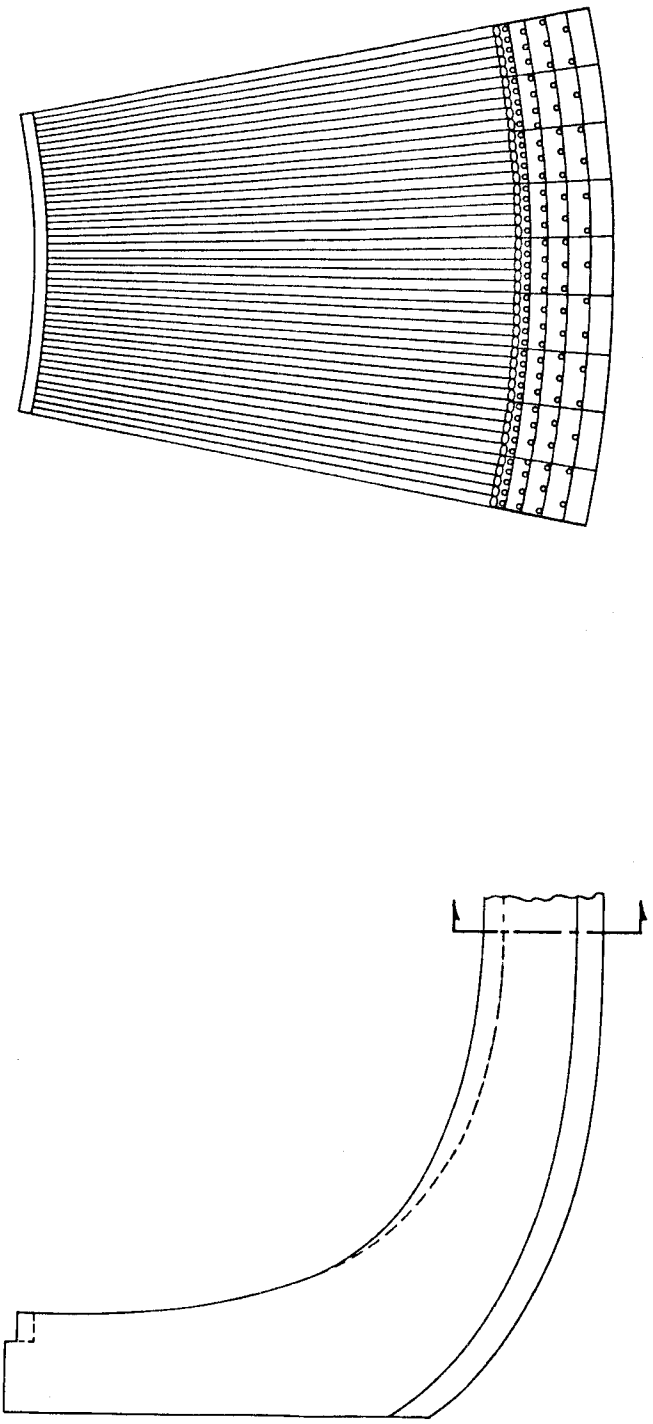


Fig. VII-H-6 Cross section of outer blanket module at midplane

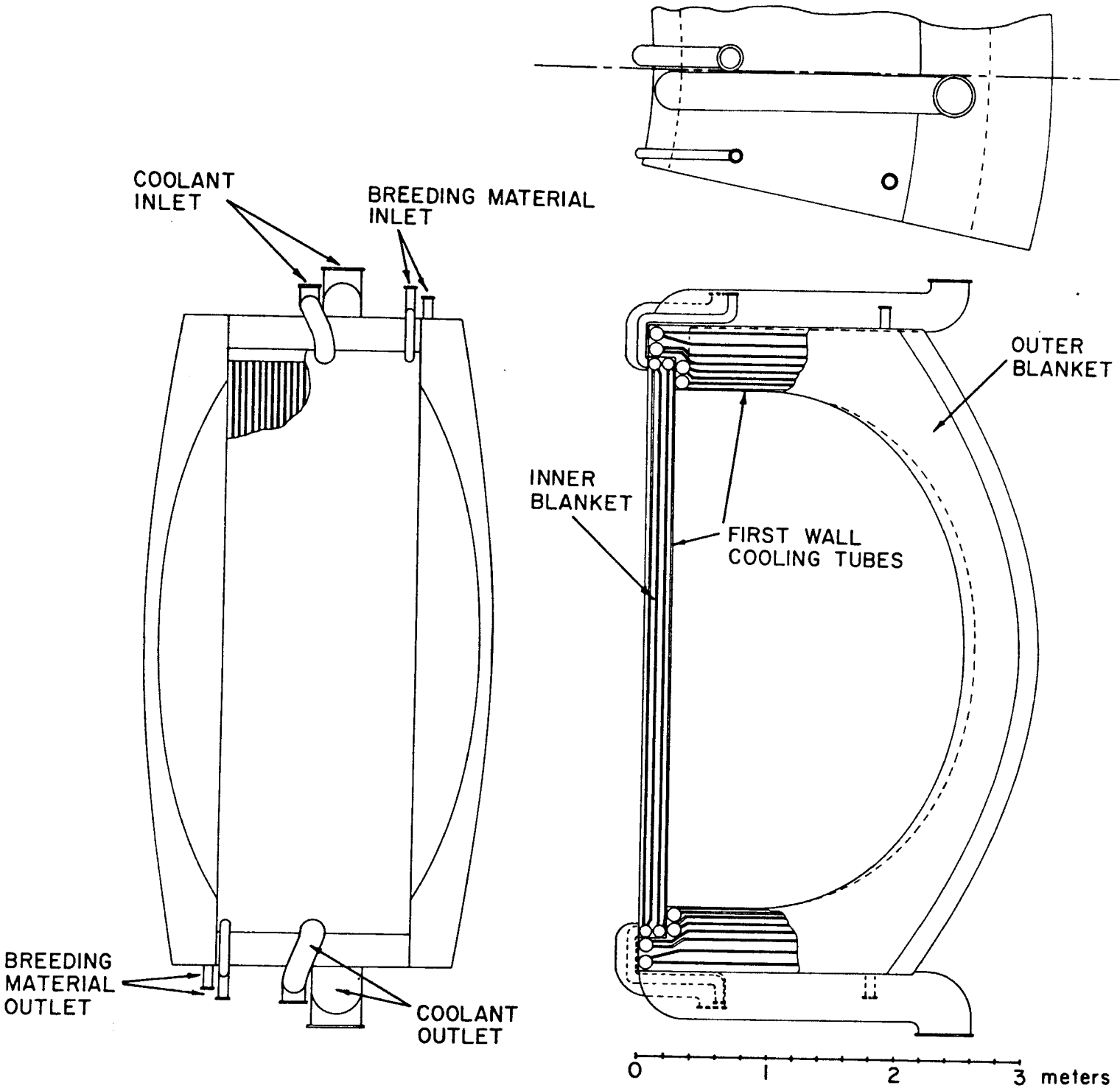


Fig. VII-H-7. Cross-Sectional View of Blanket

feeds saturated water at 300°C to the circumferential headers. The water then flows upward through the banks of tubes, boiling in the process and emerging into the top circumferential headers with about 10% steam. A single return line them connects into a header outside the toroidal enclosure. The 10% saturated mixture then goes to a steam drum where the steam is separated to drive a steam turbine while the water is recycled back to the reactor.

From the heat transfer standpoint the breeding material in the blanket is essentially static. However, for tritium removal, the breeding material has to be circulated. Each inner and outer blanket module has a supply and return line for circulating the breeding material. This provision also serves another important aspect of this design, namely that the breeding material can be drained out of the blanket during maintenance. During blanket module changeout, the mass handled is only a small fraction of the weight of the module during reactor operation.

The inner and outer blanket modules have been provided with separate coolant and breeding material lines. However, the two sections are joined together, and are inserted and taken out as a unit. It was thought that by providing separate lines for the inner and outer blanket modules it would simplify flow control and manifolding. This, of course, means that there are twice as many connections to make and break, a distinct disadvantage. It is not out of the question, however, to consider providing common coolant and breeding material lines for the inner and outer blanket modules.

As has been mentioned earlier, we have chosen not to make seals between blanket modules. Instead, the inside surface of the shield is the vacuum barrier everywhere except on the periphery of the removable shield gates located between TF coils. These removable shield segments will be equipped with seals that can be undone from the outside.

The blanket modules within the reactor are butted against each other such that the gaps between them are long and narrow, presenting a high impedance to the leakage of gas in the molecular flow regime. This will allow a pressure gradient to be maintained across the gaps between the plasma chamber and the region behind the blanket. Eliminating the seals between blanket modules makes the maintenance of the blanket considerably simpler.

VII-H-3. Structural Considerations

A thorough stress analysis of the first wall and blanket has not been performed. In this section we obtain a very rough estimate of the magnitude of the stesses.

VII-H-3-a. First Wall and Blanket Stresses

The first wall is the most severely stressed element of the blanket because it is subjected to both thermal and pressure stresses. The problem is further complicated by the fact that the first wall tubes are not uniformly round as described in Section VII-E-2. Figure VII-H-5 shows the different cross sections of the first wall tubes at three locations in the outer blanket.

To simplify the analysis we will assume that the shape of the tubes is ellipsoidal (wherever they are not round). At the midplane of the outer blanket the width of the squashed outer tube is 63% larger than the width at the junction between the outer and the inner blanket. If we designate the major dimension of the ellipse as 2a and the minor dimension as 2b, then the radius of curvature at any point is:

$$r = \frac{a^2 b^2}{(a^2 \sin^2\phi + b^2 \cos^2\phi)^{3/2}}$$

where ϕ is the angle measured from the major axis of the ellipse. At midplane 2a = 1.4 cm, 2b = 0.92 cm and the major radius of curvature ($\phi = 90^o$) is 1.07 cm. For this ratio of r/t, membrane theory dominates and bending is negligible. The pressure stress is, therefore, simply Pr/t, where P is the operating pressure and t the wall thickness of the tube. Steam pressure in the first wall is 8.62×10^6 N/m^2 (1250 psi) and the wall thickness is 0.07 cm, giving a hoop stress

$$\sigma_p = 1.29 \times 10^8 \text{ N/m}^2 \text{ (18,710 psi)} .$$

Elsewhere in the tube, the stresses are lower since they are proportional to r. At the minimum radius where r/t is high, the bending component adds about 10% to the stress. The total stress at this point ($\phi = 0$) is 4.2×10^8 N/m^2 (6092 psi).

The nuclear heating ω_n in the first wall is 20 W/cm^3 and the surface heating ω_s is 108 W/cm^2. The thermal stress is given as:

$$\sigma_{th} = \pm \frac{\alpha}{2} \frac{E}{k(1-\nu)} (\omega_s + \frac{\omega_n}{2} t)\ t$$

where α is the coefficient of expansion, E the modulus of elasticity, k the thermal conductivity, ν Poisson's ratio and t the thickness of the tube. For Ti-6-4 at 400°C these values are:

$$\alpha = 10 \times 10^{-6}\ cm/cm^{o}C$$
$$E = 85 \times 10^{9}\ N/m^2$$
$$k = 0.12\ W/cm^{o}C$$
$$\nu = 0.3$$
$$t = 0.07\ cm$$

The thermal stress is:

$$\sigma_{th} = \pm\ 3.85 \times 10^{7}\ N/m^2\ (\pm\ 5584\ psi)$$

with compression on the outer tube surface and tension on the inner. At midplane of the outer blanket first wall, the side of the tubes facing the plasma will have a tensile stress of 9.05×10^{7} N/cm^2 (13,126 psi) on the outer surface and a tensile stress of 1.675×10^{8} N/m^2 (24,290 psi) on the inner surface. During down time, these stresses equalize at 1.29×10^{8} N/m^2 (18,710 psi) as the temperature gradient across the wall of the tube goes to zero.

This simple analysis assumes that the outer tube carries the full load of the coolant. In the actual case, the inner tube will yield until the two surfaces come in contact with each other and then the load will be shared by them. However, should the inner tube start leaking, then the outer tube will have the full load stresses imposed on it. This scheme thus gives a measure of redundancy to the first wall.

Other sources of stresses within the blanket are due to the hydrostatic pressure of the breeding material and to mechanical supports.

The maximum hydrostatic pressure at the bottom of the blanket is 2.75×10^5 N/m^2 (~ 40 psi) and acts over a distance of 20 cm of the first wall which is the distance between the 0.2 cm thick spacers joining the first wall to the back plate. This produces a negligible stress in the first wall. However, the blanket module side plates which are 0.3 cm thick will be over-stressed by this pressure. It will, therefore, be necessary to reinforce the side plates with internal ribs.

It is envisaged that the blanket module will be supported on rails fixed to the shield structure. The rails will guide the blanket modules during changeout. We believe this support scheme would not produce excessive stresses in the blanket; however, this problem has not been thoroughly addressed.

VII-H-3-b. Blanket and Shield Support

We have mentioned earlier that the blanket modules are supported on rails fixed to the shield. When full of breeding material, a blanket module weighs 57.9 metric tons of which 84% is breeding material, 11% is graphite and 5% is Ti structure. During blanket changeout, the breeding material is drained out leaving the Ti structure and the graphite reflector weighing only 9.3 metric tons.

The weight of all the reactor components within the toroidal enclosure which includes the shield, blanket, trimming coils and cryogenic VF coils is ~ 5200 metric tons. All this weight is transferred to the floor of the reactor containment building either by direct bearing (Fig. VII-H-4) or by columns protruding between TF coils. Tables VII-H-2 and VII-H-3 give the masses of the materials used in the blanket and shield, respectively.

Table VII-H-2
Materials in the NUWMAK Blanket

Material	Inner Blanket (tonnes)	Outer Blanket (tonnes)	Total (tonnes)
Ti Structure	8	38.4	46.4
Li_{62} Pb_{38}	70.4	726	796.4
Graphite	None	106	105
		Total	947.8

Table VII-H-3
Materials in the NUWMAK Shield

Material	Inner Shield (tonnes)	Outer Shield (tonnes)	Total (tonnes)
Ti Structure	16.2	130.3	146.5
Pb	98.3	1033	1131.3
B_4C	87.5	1813	1900.5
W	693.5	None	693.5
		Total	3871.8 tonnes

Appendix
Effect of Gas Puffing on the First Wall and Limiter Design

The gas puffing fueling scheme proposed in the NUWMAK study results in a plasma power output variation corresponding to a puffing cycle. The plasma calculations are discussed in the plasma section. The time dependent neutron power output, energy to the first wall and energy to the limiter are shown on Fig. VII-1, VII-2, VII-3, respectively.

The purpose of the limiter is to define the boundary of the plasma. In NUWMAK, there are three toroidal limiters located at the outer edge of the first wall. Each limiter is divided into sixteen sections, one for each blanket module. The limiter is 10 cm high and consists of two banks of copper tubes cooled by forced convection. Water is the coolant. The thermal load on the limiter is 10 kW/cm^2. The parameters for the limiter are listed on Table VII-1.

A cross-sectional view of the limiter is shown on Fig. VII-4. This configuration is chosen because it was analyzed and tested by RCA[7]; a water cooled heat sink develops, capable of absorbing 2 kW/cm^2 from a neutral beam source for the TFTR. The temperature distribution, the finite element model for stress calculations and the calculated stress are shown on Fig. VII-5, VII-6, and VII-7, respectively. The results presented in Ref. 7 are for different wall loadings and are normalized to the case of 1 kW/cm^2. The high surface stress values predicted for the attachment

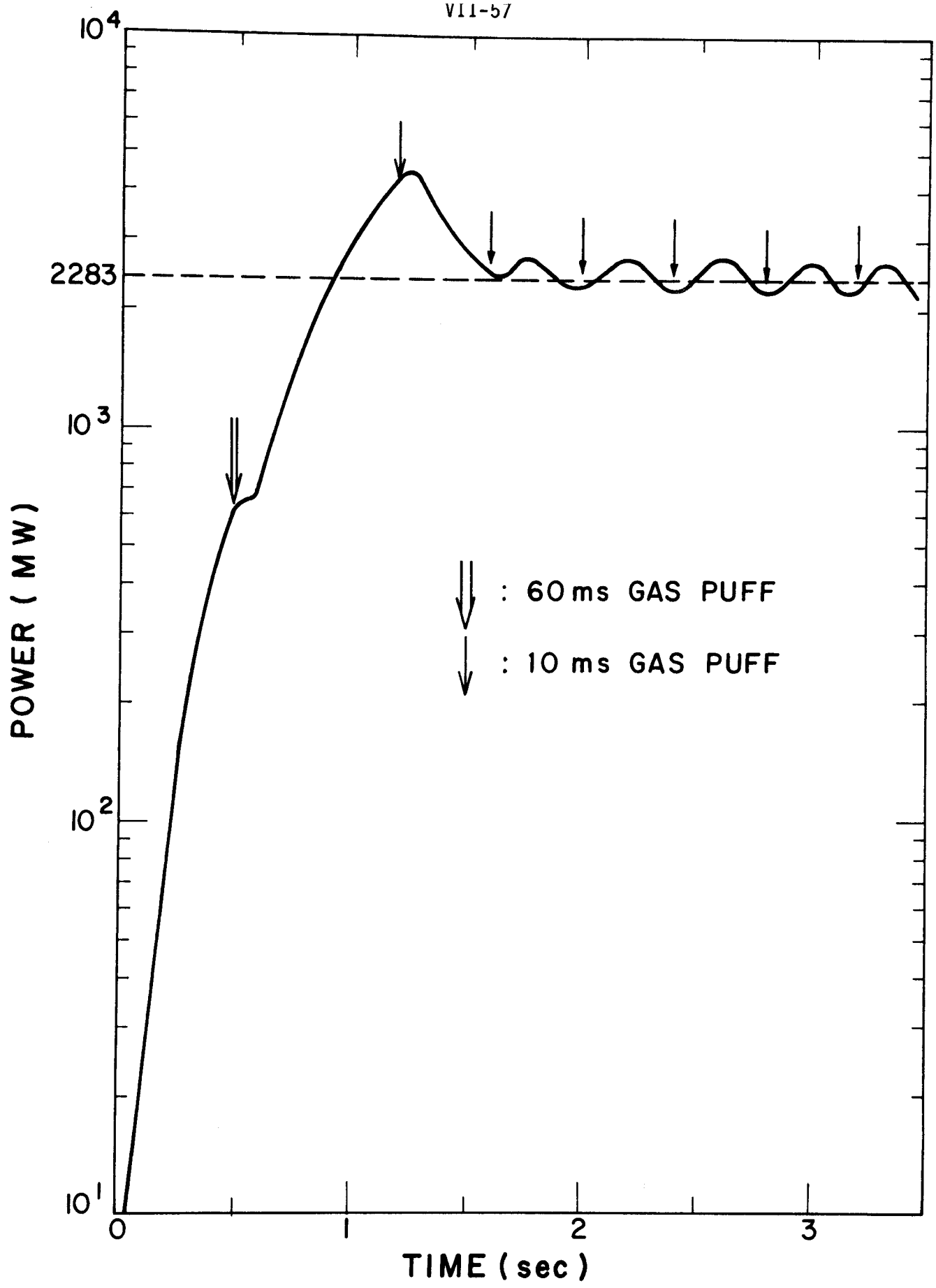


Fig. VII-1 Time history of NUWMAK plasma power: Case B

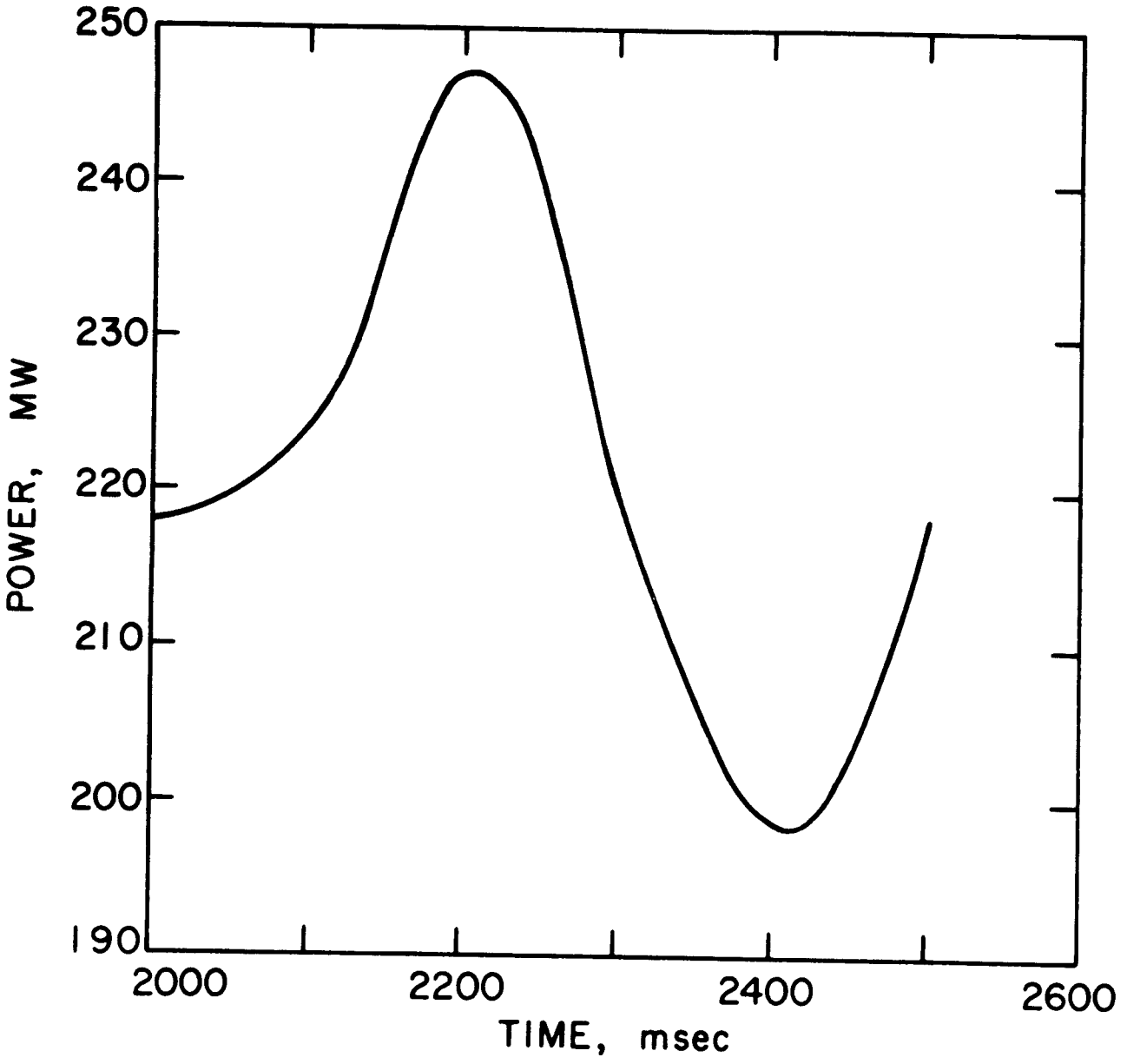


Fig. VII-2 POWER TO THE LIMITER DURING A PUFFING CYCLE

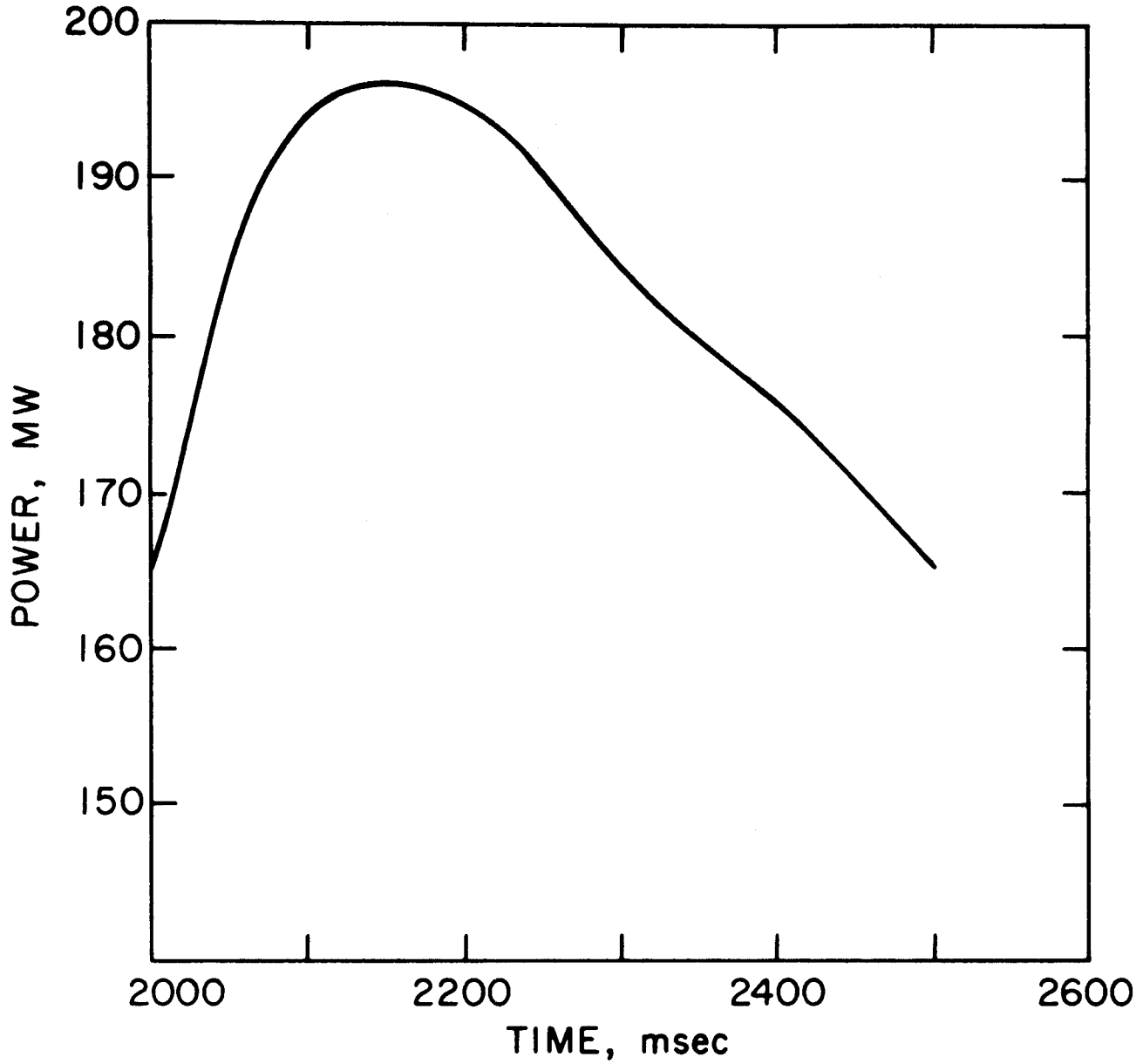


Fig. VII-3 POWER TO THE FIRST WALL DURING A PUFFING CYCLE

Table VII-1 Parameters of the Limiter

Type of Limiter	Toroidal
No. of Limiter	3
Section for Each Limiter	16
Length for Each Limiter Section	2.36 m
Height of the Limiter	10 cm
Total Limiter Area	22.2 m^2
Average Energy to Limiter	222 MW
Energy Variation During a Puffing Cycle	$\pm$ 8%
Normal Thermal Flux	1 kW/cm^2
Coolant	Water
Coolant Velocity	1.5 m/sec
Coolant Temperature In	75^oC
Coolant Temperature Out	150^oC
Coolant Pressure Drop	.5 MPa
Maximum Structure Temperature	250^oC
Maximum Stress	173 MPa

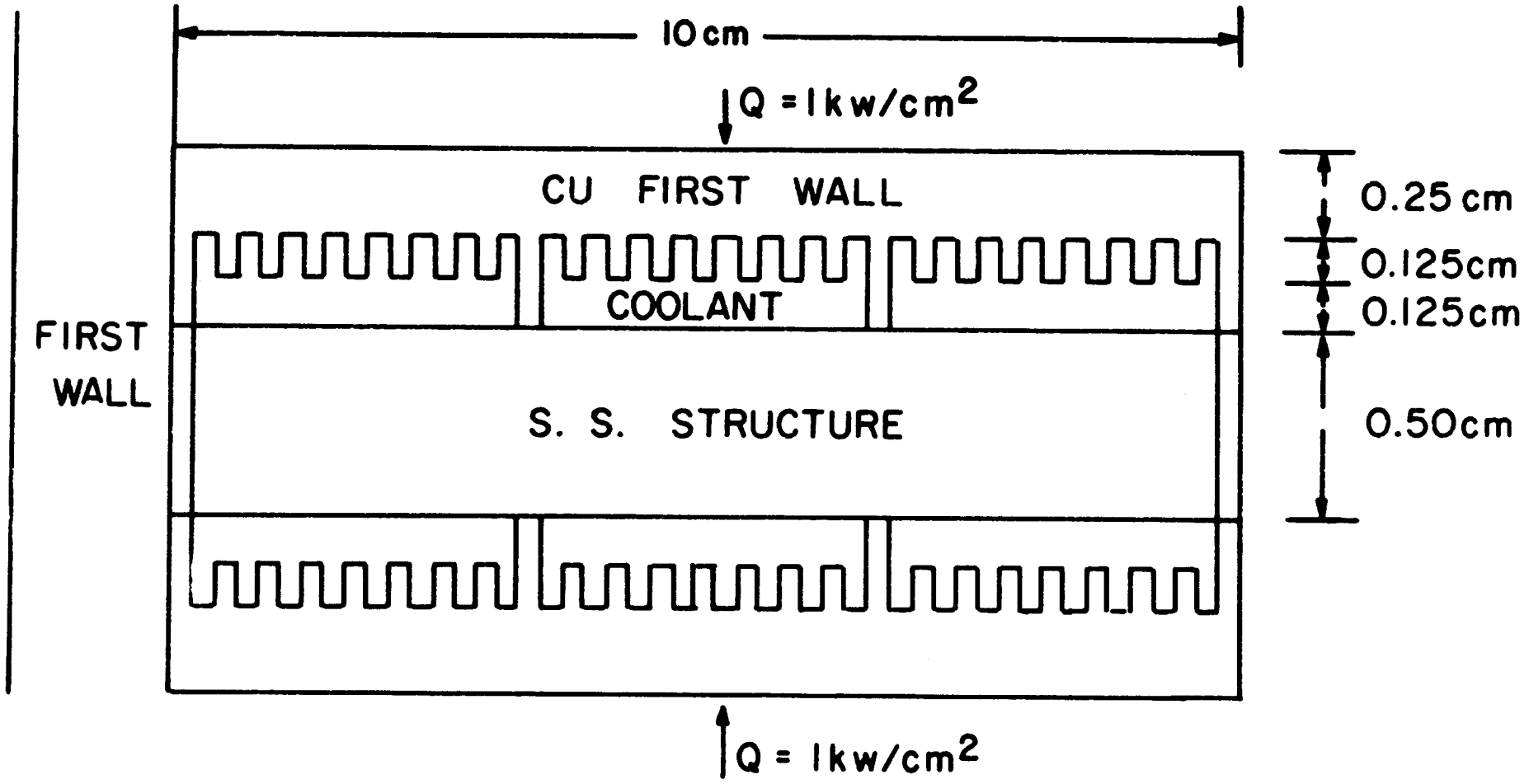


Fig. VII-4 CROSS-SECTIONAL VIEW OF THE LIMITER

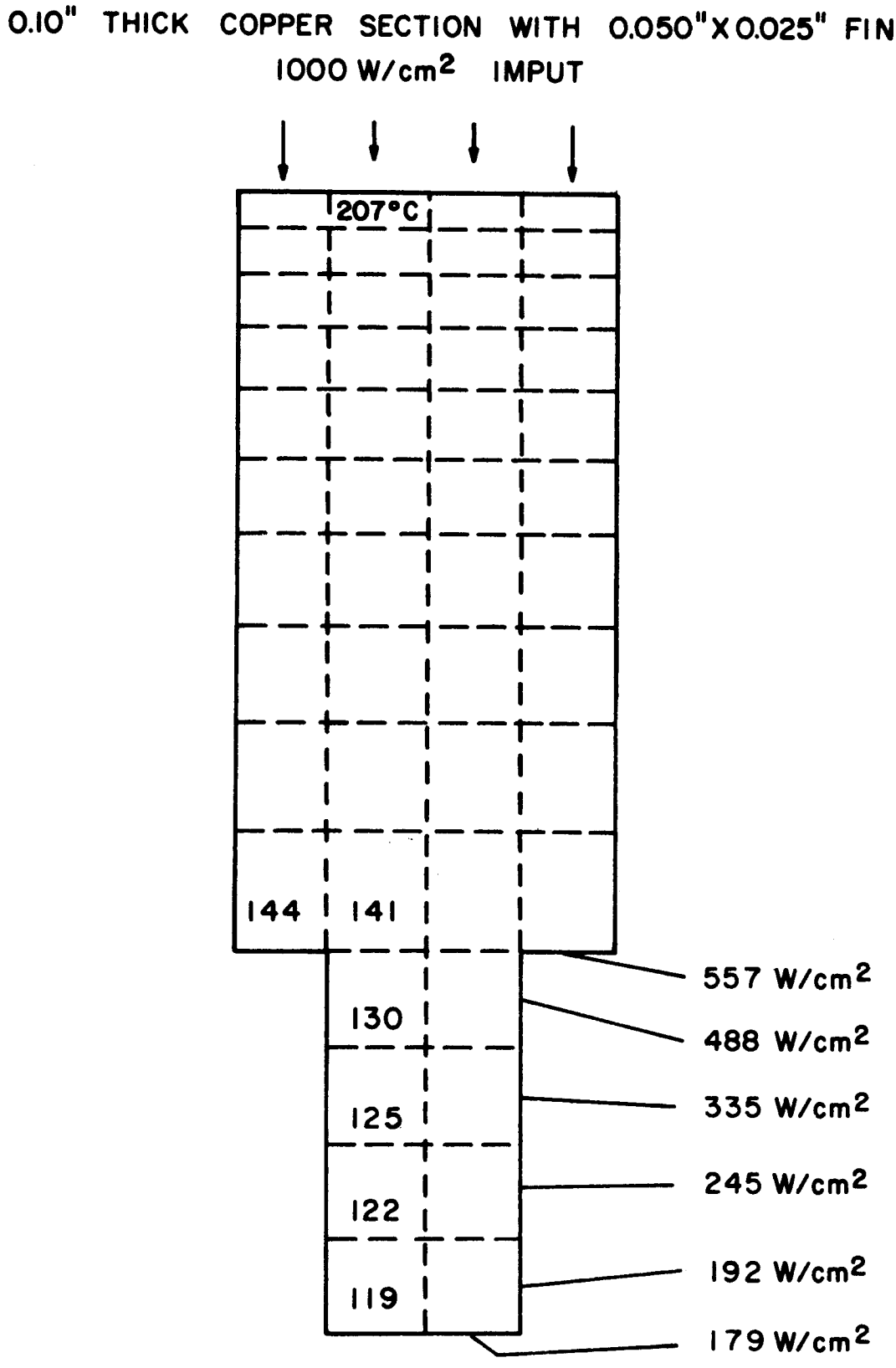


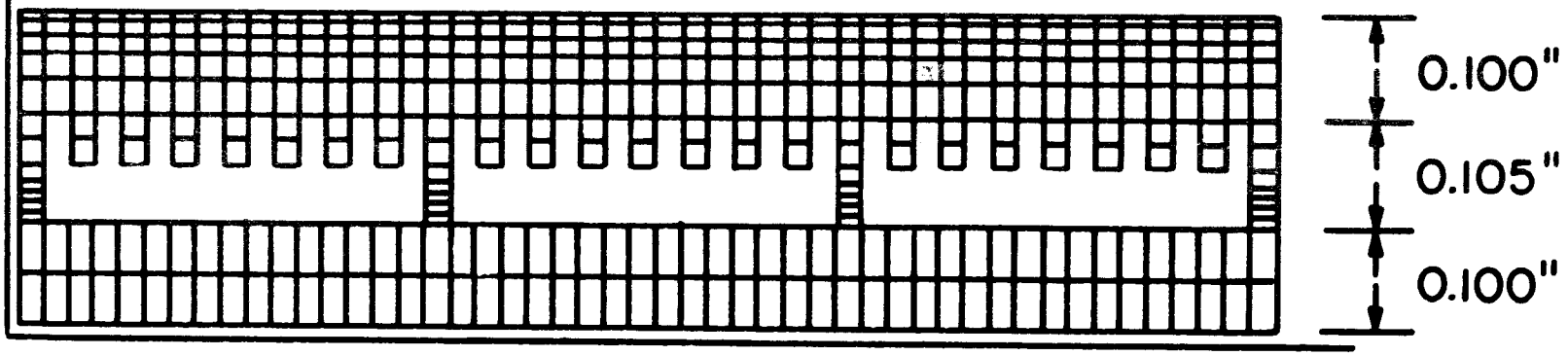
Fig. VII-5 Temperature of the limiter.

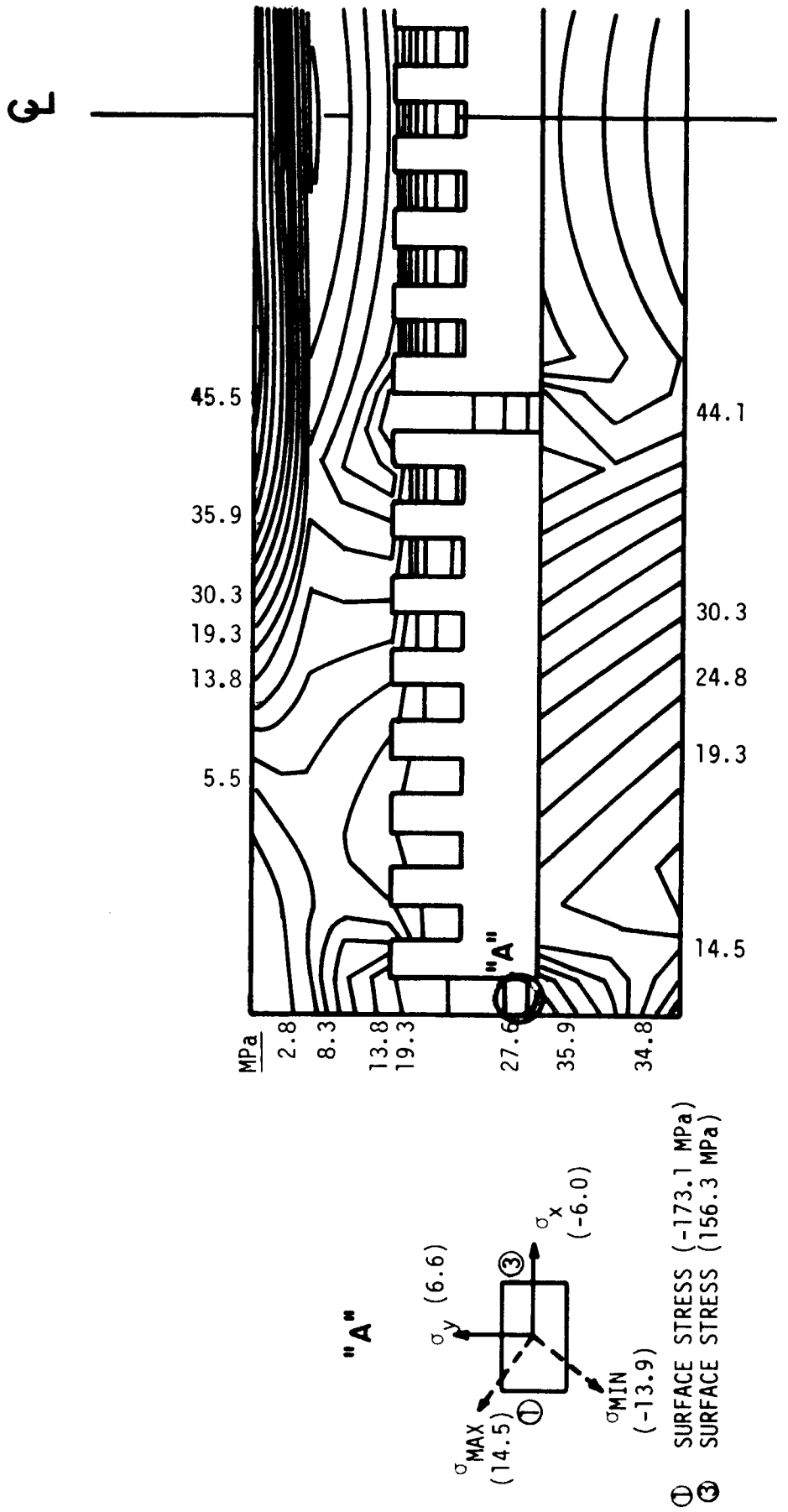
Fig. VII-6

FINITE ELEMENT MODEL - THREE SECTIONS - FOUR SUPPORTS

COPPER WITH 304 STAINLESS BACK

CONFIGURATION "C"





STRESS DISTRIBUTION OF THE LIMITER

Fig. VII-7

points between the copper and stainless steel backing plate are disturbing. However, a model survived over 6000 testing cycles with the wall loading varying between 1.2 and 2.6 kW/cm^2.

The thermal load to the limiter varies $\pm$8% for every .5 second due to the gas puffing scheme. The temperature response time for a 1 mm copper plate is less than .1 second. Therefore, the temperature response of the limiter wall facing the plasma can be considered instantaneous. The impact of this fast cycling on stress to the structure of the limiter over years of operation cannot be determined without further experimental work. The high stress, thermal fatigue and the effect of sputtering, which will be discussed in the materials section, will most likely have a detrimental effect on the life expectancy of the limiter.

The thermal cycling will not have any impact on the interior of the blanket due to the phase change energy storage of $Li_{62}\ Pb_{38}$. The temperature response of the first wall will also be instantaneous, and is shown on Fig. VII-8. The thermal load on the first wall is much smaller than that on the limiter, and a 8% variation will result in a $\pm$ 10^{o}C temperature variation.

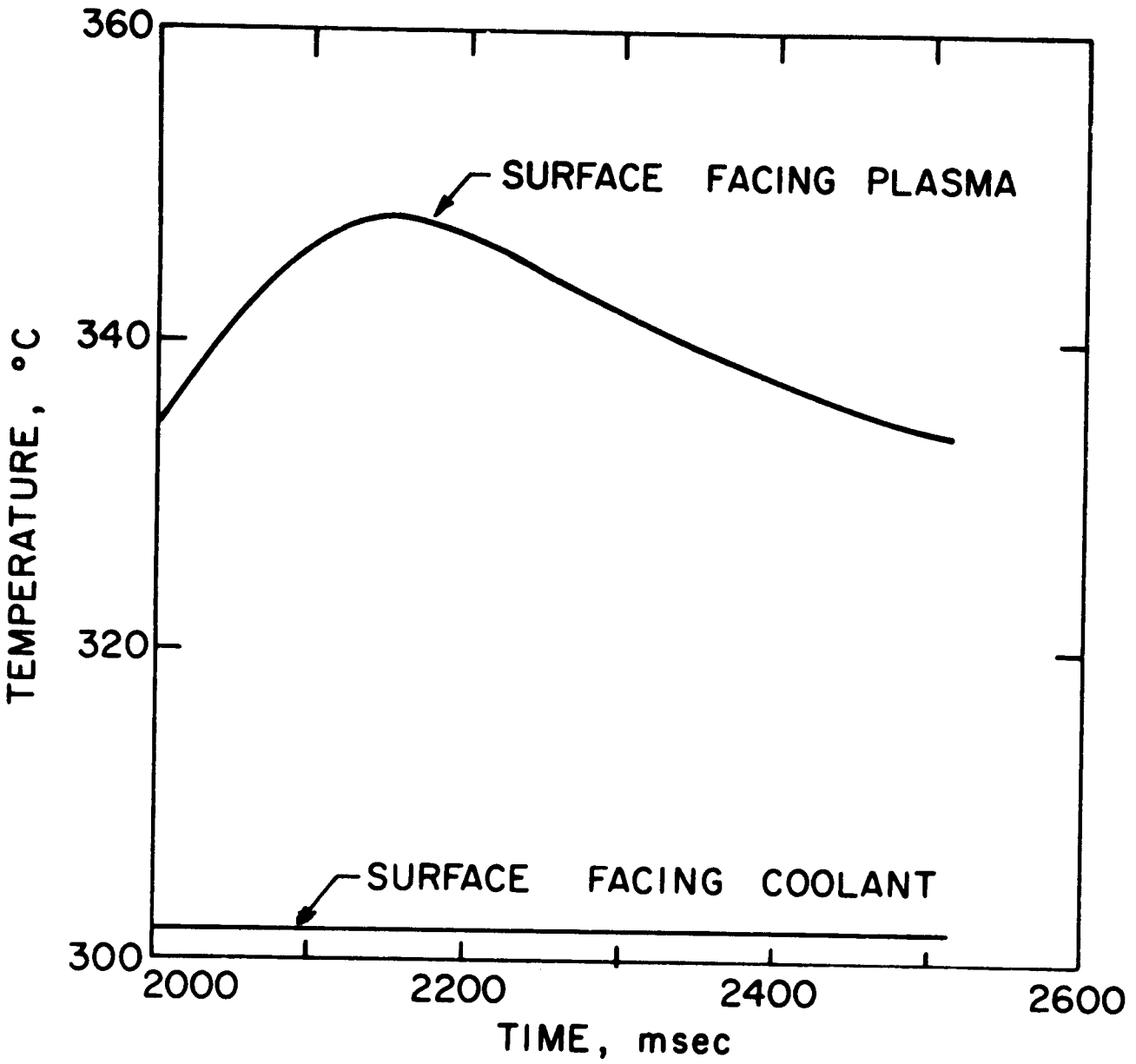


Fig. VII-8 TEMPERATURE RESPONSE OF THE FIRST WALL DURING A PUFFING CYCLE

References for Chapter VII

1. J.R. Powell, J.A. Fillo, B.G. Twining, and J.J. Dorning, "Proceedings of the Magnetic Fusion Energy Blanket and Shield Workshop", Brookhaven National Lab., Upton, N.Y., 1976.

2. D.K. Sze, E.M. Larsen, E.T. Cheng, R.G. Clemmer, "A Gas-Carried Li_2O Cooling/Breeding Fusion Reactor Blanket Concept", Trans. Am. Nucl. Soc. 22 (1975) 21.

3. Yasushi Seka, Kiyoshi Sako, Kichizo Tanaka and Torn Hiraoka, "Tritium Breeding in Ceramic Lithium Compound Blanket", JAERI, Tokai, Ibaraki, Japan.

4. D. Kearney, et al., "Design Considerations for a Noncircular Tokamak Demonstration Plant", Proceedings of the Second Topical Meeting on the Technology of Controlled Nuclear Fusion, Richland, Washington, September 1976.

5. R.H. Wiswall and E. Wirsing, "Tritium Recovery From Fusion Blankets Using Solid Lithium Compound", Radiation Effects and Tritium Technology for Fusion Reactors, Gatlinburg, Tennessee, 1975.

6. N.A. Frigerio and L.L. LaVoy, "The Preparation and Properties of LiPb, A Novel Material for Shields and Collimators", Nuclear Technology, 10, 322, 1971.

7. W.E. Harbaugh, et al., "Water Cooled D.C. Heat Sink Development", RCA Report No. 2660502, September 30, 1977.

8. B. Badger, et al., "UWMAK-I, A Wisconsin Toroidal Fusion Reactor Design," Fusion Research Program Report UWFDM-68, Univ. of Wisconsin (1974).

9. B. Badger, et al., "UWMAK-II, A Conceptual Tokamak Power Reactor Design", Fusion Research Program Report UWFDM-112, Univ. of Wisconsin (Oct. 1975).

10. B. Badger, et al., "UWMAK-III, A Noncircular Tokamak Power Reactor Design", Electric Power Research Institute Report ER-368, EPRI (July 1976).

VIII. Neutronics Analysis and Radioactivity

VIII-A. Introduction

A compact tokamak fusion reactor design[1] has evolved from the series of UWMAK designs, namely UWMAK-I,[2] II[3] and III.[4] This new conceptual design, NUWMAK, is characterized by a high value of plasma power density (11 MW/m^3) and spatially averaged neutron wall loading (4.34 MW/m^2). It has a major and minor radius of 5.13 and 1.13 meters, respectively, and a height to width ratio of 1.64. The on-axis magnetic field is 6.05 tesla and maximum field at the magnet is 11.5 tesla. There are only eight superconducting coils in this design and this provides extensive space for access and maintenance.[5] The major features and cross sectional view of the NUWMAK design are tabulated and depicted in Table VIII-A-1 and Fig. VIII-A-1, respectively.

In this paper we present the nucleonic design for the NUWMAK blanket and shield. The general design goals for this type of compact reactor are as follows: A tritium breeding ratio of no less than 1.10; a blanket/shield energy deposition of no less than 17 MeV per D-T neutron; the maximum resistivity change in the superconducting stabilizer and the critical current density change in the superconductors smaller than 50% and 2%, respectively; an endurable dose on the superinsulators for the entire plant lifetime; and low radioactivity. All the above considerations are discussed in detail in Sec. VIII-B. Sec. VIII-C presents methods of neutronic calculations and analyses which include one and two dimensional problems. In Sec. VIII-D preliminary survey and design calculations are given in which the tritium breeding ratio as a function of lithium lead composition and percent ^6Li in total lithium are considered. Included in this section are magnet protection considerations with each shield zone thickness and height, such as the tungsten zone, discussed. The final results for the NUWMAK blanket and shield design are presented in Sec. VIII-E. The discussion of radioactivity, afterheat, biological hazard potential (BHP) and dose rate after shutdown is given in Sec. VIII-F. Finally, the conclusions of this nucleonic design for a compact tokamak fusion reactor blanket and shield are summarized in Sec. VIII-G.

Table VIII-A-1

Major Features of NUWMAK Design

Power	
Total Thermal Power	2097 MW_t
Net Electric Power	660 MW_e
Plasma	
Major Radius	5.13 m
Minor Radius	1.13 m
Plasma Height to Width Ratio (b/a)	1.64
Plasma Current	7.2 MA
Toroidal Beta	6%
$n_e\tau_E$	2×10^{14} cm^{-3}-sec
q(a)	2.64
Magnet	
On-Axis Toroidal Field	6.05 Tesla
Toroidal Field at NbTi Conductor	11.5 Tesla
Stabilizer	Aluminum
Number of Toroidal Field Coils	8
Number of Cu Trim Coils	16
Blanket	
Structural Material	Titanium Alloy
Coolant	Boiling Water
Breeding Material	$Li_{62}Pb_{38}$
Average Neutron Wall Loading	4.34 MW/m^2

CROSS-SECTIONAL VIEW OF NUWMAK

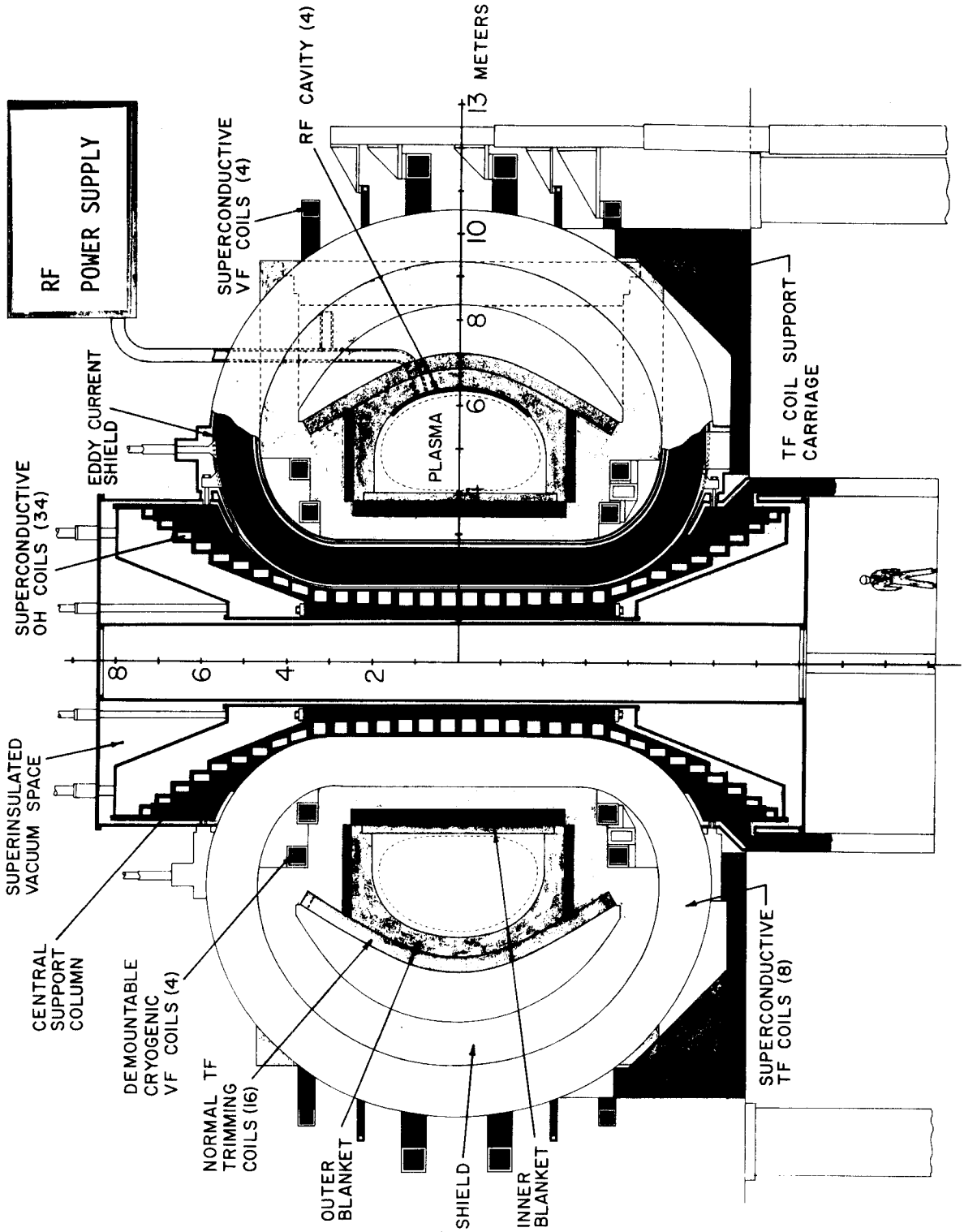


Figure VIII-A-1

VIII-B. Design Goals for NUWMAK Blanket and Shield

The design goals for the NUWMAK blanket and shield have evolved from our previous conceptual tokamak fusion reactor designs[2-4] and from those discussed in the literature[7-12]. Here, we will briefly review some of the important features related to the blanket and shield design and summarize the design requirements on the characteristic roles of the blanket and shield, namely, tritium breeding, nuclear energy deposition and magnet shielding.

VIII-B-1. Tritium Breeding

It has been shown that a tritium breeding ratio of ~ 1.02 tritons per D-T neutron is capable of producing a doubling time of 2-7 years[7]. This means that a tritium breeding ratio of slightly greater than unity would meet the refueling requirement of a D-T fusion reactor for the whole plant lifetime of about 30 years. However, considering the uncertainties inherent in the neutron transport calculation due to the geometric homogeneity assumed in the calculational model, and the nuclear data uncertainty, it is very often required that the tritium breeding ratio is to be greater than 1.10 in order to assure the adequacy of the breeding capability.[8]

VIII-B-2. Nuclear Energy Deposition

One of the basic functions of the blanket is to intercept the 14 MeV neutrons and convert their kinetic energy into heat. The blanket energy multiplication, M, is given by the ratio of the heat deposited in the blanket to the source neutron kinetic energy, i.e.,

$$M = \frac{\text{Blanket Heat Deposition (MeV per D-T Neutron)}}{\text{Source Neutron Energy (14.1 MeV per Neutron)}} \quad .$$

In order to obtain a higher thermal power output, the blanket energy multiplication is to be as large as possible. It is desired that $M \geq 1.2$, i.e., the blanket heat deposition is greater than 17 MeV per D-T fusion neutron. Since the heat deposited in the cold shield will not be recoverable, this heat should be designed to be as small as possible. In this study we have limited the non-recoverable heat to less than one percent of the total thermal output.

VIII-B-3. Magnet Shielding

In a fusion reactor shield design, the most severe problem is to protect the superconducting magnet. The function of a superconducting magnet can be affected during reactor operation through radiation damage to the magnet components, namely, superconductors, structural, stabilizing, and super-insulating materials.

In the superconductors, the radiation damage is primarily due to neutron bombardment and affects the critical temperature, T_c, and the critical current density, J_c. It has been reported that the reduction of T_c in NbTi is very small under a neutron fluence of 10^{18} n/cm^2. The reduction of J_c in NbTi is less than 0.5% if the irradiating neutron fluence is no more than 10^{17} n/cm^2. However, it will be more than 16% or 170% if the neutron fluence is 5×10^{18} or 10^{19} n/cm^2, respectively.[9]

As far as the stabilizing material is concerned, the radiation damage results in an increase of the electrical resistivity under neutron irradiation. For the aluminum stabilizer studied here the electrical resistivity is not sensitive to an applied magnetic field of more than 2 tesla.[10] The neutron irradiation effect is measured by the extent of atomic displacement (displacement per atom, dpa) in metals. For an atomic displacement of 10^{-5} dpa, the resistivity will increase by $\sim 1.3 \times 10^{-8}$ ohm-cm, which is ~ 1.3 times that of the resistivity without irradiation.* However, the increase of the electrical resistivity is $\sim$ 13% if the atomic displacement is $\sim 1 \times 10^{-6}$ dpa. The resistivity change below 10^{-5} dpa is roughly linear and can be expressed as

$$\rho_c = 1.33 \times 10^{-3} \times \text{dpa (ohm - cm) for dpa} \leq 10^{-5} .$$

For the design of a superconducting magnet the magnetic field strength and the heat transfer characteristics are very important considerations during operation. The magnetic field strength and the ohmic heat generation are proportional to the current density in the superconductors and the resistivity in the stabilizer, respectively. Hence, the reduction of the critical current density in the superconductor, as well as the increase of the

*The electrical resistivity of the aluminum adopted in the UWMAK-III (Ref. 4) and NUWMAK designs is 1×10^{-8} ohm-cm. This is higher than the predicted value, $\sim 7 \times 10^{-9}$ ohm-cm, for safety purposes.

resistivity in the stabilizer will limit as well as determine the functioning of the magnet. However, the resistivity change and critical current density reduction are recoverable as the magnet is brought back to higher temperature for annealing. For example, the recovery of the aluminum resistivity is almost 100% at room temperature.[10] Thus, it is very important to expect a reasonable period of down time for both blanket replacement and magnet annealing in order to maximize the plant utilization.

In the design of the NUWMAK magnet, a maximum increase of 50% for the resistivity in the aluminum stabilizer is used as the limit. As the value of resistivity reaches this limit, the plant will be shut down and the magnet annealed while the blanket is replaced. Corresponding to this limit, $\sim 4 \times 10^{-6}$ dpa at the aluminum stabilizer is expected.

While the radiation damage to the superconductors and stabilizer can be restored, the effects on the superinsulation materials are irreversible.[11] Radiation damage to the superinsulation materials is measured in terms of the dose or the amount of nuclear energy, including neutrons and gamma-rays, absorbed in them expressed in units of rads (one rad is defined as the absorption of 100 ergs of energy by a gram of material mass). It has been reported[11,12] that mylar based superinsulators suffer severe property changes if the dose is more than 1×10^8 rads. However, the endurable dose for epoxy based superinsulators is in the range of $1\text{-}5 \times 10^9$ rads. Therefore, for a plant lifetime of $\sim$ 30 years, a dose rate of less than 3×10^6 and $3\text{-}15 \times 10^7$ rads/year is desired if mylar and epoxy based superinsulators are to be employed for the magnet design.

In summary, in the design of the NUWMAK blanket and shield, we aim at the following criteria:

1. A tritium breeding ratio of no less than 1.10 tritons per D-T neutron.
2. A blanket/shield energy deposition of no less than 17 MeV per D-T neutron, of which $\sim$ 99% is recoverable.

3. The maximum resistivity change in the aluminum stabilizer and the critical current density reduction in the superconductors is no greater than 50% and 2%, respectively, before magnet annealing takes place.
4. An endurable dose to the superinsulation materials for the plant lifetime.

VIII-C. Methods of Calculation

The neutronics calculations make use of one and two-dimensional discrete ordinates transport codes, ANISN[13] and DØT[14] for either survey or design purposes. The calculations were performed with the P_3S_4 approximation in cylindrical or r-z geometry depending on whether one or two-dimensional models are used. The nuclear cross section library used is the same as described elsewhere[15] and is collapsed into coupled 25 neutron and 21 gamma-ray groups. In Table VIII-C-1 the neutron group structure is given and compared to that from Ref. 15. The gamma-ray group structure is kept unchanged. The displacement cross sections were obtained from Ref. 16. The neutronics model, which is used to provide detailed spatial neutron and gamma-ray fluxes and nuclear responses, consists of the important components of fusion reactors; namely the magnet, the shield, the blanket, and the plasma and vacuum core. Two-dimensional models, as shown in Fig. VIII-C-1, provide for the poloidal variation in zone thicknesses and the different design of the inner shield. The blanket and shield are made of the titanium alloy, Ti-6242. The piping material is another titanium alloy, Ti-6Al-4V. However, in the flux calculations, both structural and piping materials are treated as the alloy Ti-6Al-4V, and this has almost no effect on the neutronic results. The coolant is boiling water. At the midplane, the inner blanket/shield consists of a 20 cm breeding zone, a tungsten hot shield, a boron carbide cold shield and a lead zone. The individual zone thickness is to be decided after an analysis of the survey calculations according to the design goals discussed in the previous section. The total thickness of this shield zone is fixed at 85 cm. Thus, the distance from the first wall to the dewar of the superconducting coils is only 1.05 meters. The outer blanket/shield region consists of a 50 cm breeding blanket,

Table VIII-C-1

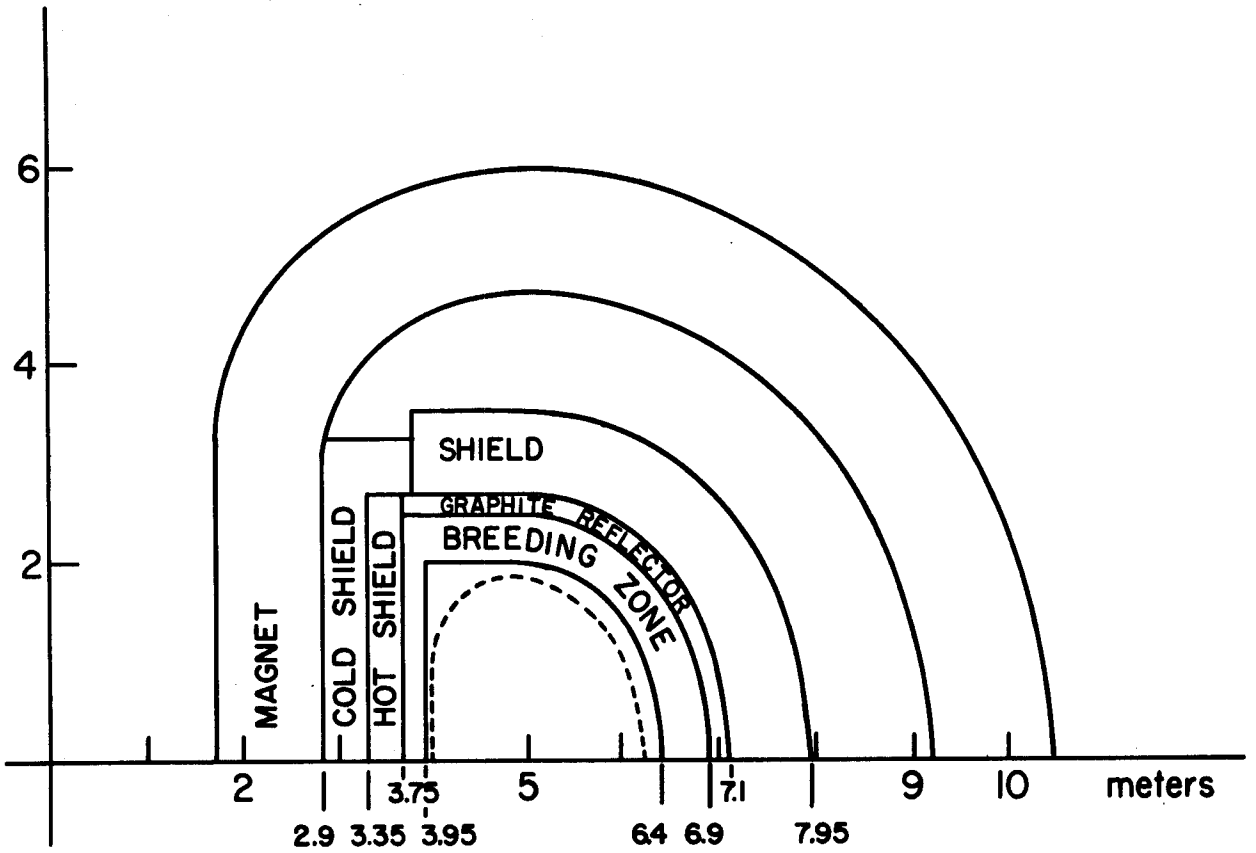
Neutron 25 Energy Group Structure in eV

Group Limits

Group	E(Top)	E(Low)	E(Mid Point)	Corresponding Fine Groups in 100 Group Structure[a]
1	1.4918 (+7)	1.3499 (+7)	1.4208 (+7)	1
2	1.3499 (+7)	1.2214 (+7)	1.2856 (+7)	2
3	1.2214 (+7)	1.1052 (+7)	1.1633 (+7)	3
4	1.1052 (+7)	1.0000 (+7)	1.0526 (+7)	4
5	1.0000 (+7)	9.0484 (+6)	9.5242 (+6)	5
6	9.0484 (+6)	8.1873 (+6)	8.6178 (+6)	6
7	8.1873 (+6)	7.4082 (+6)	7.7979 (+6)	7
8	7.4082 (+6)	6.7032 (+6)	7.0557 (+6)	8
9	6.7032 (+6)	6.0653 (+6)	6.3843 (+6)	9
10	6.0653 (+6)	5.4881 (+6)	5.7787 (+6)	10
11	5.4881 (+6)	4.4933 (+6)	4.9907 (+6)	11 - 12
12	4.4933 (+6)	3.6788 (+6)	4.0860 (+6)	13 - 14
13	3.6788 (+6)	3.0119 (+6)	3.3453 (+6)	15 - 16
14	3.0119 (+6)	2.4660 (+6)	2.7390 (+6)	17 - 18
15	2.4660 (+6)	1.3534 (+6)	1.9097 (+6)	19 - 24
16	1.3534 (+6)	7.4274 (+5)	1.0481 (+6)	25 - 30
17	7.4274 (+5)	4.0762 (+5)	5.7518 (+5)	31 - 36
18	4.0762 (+5)	1.6573 (+5)	2.8667 (+5)	37 - 45
19	1.6573 (+5)	3.1828 (+4)	9.8779 (+4)	46 - 54
20	3.1828 (+4)	3.3546 (+3)	1.7591 (+4)	55 - 63
21	3.3546 (+3)	3.5358 (+2)	1.8541 (+3)	64 - 72
22	3.5358 (+2)	3.7267 (+1)	1.9542 (+2)	73 - 81
23	3.7267 (+1)	3.9279 (+0)	2.0597 (+1)	82 - 90
24	3.9279 (+0)	4.1399 (-1)	2.1718 (+0)	91 - 99
25	4.1399 (-1)	2.200 (-2)	2.1800 (-1)	100

a. the original EPR library group structure

SCHEMATIC OF THE BLANKET AND SHIELD FOR NUWMAK



COLD SHIELD	HOT SHIELD	BREEDING ZONE	GRAPHITE REFLECTOR	SHIELD
3.5% Ti alloy	4% Ti alloy	5.7% Ti alloy	3.5% Ti alloy	3.5% Ti alloy
95.25% B_4C	93% W	89.4% Pb Li	95.25% C	95.25% B_4C
1% H_2O	2% H_2O	3.7% H_2O	1% H_2O	1% H_2O
0.25% Pb	1% Pb	1.2% Pb	0.25% Pb	0.25% Pb

Figure VIII-C-1

a 20 cm graphite reflector and a boron carbide cold shield thick enough to protect the magnet close to the outer portion of the torus. Note the blanket zones are divided into several (five as shown in Table VIII-E-1) subzones to account for various amounts of structure/piping and coolant inferred from nuclear heating distributions (two and three subzones for inner and outer blankets, respectively). The volume present for the structure/piping ranges from 12 to 4% as one moves through the blanket region away from the first wall. The volume percent for the coolant ranges from 9 to 2%. The breeding material thus varies from 79 to 94% by volume. As discussed in Ref. 6, the lithium lead eutectic Li_{62} Pb_{38} is employed as the breeding material. The advantages resulting from the use of this eutectic are twofold. One is that it will be easy to obtain a tritium breeding ratio greater than 1.10, as will be discussed later. The other is that this blanket will provide an internal energy storage through its phase change during plasma burn and down time by operating the blanket at a temperature around the melting temperature of the Li_{62} Pb_{38} eutectic, 464°C. The solid and liquid (at 500°C which is the maximum operating temperature in the blanket) densities for this Li_{62} Pb_{38} eutectic are estimated to be 6.5 and 5.0 g/cm^3, respectively. The volume fraction of these two phases during blanket operation is roughly equal,[6] hence the average value of these two densities is taken as the calculational Li_{62} Pb_{38} density in this study. As for the density of each shield material, from the present attainable technology, density factors of 0.9, 0.9 and 0.95 are taken into consideration when tungsten, lead and boron carbide are employed. The average density for the boiling water in each zone is estimated and used in the calculation.

VIII-D. Survey Calculations and Discussions

In this section, we present and discuss results of several survey calculations. The computational results for the final design of NUWMAK are given in the next section.

Based on the design goals described in Sec. VIII-B, we investigate here the tritium breeding, nuclear heating and the magnet shielding arrangement. However, two of the most important design criteria which are sensitive to the design variations will be emphasized in this study. One is the tritium breeding, in which we study the tritium breeding potential of the lithium lead compositions, such as $LiPb_4$, LiPb and $Li_{62}\ Pb_{38}$. The sensitivity to the percent ^6Li in total lithium in the $Li_{62}\ Pb_{38}$ eutectic chosen for this blanket breeding material of the tritium breeding is also studied. The other is the magnet shielding arrangement in which we look at the effect on the magnet damage responses of the thickness for each shield material zone in the inner shield region, namely tungsten, B_4C and the lead zone (for a fixed total thickness of 85 cm). The effect of the height of the tungsten zone is also considered.

VIII-D-1. Tritium Breeding vs. Lithium Lead Composition

The choice of the $Li_{62}\ Pb_{38}$ eutectic as the breeding material is mainly based on thermal design considerations.[6] Its melting temperature, 464^oC, coupled with the use of Ti-6Al-4V alloy as piping/structural material, which operates best in the range of $300\text{-}390^oC$, makes it a suitable blanket material for high thermal efficiency and for providing internal energy storage to minimize the thermal cycling and eliminate external storage. Nevertheless, it is of interest to investigate the tritium breeding potential over the various compositions of the lithium lead alloys or eutectics. For simplicity we fix all the alloys at 500^oC and use the ideal solution approximation to estimate their densities. In Table VIII-D-1, a list of solid and liquid (500^oC) densities for several lithium lead alloys is given for comparison. At practical operating conditions, the tritium breeding ratio may be expected to be no less than obtained in this study.

Fig. VIII-D-1 shows the tritium breeding ratio as a function of the lithium (natural lithium) atom percent in lithium lead alloys. It is found in this figure that as long as the atomic percent lithium in the lithium lead alloy is r less than 20%, i.e., $LiPb_4$, the tritum breeding ratio is adequately bracketed

Table VIII-D-1

Solid and Liquid Densities of Pb, Li and Their Alloys

Material	Solid Density-g/cm^3	Liquid Density at 500°C-g/cm^3
Pb	11.34[a]	10.45[b]
PbLi	8.1[c]	6.31[d]
$Pb_{38}Li_{62}$-eutectic	6.5[e]	5.01[d]
Li_5Pb_2	5.33[c]	4.04[d]
Li	0.534[a]	0.485[b]

(a) From CRC Handbook of Chemistry and Physics, 56th Ed. pp. B-104, 107.

(b) For Pb

$$\rho_{Pb} = 10.71 - 0.00139\ (t-327) \qquad 327°C < t < 800°C$$

For Li

$$\rho_{Li} = 0.515 - 1.01 \times 10^{-4}\ (t-200) \qquad 200°C < t < 1600°C$$

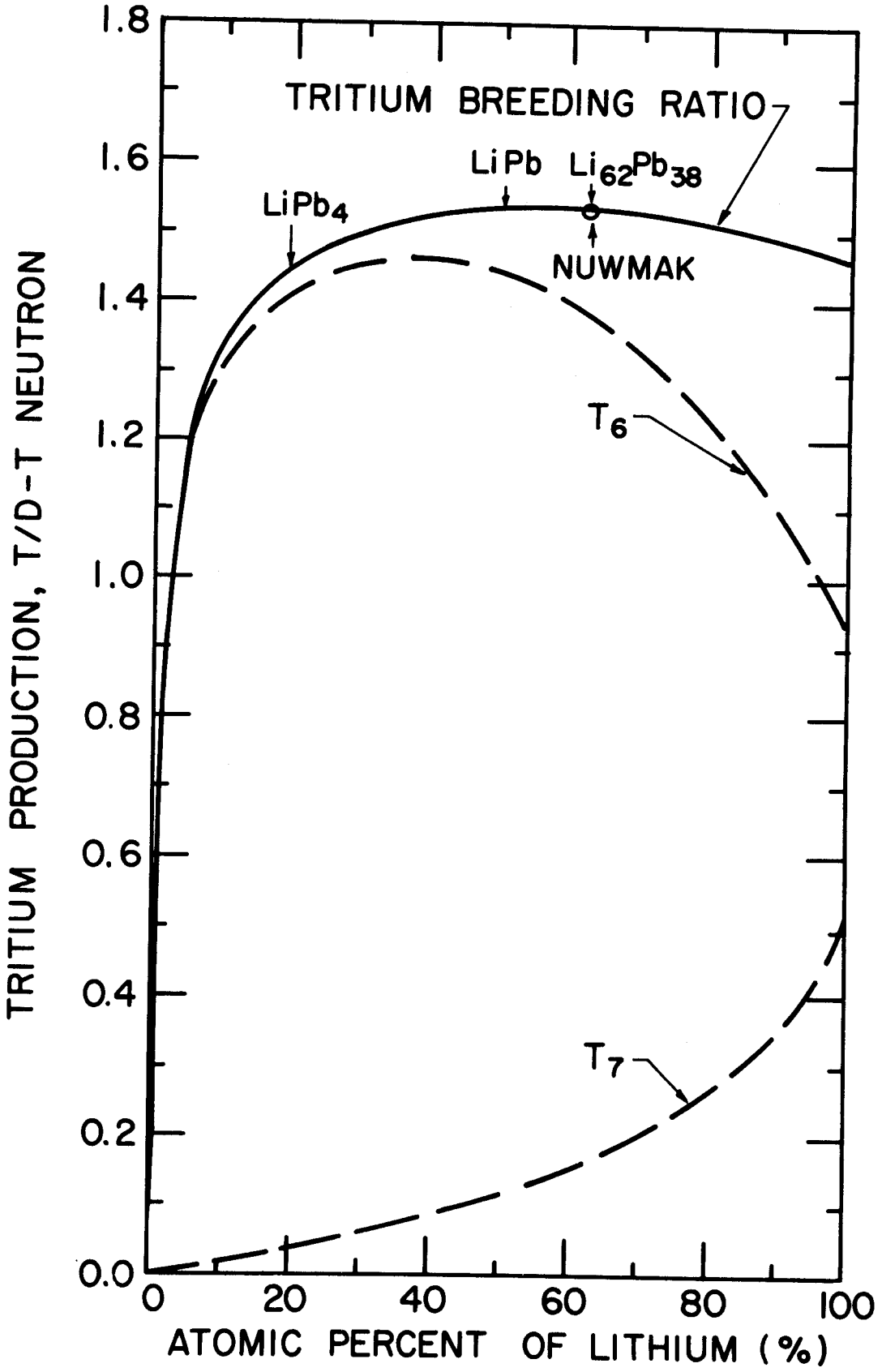
These formulas giving the liquid metal density as a function of temperature are from p. B-240 of CRC Handbook of Chem. and Phys.

(c) From Gmelins Handbuch Der Anorganischen Chemie, Blei: Teil C3, #47, page 982.

(d) Calculated assuming ideal solution of Pb and Li.

(e) Interpolated between the experimental values of 8.1 for PbLi and 5.33 for Li_5Pb_2.

FIGURE VIII-D-1



between 1.45 and 1.55 tritons per D-T neutron. At 100% lithium atom percent, i.e., pure lithium, it is ~ 1.46 which is about the same as found in the UWMAK-I design. The resulting approximately constant tritium breeding is primarily due to the competition between $^{7}Li(n,n'\alpha)T$ and Pb(n,2n) reactions, while all the secondary neutrons are absorbed by ^{6}Li and result in production of additional tritons. This can be easily revealed by comparing the contribution from the $^{6}Li(n,\alpha)T$ (T_6) and $^{7}Li(n,n'\alpha)T$ (T_7) reactions shown in Fig. VIII-D-1.

VIII-D-2. Tritium Breeding vs. Percent ^{6}Li in Total Lithium

Natural lithium consists of only 7.42% of ^{6}Li. Percents of ^{6}Li other than the natural content in total lithium have been employed in reactor blanket design.[3] In this subsection we will discuss the effect of the percent ^{6}Li in total lithium on the tritium breeding ratio.

Due to thermal design considerations, we choose $Li_{62}Pb_{38}$ eutectic as the tritium breeding and nuclear energy deposition material in the blanket. Here we will also employ this candidate eutectic in this study although the results may be equally applicable to most lithium lead alloys whose tritium breeding potential were discussed in Sec. VIII-D-1. Note the $Li_{62}Pb_{38}$ density used here is the average value of solid and liquid densities as will be used in the final design calculations. Fig. VIII-D-2 shows the calculational results. The maximum tritium breeding ratio, ~ 1.65 tritons per D-T neutron, is obtained at ~ 30% ^{6}Li in total lithium. However, at 7.42% ^{6}Li (natural lithium) and 90% ^{6}Li, the tritium breeding ratios are very close, 1.54 and 1.51 tritons per D-T neutron, respectively. The contribution from T_6 increases from 90 to more than 99% as the ^{6}Li in total lithium increases from 7.42 to 90%. It is noticed that the increase of the tritium breeding ratio from that of the natural-lithium lead eutectic blanket to the maximum value is only 6%. The blanket spatial distributions of the tritium breeding at the midplane for 7.42, 30 and 90% ^{6}Li in total lithium are depicted in Fig. VIII-D-3.

Figure VIII-D-2

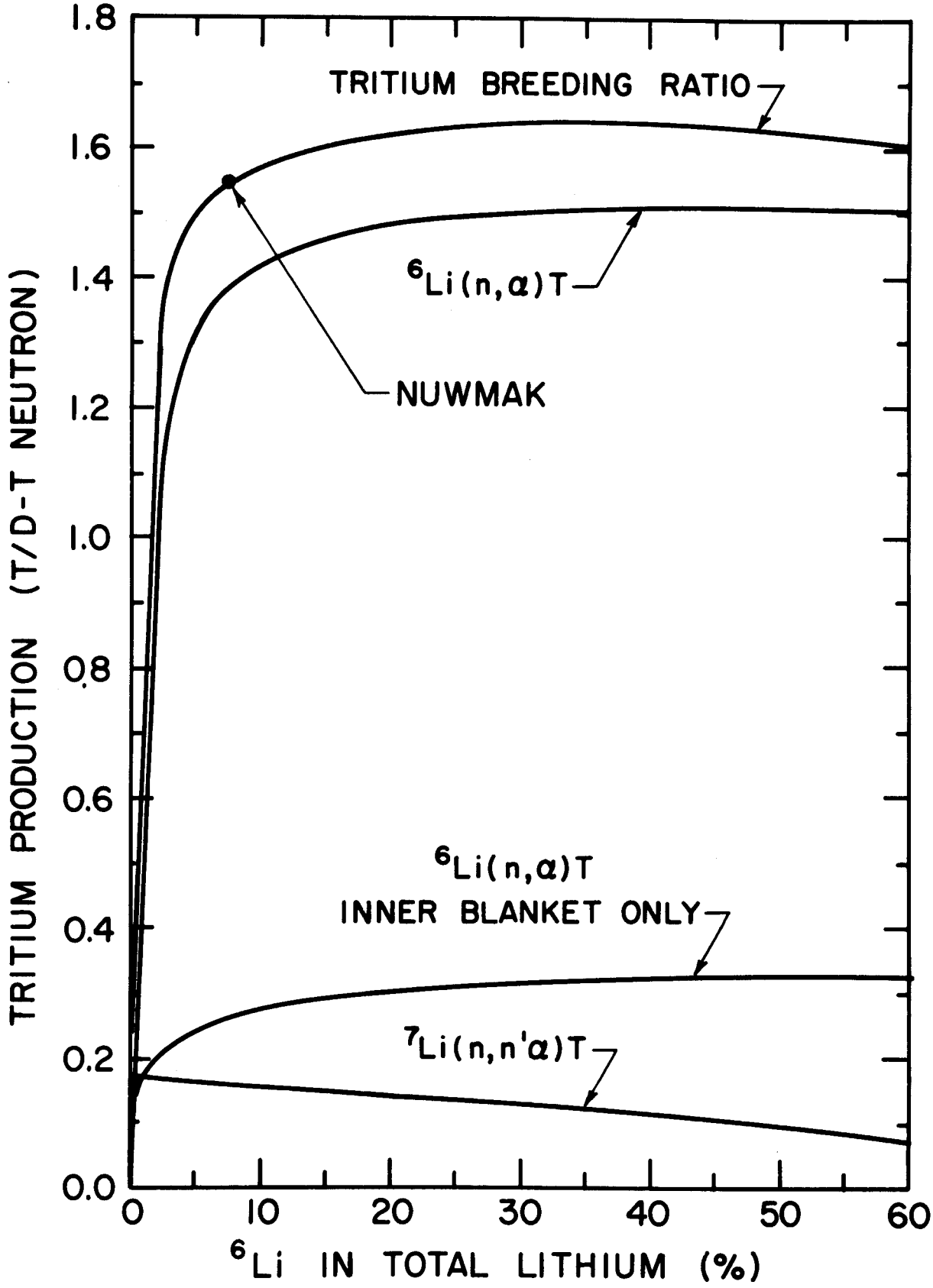
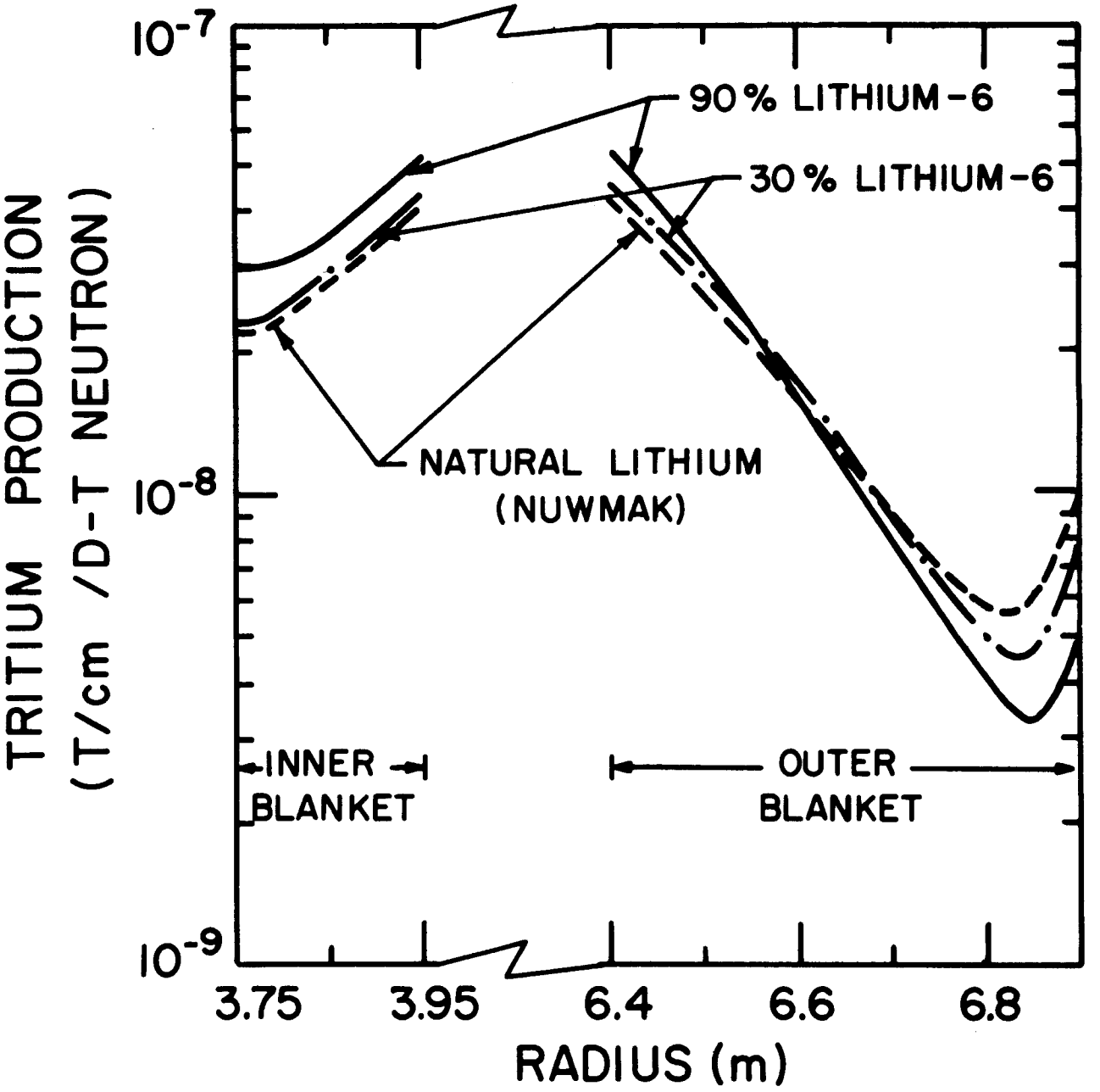


Figure VIII-D-3



From the above considerations, we conclude that there is no incentive to increase the percent ^{6}Li in total lithium in the lithium lead eutectic for tritium breeding purposes.

VIII-D-3. Magnet Protection Considerations

The NUWMAK magnet system consists of NbTi superconductors, aluminum stabilizer and structure, and superinsulation. The superconductor operates at 1.8 K and is cryogenically cooled by superfluid helium. Due to the design space requirements for the magnet and the plasma ohmic heating coils, the minimum space available for the magnet shielding appears at the midplane close to the toroidal axis (inner blanket/shield region) and is only 1.05 meters from the plasma chamber first wall to the dewar of the magnet. Excluding 20 cm for the blanket zone, a space of only 85 cm is actually available to provide adequate shielding for the protection of the superconducting magnet from the environment of intense nuclear radiation ($\sim$ 5 MW/m^2 neutron wall loading). Although the existence of large amounts of lead in the Li_{62} Pb_{38} eutectic in the inner blanket provide a good attenuation of the D-T neutrons through (n,2n) and inelastic scattering reactions, metallic tungsten is essential for effectively attenuating both high energy neutron and gamma radiations coming through the blanket. The lowest threshold energies for (n,2n) and inelastic reactions among the tungsten isotopes existing in nature are 6.3 MeV and 46.7 keV for ^{183}W, respectively. These values are comparatively lower than those of other candidate materials such as Fe, Nb, Mo and Pb. Moreover, the macroscopic interaction cross section, which is directly related to the attenuation of neutron radiation, depends on the atomic density of the material. Tungsten metal is a relatively dense material as far as high atomic mass number materials are concerned with an atomic density of 0.0629×10^{24} atoms/cm^3 as compared to 0.03348×10^{24} atoms/cm^3 for lead.

The secondary neutrons coming through the blanket are energetically peaked in the range 0.74 - 2.5 MeV (groups 15-17 in the 25 neutron group structure). The mean free path due to inelastic scattering processes for neutrons of this energy range in the tungsten material is $\sim$ 8 cm, which is about one-half of that in iron, niobium and molybdenum, and about one-fourth of that in lead. However, for source neutrons (14 MeV energy), the

overall mean free path in tungsten is ~ 3 cm, which is less than 80% of that in comparable materials. Nevertheless, the neutron energy and particle attenuation depend on the actual neutron spectrum and the composition of the medium, and the attenuation process is too complicated to be fully described by partial or even total interaction cross sections. The solution must be obtained from transport calculations or experimental measurements depending on the attenuation goal. In order to quantitatively describe the superiority of the use of tungsten metal as the most effective shielding material, we completed several transport calculations. The shielding materials considered here are stainless steel (SS), lead (Pb) and tungsten (W) mixed with boron carbide (B_4C). The composition used is the same as was reported in Ref. 17 as being the best energy attenuating shielding composition for metal and B_4C mixtures, i.e., 70% metal and 30% B_4C by volume. From these calculations, we found that for the same amount of radiation attenuation for atomic displacement rate and neutron fluence in the magnet, SS + B_4C and Pb + B_4C zones needed to be ~ 50% thicker than a W + B_4C mixture. The maximum atomic displacement rate at the aluminum stabilizer is required to be of the order of 10^{-6} dpa/year while it is more than 100 dpa/year at the first wall. More than seven orders of magnitude attenuation is required for the atomic displacement rate from the back of the blanket to the magnet assuming one order of magnitude is achieved by the 20 cm blanket region. It seems that tungsten is the only candidate for the design of the magnet shield described above.[18]

VIII-D-3-a. Tungsten Zone Thickness vs. Atomic Displacement Rate in Aluminum Stabilizer

In the following survey calculations, tungsten and B_4C will be employed to study the attenuation effectiveness as a function of tungsten zone thickness. However, the tungsten metal is put before the B_4C shield in order to efficiently utilize its high energy attenuation property and to decrease the total amount of tungsten in the shield design because of its expense.

Fig. VIII-D-4 shows the atomic displacement rate in the aluminum stabilizer as a function of the tungsten zone thickness. Note here the total thickness for the shield material is 85 cm and a lead zone of 5 cm is already taken into account for the purpose of decreasing the nuclear dose in the superinsulation as well as the whole magnet. In this figure, it is found that the minimum radiation damage level to the aluminum stabilizer is $\sim 2 \times 10^{-7}$ dpa/year at $\sim$ 55 cm of tungsten zone thickness. Using a tungsten zone thicker than this value, the radiation damage level increases rather than decreasing further. The reason is primarily that the remaining B_4C zone is not thick enough and does not absorb enough of the neutrons. For a tungsten zone of between 35 and 40 cm, the value for the atomic displacement rate in the aluminum stabilizer lies between $\sim 2 \times 10^{-6}$ and 1×10^{-6} dpa/year, which will cause a resistivity increase of between $\sim$ 25 and 13% after one year of operation.

VIII-D-3-b. Lead Zone Thickness vs. Dose and Atomic Displacement Rates

From the results discussed in the previous subsection, a reasonable tungsten zone thickness is found to be between 35 and 40 cm. In order to know more about the dose rate on the superinsulator as well as the magnet, the lead zone thickness is varied for these two designs. The results are shown in Fig. VIII-D-5 where the atomic displacement rate ranges from 1×10^{-6} and 2×10^{-6} to 1.8×10^{-6} and 3×10^{-6} dpa/year as the lead zone increases from 5 to 10 cm for the design of a tungsten zone of 40 and 35 cm, respectively. However, the dose rate on the superinsulator will be about three times less as the lead zone increases from 5 cm to 10 cm. For a 5 cm lead zone thickness, the dose rate on the superinsulator is about 3×10^7 and 1.7×10^7 rads/year for the design with a 35 and 40 cm tungsten zone, respectively. As far as the heat load on the magnet is concerned, it increases from $\sim$ 60 to 515 watts* as the lead zone thickness decreases from 10 to 5 cm. However, this amount of heat is still small compared to the total heat generated and being transferred from the magnet system.

*This is the total energy deposited in the inner magnet, i.e., the portion of the magnet close to the toroidal axis. For the heat load deposited in the whole magnet, another $\sim$ 50 watts is to be added to the above.

Figure VIII-D-4

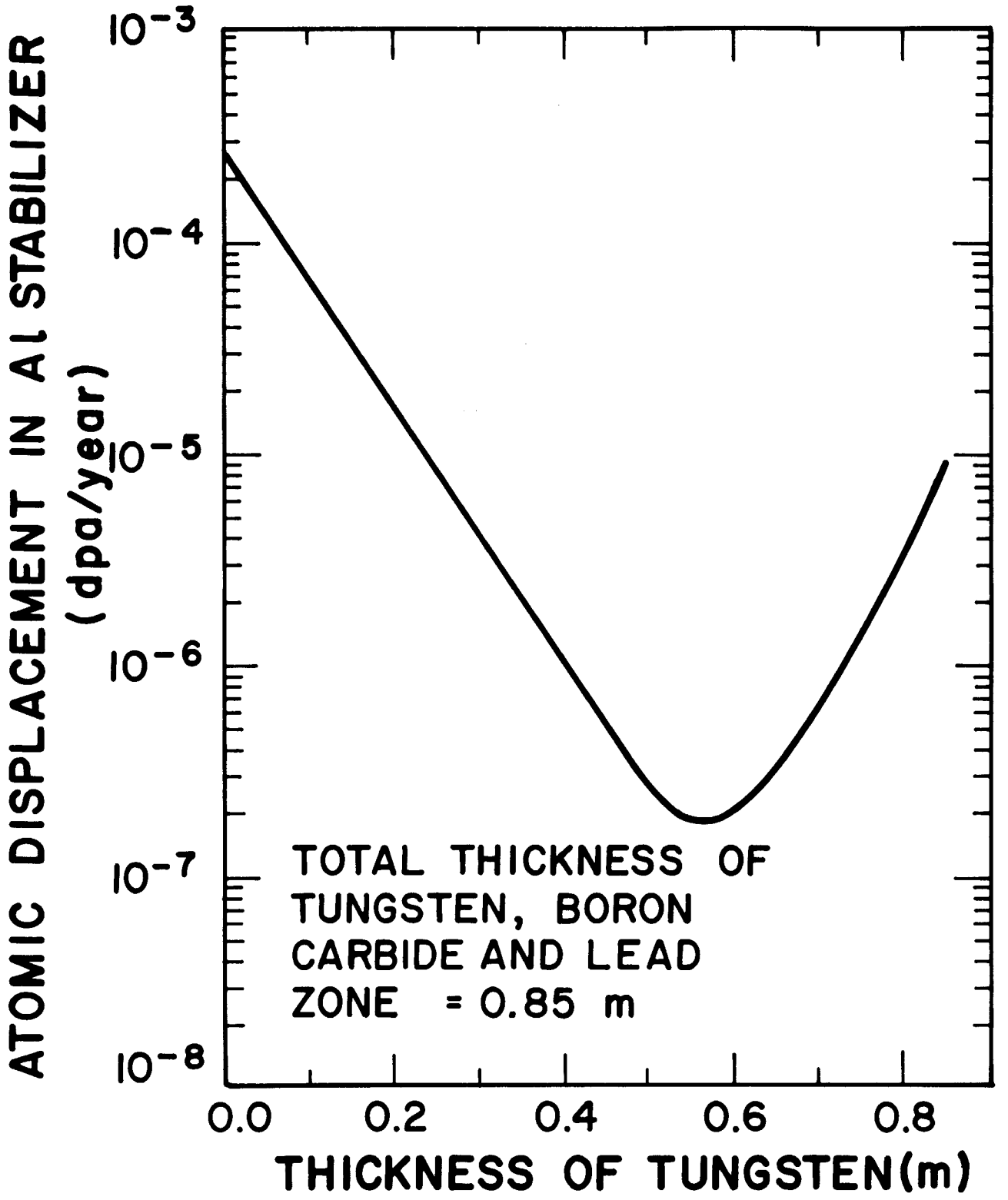
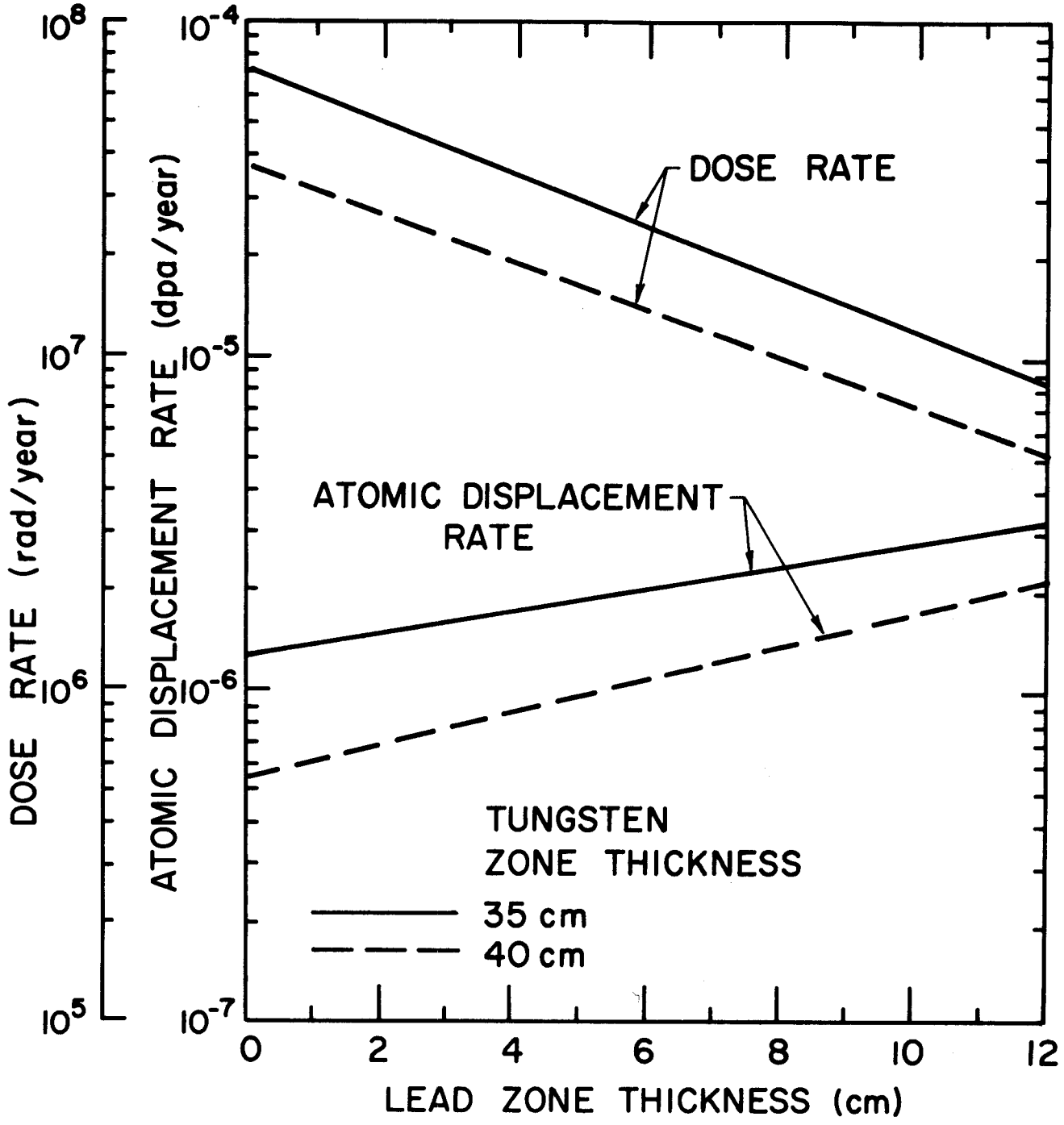


Figure VIII-D-5



VIII-D-3-c. Tungsten Zone Height vs. Atomic Displacement, Dose Rate and Neutron Fluence

The importance of the radiation protection is not only for the superconducting magnet at the midplane region but also for the entire magnet. It is very necessary to look at the radiation damage for the magnet region close to the plasma as a function of height above the midplane, for the magnet region shown in Fig. VIII-C-1. A survey study is given here for the case of a 35 cm tungsten zone with a 5 cm lead zone. The height of the tungsten zone is varied from 2 to 2.5 meters for survey purposes.

Figs. VIII-D-6-8 show the results of these calculations. In these figures, the atomic displacement rate in the aluminum stabilizer, the maximum neutron fluence and dose rate on the superinsulator as a function of magnet region height above the midplane are presented for the cases of tungsten zone heights of 2, 2.25 and 2.5 meters, respectively. For a tungsten zone height of 2 and 2.25 meters, the atomic displacement rate at $\sim$ 2.2 meters above the midplane is about two and one order of magnitude higher than that at the midplane, respectively. The maximum resistivity change occurring in these designs would be correspondingly $\sim$ 40 and 2 times that of the unirradiated resistivity after one year of operation. However, for the 2.5 meter tungsten zone height design, the atomic displacement at the magnet region above midplane is always less than that at midplane. The maximum resistivity change is only $\sim$ 25% for one year of irradiation. These effects can be easily seen in Fig. VIII-D-9 where contours of the atomic displacement rates are depicted for designs with 2.25 and 2.5 meter high tungsten zones. If the parameter value at midplane is designed to be an optimum then the values for the region above midplane would not be acceptable in the 2.5 m design. Hence, a tungsten zone height of no less than 2.5 meters seems to be unavoidable in the NUWMAK design. The situation for dose rate and neutron fluence is similar to that for atomic displacement considerations.

VIII-E. Final Results for NUWMAK Blanket and Shield Design

In the following, computational results for the final NUWMAK blanket and shield, which evolved from the parametric survey studies in previous

Figure VIII-D-6

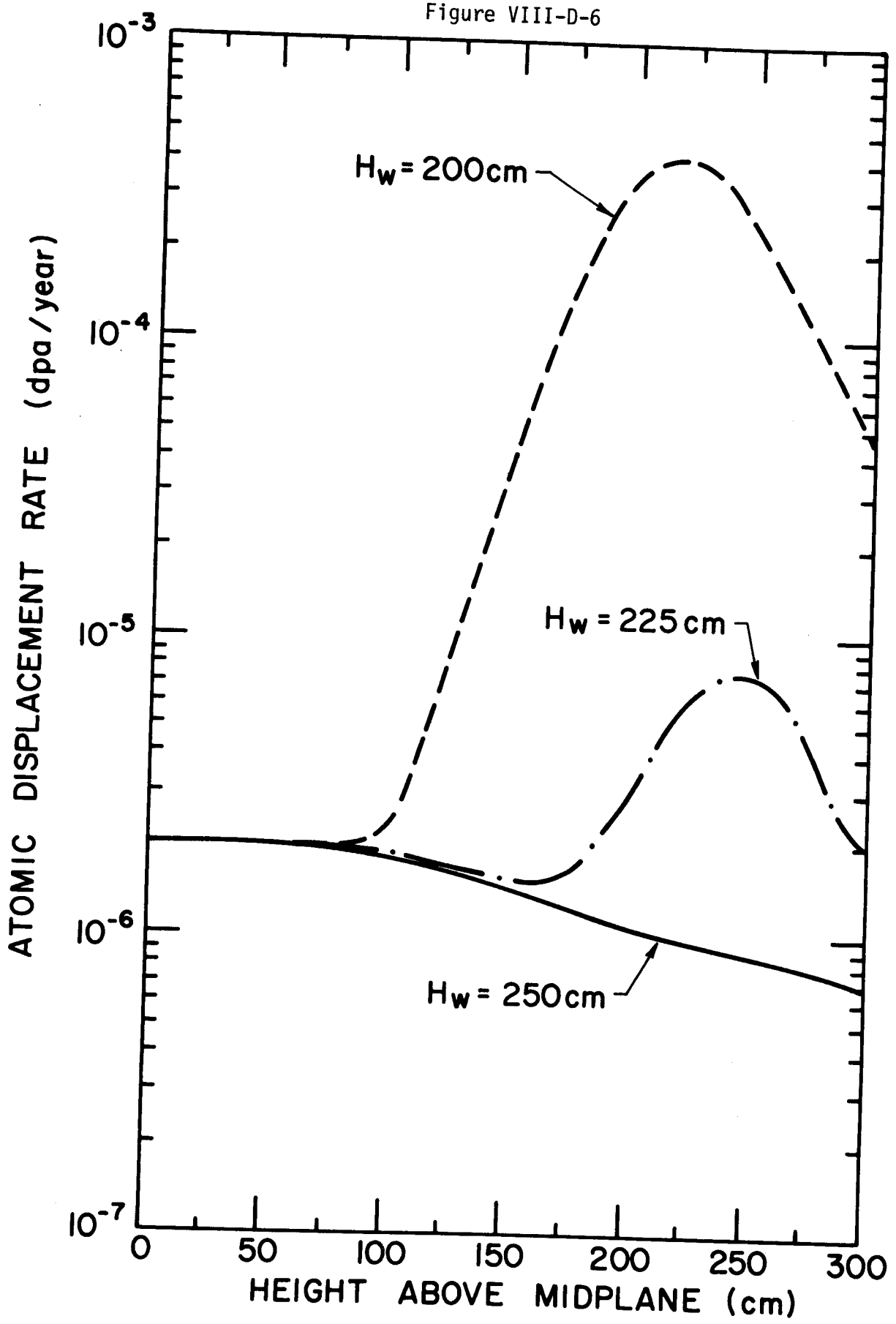


Figure VIII-D-7

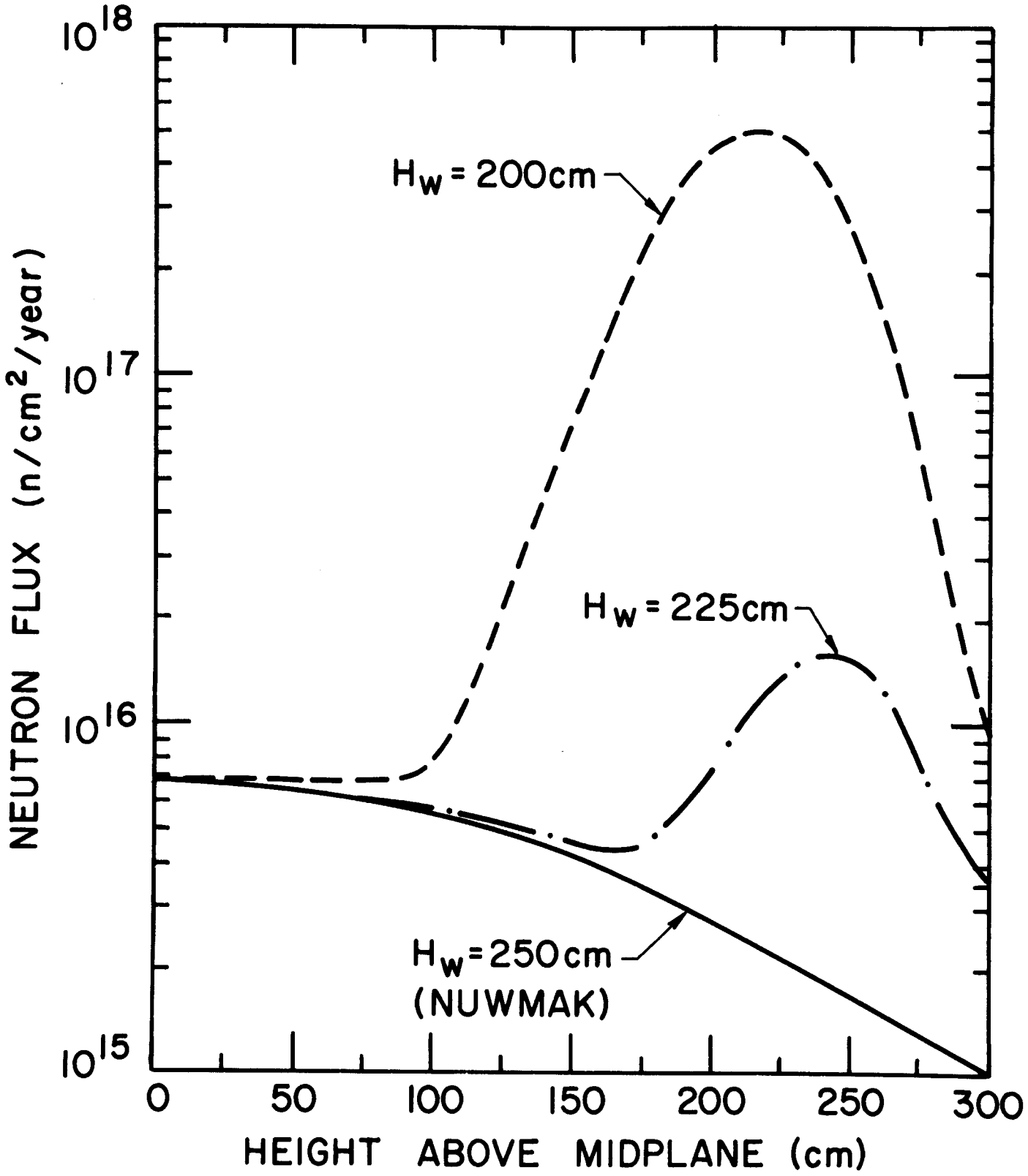


Figure VIII-D-8

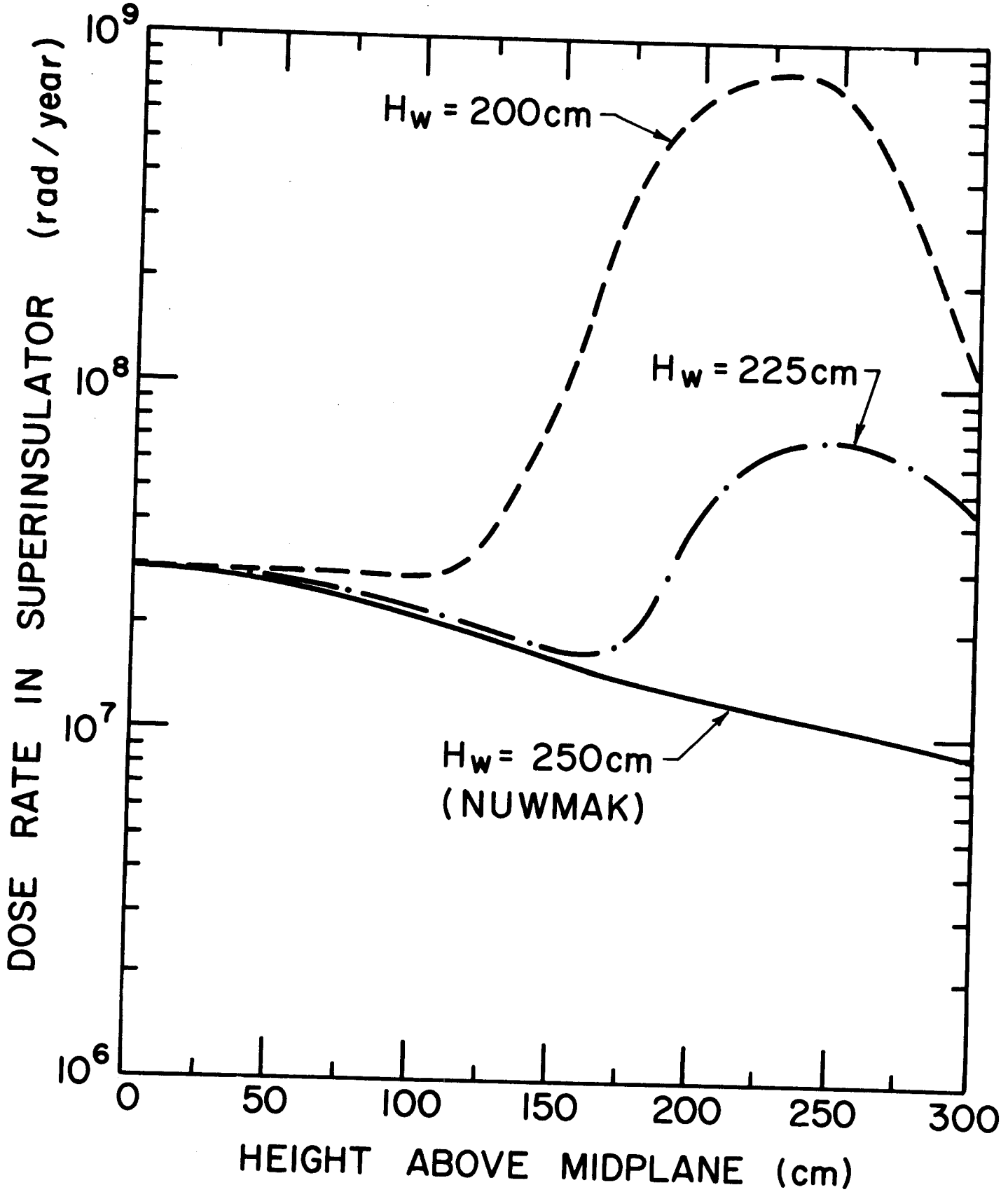
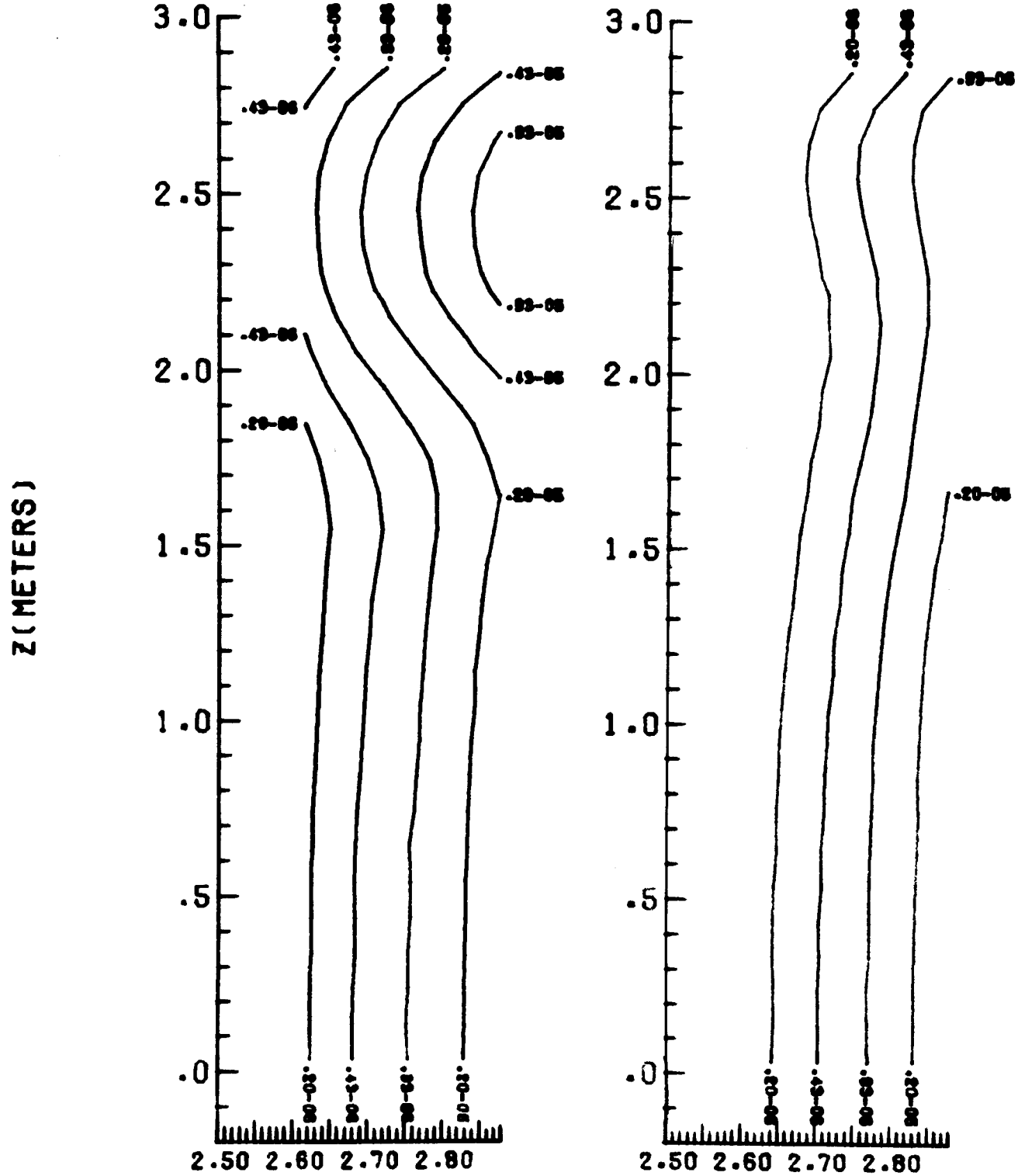


Figure VIII-D-9

(A) 2.25 m tungsten zone height (B) 2.5 m tungsten zone height



ATOMIC DISPLACEMENT RATES IN ALUMINUM STABILIZER

sections will be presented. In this final design model, the 20 cm Li_{62} Pb_{38} blanket will be followed by a 35 cm tungsten zone, a 45 cm boron carbide zone and a 5 cm lead zone. The tungsten zone height is designed to be 2.5 meters. The specific composition and dimensions for each zone are tabulated in Table VIII-E-1. (The zone thicknesses given here are those at the midplane,) Natural lithium is employed in the Li_{62} Pb_{38} eutectic.

VIII-E-1. Tritium Breeding, Neutron Multiplication and Nuclear Heating

In Table VIII-E-2 are shown the tritium breeding, neutron multiplication and nuclear heating for the final blanket and shield design. The tritium breeding ratio for this system is 1.54 tritons per D-T neutron, of which about 90% is from $^6Li(n,\alpha)$ reactions. The tritium breeding from the outer blanket alone is about 1.24 tritons per D-T neutron which is already more than is required for the design goal described in Sec. VIII-B. As discussed in Ref. 1 and 6, the placing of Li_{62} Pb_{38} eutectic in the inner blanket is primarily due to the internal energy storage requirement to minimize the thermal cycling of the structure and coolant output temperature.

The neutron multiplication in this system which is dominated by Pb(n,2n) reactions is ~ 0.57 neutrons per D-T neutron as shown in this table. The total nuclear heating in the blanket/shield system is ~ 17.15 MeV per D-T neutron, of which ~ 35% is contributed by gamma-ray heating. Note that the gamma-ray heating itself is more than 50% as far as the nuclear heating in the inner blanket/shield is concerned. This can be attributed to the contribution of the nuclear heating in the tungsten zone (zone 4) as shown in Table VIII-E-4. It is 1.22 MeV per D-T neutron, most of which is from gamma-ray heating reflecting the fact that the Q values for $W(n,\gamma)$ reactions are on average ~ 6 MeV, which is higher than for $^6Li(n,\alpha)$ reactions, ~ 4.8 MeV. In Table VIII-E-3, the nuclear heating in the structure and coolant is shown to be 2.14 MeV per D-T neutron, which is ~ 12% of the total. The energy deposition in the coolant alone is ~ 8% of the total. The recoverable energy for this system can be collected from the total energy deposited in the blanket/shield zone shown in Table VIII-E-4 excluding zones 2, 3 and 14. Hence, the total recoverable energy is found to be more than 99%

Table VIII-E-1

Material Compositions for the NUWMAK Blanket and Shield Neutronics Model at Midplane

Specification	Zone Number	Thickness (meter)	Composition (All percentage by Volume)
Magnet	1	0.30	80% Al + 12.8% Epoxy + 7.2% He (liquid)
Lead Shield	2	0.10	4% Ti Alloy + 2% H_2O + 1% Pb + 93% Pb[a]
B_4C Shield	3	0.40	4% Ti Alloy + 2% H_2O + 1% Pb + 93% B_4C[b]
Tungsten Shield	4	0.35	4% Ti Alloy + 2% H_2O[c] + 1% Pb + 93% W[d]
Inner Breeding Blanket	5 (B-2)	0.10	6% Ti Alloy + 3.9% H_2O[e] + 1.0% Pb + 89.1% Li_{62} Pb_{38}[f]
	6 (B-1)	0.10	9.6% Ti Alloy + 8.6% H_2O[e] + 2.4% Pb + 79.4% Li_{62} Pb_{38}[f]
Plasma and Vacuum	7	0.05	Vacuum
	8	2.25	Plasma
	9	0.15	Vacuum
Outer Breeding Blanket	10 (B-1)	0.10	9.6% Ti Alloy + 8.6% H_2O[e] + 2.4% Pb + 79.4% Li_{62} Pb_{38}[f]
	11 (B-2)	0.15	6% Ti Alloy + 3.9% H_2O[e] + 1.0% Pb + 89.1% Li_{62} Pb_{38}[f]
	12 (B-3)	0.25	3.8% Ti Alloy + 1.8% H_2O[e] + 0.3% Pb + 94.1% Li_{62} Pb_{38}[f]
Graphite Reflector	13	0.20	3.5% Ti Alloy + 1% H_2O[e] + 0.25% Pb + 95.25% Graphite
B_4C Shield	14	0.20	3.5% Ti Alloy + 1% H_2O + 0.25% Pb + 95.25% B_4C[b]

a. 90% dense b. 95% dense c. average density factor is 94% d. 90% dense e. average density factor 90% f. average density between solid and liquid phases is 5.75 g/cc

Table VIII-E-2

Tritium Breeding, Neutron Multiplication and Nuclear Heating in NUWMAK

Tritium Production (T/D-T Neutron)	INNER	OUTER	TOTAL
$^{6}Li(n,\alpha)$ (T_6)	0.2604	1.1249	1.3853
$^{7}Li(n,n'\alpha)$ (T_7)	0.0375	0.1192	0.1567
$T_6 + T_7$	0.2979	1.2441	1.5420

Neutron Multiplication (Reaction/D-T Neutron)	INNER	OUTER	TOTAL
Pb(n,2n)	0.1339	0.4181	0.5520
W(n,2n)	0.0137	------	0.0137
Total	0.1476	0.4181	0.5657

Nuclear Heating (MeV/D-T Neutron)	INNER	OUTER	TOTAL
Neutron	2.2665	8.9298	11.1963
Gamma-Ray	2.4143	3.5422	5.9565
Neutron + Gamma-Ray	4.6808	12.4720	17.1528

Table VIII-E-3

Nuclear Heatings by Zone in the Structure/Piping and Coolant in NUWMAK (in units of MeV per D-T neutron)

Zone Number	Ti	Al	V	Pb	H	O	Subtotal
2	1.48(-7)	5.33(-9)	6.98(-9)	1.64(-7)	7.88(-9)	1.54(-8)	3.47(-7)
3	1.26(-4)	4.46(-6)	6.00(-6)	1.30(-4)	1.22(-5)	7.64(-6)	2.80(-4)
4	9.46(-3)	4.82(-4)	4.52(-4)	9.00(-3)	1.28(-2)	1.89(-3)	3.41(-2)
5	1.64(-2)	1.34(-3)	7.65(-4)	3.57(-3)	5.32(-2)	7.30(-3)	8.26(-2)
6	7.97(-2)	7.22(-3)	3.38(-3)	2.35(-2)	2.56(-1)	4.90(-2)	4.19(-1)
10	2.44(-1)	2.19(-2)	1.04(-2)	7.27(-2)	7.95(-1)	1.49(-1)	1.29
11	4.52(-2)	3.93(-3)	2.17(-3)	8.98(-3)	1.71(-1)	2.22(-2)	2.53(-1)
12	7.52(-3)	6.49(-4)	4.39(-4)	6.64(-4)	3.34(-2)	3.14(-3)	4.58(-2)
13	5.09(-3)	2.14(-4)	5.50(-4)	2.60(-3)	2.09(-3)	3.84(-4)	1.09(-2)
14	1.91(-3)	6.58(-5)	9.06(-5)	1.95(-3)	1.15(-4)	1.10(-4)	4.24(-3)
Sum	4.09(-1)	3.58(-2)	1.82(-2)	1.23(-1)	1.32	2.33(-1)	2.14

Table VIII-E-4

Nuclear Heatings by Zone in Breeding and Shield Materials in NUWMAK (in units of MeV per D-T neutron)

Zone Number	W	Pb	^{6}Li	^{7}Li	^{10}B	^{11}B	C	Subtotal	Total[a]
2	-----	1.527(-5)	-----	-----	-----	-----	-----	1.527(-5)	1.562(-5)
3	-----	-----	-----	-----	4.689(-3)	9.793(-4)	4.482(-5)	5.713(-3)	5.993(-3)
4	1.2209	-----	-----	-----	-----	-----	-----	1.2209	1.2550
5	-----	0.3179	0.4299	0.1388	-----	-----	-----	0.8866	0.9692
6	-----	0.7769	0.8769	0.3776	-----	-----	-----	2.0314	2.4504
10	-----	2.4046	2.8440	1.1549	-----	-----	-----	6.4035	7.6935
11	-----	0.8000	1.7221	0.4328	-----	-----	-----	2.9549	3.2079
12	-----	0.2082	1.0250	0.1337	-----	-----	-----	1.3669	1.4127
13	-----	-----	-----	-----	-----	-----	0.0752	0.0752	0.0861
14	-----	-----	-----	-----	4.936(-2)	1.370(-2)	5.064(-3)	0.0681	0.0724
Sum	1.2209	4.5076	6.8979	2.2378	0.0540	0.0147	0.0803	15.013	17.153

a. includes heatings in the structure/piping and coolant shown in Table VIII-E-3.

of the total. The total thermal output (including alpha heating) for the NUWMAK blanket/shield is thus 2292 MW during the burn. The net electrical output is 660 MW, if a duty factor of 0.91 and a net efficiency of 31.5% are assumed. The spatial nuclear heating rates in the inner as well as outer blanket/shield at the midplane are shown in Fig. VIII-E-1.

VIII-E-2. Radiation Damage of Superconducting Magnet

The maximum atomic displacement rate in the aluminum stabilizer, neutron fluence in the superconductors, and dose rate in the superinsulators for NUWMAK are given in Table VIII-E-5 and are 2×10^{-6} dpa/year, 7×10^{15} n/cm^2 per year and 3×10^7 rads/year, respectively. The corresponding magnet operation parameters after one year of continuous operation are as follows. The resistivity change in the aluminum stabilizer is found to be less than 25%, the critical current density change in the NbTi conductors is less than 0.5%. The most crucial design consideration is that after two years of continuous operation, the resistivity change will reach the design limit as discussed in Sec. VIII-B. In fact, this is designed to be consistent with the blanket lifetime.[19] Hence, the plant will be shut down, the magnet annealed and the blanket replaced after every two years of operation.

For the integrity and thermal insulation properties of the super-insulation materials, after 30 years of continuous operation, which is about the plant lifetime, the dose in the superinsulator will be $\sim 1 \times 10^9$ rads. Under such a dose, mylar based superinsulators would experience severe radiation damage while the epoxy based superinsulators would only show incipient to mild damage. Hence, epoxy based superinsulators must be used in regions where intense radiation dose occurs.

The spatial atomic displacement, neutron fluence and dose rate in the magnet are shown in Figs. VIII-E-2 and VIII-E-3. The spatial nuclear heating rate as well as the gas production rates are also depicted in Fig. VIII-E-4.

Figure VIII-E-1

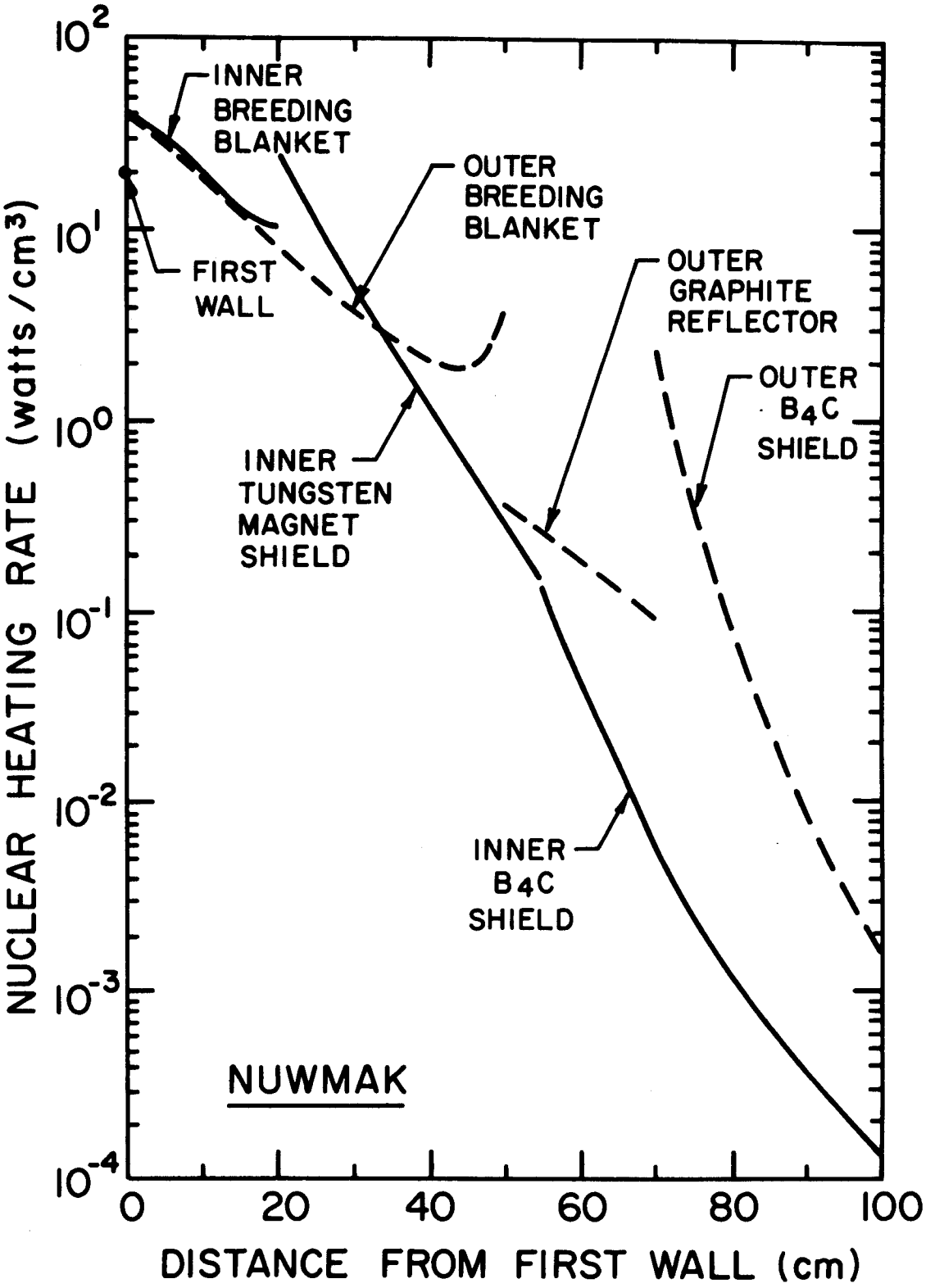


Table VIII-E-5

Radiation Damage Parameters for the Superconducting Magnet in NUWMAK

Maximum Atomic Displacement Rate in the Aluminum Stabilizer (dpa/year)	2×10^{-6}
Maximum Dose Rate in the Epoxy-Base Superinsulators (rad/year)	3×10^{7}
Maximum Neutron Flux in the NbTi Superconductors (n/cm^2/year)	7×10^{15}
Total Nuclear Heatings in TF Coils (Watts)	~ 500

Figure VIII-E-2

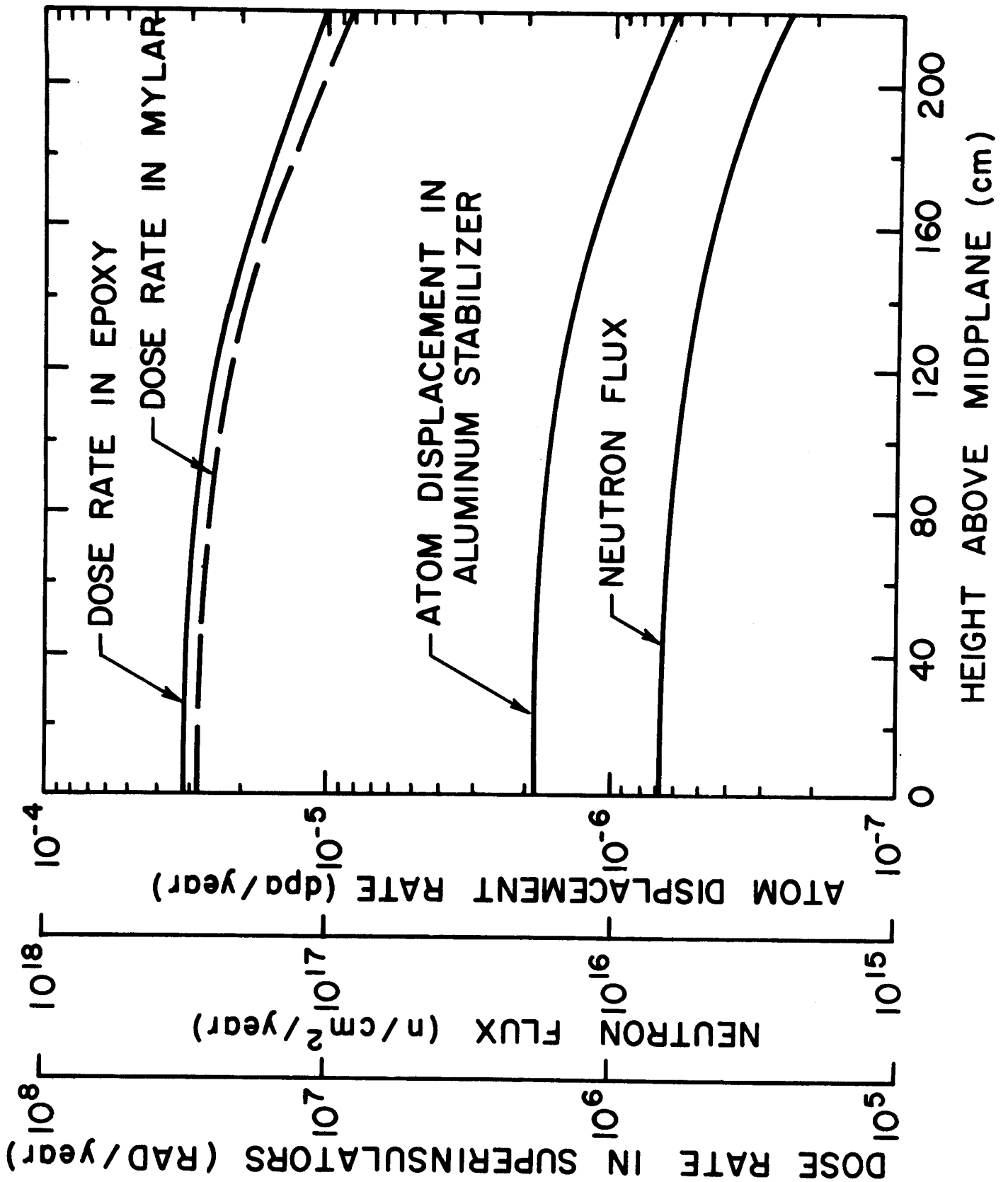


Figure VIII-E-3

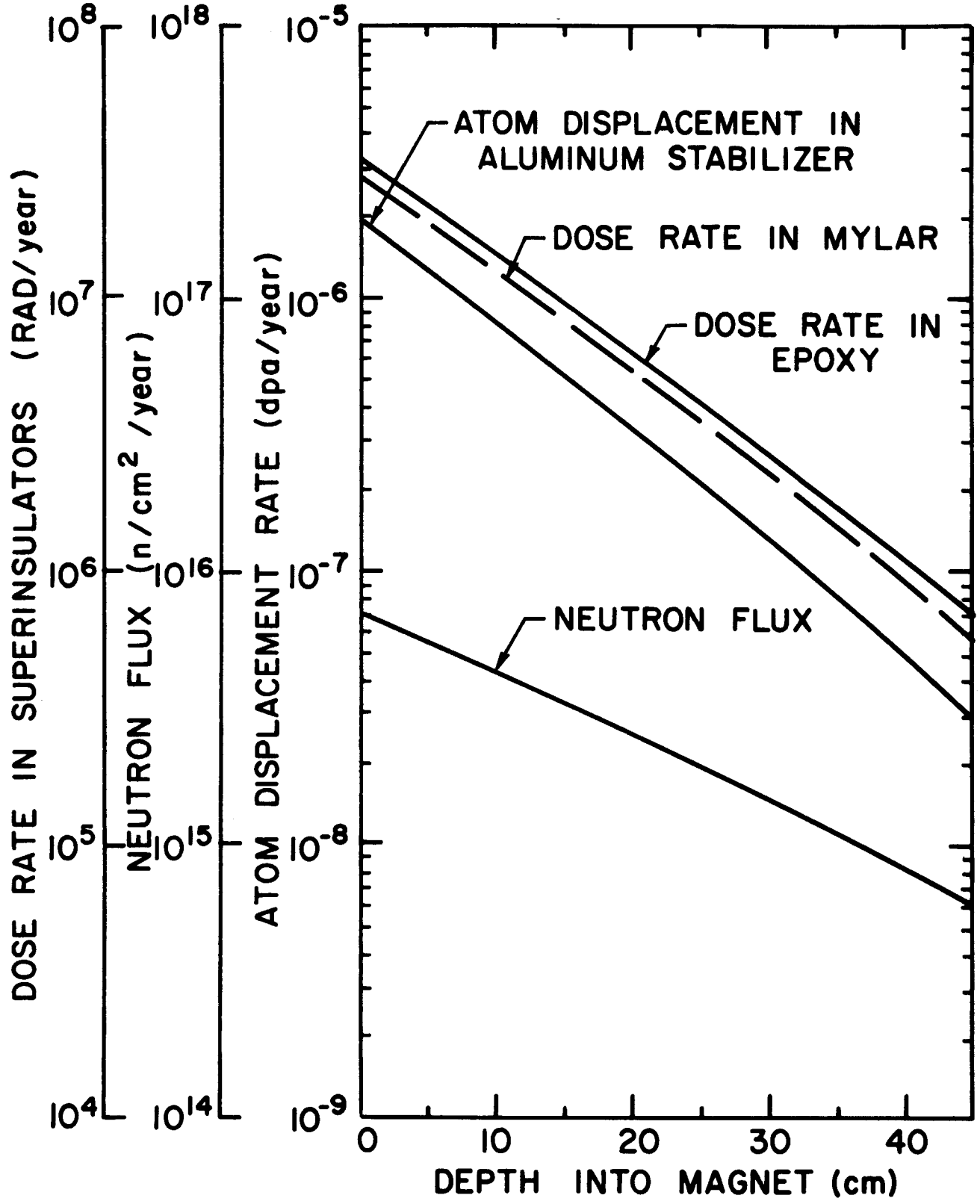
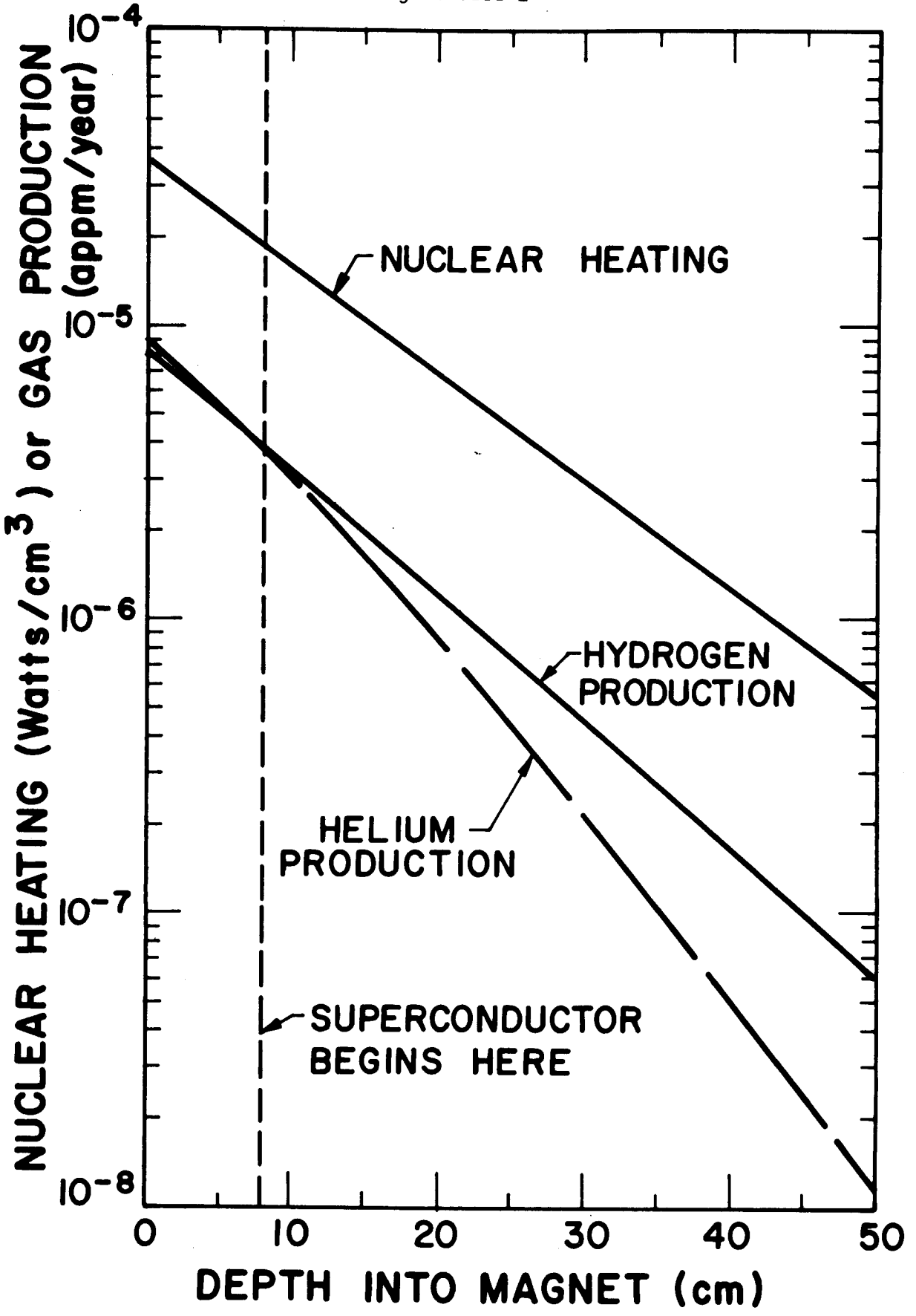


Figure VIII-E-4



VIII-E-3. Contour Plots and Neutron Fluxes

Additional results have been depicted as contour plots and are given in Figs. VIII-E-5-17. They include tritium production rate (Fig. VIII-E-5), Pb(n,2n) reaction rate (Fig. VIII-E-6), total nuclear heating rate (Fig. VIII-E-7), titanium atomic displacement rate (Fig. VIII-E-8), hydrogen production rate (Fig. VIII-E-9) and helium production rate (Fig. VIII-E-10), total neutron flux (Fig. VIII-E-11), neutron flux at energy 14.9-13.5 MeV and 0.41-0.17 MeV (Fig. VIII-E-12 and 13, respectively).

Some scalar neutron fluxes are also given in this subsection. Figs. VIII-E-14, 15, 16, 17 show the neutron flux at the tungsten zone 52 cm from the first wall, the neutron flux at the graphite reflector 62 cm from the first wall, at the magnet region closest to the lead shield at mid-plane, and at the outer breeding zone 32 cm from the first wall. All are compared with the neutron flux at the first wall (dashed curve). The numerical values of these scalar neutron fluxes are also tablulated in Table VIII-E-6 for application purposes.

VIII-F. Radioactivity

The calculation of activity and related quantities in NUWMAK have been performed using the techniques developed for use in previous studies.[2,3,4] Specifically the code DKR[20] was used to calculate specific activities using the flux spectrum from the neutronics calculations and nuclear data from the DCDLIB[12] code. As in previous calculations the energy from decay gammas is assumed to be deposited at the site of the decay unless gamma transport calculations are to be performed to obtain shielding information.

The calculations in previous studies were for the most part performed on a one-dimensional basis, i.e., the neutron flux and blanket materials were assumed to be independent of the poloidal angle. In NUWMAK, however, because of the heterogeneous nature of the blanket, involving several regions with different materials, and the two-dimensional shape of the plasma, an attempt was made to make the calculations reflect these effects more realistically than in the past.

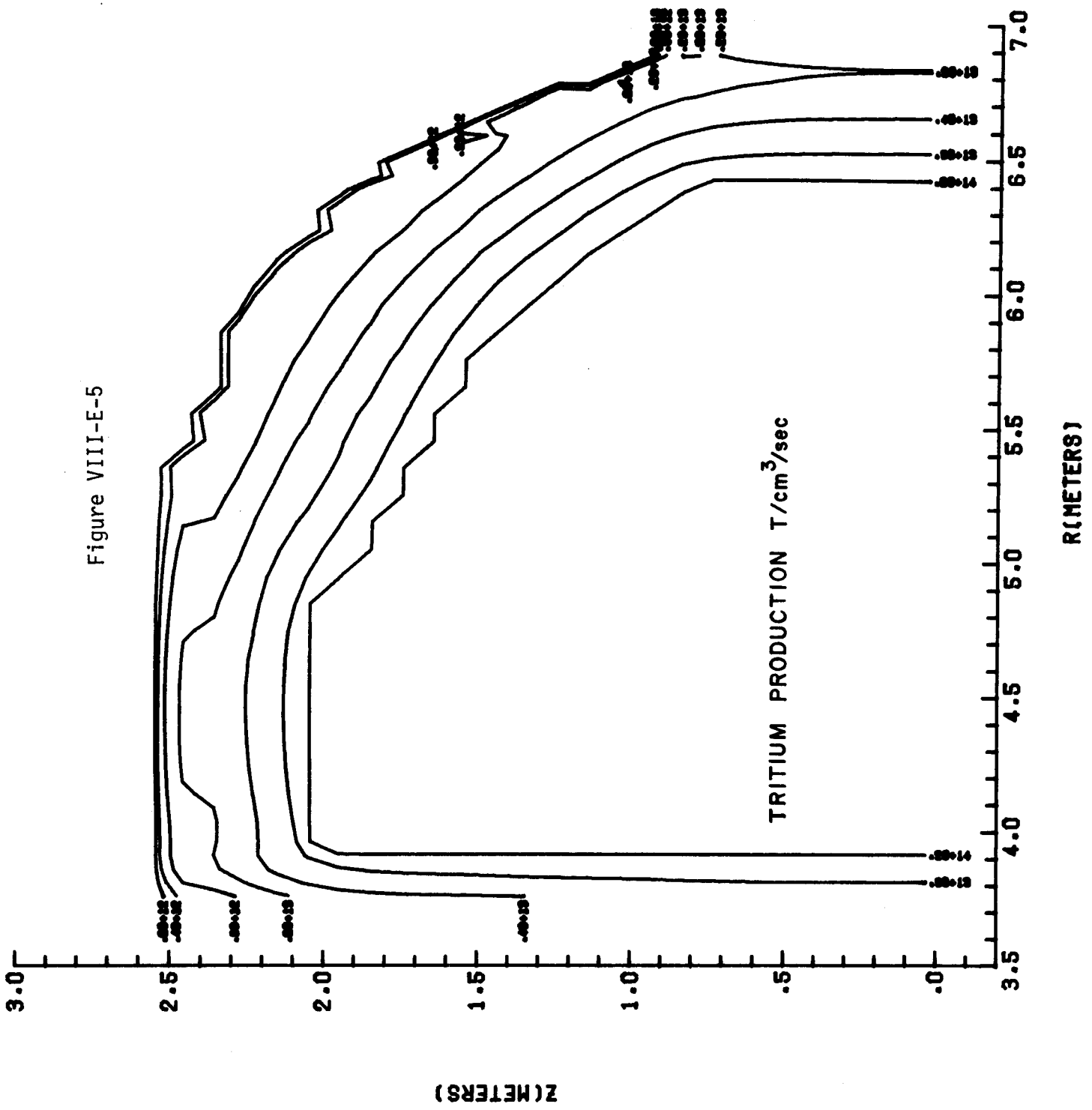


Figure VIII-E-5

Figure VIII-E-6

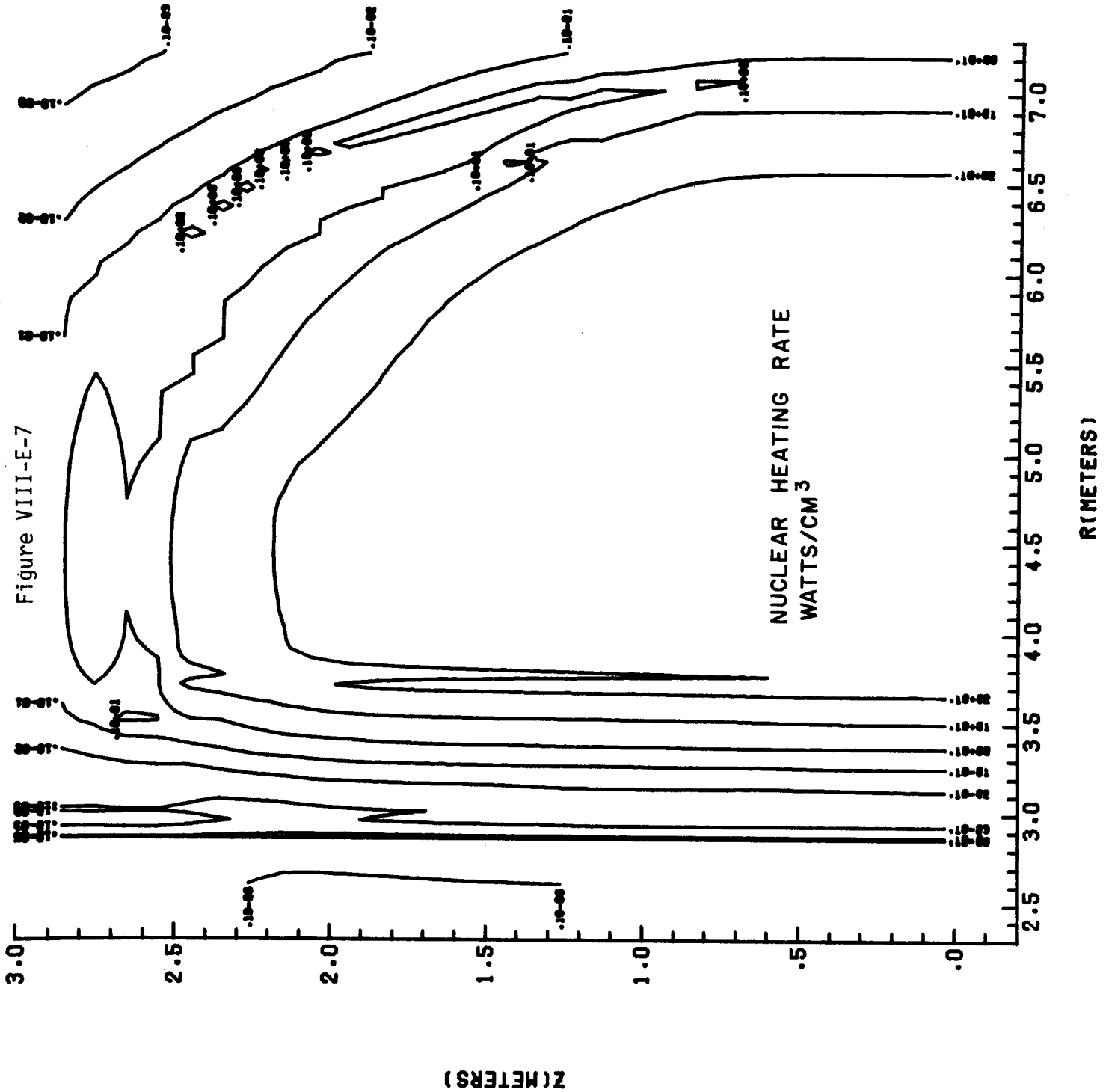


Figure VIII-E-7

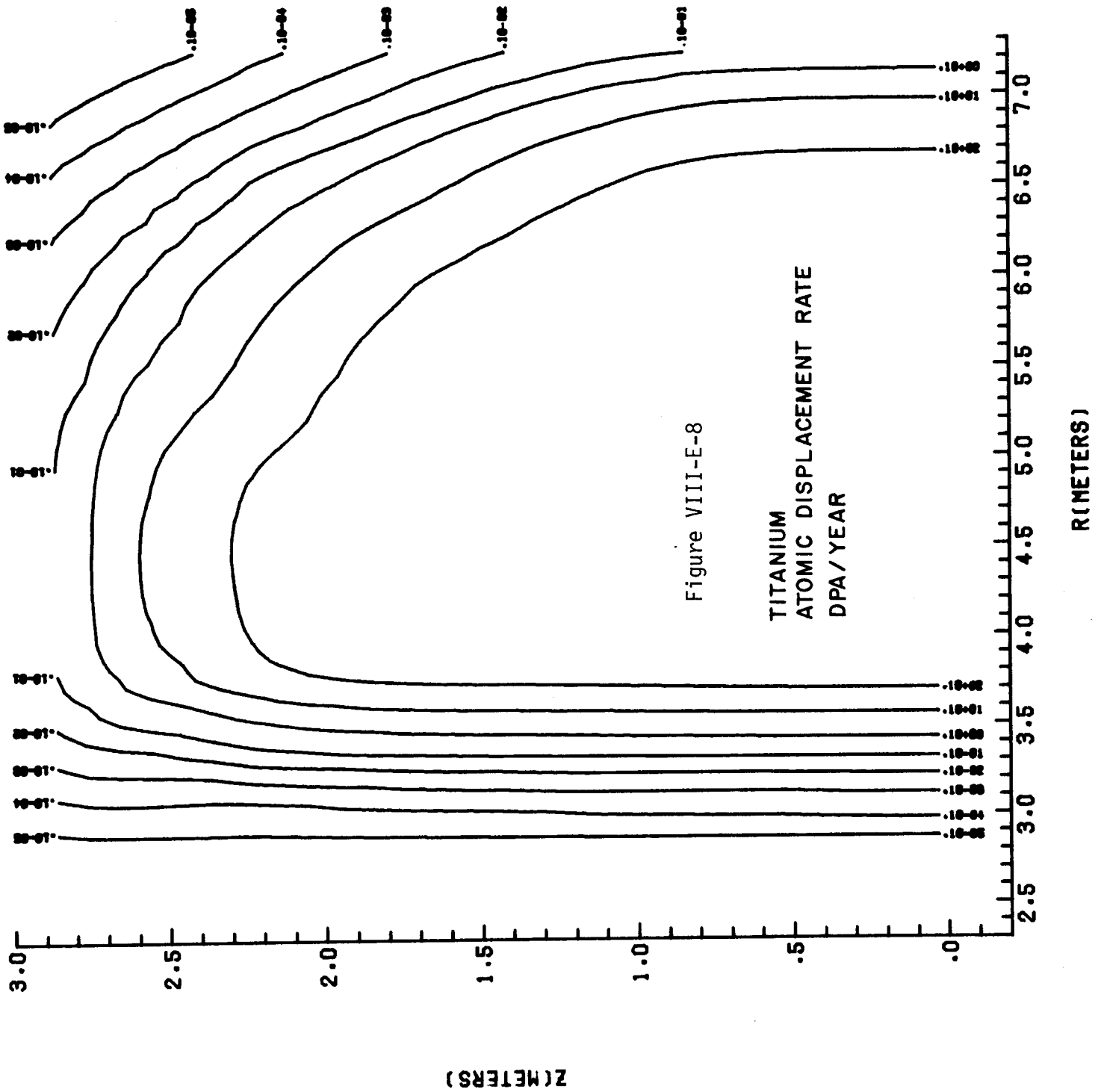


Figure VIII-E-8

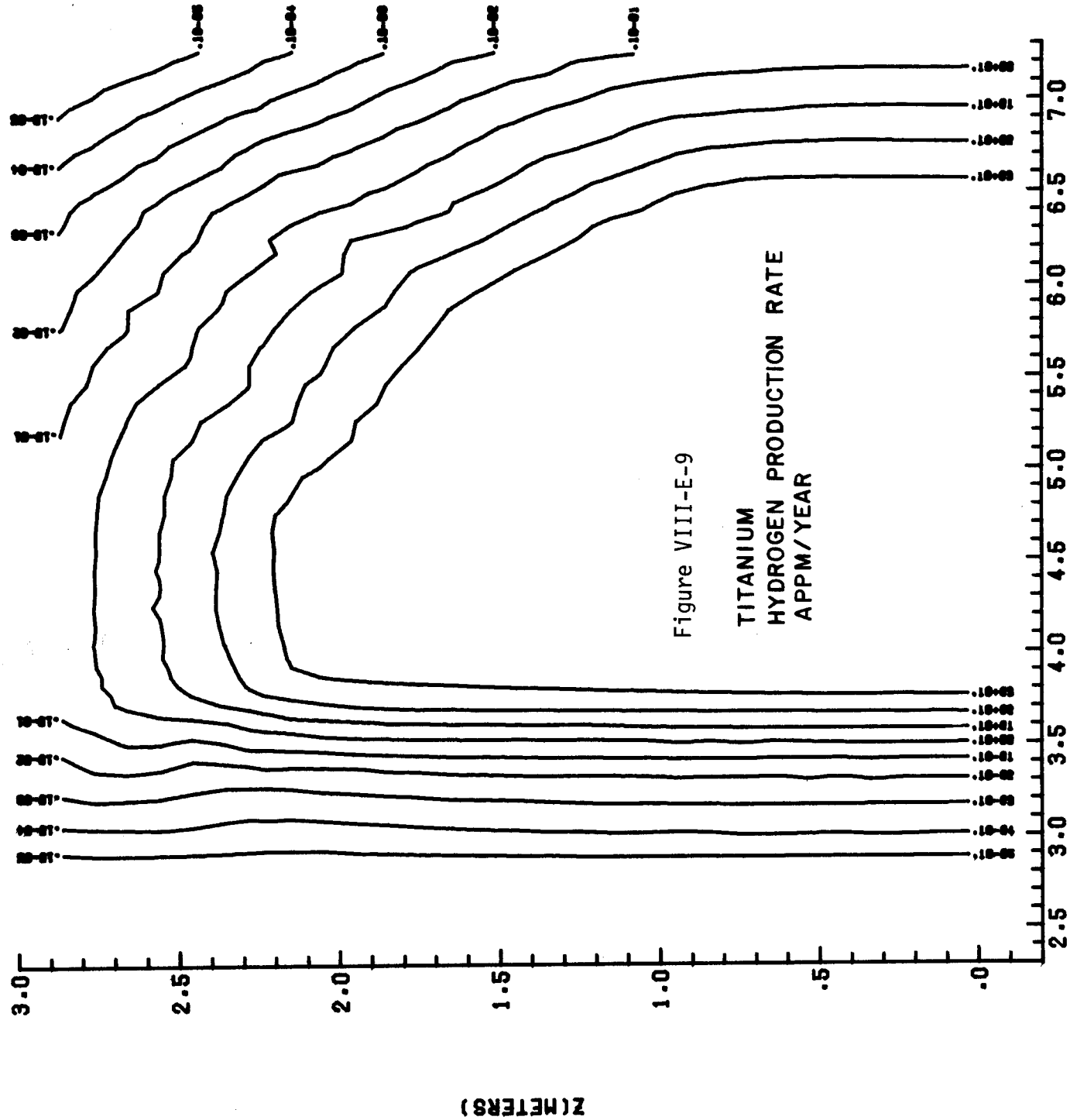


Figure VIII-E-9

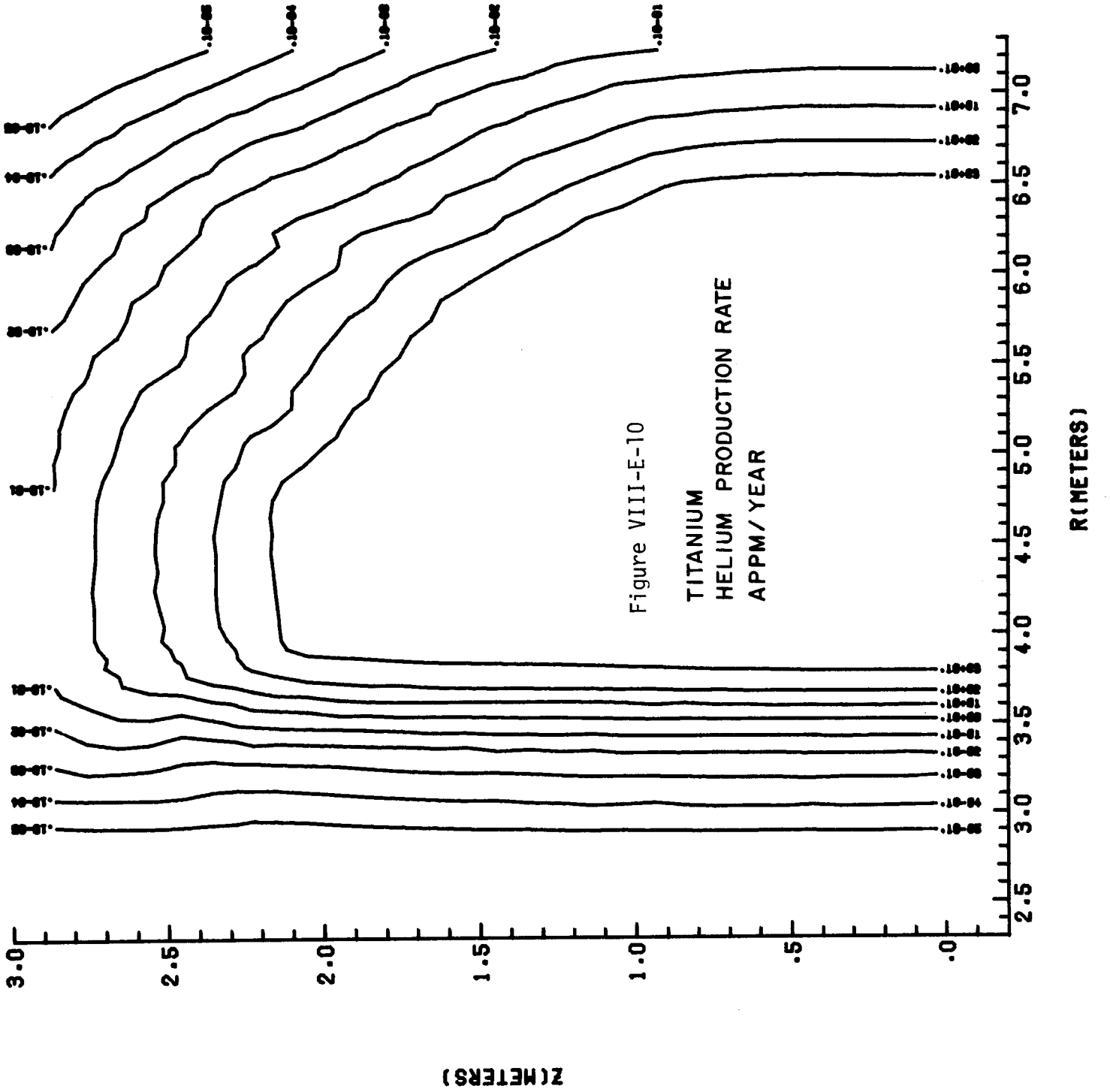


Figure VIII-E-10

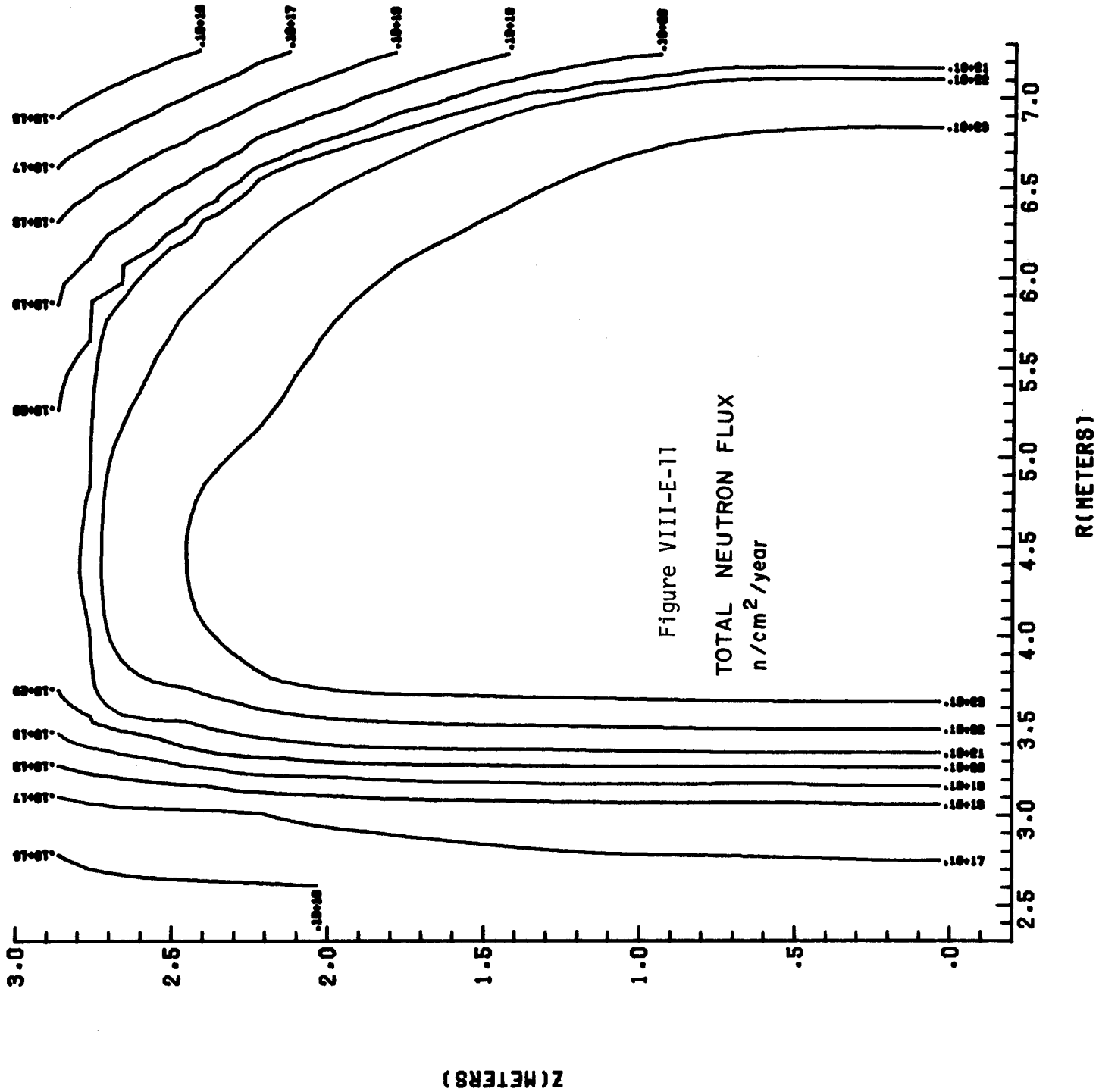


Figure VIII-E-11

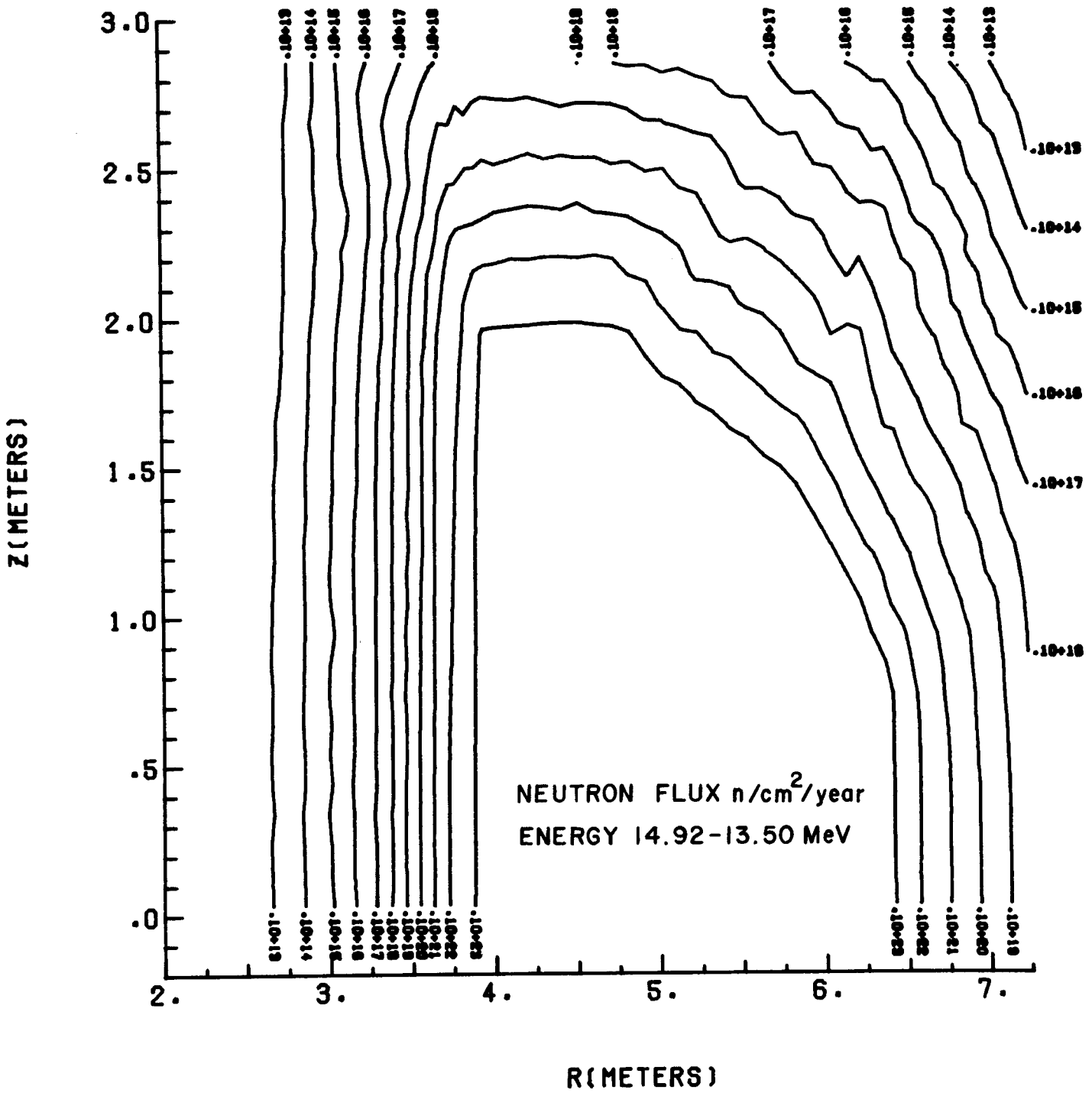


Figure VIII-E-12

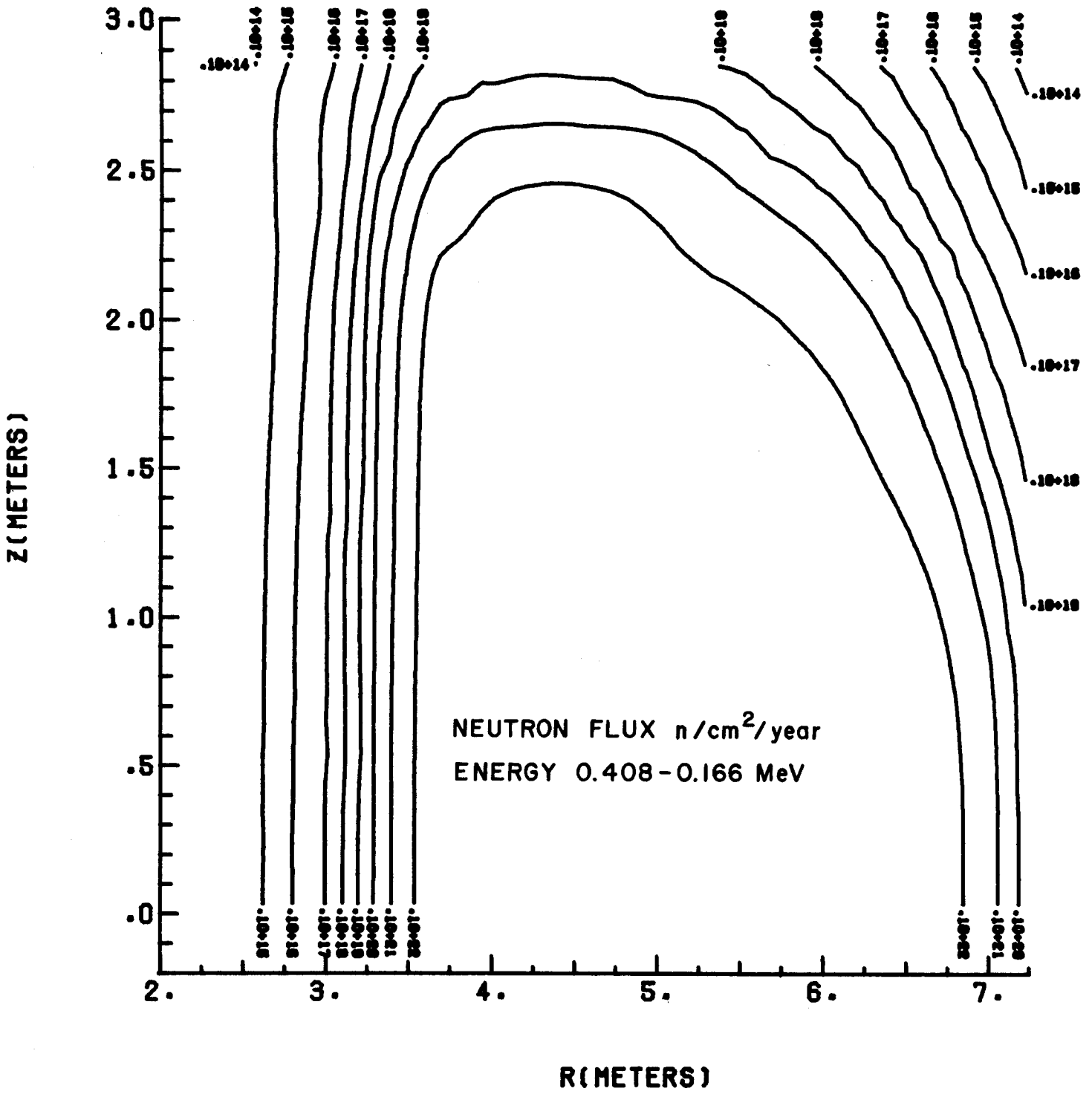


Figure VIII-E-13

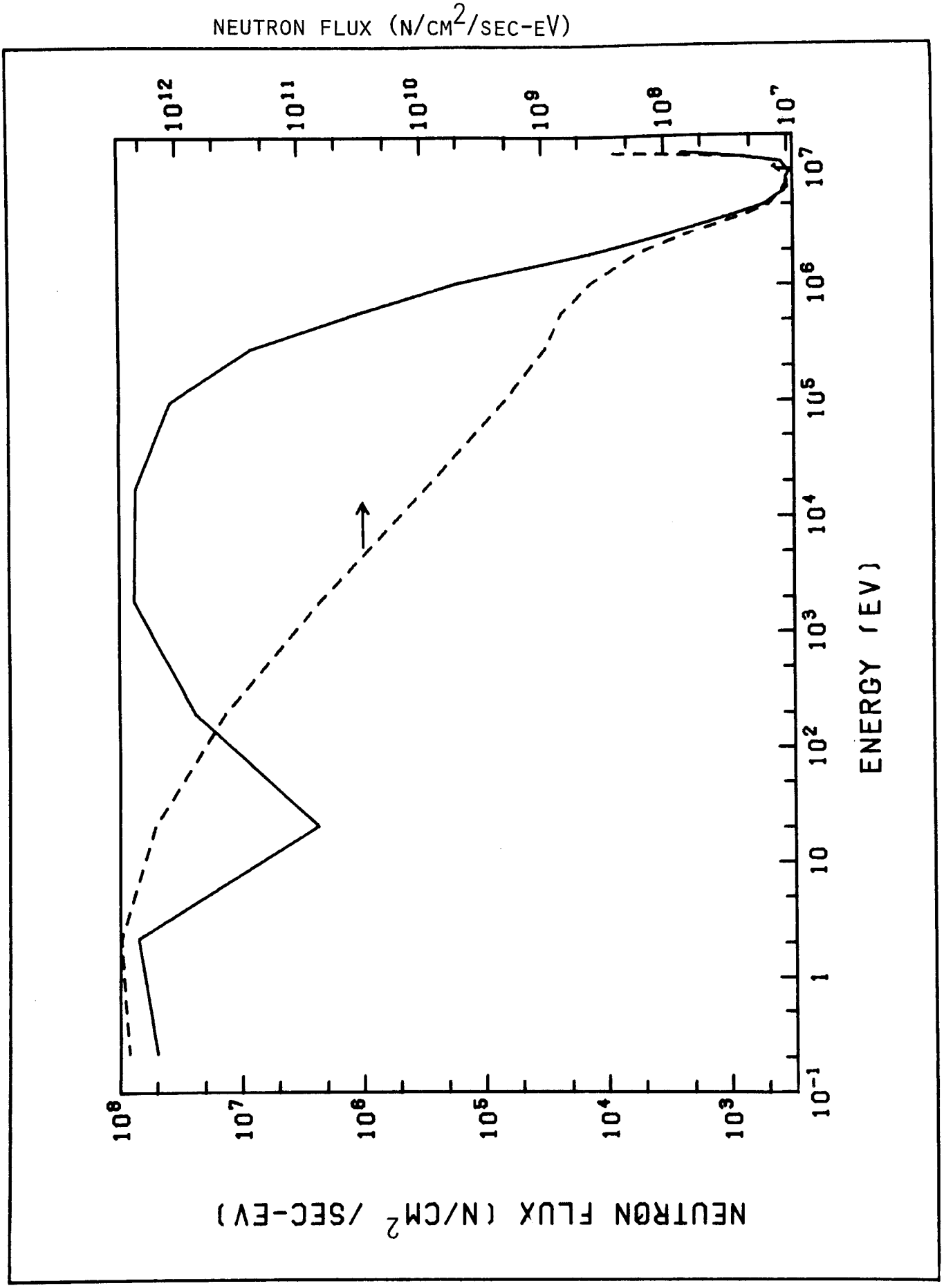


Fig. VIII-E-14 Neutron flux at tungsten zone 52 cm from the first wall

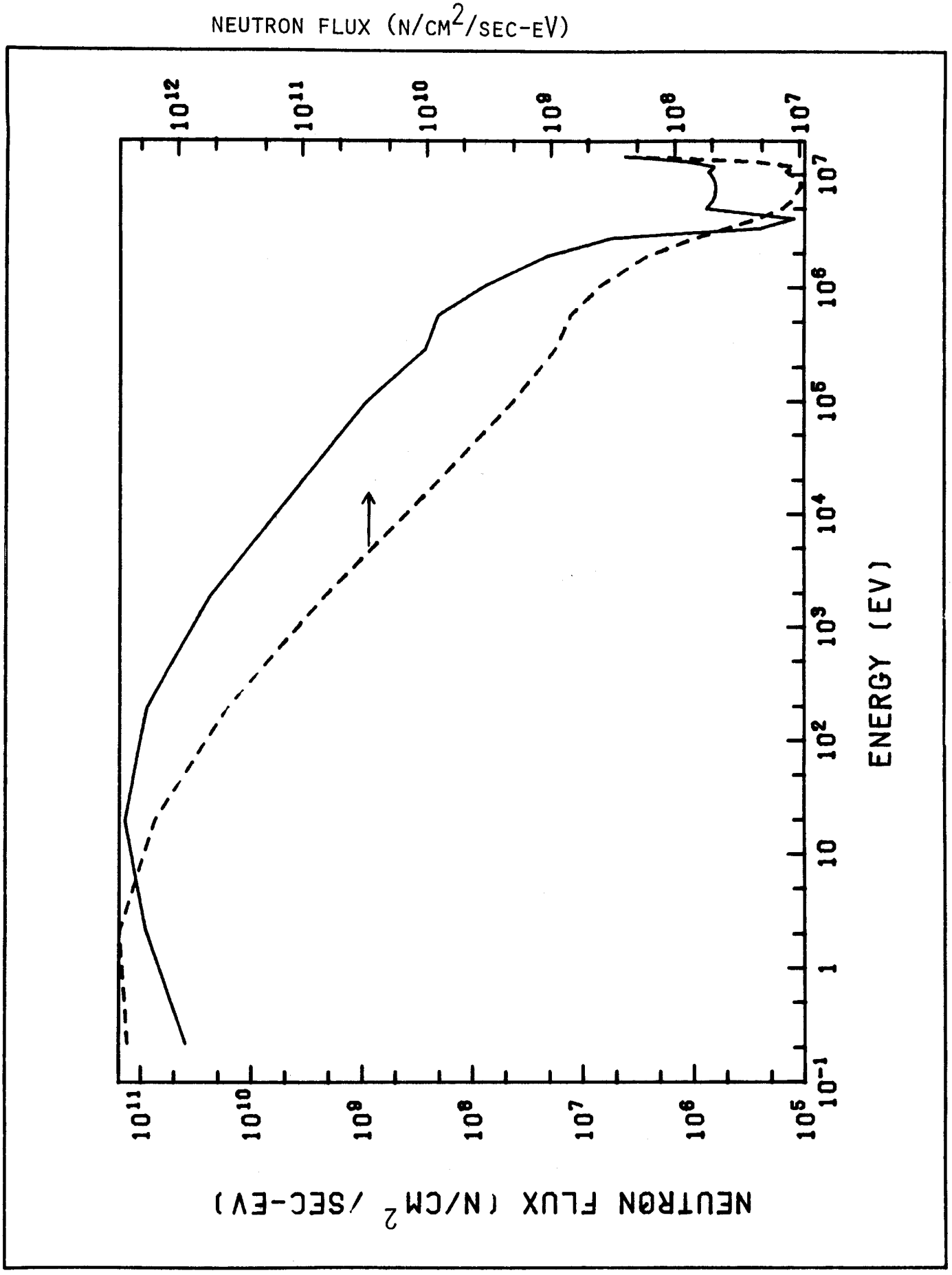


Fig. VIII-E-15 Neutron flux at the graphite reflector 62 cm from the first wall

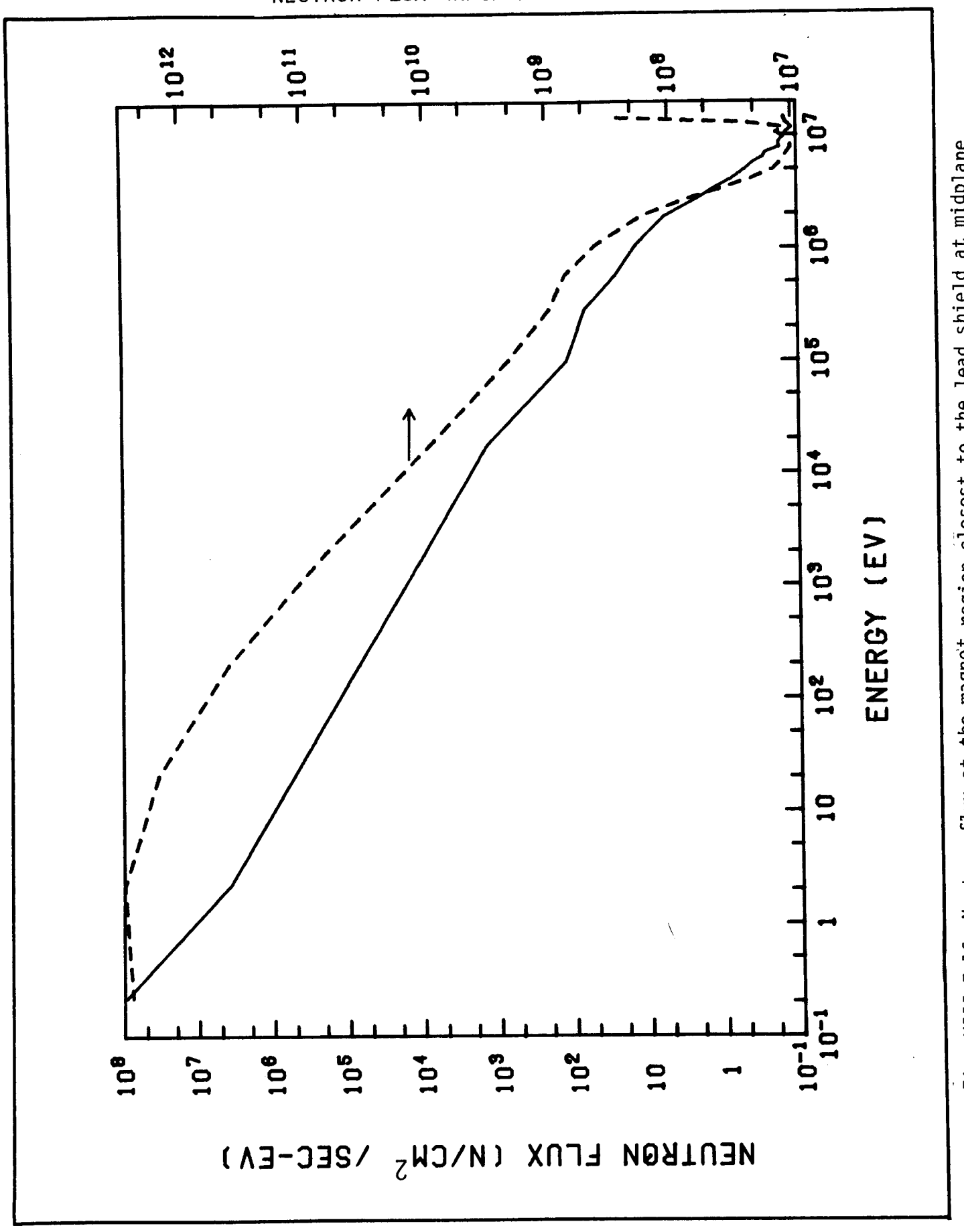


Fig. VIII-E-16 Neutron flux at the magnet region closest to the lead shield at midplane

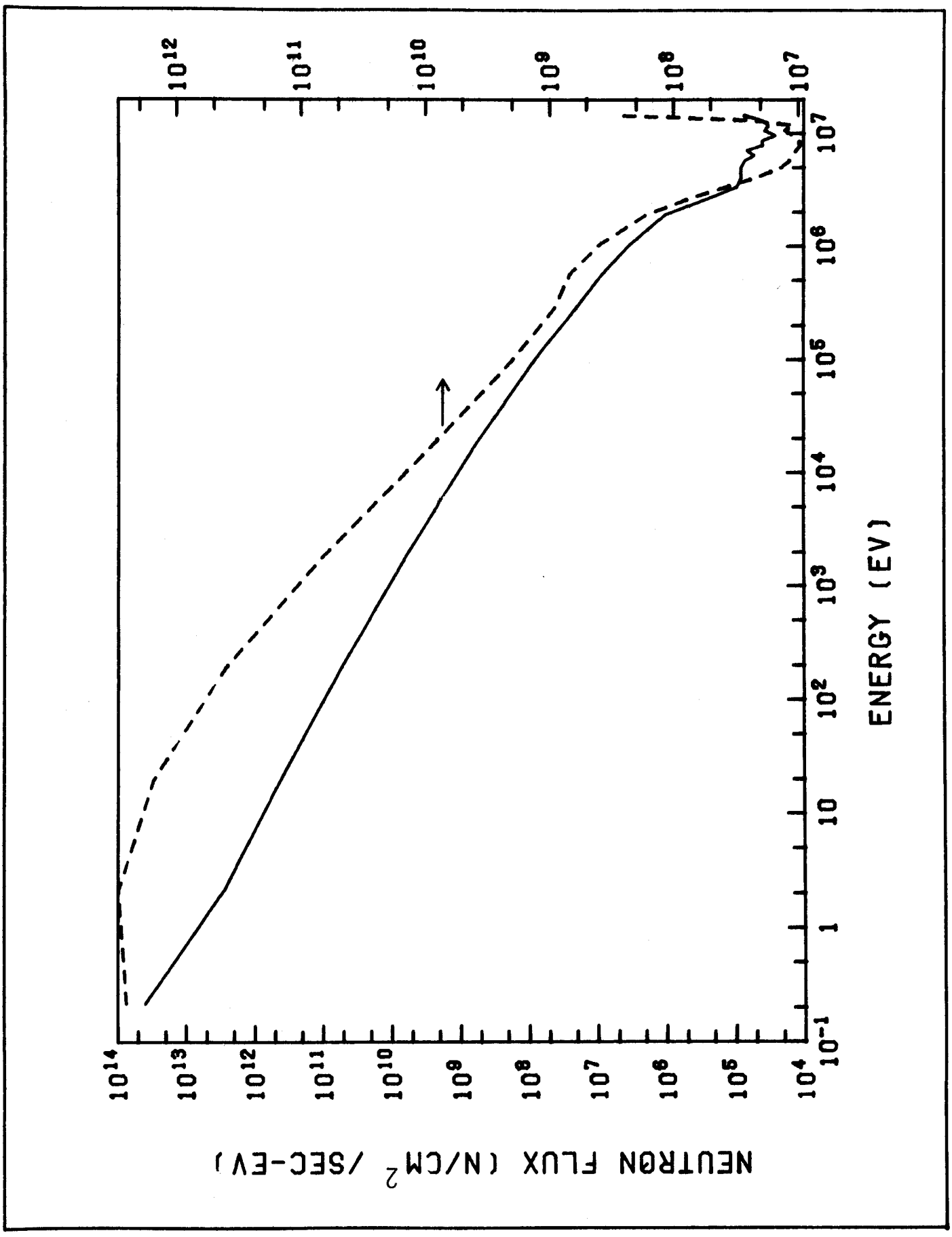


Fig. VIII-E-17 Neutron flux at the outer breeding zone 32 cm from the first wall

Table VIII-E-6

Some Group Scalar Neutron Fluxes ($n/cm^2/sec$) Found in the NUWMAK Blanket and Shield at Positions at Midplane $\theta=0°,180°$

	Inner Blanket/Shield			Outer Blanket/Shield	
Neutron Energy Group	Magnet Region Close to the Lead Shield	Tungsten Region 52 cm From the First Wall	Outer/Inner First Walls	Breeding Region 32 cm From the First Wall	Reflector Region 62 cm From the First Wall
1	2.032+5	3.401+9	3.553+14	4.870+12	1.631+11
2	1.731+5	9.745+8	3.031+13	1.440+12	4.933+10
3	1.330+5	4.341+8	1.263+13	7.586+11	3.815+10
4	1.440+5	3.656+8	1.341+13	7.740+11	3.898+10
5	1.419+5	3.026+8	1.037+13	6.524+11	2.464+10
6	1.504+5	2.916+8	8.603+12	5.520+11	3.482+10
7	1.287+5	2.678+8	7.565+12	4.958+11	3.041+10
8	1.816+5	2.311+8	7.343+12	4.519+11	4.821+10
9	1.766+5	2.307+8	7.089+12	4.163+11	3.336+10
10	2.152+5	2.445+8	6.729+12	3.999+11	4.178+10
11	4.775+5	5.038+8	1.357+13	7.698+11	8.159+10
12	6.141+5	7.363+8	1.737+13	1.013+11	6.578+10
13	8.695+5	1.148+9	2.510+13	1.709+11	6.344+10
14	1.130+6	1.785+9	3.631+13	3.003+12	1.129+11
15	6.439+6	1.495+10	1.841+14	2.380+13	1.157+12
16	8.469+6	1.057+11	2.402+14	4.684+13	2.061+12
17	8.661+6	3.836+11	2.307+14	6.887+13	2.919+12
18	1.616+7	1.983+12	2.222+14	6.571+13	5.124+12
19	1.579+7	5.107+12	2.700+14	1.242+14	1.146+13
20	3.866+7	2.100+12	2.539+14	1.098+14	1.790+13
21	2.855+7	2.284+11	2.001+14	7.294+13	1.860+13
22	2.232+7	7.522+9	1.281+14	2.860+13	1.726+13
23	1.724+7	7.842+7	5.158+13	4.711+12	1.374+13
24	1.311+7	2.473+8	1.043+13	3.161+11	9.780+12
25	3.605+7	1.940+7	9.990+11	1.549+10	1.547+13

A schematic of the NUWMAK blanket as considered for the radioactivity calculations is shown in Fig. VIII-F-1. The composition of the various regions is given in Table VIII-E-1. As discussed in previous sections of this report, the inner regions of the blanket (zones A-C) are mainly shields to reduce the radiation and heat loads on the magnets and associated components. For the activity calculations to be performed with the same detail as the flux calculations a DKR calculation would have to be made at each mesh point resulting in some 1600 calculations which would then have to be properly volume weighted and processed together. This course of action was not taken for two reasons. First, the amount of effort required was deemed to be too large and second, at this stage of the study it was judged that such detailed calculations were not necessary to determine the activity of the design adequately for comparison with other results and to evaluate the effects of the radioactive decay. Consequently, calculations were made only along those traverses shown in Fig. VIII-F-1. Further, simplification was obtained by breaking the various regions along the traverses into subregions using an average flux in each of these regions. This procedure was also used in previous one-dimensional studies. The specific activities calculated along each of these traverses were then taken to be representative of the average activity in an associated zone so that with proper volume weighting the total activity of a zone or combination of zones could be found. Since the highest specific activity occurs in the first wall additional calculations were made at additional first wall points around the plasma cavity.

VIII-F-1. Radioactivity, Afterheat and BHP

The results of the calculations are shown in Figs. VIII-F-2-4. Fig. VIII-F-2 shows the radioactivity of the reactor in curies per watt thermal. For comparison purposes the activity of UWMAK-I is also shown. The activity changes very little during the time immediately after shutdown being almost constant for the first month or so. This means that very little

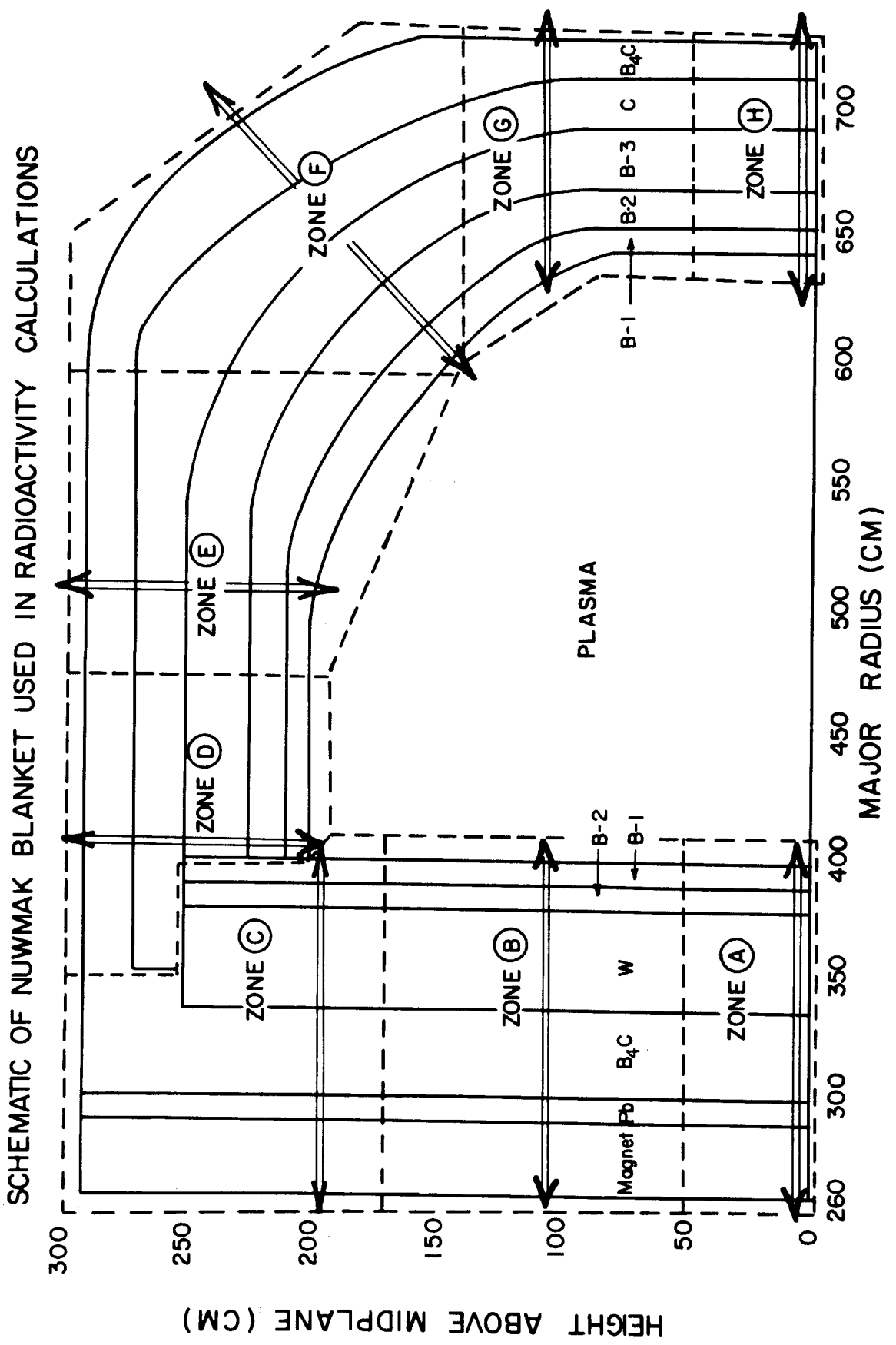


FIGURE VIII-F-1

Fig. VIII-F-2

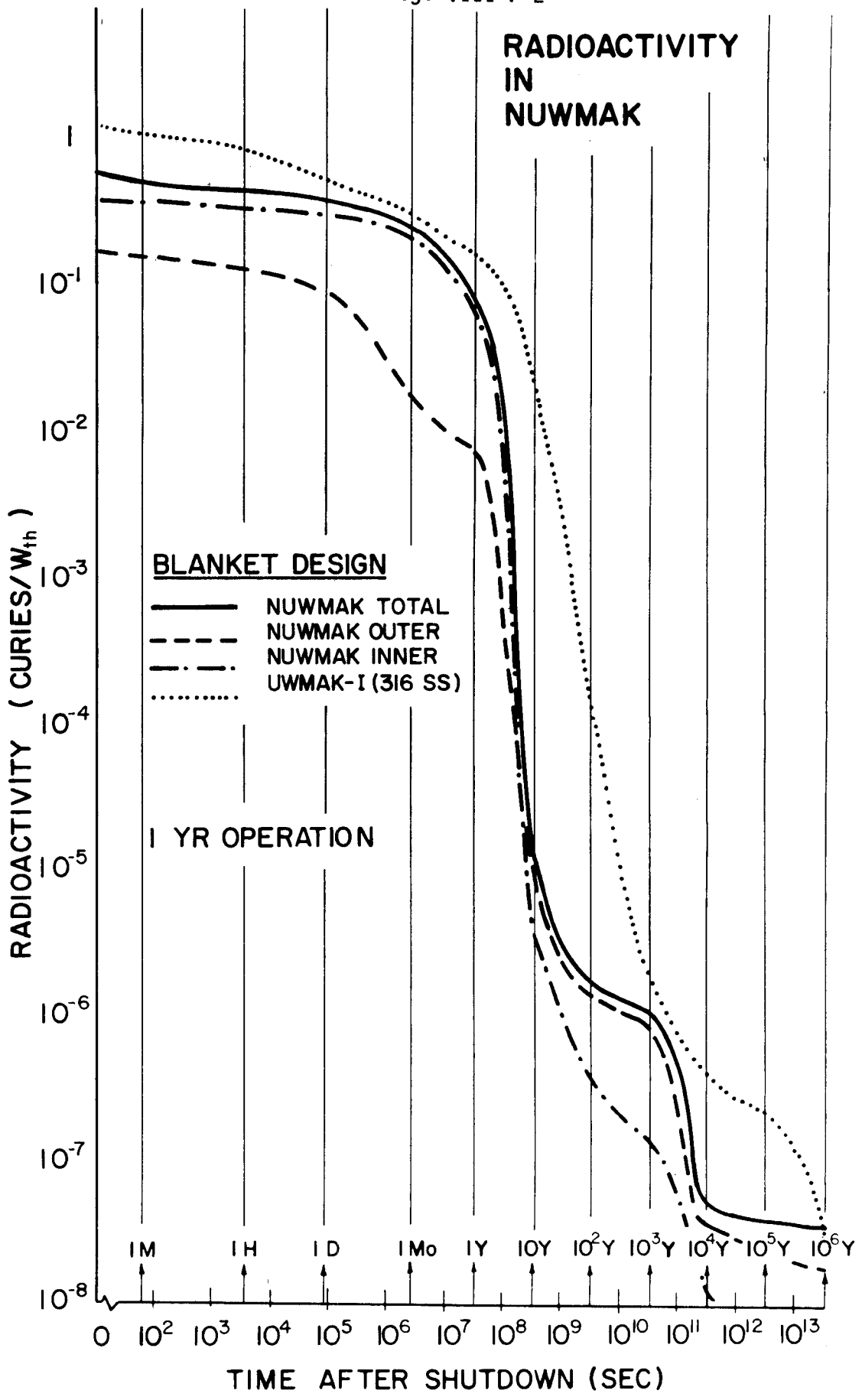

RADIOACTIVITY
IN
NUWMAK
BLANKET DESIGN
NUWMAK TOTAL
NUWMAK OUTER
NUWMAK INNER
UWMAK-I (316 SS)
1 YR OPERATION
RADIOACTIVITY (CURIES/W$_{th}$)
1
10^{-1}
10^{-2}
10^{-3}
10^{-4}
10^{-5}
10^{-6}
10^{-7}
10^{-8}
1M
1H
1D
1Mo
1Y
10Y
10^2Y
10^3Y
10^4Y
10^5Y
10^6Y
0
10^2
10^3
10^4
10^5
10^6
10^7
10^8
10^9
10^{10}
10^{11}
10^{12}
10^{13}
TIME AFTER SHUTDOWN (SEC)

Fig. VIII-F-3

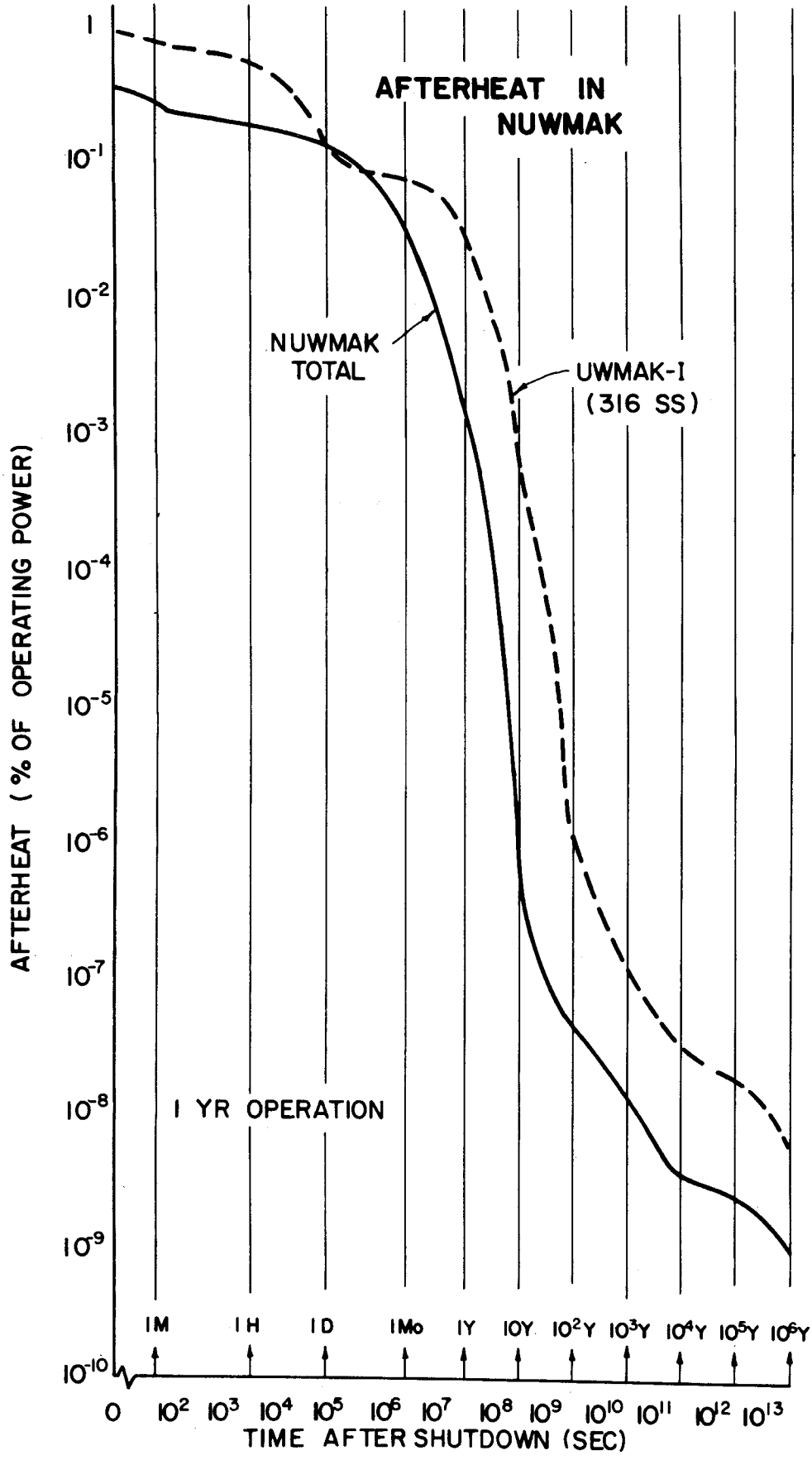
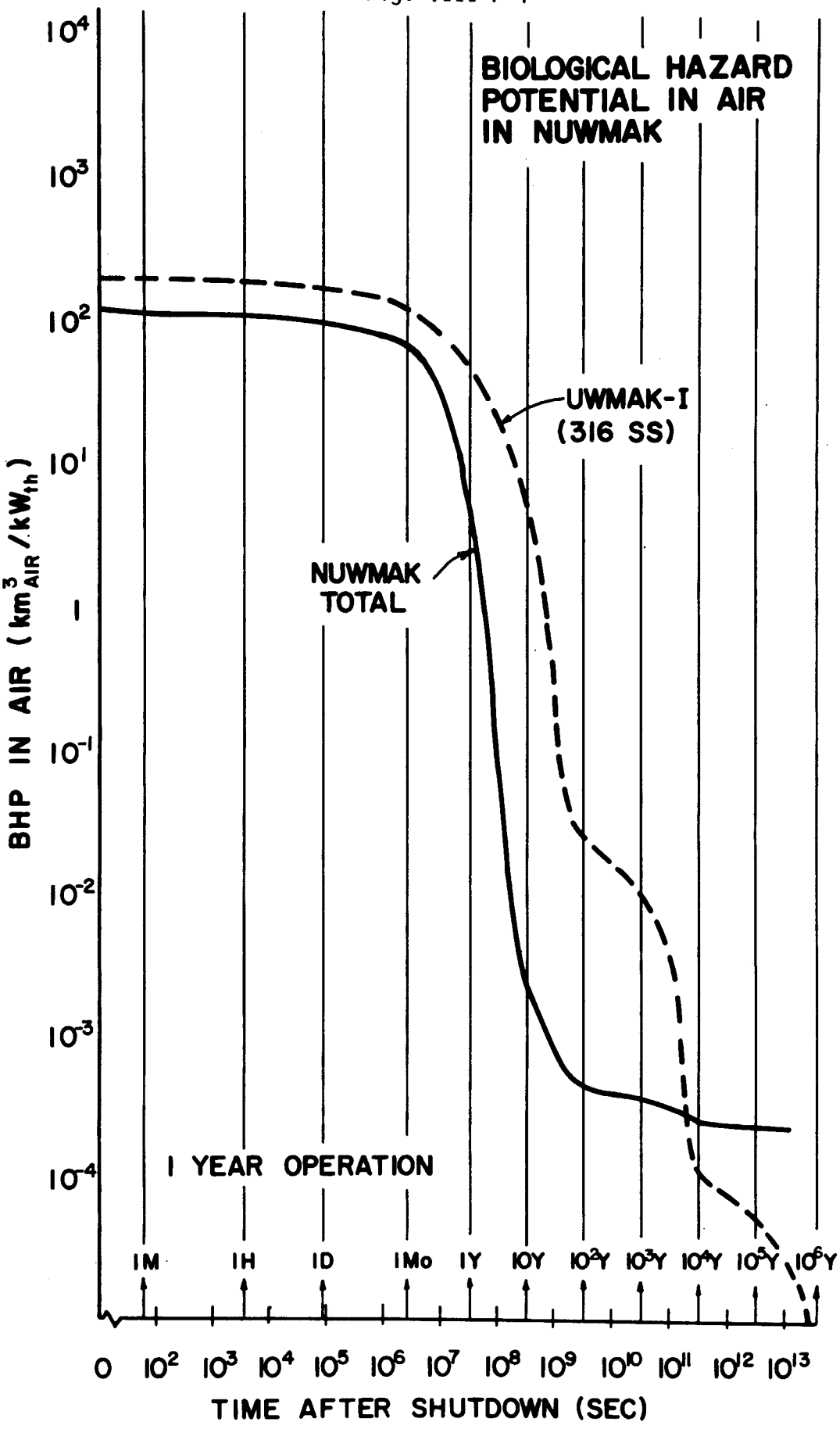

AFTERHEAT IN NUWMAK
NUWMAK TOTAL
UWMAK-I (316 SS)
1 YR OPERATION
AFTERHEAT (% OF OPERATING POWER)
1
10-1
10-2
10-3
10-4
10-5
10-6
10-7
10-8
10-9
10-10
1M
1H
1D
1Mo
1Y
10Y
10²Y
10³Y
10⁴Y
10⁵Y
10⁶Y
0
10²
10³
10⁴
10⁵
10⁶
10⁷
10⁸
10⁹
10¹⁰
10¹¹
10¹²
10¹³
TIME AFTER SHUTDOWN (SEC)

Fig. VIII-F-4


BIOLOGICAL HAZARD POTENTIAL IN AIR IN NUWMAK
UWMAK-I (316 SS)
NUWMAK TOTAL
1 YEAR OPERATION
BHP IN AIR (km^3_{AIR}/kW_{th})
10^4
10^3
10^2
10^1
1
10^{-1}
10^{-2}
10^{-3}
10^{-4}
1M 1H 1D 1Mo 1Y 10Y 10^2Y 10^3Y 10^4Y 10^5Y 10^6Y
0 10^2 10^3 10^4 10^5 10^6 10^7 10^8 10^9 10^{10} 10^{11} 10^{12} 10^{13}
TIME AFTER SHUTDOWN (SEC)

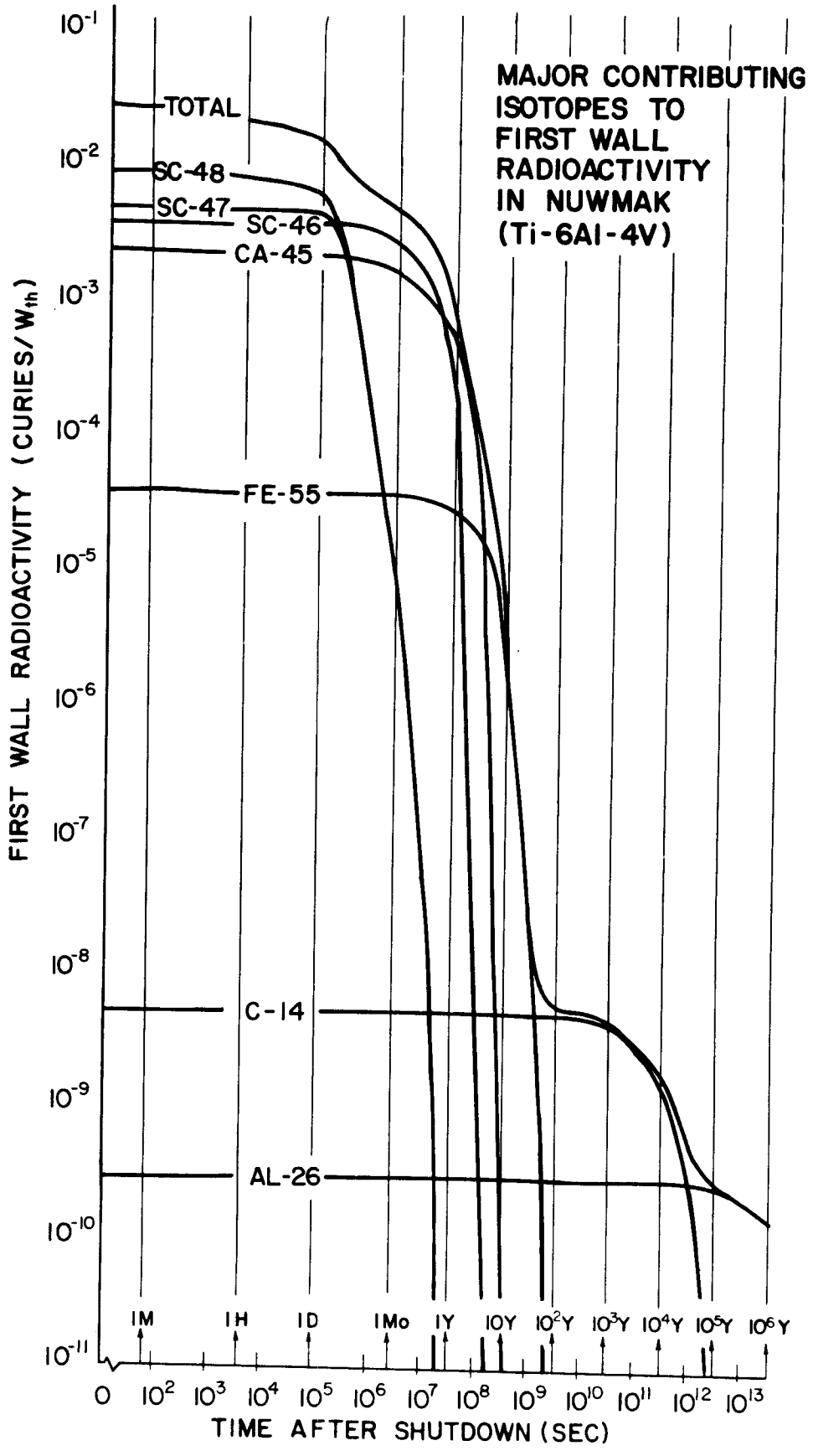
relief in activity levels around the reactor can be obtained by using a waiting period after shutdown. However, since the dose rates occurring outside of the shield are primarily the result of gammas emitted near the edge of the shield, it does not necessarily follow that the dose rates in that region will follow this same pattern. This will be discussed in the next subsection. From the point of view of intermediate term activity the curves show that after about 10 years the activity levels are down by between 4-5 orders of magnitude. It may be also noted that most of the activity originates in the inner region of the blanket.

In comparing the activity with the stainless steel UWMAK-I design it is seen that some improvement has been made especially in the one year to 1000 year time span. Initially the activity per watt is only lower by a factor of about two. The afterheat results (Fig. VIII-F-3) and BHP results (Fig. VIII-F-4) show qualitatively similar behavior with the primary difference being the very long term behavior of the BHP for NUWMAK.

As seen in Fig. VIII-F-4, it would appear that at very long times the biological hazard potential (BHP) of NUWMAK is significantly higher than the BHP of a stainless steel system such as UWMAK-I. This would imply a long term radioactivity problem in any machine with a Pb-Li blanket with all its attendant difficulties and problems. It is unlikely that this is the case. In calculating the BHP the allowable concentrations used are taken from chapter 10 part 20 of the Code of Federal Regulations. In the case of ^{205}Pb no limits are given and therefore the default value of 10×10^{-10} μCi/ml is used. However, ^{205}Pb decays by electron capture to the ground state of ^{205}Tl. Furthermore, the Q value for this reaction is so low that the electron captured is from the L shell. Consequently, the X-rays emitted following a transition are of low energy viz. ~ 11 keV. It would seem then that ^{205}Pb should be no worse than ^{203}Pb which has an allowable concentration of 6×10^{-8} μCi/ml and likely would be significantly less of a problem. Even raising the allowable concentration by a factor of 20 means that at these very long times it is the ^{26}Al activity that would dominate.

It is of interest to determine the source of the activity in the system. Figure VIII-F-5 shows the activity of the first wall. The activity for the first 10 years is dominated by four isotopes - ^{46}Sc, ^{47}Sc, ^{48}Sc,

Fig. VIII-F-5


MAJOR CONTRIBUTING ISOTOPES TO FIRST WALL RADIOACTIVITY IN NUWMAK (Ti-6Al-4V)
TOTAL
SC-48
SC-47
SC-46
CA-45
FE-55
C-14
AL-26
FIRST WALL RADIOACTIVITY (CURIES/W$_{th}$)
10^{-1}
10^{-2}
10^{-3}
10^{-4}
10^{-5}
10^{-6}
10^{-7}
10^{-8}
10^{-9}
10^{-10}
10^{-11}
1M
1H
1D
1Mo
1Y
10Y
10^{2}Y
10^{3}Y
10^{4}Y
10^{5}Y
10^{6}Y
0
10^{2}
10^{3}
10^{4}
10^{5}
10^{6}
10^{7}
10^{8}
10^{9}
10^{10}
10^{11}
10^{12}
10^{13}
TIME AFTER SHUTDOWN (SEC)

and ^{45}Ca - all of which are produced by reactions in titanium. After the decay of these isotopes the activity is dominated by ^{55}Fe which is produced from the iron impurities (0.3%) present in the Ti-6Al-4V alloy. Similarly the very long lived components ^{14}C and ^{26}Al originate with the carbon impurities and the aluminum alloying constituents respectively.

The activity sources in the outer blanket (including the first wall) are somewhat different for two reasons. One is the fact that the titanium alloy in the blanket structure is different, being Ti-6Al-2Sn-4Zr-2Mo. The second difference is due to the lead in the lead-lithium breeding material. The fractional contribution to the activity of the outer blanket is shown in Figure VIII-F-6. Here we see that at short and very long times the major activity originates in the lead isotopes. At intermediate times the activity is first dominated by isotopes originating in titanium, then in the iron impurity and finally in the molybdenum alloying constituent.

If, however, the BHP of the outer blanket (Figure VIII-F-7) is considered rather than the activity the situation is changed. At times up to a few years the activity is dominated by isotopes originating in titanium followed by a time when ^{204}Tl from lead dominates. Beyond this time the BHP is dominated by ^{205}Pb from lead with some smaller contributions from the ^{93m}Nb originating in the molybdenum component. The previous comments concerning the BHP values of ^{205}Pb apply equally well here.

The situation in the inner blanket is similar being affected at short times by the presence of the tungsten in the shield. The contribution of the various isotopes to activity and BHP are shown in Figure VIII-F-8 and VIII-F-9. Initially the activity of the tungsten dominates but following the decay of ^{181}W and ^{185}W the situation is very similar to the outer blanket, e.g., the isotopes from molybdenum and lead dominate at the longer times. It thus appears that with the exception of ^{55}Fe the activity levels are determined by the primary materials in the system rather than the impurities considered in these calculations.

Fig. VIII-F-6

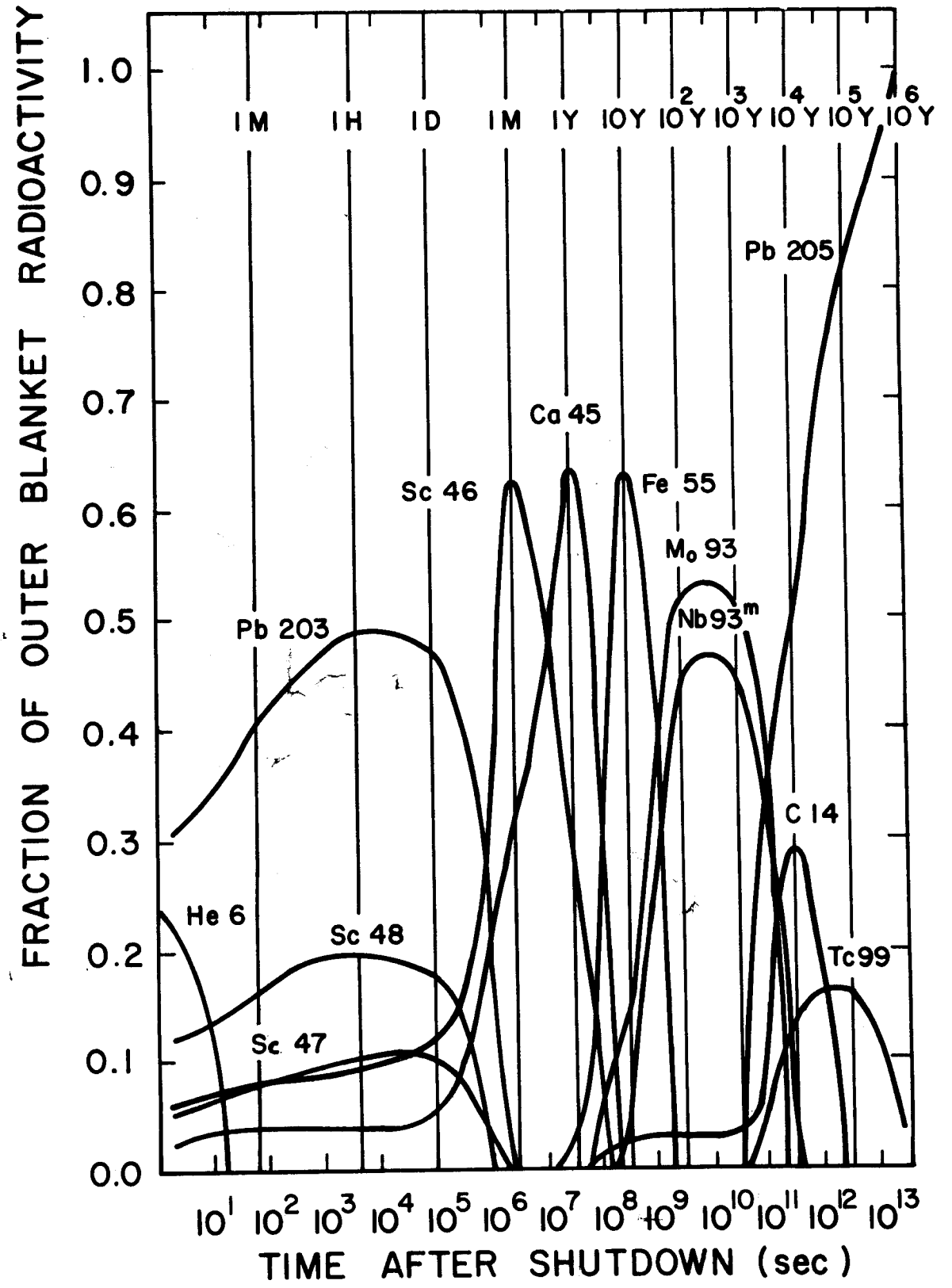

FRACTION OF OUTER BLANKET RADIOACTIVITY
1.0
0.9
0.8
0.7
0.6
0.5
0.4
0.3
0.2
0.1
0.0
1M
1H
1D
1M
1Y
10Y
10^2 Y
10^3 Y
10^4 Y
10^5 Y
10^6 Y
Pb 205
Ca 45
Sc 46
Fe 55
Mo 93
Nb 93^m
Pb 203
C 14
He 6
Sc 48
Tc 99
Sc 47
10^1 10^2 10^3 10^4 10^5 10^6 10^7 10^8 10^9 10^10 10^11 10^12 10^13
TIME AFTER SHUTDOWN (sec)

Fig. VIII-F-7

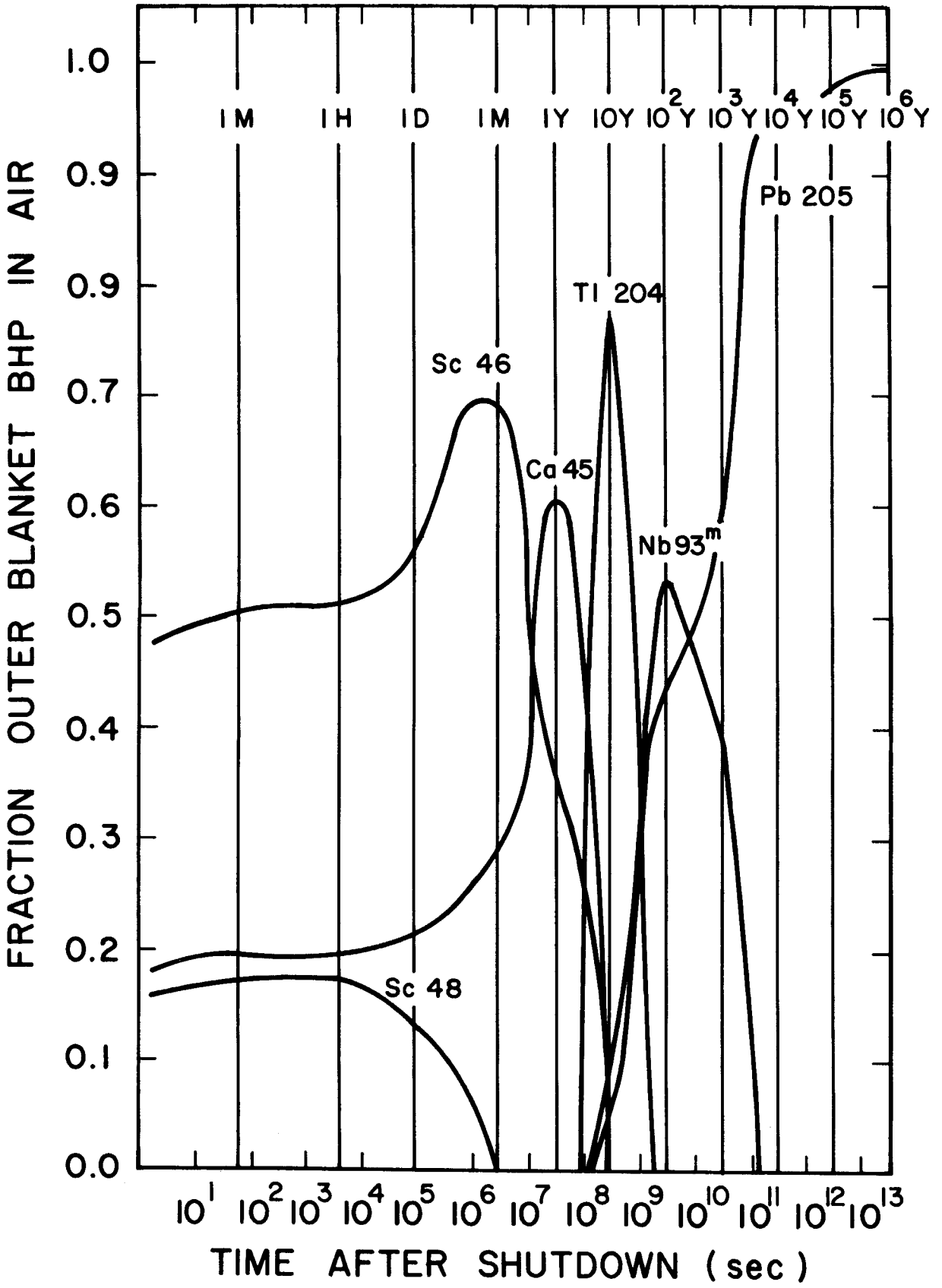

1.0
0.9
0.9
0.7
0.6
0.5
0.4
0.3
0.2
0.1
0.0
FRACTION OUTER BLANKET BHP IN AIR
1 M
1 H
1 D
1 M
1 Y
10 Y
10^2 Y
10^3 Y
10^4 Y
10^5 Y
10^6 Y
Pb 205
Tl 204
Sc 46
Ca 45
Nb 93^m
Sc 48
10^1 10^2 10^3 10^4 10^5 10^6 10^7 10^8 10^9 10^10 10^11 10^12 10^13
TIME AFTER SHUTDOWN (sec)

Fig. VIII-F-8

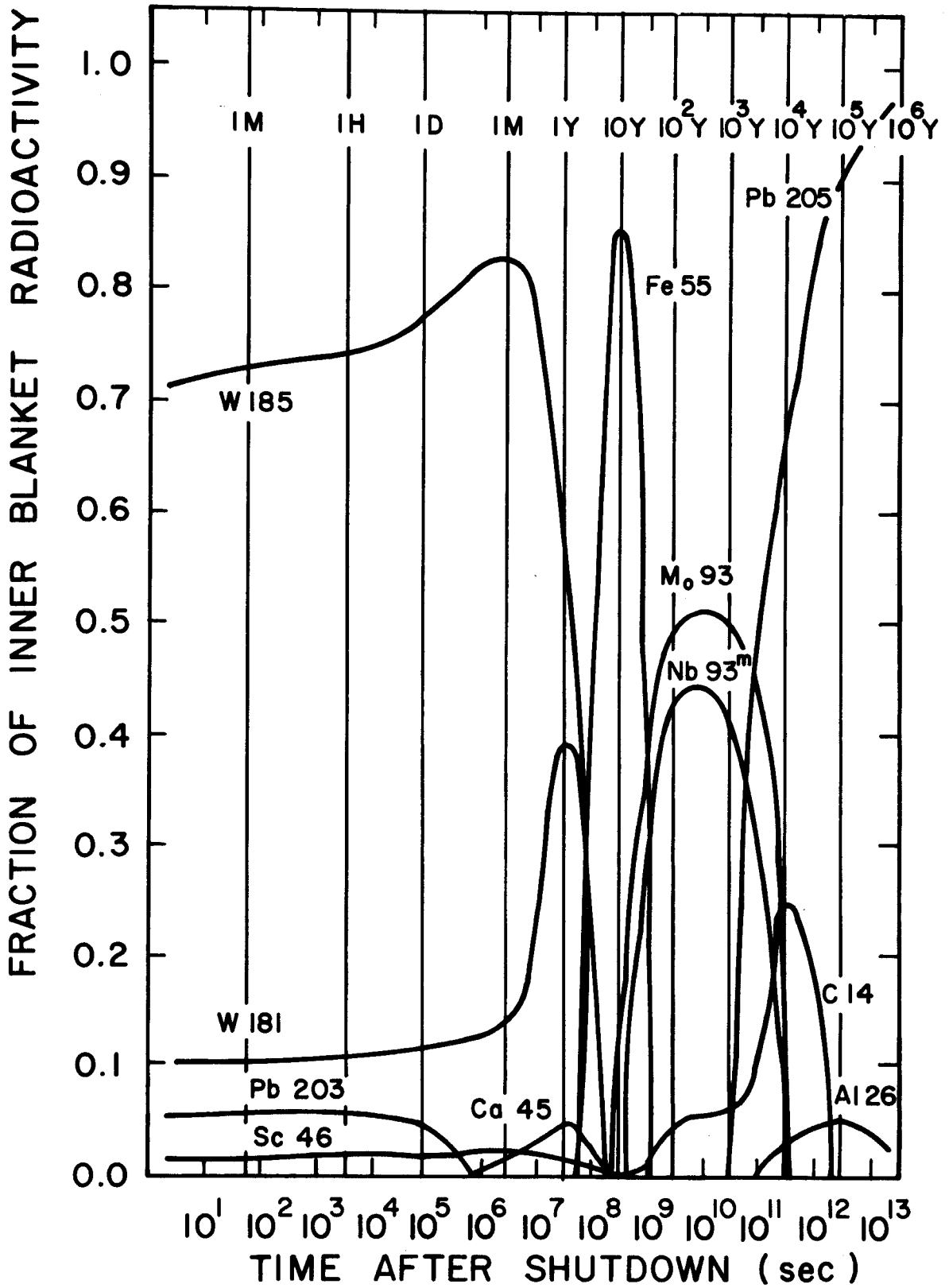
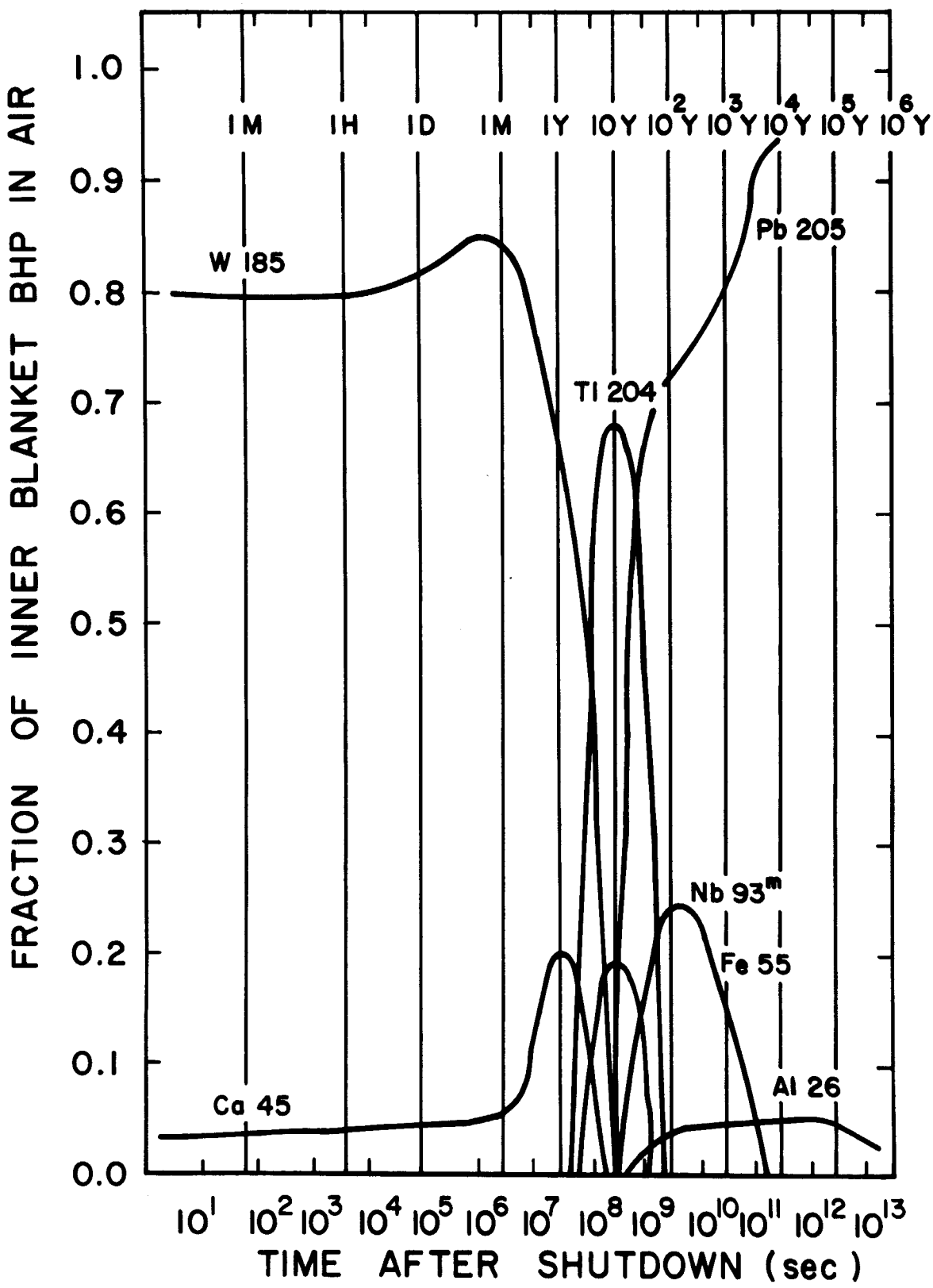

FRACTION OF INNER BLANKET RADIOACTIVITY
1.0
0.9
0.8
0.7
0.6
0.5
0.4
0.3
0.2
0.1
0.0
1M
1H
1D
1M
1Y
10Y
10²Y
10³Y
10⁴Y
10⁵Y
10⁶Y
W 185
W 181
Pb 203
Sc 46
Ca 45
Fe 55
Mo 93
Nb 93m
Pb 205
C 14
Al 26
10¹ 10² 10³ 10⁴ 10⁵ 10⁶ 10⁷ 10⁸ 10⁹ 10¹⁰ 10¹¹ 10¹² 10¹³
TIME AFTER SHUTDOWN (sec)

Fig. VIII-F-9


FRACTION OF INNER BLANKET BHP IN AIR
1.0
0.9
0.8
0.7
0.6
0.5
0.4
0.3
0.2
0.1
0.0
1M
1H
1D
1M
1Y
10Y
10^2Y
10^3Y
10^4Y
10^5Y
10^6Y
W 185
Pb 205
Tl 204
Nb 93^m
Fe 55
Al 26
Ca 45
10^1 10^2 10^3 10^4 10^5 10^6 10^7 10^8 10^9 10^10 10^11 10^12 10^13
TIME AFTER SHUTDOWN (sec)

VIII-F-2. ^{210}Po Production in NUWMAK

The special problem of ^{210}Po production was raised during the design of NUWMAK, because of the large quantities of lead involved in the breeding blanket. The ease of diffusion and the volatility of the radionuclide were seen as possible problems.

Originally, it was thought that the major route of production was double neutron capture in ^{208}Pb by one of two paths:

$$^{208}Pb(n,\gamma)\ ^{209}Pb(n,\gamma)\ ^{210}Pb \xrightarrow[22y]{\beta^-} {}^{210}Bi \xrightarrow[5.0d]{\beta^-} {}^{210}Po$$

or

$$^{208}Pb(n,\gamma)\ ^{209}Pb \xrightarrow[3.3h]{\beta^-} {}^{209}Bi(n,\gamma)\ ^{210}Bi \xrightarrow[5.0d]{\beta^-} {}^{210}Po$$

The latter would seem to be more likely since the half life of ^{209}Pb is relatively short. However, the major pathway for ^{210}Po production will probably be the direct path from ^{209}Bi impurities in the Pb mixture. For example, commercial silver free lead obtained for a slowing down spectrometer was found to have 42 appm of Bi impurity. In this case the activation chain is just

$$^{209}Bi(n,\gamma)\ ^{210}Bi \xrightarrow[5.0d]{\beta^-} {}^{210}Po \xrightarrow[138.4d]{\alpha} {}^{206}Pb$$

This lead is of fairly high purity, and it is reasonable to assume that it is not unlike that which would be obtained in the large quantities required by NUWMAK.

Since ^{209}Bi cross sections were unavailable, an estimate was made based on ^{10}B and ^{6}Li reaction rates in the breeding zone. This procedure may be used since ^{209}Bi is a 1/v absorber with very little resonance structure (for example the resonance integral is less than 0.5 barns). ^{10}B is a 1/v absorber and ^{6}Li is also 1/v but with a high energy resonance at ~ 3 MeV. To normalize, the results must be modified by the ratio of the ^{209}Bi and the ^{10}B or ^{6}Li thermal neutron cross sections and must be adjusted by the ratio of the number densities.

There are 796 metric tons of $Li_{62}Pb_{38}$ eutectic in the NUWMAK breeding zones. About 95% of the weight is due to the Pb, so that there are 756 metric tons of Pb in this region. Thus, there are 2.195×10^{30} atoms of Pb and 9.219×10^{25} atoms of ^{209}Bi; Bi number density is then 6.984×10^{17} ^{209}Bi atoms/cm^3.

From the neutronics work , the ^{6}Li and ^{10}B activities are 1.111 and 0.294 reactions per second per atom per cm^3, respectively. For ^{10}B modeling the reaction rate is

$$0.294 \frac{\text{reactions}}{\text{sec}} \cdot \frac{cm^3}{\text{atom}} \times 6.984 \times 10^{17} \frac{^{209}Bi \text{ atoms}}{cm^3} \times \frac{0.019 \text{ b}}{940 \text{ b}} = 4.15 \times 10^{12} \frac{\text{react}}{\text{sec}}$$

and for ^{6}Li modeling it is

$$1.111 \frac{\text{react}}{\text{sec}} \cdot \frac{cm^3}{\text{atom}} \times 6.984 \times 10^{17} \frac{^{209}Bi \text{ atom}}{cm^3} \times \frac{0.019 \text{ b}}{3838 \text{ b}} = 3.825 \times 10^{12} \frac{\text{react}}{\text{sec}}$$

At steady state the activity of ^{210}Po equals the reaction rate of the $^{209}Bi(n,\gamma)$ reaction, thus

$$\lambda N(^{210}Po)_B = 4.15 \times 10^{12} \text{ dps or } 112.0 \text{ Ci}$$

and

$$\lambda N(^{210}Po)_{Li} = 3.82 \times 10^{12} \text{ dps or } 103.4 \text{ Ci.}$$

However, since these calculations were done for only half of the blanket, the total NUWMAK breeding blanket ^{210}Po activity would be

$$\lambda N(^{210}Po)_B^{total} = 224.0 \text{ Ci}$$

$$\lambda N(^{210}Po)_{Li}^{total} = 206.8 \text{ Ci.}$$

The actual activity would be expected to fall somewhere between these two values probably closer to the calculation based on the ^{10}B cross section. Even 224 Ci of ^{210}Po radioactivity is dwarfed by the magnitude of the activity from the rest of the nuclides in the blanket. Therefore,

from a radioactivity viewpoint, ^{210}Po seems to be negligible. Also, since the half life γ is short (138.4 days), ^{210}Po poses no long term storage problem.

The gamma dose rate following shutdown has been calculated at two positions, the center of the plasma region and the outside of the shield at the mid-plane of the outer blanket. The calculation of the latter presented more difficulty since neutronics calculations were made only out to a major radius of 7.25 m and thus it was not possible to determine decay gamma sources beyond this point. In an attempt to obtain an estimate of the dose outside the shield it was assumed the shield would be extended to a thickness of 85 cm thus ending the shield at a major radius of 7.95 m. In this extended region of the shield the decay gamma source was taken to be a constant with the same strength as in the outermost region of the neutronics calculation, i.e., at 7.25 m. As the decay gamma source is expected to drop off between 7.25 and 7.95 m, this calculation should overestimate the dose outside the shield. The results of the calculations are shown in Table VIII-F-1. As anticipated, the radiation levels inside the torus are quite high being about 7.5×10^5 rem/hr at shutdown. The reduction in level with time is quite slow requiring about one month to be reduced by a factor of ten and about one year for a factor of 100. Even after ten years the predicted dose level is still about 3 rem/hr.

It is interesting to note the effect the selection of materials has on the contribution to the dose rate. For example, the activity levels of the inner and outer blankets are about the same. However, the inner blanket contributes much less to the dose rate inside the torus. This is because of the presence of tungsten in the inner region which provides a substantial amount of self shielding. Consequently, the contribution of the inner blanket to the dose rate is about two orders of magnitude less than that of the outer blanket.

The situation outside the shield appears to be rather favorable. The predicted dose rates are low even at shutdown being $\sim$ 60 mrem/hr and dropping in one hour to 6.1 mrem/hr, and to 2.6 mrem/hr after one

Table VIII-F-1

Calculated Dose Rates in NUWMAK for Times After Shutdown

Position: Inside Torus

Time After Shutdown	From Inner Blanket (mRem/hr)	From Outer Blanket (mRem/hr)	Total (mRem/hr)
0	3.37 + 06	7.46 + 08	7.49 + 08
1 Min	3.28 + 06	6.16 + 08	6.19 + 08
1 Hr	2.92 + 06	5.66 + 08	5.69 + 08
1 Da	1.79 + 06	3.85 + 08	3.87 + 08
1 Mo	2.90 + 05	7.56 + 07	7.59 + 07
1 Yr	1.93 + 04	5.43 + 06	5.45 + 06
10 Yr	1.02 + 00	3.31 + 03	3.32 + 03
100 Yr	8.31 - 02	1.35 + 02	1.36 + 02
1000 Yr	7.42 - 02	8.35 + 01	8.36 + 01
10 kYr	6.19 - 02	1.96 + 01	1.97 + 01
100 kYr	5.62 - 02	1.59 + 01	1.60 + 01
1 MYr	2.49 - 02	9.80 + 00	9.82 + 00

Position: Outside Shield

Time After Shutdown	Dose Rate (mRem/hr)
0	6.08 + 01
1 Min	2.51 + 01
1 Hr	6.10 + 00
1 Da	2.62 + 00
1 Mo	2.18 - 01
1 Yr	1.44 - 02
10 Yr	2.91 - 06
100 Yr	2.74 - 07
1000 Yr	2.51 - 07
10 kYr	1.18 - 07
100 kYr	4.70 - 08
1 MYr	2.36 - 08

day. However, this result should be viewed with some caution even though the gamma decay source has been overestimated in the outer shield region. The dose rate outside the shield is determined to a large degree by the activity in the outer region of the shield if the shield is assumed to completely cover the blanket. Variations in structure in this region can alter the predicted dose rate considerably. In addition, streaming problems due to the necessity of penetrations in the blanket and shield less carefully attended to could raise the dose levels significantly. Nevertheless, it appears that with care the post shutdown dose rates can be low enough to consider hands on shift maintenance, if not immediately after shutdown, within a relatively short time.

VIII-G. Conclusions

The nucleonic design of the blanket and shield for a high power density, compact, boiling water cooled tokamak fusion reactor, NUWMAK, has been completed. The calculational analysis results are summarized as follows.

1. A tritium breeding ratio of 1.54 tritons per D-T neutron is obtained. More than 90% of the breeding is contributed from $^{6}Li(n,\alpha)T$ reactions. The outer breeding blanket alone contributes 1.24 tritons per D-T neutron which is more than adequate.
2. There is no incentive to employ enriched lithium in the $Li_{62}\ Pb_{38}$ eutectic.
3. The total recoverable nuclear heat deposited in the blanket and shield is 17.15 MeV per D-T neutron, of which ~ 35% comes from gamma-ray heating. This amount of heat represents more than 99% of the total energy output in the system (exclusive of alpha power).
4. The total thermal power output is 2292 MW. The net electric output is 660 MW if a duty factor of 0.91 and a net efficiency of 31.5% are considered.
5. The atomic displacement in the aluminum stabilizer is ~ 4×10^{-6} dpa after two years of continuous operation. The corresponding resistivity

change is ~ 50%. While the neutron fluence at the superconductor is ~ 1.4×10^{16} n/cm^2, the reduction of its critical current density is no more than 1%.

6. With the dose of ~ 1×10^9 rads after 30 years of operation, the only endurable organic superinsulator is an epoxy-base superinsulator. The mylar-base superinsulator will be excluded in the most severely damaged regions.
7. The radioactivity, afterheat and biological hazard potential after one year of continuous operation are 0.8 curie/W_{th}, 0.5% of operating power and 2×10^2 km^3 air/kW_{th}, respectively. However, they drop by between 4-5 orders of magnitude 10 years after shutdown.
8. The post shutdown dose rates outside the regular outer shield are favorable to hands on shift maintenance. They drop to less than 2.6 mrem/hr one day after shutdown.

References for Chapter VIII

1. R. W. Conn et al., "NUWMAK: An Attractive Medium Field, Medium Size, Conceptual Tokamak Reactor", Proc. of Third Topical Meeting on the Technology of Controlled Thermonuclear Fusion, American Nuclear Society, Santa Fe, New Mexico, 9-11 May 1978.

2. B. Badger et al., "UWMAK-I, A Wisconsin Toroidal Fusion Reactor Design", Fusion Research Program Report UWFDM-68, University of Wisconsin (1973).

3. B. Badger et al., "UWMAK-II, A Conceptual Tokamak Power Reactor Design", Fusion Research Program Report UWFDM-112, University of Wisconsin (1975), See also Nucl Engr. and Design, 39, 5 (1976).

4. B. Badger et al., "UWMAK-III, A High Performance Noncircular Tokamak Power Reactor Design", Electric Power Research Institute Report ER-368, EPRI (1976).

5. I. N. Sviatoslavsky, "Engineering Design Considerations for Facilitating Maintainability of Fusion Reactors", Proc. of Third Topical Meeting on the Technology of Controlled Thermonuclear Fusion, American Nuclear Society, Santa Fe, New Mexico, 9-11 May 1978.

6. D. K. Sze et al., "A BWTR (Boiling Water Tokamak Reactor) Blanket Study", ibid.

7. W. F. Vogelsang, "Breeding Ratio, Inventory, and Doubling Time in a D-T Fusion Reactor", Nuclear Technology 15, 470 (1972).

8. M. A. Abdou and R. W. Conn, "A Comparative Study of Several Fusion Reactor Blanket Studies", Nucl. Sci. Eng. 55, 256 (1974).

9. M. A. Abdou, "Radiation Considerations for Superconducting Fusion Magnets", ANL/FPP/TM-92, Argonne National Laboratory report. (1977)

10. G. M. McCracken and S. Blow, "The Shielding of Superconducting Magnets in a Fusion Reactor", CLM-R120, Culham Laboratory (1972).

11. C. A. M. Van der Klein, "The Organic Insulation in Fusion Reactor Magnet Systems", RCN-240, Reactor Centrum Nederland (1975).

12. R. D. Hay, "Superconducting Magnetic Electrical Insulations", Proc. of the Meeting on CTR Electrical Insulators, May 17-19, 1976, LASL, CONF-760558 (Feb. 1978), p. 65.

13. W. W. Engle, Jr., "A User's Manual for ANISN", K-1693, Oak Ridge Gaseous Diffusion Plant (1967).

14. F. R. Mynatt et al., "The DOT-III Two-Dimensional Discrete Ordinates Transport Code", Oak Ridge National Laboratory, ORNL-TM-4280 (1973).

15. D. M. Plaster et al., "Coupled 100 Group Neutron and 21 Gamma Ray Cross Sections for EPR Calculations", ORNL-TM-4873, Oak Ridge National Laboratory (1975).

16. T. A. Gabriel et al., "Radiation Damage Calculations: Primary Knock-On Atom Spectra, Displacement Rates, and Gas Production Rates", Nucl. Sci. Eng. 61, 21 (1976).

17. M. A. Abdou and C. W. Maynard, "Nuclear Design of the Magnet Shield for Fusion Reactors", Proc. First Topical Meeting Technology of Controlled Nuclear Fusion, CONF-740402-R1, Vol. I, p. 685, U. S. Atomic Energy Commission (1974).

18. M. A. Abdou, "Nuclear Design of Blanket/Shield System for a Tokamak Experimental Power Reactor", Nuclear Technology 29, 7 (1976).

19. The blanket lifetime for NUWMAK is estimated ~10 MW-Yr/m^2, and is ~2 years of continuous operation. Private communications with R. W. Conn and G. L. Kulcinski.

20. T. Y. Sung and W. F. Vogelsang, "DKR: A Radioactivity Calculation Code for Fusion Reactors", UWFDM-170, Nuclear Engineering Department, University of Wisconsin (Sept 1976).

21. T. Y. Sung and W. F. Vogelsang, "Decay Chain Data Library for Radioactivity Calculations", UWFDM-171, Nuclear Engineering Department, University of Wisconsin (Sept 1976).

IX. Materials Analysis

IX-A. Introduction

IX-A-1. Materials Design Philosophy for Advanced Reactors

One of the characteristics of fusion power plants is the wide variety of materials that are required for their safe and efficient operation. In contrast to fission and fossil plants, the fusion facilities require materials that can stand the intense bombardment of both neutron and charged particles and the operating temperatures can range from very high (up to one half of the melting point) to almost absolute zero (i.e., in the magnets). The requirements are for both metallic and insulating materials which can retain their original properties in the face of a rather corrosive and sometimes transient radiation environment. Therefore, it is impossible to speak about the materials problems in a fusion power plant; one must be very specific about which phase of the materials problem he is addressing.

The major emphasis in this chapter will be on the structural materials, and in particular those structural components in the blanket region which must contain the tritium breeding materials and coolants. The choice of these structural materials is very complicated as discussed in previous UWMAK[1-3] and TETR[4] reports. We will only briefly review some of the highlights of those studies here.

If the design engineer was able to designate the ideal materials for the blanket, he would probably chose one which has the following properties:

a. Easily fabricable and weldable in the field.
b. Supported by a well-established mining-processing-manufacturing industrial complex.
c. Supported by a large body of experimental data (both irradiated and unirradiated) which has been critically examined by engineers and incorporated into design codes.
d. Possess a high yield strength at the operating temperatures and sufficient ductility to withstand off-normal operating conditions without fracturing.
e. Resistant to corrosive liquid metals, steam, and environments which could contain high hydrogen isotope concentrations.
f. Have a low solubility for hydrogen isotopes and a low permeability.

g. Be resistant to the damage produced by the fusion neutron spectrum and retain its dimensional and desirable mechanical properties after a lifetime exposure (normally 30 years).
h. Be resistant to the bombardment of plasma particles or be amenable to the application of protective coatings. The material or its coatings should not have any deleterious effects on the plasma.
i. Possess well-defined physical and thermal properties such as high (blankets) or low (magnets) electrical resistivity, low vapor pressure, high thermal conductivity, etc.
j. Be relatively inexpensive in comparison to today's costs for high quality metals and alloys (e.g., fabricated costs of less than 40$/kg).
k. Be relatively abundant and available to all nations, at least up to the level of $\sim 10^6$ metric tonnes.
l. Will not interfere with the neutronics of the system, and if possible, actually provide more neutrons via (n,2n) reactions.
m. Does not produce long-lived radioisotopes or those which have low maximum permissible concentrations with respect to the biosphere.

One would like this "ideal" material to last for the lifetime of the plant and be in a condition such that it could be easily removed and recycled for use in a future facility.

Obviously, no such material now exists nor is there much hope for one in the near future. The best one can do at the present time is to make compromises on the basis of the above properties and the current approach is to insure the near-term viability at the expense of long service lifetime. That is, recent designers have accepted the fact that the structural components will <u>not</u> last the life of the reactor and they base their present efforts on service for a few years.

Early in the fusion reactor design studies (late 1960s and early 1970s) refractory metals (Nb, Mo) were the favorite structural materials for the blanket. This decision seemed to be based on the sole function of producing and containing high temperature ($\sim$1000°C) heat at very high wall loadings (up to 10 MW/m^2). As designers became more realistic about contamination,

fabrication, industrial base, cost and radiation effects there was a swing away from the refractory metals to better understood (especially in an irradiation environment) alloys like stainless steel. This shift required a drop in the coolant temperatures to ~500°C as well as a drop in the wall loadings to ~1 MW/m^2 because of thermal stress problems. At the same time more realistic estimates of wall lifetimes were made and the associated impact on down time and disposal of highly radioactive structures was rather negative in the fusion community. Several attempts to alleviate that problem by using Al and graphite were not successful for a variety of reasons.

In an effort to increase the neutron wall loading above that allowed by steel and minimize the induced radioactivity problems, suggestions to use the Ti alloy system were made.[5] The reasons behind that choice over steel and the refractory metals are documented in reference 5. The major point of the Ti choice is to allow higher wall loadings with fewer maintenance and long term waste storage problems. This is not to say that Ti alloys will be the perfect answer because, as will be seen, they are not. However, that system has some unique properties that we thought could be explored by the fusion community to its advantage.

IX-A-2. General Objectives for Materials in NUWMAK

The main objectives of the structural materials in the NUWMAK design are to reduce the down time due to replacement (i.e., have a long service lifetime), to reduce the post operation impact on the environment (i.e., have no extremely long-lived isotopes), and to allow higher power density operation for better economical performance. The objectives for the other materials in NUWMAK are varied but a common desire is for the materials to provide a full lifetime service (i.e., 30 years at a 70% plant factor). This means that we would like the shield, magnet, and support structures to withstand their particular radiation, chemical, thermal, and mechanical environment without failure. It may not be possible to meet such a requirement but at least that is the goal and the degree to which it is met will be a measure of the viability of the NUWMAK concept. More specific requirements will be given later in this chapter.

IX-A-3. Outline of Chapter

After this introduction to the philosophy of the materials choice for NUWMAK we will discuss the attributes of Ti alloys for fusion reactors. This discussion will include a general description of the Ti alloy system followed by special physical, mechanical, chemical, neutronic, resource, and cost features. Next the operating environment for Ti alloys and other materials in NUWMAK will be discussed and this will be followed by the anticipated performance of the various NUWMAK materials. The performance of the non-Ti alloy structural components will then be considered and this will be followed by a summary of how well we think the goals of the NUWMAK reactor have been met and where future work is necessary.

References for Section IX-A

1. B. Badger et al.,"UWMAK-I - A Wisconsin Toroidal Fusion Reactor Design", University of Wisconsin, UWFDM-68, September 1973.

2. B. Badger et al.,"UWMAK-II, A Conceptual D-T Fueled, Helium-Cooled, Tokamak Fusion Power Reactor Design", University of Wisconsin, UWFDM-112, May 1975.

3. B. Badger et al.,"UWMAK-III, A High Performance, Noncircular Tokamak Power Reactor Design", University of Wisconsin, UWFDM-150, December 1975.

4. B. Badger et al.,"TETR, A Tokamak Engineering Test Reactor to Qualify Materials and Blanket Components for Early DT Fusion Power Reactors", University of Wisconsin, UWFDM-173, September 1976.

5. J. Davis and G. L. Kulcinski,"Assessment of Titanium for Use in the 1st Wall/Blanket Structure of Fusion Power Plants", EPRI-ER386, (1977).

IX-B. General Description of Titanium Alloy Systems

IX-B-1. Introduction

There is a great deal of information on titanium alloys which has been generated in the aircraft industry and it would not be possible, or even prudent, to attempt to summarize it here. Rather, we will cover only those selective aspects of the Ti alloy system which we think have the greatest impact on its potential use in fusion reactors. We will first consider the complex nature of the microstructure of Ti alloys and then this will be related to the mechanical properties of those systems.

Because of the large number of potential Ti alloys that have been investigated, we will concentrate our efforts on only three representative alpha + beta ($\alpha + \beta$) phase alloys: Ti-6Al-4V (Ti-64), Ti-6Al-2Sn-4Zr-6Mo (Ti-6246) and Ti-6Al-2Sn-4Sr-2Mo (Ti-6242). These alloys are representative because they comprise the highest usage medium strength alloy (Ti-64), a high strength alloy (Ti-6246) and a high temperature creep resistant alloy (Ti-6242). Reference will be made to other alloy systems as the need arises, but the reader should recognize that there are literally hundreds of possible alloys that could be considered for fusion application. The process of selecting the most promising Ti alloy has only just begun.

Comparison between one Ti alloy (Ti-64) and other potential fusion reactor materials has already been made in a document entitled, "Assessment of Titanium for Use in the 1st Wall/Blanket Structure of Fusion Power Reactors," EPRI-ER-386, April 1977. The reader is urged to include that document along with the additional information in this chapter.

IX-B-2. Microstructure Development in $\alpha+\beta$ Ti Alloys

Pure Ti has two allotropic forms, a low temperature hexagonal close packed form (the α-phase) and an elevated temperature body centered cubic form (the β-phase). In pure Ti the allotropic transformation temperature is $\sim$882°C. The transformation from $\beta \rightarrow \alpha$ on cooling occurs by nucleation and growth during slow cooling or by nucleation and shear (martensitically) during rapid cooling. Additions of alloying elements such as Al, V, Mo, Zr and Sn can raise, lower or leave unaltered, the allotropic transformation temperature (also called the β-transus). Accordingly, alloying elements are categorized as α stabilizers if they raise the β-transus, as β-stabilizers

if they lower the transus or as neutral elements if they leave it unaltered. Among the alloying elements of interest in commercial α+β alloys are Al and oxygen, the latter of which is present as a controlled impurity. The Al and oxygen are α-stabilizers, while Mo, V and Cr are β-stabilizers and Sn and Zr are neutral elements. Some typical binary Ti phase diagrams are shown in Figure IX-B-1.

In addition to categorizing alloying elements according to their effect on the β-transus, it also is common to categorize alloys according to their equilibrium constitution. That is, alloys with sufficient concentration of β-stabilizing elements such as Mo or V lie in the two phase α+β region of phase diagrams such as the Ti-V or Ti-Mo diagrams shown in Figures IX-B-1(a) and IX-B-1(b). Thus at equilibrium, these alloys contain both the α and β phases and are described as α+β alloys. Other lower strength alloys are categorized as α-phase alloys whereas there also is a third class of alloys known as β alloys. Representative compositions of these alloys are shown in Table IX-B-1.

In commercial multi-component α+β alloys the quantitative phase relationships are known only empirically. This is because the extent of partitioning of the various components between the α and β phases cannot be readily determined. However, in commonly used alloys such as Ti-6Al-4V detailed microprobe studies have been performed.[2] These studies have shown that Al partitions nearly equally between the α and β phases but does slightly partition to the α phase; in contrast, V partitions heavily to the β-phase. These results permit the constitution of α+β alloys to be represented qualitatively by a constant Al pseudobinary phase diagram such as that shown in Figure IX-B-2(a). This diagram shows the partitioning of V to the β-phase and also shows that increasing V contents lead to lower β-transus temperatures. In addition, the alloy composition affects the temperature at which martensite first forms during quenching. This temperature is called the M_s temperature. The composition dependence of the M_s temperature for the martensitic $\beta \rightarrow \alpha'$ transformation also is shown in Figures IX-B-2(a) and (b). The α' martensite has a hexagonal structure and a composition which is enriched (supersaturated) in β-stabilizing elements. The overall significance of this will be discussed below, but

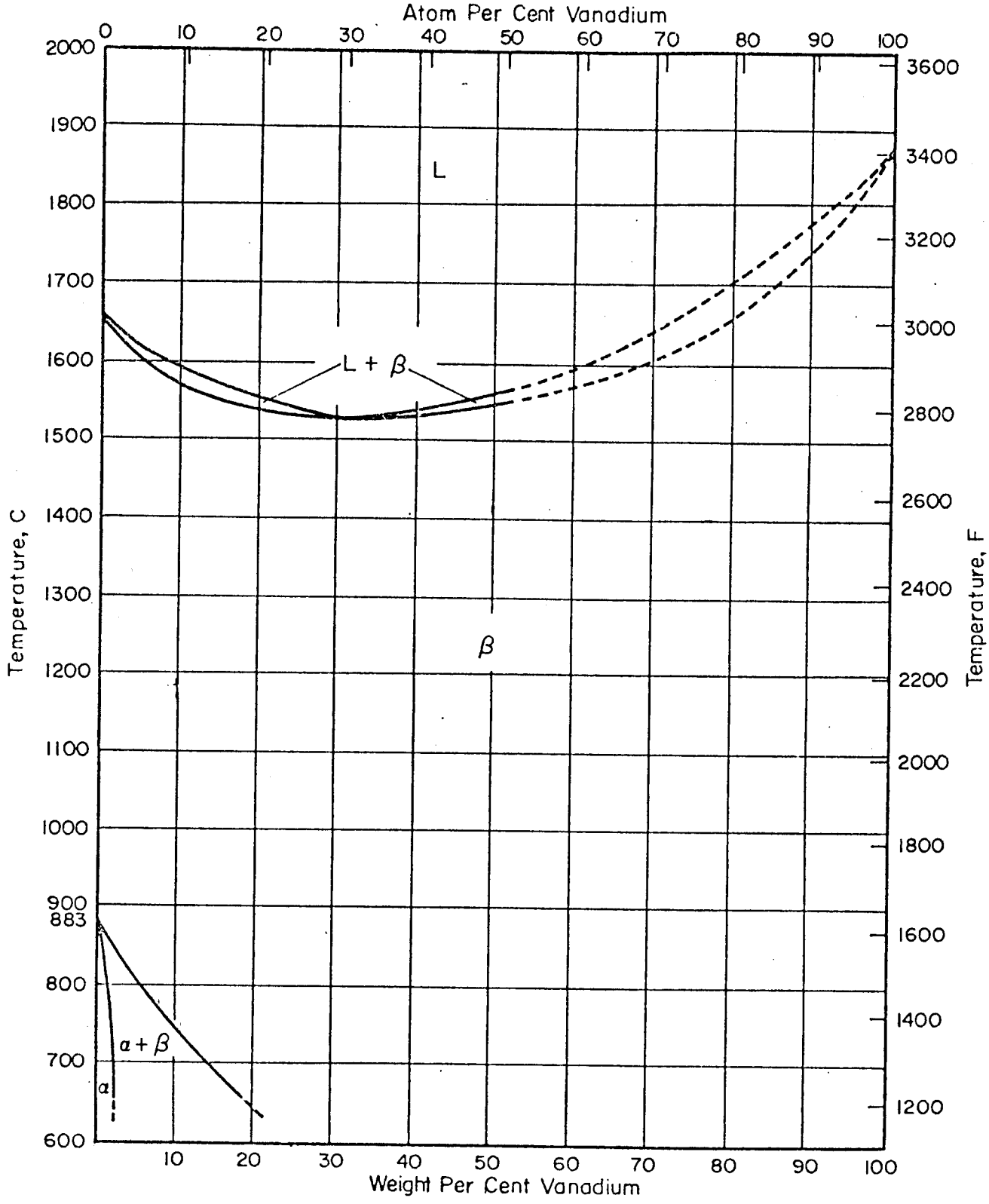

Atom Per Cent Vanadium
0
10
20
30
40
50
60
70
80
90
100
2000
1900
1800
1700
1600
1500
1400
1300
1200
1100
1000
900
883
800
700
600
3600
3400
3200
3000
2800
2600
2400
2200
2000
1800
1600
1400
1200
L
L + β
β
α + β
α
Temperature, C
Temperature, F
Weight Per Cent Vanadium

Fig. IX-B-1(a)

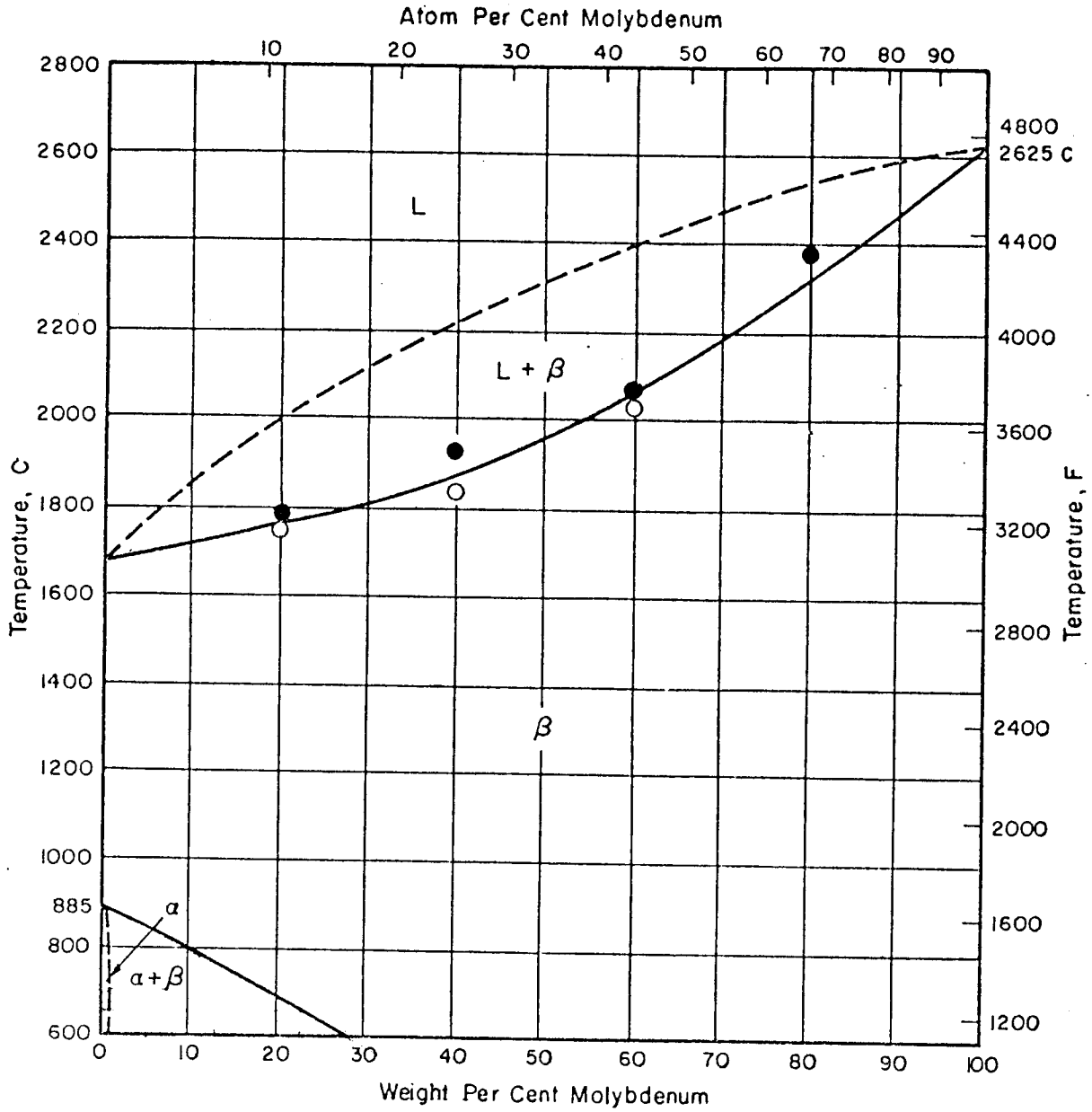

Atom Per Cent Molybdenum
10
20
30
40
50
60
70
80
90
2800
2600
2400
2200
2000
1800
1600
1400
1200
1000
885
800
600
4800
2625 C
4400
4000
3600
3200
2800
2400
2000
1600
1200
L
L + β
β
α
α+β
Temperature, C
Temperature, F
0
10
20
30
40
50
60
70
80
90
100
Weight Per Cent Molybdenum

Fig. IX-B-1(b)

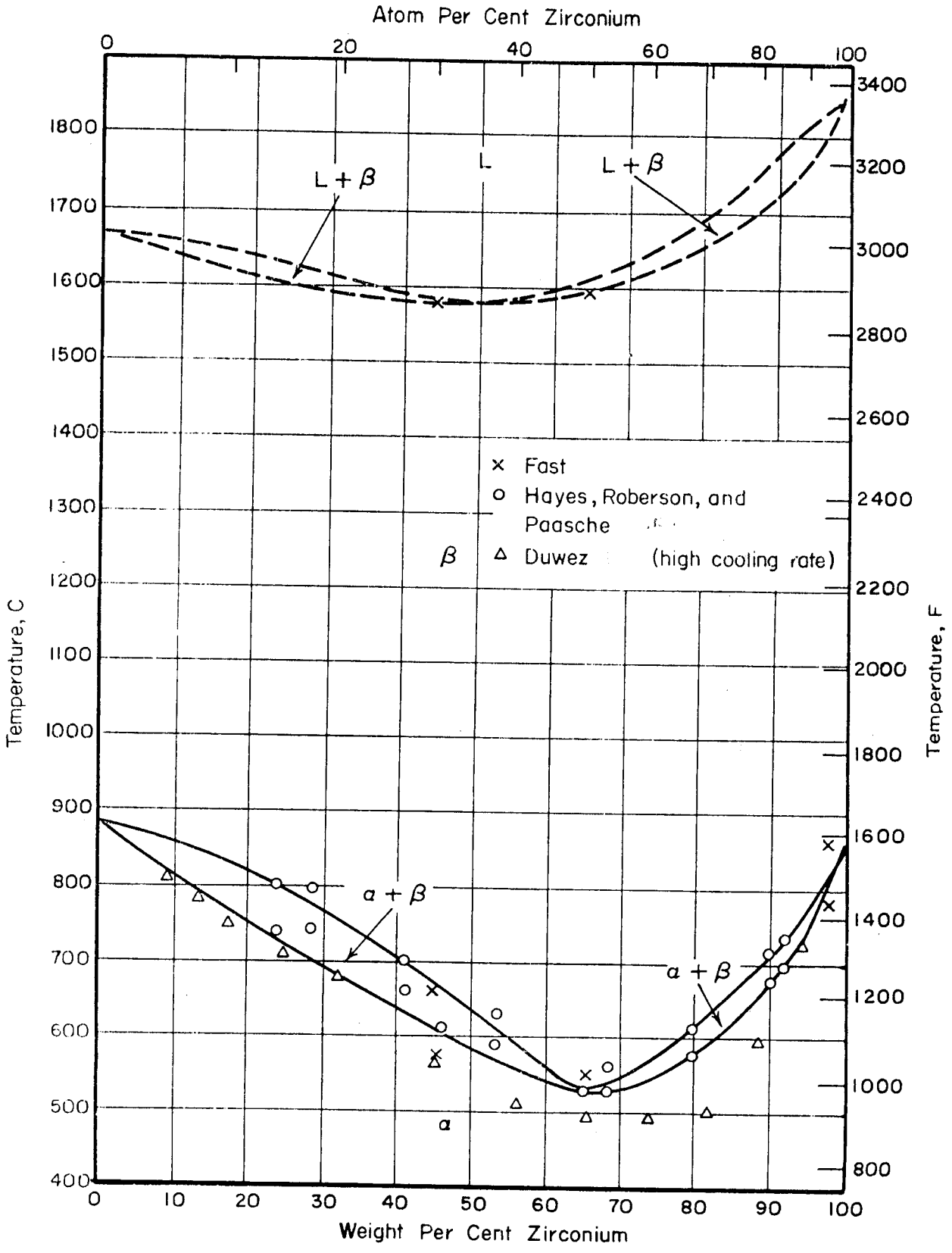

Atom Per Cent Zirconium
0
20
40
60
80
100
1800
1700
1600
1500
1400
1300
1200
1100
1000
900
800
700
600
500
400
3400
3200
3000
2800
2600
2400
2200
2000
1800
1600
1400
1200
1000
800
L + β
L
L + β
× Fast
○ Hayes, Roberson, and Paasche
β
△ Duwez (high cooling rate)
α + β
α + β
α
Temperature, C
Temperature, F
0
10
20
30
40
50
60
70
80
90
100
Weight Per Cent Zirconium

Fig. IX-B-1(c)

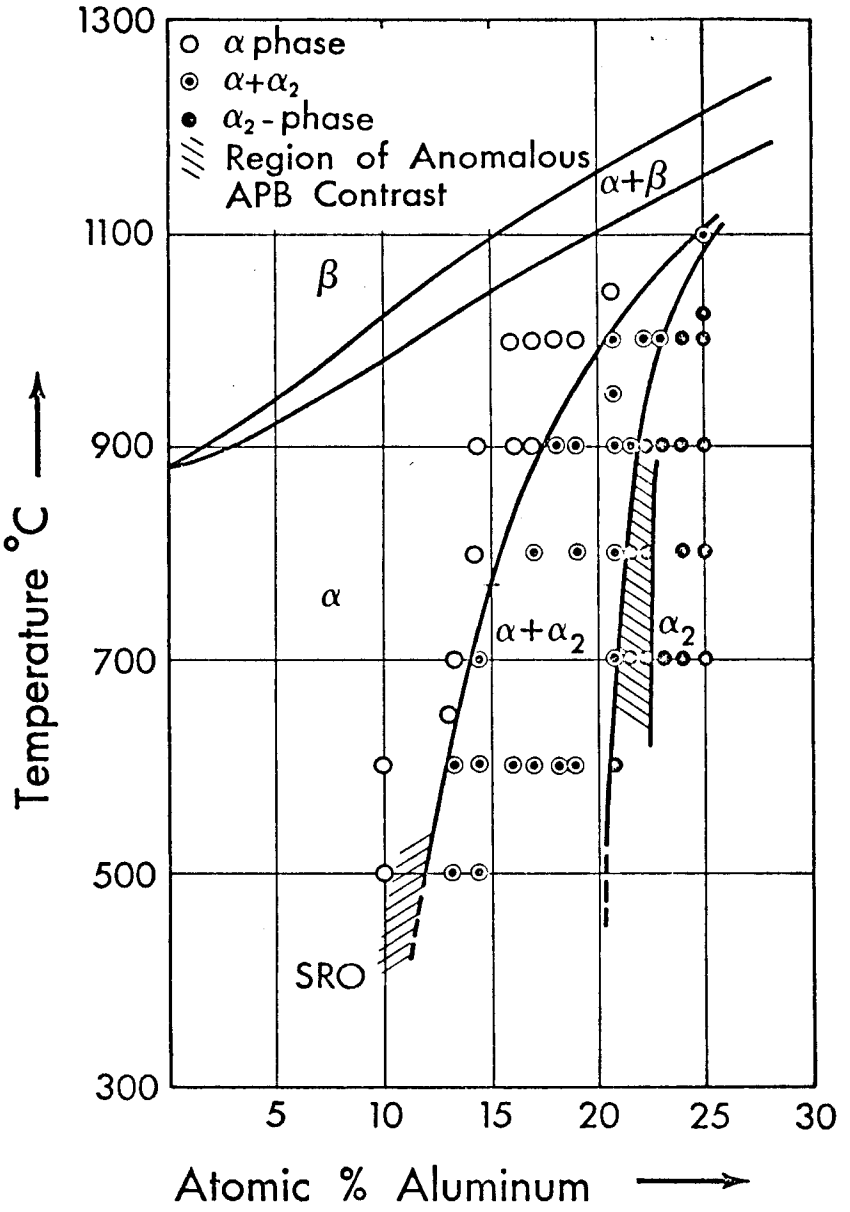

1300
1100
900
700
500
300
5
10
15
20
25
30
α phase
α+α2
α2 - phase
Region of Anomalous APB Contrast
α+β
β
α
α+α2
α2
SRO
Temperature °C
Atomic % Aluminum

Fig. IX-B-1(d)

Table IX-B-1

Compositions and Alloy Designations of Selected Ti Alloys

Designation	Composition (in wt%)
α-Phase Alloys	
Ti-35A	Ti-.18 O*-.12 Fe*
Ti-50A	Ti-.25 O*-.20 Fe*
Ti-75A	Ti-.40 O*-.30 Fe*
Ti-5-2.5	Ti-5Al - 2.5Sn
α+β Phase Alloys	
Ti-64	Ti-6Al-4V
Ti-6242	Ti-6Al-2Sn-4Zr-2Mo-.1Si
Ti-6246	Ti-6Al-2Sn-4Z-6Mo
Ti-5621-S	Ti-5Al-6Sn-2Zr-1Mo-.25Si
Ti-811	Ti-8Al-1Mo-1V
β Alloys	
Beta-III	Ti-11.5Mo-6Zr-4.5Sn
Beta C	Ti-3Al-8V-6Cr-4Zr-4Mo
Ti-8823	Ti-8Mo-8V-2Fe-4Al
Ti-15-333	Ti-15V-3Cr-3Al-3Sn
Ti10-23	Ti-10V-2Fe-3Al
VCA120	Ti-13V-11Cr-3Al

*Maximum Value

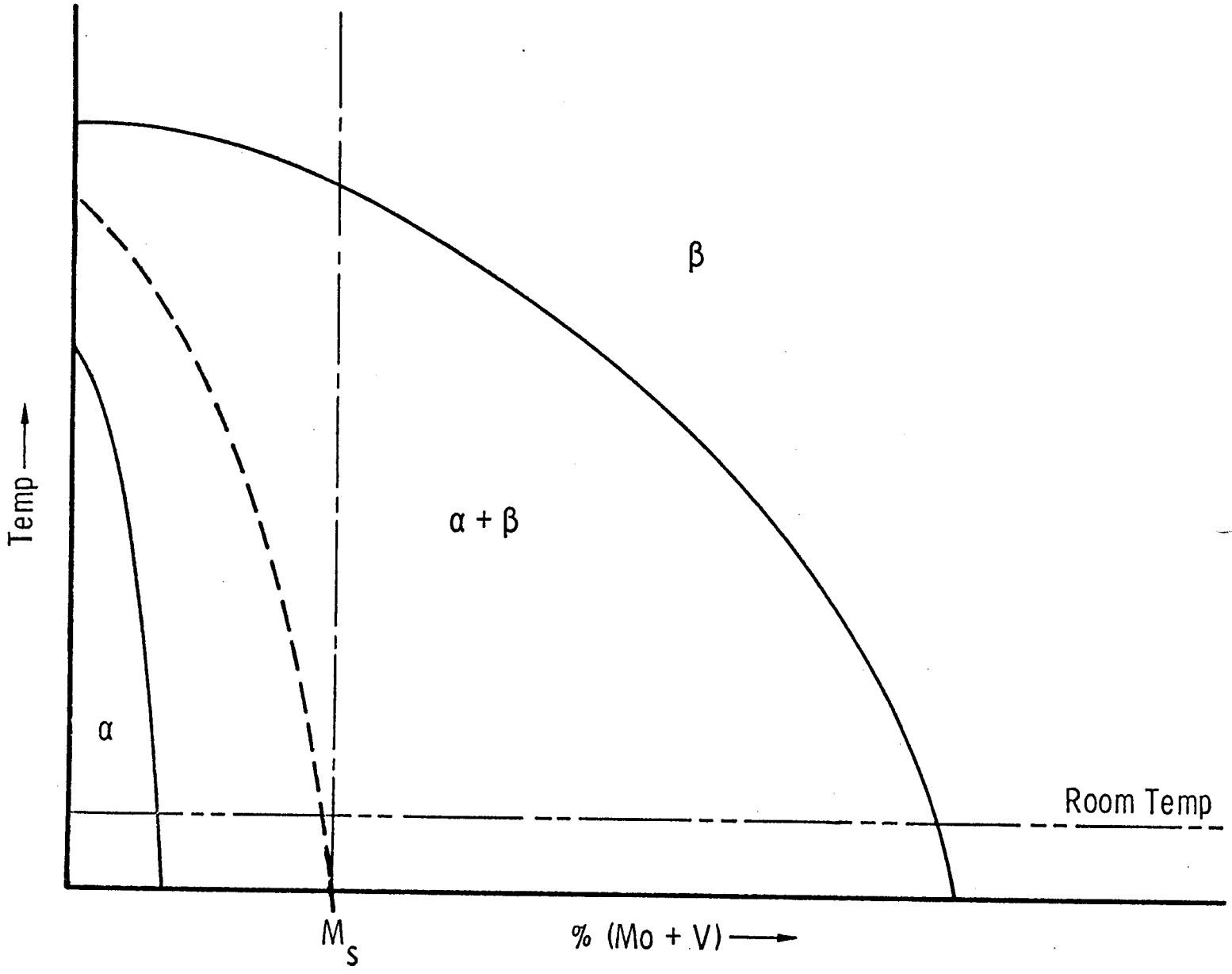


Fig. IX-B-2(a)

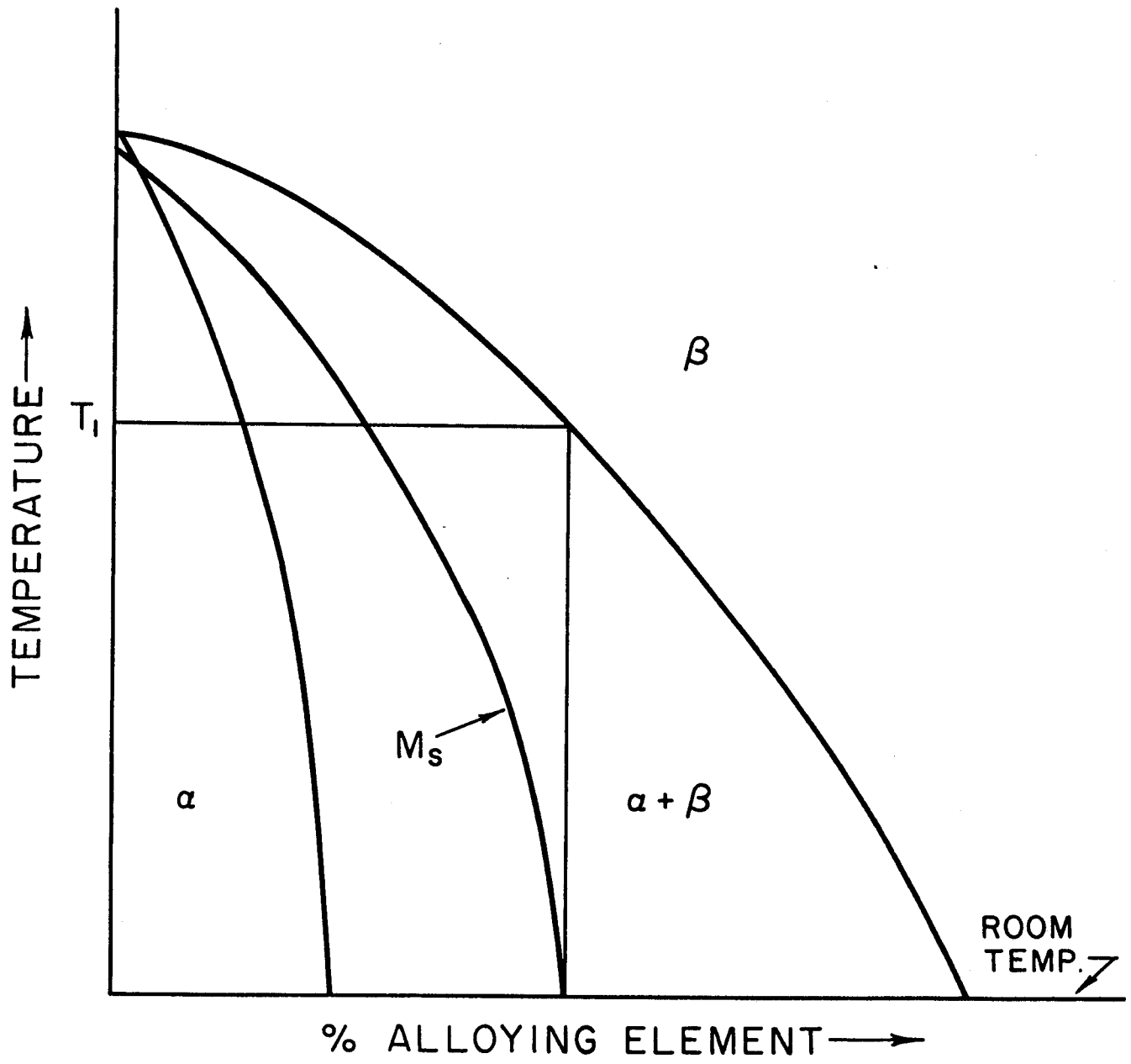

TEMPERATURE
T_1
β
M_s
α
$\alpha + \beta$
ROOM TEMP.
% ALLOYING ELEMENT

Fig. IX-B-2(b)

it is important to mention here that β-phase is retained in a metastable state during quenching if the composition of the β-phase leads to a M_s temperature which is below room temperature. This point is more readily illustrated in a binary phase diagram such as Figure IX-B-2(b). The maximum temperature for β retention during quenching is shown as T_1 in the schematic diagram, Figure IX-B-2(b). Adjustment of the β-phase composition can be achieved by solution treating at different temperatures in the two phase α+β region as predicted by phase equilibrium considerations. This can be seen by examining the schematic phase diagram in Figure IX-B-2(b). The volume fraction of β-phase can be adjusted by changing the alloy composition to increase the β-stabilizer content. The leanest alloy composition corresponds to the minimum alloy content for complete retention of the β-phase during quenching. In a fixed alloy composition, the β-phase composition can be adjusted by solution treating in the α+β phase field. From this it follows that there is a solution treatment temperature which has a corresponding β-phase composition whose M_s temperature is room temperature. Solution treating above this critical temperature and quenching leads to the formation of martensitic α'. Solution treating and quenching from below this temperature results in retention of metastable β-phase.

In addition to the α' martensite which is commonly observed in Ti-64, Ti-6242 and other α+β alloys, a second type of martensite can be formed under certain circumstances. This second martensite has an orthorhombic structure and is designated α". It forms on quenching in alloys or β-phase compositions with Mo, Nb or V* contents which are greater than that for α' formation and less than that for retention of the metastable β-phase. The α" can be formed athermally or can be strain-induced. It is especially prevalent in alloys which contain Mo as a β-stabilizing addition. For example, it forms in Ti-6246 on quenching from above the β-transus. The details of α" formation have been discussed elsewhere[2a,2b] and thus will not be reiterated here. However, it is important to be aware of the existence of α" since its tempering behavior is quite different as will be discussed later.

---

*α" forms in Ti-V-Al alloys but not in Ti-V alloys. The minimum Al content appears to be ~6wt%.

The phase diagram discussed above provides the basis for understanding the microstructure and property alterations achievable by heat treatment. The microstructures which are commonly encountered in $\alpha+\beta$ alloys are non-equilibrium in nature and result from the ability to control the kinetics of two competing β decomposition reactions: the nucleation and growth of α and the martensitic transformation. The kinetics of these two reactions are best represented on a time-temperature-transformation (T-T-T) diagram and a schematic of such a diagram is shown in Figure IX-B-3.

The T-T-T diagram shows the C-shaped curve which defines the locus of the minimum time required to initiate the $\beta \rightarrow \alpha+\beta$ nucleation and growth reaction during isothermal reaction. In addition, it shows as a horizontal line the M_s temperature for the β-phase composition pertinent to the diagram. The characteristics both of nucleation and growth and of martensitic reactions are illustrated by this diagram. That is, nucleation and growth reactions typically proceed at a maximum rate at an intermediate reaction temperature but have a finite incubation time, whereas the onset of martensitic reactions depends only on reaction temperature. Because the volume fraction of martensite develops instantaneously at any reaction temperature below M_s and increases with decreasing reaction temperature, martensitic reactions are often called athermal reactions. From Figure IX-B-3 it can be seen that nucleation and growth of α is the slower of these two decomposition reactions but this reaction also leads to the more stable decomposition product, the α-phase. Nucleation and growth (N&G) of α is slower than formation of martensite, and growth C-curve must be achieved in a matter of seconds, rather than minutes if the N&G reaction is to be suppressed. Thus water quenching to a temperature below M_s is required to obtain the martensitic phase which is designated α'. The α' is hexagonal close packed and is supersaturated in β-stabilizing elements such as V or Mo. Subsequent aging causes decomposition of the α' martensite to form precipitates of β-phase in a matrix of equilibrium α which was formerly supersaturated martensite. This aging reaction and the decomposition of α'' will be discussed further below.

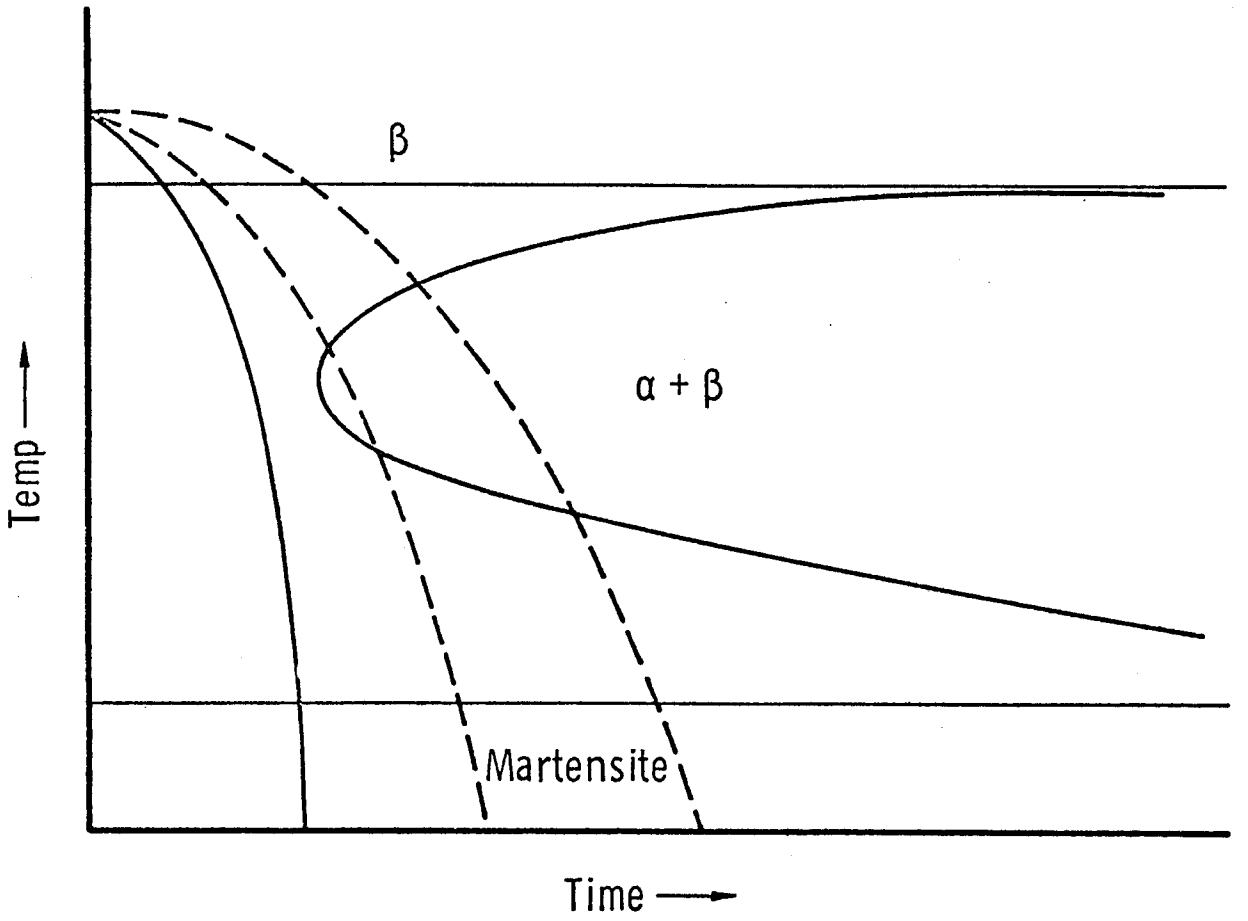


Fig. IX-B-3

The nucleation and growth α forms as plates which are immersed in the β-phase. This β-phase has a higher concentration of β-stabilizing elements than the elevated temperature β-phase due to the rejection of β-stabilizing elements from the β-phase which is growing by a diffusion controlled process. In an alloy such as Ti-64, which has a relatively high β-transus, the N&G α forms as colonies of plates, each separated by a thin region of β-phase. In more heavily β-stabilized alloys such as Ti-6246, which have lower β-transus temperatures, the plates form individually in a more random arrangement.

The N&G plates of α-phase grow along specific crystallographic directions in the parent β-phase and have the broad, flat interfaces parallel to specific crystallographic plates. The selection of these planes and directions are determined by numerous factors but probably the most important are the direction of easy, and therefore rapid, growth and the planes of good matching and, therefore, low energy. These plates, therefore, form characteristic patterns when viewed under the light microscope and are called Widmanstatten plates or Widmanstatten α.

There also is a third constituent present in the Widmanstatten α+β mixtures. This constituent occurs at the α/β interfaces and has been named interface phase.[3] There is some disagreement regarding the details of the origin of this constituent but it is agreed that it consists of a layer of finely divided α-phase.[3,4] The layer is sufficiently thin that it is not resolvable by light metallography; thus its presence was not discovered until the microstructure of α+β Ti alloys was investigated by thin foil electron microscopy techniques. As will be discussed later, a prevalent secondary crack path in Widmanstatten α+β microstructures is along α/β interfaces. This cracking mode has been suggested to be related to the presence of the interface phase and thus an awareness of the presence of this constituent is important.

The commonly used commercial heat treatments which make use of the β decomposition reactions are designated duplex anneal (DA), solution treat and age (STA), β-anneal (BA) and β-quench (BQ) or β solution treat and age (BSTA). Since BQ and BSTA are synonomous, BQ will be used in

this article. The microstructures which result from these heat treatments are illustrated in Figure IX-B-4 and summarized in Table IX-B-2. From this table it can be seen that significant flexibility is present in the exact heat treatment temperatures, especially those used for aging. The exact temperatures chosen depend on the strength level and detailed microstructure desired for a particular application. The relation between heat treatment and strength will be discussed in a subsequent section.

In addition to the effect of heat treatment of microstructure, elevated temperature mechanical working (thermomechanical processing or TMP) also can be utilized to manipulate the microstructure of $\alpha+\beta$ Ti alloys. The principal microstructural variable affected by TMP is the α-phase morphology. Working in the $\alpha+\beta$ phase region plastically deforms the acicular or Widmanstatten α plates. Depending on the extent of working and the working temperature, these α plates undergo dynamic recrystallization or store significant amounts of work which can lead to recrystallization during subsequent annealing. The resulting α-phase morphologies change with increasing amounts of work from round-ended, highly elongated plates to globular, equiaxed particles. The controlling factor is the working temperature and the extent of working in the $\alpha+\beta$ field. Excellent examples of the effect of $\alpha+\beta$ working on α-phase morphology can be found elsewhere.[5,6] The $\alpha+\beta$ worked materials have more equiaxed microstructures. As a result, the microstructures of $\alpha+\beta$ alloys are often described according to working history as well as heat treatment. For example, a microstructure described as equiaxed primary α implies that the material has been $\alpha+\beta$ worked and has recrystallized. On the other hand, a microstructure described as β-processed or β-annealed implies a Widmanstatten $\alpha+\beta$ microstructure.

Quite apart from the effect of working history on primary α morphology, is the relation between primary α grain size and working history. Recent work[7] has shown that the recrystallized primary α grain size becomes smaller as the amount of working increases, as the working temperature decreases and as the initial size of the α-phase regions decreases. For example, subsequent $\alpha+\beta$ working of BQ Ti-64,

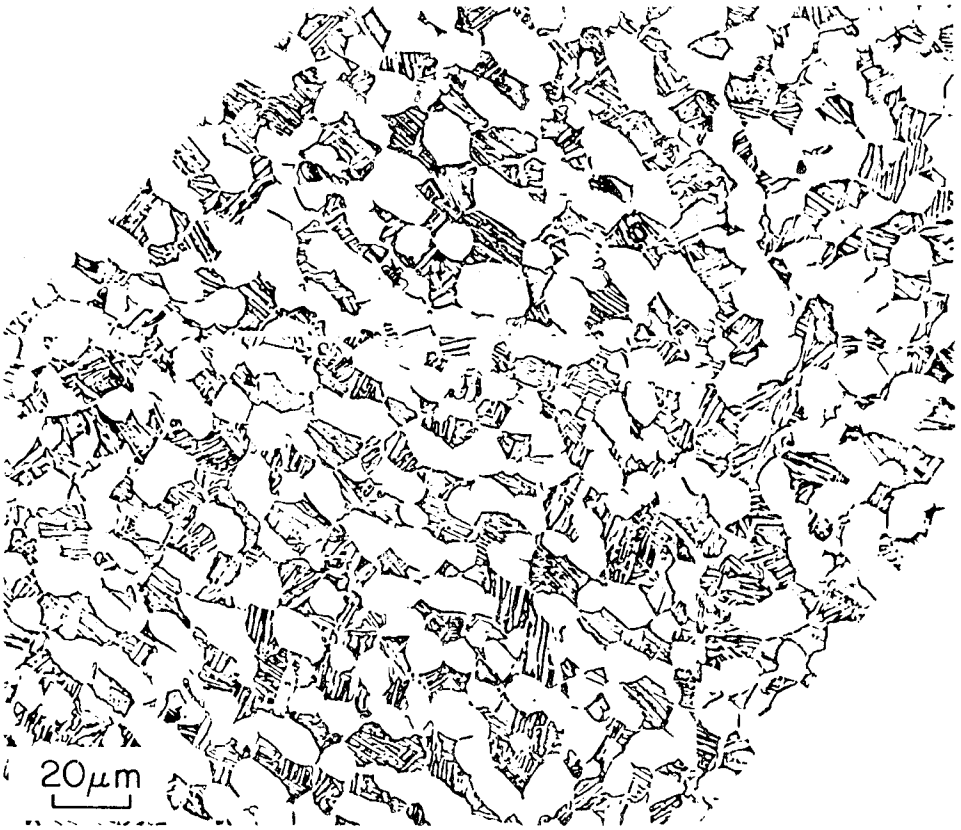


Fig. IX-B-4(a) Ti-6Al-4V, Condition DA

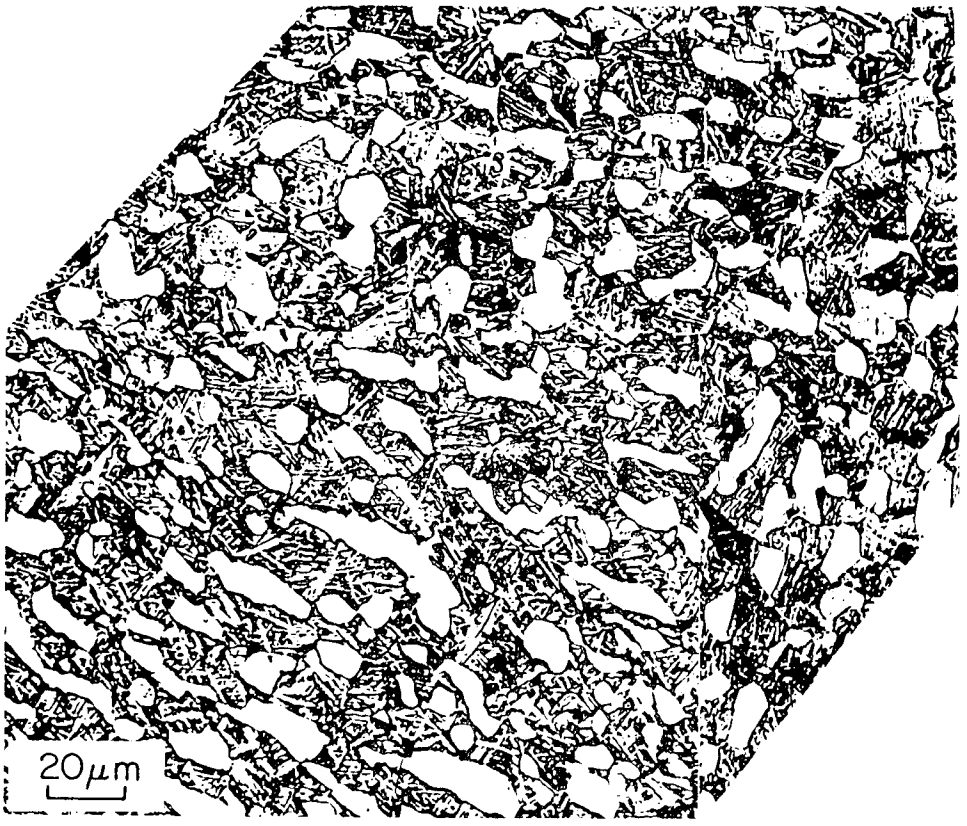


Fig. IX-B-4(b) Ti-6Al-4V. Condition STA

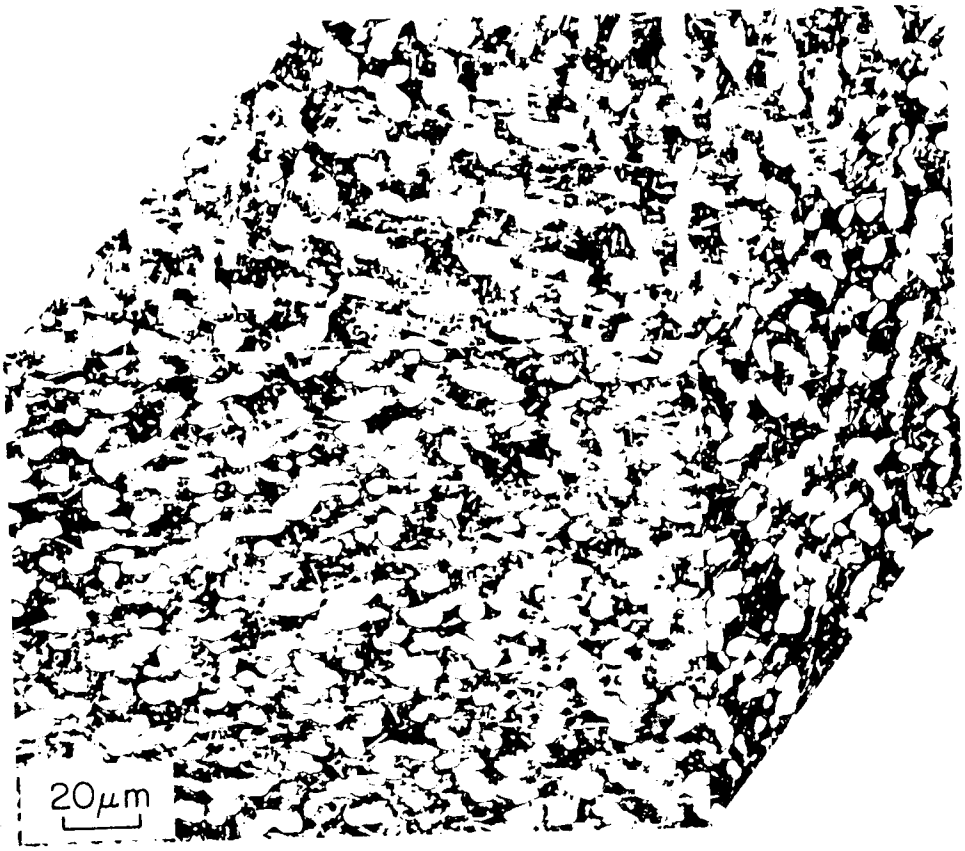


Fig. IX-B-4(c) Ti-6Al-2Sn-4Zr-6Mo, α+β Forge + STA

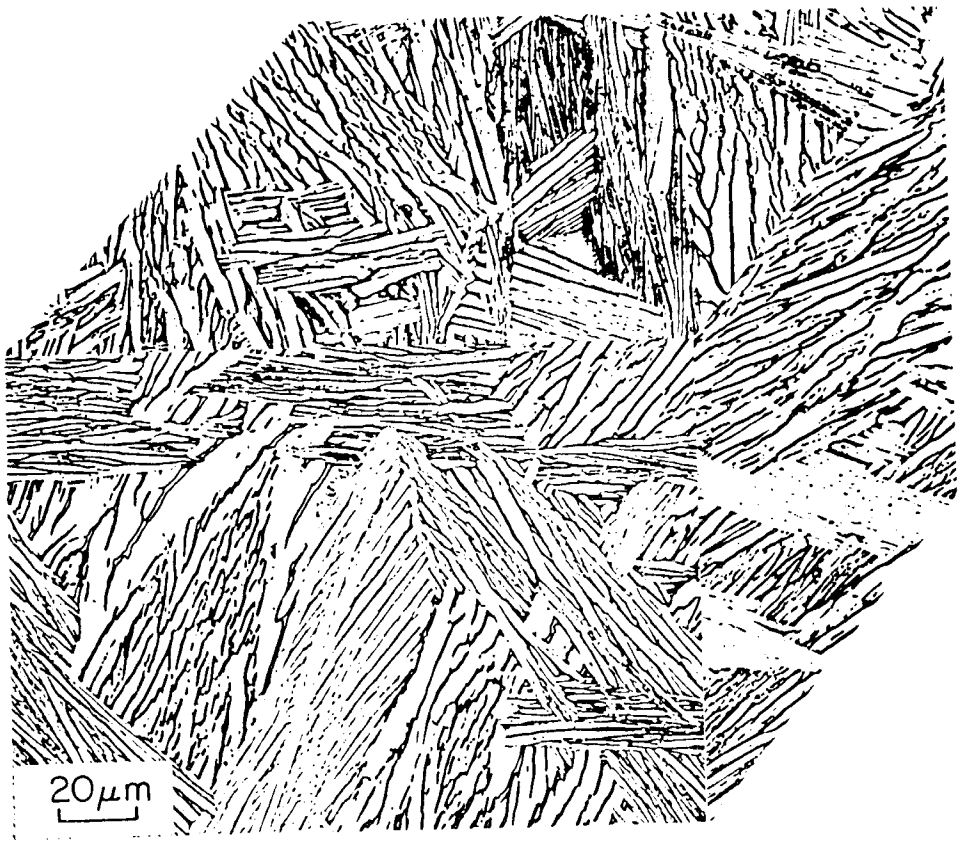


Fig. IX-B-4(d) Ti-6Al-4V, Condition BA

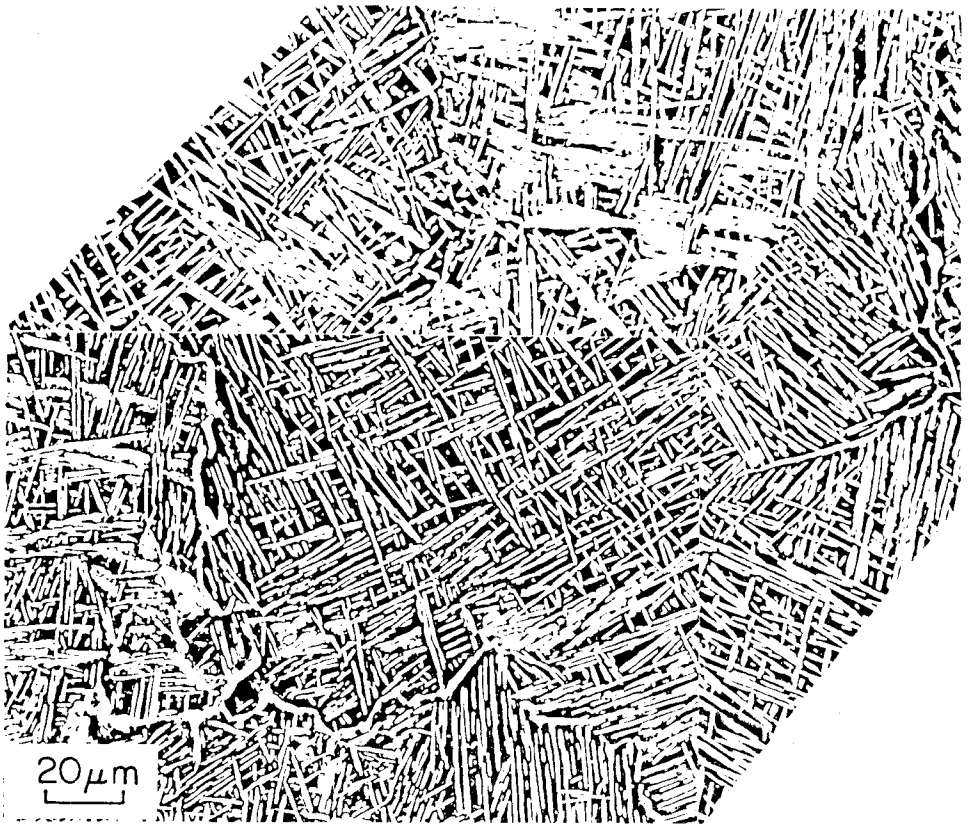


Fig. IX-B-4(e) Ti-6Al-2Sn-4Zr-6Mo, β Forge + STA

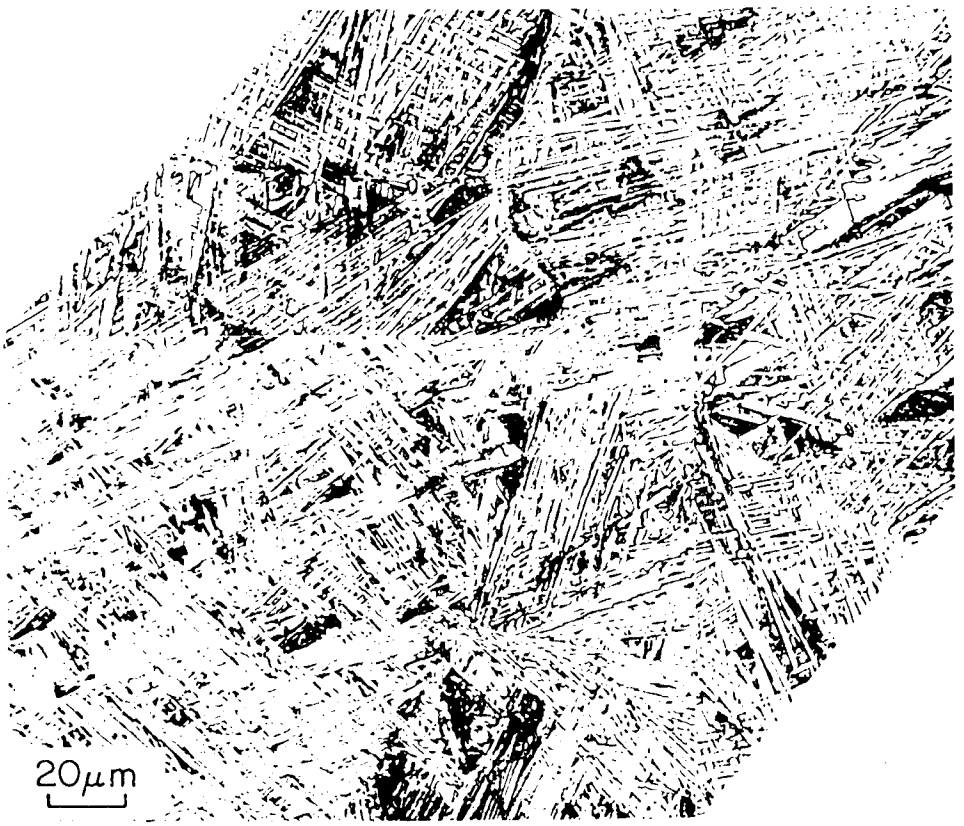


Fig. IX-B-4(f) Ti-6Al-4V, Condition BQ

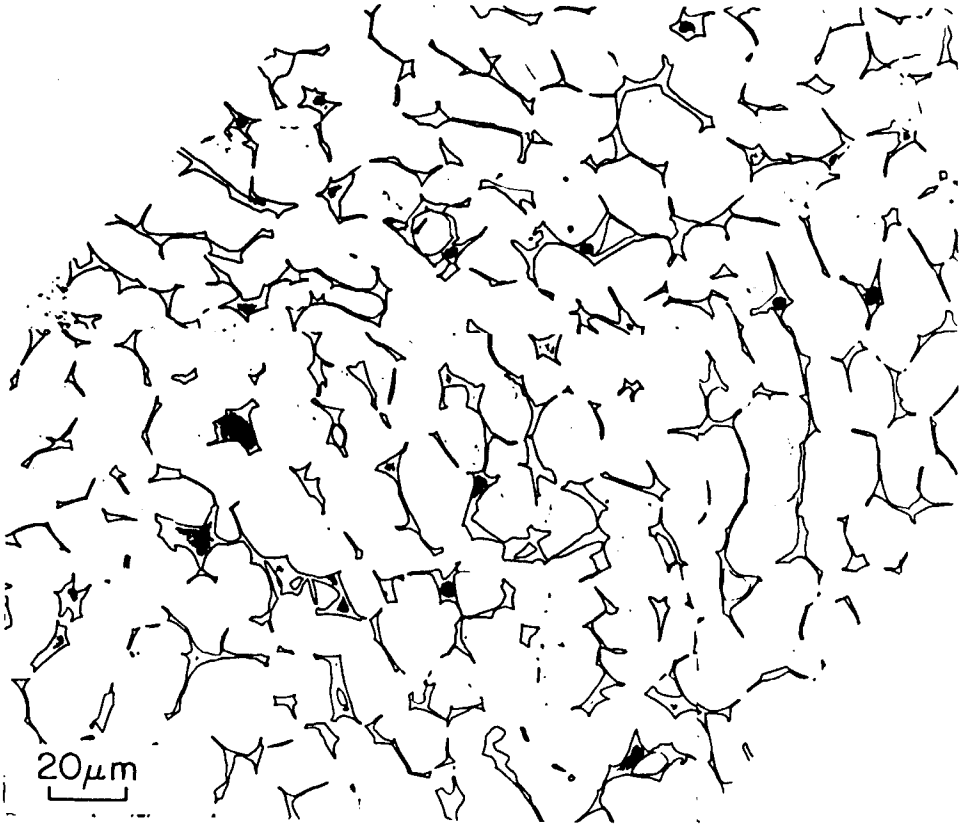


Fig. IX-B-4(g) Ti-6Al-4V Condition RA

Table IX-B-2

Summary of Heat Treatments in $\alpha+\beta$ Ti Alloys

Heat Treatment Designation	Heat Treatment Cycle	Microstructure
Duplex Anneal (DA)	Solution Treat at 55-85°C below T_β^*, air cool and age for 2-8h at 540-680°C	Primary α, plus Widmanstatten $\alpha+\beta$ regions
Solution Treat and Age (STA)	Solution Treat at 40°C below T_β, water quench and age for 2-8h at 540-680°C	Primary α, plus tempered α' or a $\beta+\alpha$ mixture
Beta Anneal (BA)	Solution Treat at ~15°C above T_β, air cool and stabilize at 650-760°C for 2h	Widmanstatten $\alpha+\beta$ colony microstructure
Beta Quench (BQ)	Solution Treat at ~15°C above T_β, water quench and temper at 650-760°C for 2h	Tempered α'
Recrystallization Anneal (RA)	930°C/4h/cool at 50°C/h to 760°C/air cool	Equiaxed α with β at grain boundary triple points

* T_β is the β transus temperature for the particular alloy in question.

** In more heavily β-stabilized alloys such as Ti-6Al-2Sn-4Ar-6Mo or Ti-6Al-6V-2Sn, the solution treatment is followed by air cooling. Subsequent aging causes precipitation of α-phase to form an $\alpha+\beta$ mixture.

which has a very fine α' plate size, equiaxed primary α grains of <5μm diameter have been achieved. This is in contrast to conventional $\alpha+\beta$ working practice which is performed on β-forged Ti-64, which has coarser Widmanstatten α plates and leads to equiaxed primary α grains ~15-20μm in diameter. The strength, ductility and fatigue life of this fine grained material is significantly better[7] than the coarsest grained conventionally processed Ti-64.

The above discussion has outlined the β-phase decomposition modes and the effects of TMP on primary α-phase morphology. In addition to these factors there is an α-phase decomposition reaction which affects the properties of alloys which contain $\geq$ 10at% Al or Al plus Sn. This reaction is the precipitation of the ordered α_2 phase which is based on the composition $Ti_3(Al,Sn)$. The α_2 phase precipitates as a uniform dispersion of coherent precipitates, which form by nucleation and growth. As in other such precipitation reactions, the particle size, spacing and volume fraction depends on alloy content and on aging time and temperature. In dilute alloys such as Ti-64, Ti-6242 or Ti-6246, the kinetics of α_2 formation are quite sluggish and it thus is difficult to precipitate it during aging. However α_2 can form during long term, elevated temperature service. This leads to a reduction in subsequent room temperature ductility. Thus, the potential presence of α_2 must be accounted for when assessing the room temperature ductility requirements of an alloy intended for use at elevated temperatures.

In addition to the factors discussed above which affect the type and morphology of the microstructural features present, there is an additional factor which has a pronouced influence on the properties of $\alpha+\beta$ Ti alloys. This factor is preferred orientation or texture as it is more frequently called. Texture is the alignment of grains in a polycrystalline aggregate in a manner such that many grains have particular crystallographic planes and directions aligned in a specific orientation relative to the principal axes of the sample. In wrought products texture is most frequently developed as the result of grain rotation during working or drawing operations. The type and severity of texture present in a material is expressed as a pole figure. The pole figure expresses on a stereographic projection the spatial distribution of the density poles of a particular crystallographic plane. The pole figure is indexed relative to the coordinates of the sample. For example, in sheet or plate pole

figures the rolling direction is usually the North Pole. Thus the basal pole figure for plate would depict the spatial distribution of the density of basal poles relative to the rolling direction. Typical textures which are frequently observed in Ti alloys are shown in Fig. IX-B-5.

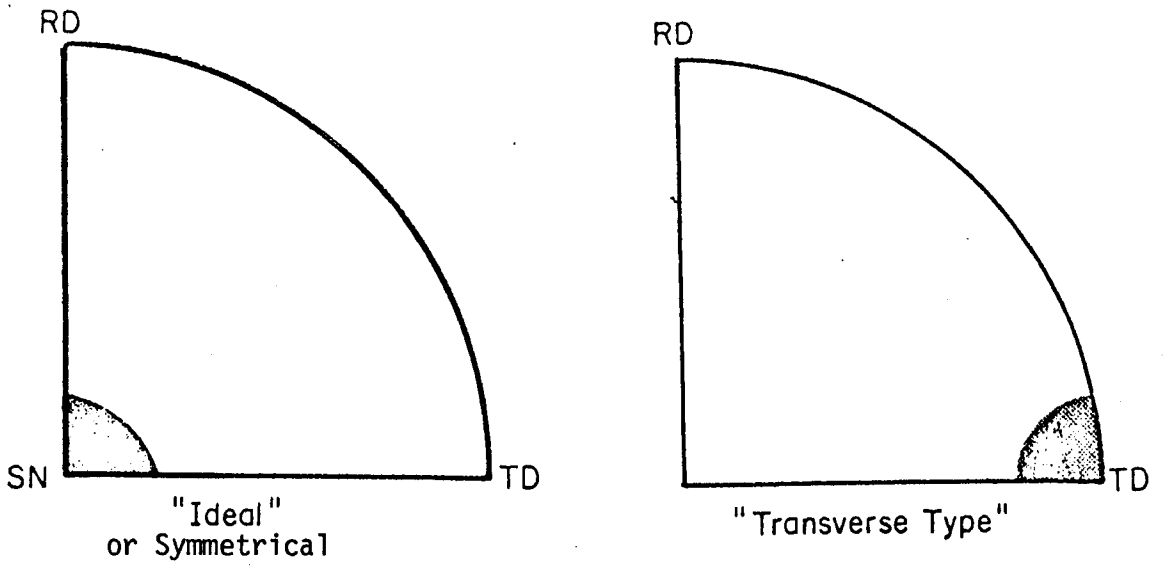
Because the lowest multiplicity plane in the hexagonal α_2 phase is the basal plane, the plastic anisotropy of the α-phase in polycrystalline samples is most readily determined from basal plane pole figures. In $\alpha+\beta$ alloys, the most frequently observed texture is the basal transverse texture. This texture leads to alignment of basal planes perpendicular to the surface of the plate and parallel to the rolling direction. The corresponding basal pole figure thus has a high concentration of basal poles in the transverse direction which would be in the east-west positions on the pole figure. Since texture is developed during working it follows that α-phase,which is present during working,is responsible for texture. Thus texture is most severe in $\alpha+\beta$ worked materials. In β-worked materials the β-phase also can develop texture, but this typically does not lead to significant texture in the α-phase which forms during cooling. This is because there are 12 variants of the α/β orientation relation. Thus even strongly textured α-phase transforms to a much more random distribution of α-phase orientations. As a result the intensity of texture decreases as the primary α volume fraction decreases. This makes comparison of microstructural effects on properties more difficult because of similarities in texture.

IX-B-3. The Relationship Between Microstructure and Tensile Properties of Selected $\alpha+\beta$ Ti Alloys

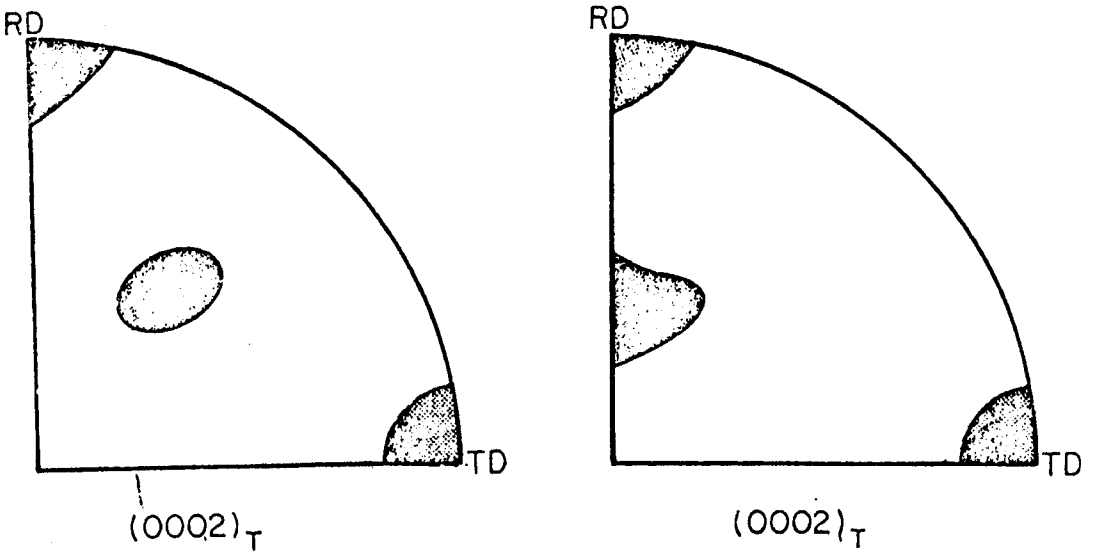
The variations in microstructure discussed above also have a significant effect on strength and ductility. For many applications these properties represent the first and primary consideration in selecting a processing/heat treatment combination. This section contains a brief summary of the relationship between microstructure and tensile properties of three alloys: Ti-6Al-4V, Ti-6Al-2Sn-4Zr-2Mo, and Ti-6Al-2Sn-4Zr-6Mo.

IX-B-3-a. General Trends

All $\alpha+\beta$ Ti alloys show reductions in ductility with increasing strength in much the same way that is well-known for other Fe, Ni and Al based



α+β worked textures



β Transformation Textures

Fig. IX-B-5

structural alloys. However, unlike these alloys, the primary α morphology also is a controllable variable which has a significant effect on ductility. As a general rule, the tensile ductility of α+β processed-material is from 1.5 to 2 times that of β processed-material of comparable or somewhat lower strength level. As will be discussed further in a subsequent section, the fracture toughness K_{IC} exhibits the reverse trend. These unusual trends in properties have led to considerable confusion in material selection criteria, especially during the period when fracture mechanics properties such as K_{IC} were gaining recognition and acceptance. Nevertheless, tensile ductility is still a reasonable indicator of low cycle fatigue behavior via the Coffin-Manson law[8] and thus can be important. It can also be important for material which will be subjected to room temperature deformation such as forming or straightening operations.

In general, the yield strength of α+β Ti alloys is somewhat higher than can be accounted for on theoretical grounds. Consider the example of α+β worked and annealed Ti-6Al-4V. In this condition this alloy consists of ~85 vol% α present as equiaxed grains ~15μ in diameter and small regions of β phase located largely at grain boundary triple points. The strength of a monolithic specimen of α-phase would be ~95 ksi (~655 $\frac{MN}{m^2}$), whereas the strength of the β-phase would be ~100 to 111 ksi (~690 to 760 $\frac{MN}{m^2}$). Nevertheless, the relatively coarse mixture of the two phases described above will invariably exhibit yield strengths in excess of 125 ksi (860 $\frac{MN}{m^2}$). The detailed reasons for the higher than anticipated yield stress are not clear but it has been pointed out elsewhere that this effect is general to dispersions of two deformable phases.[9] In this connection, it has been suggested[9] that the increase in yield stress reflects the difficulty in transferring slip across interphase boundaries; in this case slip transfer across bcc/hcp boundaries between the β and α-phases would be the pertinent consideration.

Another factor which affects both strength and ductility is preferred orientation or texture. Texture was defined earlier as the development of preferentially aligned grains such that particular crystallographic planes

and directions within individual grains lie along specific directions in the sheet, plate, bar or rod. The effect of texture is to give an oriented polycrystalline material rather than a random one. Since the α-phase is hexagonal close packed, it is plastically anistropic. Thus the presence of texture introduces variability and directionality of properties. Because of texture, comparisons of properties of alloys with different microstructures must be approached cautiously to ensure that a part of the observed property variations are not due to the presence of texture of varying type and/or intensity. There are several common α-phase textures observed in α+β Ti alloys.[10] Of these, two of the most common are related to preferred orientation of the basal plane and are called basal transverse and symmetrical basal textures. Schematic pole figures which illustrate these are shown in Fig. IX-B-5.

The effect of texture on the properties of Ti alloys has been reviewed by Larson.[10] This review presents an account of texture development and of the variations in properties in textured Ti alloys. For the purposes of examining the magnitude of texture effects, this article is quite useful. However, for readers interested in mechanisms of texture strengthening or in mechanistic interpretation of the role of texture in fracture or fatigue, the article is frequently misleading or incorrect. For example, it is well established that $\bar{c}+\bar{a}$ slip is an important deformation mode in the α-phase[11,12] yet Larson tends to ignore it and most certainly underestimates the importance of this non-basal slip mode. Other investigators have provided thoughtful interpretations of the effect of texture on certain properties. These will be mentioned later in appropriate sections.

The most readily controlled and thus must extensively studied factor which affects tensile properties is microstructure. As a general rule, the yield stress of α+β Ti alloys is highest in the BQ or STA conditions and lowest in the recrystallization annealed or BA conditions. Further, the strength of the STA condition can be varied by proper selection of aging time and temperature. In alloys such as Ti-6242 or Ti-64 the solution treatment is followed by a water quench which transforms most of the β-phase to α' martensite. In more heavily β-stabilized alloys such as Ti-6246 the

solution treatment is followed by an air cool which retains much of the β-phase in a metastable state. As might be expected, subsequent aging of the as-quenched α' or the metastable β-phase leads to different metallurgical reactions. These reactions have been described in detail elsewhere[6,13-15] but will be summarized here since they have a direct bearing on the strength of STA alloys.

IX-B-3-a-i. Decomposition of α' Martensite

The α' martensite inherits the composition of the parent β-phase and thus is supersaturated in β-stabilizing elements such as Mo and V. The α' also contains a high density of dislocations which result from both the accommodation strains and the lattice invariant deformation which are attendant to the martensitic reaction. This dislocation substructure undergoes extensive recovery during aging, especially at higher temperatures such as 680°C. Concurrent with this recovery process, the nucleation and growth of β-phase occurs. Because of the high density of dislocations and interfaces, this nucleation of β-phase occurs almost entirely heterogeneously at these sites. Since the nucleation is heterogeneous, there is very little effect of aging temperature on the nucleation rate. Thus apart from the recovery effects mentioned above, the most significant effects of aging time and temperature on α' decomposition are related to the time-temperature combinations required to permit growth of the β-phase precipitates to the equilibrium volume fraction. It is a common misconception that aging significantly increases the strength of α'. While a small peak in strength is observed it is not significant. The aging treatment is used to stabilize the martensitic structure against further changes during elevated temperature service and to improve the tensile ductility through recovery of the substructure of the martensitic α'.

IX-B-3-a-ii. Decomposition of Metastable β-phase

The decomposition of metastable β-phase occurs by the precipitation of α-phase at aging temperatures above 510°C. This precipitation reaction occurs by uniform nucleation and growth. Thus the precipitate size and spacing are smaller at lower aging temperatures. As a result, the strength of the resulting α+β alloys such as Ti-6Al-2Sn-4Zr-6Mo are not very high.

Another β-phase decomposition product which is known to adversely affect ductility is the ω-phase. The ω-phase is a solute lean transition phase which forms more rapidly than the equilibrium α-phase. A detailed discussion of factors which effect the formation of ω-phase can be found elsewhere.[2a] However, because the ω-phase is a well-known β-phase decomposition product in Ti alloys, it is important to comment on it with respect to α+β alloys. Alloys which contain $\geq$6wt%Al do not exhibit ω-phase formation. Thus this phase is not a factor in β-phase decomposition in the α+β alloys considered here.

IX-B-3-a-iii. Decomposition of α" Martensite

The tempering behavior of α" martensite is different from that of α'. During tempering of α" a very fine dispersion of α platelets forms. This dispersion leads to very high strengths and attendant low ductility values. In fact, tensile strengths in excess of 1590 $\frac{MN}{m2}$ have been reported in Ti-6246 which contains tempered α".(18)

IX-B-3-b. Property Variations

The previous discussion provides a qualitative basis for understanding the effect of heat treatment on the strength and, to a lesser extent, the ducility of α+β Ti alloys. It will now be useful to examine tensile data for various heat treatments to see how the trends pertain.

There has been considerable effort expended on studying the effect of microstructure and processing history on properties of α+β Ti alloys. Of all the available information, there are several systematic studies which are especially helpful to establish property trends.(5,16,17) The Sparks and Long(5) work probably represents the most extensive study of properties of forgings made with material from the same heat and with the same billet microstructure. Further, since Sparks and Long and also Chesnutt et al.,(16) investigated forgings, a minimum amount of texture was present to complicate the interpretation of the effect of microstructure on properties.

Tensile properties of the three α+β alloys of interest are shown in Table IX-B-3. From this table it can be seen that heat treatment has the greatest effect on strength, whereas forging practice has the greatest effect on tensile ductility. For example, the effect of forging practice is reflected by the properties of Ti-64 in the BA and STOA conditions. The tensile ductility of the BA material is lower as is the strength. To examine the effect of heat treatment on strength compare the properties of Ti-64 in the recrystallization anneal (RA) and the STA or STOA conditions. It also should be noted that the strength of the STOA condition is higher than that of the STA condition. This result is not well understood but the data in Table IX-B-3 was obtained from lower oxygen material than in

Table IX-B-3. Tensile Properties of Three α+β Ti Alloys at Room Temperature

	YS		UTS				
Ti-6Al-4V	ksi	MN/m^2	ksi	MN/m^2	%Elong	RA%	Ref
α+β Forge + Recrystallization Anneal*1	103	710	127	190	12.4	36	16
α+β Forge + Mill Anneal							
α+β Forge + STA (age 4h/590°C)	127	875	136	940	15.2	34	16
α+β Forge + STOA (age 24h/590°C)	131	903	141	970	15.5	47	16
β Forge + AC {BA} (+700°C/2h/AC)	112	772	124	850	11.2	23	16
β Forge + WQ {WQ} (+700°C/2h/AC)	125	862	135	930	5.9	6	16
α+β Forge DA (870°C/2h/AC+700°C/2h/AC)	124	855	132	910	15.3	47	16
Ti-6Al-2Sn-4Zr-6Mo							
10-20% Primary α + STA*2	162	1117	176	1213	13	37	5
+ STOA*3	148	1020	158	1089	16	42	5
40-50% Primary α + STOA*2	167	1151	180	1241	14	42	5
+ STOA*3	155	1069	166	1145	14	41	5
β Forge + STA	152	1048	174	1200	6.5	13	5
Ti-6Al-2Sn-4Zr-2Mo							
α+β Forged + STA*4	149	1027	136	938	16	35	18
Ti-6-2-4-2 + .25 wt%Si							
α+β Forge + 965°C/1h/AC+590°C/8h/AC	146	1007	154	1062	13	34	18
α+β Forge + 965°C/1h/OQ+590°C/8h/AC	158	1089	172	1186	12	20	18
β Forge + 965°C/1h/AC+590°C/8h/AC	138	952	150	1034	11	25	18
β Forge + 965°C/1h/AC+590°C/8h/AC	151	1041	166	1145	7	15	18

*1 RA = 930°C/4h/cool at 55°C/h to 760°C/Air Cool
*2 STA = 885°C/1h/Air Cool + 590°C/8h/Air Cool
*3 STOA = 885°C/1h/Air Cool + 700°C/1h/Air Cool
*4 STA = 985°C/1h/Air Cool + 590°C/8h/Air Cool

typically used in the STA or STOA condition. The aging response of the lower oxygen material may be quite different; this would account for the above result. Oxygen content has a large effect on strength and ductility as will be discussed later.

Comparable, but larger effects of processing and heat treatment on tensile properties can be seen in the data for Ti-6246 also shown in Table IX-B-3. For example, the differences in strength between the STA and STOA conditions reflect the effect of heat treatment whereas the differences in ductility of β-forged-STA and the α+β forged 40-50% primary α-STA material reflects the effect of processing on ductility.

Similar trends to those mentioned above exist in the data for Ti-6242 except the heat treatment response is not as great. Thus while the effect of processing on ductility is comparable to that observed in the two alloys already described, the ability to achieve increases in the strength of Ti-6242 by heat treatment is much more limited. This is typical of alloys which contain low concentrations of β-stabilizing elements.

Most of the Ti-6242 data in Table IX-B-3 is for the alloy which contains 0.25wt%Si although baseline data for Si-free material is also included. Silicon is added to the alloy to impart creep resistance as will be discussed later. In addition to improving creep resistance, Si also improves the heat treatment response, probably because is is a relatively potent β-stabilizer. Concomitant with the increased hardness response in the Si bearing alloys is an increased tendency for metallurgical instability during elevated temperature service. This will be discussed further in the section on creep.

The magnitude of the heat treatment response of the three alloys addressed in Table IX-B-3 increases with increasing β-stabilizer content. This trend is quite general among α+β Ti alloys. This is because alloys with higher concentrations of β-stabilizing elements have larger volume fractions of β-phase. As described earlier, it is the β-phase decomposition reactions which lead to increased strength after heat treatment. Thus alloys with increased volume fraction β-phase have a higher overall hardening response when these β-phase regions are strengthened by a decomposition reaction.

As mentioned previously, increasing oxygen content significantly increases the strength of $\alpha+\beta$ Ti alloys. This is because oxygen is a potent solid solution strengthening agent in the α-phase. This effect is most clearly documented in commercial purity Ti where increasing oxygen content from 0.1 to 0.3wt% can change the yield stress from < 20ksi to > 50ksi. Significant strength increases also are observed in the higher strength alloys. Some tensile data for Ti-64 with constant microstructure and different oxygen contents is shown in Table IX-B-4. From this table it can be seen that the strength increases significantly in the higher oxygen material. The variations in tensile ductility are minor and in some cases seem to favor the higher oxygen material, but this may reflect other factors such as grain size. As will be shown later, increasing oxygen always results in lower fracture toughness.

Finally, the effect of texture on the tensile properties of one alloy (Ti-64) in one microstructural condition will be shown to demonstrate the magnitude of texture effects. The material from which this data was obtained had 14 times the random number of basal plane poles concentrated parallel to the transverse direction.[20] The data in Table IX-B-5 shows that the textured material is much stronger when loaded parallel to the basal poles. Also shown in the table is the high modulus in this direction. As mentioned earlier, these property variations are the result of the elastic and plastic anisotropy of the hexagonal α-phase which is the majority phase in all alloys dealt with in this review.

IX-B-4. The Effect of Microstructure on the Fracture Toughness of $\alpha+\beta$ Ti Alloys

Fracture toughness is the measure of the resistance of a material to catastrophic propagation of a pre-existing sharp crack. Since many applications for moderate to high strength Ti alloys involve heavy sections which are fracture critical, resistance to catastrophic fracture is an important consideration in the selection of an alloy and a heat treatment condition. Another important aspect of high toughness is that, at constant strength level, the maximum pre-existing flaw size that cannot

Table IX-B-4

Effect of Oxygen on the Tensile Properties of Ti-6Al-4V at Room Temperature

		YS		UTS				
		MN/m^2	ksi	MN/m^2	ksi	%Elong	%RA	Ref
BA	lo oxy*1	772	112	855	124	11	23	16
	std oxy*2	883	128	993	144	11	20	5
STOA	lo oxy	903	131	972	141	16	47	16
	std oxy	945	137	1041	151	14	33	5
RA	lo oxy	710	103	876	127	12	36	16
	std oxy*3	1055	153	1076	156	13	Not avail.	19
BQ	lo oxy	862	125	931	135	6	6	16
	std oxy	1020	142	1076	156	10	20	5

*1 0.12 wt% Oxygen

*2 0.19 wt% Oxygen

*3 0.20 wt% Oxygen (plate)

Table IX-B-5

Effect of Basal Texture on Tensile Properties of Ti-6Al-4V at Room Temperature

	YS		UTS		Young's Modulus		
	MN/m^2	ksi	MN/m^2	ksi	%Elong	%RA	ksi
Longitudinal (test direction normal to high density of basal poles)	883	128	917	133	13	32	16.0×10^6
Transverse (test direction parallel to high density of basal poles)	1062		1131		16	33	21.2×10^6

propagate unstably is proportional to the square of the ratio of the fracture toughness to the yield stress. Thus as toughness increases the critical flaw size also increases dramatically. As a result, metallurgical factors which can be controlled to improve toughness offer the potential for improved structural integrity and efficiency.

In subsequent sections some general trends regarding microstructure/toughness relations which appear to generally pertain to $\alpha+\beta$ alloys will be discussed. Following this, toughness data for each of the three alloys discussed herein will be presented and examined. In this regard, most fracture toughness testing has focussed on test conditions which result in plane strain since these conditions are pertinent to heavy sections. As a result, the data presented will be largely K_{IC} or plane strain fracture toughness. For the purpose of comparison, K_{IC} is the most useful toughness parameter to consider since it is independent of thickness and also represents a lower bound value for the toughness.

The plane stress fracture toughness (K_c) of $\alpha+\beta$ Ti alloys rolled into sheet for thin section applications is generally excellent and, as a result, virtually is never a design limiting factor in structures which are built up from sheet (such as in the NUWMAK design). As a result, other factors such as strength, ductility and creep resistance usually dominate the design decisions in thin section components. Thus all subsequent discussions of the effect of microstructure on toughness will pertain to variations in K_{IC}.

IX-B-4-a General Trends

As is the case with other structural materials, $\alpha+\beta$ Ti alloys typically have lower plane strain fracture toughness (K_{IC}) at higher strength levels. However, unlike Al alloys and high strength steels, the processing and heat treatment combinations which lead to variations in strength have much larger attendant variations in microstructure. These variations already have been discussed previously so it is sufficient to point out that changes in morphology, size of precipitates and distribution of microstructural constituents (which occur on a scale comparable to the crack tip plastic zone size at the onset of unstable fracture) can be expected to influence the crack path and fracture toughness. Microstructural features or constituents which are much smaller or larger than the crack tip effect on toughness. Thus in $\alpha+\beta$ Ti alloys gross

microstructural variations such as between equiaxed $\alpha+\beta$ and BA material might be expected to effect toughness independently of strength and this is observed; moreover, as a general rule, BA materials have a significantly higher fracture toughness than do materials which have equiaxed $\alpha+\beta$ microstructures. These toughness variations have been shown to have an accompanying change in fracture topography[6] from intergranular fracture along prior β grain boundaries in BA material to transgranular fracture across and around equiaxed primary α grains in $\alpha+\beta$ processed material. This change in fracture mode will be discussed further below; and here it is sufficient to say that changes in microstructure which lead to more tortuous, irregular fracture paths also lead to higher fracture toughness values, provided that variations in strength also are taken into account. Further, this trend becomes more pronounced at higher strength levels.

Other material variables such as oxygen content and texture also affect fracture toughness of Ti alloys. Toughness decreases relatively rapidly as oxygen is increased, thus material containing $\leq$ 0.13wt% oxygen is usually used for toughness critical applications. Because toughness also decreases with strength, higher strength alloys sometimes are specified with even lower oxygen contents, e.g., 0.10wt%. However, as mentioned earlier, oxygen also increases the strength. As a result unnecessarily low oxygen levels can lead to superfluous toughness and thus unexpected variations in toughness at constant strength, oxygen content and microstructure may be traceable to texture variations. This is especially true in flat-rolled products such as plate and sheet which typically exhibit more severe textures.

IX-B-4-b. Toughness Variations

As mentioned above, there is a strong effect of microstructure on K_{IC}. Some data which illustrate these variations are shown in Table IX-B-6.

The data for Ti-64 show that the alloy generally exhibits attractive properties, although the toughness of the mill annealed (MA) plate can be quite low. The toughness of the mill annealed material can be significantly improved with little loss of strength by re-annealing as shown by the increased toughness of the RA plate. These data for the MA and RA conditions were obtained from the same plate, thus the RA properties accurately reflect the effect of re-annealing. The highest toughness in plate material is typically achieved by beta annealing as also seen in Table IX-B-6.

Table IX-B-6. Fracture Toughness Variations in α+β Ti Alloys

	YS		UTS			$K_{IC}(K_Q)$	
Ti-6Al-4V	ksi	MN/m^2	ksi	MN/m^2	%Elong	$ksi\sqrt{in}$	$MN/m^{3/2}$
Plate							
α+β roll + Mill Anneal	159	1096	170	1177	14	29.4	32.3
α+β roll + Recrystallization Anneal (RA)	153	1145	166	1145	13	46.2	50.8
α+β roll + Duplex Anneal (950°C/1.5h/AC + 760°C/1h/AC)	128	972	141	972	14	54.	59
BA roll (1040°C/20m/AC + 730°C/2h/AC)	128	876	138	952	11	79	87
Forging							
α+β forge + RA	103	710	127	876	12	(110)	(121)
α+β forge (15% primary α)+DA	118	814	129	889	12	(112)	(123)
α+β forge (50% primary α)+DA	124	855	132	910	15	(101)	(111)
β-forge (BA)	112	772	124	855	11	(108)	(119)
β-forge + Quench (BQ)	125	862	135	931	6	92	68
α+β forge + STA	127	876	136	938	15	(84)	(92)
α+β forge + STOA	131	903	141	972	16	76	84
Ti-6Al-2Sn-4Zr-6Mo							
Forging							
α+β forge + STA* (10% primary α)	162	1117	176	1213	13	31	34
α+β forge + STA* (50% primary α)	167	1151	180	1241	14	24	26
α+β forge + Ann** (50 % primary α)	154	1062	164	1131	13	24	26
β-forge + STA*	152	1048	174	1200	7	52	57
Ti-6Al-2Sn-4Zr-2Mo							
Forging							
α+β forge - β ST+Age	131	903	---	----	12.5	74	81
β-forge - α+β ST+Age	130	986	---	----	11.0	76	84

*885°C/1h/AC + 590°C/8h/AC
**700°C/1h/AC

The properties of the Ti-64 forgings in the BQ and the DA (50% primary α) conditions shown in Table IX-B-6 permit comparison of the effect of acicular and equiaxed microstructures on the toughness and tensile ductility at essentially constant strength. These data show that the $\alpha+\beta$ forged + DA materials have superior strength-toughness and strength-ductility combinations to either BA or BA material. This result is at variance with the data for plate. Although the reasons are not entirely clear, it is possible that the inevitable presence of texture in $\alpha+\beta$ processed plate affects the apparent toughness-microstructure comparisons in this product form. In this connection, it is important to note that the forgings from which the data in Table IX-B-6 were obtained were virtually untextured. If the role of texture suggested here is correct, then it would appear that any texture may be deleterious to toughness.

Fractographic analysis has shown that the fracture surfaces of K_{IC} specimens are much rougher and more irregular for acicular than for equiaxed microstructures. The irregularity of the fracture surface and the density of secondary cracks is higher in the BA than in the BQ condition. In the former condition is appears that prior β grain boundaries and Widmanstatten colony boundaries are the primary sites for crack deviation and secondary crack formation. Such irregular fracture paths tend to increase the toughness. This correlation between irregular crack path and high toughness is especially evident in the higher strength alloys such as Ti-6Al-2Sn-4Zr-6Mo. The relationship between fracture topography toughness has been discussed in detail elsewhere.[6]

The inverse trends in tensile ductility and fracture toughness between equiaxed and acicular microstructures is important to notice. This is characteristic of all $\alpha+\beta$ alloys but is especially pronounced in higher strength alloys such as Ti-6246.

The data in Table IX-B-6 shows that β processed forgings of Ti-6246 have decidedly superior strength-toughness combinations. Moreover, in the $\alpha+\beta$ processed condition this alloy can exhibit very low toughness values. For example, at the 167ksi (1151 MN/m^2) yield strength level, a toughness

of 24ksi$\sqrt{in}$ (26 MN/m$^{3/2}$) corresponds to a critical flaw size of ~5.08 x 10^{-2}cm. The high toughness of the β-forged material has been correlated with the change from a flat transgranular fracture in α+β forged material to an irregular intergranular fracture in β-forged material as discussed above. This alloy is currently used almost exclusively as a forging alloy, as a result, there is no data available for plate.

The data in Table IX-B-6 for Ti-6242 also shows that this alloy is generally quite tough. Thus the improvement in toughness achieved by β-forging is less significant than that for Ti-6246. Fortunately, this condition also has other attractive properties as will be discussed later.

The effect of oxygen content on toughness is illustrated by the data for Ti-64 shown in Table IX-B-7. These data have been selected to reflect the effect of oxygen on toughness while maintaining a constant microstructure. These data shown that increasing oxygen leads to substantial decreases in toughness. In this connection it has been shown that increasing oxygen leads to more intense planar slip with a resultant stronger tendency toward strain localization. The details of how strain localization causes reductions in toughness are not well understood but empirical correlations exist which strongly suggest this cause-effect relationship.

The role of texture on toughness has been the subject of limited study in Ti-64 and Ti-6246.[20] These studies have shown that material which contains relatively intense transverse basal textures has greater fracture resistance when the crack propagation direction is perpendicular to the majority of the basal planes, i.e., the transverse direction. The one exception to this appears to be in ELI (extra low interstitial) Ti-64 where the opposite appears to be true. Fracture resistance data obtained from R-curves of material with strong basal transverse texture is shown in Table IX-B-8. Note that the R-curves for the ELI material differed from the others inasmuchas the incremental crack growth, Δa, which preceded unstable fracture was smaller by a factor of 5 in the LT specimens compared to the TL specimens. This may account for the apparent reversal in the effect of texture on K_R in this material. One possible explanation for the apparent reversal in the effect of texture on toughness in Ti-64 as a function of oxygen content is based on the relative amounts of twinning

Table IX-B-7. Effect of Oxygen Content on Toughness

Ti-6Al-4V	YS ksi	YS MN/m^2	UTS ksi	UTS MN/m^2	%El.	%RA	$K_{IC}(K_Q)$ $ksi\sqrt{in}$	$K_{IC}(K_Q)$ $MN/m^{3/2}$
BA ℓo oxy*	112	772	124	899	11	23	(108)	(119)
BA std oxy**	128	883	144	993	11	20	73	80
BQ ℓo oxy	125	862	135	931	6	6	92	101
BQ std oxy	142	979	156	1076	10	20	60	66
RA ℓo oxy	103	710	127	876	12	36	(110)	(121)
RA std oxy	141	972	155	1069	14	35	69	76

* 0.12wt% oxygen
** 0.19wt% oxygen

Table IX-B-8. Toughness Directionality in Textured Material

	K_R^*			
	TL Orientation		LT Orientation	
Alloy (Grade)	$ksi\sqrt{in}$	$MN/m^{3/2}$	$ksi\sqrt{in}$	$MN/m^{3/2}$
Ti-6Al-4V (ELI) (Ref 20)	112**	123	103**	113
Ti-6Al-4V (Ref 20)	103	113	113	124
Ti-6Al-2Sn-4Zr-6Mo (Ref 20)	96	106	113	124

* Maximum K prior to onset of unstable fracture

** Δa corresponding to K_R^{max} was 5 times smaller for the LT orientation than the TL orientation

	K_{IC}-$MN/m^{3/2}$	loaded along <0001>
Ti-6Al-4V plate (Ref 22)	80	46

which occurs in low and high oxygen material. Increasing oxygen dramatically reduces the incidence of twinning.[21] Thus in the low oxygen material crack tip plasticity may be enhanced by twinning with an attendant increase in toughness.

The use of R-curves to determine the toughness of the textured material was necessitated because the material was fabricated in sheet thickness. Thus the LT and TL K_R values must be examined on a relative basis although the absolute relationship between these values and K_{IC} values which would be expected from thicker plate are not obvious. One advantage of measuring texture effects in sheet is that the texture is much more uniform in the thickness direction. In thick plate, a surface to center texture gradient is nearly always present. This is because during continuous rolling the amount of work near the surface increases as the working temperature decreases. Since the final texture depends on both amount of work and working temperature, it is understandable that surface to center texture gradients are developed in plate during continuous rolling.

There also are some K_{IC} data on textured plate. These data also are shown in Table IX-B-8. These toughness data agree with the variation in crack propagation resistance, K_R, shown earlier. This provides further support for the incidence of lower toughness values when the crack propagates along the basal plane.

IX-B-5. The Effect of Microstructure on the Fatigue Behavior of $\alpha+\beta$ Ti Alloys

The wide variations in microstructure attainable in $\alpha+\beta$ Ti alloys by controlled thermal and thermomechanical processing lead to substantial variations in fatigue performance. Moreover, because of the large changes in tensile ductility with variations in microstructure, different measures of fatigue performance, e.g., notched vs. smooth and low cycle vs. high cycle tests, show different microstructural dependences. As a result, the optimum microstructure for a particular application depends on the particular loading situation and relevant design philosophy. The ensuing sections will attempt to review the effect of microstructure on smooth and notch fatigue life in the high and low cycle regimes and on the fatigue crack propagation (FCP) rate.

IX-B-5-a. Fatigue Life

Fatigue life is usually divided into two regimes; low cycle fatigue (LCF) in which failure occurs in 10^4 cycles or less and high cycle fatigue (HCF) in which failure occurs in more than 10^4 cycles. Coffin and Manson[23] have shown that at $\sim 10^4$ cycles there is a transition from the life being dominated by the plastic strain amplitude at shorter lifetimes to the elastic strain (stress) amplitude at longer lifetimes. In addition, the fatigue life of smooth test bars is generally considered to represent the combined result of crack initiation and propagation. The conventional wisdom is that initiation comprises 85-95% of total life in smooth bar tests, although Tompkins[24] has recently questioned this. In the case of notched fatigue tests, the foreshortened lifetimes are usually considered to result from very early crack initiation. Thus, the notched fatigue life depends more critically on the factors which affect FCP rate.

With the foregoing factors in mind, the available fatigue life data for specimens with controlled microstructures will be examined.

IX-B-5-a-i. Smooth Bar Fatigue Life

There now is compelling evidence for Ti-64 which indicates that superior high cycle ($N_f = 10^7$ cycles) fatigue strength is obtained when the slip length is small.[25-27] Small slip lengths can be obtained by producing very fine grained equiaxed material or by quenching from the β-phase field to produce fine, acicular α'. There is general agreement that the Widmanstatten $\alpha+\beta$ microstructure has decidedly poorer fatigue strength as shown in the two sets of S-N curves, Figure IX-B-6. In coarser equiaxed microstructure the fatigue strength is significantly lower but still better than in the Widmanstatten structure.[28] STA material has good fatigue strength but not as good as the fine grained equiaxed material or the beta quenched material.[29] These trends in microstructure-fatigue strength dependency follow from the general body of available data on this subject. However, it is difficult to find a single set of data which includes all microstructures in the above ranking. There are several reasons for the scarcity of self-consistent data. These include variations in texture, variations in test method (axial vs. bending), variations in test conditions (load ratio, frequency) and finally, but possibly most important, variations in surface preparation method. In this connection, Leverant et al.[29] have shown that any machining method which leaves a compressive surface stress results in increased fatigue strength. This is presumably due to an extended pre-initiation portion of the overall specimen life.

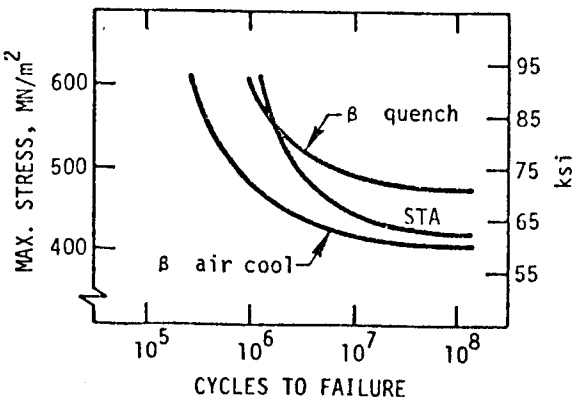


Fig. IX-B-6(a) Effect of microstructure on fatigue life in Ti-6Al-4V forgings. Stresses are maximum alternating stress; all tests were done with 300 MN/m^2 mean stress. Heat treatments were as follows: β air cool, 1285 K (1010°C)/ 90 min/AC + 1005 K (730°C)/3h/AC; β quench, 1285 K/90 min/wa + 1005 K/3h/AC (25).

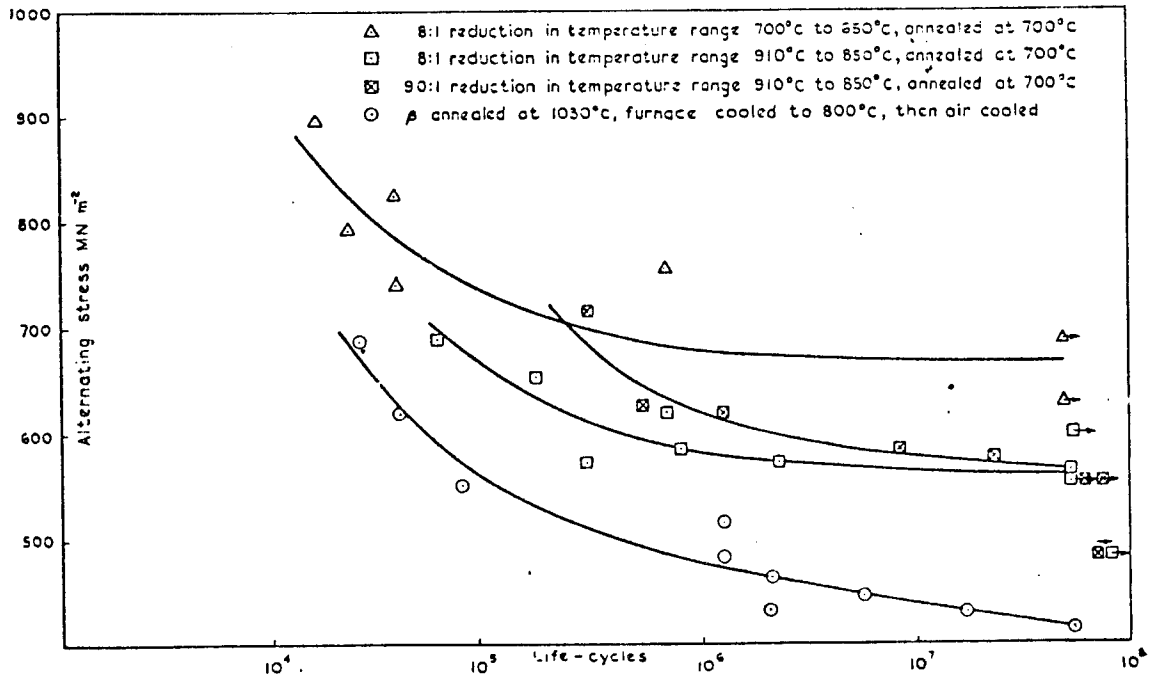


Fig. IX-B-6(b) S-N curves for rotating cantilever fatigue tests on Ti-6Al-4V bars β annealed, and β annealed and α+β worked at high and low temperatures in the α+β field, and subsequently annealed.

A broader range of microstructures have been exampled by Sparks and Long[5] who have presented extensive tensile and smooth bar fatigue data for 23 different conditions of Ti-64. Some of this data is summarized in Table IX-B-9. Using their data, regression analysis has been performed to see if a correlation exists between 10^7 cycle fatigue strength and yield or tensile strength. In both cases the co-efficient of correlation was smaller than 0.1 indicating that essentially no correlation exists.

The low cycle fatigue of Ti-64 appears to be most attractive in the STA condition[30] although systematic studies of the effect of microstructure of LCF life are not readily available in the open literature. The data of Lucas[25] shown earlier also shows that LCF life is best in STA material. One of the difficulties in using Lucas' data for LCF is that his tests were constant stress (HCF type) tests. Such tests have only limited use in the LCF regime where plastic strain amplitude dominates life. In contrast to the HCF case, the effect of primary α grain size on LCF life has not been systematically studied. In a different study, Gilmore and Imam[31] have shown that specimens solution treated at 900°C (1650°F) have excellent LCF life. The applicability of these results is subject to question, however, because Gilmore and Imam perform their testing in torsion. Since torsion suppresses crack opening, the torsion initiated cracks propagate in Mode II. Thus comparison of the life data from this type test to an axial (model 1) test is very difficult. Further, Gilmore and Imam tested as-quench materials which are metallurgically unstable. Thus the principal result which can be safely extracted from their work is corroboration of the earlier result that LCF life is optimized in STA material which contains primary α in an α' matrix.

In connection with the general low cycle fatigue behavior of $\alpha+\beta$ alloys, the cyclic stress-strain behavior of Ti-64 during fully reversed loading recently has been shown to vary with microstructure.[28] Seven microstructures were examined: RA, two DA conditions, BA, BQ, STA and STOA. Of these, 3 showed pronounced cyclic work softening whereas the

Table IX-B-9. Fatigue and Tensile Data for Various Microstructural Conditions at Room Temperatures

Condition	YS ksi	YS MN/m^2	TS ksi	TS MN/m^2	%Elong	%RA	$\sigma@10^7$ Smooth ksi	$\sigma@10^7$ Smooth MN/m^2	$\sigma@10^7$ Notch ksi	$\sigma@10^7$ Notch MN/m^2
Ti-6Al-4V										
10% Equiaxed primary α + Ann[a]	141	972	155	1069	14	35	78	538	31	214
40% Equiaxed primary α + Ann	135	931	147	1041	15	41	84	579	37	255
10% Equiaxed primary α + STOA[b]	142	979	154	1062	15	41	71	490	32	221
10% Equiaxed primary α + Ann[c]	139	958	151	1041	14	37	88	607	38	262
50% Elongated primary α + Ann[c]	134	924	148	1020	13	32	90	621	33	228
β forge + Ann	128	883	144	993	11	20	82	565	32	221
β forge/water quench + Ann	138	952	153	1055	10	21	88	607	27	186
β forge + STOA	142	979	156	1076	10	20	85	586	32	221
10% Equiaxed primary α + Ann[d]	128	883	143	986	13	33	90	621	31	214
Ti-6Al-2Sn-4Zr-6Mo										
10% Equiaxed primary α + Ann[e]	148	1020	161	1110	15	37	90	621	42	290
10% Equiaxed primary α + STA[f]	162	1117	176	1213	13	37	90	621	36	248
50% Equiaxed primary α + Ann	154	1062	164	1131	13	34	90	621	41	282
50% Equiaxed primary α + STA	167	1151	180	1241	14	42	98	676	38	262
50% Equiaxed primary α + STOA[g]	155	1069	166	1145	14	41	90	621	38	262
50% Elongated primary α + STA	159	1096	175	1207	10	23	109	752	40	276
20% Elongated primary α + STA	161	1110	175	1207	11	26	90	621	41	282
βforge + STA	152	1048	174	1200	7	13	98	676	38	262

a) Ann = 700°C/2h/air cool
b) STOA = 950°C/1h/WA+700°C/2h/air cool
c) Water quenched off of forging press
d) Low oxygen material
e) Ann = 700°C/1h/air cool
f) STA = 885°C/1h/air cool+590°C/8h/air cool
g) STOA = 885°C/1h/air cool+700°C/1h/air cool

others showed cyclic σ-ε curves which crossed the monotonic curves. The 3 conditions which softened were BQ, STA and STOA. This is not surprising since the α' in these structures contains a high initial dislocation density which tends to "shake-down" during cyclic straining. The effect of these variations in cyclic stress-strain behavior on LCF life merit systematic investigation. Nevertheless, the softening behavior is generally undesirable in applications which are load (as opposed to displacement) limited since the plastic strain amplitude decreases during service.

An additional type of LCF test utilizes the half bolt hole specimen.[5] This specimen localizes the strain so that periodic inspection can be effectively used to identify the number of cycles which correspond to crack initiation. Since the pre-initiation stage can be as much as 50% of total LCF life, data from such tests is useful in selecting LCF resistant microstructures. In this connection, half bolt hole data is available[32] for the 23 conditions of Ti-64 which Sparks and Long studied. These data show that the most resistant conditions to LCF crack initiation are BQ plus aged 700°C for 2h and 3 conditions which were $\alpha+\beta$ forged according to different schedules, then annealed 2h at 700°C. Conditions in which either blocky α or continuous α-phase networks at prior β grain boundaries were present showed consistently poor resistance to LCF crack initiation.

The microstructural reasons for the above trends in LCF behavior are not completely clear. Moreover, since each test was run at only one plastic strain amplitude, the relative rankings might be reordered at different plastic strain amplitudes. This suggestion is strengthened by the cyclic stress strain data mentioned earlier[28] where several microstructures soften at low strain amplitudes and harden at higher ones.

Another and possibly very important observation is that the microstructural conditions mentioned above as having good LCF crack initiation resistance also have fracture toughness values which vary from 59 to 86 $ksi\sqrt{in}$ (65 to 95 $MN/m^{3/2}$) while the tensile strengths range from 143 to 156 ksi (986 to 1076 MN/m^2). Thus selection of a material for attractive LCF performance may be done at the expense of toughness or tensile strength or both. Again, this underscores the importance of identifying the performance limiting property in design.

Finally, Bowen[33] has examined the effect of texture on the smooth HCF behavior of Ti-64 bar. He tested bar with a transverse basal texture and a microstructure in which the primary α grains were elongated in the rolling direction. Bowen's data is summarized in Table IX-B-10. From this it can be seen that the fatigue strength is significantly lower when the loading axis coincides with the direction of maximum basal pole density (in this case the transverse direction). These data also show that the fatigue strength is greater in the short transverse than in the longitudinal direction. Bowen has attributed this to the elongated grain structure which makes the short transverse grain size effectively smaller when compared to the longitudinal direction. The orientation dependence of the yield stress values also shown in Table IX-B-10 is consistent with this interpretation. This is because the rotational symmetry of the texture about the transverse direction excludes strength differences in the longitudinal and short transverse directions. Thus the observed strength differences probably result from grain size effects.

The amount of fatigue data available for Ti-6246 is small compared to that for Ti-64. Nevertheless, there is HCF data for the 11 conditions studied by Sparks and Long.[5] Of these conditions no systematic trends are evident. Good HCF strength at 10^7 cycles was obtained in material with both equiaxed and elongated primary α. The best fatigue performance in this alloy was obtained in the STA condition which corresponds to a 885°C/1h/air cool solution treatment followed by an aging treatment of 590°C/8h/air cool. This is in contrast to Ti-64 where the highest fatigue strengths were obtained by annealing for 2h at 700°C after forging. It should be noted that the air cooled microstructures in Ti-6246 do not have Widmanstatten $\alpha+\beta$ colonies such as those present in Ti-64. As a result, BA or β-forged material does not have an increased slip length in Ti-6246, in contrast to Ti-64. Thus there is no significant lowering of the HCF strength in this alloy when elongated α is present.

There is also half bolt hole specimen LCF data for the 11 conditions of Ti-6246.[32] These data show that the best LCF crack initiation resistance is in material with ~50% equiaxed primary α. Moreover, the conditions which exhibit good LCF properties generally have high tensile ductility. Detailed examination of the data shows that the correlation

Table IX-B-10. The Effect of Texture on Fatigue Strength of Ti-6Al-4V (Ref. 33) at Room Temperature

Specimen Orientation	YS		UTS		E		σ_f (ksi) at 10^7 cycles
	ksi	MN/m^2	ksi	MN/m^2	psi	MN/m^2	
Longitudinal	118	814	129	889	16.1×10^6	111×10^3	70
Transverse	132	910	139	958	18.1×10^6	125×10^3	60
Short Transverse	126	869	138	952	16.1×10^6	111×10^3	80

between tensile ductility and LCF crack initiation resistance is only qualitatively valid. A list which ranks the microstructural conditions in order of decreasing ductility does not exactly coincide with the ranking in order of decreasing LCF crack initiation resistance. Nevertheless, the conditions at the top of the LCF list are consistently the more ductile ones whereas the conditions near the bottom are the least ductile.

There is only limited data which shows the effect of texture on the fatigue behavior of Ti-6246.[20] The availabe data pertains to $\alpha+\beta$ rolled and annealed material. These data show that the fatigue strength at 10^6 cycles is ~15ksi (~100 MN/m^2) greater when the stress axis is perpendicular to the basal pole texture direction ($<0001>_\alpha$) than when it is parallel to it.

The effects of microstructure on the fatigue behavior of Ti-6242 are not extensively treated in the open literature. Further, those data which are available usually do not systematically relate properties to microstructure. Since the alloy is microstructurally more similar to Ti-64 than to Ti-6246, it is useful to examine the available data in light of the Ti-64 data reviewed earlier. The HCF fatigue strength of Ti-6242 in the duplex annealed condition is ~75ksi (~520 MN/m^2). This corresponds to a fatigue ratio $\frac{\sigma f}{\sigma uts}$ of ~0.51. In duplex anneal sheet the fatigue strength increases to ~85ksi (~590 MN/m^2). The increase may be due to the characteristically smaller grain size in sheet or due to the presence of texture. As discussed earlier, caution must be exercised to separate the contributions of these two variables. Decreasing the solution treatment temperature in the duplex anneal from 970°C to 900°C increases the low cycle fatigue resistance of bar stock significantly. Again the paucity of data makes it hard to separate microstructure effects from texture effects since lower solution treatment temperatures increase the volume fraction of primary α which, in turn, intensifies any texture which may be present. In the BA condition Ti-6242 exhibits a well-developed Widmanstatten $\alpha+\beta$ colony structure. Thus it is anticipated that the smooth HCF life of beta forged Ti-6242 is inferior to that of $\alpha+\beta$ forged

material. Similarly, the LCF life of β-forging is reduced. Systematic studies of the effect of microstructure on fatigue behavior are needed for this technologically important alloy.

Some discussion of the smooth bar fatigue life data summarized above seems appropriate. The low fatigue strength of Ti-64 in the BA condition has been examined by Stubbington and Bowen[27] who found that Stage I cracks initiate at α/β interfaces. Since the density of α/β interfaces is very high in the Widmanstatten structure of the BA condition, this microstructure should be susceptible to initiation of Stage I cracks. Moreover, the presence of the interface phase retards slip transfer across the α/β interfaces and thus a local strain incompatibility exists in the region of the interface. Finally,since all α plates in a single colony have the same orientation, Stage I cracks can propagate for larger distances in a constant maximum shear stress orientation. In contrast, fine grained equiaxed microstructures contain many α/α boundaries but few α/β boundaries. Moreover, smaller grain sizes reduce the strains which accumulate at grain boundaries by reducing the slip length and, therefore, the dislocation pile-up size. Also since α/α boundaries are most prevalent in this microstructure, occurrence of the strain incompatibility mentioned earlier is minimized. Finally, Stage I crack propagation is more difficult because the crack is re-oriented each time it crosses an α/α grain boundary. Thus, there are a number of factors which help explain the superior HCF behavior of fine grained equiaxed microstructures relative to Widmanstatten BA microstructures. From the standpoint of HCF life and Stage I crack initiation, the fine acicular α' in BQ material has several features in common with the fine grained equiaxed microstructures. These include almost no α/β interfaces, small grains (in this case the individual martensite plates) and frequent changes in crystallographic orientation. It is thus not surprising that the HCF life of BQ material also is very good. Further, since BQ material typically contains almost no texture, the even more frequent changes in Stage I crack propagation orientation may account for the BQ material being typically better than even the fine grained equiaxed material.

IX-B-5-a-ii. Notched Bar Fatigue Life

In contrast to the smooth bar case, notched bar fatigue life is generally considered to result in early crack initiation. Further, because of the stress state due to the notch, the extent of Stage I crack growth is extremely limited. Thus notched life is dominated by the rate at which Stage II cracks propagate. In this regard, Eylon and Pierce[34] have shown that the notched life of BA material is superior to RA, MA, DA or STA material. However, these authors are somewhat vague in their explanation of this effect, leaving two possible causes: large numbers of cycles to crack initiation or longer Stage I crack lengths.* They further show that microstructure has a significant effect on the extent of Stage I crack propagation prior to the transition to Stage II cracking. Even though these authors studied notched specimens, their finding must be compared to the earlier discussion of Stage I cracking in smooth specimens. In this connection it is appealing to relate good notched fatigue strength to lower fatigue crack propagation rates. However, other available data, especially that of Sparks and Long[5] make this appear to be an oversimplification. For example, their data shows that the BA and BQ conditions are among the better conditions but that a DA condition has the best notched fatigue strength. Thus the factors which control notched fatigue strength appear to be more complex than suggested above or by others.[34]

In an attempt to produce an empirical correlation, regression analysis similar to that mentioned earlier in connection with smooth fatigue of Ti-64 was also conducted on notched fatigue data for 23 conditions of Ti-64 and on 11 conditions of Ti-6246. There was essentially no correlation between 10^7 notched fatigue strength and either the tensile or yield strengths. However, the variations in notched fatigue strength are also smaller so that uncertainties in this property only lead to minimal weight penalties.

The effect of texture on notched fatigue is neither well-characterized nor well-understood. However, limited test data[20] show that the trends in Ti-64 follow those for smooth bar fatigue. That is, the fatigue strength is lower when the stress axis is parallel to the basal texture direction. In Ti-6246 the presence of basal texture tends to reverse the trends between smooth and notched strength. In this latter case the notched fatigue strength is higher when the loading direction is parallel to the basal texture direction whereas the smooth bar fatigue strength is lower for the orientation. No obvious explanation is available for this result.

IX-B-5-b. Fatigue Crack Propagation

There is now a significant quantity of data available which shows that microstructure variations can alter the FCP rates at constant cyclic stress intensity (ΔK) by more than an order of magnitude.[6,14,16,26,35-38]

*Eylon and Pierce call this initial crack the initiated crack but examination of their Figure 14(b) strongly suggests that this crack is a Stage I crack.

It is well known that a log-log plot of FCP rate vs. ΔK for all materials has the characteristic shape shown in Figure IX-B-7. In this figure it can be seen that the curve bends downward at low growth rates and eventually becomes parallel to the ordinate. When the curve becomes parallel to the ordinate, the ΔK intercept represents a threshold value (ΔK_{th}) below which no crack growth occurs. The crack growth rate at ΔK_{th} is typically $\sim 10^{-10}$ m/cycle. Referring again to Figure IX-B-7 it can be seen that at higher growth rates there is a linear portion of the curve. This linear portion was represented as ΔK^m by Paris and Erdogan[39] and is now frequently referred to as the Paris Law regime of fatigue crack growth. Most structural materials show variations in near threshold FCP rate and in ΔK_{th} but seldom show significant variations in FCP rate in the Paris Law regime.[40] In contrast Ti alloys show significant variations in FCP rate over the entire range. At the highest crack growth rates shown in Figure IX-B-7, the FCP rate curve bends upward. This is controlled by fracture toughness. However, since crack growth rates are uncontrollably rapid in this regime it is of little interest and will not be discussed further here. Moreover, since the majority of the lifetime of a cracked component is spent in the low FCP rate regime, factors which control FCP rate in this regime are probably most important. These factors include microstructures and texture. Each will be discussed below.

IX-B-5-b-i. Microstructure Effects

Among the commonly used microstructures described in Table IX-B-2, the FCP rate is typically lowest for BQ and BA and highest for MA and STA or STOA. The FCP rates for the other microstructures fall between these extremes. Further, the FCP rate for BQ is consistently lower than for BA at very low rates. Recent work[26] has shown that the FCP rate curves for these two microstructures cross at $\sim 10^{-7}$ m/cycle. Above this rate the BA condition is superior. In addition, the BQ material has a ΔK_{th} of $\sim 8 ksi\sqrt{in}$ ($9 MN/m^{3/2}$), whereas the BA anneal material has a ΔK_{th} of $\sim 5 ksi\sqrt{in}$ (~ 5.5 $MN/m^{3/2}$). Such variations are consistent with the higher fatigue strength of BQ material which was verified in the same study.[26] That is, higher fatigue strength and higher ΔK_{th} are self-consistent inasmuch as they both indicate a low rate of growth of short (low ΔK) cracks.

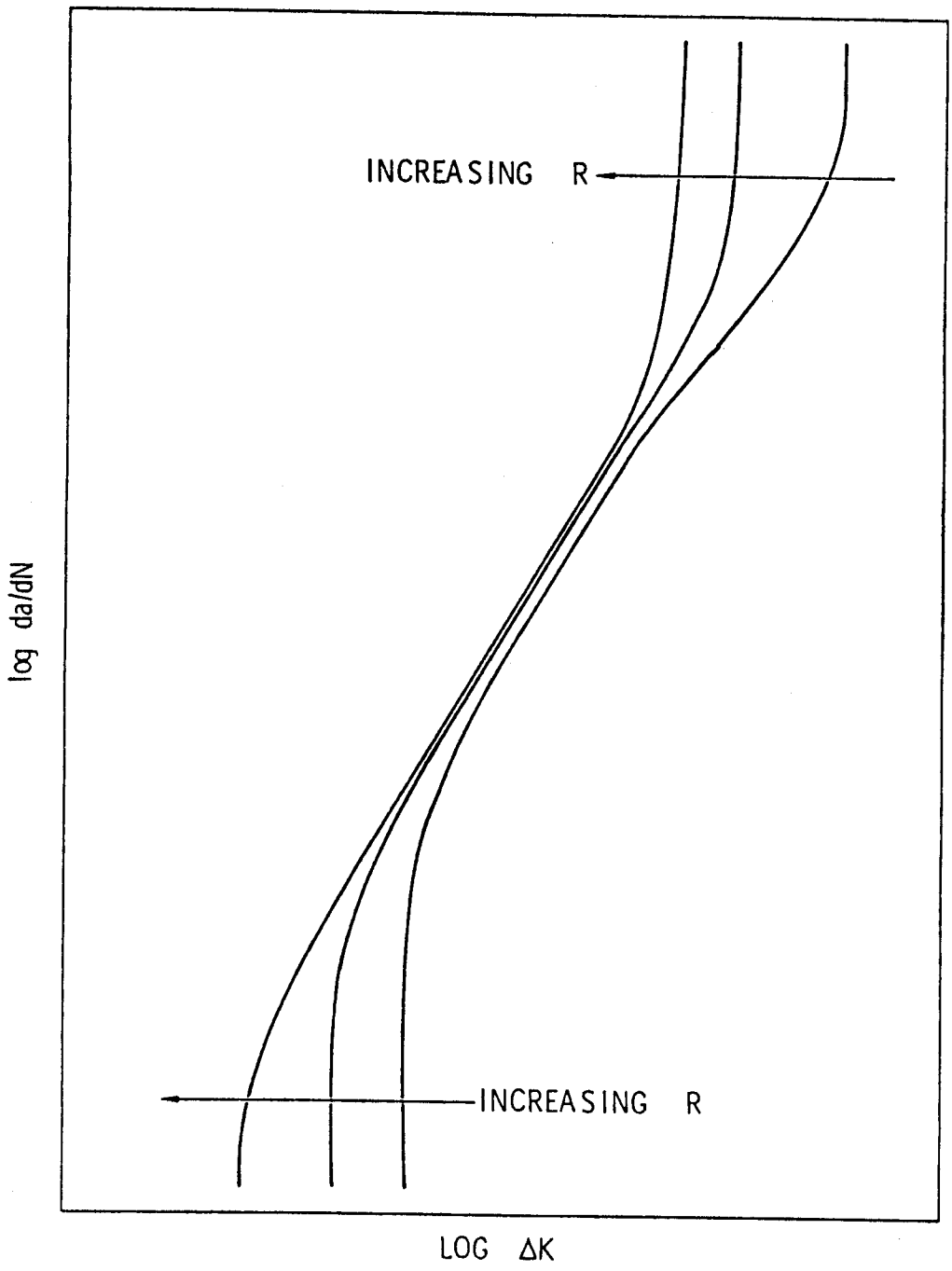


Fig. IX-B-7

In an attempt to provide an improved understanding of the role of microstructure on FCP rate, detailed electron fractography(6,26,16,35) has been conducted on FCP specimens with different microstructures.

These fractographic studies have shown that, depending on ΔK level, FCP is accompanied by formation of either of two distinctly different fracture features. These features occur with dimensions which depend on microstructure but which typically lie in the 5-150μ range.

At low ΔK levels (low FCP rates) the crack growth occurs by a faceted growth mode whereas at higher ΔK levels crack propagation is accompanied by formation of ductile fatigue striations. Further, the details of the topography of the facets at the sub-micron scale vary with microstructure. For those microstructures which exhibit low FCP rates (BQ and BA), the fracture surfaces contain facets which have extensive secondary cracking. In contrast, the facets on the fracture surfaces of MA or RA conditions are smooth and exhibit no evidence of secondary cracking. It has been reasoned(16) that the secondary cracking reduces the local effective stress intensity and thereby leads to lower FCP rates.

At higher FCP rates, where ductile fatigue striations are observed, the crack growth rate is consistently lower in those microstructures which have more tortuous crack propagation paths. In order to effectively reduce FCP rate, the wavelength of the tortuousity must be hundreds of times that of the crack growth rate per cycle. Thus in structures such as DA or STA the individual martensite or Widmanstatten α plates are too small to re-orient the crack. This probably is because these microstructural units fail in a single load cycle and thus cannot divert the crack. Fractographic examination bears this out because FCP specimens with these structures exhibit a high density of tear ridges in the $\alpha+\beta$ or α' regions and striations in the primary α regions.

The above discussion raises questions regarding the low FCP rates in BQ material in the near threshold regime. It appears that the α' plates in BQ material are significantly larger than in STA material. Similar trends pertain to the Widmanstatten α plate sizes in BA and DA material. The reasons for these microstructural scale variations have not been analyzed in detail but it is suggested that the size of these transformation products (Widmanstatten α and α' plates) is very important. Thus in BA and BQ materials the α' or Widmanstatten α plates are much larger because the sample is fully β at the onset of the transformation. It is also noteworthy that the larger α' plate size in the BQ condition may not be large enough to divert the crack at higher ΔK values. Thus the crossing of the FCP rate curves for BA and BQ may be accounted for on this basis.

The effect of microstructure on the FCP rate of Ti-6246 is smaller(16) with the maximum variation being a factor of 4 or 5. As in the Ti-64 case, the lowest FCP rates correspond to β-forged material whereas the fastest FCP rates correspond to the $\alpha+\beta$ forged material. Fractographic examination of these specimens showed a significantly higher density of secondary cracking in the β-forged condition. This observation is

consistent with the earlier discussion of the effect of secondary cracking on FCP rate. The smaller differences in FCP rate between microstructures in Ti-6246 may be due to the considerably finer microstructural scale which typifies all conditions of this alloy. The effect of increased alloy content on reducing the microstructural scale of $\alpha+\beta$ alloys has been discussed elsewhere.(6)

IX-B-5-b-ii. Texture Effects

Separation of the effect of texture on FCP rate from that of microstructure can be tricky. This is in part due to the increased intensity of texture which is typically found in equiaxed microstructures when compared to acicular microstructures. The reason for this is related to the randomizing effect of the nucleation and growth or martensitic β-phase decomposition reactions. Since there are twelve variants of the α/β orientation relation, the β-phase decomposition products tend to exhibit a relatively random texture which reflects a nearly random population of these twelve variants.

Since examination of microstructure effects on FCP rate should be conducted under conditions of constant texture, comparison of FCP rates in RA or MA material with those in BA or BQ material is almost certainly complicated by variations in texture. Such complications may account for the apparent variability in FCP rates in the same microstructure. This is particularly true for $\alpha+\beta$ microstructures which contain equiaxed primary α which is most prone to texture. Further, since texture also affects modulus and yield strength, variations in texture lead to changes in other factors such as crack opening displacement (COD) and plastic zone size (r_p). Thus variations in texture complicates the design of FCP experiments which permit a fair assessment of microstructure effects.

In view of the above complications Bowen(41) has attempted to assess the intrinsic effect of texture on FCP in Ti-64. In order to minimize microstructure effects he has used $\alpha+\beta$ worked material with a single microstructure and with a strong transverse basal texture. He has compared the FCP rate for all six possible orientations in a directionally worked product. He has found that the FCP rate in the Paris Law regime exhibits different exponents, m, for different crack growth directions. Where the FCP rate is proportional to $(\Delta K)^m$ the corresponding m values are shown in Table IX-B-11. The orientation designations are shown in Figure IX-B-8. From these experiments Bowen has concluded that texture affects the symmetry of the plastic flow in the crack tip region. When flow is symmetrical the m values are low. When flow is asymmetric the m values are high. He also has shown that the crack plane is normal to the stress axis when the local orientation permits.

More recently another study(20) of the effect of texture on FCP rate has been reported. This study shows that for specimens of Ti-64, the FCP rate was approximately 5-6 times faster when the loading direction was parallel to <0001> so that the crack was growing along the basal plane, compared to samples rotated 90° so that the crack growth direction was

Table IX-B-11. Fatigue Crack Growth Exponents for Textured Ti-64

Test Piece Orientation (See Figure IX-B-8)	m value
LS	2.7
LT	4.1
SL	2.4
ST	3.6
TS	2.5
TL	3.1

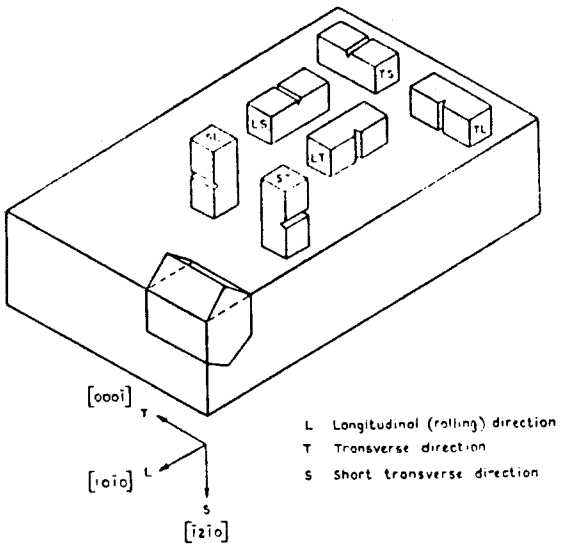


Fig. IX-B-8

parallel to <0001>. A similar but much smaller effect also was observed for textured Ti-6246, but in this alloy the differences in FCP rate were about a factor of 2-3. In the same study, textured ELI (extra low interstitial) Ti-64 was also tested. In this material there was essentially no difference in FCP rate in the two orientations. One possible explanation for this is the significant increase in propensity for twinning in the ELI material compared to normal interstitial material. The twinning alters the flow characteristics in the crack tip plastic zone which might cause the FCP rate to slow down in the orientation where cracking is along $<0001>_\alpha$. These data also show that texture does have an intrinsic effect on FCP rate but they do not provide information regarding the relative FCP rates in textured and random material. It does not necessarily follow that the lowest FCP rate in textured will be lower than the corresponding rate for random material. This may be particularly true at low FCP rates where the faceted mode of crack growth occurs. Since the facet plane is near $(0001)_\alpha$ random material should lead to more frequent reorientation of the crack front. The situation for FCP in textured material when $(0001)_\alpha$ is parallel to the loading axis is not clear since there has not been combined FCP rate measurements and fractographic examination for these circumstances. At any rate it is clear that further investigation of FCP rate and attendant fracture mode in materials with varying controlled texture and microstructure is needed.

IX-B-6. The Effect of Microstructure on Creep of α+β Ti Alloys

Ti alloys are commonly used up to 535°C in gas turbine engine applications. At these temperatures creep is frequently the limiting factor. As a result several α+β alloys are used nearly exclusively at elevated temperatures because they have excellent creep resistance and good, or at least acceptable, metallurgical stability during long time, elevated temperature service. The most common of these alloys is Ti-6Al-2Sn-4Zr-2Mo(+Si). Since essentially all of the Ti-6242 alloy produced in the U.S. now contains between .05 and .10wt%Si the designation Ti-6242 implies the Si bearing version of this alloy. The role of Si will be discussed further below.

IX-B-6-a. The Creep Behavior of α+β Ti Alloys

In general, the interaction between applied stress, temperature and creep rate is not well understood. As a result the time and temperature effects are combined empirically in terms of the Larson-Miller parameter.[42] This parameter is given by the following relationship:

$$P = (T + 460)\ (C + \log t) \times 10^{-3}\ .$$

Here T is temperature in °F, t is time in hours and C is a constant taken to be 20. Creep data is often presented as plots of applied stress versus P for a given total creep strain or for stress rupture. Such plots yield families of curves which bend downward at higher P values. In the open literature there is very limited creep data available for Ti alloys. If, in addition, the available data are restricted to include only those which pertain to controlled microstructure, the amount of data becomes almost vanishingly small. Nevertheless available data shows that Ti-6Al-4V has acceptable creep resistance at temperatures up to and including 400°C. Further the available data shows that there is essentially no difference between the MA and STA conditions with respect to creep. Above this temperature Ti-6242 is decidedly superior. Even in the 350°C - 400°C range Ti-6242 in the conventionally $\alpha+\beta$ forged condition is ~3 Larson Miller parameters better than Ti-64. Ti-6242 is 4.5-5 parameters better than Ti-64 in the β-forged condition. These data show that, for high creep strength applications, Ti-6242 is significantly better. As a result most of the available creep data pertains to this alloy. The balance of this discussion will focus on the relationship between microstructure, alloy composition and creep behavior.

The creep behavior of Ti-6242 is strongly dependent on microstructure.[43,44] In general, β-processed material has better creep resistance than $\alpha+\beta$ processed material. However, there are numerous combinations of heat treatment and processing each of which lead to differences in creep rate. For example, $\alpha+\beta$ solution treatment following β forging appears to consistently improve the creep strength in comparison to forging well above the transus. The origins of these subtle differences must lie in small microstructural differences although at present detailed microstructural characterization has not been performed on each of these processing conditions. Some possible causes of the differences will be discussed in the section on creep mechanism.

The effect of chemistry on creep rate has also been evaluated.[18,45,46,47] These studies have found that Si significantly increases the creep strength of $\alpha+\beta$ Ti alloys of the Ti-6242 type. In an alloy of base composition

Ti-6Al-2Sn-2Zr-1Mo, the creep rate fell continuously over a wide range of applied stress with increasing Si content up to 0.5wt%. Increasing the Mo content from 0 to 2.0wt% also reduced the creep rate. However, when both the Si and Mo contents were varied simultaneously the optimum creep strength was observed at 1% Mo and 0.5% Si. Thus complex interaction effects exist with respect to the varying alloying elements. The same study also showed that increasing Fe content is deleterious to creep resistance. This also has been found empirically in Ti-6242. As a result the high strength grades of Ti-6242 have specified maximum Fe contents. These maximum contents vary with specification, but typically lie in the range 0.05 to 0.1wt% Fe. In any evaluation of chemistry effects it is imperative that microstructure be held constant. This requirement places limitations on the range over which the chemistry can be varied. This is because changes in Fe, Mo or Si content also change the equilibrium volume fraction of β-phase and, possibly more importantly, change the transformation kinetics to that the Widmanstatten α plate and packet sizes vary simultaneously.

IX-B-6-b. The Mechanism of Creep

The mechanism of creep in Ti alloys has not been the subject of extensive investigation at least by comparison to the Ni based superalloys. Moreover, the maximum operating temperature for Ti is low on a homologous scale, being $< .4T_m$. Thus pertinence of the mechanisms of creep which have been extensively investigated for service temperatures $> .6T_m$ is not obvious in the case of α+β Ti alloys.

Investigations of creep mechanisms[45,46,48] have shown that the principal contribution to creep strain is the motion of dislocations, called dislocation creep. In addition there is a small contribution to the creep strain from boundary sliding.[45] The boundaries which show the greatest tendency for sliding are the prior β boundaries. However, the rate controlling creep mechanism is dislocation creep.

The two major factors which reduce creep rate are β-forging to produce Widmanstatten α+β structures and additions of Si. A less important factor which improves creep resistance is the addition of Mo.

It has been shown in Ti alloys that Si forms atmospheres around moving dislocations in the α-phase during creep. These atmospheres retard the motion of the dislocations and, as a result, reduce the creep rate. Thus the beneficial effect of Si additions on creep rate is due to reductions in the mobility of the dislocations which give rise to the creep strain.

The better creep strength in Widmanstatten microstructures than in equiaxed microstructures is less well understood. However, as described earlier, the Widmanstatten α+β microstructures consist of parallel plates of α-phase separated by thin regions of β-phase.

In addition each α/β interface contains a layer of interface phase. During creep by a dislocation mechanism the dislocations must pass from one Widmanstatten α plate to the next in order to move over significant distances. In Widmanstatten microstructures this requires that the dislocations pass through the β-phase regions. Since the β-phase has a different crystal structure this requires significant adjustments in the detailed nature of the displacement field surrounding the dislocation core. These readjustments also impede the motion of the dislocations and this also reduces the creep rate. By comparison equiaxed α+β microstructures have mostly α/α grain boundaries. The transfer of dislocations across these boundaries does not require such extensive adjustments and therefore should be significantly easier.

The additions of Mo improve the creep resistance by increasing the β-phase volume fraction. This insures that there is β-phase between each of the Widmanstatten α plates. In addition it has been shown that Mo additions raise the athermal component of the flow stress.[47] This apparently is due to solid solution strengthening of the β-phase. Elevated temperature solid solution strengthening is greater from low diffusivity solutes. Thus Mo is much more beneficial than Fe.

It also appears that there is an optimum β-phase volume fraction necessary to obtain the best creep resistance. This appears to be ~5 volume %. Lower β-phase volume fractions result in wider β-regions so that the regions can deform by dislocation creep. Since the Si is much more soluble in the β-phase it does not tend to form atmospheres around

dislocations. Thus the β-phase regions should have a lower resistance to dislocation creep. If they are very thin, plastic constraint from the adjacent α-phase plates retards the creep deformation. This description of the effect of β-phase volume fraction, while somewhat speculative, does account for the apparent maximum creep strength at a small, intermediate β-phase volume fraction.

IX-B-7. The Physical Properties of Ti Alloys

The physical properties of Ti alloys which are of interest in fusion reactor applications include density, electrical resistivity, thermal expansion, thermal conductivity and elastic moduli. These properties vary appreciably between the three classes of alloys (α, α+β and β) but the variations are much smaller within each class of alloy. In addition, the modulus of α and α+β alloys can vary by as much as ~35% when texture is present. Some selected physical property data are shown in Table IX-B-12.

The high electrical resistivities of these alloys are a positive factor in tokamak reactor design. Such high values will tend to reduce the generation of eddy currents as the plasma current is ramped up and down.

The relatively low thermal conductivity is a disadvantage because of the thermal gradients which can be set up. In fact, titanium has a thermal conductivity only slightly better than stainless steel in this regard. The lower Young's modulus and thermal expansion coefficient (compared to steel) counter the low thermal conductivity such that the thermal stresses generated are less than in steel.

Overall, the physical properties of Ti alloys are neither extremely good nor bad for tokamak operation.

IX-B-8. Titanium Industry and Fabrication Techniques

IX-B-8-a. The Titanium Industry

The U.S. Ti industry achieved commercially viable status about 20 years ago. Today the industry consists of two major fully integrated producers plus a number of other producers which melt alloys and fabricate both semi-finished products such as sheet bar and billet and finished products such as sheet, rod, bar, tube and plate. The combined U.S. titanium production in 1977 was approximately 24,000 tonnes and is

Table IX-B-12. Selected Physical Properties of Three $\alpha+\beta$ Ti Alloys at Room Temperature

Property	Alloy → Ti-64	Ti-6242	Ti-6246
Young's Modulus (psi)	16.5×10^6	16.5×10^6	16.5×10^6
(MN/m^2)	114×10^3	114×10^3	114×10^3
Electrical Resistivity ($\mu\Omega$-cm)	171 (at R.T) 187 (at 425°C)	191 (at R.T.) 199 (at 425°C)	
Thermal Conductivity (watt/cm°C)	0.073 (at R.T.) 0.118 (at 425°C)	0.061 (at R.T.)	0.071 (at R.T.) 0.109 (at 315°C) 0.135 (at 450°C)
Thermal Expansion ($x10^{-6}$ $°C^{-1}$)	8.8	9.9	9.4 (at R.T.)
Density (gms/cm^3)	4.44	4.55	4.66

anticipated to be ~27,000 tonnes in 1978. Of this between 25 and 30% is produced for commercial applications in unalloyed form. The remainder is produced as alloyed material for high strength applications in gas turbine engines, commercial and military fixed wing aircraft and in helicopters.

The increasing usage of Ti alloys in various types of high performance applications reflects the increasing recognition of the fact that Ti alloys exhibit good fabricability, excellent specific strength (strength/density), excellent creep resistance up to 1000°F (535°C), outstanding fatigue strength and superior corrosion resistance. These factors combine to make Ti alloys attractive for applications where total system life costs overwhelm the higher initial costs.

In addition there is emerging a significant amount of new fabrication technology for Ti alloys. This new technology utilizes some of the unique properties of Ti alloys in ways which permit more cost effective production of complex Ti components. The result of this new technology has been to improve the initial cost competitiveness of Ti alloys. Some of the fabrication techniques will be described below.

IX-B-8-b. Current Fabrication Techniques

The fabrication of sheet gage components from Ti alloys such as Ti-6Al-4V has been possible for a long time but it has also been costly. The high costs are due to two factors. First, the high strength of the alloys requires high press, or drop hammer, capacities. Second, the relatively low modulus and high yield stress results in large amounts of elastic deformation which lead to large "spring-back" strains. Thus cold formed parts required subsequent hot sizing to offset this spring-back problem.

Over a decade ago $\alpha+\beta$ Ti alloys were shown to exhibit microstructural superplasticity.[49-51] This superplasticity is derived from the stable, fine-grained microstructure which is typical of Ti alloy sheet. Superplasticity is manifested as a high strain rate sensitivity of the flow stress. This tends to stabilize regions such as diffuse necks against plastic instability and permits large strains to be achieved without fracture. The flow stress is expressed as

$$\sigma = \kappa \dot{\varepsilon}^{m} ,$$

where κ is a material parameter which depends on test temperature and m is the strain rate sensitivity exponent. Ti alloys in the equiaxed $\alpha+\beta$ condition typically exhibit m values in the range 0.6 - 0.9. Such m values permit elongations of several hundred percent. Moreover, superplastic forming is performed at elevated temperatures, typically 1700°F (925°C) and very low pressures, typically 30-100 psi (0.21 → 0.69 MN/m^2). As a result, there is essentially no elastic strain and, therefore, no springback. An additionally attractive feature of superplastic forming is that it can be done with a single die rather than a matching die set. The metal is essentially "blown" into the die cavity with a low pressure of inert gas such as argon. This technique has been successfully used for fabrication of large, complex-shaped sheet metal parts for the aircraft industry. It should be readily adaptable to the relatively simple corrugated structure of the first wall of NUWMAK.

Ti alloys of the type being incorporated into NUWMAK are readily welded using GTA techniques. Moreover, the growth of the commercial applications area has promoted development of reliable and reasonably economical automatic tube welding equipment. Thus the extensive tube structure in the blanket can be fabricated without any significant technique development. Likewise, the corrugated sheet structure of the first wall can be superplastically formed in symmetrical sections and then welded together using GTA or plasma arc techniques. Based on aerospace industry experience, the superplastically formed sections will have unusually good dimensional reproducibility. This will minimize the fit-up problems both from a joint make-up standpoint and from a subsequent residual stress standpoint.

IX-B-9. Corrosion of Ti in Liquid Metals

IX-B-9-a. Introduction

The corrosion of metals and alloys by liquid metals generally follows the pattern of the formation of metallic alloys. The solid structural materials either dissolve, form inter-metallic compounds or both. In any case, simple solution of the solid is a necessary precursor of the reaction. In liquid alkali metals, solubility is often very low and so isothermal equilibrium can easily be attained when further dissolution ceases. Continued corrosion will then occur only if the equilibrium is disturbed, by circulation of the liquid or by temperature gradients for example. It should be noted that the NUWMAK near isothermal blanket system minimizes both of these by its inherent temperature stability and the slow circulation of the Li-Pb eutectic.

The solution process may occur uniformly or it may be localized, the latter being potentially much more damaging. Local attack implies a preferential dissolution and this can take two forms:

a) Leaching - one component of an alloy is preferentially dissolved. An important example is the leaching of nickel from stainless steels by molten lithium or bismuth, sometimes to the extent that voids are left in the steel.

b) Intergranular attack. The liquid penetrates along grain boundaries in the solid, opening up cracks. This is because alloying elements in the alloy may be concentrated at a grain boundary and are then selectively dissolved, or because of the development at the junction of a grain boundary and the surface, of a low dihedral angle to satisfy surface energy relationships. The crack can then grow with a decrease in surface energy. When this is accompanied by stress, catastrophic failure can occur, a classic example being the catastrophic cracking of brass tubes by mercury.

In complex systems using liquid metals, mass transfer by the dissolution mechanism may occur driven by temperature or chemical gradients. Since the solubility of the solid is temperature dependent (often decreasing exponentially with temperature) the solid can dissolve in high temperature regions and reprecipitate in low temperature regions. In cases where dissimilar metals (including different alloy compositions of the same basic metal system) are in contact with the liquid, a similar mass transfer

can occur driven by the different chemical activities of the solute elements in the different alloys (i.e., a chemical activity gradient driving the transport via the liquid metal).

Important examples of chemical gradient mass transfer apply in the cases of oxygen, nitrogen, carbon and hydrogen. These are often present in liquid metals due to leakages or to impurities left after construction. In the case of hydrogen, the fusion system itself generates both tritium in the blanket and hydrogen in all parts due to (n,p) reactions. All these elements will distribute themselves in the various solid and liquid materials so as to minimize the energy of the system. In the case of hydrogen and its isotopes the tritium removal process prevents the system from approaching equilibrium. However, redistribution of the elements can occur and such elements (N,O,C) are sources of embrittlement in titanium and other structural alloys.

Finally, it should be noted that all these processes and particularly the primary one of dissolution are kinetically controlled. The most general approach to corrosion prevention has been to induce a drastic slowing down of these kinetics by either controlling the temperature or interposing diffusion barriers. In the particular case of the NUWMAK blanket, the low temperature already limits many of the possible reactions to such slow rates that they may be neglected. In addition, the usual techniques of interposing oxide and nitride layers on the surface readily apply to titanium alloys naturally, so that the dissolution processes will rarely approach equilibrium.

IX-B-9-b. The Solubility of Tritium and Its Alloys in Liquid Lithium and Lead

From the point of view of compatibility titanium is a preferred material for the containment of liquid lithium because of its very low solubility, an order of magnitude lower even than iron and chromium and comparable with Nb and Mo.

The solubility data for several metals, including titanium, have been reviewed by Cleary, et al.,[52] and their summary graph is shown in Figure IX-B-9. Also included are the best recent data from both U.S. workers[53]

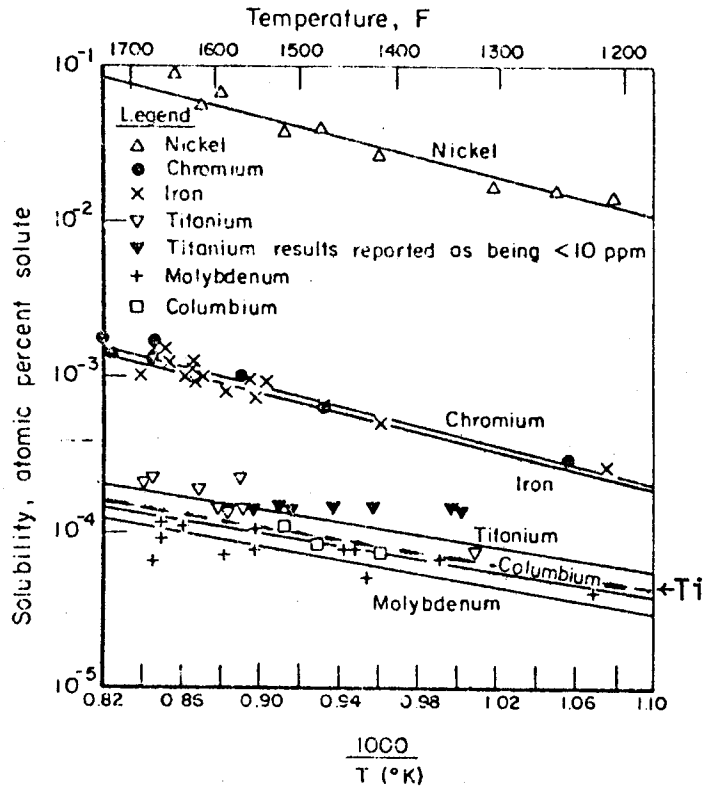


Fig. IX-B-9

Solubility for several metals in liquid lithium from ref. 52. The dashed line is for recent results on titanium in refs. 53 and 54.

and Russian workers[54] which are in excellent agreement. It is clear that titanium is almost as insoluble as molybdenum in pure lithium.

The kinetics of titanium dissolution in pure lithium are so slow that experiments show little or no attack even at temperatures as high as 800°C[55] and the presence of up to 2000 ppm of oxygen in the titanium did not affect this rate. The evidence therefore indicates that in the temperature range of NUWMAK no difficulty should be experienced from corrosion by liquid lithium.[56,57]

Liquid lead is a much more aggressive corrodent than the alkali metals. The corrosion is usually by a straightforward dissolution reaction. The existence of the stable intermetallic[58] compound Ti_4Pb which remains solid up to 1200°C suggests that a surface reaction may occur between titanium and lead. No data on the solubility of titanium in liquid lead are available in the literature.

Short term corrosion tests have been carried out at 814°C - 1000°C.[59,60] In this temperature range lead attacks titanium at a rate of 440 mils/yr (at 1000°C) principally by pitting. It is difficult to evaluate these experiments since the resistance to corrosion is almost certainly due to oxide protection. Where cracking of the oxide occurs, pitting corrosion will no doubt occur by direct dissolution of the metal. The process is therefore strongly dependent on the oxygen contents in the Pb which is generally not reported. Applied stresses could be critical for corrosion under such conditions.

Provided an oxide or nitride layer is maintained, corrosion will probably not occur by dissolution into liquid lead either in the blanket where the lead is mixed with lithium or in the intertube space where pure lead is used. The maintenance of a small concentration of nitrogen in the liquid metals would probably be helpful in maintaining the resistance of the nitride coating.

IX-B-9-c. Distribution of Oxygen, Nitrogen, and Carbon in Ti Alloys and Li-Pb Liquid

The free energies of formation of oxides relevant to the titanium alloys and liquid metals in NUWMAK are shown in Fig. IX-B-10. The titanium,

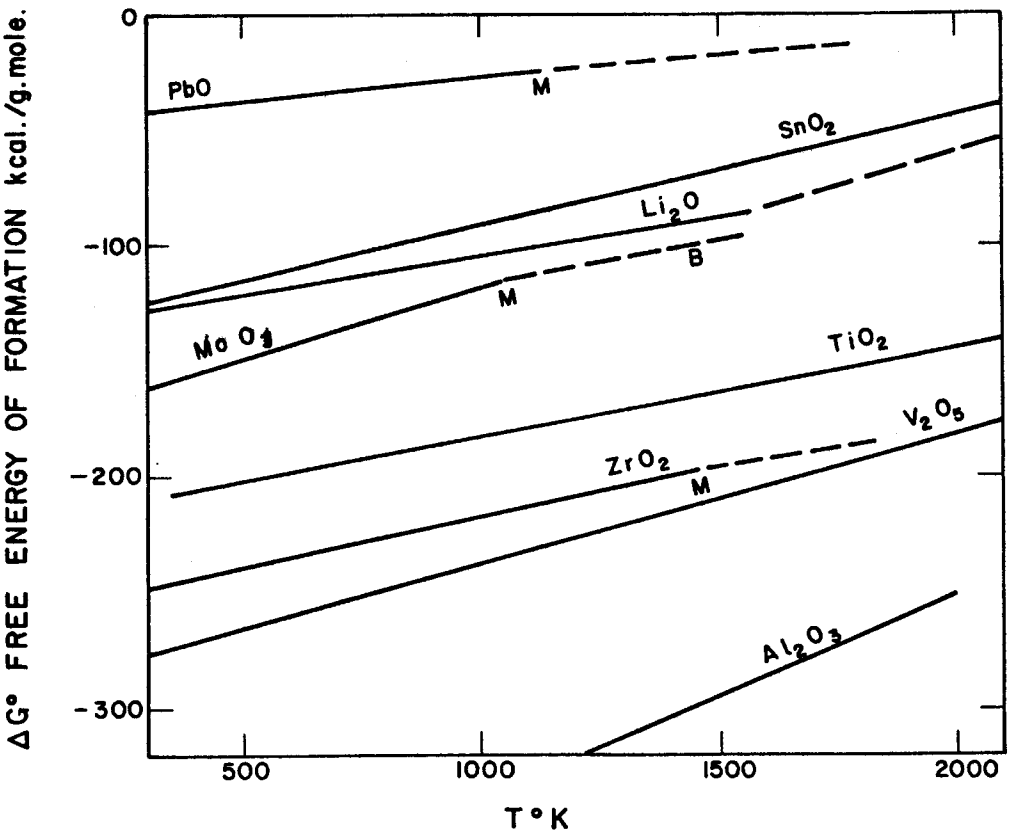


Fig. IX-B-10. The free energy of formation of metal oxides as a function of temperature. (Data from ref. 61)

vanadium, zirconium, and aluminum oxides are far more stable than the lithium or lead oxides. This means that most of the oxygen in the system will end up combining with the former metals (an even more stable form of titanium oxide Ti_3O_5 exists and it is off the bottom of the graph entirely, meaning that it is even more stable than Al_2O_3).

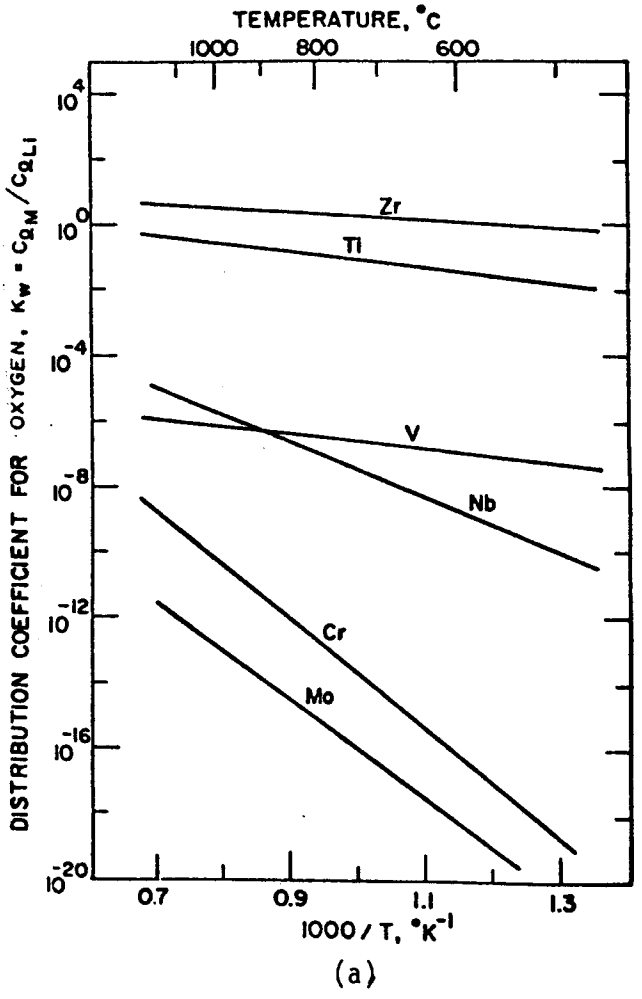
However, low free energy plots of the oxides do not of themselves guarantee alloy stability. There is also the question of distribution of oxygen in solution in both liquid and solid phases which is distinct from compound free energy of formation. This is true even though large negative free energies are usually associated with low equilibrium solubilities.

The partition coefficient (the ratio of equilibrium oxygen solubilities in a pure solid metal and a pure liquid metal) can be readily calculated from the Nernst equation. This has been done for several metals (including titanium) in contact with liquid lithium.[62] The simplifying assumptions are that Henry's Law is obeyed by oxygen in solution in both solid and liquid metals and that the latter are insoluble in each other. The partition coefficient is then

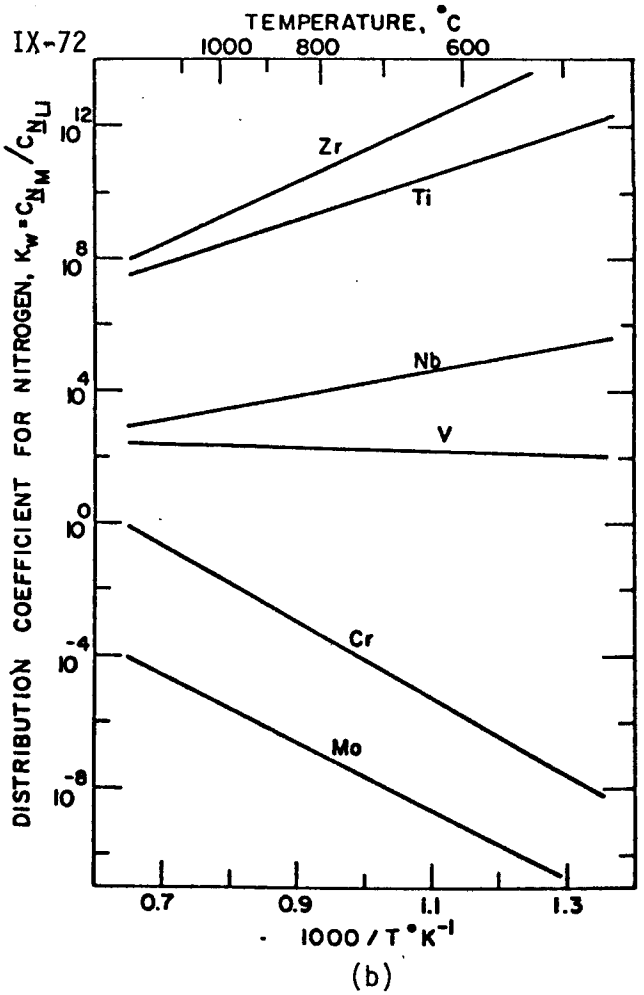
$$K = \frac{C_M}{C_{Li}} = \frac{C_M^0}{C_{Li}^0} \exp\left(\frac{\Delta G_{Li}^0 - \Delta G_M^0}{RT}\right)$$

where C_M and C_{Li} are the solubilities in solid metal and liquid lithium respectively in equilibrium with each other, and the superscript zero refers to the solubility of oxygen in the separated metal-oxygen and Li-oxygen systems. The free energies ΔG^0 are the free energies of formation of the stable oxides (as in Fig. IX-B-10).

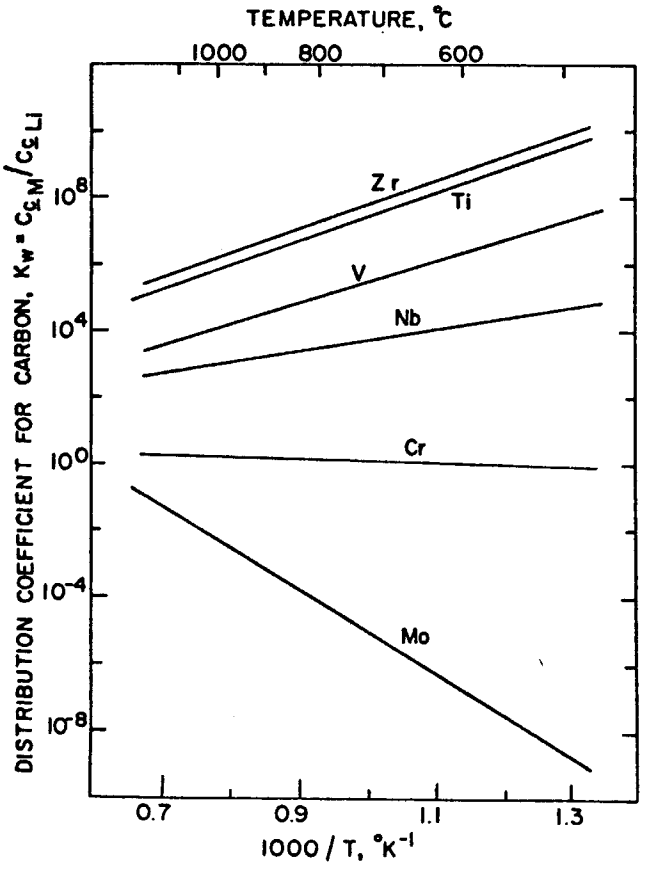
The partition coefficients from these calculations are shown in Figure IX-B-11. A value greater than unity implies that the oxygen is found in the solid metal at a higher equilibrium concentration than in liquid lithium. Titanium and lithium contain approximately equal concentrations (K~1) at higher temperatures but at the temperature of NUWMAK the ratio reaches $\sim 10^{-2}$ indicating that only 1/100 of the oxygen remains in the solid titanium. The other alloying elements all have much smaller K values. Aluminum however was not included in these



(a)



(b)



(c)

Fig. IX-B-11.

Temperature dependence of the equilibrium distribution coefficients K, for oxygen (a), nitrogen (b), and carbon (c), between the metals shown and lithium liquid. (Taken from ref. 62)

calculations and would probably come an order of magnitude higher because of the stability of Al_2O_3. This implies that aluminum could be internally oxidized inside the titanium alloy removing it from solution. However, since alumina could also form on the surface it might remain undissolved and prevent further pickup of oxygen from the lithium. The presence of hydrogen in the lithium in NUWMAK will further decrease the availability of dissolved oxygen. It is highly probably that oxygen absorption by the solid phase, including all the alloying elements will not occur.

Note however, that experiments[55] on titanium containing up to 2000 ppm of oxygen show no tendency for oxygen pickup by the lithium and the authors in that case argued[55] that oxygen is in fact being transferred to the titanium, but very slowly.

The calculations described above refer to pure lithium. The dilution of lithium by lead will probably not have a major effect on the oxygen partition--the higher affinity of the lithium for oxygen will probably still dominate. However since the activity of lithium in molten solution with lead is not known at the present time it is not possible to calculate the partition values.

Provided that the oxygen content is low in the titanium alloy (<50 ppm usually specified) no difficulty is anticipated from the extraction of the oxygen from the Ti into the liquid.

Calculations similar to those described above are available for partition of nitrogen and carbon also.[62] The calculated partition coefficients are shown in Figs. IX-B-11b and c.

For these elements the situation is reversed and both will segregate to the titanium alloy. One method of preventing this process is the reduction of nitrogen and carbon available in the lithium. The critical concentration for carbide or nitride formation is just,

$$\ell n\ C(crit) = \ell n\ C_M^0 - \ell n\ K \quad .$$

This is plotted for both carbide and nitride formation in Figures IX-B-12-a-b. In both cases the concentration of nitrogen in the lithium to prevent nitride formation is much less than 1 part per million, which demonstrates the impracticability of this approach. It is therefore inevitable that nitrogen and carbon pickup by the titanium will occur.

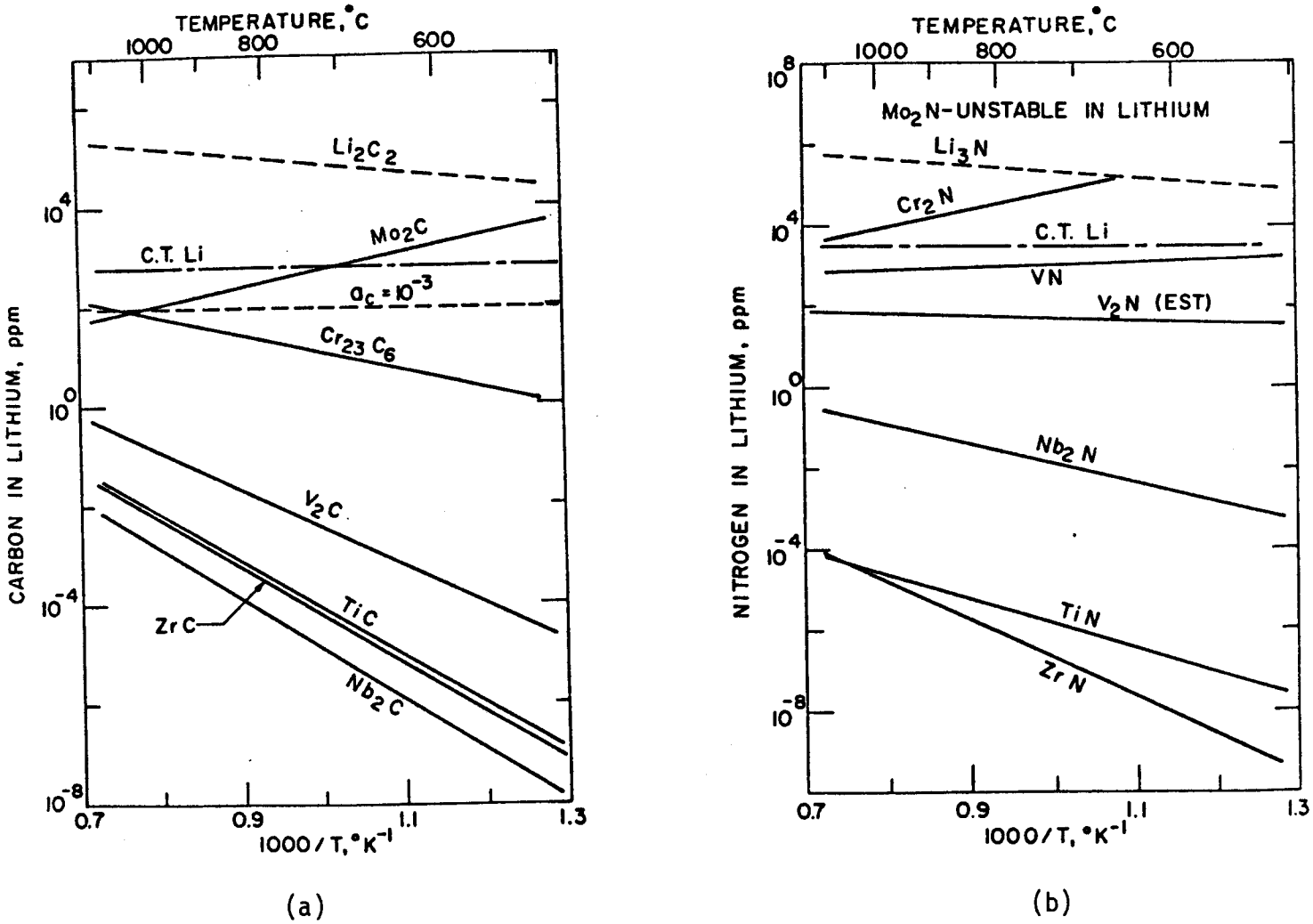


Fig. IX-B-12. Temperature dependence of the nitrogen concentrations in lithium at which certain metal carbides (a), and nitrides (b) are stable.

However since the titanium alloy in NUWMAK already has a nitride coating, there is a diffusion barrier to further nitride growth. In fact any cracks or local spalling of the nitride layer will be healed by the formation of new nitride.

The resistance of the titanium to corrosion then becomes a matter of adhesion of the nitride. There is ample evidence that nitriding produces an adherent layer,[63] however thermal cycling is inimical to adhesion. In this respect the isothermal nature of the NUWMAK blanket should provide ideal conditions for the maintenance of the nitride layer in service.

The presence of lead in the liquid phase will not alter these conclusions and will probably simply reduce the activity of the lithium a little, its chief influence being on solubility rather than on reactivity and partitioning of carbon and nitrogen.

In summary, oxygen, carbon, and nitrogen partitioning will probably not be a problem in NUWMAK. Oxygen will remain in the liquid phase and will be extracted from the titanium. Design data for oxygen free titanium alloys should therefore be used. Carbon and nitrogen will end up as titanium compounds and this will probably stabilize the nitride layer and maintain its integrity. Since the nitride barrier is important as a barrier to hydrogen diffusion this will be a valuable feature.

IX-B-10. Permeability and Solubility of Hydrogen Isotopes in Ti and Ti-6Al-4V.

One of the major concerns with the use of Ti alloys is the diffusion of T from the breeding zone into the coolant and subsequently out of the reactor. This concern is prompted by the known fact that hydrogen readily diffuses in pure Ti[64] and pure titanium has a large solubility for hydrogen at low temperatures.[65-68] However, recent experimental evidence shows that small amounts of oxide films can greatly inhibit the permeability of alpha titanium to hydrogen[69] and there is currently work being done on the use of TiN films to accomplish the same effect.[70] We will now proceed to examine the two major consequences of such diffusion:

a. loss of T_2 to coolant,

b. inventory of T_2 in Ti alloy structure.

IX-B-10-a. Model for Hydrogen Permeability

The geometrical model used to calculate the diffusion of hydrogen isotopes (from now on we will refer to tritium only) from the breeding material, through the double walled tubes containing the steam coolant, is shown in Figure IX-B-13. The tritium has to diffuse from the breeder material (solid Pb-Li alloy in NUWMAK), through successive layers of a 0.7 mm thick Ti alloy tube wall, 0.1 mm of Zr coating, 0.1 mm of liquid Pb and finally 0.7 mm of the inner Ti alloy tube before reaching the steam coolant at 300°C.

The permeation rate of tritium in nitrided Ti can be given as

$$R = P\ C\ p^{1/2}\ \frac{a}{t}$$

where

R = permeation rate (moles/hr)

P = permeation rate $[cm^3(STP)\text{-}mm/cm^2 \cdot hr \cdot torr^{1/2}]$

C = constant = $4.46 \times 10^{-5}\ \frac{mole}{cm^3(STP)}$

a = area, cm^2

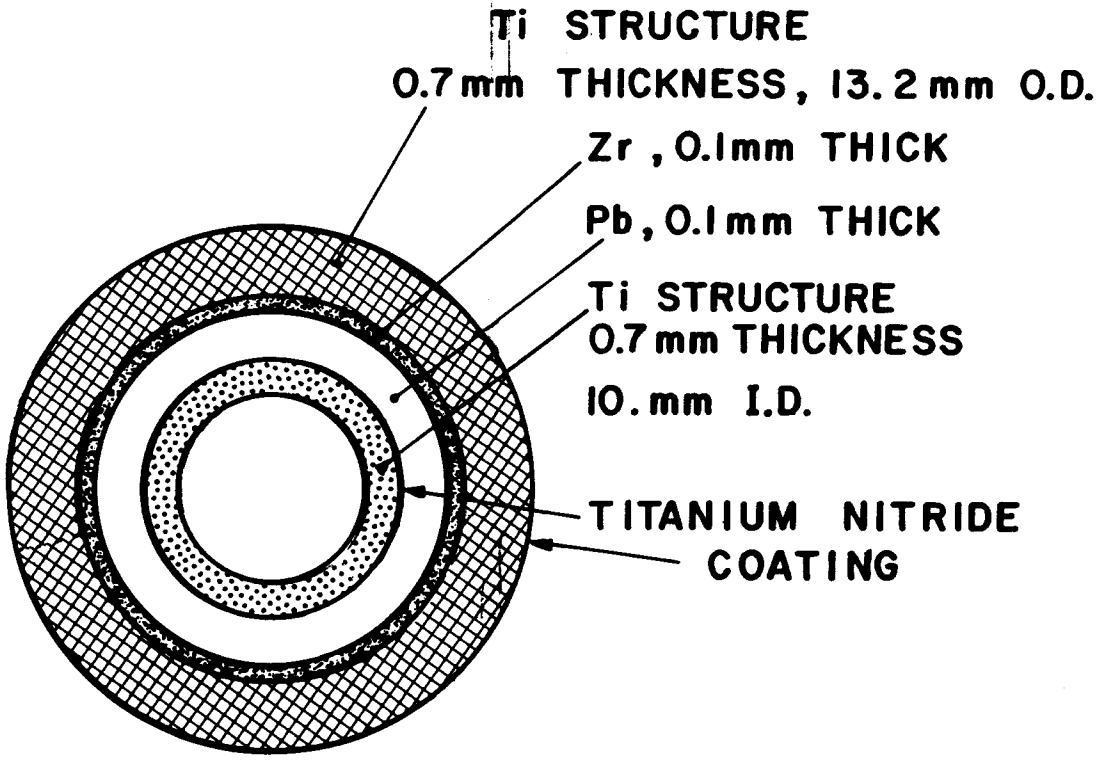
t = thickness, mm

The partial pressure difference of tritium across a membrane is

$$p = (p_0 - p_{eq})$$

FIGURE IX-B-13

GEOMETRIC MODEL FOR TRITIUM DIFFUSION INTO NUWMAK COOLANT



where p_0 = partial pressure in torr of the tritium on the upstream side (e.g., the blanket side), torr

p_{eq} = equilibrium tritium partial pressure on the downstream side (e.g., the coolant), torr.

The pressure on the downstream side of titanium coated with Zr should be taken as the pressure at the Ti-Zr interface when the tritium is in equilibrium with the Zr. That is,

$$P_{eq} = \frac{C_Z^2}{S^2} \quad \text{(torr)}$$

where C_Z = concentration of tritium in the Zr, atom fraction

S = solubility of tritium in Zr, atom fraction per $(\text{torr})^{1/2}$.

Thus, the permeation rate across the outer wall of the tubing of Figure IX-B-13 is,

$$R_{IN} = \frac{PCa_0}{t_0} \left(p_0 - \frac{C_Z^2}{S^2}\right)^{1/2} \quad \frac{\text{moles}}{\text{hr}} .$$

Assuming that the liquid Pb represents no barrier whatsoever to the diffusion of tritium, and the partial pressure of T_2 in the steam is zero, the permeation through the second wall is

$$R_{OUT} = \frac{PCa_1}{t_1} \frac{C_Z}{S} \left(\frac{\text{moles}}{\text{hr}}\right) .$$

The rate of change of tritium concentration in the Zr is:

$$\frac{dC_Z}{d\theta} = B(R_{IN} - R_{OUT}) \left(\frac{\text{moles}}{\text{hr}}\right) \quad \text{per cm of tube length}$$

where $B = \frac{N_T}{2\pi r \Delta t N_{Zr}}$

N_T is the number of tritium atoms per mole

N_{Zr} is the atomic density of Zr atoms

Δt is the thickness of the Zr layer .

The expression for the tritium concentration in zirconium is

$$\frac{dC_Z}{d\theta} = \frac{PCB}{t}\left[\left(p_0 - \frac{C_Z^2}{S^2}\right)^{1/2} a_0 - \frac{C_Z a_1}{S}\right] .$$

Integrating and changing variables to C_Z',

$$PC\theta B = t \int_{C_0}^{C_Z} \frac{dC_Z'}{\left[\left(p_0-\left(\frac{C_Z'}{S}\right)^2\right)^{1/2} a_0 - \frac{C_Z'}{S} a_1\right]}$$

For small times,

$$\left(\frac{C_Z'}{S}\right)^2 << p_0$$

$$\theta = \frac{t}{PCa_1B} \int_{C_0}^{C_Z} \frac{dC_Z'}{\left[\frac{a_0}{a_1} p_0^{1/2} - \frac{C_Z'}{S}\right]} .$$

Finally,

$$C_Z = S\, p_0^{1/2} \frac{a_0}{a_1}\left[1-\exp\left(\frac{-BPCa_1\theta}{tS}\right)\right] .$$

IX-B-10-b. Sample Calculation for NUWMAK

In order to get a feeling for whether tritium permeability through Ti tubing is a problem we will perform a simple calculation for the anticipated operating conditions of NUWMAK. The reader is cautioned that this calculation is illustrative only and the final conditions for NUWMAK may be slightly different.

Let us assume the following operating conditions.

1. Temperature of both inner and outer Ti alloy walls as well as in the Zr = 350°C.
2. Partial pressure of tritium in Pb-Li alloy is equal to 10^{-4} torr at 350°C.
3. . Outside area of Ti outer tube = 4.15 cm^2 per cm of length
   . Inside area of Ti inner tube = 3.14 cm^2 per cm of length
   . Areas normalized per 1 cm length of tube
   . There are 4300 m^2 of tube surface in the NUWMAK blanket.

4. Solubility of tritium in Zr at 350°C is,[67]

$$15.4 \frac{\text{tritium atoms}}{\text{atom Zr} \cdot \text{torr}^{1/2}}$$

for hydrogen partial pressures between 10^{-4} to 10^{-2} torr.

5. Permeability of tritium through Ti structure is taken from unpublished data by Maroni.[71]
6. Permeability data on alpha titanium,[64,69] on oxidized alpha-Ti,[69] Ti-64 alloy,[71a] nitrided Ti-64 alloy,[71] Ti-5621,[70,71a] and 316 steel are compared in Figure IX-B-14. The permeation rate is also expressed in grams of tritium per year for a total area of 4300 m^2 and a 1 mm thick wall.
7. The value of B is $\frac{6 \times 10^{23}}{2 \times \pi \times 0.58 \times 0.01 \times 4 \times 10^{22}} = 4.12 \times 10^2$

Using the data in Figure IX-B-14, we obtain at 10^{-4} torr a permeability of 3×10^{-5} $cm^3(STP) \cdot mm/cm^2 \cdot hr$. We can then calculate the concentration of tritium in the Zr getter as a function of time.

$$C_Z = \left(\frac{15.4 \text{ Tritium Atoms}}{\text{Zr Atom} \cdot \text{torr}^{1/2}}\right) \cdot \left(10^{-4} \text{torr}\right)^{1/2} \cdot \left(\frac{4.15 \text{ cm}^2}{3.08 \text{ cm}^2}\right) \cdot$$

$$\left\{1-\exp\left[-\left(\frac{4.12 \times 10^2 \text{ Trit. atoms}}{\text{Mole Tritium} \cdot \text{Zr atom}}\right) \cdot \left(\frac{3 \times 10^{-5} \text{cm}^3\text{(STP)} \cdot \text{mm}}{\text{cm}^2 \cdot \text{hr}}\right) \cdot \left(\frac{1}{0.7 \text{ mm}}\right)\left(\frac{1}{10^{-2} \text{torr}^{1/2}}\right)\right.\right.$$

$$\left.\left. \cdot \left(\frac{4.46 \times 10^{-5} \text{mole tritium}}{\text{cm}^3\text{(STP)}}\right) \cdot \left(3.08 \text{ cm}^2\right) \cdot \left(\frac{1}{15.4} \frac{\text{Tritium atom}}{\text{Zr atom torr}^{1/2}}\right) \cdot \theta \right] \right\}$$

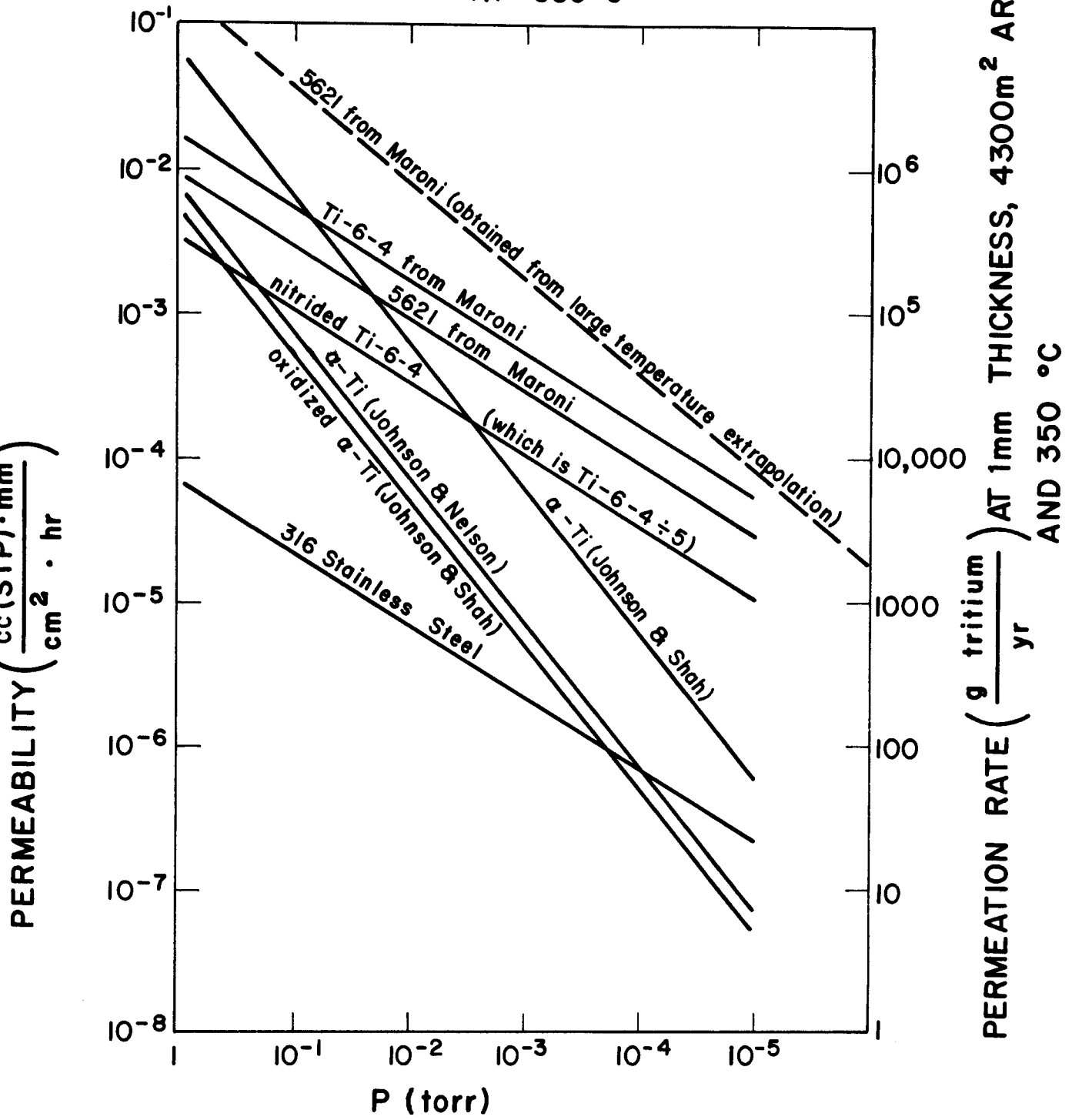
$$C_z = 0.21 \left[1-\exp(-1.58 \times 10^{-5} \theta)\right] .$$

After one year of operation

$$C_Z = 0.027 \quad \text{Tritium atom per Zr atom.}$$

From $R_{out} = \frac{PC_{a_1}}{t} \frac{C_Z}{S}$,

Figure IX-B-14 HYDROGEN PERMEATION RATE IN TITANIUM AT 350°C



$$= \frac{3 \times 10^{-3}\ cm^3(STP)\cdot mm}{cm^2\cdot hr\ torr^{1/2}} \times \frac{4.46 \times 10^{-5}\ mole}{cm^3(STP)} \times \frac{3.08\ cm^2/cm}{0.7\ mm}$$

$$\times \frac{0.027\ atom\ T/atom\ Zr}{15.4\ Tritium\ atom/atom\ Zr\cdot torr^{1/2}}$$

$$= \frac{1.03 \times 10^{-9}\ mole}{cm\ hr} \times \frac{6g}{mole} \times \frac{8760\ hr}{yr} \times 1.04 \times 10^7\ cm$$

R_{out} = 564 g/yr at one year,

$R_{out} \cong$ 1060 g/yr at two years.

Note that these values correspond to the release rates at the end of the periods indicated. The total release rate would be the instantaneous rate integrated over time and hence would be less than indicated above. Depending on the lifetime of the tubes (i.e., 2 vs. 4 years) the maximum release of tritium into the NUWMAK cooling system would be less than 1000 grams per year ($\sim 10^7$ curies). This number of ~30,000 curies per day means that a water cleanup system is needed* but the leakage of T_2 should not have any significant impact on the tritium breeding ratio.

Finally, we need to calculate the tritium inventory in the structural material. If all of the Zr had the equilibrium value of T_2 in it, there would be a maximum 0.154 tritium atom per Zr atom. Assuming the area of the Zr is ~3.5 cm^2 per cm of length and that there are 1.04×10^7 cm of tube surface, then a 100 micron Zr layer yields 3.7×10^5 cm^3 or 2.4×10^6 g or 2.6×10^4 moles. This means 2040 moles of tritium or 12.2 kg of tritium. However, it takes some time to build up such a high concentration of tritium and the previous calculations show that it takes roughly 5 years to build up the saturation level. Hence after 1 year the amount of tritium in the Zr is about 2 kg. The value is considered to be a significant problem.

The amount of tritium in transit in the titanium was calculated by assuming the dynamic equilibrium produced by a 10^{-4} torr upstream driving

*A release of 1000 g/year into the 2.5×10^8 g of cooling water represents a 4 wt part per million increase in T_2 concentration per year.

pressure of tritium and a downstream value of 0 torr. This can be expressed[64] as a concentration of

$$C_{Ti} = + F \frac{1}{2\pi \ell D} \ell n \left(\frac{b}{a}\right)$$

where F is the flow rate of tritium through the Ti alloy, moles per second,
D is the diffusivity of tritium in Ti, cm^2/sec,
ℓ is the length of the tubes, cm,
a, b are the inner and outer radii of the tubes, cm.

For a permeability at 10^{-4} torr of 3×10^{-5} cm(STP) per cm^2-hr, the concentration in the Ti is

$$C_{Ti} = 3 \times 10^{-5} \times \frac{4.3 \times 10^{7} cm^2}{3600\ s/hr} \times \frac{mole}{22{,}400\ cm^3} \times \frac{1}{2\pi} \times \frac{1}{1 \times 10^{+7} cm} \times \frac{1}{8.03 \times 10^{-7} cm^2/s} \times \ell n\left(\frac{0.66}{0.59}\right)$$

$C_{Ti} = 3.6 \times 10^{-8}$ mole T_2 per cm^3 Ti

$C_{Ti} = 4.7 \times 10^{-8}$ g tritium/g titanium .

Since the weight of Ti in the blanket is 41 tonnes, this translates into about 2 g of tritium in transit in the tubing.

The background concentration is assumed to be that in equilibrium with the tritium partial pressure at the downstream surface of the titanium membrane. For the inner wall, this is assumed to be negligible. For the outer wall, the tritium partial pressure is that which is in equilibrium with the tritium concentration in the zirconium. The tritium concentration in titanium is given by the expression by Nagasaka, et al.:

$$C_{Ti} = p_{eq}^{1/2}(4.8 \times 10^{-5}) \exp(12600/RT) \ \frac{\text{atoms T}}{\text{atoms Ti}}$$

or

$$C_{Ti} = 1.26 p_{eq}^{1/2} \ \frac{\text{atoms T}}{\text{atoms Ti}}$$

at 623 K. The pressure in equilibrium with the tritium in zirconium is

$$p_{eq} = \frac{C_Z^2}{S^2} \quad ,$$

then

$$C_{Ti} = 1.26 \frac{C_Z}{S} = \frac{1.26}{15.4} C_Z \quad .$$

After one year

$$C_{Ti} = \frac{1.26 \times 0.027}{15.4} = 0.0022 \text{ tritium atom/titanium atom}$$

$$= 1.35 \times 10^{-4} \text{ gm T/gm Ti.}$$

The mass of titanium in the outer tubes is about 12.7 tonnes. The total inventory of tritium in the titanium structure is 1.7 kg.

In summary, this means that roughly 4 kg of tritium is tied up in the metallic blanket components after 1 year. While such a number is not large compared to the burnup of ∿80 kg/year, it may be a problem for accident analysis.

IX-B-11. Previous Radiation Damage Studies of Ti and Its Alloys

In contrast to the situation for stainless steels, there has been very little radiation damage work on the Ti system. This lack of data greatly hampers our analysis of the potential lifetime of Ti alloys and we are only able to infer such values based on meager information. We will not go into an extensive review of the data that is available because the testing conditions bear little resemblance to the NUWMAK environment. Therefore we will simply list what data we have been able to obtain up to the publication of this report, comment briefly on its significance for NUWMAK, and then outline where the current research efforts in this area are expected to make a contribution. We will discuss the neutron irradiations separate from the ion bombardment work.

II-B-11-a. Neutron Irradiation

A summary of the neutron irradiation studies conducted to data is given in Table IX-B-13. The first reported work was in 1956[72,73] and then there was a period of ~15 years before interest was again rekindled. The early work was conducted on commercial purity Ti at ~100°C to relatively low neutron fluences (0.5 to 6 x 10^{20} n/cm^2). This corresponds to roughly 0.03 to 0.4 dpa. The investigations revealed the traditional increase in yield strength and decrease in ductility.

In the early 1970's three studies[74-76] briefly investigated the high temperature (335 to 800°C) behavior of high purity Ti from 5 x 10^{20} to 3 x 10^{21} n/cm^2. This damage region is roughly 0.3 to 2 dpa. The studies were mainly microstructural in nature and revealed two surprising features.

1.) No void swelling was observed even though the irradiations were carried out at 0.3 to 0.55 T_m.

2.) Vacancy loops were found in contrast to the more traditional interstitial loop observations of that time.

The first Ti alloy work was carried out in the 1972 to 1973 period,[77-78] again at low temperatures (<70°C) and low neutron fluences (<10^{21} n/cm^2, <0.6 dpa). Again increases in yield strength and decreases in ductility were the observations.

Table IX-B-13 Summary of neutron irradiation studies on Ti and Ti alloys

Material	Fluence (n/cm^2)	Temperature (°C)	Main Results	Ref.
CPTi	$2.2\text{-}6.6\times10^{20}$ (Thermal)	90	increase in Y.S. (74%) decrease in elongation (53%) increase in resistivity (7.8%)	72
99.9 Ti	5.1×10^{19} (Fast)	100	increase in Y.S. (10-25% decrease in elongation (10%)	73
HP Ti	3×10^{21} (E>0.1 MeV)	450	dislocation loops, 200-1500 Å density 2.5×10^{5} cm^3 vacancy type, $\bar{b} = \frac{1}{3}\langle 11\bar{2}0\rangle$	74,75
HP Ti	5×10^{20} (E>0.1 MeV)	335 435 600 800	dislocations; no swelling	76
Ti-6Al-4V	$2\times10^{18}\text{-}1\times10^{21}$ (E>1.0 MeV)	67	increase in Y.S.; U.S. (40%) decrease in elongation (70%)	77
Ti-5Al-2.5Sn	2×10^{20} (E>1.0 MeV)	67	increase in Young's Modulus (11%) decrease in ductility (25%) increase in Y.S.(11%) increase in U.S. (6%) slight decrease in fatigue life	78
CPTi	1.3×10^{20} (E>1 MeV)	150	increase in resistivity (20%) increase in hardness (30%) dense black spot damage (60 Å) precipitation of solute atoms	79
CPTi	6.9×10^{18} 8.6×10^{18} 3.0×10^{19} (E>1 MeV)	100-150°C	increase in Y.S. (15-50% at 77°K, 100-500% at 600°K) dislocation loops, $\bar{b} = \frac{1}{3}\langle 11\bar{2}0\rangle$	80,81
Ti-6%Al-2%Sn-4%Zr-2%Mo-0.09%Si (Ti-62425)	3.7×10^{21} (E>0.1 MeV)	400	No significant microstructural changes Dense distribution of small dislocation loops No voids observed	82
Ti-6Al-4V	3.4×10^{21} (E>0.1 MeV)	450	Some beta phase observed in alpha structure No voids observed Increased hardness (18-36%)	83

More recently a group of Japanese scientists have irradiated commercial purity Ti at low temperatures (<150°C) and low fluences (<1.3 x 10^{20} n/cm^2). The microstructural observations were made and found not to be particularly different than previous work. There was an increase in yield strength again and some precipitation was observed.

Finally, there have been two recent neutron irradiation studies released on Ti-62425[82] and Ti-6Al-4V[83]. These samples were irradiated at roughly 3 x 10^{21} n/cm^2 (E>0.1 MeV) at 400-450°C. Such a radiation corresponds to ~2 dpa. No major microstructural effects (such as voids) were observed in either alloy. However some irradiation produced precipitation of beta phase was observed which probably accounts for the 18 to 36% increase in microhardness.

To sum up the above results we find that irradiation of Ti alloys to a few dpa (less than 1 month of NUWMAK irradiation) at temperatures equal to or above those in NUWMAK caused no significant dimensional or microstructural changes. Irradiation at lower temperatures than expected in NUWMAK to fluences (and damage levels) typical of less than one day in NUWMAK cause measurable increases in yield strength and a slight loss in ductility. Obviously, one cannot extrapolate such data with confidence to higher energy neutron or higher helium content irradiation conditions.

Before leaving this area, it should be mentioned that several alloys are currently being irradiated in the ORR and EBR-II reactors (see Table IX-14). Information in the 350-550°C, 3 x 10^{22} n/cm^2 (20 dpa) range will be very valuable in assessing the overall resistance of Ti to the formation of voids and the phase stability of the more complex alpha, beta, and alpha + beta alloys.

IX-B-11-b. Ion Irradiation Studies on Ti Alloys

The irradiation of Ti alloys with high energy heavy ions or high energy light ions is a relatively recent phenomenon (See Table IX-B-15). Starting from 1977, Ti-6Al-4V samples have been irradiated with 17.5 MeV copper ions[84] in the 250 to 450°C range and with both 2.4 MeV vanadium ions and 0.95 MeV helium in the 450-650°C range [85]. Both studies concentrated on the microstructure and both revealed the existence of nonequilibrium precipitates presumably of the coherent beta phase type.

Table IX-B-14

Summary of Current Irradiation Experiments
Being Conducted on Ti Alloys

Reactor	Alloy*	$T_{nominal}$ °C	Expected n/cm^2 (E>0.1 MeV)
ORR (MFE-1) (MFE-2)	Ti-6Al-4V Ti-6242S Ti-5621S Ti-38-6-44	450-600	$\sim 10^{21}$ to 10^{22}
EBR-II	Ti-6Al-4V Ti-6242S Ti-5621S Ti-38-6-44	370-550	3×10^{21} to 3×10^{22}

*Ti-6242S = Ti-6Al-2Sn-4Zr-2Mo-0.09Si
*Ti-5621S = Ti-5Al-6Sn-2Zr-1Mo-0.25Si
Ti-38-6-44 = Ti-3Al-8V-6Cr-4Mo-4Zr.

Table IX-B-15 Summary of ion-irradiation studies on Ti and Ti alloys

Material	Ion	Dose Rate (dpa/s)	Dose (dpa)	Nominal Temp. (°C)	Results	Ref.
Ti-6Al-4V	17.5 MeV Cu^{4+}	3×10^{-4}	1.5	250, 350, 450	Loop structure at all temperatures, coherent β-phase precipitate at 450°C	84
Ti-6Al-4V	2.4 MeV V^{+} 0.95 MeV ^{3}He	3×10^{-3}	3-25, 25 w/ 10:1 appm He:dpa	450, 550, 650	β-phase precipitate in all samples. Voids at 660°C for single-ion (0.07% swelling) voids at all temperatures for dual-ion (0.02% at 560, 0.6% at 620)	85
Ti-14.4Al	3.0 MeV Ni^{+}	2.2×10^{-3}	0.6 - 6.8	570-700	No swelling below 600°C Voids at all doses above 600°C; 0.6% swelling at 6.8 dpa γ'-Ti_3Al precipitate at sinks.	86
Ti-6Al-4V	16 MeV Proton	2.4×10^{-6}	0.35	325	Creep rate same order of magnitude as 20% CW 316 SS	87

No voids were observed up to 1.5 dpa at 250-450°C nor in the 450 and 550°C studies up to 25 dpa. However voids (~ volume change of 0.07%) were observed at 660°C, 25 dpa level in the case of single V ion irradiation. When the dual beam was used,voids were found in specimens irradiated to 25 dpa and 250 appm He at 541, 556 and 625°C. The swelling values in the dual ion irradiation were 0.02% at 556°C and 0.6% at 624°C. Note that all of these irradiation temperatures are far above the NUWMAK conditions but the corresponding irradiation temperature at lower damage rates might be ~450-500°C due to the "temperature shift" phenomenon characteristic of ion beam irradiation. The ANL study does point out that voids can be produced in Ti-6Al-4V if the temperature is high enough and if helium is simultaneously injected (generated).

A study by Erck et al., on Ti-14.4Al with single ion 3 MeV Ni bombardment revealed that up to 6.8 dpa (and below 600°C) no voids could be formed. However above 600°C voids could be formed and cause the solid to swell as much as 0.6% at 6.8 dpa. A significant amount of gamma prime Ti_3Al precipitates were observed in the alloy after irradiation. Finally, five wires of Ti-6Al-4V were bombarded at 325°C with 16 MeV protons at 2.4×10^{-6} dpa per sec[87] to 0.35 dpa. The creep rate of the Ti alloy was found to be essentially that of 20% CW 316 SS under these conditions. This result is significant in that one might have expected the anisotropic Ti alloy to yield higher creep rates.

The conclusions that one can draw from the ion studies are:

1.) Irradiation induced precipitation of beta phase in Ti-6Al-4V, and gamma prime phase in Ti-14.4Al may be expected.

2.) Voids will form in Ti alloys if irradiated above 600°C and above 7-25 dpa.

3.) Helium seems to stimulate the nucleation of voids in Ti alloys at somewhat lower temperatures.

IX-B-12. Displacement and Gas Production Cross Sections for Ti

The displacement cross sections for Ti have been calculated by H. Avci using the MODISS code.[88] We have used a threshold displacement energy of 19 eV and included the charged particle reactions. Table IX-B-16 lists the cross sections and compares them to several other CTR materials. The cross sections are plotted in Figure IX-B-15 compared to 316 SS, Al, and Nb. Note that the Ti displacement cross section is higher than all three of the other materials above ~ 3 MeV. This high dpa cross section is due to the large inelastic contribution above 3 MeV and a large contribution from the (n, 2n) reaction starting at ~ 12 MeV. This is illustrated in Figure IX-B-16 where the various contributions to the total displacement cross section are given. The values do not exactly agree with the reference set of cross sections because of the difference in ENDF-III (Figure IX-B-16) and ENDF-IV (Figure IX-B-15). However, the qualitative points are still the same. Elastic reactions dominate up to ~ 2 MeV wherein the inelastic events become important. Finally, the charged particle and (n,2n) reactions become important in the 10 - 12 MeV region.

The charged particle cross sections used for NUWMAK are given in Table IX-B-17. Note that the helium production cross section is ~ 40 millibarns at 14 MeV, a factor of 4 to 5 lower than stainless steel. However, when the alloy components of V and Al are added this difference becomes somewhat smaller.

Table IX-B-16

Displacement Cross Sections For Potential CTR Materials As Calculated by the MODISS Code[88].

Energy Group	Upper Energy - eV	Al	Fe	Ni	Cr	316 SS	Ta	W	Ti	Cu	Nb
1	1.4918(+7)	2605.	3058.	3245.	2773.	3029.	1043	898.2	3676.	3788.	1871.
2	1.3499(+7)	2526.	2884.	3094.	2706.	2877.	968.4	848.4	3536.	3653.	1736.
3	1.2214(+7)	2455.	2753.	2939.	2582.	2745.	907.2	804.0	3524.	3530.	1657.
4	1.1052(+7)	2315.	2606.	2794.	2441.	2599.	874.2	757.8	3324.	3402.	1603.
5	1.0000(+7)	2224.	2469.	2630.	2309.	2460.	810.	713.4	3224.	3223.	1537.
6	9.0484(+6)	2161.	2329.	2392.	2216.	2316.	742.8	661.2	3189.	3041.	1467.
7	8.1873(+6)	2174.	2203.	2247.	2146.	2198.	708.6	630.6	3126.	2861.	1409.
8	7.4082(+6)	2143.	2080.	2140.	2075.	2086.	654.6	601.8	3052.	2702.	1339.
9	6.7032(+6)	2099.	1960.	2045.	2005.	1978.	610.8	563.0	2962.	2578.	1249.
10	6.0653(+6)	2068.	1859.	1978.	1933.	1887.	573.6	528.1	2860.	2438.	1166.
11	5.4881(+6)	2039.	1772.	1844.	1877.	1800.	543.	492.7	2752.	2314.	1103.
12	4.9659(+6)	1956.	1691.	1689.	1814.	1713.	505.5	460.1	2593.	2194.	1037.
13	4.4933(+6)	1919.	1594.	1585.	1666.	1606.	464.4	430.3	2409.	2018.	957.0
14	4.0657(+6)	1948.	1509.	1472.	1599.	1521.	433.6	403.5	2264.	1847.	877.2
15	3.6788(+6)	1940.	1388.	1382.	1525.	1412.	414.7	379.6	2165.	1684.	814.2
16	3.3287(+6)	1860.	1372.	1234.	1476.	1374.	393.5	355.9	2058.	1545.	764.4
17	3.0199(+6)	1847.	1280.	1217.	1423.	1298.	372.3	335.0	1935.	1415.	710.4
18	2.7253(+6)	1951.	1286.	1084.	1383.	1279.	351.6	315.9	1795.	1292.	669.0
19	2.4660(+6)	1732.	1035.	904.5	1134.	1037.	306.7	278.5	1460.	1107.	600.9
20	1.8268(+6)	1543.	793.8	752.6	978.0	822.0	250.2	226.9	1236.	907.4	481.7
21	1.3534(+6)	1342.	557.6	668.3	677.4	592.4	189.2	194.2	888.4	832.4	419.6
22	1.0026(+6)	1316.	442.1	512.4	551.1	470.2	145.5	156.0	750.9	725.8	398.7
23	7.4274(+5)	1069.	317.5	391.0	454.5	351.0	116.6	119.2	561.8	619.0	364.4
24	5.5023(+5)	1059.	362.3	387.9	405.7	373.2	91.9	92.20	400.2	520.0	318.8
25	4.0762(+5)	713.8	288.2	349.6	227.4	284.6	74.06	72.96	255.4	421.7	273.7
26	3.0197(+5)	562.8	182.3	356.8	231.7	212.1	62.22	59.26	251.8	367.1	223.6
27	2.2371(+5)	575.8	217.5	299.2	230.8	229.7	50.92	49.07	175.0	295.9	176.6
28	1.6573(+5)	697.6	159.6	226.3	278.6	189.0	38.91	41.07	92.19	242.9	137.0
29	1.2277(+5)	449.4	122.9	147.5	169.3	134.2	29.85	32.36	127.8	185.0	71.20
30	6.7379(+4)	225.9	73.06	106.3	78.25	77.98	18.22	21.33	252.6	118.6	36.14
31	3.1828(+4)	18.53	88.48	168.6	22.42	86.20	9.78	12.98	536.3	103.6	18.61
32	1.5034(+4)	10.88	21.67	80.85	32.82	30.78	6.56	8.337	171.7	71.94	10.06
33	7.1017(+3)	8.075	11.00	31.30	40.88	18.81	5.11	6.152	24.70	19.91	7.684
34	3.3546(+3)	2.802	5.415	11.81	6.395	6.359	3.33	1.831	9.718	20.19	6.196
35	1.5846(+3)	1.381	4.901	6.457	1.371	4.452	5.37	1.901	2.542	2.209	6.121
36	7.4852(+2)	.7241	2.003	3.073	.1276	1.794	8.41	2.761	1.550	13.58	2.187
37	3.5358(+2)	.4371	.1214	.2373	.0	.1135	16.12	5.887	.6125	1.802	5.982
38	1.6702(+2)	.2193	.1536	.3381	.0	.1481	21.61	4.756	.5313	.4623	4.039
39	7.8893(+1)	.2302	.2218	.4884	.0	.2139	30.26	9.406	.7138	.5816	.3691
40	3.7267(+1)	.2598	.3210	.7076	.0	.3096	47.68	138.7	.9834	.7612	.6013
41	1.7603(+1)	.3026	.4677	1.027	.0	.4506	64.03	5.284	1.353	1.021	.1183
42	8.3153(+0)	.3666	.6831	1.492	.0	.6572	349.8	69.05	1.899	1.376	.1711
43	3.9279(+0)	.4596	.9890	2.181	.0	.9540	11.84	3.604	2.687	1.918	.2477
44	1.8554(+0)	.5948	1.445	3.171	.0	1.392	2.89	1.668	3.844	2.707	.3580
45	8.7643(-1)	.7922	2.119	4.615	.0	2.037	3.09	2.159	5.562	3.829	.5192
46	4.1399(-1)	2.613	8.100	18.01	.0	7.831	10.06	7.776	21.33	14.21	1.978

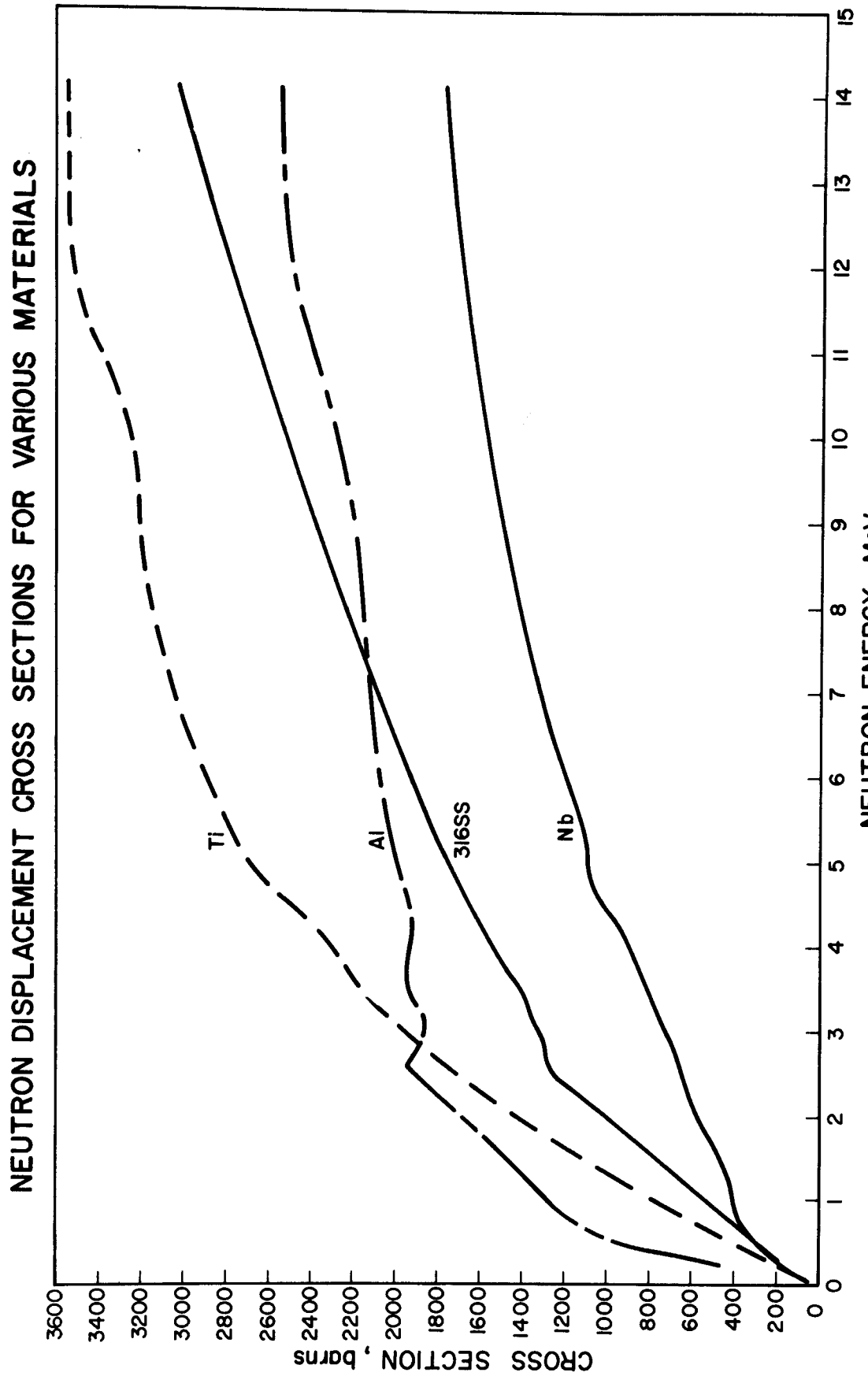


Figure IX-B-15

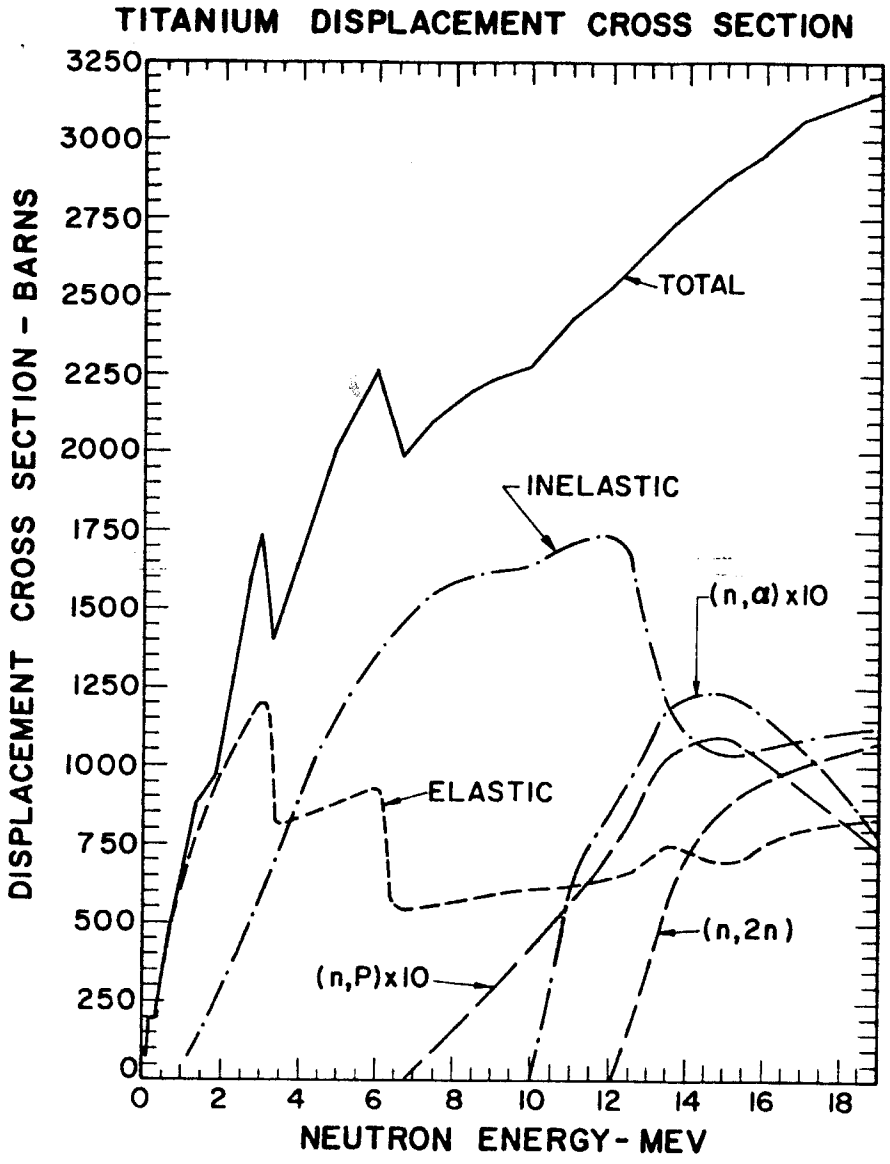


Figure IX-B-16

Contributions of various nuclear reactions to the displacement cross section of titanium[89]. Data differ slightly from Figure IX-B-15 because of different input reaction cross sections.

Table IX-B-17

Summary of Gas Production Cross Sections Used for NUWMAK

Millibarns

Upper Neutron Energy--MeV	(n, p)		(n, α)	
	Ti	Ti-64	Ti	Ti-64
14.92	63.5	68.9	43.8	50.7
13.50	61.0	66.4	40.0	47.9
12.21	43.0	49.2	27.2	35.3
11.05	34.1	41.4	18.9	26.4
10.00	25.6	33.9	13.2	19.5
9.05	18.1	26.2	10.0	14.5
8.19	11.4	18.9	7.1	9.6
7.41	5.5	12.2	4.1	5.2
6.70	1.8	7.6	1.5	1.8
6.06	0.002	9.6	0.001	0.08
5.49	0	3.2	0	0.01
4.97	-	2.1	-	-
4.49	-	1.1	-	-
4.07	-	0.8	-	-
3.68	-	0.7	-	-
3.33	-	0.2	-	-
3.02	-	0.08	-	-
2.73	-	0.01	-	-
2.47	-	-	-	-

References for Section IX-B

1. D. J. Maykuth, H. R. Ogden and R. I. Jaffee; DMIC Report 136A, Sept. 1960.

2. R. H. Olsen and A. L. Wingert; unpublished research, The Boeing Company, 1966.

2a. J. C. Williams; "Titanium Science and Technology," R. I. Jaffee and H. M. Burte, eds. Plenum Press, 1973, vol. 3, pg 1433.

2b. J. C. Williams; to be published in AIME Precipitation Symposium.

3. C. G. Rhodes and J. C. Williams; Met. Trans., 6A, 1670 (1975).

4. H. Margolin, E. Levine and M. Young; Met. Trans., 8A, 373 (1977).

5. R. B. Sparks and J. R. Long: AFML-TR-73-301, Feb. 1974.

6. J. C. Chesnutt, C. G. Rhodes and J. C. Williams; ASTM STP600, ASTM, Philadelphia, 1976, pg 99.

7. G. Lütjering; private communication, 1978.

8. See for example: S. S. Manson, "Thermal Stresses and Low Cycle Fatigue," McGraw-Hill, New York, 1966, pg 132 et seq.

9. S. M. Copley and J. C. Williams; "Alloy Design," J. Tien and G. Ansell, eds., Academic Press, 1976, pg 3.

10. F. R. Larson and A. Zarkades; "Properties of Textured Ti Alloys," MCIC-74-20, June, 1974.

11. J. C. Williams and M. J. Blackburn; Phys. Stat. Sol., 25, K1 (1968).

12. N. E. Paton, G. P. Rauscher and J. C. Williams; "Titanium Science and Technology," R. I. Jaffee and H. M. Burte, eds. Plenum Press, 1973, vol. 2, pg 1049.

13. J. C. Williams and M. J. Blackburn; ASM Quart Trans., 60, 373 (1967).

14. J. C. Williams, N. E. Paton, P. J. Stocker and H. L. Marcus; "Space Shuttle Materials," SAMPE, 1971, pg 643.

15. M. Young, E. Levine and H. Margolin; Met. Trans., 5, 1891 (1974).

16. J. C. Chesnutt, A. W. Thompson and J. C. Williams; AFML-TR-78-68.

17. R. R. Boyer and R. Bajoraitis; Boeing Document D6-48016, July 1978.

18. M. M. Allen; AFML TR-71-78, February 1976.

19. J. C. Williams; unpublished research, 1974.

20. A. W. Sommer and M. Creager; AFML-TR-76-222,January 1977.

21. J. C. Chesnutt and J. C. Williams; unpublished research, 1973.

22. A. W. Bowen; RAE TR 76150, 1976.

23. See for example: ref. 8.

24. B. Tomkins, Proceedings Storrs Conference on Corrosion Fatigue, 1971.

25. J. J. Lucas; "Titanium Science and Technology," R. I. Jaffee and H. M. Burte, eds, Plenum Press, 1973, pg 2081.

26. P. C. Kelly and J. C. Williams; unpublished research, 1977.

27. C. A. Stubbington and A. W. Bowen, J. Matls. Sci. 9, 941 (1974).

28. J. C. Chesnutt, A. W. Thompson and J. C. Williams; same as ref. 16.

29. G. R. Leverant, B. S. Langer, A. Yuen and S. W. Hopkins; submitted to Met. Trans.

30. R. A. Sprague, D. L. Ruckle and M. P. Smith; "Titanium Science and Technology," R. I. Jaffee and H. M. Burte, eds., Plenum Press 1973, pg 2069.

31. C. M. Gilmore and M. A. Imam, Report 3-B, The George Washington University, Washington, D.C., August 1976.

32. Appendix C in ref. 5.

33. A. W. Bowen; "Titanium Science and Technology," R.I. Jaffee and H. M. Burte, eds. Plenum Press, 1973, pg 1271.

34. D. Eylon and C. M. Pierce; Met. Trans., 7A, 111 (1976).

35. N. E. Paton, J. C. Williams, J. C. Chesnutt and A. W. Thompson; AGARD Conf. Proc. #185, Pg 4-1 (1976).

36. A. W. Thompson, J. C. Williams, J. D. Frandsen and J. C. Chesnutt; Proceedings of Moscow Ti Conference (in press).

37. G. R. Yoder, L. A. Cooley and T. W. Crooker; Met. Trans, 8A, 1737 (1977).

38. G. R. Yoder, L. A. Cooley and T. W. Crooker; Jl. Eng. Mat'ls and Tech., Pg. 313, October 1977.

39. P. C. Paris and F. Erdogan; Trans ASME, Series D, 85, 528 (1963).

40. See for example R. O. Ritchie, Metal Science, Aug/Sept (1977), Pg 368.

41. A. W. Bowen; Acta Met, 23, 1401 (1975).

42. F. R. Larson and J. Miller; Trans. ASME, 74, 765 (1952).

43. C. C. Chen; Wyman-Gordon Company Report RD-88-110, October 1977.

44. C. C. Chen; Syman-Gordon Company Report RD-77-111, October 1977.

45. N. E. Paton, M. W. Mahoney and J. C. Williams; Final Report SC532.8FR, July 1973.

46. M. W. Mahoney and N. E. Paton; Final Report SC5003.7FR, September 1975.

47. M. W. Mahoney, N. E. Paton, W. M. Parris and J. A. Hall, AFML-TR-77-56, May 1977.

48. N. E. Paton, M. W. Mahoney and J. C. Williams; Final Report SC564.7FR, August 1974.

49. W. A. Backofen, I. R. Turner and D. H. Avery, Trans. Quart. ASM, 57, 980 (1964).

50. D. H. Avery and W. A. Backofen, ibid 58 551 (1965).

51. D. H. Avery and W. A. Backofen; ibid, 59 359 (1966).

52. R.E. Cleary, S.S. Blecherman, J.E. Corliss, USAEC Report TIM-850 (Nov. 1965).

53. H.W. Leavenworth, R.E. Cleary, Act Met. 9 (1961) p. 519.

54. Y.F. Bychkov, A.N. Rozanov, V.B. Yakovleva, At. Energ. (USSR) 7 (1959) p. 531, Soviet Int. At. Energy 7 (1961) p. 987.

55. J.R. DiStefano, USAEC Report ORNL-3551 (March 1964).

56. W.E. Berry, "Corrosion in Nuclear Applications," J. Wiley, NY (1971) p. 298.

57. C. DeVries, "Corrosion in Liquid Metals," AIME Conf. eds. K. Draley, J.R. Weeks (1969) p. 251.

58. M. Hansen, "Constitution of Binary Alloys," McGraw-Hill (1958).

59. W.D. Wilkinson, E.W. Hoyt, H.V. Rhude, USAEC Report ANL 54 (Oct. 1955).

60. R. Parkman, O.C. Shephard, USAEC Report ORO-45 (June 11, 1951).

61. C.E. Wicks, F.E. Block, Bulletin 605, Bureau of Mines (1963).

62. D.L. Smith and K. Natesan, Nuclear Tech., 22 (1974) p. 392.

63. M. Konumar, O. Matsumoto, J. Less Common Metals, 52 (1977) p. 145.

64. D.L. Johnson and H.G. Nelson, Metallurgical Transactions 4, 569 (1973).

65. A.O. McQuillan, Proc. Royal Soc. London, Sev. A, 204, 309 (1950).

66. T.A. Giorgi and F. Ricca, Supplemento Al Nuovo Cimento, 5, 2, 472 (1967).

67. M. Nagasaka and T. Yamashina, J. Less Common Metals, 45, 53 (1976).

68. J.L. Waisman, G. Sines, and L.B. Robinson, Met. Trans., 4, 291 (1973).

69. K.K. Shah and D.L. Johnson, Hydrogen in Metals, (1974).

70. V. Maroni, D. Gruen of Argonne National Laboratory and C. O'Donnell University of Wisconsin, unpublished results.

71. V. Maroni, to be published.

71a. V.A. Maroni and E.H. Van Deventer, Proc. of the First Topical Meeting on Fusion Reactor Materials, January 29-31, 1979, Miami Beach FL.

72. C.A. Bruch, W.E. McHugh, R.W. Hockenbury, Journal of Metals, Trans AIME, 206, 1362 (1956).

73. M.J. Makin, F.J. Minter, Journal of the Institute of Metals, 85, 397 (1956).

74. J.L. Brimhall, G.L. Kulcinski, H.E. Kissinger, B. Mastel, Radiation Effects, 9, 273 (1971).

75. J.L. Brimhall, H.E. Kissinger, G.L. Kulcinski, USAEC Symp. Series 26, CONF-710601, 338 (1972).

76. Y. Adda, USAEC Symp. Series 26, CONF-710601, 31 (1972).

77. R.A. Hasse, C.B. Hartely, NASA-TM-X-2678 (1972).

78. C.E. deBogdan, NASA-TM-X-2883 (1973).

79. Y. Higashiguchi, H. Kayano. S. Yajima, Journal of Nuclear Science and Technology, 13 (8), 454 (1976).

80. Y. Higashiguchi, H. Kayano, Journal of Nuclear Science and Technology, 12 (5), 320 (1975).

81. H. Kayano, Y. Higashiguchi, S. Yajima, Journal of Nuclear Science and Technology, 14 (2), 117 (1977).

82. J.A. Sprague and F.A. Smidt, Jr., P. 67 in DOE/ET/0058/4 (1979).

83. S.M.L. Sastry, J.E. O'Neal and J.W. Davis, P. 72, ibid.

84. P. Wilkes, G.L. Kulcinski, J. Nucl. Matl, 78, 427 (1978).

85. F.V. Nolfi, Jr., A. Taylor, K.S. Grabowski, to be published.

86. R.A. Erck, D.I. Potter, H. Wiedersich, submitted to Journal of Nuclear Materials, May, 1978.

87. E. Opperman, to be published.

88. H.I. Avci, PhD. Thesis, University of Wisconsin, 1978.

89. H.I. Avci, unpublished data.

IX-C. Use of Ti Alloys in NUWMAK

IX-C-1. Operating Environment

One of the more useful functions of fusion reactor design exercises is to establish a set of operating parameters which are detailed enough so that assessments of potential materials performance can be made. Therefore, we will try to be as specific as possible about neutron spectra, neutron flux, neutron fluence, displacement rates, transmutation rates, etc. Much of the data in this chapter is reported in other chapters of the report. Our objective here is to gather information, into one place, that is of interest mainly to the materials scientist.

The rest of this section is organized as follows. First, we will address the neutron environment with respect to spectral, spacial, and temporal variations. Next, we will consider the particle fluxes of plasma atoms to the first wall in NUWMAK. The damage and transmutation rates will be addressed followed by a brief summary of the temperature and stress levels of importance. At times we will extend the summary of operating environment into the non-Ti alloy areas to avoid having to repeat this information in Section IX-D.

IX-C-1-a. Neutron Environment

There are two important parameters of interest here.

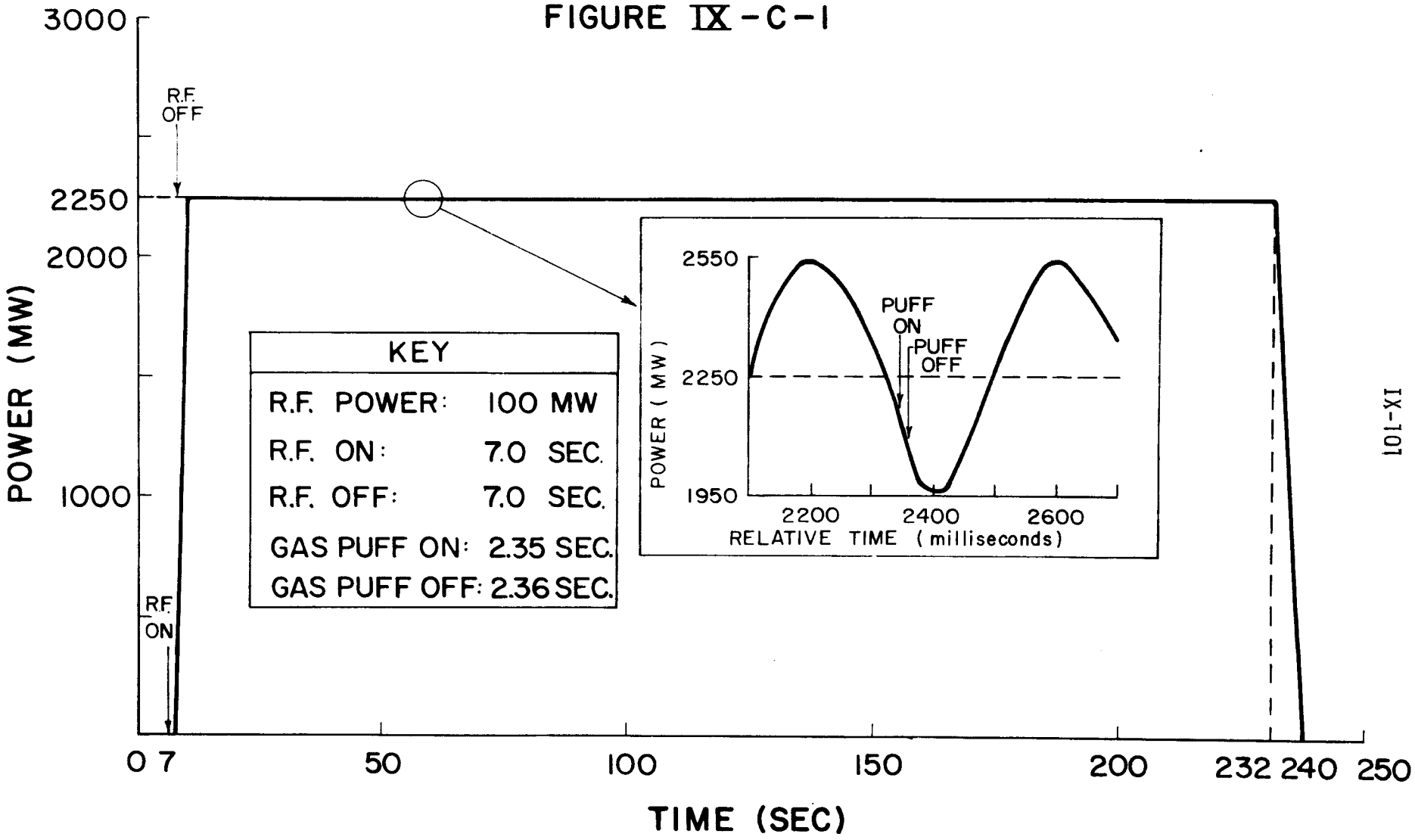
- Neutron flux and fluence, as a function of time during the burn and position in the reaction $\phi(t,x,\theta)$.
- Neutron energy spectra as a function of distance from the first wall and poloidal angle $\phi(E(x,\theta))$.

Let us consider each one separately.

IX-C-1-a-i. Neutron Flux and Fluence

The burn sequence of NUWMAK has been described in Chapter IV and it is noticed that there is a 8 second rise time in which the neutron flux is changing rapidly before the 224 second burn. After the burn there is another 8 second decay time followed by a 10 second period during which no neutrons are being produced. However, it is important to note that there is even more substructure within the burn which is of importance to the materials scientist. The 224 seconds of the burn cycle is made up of 560 cycles during which the power from the plasma has the behavior shown in Figure IX-C-1. During the

FIGURE IX-C-1


3000
2250
2000
1000
POWER (MW)
R.F. OFF
R.F. ON
KEY
R.F. POWER: 100 MW
R.F. ON: 7.0 SEC.
R.F. OFF: 7.0 SEC.
GAS PUFF ON: 2.35 SEC.
GAS PUFF OFF: 2.36 SEC.
2550
2250
1950
POWER (MW)
PUFF ON
PUFF OFF
2200
2400
2600
RELATIVE TIME (milliseconds)
0 7
50
100
150
200
232 240 250
TIME (SEC)

puffing sequence the output power from the plasma varies by approximately ±13% over a 0.4 second period. Such power swings will not be too much of a problem for the energy conversion system but they could have substantial effects on the radiation damage response as we shall see later.

The first solid surface to be bombarded by the neutrons is the V-Ti water cooled RF cavity and the Ti-64 alloy first wall. The spatially averaged first wall flux is 4.34 MW/m^2 during the burn but due to the aforementioned substructure, the peak neutron wall loading (with respect to time) is ~4.92 MW/m^2. The minimum during the burn is 3.84 MW/m^2. It would be difficult to continually include in our discussion the time structure of the neutron flux at every point in the reactor, so consequently we will only quote the time averaged flux (over a puffing cycle) and the reader can apply the ±13% variations.

A repeat of the neutronics model (Chapter VIII) for the NUWMAK blanket is given in Table IX-C-1 and Figure IX-C-2 for the readers' convenience. The average flux of neutrons in the first energy group (13.5 to 14.9 MeV) is shown in Figure IX-C-3 indicating that the average flux (over the burn) is 5×10^{14} $cm^{-2}s^{-1}$ at the first wall. The poloidal variation in the 14.1 MeV neutron wall loading is shown in Figure IX-C-4. The maximum 14 MeV neutron current is 60° and the minimum is at the top of the chamber (110°). The ratio of maximum to minimum on both the outer and inner first wall is ~2.1. This means that the maximum time averaged wall loading is ~5.2 MW/m^2 at the midplane and the maximum at the peak of fluctuations (Figure IX-C-1) is 6.1 MW/m^2. The minimum wall loading at 110° is 2.2 MW/m^2 at the low point of the power cycle which represents a variation of a factor of 2.8 around the first wall.

The 14 MeV neutron flux drops by 5 orders of magnitude through the inner breeding zone and hot shield and another 3 orders of magnitude before the superconducting magnet is reached. The total neutron flux (E>0) is displayed graphically in Figures IX-C-5a and IX-C-5b. The maximum time averaged neutron flux is not at 0° in contrast to 60° for the neutron current and the maximum flux is 2.5×10^{15} n $cm^{-2}s^{-1}$. The spacial variations are slightly less pronounced for the total flux than the 14 MeV values and

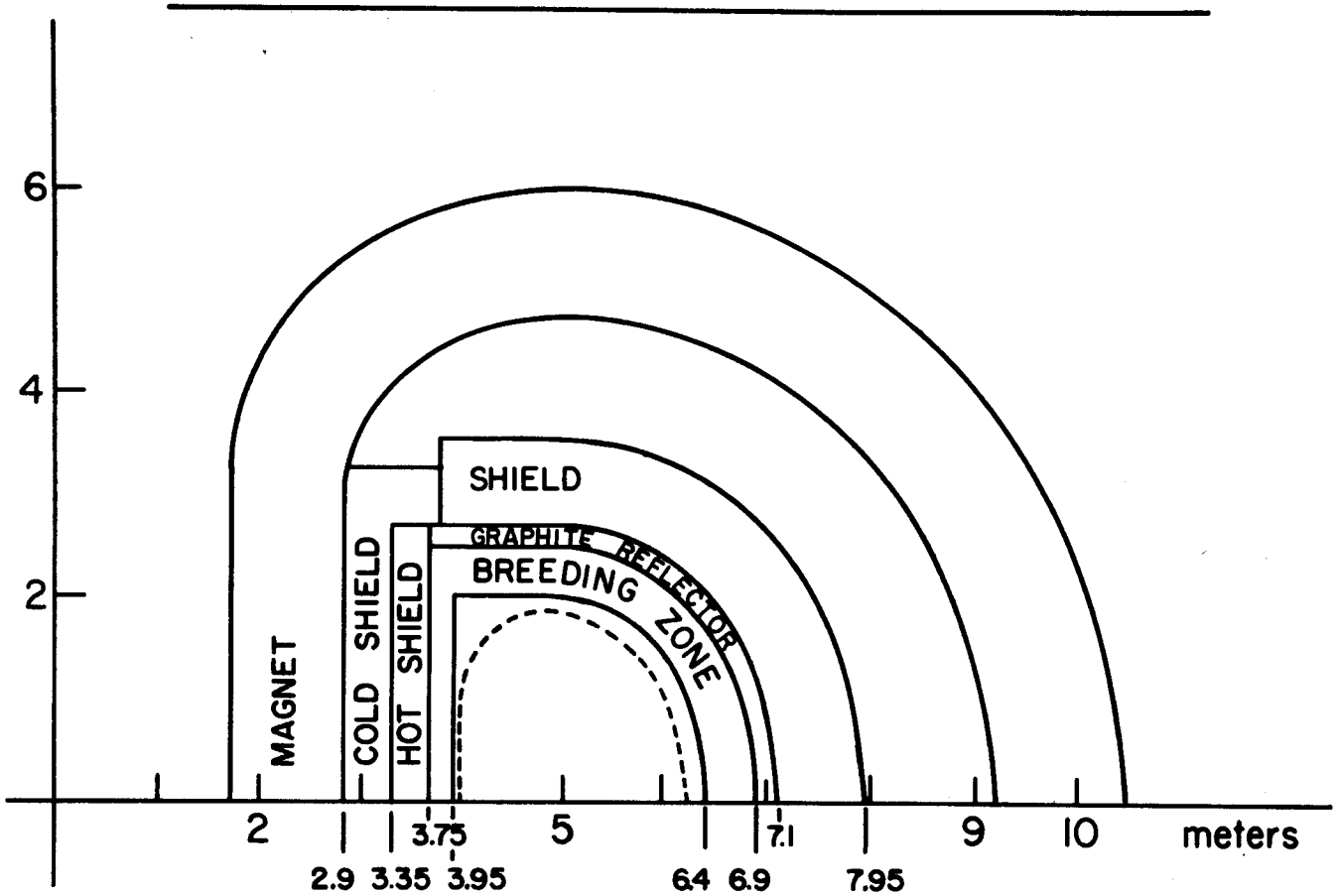
Table IX-C-1

Material Compositions for the NUWMAK Blanket and Shield Neutronics Model at Midplane

Specification	Zone Number	Thickness (meter)	Composition (All percentage by Volume)
Magnet	1	0.30	80% Al + 12.8% Epoxy + 7.2% He (liquid)
Lead Shield	2	0.10	4% Ti Alloy + 2% H_2O + 1% Pb + 93% Pb[a]
B_4C Shield	3	0.40	4% Ti Alloy + 2% H_2O + 1% Pb + 93% B_4C[b]
Tungsten Shield	4	0.35	4% Ti Alloy + 2% H_2O[c] + 1% Pb + 93% W[d]
Inner Breeding Blanket	5 (B-2)	0.10	6% Ti Alloy + 3.9% H_2O[e] + 1.0% Pb + 89.1% $Li_{62}Pb_{38}$[f]
	6 (B-1)	0.10	9.6% Ti Alloy + 8.6% H_2O[e] + 2.4% Pb + 79.4% $Li_{62}Pb_{38}$[f]
Plasma and Vacuum	7	0.05	Vacuum
	8	2.25	Plasma
	9	0.15	Vacuum
Outer Breeding Blanket	10 (B-1)	0.10	9.6% Ti Alloy + 8.6% H_2O[e] + 2.4% Pb + 79.4% $Li_{62}Pb_{38}$[f]
	11 (B-2)	0.15	6% Ti Alloy + 3.9% H_2O[e] + 1.0% Pb + 89.1% $Li_{62}Pb_{38}$[f]
	12 (B-3)	0.25	3.8% Ti Alloy + 1.8% H_2O[e] + 0.3% Pb + 94.1% $Li_{62}Pb_{38}$[f]
Graphite Reflector	13	0.20	3.5% Ti Alloy + 1% H_2O[e] + 0.25% Pb + 95.25% Graphite
B_4C Shield	14	0.20	3.5% Ti Alloy + 1% H_2O + 0.25% Pb + 95.25% B_4C[b]

a. 90% dense b. 95% dense c. average density factor is 94% d. 90% dense e. average density factor 90% f. average density between solid and liquid phases is 5.75 g/cc

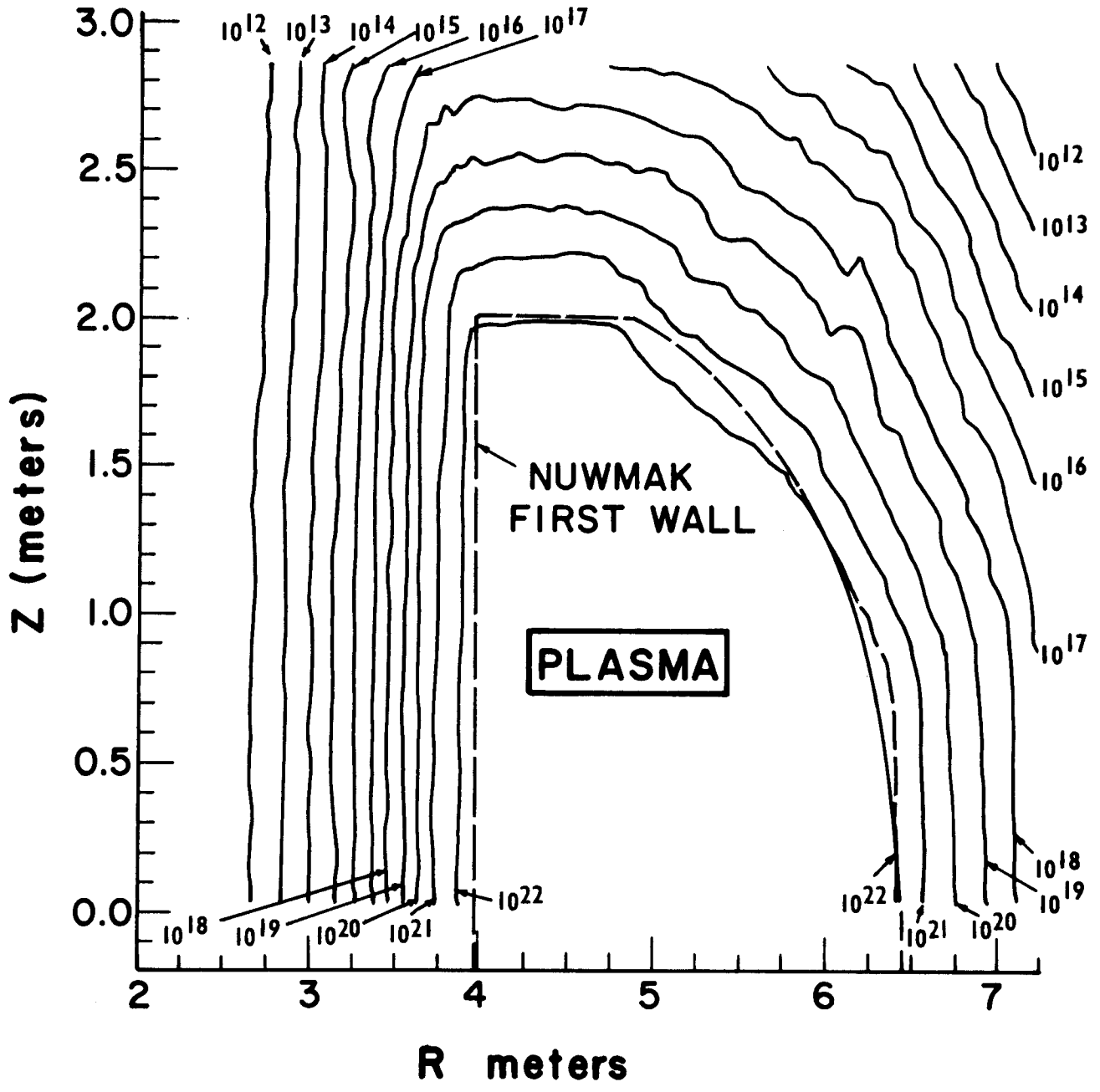
SCHEMATIC OF THE BLANKET AND SHIELD FOR NUWMAK



COLD SHIELD	HOT SHIELD	BREEDING ZONE	GRAPHITE REFLECTOR	SHIELD
3.5% Ti alloy	4% Ti alloy	5.7% Ti alloy	3.5% Ti alloy	3.5% Ti alloy
95.25% B_4C	93% W	89.4% Pb Li	95.25% C	95.25% B_4C
1% H_2O	2% H_2O	3.7% H_2O	1% H_2O	1% H_2O
0.25% Pb	1% Pb	1.2% Pb	0.25% Pb	0.25% Pb

Figure IX-C-2

Figure IX-C-3 SUMMARY OF FIRST WALL NEUTRON FLUX, $n\,cm^{-2}\,y^{-1}$ IN THE ENERGY RANGE 13.5 TO 14.92 MeV .



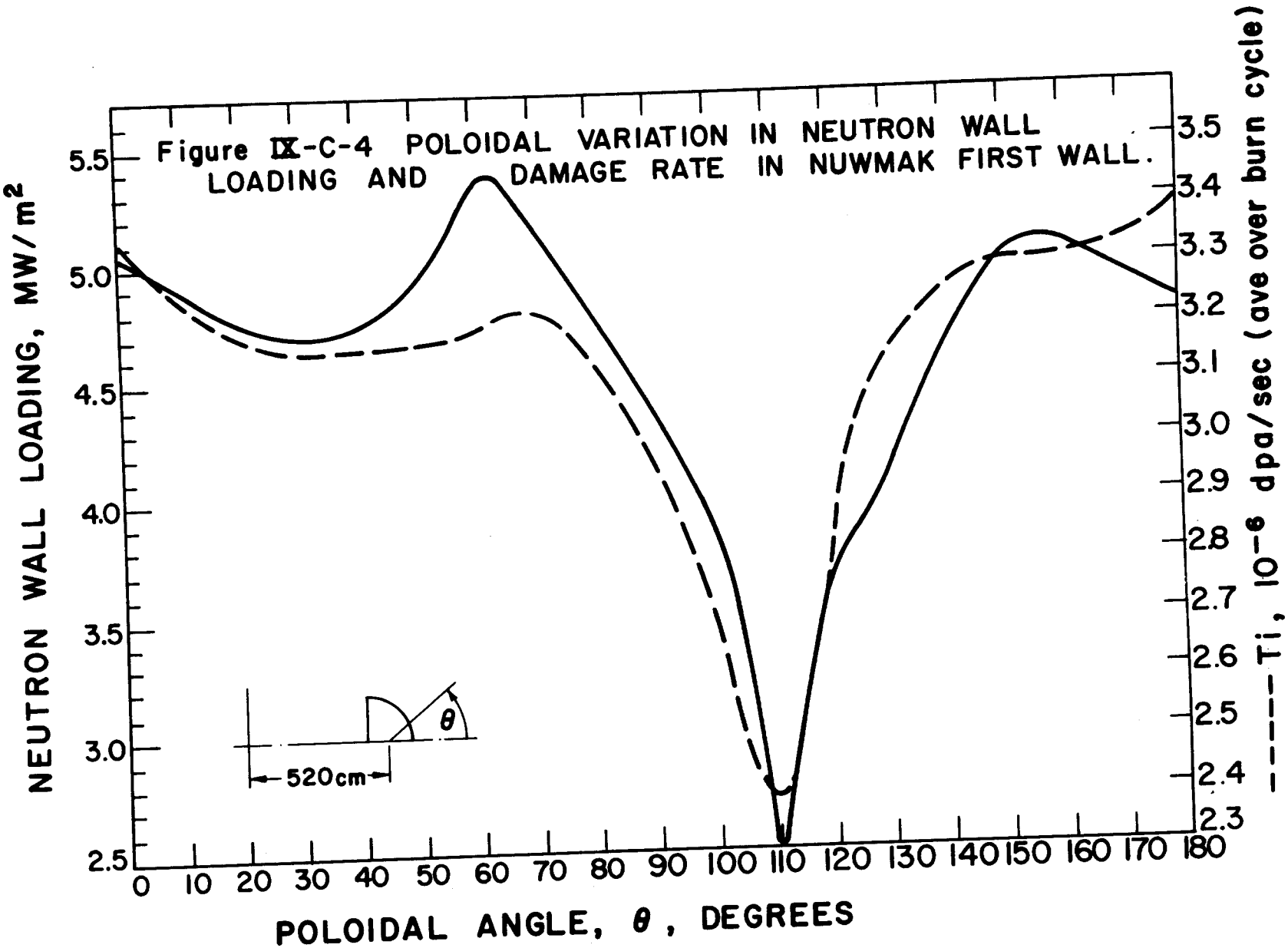
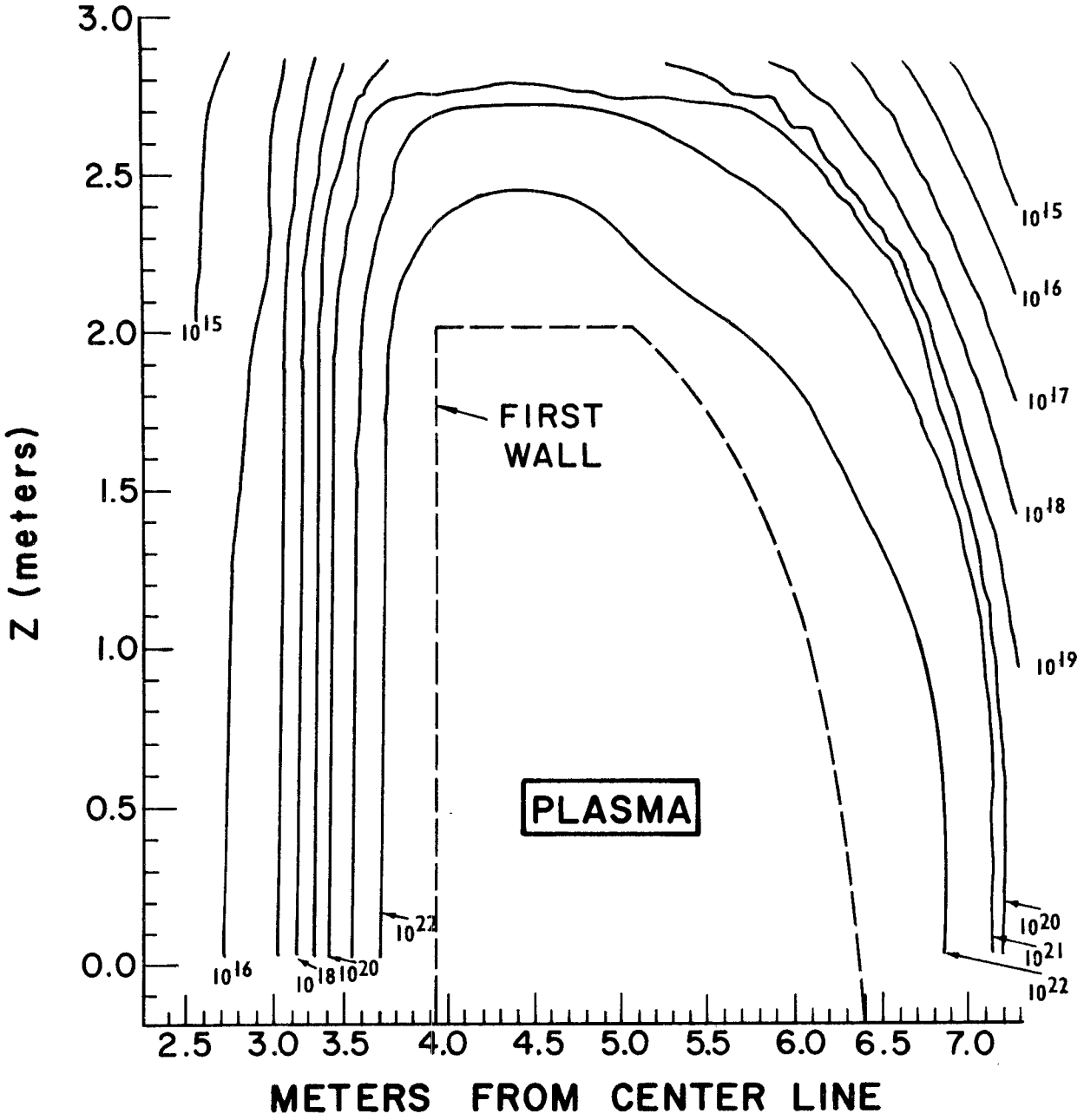

Figure IX-C-4 POLOIDAL VARIATION IN NEUTRON WALL LOADING AND DAMAGE RATE IN NUWMAK FIRST WALL.
NEUTRON WALL LOADING, MW/m²
Ti, 10⁻⁶ dpa/sec (ave over burn cycle)
POLOIDAL ANGLE, θ, DEGREES
θ
520cm
5.5
5.0
4.5
4.0
3.5
3.0
2.5
3.5
3.4
3.3
3.2
3.1
3.0
2.9
2.8
2.7
2.6
2.5
2.4
2.3
0 10 20 30 40 50 60 70 80 90 100 110 120 130 140 150 160 170 180

Figure IX-C-5a SPACIAL DISTRIBUTION OF TOTAL (E>o MeV) NEUTRON FLUX ($cm^{-2} yr^{-1}$) IN NUWMAK



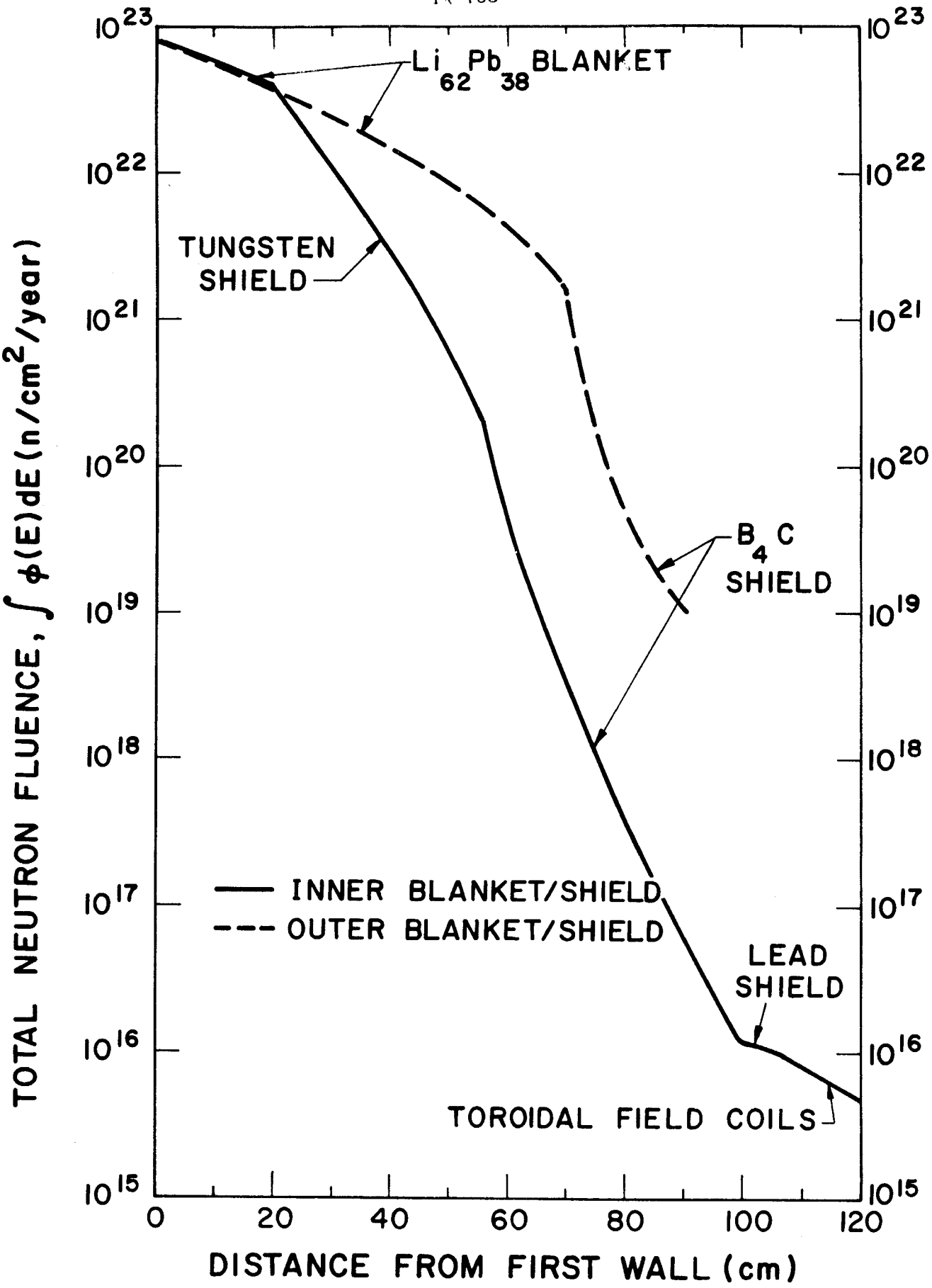

$Li_{62}Pb_{38}$ BLANKET
TUNGSTEN SHIELD
B_4C SHIELD
INNER BLANKET/SHIELD
OUTER BLANKET/SHIELD
LEAD SHIELD
TOROIDAL FIELD COILS
TOTAL NEUTRON FLUENCE, $\int \phi(E)dE$ (n/cm^2/year)
DISTANCE FROM FIRST WALL (cm)
10^{23}
10^{22}
10^{21}
10^{20}
10^{19}
10^{18}
10^{17}
10^{16}
10^{15}
0
20
40
60
80
100
120

Fig. IX-C-5(b)

there is approximately seven orders of magnitude drop from the first wall to the most critical S/C toroidal magnet surface.

A summary of the important parameters for the neutron environment is given in Table IX-C-2.

IX-C-1-a-ii. Neutron Energy Spectrum

The neutron energy spectra at 3 selected positions are shown in Figs. IX-C-6, 7, and 8 for the first wall at 0° (dotted line in all Figures), the middle of the hot shield (X = 3.43m, θ = 180°), the middle of the outer breeding zone (X =6.72m, θ = 0°) and the superconducting magnet (X = 2.9 m, θ = 180°) respectively. Tabular values are given in Table IX-C-3. The main feature of these curves is the drop in the high energy neutron flux as one progresses into the blanket-shield-magnet areas. There is a drop in the 14 MeV flux of 7 orders of magnitude to the S/C magnet while the drop in the thermal flux is only 4 orders of magnitude. The reader is urged to study the numbers at his leisure.

IX-C-1-b. Particle Flux to the First Wall

The unique nature of the NUWMAK plasma operation, that is a "cold" gas surrounding a "hot" plasma, coupled with good magnetic confinement means that very few energetic charged particles will strike the first wall. However, charge exchange neutrals can be formed in the plasma and could escape into the cold gas region and even strike the first wall. Calculations described earlier show that the charge exchange neutrals in the NUWMAK plasma have the energy spectrum shown in Figure IX-C-9. The average energy of the neutral D and T atoms is 262 eV and the average flux of atoms is $2.1 \times 10^{17} cm^{-2} s^{-1}$. The time behavior of the neutral flux is shown in Section IV-A. This produces a 8.8 watt/cm^2 heat load during the burn.

IX-C-1-c. Displacement Rate Effects

The bombardment of the NUWMAK components with neutrons will produce two primary reactions. First, atoms will be displaced from their equilibrium sites and we will measure the production of defects with the dpa (displacements per atom) unit. Secondly, nuclear reactions will cause many of the original compositions to change and in some cases large concentrations of hydrogen and helium will be produced. It is convenient to separate the two phenomena

Table IX-C-2

Neutron Fluxes in NUWMAK

Position	Distance from Reactor Center-m	Total Flux n $cm^{-2}y^{-1}$ (100% PF)
Inner Zone, $\theta = 180°$		
S/C TF Magnet	2.90	7×10^{15}
Cold/Hot Shield Interface	3.35	3×10^{19}
Hot Shield/Breeding Zone Interface	3.75	3×10^{22}
First Wall/RF Cavity	3.95	6×10^{22}
Outer Zone, $\theta = 0°$		
First Wall/RF Cavity	6.4	6×10^{22}
Breeding Zone/Graphite Reflector Interface	6.9	6×10^{21}
Graphite Reflector/Shield Interface	7.1	1×10^{21}
Back of Shield	7.95	$< 10^{14}$
S/C TF Coil	9.1	$<<10^{14}$

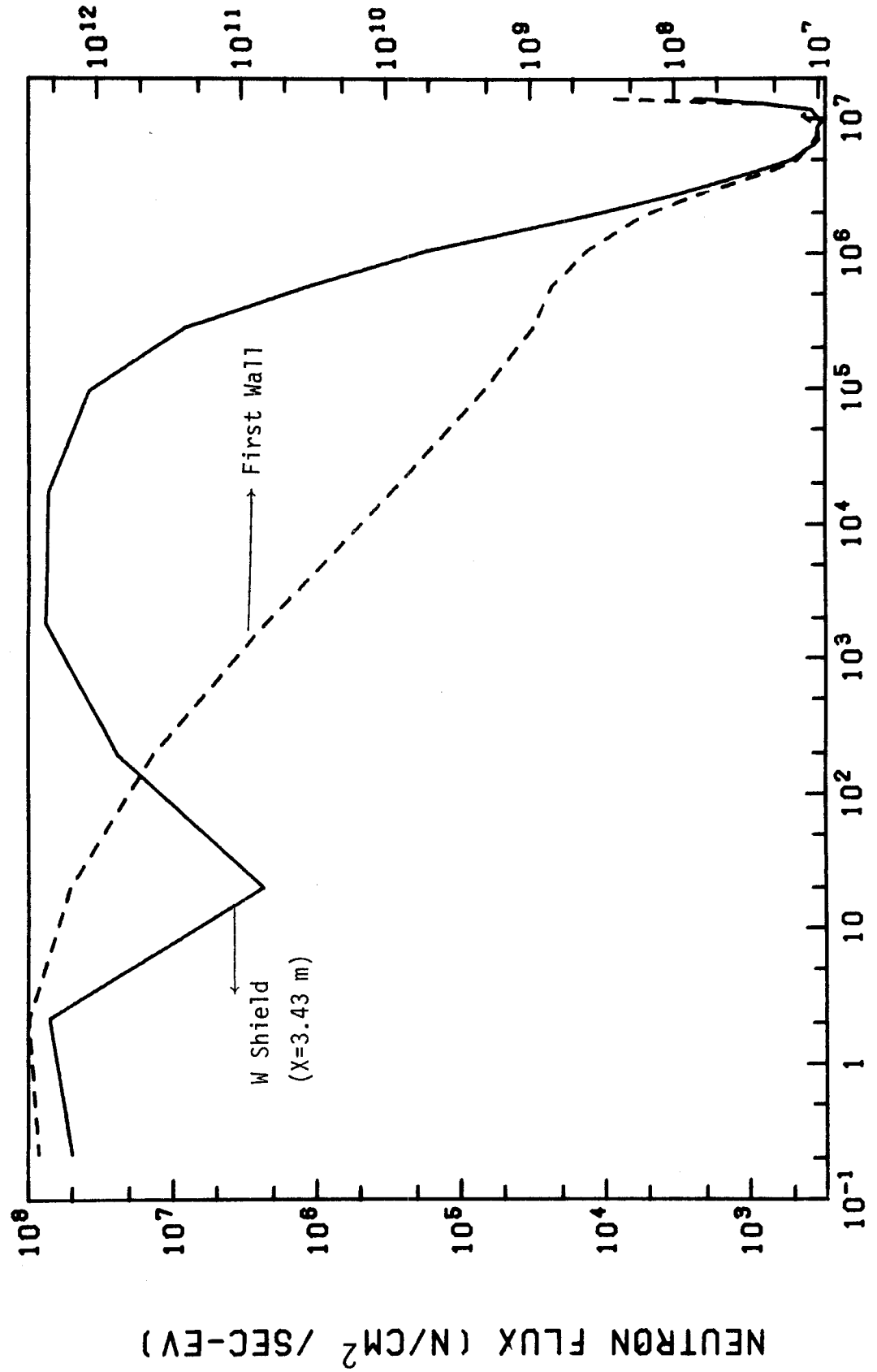


Fig. IX-C-6

Comparison of the Neutron Energy Spectra at the First Wall to that in the Tungsten Shield Area

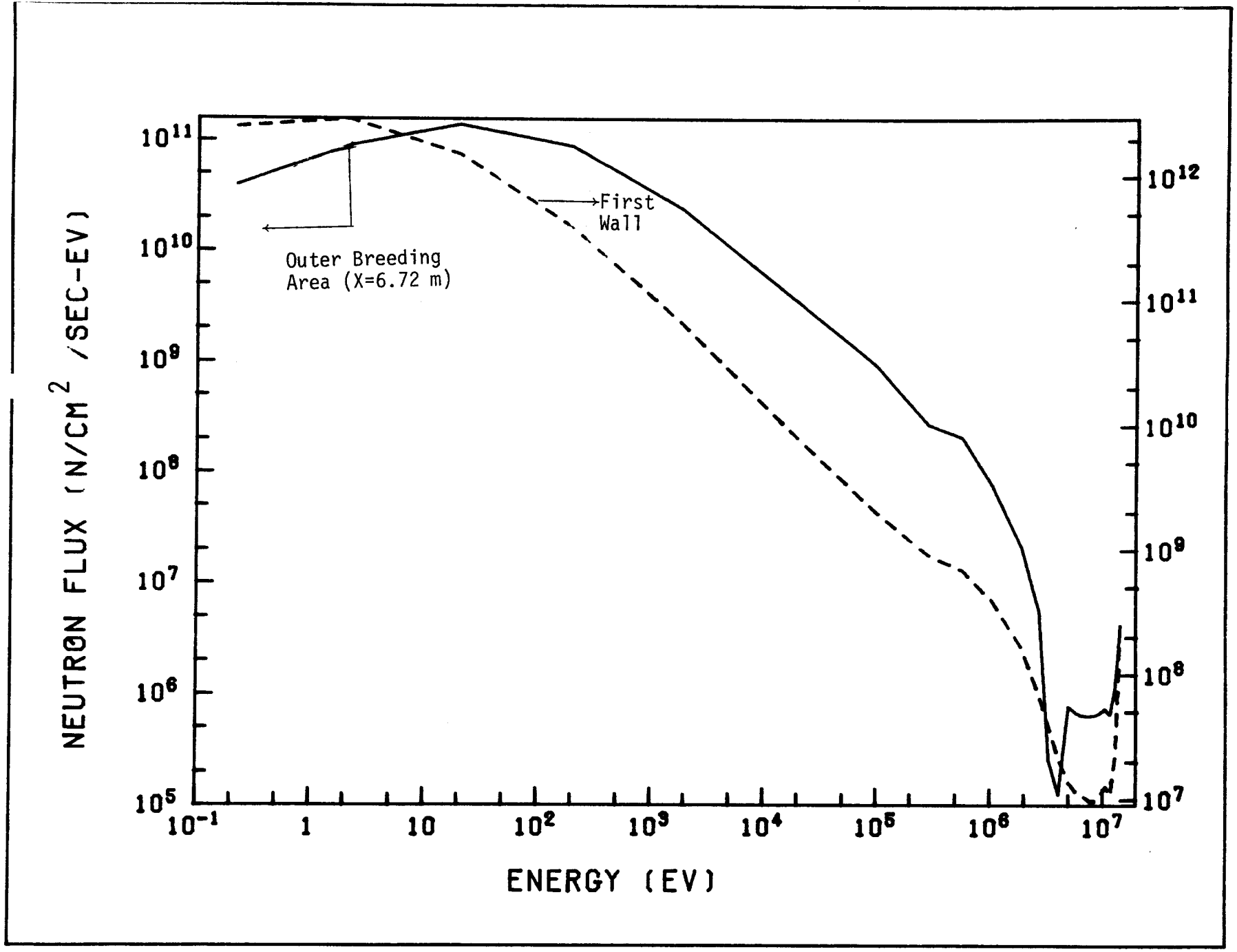


Fig. IX-C-7
Comparison of Neutron Energy Spectra at the First Wall to that in the Outer Breeding Zone

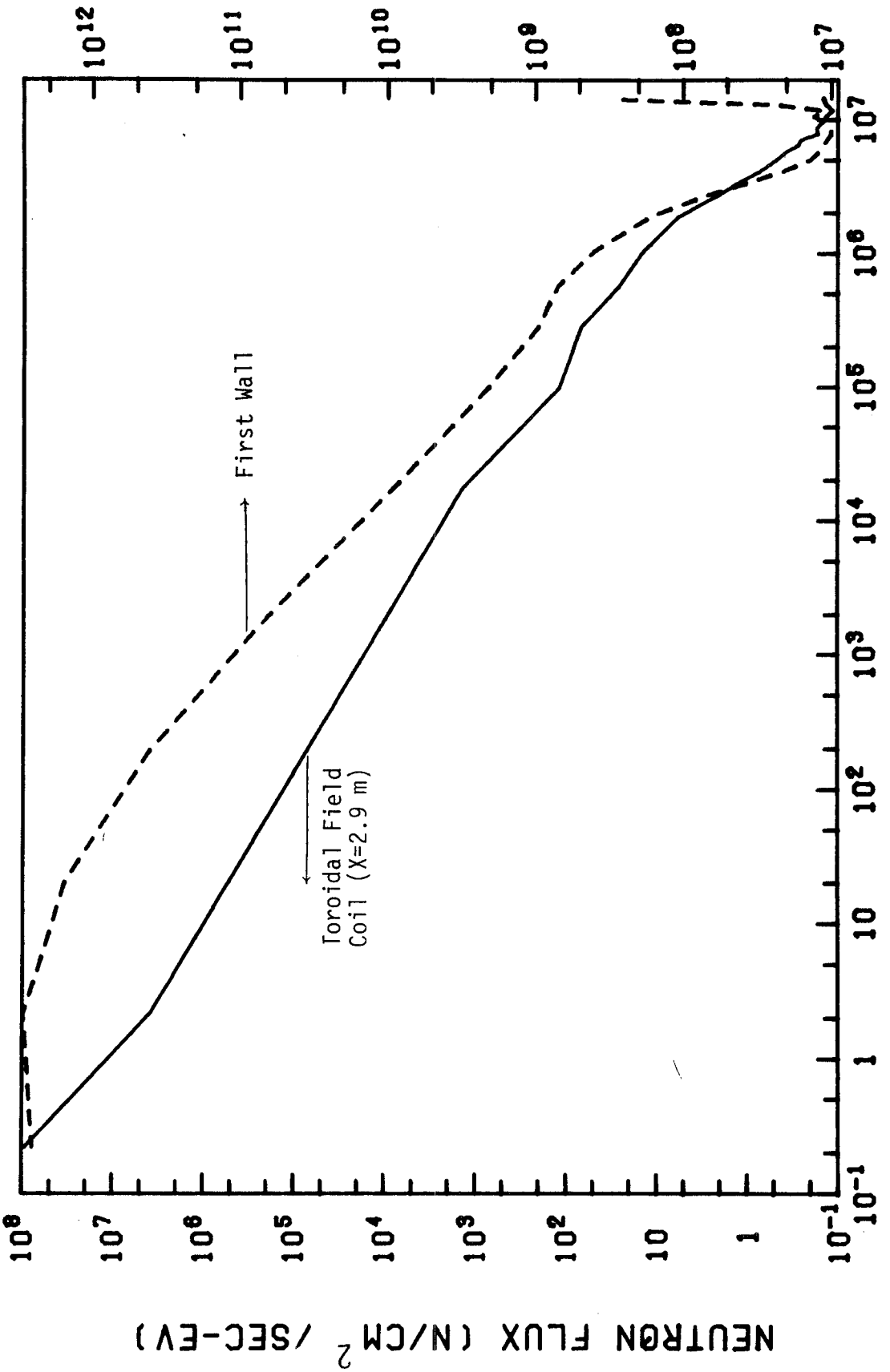


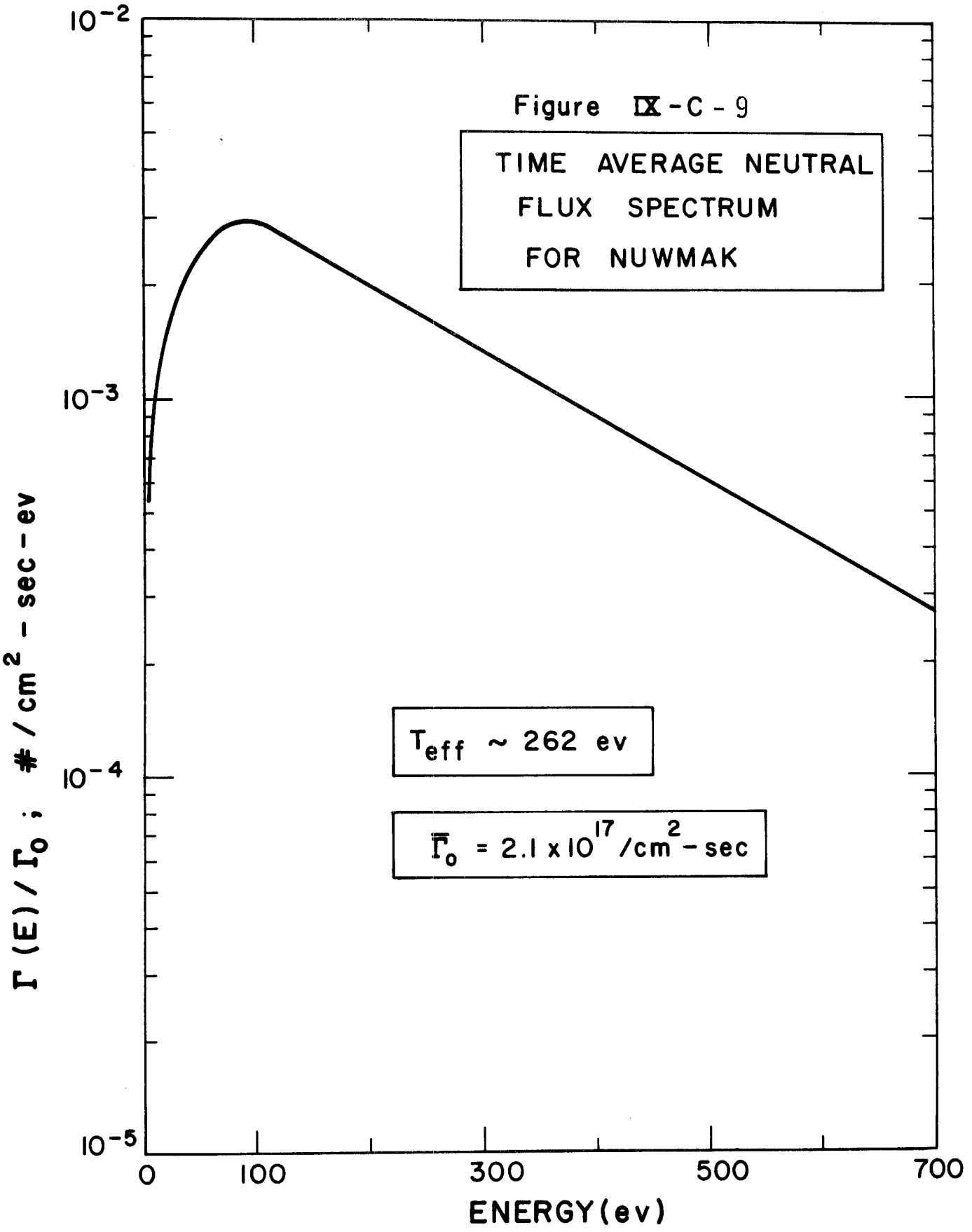
FIGURE IX-C-8

Comparison of the Neutron Energy Spectra at the First Wall to that in the Closest Toroidal Field Coil

Table IX-C-3

Some Group Scalar Neutron Fluxes ($n/cm^2/sec$) Found in the NUWMAK Blanket and Shield at Positions at Midplane $\theta=0°,180°$

	Inner Blanket/Shield			Outer Blanket/Shield	
Neutron Energy Group	Magnet Region Close to the Lead Shield	Tungsten Region 52 cm From the First Wall	Outer/Inner First Walls	Breeding Region 32 cm From the First Wall	Reflector Region 62 cm From the First Wall
1	2.032+5	3.401+9	3.553+14	4.870+12	1.631+11
2	1.731+5	9.745+8	3.031+13	1.440+12	4.933+10
3	1.330+5	4.341+8	1.263+13	7.586+11	3.815+10
4	1.440+5	3.656+8	1.341+13	7.740+11	3.898+10
5	1.419+5	3.026+8	1.037+13	6.524+11	2.464+10
6	1.504+5	2.916+8	8.603+12	5.520+11	3.482+10
7	1.287+5	2.678+8	7.565+12	4.958+11	3.041+10
8	1.816+5	2.311+8	7.343+12	4.519+11	4.821+10
9	1.766+5	2.307+8	7.089+12	4.163+11	3.336+10
10	2.152+5	2.445+8	6.729+12	3.999+11	4.178+10
11	4.775+5	5.038+8	1.357+13	7.698+11	8.159+10
12	6.141+5	7.363+8	1.737+13	1.013+11	6.578+10
13	8.695+5	1.148+9	2.510+13	1.709+11	6.344+10
14	1.130+6	1.785+9	3.631+13	3.003+12	1.129+11
15	6.439+6	1.495+10	1.841+14	2.380+13	1.157+12
16	8.469+6	1.057+11	2.402+14	4.684+13	2.061+12
17	8.661+6	3.836+11	2.307+14	6.887+13	2.919+12
18	1.616+7	1.983+12	2.222+14	6.571+13	5.124+12
19	1.579+7	5.107+12	2.700+14	1.242+14	1.146+13
20	3.866+7	2.100+12	2.539+14	1.098+14	1.790+13
21	2.855+7	2.284+11	2.001+14	7.294+13	1.860+13
22	2.232+7	7.522+9	1.281+14	2.860+13	1.726+13
23	1.724+7	7.842+7	5.158+13	4.711+12	1.374+13
24	1.311+7	2.473+8	1.043+13	3.161+11	9.780+12
25	3.605+7	1.940+7	9.990+11	1.549+10	1.547+13


Figure IX-C-9
TIME AVERAGE NEUTRAL FLUX SPECTRUM FOR NUWMAK
T_{eff} ~ 262 ev
$\bar{\Gamma}_o$ = 2.1 x 10^17 /cm^2 - sec
$\Gamma(E)/\Gamma_o$; # / cm^2 - sec - ev
10^{-2}
10^{-3}
10^{-4}
10^{-5}
0
100
300
500
700
ENERGY (ev)

for discussion purposes, but the reader should recognize that they both must be considered together before the final damage state is determined.

IX-C-1-c-i. Displacement Rates

The displacement cross sections used for this work have been described in Section IX-B. This total cross section was used in conjunction with the neutron fluxes of Section IX-C-1-a to arrive at the instantaneous displacement rates.

An example of the spacial variation in dpa rate is shown in Figures IX-C-10, 11 and 12. These figures show that the dpa rate in the Ti alloy varies from the mid-10^{-6} per second range at the first wall to ~$10^{-13} s^{-1}$ at the inner S/C TF magnet surface. More detail about the dpa rate variation in the poloidal direction is given in Figure IX-C-4 and it is seen that the maximum dpa rate is at the midplane in the 3.4 x $10^{-6} s^{-1}$ range. The ratio of the maximum to minimum damage rate in the first wall is 1.5.

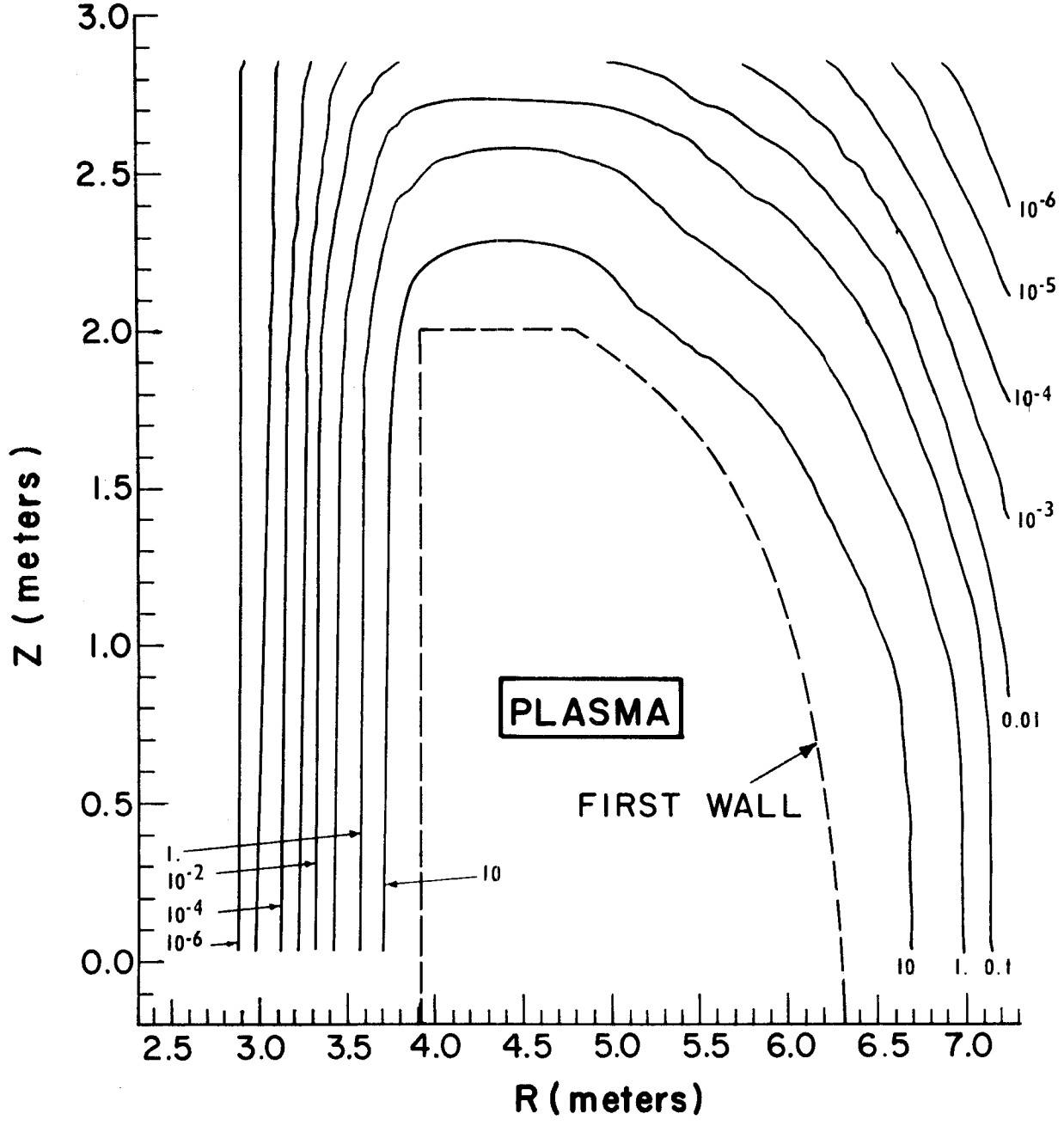
Table IX-C-4 lists the dpa rates at various positions in the NUWMAK reactor. It also includes the variation to the power oscillation during the burn (see Section IX-C-1-a-i). Note that the maximum dpa rate is ~4.3 x $10^{-6} s^{-1}$ in Ti-64 for a few milliseconds of the burn. This drops to 10^{-8} dpa s^{-1} at the graphite reflector and cold shield areas.

The dpa rate in the V-Ti cavity ranges from 50-60 dpa/yr while that in the graphite reflector is 1-10 dpa/year. The W undergoes damage at <0.1 dpa/yr while that in the Al stabilizer is 10^{-8} dpa/yr. The maximum dpa rate in the NbTi superconductor is 10^{-9} dpa/yr.

The depth dependent dpa rate in the magnet is shown in Figure IX-C-13. The results are self-evident and representative of the modification of the neutron spectrum due to blanket and magnet thicknesses.

Finally, the dpa rate in the Al and copper of the VF coils is shown in Figure IX-C-14. Obviously the farther the coils are above the midplane the lower the dpa rate is. However, at the design point of 335 cm above the midplane the damage rate in the Al and copper is 2 x 10^{-5} dpa/full power year or 6 x 10^{-13} dpa/sec during the burn. At a 70% plant factor the damage incurred per year is 1.4 x 10^{-5} dpa.

Figure IX-C-10. SPACIAL VARIATION IN TITANIUM STRUCTURE, dpa PER FULL POWER YEAR



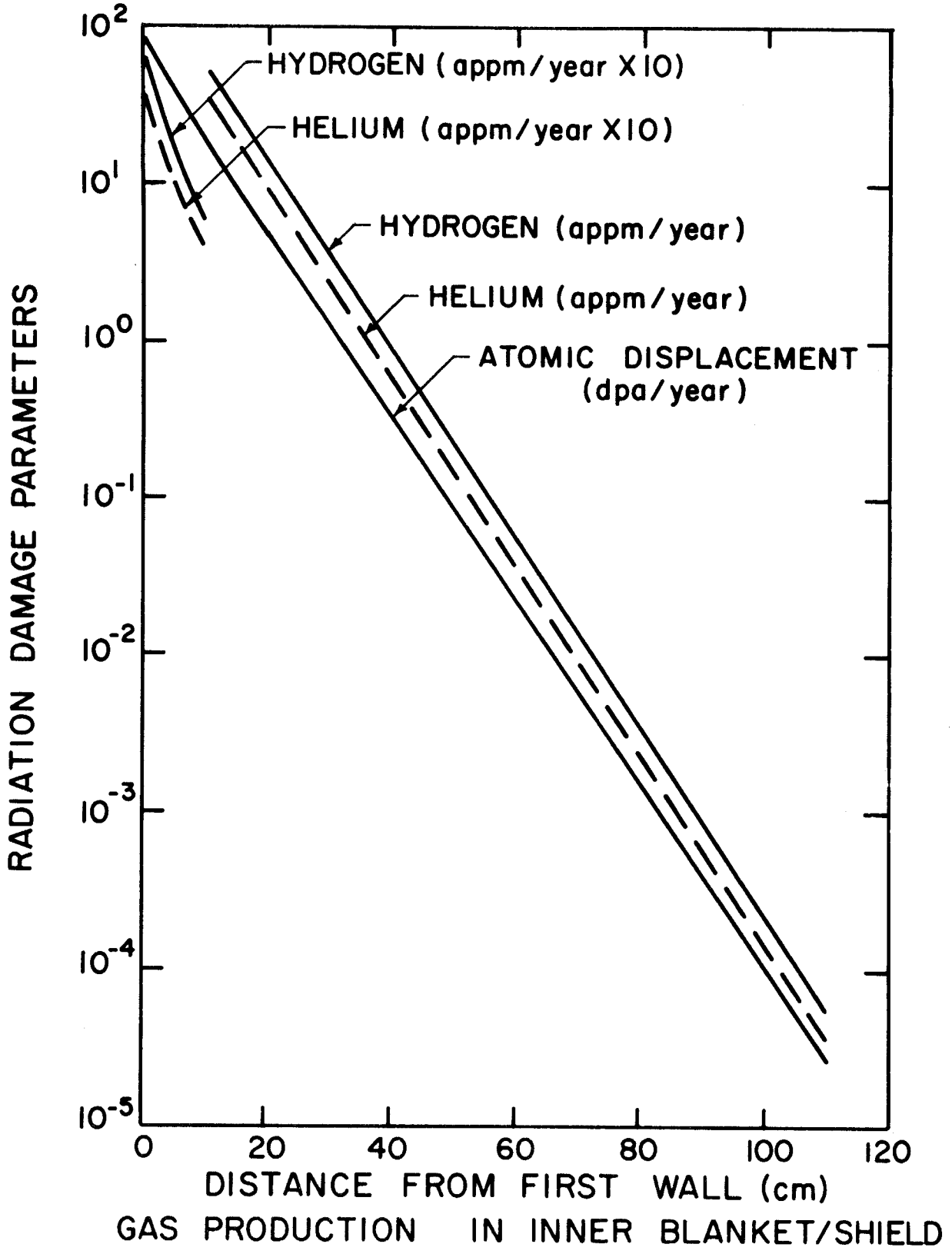


Fig. IX-C-11 Variation in Displacement and Gas Production Rates per Full Power Year for the NUWMAK Inner Blanket/Shield

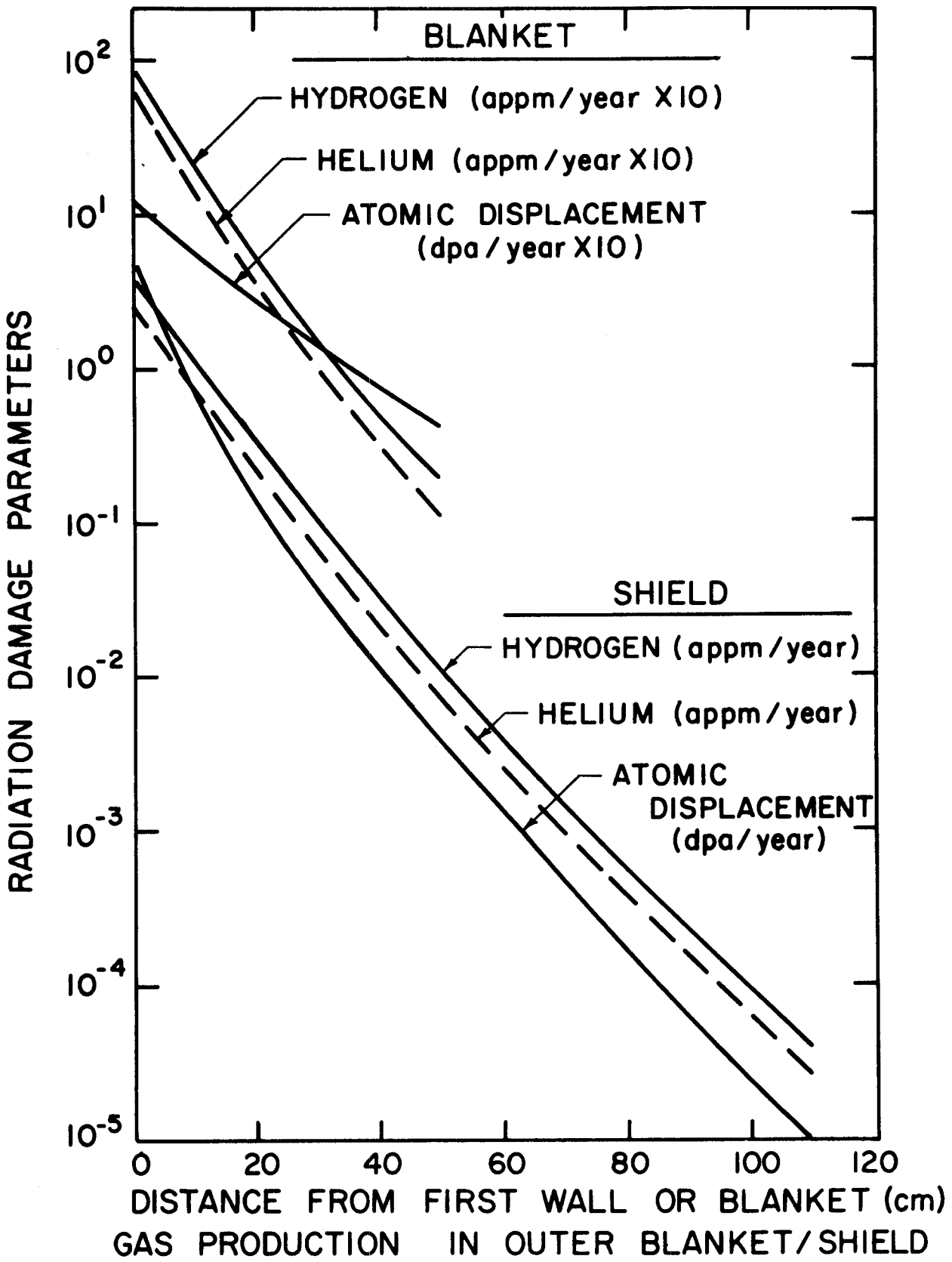


Fig. IX-C-12 Variation in Displacement and Gas Production Rates per Full Power Year in the NUWMAK Outer Blanket/Shield

Table IX-C-4

Position	At Midplane X-m	dpa/s Ave[a]	dpa/s Maximum During Burn	dpa/yr (70% PF)
S/C TF Coil	2.9			
Al (stabilizer)	2.9	6×10^{-14}	7×10^{-14}	1.4×10^{-6}
NbTi (superconductor)	<2.9	$\sim3\times10^{-14}$	3.4×10^{-14}	7×10^{-7}
Ti-64 alloy (cold shell)	3.35	7×10^{-10}	8×10^{-10}	1.5×10^{-2}
Ti-64 alloy (hot shell)	3.75	7×10^{-7}	8×10^{-7}	15
Ti-64 alloy (first wall)	3.95	3.8×10^{-6}	4.3×10^{-6}	84
V-Ti cavity	3.95	2.5×10^{-6}	2.8×10^{-6}	57
V-Ti cavity	6.40	2.5×10^{-6}	2.8×10^{-6}	57
Ti-64 first wall	6.4	3.8×10^{-6}	4.3×10^{-6}	84
Ti-64 (reflector)	6.9	5.2×10^{-8}	5.9×10^{-8}	10.5
Graphite	6.9	9×10^{-8}	1×10^{-7}	2.0
Ti-64 (shield)	7.1	8.7×10^{-9}	9.9×10^{-9}	0.18
Ti-64 (shield)	7.95	$<10^{-14}$	$<10^{-14}$	$<10^{-7}$
Cu in saddle coils	7.95	$<10^{-14}$	$<10^{-14}$	$<10^{-7}$
S/C TF coil Al (stabilizer)[b]	9.1	$<<10^{-14}$	$<<10^{-14}$	$<<10^{-7}$
S/C TF coil NbTi[b]	9.1	$<<10^{-14}$	$<<10^{-14}$	$<<10^{-7}$

(a) Average during the burn

(b) Depends on the amount of shielding afforded by saddle coils and other portable shielding

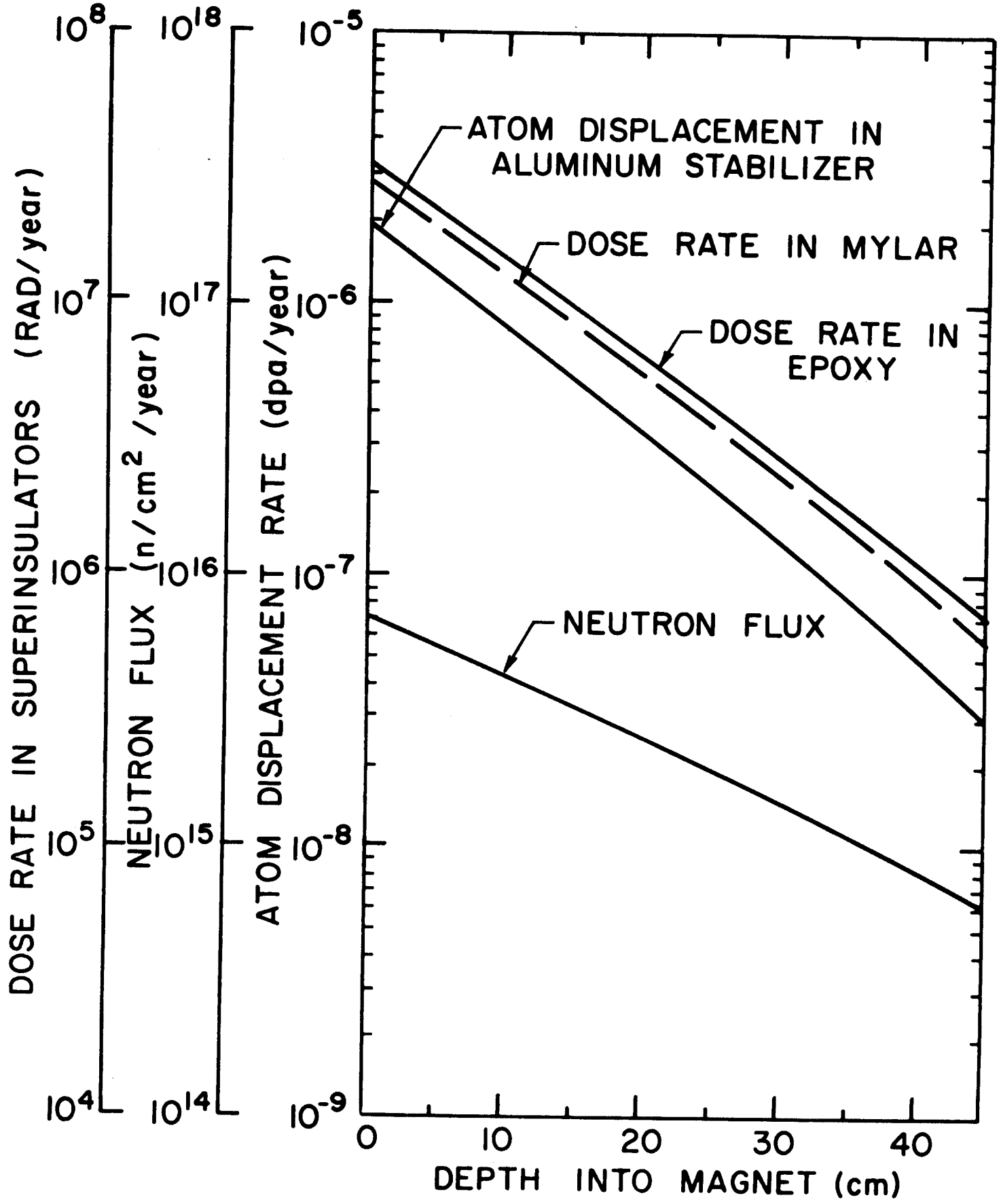
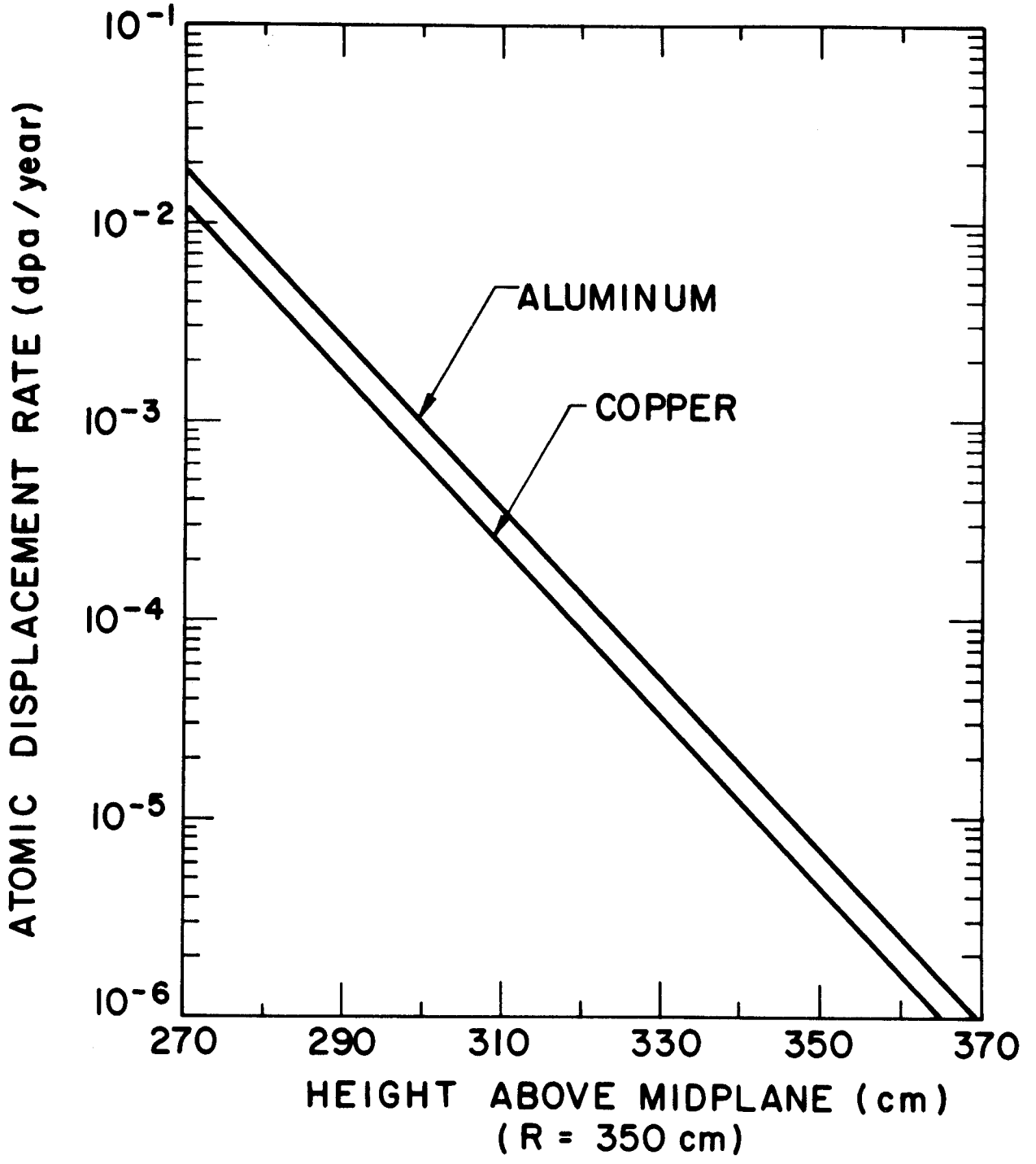


FIGURE IX-C-13

Variation in Damage Rates for Toroidal Field Coils

Figure IX-C-14 DISPLACEMENT RATE IN NUWMAK VERTICAL FIELD COILS.



IX-C-1-d. Transmutation Rates in NUWMAK

The production of gaseous (H, He) and nongaseous transmutation products in materials is known to have a deleterious effect on the mechanical properties of metals. Therefore, it is important to know these transmutation rates in order to establish useful lifetime predictions. It is convenient to divide the discussion now along the lines of gaseous and nongaseous elements.

IX-C-1-d-i. Production of Hydrogen and Helium in NUWMAK Materials

The cross sections for producing hydrogen and helium in the major elemental components of the NUWMAK blanket are shown in Table IX-C-5.

When these cross sections are combined with the earlier neutron fluxes we obtain the spatially distributed source of gas production in appm per year as shown in Figs. IX-C-15 and 16 for the Ti-64 alloy. Both the helium and hydrogen gas production is 800 to 1000 appm per full power year at the first wall (550 to 700 appm at 70% PF). The poloidal variation of the helium production is similar to the wall loading of Figure IX-C-4 and one finds that the helium production rate is ~10% higher than the average at 60°. The hydrogen production rate peaks at ~1100 appm/yr in the same position.

The variation in hydrogen and helium production rate in Ti-64 as a function of distance from the first wall was shown earlier in Figures IX-C-11 and 12. These figures show that the production rate falls to less than 1 appm/year at ~50 cm for the first wall.

The helium and hydrogen production rate in the V-5Ti cavity will display the same poloidal angle dependence as in the Ti alloy. At a 70% plant factor, the production of helium is greatest at 60% with ~350 appm/year while the hydrogen production is ~550 appm/yr.

Finally, the spacial variation of helium and hydrogen production in vanadium cavity leads and carbon is shown in Figure IX-C-17. The helium production rate in the RF cavity leads ranges from 350 appm/year (70% PF) to less than 10 appm/yr at 20 cm behind the wall. The helium production rate in C ranges from 15 appm/yr at the front of the reflector to ~1.5 appm/year at the back (70% PF).

The significance of the alloying elements on gas production can be appreciated by noting that elements produce much more helium per unit of concentration. For example, Al is only 10 atomic percent of the Ti-64 alloy

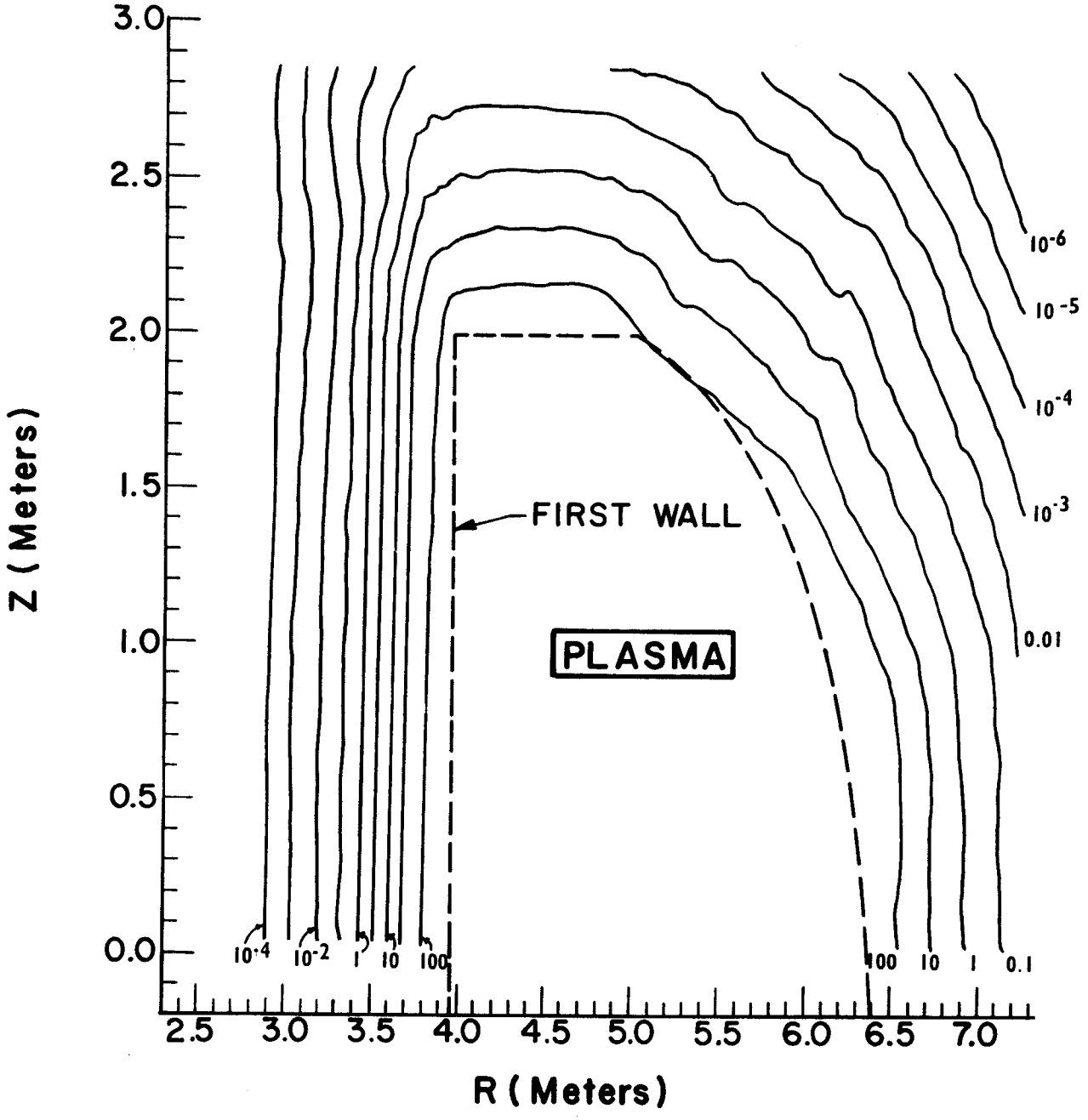
Table IX-C-5

Summary of Gas Production Cross Sections Used for this Study

Millibarns

Energy Group	Ti	V	Al	Ti	V	Al
1	43.8	20.0	123.1	63.5	98.1	103.7
2	40.0	16.5	128.2	61.0	85.2	104.9
3	27.2	8.6	116.2	43.0	61.9	105.6
4	18.9	4.9	99.8	34.1	51.6	106.3
5	13.2	2.7	80.9	25.6	40.9	102.7
6	10.0	1.5	58.3	18.1	29.0	93.7
7	7.1	0.6	34.7	11.4	22.4	81.6
8	4.1	0.3	16.6	5.9	18.1	68.2
9	1.5	0	5.0	1.8	14.2	54.1
10	0		0.7	0	11.0	41.2
11			0		8.5	28.7
12					4.2	19.0
13					1.0	10.6
14					0.2	7.6
15					0.1	6.9
16					0	2.3
17						0.7
18						0.1
19						0

Figure IX-C-15 SPATIAL VARIATION OF HELIUM PRODUCTION IN NUWMAK. Ti ALLOY, (appm He / Full Power Year)



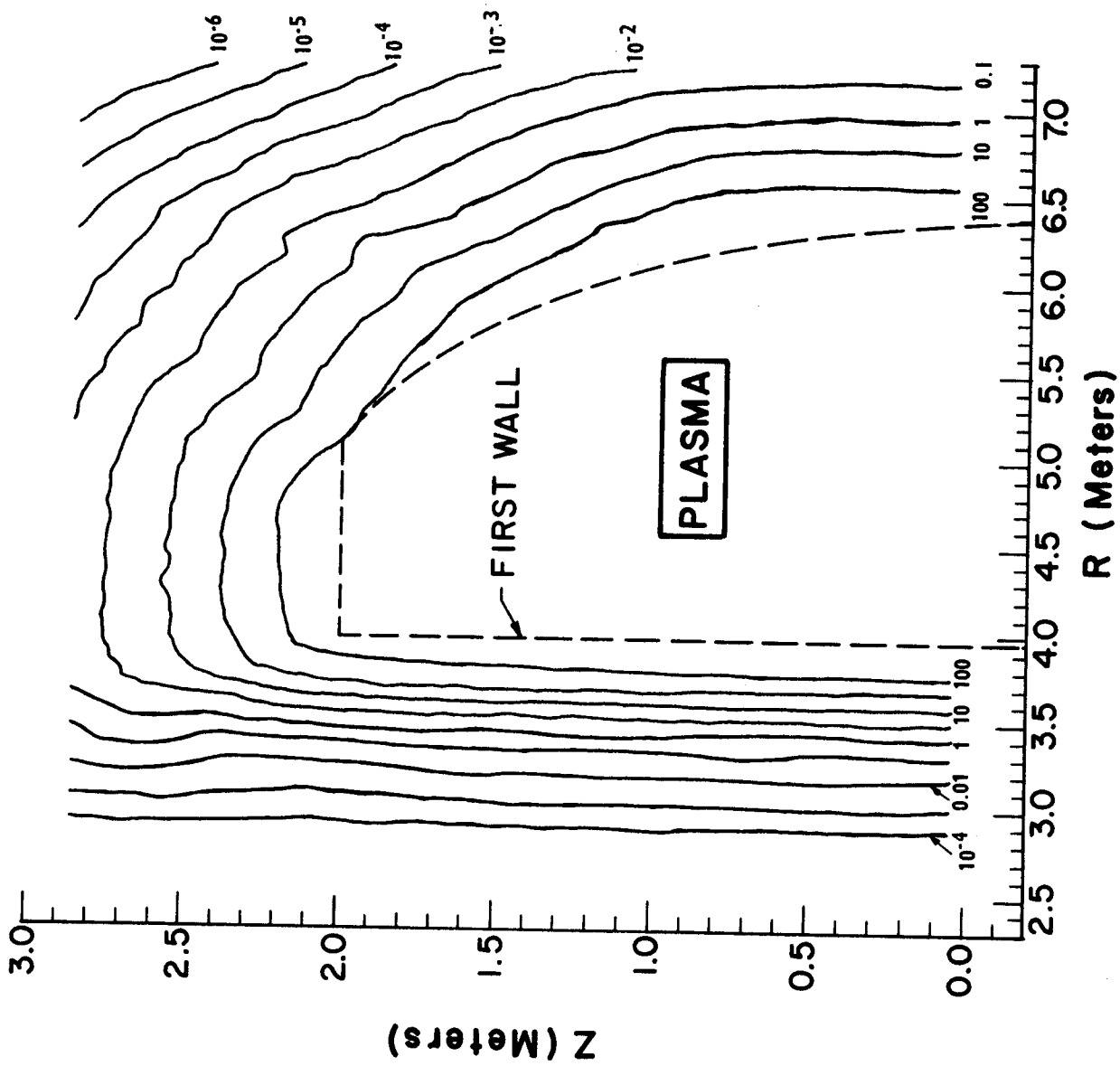
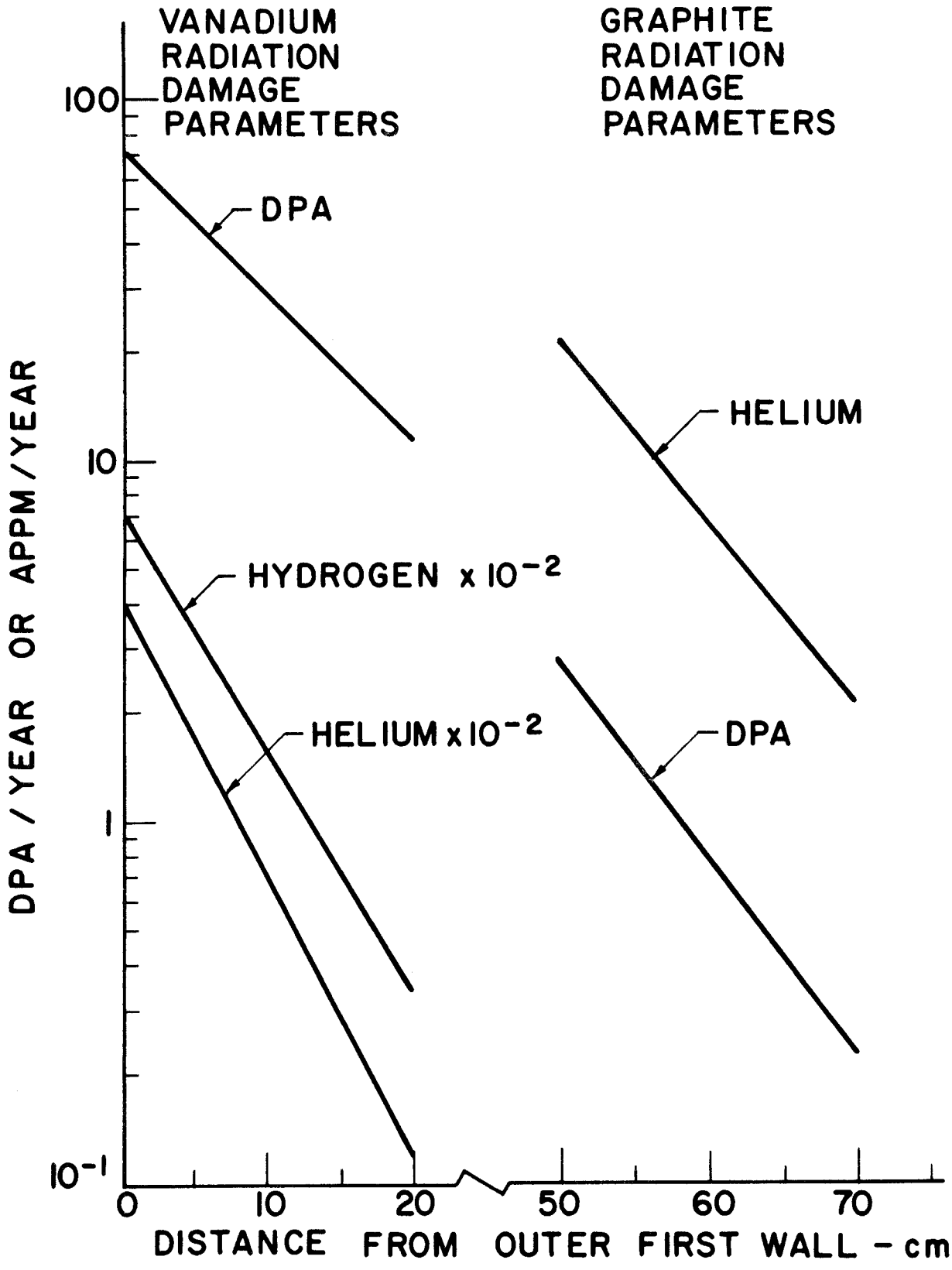


Figure IX-C-16

Figure IX-C-17 VARIATION IN DAMAGE RATES FOR V CAVITY LEADS AND GRAPHITE REFLECTOR



and yet it produces 25% of the helium and 15% of the hydrogen. In the RF cavity, Ti is only 5 atomic percent of the alloy but it produces 10% of the helium. (See Table IX-C-7.)

Table IX-C-7

Contribution to Gas Production Rates by Alloying Elements

Element	wt%	at%	He Production %	H Production %
			Ti-6Al-4V Alloy	
Ti	90	86.2	74	80
Al	6	10.2	25	15
V	4	3.6	1	5
			V-5Ti Alloy	
V	95	95	90	94
Ti	5	5	10	6

IX-C-1-d-ii. Production of Solid Transmutation Products

We will only consider the first wall of Ti-64 alloy composition here. The initial and final composition of the wall is given in Table IX-C-8. The preliminary calculations show that there is relatively little change in the chemical makeup of the alloy with only Sc and Ca appearing in small amounts after 10 full power years. It is not anticipated that these elements will have a major effect on the physical or mechanical properties of the alloy.

IX-C-1-e. Radiation Exposure to the Organic Thermal and Electrical Insulators of NUWMAK Magnets

A detailed discussion of the radiation exposure (in Rads/hr or Rads/year) to organic insulators has been given in Chapter VIII. We will only summarize the results of those parameter studies here as they pertain to the final NUWMAK design. The location of the two most critical insulators is shown in Figure IX-C-18 and the exposure levels at inner TF coil (A) and the closest VF coil (VI) are listed in Table IX-C-9. The most critical point seems to be the insulators in the VF coil. Dose rates of 3×10^8 Rad/yr will be accumulated there. The dose rates are a factor of ten lower in the TF coil (see Figure IX-C-13). These levels will drop with height above the midplane according to the curves in Figure VIII-E-2.

IX-C-1-f. Temperature Levels in NUWMAK Components

The temperature distributions in the blanket of NUWMAK have been discussed in Chapter VII and those in the magnets in Chapter VI. We will only summarize some of these values here for the readers' convenience.

Table IX-C-10 lists the temperature ranges to be expected during normal operation and between burns in the critical components. The temperature oscillation between burns is ~30°C for both the V-5Ti cavity and the Ti-64 first wall.

IX-C-1-g. Stress Levels in NUWMAK Components

There are three alloys of interest here; the V-Ti in the RF cavity, the Ti-64 in the first wall coolant tubes and the coolant tubes that run through the blanket, and the Ti 5626 alloy for structural support. Analysis of the stress levels in these components were presented in Chapter VII and we will only quote the maximum levels in Table IX-C-11.

Table IX-C-8
Transmutation Effects in First Wall of NUWMAK

Element	Initial Atomic %	Composition After 10 Full Power Years,%
C	0.38	0.39
N	0.16	0.16
O	0.57	0.57
Al	10.12	9.92
V	3.58	3.52
Ti	84.95	84.95
Fe	0.24	0.24
Mg		4.1 appm
Sc		1024 appm
Ca		1176 appm
Cr		0.3 appm
Mn		7.8 appm

Table IX-C-9
Summary of Most Critical Insulator Exposure Levels

Components	Rad/year
Epoxy, TF coil, position A	3×10^7
Mylar, TF coil, position A	3×10^7
Electrical Insulator, VF coil, position V_1	3×10^8
Thermal Insulator, VF coil, position V_1	3×10^8
Graphite Insulator, Saddle Coil	---

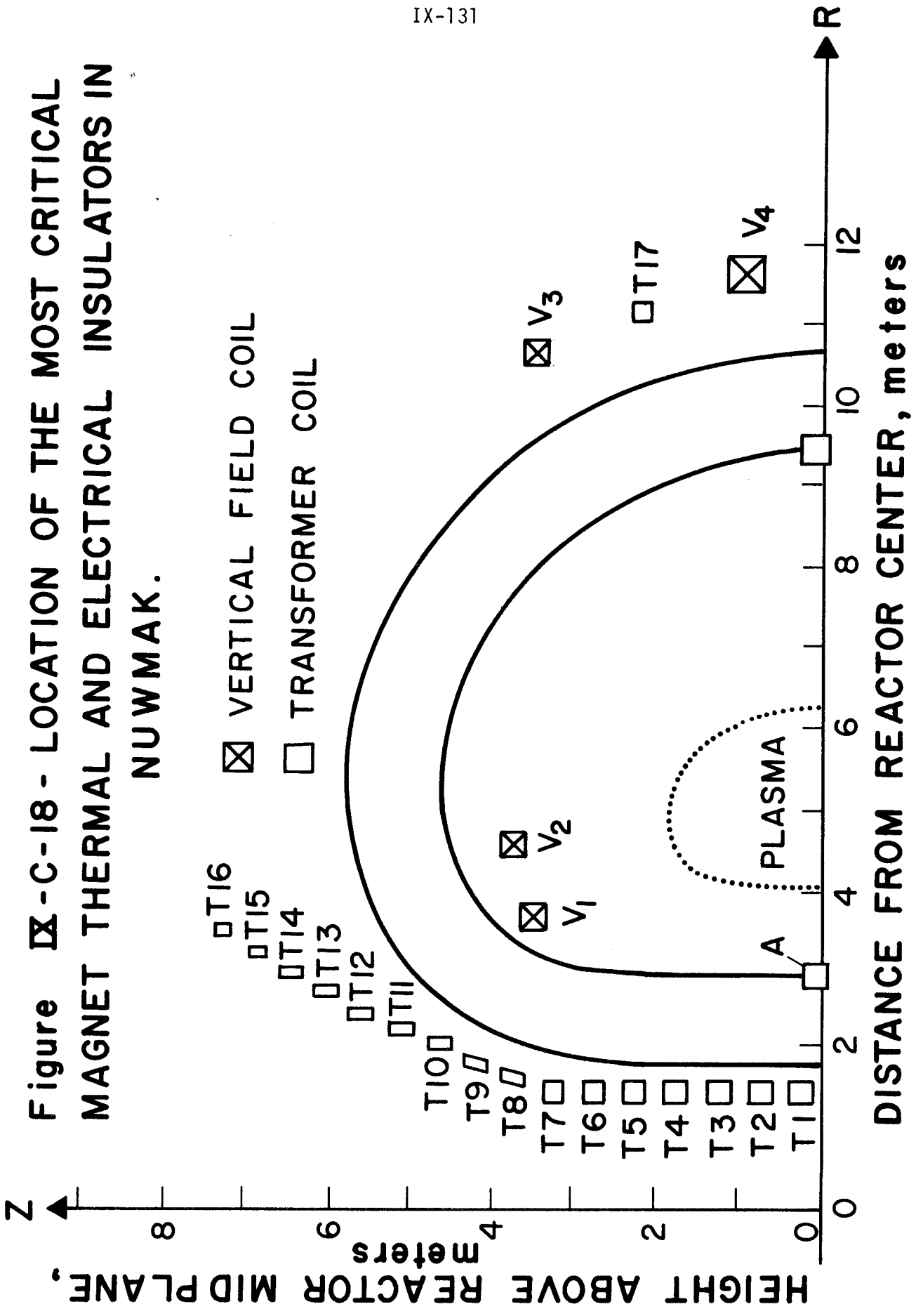


Figure IX-C-18 - LOCATION OF THE MOST CRITICAL MAGNET THERMAL AND ELECTRICAL INSULATORS IN NUWMAK.

Table IX-C-10

Summary of Temperatures in Critical NUWMAK Components

Component		Position	Temperature - °C During Burn	Between Burns
V-5Ti RF Cavity		Plasma Surface	340	300
		Inside Coolant Tube	305	300
Ti-64 First Wall		Plasma Surface	400	305
		Inside Coolant Tube	315	300
Ti-64 Blanket Structure		Coolant Tube - Outside	390	390
		Coolant Tube - Inside	300	300
Ti-64 Shield Structure		Maximum Temp. Position	100-150	100-150
Ti-5262 -Strut		Maximum Temp. Position	500	465
Graphite		Maximum Temp. Position		
Tungsten		Maximum Temp. Position	100-150	100-150
B_4C		Maximum Temp. Position	100-150	100-150
TF Coil	Thermal Insulator	---	77°K to 1.8°K	77°K to 1.8°K
	Al	Stabilizer	1.8°K	1.8°K
	NbTi	Superconductor	1.8°K	1.8°K
	Epoxy		1.8°K	1.8°K
VF Coil	Al	Structure	20°K to 25°C	20°K to 25°C
	Electrical & Thermal		20°K	20°K
Saddle Coil	Copper	Conductor	60°C	60°C
	Graphite Insulator	---	60°C	60°C
	Ti-64	Casing	60°C	60°C

Table IX-C-11

Summary of Anticipated Stress Levels in NUWMAK Components

		Maximum Stress	
		During Burn[a]	During Down Time
V-5Ti	RF Cavity Coolant Tube	20 ksi	10 ksi
Ti-64	First Wall	15 ksi	5 ksi
	Blanket	10 ksi	10 ksi

[a]Not considering cycling during puffing cycle

1 ksi = 6.89 MPa

It can be seen that the maximum stresses occur in the RF cavity and the Ti-64 first wall coolant tubes during the burn phase. The maximum levels are in the 15-20 ksi range but we have not included the variation on a 1-2 second time scale of the gas puffing. We have also not included any effects of creep relaxation during the burn or its subsequent affects during the downtime.

IX-C-2. Anticipated Performance for NUWMAK Structure

It is impossible to establish a definitive lifetime for the Ti-64 alloy in NUWMAK because of the lack of theory and experimental data. However, it is important to put some lower bound limit on the lifetime so that the economics, plant factor, maintenance, and resource questions can beaddressed. To that end we will speculate on what factors might limit the useful lifetimeof aTi-64 first wall assuming that all other components will last at least that long.

The first question to address is that of swelling. As seen in Section IX-B-11 no voids have been observed as of now up to $3.4 \times 10^{21} n/cm^2$ ($E > 0.1$ MeV). This corresponds to roughly 2 dpa (or about 0.13 MW-yr/m^2) and the samples contained 0.3 appm He. Data will shortly be available up to 20 dpa and 3 appm He from EBR-II. It was also noticed (in Table IX-B-15) that ion bombardment to 25 dpa (no helium injection) produced only phase transformation and no voids. Ion bombardment at 550°C to 25 dpa with 250 appm helium produced only 0.02% swelling and the same irradiation conditions at 670°C produced 0.6% swelling. Such a damage level (ignoring rate effects for the minute) corresponds to ~2 MW-y/m^2 in NUWMAK. Hence one might be tempted to assume that damage levels of 1-2 MW-y/m^2 in NUWMAK could be achieved without excessive swelling.

It is difficult to extrapolate these results to what could be found after 1 year of irradiation in NUWMAK (84 dpa on average per year at 70% P.F.) butone way to gain some insight might be to assume a linear swelling rate. If we assume that the incubation dose for swelling in Ti-64 is at least ~10 dpa, then to produce 10% swelling in Ti alloys would take ~ $\frac{15}{0.6} \times 10$ ~250 dpa. This would correspond to ~16 MW-yr/m^2 or roughly 2.6 years of NUWMAK operation at 70% P.F. The above analysis is highly speculative and relies on the fact that the temperature shift for 10^{-3} dpa vs. 4×10^{-6} dpa (maximum in NUWMAK) is ~250°C. It also assumes that the higher damage rate and simultaneous helium injection rates can correctly simulate the fusion environment. With such uncertainty, we will assume that 2 years of NUWMAK operation (~170 dpa) would be a prudent number to design for on the basis of swelling.

Another way of estimating the useful lifetime might be on the basis of unirradiated fatigue life information. There is some indication from work at NRL that, if anything, irradiation improved fatigue life, so assuming that it is unaffected may be a conservative assumption. From Figures IX-B-6a & b and Table IX-B-9 we see that the most limiting fatigue conditions at room temperature would be 27 ksi (186 MN/m^2) for 10^7 cycles. This number of cycles corresponds to ~40,000 burn cycles or about 4 months of continuous operation of the reactor. However, the stresses in the Ti-64 structure are less than 27 ksi, in fact in the neighborhood of 15-20 ksi. This would certainly extend the lifetime by two or more orders of magnitude (see Figure IX-B-6). The effect of temperature is generally to lower the fatigue life of materials and in the absence of data for 400°C operation, we would estimate that it might lower the useful life by an order of magnitude. The net effect would be a useful life on the basis of fatigue data of at least 2 years. Obviously, more data is needed to substantiate this estimate, but it is probably in the general range of what we might expect.

The tentative conclusion that we come to is that the first wall of the NUWMAK reactor could have a lifetime of ~10 MW-yr/m^2 or ~2 years of operation. Much more detailed analyses are in progress and will be reported in the future.

X. Tritium Systems

X-A. NUWMAK Fueling System

X-A-1. Introduction

NUWMAK is a second generation power reactor with a number of optimized functions. The design goals involve high burn fractions to minimize tritium inventories along with a simplified breeding blanket design and facile removal of bred tritium. An effective particle confinement scheme which minimizes tritium losses from the plasma is employed to maximize burn fractions. This technique consists of introducing a cold gas which forms a blanket surrounding the plasma. Periodically a mixture of hydrogen isotopes is "puffed" into the reactor chamber forming a 10 cm layer surrounding the plasma. This has the effect of inverting the plasma density profile so that the plasma is densest at the edge. This effectively limits particle losses from the plasma to that resulting from changes in plasma density during the burn cycle. Since the puffed gas is pulled into the plasma in the density profile inversion, the cold gas blanket serves as a fueling mechanism.

The plasma is composed of a 50-50 mixture of deuterium and tritium. The details of fueling this plasma are discussed in Section X-A-2. The plasma exhaust is purified of non-hydrogenic impurities, pumped by cryosorption pumps, and passed to a cryogenic distillation system for separation and purification of the hydrogen isotopes with subsequent return to the fuel storage vessels. The fueling system is divided into eight identical systems, each serving an eighth of the torus. This eases servicing the system since the blanket and shield are divided into eight units, one associated with each of the eight superconducting magnets. The redundancy means that, in the event of the failure of one system, no more than one-eighth of the tritium in the fueling system will be released to the emergency containment system.

Tritium is bred in the NUWMAK blanket in the eutectic, $Li_{62}\ Pb_{38}$, operating at its eutectic temperature ($464^{o}C$). The blanket, then, consists of a mixture of solid and liquid $Li_{62}\ Pb_{38}$, the proportion of each phase varying with the amount of energy deposited in the blanket. The total weight of $Li_{62}\ Pb_{38}$ in the blanket is 8×10^{5} kg. The heat of fusion of $Li_{62}\ Pb_{38}$ permits the blanket to function as a thermal flywheel, smoothing out the variations in energy delivered to the steam generating system. The equilibrium concentration of tritium in $Li_{62}\ Pb_{38}$

is 0.11 wppm, the equilibrium tritium pressure is estimated to be 10^{-4} torr and the blanket tritium inventory is 88 g. Separation of the bred tritium from Li_{62} Pb_{38} is accomplished by continually pumping a small fraction of the liquid blanket to a processing unit where 50% of its tritium content is removed. Several processing schemes will be evaluated.

1) Extraction of the tritium species from the eutectic with a molten salt and electrolysis of the extracted LiT to isolate T_2 or HT.
2) Sweeping the surface of the eutectic with an inert gas to remove the equilibrium vapor phase tritium.
3) Passing a fine spray of Li_{62} Pb_{38} through an evacuated chamber under such conditions that the tritium within the droplets has time to diffuse to the surface.
4) Sparging the eutectic with an inert gas and removal of the tritium from the gas phase.

The blanket is steam cooled with the coolant tubes passing through the eutectic. The first wall and cooling tubes are fabricated from a titanium alloy containing 6% aluminum and 4% vanadium. The cooling tubes are double walled and each wall is constructed of layers of zirconium and titanium alloy with a nitrided surface. The annulus of the tube is filled with molten lead to facilitate thermal conductance across the tube wall (Chapter VII).

The containment system for NUWMAK consists of three levels during normal operation. Off-normal conditions will be handled via an emergency containment system designed to quickly process large volumes of tritium-contaminated air. The presence of tritium must be evaluated for the many subunits of the reactor which contact tritium during normal operation. The total tritium inventory in NUWMAK is about 22 to 23 kg (see Table X-A-2). Unlike the structural materials of previous tokamak designs, hydrogen isotopes are very soluble in the NUWMAK alloy of construction; therefore, an additional inventory of tritium resides in the alloy of construction itself. The reactor structure will contain an equilibrium quantity of tritium due to the solubility of tritium in titanium. The implications of this are considered in Chapter IX of this report.

The fueling of NUWMAK is considered in Section X-A of this report, the blanket and reactor cooling concerns in Section X-B and tritium containment in Section X-C.

X-A-2. Fueling Scenarios

During normal operation, NUWMAK will produce an average of 2376 $MW_{(th)}$ from a 50-50 deuterium-tritium plasma. RF heating at 92 MHz and 80 MW is sufficient to ignite the plasma in 3.0 seconds. When the RF is shut off, the periodic puffing of hydrogen isotopes is begun. Table X-A-1 lists the design parameters of importance to the evaluation of the tritium requirements for two fueling schemes.

In the first scheme (case I), the cold gas blanket consists of puffed DT. The inverted density profile at the edge of the plasma causes all of the DT to be pulled into the plasma. The plasma is thus fueled by the cold gas blanket. The burn fraction is evaluated from the amount of tritium burned as compared to the amount of tritium handled in the course of a burn. Table X-A-2 lists the reactor tritium inventories for case I fueling.

The partial pressure of DT at the first wall in this case is about 10^{-5} torr averaged over the puff cycle. Since the fraction of coolant tube area on the first wall is small and since the partial pressure of T_2 in the Li_{62} Pb_{38} eutectic is about 10^{-4} torr, the tritium leakage to the coolant due to the cold gas blanket should not amount to more than 1% of that leaked to the coolant from the eutectic and will not be considered in this analysis.

In a second scheme (case II), the cold gas blanket is composed of D_2. Tritium fueling is accomplished by the injection of frozen tritium pellets into the plasma at a speed slow enough to match the rate of deuterium diffusion into the plasma and fast enough to penetrate through the gas blanket with minor ablation losses. Only the amount of tritium required to produce a 50-50 plasma and the required power levels will be introduced. Again, the burn fraction is determined by the tritium burned compared to the tritium handled in the course of a burn. The tritium leakage to the coolant should be virtually nonexistent in this case since there is almost no tritium in the cold gas blanket.

Table X-A-1

Operating Parameters Governing Deuterium and Tritium Flow

Average Thermal Power	2376 $MW_{(th)}$
Energy/D-T Fusion	20.97 MeV
Torus Volume	2.1×10^{8} cm^3
Torus Area	3.60×10^{6} cm^2
Gas Blanket Volume	3.6×10^{7} cm^3
Gas Blanket Thickness	10 cm
Initial Plasma Particle Density	$1.86 \times 10^{14}/cm^3$
Burn Time	225 sec
Down Time	20 sec
Puff Cycle Duration	9 msec
Chug Cycle Duration	391 msec
Maximum Blanket Particle Density (during puff cycle)	10^{12} cm^{-3}
Minimum Blanket Particle Density (during chug cycle)	10^{10} cm^{-3}
Average DT Particle Density	2.5×10^{11} DT/cm^3

Table X-A-2
NUWMAK Tritium Inventory
(Case I Fueling)

Fueling System	
Cryopumps (4 hr cycle time)	1.6 kg
Storage (1 day's supply, 91.8% duty factor)	19.4 kg
Purification System	
Distillation Columns	0.34 kg
Blanket	
Li_{62} Pb_{38} eutectic	0.088 kg
Processing of breeder	0.01 kg
Reactor Coolant	
Coolant (H_2O)	Neglibible
TOTAL	21.4 kg

X-A-3. Deuterium and Tritium Flow Rates

In order to size the tritium handling systems associated with fueling, it is necessary to evaluate the deuterium and tritium flow rates for the fueling scheme of choice. To reconcile the cycle time of the cryopumps with the continuous operation of the cryogenic distillation system, average flow rates (taking into account the duty factor of the reactor's burn cycle) are calculated.

X-A-3-a. Case I: A DT Gas Blanket

In the case of a DT cold gas blanket, the cyclic variation in the edge density profile results in a cyclic variation in the average particle density in the plasma. Thus, the tritium (and an equivalent amount of deuterium) lost from the plasma during a drop in the average plasma density is replaced during the next puff cycle. This results in an increase in the average particle density in the plasma. So the amount of tritium handled on a per second basis is represented by the amount of tritium lost during the plasma density drop. On the average, the plasma particle density varies between 3.65×10^{14} cm^{-3} and 2.47×10^{14} cm^{-3} over a 250 msec interval and is composed of a 50-50 mixture of deuterium and tritium atoms. The average tritium flow rate into the pumps during a burn cycle with 91.8% duty factor is then 4.55×10^{22} T atoms/sec or 0.225 g tritium per second. The burn fraction is then calculated from the average tritium burn rate, 6.72×10^{20} T atoms per second, the above calculated flow rate, and is equal to 1.48%. The amount of tritium present in the cold gas blanket and in the initial charge of DT in the torus is not included in the above calculations since, averaged over the burn cycle, it accounts for less than 1% of the total tritium flow rate.

The amount of deuterium handled will be equivalent to the amount of tritium handled; 0.075 moles D atoms per second or 0.150 grams of deuterium per second. The plasma exhaust will also be assumed to contain about 1% hydrogen due to back diffusion and minor products of less probable fusion reactions.

X-A-3-b. Case II: A D_2 Gas Blanket - Tritium Pellet Fueling

It may be possible to employ the impurity control mechanism of the cold gas blanket and to fuel in such a way as to increase the burn fraction over that resulting from the use of DT in the blanket. The ability of the gas blanket to achieve an inversion of the density at the edge of the plasma

is not sensitive to which hydrogen isotope is used. Thus, if pure deuterium is puffed into the blanket and tritium is injected as frozen pellets at a speed sufficient to match the rate at which puffed deuterium moves into the plasma, no residual tritium remains unused in the blanket; all tritium present resides in the plasma; thus, conceivably increasing the burn fraction substantially.

At this time, however, the necessary plasma calculations from which to derive the tritium flow rates for this mode of fueling are not available. This method represents an ideal case for fueling and one which merits further attention.

X-A-4. Tritium Consumption and Inventory in Storage

Case I will be the one examined throughout this chapter. If the tritium pellet fueling scenario is developed more concretely, it will obviously represent the desirable choice of fueling schemes.

The average burn rate of 6.72×10^{20} T atoms/sec takes into account only the duty factor accruing to the lengths of the burn time and down time during a burn cycle. The plant duty factor will certainly be lower owing to shutdowns for repairs and routine maintenance and may be about 70%. At a 91.8% burn cycle duty factor, 105.5 kg of tritium are burned per year. If a single day's supply at a handling rate of 0.225 g T/sec is to be kept in storage so that the tritium only cycles through the torus once per day, the amount of tritium which must be kept in storage is 19.4 kg.

X-A-5. The Deuterium-Tritium Separation System

The deuterium-tritium separation system includes all purification procedures used to treat the plasma exhaust gas between removal from the torus and storage. Particulate removal, gaseous impurity removal and separation of the hydrogen isotopes into pure gases for storage are all considered part of the separation system. Isotopic separation is included even though the plasma is fueled by a 50-50 mixture of deuterium and tritium because imbalances of the deuterium-tritium ratio will occur as a result of (1) the addition of the tritium-inert gas mixture from the breeding system to the plasma exhaust stream for processing and (2) the presence of a few percent of hydrogen in the plasma exhaust due to back diffusion during a burn. So to more completely control the composition of the fueling mixture, an isotopic separation system is included in NUWMAK. The proposed

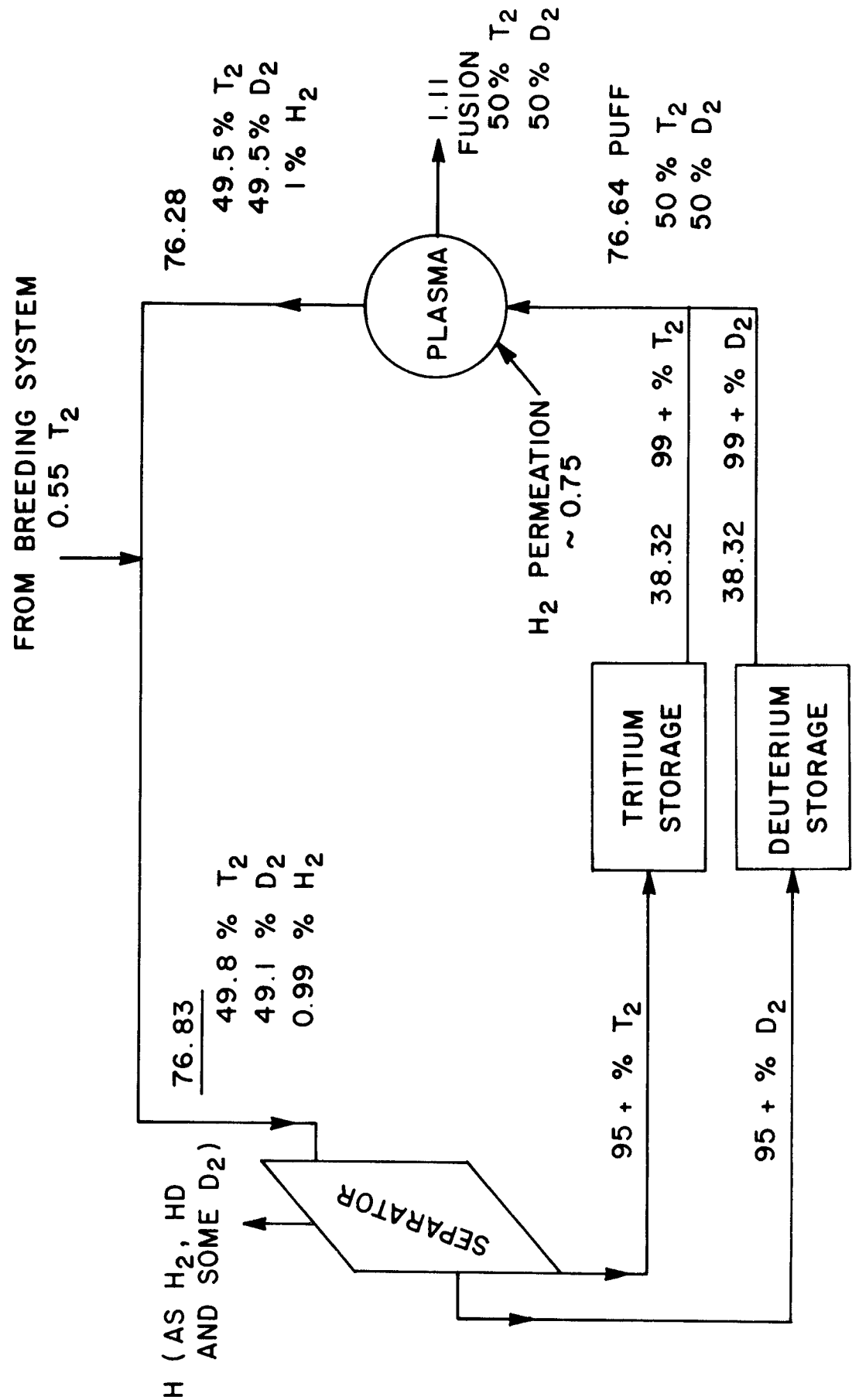
system is largely based on that described in UWFDM-191, the TETR conceptual design.[1] This system, as applied to NUWMAK, is scaled up on the basis of material handling requirements.

X-A-5-a. The Impurity Separation System

From the calculations made in section X-A-3-a, it is possible to construct a preliminary block diagram of the isotopic flow routes in the the fueling system (Figure X-A-1). The composition of the exhausted fuel determines the components of the processing system. In addition to the unburnt fuel, gaseous impurities such as helium, carbon (as methane), oxygen, and nitrogen, and solid impurities such as carbon, titanium, vanadium and aluminum will be exhausted from the torus. These impurities are removed before the hydrogen isotopes are separated. The fuel processing system is divided into eight identical systems, one for each eighth of the torus defined by the eight superconducting magnets. In the event of a system failure in one octant, fuel may continue to be processed in the other seven systems. Since the amount of fuel handled is large compared to the TETR design, the extra redundancy is necessary to reduce to a manageable level the amount of tritium lost in the event of an accidental release. Figure X-A-2 shows the components of one of the eight fuel processing systems. The plasma exhaust will be pumped by cryosorption pumps. Pumping is phased so that half of the pumps are pumping while the other half are regenerating. Pumping and regenerating times are equal and are long compared to the burn time, so average fuel flow rates are used to calculate pump inventories. With a 50% duty cycle, if the regeneration rate is approximately constant, the highest pump inventory is equal to the circulation rate multiplied by half the cycle length. Tritium is exhausted from the torus at an average rate of 0.038 moles T_2 per second. For one-eighth of the torus, the amount of tritium handled is 0.00475 moles T_2 per second. With a cycle length of four hours, the tritium inventory is about 34 moles of T_2 or 205 grams. There will be about 2.05×10^6 Ci per octant and 1.6 kg of tritium in the cryopumps for the whole reactor.

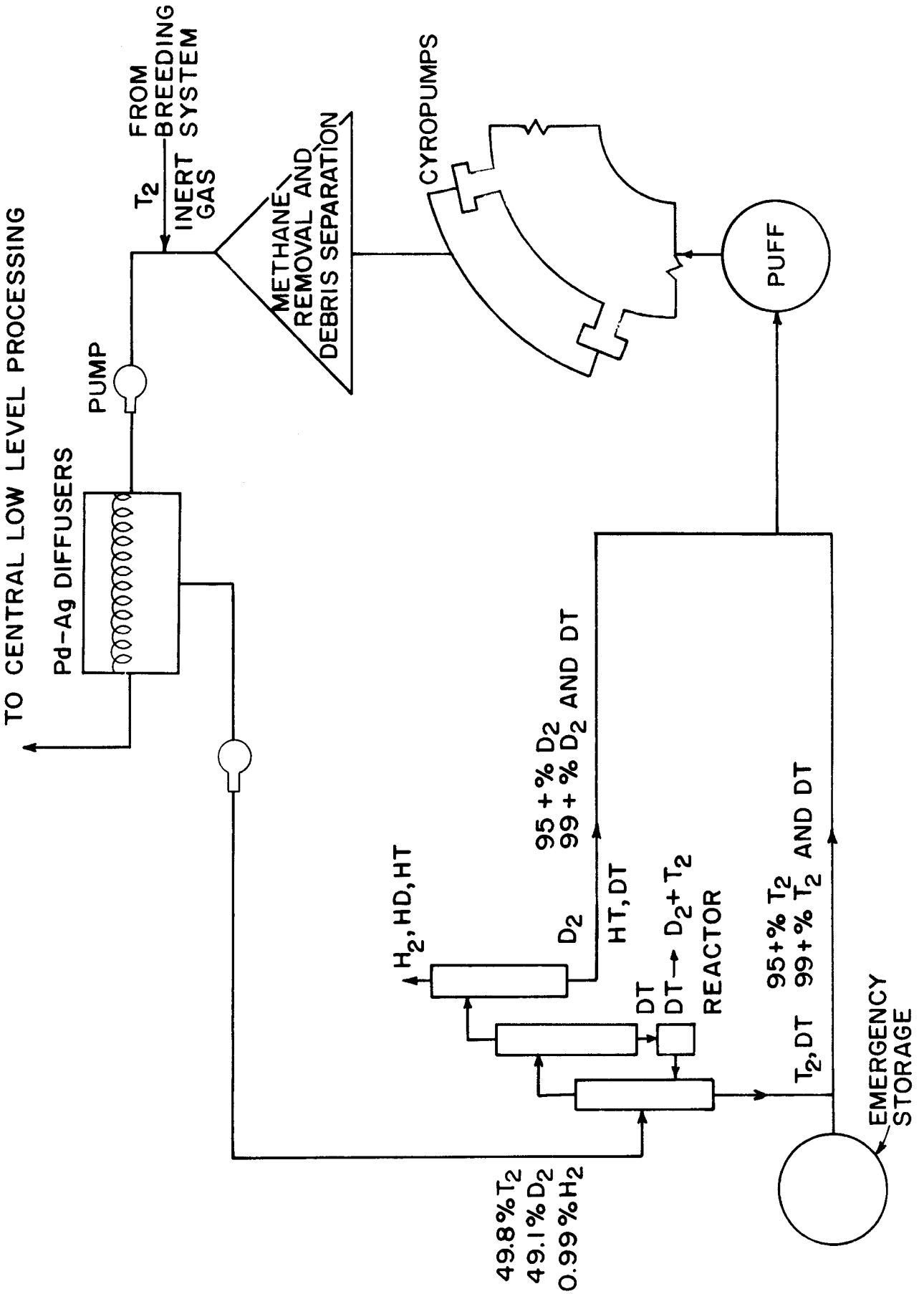
Separation of larger solid debris particles is achieved by the water-cooled chevron shields upon which most solids are expected to plate out. Smaller particles which remain entrained in the hydrogen isotope stream should remain with the stream during the pumping cycle and pass out of the cryopumps during the regeneration cycle.

FIG. X - A - 1 NUWMAK ISOTOPIC FUEL FLOW DIAGRAM



ALL FLOW RATES IN mMOLES / SEC

FUEL PROCESSING SYSTEM FOR ONE OCTANT OF NUWMAK



These solids will however separate out in the Pd-Ag diffuser (see below) and must be removed periodically. These solids must be processed for tritium including, possibly, a high-temperature bakeout to collect absorbed tritium.

After the particulates have been separated, the remaining gaseous mixture is passed to a high temperature cracker to break down organic impurities (principally methane). The stream from the breeding system consisting of 0.5 mol % T_2 in an inert gas is added to the exhaust stream and then passed to a Pd-Ag diffuser to remove all non-hydrogenic gaseous impurities.

A model system of Pd-25 wt % Ag having an effective area of about 580 cm^2 was found to efficiently separate mixtures of H_2 and D_2 from an approximately equal amount of He. Rates were of about 0.4 to 0.5 moles hydrogen isotopes per minute at a temperature of 400°C and high driving pressures (1000 psia or about 52,000 torr).(2) The NUWMAK diffuser system is required to separate about 4.62 moles of hydrogen isotopes from about ten moles of an inert gas and other impurities per minute for the whole reactor. Since permeation follows a square root dependence on the pressure of the hydrogen isotopes and a linear dependence on area, at a reasonable driving pressure of about 1000 torr (a reduction by a factor of 52 from the model system), the NUWMAK diffuser system as a whole must have an effective area of about 4.32 m^2 to process the required amount of hydrogen isotopes. It will be necessary to employ booster pumps to increase the diffuser input pressure over the few torr output of the cryopumps and to increase the diffuser output pressure to that required by the distillation columns. The product gas stream from the diffuser, which contains only hydrogen isotopes, is cooled to 25 K and admitted to the isotope separation system.

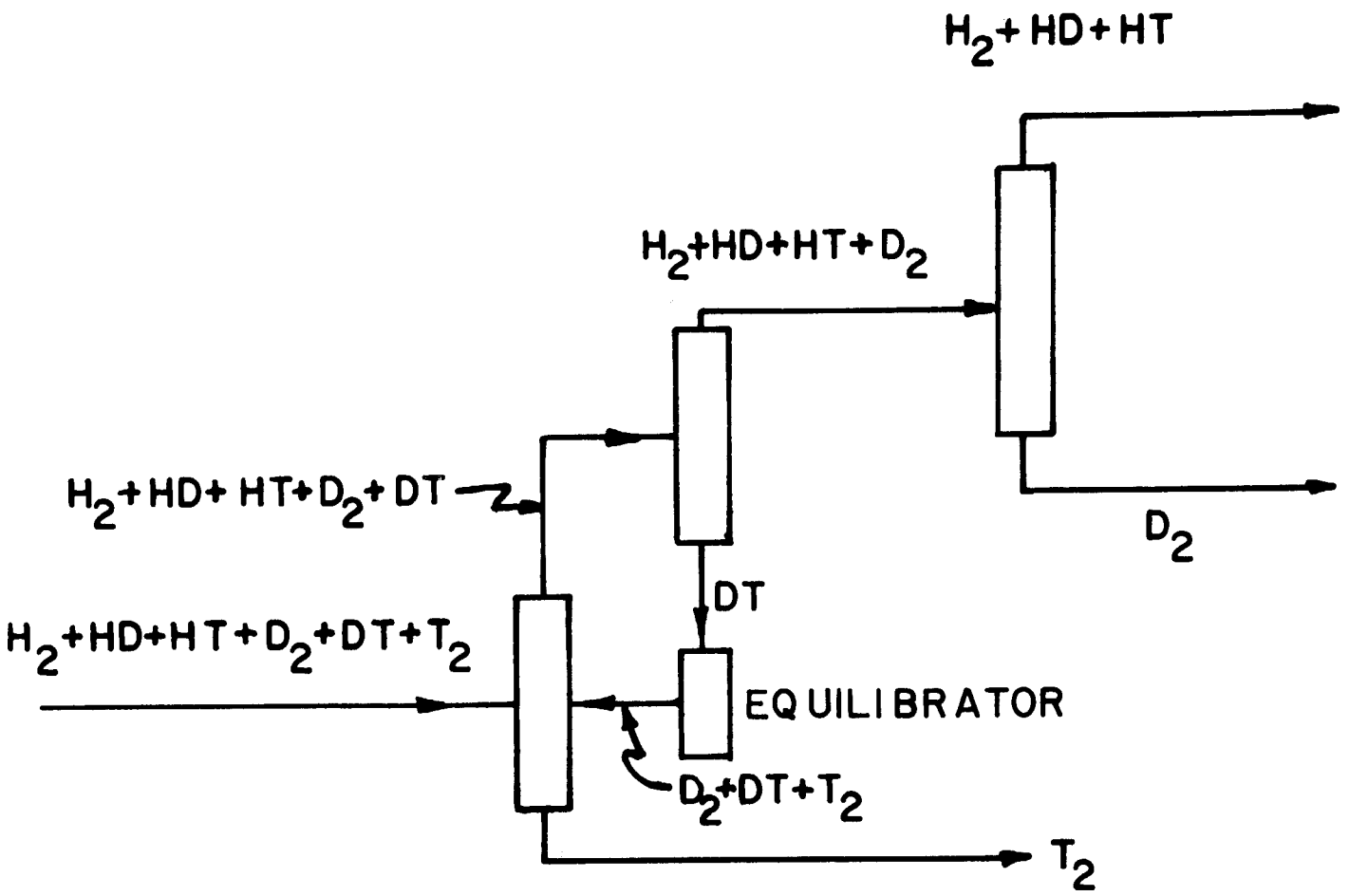
X-A-5-b. The Isotope Separation System

Isotopic separation is accomplished by cryogenic distillation with columns operating at slightly above atmospheric pressure.(1) In this mode, inleakage of the glove box atmosphere surrounding the columns is prevented. The separated isotopes are either stored or passed directly to the puffing system. Tritium may be diverted to a device generating frozen fuel pellets if such a fueling system is employed. In this case, tritium is drawn from storage as needed so that there is no tritium inventory associated with the pellet making process.

Storage of the isotopes may be provided by gas cylinders or hydride beds. The waste hydrogen from the distillation columns as well as the rejected gases from the diffusers will contain some tritium impurities. These wastes must be collected and monitored for tritium content to determine whether further processing is required before disposal. Emergency storage for the fuel system is provided by evacuated tanks with a total volume of about 1000 liters for the entire reactor. This is enough to accommodate more than 35 moles of gas at NTP (the cryopump inventory is about 34 moles of tritium).

Figure X-A-3 diagrams a scheme for the separation of the three hydrogen isotopes and is based on the TETR separation system.[1] Such a system is capable of producing 95+ % pure streams of deuterium and tritium. In TETR, the system for one quadrant of the torus handled 6.69 mmoles/sec of hydrogen isotopes. In NUWMAK, the system in each octant is required to handle about 9.6 mmoles/sec of hydrogen isotopes. At a feed stream composition of T:D:H of about 50:49:1, the contamination of the waste hydrogen should be minimal since 99+% of the tritium occurs as T_2 or DT. Since the capacity of the system in one octant of NUWMAK is only about one and one-half the capacity of the system in one quadrant in TETR, the design of the system can be described by comparable equipment and power requirements, scaled up according to the tritium handling requirements.

The system consists of a multi-stage, multi-component distillation column. The feed stream is introduced at a low temperature to a column operating at 25.1 K. The bottom product of the first column is mostly tritium. The upper product of the first column is fed to a second column, the upper product of which is mostly D_2 with small amounts of HT, HD and H_2. The lower product of the second column is mostly DT and is catalyzed to the equilibrium composition 25% T_2, 25% D_2 and 50% DT. This is passed back to the first column for separation of the T_2. The upper product of the second column is also equilibrated. Since this product is almost entirely deuterium, equilibration will result in almost all of the tritium being converted to DT which remains in the D_2 stream produced at the bottom of a third column. The upper product of the third column is almost tritium-free and may be disposed of by a method appropriate to its tritium content.



THREE COMPONENT SEPARATION SCHEME FOR A MIXTURE OF D AND T

Fig. X-A-3

Heat exchangers may be used to minimize the refrigeration load accruing to the use of the relatively high temperature (i.e., room temperature) equilibration devices.

The tritium inventory of one quadrant in TETR processing 6.69 mmoles isotopes/sec at about 80% tritium is about 47 grams. If this system is scaled down to correspond to a stream which is 50% tritium (as in NUWMAK), the inventory for the system is roughly (50/80) x 47 grams or about 29 grams. If the system is now scaled up to the NUWMAK flow rate of 9.6 mmoles per second of isotopes, the inventory for the system is roughly (9.6/6.7)x(29 grams) or 42 grams of tritium. There are eight such systems in NUWMAK, so the tritium inventory for the reactor's entire distillation system is about 336 kg. This is only a rough estimate since many of the distillation system parameters can be expected to change due to a radically altered T:D:H ratio.

Table X-A-3 lists some of the estimated costs for the distillation system derived from values for the TETR system. Diffusers, refrigeration power, distillation columns and emergency storage costs were scaled by both the number of systems required (8 in NUWMAK vs. 4 in TETR) and the required handling capacity (9.6 mmoles/sec in NUWMAK vs. 6.7 mmoles/sec in TETR). Cracking units, glove boxes and control systems were costed according to the number of such systems in the reactor.

References for Section X-A

1) B. Badger, et al., "TETR - A Tokamak Engineering Test Reactor to Qualify Materials and Blanket Components for Early DT Fusion Power Reactors", UWFDM-191 (June 1977), Section XII-A.

2) F.J. Ackerman, G.J. Koskinas, "A Model for Predicting the Permeation of Hydrogen-Deuterium-Inert Gas Mixtures Through Palladium Tubes", Ind. Eng. Chem. Fundam. 11, 332 (1972).

Table X-A-3

NUWMAK Costs for Fuel Separation

	TETR[1] x 10^3 $	NUWMAK x 10^3 $
Refrigeration Power	280	780
Distillation Columns	200	560
Palladium Diffusers Including Furnaces	20	80
4 Diffuser Systems w/3 Diffusers in Each	96	190
Methane Crackers	40	80
Glove Boxes	500	1000
Control Systems	120	240
Emergency Storage	20	56
	1.276 M $	2.986 M $

X-B. Tritium Properties in and Extraction from Li_{62} Pb_{38}

X-B-1. The Li_{62} Pb_{38} Blanket

The tritium breeding material in NUWMAK is a lithium-lead alloy (8×10^5 kg) of composition 62 atom % Li: 38 atom % Pb. The energy deposited in the blanket and first wall is transported to steam generators by boiling water flowing through Ti-6-4 tubes. The $Li_{62}Pb_{38}$ operates around its eutectic temperature (464^oC) and the solid-liquid phase change is used as a thermal flywheel to supply energy to the steam generators during the plasma downtime. The solid portion of the alloy encircles the coolant tubes and its volume contracts during the plasma burn and expands during the downtime. At the conclusion of the 225 second burn the alloy is 64% liquid and after the 15 second downtime it is only 54% liquid. Selected blanket temperatures are given in Table X-B-1.

Tritium is bred in the Li_{62} Pb_{38} eutectic by the reaction of neutrons with lithium. Consequently, there is a small concentration of tritium in the alloy and it is necessary to know the properties of the lithium-lead-hydrogen isotope system in order to devise a tritium extraction scheme. Unfortunately, data on lithium-lead systems interacting with hydrogen are scarce. Therefore, it is necessary to estimate the pertinent thermodynamic data and kinetic properties of the Li_{62} Pb_{38}-T_2 system. To accomplish this, first the properties of the lithium-hydrogen isotope, lead-hydrogen isotope and lithium-lead systems are surveyed, then experimental observations on the lithium-lead-hydrogen isotope system are given and finally a prediction of the thermodynamic properties and diffusivity of tritium in Li_{62} Pb_{38} is made with support from analogous metal alloy-hydrogen systems.

X-B-2. Thermodynamics of the Lithium-Lead-Tritium System

X-B-2-a. The Liquid Lithium-Hydrogen Isotope System

Recent investigations[1-5] into Sievert's constants for solutions of hydrogen isotopes in liquid lithium are given in Figure X-B-1 and Table X-B-2. The data are in good agreement and show that there is an isotope effect associated with hydrogen solubility in liquid lithium. Only one study[1] has been conducted on tritium solubility. These results are consistent with those expected from extrapolation of hydrogen and deuterium data and are given by the expression:

Table X-B-1

Blanket Temperatures

	Temp. During Burn (^{o}C)	Temp. Between Burn (^{o}C)
First Wall		
Plasma Side	400	300
H_2O Side	305	300
Tubes		
Li_{62} Pb_{38} Side	390	390
H_2O Side	305	300
Maximum in Li_{62} Pb_{38}	500	464

SIEVERT'S CONSTANT FOR HYDROGEN ISOTOPES IN LIQUID LITHIUM

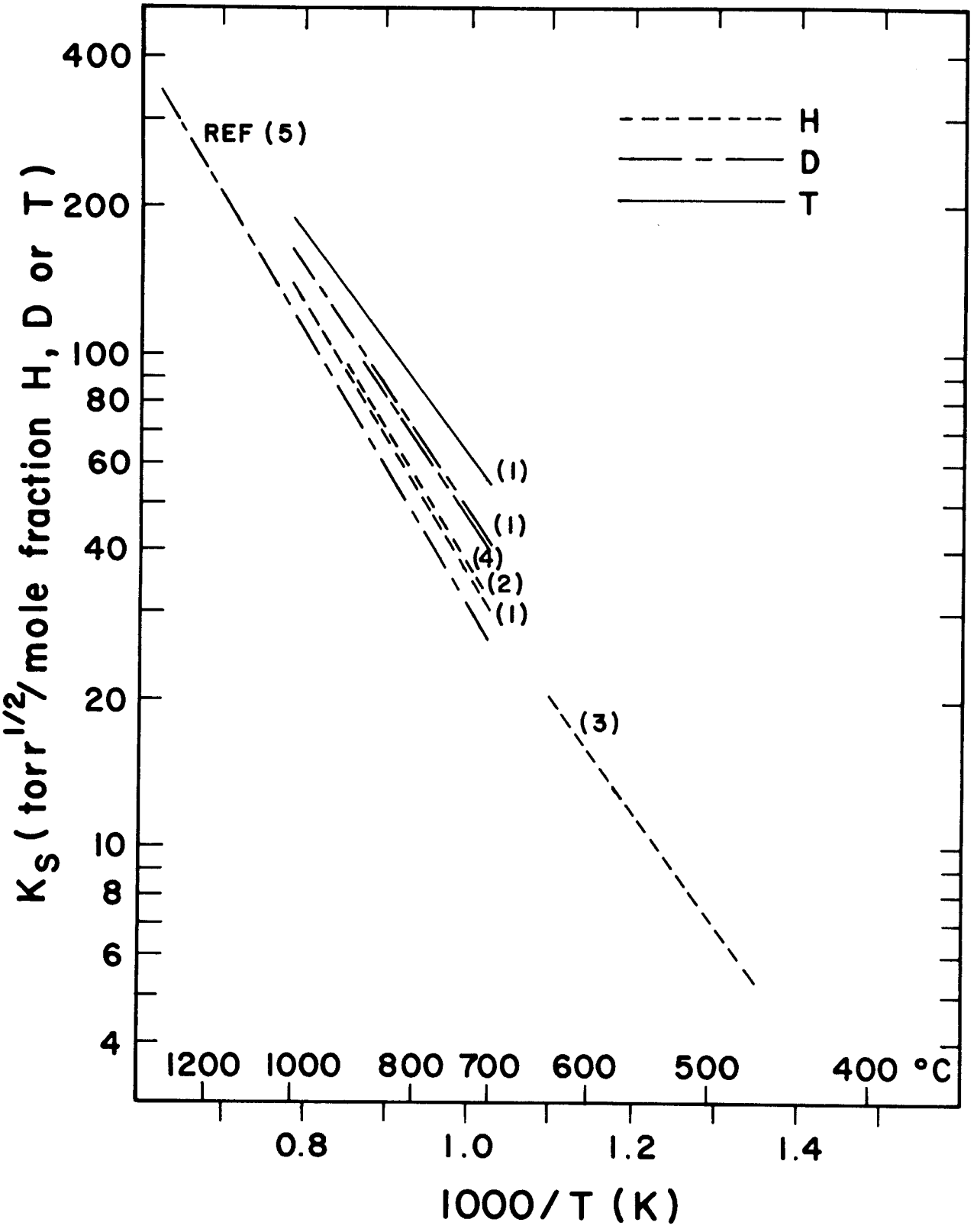


Fig. X-B-1

Table X-B-2

Hydrogen Isotope Solubility in Liquid Lithium

Isotope	Mole Fraction	Sievert's Constant ($torr^{1/2}$/mole fraction LiH,D,T)	Reference
H	0.01-0.1	exp (9.842-6242/T(K))	Smith et al.[1]
H	0.005-0.99	exp (9.815-6182/T(K))*	Veleckis et al.[2]
H	0.002-0.012	exp (8.89-5340/T(K))	Katsuta et al.[3]
D	0.01-0.1	exp (9.515-5644/T(K))	Smith et al.[1]
D	0.01-0.99	exp (9.455-5599/T(K))*	Veleckis[4]
D	$5x10^{-7}$ - 10^{-4}	exp (9.8 - 6381/T(K))	Ihle and Wu[5]
T	0.01-0.1	exp (9.226-5085/T(K))	Smith et al.[1]

*Equations valid for dilute solutions only

$$K_s = \frac{P_{T_2}^{1/2} \ (\text{torr}^{1/2})}{N_{LiT} \ (\text{mole fraction})} = \exp\left(9.226 - \frac{5085}{T(K)}\right) \quad (1)$$

X-B-2-b. The Lead-Hydrogen System

The solubility of hydrogen in liquid lead has been the subject of several investigations. Opie and Grant[6] found hydrogen to follow Sievert'srelation over the temperature range 500 to 900°C. At 600°C and 1 atm pressure the hydrogen solubility was determined to be 0.25 cm^3/100 g of liquid lead. However, this value was not corroborated by subsequent investigators. Under similar conditions Hofmann and Maatsch[7] and Cerjak and Erdmann-Jesnitzer[8] found the solubility of hydrogen to be less than 0.01 cm^3 and ~ 0.03 cm^3/100 g of lead, respectively. In addition, Mannchen and Baumann[9] observed that lead does not absorb hydrogen, even on melting in a hydrogen atmosphere. The high solubility results of Opie and Grant are attributed[7] to oxygen impurities in the lead, which combine with the hydrogen forming water.

Molecular hydrogen is not soluble in solid lead at room temperature,[7,8] though experiments[10,11] have shown that evaporated and sintered lead films absorb gas phase hydrogen atoms (10^{-3} to 10^{-2} torr) to a maximum bulk composition $PbH_{0.19}$ at 0°C. When the hydride is heated, 25% of the hydrogen is desorbed by 140°C[10] and by 190°C about 50% of all the hydrogen incorporated at 0°C has been desorbed.[11]

X-B-2-c. The Lithium-Lead System

The thermodynamics of molten lithium-lead alloys have been investigated at temperatures ranging from 477 to 800°C.[12-15] The activity of lithium has been found to be greatly reduced at mole fractions of less than ~ 0.8. The activity of lithium in molten $Li_{62}Pb_{38}$ as a function of temperature is given in Figure X-B-2. From the figure the lithium activity is 0.0048 and 0.0067 at 464 and 500°C, respectively.

X-B-2-d. Observations on the Lithium-Lead-Hydrogen Isotope System

The following experimental observations of the lithium-lead-hydrogen isotope system have been made:

(1) When LiH is dropped into molten lead in approximate mole ratios of 1 to 3:3 of LiH:Pb at a temperature of ~ 600°C, the hydrogen is released quantitatively.[16] This is the basis of a common technique for the analysis

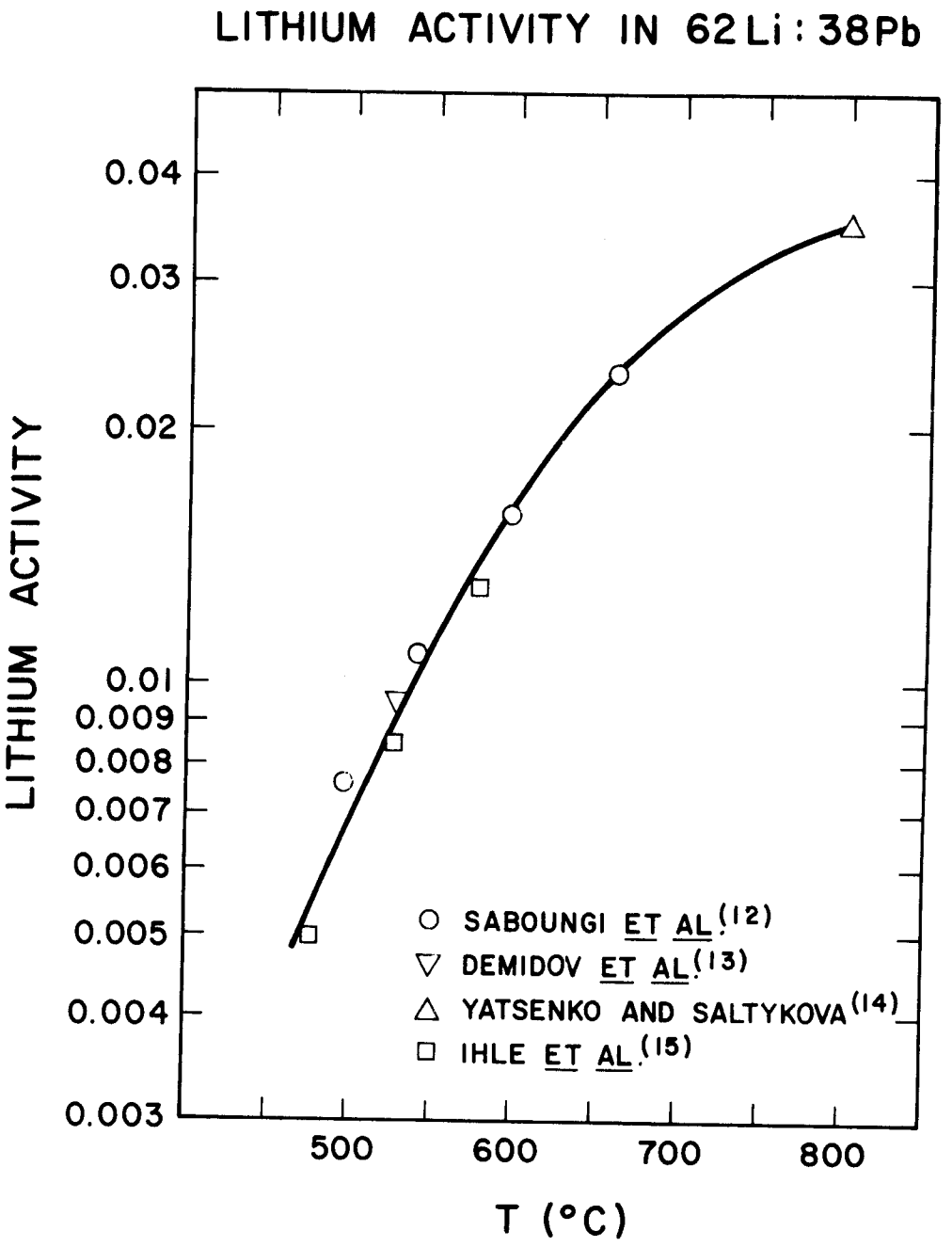

LITHIUM ACTIVITY IN 62Li : 38Pb
LITHIUM ACTIVITY
0.04
0.03
0.02
0.01
0.009
0.008
0.007
0.006
0.005
0.004
0.003
500
600
700
800
T (°C)
SABOUNGI ET AL.(12)
DEMIDOV ET AL.(13)
YATSENKO AND SALTYKOVA(14)
IHLE ET AL.(15)

FIGURE X - B - 2

of hydrogen.[16,17] At lower temperatures the reaction is too slow for analytical purposes and at LiH:Pb mole ratios much greater than 1:1, incomplete decomposition of the LiH is observed.[16]

(2) In lead alloys containing 0.009 to 0.076 weight percent of lithium, there is considerable solubility of hydrogen.[18,19] When the alloys are degassed at 5×10^{-2} torr, hydrogen is evolved in two different stages. In one, found in all the alloys, the hydrogen begins to escape at 425°C and the rate of escape is a maximum at 450 to 500°C. In the other, found only in alloys containing the intermetallic Pb-Li phase, the rate of escape of hydrogen is a maximum at 700 to 800°C.[18]

(3) Experiments[20,21] on the rate of removal of tritium (generated by exposure to thermal neutrons) from solid $Li_7 Pb_2$ have been done. Substituting data from these experiments into Equation (8) in Section X-B-4-a yields a lower limit for Sievert's constant. This analysis is based on the assumption that the tritium leaving the sample is in equilibrium with a surface whose tritium content is the same as the average tritium concentration in the sample.[22] These values for Sievert's constant in the temperature range 400 to 550°C are reported in Table X-B-3, along with the corresponding values for tritium in pure liquid lithium.[1] Also given is a value[15] obtained by introducing a known amount of deuterium into $Li_7 Pb_2$ at 677°C. The result for deuterium is in qualitative agreement with those for generated tritium. From Table X-B-3 it can be seen that the presence of lead increases the value of Sievert's constant as compared with pure lithium.

(4) Recently the solubility of deuterium in liquid lithium-lead alloys was measured at 677 and 767°C.[15] The Sievert constant was found to increase with decreasing lithium content and it was concluded that the solubility of deuterium in lithium-lead alloys changes in accordance with the activity of lithium.

The above experimental observations do not quantitatively describe the $Li_{62} Pb_{38}$-tritium system operating at 390 to 500°C, but they do serve to give some qualitative indication of the expected tritium interaction with the alloy. The first part of observation (1) and observations (3) and (4) imply that the tritium pressure above lithium-lead alloys is substantially greater than above pure lithium at similar temperatures while the second part of observation (1) and observation (2) indicate that

Table X-B-3

Sievert's Constant ($torr^{1/2}$/mole fraction T in Li) for Tritium in Solid $Li_7 Pb_2$ Compared to Liquid Lithium

Temperature (^oC)	Solid $Li_7 Pb_2$[19,20]	Liquid Lithium[1]
400	2,700*	5.3
450	5,500*	9.0
500	10,000*	14
550	18,000*	21
677	12,000+	36+

*Lower limits

+Deuterium

tritium will be more strongly bound in lithium-lead alloys than in pure lead, with a subsequent lower hydrogen isotope pressure above lithium-lead alloys than above pure lead.

X-B-2-e. Estimate of the Thermodynamics of the $Li_{62}Pb_{38}$ - Tritium System

To estimate quantitatively the tritium pressure above $Li_{62}Pb_{38}$, the following equilibrium is postulated in the lithium-lead-tritium system:

$$LiT_{(soln)} \xrightarrow[\text{solvent}]{Li_{62}Pb_{38}} Li_{(soln)} + 1/2\ T_{2(g)} \cdot \qquad (2)$$

The above equilibrium assumes the only manner in which lead enters into the lithium-tritium equilibrium system is to chemically bind the lithium making it less available to interact with the tritium. The equilibrium constant for the above reaction is

$$K' = \frac{a_{Li}\ P_{T_2}^{1/2}}{a_{LiT}} \qquad (3)$$

where a denotes activity. For dilute solutions of LiT in lithium when no lead is present, the activity of lithium is unity and the activity of LiT is incorporated into the Sievert's law expression as given by Equation (1). For this case Equations (1) and (3) are equivalent and K_s is equal to K'. To evaluate Equation (3) when lead is present, the assumption is made that K' remains equal to K_s and is independent of the lithium activity. This assumption implies that there is no lead-hydrogen interaction (Section X-B-2-b). By combining Equations (1) and (3) a Sievert's expression for tritium solubility in liquid $Li_{62}Pb_{38}$ is obtained:

$$\frac{P_{T_2}^{1/2}\ (torr^{1/2})}{N_{LiT}(\text{mole fraction LiT in Li})} = \frac{\exp(9.226-5085/T(K))}{a_{Li}} \qquad (4)$$

The lithium activity in lead is assumed to be unaffected by ppm quantities of tritium and is given in Figure X-B-2. From these activities and Equation (4), the Sievert's constant ($torr^{1/2}$/mole fraction LiT in Li) for tritium in liquid $Li_{62}Pb_{38}$ at 464 and 500°C is calculated to be

~ 2100 at either temperature.

To minimize tritium losses due to permeation into the coolant water, the tritium pressure is limited to 1.0×10^{-4} torr (Chapter IX). This corresponds to a tritium blanket inventory of 88 g (0.11 wppm or 4.8 appm T/Li).

To gain confidence in the preceding method of estimating Sieverts constant for tritium in liquid Li_{62} Pb_{38} at 464 and 500°C, this method was applied to existing data on deuterium in lithium-lead[15] and tritium in lithium-bismuth alloys.[23] Lithium-bismuth alloys were included because this system should be similar to the lithium-lead system as both hydrogen-bismuth[24] and hydrogen-lead (Section X-B-2-b) interactions are very weak. (The lithium activity in liquid Li_{15} Bi_{85} is 3.6×10^{-6}, 1.2×10^{-5} and 3.6×10^{-5} at 500, 600 and 700°C, respectively.[25,26]) The results of estimating Sievert's constant for deuterium in liquid lithium-lead alloys and of estimating the tritium pressure above liquid Li_{15} Bi_{85} are compared with the experimental data in Figures X-B-3 and X-B-4, respectively. These figures indicate that although these estimates do provide a first approximation to the data, the accuracy of this method does not extend beyond this stage.

X-B-3. Diffusivity of Tritium in $Li_{62}Pb_{38}$

X-B-3-a. Hydrogen Isotopes in Liquid Lithium

The diffusion of hydrogen[27] and deuterium[28] in liquid lithium has been studied over the temperature range 600 to 900°C. Since the data for the diffusion of deuterium were later discovered to depend on erroneous assumptions,[29] the hydrogen data were used in further calculations (Section X-B-3-c). There is no obvious way to adjust these data for an isotope effect, so the hydrogen data were used as if it were tritium data. The hydrogen data fit the equation

$$D(cm^2/sec) = 13 \exp\left(\frac{-25{,}000 \text{ cal/mole}}{RT}\right) . \qquad (5)$$

The diffusion coefficients are 5.0×10^{-7} and 1.1×10^{-6} cm^2/sec at 464 and 500°C, respectively.

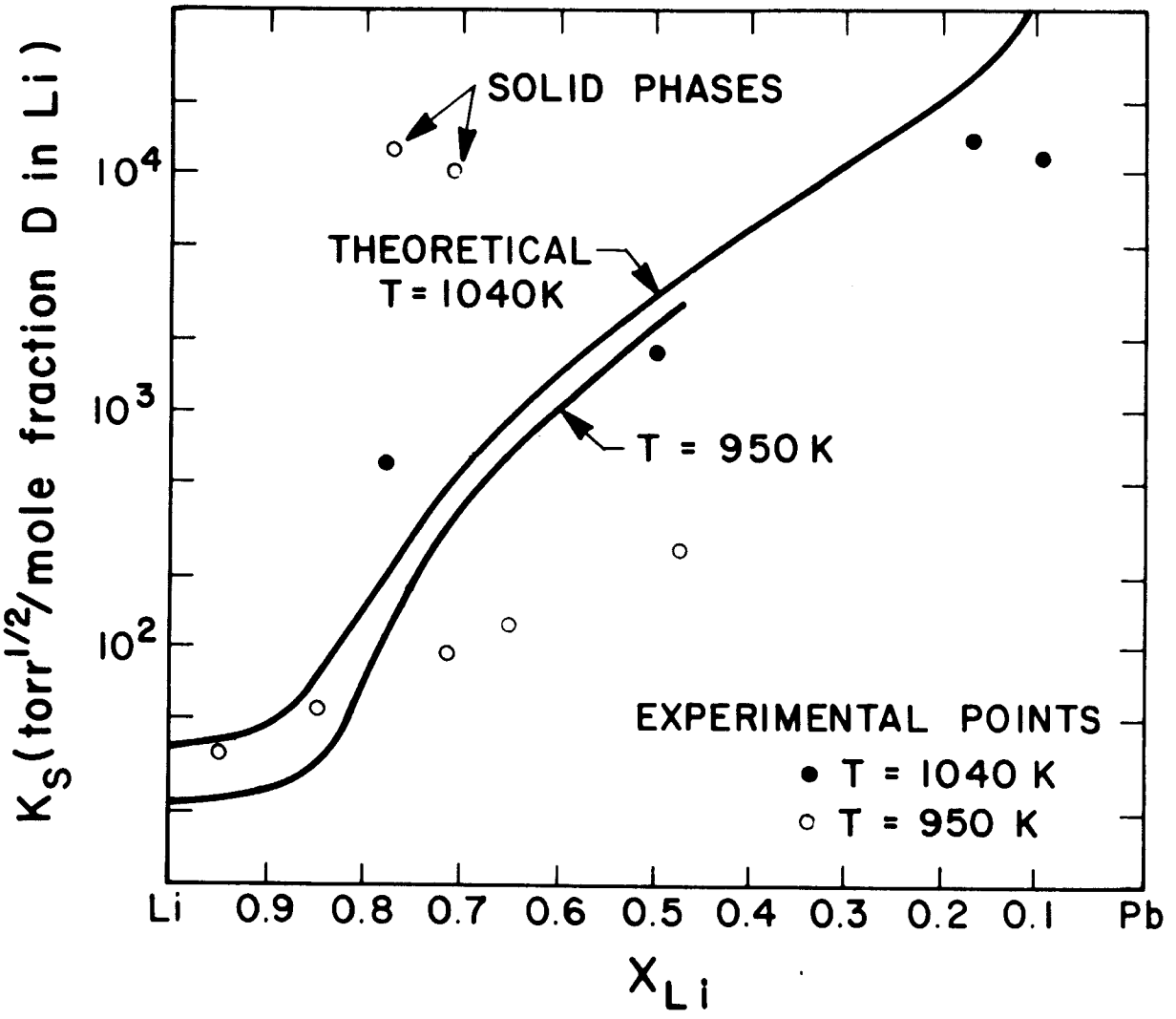


FIG. X-B-3 THE SIEVERT CONSTANT OF DEUTERIUM IN THE Li-Pb SYSTEM AS A FUNCTION OF ATOM FRACTION OF LITHIUM.

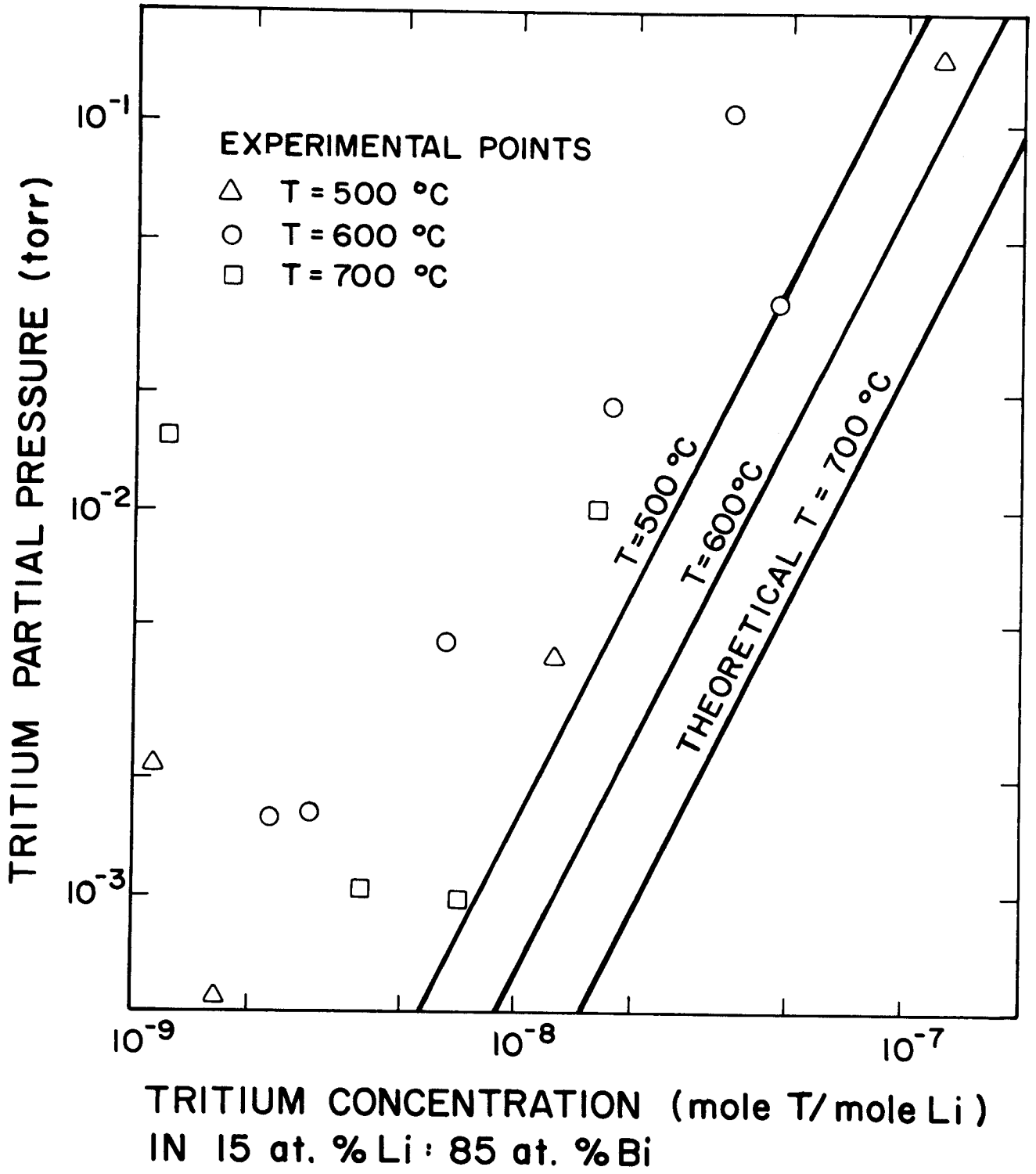

EXPERIMENTAL POINTS
△ T = 500 °C
○ T = 600 °C
□ T = 700 °C
T=500 °C
T=600°C
THEORETICAL T = 700 °C
TRITIUM PARTIAL PRESSURE (torr)
10^-1
10^-2
10^-3
10^-9
10^-8
10^-7
TRITIUM CONCENTRATION (mole T/ mole Li)
IN 15 at. % Li : 85 at. % Bi

FIGURE X-B-4

X-B-3-b. Estimate of the Diffusivity of Hydrogen in Liquid Lead

The diffusivity of hydrogen in molten lead has not been determined. The diffusion coefficient of hydrogen in liquid tin, which is also a Group IVA metal, has been measured at roughly 1 cm^2/sec at 1009°C.[30] The energy of activation for hydrogen diffusion in liquid tin could not be unequivocally determined from this study, though it was expected to be lower than liquid silver which was only 1.359 kcal.[30] It is unlikely the results for hydrogen diffusion in liquid lead would differ greatly from those for liquid tin. Therefore, the diffusion coefficient of hydrogen in liquid lead at ~ 500°C is expected to be > 10^{-2} cm^2/sec.

X-B-3-c. Estimate of the Diffusivity of Tritium in Liquid $Li_{62}Pb_{38}$

Few results are available on which to base an estimate of the diffusivity of tritium in liquid Li_{62} Pb_{38}. However, a qualitative idea of what can be expected can be obtained from studies on the diffusion of hydrogen in liquid iron[31] and nickel[32] alloys. It was found in the experiments on liquid iron alloys[31] that the addition of nickel decreased the diffusivity of hydrogen while copper and tin increased it. In each case the diffusivity was intermediate between the values of the two pure components.[30]

The study on hydrogen diffusion in liquid nickel alloys[32] found an inverse relationship between the hydrogen diffusion coefficients in these alloys and the hydrogen solubility in the same alloys. This negative correlation between solubility and diffusivity of hydrogen has also been found to hold for pure liquid metals.[30] Since the solubility of tritium in liquid Li_{62} Pb_{38} compared with pure lithium is expected to be decreased by the activity of lithium in the alloy (Section X-B-2-e), the diffusivity of tritium is expected to be increased in the alloy compared with pure lithium by roughly an equal magnitude. Dividing the diffusion coefficients obtained for tritium in pure lithium (Section X-B-3-a) by the activity of lithium in Li_{62} Pb_{38} (Figure X-B-2) yields 1.0×10^{-4} and 1.6×10^{-4} cm^2/sec for the diffusion coefficients in liquid Li_{62} Pb_{38} at 464 and 500°C, respectively. These coefficients are then used in the following section on calculations involving the design of a tritium extraction unit.

X-B-4. Tritium Extraction From Li_{62} Pb_{38}

Tritium is bred in the blanket at a rate of 450 g/day or 0.0052 g/sec and must be extracted at this rate. The first process that was examined was the possibility of extracting tritium from Li_{62} Pb_{38} with a molten alkali halide salt. This process has shown considerable promise for removing hydrogen isotopes at the ppm level from liquid lithium.[33,34] In this method liquid lithium and a molten salt are contacted and the LiT is preferentially distributed in the salt phase.[33] The salt is then electrolyzed to yield T_2[34]. However, the data indicate that lithium-lead alloys behave differently than pure lithium.[12,35] Two specific concerns that arise are possible unfavorable tritium distribution coefficients between the liquid alloy and the molten salt and possible excessive mutual solubilities of the alloy and the molten salt. The latter concern is of particular importance as it is undesirable to transport alkali halides to the blanket due to both neutronic and corrosion considerations. Heymann and Weber[36] found that when binary liquid alloys of sodium with metals such as tin, bismuth, antimony and gold were contacted with molten NaBr or NaI at 770°C, the alloying metal was passed into the salt phase to an appreciable extent. More recent experiments[37] have shown this to also be the case for the molten solvent NaCℓ-NaI (37:63) in the temperature range 600 to 1000°C. The Na-Bi and Na-Sb phase diagrams in particular, and the Na-Au and Na-Sn phase diagrams to a lesser extent, are similar to the Li-Pb phase diagram.[24] Also, in experiments in which liquid lithium-bismuth alloys were contacted with molten LiCℓ[38] and molten LiCℓ-LiF(70:30)[39] in the temperature ranges 650 to 800°C and 600 to 1000°C, respectively, the lithium-bismuth alloy was found to have a finite solubility in the molten salt. Consequently, although molten salt extraction may be applicable to the NUWMAK design, uncertainties are such at this time that other extraction schemes were pursued. Liquid alloy getters[40,41] also suffer from the possibility of mutual solubility with Li_{62} Pb_{38} and are, therefore, undesirable in the NUWMAK design.

The tritium in Li_{62} Pb_{38} is less tightly bound chemically than in pure lithium (Section X-B-2-d) and some type of physical extraction of the tritium should be possible. Three processes examined were (1) removal of the tritium with a sweep gas, (2) vacuum extraction of the tritium and (3) inert gas purging of the alloy. To determine which schemes warrant further investigation and which are obviously untenable, certain parameters were arbitrarily set to values that are reasonable but not optimized. To achieve this the alloy is assumed to be at ~ 500°C to ensure liquid conditions throughout its residence time in the extractor. Also a maximum residence time in the extractor of 300 sec is assumed during which 50% of the tritium is removed. The alloy flow rate through the extractor, calculated by multiplying the alloy blanket inventory (8×10^5 kg) by the tritium breeding rate (0.0052 g/sec) and dividing by the tritium inventory (88 g) and the extractor efficiency (0.50) is 95 kg/sec.

X-B-4-a. Tritium Extraction With a Sweep Gas

Under the most favorable conditions in which an inert gas sweeps the surface of the Li_{62} Pb_{38} to collect the tritium, diffusion of the tritium to the surface is essentially instantaneous and an equilibrium partial pressure of tritium continually exists above the alloy. Then the rate of removal of tritium is governed by Sievert's Law and the tritium extraction equation can be expressed as

$$\left(\frac{RK[T]n_{Li}}{2F_g}\right)\frac{dy}{dt} = (K_s[T]y)^2 \qquad (6)$$

where y is the fraction of tritium remaining in the Li_{62} Pb_{38} after time t (sec) in the extractor,

R is the gas constant,

K is the temperature in Kelvin,

$[T]_{Li}$ is the initial tritium concentration in the Li_{62} Pb_{38} in mole T/mole Li,

n_{Li} is the moles of lithium in the extractor,

F_g is the flow rate of inert gas in ℓ/sec,

K_s is Sievert's constant for tritium in Li_{62} Pb_{38} in $torr^{1/2}$/mole fraction T in Li, and

2 converts moles T to moles T_2.

Rearrangement and integration of Equation (6) gives

$$\int_{y}^{1} \frac{dy}{y^2} = \frac{2K_s^2[T]F_g}{RKn_{Li}} \int_{o}^{t} dt \quad , \tag{7}$$

which yields

$$1/y - 1 = \frac{2K_s^2[T]F_g t}{RKn_{Li}} \quad . \tag{8}$$

The flow rate, F_g, necessary to extract 50% of the tritium (y=0.5) in 300 seconds when

$$R = 62.36 \frac{\text{torr-}\ell}{\text{mole K}}$$

$$K = 773 \text{ K}$$

$$[T] = 4.8 \times 10^{-6} \text{ moles T/mole Li}$$

$$n_{Li} = 95 \frac{\text{kg}}{\text{sec}} Li_{62} Pb_{38} \times \frac{7.47 \text{ moles Li}}{\text{kg } Li_{62} Pb_{38}} \times 300 \text{ sec}$$

$$= 2.1 \times 10^5 \text{ moles Li, and}$$

$$K_s = 2100 \text{ torr}^{1/2}\text{/mole fraction LiT in Li}$$

is 8.0×10^5 ℓ (STP)/sec or 3.6×10^4 moles/sec. A flow rate of this magnitude is clearly unreasonable so this scheme was not pursued further.

X-B-4-b. Vacuum Extraction of Tritium

Hydrogen can be removed from liquid metals by exposing the metal to a vacuum at a pressure less than the equilibrium tritium partial pressure above the metal.[42] If a 50% efficient extraction scheme is desired, the exiting Li_{62} Pb_{38} will have a tritium concentration of only 2.4×10^{-6} mole T/mole Li, and by Equation (4) the tritium pressure in the chamber must be $\leq 2.5 \times 10^{-5}$ torr. The quantity of tritium that must be extracted from the alloy is 5.2×10^{-3} g/sec or 8.7×10^{-4} mole T_2/sec. This is 1.7×10^6 ℓ/sec at 300 K and 9.7×10^{-6} torr (2.5×10^{-5} torr x 300 K/773 K) which is a very high pumping speed for conventional, mechanical pumps. For this reason the feasibility of cryosorption pumping was examined.

Cryosorption pumps are useful only if their surfaces remain clean. Therefore, it is imperative that excessive quantities of lead or lithium are not transported into the vapor phase. The vapor pressure of lead over lithium-lead alloys can be approximated by multiplying the vapor pressure of pure liquid lead, given by the equation [43]

$$P_{Pb}(\text{torr}) = \exp\,(17.86 - 2.23 \times 10^4/T(K)) \qquad (9)$$

by the activity of lead in $Li_{62}\ Pb_{38}$ at 500°C. The activity of lead is 0.025[12-14] so the alloy has a lead vapor pressure of 4.2×10^{-7} torr which is much less than the pressure of 2.5×10^{-5} torr in the vacuum chamber.

The lithium vapor pressure above the alloy can be determined in a similar manner. The vapor pressure of liquid lithium is given by:[5]

$$P_{Li}(\text{torr}) = \exp\,(18.2 - 18{,}690/T(K)) \; . \qquad (10)$$

The activity of lithium at 500°C is 0.0067 (Fig. X-B-2). Multiplication of the pure lithium vapor pressure by the activity of lithium will give a lithium pressure of 1.7×10^{-5} torr at 500°C. This is close to the pressure in the chamber which results in the evaporation of some lithium and subsequent condensation on the cryosorption pumps, thus rendering them ineffective.

These calculations on the lithium vapor pressure indicate that even if conventional pumps were used, baffling would be necessary to condense out the lithium before it reaches the pumps. This would place a large impedance on the pumps and necessitate design of a system with a capacity in excess of the 1.7×10^6 ℓ/sec stated above. Therefore, it appears the lithium pressure is too near the T_2 pressure for vacuum extraction to be viable.

X-B-4-c. Tritium Extraction With a Purge Gas

The final method for the removal of tritium is to introduce inert gas bubbles at the bottom of the melt.[44,45] Either of two conditions may then govern tritium removal. In the first case the mass transfer of tritium to the inert purge gas bubble is rapidly achieved, and the

equilibrium pressure of tritium in the purge bubble is reached during the rise of the bubble through the liquid metal. In the second case the mass transfer of tritium from the liquid metal to the inert purge gas bubble limits the rate of hydrogen extraction and equilibrium conditions are not reached. Industrially the first case holds approximately for hydrogen extraction from liquid iron[44,46] and the second case holds for hydrogen in liquid aluminum.[44,47]

For the case where equilibrium between tritium in the liquid phase and the inert gas bubble exists, Geller[48] has derived the basic relation whereby the quantity of purging gas required to reduce the dissolved gas in the liquid metal to a predetermined minimum may be calculated. The equation for a purging gas of infinitesimal bubble size is given as:

$$F_g = \frac{11.2 n_{Li}}{t}\left[\frac{P}{K_S^2}\left(\frac{1}{[T]_f} - \frac{1}{[T]_i}\right) + [T]_i - [T]_f\right] \quad (11)$$

where F_g is the ℓ(STP)/sec of purging gas required. P is the external pressure on the alloy and is equal to 760 torr. The other parameters in Equation (11) are given as follows:

K_S is Sievert's constant
= 2100 $torr^{1/2}$/mole fraction LiT in Li,
$[T]_i$ is the initial concentration of tritium
= 4.8×10^{-6} mole of T/mole of Li,
$[T]_f$ is the final concentration of tritium
= 2.4×10^{-6} mole T/mole Li,
n_{Li} is the moles of lithium in the extractor
= 95 kg/sec Li_{62} Pb_{38} x $\frac{7.47 \text{ moles Li}}{\text{kg } Li_{62} Pb_{38}}$ x 300 sec = 2.1×10^5 moles Li,
t is the time in the extractor = 300 sec, and
11.2 converts moles T to ℓ of gas.

For the above parameters F_g must be 2.8×10^5 ℓ/sec at STP. This appears unworkable. However, if the external pressure, P, is kept at 10^{-2} torr, then Equation (11) gives a flow rate of only 3.7 ℓ(STP)/sec. The vacuum system must then handle 3.1×10^5 ℓ/sec at 10^{-2} torr and 300 K which is 3.1×10^3 torr-ℓ/sec. This is a relatively large, but not unfeasible pumping speed. However, if the extraction process is in fact not controlled by equilibrium conditions within the melt, the pumping speed may rise to an unreasonable level.

A calculation was made to check that the extraction process was indeed equilibrium, and not mass transfer, controlled. Pehlke[49] gives the expression for such a case as:

$$\ell n\ y = -\left(\frac{DA_s}{\delta} + \frac{3000 k_T F_g h}{r_b v_t}\right)\ t/V_m \qquad (12)$$

where y is the fraction of tritium remaining in the $Li_{62}\ Pb_{38}$ after time t (sec) in the extractor,

D is the diffusion coefficient of tritium in $Li_{62}\ Pb_{38}$ in cm^2/sec,

A_s is the surface area of the melt in cm^2,

δ is the boundary layer thickness at the top of the melt in cm,

k_T is the mass transfer coefficient for tritium from $Li_{62}\ Pb_{38}$ to a flowing gas bubble in cm/sec,

F_g is the flow rate of the purge gas in ℓ/sec,

h is the height of the melt above the exit of the bubble from the delivery mechanism in cm,

r_b is the bubble radius in cm,

v_t is the terminal rise velocity of a bubble in the melt in cm/sec and is equal to $c(gr_b)^{1/2}$ where g is the acceleration due to gravity (981 cm/sec^2) and c is 2.54 and 1.15 for bubbles in liquid aluminum[49] and liquid steel,[50] respectively, and is estimated to be ~ 1.5 for liquid $Li_{62}\ Pb_{38}$ and

V_m is the volume of $Li_{62}\ Pb_{38}$ in the extractor in cm^3.

The bubble radius is assumed to be twice the radius of the orifice through which the gas is delivered to the alloy.[49] An orifice radius of 0.05 cm should yield a bubble radius (r_b) of ~ 0.1 cm. Then v_t will be 15 cm/sec. The geometry of the extraction unit will determine the parameters V_m, $\underline{h}$ and A_s. For a 300 second residence time and an alloy flow rate of 95 kg/sec the extractor must contain 2.9×10^4 kg of liquid alloy. The density of $Li_{62}\ Pb_{38}$ at 500°C is 5.8 g/cm^3,[51] which results in an extractor volume (V_m) of 5.0×10^6 cm^3. If $\underline{h}$ is set at 250 cm, A_s will be 2.0×10^4 cm^2. The diffusion coefficient, $\underline{D}$, has already been estimated to be 1.6×10^{-4} cm^2/sec (Section X-B-3-c). The boundary layer thickness, δ, is unknown but is in the region of 4×10^{-4} to 2×10^{-3} cm for liquid lead at 700°C[52] and arbitrarily estimated to be 10^{-3} cm here. The fraction of tritium remaining in the $Li_{62}\ Pb_{38}$ after passage through the extractor, y, is 0.50.

Equation (12) can then be solved for the minimum mass transfer coefficient (k_T) necessary such that the rate of mass transfer of tritium from the $Li_{62}\ Pb_{38}$ to the inert gas does not limit the degassing of $Li_{62}\ Pb_{38}$ where the flow rate of the flush gas, F_g, was determined from Equation (9) to be 10.5 ℓ/sec at 500°C. The mass transfer coefficient must be at least 1.6×10^{-3} cm/sec for equilibrium conditions to prevail in this degassing scheme. Generally, transfer coefficients higher than this are found. A value of 3.9×10^{-2} cm/sec for hydrogen in liquid aluminum at 700°C[49] and of 1 cm /sec for hydrogen in liquid steel at 1600°C[45] gives an idea of the order of magnitude for hydrogen mass transfer in liquid metals. From theoretical considerations[52] a transfer coefficient in the range 10^{-2} to 10^{-1} cm/sec is expected for the mass transfer of tritium dissolved in the alloy (500°C) to single bubbles of radius 0.1 cm which are flowing through the alloy. Therefore, it appears that equilibrium conditions rather than mass transfer will govern the extraction of tritium from $Li_{62}\ Pb_{38}$ at the concentrations found in NUWMAK.

Roots blowers, sometimes called "mechanical booster pumps," are used in NUWMAK to maintain the surface of the alloy at 10^{-2} torr. Lithium that is vaporized must be condensed on cooled baffles before it reaches the pumps. The lithium is condensed at a temperature above its melting point,

drained from the baffles and reunited with the alloy. This quantity of lithium can be roughly approximated by multiplying the moles of T_2 removed per day (75) by the ratio of the lithium and tritium pressures at 500°C (1.7×10^{-5} torr: 2.5×10^{-5} torr) to give 51 moles or only 350 g of lithium per day.

The vacuum pumping system is designed with primary blowers to raise the pressure from that of the extraction unit (10^{-2} torr) to that of the cryopumped plasma exhaust after particulate removal. This extracted tritium is thus merged with the plasma exhaust (Section X-A-5-a). The complete tritium extraction scheme is shown in Fig. X-B-5.

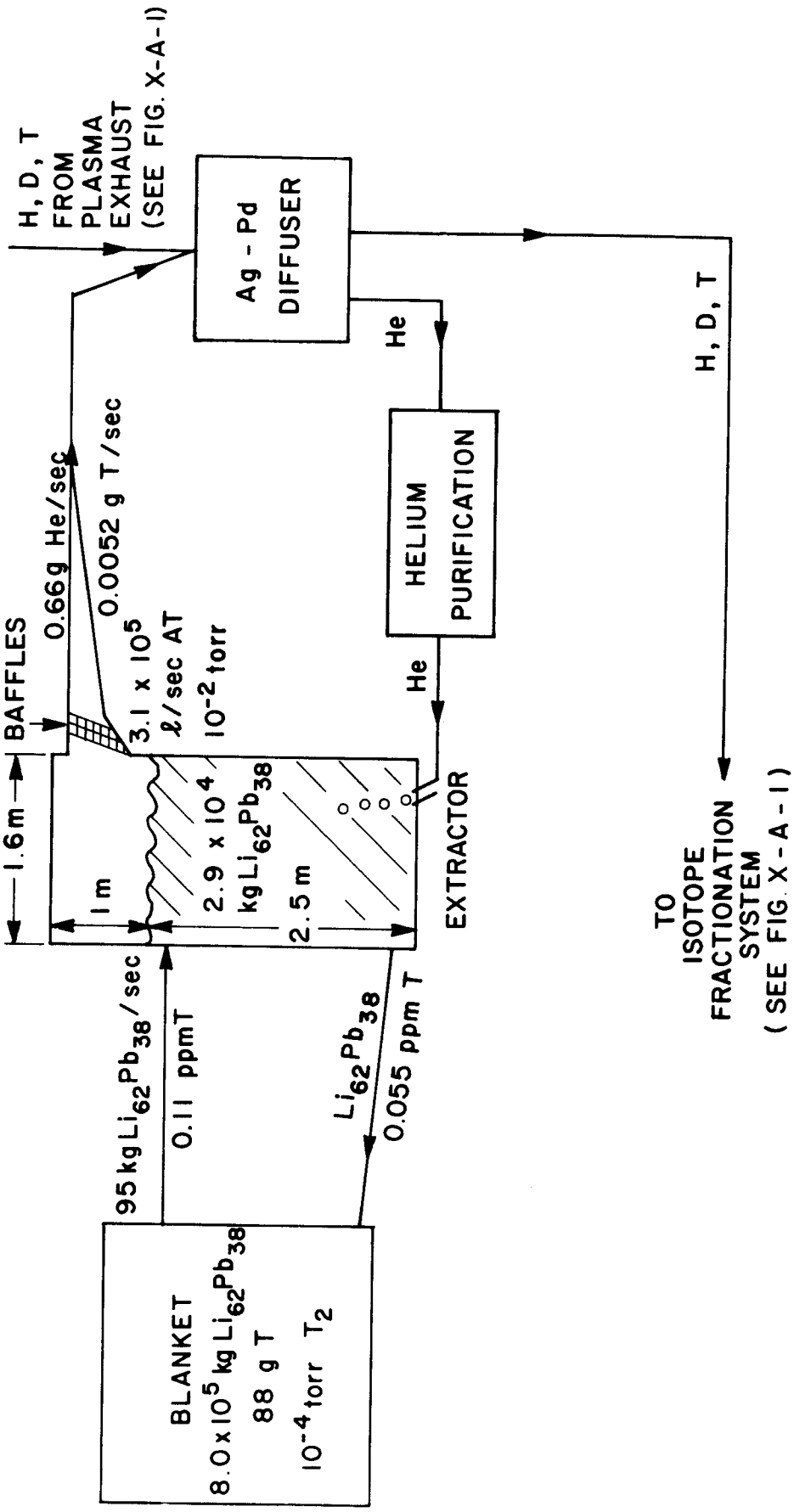


FIG. X - B - 5 TRITIUM EXTRACTION SCHEME

References for Section X-B

1. F.J. Smith, A.M. Batistoni, G.M. Begun, J.F. Land, "Solubility of Hydrogen Isotopes in Lithium", Report 1976 Conf. 760631-1.

2. E. Veleckis, E.H. Van Deventer and M. Blander, "The Lithium-Lithium Hydride System", J. Phys. Chem. 78 (1974), 1933-1940.

3. H. Katsuta, T. Ishigai and K. Furukawa, "Equilibrium Pressure and Solubility of Hydrogen in Liquid Lithium", Nucl. Technol. 32 (1977), 297-303.

4. E. Veleckis, "Thermodynamics of the Lithium-Lithium Deuteride System", J. Phys. Chem. 81 (1977), 526-531.

5. H.R. Ihle and C.H. Wu, "The Solubility of Deuterium in and Its Separation From Liquid Lithium by Distillation", Hydrogen in Metals, Vol. 1, Proceedings of the 2nd International Congress, Paris, France, June 6-10, 1977, Pergamon Press, New York (1977).

6. W.R. Opie and N.J. Grant, "Solubility of Hydrogen in Molten Lead", Trans. AIME 191 (1951) 244-245.

7. W. Hofmann and J. Maatsch, "The Gas Content of Lead", J. Erzbergbau u. Metallhüttenw. 10 (1957) 313-317.

8. H. Cerjak and F. Erdmann-Jesnitzer, "Increasing the Creep Strength Through Reaction Products Formed in the Melt. I. Lead-Lithium-Hydrogen Alloys", Metall. 22 (1968) 113-123, as cited by ref. (18).

9. W. Mannchen and M. Baumann, "The Absorption of Hydrogen by Lead and Alloys of Lead With Magnesium and Calcium", Metall. 9 (1955) 686-688, Chem Abst. 49:14410c.

10. B.R. Wells and M.W. Roberts, "A Lead Hydride of High Stability", Proc. Chem. Soc. (1964) 173-4.

11. M.W. Roberts and N.J. Young, "Interaction of Atomic Hydrogen With Evaporated Lead Films", Trans. Faraday Soc. 66 (1970) 2636-2643.

12. M.L. Saboungi, J. Marr and M. Blander, "Thermodynamic Properties of a Quasi-Ionic Alloy From Electromotive Force Measurements - The Li-Pb System", J. Chem. Phys. 68 (1978), 1375-1384.

13. A.I. Demidov, A.G. Morachevskii and L.N. Gerasimenko, "Thermodynamic Properties of Liquid Lithium-Lead Alloys", Sov. Electrochem. 9 (1973), 813-814.

14. S.P. Yatsenko and E.A. Saltykova, "Thermodynamic Properties of Liquid Lithium-Lead Alloys", Russ. J. Phys. Chem. 50 (1976), 1278.

15. H.R. Ihle, A. Neubert, and C.H. Wu, "The Activity of Lithium and the Solubility of Deuterium in Lithium-Lead Alloys", presented at the 10th Symposium on Fusion Technology, Ispra, Italy, September 1978.

16. K.S. Bergstresser and G.R. Waterbury, "Determination of Hydrogen in Lithium Hydride", LAMS-1698, Los Alamos National Lab. (1954).

17. H. Lefevre, G. Reversat and J.C. Putaux, "Analyse du deutériotritiure de lithium", Bull. Inform. Sci. Tech., Commis. Energ. At. (Fr.) 178 (1973), 51-54.

18. F. Erdmann-Jesnitzer, A.P. Van Peteghem and R. De Wilde, "Untersuchungen zur Verbesserung des Kriechverhaltens von Blei-Lithium-Legierungen durch Wasserstoff", Metall. 28 (1974), 449-455.

19. F. Erdman-Jesnitzer, "Hydrogen, A Useful Alloy Element in Metal Alloys", Ref. (5), Vol. 10.

20. R. Wiswall and E. Wirsing, "The Removal of Tritium From Fusion Reactor Blankets", BNL-50748, Brookhaven National Lab. (Oct. 1, 1977).

21. R.H. Wiswall and E. Wirsing, "Tritium Recovery from Fusion Blankets Using Solid Lithium Compounds-II: Experiments on Tritium Removal and Absorption", Proc. Int. Conf. Radiation Effects and Tritium Technology for Fusion Reactors, Gatlinburg, Tenn., Oct. 1-3, 1975, CONF-750989, U.S. Energy Research and Development Administration (1976), III-232-252.

22. R.H. Wiswall and E. Wirsing, "Removal of Tritium From Solid CTR Blanket Materials Progress Report", BNL-19766, Brookhaven National Lab. (Feb. 11, 1975).

23. J.B. Talbot, "A Study of Tritium Removal From Fusion Reactor Blankets of Molten Salt and Lithium-Aluminum", ORNL/TM-5104, Oak Ridge National Lab. (March 1976).

24. M. Hansen, Constitution of Binary Alloys, Second Edition, McGraw-Hill Book Company, Inc., New York (1958).

25. W. Weppner and R.A. Huggins, "Thermodynamic Properties of the Intermetallic Systems Lithium-Antimony and Lithium-Bismuth", J. Electrochem. Soc. 125 (1978), 7-14.

26. A.I. Demidov and A.G. Morachevskii, "Thermodynamic Properties of Liquid Lithium-Bismuth Alloys", Sov. Electrochem. 9 (1973),1321-1322.

27. R.M. Alire, "Transport of Hydrogen in Liquid Lithium", J. Chem. Phys. 65 (1976), 1134-1137.

28. G.M. McCracken, D.J.H. Goodall, R.T.P. Whipple and G. Long, "Extraction of Tritium From Liquid Lithium", Nucl. Fusion Special Supplement (1974), 439-448.

29. D.H.J. Goodall, G.M. McCracken and G.E. Austin, "Experimental Measurement of the Permeation of Hydrogen Isotopes in Lithium Filled Niobium Cells", Ref. (21), IV-274-289.

30. E.M. Sacris and N.A.D. Parlee, "The Diffusion of Hydrogen in Liquid Ni, Cu, Ag, and Sn", Met. Trans. 1 (1970),3377-3382.

31. P.J. Depuydt and N.A.D. Parlee, "The Diffusion of Hydrogen in Liquid Iron Alloys", Met. Trans. 3 (1972), 525-532.

32. A.B. Shal'kevich and B.V. Linchevskiy, "Diffusion of Hydrogen in Nickel-Based Melts", Met. No. 4 (1975), 50-52.

33. V.A. Maroni, R.D. Wolson and G.E. Staahl, "Some Preliminary Considerations of a Molten-Salt Extraction Process to Remove Tritium From Liquid Lithium Fusion Reactor Blankets", Nucl. Technol. 25 (1975), 83-91.

34. W.F. Calaway, "Electrochemical Extraction of Hydrogen From Molten LiF-LiCl-LiBr and Its Application to Liquid-Lithium Fusion Reactor Blanket Processing", Nucl. Technol. 39 (1978), 63-74.

35. V.T. Nguyen and J.E. Enderby, "The Electronic Structure of Lithium-Based Liquid Semiconducting Alloys", Philos. Mag. 35 (1977), 1013-1019.

36. E. Heymann and H.P. Weber, "The Distribution Equilibrium of Sodium Between Molten Sodium Halides(NaBr, NaI) and a Molten Metal Phase (Cd, Pb, Tℓ, Sn, Bi, Sb, Au)", Trans. Faraday Soc. 34 (1938), 1492-1501.

37. M. Okada, R.A. Guidotti and J.D. Corbett, "The Solution of Sodium Alloys of Some Post-Transition Metals in Molten Sodium Halides. Evidence for Anions of Bismuth and Antimony", Inorg. Chem. 7 (1968), 2118-2124.

38. L.M. Ferris, M.A. Bredig and F.J. Smith, "Equilibrium Distribution of Lithium and Bismuth Between Liquid Lithium-Bismuth Alloys and Molten Lithium Chloride at 650-800°", J. Phys. Chem. 77 (1973), 2351-2357.

39. M.S. Foster, C.E. Crouthamel, D.M. Gruen and R.L. McBeth, "First Observation of a Solution of Li_3Bi, An Intermetallic in Molten Lithium Chloride and Lithium Chloride-Lithium Fluoride", J. Phys. Chem. 68 (1964), 980-981.

40. D.H.W. Carstens, "The Extraction of Tritium From Helium Streams Using $La_{5.25}$ Ni", LA-7209-MS, Los Alamos Scientific Lab. (March 1978).

41. D.H.W. Carstens, "Use of Binary Alloys of the Lanthanides for Tritium Recovery From CTR Blankets", presented at the Third ANS Topical Meeting on the Technology of Controlled Nuclear Fusion, Santa Fe, New Mexico, May 9, 1978.

42. K. Rüttiger, "Vacuum Degassing in the Liquid State", Vacuum Metallurgy, ed. by O. Winkler and R. Bakish, Elsevier Pub. Co., New York (1971), 337-463.

43. D.H. Shiu and Z.A. Munir, "The Heat of Vaporization and Vapor Pressure of Liquid Lead", Met. Trans. 2 (1971), 2953-2955.

44. P.M. Hulme, "Removing Dissolved Gases From Molten Metals", Steel no. 15, 108-111, 160-163 and no. 16, 110-111, 122-128,(1946).

45. C.B. Alcock, Principles of Pyrometallurgy, Academic Press, New York (1976), 305-312.

46. A.V. Bradshaw and F.D. Richardson, "Thermodynamic and Kinetic Aspects of Vacuum Degassing", Vacuum Degassing of Steel, Spec. Rept. 92, The Iron and Steel Inst., London (1965), 24-44.

47. K.J. Brondyke and T.F. McCormick, "Degassing", Aluminum, Vol. III, Fabrication and Finishing, K.R. Van Horn (ed.), American Society for Metals, Metals Park, Ohio (1967), 31-33.

48. W. Geller, "Zur Theorie der Auf-und Entgasung flüssiger Metallbäder", Z. Metallk. 35 (1943), 213-217.

49. R.D. Pehlke and A.L. Bement, Jr., "Mass Transfer of Hydrogen Between Liquid Aluminum and Bubbles of Argon Gas", Trans. A.I.M.E. 224 (1962), 1237-1242.

50. D. Papamantellos, K.W. Lange, K. Okohira and H. Schenck, "A Mathematical Approach for the Mass Transfer Between Liquid Steel and an Ascending Bubble", Met. Trans. 2 (1971), 3135-3144.

51. H. Ruppersberg and W. Speicher, "Density and Compressibility of Liquid Li-Pb Alloys", Z. Naturforsch. 31a (1976), 47-52.

52. A. Ali and H.S. Ray, "Interaction of Gas Bubbles With Liquid Lead", J. Appl. Chem. Biotechnol. 24 (1974), 539-556.

X-C. Tritium Containment Systems

X-C-1. Introduction

The total tritium inventory in NUWMAK may amount to more than 10^9 Ci. In order to limit tritium releases from NUWMAK to less than 10 Ci per day, tritium losses must be limited to one part in one hundred million on a daily basis. Such a monumental task must rely on the most conservative containment measures possible. Essentially perfect containment of tritium depends on clearly identifying possible routes of tritium release. During normal operation, plasma fueling and fuel purification components, storage (both normal and emergency), breeding and tritium extraction system components and the first wall and blanket coolant are all sources of potential tritium losses. Tritium containment associated with each of these systems is examined in the analysis of a multi-layer containment system. Such a system has been studied in TETR.[1]

The three-level containment system (Figure X-C-1) is designed to deal with tritium release under both normal and off-normal conditions. Each level prevents the dilution of released tritium so that it can be recovered before permeating to the next barrier. These barrier systems are described in Sections X-C-2,3,4. Tritium loss to the coolant water is considered in Section X-C-5.

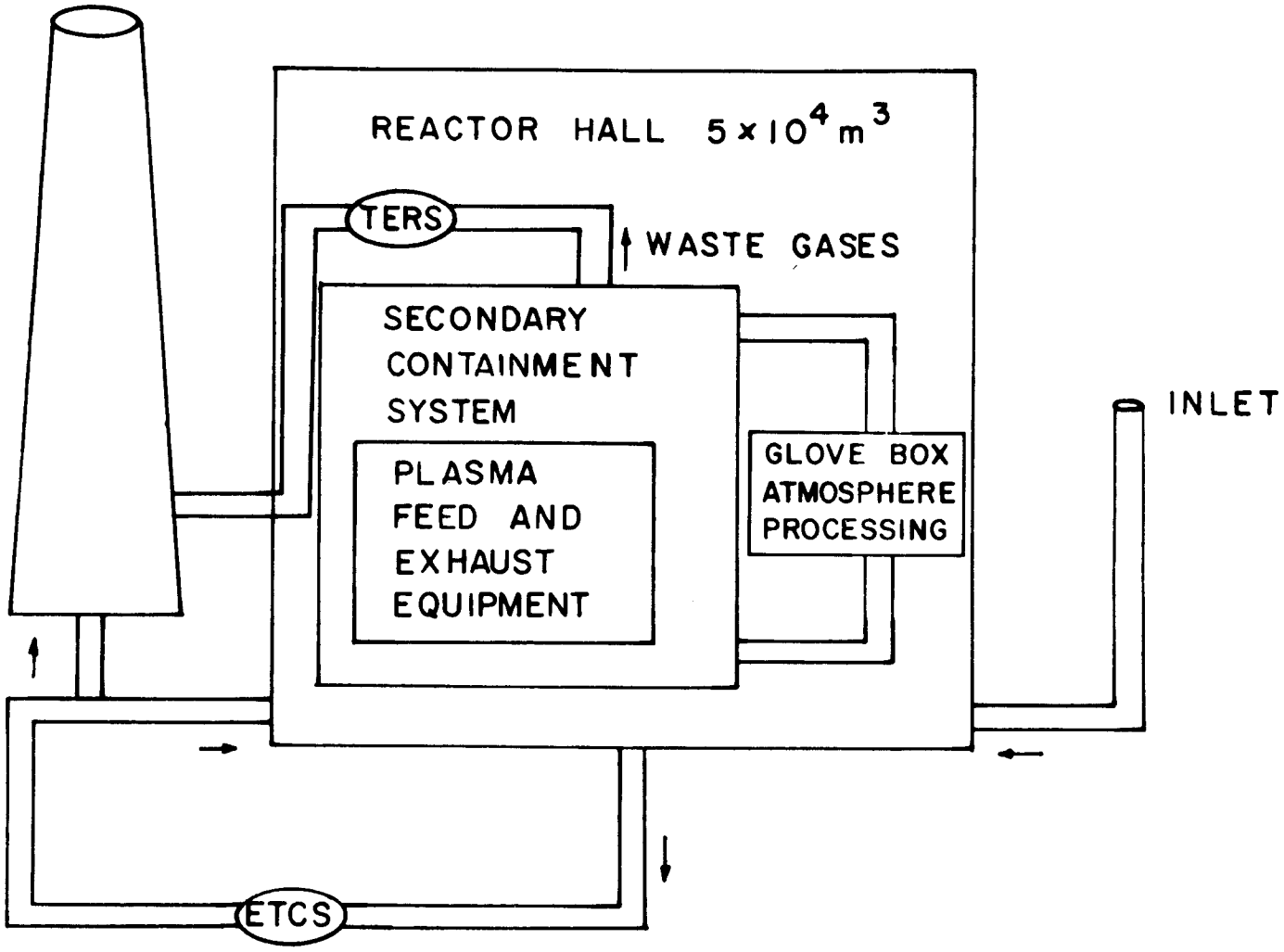
X-C-2. Primary Containment

The primary containment system consists of those pipes and other structural elements which contain tritium or tritium-bearing materials. These components must demonstrate high structural integrity for the containment of tritium. Connections must be welded and leak tested extensively with helium prior to the introduction of tritium. Division of the fueling and fuel storage system into eight identical units reduces the size of the maximum tritium release possible.

X-C-3. Secondary Containment

The secondary containment system consists mainly of a second physical barrier around primary system components. Thus, primary system piping outside the plasma chamber is contained within larger diameter piping. A slowly flowing inert gas is passed through the annulus and monitored for tritium leakage. Large pieces of equipment

TRITIUM EFFLUENT SYSTEM DESIGN FOR TETR



LEGEND:

TERS = TRITIUM EFFLUENT REMOVAL SYSTEM
ETCS = EMERGENCY TRITIUM CONTAINMENT SYSTEM

Fig. X-C-1

requiring maintenance or adjustment are enclosed in glove boxes. Estimates currently hold that approximately 1% of the building volume will contain high enough levels of radioactivity to require enclosure within glove boxes.[2] These glove boxes will contain a circulating inert gas which is monitored for tritium.

Wittenberg[2] experimentally confirmed several aspects of glovebox usage in successful tritium containment. Tritium losses from the glove-box system can be kept to about 1 Ci per day through the use of the following devices. The major pathway of tritium escape is through the glovebox rubber gloves. Summarized data[2] on the permeation of HTO and dry HT indicate that butyl rubber has the lowest permeability to HTO where the permeation of HTO through any film examined is 20 to 100 times higher than that of HT. A laminate of 0.5 mm butyl rubber and 0.25 mm neoprene is used to improve abrasion resistance. The glove boxes should be operated below atmospheric pressure to limit tritium loss in the event of leakage.

The condition of the glove box atmosphere is of major importance in the control of tritium losses. Molecular HT exchanges with water in the atmosphere to form HTO. Prevention of the formation of HTO has twofold importance: (1) the permeability of HT through human tissues is lower than that of HTO, so in the event of a major system rupture, less dangerous tritium species are released, (2) HTO permeates through the gloves more quickly than HT. Reduced oxygen and water levels will reduce the level of HTO in the glove box atmosphere. The oxygen level can be controlled to 10 ppm by Dow Q-1 reactant. The water level can be kept to 1 ppm by molecular sieves operating at the ambient temperature and by circulating the atmosphere through them at a rate comparable to the calculated permeation rate of water through the gloves from the room atmosphere. By control of the oxygen and water content of the glovebox atmosphere and continuous monitoring for tritium leakage from the primary system, an atmospheric concentration of 1 ppm HT should not result in the release of more than 1 Ci per day from the glove boxes where there is 1 pair of gloves per m^3 of box volume with a surface area of 1 m^2 per pair.

If the level of tritium goes above 2 ppm, the glove box atmosphere can be diverted to a tritium removal system (TERS)[1] or an emergency detritiation system (ETCS)[1] as needed. Especially leaky components of the primary system can be enclosed in special glove boxes equipped with cryogenic absorption or hydrogen getters to control tritium losses when needed. Table X-C-1 lists some of the glove box parameters.

X-C-4. Tertiary Containment

The tertiary containment system includes the reactor hall, rooms containing tritium processing equipment, the reactor building itself, the tritium effluent removal system (TERS), and the emergency tritium containment system (ETCS). The TERS is designed to operate on routine tritium losses while the ETCS is only used under off-normal conditions.

As with the primary and secondary systems, the reactor building is subdivided to reduce both the extent of loss and the extent of contamination in the event of a leak. The reactor hall has a volume of 8.7×10^4 m^3 and may be divided radially to provide the least impediment to maintenance operations. The reactor building is maintained at 70 torr during operation, with the capability of attaining 10 torr under emergency conditions.
About 20% of the building volume atmosphere should be circulated per day through the building from areas of smallest to largest radioactive hazard before leaving through a stack of sufficient height to guarantee proper dispersal of the effluent. Under normal operation, this stack effluent would contain about 1 Ci per day. The main reactor hall should not be ventilated routinely due to the existence of the short-lived, but hazardous isotopes ^{13}N, ^{16}N, and ^{41}Ar created by neutron leakage from the reactor.

Routine processing of exhaust gases from vacuum pumps and purge gases is performed by the TERS. The TERS converts gaseous waste (HT, tritiated hydrocarbons, etc.) to tritiated water which is collected. This water and other liquid and solid tritiated waste is then fixed for burial in a solid matrix such as concrete.

The TERS for TETR, which has a 12 kg tritium inventory, a power rating of 346 $MW_{(th)}$ and a building volume of 5×10^4 m^3 was sized at an air processing rate of 0.06 m^3/sec.[1] NUWMAK is a power reactor with

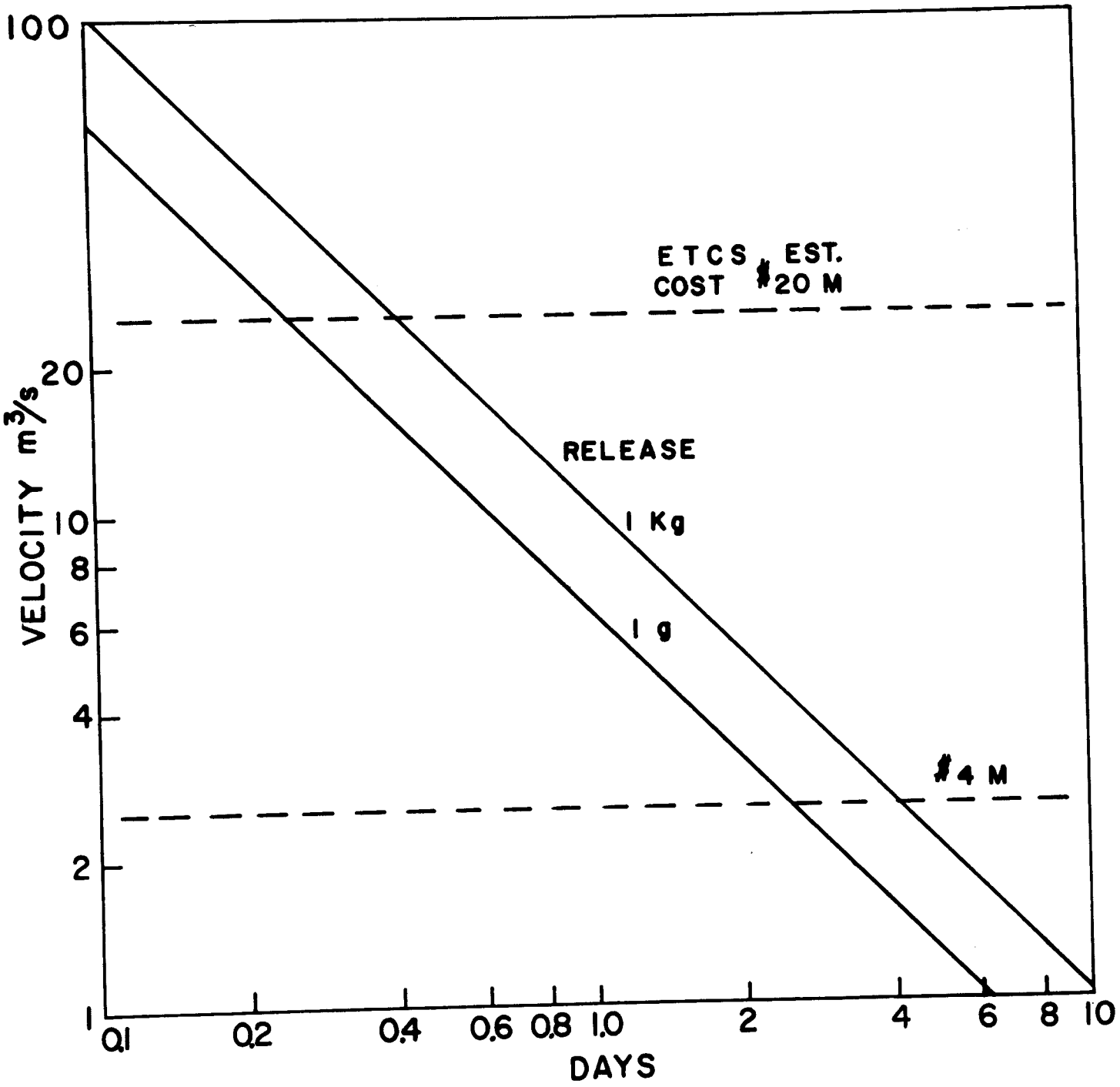
Table X-C-1

Glove Box System Parameters

Volume of Glove Boxes	870 m^3
Pressure in Glove Boxes	2.5×10^{-3} atm
Number of Gloves	870
Surface Area/Glove	0.5 m^2
Dryer and Oxygen Removal Rate (Entire Glove Box Volume)	~ 1.75 m^3/sec

a tritium inventory of about 25 kg, a power rating of 2300 $MW_{(th)}$ and a building volume of 8.7×10^4 m^3. However, due to comparably small burn fractions (1.48% in NUWMAK vs. 0.33% in TETR) most of the tritium inventory is circulating through the fueling and storage system. The atmospheric concentration of tritium in NUWMAK is not expected to be higher than that in TETR. Thus, to process the NUWMAK glove box atmosphere on the same timescale as in TETR requires a processing rate scaled up on the basis of the volumes processed and, in NUWMAK, this rate should be about (870/500)x(0.06 m^3/sec) or 0.104 m^3/sec.

The emergency tritium containment system (ETCS) consists of a heated catalyst to oxidize HT and T_2 to HTO and T_2O, alumina beds presaturated with water at 100% humidity and the required air handling equipment. The ETCS is used in the event of a simultaneous breakdown of both the primary and secondary systems to rapidly detritiate air from contaminated areas of the reactor building. During cleanup, the inlet dampers of contaminated areas are closed and only a small fraction of fresh air is allowed to circulate to reduce tritium losses from the stack. While the cost of such a system is not very sensitive to the size of the spill (within the range of 1 g to 1 kg), it is very sensitive to the required handling capacity. Figure X-C-2[1] shows the relationship between the processing velocity and the time required to reduce the building atmosphere to the RCG level (5 $\mu Ci/m^3$) in a volume of 5×10^4 m^3. Since NUWMAK is a power reactor, it is desirable to reenter a contaminated area as soon as possible so that the reactor may be returned to full power. In TETR, a 1 kg spill in a 50,000 m^3 building could be cleaned up in 1 day at a processing velocity of 10 m^3/sec.[1] In an 87,000 m^3 building, this would take ~ 1.75 days. Alternatively, cleanup could be achieved in 1 day if the processing rate were increased to ~ 17.5 m^3/sec, assuming linearity between building volume, detritiation time and processing velocity. The cost of such a system is estimated at ~ \$17 M.[1]



TIME REQUIRED TO REDUCE BUILDING ATMOSPHERE TO RCG FOLLOWING TRITIUM RELEASE AS A FUNCTION OF THE VELOCITY OF EMERGENCY TRITIUM CONTAINMENT SYSTEM IN A SYSTEM OF VOLUME 5×10^4 M^3

Fig. X-C-2

It may be useful to consider other schemes in the effort to hasten the return of the reactor to full operation. If the building is detritiated to ~ 570 $\mu Ci/m^3$, the entire building volume would contain only 50 Ci which could be vented with little hazard to the public. This would permit either the use of a lower capacity (and less expensive) system or earlier reentry. At 50% relative humidity and a temperature of 20°C, 5700 liters of water at an average concentration of 1756 Ci/ℓ will be collected following a 1 kg spill. This tritium may be regenerated for further use.

Also, the use of bubble-suited workers would permit functioning by those workers in atmospheres of up to 20,000 $\mu Ci/m^3$. Reentry and working in such an atmosphere is also dependent on the fraction of HTO in the spill. If it is less than 10%, workers in bubble suits may reenter when the atmosphere reaches 200,000 $\mu Ci/m^3$, which is to say, almost immediately in the event of a spill of less than ~ 2 grams. In these cases both reactor and cleanup can operate simultaneously. Table X-C-2 lists some parameters of the tertiary containment system.

X-C-5. Tritium Removal From Cooling Water

It has been calculated that the leak rate of tritium into the cooling water will be limited to a few curies per day. In the event that the leak rate increases, it is possible, at comparable costs, to remove tritium (in the range of 0.001 to 10 $\mu Ci/m\ell$), either by combined electrolysis-catalysis or by molecular photo-excitation.[3]

References for Section X-C

1. B. Badger, et al., "TETR - A Tokamak Engineering Test Reactor to Qualify Materials and Blanket Components for Early DT Fusion Power Reactors", UWFDM-191 (June 1977), Section XII-C.

2. L.J. Wittenberg, "Experimental Verification of Tritium Control by Glove-Box Containment", Nuclear Technology 38, 434 (1978).

3. T. Ben Rhinehammer and L.J. Wittenberg, "An Evaluation of Fuel Resources and Requirements for the Magnetic Fusion Energy Program", Appendix B, MLM-2419 (October 31, 1978).

Table X-C-2
Tertiary Containment System

Volume of Reactor Building	8.7×10^4 m^3
Pressure in Reactor Building	70 torr
Maximum Volume of Any Room	1.74×10^4 m^3
Building Inleakage Rate (fraction of building volume)	~ 0.1%/day
TERS Flow Rate	0.104 m^3/sec
ETCS Flow Rate	17.5 m^3/sec

X-D. Addendum

Since the first analysis was made of the NUWMAK fueling parameters a new fueling scenario has been developed involving injection of fuel by pellets as well as via a cold gas blanket. There are two alternate schemes, the "shallow pellet" method in which tritium is injected as a DT gas blanket and as DT pellets at the edge of the plasma, and the "deep pellet" fueling technique wherein the cold gas blanket is composed only of D_2 and tritium pellets which are injected deep into the center of the plasma (Section IV-D). Of the two techniques the "shallow pellet" method represents the worst case for NUWMAK fueling. In this fueling scheme, 6.91×10^{20} T atoms/sec are burned to produce 2283 $MW_{(th)}$. Tritium is injected as a DT gas blanket at a rate of 2.03×10^{22} T atoms/sec and as DT pellets at a rate of 9.03×10^{22} T atoms/sec. This results in a burn fraction of only 0.62%. (Burn fraction is defined here as $\frac{T_{burned} \times 100}{T_{injected\ in\ all\ forms}}$.) Tritium is handled at a rate of 11.14×10^{22} T atoms/sec or 0.185 moles T/sec. As a consequence, the tritium in storage for a 1 day's supply at a burn cycle duty factor of 91.8% is now 44.0 kg. In the original fueling scenario, the burn fraction was 1.48% and a 1 day's supply was 19.4 kg. Thus, the "shallow pellet" fueling technique results in an increase in the amount of tritium to be stored by a factor of 2.4.

All aspects of fuel processing are adversely affected in this fueling scheme. The cryopump inventory is increased from 1.6 kg to 4.0 kg. The Pd-Ag diffusers must handle about 11.1 moles/min of hydrogen isotopes, requiring an increase in the surface area of the diffusers from 4.3 m^2 to 10.4 m^2. It is assumed that the proportion of inert gas in the exhaust fuel will be comparable so that, with an appropriate increase in surface area, the separation of hydrogen isotopes from the inert gas and other exhausted impurities can be accomplished at the temperatures and driving pressures given in Section X-A-5-a.

The isotope separation system must handle about 23 mmoles/sec in this fueling scheme. The feed stream composition should be similar to that in the original design, however. This increase will necessitate a concomitant increase in the capacity of the system by a factor of 2.4 over that designed to handle the original feed stream of 9.6 mmoles/sec. The required increase in capacity may be accomplished by increasing the number of columns in each octant or increasing the capacity of the original number of columns. The total column inventory increases to about 0.8 kg.

In conclusion, the tritium requirements of this fueling scheme are clearly unacceptable. In addition to the increased handling capacity required and the increased inventory, Table X-D-1, the cost increase for such a system can be expected to be more than twice the original, since most component costs are capacity-dependent and, effectively, over twice the system is required under this scenario. Also, the added risks associated with the containment of the higher tritium inventory (Table X-D-1) should be considered. The containment system design features are not expected to change. However, as the average size of a spill may be expected to be larger in a plant with a high inventory, the plant's leak prevention and cleanup capability may need to be improved.

The detailed calculations for the "deep pellet" fueling have not yet been worked out. However, it has been found that injection of tritium deep into the center of a plasma surrounded by a cold gas blanket of D_2 should increase the particle confinement time at the plasma's center by a factor of ten compared to the "shallow pellet" fueling technique. Thus, the anticipated burn fraction would be about 6%. This represents a best case fueling scheme and would have associated with it inventories and handling capacities reduced by a factor of about ten.

Table X-D-1

Tritium Inventory Under a DT Pellet Fueling Scheme

Fueling System	
Cryopumps (4 hr. cycle time)	4.0 kg
Storage (1 day's supply, 91.8% duty factor)	44.0 kg
Purification System	
Distillation Columns	0.8 kg
Blanket (no change over original case)	0.088 kg
TOTAL	48.9 kg

XI. Assembly and Maintenance

XI-A. Introduction

The answer to whether fusion will become a viable source of energy hinges on many problems that are being worked on today. However, for fusion reactors to become economical sources of energy, they must demonstrate a high degree of serviceability and maintainability. The large capital investment in a fusion reactor will necessitate that downtime for routine and unexpected maintenance must be kept to a minimum in order to have a reasonable availability and decrease the cost of energy. For this reason, problems of accessibility, blanket and first wall replacement, servicing of magnets, ease of connecting and disconnecting coolant lines, and many other functions needed to maintain fusion reactors become of paramount importance.

Conceptual designs of tokamak fusion reactors have undergone a tremendous evolution as new ideas continue to emerge and problem areas are identified. The designs of today bear little resemblance to the designs of the early 1970's. Recognition of the importance of maintainability of fusion reactors has been one of the driving forces in the evolution of reactor designs. Sizes and weights of current fusion reactor components have been drastically reduced, plasma chambers have been simplified, magnet system designs are making accessibility a prime consideration and problems of fueling, impurity control, plasma heating, vacuum pumping and ash removal are receiving even greater attention.

Early studies have indicated that an optimally sized power plant is on the order of 5000 MW_{th}[1]. That, coupled with a very low neutron wall loading based on incomplete radiation damage data, produced reactor designs monstrously large and unwieldy.[2,3] Later studies, however, have shown that the cost of energy is only marginally dependent on the power output of a reactor between 3000-7000 MW_{th}[4]. At the same time new radiation damage data predicted a more optimistic material lifetime at lower temperatures on the order of 300-350°C.[5] Concurrently, results of remote maintenance studies indicated that it would be virtually impossible to maintain these large reactors economically.[6] All of these factors combined to reduce the power output and consequently the sizes and weights of the second generation of conceptual reactor designs. As the plasma size was reduced, the size and weights of the magnets and other components came down correspondingly.

Similarly the drive to provide more access to the blanket and inner reactor components has spurred the effort toward reducing the number of toroidal field (TF) coils and the number and placement of the vertical field (VF) coils. Some early designs have placed the return leg of the TF coils far enough back to allow unimpeded radial extraction of blanket segments. This concept was used in UWMAK-II[3] and more recently, in the Culham Mk-II[7] design. Although this scheme provides good accessibility for blanket maintenance, the magnet system, particularly the TF coils,end up very large, expensive and difficult to service. In order to minimize the stored energy in these designs the VF coils are usually placed within the bore of the TF coils, creating the so called "Gordian knot".

In NUWMAK we have made an attempt to consider the maintainability of the major reactor systems from the earliest stages of the design. The areas which we feel will necessitate long reactor downtime for servicing are:

1 - First wall/blanket
2 - Toroidal field coils
3 - Vertical field coils and trimming coils
4 - Ohmic heating coils

Each of these areas will be discussed separately below.

XI-B. First Wall/Blanket Maintenance

This section includes the maintenance of all the components located within or in close proximity to the plasma chamber, such as limiters, RF launching structures, RF waveguides, vacuum ducts, etc. The most important criterion in these considerations (aside from safety) is the speed with which these components can be fixed or replaced because it will determine the plant availability and will ultimately be reflected in the busbar cost of electricity. If one makes the assumption that any repair or maintenance within the toroidal bore will be by remote control, then the major considerations which will determine the amount of downtime needed are:

- Rapid and abundant accessibility to the interior of the reactor
- Ease of disengagement of the components in question
- Bulkiness and weight of the components
- Ease of testing and qualification after repair or replacement.

In NUWMAK we have attempted to address these issues from the start of the study. The last issue, having to do with testing and qualification, is a very complicated one and since there are no codes and standards established for fusion reactors, it can only be addressed in a very general way. For this reason, more time will be devoted to the first three issues.

The original motiviation for reducing the number of TF coils in NUWMAK came from two considerations, accessibility and economics. By reducing the number of TF coils, the spaces between them became larger providing the potential for good accessibility. However, the field ripple thus created at the edge of the plasma has to be trimmed to some value less than two percent, and in NUWMAK this is done with normal copper water cooled saddle shaped coils described in detail in Chapter VI. In terms of economics, reducing the number of TF coils by 30% and adding trimming coils accounts for a 3% reduction in the capital cost of the plant. The effect on the busbar cost is less dramatic amounting to only 0.2% ($\sim$ 0.1 mills/kWhr) because the addition of the trimming coils drains 16 MW from the total electrical plant capacity.

The improvement in the accessibility to the reactor interior is quite dramatic. In NUWMAK, access is provided through large removable shield doors located between the TF coils. These doors,which weigh on the order of 80 tonnes each,can be handled by the overhead crane. However, as described in Chapter XII, the mobility of the overhead crane will be limited by some of the equipment located at a level immediately above the reactor. For this reason it has been proposed that the components be manipulated by vehicles operating on the reactor floor assisted by the overhead crane. Each access port thus provided is 3.3 m wide and 7.8 m high, more than adequate for servicing the equipment located in the immediate area.

Figure XI-B-1 shows the sequence for component removal. The operation is initiated with the lowering of the external VF coils into the annular well provided for that purpose as shown in the figure. Before a shield door can be opened, a seal weld must be machined off. This is a relatively simple operation especially since the area is very accessible with plenty of space for maneuvering. A shielded vehicle having space for three workers inside will latch onto the door while structural bolts are removed to free it from the rest of the shield. The vehicle then moves radially back and takes the door to a designated area for storage until it is needed again.

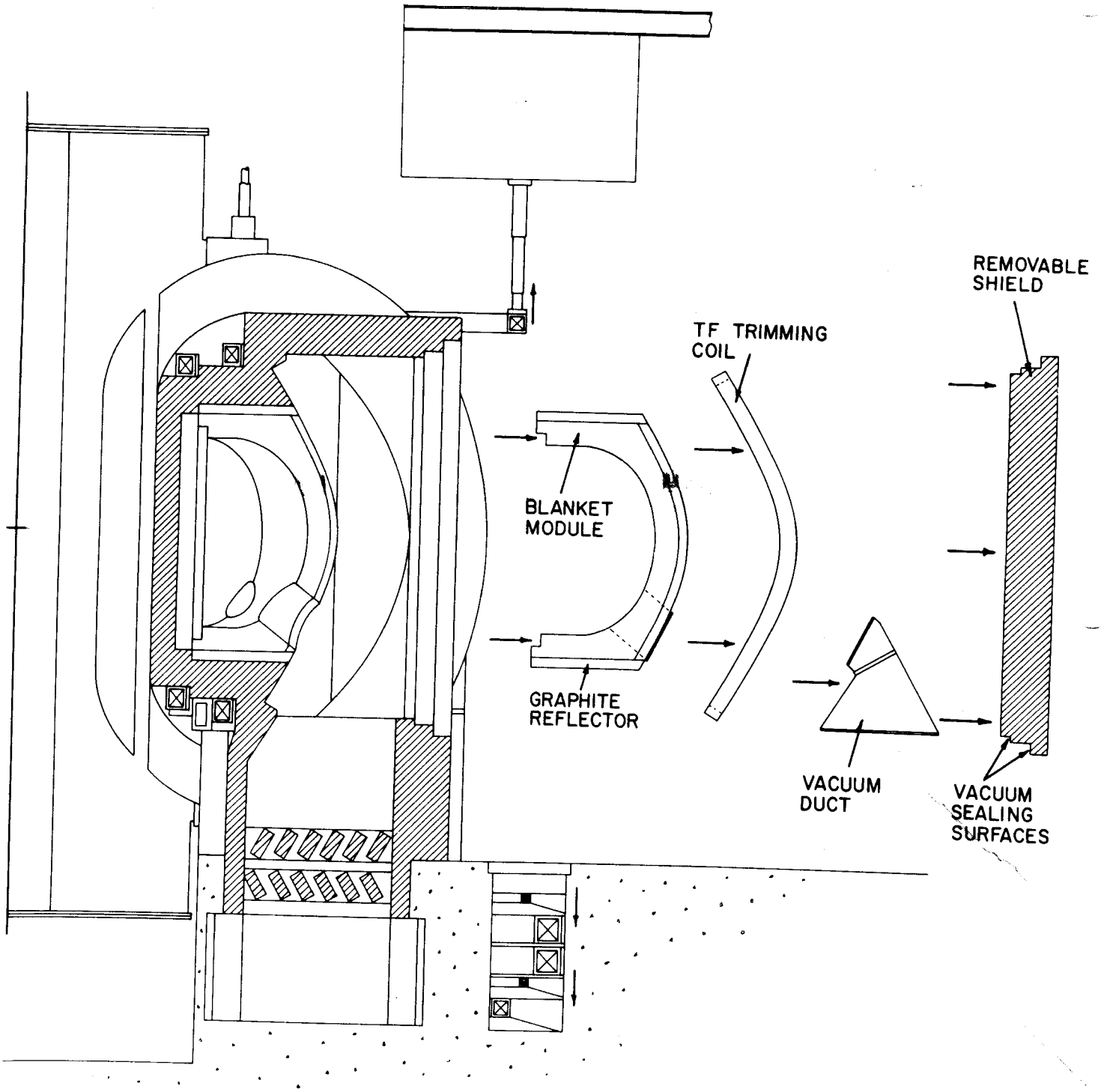


Fig. XI-B-1 Sequence for NUWMAK component removal.

The second consideration for reducing the downtime in the blanket changeout operation is the ease of disengagement of the components. One of the most difficult jobs facing a fusion reactor designer is the first wall seal. Conventional plasma experiments operate in hard vacuum environments, where the first wall of the plasma chamber is sealed with a weld or a metal wire mechanical seal. In either case, it is a very difficult operation to undo the seal, whether by machining off a weld or by removing mechanical fasteners.

In NUWMAK we have proposed a somewhat unconventional method for providing the vacuum needed in the plasma chamber. In this design, the blanket modules are butted up against each other such that the gap between them is long and narrow providing a very high impedance to the flow of gases. The region immediately behind the blanket bounded by the blanket on one side and the shield on the other is evacuated to some intermediate pressure, one or two orders of magnitude higher than the plasma chamber. In this way, the atmospheric loading on the blanket/first wall is eliminated and the seal problem is transferred to the shield. The plasma chamber is connected to eight large pumping stations by short low impedance ducts which fit between the trimming coils on the lower part of the reactor. These ducts are closely fitted to the blanket on one end and to the pumping station on the other. The seal at the shield gate as mentioned earlier is made with a non-structural weld located on the outside, accessible to both servicing in the event of a leak and to machining off for blanket maintenance.

There are several questions that have to be investigated in detail before the viability of such a scheme can be verified. They are:

- What are the implications of contaminating the shield enclosure with tritium? This question is critical and depends on many issues which cannot be answered at this time.
- Can a sufficiently high impedance be maintained in the gaps between blanket modules to support a pressure difference of one or two orders of magnitude with the available pumping speeds? Rough calculations indicate that it can.
- Can the surfaces in the shield enclosure be kept sufficiently clean as to prevent outgassing problems? This also does not seem to be a major impediment.

- How serious is the problem of neutron streaming through the vacuum ports? This problem is generic to all DT fusion reactors in varying degrees. Very careful investigation is needed in this area.

The other disengagements that will be needed are of the power and coolant connections for the trimming coils and the coolant and drain connections for the blanket. Fasteners which hold down the trimming coils at the top and bottom will also have to be disconnected before they can be removed. Each trimming coil weighs ~ 9 tonnes. Those blanket modules which have built-in cavity backed aperture antennae for RF power will also require disconnection of the RF waveguide located in the back.

Trimming coils and blanket modules located in line with TF coils will have to be translated circumferentially prior to radial extraction through the shield port. In case of routine maintenance this would not present a problem since more than one blanket will be replaced at any one shutdown. However, if the need for extracting a blanket module is for other than routine maintenance, then it may be necessary to remove more than one module in order to reach the one that needs replacing.

Figure XI-B-1 shows only the outer blanket module being removed from the reactor. This need not be the case. Manifolding could be arranged such that both inner and outer module elements can be extracted simultaneously. With the graphite reflectors in place, the blanket modules (drained of the breeding material) each weigh 9.5 tonnes. If the graphite blocks are removed first, the weight is reduced to only 3 tonnes. Since the blanket modules are rather bulky, it would be prudent to provide guides for circumferential translation and radial extraction. These guide grooves can be built into the surrounding shield structure.

Checking out the blanket module prior to closing the shield door would primarily entail testing the coolant and drain connections. Several ways for making the connections have been proposed. The one favoured by the author is the internal weld such as proposed by the Culham group.[8] The seal can also be checked internally by replacing the welding head with a special device designed for that purpose.

XI-C. Toroidal Field Coil Maintenance

Early conceptual designs of fusion reactors have essentially either ignored the problem of maintaining the TF coils or attempted to provide redundancy by using conservative design parameters. It is generally agreed that maintenance of the TF coils is desirable and perhaps essential. The likelihood of a major failure of a TF coil is probably small, but it is the minor problems, such as vacuum leaks or leaks in the helium vessel, that are more likely to happen. Most of such problems can be usually fixed in situ. However, there is always the probability that such a minor failure will necessitate a major repair shutdown, especially if it means removal of a TF coil from the reactor. We have anticipated such a possibility and have taken measures to alleviate the consequences.

In NUWMAK, as in most reactor designs, some of the vertical field (VF) coils are located within the toroidal bore. The four coils located thus have been made cryogenic rather than superconducting and each has a removable section large enough to allow a TF coil to pass through. Provision has been made to rotate the coils circumferentially in order to be able to align the removable section with the TF coil being removed. Although some researchers[9] have proposed demountable superconducting joints in coils, they have not yet been demonstrated. Reliable joints in cryogenic coils are relatively easy to make. Further, a lossy cryogenic joint would generate additional local resistive heating but would not jeopardize the operation or safety of the system.

In addition to untangling the VF and TF coils, removal of a TF coil will entail breaking the seal which is the vacuum barrier between the toroidal enclosure and the reactor containment building. This would be done after the blanket modules had been removed and the seal weld on the inside of the shield is exposed.

Each TF coil in NUWMAK has an individual dewar and is supported on permanent carriages. Once it is disengaged from its surroundings, a coil along with a sector of shield can be removed radially from the reactor as shown in Fig. XI-C-1 and then taken via the service corridor to the maintenance area.

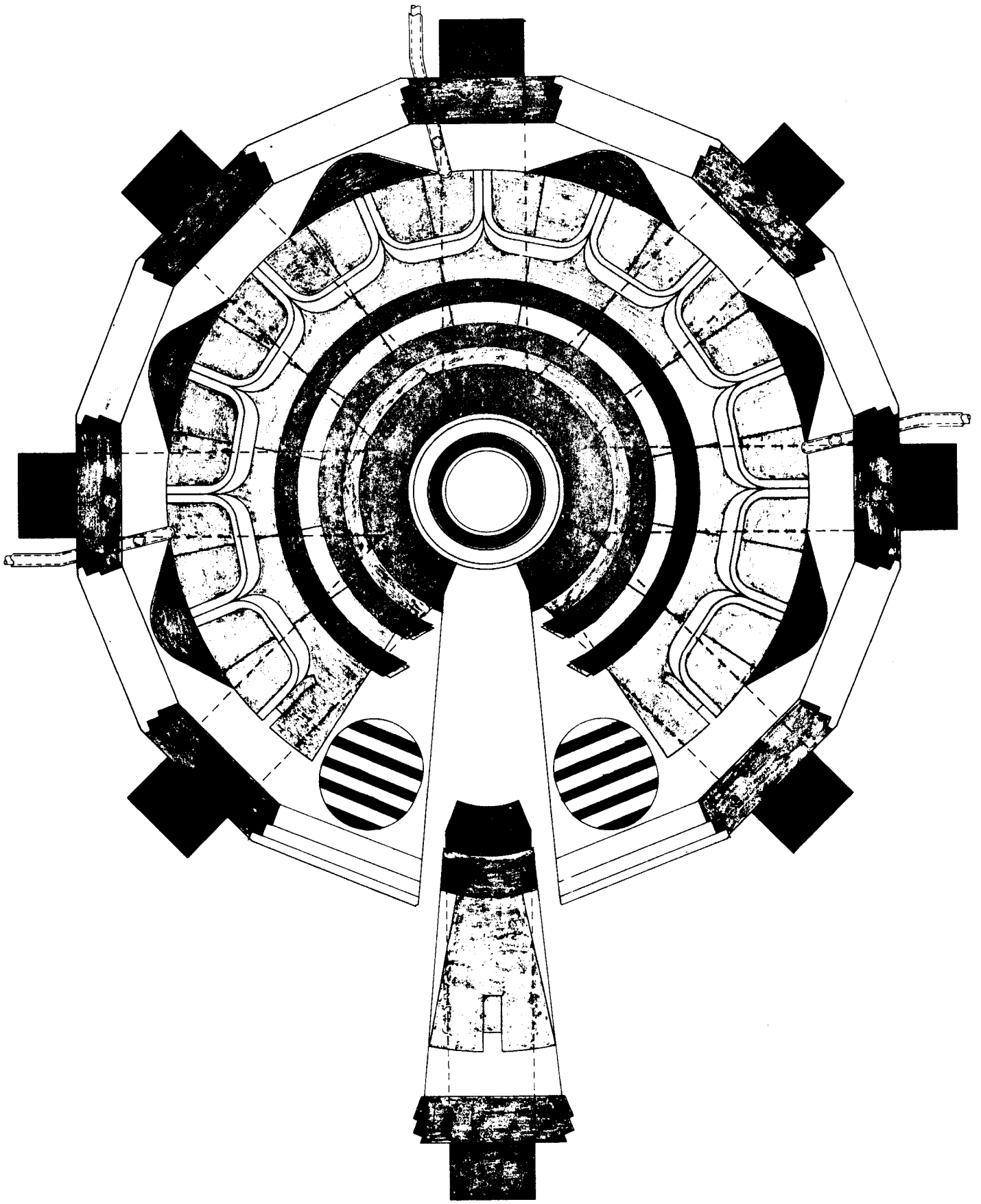


Fig. XI-C-1 TF Coil Removal in NUWMAK

A breakdown in a TF coil necessitating its removal from the reactor would constitute a major shutdown of the facility for several months. Without the design features incorporated in NUWMAK, a breakdown of this magnitude would shut the plant down for over a year and would entail dismantling a sizeable fraction of the nuclear island.

XI-D. Vertical Field Coil Maintenance

Any coils located within the toroidal bore would be extremely difficult to maintain and service. This is particularly true of superconducting coils. In order to alleviate this problem somewhat, the vertical field (VF) coils in NUWMAK have been divided into two groups:

(1) Cryogenic coils within the toroidal bore

(2) Superconducting coils outside the toroidal bore.

In order to provide the capability for removing a TF coil from the reactor, the cryogenic coils were designed with a demountable section. This feature aids in the capability for disassembling these coils should it become necessary. A detailed description of the cryogenic coils and the procedure for taking apart a demountable section is given in section VI-D-2.

One of the attractive features of a cryogenic coil is its dependability and reliability. Unlike a superconducting coil, a less than perfect joint will result in some excessive local ohmic heating without any other major consequences.

Taking apart a cryogenic coil would first require the removal of a TF coil from the reactor. This will provide access to the coils and will also provide the space needed for taking out sections of the conductors which make up the coils.

The coil conductors are made up of rectangular aluminum discs stacked on top of each other with spaces in between for the coolant gas to pass through. One turn of conductor consists of two half discs, each covering 180^{o} of the circumference. The individual turns of each coil have to be taken apart separately and replaced in the same way. They are mounted on beds designed to be capable of 360^{o} circumferential rotation. This will aid tremendously in the procedure for taking out the conductor segments.

As in the case of the TF coils, in situ repair of a cryogenic coil may be possible. This is particularly true since all of the coil will be accessible and rotatable. However, in the rare event that the coil has to be entirely replaced, we have taken the precaution of providing for such a contingency.

The superconducting VF coils which are outside the toroidal bore are accessible for maintenance. Replacement of such coils would either necessitate winding them in place, or winding them elsewhere and then transporting them to the reactor for installation. The latter option is not open in NUWMAK because the reactor building will not be equipped with a port large enough to allow a 23 m diameter coil to pass through. In order to wind such a coil in situ, one would have to assemble a circumferential track around the reactor. Such a track will be available from the original winding of the coils, but may need some modification for subsequent use with the reactor in place.

XI-E. Trimming Coil Maintenance

As mentioned frequently, the trimming coils will be the easiest to service and to replace. Access is provided by lowering the external VF coils into the annular well provided for this purpose, and then removing a shield door closest to the trimming coil in question. Next, the vacuum duct is unfastened and removed. Final disengagement of a trimming coil from the reactor will entail removing the coolant and electrical connections, unbolting structural brackets at the top and the bottom of the coil, and then radially extracting it through the access port. Since all the coils are identical in every respect, there will be spares available for replacement.

XI-F. Ohmic Heating Coil Maintenance

XI-F-1. General Discussion

The maintenance of the ohmic heating (OH) coils is another area that has been neglected in the past. The OH coils are usually buried within the central column in a very inaccessible region. These coils, which are usually superconducting, are pulsed at the start and the end of each burn cycle. Consequently, they are subjected to substantial cyclic stresses and should, therefore, be regarded as vulnerable. Provision should be made for maintaining them.

One of the problems with the OH coils is that they share the space in the central column with the bucking cylinder needed for reacting the TF coil centering forces. Because a fixed amount of flux swing is needed for a certain reactor to induce the plasma current, it is advantageous to make the OH coils with the largest possible bore, since the flux is determined by

the product of the field and the area in the coil bore. If the area is larger, then the field can be lower, and consequently the ampere turns can be lower making the cross section of the coils smaller. The lower field also means a smaller energy storage system needed to drive the coils as well as a lower $\frac{dB}{dt}$, which impacts on coil design and the design of other components in the vicinity of the central column. Two choices are open to the OH coil designer. They are:

1 - Making the OH coils of the largest possible diameter, placing the bucking cylinder on their inside and providing for the transfer of the centering forces to the bucking cylinder without compromising the performance of the coils.

2 - Placing the bucking cylinder at the maximum possible diameter and locating the OH coils on its inside. This ends up with higher field coils, more ampere turns and a higher $\frac{dB}{dt}$.

From the standpoint of coil technology the first option wins out. However, from the standpoint of maintainability the latter option is more desirable.

In NUWMAK we were forced into using the first option primarily for one reason, the desire not to exceed a maximum field of 8 tesla at the conductors. As designed, the maximum field in the OH coil system is 7.3 tesla in coil no. T-7 (see Fig. VI-D-1) and the maximum $\frac{dB}{dt}$ is 1.8 T/s. If the coils were on the inside of the bucking cylinder, the maximum field would have exceeded 8 tesla and would have required operation at a temperature lower than 4.2 K in order to achieve the needed current density in the coil. We have chosen not to do so.

XI-F-2. OH Coil Maintenance Procedure

The following design features were incorporated into NUWMAK to facilitate the maintainability of the OH coil system:

- The OH coils were wound on coil forms capable of transmitting the TF coil centering forces to a bucking cylinder located on the inner radius of the OH coils.

- The central column including the bucking cylinder was made as a self-contained liquid helium dewar which houses the OH coils.
- The OH coils were divided into two groups, one serviced from the top, the other from the bottom.
- The separation between the two groups was used for structure linking the bucking cylinder to the central column.
- Some coils were grouped together on common coil forms in places where individual coils could not be conveniently removed.
- The central column is supported on three columns and is not built into the floor.
- A service bay is provided below the central column for maintaining the lower group of coils.
- The power leads to each group of coils were brought to the top or bottom of the dewar (depending on the group) for ease of connection.

Figure XI-F-1 shows a group of four coils being removed from the top of the central column. The vacuum dewar lid has been disconnected and the liquid helium dewar lid also removed. Mechanical fasteners which are used to damp the coil forms together are removed and the coil forms can now be lifted up. Obviously, removal of any coil in the upper group will necessitate the removal of all the coils in the straight section ahead of it. Figure XI-F-2 is a cross section of the structural part of the central column without the coils and without the dewar. Section A-A shows the radial ribs between which the TF coils fit. The figure also shows the structural support of the bucking cylinder at the separation between the upper and lower groups of the OH coils.

The most difficult aspect of this scheme is maintaining the clearance between the coil forms and the central column, in order to transfer the centering force to the bucking cylinder and still be able to extract the coil forms. This problem needs further investigation.

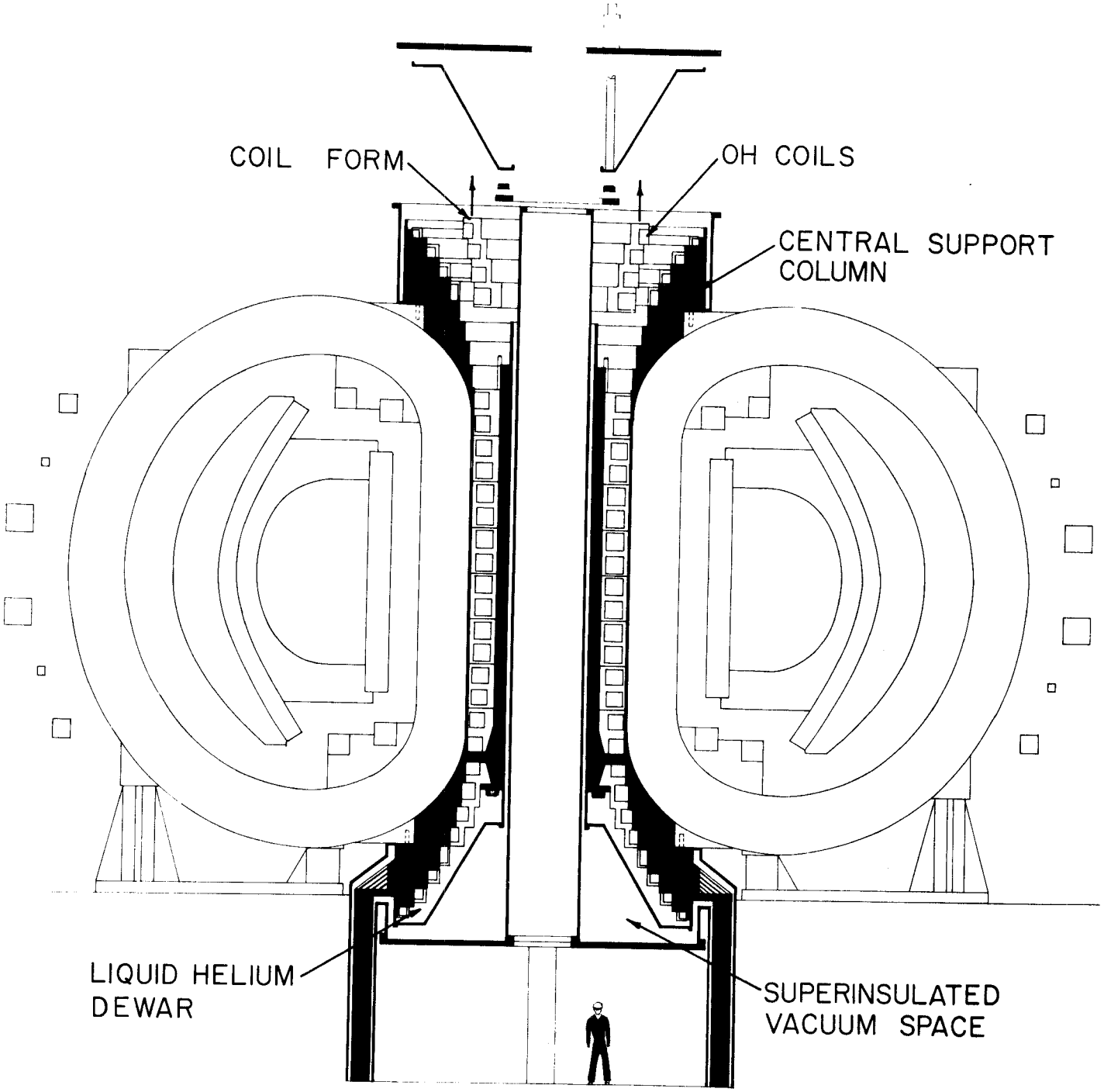


Fig. XI-F-1

DESIGN OF A SERVICEABLE OH COIL SYSTEM FOR NUWMAK

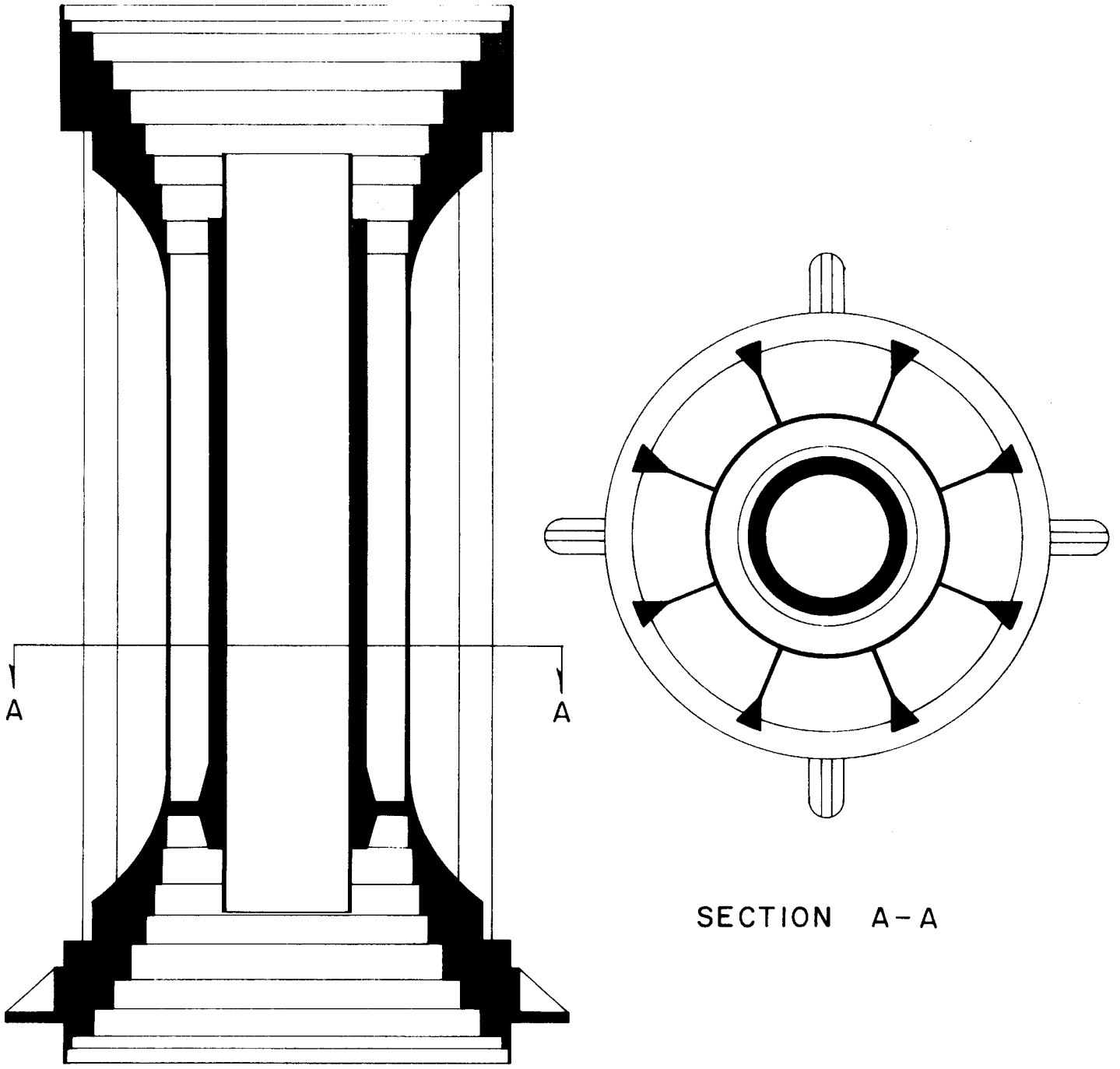


Fig. XI-F-2

CENTRAL SUPPORT COLUMN
NUWMAK

References for Chapter XI

1. D. Klein, G.A. Emmert, and T. Yang, "Optimization Considerations in the Design of a Tokamak Reactor", Nucl. Eng. Dept. Report FDM-44, University of Wisconsin, 1973.
2. B. Badger, et al., "UWMAK-I, A Wisconsin Toroidal Fusion Reactor Design", Nucl. Eng. Dept. Report FDM-68, University of Wisconsin, 1973.
3. B. Badger, et al., "UWMAK-II, A Conceptual Tokamak Power Reactor Design", Nucl. Eng. Dept. Report FDM-112, University of Wisconsin, 1975.
4. D.A. DeFreece, G.M. Fuller, and L.M. Waganer, "The Impact of Neutron Wall Loading on the Cost of Tokamak Fusion Power Systems", McDonnell Douglas Co. East (Proc. 2nd Topical Meeting on Tech. of Controlled Nuclear Fusion), ANS, Richland, Washington, September 1976.
5. E.E. Bloom, F.W. Wiffen, P.J. Maziasz, and J.O. Stiegler, "Temperature and Fluence Limits for a Type 316 SS CTR First Wall", Nucl. Technology, 31, 115 (1976).
6. H.S. Lahn, et al., "Developing Maintainability for Tokamak Fusion Power Systems", COO-4184-4, McDonnell Douglas Co. East, October 1977.
7. J.T.D. Mitchell, "Blanket Replacement in Toroidal Fusion Reactors", Culham Lab., Abingdon Oxon, UK, Proceed. 3rd Topical Meeting on the Tech. of Controlled Nuclear Fusion, May 1978, Santa Fe, NM.
8. D.A. Briaris and J.R. Stanbridge, "The Feasibility of Remotely Separating and Rejoining the Main Coolant Pipes of a Fusion Reactor", CLM-R 174, UKAEA Culham Lab., Abingdon, Oxon, UK, September 1977.
9. J. Powell, D. Hsieh, J. Lerner, "Deals: A Demountable Externally Anchored Low Stress Superconducting Magnet System for Fusion Reactors", BNL 50616.

XII. Balance of Plant

XII-A. Introduction

The balance of plant designs in the three UWMAK series of conceptual power reactors were produced by participating architect and engineering firms. Unfortunately, that is not the case in NUWMAK. This chapter will, therefore, not be as detailed and as complete as in the earlier reports.

Basically there are three major differences between NUWMAK and the three UWMAK reactor designs which are relevant to the BOP:

I. NUWMAK has a smaller net power output.

II. NUWMAK does not have an intermediate loop.

III. The NUWMAK blanket provides ~ 83% of the energy needed to keep the turbines operating during down time; therefore, the system requires a much smaller thermal flywheel.

These three factors have a considerable impact on the balance of plant from the standpoint of size, complexity and cost.

There is no heat exchanger building in the NUWMAK power station. Steam is generated directly in the blanket and transported to steam drums where it is separated from the water. The steam then goes directly to the turbine while the water is pumped back to the blanket. Hot water is stored at high pressure in four cylindrical vessels. During down time, it is discharged into the steam drums providing the remaining 17% of stored energy needed to keep the turbines at constant speed. The steam drums and the hot water storage vessels are located in the turbine building, obviating the need for a separate heat exchanger building.

The smaller net power output reduces the overall size of the turbine and electric plant equipment. Since the NUWMAK power cycle is almost identical to a BWR, the sizing and costing of the buildings and equipment was based on actual cost estimates of BWR plants of comparable power output.

XII-B. Description of Reference Site

XII-B-1. Topography and General Site Characteristics

The NUWMAK site is located on the east bank of the North River at a distance of twenty-five miles south of Middletown, the nearest large city. The North River flows from north to south and is one-half mile (2600 feet) wide adjacent to the plant site. A flood plain extends from both river banks an average distance of 1/2 mile, ending with hilltops generally 150 to 250 feet above the river level. Beyond this area, the topography is gently rolling, with no major topographical features. The plant site itself extends from river level to elevations of fifty feet above river level. The reactor building, other structures and the switch yard will be located on level ground at an elevation of eighteen feet above the mean river level. This elevation is ten feet above the 100-year maximum river level, according to U.S. Army Corps of Engineers studies of the area.

In order to optimize land area requirements for the fusion power plant site, maximum use of the river location is employed. The reactor building structure is located 400 feet from the east bank of the river.

XII-B-2. Site Access

Highway access is provided by five miles of secondary road connecting to a state highway; this road is in good condition and needs no additional improvements. Railroad access will be provided by constructing a railroad spur which intersects the B&M Railroad. The length of the required spur from the main line to the plant site is assumed to be five miles in length for all plant sizes. The North River is navigable throughout the year with a forty-foot wide channel, 12 feet deep. The distance from the shoreline to the center of the ship channel is 2000 feet. All plant shipments will be made overland except that heavy equipment (such as generator stator) may be transported by barge. The Middletown Municipal Airport is located 3 miles west of the state highway, 15 miles south of Middletown, and 10 miles north of the site.

XII-B-3. Population Density and Land Use

The NUWMAK site is near a large city (Middletown, 250,000 population) but in an area of low population density. Variation in population with distance from the site boundary is:

Miles	Cumulative Population
0.5	0
1.0	310
2.0	1,370
5.0	5,020
10.0	28,600
20.0	133,000
30.0	1,010,000

The nearest residence to the plant is on the opposite bank of the North River, directly west of the reactor location, 2600 feet west of the plant boundary, and 3000 feet west of the reactor building.

There are five industrial manufacturing plants within 15 miles of the NUWMAK site. Four are small plants employing less than 100 people each. The fifth, near the airport, employes 2500 people. Closely populated areas are found only in the centers of the small towns so the total land area used for housing is small. The remaining land, including that across the river, is used as forest or cultivated crop land, except for railroads and highways.

XII-B-4. Cost of Land

The cost of land and land rights, including clearing and relocating highways, bridges, rail lines, utilities, etc., is $2500 per acre.

XII-B-5. Cooling Water and Public Utility Services

Utilities are available as follows:

- The North River provides an adequate source of raw make up and condenser cooling water for the ultimate station capacity. The average maximum temperature is $75^{o}F$ and the average minimum is $39^{o}F$. The mean annual temperature is $57^{o}F$. (These temperatures are such as to enable the turbine back-pressure to be specified as 1.5 inches Hg absolute.)
- Natural gas service is available two miles from the site boundary on the same side of the river.
- Communication lines will be furnished to the project boundaries at no cost.
- Power and water for construction activities are available at the southwest corner of the site boundary.
- The distribution system in the area is a single source transmission, and is subject to occasional outages.

XII-B-6. Meteorology and Climatology

XII-B-6-a. Prevailing Wind

According to Weather Bureau records at the Middletown Airport, located ten miles north of the site on a low plateau just east of the North River, surface winds are predominantly southwesterly 4 - 10 knots during the warm months of the year, and westerly 6 - 13 knots during the cool months. There are no large daily variations in wind speed or direction. Observations of wind velocities at altitude indicate a gradual increase in mean speed and a gradual veering of the prevailing wind direction from southwest and west near the surface to westerly and northwesterly aloft.

Studies of the area indicated that there is a significant channeling of the winds below the surrounding hills into the north-south orientation of the North River. It is estimated that winds within the river valley blow approximately parallel to the valley orientation in excess of 50 percent of the time.

XII-B-6-b. Atmospheric Diffusion Properties

During the warm months of the year, according to analysis of weather bureau records, the atmospheric conditions near the surface are 25 percent unstable (Pasquill A, B, and C), 40 percent neutral (Pasquill D), and 35 percent stable (Pasquill E and F). Average wind speeds are approximately six miles per hour during unstable conditions, ten miles per hour during neutral conditions, and four miles per hour during stable conditions.

During the cool months of the year, the atmospheric conditions are 15 percent unstable, 50 percent neutral, and 35 percent stable. Average wind speeds are six miles per hour during unstable conditions, twelve miles per hour during neutral conditions, and four miles per hour during stable conditions.

XII-B-6-c. Severe Meteorological Phenomena

A maximum instantaneous wind velocity of 100 mph has been recorded at the site. During the past 50 years, three tropical storms, all of them in the final dissipation stages, have passed within 50 miles of the site. Some heavy precipitation and winds in excess of 40 miles per hour were recorded, but no significant damage other than to crops resulted.

The area near the site experiences an average of 35 thunderstorms a year, with maximum frequency in early summer. High winds near 60 mph, heavy precipitation, and hail are recorded about once every four years.

In forty years of record, there have been twenty tornadoes reported within fifty miles of the site. Maximum tornado frequency occurs in May and June.

During the past forty years, there have been ten storms in which freezing rain has caused power line disruptions. Most of these storms have occurred in early December.

XII-B-6-d. Potential Accidental Release Meteorology

A review of weather bureau reacords taken at the Middletown Municipal Airport over the past ten years indicates that the poorest atmospheric diffusion conditions occur in the autumn. The following conditions were noted:

- Nocturnal inversions occur on four of five nights.
- Stagnating high-pressure systems have occurred each year for the past ten years during the fall, causing a persistent subsidence inversion over the entire area. Average duration of these stagnating anticyclones has been five days, with the longest occurrence being nine days.
- The longest wind persistence (duration of time winds blew constantly from one 22-1/2^{o} sector) during the period of records was for 96 hours from the south, along the river valley. During this time, stabilities were 20 percent unstable (Pasquill B and C), 30 percent neutral (Pasquill D), and 50 percent stable (Pasquill E and F). This occurred during a stagnation period, so that there was also a persistent subsidence inversion aloft at an average height of 3000 feet.

From these data, 30 day accident meteorological regimes are assumed to be as given in Tables XII-B-1 and XII-B-2 for a ground level release and an elevated release.

XII-B-b-e. Dispersion Characteristics

The accident meteorology presented in Tables XII-B-1 and XII-B-2 provide the basic data for calculating dispersion factors (χ/Q) using equations based upon the Pasquill dispersion model. (χ/Q) values for center-line, ground level locations as a function of downwind distances are given in Figures XII-B-1 and XII-B-2 for ground level and elevated releases, respectively. A lateral restriction at 1200 meters imposed

by the river valley and a building wake factor of C = 1/2 have been used in the ground level release calculations.

Table XII-B-1 Accident Meteorology for a Ground Level Release

Time Period	Pasquill Stability Category	Stability Frequency	Direction Frequency	Wind Speed (m/sec)	Wind Direction type *
0-2 hrs	F	1.0	1.0	1.0	Invariant
2-24 hrs	F	1.0	1.0	2.0	Invariant
1-5 days	B	0.2	1.0	2.0	Variant
	D	0.3	1.0	4.0	Variant
	F	0.5	1.0	2.0	Variant
5-30 days	B	0.15	0.5	3.0	Variant
	D	0.50	0.5	5.0	Variant
	F	0.35	0.5	2.0	Variant

* Lateral dispersion restricted to 1200 meters from center line for all time periods.

Table XII-B-2 Accident Meteorology for an Elevated Release

Time Period	Pasquill Stability Category	Stability Frequency	Direction Frequency	Wind Speed (m/sec)	Wind Direction type *
0-2 hrs	B*	1	1	1	Invariant
2-24 hrs	B	1	1	2	Invariant
1-5 days	B	0.33	0.75	3	Variant
	D	0.33	0.75	5	Variant
	F	0.33	0.75	2	Variant
5-30 days	B	0.15	0.5	4	Variant
	D	0.15	0.5	6	Variant
	F	0.35	0.5	3	Variant

* Inversion cap at release height.

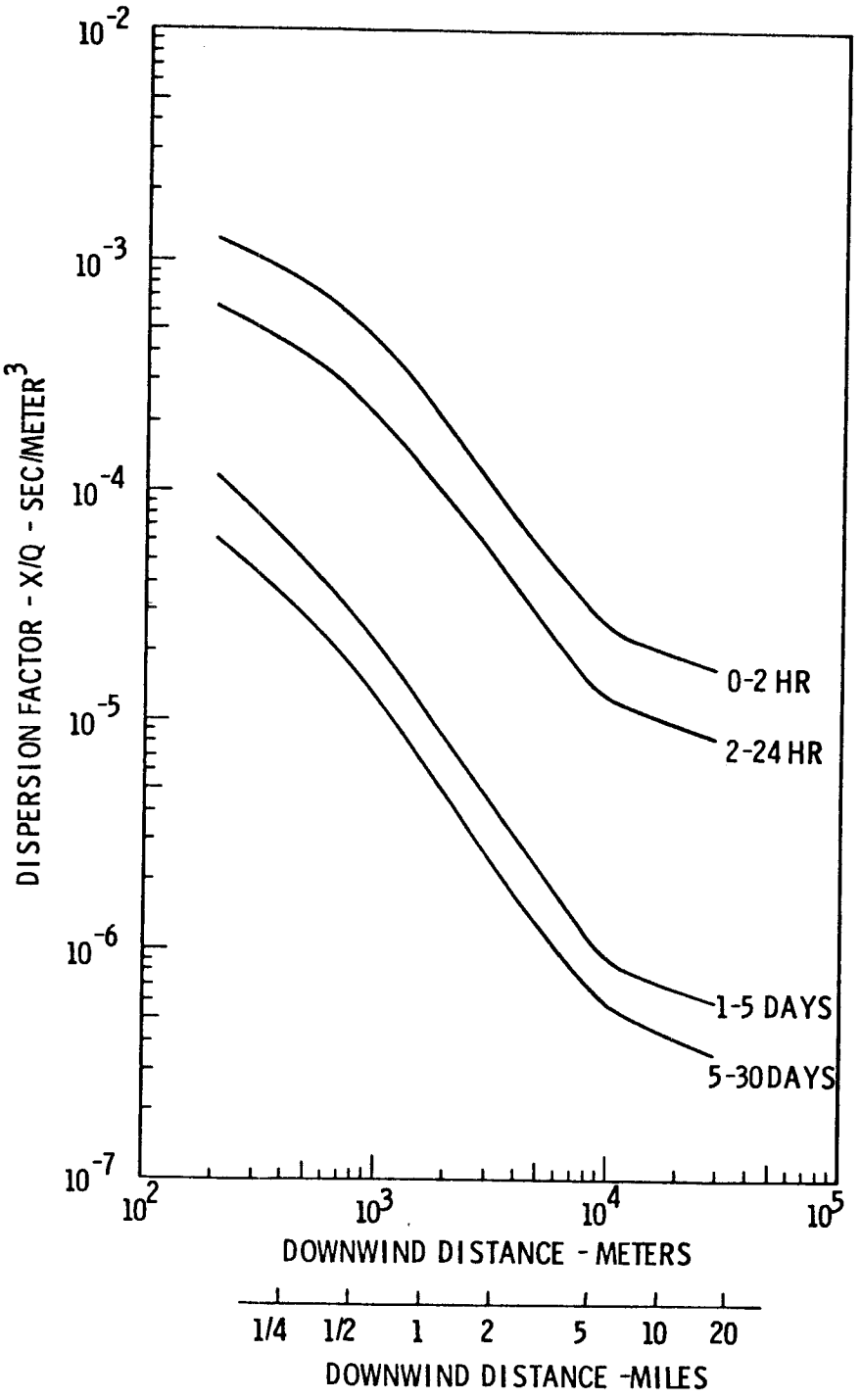


Fig. XII-B-1 Dispersion Factor χ/Q, s/m^3

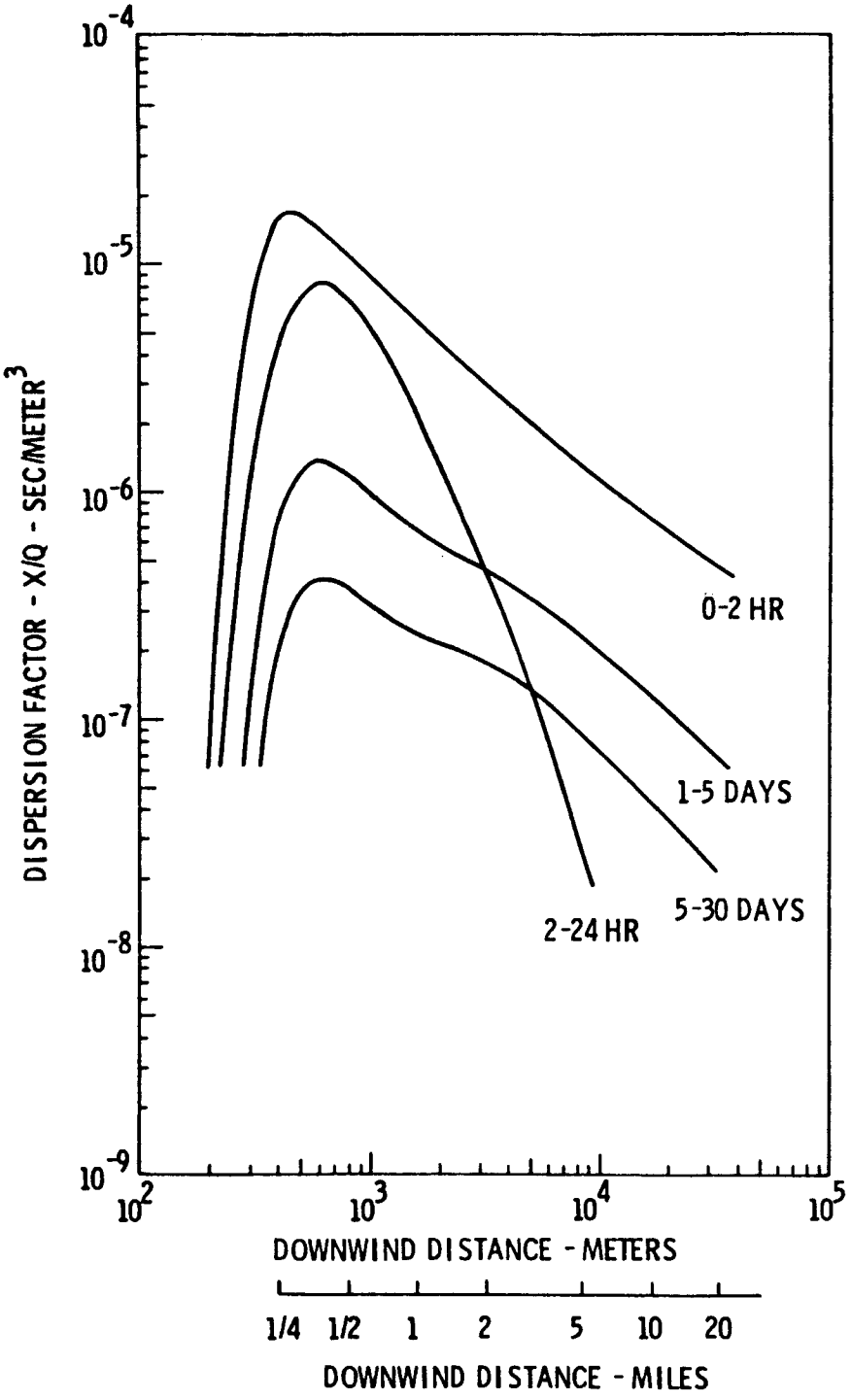


Fig. XII-B-2 Dispersion Factor χ/Q, s/m^3

XII-B-7. Geology and Seismology

XII-B-7-a. Soil Profiles and Load Bearing Characteristics

Soil profiles for the site show alluvial soil and rock fill to a depth of eight feet; Brassfield limestone to a depth of 30 feet; blue weathered shale and fossiliferous Richmond limestone to a depth of 50 feet; and bedrock over a depth of 50 feet. Allowable soil bearing is 6000 psf and rock bearing characteristics are 18,000 psf and 15,000 psf for Brassfield and Richmond strata, respectively. No underground cavities exist in the limestone.

XII-B-7-b. Seismology

This is a Zone 1 site, as designated by the Uniform Building Code, based on the observation of three earthquakes of seismic intensities 4-6 on the modified mercall scale during the period 1870-1958, causing minor damage to towns in the surrounding area.

XII-B-8. Sewage and Radioactive Waste Disposal

XII-B-8-a. Sewage

All sewage will receive primary and secondary treatment prior to discharge into the North River.

XII-B-8-b. Gaseous and Liquid Radioactive Wastes

Maximum permissible concentrations or dosages shall be as prescribed in the current revision of 10 CFR 20. The activity level of the liquid effluent will be measured as it leaves the plant. No credit for dilution in the North River will be assumed.

XII-B-8-c. Solid Radioactive Wastes

Storage onsite for decay will be used but no ultimate disposal on site will be made.

XII-C. Description of Buildings

XII-C-1. Introduction

The buildings are divided into two categories. Category I buildings are required to withstand the effects of earthquakes, floods, tornadoes and other natural disasters, as well as the impact of wind generated or plant generated missiles. Non-category I buildings are designed such that their failure will not cause a loss of safety function of any category I system.

In the following section each building will be described as to its category, function, location and size.

XII-C-2. Reactor Building

The main reactor building will be divided into two parts, the central part which will be 40 m in diameter and 35 m high and the outer service corridor which will be 10 m wide and 18 m high. The central part will be connected to the annular service corridor with eight archways, large enough to allow a TF coil to pass through. These archways will be located directly behind the TF coils, such that a TF coil can be extracted radially into the corridor and then moved to a service area in the auxiliary building adjacent to the reactor building. The reactor building will provide the primary containment. The function of the primary containment building is to:

- Provide a protective barrier against radiation and leakage of radioactive material from the nuclear island to the environment under all possible accident conditions.
- Contain internal pressure in the event of a liquid helium or a steam line break.
- Protect the reactor and its components against missiles and other conditions of adverse nature.

Figure XII-C-1 shows a cross section of the reactor building. To the right is the turbine building with one steam drum visible and to the left is the auxiliary building. A TF coil mounted on its own carriage is shown in the service corridor on its way to a service area.

The central building will have many wells and access areas built into the floor. In the middle, there is an 8 m x 4.5 m deep circular well which will contain the lower part of the central support structure and will provide the access for servicing the lower set of OH coils. There will also be eight circular wells 4.5 m in diameter and 3.5 m deep, equally distributed at a radius of 6.4 m. These wells will house the main cryopumps for the reactor vacuum chamber. An annular trench, 1.5 m wide and 3.5 m deep, will also be provided at a radius of 11.2 m from the reactor center. The external VF coils will be retracted into this trench when access to the reactor is needed. There will also be an annular service

SIDE VIEW OF THE NUWMAK
REACTOR BUILDING

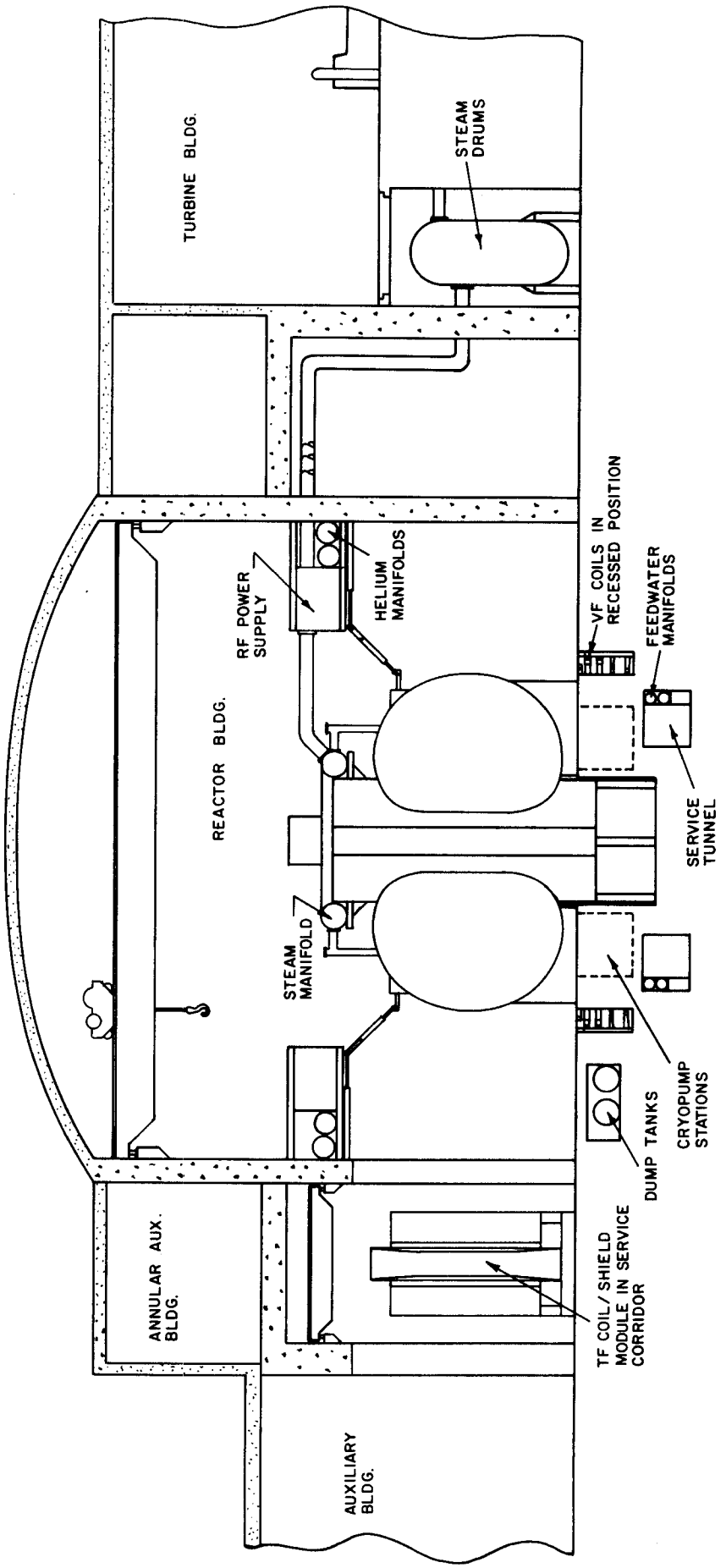


Fig. XII-C-1

tunnel 3.5 m wide and 3.5 m high at an average radius of 7.5 m from the center and 4 m below grade. The coolant supply manifolds will be located in this tunnel as well as other gas, electric, water and instrumentation services. This tunnel will also provide access to the cryopumps. The dump tanks for the LiPb will be located below grade on the side of the auxiliary building which will contain the tritium handling facilities.

With the VF coils extended, the reactor occupies a space 25 m in diameter; however, when the VF coils are retracted, it only occupies a space which is 21 m in diameter. The annular space between the reactor and the entrance to the corridor is 9.5 m wide. This is ample space for local maneuvering of service vehicles. Furthermore, circumferential transfer of equipment and parts can proceed in the service corridor unimpeded by activity in the central part. This feature of the design is particularly useful during routine maintenance, where several crews can be working on the reactor at several locations without getting in each others way.

The central part of the reactor building will be equipped with a 150 T (tonne) polar crane. Except for the TF coils which weigh 140 T each, none of the other reactor components weigh in excess of 120 T. The TF coils are transported on individual carriages which are permanent parts of their support structure. They will only require a supportive role from the polar crane. Actually, the heaviest use of the polar crane is during the reactor assembly operation at which time it is indispensable. Thereafter, its utility will be limited by some of the equipment which will be in the way such as the RF power supply systems and the manifolds located at a level of 16 m from the floor.

The service corridor will also have a 150 tonne crane. This crane will be able to navigate circumferentially from the auxiliary building in both directions to the junction between the reactor and the turbine buildings. A strip of the service corridor ~ 10 m wide at the junction will be used as the piping chute connecting the reactor with the turbine room. It will also house some of the valves, controls and the feedwater treatment equipment needed at this interface. The service crane will, therefore, be limited to about 350^{o} circum-navigation of the reactor building.

The radiological barrier in the reactor building will be a 2.5 m thick reinforced concrete wall. This barrier will cover the upper half of the main reactor building and the ceiling and outer wall of the service corridor. The ceiling of the central building will be a 1 m thick reinforced concrete spherical shell.

Both the reactor central building and the service corridor will be category I primary containment. A 0.3 cm thick steel liner will cover the ceiling, floor and walls. The doorway between the service corridor and the auxiliary building will have a sealed hatch to provide the capability of evacuating the reactor building to a pressure of ~ 10 torr. In the event of an accidental tritium release within the reactor building, it will be evacuated and the effluent treated for tritium recovery. Under normal operating conditions the reactor building will be maintained at a pressure of ~ 70 torr, but will be designed to withstand an over-pressure of 15 psi, in the event of a liquid helium or a steam line break.

The floor above the access corridor will be considered a part of the auxiliary building and will be discussed in the following section.

XII-C-3. Auxiliary Building

The reactor will have two auxiliary buildings comprised of the following: I - the second floor above the access corridor and II - a separate building on the ground floor adjacent to the reactor building. Both of these buildings will be category I.

The floor above the access corridor is an excellent location for one of the auxiliary buildings. This annular building, 9.5 m wide and 10 m high, completely surrounds the reactor containment structure, providing places for penetration between them at any number of locations. It will be compartmentalized to contain equipment of various kinds. Equipment which will handle radioactive material, such as the building vacuum system pumps and the associated tritium processing apparatus, will be housed in compartments with liners on the side opposite from the turbine building. Other equipment such as the cryogenerator-liquifiers, liquid helium storage vessels and diesel generators will be housed in shielded compartments on the side of the turbine building. This will make hands-on maintenance in those areas possible during reactor operation.

The second auxiliary building will be on the ground floor adjacent to the reactor and 180^{o} from the turbine building. This building, which is 30 m x 30 m and 20 m high, will be completely surrounded with a liner because it will contain the primary tritium handling equipment. Thus, the primary reactor vacuum pump effluent processing and the coolant detritiation will take place in this building. There will also be a doorway connecting this auxiliary building with the service corridor, and any transfer of equipment between the two buildings will take place through it. This door will be sealed during reactor operation and removable shielding blocks will be used to provide radiation isolation. During reactor blanket changeout, spent blanket modules will be transported through the auxiliary building to the hot cell for processing and ultimate storage in the radwaste area. New blanket modules will then be transported to the reactor building for installation in the reactor.

XII-C-4. Hot Cell

The hot cell is located adjacent to the reactor containment building and the lower auxiliary building as shown in Fig. XII-C-2. The entrance into it will be from the auxiliary building. It will be 20 m x 30 m and 20 m high. The hot cell will also be category I and equipped with a liner. For this reason the entry way into the auxiliary building will not need to be sealed.

The chief function of the hot cell is to receive and process irradiated blanket and other reactor components. It will, therefore, be equipped with temporary storage for a radioactive decay period, after which the components will be decontaminated, crushed and packaged. These packages will then be stored for an additional period of time before off site disposal can be provided.

XII-C-5. Radwaste Building

The function of the radwaste building is to process all the radioactive waste from the tritium handling and coolant purification systems. It is, therefore, located adjacent to the hot cell and the lower auxiliary building.

This building will be 20 m x 25 m x 20 m high. It will be category I and like the hot cell will have a liner. There will be one entry way into it from the auxiliary room.

NUWMAK REACTOR BUILDING LAYOUT

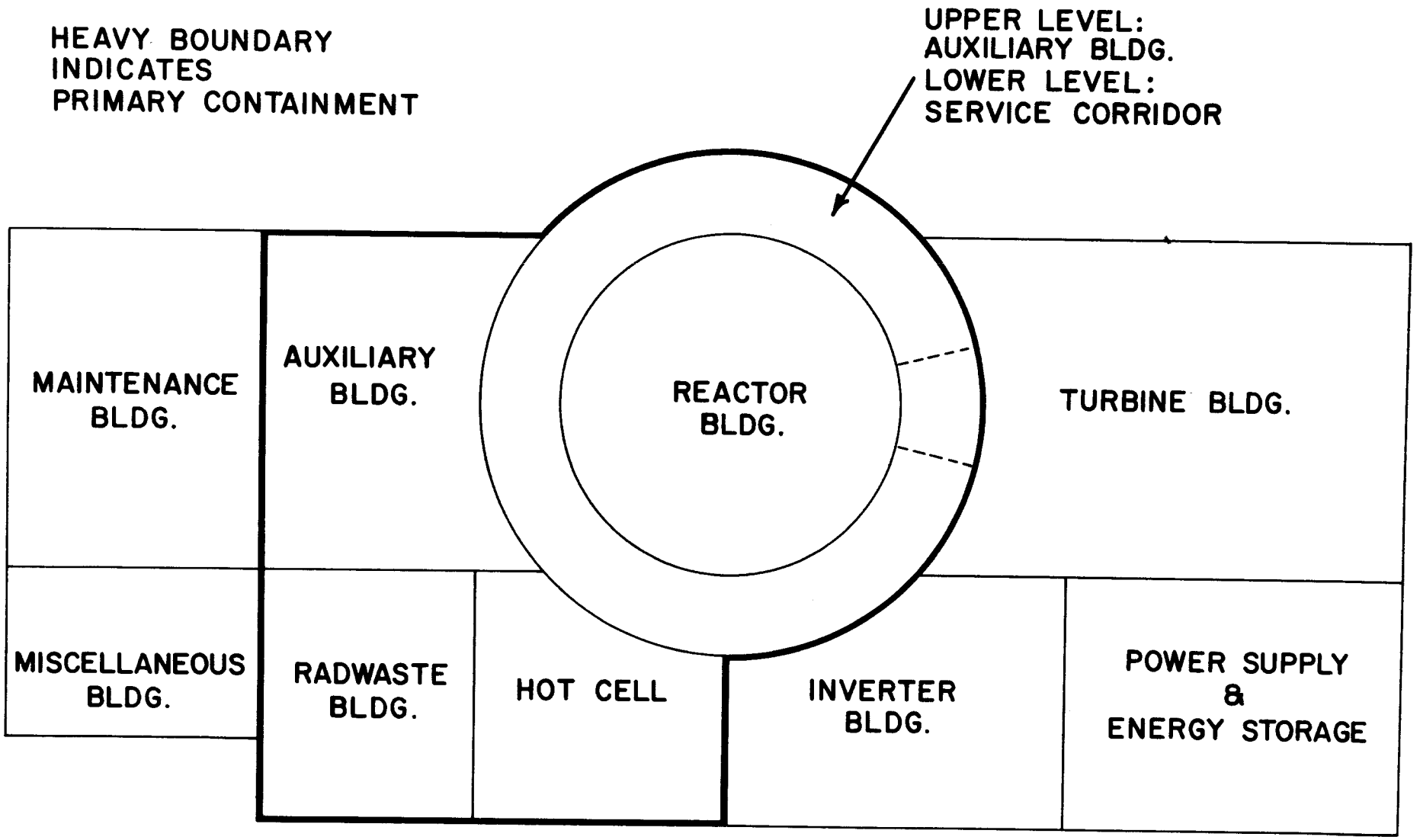


Fig. XII-C-2

The equipment in this building will be capable of solidifying and packaging the radioactive wastes in preparation for off site disposal or storage.

XII-C-6. Turbine Building

The blanket in NUWMAK is cooled with boiling water which goes directly to steam drums located on the ground floor of the turbine building. In this design, steps have been taken to inhibit tritium diffusion into the steam. However, at this time it is not clear that these steps will be adequate to prevent the buildup of tritium in the steam cycle. Diffusion tests will soon provide data on the basis of which this question will be answered. For the present, we will assume that direct turbine operation is possible without an intermediate loop.

Because there is no intermediate loop, there is no need for a heat exchanger building. The saturated steam from the reactor blanket goes directly to four steam drums where the vapor is separated from the moisture and goes to drive the steam turbines. The water is pumped back to the reactor to repeat the cycle.

The four steam drums, each 4 m in diameter and 10 m high, are located on the ground floor of the turbine building adjacent to the part of the service corridor which is devoted to the piping interface between the reactor and the turbine buildings. In addition, there are four water storage tanks 2.2 m in diameter and 10 m high, and two accumulators 1.5 m in diameter and 6 m high located near the steam drums. They are part of a load leveling scheme described elsewhere in the report.

The turbine building is 40 m wide, 55 m long and 30 m high. The level of the turbine generators is 12 m above the ground floor. Most of the equipment needed by the turbine generators, such as condensers, reheaters, etc. will be located on the ground floor below the turbines. An overhead crane with a capacity consistent with the heaviest item in the turbine building is provided for servicing the system. Removable floor covers make it possible to reach the steam drums and other components located on the ground floor.

The two 365 MWe turbine generators will be located side by side with their axes pointing away from the reactor. In this way any disintegrating part of the turbines or generators will not be directed toward the reactor. Each turbine-generator unit is ~ 30 m long and 5 m wide. They are supported on massive reinforced concrete pedestals designed to withstand earthquake conditions and to prevent settling which would cause misalignment problems.

XII-C-7. Maintenance Building

This building contains the equipment needed to maintain the radioactive components of the reactor. It will also be used to serve the remote handling vehicles used in the containment building.

It will be a 30 m x 40 m x 20 m high, category I single story building without a liner located adjacent to the auxiliary building. Transfer of equipment and components from the auxiliary building to the maintenance building will be through an air lock.

XII-C-8. Administration and Control

The administration and control building will be located separate from the reactor building complex as shown in Fig. XII-C-3. Administrative functions will be handled in one wing of the building roughly one-half the floor area and the other will be devoted to the control of the reactor.

The control building is placed at a distance from the reactor so that it would not be affected by the stray fields from the poloidal coils and in particular by the energy storage coil. It will be a category I building and will contain all the controls for reactor operation as well as the controls for regulating the movement of equipment and placed well within the reactor complex. The overall size of the administration and control building will be 20 x 30 m. The administration wing will be two stories high and the control wing, one story high.

Some facilities that are usually housed in the control room will be instead located in the miscellaneous building. These will include the radiation chemistry lab, clean chemistry lab, counting room, health physics office and first aid facilities.

PLAN VIEW OF THE NUWMAK POWER PLANT

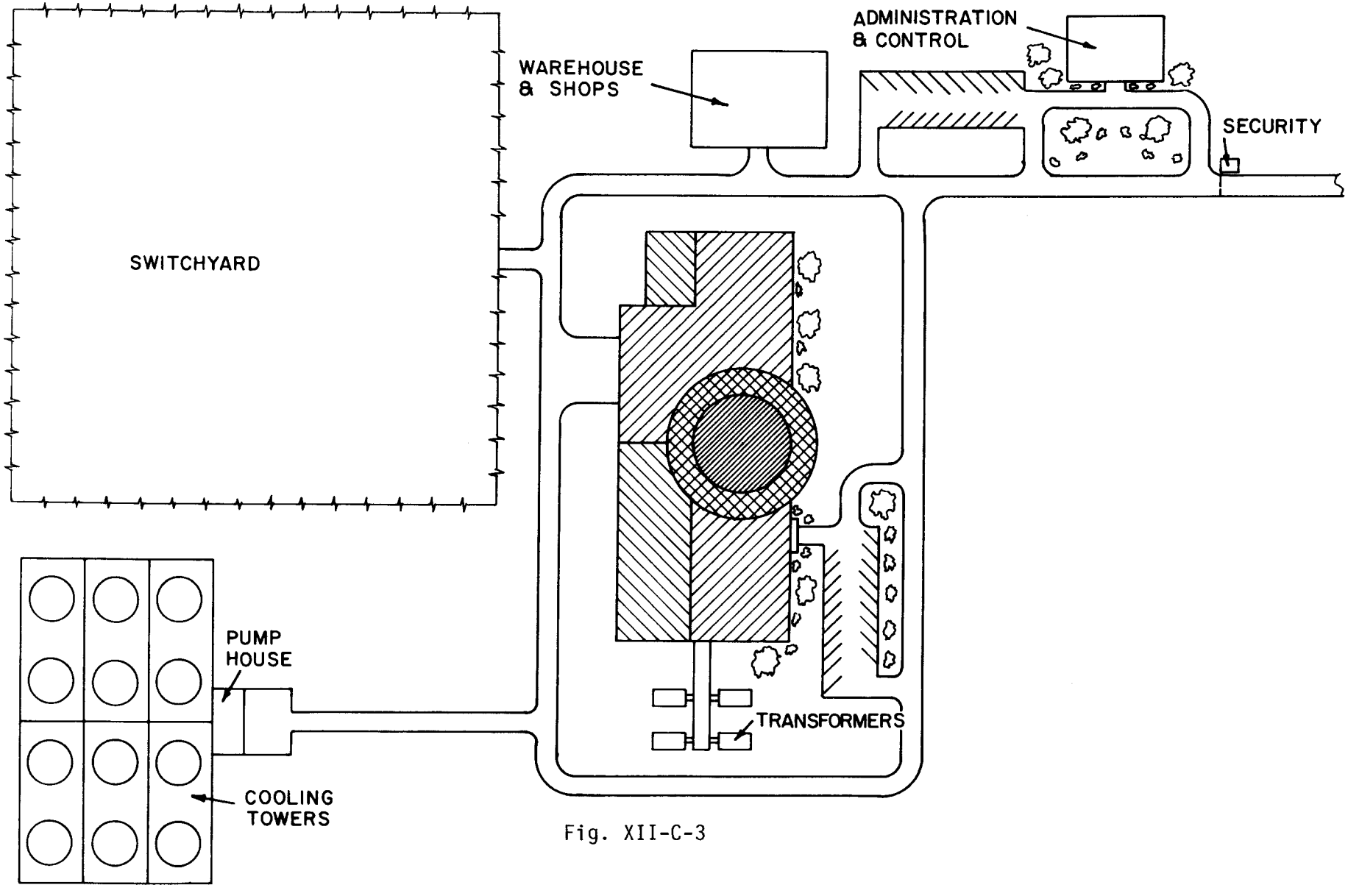


Fig. XII-C-3

XII-C-9. Other Buildings

The remaining buildings are;

a) Energy storage

b) Inverter

c) Miscellaneous

Figure XII-C-1 shows the location of these buildings within the reactor complex. All three buildings will be single story, non-category I frame structures with insulated metal panel walls and built up roofing. They will be reinforced with trusses and purlins.

The energy storage building will be located adjacent to the turbine building, in close proximity to the helium liquifiers. The building itself is 30 m x 40 m x 10 m high. It will house a 2 MW-hr superconducting energy storage solenoid, approximately 24 m major diameter. About 40% of this stored energy is used to supplement energy taken from the grid to drive the poloidal coils in the reactor. The DC/AC/DC conversion takes place in the inverter building which adjoins the turbine and energy storage buildings. The inverter building is 20 x 40 m x 10 m high.

Finally, the miscellaneous building houses such facilities as the radiation chemistry laboratory, the clean chemistry laboratory, the counting room, contaminated clothing laundry, health physics office, first aid station and showers. It will be 30 m x 20 m x 10 m high.

Table XII-C-1 lists the specifications of the buildings in the NUWMAK power plant.

Table XII-C-1

Specifications of Buildings in the NUWMAK Power Plant

Building	Classification	Liner	Special Design	Dimensions (m)
Reactor Containment	Category I	Yes	0.1 MPa (1 atm) Pressure 10 Torr Vacuum Shielding	40 dia. x 35 m High Service Corridor 10 m x 18 m High
Auxiliary	Category I	Partly	Partly - 0.1 MPa (1 atm) Pressure 10 Torr Vacuum Shielding	30x30x20m High 10 m x 10 m High Annular
Hot Cell	Category I	Yes	Shielding	20x30x20 m High
Radwaste	Category I	Yes	Shielding	20 m x 25 m x 20 m High
Turbine	Category I	No	None	40 m x 55 m x 30 m High
Maintenance	Category I	No	None	30x40x20 m High
Control	Category I	No	None	15x20x5 m High
Administration	Category I	No	None	15x20x10 m High
Energy Storage	Non-Category I	No	None	30 m x 40 m x 10 m
Inverter	Non-Category I	No	None	20 m x 40 m x 10 m
Miscellaneous	Non-Category I	No	None	20 m x 30 m x 10 m

XII-D. Plant Electric System

The electric power system for NUWMAK has not been designed in detail as was the case in the UWMAK series. It is envisaged that this system will be similar to the earlier designs but smaller in total output. In some ways it will also be simpler because there is only one thermal output cycle. Those who are interested in more details of how the electric power plant of a fusion reactor looks are referred to the UWMAK-III report. In this section we will only briefly review some of the safety and the main design characteristics of the power generation system.

The main function of the electric power system is to generate electric power and transmit it to an electric grid through suitable transformers. The system should be capable of generating enough auxiliary power to operate the essential plant equipment in the event of an emergency.

From the safety standpoint, there will be adequate on-site power provided to meet plant emergency power requirements. Further, this on-site power supply system will be fully redundant and will consist of an AC system, DC system and instrumentation and control system. As another measure of safety, the on-site power supply system will be connected to two off-site power sources.

The power will be produced by two turbine generator units rated at 400 MVA each and will be 3 phase, 60 cycle and at 24 kV. Each generator will be connected to a circuit breaker and a switch through an isolated phase bus duct. An isolated phase bus duct also connects each generator at the load side of the disconnect switch to a step-up transformer connected to the switch yard. The step-up transformer is made up of three single phase units and a spare. The single phase units have a low voltage rating of 26 kV and a high of 404 kV. When the three units are connected in a delta-wye mode, they develop 700 kV which matches the switch yard voltage.

The following are some of the main design characteristics of the power generation system:

a) High reliability of power supply is insured by the provision that each main bus of the auxiliary distribution system is transferable between two redundant connections to the switch yard power sources.

b) Isolation is provided for each of the redundant components of the plant distribution system in order to make it possible to service

the equipment without plant shutdown.

c) The turbine-generators are provided with a separate overload protection and an isolation device. Each generator will be provided with the means to synchronize the output with the switch yard sources.

d) The high cost of the superconducting energy storage and inverter systems makes the provision of redundancy economically prohibitive. It is postulated, however, that the likelihood of failure of the energy storage system will be low.

XIII-A. Materials Resource Analysis

In Table XIII-A-1, total materials requirements (nuclear island plus balance of plant) for 10^6 MW_e capacity (1500 reactors) are given based on the NUWMAK design. Tables XIII-A-2 and XIII-A-3 give the material requirements in the nuclear island and the balance of plant, respectively. The materials are listed in three groups, according to availability from domestic sources. Helium is omitted.

Group A consists of metals, plus carbon, that should be available from domestic mines during the period 2000 to 2020 at market prices then current. Those prices will reflect whatever inflation the future may bring, plus increases due to development of lower-grade ores. However, domestic reserves of these materials are adequate. Appropriate increases in production capacity are assumed, to meet the increases over normal U.S. consumption that would be involved in meeting reactor requirements.

Group B consists of Aℓ, V, Ti, Ni, Cr, and Mn. Reserves of the first four metals will probably be too depleted by the year 2000 to furnish the required amounts. However, at prices 3 times normal prices all five metals could be obtained from domestic deposits that are not now economically viable. Those deposits could be brought into production over a period of 3 to 5 years.

Group C consists of W, Nb and Co. U.S. reserves of W are only about one-fourth of the requirement. They furnish only about 40 percent of current U.S. consumption and they are steadily being depleted. It is increasingly difficult to find new tungsten deposits in the U.S. since Canadian reserves are twice those of the U.S. and could help in supplying requirements, but major reserves outside North America would have to be tapped. The requirement is about 22 times total world annual production, hence tungsten availability should be a matter of concern.

Niobium is also a problem. At three times present prices, perhaps 60 percent of the requirement could be obtained from the Powderhorn (Colorado) deposits. World reserves of niobium, however, are very large relative to the requirement. If the NUWMAK design is selected, it would be well to consider stockpiling Nb over a period of years to take advantage of the production capability that exists abroad, and could be increased, especially in Canada and in Brazil.

Cobalt is a severe problem. There is no production of Co in the U.S. The requirement is twice world annual production of the metal. At present, Co is produced as a byproduct of mining for copper or nickel, or both. This would also be true for Co produced from seafloor nodules. Any large increase in world Co production would require a price several times the present price, perhaps 10 times the price, and the resulting greatly increased production of Ni or Cu, or both, would cause severe dislocations in the present Ni and Cu-producing industries. It would seem worthwhile to consider stockpiling Co, over a period of years, as the metal may be available in world markets. No crash program of procurement of Co in the amounts required for 10^6 MW_e capacity can be successful.

Table XIII-A-1

Group & Metal	Total requirement for 10^6 MW_e, in m.t. x 10^3
Group A - Materials available from domestic mines at market prices	
Boron	2,232
Carbon	1,093
Copper	1,183
Iron	56,362
Lead	2,829
Lithium	63
Magnesium	8
Zr	1.5
Mo	68
Group B - Materials available from domestic mines at 3X market prices	
Aluminum	2,240
Chromium	346
Titanium	1,286
Manganese	53
Vanadium	117
Ni	44
Group C - Materials available in adequate amounts only from foreign sources	
Niobium	75
Tungsten	1,040
Cobalt	68

Table XIII-A-2

Material Requirements - NUWMAK Nuclear Island

	Blanket & RF			Magnets & Dewars									
Element	Initial	Replacem. 30 yr	Shield	TF	Cryog. VF	Super. VF&OH	Trimm. Coils	Central Support Struc.	Vacuum Pumps & Ducts	Reactor Support Struc.	Other	Total (MT)	Tonnes / MW_e
Al	2.6	36.4	8.8	979.1	103		1	111.23	24.95	49.2	147.6	1463.9	2.218
B			1488									1488	2.254
C	105	210	412.5				1.8					729	1.104
Cr				0.4	.03	11.6		0.3	.86	.13	8.9	22.2	0.034
Nb				28.2		2.6						40.9	0.062
Cu				23.6	2.74	143.6	144	0.34	.01	.15	0.5	314.9	0.477
He												370×10^3 Liters	
Fe						47.1			3.35		33.5	83.95	0.127
Pb	755		1131.3									1886.3	2.858
Li	41.4											41.4	0.063
Ti	42	588	131.9	20.4	.03	1.3	14.4					798	1.209
Mn				1.2	.14				0.1		1.0	2.4	0.004
Mg				2.2	.12			1.13	.03	0.5	1.5	5.5	0.008
V	4.6	64.4	5.9	0.4	.05		0.6					76	0.115
Ni						8.2			0.6		6	14.8	0.022
Zr				0.77	.10							0.9	0.001
W			693.5									693.5	1.051
Mo						1.4			0.1		1.0	2.5	0.004
												TOTAL	11.611
Material													
$Li_{62}Pb_{38}$	796.4											796.4	
Ti-6Al-4V	44.14	618	146.5				16					824.6	
Ti	2.26	31.6										33.9	
Solder						18.8						18.8	
B_4C			1900									1900	
Al(2219)				384	45.2							429.2	
Al(6061)				220	12.6			113	25	50	150	570.6	
Al(MPA)				404	48.4							452.4	
316SS						47.1			5		50	102.1	
NbTi				58.2		3.9						62.1	
Fiberglass Epoxy				66.5	16.5	3.6						86.6	

Table XIII-A-3

Material Requirements - NUWMAK Balance of Plant

Element	Piping	Steam Drums & Water Storage	Dump Tanks	Pumps	Liquid Helium Storage	Cryogen-erators	Energy Storage Unit	Building Liners	Buildings	Turbine	Generator	Total (MT)	Tonnes MW_e
Al	2.2		0.9			80				12.5		95.6	0.145
Cr	58	1.1		1.8	1.7	10.2	97			37.5	1.4	208.7	0.136
Nb							9					9	0.014
Cu						20	434				20	474	0.718
Fe	2483	410.3		13.6	36.3	60.2	323	493.8	32.500	752.5	418	37.491	56.80
Pb													
Li													
Ti	32.4		13.5				4.8						
Mn	12.9	2.1		0.2	0.6	1.2	9.6	6.25		8.8		59.5	0.090
Mg												32.9	0.050
V	1.4		0.6										
Ni		2.1		1.2	1.2	7.2	59					2	0.003
Zr		0.02								131		201.7	0.305
W													
Mo	25.8	2.3		0.2	0.2	1.2							
Co										12.5	0.6	42.8	0.065
										45		45	0.068
Material												TOTAL	58.574
CROLOY	2580												
Mn-Mo-Ni	Alloy	420										2580	
Ti-6Al-4V	36		15									420	
316 SS				10	10	60	488.6					51	
A-242					30			500				568.6	
1020				5		20			32.500	750	200	530	
UDIMET -700										250		33.475	
Silicon Steel											160	250	
2-1/2 Cr-1Mo				2					3		60	160	
Concrete									$125x10^3 m^3$			62	
												$125x10^3 m^3$	

XIV. System Economics

XIV-A. Introduction

The economic analysis for NUWMAK conforms to the guidelines provided by the Department of Energy through the"Fusion Reactor Design Studies - Standard Accounts for Cost Estimates" report issued in May 1978.

Two modes of economic analysis are used. The first is a current dollar mode (nominal dollar) which assumes that the purchasing value of the dollar changes over time. The second is a constant dollar mode which assumes the purchasing value of the dollar remains constant over time or that the inflation rates and component escalation rates are equal to zero. The cost of energy figures obtained by the constant dollar mode will be higher than the cost of energy today because the present dollar value is used without deescalation to its value eight years ago (assuming an eight year construction period) and the interest during construction is based on the present day cost. This is an important factor to be kept in mind if one has to compare the cost of energy from NUWMAK obtained by the constant dollar mode with the cost of present day energy (fossile fuel, etc.).

In the current dollar mode the cost escalation on the estimated capital costs is assumed to exist and is accounted for in a single escalation during construction account. Further, the cost escalation on estimated operating and maintenance, scheduled component replacement and fuel costs is also assumed to exist, and is accounted for within the respective parent cost account. The current dollar analysis mode is, therefore, essentially a nominal first year facility cost and the cost of energy obtained in this way should be compared with the cost of energy from other sources eight years from now.

XIV-B. Level of Technology

There are many levels of technology utilized in the design of fusion reactor systems and their supporting subsystems, ranging from current to advanced. Advanced technology is usually defined as any technology which has not been demonstrated on a commercial scale.

Generally speaking most of the technology used in the nuclear island is advanced. There are some exceptions. On the other hand, certain technology that may be classified as current under ordinary conditions has to be classified as advanced because of the unique fusion reactor environment. For example, NUWMAK has a first wall and blanket made of Ti-6Al-4V titanium alloy. This alloy is used extensively in the aircraft industry, has a large technical base for fabrication and its use has been demonstrated on a commercial scale. However, in a fusion environment and in particular with respect to radiation damage, this technology would have to be classified as advanced.

In the balance of plant, however, most of the technology is current. This is particularly true in the case of NUWMAK which has a boiling water cooled blanket utilizing straightforward BWR technology in the power cycle. The turbine and electric plant equipment, condensing and heat rejection equipment and the miscellaneous plant equipment would, therefore, be considered as current technology. Such areas as tritium extraction, superconducting energy storage and certain aspects of radioactive waste handling would obviously have to be classified as advanced technology.

XIV-C. Design Allowance, Contingency and Spare Parts

The design allowance is a sum of money included in the estimate to account for items overlooked or underestimated in the original design. Thus, the level of technology in a particular area dictates the percentage of design allowance allocated to the different accounts. In the NUWMAK economic analysis, a 10% allowance was used in all the accounts except the reactor plant equipment account for which a 15% design allowance was used.

By definition, contingency is a sum of money added to an estimate to provide for items not specified in the engineering detail but which are known from experience to be a necessary part of a facility. Implicitly, it will be used, and it is not a drawdown fund to compensate for overruns or changes and additions to the project scope. In NUWMAK, a 10% contingency was used throughout the report.

The spare parts allowance is the purchase cost and inventory cost prior to facility operation of the initial inventory of spare parts required onsite.

Reactor parts rotated into service as part of a scheduled maintenance program are not considered as spare parts. The following spare parts allowances were used: 2% for reactor plant equipment, 1% for the turbine plant and miscellaneous plant equipment, and 0.5% for the electric plant equipment and the structure and site facilities.

XIV-D. Nuclear Island Unit Costs

In this section the unit costs used in estimating the major components in the nuclear island will be given and the reasoning used for arriving at them will be discussed. The order used in section XIV-G accounts will be followed.

Blanket and First Wall (Acct. 22.01.01)

The cost of the $Pb_{38}Li_{62}$ breeding material used is \$3.5/kg based on vendors' quotes for Pb of \$3.0/kg and for Li of \$13.00/kg.

The cost estimates obtained for the TFTR vacuum vessel ranged from \$46.25-82.72/kg. Based on these values, the stainless steel ORNL-TNS vacuum vessel was estimated at \$120/kg. Some fairly complex and detailed structures have been fabricated from Ti-6Al-4V in the aerospace industry for \$55-60/kg.[2] Taking all these factors into account we have taken a unit cost of \$150/kg for the first wall, blanket and limiter. This gives an average cost of \$72.6 x $10^3/m^3$ for the first wall/blanket/limiter. Table XIV-D-1 summarizes these costs.

Shield (Acct. 22.01.02)

The complexity of the structure in the shield varies substantially and it was, therefore, decided to estimate it using three different unit costs, \$40/kg, \$60/kg and \$100/kg (Table XIV-D-2). Some of the lead in the shield will have to be fabricated into certain shapes; however, the bulk of it will most likely be poured into prepared cavities. A fabricated lead shield was estimated at \$8/kg for the ORNL TNS[1] and we have obtained a price of \$3/kg for unfabricated lead. We have taken an intermediate figure of \$5/kg.

The base cost of tungsten powder is taken as \$23/kg[1] and this cost will double when fabricated into plate or laminations. We have taken a unit cost of \$50/kg for the tungsten in the shield.

Table XIV-D-1
Blanket Unit Costs

	Unit Cost ($/kg)	Quantities (Tonnes)	Cost ($x10^6$)
Breeding material	3.5	800	2.800
First Wall/Blanket	150	46.2	6.930
Limiter	150	6.93	1.040
		TOTAL	10.770

Table XIV-D-2
Shield Unit Costs

	Unit Cost ($/kg)	Quantity (Tonnes)	Cost ($x10^6$)
Ti Alloy	100	10	1.000
	60	25	1.5000
	40	112	4.4800
Lead	5	1131	5.655
Tungsten	50	693	34.650
B_4C	50	87	4.350
	6	1813	10.878
Graphite	5	105	0.525
		TOTAL	63.038

The average unit cost of the shield comes out to \$15.9/kg or \$56.6 x $10^3/m^3$.

The B_4C in the inner shield amounting to ~ 90 tonnes will be in the form of fabricated high density blocks for which we have used a unit cost of \$50/kg. The rest can be in the form of borated water at a cost of \$6/kg.[1]

The graphite reflector will not be very complex. A unit cost of \$5/kg was used based on similar shapes used in the HTGR.

Magnets (Acct. 22.01.03)

The magnets in a tokamak usually account for a sizeable fraction of the cost of the nuclear island. It is, therefore, appropriate that we elaborate on the unit costs used.

The following assumptions were made in costing out the magnets in NUWMAK:

1 - NUWMAK is not a one of a kind device, but is part of an established industry.

2 - The use of high purity aluminum as a stabilizer has been demonstrated and fabrication of the conductor has been developed.

3 - TF coil discs are fabricated and the conductors embedded in them at a magnet factory offsite. Discs can be transported individually or in groups from the magnet factory to the site where they are assembled. Although the discs are too large for over the road or rail transportation, they can be transported by barge or helicopter easily. The weight of a single disc is ~ 4.4 tonnes. We, therefore, assume that an onsite winding facility for TF coils is not necessary.

4 - The superconducting VF coils are wound onsite and are placed within the well provided for them prior to assembly of the reactor. A spare coil is provided within the well for the lowest VF coil. The reason for doing this is because the lowest VF coil is the only one which cannot clear the TF coils and a replacement for it would have to be wound in situ.

Only the external superconducting VF coils will be wound onsite. However, such a winding facility would be very simple and cheap.

5 - The cryogenic VF coil conductors will be fabricated at a factory and shipped to the site in long straight sections. Onsite, they will be bent into the correct curvature, drilled and assembled.

6 - The trimming coils will be fabricated in their entirety offsite. They can be shipped by rail, truck, barge or helicopter. This is also true of all the OH coils.

The cost of the superconducting NbTi material delivered on a spool is taken as \$50/kg.[1] The high purity aluminum stabilizer (RRR $\simeq$ 2000) is taken as \$10/kg although figures of \$6/kg[3] have been mentioned for very large quantities. The fabrication cost is taken as \$40/kg for the TF coil conductor. Although the technological problem of making a good electrical bond to aluminum has not yet been resolved, it is assumed that the fabrication of such a conductor will not be too difficult. The overall unit cost of this conductor is \$58.6/kg or \$55/m. It is interesting to note that the relatively complex conductor for MFTF had a unit cost of $\sim$ \$35/m.

The high strength aluminum discs are costed at \$30/kg. Although rather big and bulky, their fabrication will be fairly straightforward. The discs will start out as long rectangular extrusions with straight grooves on both sides. The rectangular bars will then be bent into the proper D shape but without the straight section of the D. The straight section will be made separately, because it will contain the transition grooves which will make it possible to wind the conductor in a helical fashion. Thus, one side of the straight section will have grooves which will make it possible to wind a clockwise helix while the other side, a counter-clockwise helix. The straight section will then be welded to the disc to complete the D shape. The final step will be to do a clean-up machining of the grooves. This will be done by a numerically controlled multi-spindle milling machine and will account for the bulk of the fabrication cost.

The dewars are fairly complex structures requiring much inspection and leak checking, and for this reason a value of \$40/kg has been used. A unit cost of \$42/kg is given for a stainless steel dewar for the ORNL TNS.[1]

We have taken a value of 6×10^5 man hours for the assembly and erection of the TF coils at an average cost of \$12.5/man hour. This amounts to three, thirty man crews working for a period of 3-1/2 years.

The average unit cost of the TF coil system comes out to be $45.45/kg.

Although the conductor used in the OH coils is different in design from that used in the external superconducting VF coils, they both use NbTi with copper stabilizer and stainless steel structure. For this reason the same unit costs have been used to estimate their cost. Since both conductors have already been produced and are in use today a fabrication cost of $25/kg was taken which gives an overall conductor unit cost of $45/kg. The overall coil system unit cost is $59.2/kg.

The conductor used in the cryogenic VF coils is fairly straightforward. It consists of a high purity aluminum rectangular bar surrounded by a casing of high strength aluminum. A fabrication cost of $20/kg was used here. The high strength aluminum structural rings were costed at $15/kg because of their simple geometry compared with the structural discs in the TF coils which were costed at $30/kg. The average unit cost of the conductor is $30/kg and the average unit cost of the coil system is $34.5/kg.

The trimming coil conductor is conventional and although copper bus bars with eight cooling holes may not have yet been produced, they are within the present day state-of-the-art. It is envisaged that the conductor will be extruded and subsequently cold worked to the 1/4 hard condition. No machining except at the joints will be required. A unit cost of $30/kg[1] was used for the conductor which gives an average unit cost of $46/kg for the whole coil system. Tables XIV-D-3 to 6 summarize the magnets' cost.

Supplemental Heating (Acct. 20.01.04)

A unit cost of $0.45/W of injected power has been used. This figure is based on $21 x 10^6 for hardware and $15 x 10^6 for labor. Some of the figures were extrapolated from manufacturer supplied costs while a major portion was based on a similar cost analysis for the TEPR-1[4] reactor design.

Although studies on neutral beams and lower hybrid wave heating systems invariably arrive at unit costs in excess of $1/W, we feel that ICRF is comparatively simpler in terms of system integration and RF high power engineering in the 10-100 MHz range. Technology for improving high power tubes (5 MW) is well known and thus, development costs can be minimized. High power transmission

Table XIV-D-3
TF Magnet Unit Costs

	Unit Cost ($/kg)	Quantity (Tonnes)	Cost ($x10^6)
1. NbTi s/c	50	58.2	2.91
2. Aluminum Stabilizer	10	212	2.12
3. Conductor Fabrication	40	270.2	10.808
4. Fabricated Al Structure	30	384	11.52
5. Fiberglass Epoxy	10	23	0.23
6. Fabricated Micarta Spacers	15	34	0.51
7. Dewar (TF)	40	85	3.40
Dewar (Central Support)	40	15	0.60
8. Aluminum Shield	20	192	3.84
9. Superinsulation	$100/m^2	2000 m^2	0.20
10. Epoxy Struts	15	9.5	0.143
11. Central Support Structure	30	113	3.390
12. Motorized Carriages	$0.5x10^{6}ea	8	4.000
13. Assembly & Erection	$12.5/man-hr	$6x10^5$man-hr	7.500
			51.171

Total mass of TF coil is 1125.7 x 10^3 kg.
Average unit cost of conductor $58.6/kg.
Avg. unit cost of coil system $45.45/kg.

Table XIV-D-4
OH & VF Coils Unit Costs

	Unit Cost($/kg)	Quantity (Tonnes)	Cost ($x10^6)
1. NbTi s/c	50	3.9	0.195
2. Cu Stabilizer	20	143.6	2.872
3. S/S Structure	20	68.3	1.366
4. Conductor Fabrication	25	217.8	5.449
5. Solder	10	18.8	0.188
6. Fabricated Micarta Spacers	15	3.6	0.054
7. Superinsulation	$100/m^2	583 m^2	0.058
8. Dewar	40	40	1.600
9. Support Structure	35	75	2.625
10. Winding, Assembly & Erection	$12.5/man-hr	$1.5x10^5$man-hr	1.875
		TOTAL	$16.282

Total mass of coils 275 x 10^3 kg.
Average unit cost of conductor $45.4/kg.
Avg. unit cost of coil system $59.2/kg.

Table XIV-D-5

Cryogenic VF Coils Unit Costs

		Unit Cost ($/kg)	Quantity (Tonnes)	Cost ($x10^6)
1.	High Purity Aluminum	10	48.4	0.484
2.	High Strength Aluminum in Cond.	10	28.6	0.286
3.	Conductor Fabrication	20	77	1.540
4.	High Strength Aluminum in Structural Rings (Fabricated)	15	16.6	0.249
5.	Micarta Spacers (Fabricated)	15	16.47	0.247
6.	Fabricated Dewars	40	12.58	0.503
7.	Aluminum Bolts	$20 ea	$10x10^3$	0.200
8.	Superinsulation	$100/$m^2$	152 m^2	0.015
9.	Assembly & Erection	$12.5/ man-hr	$7.5x10^4$ man-hr	0.967
			TOTAL	$4.491

Mass of coils 130 x 10^3 kg.

Avg. unit cost of conductor $30/kg.

Avg. unit cost of coil system $34.55/kg.

Table XIV-D-6
Trimming Coils Unit Costs

	Unit Cost ($/kg)	Quantity (Tonnes)	Cost ($x10^6$)
1. Fabricated Cu Conductor	30	144	4.320
2. Ti Alloy Casing	50	16	0.8
3. Graphite Insulation	22	1.8	0.04
4. Assembly & Erection	$12.5/man-hr	$1x10^5$ man-hr	1.25
			6.410

Total mass of trimming coils is $161.8x10^3$ kg.
Average unit cost of coils system $46/kg.

in this frequency range can be achieved with coaxial lines which are being commercially produced today.

Reactor Vacuum System (Acct. 22.01.06)

The highest expense in the reactor vacuum system is in the cryopumps. The proposed cryopumps will have two pumping surfaces back-to-back, such that one surface can be in use while the other is being regenerated. Some development is needed to produce such a pump especially in the area of the seal. NUWMAK will have 140 m^2 of cryopump surface in operation or 280 m^2 altogether. The unit cost used is $\$30x10^3/m^2$ based on discussions with cryopump manufacturers[5] and extrapolation of present day units. The pumps and compressors used for regenerating the cryopumps are estimated to cost an additional $\$1x10^6$. The values given here do not include the costs of the cryogenerators which are estimated in Acct. No. 22.03.03.01. The reactor vacuum ducting and the cryogenic piping is estimated at $100/kg.

There are twenty separate magnet vacuum systems altogether. These systems are estimated at $\$175x10^3$ each. They will most likely consist of a turbomolecular pump backed up by a roughing pump and the associated valves and controls.

XIV-E. Supplemental Systems Unit Costs

Power Supply Switching & Energy Storage (Acct. 22.01.07)

The cost of a 2 MW-hr superconducting energy storage unit of $\$25x10^6$ was arrived at using the magnet system unit costs adapted to an extrapolated design produced for Fermilab by the UW superconductive energy storage group.[6]

The cost of the power supply and controls comes from two sources. The controls for the 7 sec, 1000 MW peak pulse were costed at $20/kW. The protective Graetz bridges figured to handle 62 MW were costed at $35/kW. These two quantities add up to $\$22.17x10^6$.

Primary Coolant (Acct. 22.02.01)

The major cost item here is the piping. It is estimated that there are about 2174 tonnes of piping in the primary coolant loop. These include the steam manifolds and all the pipes leading to the steam drums and the intermediate equipment. Although the cost of piping ranges from $12/kg to $30/kg depending on the size and complexity, the average is usually about

$13-15/kg. We have used a unit cost of $15/kg. Supports and hangers usually amount to ~ 22% of the piping mass and these are costed at $5/kg.

The steam drums, hot storage tanks and dump tanks are costed at $16.5/kg.

Magnet Cooling (Acct. 22.03.01)

The following table gives a breakdown of the cooling loads required:

Table XIV-E-1 Cooling Loads in Magnets

	Power in kW			
Temp. →	1.8 K	4.2 K	18 K	25 K
TF Coils	1.3	25.2	95.7	
Cryogenic VF Coils				336
Superconducting OH & VF Coils		5.4		
TOTAL	1.3	30.6	95.7	336
Refrigeration factor to convert to room temp. power requirement	830	280	64	40
Room temp. power MW	1.08	8.57	6.12	13.44

Total room temp. power required is 29.21 MW

Many different algorithms have been suggested for estimating the cost of refrigeration. In 1974 Strobridge[7] gave the following for refrigerators and liquifiers operating in the range 1.8-90 K.

$$C = 6000\ p^{0.7} \qquad \text{(1974 dollars)}$$

where p is the installed input power in kilowatts. If this figure is inflated at 10% per year, it becomes

$$C = 9660\ p^{0.7} \qquad \text{(1979 dollars)}\ .$$

This figure, however, does not include the distribution system, gas handling and electrical substations. The refrigeration system cost for the large coil

project was $\$3.5 \times 10^6$ and had a power input of ~ 800 kW. This figure covered all the peripheral items including a closed cycle helium distribution system. Based on these values, the following algorithm is obtained:

$$C = 32{,}550\ (p)^{0.7}\ .$$

We estimate that a system which is 35 times larger than the LCP system will have a 20% cost advantage and we, therefore, used the following algorithm:

$$C = 26{,}000\ (p)^{0.7}$$

of which 29% is the cost of the refrigerator, 35% the cost of the distribution system and the remainder is the cost of the peripheral equipment.

Vacuum System Cooling (Acct. 22.03.03)

The total heat load needed for the cryosorption pumps is 3.7 kW at 4.2 K and 436 kW at 77 K which amounts to 4.175 MW at room temperature. If this power is added to the power in the main magnet refrigeration system the cost increment would be $\$3.41 \times 10^6$. This figure was then divided in the same proportion as in account 22.03.01. It should be borne in mind that although the numbers appear small, they are only a part of the overall refrigeration system described in 22.03.01.

Radwaste Treatment & Disposal (Acct. 22.04)

This number of $\$5.5 \times 10^6$ was obtained by scaling down the UWMAK-III system which was costed out by Bechtel Corporation.

Maintenance Equipment (Acct. 22.06.01)

The equipment listed in Table XIV-E-2 is deemed necessary for day-to-day servicing of the reactor. This is not to say that additional equipment is not needed in the event of a major breakdown requiring very special servicing. The unit costs were obtained from the Westinghouse estimate for the ORNL TNS.[1]

Instrumentation and Control (Acct. 22.07)

Typically, the instrumentation and control for an LWR or BWR runs about 2% of the total direct costs. Thus, for a 1200 MW_e system the I&C cost is $\sim\$9 \times 10^6$. However, earlier estimates for tokamaks[8,9] were 1-1.5% of the TDC. We have used $\$15 \times 10^6$ which is 1.8% of the TDC.

Table XIV-E-2 Maintenance Equipment

Number of Units	Description	Cost ($\$ \times 10^6$)
3	Self-propelled shielded maintenance modules with internal space for 3 people - manipulators mounted outside but controlled from inside - unit cost $\$1 \times 10^6$	3.000
1	Overhead crane supported shielded maintenance module with internal space for 3 people - manipulators attached externally controlled from inside - unit cost $\$2 \times 10^6$	2.000
3	Special cutting and welding equipment	1.800
2	Remotely operated cars and tracks	2.5000
10	Wall mounted manipulators	0.750
10	Moveable - post mounted manipulators	1.500
	Portable shielding	1.000
	Viewing equipment, boroscopes, TV monitors, telescopes, etc.	2.000
	Special handling devices, fixtures, frames, support stands, etc.	0.300
	Remote controllers	2.000
	Special tools	0.650
	TOTAL	17.500

XIV-F. Balance of Plant Unit Costs

The unit costs for the turbine plant equipment, electric plant equipment and miscellaneous plant equipment were obtained from the energy economic data base program for DOE operated by United Engineers and Constructors. Detailed costs exist for BWR plants of 600 and 1190 MW_e.

For the turbine plant equipment the following algorithm seems to hold true:

$$C = 2.281 \times 10^6 \, (PMW_e)^{0.58} \, .$$

This cost includes the main condenser and heat rejection system which normally appears in Acct. 26 in the NUS-531 code of accounts used by the energy economic data base program. Thus, the turbine plant equipment (acct. 23) in the NUWMAK cost estimate is equal to $\$98.03 \times 10^6$ and contains what would be normally included in Accts. 23 and 26 in the NUS-531 code of accounts.

The electric plant equipment is not too sensitive to the electric power output of the plant. For example in a 600 MW_e BWR the electric plant equipment is $\$35 \times 10^6$ while in a 1190 MW_e it is $\$40.7 \times 10^6$. We have used a value of $\$38 \times 10^6$.

In the miscellaneous plant equipment account we used a value of $\$11 \times 10^6$ which is the same as that in an 1190 MW_e BWR plant.

Table XIV-F-1 gives a breakdown of the buildings in the NUWMAK power plant, their volumes and the unit costs used in each type of structure. These unit costs have been arrived at by using data from earlier cost estimates produced by architect and engineering firms. We believe that these costs are reliable.

Table XIV-F-1 Building Unit Costs

Building	Classification	Liner	Volume (m^3)	Unit Cost $/$m^3$	Cost $x10^6
Reactor	Category I	Yes	75,626	560	42.35
Auxiliary	Category I	Partly	33,707	500	16.85
Hot Cell	Category I	Yes	12,000	500	6.00
Radwaste	Category I	Yes	10,000	500	5.00
Turbine	Category I	No	66,000	360	23.76
Maintenance	Category I	No	24,000	360	8.64
Control	Category I	No	1,500	360	0.54
Administration	Category I	No	3,000	360	1.08
Energy Storage	Non-Category I	No	12,000	100	1.20
Inverter	Non-Category I	No	8,000	100	0.80
Miscellaneous	Non-Category I	No	6,000	100	0.60
				TOTAL	106.82

XIV-G. Direct Cost Accounts

			$x10^6	
22	Reactor Plant Equipment			
	22.01 Reactor Equipment			
	22.01.01 Blanket and First Wall			
	22.01.01.01	Breeding Material (T_2)	2.8000	
	.02	First Wall and Structural Mtl.	6.9300	
	.03	N/A		
	.04	Limiters	1.0400	
	.05	Other		
		Blanket/First Wall Total		10.7700
	22.01.02 Shield			63.0380
	22.01.03 Magnets			
	22.01.03.01	TF Magnets	51.1710	
	.02	OH & s/c VF Coils	16.2820	
	.03	Cryogenic VF Coils	4.4910	
	.04	Trimming Coils	6.4100	
		Magnets Total		78.3540
	22.01.04 Supplemental Heating			
	22.01.04.01	RF Heating		36.0000
	22.01.05 Primary Structure & Support			
	22.01.05.01	Reactor Structure	0.6284	
	.02	Equipment Support	0.3000	
		Total Primary Structure		0.9284
	22.01.06 Reactor Vacuum Systems			
	22.01.06.01	Plasma Chamber Vacuum		
	22.01.06.01.01	Pumps/Comp.	9.4000	
	.02	Piping	1.5000	
	22.01.06.02	Magnet Dewar Vacuum		
	22.01.06.02.01	Pumps/Comp.	3.5000	
	.02	Piping	1.5000	
	22.01.06.03	Supplemental Heating Vacuum		
	22.01.06.03.01	Pumps/Comp.	0.1000	
	.02	Piping	0.3000	
	22.01.06.04	N/A		
	22.01.06.05	Reactor Vacuum System		
	22.01.06.05.01	Pumps/Comp.	0.1300	
	.02	Piping	0.4000	

22.01.06.06	Venetian Blind Flow Control		
22.01.06.06.01	Structure	2.000	
.02	Drives	1.000	
.03	Control	0.2000	
	Total		20.0300
22.01.07	Power Supply Switching and Energy Storage		
22.01.07.01	Heating (N/A)		
.02	Confinement (N/A)		
.03	Control	22.1700	
.04	Central Energy Storage	25.0000	
	Total		47.1700
22.01.08	Impurity Control		
22.01.08.01	Valves	0.2000	
.02	Piping	0.0500	
.03	Control	0.5000	
	Impurity Control Total		0.7500
22.02	Main Heat Transfer and Transport System		
22.02.01	Primary Coolant		
22.02.01.01	Pumps, Motor Drives	3.0000	
.02	Piping	35.000	
.03	Steam Drums	5.8400	
.04	Hot Water Storage	2.1500	
		1.0000	
	Primary Coolant Total		46.9900
22.02.02	Tritium Extraction		
22.02.02.01	T_2 Extraction From LiPb		0.3740
22.03	Auxiliary Cooling Systems		
22.03.01	Magnet Cooling		
22.03.01.01	Refrigeration	9.7300	
.02	Piping	8.2600	
.03	Fluid Circulation	0.9000	
.04	Tanks	3.0000	
.05	Other Peripheral	12.8500	
	Magnet Cooling Total		34.7400

22.03.02	Shield and Structure Cooling		0.2000
22.03.03	Vacuum System Cooling		
22.03.03.01	Refrigeration	0.9600	
.02	Piping	0.8100	
.03	Fluid Circulation	0.0900	
.04	Tanks	0.2900	
.05	Other Peripheral	1.2600	
	Vacuum System Cooling Total		3.4100
22.03.04	Power Supply Cooling		0.3000
22.04	Radioactive Waste Treatment and Disposal		5.5000
22.04.01	Liquid Waste Processing and Equipment		
.02	Gaseous Wastes and Off-Gas Processing		
.03	Solid Wastes Processing		
22.05	Fuel Handling and Storage (Fuel Injection)		
22.05.01	Fuel Purification System	3.0410	
22.05.02	Emergency Air Detritiation	20.4000	
	Fuel Handling & Storage Total		23.4410
22.06	Other Reactor Plant Equipment		17.5000
22.06.01	Maintenance Equipment		
22.07	Instrumentation and Control		15.0000
	Reactor Plant Equipment Total		404.4954
23	Turbine Plant Equipment		
23.01	Turbine-Generators		
23.01.01	Turbine Generators and Accessories	45.3830	
	Turbines		
	Generator		
	Non Standard Accessories		
	Steam By-Pass		
	Live Steam Reheaters		
	Piping, Value and Heaters for By-Pass System		
	Thermal Insulation		

23.01.02	Foundations	3.9730
.03	Standby Exciters	
.04	Lubricating System	
.05	Gas System	
.06	Reheaters	
23.03	Heat Rejection Systems	14.7570
23.03.01	Waste Intake Common Facilities	
	Traveling Screens	
	Screen Wash Pumps	
	Chlorination	
.02	Circulating Water Systems	
	Circulating Water-Pumps and Drives	
	Pumps to Condensers and Cooling Tower	
.03	Cooling Towers	
	Foundations and Basics	
	Primary Cooling Towers	
	Waste Heat Cooling Towers	
	Waste Heat System Heat Exchanger	
.04	Other Systems Rejecting Heat to the Atmosphere	
23.04	Condensing Systems	10.3970
23.04.01	Condensers	
	Condensers Complete Including Shells, Tube	
	Plates, Water Boxes, Hot Wells, etc.	
	Condenser Tubes	
	Expansion Joints	
	Foundations	
23.04.02	Condensate System	
	Condensate Pumping Units	
23.04.03	Gas Removal System	
	Vacuum Pumps	
	Air Ejector Equipment	
	Priming Ejectors	
23.04.04	Turbine By-Pass Systems (Excluding Piping)	

23.05 Feed Heating System	9.7880	
23.05.01 Regenerators and Recuperators		
23.05.02 Pumps		
Turbine Driven Feed Pumps, Bedplates, etc.		
Motor Driven Feed Pumps, Bedplates, etc.		
Turbine Drives		
Exhaust Ducts		
23.05.03 Tanks		
Condensate, Chemical, Oil, etc.		
23.06 Other Turbine Plant Equipment	12.8410	
23.06.01 Turbine Auxiliaries (Excluding Piping)		
.02 Auxiliary Cooling Systems (Excluding Piping)		
.03 Make-up Treatment (Excluding Piping)		
.04 Chemical Treatment and Condensate Purification		
Filtration, Aeration, Retention Tanks		
Demineralization - Regeneration		
Polishing Units		
Instrumentation and Control		
Chemical Feed		
23.06.05 Central Lubrication Service System (Excluding Piping)		
23.07 Instrumentation and Control Equipment	0.8960	
Turbine Plant Equipment Total		98.0350
24 Electrical Plant Equipment		
24.01 Switchgear	5.0830	
24.01.01 Generator Circuits		
.02 Station Service		
24.02 Station Service Equipment	9.2130	
24.02.01 Station Service and Startup Transformers		
.02 Low Voltage Unit Substation and Lighting Transformers		
.03 Battery System		
.04 Diesel Engine Generators		
.05 Gas Turbine Generator		
.06 Motor Generator Sets		

24.03	Switchboards (Including Heat Tracing)	0.6050	
24.03.01	Main Control Board for Electrical System		
.02	Auxiliary Power and Signal Boards		
24.04	Protective Equipment	1.5000	
24.05	Electrical Structures and Wiring Containers	7.9540	
24.05.01	Concrete Cable Tunnels		
.02	Cable Traps and Supports		
.03	Conduit		
.04	Other Structures		
24.06	Power and Control Wiring	13.6450	
24.06.01	Generator Circuits Wiring		
.02	Station Service Power Wiring		
.03	Control Wiring		
.04	Instrument Wiring		
.05	Containment Penetration		
	Electric Plant Equipment Total		38.0000
25	Miscellaneous Plant Equipment		
25.01	Transportation and Lifting Equipment	2.0020	
25.01.01	Cranes, Hoists, Monorails and Conveyors		
25.01.02	Railway		
.03	Roadway Equipment		
.04	Watercraft		
.05	Vehicle Maintenance Equipment		
25.02	Air and Water Service Systems	6.7000	
25.03	Communications Equipment	1.4070	
25.04	Furnishing and Fixtures	0.8910	
	Miscellaneous Plant Eq. Total		11.0000
26	Special Materials		
26.01	Reactor Coolant		
26.02	Intermediate Coolant		
26.03	Turbine Cycle Fluids		
26.04	Other Materials (Liquid Helium)		1.3000

XIV-H. Capital Costs

XIV-H-1. Direct Costs Summary

Acct. No.	Description	Acct. Total ($ x 10^6)	Cost (x10^6$)
20	Land and land rights	(2.500)	2.500
21	Structures & site facilities		106.824
	Design allowance (10%)		10.682
	Contingency (10%)		10.682
	Spare parts (0.5%)	(128.723)	0.534
22	Reactor plant equipment		404.495
	Design allowance (20%)		80.899
	Contingency (10%)		40.450
	Spare parts (2%)	(533.934)	8.090
23	Turbine plant equipment		98.035
	Design allowance (10%)		9.803
	Contingency (10%)		9.803
	Spare parts (1%)	(118.621)	0.980
24	Electric plant equipment		38.000
	Design allowance (10%)		3.800
	Contingency (10%)		3.800
	Spare parts (0.5%)	(45.790)	0.190
25	Miscellaneous plant equipment		11.000
	Design allowance (10%)		1.100
	Contingency (10%)		1.100
	Spare parts (1%)	(13.310)	0.110
26	Special materials	(1.300)	1.300
	TOTAL DIRECT COSTS		844.178

XIV-H-2. Indirect Costs

91	Construction facilities Equipment of Service (15% of T.D.C.)	126.627
92	Engineering and construction Management service (15% of T.D.C.)	126.627
93	Owner's costs (5% of T.D.C.)	42.210
	TOTAL INDIRECT COSTS	295.464
	TOTAL DIRECT AND INDIRECT COSTS	1,139.642

XIV-H-3. Time Related Costs

As mentioned at the start of the chapter the busbar cost and the total capital cost will be based on two economic analysis modes as directed in the DOE "Fusion Reactor Design Studies - Standard Accounts for Cost Estimates".

They are the constant dollar mode and the current dollar mode. In the constant dollar mode, interest on capital is taken at 5% and escalation is assumed to be zero. This kind of estimate then reflects the cost of energy comparable with today's cost and in this sense, a zero escalation is justified since the costing is done in present day dollar values. Similarly, the interest on the capital is taken as what it may have been eight years ago when the plant construction was initiated.

In the current dollar economic mode, a 10% interest on capital is taken and escalation is assumed to be at a 5% rate. These values appear somewhat low judging by the present inflationary rates, but since all the users of these standard costing procedures will be guided by them, the estimates will be comparable.

We have assumed an eight-year construction period for NUWMAK. This may seem optimistic, but it is difficult to judge since nobody has built a fusion reactor under the assumed conditions of an ongoing developed industry. Bechtel Corp. estimated a ten-year construction period for UWMAK-III and NUWMAK is a much smaller and less complicated reactor which utilizes current BWR technology in the power cycle.

The cash flow profile used to determine the F_{IDC} (interest during construction factor) and F_{EDC} (escalation during construction factor) is the classic S-curve biased about 20% to the right. This kind of profile seems to hold for major fossile and nuclear power plants constructed thus far. The factors used below have been taken from Table 2, page 21 of PNL-2648 (Fusion Reactor Design Studies - Standard Accounts for Cost Estimates).

Acct.	Description	Constant Dollar $\$x10^6$	Current Dollar $\$x10^6$
94	Interest during const. F_{IDC} (constant dollar)=0.170	193.739	
	F_{IDC} (current dollar)=0.466		531.073
93	Escalation during const. F_{EDC} (constant dollar)=0		
	F_{EDC} (current dollar)=0.261		297.447
	TOTAL TIME RELATED COSTS	193.739	828.520

Capital Costs Summary

	Const. Dollar $\$x10^6$	Current Dollar $\$x10^6$
Direct Costs	844.178	844.178
Indirect Costs	295.464	295.464
Time Related Costs	193.739	828.520
TOTAL CAPITAL COSTS	1,333.381	1,968.162
CAPITAL COST OF POWER FROM NUWMAK (660 MW_e)	$\$2020/kW_e$	$\$2982/kW_e$

XIV-I. Operation and Maintenance

The cost of operation and maintenance is taken as 2% per year of the total direct and indirect costs.

Scheduled component replacement cost of $\$3.988x10^6$ was arrived at by assuming that all the first wall/blanket material and the limiters will be replaced every two years. The likely way that this will be done is to have one-half of the first wall/blanket/limiter material replaced each year on a regular schedule.

In figuring the cost of fuel we assumed that a surplus of tritium will be available for startup purposes from an existing fusion industry. Thus, the fuel cost is only for replenishing the burned lithium and for the purchase of deuterium which is costed at \$1200/kg.

		$\$x10^6$
40-47	Operation and Maintenance	22.793
50-51	Scheduled Component Replacement	3.988
02-03	Annual Fuel Cost	0.449

XIV-J. Plant Availability

In figuring the plant availability one has to know the amount of scheduled and unscheduled down time which will be needed per year.

We have used four weeks (672 hours) of unscheduled down time and six weeks (1008 hours) of scheduled down time. The new ideas incorporated in the NUWMAK design for replacing the first wall/blanket module make us optimistic that a six week period will be adequate for replacing eight of the modules. This amount of downtime sets the plant availability at 80.8%. The plant

capacity is, therefore:

$$\text{Plant Capacity} = 660 \times 10^3 \text{ kW}_e \times 8760 \text{ hrs/yr} \times 0.808$$
$$= 4.672 \times 10^9 \text{ kW hr/yr}$$

XIV-K. Busbar Energy Cost

Constant Dollar Mode

For figuring the busbar cost in the constant dollar mode, interest on capital is taken as 10% per year and no escalation is taken for operation and maintenance, component replacement and the fuel cost. This is consistent with the use of present value dollars for determining present day busbar cost.

$$\text{Busbar cost} = \frac{[(\text{Total Capital Cost})(\text{Interest Rate}) + (\text{Oper. \& Maintenance}) + (\text{Compon. Replacement}) + (\text{Fuel Costs})]\ 1000 \text{ (mills)}}{\text{Plant Capacity (kW hr)}}$$

$$= \frac{[(1.333 \times 10^9)(0.1) + (22.793 \times 10^6) + (3.988 \times 10^6) + (0.449 \times 10^6)]\ 1000}{4.672 \times 10^9}$$

$$= 34.3 \text{ mills/kW hr.}$$

Current Dollar Mode

In the current dollar mode interest on capital is taken at 15% reflecting interest rates in future years. Also the operating and maintenance costs, the component replacement costs and fuel costs are escalated at 5% for the eight-year construction period. Thus the busbar costs are:

$$\frac{[(1.968 \times 10^9)(0.15) + (22.793 \times 10^6 + 3.988 \times 10^6 + 0.449 \times 10^6)(1.05^8)]1000}{4.672 \times 10^9}$$

$$= 71.8 \text{ mills/kW hr.}$$

XIV-L. Results and Conclusions

The economic analysis for NUWMAK has been performed in compliance with the guidelines provided by the DOE through the "Fusion Reactor Design Studies - Standard Accounts for Cost Estimates" (PNL-2648) issued in May 1978. Although some of the allowances such as contingency, engineering services, etc. may seem low to some people, they provide a basis for comparison with other systems costed in the same way.

In Table XIV-L-1 a breakdown of the reactor plant equipment is given. As might be expected the magnets lead the way with 19.37% of the total followed by the shield at 15.58%. It should be mentioned that the shield would have been cheaper if NUWMAK was slightly larger allowing for more shielding space on the inner side of the plasma. Tungsten in the shield accounted for 55% of the cost and was used exclusively on the inner shield.

It is interesting to compare the nuclear island cost breakdown in NUWMAK with the ORNL-TNS Reference Design for which there is a fairly detailed cost analysis. The ORNL-TNS is almost identical in size to NUWMAK but produces only 63% of the power. It has 12 TF coils compared to 8 in NUWMAK and has 50 MW of injected power while NUWMAK has 75 MW. Table XIV-L-2 gives the percentage breakdown in the four major areas:

1 - Tokamak System: This comprises the first wall/blanket, magnets, support structure and shield.

2 - Electrical Power and Control: Includes the power supplies, energy storage, instrumentation, plasma diagnostics, etc.

3 - Tokamak Support System: Remote handling, tritium handling, fueling, vacuum and refrigeration system cooling and radwaste handling.

4 - Supplemental Heating: Neutral beams in the ORNL-TNS and RF in NUWMAK.

In comparing the two reactors what should be kept in mind is that the ORNL-TNS is a first of a kind device while the assumption for NUWMAK is that it is a part of an established industry. The disproportionately larger percentage for the magnets in the ORNL-TNS reactor may come from the fact that it has 50% more TF coils.

Table XIV-L-3 gives a breakdown of the direct costs in NUWMAK. These quantities include design allowance, contingency and spare parts.

Finally, in order to get an insight on whether NUWMAK is a lower cost reactor than UWMAK-III, we have prepared a table in which the two reactors are compared on an equal basis. It will be recalled that UWMAK-III was a

Table XIV-L-1

Breakdown of the Reactor Plant Equipment Costs (RPE)

Acct. No.	Description	Cost $\$x10^6$	% of Total RPE
22.01.01	Blanket/first wall	10.77	2.66
22.01.02	Shield	63.038	15.58
22.01.03	Magnets	78.354	19.37
22.01.04	Supplemental heating	36.000	8.90
22.01.05	Primary structure & support	0.9284	0.23
22.01.06	Reactor vacuum systems	20.030	4.95
22.01.07	Power supply switching & energy storage	47.170	11.66
22.01.08	Impurity control	0.750	0.19
22.02.01	Primary coolant system	46.990	11.62
22.02.02	T_2 extraction from blanket	0.374	0.09
22.03.01	Magnet cooling (refrigeration)	34.740	8.59
22.03.02	Shield and structure cooling	0.200	0.05
22.03.03	Vacuum system cooling	3.410	0.84
22.03.04	Power supply cooling	0.300	0.07
22.04	Radwaste treatment/disposal	5.500	1.36
22.05	Fuel handling/air detritiation	23.441	5.80
22.06	Other reactor plant equipment	17.500	4.33
22.07	Instrumentation and control	15.000	3.71
	Total Reactor Plant Equipment	404.4954	100%

Table XIV-L-2

Comparison of the Reactor Plant Equipment Costs Between NUWMAK and the ORNL-TNS

	ORNL-TNS		NUWMAK	
	Cost $\$x10^6$	%	Cost $\$x10^6$	%
1 - Tokamak Systems	238	53.6	171	42.2
2 - Electrical Power & Controls	79	17.9	64	15.8
3 - Tokamak Support Systems	82	18.5	134	33.1
4 - Supplemental Heating	45	10	36	8.9

Table XIV-L-3 Breakdown of Direct Costs (DC)

Acct. No.	Description	Cost $\$x10^6$	% of Total DC
20	Land and land rights	2.5	0.30
21	Structures and site facilities	128.723	15.25
22	Reactor plant equipment	533.934	63.25
23	Turbine plant equipment	118.621	14.05
24	Electric plant equipment	45.790	5.42
25	Miscellaneous plant equipment	13.31	1.58
26	Special materials	1.30	0.15
	Total Direct Costs	844.178	100%

5000 MW_{th} advanced technology reactor utilizing high temperature helium in the power conversion system. The economic analysis for it was prepared by Bechtel Corporation utilizing a modified NUS 531 costing procedure. UWMAK-III costs were taken from UWFDM-150 and escalated at 5% to 1978. The values were then used in the DOE (PNL-2648) accounts to compute the constant dollar and current dollar plant costs and busbar costs. At the same time the NUWMAK cost numbers were used according to the modified NUS531 costing procedure to obtain plant costs and busbar costs. The results are given in Table XIV-L-4.

On the average NUWMAK is 25% less costly than UWMAK-III. This may be interpreted partly as the price one has to pay for an advanced technology reactor.

XIV-L-1. Major Conclusions

1. It appears that the plant cost for a tokamak type of reactor may range from \$2000/kWe - \$3000/kWe in constant dollars and from \$3000/kWe - \$4000/kWe in current dollars.
2. It may be possible to realize a 25% plant cost saving by using current and low technology in the reactor and the power conversion system.

Table XIV-L-4
Comparison of the Plant and Busbar Costs Between NUWMAK and UWMAK-III

	Modified NUS-531 (1978\$)	Constant Dollars (1978\$)	Current Dollars (1986\$)
Plant Costs			
UWMAK-III	\$3317/kWe	\$2743/kWe	\$4039/kWe
NUWMAK	\$2476/kWe	\$2020/kWe	\$2982/kWe
Busbar Costs			
UWMAK-III	80 mills/kWh	48 mills/kWh	100 mills/kWh
NUWMAK	58 mills/kWh	34 mills/kWh	72 mills/kWh

References for Chapter XIV

1. "Unit Cost Documentation", ORNL and Westinghouse Electric Corp., WFPS-TN-057 (1978).

2. J. Williams, Carnegie Mellon University, Pittsburgh PA; private communication.

3. Griffith Metals, 31 London Terrace, New Rochelle NY; private communication.

4. B.W. Reed, O.N. Bowen, H.M. Hill, J.Q. Lawson, W.G. Newman and A.J. Sivo, PPPL Report-1410 (1977).

5. The Excalibur Corp., 50 Thayer Road, Waltham MA; private communication.

6. Cryogenic Energy Storage System Design Report, Fermi National Accelerator Lab and University of Wisconsin-Madison, FN-264, (October 1974).

7. T.R. Strobridge, "Cryogenic Refrigerators--An Updated Survey", NBS-TN-655 (June 1974).

8. D. Steiner, et al., "Oak Ridge TNS Program: Summary of FY 1978 Activities", ORNL/TM-6720.